Get Full Access and More at ExpertConsult.com



Fundamentals of Pediatric Imaging

FHB
(Radiology golden books)

EDITION 2

FUNDAMENTALS OF PEDIATRIC IMAGING

Lane F. Donnelly

ELSEVIER

FUNDAMENTALS OF RADIOLOGY SERIES

Fundamentals of Pediatric Imaging

SECOND EDITION

Lane F. Donnelly, MD

Chief Quality Officer, Hospital-Based Services, Associate Radiologist-in-Chief, Department of Radiology, Texas Children's Hospital, Professor of Radiology, Baylor University College of Medicine, Houston, Texas

ELSEVIER

Table of Contents

Cover image

Title page

Copyright

Contributors

Preface

Chapter 1. Special Considerations in Pediatric Imaging

- Pediatric Radiology As a Potential Career
- Introduction: Special Considerations in Pediatric Imaging

Chapter 2. Airway

- Acute Upper Airway Obstruction
- Lower Airway Obstruction
- Congenital Airway Obstruction

Chapter 3. Chest

- Neonatal Chest
- Roles of Imaging in Pediatric Pneumonia
- High-Resolution Computed Tomography in Children

Chapter 4. Cardiac

- Imaging Modalities in Congenital Heart Disease
- Categorization of Congenital Heart Disease
- Abnormalities of Conotruncal Rotation
- Surgeries for Congenital Heart Disease

Chapter 5. Gastrointestinal

- Neonatal

- Intestinal Obstruction in Children
- Swallowed Foreign Bodies
- Abnormalities of the Pediatric Mesentery
- Neonatal Jaundice
- Liver Masses
- Blunt Abdominal Trauma
- The Immunocompromised Child
- Complications Related to Cystic Fibrosis
- Inflammatory Bowel Disease in Children
- Pediatric Obesity

Chapter 6. Genitourinary

- Urinary Tract Infections
- Evaluation of Prenatally Diagnosed Hydronephrosis
- Renal Tumors
- Pelvic Rhabdomyosarcoma
- Sacrococcygeal Teratoma
- Scrotum
- Acute Pelvic Pain in Older Girls and Adolescents

Chapter 7. Musculoskeletal

- Normal Variants and Common Benign Entities
- Trauma
- Periosteal Reaction in the Newborn
- Lucent Permeative Lesions in Children
- Focal Sclerotic Lesions in Children
- Multifocal Bone Lesions in Children
- Constitutional Disorders of Bone
- Hip Disorders
- Metabolic Disorders
- Miscellaneous Disorders
- Disorders Affecting Primarily Soft Tissues

Chapter 8. Neuro

- Pediatric Neuroimaging Modalities: Magnetic Resonance, Computed Tomography, and Ultrasound
- Basic Review of Advanced Magnetic Resonance Imaging Techniques in Pediatric Neuroimaging
- Neonatal Head Ultrasound

- Normal Myelination
- Developmental Abnormalities
- Sequelae of in Utero Insults
- Neurocutaneous Syndromes
- Metabolic and Degenerative Disorders
- Infection
- Tumors
- Trauma
- Hydrocephalus and Ventriculoperitoneal Shunts
- Craniosynostosis
- Lacunar Skull
- Head and Neck Inflammatory and Infectious Processes
- Retinoblastoma
- Neck Masses
- Congenital Vertebral Anomalies
- Spinal Dysraphism
- Spinal Trauma
- Normal Variants and Congenital Anomalies of the Cervical Spine
- Atlantoaxial Instability
- Spondylolysis and Spondylolisthesis

Index

Copyright

ELSEVIER

1600 John F. Kennedy Blvd.
Ste 1800
Philadelphia, PA 19103-2899

FUNDAMENTALS OF PEDIATRIC IMAGING, SECOND EDITION ISBN: 978-0-323-41619-1

Copyright © 2017 by Elsevier, Inc. All rights reserved.

No part of this publication may be reproduced or transmitted in any form or by any means, electronic or mechanical, including photocopying, recording, or any information storage and retrieval system, without permission in writing from the publisher. Details on how to seek permission, further information about the Publisher's permissions policies, and our arrangements with organizations such as the Copyright Clearance Center and the Copyright Licensing Agency can be found at our website: www.elsevier.com/permissions.

This book and the individual contributions contained in it are protected under copyright by the Publisher (other than as may be noted herein).

Notices
Knowledge and best practice in this field are constantly changing. As new research and experience broaden our understanding, changes in research methods, professional practices, or medical treatment may become necessary.

Practitioners and researchers must always rely on their own experience and knowledge in evaluating and using any information, methods, compounds, or experiments described herein. In using such information or methods, they should be mindful of their own safety and the safety of others, including parties for whom they have a professional responsibility.

With respect to any drug or pharmaceutical products identified, readers are advised to check the most current information provided (i) on procedures featured or (ii) by the manufacturer of each product to be administered, to verify the recommended dose or formula, the method and duration of administration, and contraindications. It is the responsibility of practitioners, relying on their own experience and knowledge of their patients, to make diagnoses, to determine dosages and the best treatment for each individual patient, and to take all appropriate safety precautions.

To the fullest extent of the law, neither the Publisher nor the authors, contributors, or editors assume any liability for any injury and/or damage to persons or property as a matter of products liability, negligence, or otherwise or from any use or operation of any methods, products, instructions, or ideas contained in the material herein.

Previous edition copyrighted 2009

Library of Congress Cataloging-in-Publication Data
Names: Donnelly, Lane F., editor. | Preceded by (work): Donnelly, Lane F.
Pediatric imaging.

Title: Fundamentals of pediatric imaging / [edited by] Lane F. Donnelly.
Description: Edition 2. | Philadelphia, PA : Elsevier, Inc., [2017] |
Preceded by Pediatric imaging : the fundamentals / Lane F. Donnelly.
c2009. | Includes bibliographical references and index.
Identifiers: LCCN 2016029806 | ISBN 9780323416191 (pbk.)
Subjects: | MESH: Diagnostic Imaging--methods | Child | Infant
Classification: LCC RC78.7.D53 | NLM WN 240 | DDC 616.07/54--dc23
LC record available at https://lccn.loc.gov/2016029806

Executive Content Strategist: Robin Carter
Content Development Specialist: Stacy Eastman
Publishing Services Manager: Catherine Jackson
Senior Project Manager: Doug Turner
Designer: Brian Salisbury

Printed in China

Last digit is the print number: 9 8 7 6 5 4 3 2 1



Contributors

Lane F. Donnelly, MD, Chief Quality Officer, Hospital-Based Services, Associate Radiologist-in-Chief, Department of Radiology, Texas Children's Hospital, Professor of Radiology, Baylor University College of Medicine, Houston, Texas

Monica Epelman, MD, Vice-Chair, Department of Medical Imaging/Radiology, Nemours Children's Health System/Nemours Children's Hospital, Associate Professor, University of Central Florida College of Medicine, Associate Professor, Florida State University College of Medicine, Orlando, Florida

Carolina V. Guimaraes, MD, Assistant Professor, Department of Radiology, Texas Children's Hospital, Houston, Texas

Daniel J. Podberesky, MD, Radiologist-in-Chief, Nemours Children's Health System, Chair, Department of Radiology, Nemours Children's Hospital, Associate Professor, Department of Radiology, University of Central Florida College of Medicine, Associate Professor, Department of Radiology, Florida State University College of Medicine, Orlando, Florida

Alexander J. Towbin, MD, Associate Radiologist-in-Chief, Clinical Operations and Radiology, Informatics, Neil D. Johnson Chair of Radiology Informatics, Department of Radiology, Cincinnati Children's Hospital, Associate Professor, Cincinnati, Ohio

Preface

When I was a radiology resident at the University of Cincinnati, one of the senior musculoskeletal imaging faculty members was Dr. Aaron Weinstein. He had originally gone into surgery, but when he was the chief surgical resident at the University of Cincinnati, he developed rheumatoid arthritis and decided to switch to radiology. As a senior radiology faculty person, Dr. Weinstein ran Bone Conference every Thursday morning at 7 a.m. For Bone Conference, residents brought cases, often from the teaching files, and presented them as unknowns that other residents had to take. Dr. Weinstein commented on and critiqued the job done by the resident taking the unknown case (and often the resident who picked the case) and then offered his opinion of the case. Not only was Dr. Weinstein an expert in musculoskeletal imaging, but he also had been at the University of Cincinnati for so long that he had already seen every interesting musculoskeletal case there, usually multiple times; so he was impossible to stump. He was also a cantankerous old man (though much of it was a show), and he smoked constantly, even during Bone Conference, which gave the whole thing an added cinematic flare. We usually just referred to him as "the old man." The entire process was terrifying to me as a young resident. I was always concerned about being humiliated in front of my peers and superiors. So every Wednesday evening of my residency I read the little *Fundamentals of Skeletal Radiology* textbook by Clyde Helms…cover to cover. I figured that having very good grasp of the basics of musculoskeletal imaging would minimize my chance of looking like an idiot. It worked pretty well. Certainly, I learned bone radiology. I loved that book, and I often wondered why really good, short practical books about the other radiology subspecialties did not exist. I know that I retained more useful information when I read short and basic books over and over than when I read longer, more detailed texts once.

In the late 1990s, I was on the faculty in the Department of Radiology at Duke University and had the opportunity to work with and learn from Clyde Helms. I shared with him my love for his book, the story of how I read this book every Wednesday evening when I was in residency, and my disappointment that there were not other high quality fundamental books in the other subspecialties in our field. He encouraged me to write such a book on pediatric radiology and put me in contact with the folks at what was then WB Sanders (now part of Elsevier). I was in my early thirties and just a couple of years out of training at the time and probably had no business writing a textbook about anything. However, I proceeded and that led to *Fundamentals of Pediatric Radiology* and subsequently to the first edition of *Pediatric Imaging: The Fundamentals*. By medical textbook standards, the books have been very successful—more than 20,000 copies have been sold. They have been particularly popular among radiology residents and fellows. It's funny, but despite other accomplishments on which I have worked hard, my name is predominantly associated with these books.

The intention of the book you are now reading is to serve as a basic introductory text on pediatric imaging. It is written in prose, rather than as an outline, and is intended to be readable. The emphasis is on commonly encountered imaging scenarios and pediatric diseases. The topics included reflect questions commonly asked by residents on the pediatric radiology service, important issues that rotating residents often seem not to know, and commonly made mistakes. The book is intended to serve as an introduction or review for a resident or medical student who is about to begin a rotation in pediatric radiology, as a resource to a general or pediatric radiologist who wishes to brush up on pediatric radiology, or as a guide for a pediatric resident or pediatrician who wants to learn more about pediatric radiology.

Given the growing scope and complexity of pediatric imaging, for the first time I have brought in additional pediatric radiologists to contribute chapters in their areas of expertise. They include Drs. Monica Epelman ("Chest" and "Genitourinary"), Carolin V. Guimaraes ("Neuro"), Daniel J. Podberesky ("Cardiac"), and Alex J. Towbin ("Musculoskeletal"). I am deeply indebted to these authors for their

expertise, contributions, and help. Dated portions of the text have been updated, older images replaced with more modern imaging, and suggested readings updated. Thus I am pleased to present the second edition of *Fundamentals of Pediatric Imaging*. I think you will find the same practicality and easy-to-read prose as in the previous addition.

Much of what appears in this book is the summation of what numerous radiologists have taught us, and I would like to thank them for their time and efforts. I have had the honor and privilege to work at great organizations and for great leaders and mentors. The case material in this book is the result of the hard work of the faculty, technologists, and trainees in those departments and the referring physicians who care for their patients. I would like to acknowledge their efforts, without which this book would not be possible. Finally, and most importantly, I would like to thank my wife, Carolina, and children, Piper, Griffin, and Enzo, for all of their love and support.

Best of luck with pediatric imaging.

Lane F. Donnelly, MD

CHAPTER 1

Special Considerations in Pediatric Imaging

Lane F. Donnelly

▪ Pediatric Radiology As a Potential Career

Most pediatric radiologists are very happy with both their jobs and career choice. There are a number of attractive aspects about pediatric radiology. First, one of the most important elements of job satisfaction is the quality of the interactions one has with the people with whom one works. In general the physicians who choose to go into pediatric subspecialties, as well as other health care workers who choose to work at pediatric institutions, tend to be nice people. Aggressive, power-hungry people tend not to want to work with children. This makes a huge difference in the quality of daily life. In addition, pediatric subspecialists seem to rely on the opinions of pediatric radiologists more than many of their adult subspecialist counterparts. Similarly, pediatric radiology does not seem to have the same number of turf battles that many adult-oriented departments have.

Another unique feature of pediatric radiology is that one gets to be a "general specialist." Pediatric radiology is a small part of medical imaging overall, and in this sense the pediatric radiologist is very much a subspecialist. Compared with general radiologists who must have a working knowledge of a daunting amount of information, most pediatric radiologists feel comfortable that they have an adequate command of the knowledge they need to provide outstanding care. At the same time, pediatric radiologists are generalists in the sense that many pediatric radiologists deal with all modalities and organ systems. They get the best of both worlds. It is also possible in pediatric radiology to become a sub-subspecialist, such as a pediatric neuroradiologist, pediatric interventional radiologist, pediatric cardiac imager, or pediatric fetal imager.

The most powerful and fulfilling aspect of becoming a pediatric health care provider is probably the satisfaction that comes from working with and for children. Few activities are more rewarding than helping children and their families. There are many other attractive aspects of pediatric care. First, most kids recover from their illnesses, as compared with elderly adults. Most pediatric illnesses are not self-induced. Pediatric diseases are highly varied and interesting. In addition, pediatric conditions are being increasingly recognized as important precursors to adult illnesses that cause significant morbidity and mortality—obesity, osteoporosis, and glucose intolerance. Finally, children and their families are highly appreciative of pediatricians' help.

▪ Introduction: Special Considerations in Pediatric Imaging

Many issues are unique to the imaging of children as compared with that of adults. Imaging examinations that are easily carried out in adults require special adjustments to be successfully achieved in children. The rotating resident on a pediatric imaging rotation and the general radiologist who occasionally images children must be prepared to deal with these issues and to adjust imaging techniques to safely and successfully obtain imaging examinations. In this introductory chapter, several of the general issues that can arise when imaging children are addressed briefly.

Relationship Between Imager and Parents

In both pediatric and adult patient care situations, there are family members with whom the imager

must interact. However, in the pediatric setting there are several unique features in the relationship among imager, patient, and family. When caring for children, communication more often takes place between the radiologist and parent than between the radiologist and patient. Obviously, communication directly with the child is also paramount to success. In addition, the degree of interaction between the imager and the child-parent unit may be greater in the pediatric setting than in the adult setting because of associated issues, such as the potential need for sedation, the need for consent from the parent rather than the child (if the child is a minor), and the need for intense explanation of the procedure on the levels of both the child and the parent. Most people are also much more inquisitive and protective when their children are involved. Because of these reasons, descriptions of what to expect during the visit to the imaging area may have to be more detailed when dealing with pediatric patients and their parents.

The stress level of parents when their child is or may be ill is immense, and such stress often brings out both the best and worst in people. Because of the intense bonds between most parents and their children, the relationship between imager and parents is most successful when the radiologist exercises marked empathy, patience, professionalism, and effective communication.

Professionalism and Effective Communication

It is interesting to note that in pediatric health care most of the complaints by parents and families are not related to technical errors; they are more commonly related to issues of professionalism and communication. Of reported parent complaints 30% are related to poor communication and unprofessional behavior. In addition, practicing effective communication has been shown to have multiple positive outcomes, including better patient outcome, decreased cost, increased patient and family satisfaction, and decreased chance of litigation in the presence of adverse events.

Although physicians are referred to as health care professionals, historically they have not received formal training in professionalism and communication, have had poor role models, and have been seen as individual practitioners rather than as members of health care teams. Radiology departments and individual radiologists must be proactive in making improvements in this area. Having a program to improve and standardize interactions with families can be helpful. Scripting expected interactions can help improve patient and family interactions, such as defining how physicians introduce themselves to patients and families (including stating positions and roles in the upcoming procedure), as well as behaviors to avoid (such as stating that the patient's ordering physician does not know how to order or that one does not have time to talk to a referring physician because one is too busy). Scripting both the type of conversation and process in general is also very helpful for the delivery of difficult news, such as defining the process for communicating with the family when a child is diagnosed with a new tumor.

Inability to Cooperate

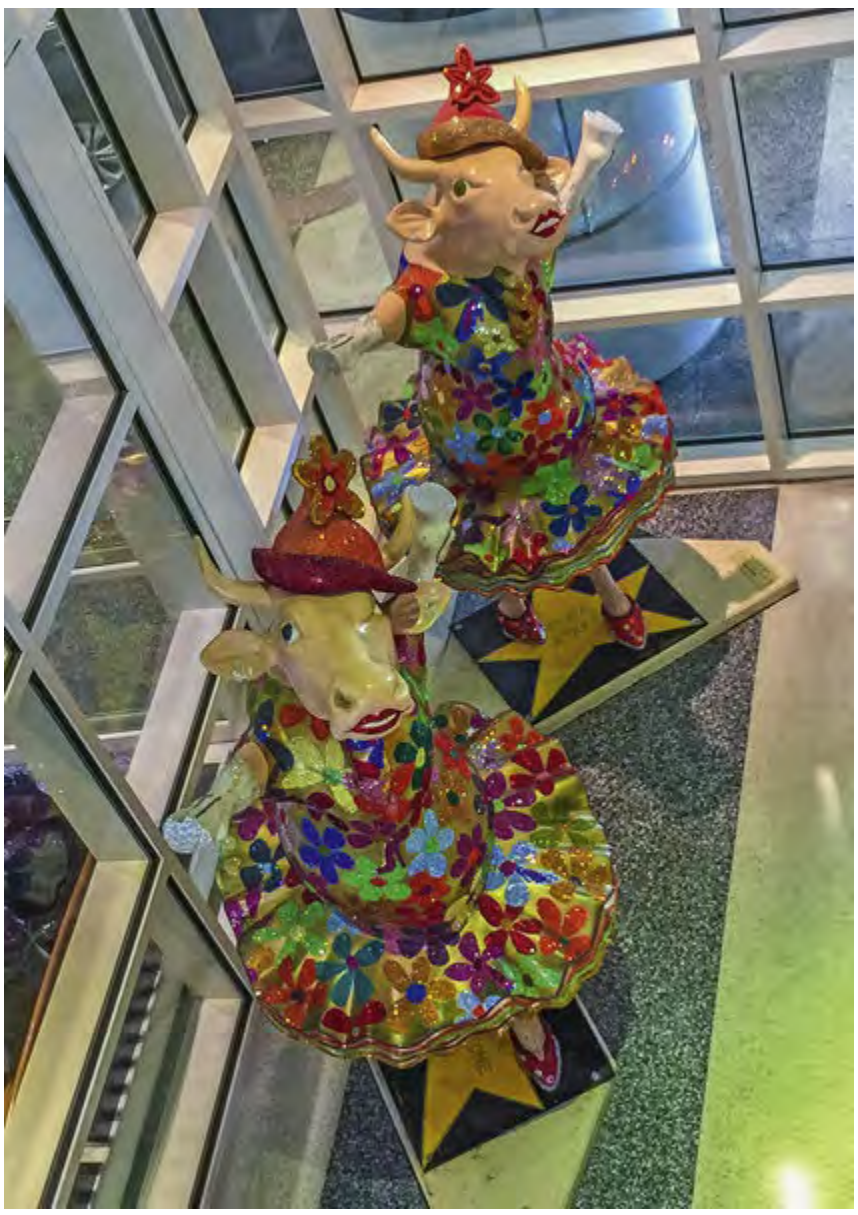
Infants and young children are commonly unable to cooperate with requirements that typically are easily met by adults. For example, they may be unable to keep still, remain in a certain position, concentrate for more than a brief moment, or breath-hold. Children of various ages have unique limitations. Infants and toddlers are unable to stay still, whereas 3-year-olds are more apt to refuse to cooperate. These limitations affect almost all pediatric imaging examinations: radiography, fluoroscopy, ultrasound, computed tomography (CT), magnetic resonance imaging (MRI), nuclear imaging, and interventional radiology. There are a number of potential solutions that can be helpful in these situations. Commonly employed techniques include distracting the child, providing child-friendly surroundings (Figs. 1-1 through 1-7), immobilization, and sedation.

Distracting the child with something other than the procedure is often a simple and easy tactic to use. Talking to older children about school and other activities can be helpful. Certified child-life specialists are very successful in helping to coach and distract children so that they can complete imaging exams without sedation. They often use rattles and noise-making toys with very young children. Video players are a very useful distraction technique for ultrasound, fluoroscopy, and CT, and video goggles (see Fig. 1-7) have been very successful in decreasing sedation for MRI. Children can be encouraged to bring their own movies or choose from the department's stock. It is amazing how cooperative many children will be when they are able to watch television. Using a combined program that includes the introduction of a child-life specialist, a combination of the tactics discussed earlier to calm infants and young children, and the promotion of a culture that avoids sedation whenever possible was shown to reduce the frequency of need for sedation in children less than 7 years of age by

34.6% for MRI and 44.9% for CT.



▪ **FIGURE 1-1** Colorful, child-friendly décor in pediatric waiting area. Many children's hospitals are now being decorated with modern, brightly colored, open areas without "cartoonish" themes.



▪ **FIGURE 1-2** Child-friendly waiting area with dancing cows.



▪ **FIGURE 1-3** CT scanner decorated with child-friendly decals.



▪ **FIGURE 1-4** Portable radiograph unit decorated with child-friendly decals.



▪ **FIGURE 1-5** SPECT/CT unit decorated with child-friendly decals.



▪ **FIGURE 1-6** Imaging room outfitted with custom lighting control, at this time turned to pink at request of child.

Providing child-friendly surroundings may help to ease a young child's anxiety and cause him or her to be more cooperative. Paintings on the walls and equipment and cartoonish figures in the examination rooms can be helpful. Eliminating or minimizing painful portions of the examination can also be very helpful in keeping a young child cooperative. The placement of an intravenous line often causes a great deal of patient anxiety and renders the child uncooperative for a subsequent imaging study, such as a CT scan. Using topical analgesia to decrease the pain of the intravenous line placement commonly makes this portion of the examination less traumatic. In addition, it is helpful to schedule appropriate sequencing of imaging examinations so that the most difficult exam is performed last. For example, it can be much easier to perform a renal ultrasound before rather than after the child has experienced a voiding cystourethrogram.

Immobilization is also a helpful technique. Infants who are bundled or "papoosed" in a blanket are more apt to stay still than infants who are not. This may make the difference between needing or not needing sedation to obtain an examination. There are also a number of commercially available

immobilization devices that are helpful when performing certain examinations, such as the use of an octagon board when obtaining fluoroscopic studies of young children. There are other devices that enhance proper positioning for specific modalities, such as chest radiographs. Imaging departments that image children should consider making such equipment available.

In certain situations, distraction and immobilization may not be successful, and sedation or general anesthesia may be necessary to obtain imaging studies. Many children younger than 6 years of age require sedation for MRI studies because of the prolonged nature of the examination and the need for the patient to be completely still. Sedation is needed much less often now than in the past for children undergoing CT examination because of the increased speed of acquisition by the newer CT scanners and the previously mentioned sedation reduction program. Other procedures that might require sedation include some nuclear medicine studies and most interventional procedures.


A


B

▪ **FIGURE 1-7** Video goggles can help young children to cooperate for MR examination, thus avoiding sedation. **A,** Video goggles on a child preparing for an MR examination. **B,** Video goggles with audio headphones in place as child is slid into scanner. Note happy demeanor.

Standards of care for conscious sedation are required by The Joint Commission and are based on standards published by several organizations, including the Committee on Drugs and the American Academy of Pediatrics. Any imaging department planning to sedate children must have a defined sedation program that is in concordance with these guidelines. The sedation program must have protocols for presedation preparation, sedative agents used, monitoring during sedation and during postsedation recovery, and discharge criteria. There has been a national shift concerning who provides sedation for pediatric imaging studies in pediatric radiology departments. In the 1990s' most pediatric radiology sedation programs were run by radiologists. Currently, multiple factors have led to such programs being run by anesthesiologists, emergency physicians, or intensive care physicians. At many institutions, such physicians have access to sedatives that are better for imaging sedation, such as propofol or dexmedetomidine.

Variable Size and Physiology

Because of the size variability from infant to adult-sized children, many adaptations must be considered for pediatric imaging studies in relation to size. The doses of contrast and drugs used in imaging examinations need to be adjusted according to a child's size, often on a per-weight (mg/kg) basis. Oral contrast dosing is also based on patient weight or age. Using CT as an illustrative example, other variables may also be affected by patient size. In small children the largest possible intravenous line may be very small, often 22 gauge or 24 gauge. The intravenous line may be placed in the foot or hand. The length of the region of interest to be imaged is variable, and the lengths of the patient's veins are variable. Physiologic parameters, such as the patient's cardiac output, are also more variable in children than in adults. These factors affect parameters such as the time between contrast injection and onset of scanning, as well as choices in contrast administration technique (hand bolus versus power injector). Slice thickness should be smaller in younger children because of the smaller anatomic parts. Similar adjustments must be considered in all other imaging modalities when applied to children. Radiation dose reduction is discussed in Patient Safety.

Age-Related Changes in Imaging Appearance

Another factor that makes imaging in children different from that in adults is the continuous changes in the imaging appearance of multiple organ systems during normal childhood development. The normal imaging appearance of certain aspects of organ systems can be different both at varying ages during childhood and between children and adults. For example, the kidneys look different on ultrasound in neonates from the way they look in a 1-year-old child. The developing brain demonstrates differences in signal at varying ages on MRI, which is related to changes in myelination. A large mediastinal shadow related to the thymus may be normal or severely abnormal depending upon the child's age. The skeleton demonstrates marked changes at all ages of childhood; this is related to the maturation of apophyses and epiphyses and the progressive ossification of structures. Knowledge of the normal age-related appearances of these organ systems is vital to appropriate interpretation of imaging studies. Lack of this knowledge is one of the more common causes of errors made in the interpretation of pediatric imaging studies.

Age-Related Differential Diagnoses

The types of diseases that affect children are vastly different from those that commonly affect adults. Therefore the differential diagnosis and significance of a particular imaging finding in a child are dramatically different from those determined by the identical imaging finding in an adult. In addition, the diseases that affect specific age groups of children are different. Therefore the differential diagnosis and significance of a particular imaging finding in a 2-month-old infant may differ dramatically from those determined by the identical imaging finding in a 10-year-old child.

Quality and Patient Safety

A lot of national attention has been paid to patient safety initiatives since the 1999 Institute of Medicine's report stating that somewhere between 44,000 and 98,000 deaths per year are caused by medical errors in the United States alone. This poor safety record would be the equivalent of the airline industry's having a large passenger plane crash in the United States every single day! If this were the case, we would probably think twice about flying. However, this is what our patients potentially face when they enter the current health care system. If looked at from the patients' perspective, even more important to them than "Heal me" (quality of care) and "Be nice to me" (customer service) is the plea "Don't harm me" (patient safety). No higher priority exists than patient safety.

There are numerous schools of thought related to both improvement and safety. Almost all of them emphasize the cultural aspects needed to reach a level of high reliability and minimize errors that may cause harm. There has to be a recognition that safety is an issue and that it is part of everybody's role to speak up in the face of uncertainty or when an individual "feels" that something is not right. The old culture of a medical hierarchy, in which the physician is in charge and is not to be questioned, does not promote safety. Medical staff, trainees, and even family members need to feel comfortable "stopping the line" and asking for clarification if things do not seem right.

Also important to create a reliable system of care that is both safe and of high quality is the acceptance of standardization. Henry Ford stated in 1926 that

> *Today's standardization is the necessary foundation on which tomorrow's improvement will be based. If you think of "standardization" as the best you know today, but which is to be improved tomorrow—you get somewhere. But if you think of standards as confining, then progress stops.*

Ideally the only variation in a health care system should be that related to the condition of the patient. There should not be variability related to technologists, protocols, care sites, or physicians. Radiologists need to work together to create evidence-based standardized imaging protocols and procedures, as well as reports, and continuously strive to improve them.

In addition, key in reaching a state in which high quality and safe care are provided is a robust daily management system. Daily management systems are designed to quickly identify issues, empower front-line areas to solve those issues, and, when the front line cannot resolve them, escalate the issues to those who can help. Increasingly in medicine, as well as other fields, tiered huddle systems are used to create daily readiness. Radiologists, technologists, and managers come together in a brief huddle each morning to make sure that they are ready to care for the patients scheduled for that day. Such processes often have three parts: daily readiness, problem accountability, and metrics evaluation. One approach to daily readiness is evaluating the volume scheduled for that day and organizing the approach to concerns around safety and the acronym MESA (Methods, Equipment, Supplies, Associates). Does anyone have any safety concerns? Do we have the right ***M***ethods to take care of the patients today (does anyone have questions around protocols or atypical patients?)? Do we have the right ***E***quipment to take care of the patients today (is there any planned downtime, broken equipment, or information technology [IT] issues?)? Do we have the ***S***upplies we need to take care of the patients today? Do we have the right ***A***ssociates to take care of the patients today (did anybody call in sick, do we have the right people with the right expertise)? Going through a set of such questions leads to a list of issues. Having a defined problem accountability process that assigns each issue a single owner and defines the immediate countermeasure and the date at which the owner will come back to report an update at the huddle is important so that issues do not go unresolved or only partially remedied.

Radiation Safety

Safety issues specific to radiology include radiation safety, MRI safety, and correct and effective communication of the information in and interpretation of imaging examinations. We will touch here on radiation safety because it is germane to pediatric radiology. Although there is much uncertainty, children are much more sensitive to the potential harmful effects of radiation than are adults, and children also have a longer expected life span during which to develop potential complications of radiation, such as cancer. Therefore attention to radiation safety in all areas of pediatric radiology is paramount. CT delivers higher doses of radiation than do other diagnostic imaging modalities. The exact radiation risk in CT examinations and even whether a risk absolutely exists are controversial topics. However, some researchers estimate the increased risk that a young child might develop cancer related to an abdominal CT scan is in the magnitude between 1:1000 and 1:10,000. Given the unknown and potentially small risk, it is essential for all radiologists to practice dose-reduction techniques in

pediatric CT. Such tactics include avoiding CT when unnecessary; using alternative diagnostic methods that do not use radiation, such as ultrasound, when possible; and adjusting CT parameters to minimize dose when CT is performed. Because children are smaller than adults and need less radiation to create the same signal-to-noise ratios, the tube current (mA), as well as kilovolts and other factors, can be greatly reduced when imaging a small child. Many other factors can be adjusted to reduce dose as well.

It is also very important not to overreact to this potentially small risk related to radiation dose for CT. For any clinically indicated examination the risk of not doing the CT and not having that information is often magnitudes greater than that related to radiation risk.

Suggested Readings

Donnelly L.F. Daily management systems in medicine. *RadioGraphics*. 2014;34:549–555.

Donnelly L.F, Dickerson J.M, Goodfriend M.A, Muething S.E. Improving patient safety: effects of a safety program on performance and culture in a department of radiology. *AJR*. 2009;193:165–171.

Donnelly L.F, Strife J.L. How I do it: establishing a program to promote professionalism and effective communication in radiology. *Radiology*. 2006;283:773–779.

Frush D.P. Overview of CT technologist for children. *Pediatr Radiol*. 2014;44:422–426.

Frush D.P, Bisset G.S. Pediatric sedation in radiology: the practice of safe sleep. *AJR*. 1996;167:1381–1387.

Frush D.P, Goske M.J. Image gently: toward optimizing the practice of pediatric CT through resources and dialogue. *Pediatr Radiol*. 2015;45:471–475.

Institute of Medicine. *Crossing the quality chasm: a new health system for the 21st century*. Washington, DC: National Academy Press; 2001.

Khan J.J, Donnelly L.F, Koch B.L, et al. A program to decrease the need for pediatric sedation. *Appl Radiol*. 2007;4:30–33.

Larson D.B, Towbin A.J, Pryor R.M, Donnelly L.F. Improving consistency in radiology reporting through the use of department-wide standardized structured reporting. *Radiology*. 2013;267:240–250.

Pichert J.W, Miller C.S, Hollo A.H, et al. What health professionals can do to identify and resolve patient dissatisfaction. *Jt Comm J Qual Improv*. 1998;124:303–312.

Thrall J.H. Quality and safety revolution in health care. *Radiology*. 2004;233:3–6.

CHAPTER 2

Airway

Lane F. Donnelly

Problems with the airway are much more common in children than in adults. It has been said that one of the differentiating features between a pediatric and general radiologist is that a pediatric radiologist remembers to look at the airway. For practical purposes, abnormalities of the airway can be divided into acute upper airway obstruction, lower airway obstruction (extrinsic compression, intrinsic obstruction), obstructive sleep apnea (OSA), and congenital high airway obstruction syndrome (CHAOS).

Clinically, children with acute upper airway obstruction (above the thoracic inlet) tend to present with inspiratory stridor, whereas children with lower airway obstruction (below the thoracic inlet) are more likely to present with expiratory wheezing. However, the categorization of a child with noisy breathing into one of these two groups can be very difficult. The primary imaging evaluation of the pediatric airway for acute conditions should include frontal and lateral high-kilovolt radiography of the airway and frontal and lateral views of the chest.

▪ Acute Upper Airway Obstruction

Acute stridor in a young child is the most common indication for imaging the pediatric airway. The most common causes of acute upper airway obstruction in children include inflammatory disorders and foreign bodies. The most common inflammatory disorders include croup, epiglottitis, exudative tracheitis, and retropharyngeal cellulitis and abscess. Anatomic structures that are especially important to evaluate on radiographs of children with acute upper airway obstruction include the epiglottis, aryepiglottic folds, subglottic trachea, and retropharyngeal soft tissues.

Croup

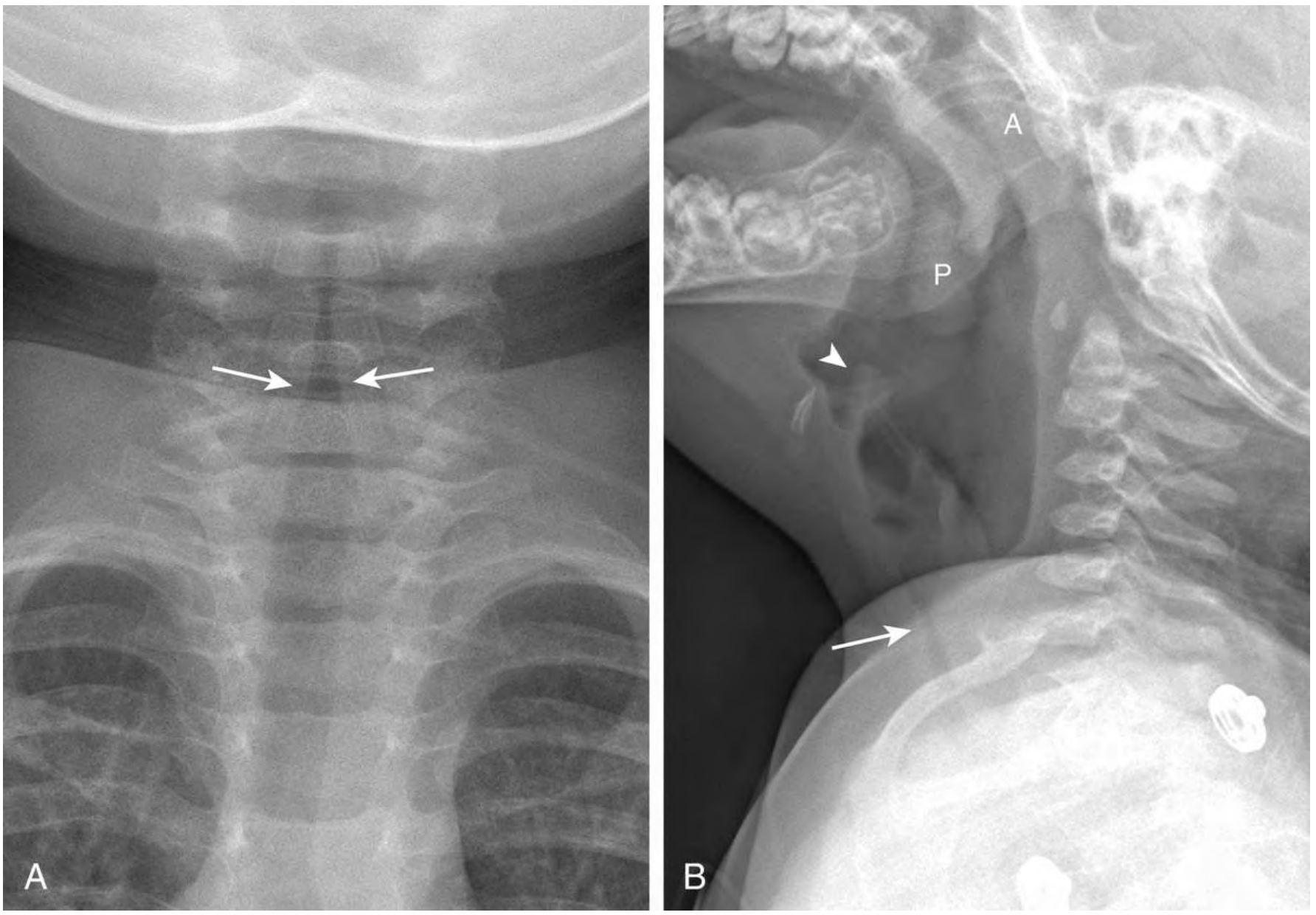
Croup (acute laryngotracheobronchitis) is the most common cause of acute upper airway obstruction in young children. The peak incidence occurs between 6 months and 3 years of age. The mean age at presentation of croup is 1 year of age. In children older than 3 years, other causes of airway obstruction should be suspected. Croup is viral in cause and is usually a benign, self-limited disease. Redundant mucosa in the subglottic region becomes inflamed, swells, and encroaches upon the airway. The children present with a barky ("croupy") cough and intermittent inspiratory stridor. It usually occurs following or during other symptoms of lower respiratory tract infection. Most children with croup are managed supportively as outpatients, and the parents are managed by reassurance. Inhaled corticosteroids are becoming a popular therapy in children with croup. They have been shown to reduce the length and severity of illness.

The purpose of obtaining radiographs in a patient with suspected croup is not so much to confirm the diagnosis but rather to exclude other, more serious causes of upper airway obstruction that require intervention. However, characteristic radiographic findings that indicate croup are best seen on frontal radiographs. With croup, there is loss of the normal shoulders (lateral convexities) of the subglottic trachea secondary to symmetric subglottic edema (Fig. 2-1). Normally, the subglottic trachea appears rounded, with "shoulders" that are convex outward (Fig. 2-2). In croup, the subglottic trachea becomes long and thin, with the narrow portion extending more inferiorly than the level of the pyriform sinuses. The appearance has been likened to an inverted V or a church steeple (see Fig. 2-1). The term *church steeple* can be confusing because some steeples look like croup and some are shaped like the normal subglottic airway (Fig. 2-3). Lateral radiographs may demonstrate a narrowing or loss of definition of the lumen of the subglottic trachea (see Fig. 2-1) or hypopharyngeal overdistention. With croup, the

epiglottis and aryepiglottic folds appear normal.

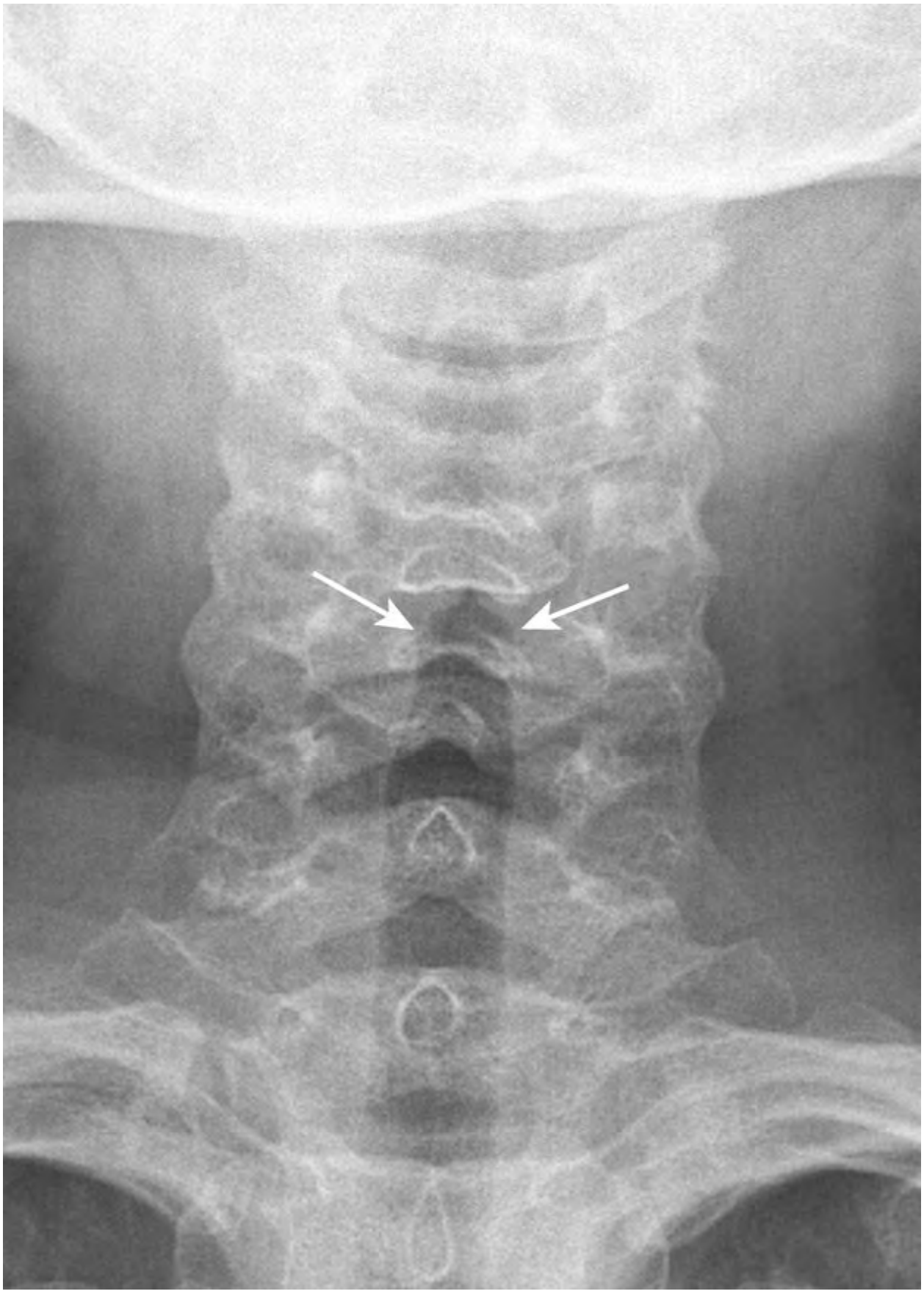
Epiglottitis

In contrast to croup, epiglottitis is a life-threatening disease that can potentially require emergent intubation. The possibility that a child with epiglottitis might arrive in a deserted radiology department was once a constant source of anxiety for on-call radiology residents. However, most cases of epiglottitis are caused by *Haemophilus influenzae* and are now preventable by immunization (HiB vaccine), so the incidence of epiglottitis has dramatically decreased. The causes of epiglottitis are now also more heterogeneous. Related to this, care of children with epiglottitis is now more of a challenge because health care workers are less used to recognizing and treating patients with this disorder. Children with epiglottitis are usually toxic appearing and present with an abrupt onset of stridor, dysphagia, fever, restlessness, and an increase in respiratory distress when recumbent. In the pre-HiB vaccine era, the classically described peak age of incidence was 3.5 years. However, since the introduction of the HiB vaccine, there has been a marked increase in the mean age of presentation to 14.6 years. Because of the risk for complete airway obstruction and respiratory failure, no maneuvers should be performed that make the patient uncomfortable. If the diagnosis is not made on physical examination, a single lateral radiograph of the neck should be obtained, usually with the patient erect or in whatever position that allows the patient to breathe comfortably. Children with epiglottitis should never be made to lie supine against their will to obtain a radiograph because it can result in acute airway obstruction and, potentially, death.



▪ **FIGURE 2-1** **Croup.**

A, Frontal radiograph showing symmetric subglottic narrowing *(arrows)* with loss of normal shouldering. The narrowing extends more inferiorly than the piriform sinuses. **B,** Lateral radiograph showing subglottic narrowing *(arrow)*. Note normal-appearing epiglottis *(arrowhead)* and thin aryepiglottic folds. Also note mildly enlarged adenoid *(A)* and palatine *(P)* tonsils.



▪ **FIGURE 2-2** **Normal frontal radiograph of the airway.**
The subglottic airway demonstrates rounded shoulders *(arrows)* that are convex outward.



▪ FIGURE 2-3 Steeple sign.

The term *steeple sign* can be confusing. It is meant to denote the pointed configuration of the subglottic trachea on a frontal radiograph of the airway when subglottic edema has effaced the normally convex lateral shoulders in this region. However, some steeples look like croup *(white arrows)*, and some look like a normal subglottic airway *(black arrow)*.



▪ **FIGURE 2-4** **Epiglottitis.**
Lateral radiograph showing marked thickening of the epiglottis *(arrow)*. The aryepiglottic folds are also narrowed.

With epiglottitis, on the lateral radiograph, there is marked enlargement of the epiglottis. A normal epiglottis typically has a thin appearance with the superior aspect being sharply pointed. The swollen epiglottis has been likened to the appearance of a thumb. With epiglottitis, there is also thickening of the aryepiglottic folds (Figs. 2-4 and 2-5). The aryepiglottic folds are the soft tissues that extend from the epiglottis anterosuperiorly to the arytenoid cartilage posteroinferiorly and normally are convex downward. When the aryepiglottic folds become abnormally thickened, they appear convex superiorly. Symmetric subglottic narrowing, similar to croup, may be seen on frontal radiography (if obtained); do not let that be confusing.



▪ **FIGURE 2-5** **Epiglottitis.**
Sagittal CT image showing low-attenuation swelling of the epiglottis *(arrowhead)*. Also note marked thickening and low-attenuation edema of the aryepiglottic folds *(arrows)*.

An obliquely imaged, or so-called omega-shaped, epiglottis may artifactually appear wide because both the left and right sides of the epiglottis are being imaged adjacent to each other. This should not be confused with a truly enlarged epiglottis. The absence of thickening of the aryepiglottic folds can be helpful in making this differentiation. With an omega-shaped epiglottis (normal variant), often both the left and right walls of the epiglottis are visible.

In current times, related to both the uncommon occurrence of epiglottitis and the frequent reliance on computed tomography (CT) to evaluate more common inflammatory neck conditions (such as retropharyngeal abscess), it is increasingly more common to see and diagnose epiglottitis on CT rather than on radiography. Although not classically advocated as a diagnostic tool for epiglottitis (given the risks of laying such patients supine and giving them intravenous [IV] contrast), the findings of epiglottitis are easily identified on CT (see Fig. 2-5). Findings include swelling and low-attenuation edema of the epiglottis and aryepiglottic folds associated with inflammatory stranding in adjacent fat.

Exudative Tracheitis

Exudative tracheitis (also known as bacterial tracheitis, membranous croup, or membranous laryngotracheobronchitis) is another uncommon but potentially life-threatening cause of acute upper

airway obstruction. The disorder is characterized by a purulent infection of the trachea in which exudative plaques form along the tracheal walls (much like those seen in diphtheria). Affected children are usually older and more ill than those with standard croup; typically their ages range from 6 to 10 years. Although initial reports described most cases to be secondary to infection by *Staphylococcus aureus*, other reports have noted multimicrobial infections. It is unclear whether the disease is a primary bacterial infection or a secondary bacterial infection that occurs following damage to the respiratory mucosa by a viral infection. A linear soft tissue filling defect (a membrane) seen within the airway on radiography is the most characteristic finding. A plaquelike irregularity of the tracheal wall is also highly suspicious (Fig. 2-6). Nonadherent mucus may mimic a membrane radiographically. In cooperative patients, having them cough and then repeating the film may help to differentiate mucus from a membrane. Other findings include symmetric or asymmetric subglottic narrowing in a child too old typically to have croup and irregularity or loss of definition of the tracheal wall. Membranes and tracheal wall irregularities may be seen on frontal or lateral radiographs and often seen on one but not the other; therefore it is important to get both views.

If one of these exudative "membranes" is sloughed into the lumen, it can lead to airway occlusion and respiratory arrest. Therefore children who are suspected to have exudative tracheitis are often evaluated endoscopically, the exudative membranes are stripped, and elective endotracheal intubation is performed.

A number of controversies regarding exudative tracheitis exist. First, it is seen with great frequency at some institutions and not at all at others. Second, although it is considered a life-threatening condition, to my knowledge, no patient has ever died at home of this disease—which seems odd. Both of these points raise the question of the validity of this diagnosis. My take is that there are definitive cases of this disease, but it is probably overdiagnosed and overtreated at some institutions.



▪ **FIGURE 2-6** **Exudative tracheitis.**
Lateral radiograph showing irregular plaquelike filling defects *(arrows)* and airway wall irregularities within trachea. Again, note the normal appearance of the nonthickened epiglottis in this patient.

Retropharyngeal Cellulitis and Abscess

Retropharyngeal cellulitis is a pyogenic infection of the retropharyngeal space that usually follows a recent pharyngitis or upper respiratory tract infection. Children present with sudden onset of fever, stiff neck, dysphagia, and occasionally stridor. Most affected children are young, with more than half of the cases occurring between 6 and 12 months of age. On lateral radiography, there is thickening of the retropharyngeal soft tissues (Fig. 2-7). In a normal infant or young child, the soft tissues between the posterior aspect of the aerated pharynx and anterior aspect of the vertebral column should not exceed the anterior-to-posterior diameter of the cervical vertebral bodies. If these soft tissues are thicker, an abnormality should be suspected. Apex anterior convexity of the retropharyngeal soft tissues provides supportive evidence that there is true widening of the retropharyngeal soft tissues (see Fig. 2-7).

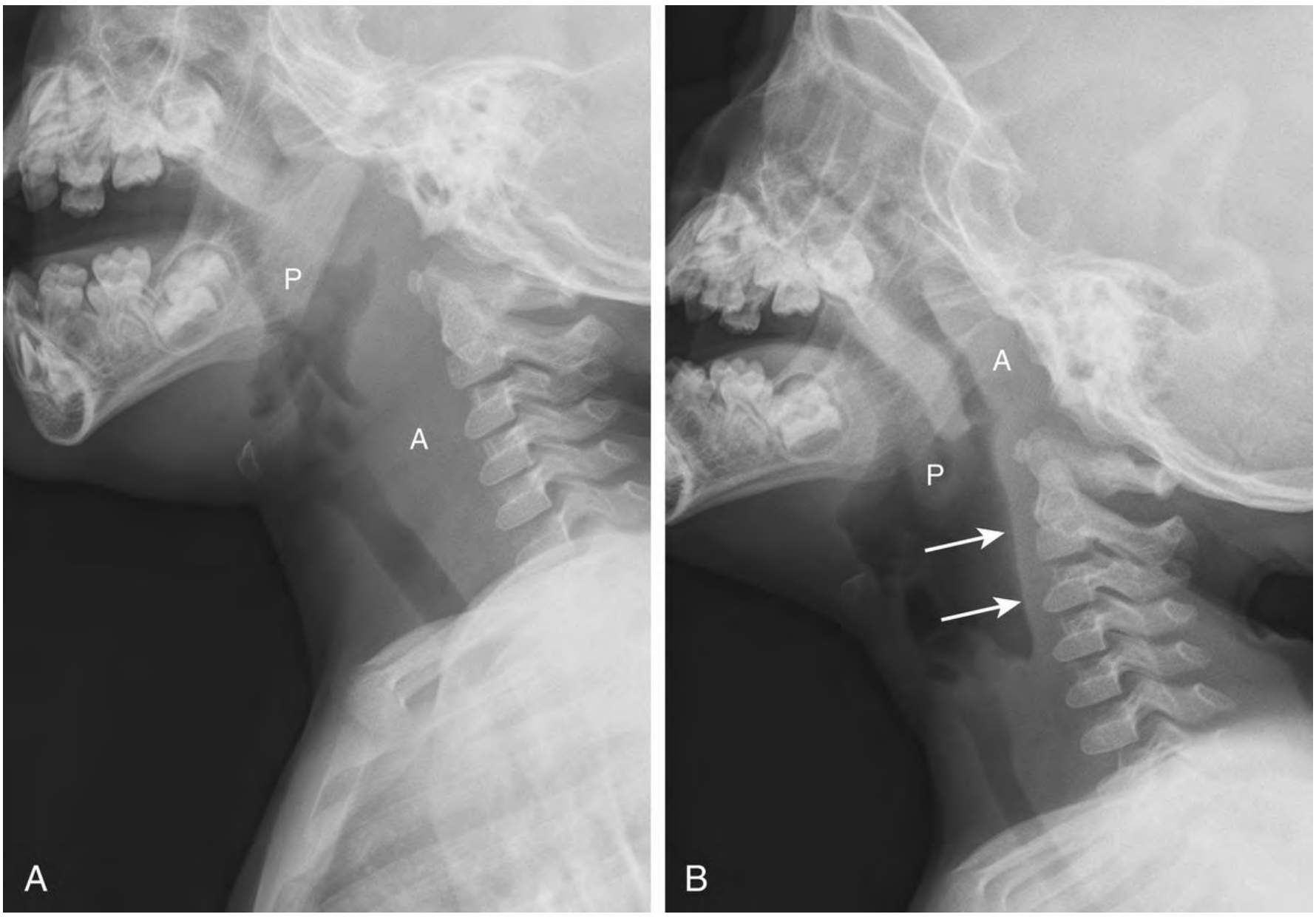
However, in infants, who have short necks, it is common to see pseudothickening of the retropharyngeal soft tissues when the lateral radiograph is obtained without the neck being well extended (Fig. 2-8). If it is unclear on the initial lateral radiograph whether the soft tissues are truly rather than artifactually widened, it is best to repeat the lateral radiograph with the neck placed in full extension (see Fig. 2-8). Fluoroscopy can also be used to evaluate whether the pseudothickening is

persistent. The only radiographic feature that can differentiate abscess from cellulitis is the identification of gas within the retropharyngeal soft tissues.



▪ **FIGURE 2-7** **Retropharyngeal abscess.**
A, Lateral radiograph showing marked thickening of the retropharyngeal soft tissues *(A)*, which are wider than the adjacent vertebral bodies. Note the anterior convexity of soft tissues. **B** and **C,** Contrast-enhanced CT in sagittal and axial planes shows a low-attenuation region with enhancing rim *(A)*, suggestive of a drainable abscess.

CT is commonly performed to define the extent of disease and to help to predict cases in which a drainable fluid collection is present (see Fig. 2-7). On CT, a low-attenuation, well-defined area with an enhancing rim is suspicious for a drainable fluid collection (see Fig. 2-7). Cellulitis without abscess is actually more common than the presence of a drainable abscess.



▪ **FIGURE 2-8** **Pseudoretropharyngeal soft tissue thickening secondary to lack of extended neck positioning.**

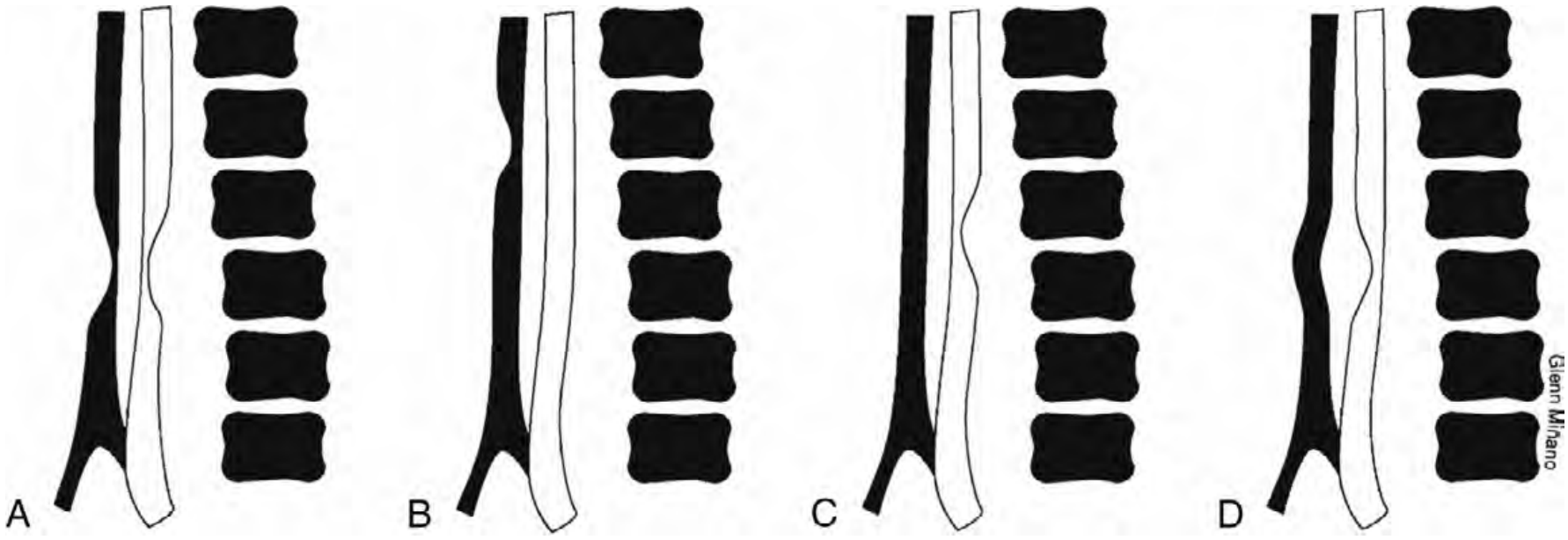
A, Initial lateral radiograph showing apparent thickening of retropharyngeal soft tissues mimicking potential retropharyngeal abscess *(A).* Note mildly enlarged palatine tonsils *(P).* **B,** Repeat lateral radiograph with neck extended, shows normal thickness of retropharyngeal soft tissues *(arrows)*, much narrower in thickness than adjacent vertebral bodies. Note palatine *(P)* and adenoid *(A)* tonsils.

▪ Lower Airway Obstruction

The most common cause of wheezing in children is small airway inflammation, such as is caused by asthma and viral illness (bronchiolitis). When the wheezing persists, presents at an atypical age for asthma, or is refractory to treatment, other reasons for lower airway obstruction are entertained. Other causes of lower airway obstruction can be divided into those that are intrinsic to the airway (such as bronchial foreign body, tracheomalacia, or intrinsic masses) and those that cause extrinsic compression of the trachea (such as vascular rings). The initial radiologic screening procedure for wheezing is frontal and lateral radiography of the airway and chest. Radiographs are used to exclude acute causes of upper airway obstruction, evaluate for other processes that can cause wheezing (such as cardiac disease), and help to categorize the abnormality as being more likely to be an intrinsic or an extrinsic airway process. Important findings to look for on the radiographs include evidence of tracheal narrowing, position of the aortic arch, asymmetric lung aeration, radiopaque foreign body, and lung consolidation. When tracheal compression is present on radiography, it is important to note both the superior to inferior level of the compression and whether the compression comes from the anterior or posterior aspect of the trachea because various vascular rings present with different patterns of tracheal compression (Fig. 2-9).

If the radiographs suggest an intrinsic abnormality, bronchoscopy is the next procedure of choice. If the radiographs suggest an extrinsic compression, cross-sectional imaging is performed. There has been a shift from using primarily magnetic resonance imaging (MRI) for the evaluation of extrinsic airway compression in the 1990s to using predominantly CT now. This shift is related to the rapid acquisition times of the newer multidetector CT scanners. The advantages of CT over MRI are that most infants can be scanned without sedation on CT (which is a significant factor in an infant with airway

difficulties) and that better evaluation of the lungs is possible. The disadvantages of CT are the radiation exposure and dependence upon IV contrast. With modern technology, both CT and MRI can be used to create dynamic cine images to depict abnormal airway motion (malacia).



▪ **FIGURE 2-9 Patterns of compression of the trachea and esophagus in common vascular rings.** The diagrams are comparable to a lateral radiograph of the chest. The trachea is black; the esophagus is white. **A,** Double aortic arch. The trachea is compressed on its anterior aspect, and the esophagus is compressed on its posterior aspect. **B,** Innominate artery compression. The trachea is compressed on its anterior aspect. The level of compression is just below the thoracic inlet, higher than other vascular causes of compression. **C,** Left arch with aberrant right subclavian artery or right arch with aberrant left subclavian artery. There is compression of the posterior aspect of the esophagus. The trachea is not compressed. **D,** Aberrant left pulmonary artery (pulmonary sling). The trachea is compressed on its posterior aspect and the esophagus is compressed on its anterior aspect.

Extrinsic Lower Airway Compression

Almost any process that causes either a space-occupying mass within the mediastinum or the enlargement or malposition of a vascular structure can lead to compression of the airway. The classically described vascular causes of lower airway compression include double aortic arch, anomalous left pulmonary artery, and innominate artery compression syndrome. However, other causes of airway compression include middle mediastinal masses, such as a bronchogenic cyst (Fig. 2-10) or large anterior mediastinal masses (Fig. 2-11); enlargement of the ascending aorta, such as is seen in Marfan syndrome; enlargement of the pulmonary arteries, as in congenital absence of the pulmonary valve; malposition of the descending aorta, as in midline descending aorta-carina-compression syndrome; enlargement of the left atrium; or abnormal chest wall configuration, such as a narrow thoracic inlet. With the congenital vascular causes of airway compression, in addition to the obvious anatomic extrinsic compression, there is also often a component of intrinsic malacia related to the long-term nature of the airway being compressed. This can cause persistent symptoms even after the extrinsic compression has surgically been remedied.

On axial imaging, the trachea is normally rounded in configuration (Fig. 2-12), sometimes with a flattened posterior wall related to the noncartilaginous portion. A normal trachea is never oblong, with a greater left-to-right than anterior-to-posterior diameter (never "pancake-shaped"). When the airway appears pancake-shaped, it is abnormal.

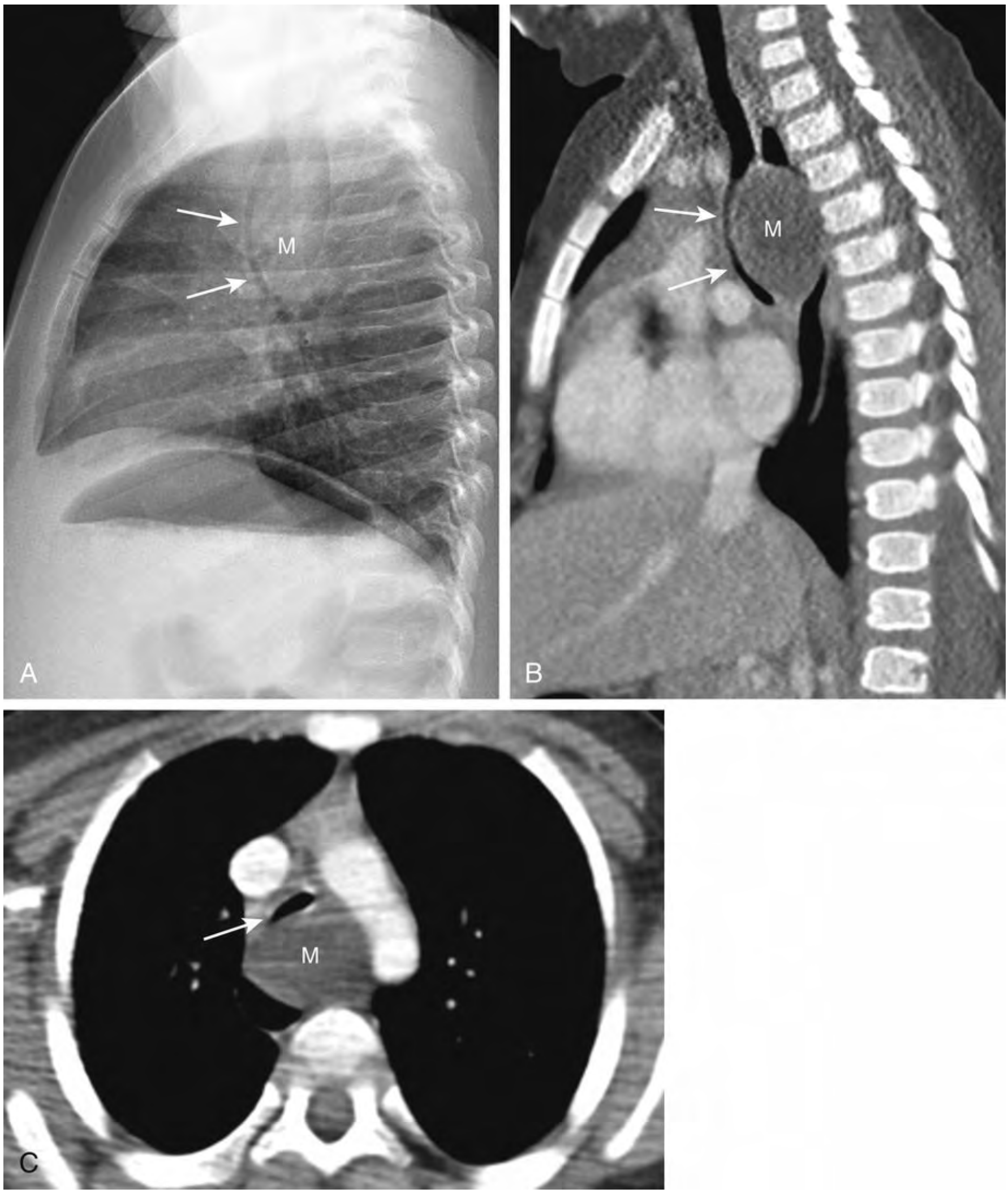
Double Aortic Arch

Double aortic arch is a congenital anomaly related to the persistence of both the left and right fourth aortic arches. It is the most common symptomatic vascular ring. Usually an isolated lesion, it typically presents with symptoms early in life (soon after birth). Anatomically, the two arches surround and compress the trachea anteriorly and esophagus posteriorly. Typically the right arch is dominant, both larger and positioned more superiorly (Fig. 2-13). In such cases, the left arch is ligated by performing a left thoracotomy. When the left arch is dominant, a right thoracotomy is performed and the right arch is ligated. Related to surgical planning, determining the dominant arch is one of the goals of cross-sectional imaging. With double aortic arch, the level of compression is the mid to lower intrathoracic

trachea. In addition, there is symmetric take-off of four great arteries from the superior aspect of the arches.

Anomalous Origin of the Left Pulmonary Artery (Pulmonary Sling)

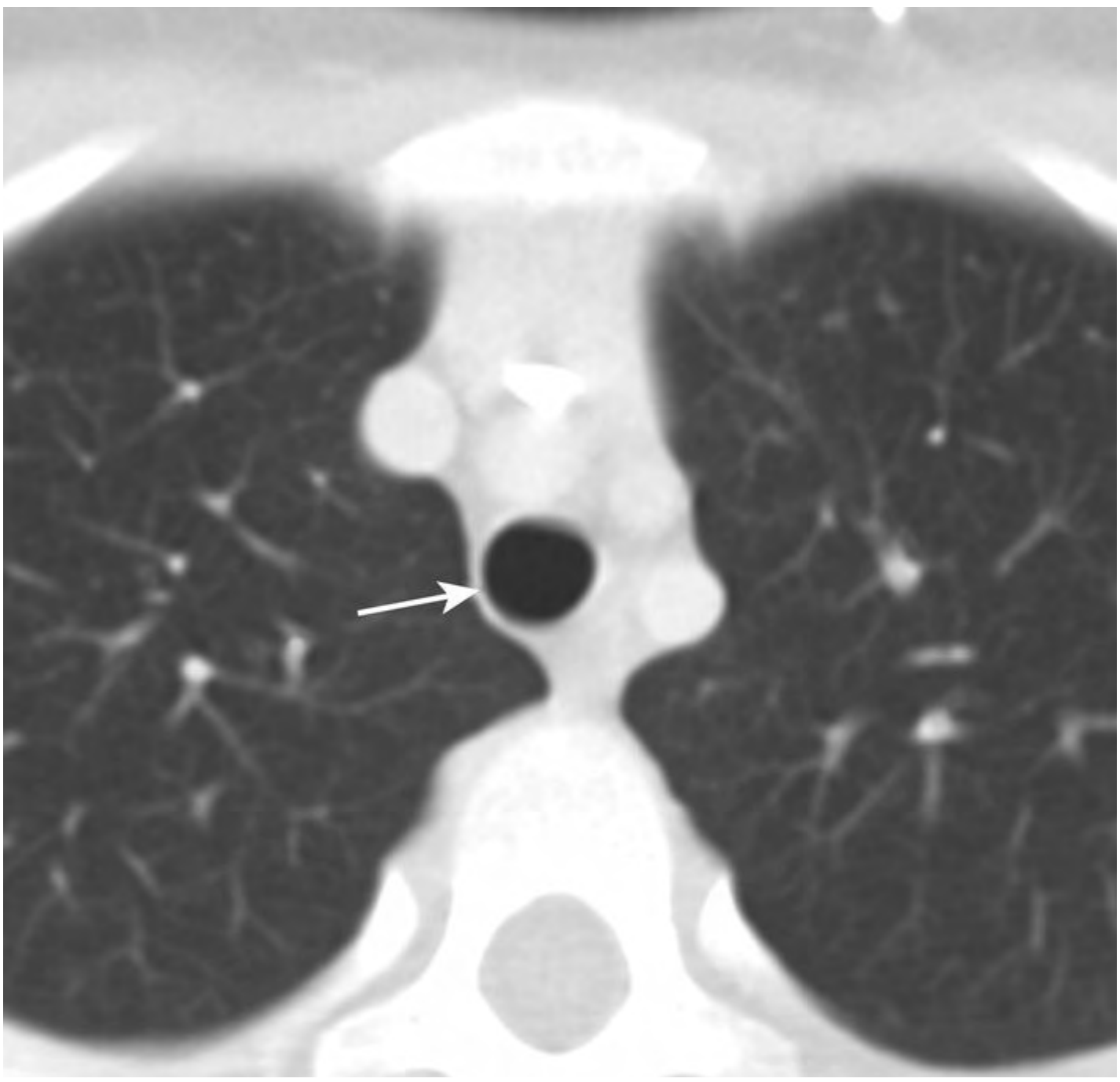
In cases of anomalous origin of the left pulmonary artery (pulmonary sling), the left pulmonary artery arises from the right pulmonary artery rather than from the main pulmonary artery and passes between the trachea and esophagus as it courses toward the left lung. The resultant sling compresses the trachea. Pulmonary sling is the only vascular anomaly to course between the trachea and esophagus (Fig. 2-14). Therefore compression of the posterior aspect of the trachea and the anterior aspect of the esophagus on lateral imaging is characteristic. It is the only vascular cause of airway compression that is associated with asymmetric lung inflation on chest radiographs (see Fig 2-14). Pulmonary sling can be associated with congenital heart disease, complete tracheal rings (an additional cause of airway problems), and anomalous origin of the right bronchus (see Fig. 2-14). On CT, the trachea is compressed at the level of the sling and appears flattened in the anterior to posterior direction—like a pancake. If complete tracheal rings are present, the rings are typically superior to the pulmonary sling, and the trachea appears very small in caliber and very round at the level of the rings (see Fig. 2-14).



▪ **FIGURE 2-10** **Bronchogenic cyst causing compression of the distal trachea.**
A, Lateral chest radiograph showing a soft tissue density mass *(M)* posterior to and anteriorly displacing the trachea *(arrows)*. **B** and **C,** Sagittal and axial contrast-enhanced CT shows mass *(M)* compressing and anteriorly displacing the adjacent trachea *(arrows)*.



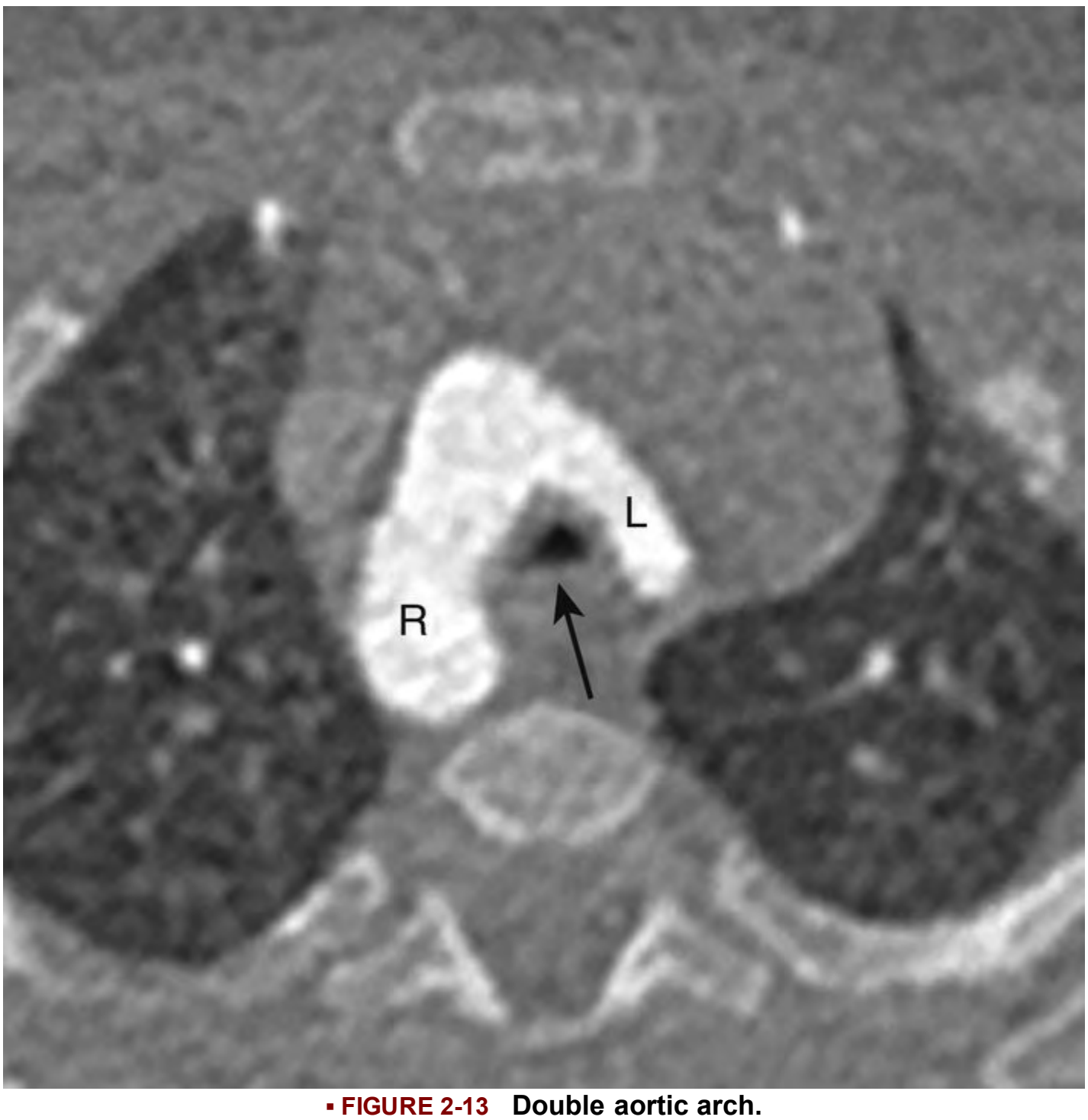
▪ **FIGURE 2-11** **Lymphoma causing compression of the trachea.**
CT shows a large anterior mediastinal mass *(M)* with posterior displacement and severe compression of the trachea *(arrow)*. The superior vena cava is also compressed *(arrowhead)*. Note multiple collateral veins on the right related to the obstructed superior vena cava.



▪ **FIGURE 2-12** Normal configuration of trachea on cross-sectional imaging is round *(arrow)*. An oval or pancake-shaped intrathoracic trachea is not normal.

Right Aortic Arch with Aberrant Left Subclavian Artery

Right aortic arch with an aberrant left subclavian artery (RAA-ALSCA) is another arch anomaly that can be associated with airway compression (Fig. 2-15). Airway compression typically occurs when there is a persistent ductus ligament completing the ring. However, you cannot see or know whether this is the case by imaging. There are several mechanisms by which RAA-ALSCA contributes to airway compression in addition to compression by the completed ring. Often there is dilatation of the subclavian artery at the origin from the right aorta (called a Kommerell diverticulum), which can contribute to airway compression. In addition, the descending aorta may lie in the midline, immediately anterior to the vertebral bodies, as the descending aorta passes from right to left as it descends (see Fig. 2-15). This midline descending aorta can contribute to airway compression as the result of the abnormal stacking of anatomic structures in the limited space between the sternum and vertebral bodies and typically causes that compression at the level of the distal tracheal carina. There is often a component of dynamic airway collapse (malacia) associated.

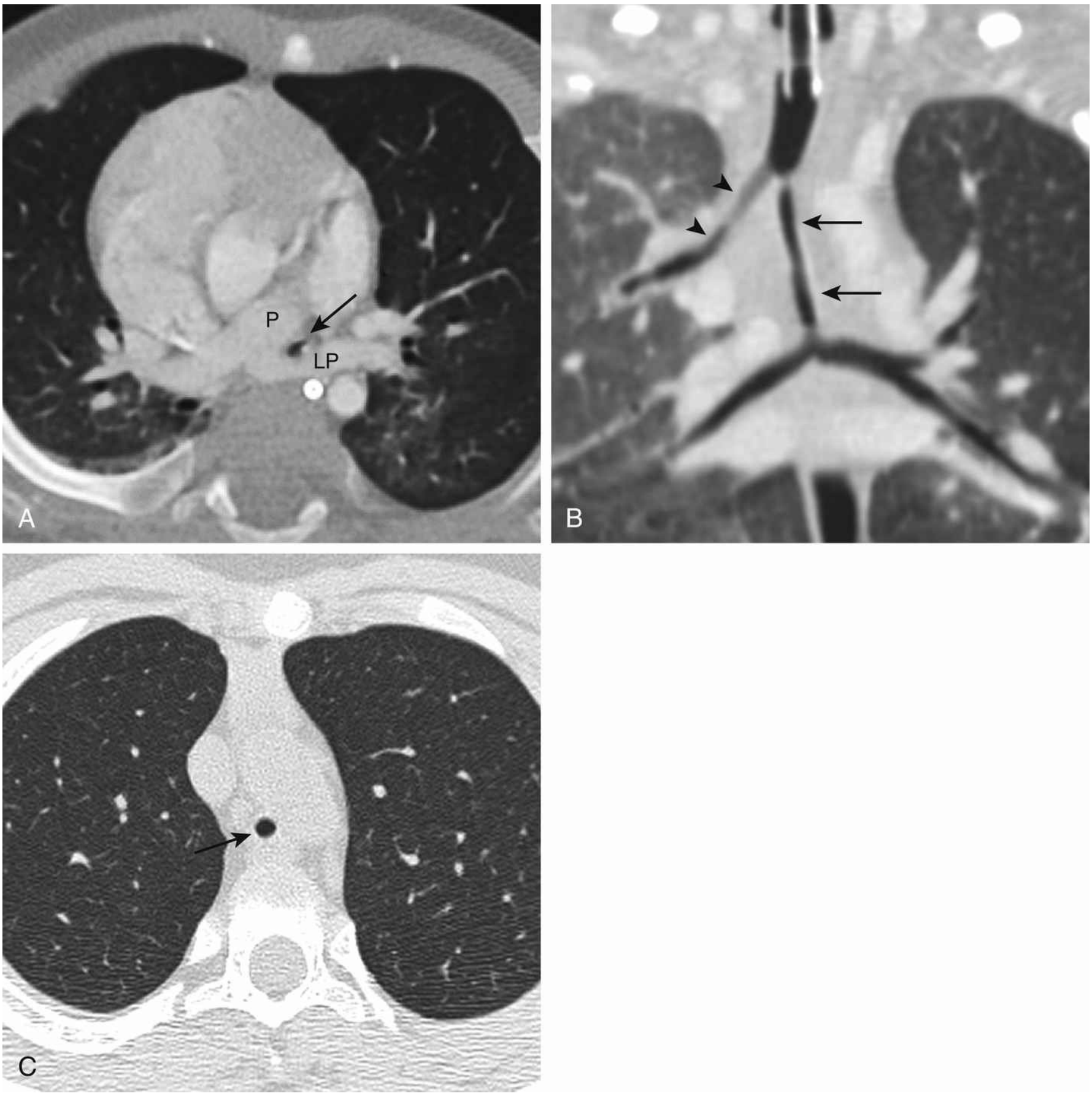


▪ **FIGURE 2-13** **Double aortic arch.**
CT image shows right and left arches *(R, L)* surrounding a small compressed trachea *(arrow)*. The arches rejoin to form the descending aorta posteriorly (not shown). The right arch is larger than the left.

Innominate Artery Compression Syndrome

The innominate artery passes immediately anterior to the trachea just inferior to the level of the

thoracic inlet. In infants, in whom the innominate artery arises more to the left than in adults and in whom the mediastinum is crowded by the relatively large thymus, there can be narrowing of the trachea at this level. There is a spectrum from normal to severe narrowing; the term *syndrome* is reserved for cases that are symptomatic. The compression and resultant symptoms decrease with time as the child grows, and surgical therapy is reserved for cases in which symptoms are severe. On lateral radiography, there is indentation of the anterior aspect of the trachea at or just below the thoracic inlet (Fig. 2-16). CT demonstrates the abnormality as anterior compression of the trachea at the level of the crossing of the innominate artery and also excludes other causes of the airway compression.

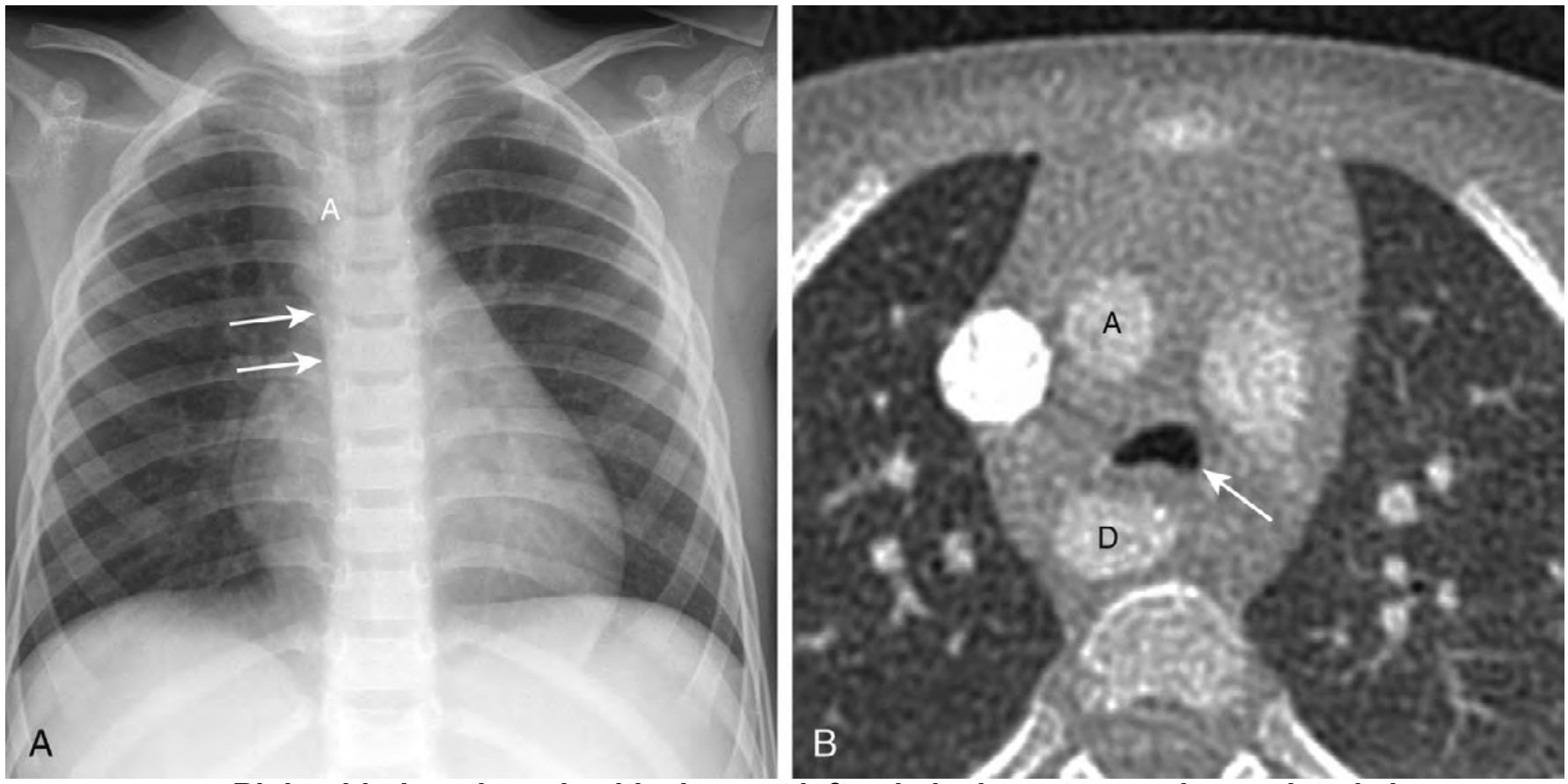


▪ **FIGURE 2-14** **Pulmonary sling.**

A, CT in axial plane shows anomalous origin of left pulmonary artery *(LP)* from the right pulmonary artery rather than from the main pulmonary artery *(P)*. The pulmonary sling wraps around and compresses the trachea *(arrow)* as it passes into the left hemithorax. Note the enteric tube in the esophagus (dense round structure), posterior to the sling. **B,** CT in coronal plane showing airway anomalies in child with pulmonary sling. Note anomalous origin of the right upper lobe bronchus (*arrowheads)* creating a "pseudocarina." The more distal trachea is very small and round in caliber *(arrows)*, consistent with complete tracheal rings. **C,** Axial CT shows small round trachea *(arrow)*, consistent with complete tracheal rings.

Intrinsic Lower Airway Obstruction

Intrinsic abnormalities of the lower airway include dynamic processes, such as tracheomalacia, tracheal stenosis, foreign bodies, and focal masses. Tracheomalacia is tracheal wall softening related to abnormality of the cartilaginous rings of the trachea. It can be a primary or secondary condition and results in intermittent collapse of the trachea. The diagnosis cannot be made on a single static radiograph. However, lateral fluoroscopy or endoscopy can demonstrate dynamic changes in the caliber of the trachea, and they are diagnostic. Cine imaging with MRI or CT may also be helpful.



▪ **FIGURE 2-15 Right-sided aortic arch with aberrant left subclavian artery and associated airway compression.**

A, Frontal radiograph shows right aortic arch *(A)* as soft tissue indentation on the rightward aspect of the trachea. The right-sided descending aorta is visualized *(arrows)*. **B,** CT showing right-sided ascending *(A)* and descending *(D)* aorta. Note aberrant left subclavian artery arising from leftward aspect of descending aorta. The trachea *(arrow)* is compressed.

The most common soft tissue masses in the trachea are hemangiomas, which most commonly occur in the subglottic region, are often associated with facial hemangiomas in a beard distribution, and appear on frontal radiographs with asymmetric subglottic narrowing. Other tracheal masses include tracheal papilloma and tracheal granuloma.

Airway Foreign Body

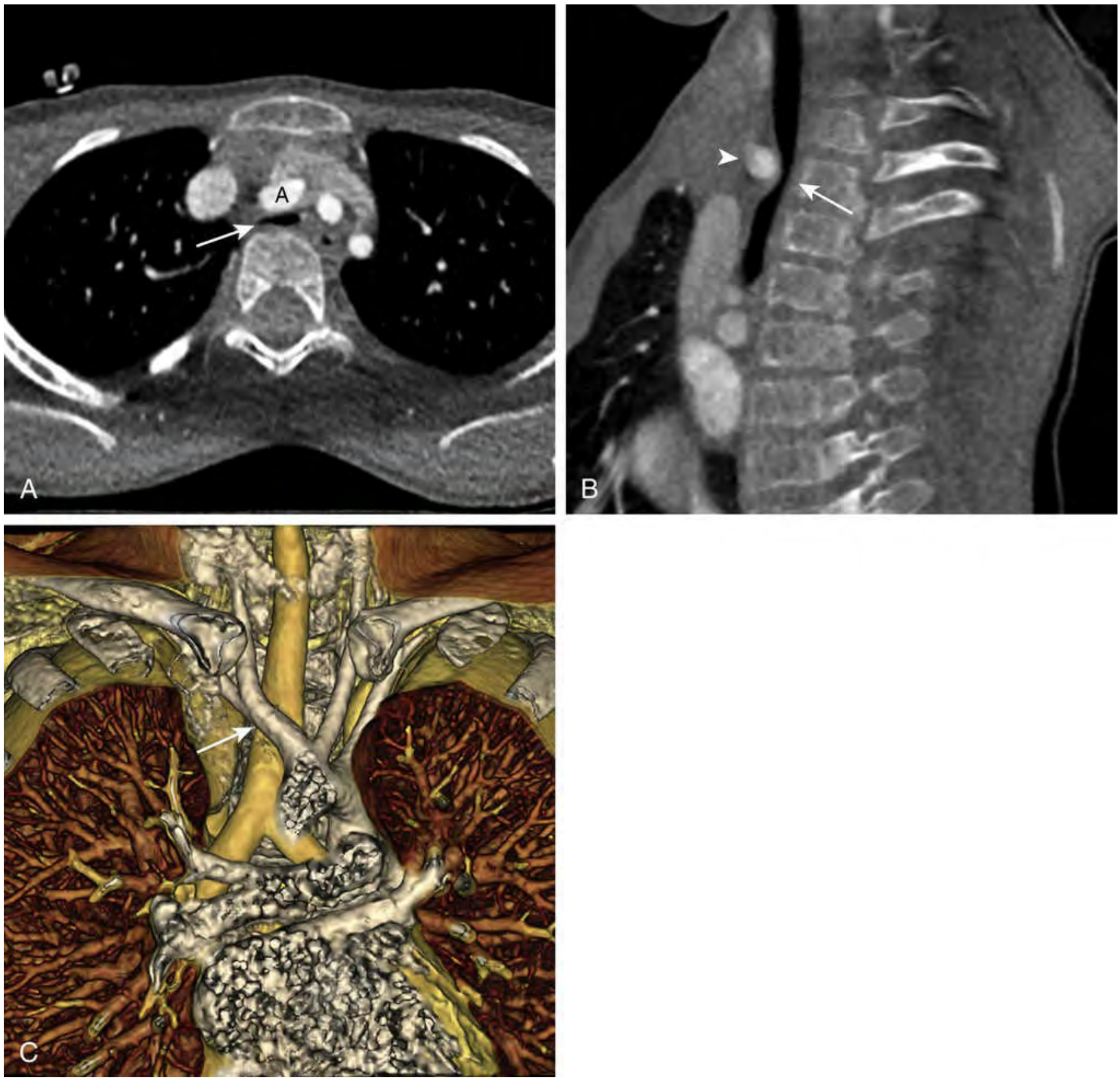
Infants and toddlers explore their environments with their mouths and will put almost anything into them. When such foreign bodies are aspirated, the bronchus is the most common site of lodgment. The aspiration commonly is not witnessed, and symptoms may be indolent, leading to an occult presentation. Radiographic findings of bronchial foreign bodies include asymmetric lung aeration, hyperinflation, oligemia, atelectasis, lung consolidation, pneumothorax, and pneumomediastinum. The vast majority of bronchial foreign bodies (as much as 97%) are nonradiopaque. Inspiratory films alone can be normal in as much as one third of patients in whom bronchial foreign bodies are present. Because the volume of the affected lung segments can be normal, increased, or decreased, the key radiographic feature is the lack of change in lung volume demonstrated at different phases of the respiratory cycle (Fig. 2-17). Evaluation at varying phases of the respiratory cycle is easily accomplished in cooperative children by taking expiratory and inspiratory films. In infants and uncooperative children, the population most at risk for foreign body aspiration, air trapping can be detected in bilateral decubitus views of the chest or by fluoroscopy. Some articles propose non–contrast-enhanced CT for the diagnosis of bronchial foreign bodies, but it is not a widespread practice at this time. The differential diagnoses for an asymmetric lucent lung include bronchial foreign body, Swyer-James syndrome, and pulmonary hypoplasia.

Laryngeal or tracheal foreign bodies are far less common than bronchial foreign bodies and usually present with abrupt stridor or respiratory distress. Radiographic findings include a radiopaque foreign body, soft tissue density within the airway, and loss of visualization (silhouetting) of the airway wall contours. Foreign bodies lodged within the proximal esophagus, most commonly coins, may also present with airway compression.

Obstructive Sleep Apnea

One of the most common clinical problems involving the pediatric airway is the presence of OSA. This disorder affects 3% of children (millions in the United States alone) and is increasingly being associated with significant morbidities, such as poor performance in school, attention-deficit disorder,

excessive daytime sleepiness, and failure to thrive. Most children with OSA are otherwise healthy children in whom there is enlargement of the adenoid and palatine tonsils, causing OSA. When the adenoid and palatine tonsils are removed, the OSA-related symptoms typically resolve.

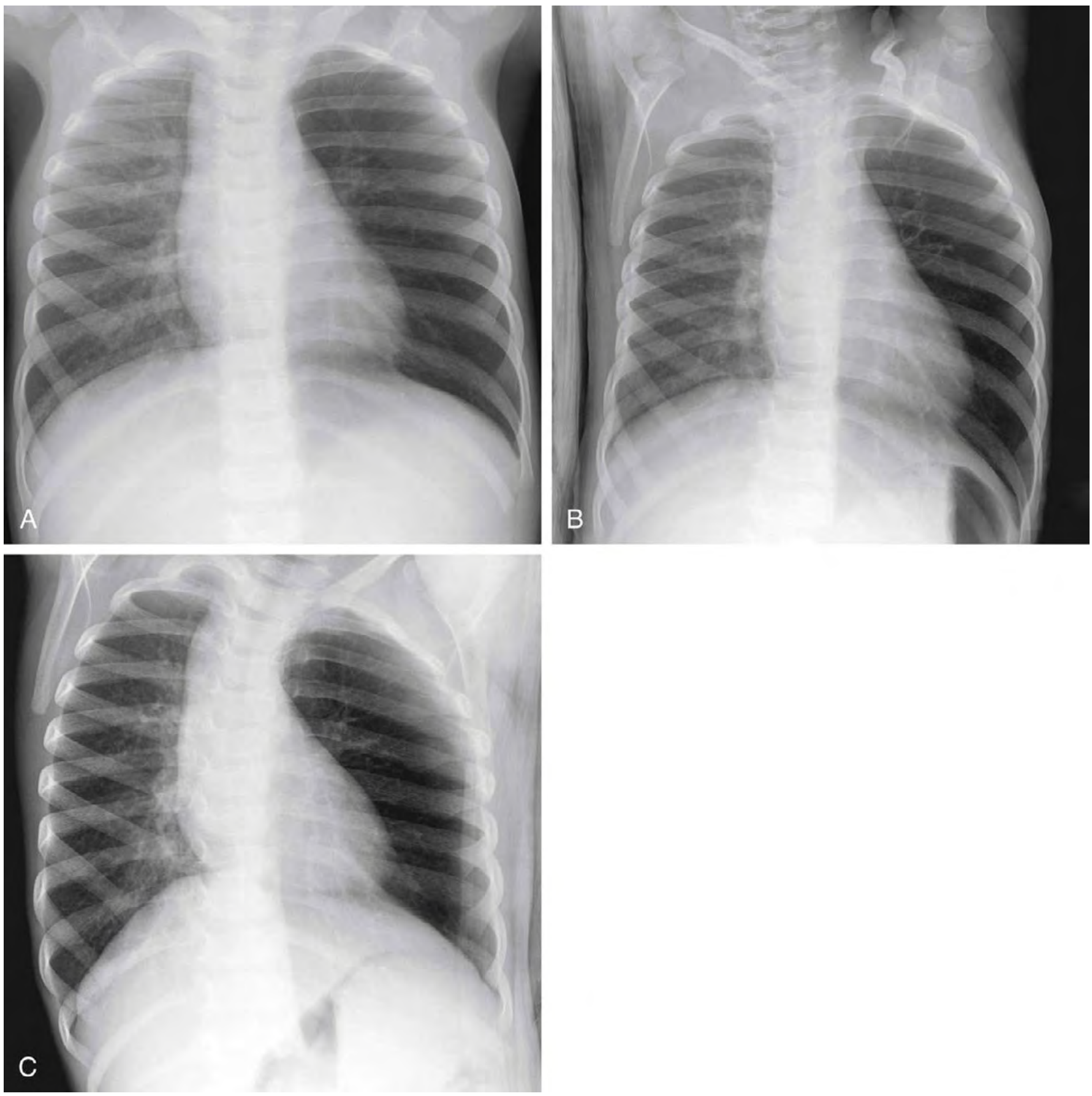


▪ **FIGURE 2-16** **Innominate artery compression syndrome.**
A, CT in axial plane shows innominate artery *(A)* compressing the trachea *(arrow)*. The trachea is oblong. Normally the trachea is round at this level. **B,** CT in sagittal plane shows trachea *(arrow)* being compressed between innominate artery *(arrowhead)* and spine. **C,** 3D reconstruction shows innominate artery *(arrow)* crossing obliquely in front of and compressing the trachea.

The palatine tonsils can be evaluated on physical examination. In these children, imaging is limited to a lateral radiograph of the airway, obtained to evaluate the adenoid tonsils. On radiography, adenoids appear as a soft tissue mass in the posterior nasopharynx. Criteria for enlargement include diameter greater than 12 mm and a convex outward anterior boarder (Fig. 2-18). Markedly enlarged adenoid tissues may completely obstruct the posterior nasopharynx. Enlarged palatine tonsils can also be seen radiographically, appearing as a large soft tissue mass projecting over the posterior aspect of the soft palate on lateral radiography (see Fig 2-18).

Certain children with OSA have more complicated airway issues. In these children, an MR sleep study may be helpful for future planning. Such studies have been shown to influence management decisions and help to plan surgical interventions in the majority of cases. Sequences performed include

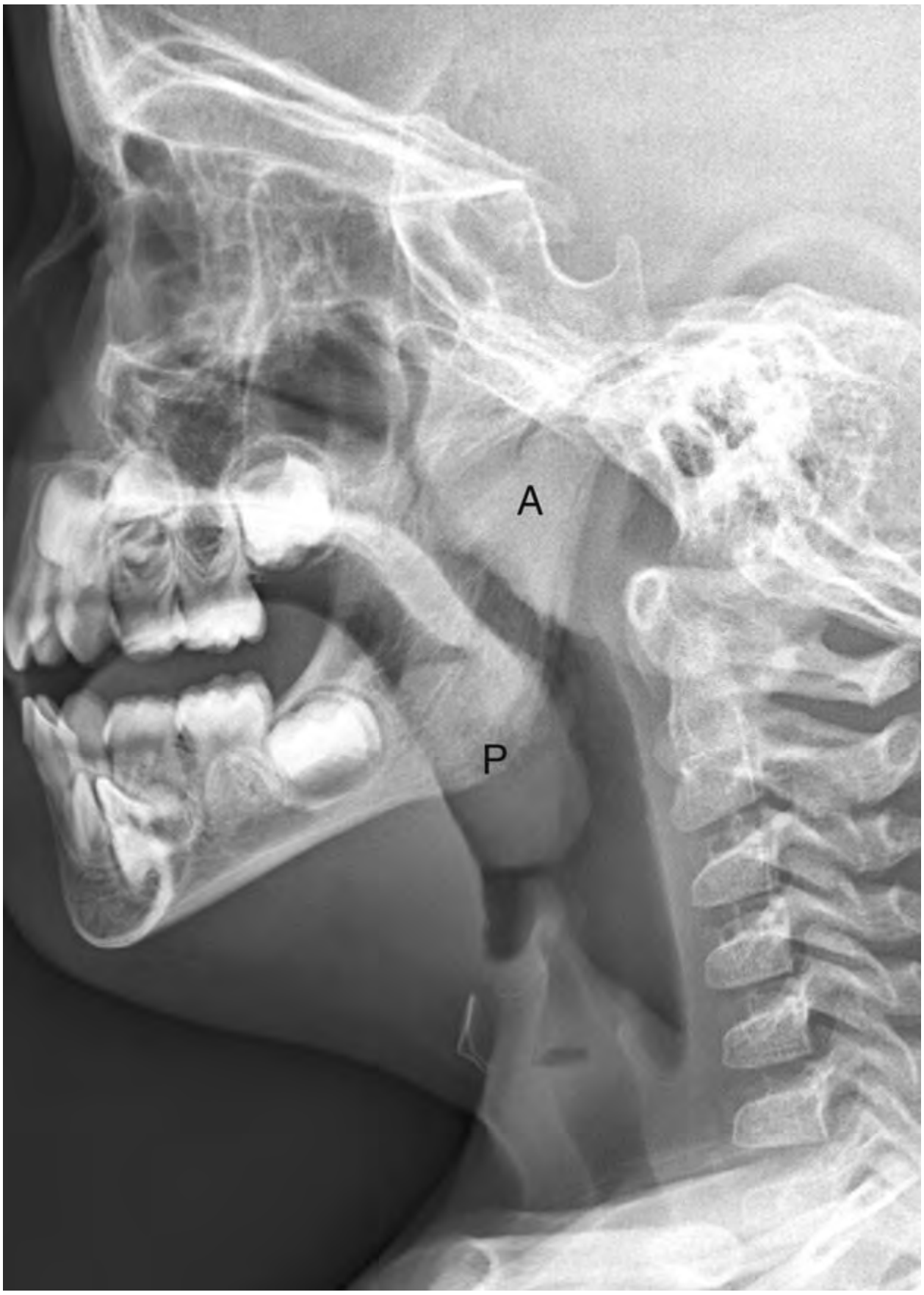
T1-weighted (for anatomy) images, T2-weighted images with fat saturation (depicts tonsillar tissue as bright on a dark background), and fast-gradient echo images that can be displayed in a cine, or movie, fashion to depict patterns of airway motion and collapse. Indications for MR sleep studies include persistent OSA despite previous airway surgery (most commonly tonsillectomy and adenoidectomy); predisposition to multilevel obstruction, such as in Down and other syndromes; OSA and severe obesity; and preoperative evaluation before complex airway surgery. Commonly encountered diagnoses include recurrent enlarged adenoid tonsils, enlarged palatine tonsils, enlarged lingual tonsils, glossoptosis, hypopharyngeal collapse, and abnormal soft palate. Cine CT has also been advocated as a way to evaluate these patients.



▪ **FIGURE 2-17** **Bronchial foreign body.**
A, Frontal radiograph show asymmetry in lung volumes, with left lung being larger and more hyperlucent. Decubitus views with right side down in **B** and left side down in **C** show a static hyperexpanded left lung and changing volume of the right lung consistent with left-sided air trapping.

Recurrent and Enlarged Adenoid Tonsils

The adenoid tonsils are absent at birth, rapidly proliferate during infancy, and reach their maximal size when children are between 2 and 10 years of age. During the second decade of life, they begin to decrease in size. It is surprising how commonly the adenoids can grow back. It is one of the most common causes of recurrent OSA after tonsillectomy and adenoidectomy. Adenoid tonsils are considered to be recurrent and enlarged (Fig. 2-19) if they are greater than 12 mm in anterior-to-posterior diameter and are associated with intermittent collapse of the posterior nasopharynx on cine images. There may also be associated collapse of the hypopharynx because the relatively superior obstruction generates negative pressure in the hypopharynx during inspiration. On axial images, the postsurgical appearance of a V-shaped defect in the midportion of the adenoid tonsil is typically seen (Fig. 2-20).



▪ **FIGURE 2-18** **Enlargement of the adenoid and palatine tonsils.**
Lateral radiograph showing enlargement of the palatine *(P)* and adenoid *(A)* tonsils, with near obstruction of the nasopharynx. Note normal epiglottis and aryepiglottid folds.

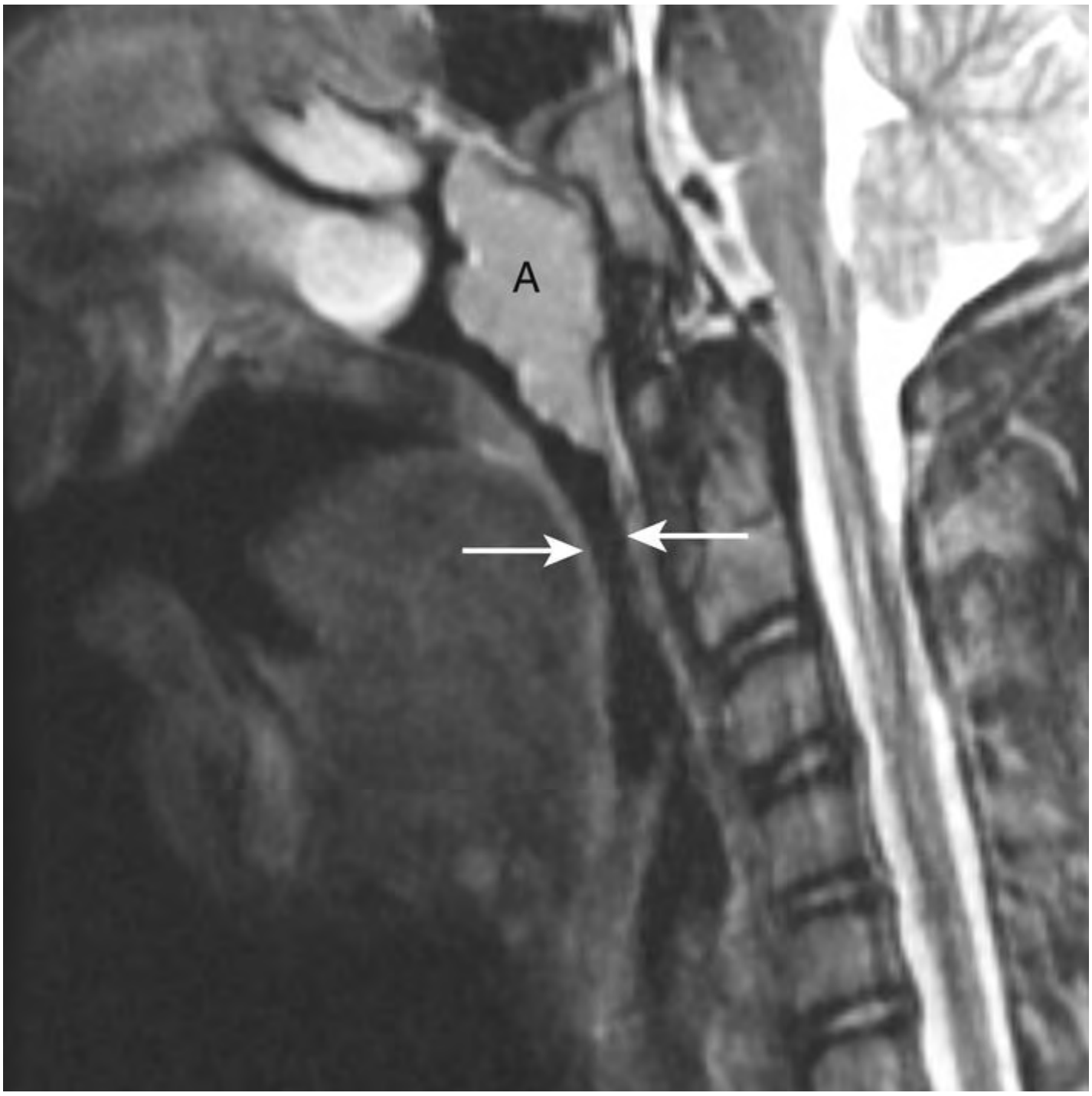
Enlarged Palatine Tonsils

Unlike the adenoid tonsils, which commonly grow back after surgical removal, the palatine tonsils do not. Therefore, because most MR sleep studies are performed after tonsillectomy, absence of the palatine tonsils is depicted in most cases. When present and enlarged (Fig. 2-21), the palatine tonsils appear as round, high T2-signal structures in the palatine fossa, and they bob inferiorly and centrally, intermittently obstructing the airway. There is no published range of normal size for palatine tonsils on imaging.

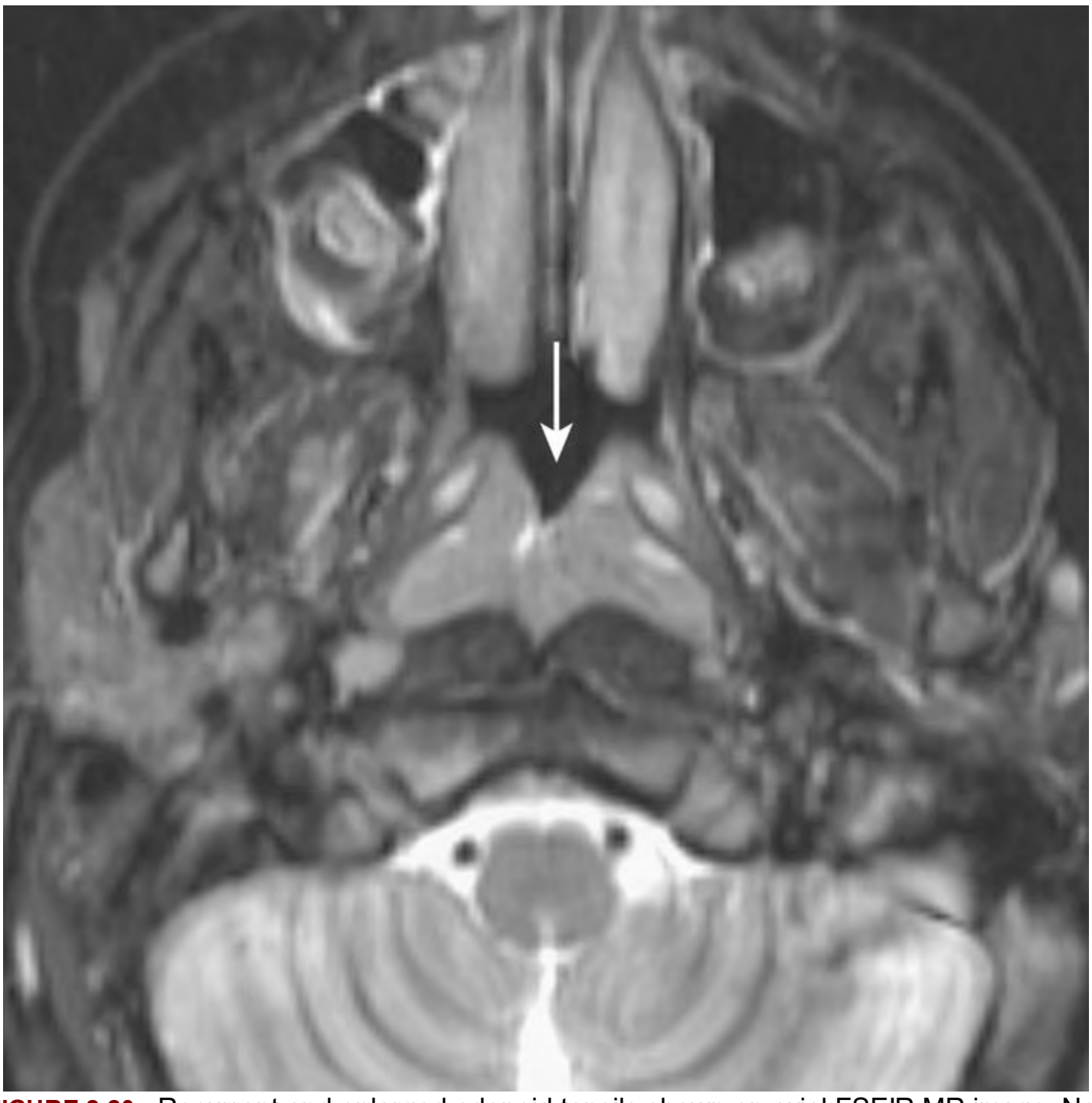
Enlarged Lingual Tonsils

Enlargement of the lingual tonsils is being recognized as a common cause of persistent OSA following previous tonsillectomy and adenoidectomy. In such patients, the lingual tonsils can become quite large and obstruct the retroglossal airway. Enlarged lingual tonsils appear as high-signal masses (Fig. 2-22) that are round or that have grown together and appear as a single dumbbell-shaped mass immediately posterior to the tongue. It is an important diagnosis to make on imaging because it is not readily seen on physical examination and is one of the more easily surgically curable causes of persistent OSA.

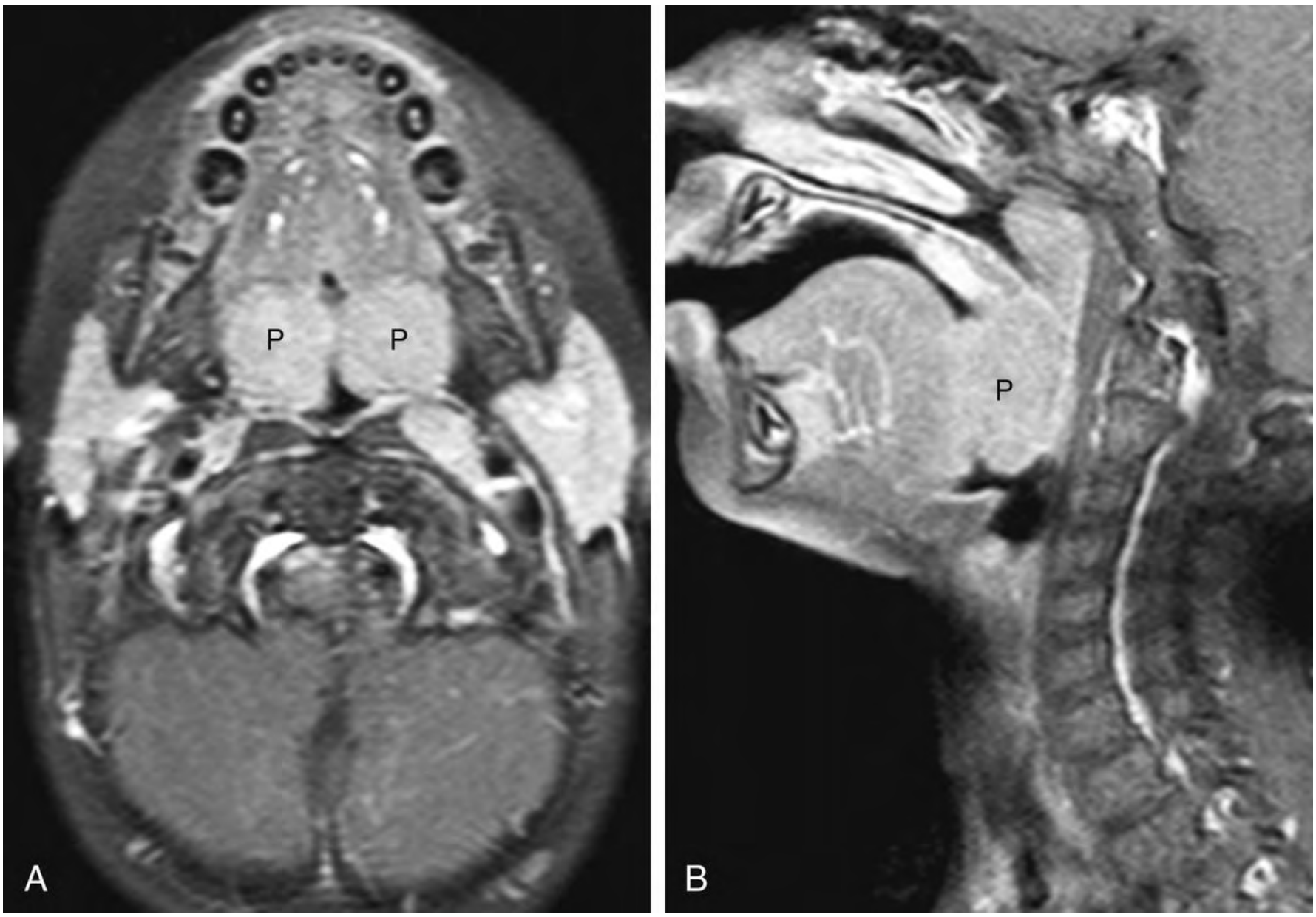
Enlargement of the lingual tonsils appears to be particularly common after tonsillectomy and adenoidectomy in obese children and in children with Down syndrome. On radiography, enlarged lingual tonsils can be seen as a soft tissue mass continuous with the posterior aspect of the tongue.



▪ **FIGURE 2-19** **Recurrent and enlarged adenoid tonsils.**
Sagittal fast-spin echo inversion recovery (FSEIR) image showing enlarged adenoid tonsils *(A)* abutting the soft palate and obstructing the posterior nasopharynx. There is narrowing of the retroglossal airway *(arrows)* related to hypopharyngeal collapse.



▪ **FIGURE 2-20** Recurrent and enlarged adenoid tonsils shown on axial FSEIR MR image. Note wedge-shaped central defect *(arrow)* in adenoid tonsil, typical of postoperative appearance.



▪ **FIGURE 2-21** **Enlarged "kissing" bilateral palatine tonsils.**

A, Axial T2-weighted image shows bilateral markedly enlarged palatine tonsils *(P)* touching in the midline and obstructing airway. **B,** Sagittal T2-weighted image shows enlarged palatine tonsil *(P)*.



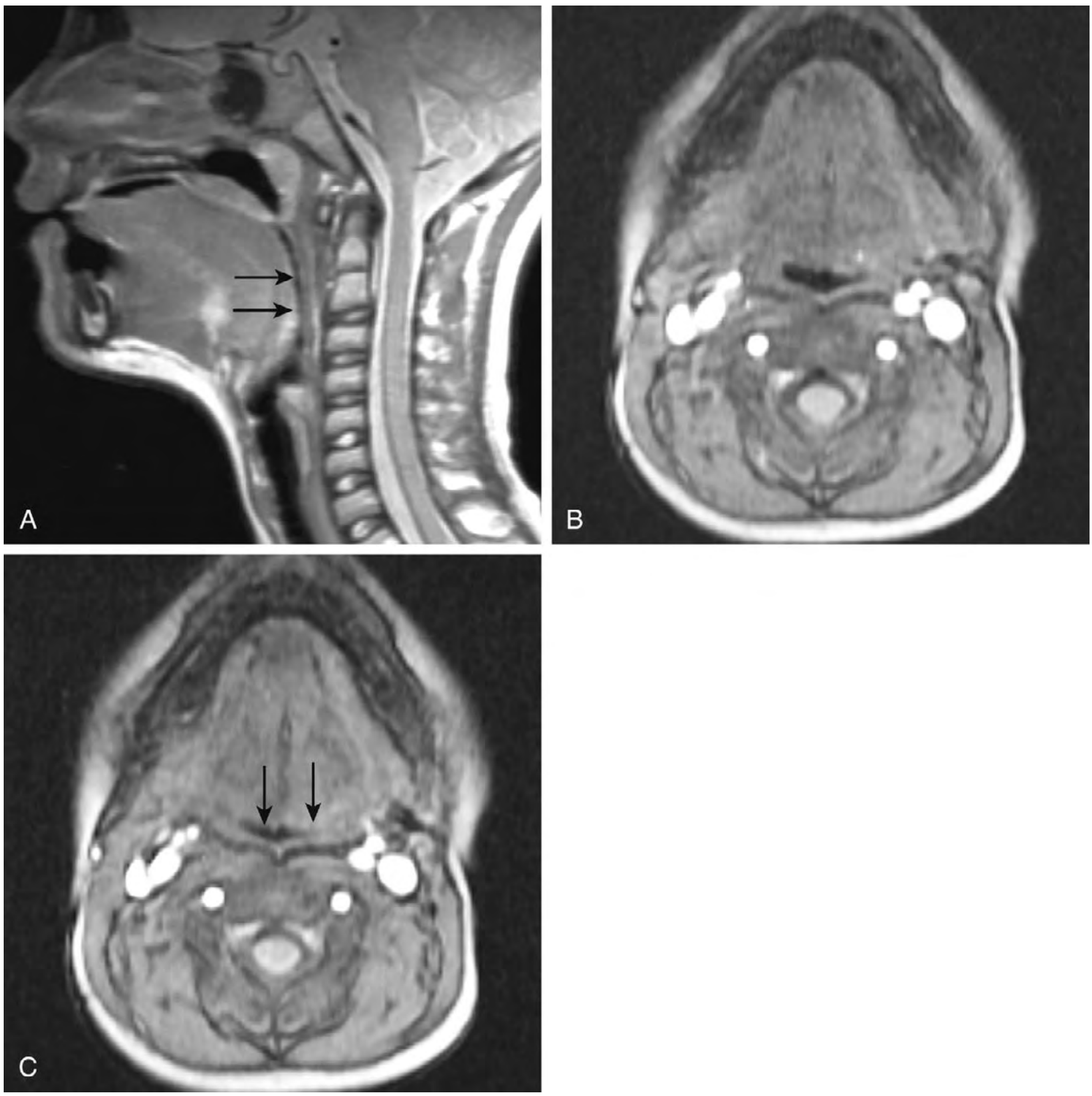
▪ **FIGURE 2-22** **Enlarged lingual tonsils.**
Sagittal FSEIR image showing enlarged lingual tonsils *(L)* obstructing the retroglossal pharynx.

Glossoptosis

Glossoptosis is defined as posterior motion of the tongue during sleep. The posterior aspect of the tongue intermittently falls posteriorly and abuts the posterior pharyngeal wall, obstructing the retroglossal airway (Fig. 2-23). It is associated with large tongues (macroglossia), small jaws (micrognathia), and decreased muscular tone. It is most commonly seen in children with Down syndrome, Pierre Robin sequence, and neuromuscular disorders, such as cerebral palsy. On imaging, intermittent posterior motion of the tongue in the anterior-to-posterior direction is depicted on cine images.

Hypopharyngeal (Retroglossal) Collapse

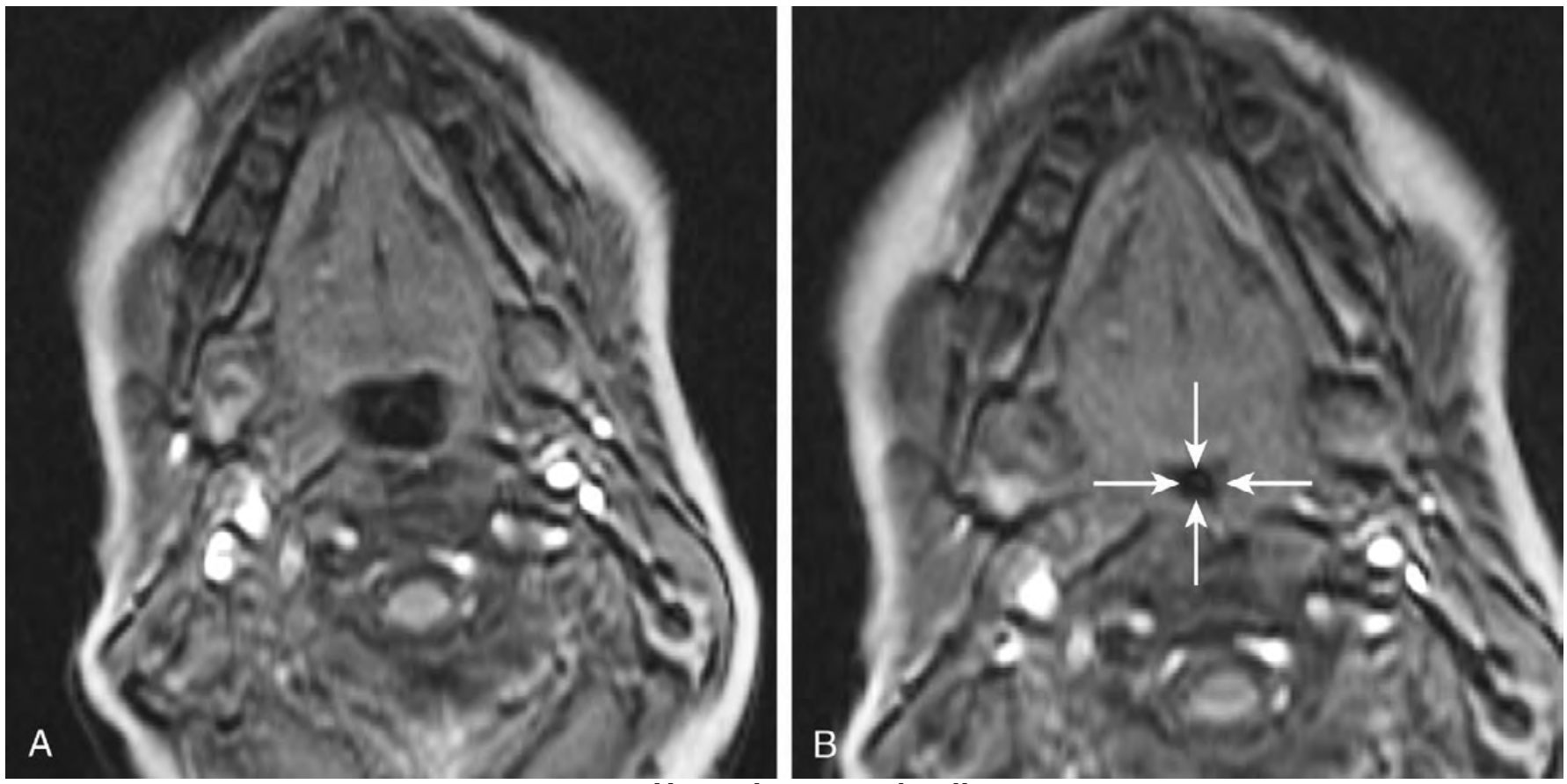
Hypopharyngeal collapse can be a primary phenomenon caused by decreased muscle tone, or it may occur secondary to negative pressure generated by a more superior obstruction (typically enlarged adenoid tonsils). With hypopharyngeal collapse, there is cylindrical collapse of the retroglossal airway, with the anterior, posterior, left, and right walls of the airway all collapsing centrally (Fig. 2-24). In contrast, with glossoptosis, the tongue moves anteriorly and posteriorly, and the lateral diameter of the airway remains unchanged. This differentiation is easiest to observe on axial cine images at the level of the midportion of the tongue, from superior to inferior. It is important to characterize the pattern of collapse of the retroglossal airway as hypopharyngeal collapse or glossoptosis because the surgical options for the two groups of patients are quite different.



▪ **FIGURE 2-23** **Glossoptosis.**
A, Sagittal proton density image showing large tongue with posterior aspect of tongue *(large arrows)* abutting the posterior pharyngeal wall and obstructing the retroglossal airway. Axial Cine MR images obtained at inspiration in **B** and expiration in **C** show intermittent anterior to posterior collapse *(arrows)* related to glossoptosis.

Abnormal Soft Palate

A prominent soft palate is one of the contributing factors in some cases of OSA, and there are surgical procedures that decrease the size of the soft palate. As you can imagine, there are no published criteria for abnormal soft palate enlargement. If the soft palate is prominent in size, is draped over the tongue and hangs more inferiorly than the midportion of the tongue, and is associated with intermittent collapse of the posterior nasopharynx or retroglossal airway, we consider it enlarged.

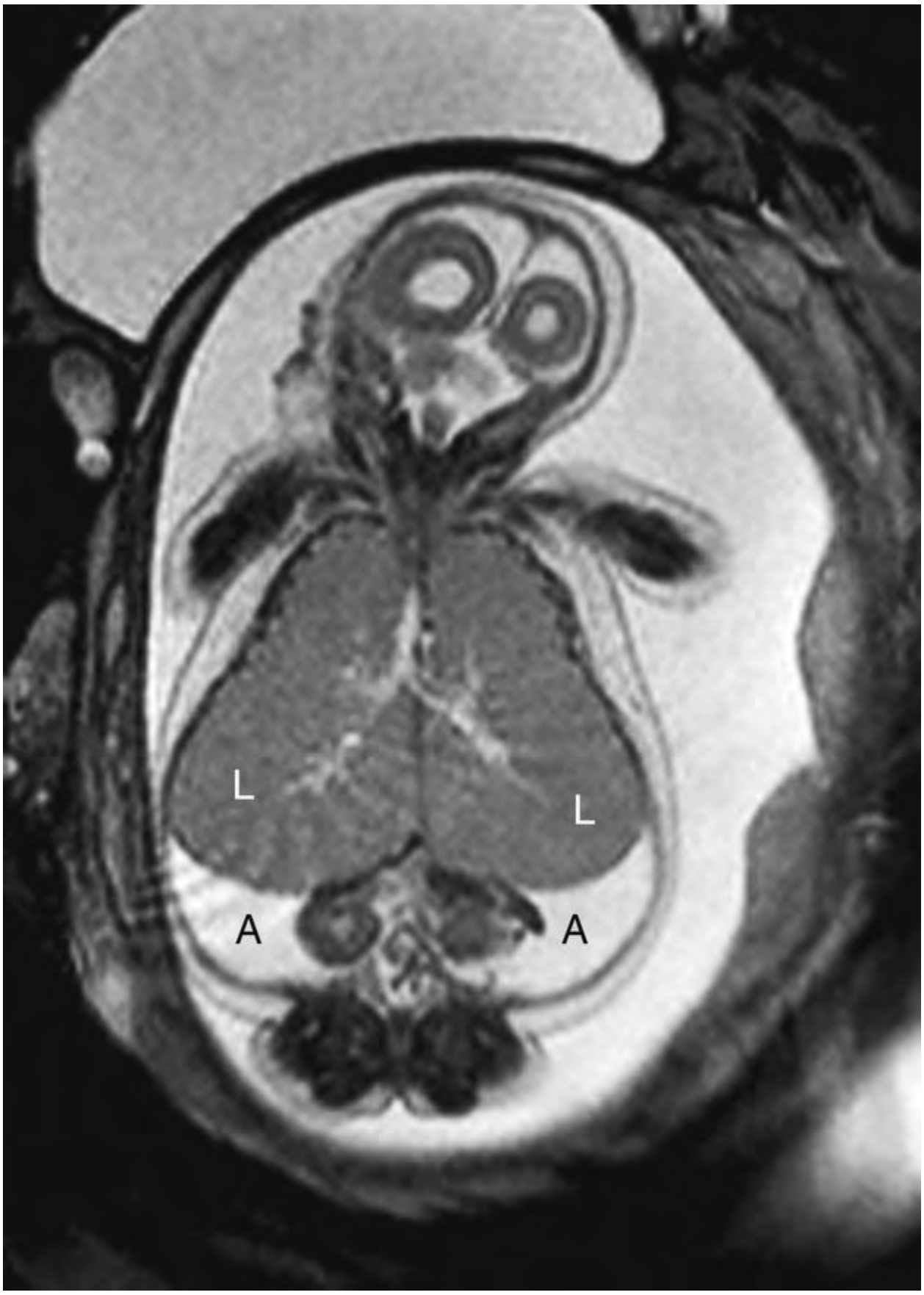


▪ FIGURE 2-24 **Hypopharyngeal collapse.**
A, Axial cine image during expiration showing open retroglossal airway. **B,** Axial cine image during inspiration showing complete collapse of the retroglossal airway *(arrows)*. Note that lateral left and right, anterior, and posterior walls all collapse cylindrically to the center of airway, in contrast to tongue moving posteriorly, as seen in glossoptosis.

The soft palate can be edematous, as seen on physical examination in patients with significant OSA. This is thought to be related to the repeated trauma of snoring. On T2-weighted MR sequences, the edema is depicted as an increased signal throughout the soft palate; in patients without OSA, the soft palate is similar in signal to that of the musculature of the tongue.

▪ Congenital Airway Obstruction

With the increase in fetal surgery centers and associated increased use of fetal ultrasound and MRI, pediatric radiologists are beginning to see an increasing number of cases of congenital obstruction of the airway, although it remains a rare entity. CHAOS is the term given to a constellation of findings resulting from this form of airway obstruction. Causes of this airway obstruction include in utero laryngeal atresia, subglottic stenosis, and head and neck masses obstructing the upper airway, most commonly lymphatic malformations or teratomas. Fetal imaging findings in CHAOS (Fig. 2-25) include massive increases in lung volumes, flattened or everted hemidiaphragms, hydrops, and polyhydramnios. Infants with airway obstruction secondary to masses (Fig. 2-26) or other causes, with or without associated CHAOS findings, may be delivered via an ex utero intrapartum treatment (EXIT). In an EXIT, the head of the infant is delivered via a cesarean section, and the airway is established by tracheotomy or intubation before the child's being taken off placental circulation. Once the airway has been established, the child can be completely delivered.



▪ **FIGURE 2-25** **CHAOS.**

Coronal MRI image shows fetus with markedly enlarged lung volumes *(L)* with inverted diaphragms, ascites *(A),* and polyhydramnios. There is also anasarca.



▪ **FIGURE 2-26** **Teratoma of the neck.**
Fetal MRI sagittal to fetal head and neck showing large complex cystic mass *(arrow)* in the region of the neck. Mass is obstructing the airway.

Suggested Readings

Berdon W.E, Baker D.H. Vascular anomalies and the infant lung: rings, slings, and other things. *Semin Roentgenol*. 1972;7:39–63.

Capitanio M.A, Kirkpatrick J.A. Obstruction of the upper airway in infants and children. *Radiol Clin North Am*. 1968;6:265–277.

Donnelly L.F, Frush D.P, Bisset G.S. The multiple presentations of foreign bodies in children. *AJR*. 1998;170:471–477.

Donnelly L.F, Strife J.L, Bisset G.S. The spectrum of extrinsic lower airway compression in children: MR imaging. *AJR*. 1997;168:59–62.

Donnelly L.F. OSA in pediatric patients: evaluation with cine MR sleep studies. *Radiology*. 2005;236:768–778.

Dunbar J.S. Upper respiratory tract obstruction in infants and children. *AJR*. 1970;109:227–246.

Guimaraes C.V, Linam L.E, Kline-Fath B.M, et al. Prenatal MRI findings of fetuses with congenital high airway obstruction sequence. *Korean J Radiol*. 2009;10:129–134.

Heyer C.M, Nuesslein T.Y, Jung D, et al. Tracheobronchial anomalies and stenoses: detection with low-dose multidetector CT with virtual tracheobronchoscopy: comparison with flexible tracheobronchoscopy. *Radiology*. 2007;242:542–549.

John S.D, Swischuk K.E. Stridor and upper airway obstruction in infants and children. *Radiographics*. 1992;12:625–643.

Pacharn P, Poe S.A, Donnelly L.F. Low-tube-current CT for children with suspected extrinsic airway compression. *AJR*. 2002;179:1523–1527.

Yedururi S, Guillerman R.P, Chung T, et al. Multimodality imaging of tracheobronchial disorders in children. *RadioGraphics*. 2008;28:e29.

CHAPTER 3

Chest

Monica Epelman

The chest radiograph is one of the most commonly obtained examinations in pediatric imaging. It is also the examination most likely to be encountered by radiology residents, pediatric residents, general radiologists, and pediatricians. Therefore topics such as chest imaging in neonates and the evaluation of suspected pneumonia are discussed in detail.

▪ Neonatal Chest

Causes of respiratory distress in newborn infants can be divided into those that are secondary to diffuse pulmonary disease (medical causes) and those that are secondary to a space-occupying mass compressing the pulmonary parenchyma (surgical causes).

Diffuse Pulmonary Disease in the Newborn

Diffuse pulmonary disease causes respiratory distress much more commonly than surgical diseases, particularly in premature infants, who make up the majority of cases of respiratory distress in the newborn. A simple way to evaluate these patients and try to offer a limited differential diagnosis is to evaluate the lung volumes and to characterize the pulmonary opacities.

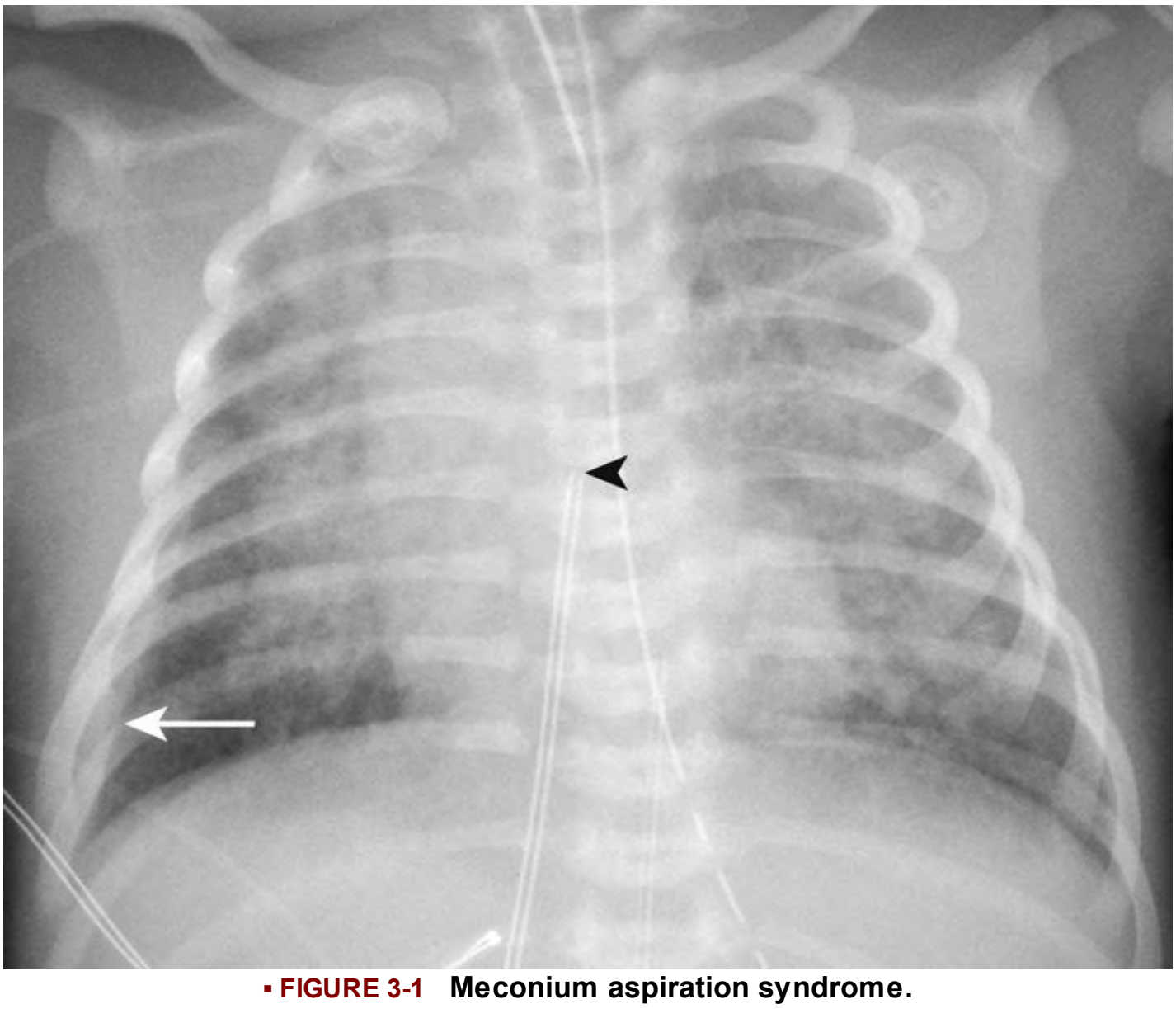
Lung volumes can be categorized as high, normal, or low. Normally the apex of the dome of the diaphragm is expected to be at the level of approximately the tenth posterior rib. If present, lung opacity can be characterized as streaky, perihilar (central) densities that have a linear quality or as diffuse, granular opacities that have an almost sandlike character. Classically cases fall into one of the following two categories: (1) cases with high lung volumes and streaky perihilar densities and (2) cases with low lung volumes and granular opacities (Table 3-1). This is more of a guideline rather than a rule because many neonates with diffuse pulmonary disease have normal lung volumes. The differential diagnosis for cases with high lung volumes and streaky perihilar densities includes meconium aspiration, transient tachypnea of the newborn (TTN), and neonatal pneumonia. Most of the neonates in this group are term. The differential for cases with low lung volumes and granular opacities includes surfactant deficiency and group B streptococcal pneumonia. Most of these neonates are premature.

Meconium Aspiration Syndrome

Meconium aspiration syndrome results from intrapartum or intrauterine aspiration of meconium. It usually occurs secondary to stress, such as hypoxia, and more often occurs in term or postmature neonates. The aspirated meconium causes both obstruction of small airways secondary to its tenacious nature and chemical pneumonitis. The degree of respiratory failure can be severe and may lead to respiratory failure, pulmonary air leaks, and persistent pulmonary hypertension. Radiographic findings include hyperinflation (high lung volumes), which may be asymmetric and patchy, and asymmetric lung densities that tend to have a ropy appearance and a perihilar distribution (Fig. 3-1). Commonly there are areas of hyperinflation alternating with areas of atelectasis. Pleural effusions can be present. Because of the small-airway obstruction by the meconium, air-block complications are common, with pneumothorax occurring in 20% to 40% of cases. Meconium aspiration syndrome is relatively common; 25,000 to 30,000 cases and 1000 deaths occur in the United States annually. Although meconium-stained amniotic fluid occurs in approximately 10% to 15% of deliveries, meconium aspiration syndrome develops in less than 5% of them.

TABLE 3-1
Differential Diagnosis of Diffuse Pulmonary Disease in the Newborn

High Lung Volumes, Streaky Perihilar Densities	Low Lung Volumes, Granular Opacities
Meconium aspiration syndrome	Surfactant deficiency
Transient tachypnea of the newborn	Group B streptococcal pneumonia
Neonatal pneumonia	



▪ **FIGURE 3-1** **Meconium aspiration syndrome.**
Newborn chest radiograph shows normal-to-large lung volumes, increased perihilar markings, and bilateral, coarse, ropy markings. Note right pleural effusion *(arrow)*. Also note umbilical venous catheter with tip *(arrowhead)* into right atrium. Tip should be at the junction of the right atrium and inferior vena cava.

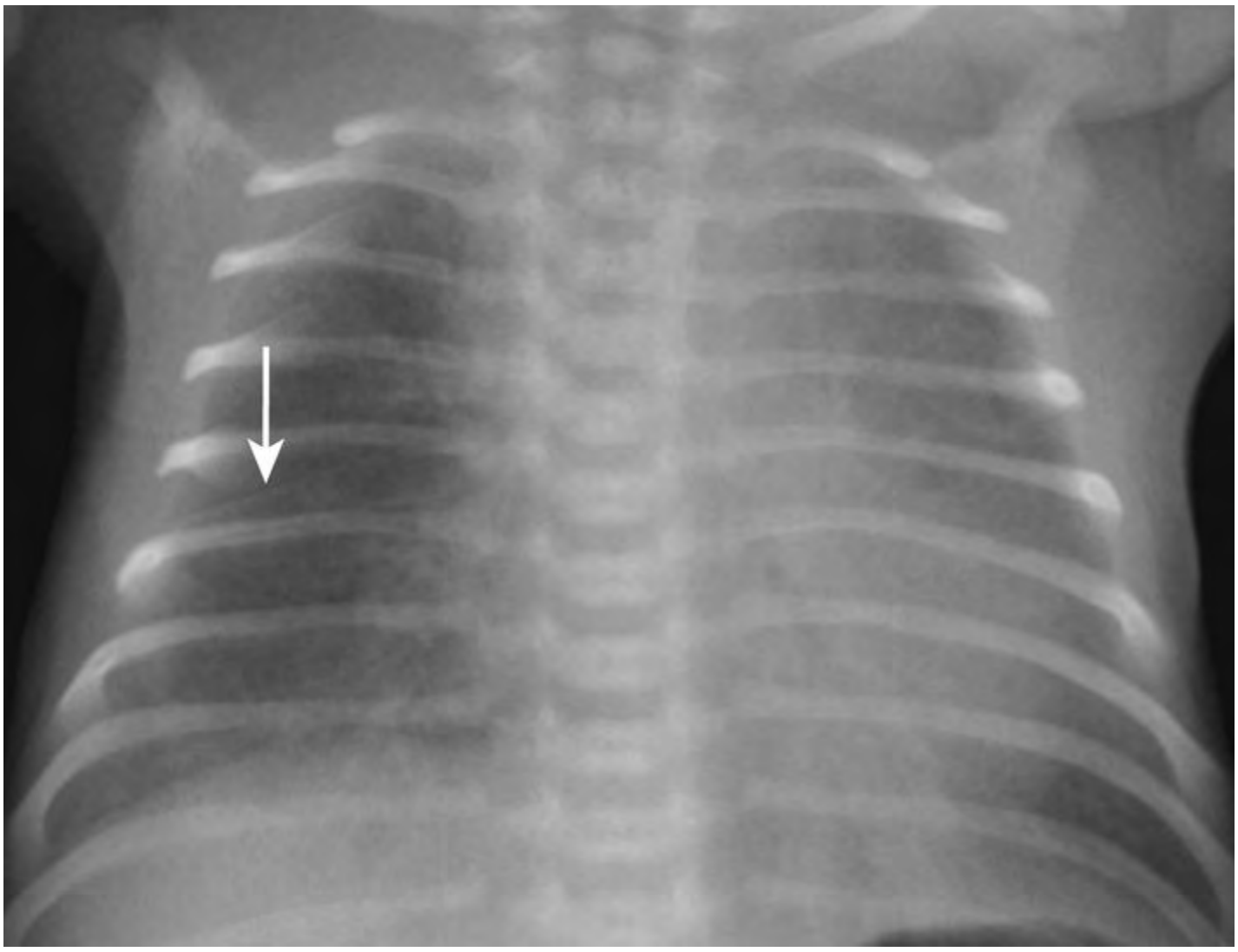
Transient Tachypnea of the Newborn

TTN is also referred to by a variety of other names, including wet lung disease and transient respiratory distress. It occurs secondary to delayed clearance of fetal lung fluid. Physiologically the clearing of fetal lung fluid is facilitated by the "thoracic squeeze" during vaginal deliveries; therefore most cases of TTN are related to cesarean section, in which the thoracic squeeze is bypassed. Other causes include maternal diabetes and fetal distress requiring anesthesia or analgesia. The hallmark of TTN is a benign course. Respiratory distress develops by 6 hours of age, peaks at 1 day of age, and is resolved by 2 to 3 days. There is a spectrum of radiographic findings similar to those seen with mild-to-severe pulmonary edema. There is a combination of airspace opacification, interstitial edema, prominent and indistinct pulmonary vasculature, fluid in the fissures, pleural effusion, and cardiomegaly (Fig. 3-2). Lung volumes are normal to increased.

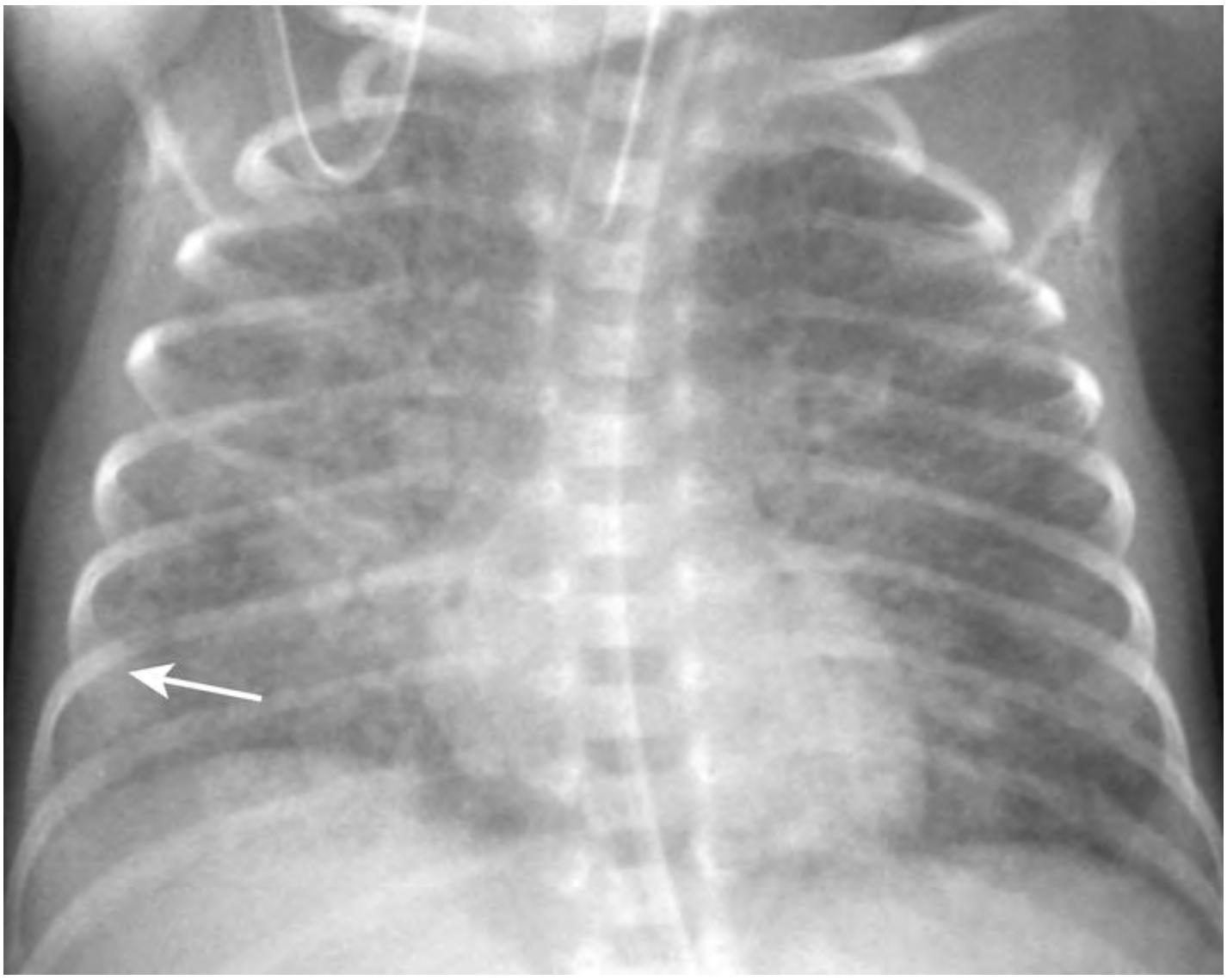
Neonatal Pneumonia

Neonatal pneumonia can be caused by a large number of infectious agents that can be acquired intrauterine, during birth, or soon after birth. With the exception of group B streptococcal pneumonia, which will be discussed separately, the radiographic appearance of neonatal pneumonia is that of

patchy, asymmetric perihilar densities and hyperinflation (Fig. 3-3). Pleural effusions may be present (Fig. 3-4). Such cases of neonatal pneumonia may have a similar radiographic appearance to and be indistinguishable from meconium aspiration syndrome, TTN, or surfactant-deficient disease (SDD) when using imaging alone.



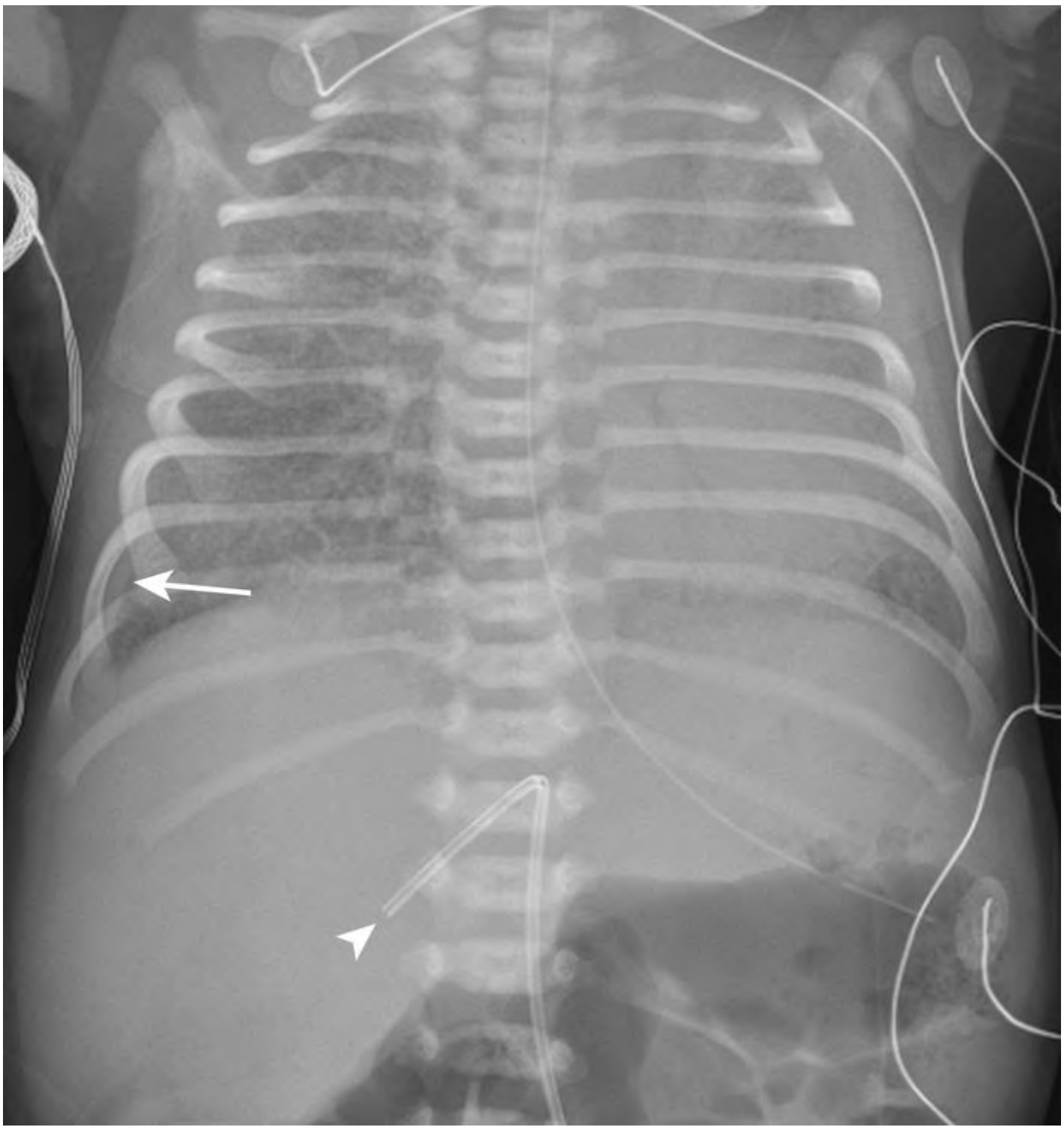
▪ **FIGURE 3-2** **Transient tachypnea of the newborn.**
Newborn chest radiograph shows normal lung volumes, cardiomegaly, indistinct pulmonary vascularity, mild diffuse haziness, and fluid in the minor fissure *(arrow)*. Within 24 hours the patient was asymptomatic.



▪ **FIGURE 3-3** **Neonatal pneumonia.**
Newborn chest radiograph shows large lung volumes and coarse, bilateral perihilar markings. Notice the small associated pleural effusion *(arrow)*.

Surfactant-Deficient Disease

SDD, or respiratory distress syndrome or hyaline membrane disease, is a common disorder, with approximately 40,000 new cases annually in the United States. It is primarily a disease of premature infants, affecting up to 50% of them, and it is the most common cause of death in live newborns. The risk of SDD increases with decreasing gestational age. SDD is related to the inability of premature type II pneumocytes to produce surfactant. Normally surfactant coats the alveolar surfaces and decreases surface tension, allowing for the alveoli to remain open. As a result of the lack of surfactant, there is alveolar collapse, resulting in noncompliant lungs. The radiographic findings reflect these pathologic changes (Fig. 3-5, *A* and *B*). Lung volumes are low. There are bilateral granular opacities that represent collapsed alveoli interspersed with open alveoli. Because the larger bronchi do not collapse, there are prominent air bronchograms. When the process is severe enough and the majority of alveoli are collapsed, there may be coalescence of the granular opacities, resulting in diffuse lung opacity. A normal film at 6 hours of age excludes the presence of SDD.

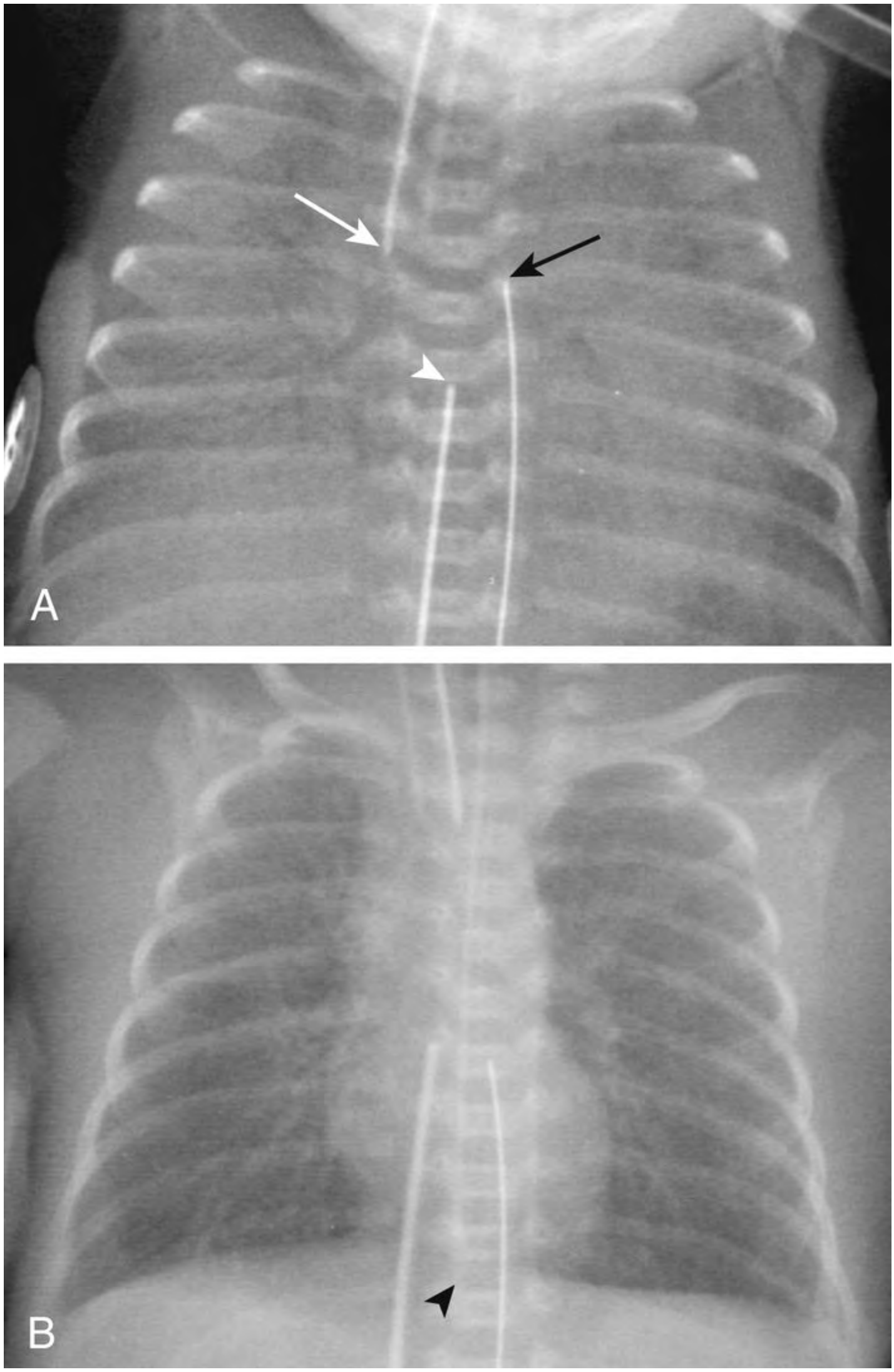


▪ **FIGURE 3-4** **Neonatal pneumonia.**
Newborn chest radiograph shows large lung volumes and coarse, perihilar markings on the right. The left lung shows diffuse ground-glass granularity with more confluent retrocardiac opacities with some air bronchograms. Note a small right pleural effusion *(arrow)*. The granularity associated with this case raises a differential diagnosis of surfactant deficiency disease. However, the right-sided pleural effusion favors infection because pleural effusions are quite uncommon with surfactant deficiency disease. Also note umbilical venous catheter with tip into right portal vein *(arrowhead)*. Tip should be at the junction of the right atrium and inferior vena cava.

Surfactant Replacement Therapy

One of the therapies for SDD is surfactant administration. Surfactant can be administered via nebulized or aerosol forms. It is administered into the trachea via a catheter or an adapted endotracheal tube. The administration of surfactant in neonates with SDD is associated with decreased oxygen and ventilator setting requirements, decreased air-block complications, decreased incidence of intracranial hemorrhage and bronchopulmonary dysplasia (BPD), and decreased death rate. However, there is an associated increased risk for development of patent ductus arteriosus and pulmonary hemorrhage, and there can be an acute desaturation episode in response to surfactant administration. Surfactant administration can be given on a rescue basis when premature neonates develop respiratory distress or can be given prophylactically in premature infants who are at risk. Prophylactic administration is commonly given immediately after birth and is becoming a more common practice. In response to surfactant administration, radiography may demonstrate complete, central, or asymmetric clearing of the findings of SDD (see Fig. 3-5). There is usually an increase in lung volumes. Neonates without radiographic findings of a response to surfactant have poorer prognoses than those who have radiographic evidence of a response. A pattern of alternating distended and collapsed acini

may create a radiographic pattern of bubblelike lucencies that can mimic pulmonary interstitial emphysema. Knowledge of when surfactant has been administered is helpful to render accurate interpretation of chest radiographs taken in the neonatal intensive care unit (NICU).



▪ **FIGURE 3-5** **SDD responding to surfactant therapy.**

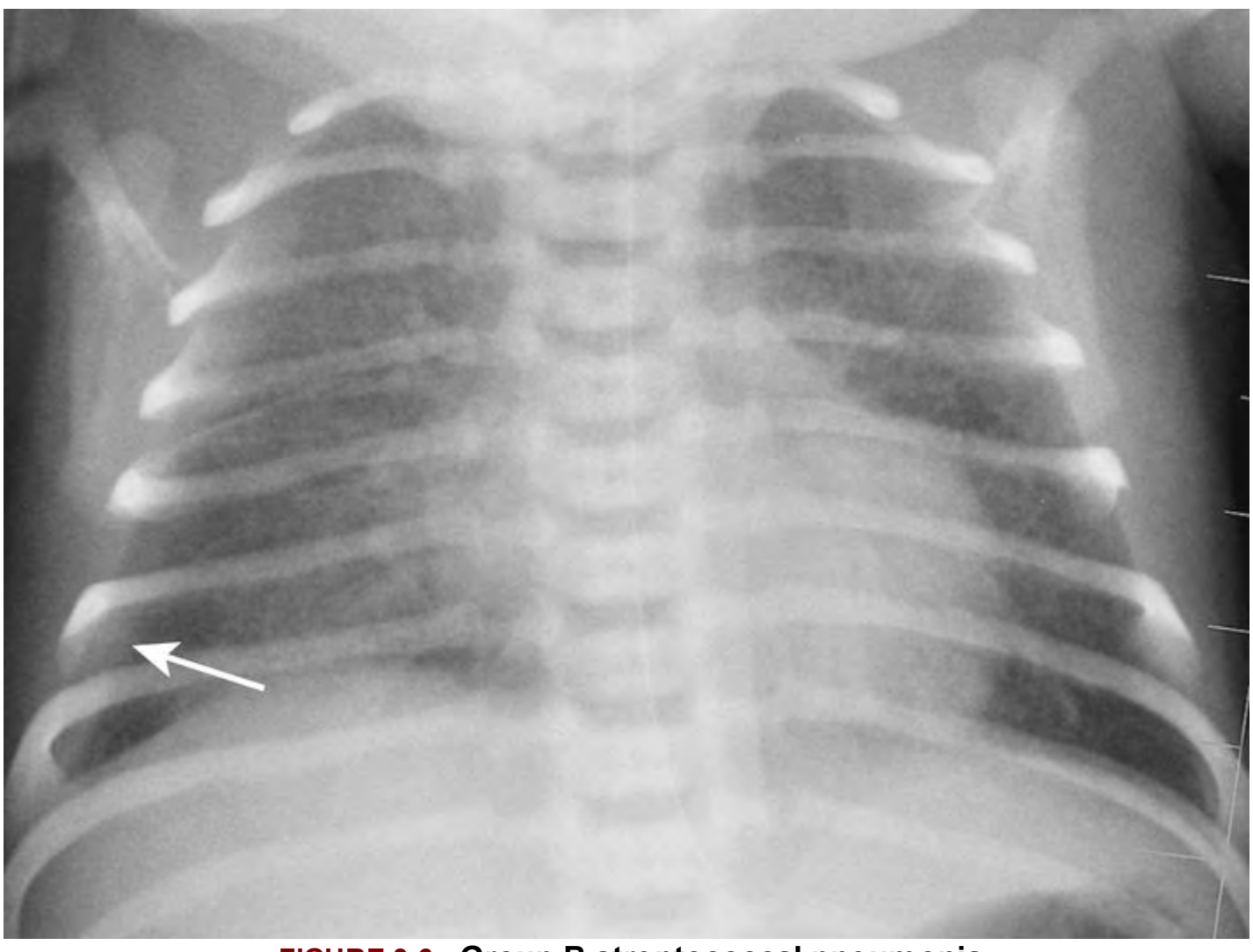
A, Radiograph shortly after birth shows low lung volumes, confluent densities, and prominent air bronchograms. Note the endotracheal tube tip *(white arrow)* terminates just above the carina and should be repositioned. There is an umbilical arterial catheter with its tip *(black arrow)* at the level of T4 and an umbilical venous catheter with its tip *(white arrowhead)* overlying the right atrium. Tip should be at the junction of the right atrium and inferior vena cava. **B,** Radiograph obtained immediately following surfactant administration shows increased lung volumes and decreased lung opacities. An enteric tube has been inserted in the interim with its tip *(black arrowhead)* overlying the lower third of the esophagus; should be advanced.

Group B Streptococcal Pneumonia

Group B (GBS) streptococcal pneumonia is the most common type of pneumonia in neonates. The infection is acquired during birth, and at least 25% of women in labor are colonized by the organism. Premature infants are more commonly infected than are term infants. In contrast to the other types of neonatal pneumonias, the radiographic findings include bilateral granular opacities and low lung volumes (Fig. 3-6), the identical findings in SDD. The presence of pleural fluid is a helpful differentiating factor because it is very uncommon in surfactant deficiency but has been reported in between 25% and 67% of cases of β-hemolytic streptococcal pneumonia.

Persistent Pulmonary Hypertension of the Newborn

Persistent pulmonary hypertension of the newborn (PPHN), or persistent fetal circulation, is a term often used in the NICU and is addressed here because it can be a source of confusion. The high pulmonary vascular resistance that is normally present in the fetus typically decreases during the newborn period. In normal conditions, after clamping the cord and with the first breaths, there is a drastic drop in pulmonary vascular resistance permitting the circulation that in utero bypasses the lungs, to perfuse the lungs. If this drastic decrease in pulmonary vascular resistance does not take place, blood would continue to bypass the lungs and pulmonary pressures would remain abnormally high; the condition is termed *persistent pulmonary hypertension*. It is a physiologic finding rather than a specific disease. It can be a primary phenomenon or it can occur secondary to causes of hypoxia, such as meconium aspiration syndrome, neonatal pneumonia, or pulmonary hypoplasia associated with congenital diaphragmatic hernia (CDH). These patients are quite ill. The radiographic patterns are variable and are more often reflective of the underlying cause of hypoxia than the presence of persistent pulmonary hypertension. Occasionally it may be seen in neonates with clear chest radiographs, and in these cases it is referred as primary PPHN.

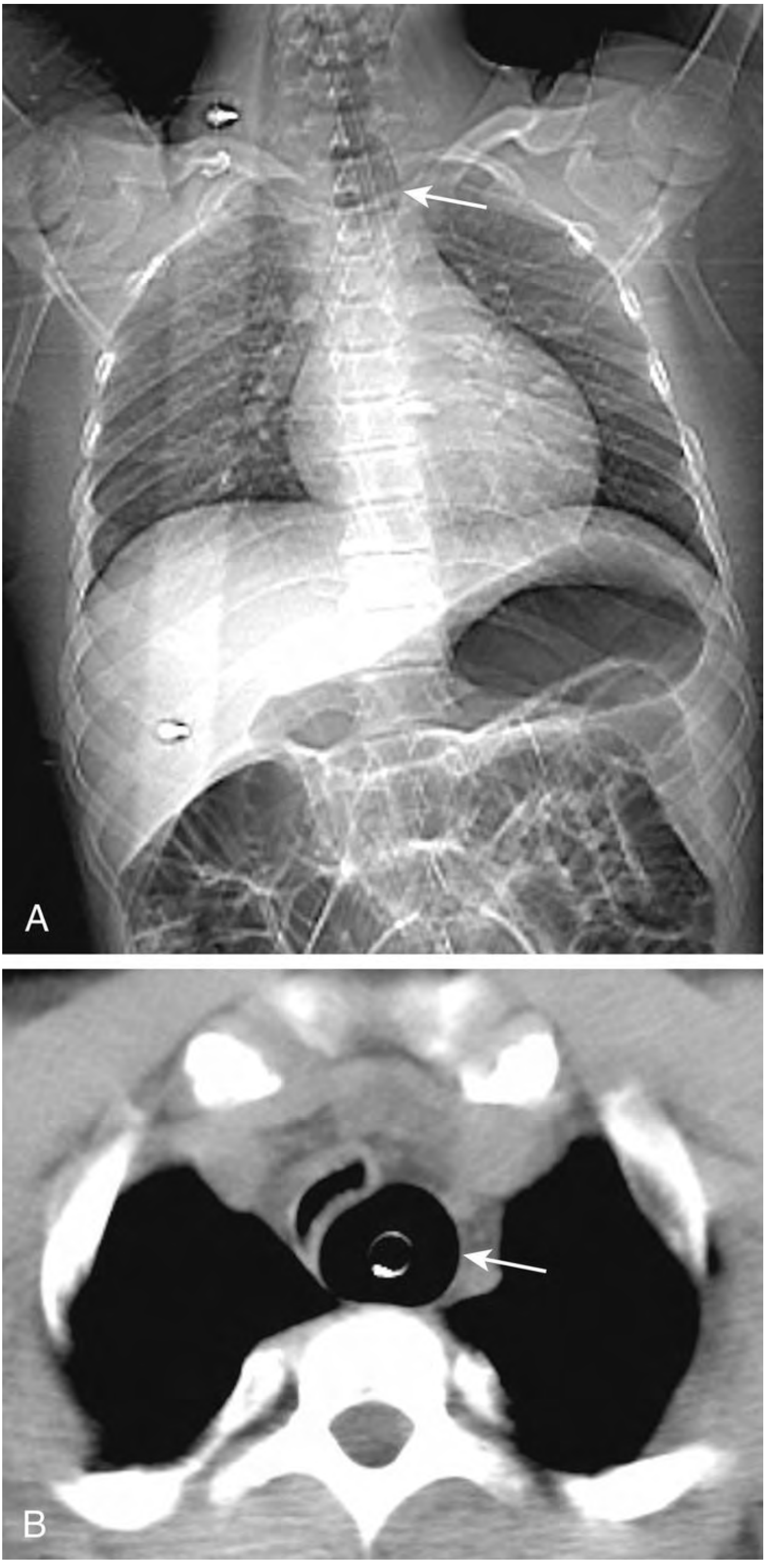


▪ **FIGURE 3-6** **Group B streptococcal pneumonia.**
Radiograph shows low lung volumes and diffuse granular opacities, similar in appearance to cases of surfactant deficiency. However, the right-sided pleural effusion *(arrow)* favors infection.

Neonatal Intensive Care Unit Support Apparatus

One of the primary roles of chest radiography in the NICU is to monitor support apparatus. They include endotracheal tubes, enteric tubes, central venous lines, umbilical arterial and venous catheters, and extracorporeal membrane oxygenation (ECMO) catheters. The radiographic evaluation of many of

these tubes is the same as that seen in adults and is not discussed here. When evaluating the positions of endotracheal tubes in premature neonates, it is important to consider that the length of the entire trachea may be only approximately 1 cm. Keeping the endotracheal tube in the exact center of such a small trachea is an impossible task for caregivers, and phone calls and reports suggesting that the tube needs to be moved 2 mm proximally may be more annoying than helpful. Direct phone communication may be more appropriately reserved for times when the tube is in a main bronchus or above the thoracic inlet. There is an increased propensity for inadvertent esophageal intubation to occur in neonates as compared with in adults. Although it would seem that esophageal intubation would be incredibly obvious clinically, this is not always the case. The authors have experienced cases in which a child has in retrospect been discovered to have been esophageally intubated for more than 24 hours. Therefore the radiologist may be the first to recognize esophageal intubation. Obviously, when the course of the endotracheal tube does not overlie the path of the trachea, the use of esophageal intubation is fairly obvious. Other findings of esophageal intubation include a combination of low lung volumes, gas within the esophagus, and gaseous distention of the bowel (Fig. 3-7).

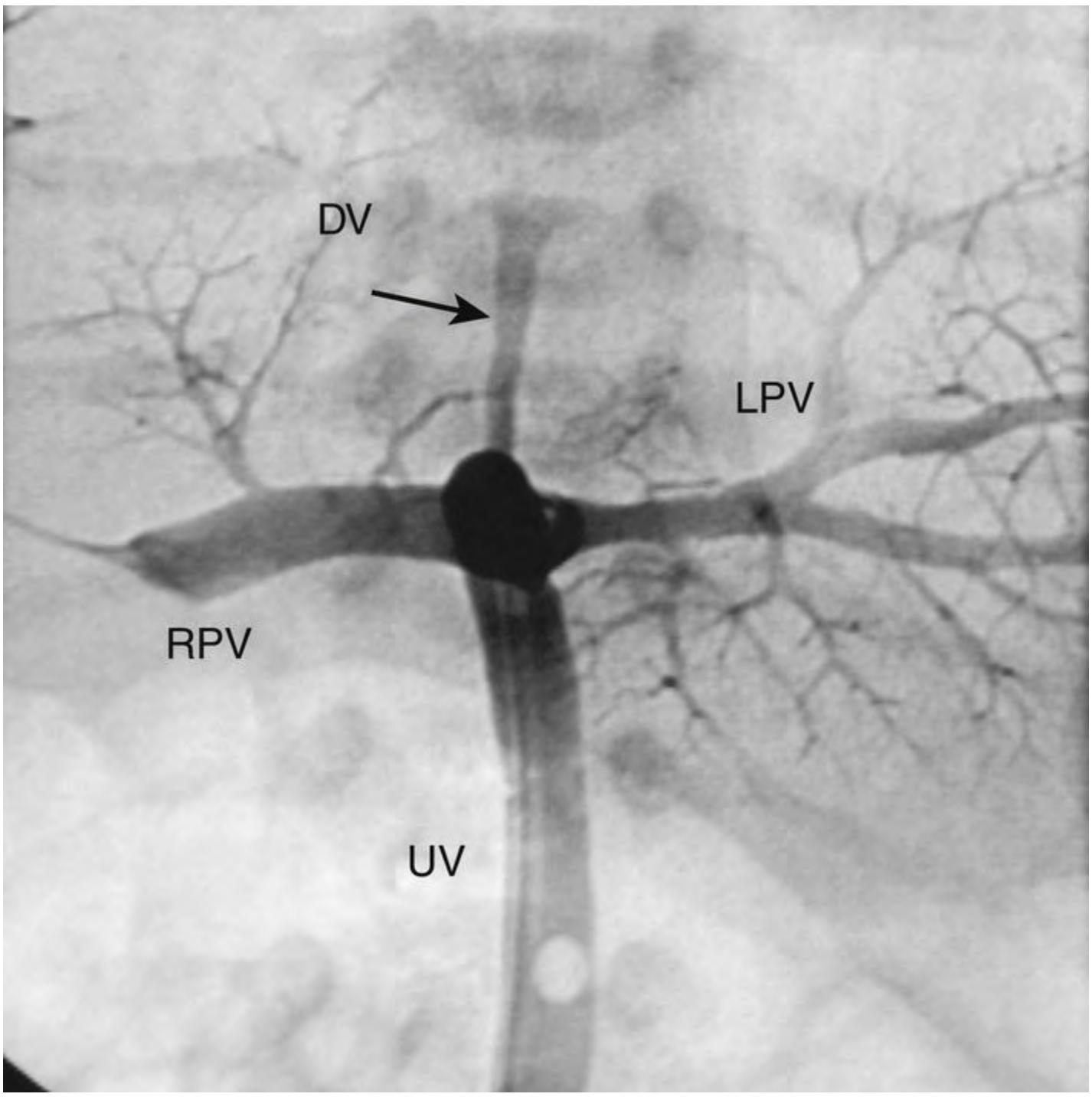

A
B

▪ **FIGURE 3-7** Esophageal intubation in an adolescent with severe craniofacial trauma and difficult intubation. **A,** Scout view shows the endotracheal tube overlying the expected location of the mid trachea. The balloon cuff *(arrow)* is quite distended. Visualized bowel loops are moderately air filled. **B,** CT shows the markedly inflated cuff of the balloon *(arrow)* within the esophagus resulting in mass effect and compression of the trachea.

Umbilical Arterial and Venous Catheters

Umbilical arterial and venous catheters are commonly used in the NICU. Umbilical arterial catheters pass from the umbilicus inferiorly into the pelvis via the umbilical artery to the iliac artery. The catheters then turn cephalad within the aorta (see Fig. 3-5). These catheters can be associated with thrombosis of the aorta and its branches. Therefore it is important to avoid positioning the catheter with the tip at the level of the branches of the aorta (celiac, superior mesenteric, and renal arteries) or at the origin of the great arteries (arch). There are two acceptable umbilical arterial catheter positions: *high lines* have their tips at the level of the descending thoracic aorta (T8-T10) and *low lines* have their tips below the level of L3. The catheter tip should not be positioned between T10 and L3 because of the risk for major arterial thrombosis. There is no clear consensus as to whether a high or low umbilical artery catheter line is better, and both positions are still currently used, although some authors advocate that the high position has fewer complications.

The pathway of the umbilical venous catheter is umbilical vein to left portal vein to ductus venosus, the most superior portion of the ductus venosus joins, or becomes part of, one of the hepatic veins as they enter the inferior vena cava (Fig. 3-8). In contrast to umbilical arterial catheters, the course is in the superior direction from the level of the umbilicus. The ideal position of an umbilical venous catheter is with its tip at the junction of the right atrium and the inferior vena cava at the level of the hemidiaphragm (see Figs. 3-4 and 3-5). The umbilical venous catheter may occasionally deflect into the portal venous system rather than passing into the ductus venosus. Complications of such positioning can include hepatic hematoma or abscess.



▪ **FIGURE 3-8** Anatomy of the course of the umbilical vein *(UV)* catheter as demonstrated by contrast injection of umbilical catheter performed because of inability to advance UV catheter. Note course of UV to portal vein to ductus venosus *(DV; arrow)*. *LPV,* Left portal vein; *RPV,* right portal vein.

Peripherally Inserted Central Catheters in Children

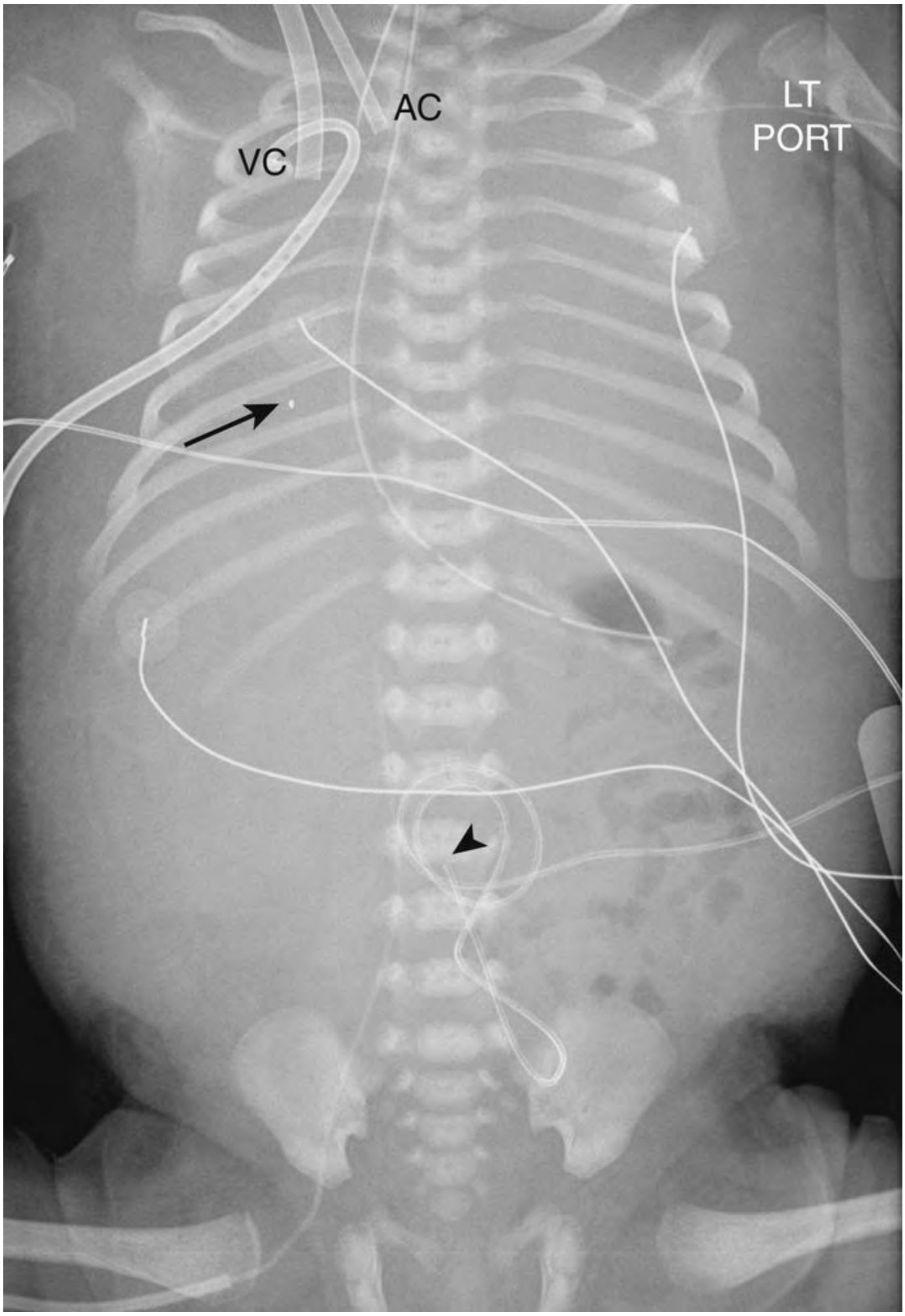
One of the more common lines now seen in children, as in adults, is peripherally inserted central catheters (PICCs). In contrast to adults, in whom some of the PICCs can be as large as 6F, the PICC lines used in children, particularly infants, are often small in caliber (2F or 3F) so that they can be placed into their very small peripheral veins. These small-caliber PICCs can be very difficult to see on chest radiography, so some of them must be filled with contrast to be accurately visualized. The tip of the PICC line that enters the child from the upper extremity or scalp should be positioned with the tip in the midlevel of the superior vena cava (see Fig. 3-27). It is essential that PICC lines not be left in place with the tip well into the right atrium. Particularly with the small-caliber lines, the atrium can be lacerated, leading to pericardial tamponade, free hemorrhage, or death. Many such cases have been reported nationally. In addition, the PICC should not be too proximal in the superior vena cava because the distal portion of the line can flip from the superior vena cava into the contralateral brachiocephalic or jugular vein. At many children's hospitals, the PICC lines are inserted in a dedicated interventional radiology suite by a team of nurses, with supervision by pediatric interventional radiologists. Ultrasound is often used to guide vein cannulation, and certified child-life specialists coach most kids through the procedure often without having to sedate them. Fluoroscopy is used at the end of the procedure to adjust and document tip position in the cavoatrial junction.

Extracorporeal Membrane Oxygenation

ECMO is a last-resort therapy usually reserved for respiratory failure that has not responded to other treatments. ECMO is essentially a prolonged form of circulatory bypass of the lungs and is used only in

patients who have reversible disease and a chance for survival. The majority of neonates who are treated with ECMO have respiratory failure as a result of meconium aspiration, persistent pulmonary hypertension (resulting from a variety of causes), severe congenital heart disease, or CDH. ECMO seems to be used less commonly now than it was in the 1990s.

There are two types of ECMO: arteriovenous and venovenous. In arteriovenous ECMO, the right common carotid artery and internal jugular veins are sacrificed. The arterial catheter is placed via the carotid and positioned with its tip overlying the aortic arch. The venous catheter is positioned with its tip over the right atrium (Fig. 3-9). One of the main roles of a chest radiograph of children on ECMO is to detect any potential migration of the catheters. Careful comparison with previous studies to make sure that the catheters are not coming out or moving too far in is critical. These patients have many bandages and other items covering the external portions of the catheters, so migration may be hard to detect on physical examination. In addition, anasarca is invariable during ECMO because the increasing soft tissue edema may result in accidental dislodgement and subsequent accidental decannulation. Note that there are various radiographic appearances of the ECMO catheters. Some catheters end where the radiopaque portion of the tube ends, and others have a radiolucent portion with a small metallic marker at the tip (see Fig. 3-9). It is common to see white-out of the lungs soon after a patient is placed on ECMO as a result of sudden decrease in airway pressure, decreased ventilator settings, and third-space shifting of fluid (see Fig. 3-9). Patients on ECMO are anticoagulated and are therefore at risk for hemorrhage.



▪ **FIGURE 3-9 Extracorporeal membrane oxygenation (ECMO) catheter placement for CDH repair.** Note venous ECMO cannula *(VC)* has a radiopaque proximal portion and a lucent distal portion. The tip of the venous catheter is marked by a small radiopaque metallic marker *(arrow)* and is actually in the right atrium. Note the arterial ECMO cannula *(AC)* with tip in region of aortic arch. In addition, note "low"-type umbilical arterial catheter with tip overlying the abdominal aorta at the level of the lower endplate of L3 *(arrowhead)*. It should be repositioned. Enteric tube terminates in the stomach, and a pleural pigtail is seen overlying the right hemithorax. The lungs are completely opacified. Notice severe anasarca.

Types of Ventilation: High-Frequency Oscillator versus Conventional Ventilation

High-frequency oscillators are commonly used to treat neonates in the NICU. In contrast to conventional ventilation, high-frequency oscillators use supraphysiologic rates of ventilation with very low tidal volumes. Conventional ventilation has been likened to delivering a cupful of air

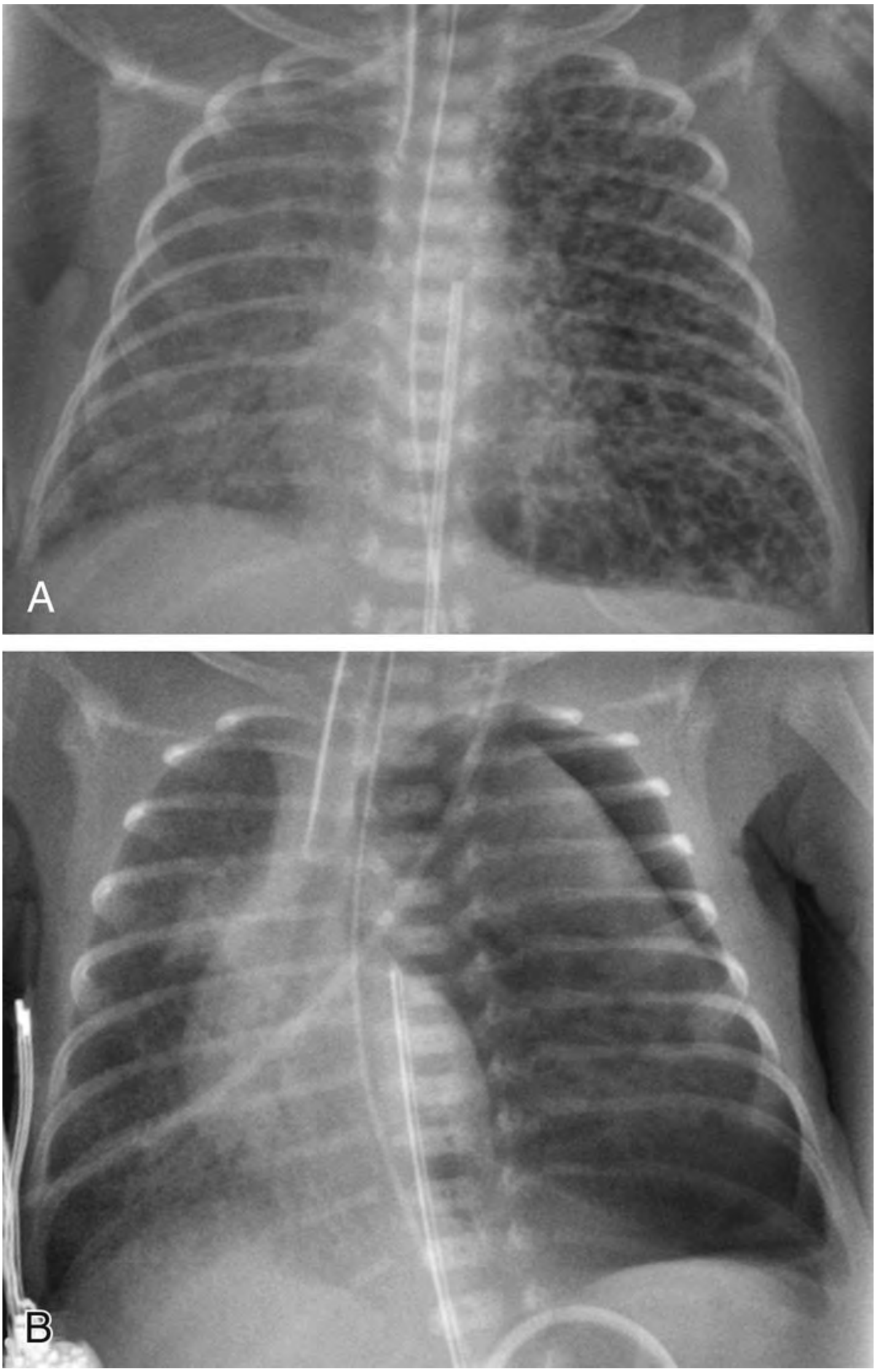
approximately 20 times a minute. In contrast, high-frequency oscillation is like delivering a thimbleful of air approximately 1000 times per minute. The air is vibrated in and out of the lung, and appropriate gas exchange occurs at significantly lower peak inspiratory pressures than those required with conventional ventilation. The mechanism of oscillators is poorly understood. In conventional ventilation, the diaphragm moves up and down, whereas during high-frequency ventilation the diaphragm stays parked at a certain anatomic level. This level can be adjusted by changing the mean airway pressure of the oscillator. Caregivers usually like to maintain the diaphragm at approximately the level of the tenth posterior ribs. In general the radiographic appearance of neonatal pulmonary diseases is not affected by whether the patient is being ventilated by conventional or high-frequency ventilation.

Complications in the Neonatal Intensive Care Unit

As in adult intensive care units, major complications detected by chest radiographs include those related to air-leak complications, lobar collapse, or acute diffuse pulmonary consolidation. Another type of complication seen in neonates is the development of BPD. Imaging findings of lobar collapse and air-block complications, such as pneumothorax, pneumomediastinum, and pneumopericardium, are similar in neonates and adults. One type of air-block complication that is unique to neonates is pulmonary interstitial emphysema.

Pulmonary Interstitial Emphysema

In patients with severe surfactant deficiency, ventilatory support can result in marked increases in alveolar pressure, leading to perforation of alveoli. The air that escapes into the adjacent interstitium and lymphatics is referred to as *pulmonary interstitial emphysema* (PIE). PIE appears on radiographs as bubblelike or linear, nonbranching lucencies and can be focal or diffuse (Fig. 3-10). The involved lung is usually noncompliant and is seen to have a static volume on multiple consecutive films. The finding is typically transient. The importance of detecting PIE is that it serves as a warning sign for other impending air-block complications, such as pneumothorax, and its presence can influence caregivers in decisions, such as switching from conventional to high-frequency ventilation.



▪ **FIGURE 3-10** **Pulmonary interstitial emphysema in a premature infant with surfactant deficiency disease.**

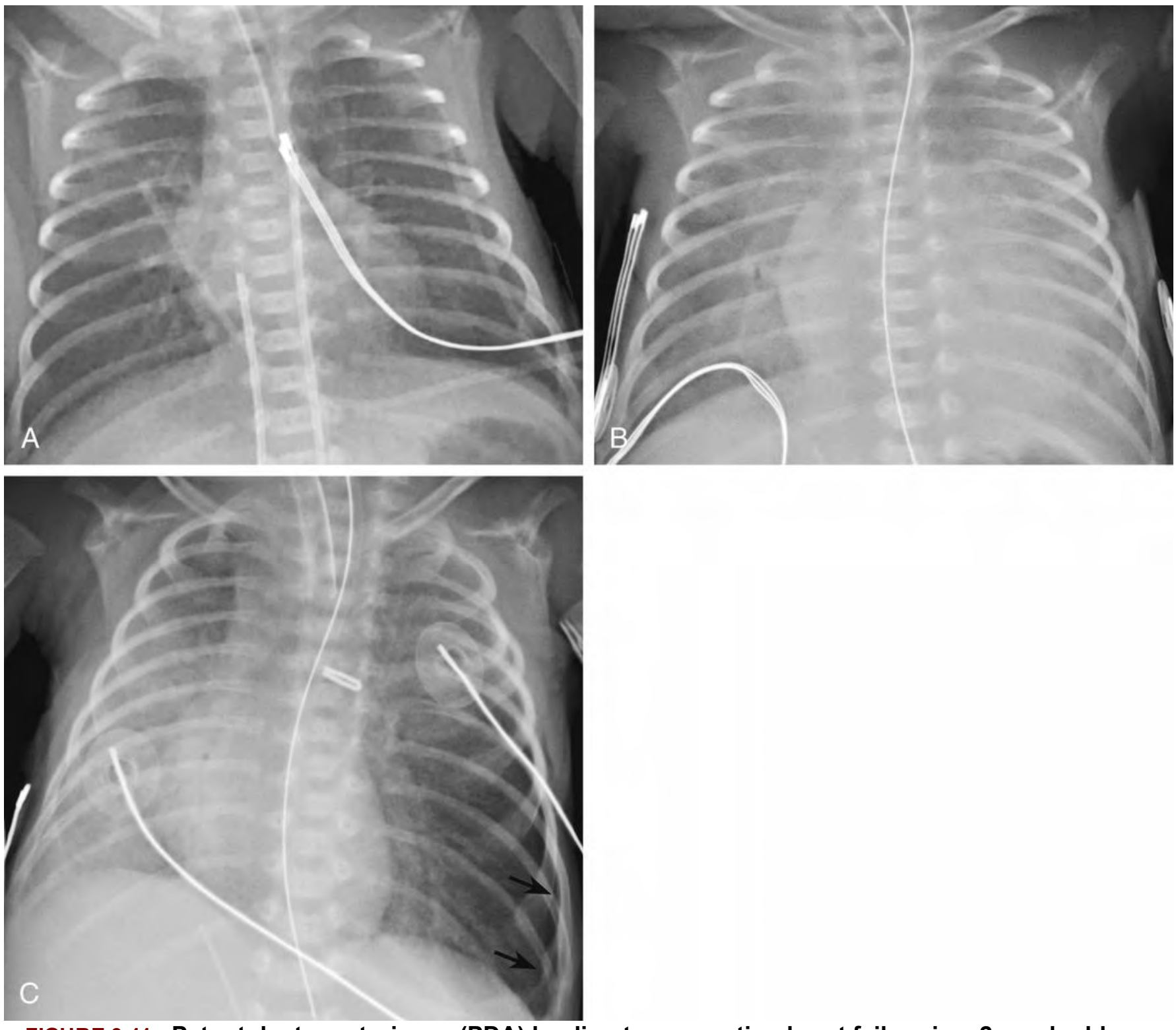
A, Chest radiograph shows asymmetric bubblelike, nonbranching lucencies within the left lung consistent with PIE. **B,** The child developed a tension pneumothorax on subsequent exam.

It can be difficult to differentiate diffuse PIE from the bubblelike lucencies that are associated with developing BPD. When encountering this scenario, the patient's age can help to determine which is more likely. Most cases of PIE occur in the first week of life, a time at which BPD is very unlikely. In patients older than 4 weeks, BPD is more likely. In addition, in patients who have undergone a series of daily films, PIE may be noted to occur abruptly, whereas BPD tends to occur gradually. As previously mentioned, SDD partially treated by surfactant replacement can cause a pattern of lucencies that may mimic PIE as well.

Rarely PIE can persist and develop into an expansive, multicystic mass. The air cysts can become large enough to cause mediastinal shift and compromise pulmonary function. Often the diagnosis is indicated by sequential radiography showing evolution of the cystic mass from original findings typical of PIE. In unclear cases, computed tomography (CT) demonstrates that the air cysts are in the interstitial space by showing the bronchovascular bundles being positioned within the center of the air cysts. The bronchovascular bundles appear as linear or nodular densities in the center of the cysts.

Causes of Acute Diffuse Pulmonary Consolidation

Acute diffuse pulmonary consolidation is nonspecific in neonates, as it is in adults, and can represent blood, pus, or water. In the neonate the specific considerations include edema, which may be secondary to the development of patent ductus arteriosus (Fig. 3-11); pulmonary hemorrhage, to which surfactant therapy predisposes; worsening surfactant deficiency (during the first several days of life but not later); or developing neonatal pneumonia (Table 3-2). Diffuse microatelectasis is another possibility because neonates have the propensity to artifactually demonstrate diffuse lung opacity on low lung volume films (expiratory technique; Fig. 3-12, *A* and *B*); this should not be mistaken for another cause of consolidation. Such radiographs showing low lung volumes offer little information concerning the pulmonary status of the patient and should be repeated when clinically indicated.



▪ **FIGURE 3-11** **Patent ductus arteriosus (PDA) leading to congestive heart failure in a 2-week-old premature neonate.**

A, Before development of PDA, radiograph shows normal-sized heart and mild right mid lung field atelectasis with otherwise clear lungs. **B,** After development of PDA, radiograph shows cardiac enlargement and bilateral lung airspace opacification. **C,** Radiograph obtained immediately following ductus ligation shows decrease in heart size and improvement in lung aeration. Notice postsurgical change in the left fourth rib, very small amount of subcutaneous emphysema, and tiny left basilar pneuthorax *(arrow)*.

Bronchopulmonary Dysplasia

BPD, or chronic lung disease of prematurity, is a common complication, seen in premature infants and is associated with significant morbidity rates. BPD typically occurs in neonates treated with oxygen and positive pressure ventilation for respiratory failure, usually SDD. The definition of BPD has evolved over time; currently, the most accepted definition is that of oxygen dependence for at least 28 days after birth, whereas the severity is graded in proportion to the respiratory support required at term. It is uncommon in children born at greater than 32 weeks of gestational age, but it occurs in more than 50% of premature infants born at less than 1000 g. BPD is the most common chronic lung disease of infancy.

TABLE 3-2

Causes of Acute Diffuse Pulmonary Consolidation in Neonates

- Edema: patent ductus arteriosus
- Hemorrhage
- Diffuse microatelectasis: artifact

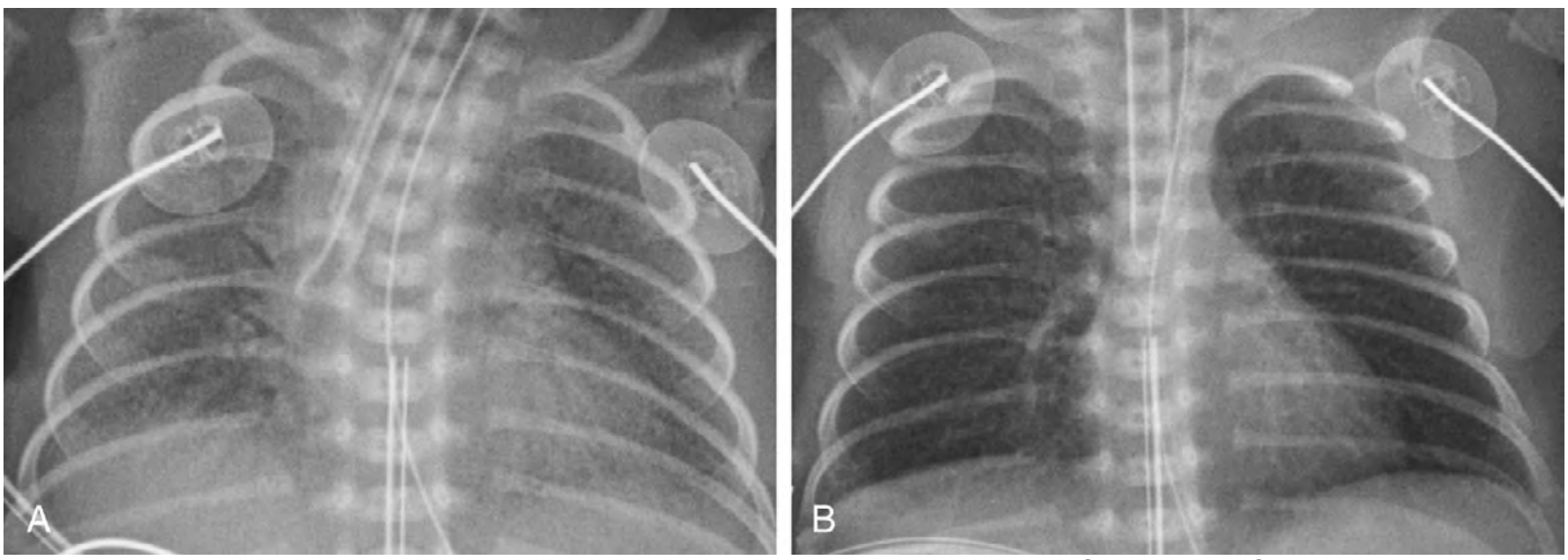
- Worsening surfactant deficiency (only during first days of life)
- Pneumonia

BPD is related to injury to the lungs that is thought to result from some combination of mechanical ventilation and oxygen toxicity. Although four discrete and orderly stages of the development of BPD were originally described, they are not seen commonly and are probably not important to know. BPD typically occurs in a premature infant who requires prolonged ventilator support. At approximately the end of the second week of life, persistent hazy density appears throughout the lungs. Over the next weeks to months a combination of coarse lung markings, bubblelike lucencies, and asymmetric aeration can develop (Fig. 3-13). Eventually, focal lucencies, coarse reticular densities, and bandlike opacities develop. In childhood survivors of BPD, many of these radiographic findings decrease in prominence over the years and only hyperaeration may persist. The radiographic findings may completely resolve. Clinically, many children with severe BPD during infancy may eventually improve to normal pulmonary function or may only have minor persistent problems such as exercise intolerance, predisposition to infection, or asthma.

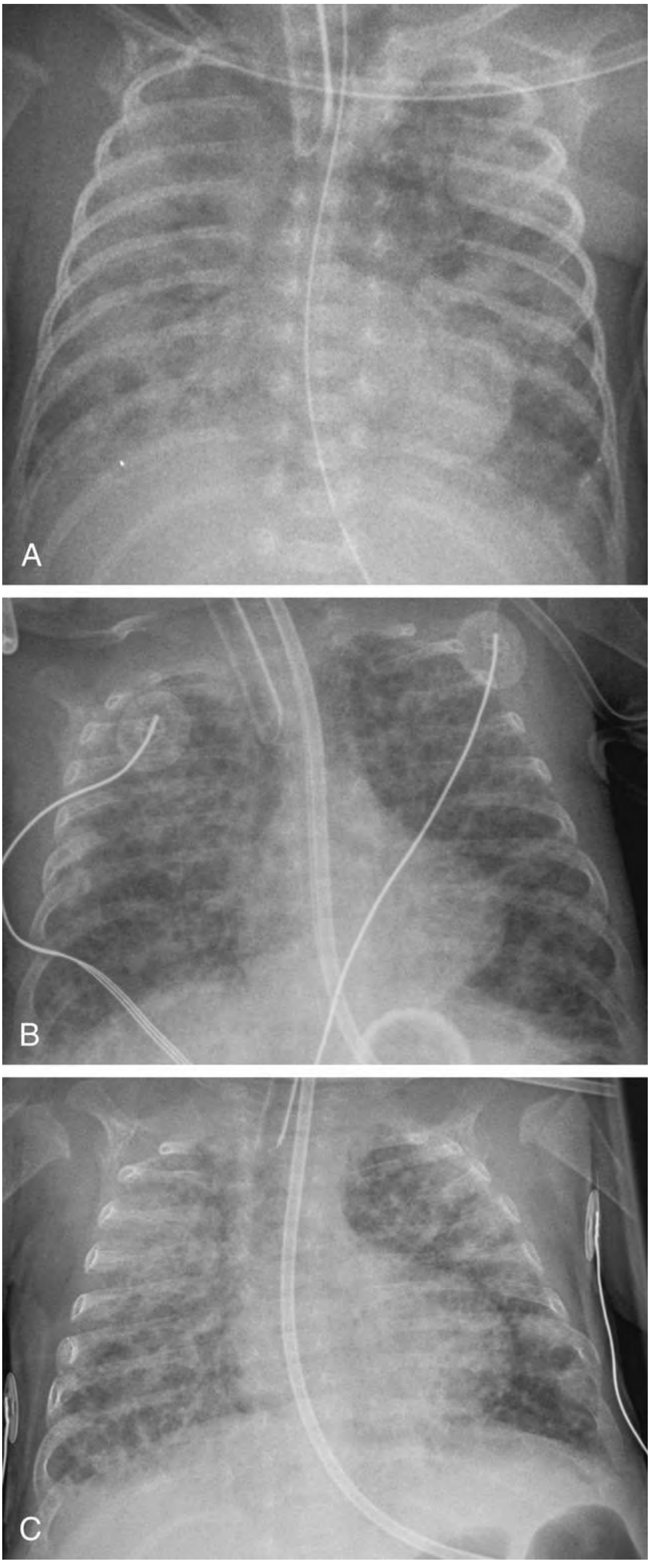
Wilson-Mikity syndrome is a confusing and controversial term. It historically refers to the development of BPD in the absence of mechanical ventilation. It is now believed to be related to an underlying alveolar growth disorder.

Focal Pulmonary Lesions in the Newborn

In contrast to diffuse pulmonary disease in newborns, focal masses can present with respiratory distress due to compression of otherwise normal lung. Most of these focal masses are related to congenital lung lesions. Congenital lung lesions may appear solid, as air-filled cysts, or mixed in appearance. The differential for a focal lung lesion can be separated on the basis of whether the lesion is lucent or solid appearing on chest radiography (Table 3-3). The most likely considerations for a lucent chest lesion in a newborn are congenital lobar emphysema, congenital pulmonary airway malformation (CPAM) persistent PIE, and CDH. CT may be helpful in differentiating among these lesions by demonstrating whether the abnormal lucency is related to air in distended alveoli, in the interstitium, or in abnormal cystic structures. Lesions that typically appear solid during the neonatal period include sequestration and bronchogenic cyst. Many of these lesions can present in children beyond the neonatal period, and those aspects of these entities are also discussed here.



▪ **FIGURE 3-12** **Expiratory chest radiograph mimicking heart failure in infant.**
A, Initial radiograph shows prominent size of cardiothymic silhouette, indistinctness of pulmonary vascularity, and low lung volumes. Note right main bronchus intubation. **B,** Repeat radiograph obtained immediately after **A** shows clear lungs and normal heart size.


A
B
C

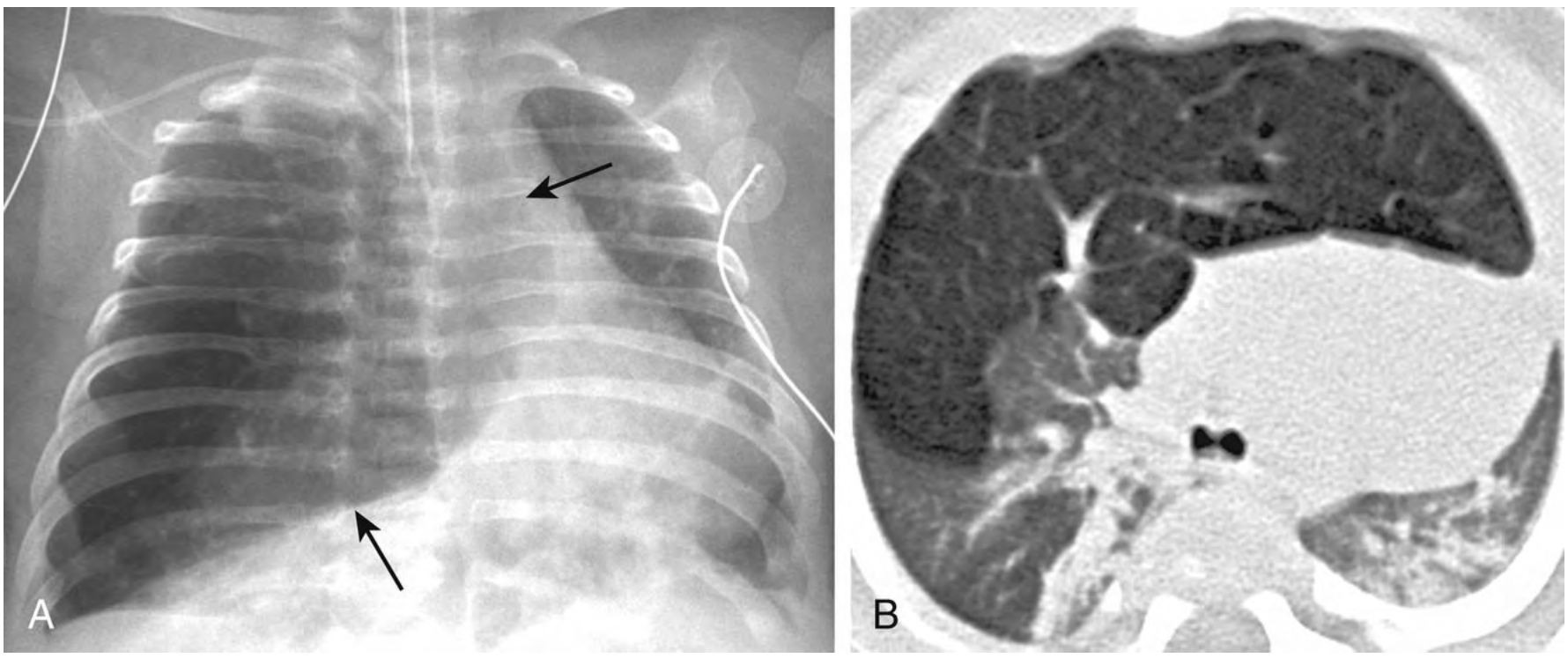
▪ **FIGURE 3-13** **Bronchopulmonary dysplasia in a premature neonatal girl.**
A, Chest radiograph at 20 days of life shows persistent bilateral lung opacities. **B,** Chest radiograph at 35 days of life shows coarsening of the lung markings. **C,** Chest radiograph at 60 days of life shows increased coarse lung markings and development of diffuse bubblelike lucencies.

The following sections are divided into specific congenital lesions. However, it has been increasingly recognized that there can be mixed or hybrid lesions, which show characteristics of more than one type of lesion (see Fig. 3-16). The most common mixed lesions are those that show characteristics of both congenital pulmonary airway malformation (CPAM) and sequestration. Currently, the majority of the congenital lung lesions are believed to be the result of fetal airway obstruction with varying degree of associated dysplastic changes. This explains the significant overlap of imaging findings of the various lesions. Bronchial atresia is the most commonly identified type of lesion on resected specimens and is found in 69% of CPAM lesions and in 100% of bronchopulmonary sequestrations.

It is also worth mentioning that there has been a change in the way these lesions present that is related to the increased use of prenatal ultrasound and magnetic resonance imaging (MRI). Historically, congenital lung lesions were identified when the infant became symptomatic. Indeed, the most common clinical presentation in cases of underlying bronchopulmonary sequestration was that of a young adult with recurrent pyogenic pneumonias of progressive severity. In the current clinical algorithms, most of the congenital lung lesions we currently see are identified and followed through fetal life, with additional postnatal imaging obtained shortly after birth. A significant number of these children are asymptomatic. This has raised issues related to when and whether to perform surgical treatment in infants with asymptomatic lesions.

TABLE 3-3
Focal Lung Lesions in Neonates on Radiography

Lucent Lesions	Solid Lesions
Congenital lobar emphysema	Sequestration
Congenital pulmonary airway malformation	Bronchogenic cyst
Pulmonary interstitial emphysema	Congenital cystic adenomatoid malformation
Congenital diaphragmatic hernia	



▪ **FIGURE 3-14** **Congenital lobar emphysema.**
A, Frontal radiograph obtained at 1 day of age shows diffuse lucency and enlargement of right upper lobe *(arrows)*. **B,** CT scan shows hyperlucent and enlarged left upper lobe with asymmetric attenuation of vascular structures and increased space between interstitial septa.

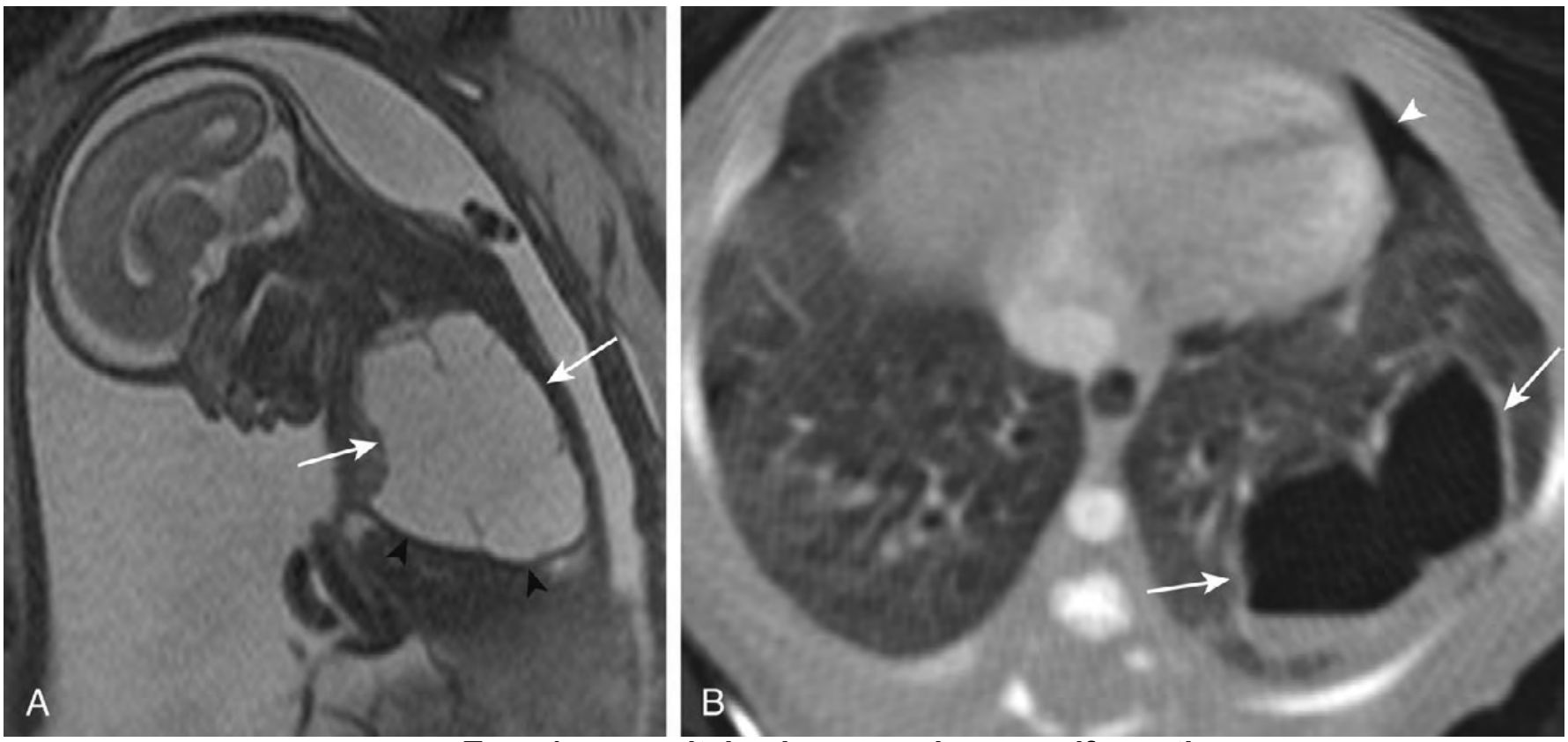
Congenital Lobar Emphysema

Also referred to as congenital lobar hyperinflation, congenital lobar overinflation, and infantile lobar

emphysema, congenital lobar emphysema is related to overexpansion of alveoli, but the mechanism is debated. The alveolar walls are maintained; therefore there is not true emphysematous change. Some reports suggest a ball-valve type of anomaly in the bronchus leading to the affected lung, which causes progressive air trapping. Most cases present with respiratory distress during the neonatal period; 50% present within the first month, and 75% present within the first 6 months of life. There can be associated anomalies, usually cardiac, but they occur in the minority of patients with congenital lobar emphysema. There is a lobar predilection; the most common site is the left upper lobe (43%), followed by the right middle lobe (35%) and right upper lobe (21%), with less than 1% in each of the other lobes. On chest radiography a hyperlucent, hyperexpanded lobe is seen (Fig. 3-14, *A* and *B*). On initial radiographs the lesion may appear to be a soft tissue density because of retained fetal lung fluid. This density resolves and is replaced by progressive hyperlucency. On CT the air is in the alveoli, so the interstitial septa and bronchovascular bundles are at the periphery (not the center) of the lucency (see Fig. 3-14). The air spaces are larger than those in the adjacent normal lung, and the pulmonary vessels appear attenuated. The treatment is lobectomy.

Congenital Pulmonary Airway Malformation

CPAM, or CCAM or dysplastic lesions caused by overgrowth of mesenchymal elements and airway maldevelopment, is a congenital adenomatoid proliferation that replaces normal alveoli. The majority are detected prenatally or are present with respiratory distress at birth. Most involve only one lobe and, in contrast to congenital lobar emphysema, there is no lobar predilection. CPAMs were originally classified by Stocker into three types based on cyst size and microscopic similarities to presumed sites of origin of the malformation along the airway. Type 1 shows cysts greater than 2 cm with probable bronchial or bronchiolar origin; type 2 shows more uniform cysts measuring less than 2 cm with probable bronchiolar origin; and type 3 appears solid or shows very small cysts (<0.2 cm) with probable bronchiolar or alveolar origin. Subsequently, Langston developed a more comprehensive pathologic classification of all congenital lung malformations, which is the most accepted at present. In this classification the type 1 CPAM is named large cyst type and the type 2 CPAM is named small cyst type based on similar cyst size and histologic criteria. In this classification type 3 CPAM is excluded because it is considered to represent a form of pulmonary hyperplasia. Stocker later expanded his CPAM classification to include five types; however, the Langston classification is the most currently accepted because it correlated well with findings. In fetal imaging the classification of these anomalies is also mainly based on cyst size as microcysts (<5 mm) and macrocysts (>5 mm). Given the controversial and confusing terminology, it is best to thoroughly describe the imaging findings that characterize the malformation to guide management because CPAMs can have multiple appearances when imaged. We include in our reports the gross number of cysts (e.g., single, several, or multiple), size of the largest cyst, lobe or lobes involved, degree of aeration of the CPAM, and presence or absence of an aberrant, systemic vessel. CPAMs communicate with the bronchial tree at birth and therefore fill with air within the first hours to days of life. On radiography and CT a completely cystic, mixed cystic and solid, or completely solid mass is seen depending on the number and size of cysts and whether those cysts contain air or fluid (Figs. 3-15, *A-C,* and 3-16, *A-C*). The management of symptomatic CPAM is surgical resection. The management of asymptomatic CPAM is currently somewhat controversial. However, many caregivers advocate elective resection because these lesions are at increased risk for infection and, rarely, type 1 or large cyst lesions may develop malignancy.



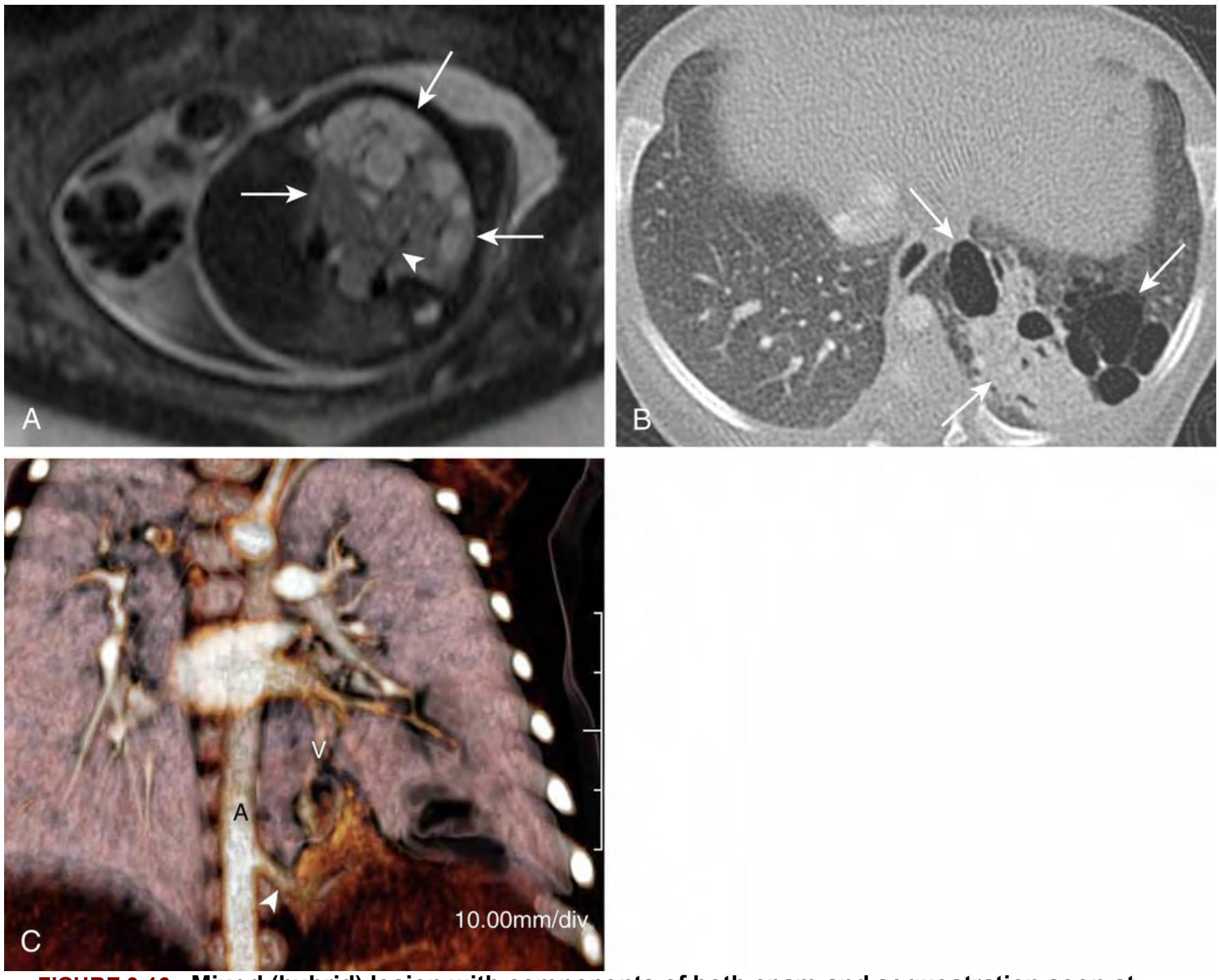
▪ **FIGURE 3-15** **Type 1 congenital pulmonary airway malformation.**
A, Sagittal fetal MR image shows hyperexpanded, high-signal lesion *(arrows)* in right lung with inversion of the diaphragm *(black arrowheads)*. The fetus developed hydrops and was treated with in utero thoracoamniotic shunt. **B,** CT soon after birth shows large, lucent, lobulated lesion *(arrows)* in left lung. Notice tiny left pneumothorax *(white arrowhead)*.

A scenario encountered with increasing frequency is a prenatally diagnosed lung mass that becomes less prominent on serial prenatal ultrasounds or MR examinations and demonstrates only subtle findings or is not detected on a chest radiograph obtained soon after birth. Almost all such lesions are CPAMs and demonstrate abnormalities on CT, even in light of a normal chest radiograph.

Many CPAMs identified prenatally are followed with MRI (see Fig. 3-15), and much has been learned about the nature of these lesions. CPAMs tend to increase in size until approximately 25 weeks of gestation. The mass of the CPAMs then tends to regress over time, sometimes dramatically. Compression of the contralateral lung by a large mass and development of fetal hydrops are associated with high mortality rates. Fetal intervention is typically reserved for cases with hydrops; management options include dominant cyst aspiration and fetal surgery with resection of the lesion. Trials using maternal steroids have shown promise in shrinking the CPAM volumes and avoiding other interventions.

Congenital Diaphragmatic Hernia

CDHs are usually secondary to posterior defects in the diaphragm (Bochdalek hernia) and are more common on the left side by a ratio of 5 to 1. CDHs are isolated in 50% to 60% of the cases, but it also may occur as part of genetic syndrome, related to chromosomal abnormalities, or as part of a complex but nonsyndromic set of findings. Most infants with CDHs present at birth with severe respiratory distress. The hernia may contain stomach, small bowel, colon, or liver. The radiographic appearance depends on the hernia contents and on whether there is air within the herniated viscera. On initial radiographs, before the introduction of air into the viscera, the appearance may be radiopaque. Later, and more commonly, the herniated viscera contain air and the hernia appears as an air-containing cystic mass. Fewer air-filled viscera in the abdomen than expected and an abnormal position of support apparatus, such as a nasogastric tube within a herniated stomach, are obvious clues that support the diagnosis (Fig. 3-17). Often a nasogastric tube becomes lodged at the esophagogastric junction because of the acute turn in the herniated stomach. This can be a supportive finding of the diagnosis.



▪ **FIGURE 3-16 Mixed (hybrid) lesion with components of both cpam and sequestration seen at pathology.**

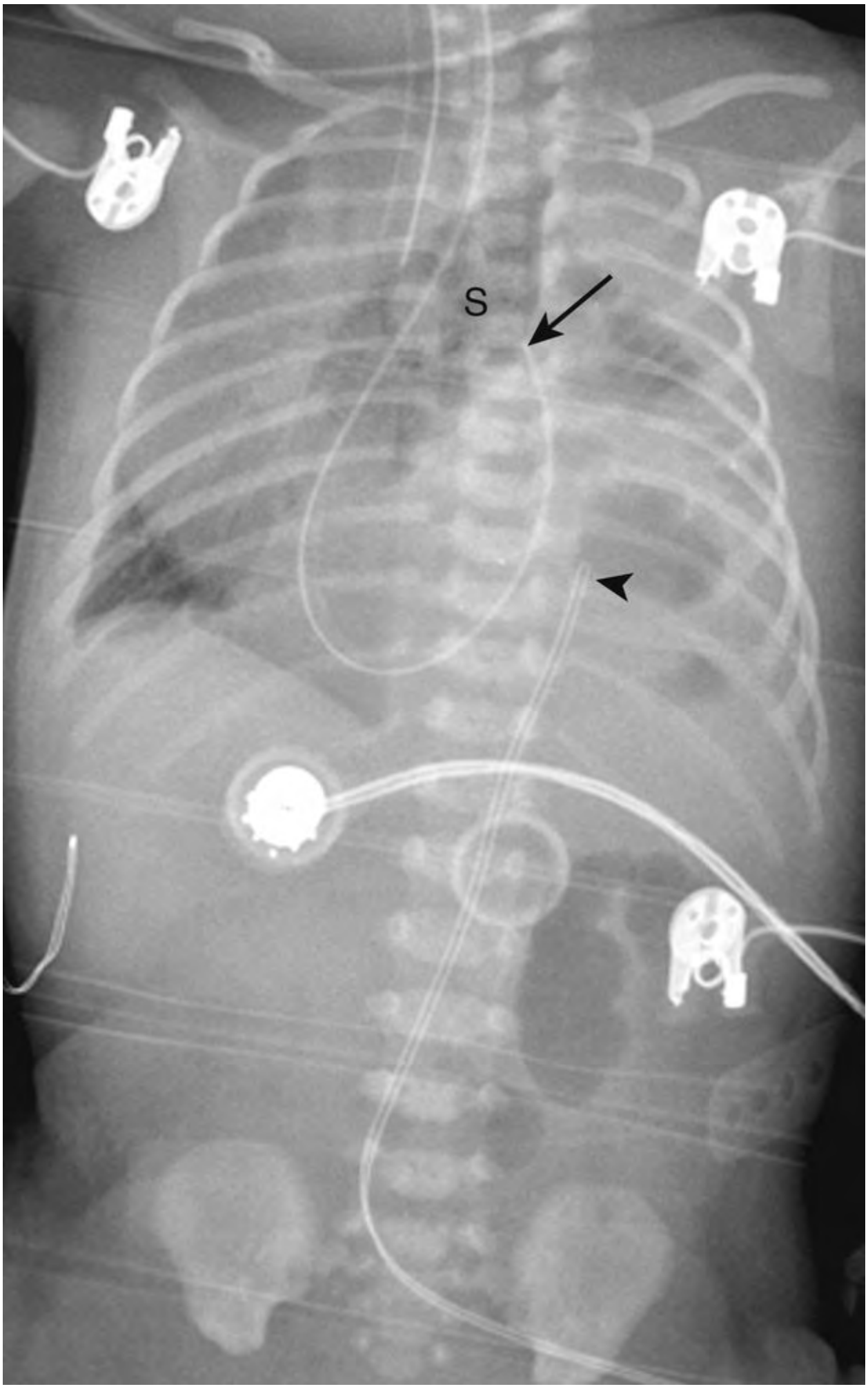
A, Fetal MR image in axial plane shows a large lesion *(arrows)* in left lower lobe with cystic components in the periphery and a feeding aortic vessel *(arrowhead)*. **B,** CT scan shows a complex lesion *(arrows)* with multiple air-filled cysts in the left lower lobe, suggestive of congenital pulmonary airway malformation. **C,** CT reformat shows systemic arterial feeder *(arrowhead)* arising from aorta *(A)* and extending into lesion. Findings are characteristic of sequestration. Note draining pulmonary vein *(V)*.

The diagnosis of CDH is commonly made prenatally by ultrasound and further evaluated by fetal MRI (Fig. 3-18, *A* and *B*). The mortality rate for CDH is related to the degree of pulmonary hypoplasia. Systems of calculating lung volumes and predicting mortality have been devised for use with fetal ultrasound, fetal MRI, and postnatal radiography. Radiographic predictors of poor prognoses include lack of aerated ipsilateral lung, low percentage of aerated contralateral lung, and severe mediastinal shift. Treatment includes support of respiratory failure, often by high-frequency ventilation or ECMO, and surgical repair. Multisystem morbidity is high among survivors, and almost all CDH patients have some degree of pulmonary hypoplasia and neurodevelopmental dysfunction. The reported mortality rates associated with CDH range from 20% to 60%. One factor contributing to mortality is the presence of associated abnormalities, which are reported in a high percentage of infants born with CDH. One report suggests that as many as 50% of patients with CDH have associated congenital heart disease, but also including syndromic cases. By the nature of the herniated bowel into the chest, most patients with CDH have associated malrotation.

Sequestration

The term *pulmonary sequestration* refers to an area of congenital abnormal pulmonary tissue that does not have a normal connection to the bronchial tree. The characteristic imaging feature of sequestration is the demonstration of an anomalous arterial supply to the abnormal lung via a systemic artery arising from the aorta or its branches (Fig. 3-19, *A-C*). All modalities that can demonstrate this abnormal

systemic arterial supply, including MRI, CT, ultrasound, and arteriography, have been advocated in making the diagnosis of sequestration. However, contrast-enhanced CT angiography is preferred because it both visualizes the systemic arterial supply when a sequestration is present (see Fig. 3-16) and further characterizes the lung abnormality if a sequestration is not present.



▪ **FIGURE 3-17** **Congenital diaphragmatic hernia.**
Radiograph shows stomach *(S)* containing tip of nasogastric tube *(arrow)* in left hemithorax. There is aerated generalized paucity of bowel gas in the abdomen. There is mediastinal shift to the right. Contralateral right lung poorly aerated related to mediastinal shift to the right. Notice the tip of the umbilical venous line *(arrowhead)* is also seen in the left hemithorax, probably reflecting also liver herniation into the hernial sac.

Sequestration can present on prenatal imaging, with respiratory distress during the newborn period, or with recurrent pneumonia in later childhood. Because sequestrations do not communicate with the bronchial tree unless they become infected, they usually appear as radiopaque masses during the

neonatal period. After infection has occurred, air may be introduced and sequestration may appear as a multiloculated cystic mass. The most common location is within the left lower lobe.

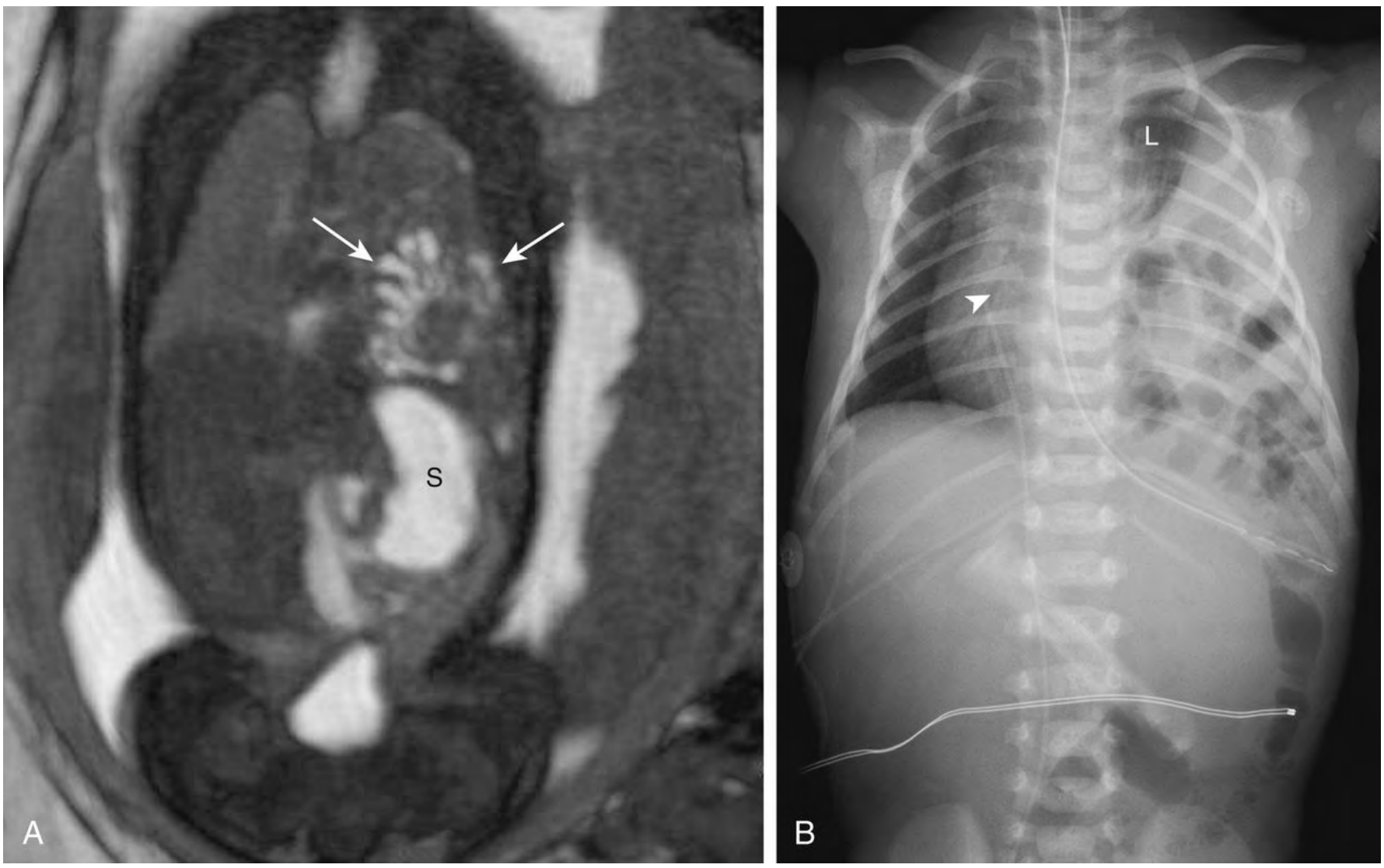
There has been much discussion concerning differentiation between intralobar and extralobar sequestrations. Extralobar sequestrations have a separate pleural covering, whereas intralobar sequestrations, which are more common, do not; however, the presence or absence of pleural covering cannot be determined at imaging. Extralobar sequestrations are associated with other abnormalities in 65% of cases, whereas intralobar sequestrations are not. Differences in venous drainage patterns between intralobar and extralobar sequestrations have been emphasized as a differentiating factor but are actually variable with both types. Visualization of the supplying systemic artery is the characteristic finding and is the documentation the surgeons are looking for before surgically removing the lesion.

Bronchogenic Cyst

Bronchogenic cysts occur secondary to abnormal budding of the tracheobronchial tree during development and occur in the lung parenchyma or the middle mediastinum. Mediastinal lesions are reportedly more common, making up between 65% and 90% of cases of bronchogenic cysts. When bronchogenic cysts occur in the lungs, they are most commonly central in location, often in a perihilar distribution. Bronchogenic cysts are almost always solitary lesions; multiple bronchogenic cysts are very uncommon. Because of the propensity for middle mediastinal and perihilar locations, compression of the distal trachea or bronchi is not an uncommon presentation. Air trapping in the lung distal to the lesion can occur. Like sequestrations, they do not contain air until they become infected and therefore may appear as well-defined soft tissue attenuation or cystic air-fluid-containing masses. They can be quite large. They appear as well-defined cystic structures on imaging.

▪ Roles of Imaging in Pediatric Pneumonia

Respiratory tract infection is the most common cause of illness in children and continues to be a significant cause of morbidity and mortality, and worldwide it is the most common cause of death in children under the age of 5. Evaluation of suspected community-acquired pneumonia is one of the most common indications for imaging in children, and it is one of the most common causes for hospitalization in children under the age of 18, second only to trauma. Because of the frequency with which this scenario arises, knowledge of the issues concerning the imaging of children with community-acquired pneumonia is important. The roles of imaging in these children are multiple: confirmation or exclusion of pneumonia, characterization and prediction of infectious agents, exclusion of other cause of symptoms, evaluation when there is failure to resolve, and evaluation of related complications.



▪ **FIGURE 3-18** **Congenital diaphragmatic hernia.**

A, Fetal MR image in coronal plane shows high signal content in multiple bowel loops *(arrows)* in left hemithorax. The stomach *(S)* remains in the abdominal cavity. **B,** Chest radiograph after birth shows multiple bubblelike lucencies in left hemithorax consistent with herniated bowel loops. There is paucity of bowel gas in the abdomen. However, note that in this case the stomach and nasogastric tube tip are not in the hernia. There is mediastinal shift to the right. The hypoplastic left lung *(L)* and right lung are well aerated. Notice the tip of the umbilical line terminates in the right atrium *(arrowhead)*; it should be repositioned.

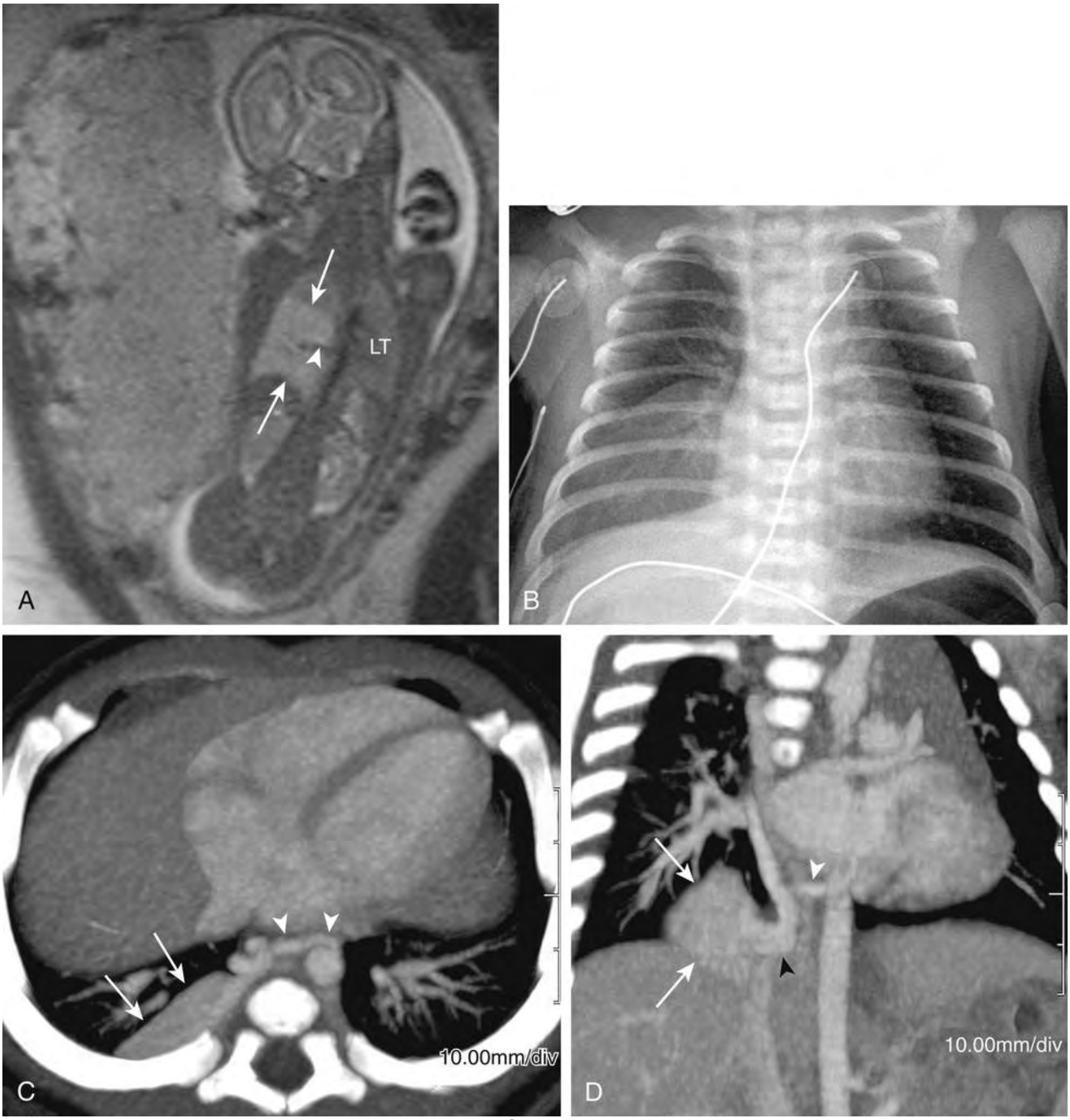
Confirmation or Exclusion of Pneumonia

Making the diagnosis of pneumonia and consequently deciding on treatment and disposition is a common but complex and difficult issue. The symptoms and physical findings in children with pneumonia are sometimes nonspecific, especially in infants and young children. Many children present with nonrespiratory symptoms, such as fever, malaise, irritability, headaches, chest pain, abdominal pain, vomiting, or decreased appetite. Findings on physical examination are also less reliable in children than in adults because young children are less cooperative with exams and have smaller anatomy and smaller respiratory cycles. Because of the inaccuracy of physical examination, radiography is often requested to evaluate children with suspected pneumonia. Several studies have shown that in a large percentage of cases, findings on chest radiography change caregivers' diagnoses and treatment plans (antibiotics, bronchodilators, and patient disposition) for children being evaluated for potential pneumonia. At our institution, we obtain both a frontal and a lateral film in the evaluation of a child with suspected pneumonia. It has been shown that obtaining both views increases the negative predictive value of chest radiography for pneumonia. In addition, some findings, such as hyperinflation in an infant, are much more easily evaluated on the lateral than on the frontal views (Fig. 3-20, *A* and *B*).

Characterization and Prediction of Infectious Agent

The historic emphasis in textbooks and articles concerning pneumonia has been on radiographic patterns that suggest a specific infectious agent, such as staphylococcal or streptococcal pneumonia. However, because of the limited ways in which the lung can respond to inflammation, findings suggestive of a specific diagnosis are usually not encountered in the radiograph of a child with suspected community-acquired pneumonia. The more general issue in the evaluation of suspected pneumonia is whether the infectious agent is likely to be bacteria or viral, which determines whether the patient should be placed on antibiotics. To answer this question, it is helpful to review the

epidemiology of lower respiratory infections in children, the classic radiographic patterns of viral and bacterial pneumonia in children, and what is known about the accuracy of chest radiography in differentiating viral from bacterial infection.

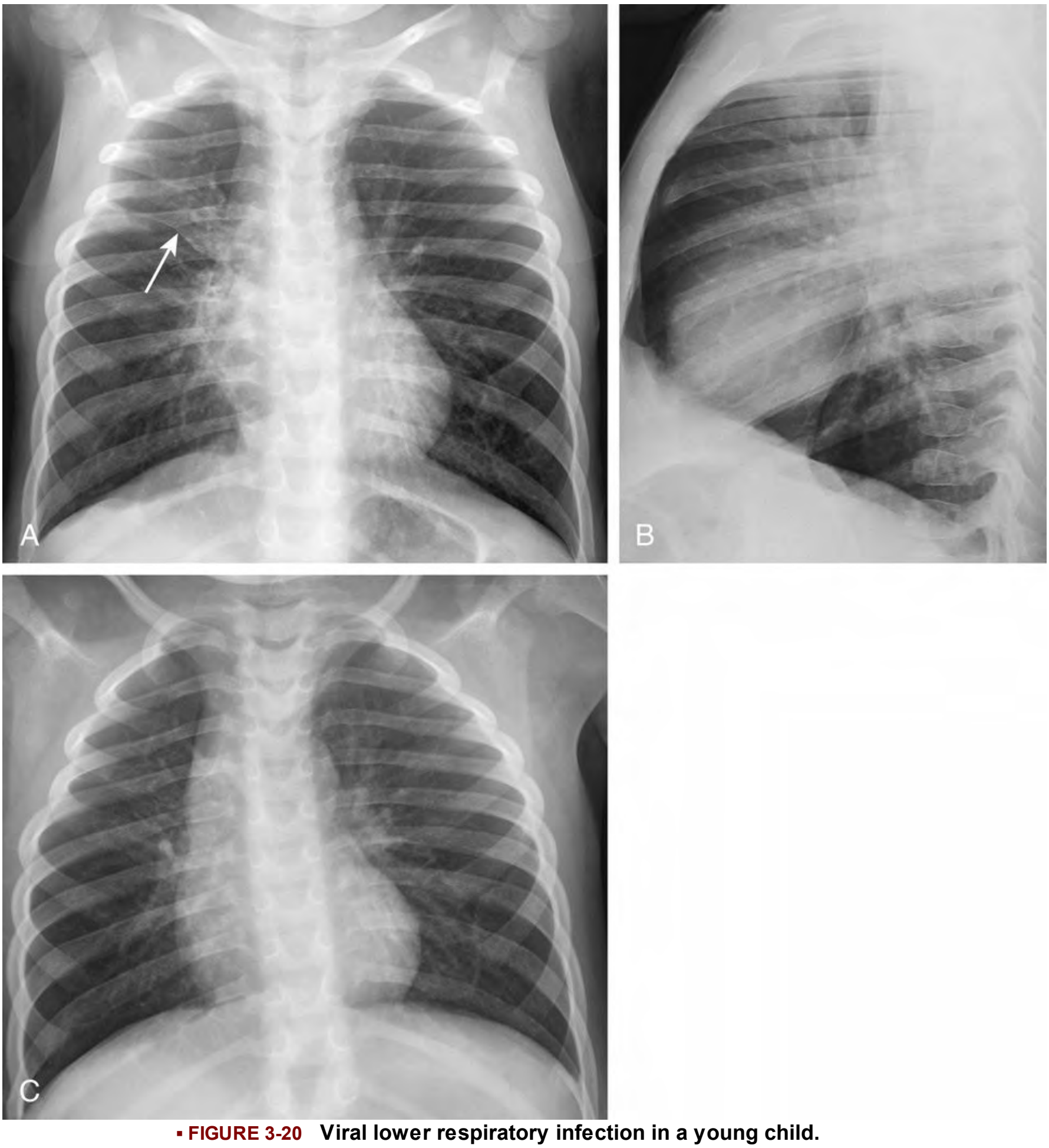


▪ **FIGURE 3-19** **Sequestration.**

A, Fetal MR image shows a large, relatively homogeneous lung lesion *(arrows)* in the right lower lobe with discrete aortic feeder *(white arrowhead)*. Note lower signal in normal left lung *(LT)*. **B,** Chest radiograph obtained at birth shows right lower lobe asymmetric opacity. Axial (**C**) and coronal (**D**) maximum intensity projection CT images performed at 5 weeks of age show feeding systemic arterial supply (*white arrowhead* in **C**) arising from aorta and extending to unaerated lesion *(arrows)* in right lower lobe. The lesion is drained by a tributary vein to the azygous system (*black arrowhead* in **D**). Notice the relatively decreased in size of the lesion when compared with fetal MRI raising the possibility of extralobar sequestration lesion.

The common causal agents of lower respiratory tract infections in children vary greatly with age. In all age groups, viral infections are much more common than bacterial infections. In infants and preschool-age children (4 months to 5 years of age), viruses cause 95% of all lower respiratory tract infections. The epidemiology is much different in school-age children (6 to 16 years of age). In school-age children, although viral agents remain the most common cause of lower respiratory tract infections,

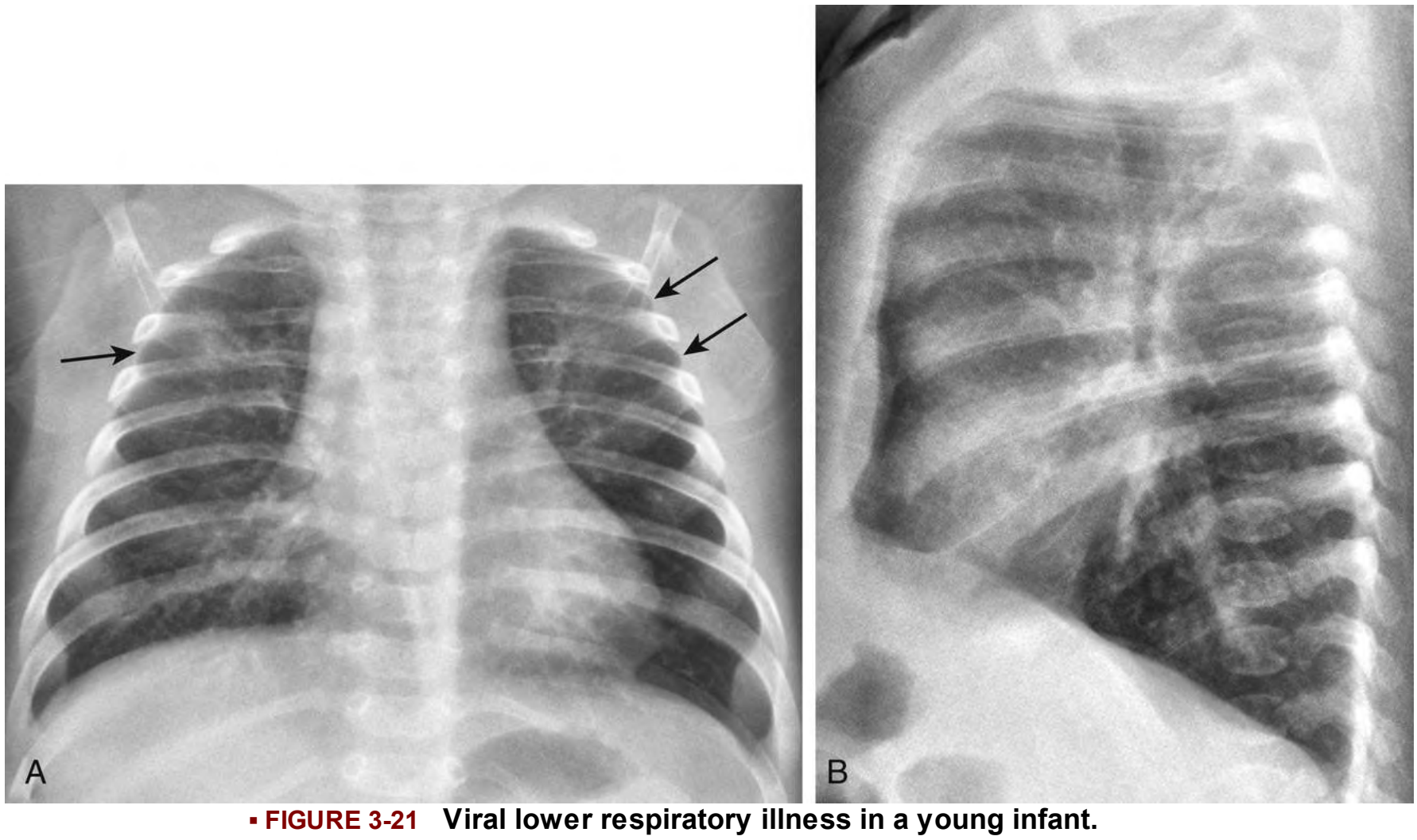
the incidence of bacterial infection by *Streptococcus pneumoniae* increases. What is most striking is that *Mycoplasma pneumoniae*, which is an uncommon cause of pneumonia in preschool infants and children, is the cause of approximately 30% of lower respiratory tract infections in school-age children. Therefore the odds that a child should be administered antibiotics for a respiratory tract infection are greatly influenced by the child's age. In addition, there has been a recent increase in the incidence of pneumonia secondary to multidrug-resistant *Staphylococcus aureus* infections. These can occur at any age.



▪ **FIGURE 3-20** **Viral lower respiratory infection in a young child.**
A, Frontal view shows increased perihilar markings and bandlike density *(arrow)* in right upper lobe, representing subsegmental atelectasis. **B,** Lateral view better shows marked hyperinflation with flattened hemidiaphragms, increased anterior-to-posterior diameter of the chest, and barrel shape of chest. Increased perihilar markings make hila appear prominent. **C,** Radiograph performed 2 months earlier in same child shows clear lungs with absence of increased perihilar markings. Note the difference between the two frontal radiographs.

Viral infections affect the airways, causing inflammation of the small airways and peribronchial edema. This peribronchial edema appears on radiography as increased peribronchial opacities—

symmetric coarse markings that radiate from the hila into the lung (Fig. 3-21, *A* and *B*; and see Fig. 3-20, *A* and *B*). The central portions of the lungs appear to be "dirty" or "busy." It is one of the most subjective findings in radiology. In addition, the combination of the bronchial wall edema, narrowed airway lumen, and necrotic debris and mucus in the airway leads to small airway occlusion. This results in both hyperinflation and areas of subsegmental atelectasis. Hyperinflation is evident on chest radiographs in children in the presence of hyperlucency, the depression of the hemidiaphragm to more than 10 posterior ribs, and the increased anterior-to-posterior chest diameter. Hyperinflation is often much better appreciated on lateral than on frontal radiographs in infants and small children (see Fig. 3-20). Subsegmental atelectasis appears as wedge-shaped areas of density, most commonly in the lower and mid lung (see Fig. 3-20, *A* and *B*). There are several anatomic differences that render small children more predisposed to air trapping and collapse secondary to viral infection than adults: small airway luminal diameter, poorly developed collateral pathways of ventilation, and more abundant mucus production. The misinterpretation of areas of atelectasis as focal opacities suspicious for bacterial pneumonia is thought to be one of the more common misinterpretations in pediatric radiology.

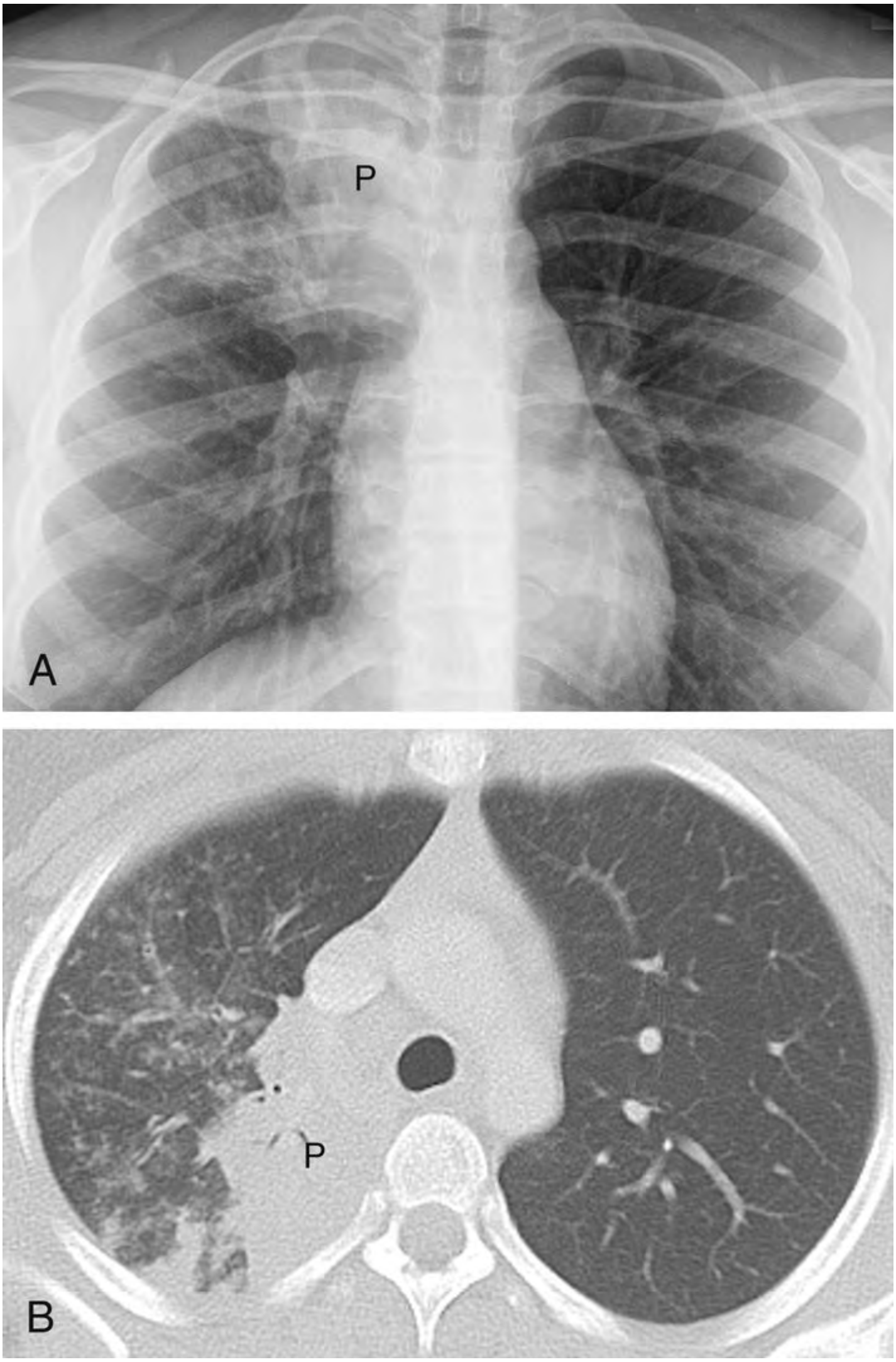


▪ **FIGURE 3-21 Viral lower respiratory illness in a young infant.**
A, Chest radiograph at peak of illness shows ropy increased perihilar markings and areas of subsegmental atelectasis. Hyperinflation can be hard to identify on the frontal view at this young age. One clue is the bulging of lung tissue between the ribs *(arrows)*. **B,** Lateral radiograph shows marked hyperinflation. Note the flattening of the diaphragms.

In contrast to the airway involvement in viral pneumonia, bacterial pneumonia occurs secondary to inhalation of the infectious agent into the air spaces. There is a resultant progressive development of inflammatory exudate and edema within the acini, resulting in consolidation of the air spaces. On chest radiography, localized air space consolidation (Fig. 3-22) occurs with air bronchograms. The typical distribution is either lobar or segmental, depending on when in the course of development of the pneumonia the radiograph is obtained. Associated pleural effusions are not uncommon. In addition, there is a propensity for pneumonia to appear "round" in younger children (Fig. 3-23). Round pneumonia is more common in children younger than 8 years of age and is most often caused by *S. pneumoniae*. The occurrence of this pattern is thought to be related to poor development of pathways of collateral ventilation. Round pneumonia tends to be solitary and occurs more commonly posteriorly and in the lower lobes. When such a lung mass is seen in a child with cough and fever, round pneumonia should be suspected. The child should be treated with antibiotics, and the chest radiograph should be repeated. It is best to avoid unnecessary CT examination in this clinical scenario. When a round opacity is seen in a child older than 8 years of age, other pathology should be suspected.

Do these classic patterns of viral and bacterial infections accurately differentiate between children

who have bacterial infection and need antibiotics and those who do not? Studies have shown that these radiographic patterns do have a high negative predictive value (92%) for excluding bacterial pneumonia. However, the positive predictive value is low (30%). In other words, 70% of children who have radiographic findings of bacterial infection actually have viral infection. In regard to decisions about administering antibiotics to children with suspected pneumonia, the goals are to treat all children who have bacterial pneumonia with antibiotics while minimizing the treatment of children with viral illnesses. Therefore the high negative predictive value of chest radiography for bacterial pneumonia is useful in identifying those children who do not need antibiotics.



▪ **FIGURE 3-22** **Bacterial pneumonia.**
Radiograph (**A**) and axial CT image (**B**) show focal lung consolidation *(P)* with air bronchograms in the medial aspect of the right upper lobe, consistent with bacterial pneumonia. Tree-in-bud opacities are noted in the remainder of the right upper lobe.

Exclusion of Other Pathologic Processes

Many of the presenting symptoms of pneumonia in children are nonspecific, and the spectrum of presentations overlaps with a number of other pathologic processes involving the chest or other anatomic regions. Therefore one of the other roles of chest radiography in the evaluation of a child who potentially has pneumonia is the exclusion of other processes. Two areas that are often blind spots for radiologists and may be involved by conditions that mimic pneumonia are the airway and chest wall.

Processes that cause extrinsic compression of the trachea and bronchi can mimic pneumonia by causing noisy breathing, lobar collapse, and recurrent infection. Evaluation of the diameter of the airway should be stressed as a routine part of evaluating radiographs. Rib abnormalities may be evidence that a lung opacity seen on chest radiography does not represent pneumonia. The presence of rib erosion or asymmetric intercostal spaces helps to differentiate neuroblastoma from chest opacity secondary to pneumonia.

Failure to Resolve

Unlike in adults, in whom postobstructive pneumonia secondary to bronchogenic carcinoma is a concern, follow-up radiography to ensure resolution of radiographic findings is not routinely necessary in an otherwise healthy child. There is a tendency to obtain follow-up radiographs both too early and too often. Follow-up radiographs should be reserved for children who have persistent or recurrent symptoms and those who have an underlying condition, such as immunodeficiency. The radiographic findings of pneumonia can persist for 2 to 4 weeks, even when the patient is recovering appropriately clinically. When follow-up radiographs are indicated, it is ideal to avoid obtaining them until at least 2 to 3 weeks have passed, if clinical symptoms allow.

Causes of failure of suspected pneumonia to resolve include infected developmental lesions, bronchial obstruction, gastroesophageal reflux and aspiration, and underlying systemic disorders. The most common developmental lung masses that may become infected and present as recurrent or persistent pulmonary infection include sequestration and CPAM. These entities have been discussed previously.

Complications of Pneumonia

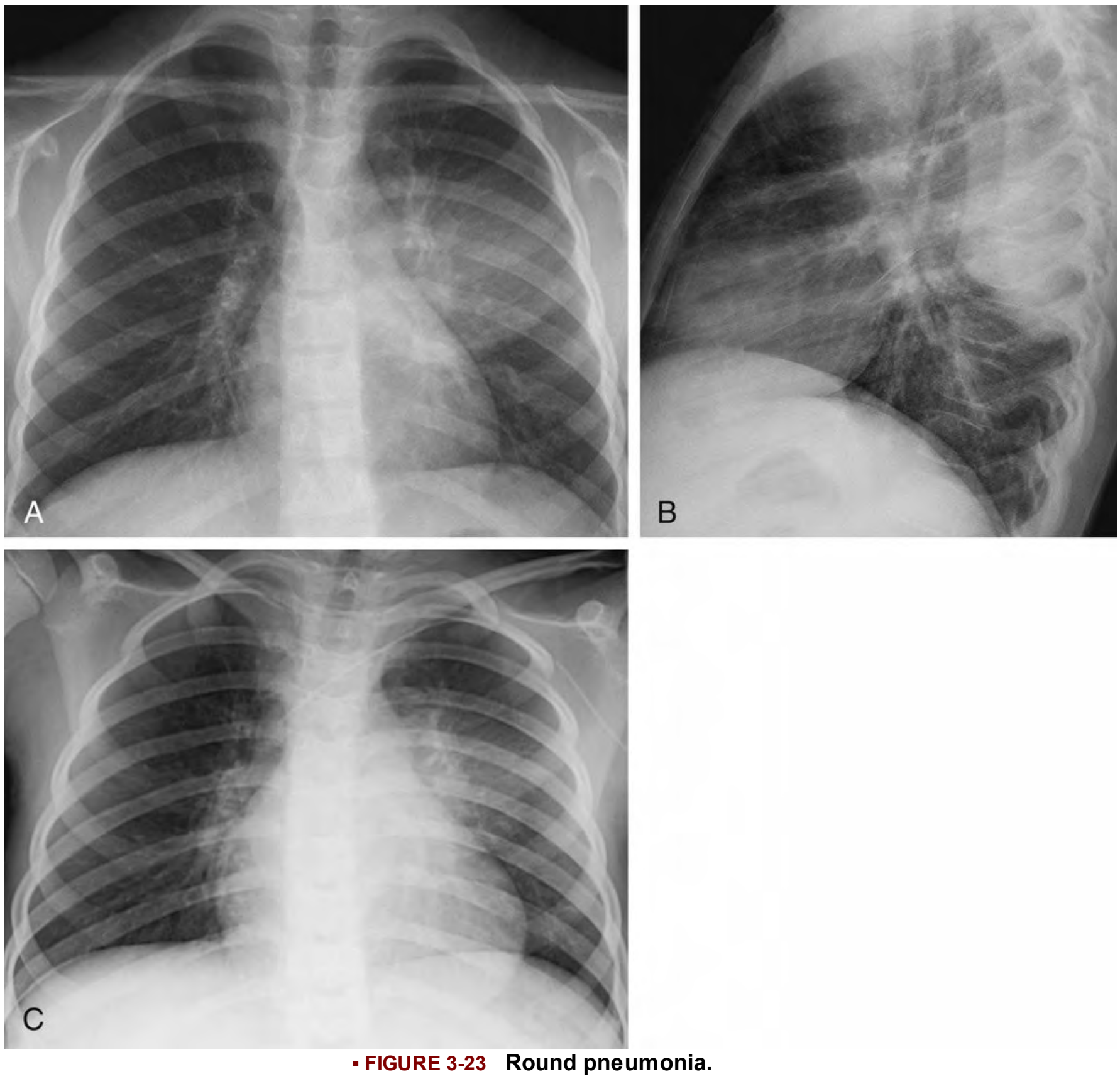
The evaluation of complications related to pneumonia can be divided into several clinical scenarios: primary evaluation of parapneumonic effusions, evaluation of a child who has persistent or progressive symptoms despite medical or surgical therapy, and the chronic sequelae of pneumonia.

Primary Evaluation of Parapneumonic Effusions

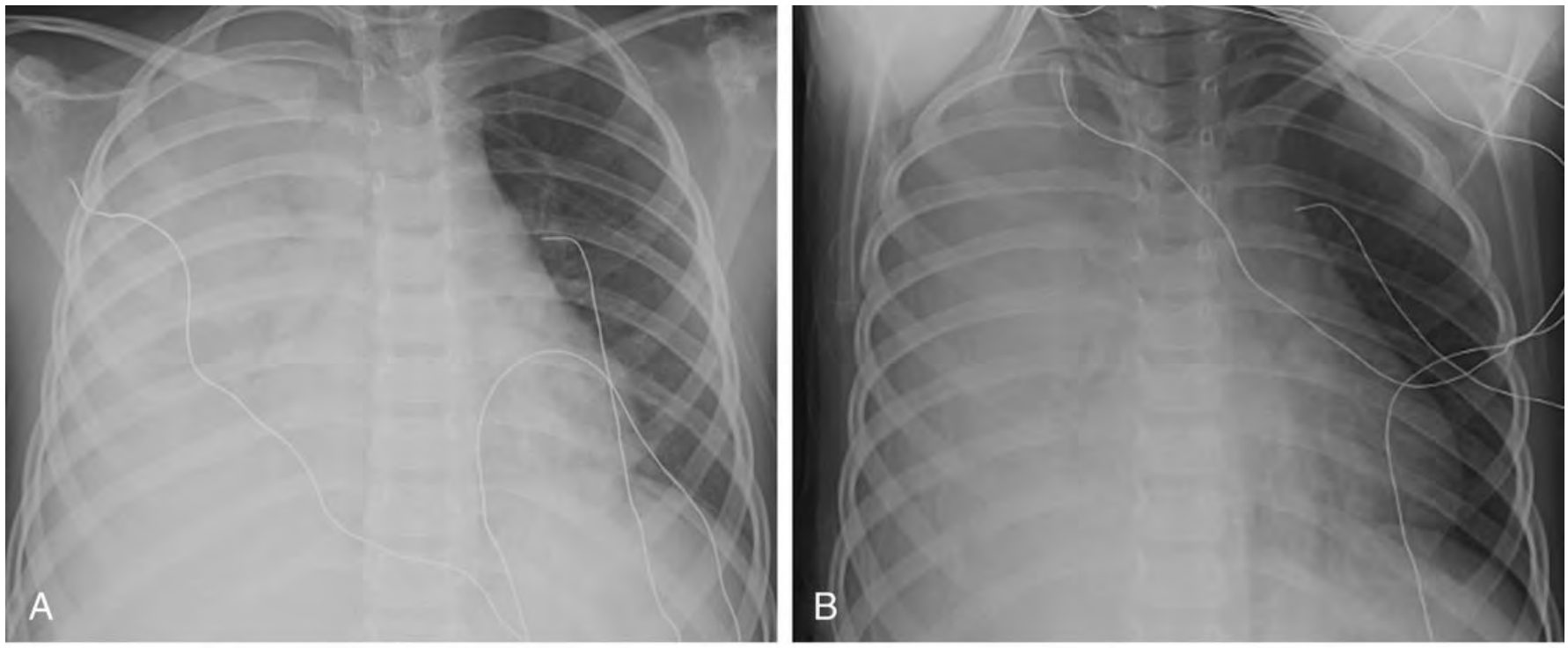
Parapneumonic effusions occur commonly in patients who have bacterial pneumonia. Multiple therapeutic options are available in the management of parapneumonic effusions, including antibiotic therapy alone, repeated thoracentesis, chest tube placement, thrombolytic therapy, and thoracoscopy with surgical debridement. Great differences in opinion exist among caregivers regarding the timing and aggressiveness of management of parapneumonic effusions. Traditionally the aggressiveness of therapy has been based on categorizing parapneumonic effusions as empyema or transudative effusion, as determined by needle aspiration and analysis of the pleural fluid.

Several imaging modalities have been advocated to differentiate empyema from transudative effusion without the use of an invasive diagnostic thoracentesis, including decubitus radiographs, ultrasound, and CT. If there is a significant change in the position and appearance of the pleural fluid on the decubitus images as compared with the upright radiograph, the fluid is considered to be free flowing and nonloculated. If there is no change in position of the pleural fluid, the fluid is considered to be loculated (Fig. 3-24, *A-C*). However, decubitus views are not helpful in cases in which the entire hemithorax is opacified because the layering fluid cannot be adequately delineated without any adjacent air. In the authors' experience, these decubitus radiographs have been more confusing than helpful, and we do not advocate the use of decubitus radiographs to evaluate pleural effusions. On CT, findings such as thickening or enhancement of the parietal pleura and thickening or increased attenuation of the extrapleural fat were previously thought to favor empyema over transudative effusion, but this has been shown to be inaccurate (Fig. 3-25, *A* and *B*; and see Fig. 3-29). The primary role of ultrasound in these instances is to identify, quantify, and characterize the effusion and empyema. Ultrasound has also been advocated as an aid in making therapeutic decisions for parapneumonic effusions because it may provide image guidance for drainage or identify any residual collection. In one study, parapneumonic effusions were categorized as low grade (anechoic fluid without internal heterogeneous echogenic structures) or high grade (fibrinopurulent organization demonstrated by the presence of fronds, septations, or loculations) (see Figs. 3-24 and 3-25). In children in whom effusions were high grade, hospital stay was reduced by nearly 50% when operative intervention was performed. The length of hospital stay in children with low-grade effusions was not affected by operative intervention. Therefore ultrasound plays a more useful role than CT in the early

evaluation of parapneumonic effusions. It is not uncommon for ultrasound to show multiple septations and in the same case to show no evidence of septations on CT (see Fig. 3-25). Ultrasound, rather than CT or decubitus radiographs, is the primary imaging modality to evaluate parapneumonic effusions.

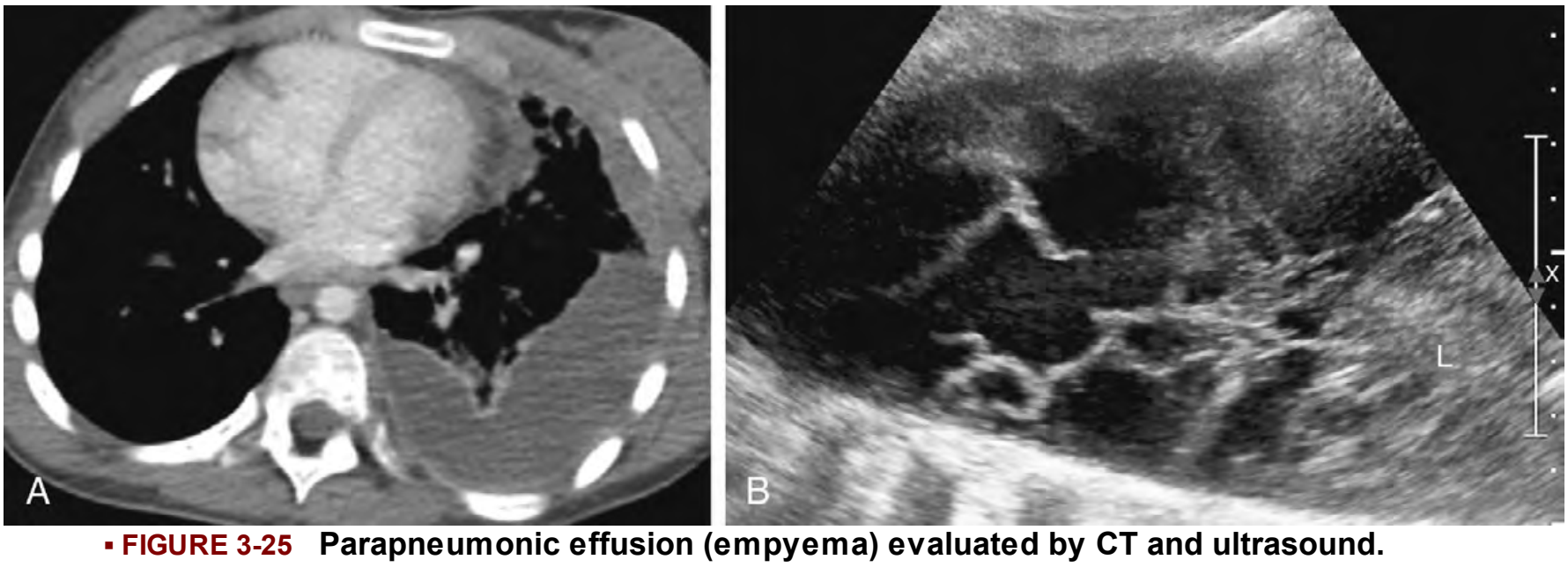


▪ **FIGURE 3-23** **Round pneumonia.**
Frontal (**A**) and lateral (**B**) radiographs show rounded opacity overlying the left hilum. This is the location of the superior segment of the left lower lobe. **C,** Radiograph obtained 4 days later show interval decrease in size. Resolution would not be expected before 2 weeks, if not more.



▪ **FIGURE 3-24 Parapneumonic effusion (empyema) evaluated by decubitus radiographs and ultrasound.**

A, Radiograph shows a large pleural effusion in child with pneumonia. **B,** Decubitus radiograph with right side down shows no change in pleural effusion. Lack of change is supposed to suggest loculation but is probably not that helpful a diagnostic tool, particularly in cases with complete or near complete opacification of a hemithorax with or without associated contralateral mediastinal shift. Neither erect nor decubitus views are helpful in determining the quantity or nature of the pleural effusion. Ultrasound is extremely helpful in these cases because it can speedily differentiate a parapneumonic effusion from extensive consolidation or an underlying mass. **C,** Ultrasound of left pleural fluid demonstrating multiple septations *(arrows)* and debris—a high-grade effusion, predictive of benefit from aggressive drainage.



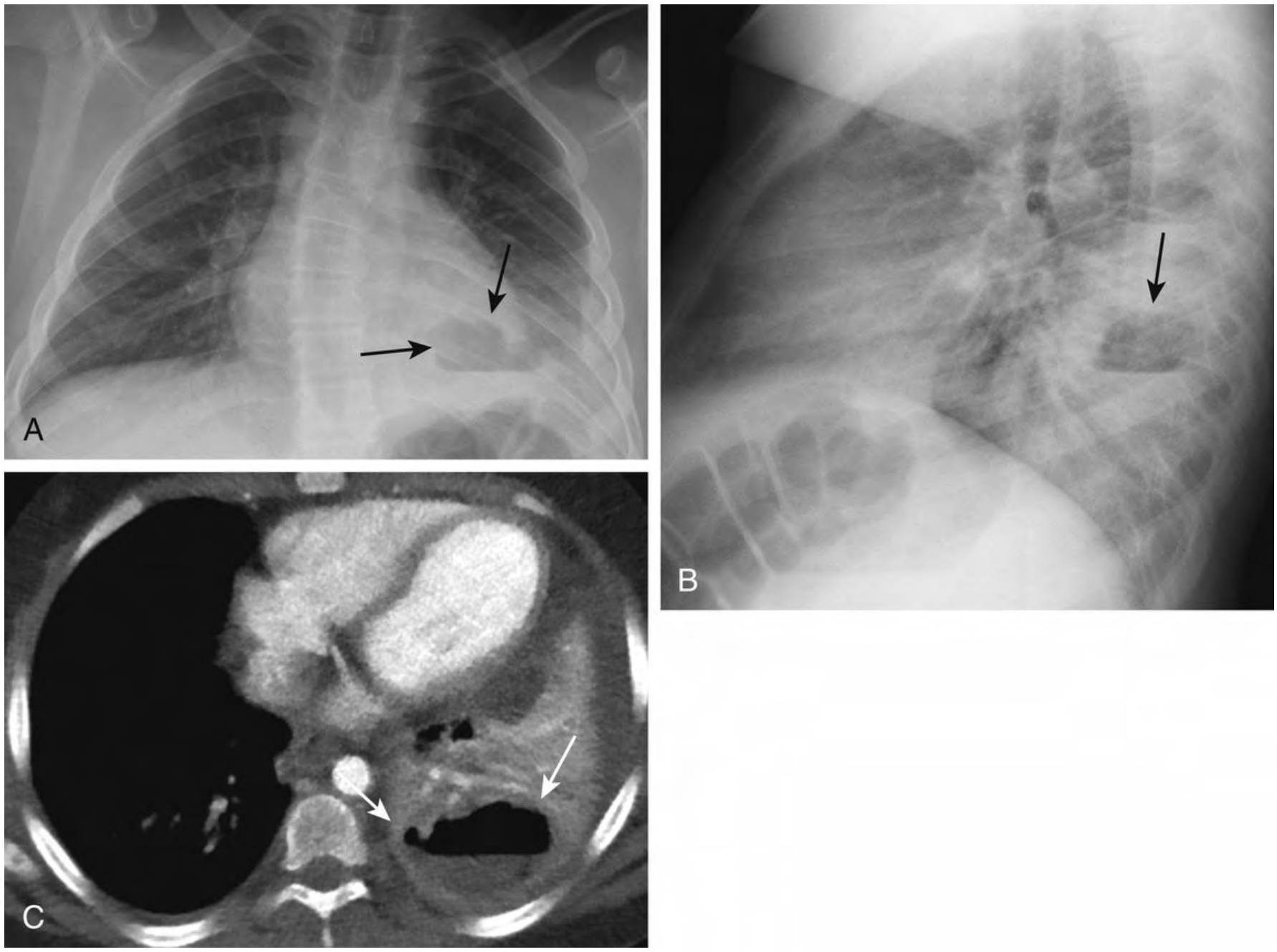
▪ **FIGURE 3-25 Parapneumonic effusion (empyema) evaluated by CT and ultrasound.**
A, CT shows left parapneumonic effusion. There are no septations seen by CT, which is typical.
B, Ultrasound shows consolidated lung *(L)* with adjacent pleural fluid. Note multiple echogenic septations consistent with complex effusion.

Evaluation of Persistent or Progressive Symptoms

When children exhibit persistent or progressive symptoms (fever, respiratory distress, sepsis) despite appropriate medical management of pneumonia, there is commonly an underlying suppurative complication. Potential suppurative complications include parapneumonic effusions (such as empyema), inadequately drained effusions, and persistent effusion due to malpositioned chest tube; parenchymal complications, such as cavitary necrosis or lung abscess; and purulent pericarditis. Although chest radiography is the primary imaging modality for detecting such complications, a significant percentage of such complications are not demonstrated by radiography. In a child who has had a noncontributory radiograph and who has not responded appropriately to therapy, contrast-enhanced CT has been shown to be useful in detecting clinically significant suppurative complications. CT can help to differentiate whether there is a pleural or a parenchymal reason for persistent illness. Administration of intravenous contrast is vital to maximize the likelihood of detection and the characterization of both parenchymal and pleural complications.

Lung Parenchymal Complications

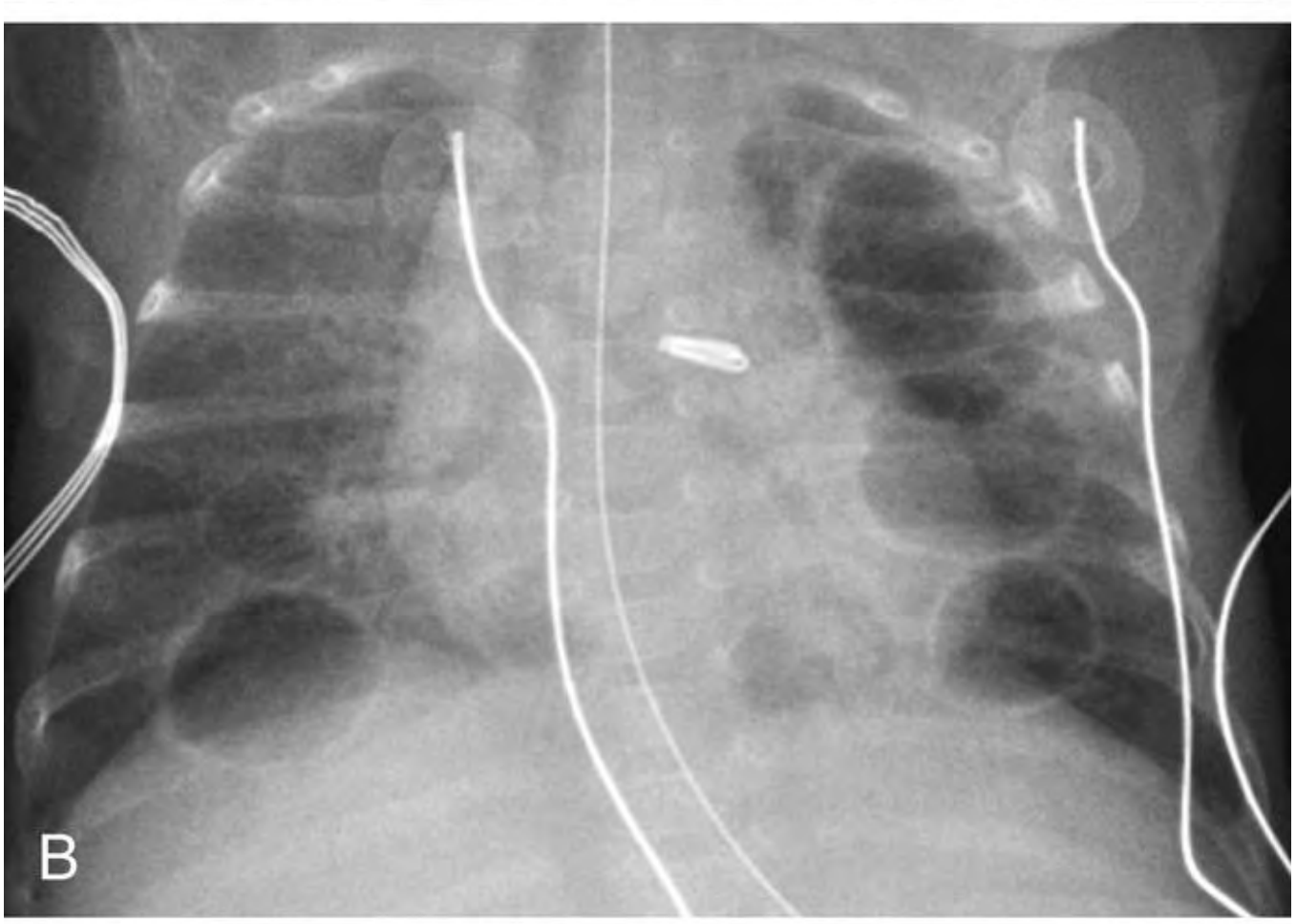
On contrast-enhanced CT, both noncompromised consolidated lung parenchyma and atelectasis enhance diffusely. Large areas of decreased or absent enhancement are indicative of underlying parenchymal ischemia or impending infarction. Suppurative lung parenchymal complications include a spectrum of abnormalities, such as cavitary necrosis, lung abscess, pneumatocele, bronchopleural fistula, and pulmonary gangrene. The name given to the suppurative process is determined by several factors, including the severity, distribution, condition of the adjacent lung parenchyma, and temporal relationship with disease resolution. Lung abscess represents a dominant focus of suppuration surrounded by a well-formed fibrous wall. Lung abscess is actually uncommon in otherwise healthy children and typically occurs in children who are immunocompromised. On contrast-enhanced CT, lung abscesses appear as fluid- or air-filled cavities with definable enhancing walls (Fig. 3-26). Typically there is no evidence of necrosis in the surrounding lung. *Pneumatocele* is a term given to thin-walled cysts seen at imaging and may represent a later or less severe stage of resolving or healing necrosis (Fig. 3-27, *A*-*C*).



▪ **FIGURE 3-26** **Lung abscess.**
Frontal (**A**) and lateral (**B**) chest radiographs show airspace consolidation in the left mid and lower lung zones with a large internal cavity with an air-fluid level *(arrows)*. **C,** Contrast-enhanced CT shows well-defined cavity *(arrows)* with thickened, irregular walls, containing an air-fluid level. There is associated pleural fluid.

Cavitary necrosis is the most commonly encountered suppurative complication. It is characterized by a dominant area of necrosis of a consolidated lobe that is associated with a variable number of thin-walled cysts (Fig. 3-28). CT findings of cavitary necrosis include loss of normal lung architecture, decreased parenchymal enhancement, loss of the lung-pleural margin, and multiple thin-walled cavities containing air or fluid and lacking an enhancing border (Fig. 3-29). Although historically described as a complication of staphylococcal pneumonia, cavitary necrosis was much more commonly seen as a complication of streptococcal pneumonia during the 1990s. Cavitary necrosis in association with multidrug-resistant *S. aureus* infection has been occurring with increased frequency recently (see Fig. 3-27). The presence of cavitary necrosis is indicative of an intense and prolonged illness. However, unlike in adults in whom the mortality rate in cavitary necrosis is high and early surgical removal of the affected lung has been advocated, the long-term outcome for children with cavitary necrosis is favorable in most cases with medical management alone. It is amazing that in children with cavitary necrosis, follow-up radiographs obtained more than 40 days after the acute illness are most often normal or show only minimal scarring.


A


B

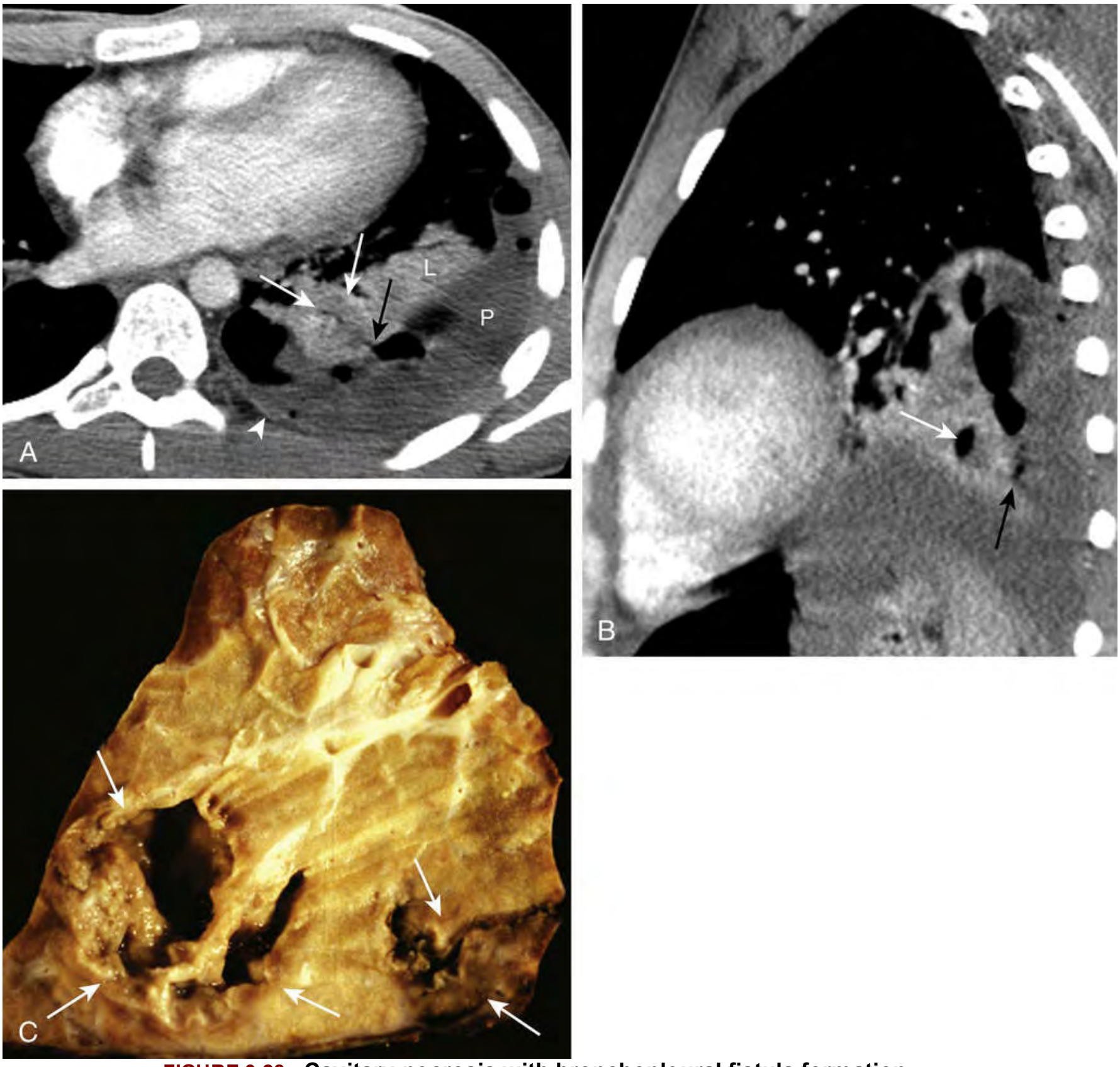

C

▪ **FIGURE 3-27** **Rapid development of necrosis and pneumatocele formation in an infant with multidrug-resistant *S. aureus* pneumonia.**
A, Radiograph obtained in the intensive care unit after intubation for respiratory failure shows several pneumatoceles in the left lung. **B,** Radiograph taken 2 days after that shown in **A** shows progressive development of necrosis and cyst formation. Not that it matters, but because many of the cysts are thin-walled and without surrounding opacification, *pneumatocele* is acceptable terminology. **C,** Axial CT image shows additional smaller cysts *(arrows)*, not well seen on conventional radiography.

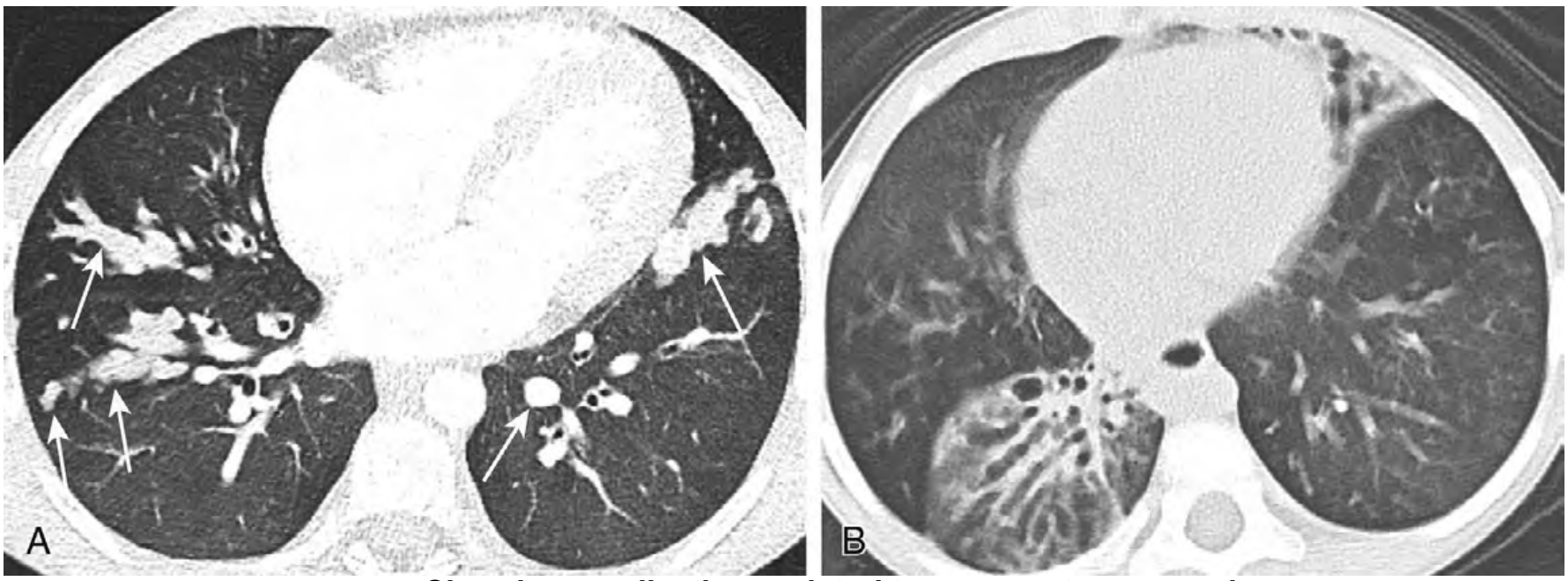
It may sometimes be difficult on a single imaging study to differentiate a suppurative lung parenchymal complication of pneumonia from an underlying cystic congenital lung lesion that has become secondarily infected. Infected CPAMs may appear very similar to cavitary necrosis. Obviously, historical imaging studies showing a lack of a cystic lesion exclude underlying CPAM, but such historical examinations often do not exist or are not available. Observable resolution of the cystic lesion on follow-up studies ensures that the lesion is no longer clinically relevant and makes cavitary necrosis much more likely. However, some CPAMs have been reported to scar down and resolve after becoming infected.

Chronic Lung Complications of Pneumonia

Acute pneumonia can lead to parenchymal damage and long-term sequelae. The most common sequelae of acute pneumonia are bronchiectasis and Swyer-James syndrome. Bronchiectasis is enlargement of the diameter of the bronchi that is related to damage to the bronchial walls. It is best demonstrated by high-resolution CT (HRCT), on which the diagnostic finding is that the bronchus in question is larger in diameter than the adjacent pulmonary artery (Fig. 3-30). Swyer-James syndrome is characterized by unilateral lung hyperlucency that is thought to be secondary to a virus-induced necrotizing bronchiolitis that leads to postinfectious obliterative bronchiolitis (see Fig. 3-30). Radiography shows a hyperlucent and enlarged lung with a static lung volume. The pulmonary vessels are less prominent than on the normal side.



▪ **FIGURE 3-28** **Cavitary necrosis with bronchopleural fistula formation.**
Axial (**A**) and sagittal (**B**) reformatted CT images show consolidation of the left lung. Portions of the lung demonstrate cavitary necrosis *(white arrows)*. There are also areas of consolidated lung that enhance *(L)* and are not compromised. There is a pleural effusion *(P)* that contains both air and fluid. There is an apparent communication between the peripheral airways and the pleural cavity *(black arrow)*, consistent with a bronchopleural fistula. There is thickening and enhancement of the parietal pleura *(white arrowhead).* **C,** Photograph of surgical specimen (in different patient) shows consolidated lung *(tan area)* with areas of necrosis and cavity formation *(arrows)*.

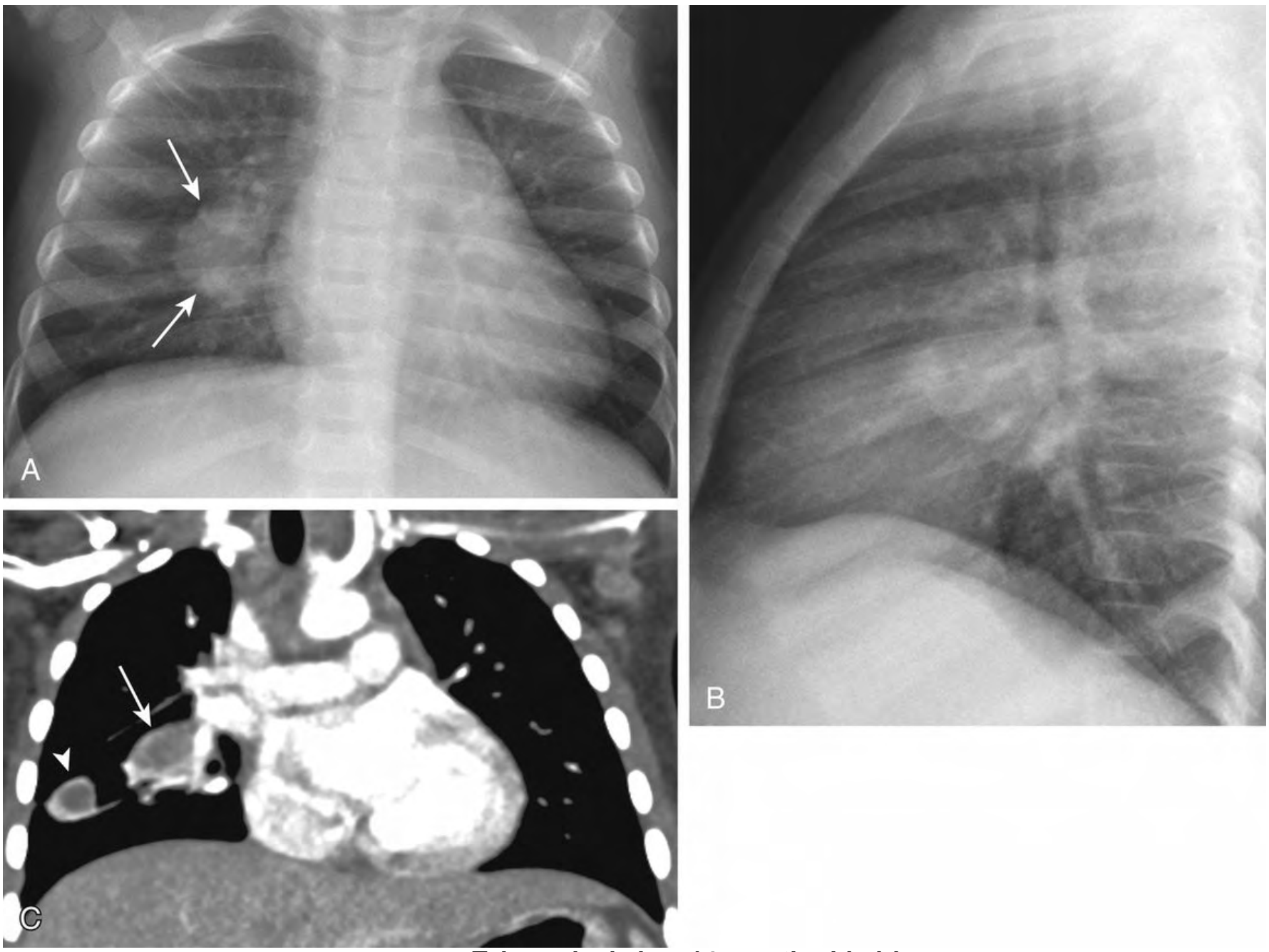


▪ **FIGURE 3-29 Chronic complications related to recurrent pneumonias.**

A, CT shows multiple round and branching, soft tissue density lesions in right middle and right and left lower lobes *(arrows)*, consistent with bronchiectasis with mucus plugging, in a 12-year-old patient with cystic fibrosis. **B,** Marked bronchiectasis with volume loss in the right lower lobe and lingula in a 4-year-old patient with cystic fibrosis. Note compensatory air trapping in the right middle and left lower lobes. These areas remained hyperlucent on expiratory images.

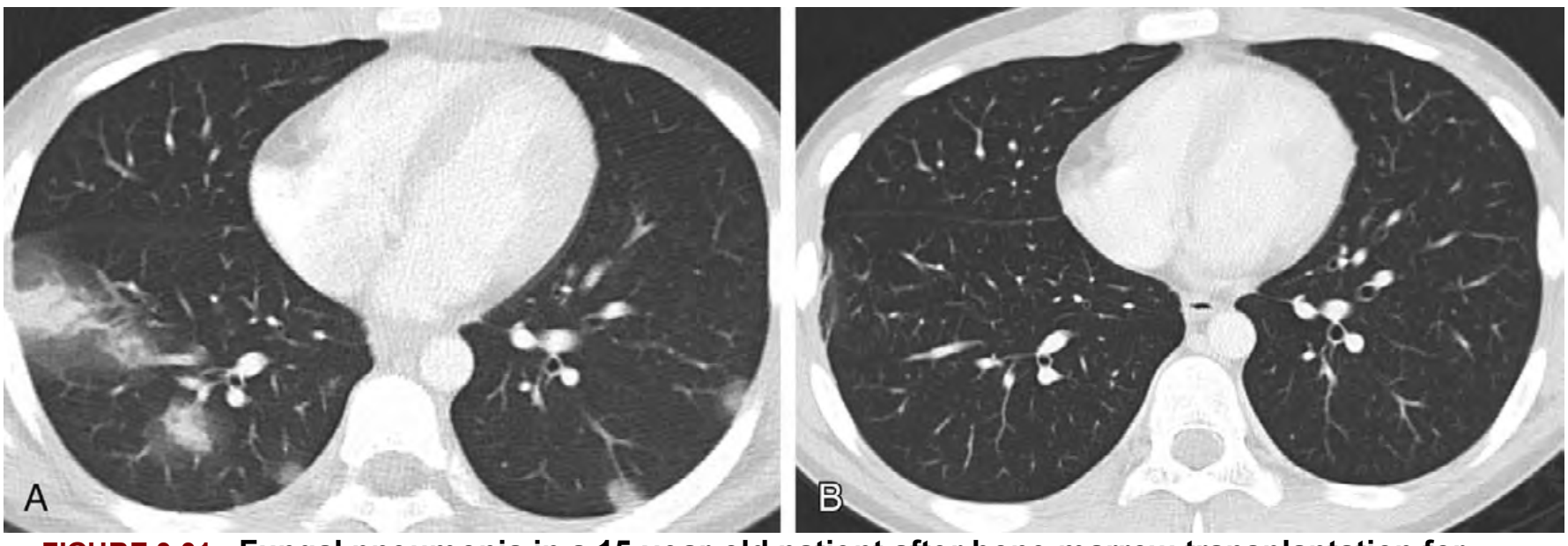
Tuberculosis

The incidence of tuberculosis in children has been increasing. Children with primary tuberculosis can present with pulmonary consolidation within any lobe. It is often associated with ipsilateral hilar lymphadenopathy or pleural effusion. Therefore, when lung consolidation is seen with associated lymphadenopathy or effusion in a child who is not acutely ill, there should be a high suspicion for tuberculosis. Unilateral hilar lymphadenopathy (Fig. 3-31, *A* and *B*) is a common presentation for tuberculosis. Such cases should be considered tuberculosis until proven otherwise.



▪ FIGURE 3-30 **Tuberculosis in a 14-month-old girl.**

A and **B,** Frontal and lateral radiographs of the chest demonstrate a right hilar mass *(arrows)* consistent with unilateral lymphadenopathy. **C,** Coronal CT image shows unilateral, right hilar lymphadenopathy with a single right middle lobe pulmonary nodule *(arrowhead)* and findings consistent with primary tuberculosis. The enlarged lymph nodes and nodule show central low attenuation and peripheral enhancement.



▪ FIGURE 3-31 **Fungal pneumonia in a 15-year-old patient after bone marrow transplantation for acute lymphoblastic leukemia.**

A, CT shows poorly defined nodules and associated ground-glass opacity. **B,** A CT taken earlier shows clear lungs. Note the striking change since this baseline study.

Common Chronic or Recurrent Pulmonary Problems in Special Populations

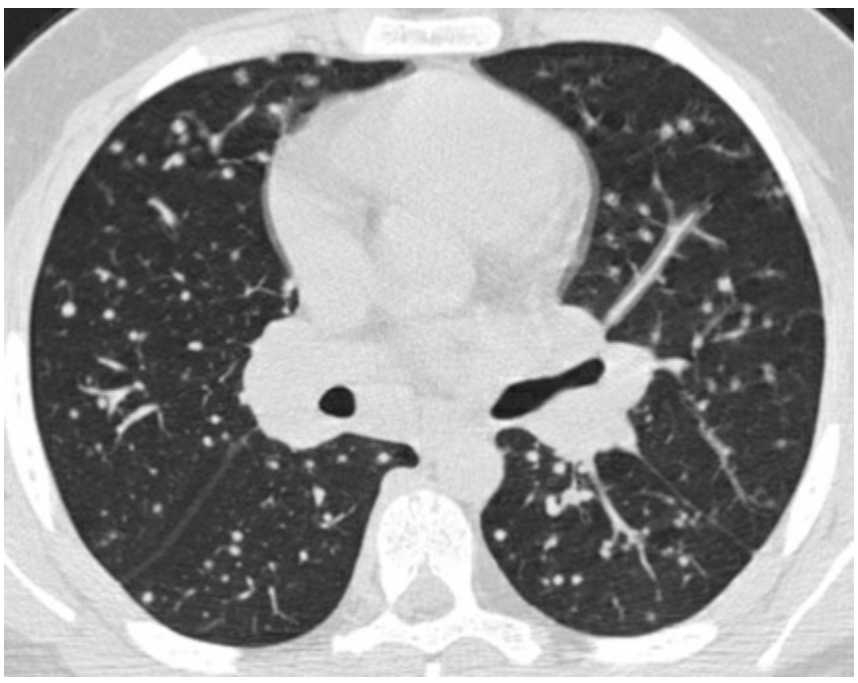
In children with certain underlying conditions, the clinical scenarios and differential diagnoses differ greatly from those seen in the general population. Commonly encountered scenarios include the

evaluation of pneumonia in immunocompromised children, acute chest syndrome in children with sickle cell anemia, and pulmonary complications in children with cystic fibrosis.

Pneumonia in Immunodeficient Children

Children can be immunocompromised for a variety of reasons, including cancer therapy, bone marrow transplantation, solid organ transplantation, primary immunodeficiency, and acquired immunodeficiency syndrome (AIDS). This is a population that continues to increase. Acute pulmonary processes are a common cause of morbidity and mortality in these patients. As with immunocompetent children, radiography is the primary modality used to confirm or exclude pneumonia. However, because many of the chest radiographs obtained in these children are portable and, because of the consequences of missing an infection, CT plays a greater role in evaluating for an acute pulmonary process when chest radiographs are noncontributory. In large children's institutions the number of chest CTs obtained in immunocompromised children is potentially greater than the number of those obtained in immunocompetent children.

In immunocompetent children, the main question is whether a pulmonary process is viral or bacterial. In immunocompromised children, there are many more possible causes of acute pulmonary processes. They include alveolar hemorrhage, pulmonary edema, drug reaction, idiopathic pneumonia, lymphoid interstitial pneumonitis, bronchiolitis obliterans, bronchiolitis obliterans with organizing pneumonia, and chronic graft-versus-host disease. The CT findings for many of these entities are overlapping and nonspecific. A clinical question often posed is this: Is there evidence of fungal infection? The hallmark CT finding indicating fungal infection is the presence of nodules (Figs. 3-32, *A* and *B*, and 3-33). Fungal infection often presents as clustered nodules and may exhibit poorly defined margins, cavitation, or a surrounding halo that has the opacity of ground glass. However, many of these findings are also nonspecific. In these cases CT does aid in directing potential interventions, such as bronchoscopy or percutaneous lung biopsy, to high-yield areas.



▪ **FIGURE 3-32 Histoplasmosis infection.**
CT shows multiple nodules bilaterally. Note bilateral hilar lymphadenopathy.

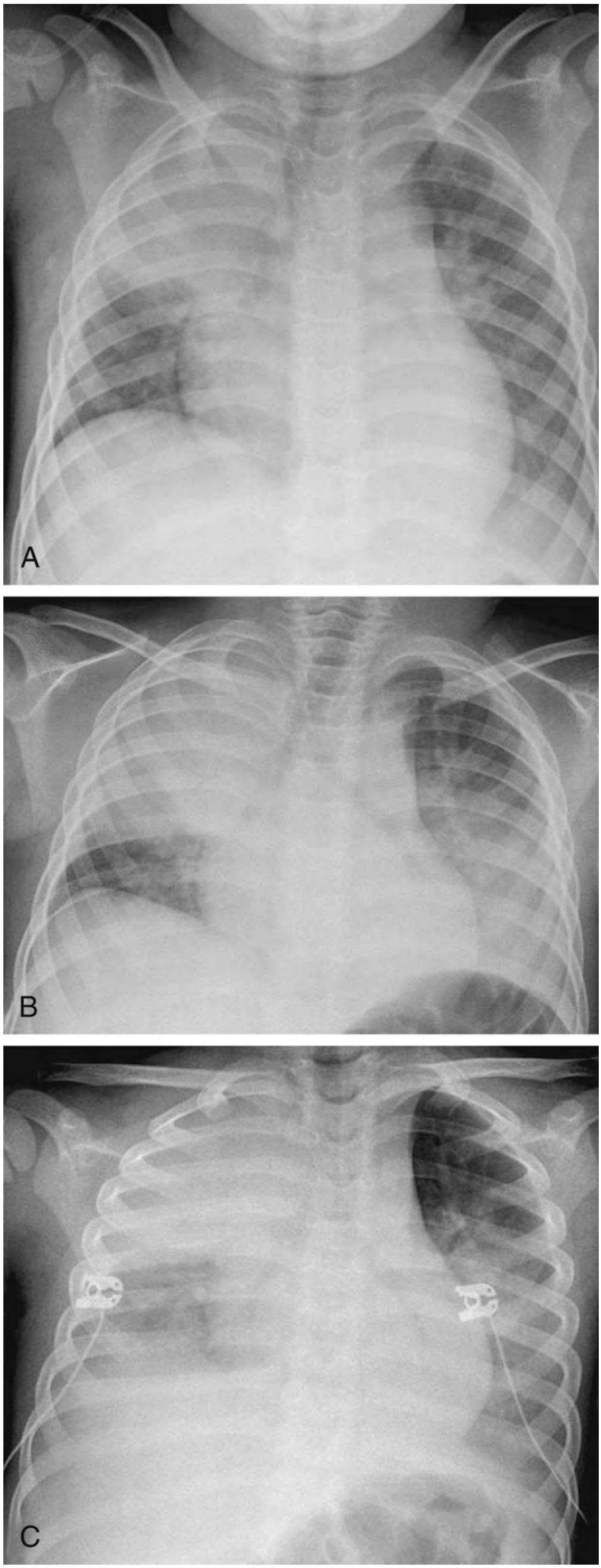
Acute Chest Syndrome in Sickle Cell Anemia

Children with sickle cell anemia can develop acute chest syndrome, which is manifested by fever, chest pain, hypoxia, and pulmonary opacities on chest radiographs (Fig. 3-34). Acute chest syndrome is much more common in children than adults with sickle cell anemia. It occurs most commonly between 2 and 4 years of age and is the leading cause of death (25% of deaths) and the second most common cause of hospitalization in those affected with sickle cell anemia. Although it is debated whether the cause of such episodes is more often related to infection or infarction, many believe the lung opacities are related to rib infarction, splinting, and subsequent areas of atelectasis. Other authors advocate fat embolism, pulmonary infarctions, hypoventilation, and pulmonary or systemic infections as possible etiologies. Radiography often shows segmental to lobar pulmonary opacities but can also be normal. There can be an associated increase in cardiomegaly. Bone scans may show rib infarcts. The children are

treated with oxygen, antibiotics, and pain control, and the pulmonary opacities are commonly monitored by radiography. Pneumonia occurs significantly more commonly in children with sickle cell disease, presumably related to impaired immune function and functional asplenia.

Cystic Fibrosis

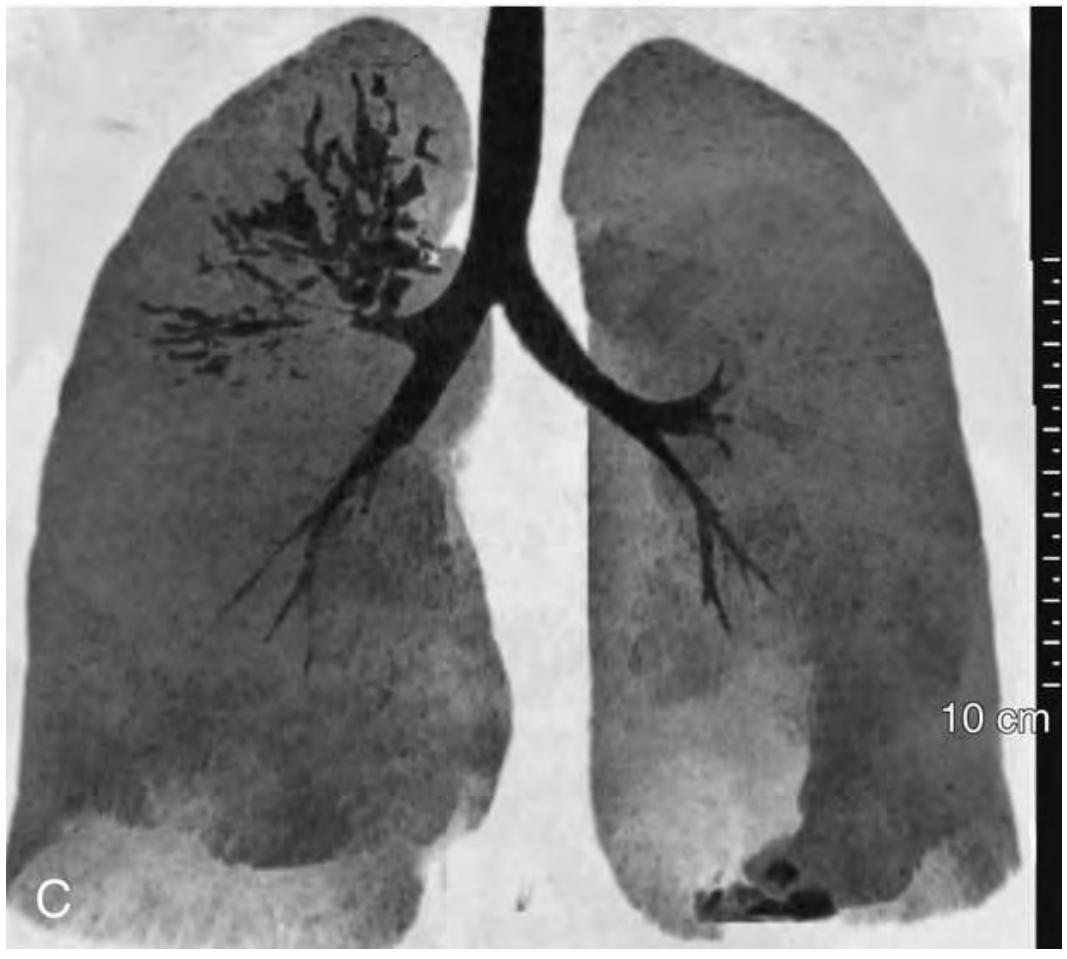
Cystic fibrosis is a genetic disease that most commonly affects the respiratory and gastrointestinal tracts. In the respiratory system, abnormally viscous mucus leads to airway obstruction and infection that causes bronchitis and bronchiectasis. Children may initially present with recurrent respiratory tract infections. Radiography may be normal at young ages but eventually demonstrates hyperinflation, increased peribronchial markings, mucus plugging, and bronchiectasis. The hilar areas can become prominent because of a combination of lymphadenopathy secondary to the chronic inflammation and enlarged central pulmonary arteries related to the development of pulmonary arterial hypertension. Chest radiography is used to monitor the disease and evaluate for complications during acute exacerbations. Such complications include focal pneumonia, pneumothorax, and pulmonary hemorrhage. To monitor the progression of disease, some institutions use low-dose CT with thin-section reconstruction, which demonstrates findings such as bronchiectasis and bronchial wall thickening in greater detail and earlier than does radiography (Fig. 3-35), often at similar radiation doses as a chest radiograph. Some authors advocate the use of MRI for follow-up imaging in patients with cystic fibrosis because it may allow the characterization of several different morphologic and functional imaging features without the use of ionizing radiation.


A
B
C

▪ **FIGURE 3-33** **Acute chest syndrome in a 3-year-old boy with sickle cell anemia.** **A,** Chest radiograph obtained at admission shows focal airspace opacity within the right upper lobe. **B,** Chest radiograph obtained 1 day later shows consolidation of a large portion of the right lung and portions of the left lower lobe. **C,** Chest radiograph obtained 2 days after **A** shows near-complete right lung opacification. Notice moderate cardiomegaly.

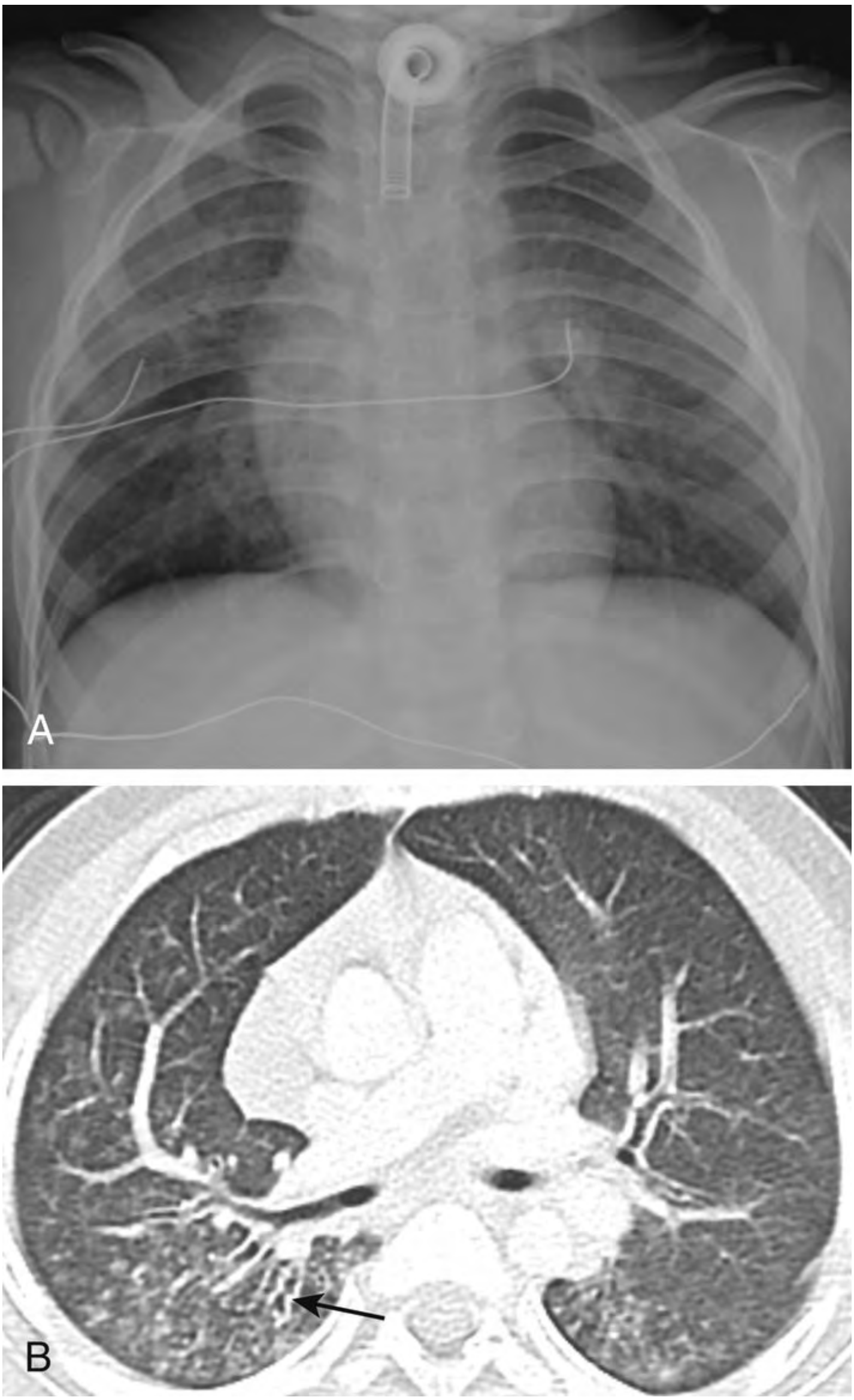

A


B


10 cm
C

▪ **FIGURE 3-34** **Cystic fibrosis.**

A, Radiograph shows areas of bronchial wall thickening and bronchiectasis, most prominent in the right upper lobe. High-resolution (**B**) and coronal minimum intensity projection (**C**) CT images show diffuse bronchiectasis and bronchial wall thickening within the right upper lobe. There are also multiple areas of poorly defined opacities in the peripheral portions of the right upper lobe. These have a tree-in-bud appearance. Notice bilateral patchy areas of air trapping throughout both lungs.



▪ **FIGURE 3-35** **Aspiration.**

A, Radiograph in a child suspected of having aspiration shows increased patchy areas of ground-glass opacification throughout both lungs. **B,** Axial high-resolution CT image shows multiple nodular opacities with tree-in-bud appearance in dependent portions of the lungs, right greater than left. Notice early bronchiectatic change *(arrow)*.

▪ High-Resolution Computed Tomography in Children

High-Resolution Computed Tomography in Questioned Chronic Aspiration

One of the more common indications for HRCT in the pediatric population is questioned chronic aspiration. Often this issue arises in children with neurologic abnormalities, such as cerebral palsy or chronic tracheotomy tubes, when decisions about methods of feeding are being entertained. HRCT findings of chronic aspiration include bronchiectasis, tree-in-bud opacities (Fig. 3-36, *A* and *B*), and increased interstitial linear opacities. Findings more often occur in lower lobes.

Childhood Interstitial Lung Disease

Occasionally, neonates and infants present with pulmonary disorders characterized by extensive lung parenchymal abnormalities and impaired gas exchange primarily related to underlying developmental or genetic disorders constituting a heterogeneous group of diseases known as childhood interstitial lung diseases (chILDs). A recently implemented classification of chILDs recognizes four main categories: (1) diffuse developmental disorders, (2) alveolar growth abnormalities, which is the most common cause of chILDs and includes conditions such as BPD and conditions associated with chromosomal abnormalities and congenital heart disease, (3) surfactant dysfunction disorders and related abnormalities, and (4) specific conditions of unknown or poorly understood etiology, including entities such as neuroendocrine cell hyperplasia of infancy (NEHI) (Fig. 3-37) and pulmonary interstitial glycogenosis (PIG).



▪ **FIGURE 3-36 Neuroendocrine cell hyperplasia of infancy.**
HRCT image shows typical geographic area of ground-glass opacity centrally in the right middle lobe with diffuse air trapping in the remainder of the lung.

On CT, NEHI is characterized by geographic areas on ground-glass opacification in paramediastinal location, particularly in the right middle lobe and lingula (see Fig. 3-37). Two forms of PIG have been described, the diffuse and the patchy forms, the later being the more common form, which is typified by the presence of numerous cystlike lucencies on the background of ground-glass opacification, septal thickening, and reticular changes.

Trauma

Rib Fractures and Lung Contusion

There is a greater component of cartilage than bone within the chest walls of children, so there is more compliance than there is in the chest walls of adults. Because of this increased compliance, the sequelae of trauma to the pediatric chest are unique in several ways. First, the incidence of rib fractures after high-speed motor vehicle accidents is lower in children than in adults. Second, the deceleration forces of high-speed collisions are more likely to be dispersed into the lung in children, resulting in lung contusion. Children with lung contusions have been shown to have higher morbidity and mortality rates than those without lung contusions. Although chest CT is not commonly performed to evaluate for lung contusion, the lower lungs are often seen on CT when it is performed to evaluate for abdominal trauma. Characteristic findings in lung contusion on CT include nonsegmental distribution, posterior location, crescent shape, and mixed confluent and nodular characteristics (see Fig. 3-37). In

children with small lung contusions, the compliance of the chest wall can result in a rim of nonopacified lung between the consolidated contusion and the adjacent ribs seen on CT (see Fig. 3-37). This *subpleural sparing* can be helpful in differentiating lung contusion from other causes of lung opacification. The CT finding that classifies an opacified area as a lung laceration rather than a lung contusion is the presence of a blood- or air-filled cyst (traumatic hematocele or pneumatocele) or both within the opacified lung (Fig. 3-38, *A* and *B*; and see Fig. 3-37). These cystic spaces result from torn lung.



▪ **FIGURE 3-37 Lung contusions and laceration after a motor vehicle accident.**
CT shows characteristic findings of contusion on the left, including posterior location, crescent shape, and nonsegmental distribution *(arrowheads)*. There is left lateral rib fracture *(white arrow)* with adjacent small air-filled pocket *(black arrow)*, consistent with a small lung laceration. Notice the presence of a small-to-moderate left hemopneuthorax.

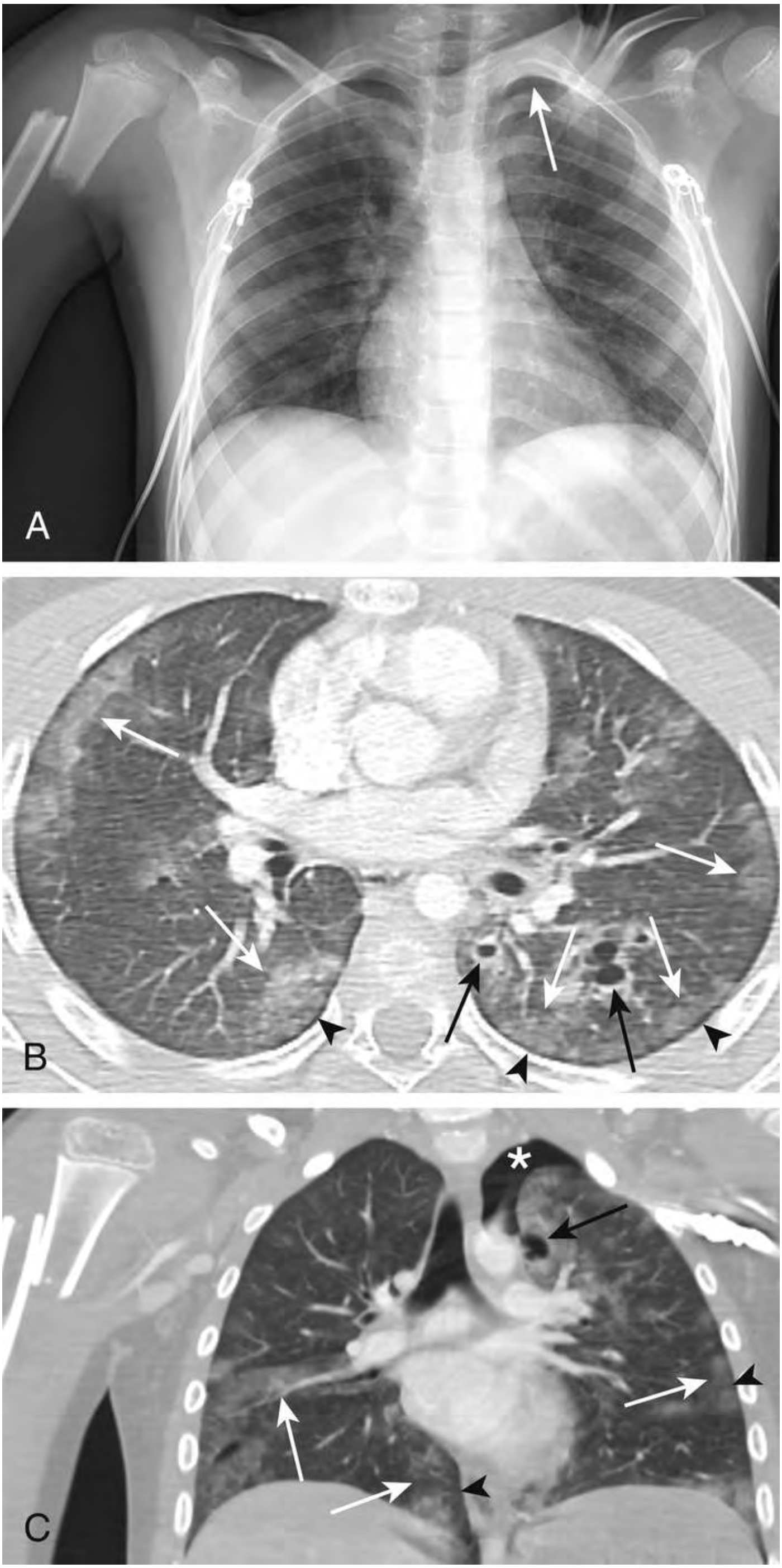
Finally, the sites of rib fracture in children differ from those in adults. Rib fractures in young children in the absence of an obvious traumatic event are highly suspicious for child abuse (Figs. 3-39 and 3-40, *A* and *B*). Pediatric rib fractures are more likely to be posterior than lateral. In child abuse, as a result of squeezing an infant's thorax, the posterior ribs can be excessively levered at the costotransverse process articulation, causing posterior fracture at this site. In the appropriately aged child, these findings are considered pathognomonic for child abuse.

Mediastinal Injury

The incidence of aortic injury is also much lower in children than in adults. This, in combination with the lower incidence of obesity in children as compared to adults, makes the "uncleared" mediastinum on a chest radiograph after trauma a much less common scenario in children than in adults. Otherwise, the use of CT and angiography and the imaging findings of aortic injuries are no different from those encountered in adults.

Hydrocarbon Ingestion

The aspiration of the hydrocarbons in gasoline, furniture polish, kerosene, or lighter fluid when young children get into and drink such liquids can cause a combination of chemical pneumonitis and atelectasis secondary to surfactant destruction. Radiographic findings may not manifest for up to 12 hours after ingestion. However, a normal radiograph at 24 hours after suspected ingestion excludes significant aspiration. The lung opacities tend to be in the lung bases (Fig. 3-41) and may persist for weeks after clinical improvement. Pneumatoceles are not uncommon sequelae.


A
B
C
*

▪ **FIGURE 3-38** **Lung contusions and lacerations with traumatic pneumatocele formation following motor vehicle accident.**

A, Radiograph shows bilateral, multifocal, peripheral areas of nonspecific opacification in nonsegmental distribution consistent with lung contusions. There is a tiny left apical pneumothorax *(arrow)*. Note displaced right humeral shaft fracture. Axial (**B**) and coronal (**C**) reformatted CT images show a few left lower lobe air-filled cysts consistent with traumatic pneumatoceles *(black arrows)*. Patchy areas of opacity are noted in the periphery of the lungs with characteristic subpleural sparing *(arrowheads)* consistent with lung contusion *(white arrows)*. No ribs fractures were present in this case. Notice the small left pneumothorax *(asterisk)* and the right proximal humeral shaft fracture in **C**.

Mediastinal Masses

The mediastinum is the most common location of primary thoracic masses in children. In addition, the majority of mediastinal masses occur in children rather than in adults. As in adults, characterizing the location of the mass as anterior, middle, or posterior mediastinal can focus the differential diagnosis of mediastinal masses (Table 3-4).

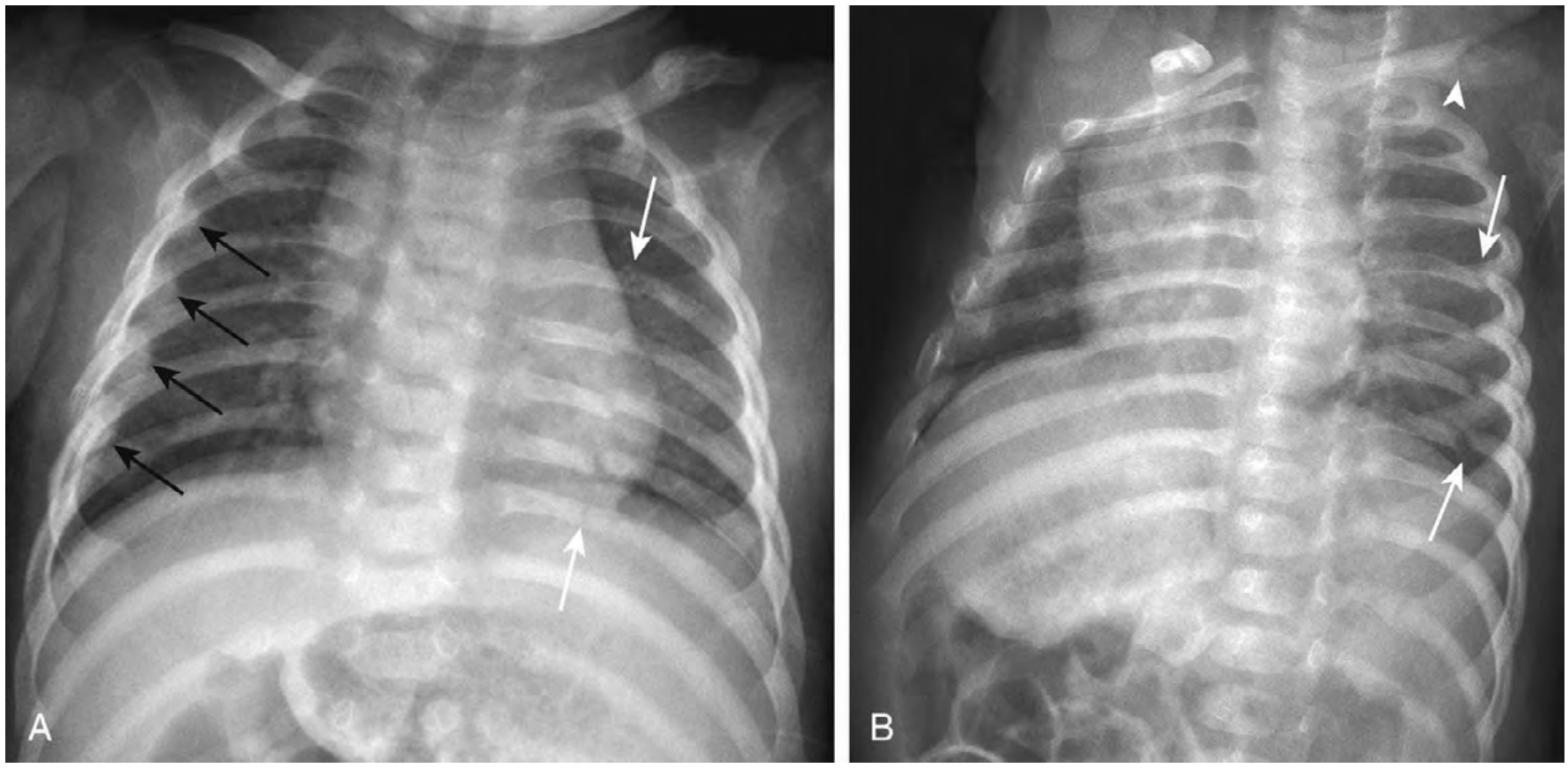
Anterior Mediastinum

By far the most commonly encountered issues in the anterior mediastinum are the normal thymus (when mistaken as a mass) and lymphoma. There are a large number of other potential but much less common causes of anterior mediastinal masses in children. They include teratoma (and other germ cell tumors), thymoma, multilocular thymic cysts seen in association with AIDS, and thymus enlargement and heterogeneity (often with calcifications or cysts) in Langerhans cell histiocytosis (in which lung cysts are also present; Fig. 3-42).

Normal Thymus

One of the most common areas of confusion in the imaging of children is related to differentiating the normal thymus from pathologic processes. This confusion led to thymic radiation therapy in the first half of the twentieth century, when children with a normal, prominent thymus on chest radiography were radiated because of the erroneous belief that a big thymus compressed the airway and predisposed to death. Interestingly, it was the fallout around the unnecessary irradiation of thousands of children related to the misinterpretation of the large thymic shadow on chest radiographs that led to the recognition that children were not just "small adults" and gave rise to the first radiology subspecialty training fellowships—which were in pediatric radiology.

Distinguishing the normal thymus from disease continues to cause diagnostic problems today, particularly for those who do not often image children. In children the thymus has a variable appearance in both size and shape. In children less than 5 years of age, and particularly in infants, the thymus can appear to be very large (Fig. 3-43). Large thymuses are said to be more common in boys but can also be seen in girls. The thymus also has variable configurations. A number of names have become associated with normal variations in the thymus, such as the sail sign (Fig. 3-44), which refers to a triangular extension of the thymus, most commonly to the right, on frontal chest radiography. It resembles a sail. This should not be confused with the spinnaker sail sign (Fig. 3-45), which is an indication of pneumomediastinum, in which the abnormally located air lifts the thymus up so it looks like the sail on the front of a racing boat. Typically it is the left lobe that is lifted by the pneumomediastinum. If both lobes are lifted, the appearance is called *angel's wing sign*.



▪ **FIGURE 3-39** **Child abuse.**

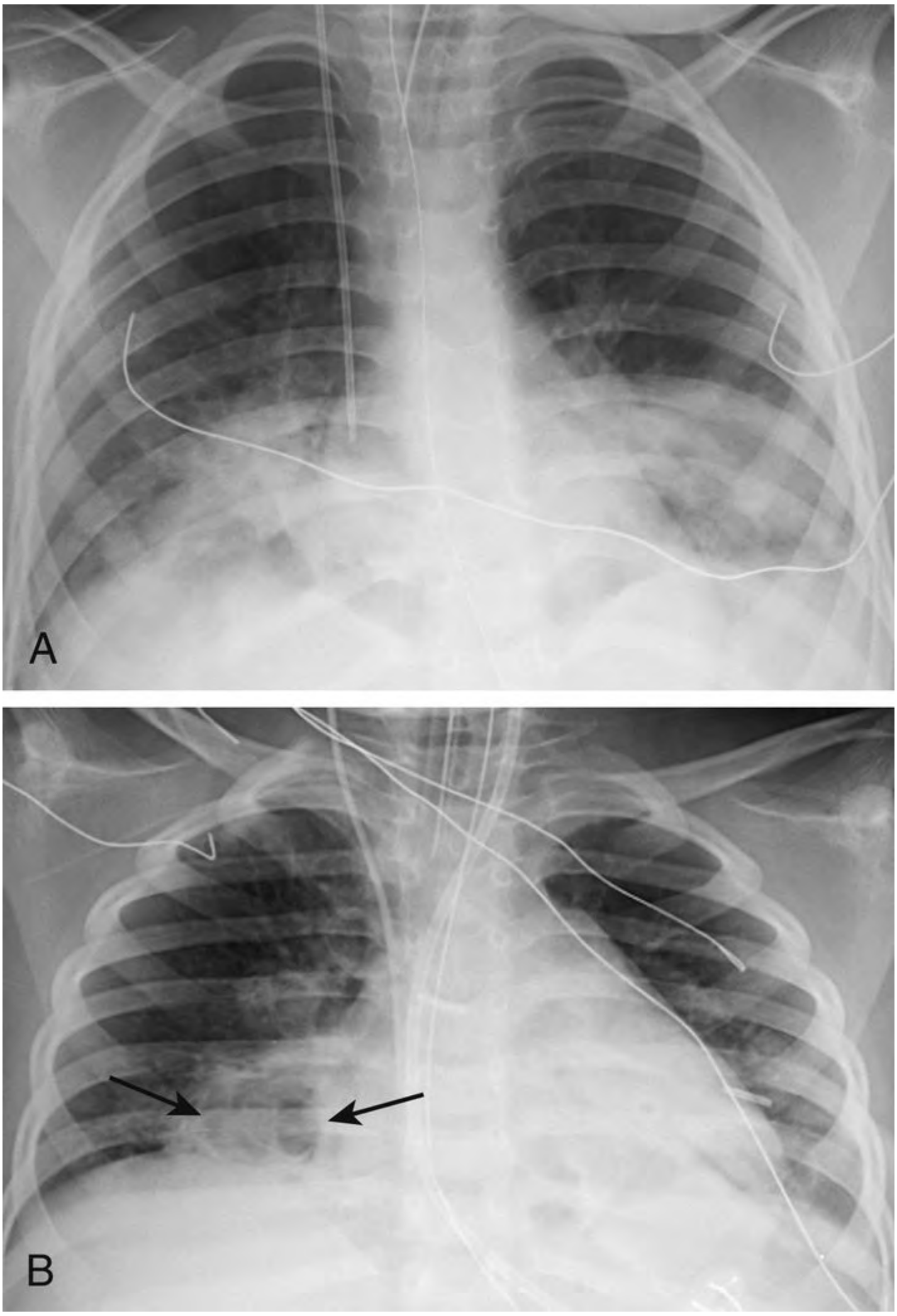
Frontal (**A**) and oblique (**B**) radiographs show healing fractures *(black arrows)* of right third, fourth, fifth, and sixth ribs. There are acute fractures *(white arrows)* of the posterior left fifth, sixth, seventh, eighth, and ninth ribs. Fractures are better appreciated on the oblique view. Note subacute healing left clavicular fracture *(arrowhead)*.



▪ FIGURE 3-40 **Child abuse.**

A, Radiograph shows multiple fractures that occurred at different times. There are multiple subacute healing rib fractures *(black arrows)* with callus formation and multiple acute right- and left-sided rib fractures *(white arrows)* without callus formation. **B,** Axial CT image shows callus around healing rib fractures *(black arrows)* on the left anterolaterally and on the right posterolaterally. A characteristic acute fracture of the posterior rib *(black arrow)* is seen on the left. **C,** Coronal reformatted CT image shows to better advantage bilateral acute *(white arrows)* and right subacute *(black arrows)*, healing rib fractures.

Between 5 and 10 years of age, the thymus becomes less prominent radiographically because of the disproportionately decreased growth of the thymus in relationship to the growth of the rest of the body. During a child's second decade, the thymus should not be visualized as a discrete anterior mediastinal mass on chest radiography.



▪ **FIGURE 3-41** **Hydrocarbon aspiration in a 4-year-old boy who accidentally drank lighter fluid.** The patient became immediately unresponsive and coughed a foamy fluid. **A,** Chest radiograph shows bibasilar lung consolidation. The patient is intubated. An enteric tube is seen coursing along the esophagus. A right-sided approach, internal jugular vein line is seen with its tip overlying the proximal right atrium. **B,** Follow-up chest radiograph obtained 12 days later shows interval development of right basilar pneumatoceles *(arrows)*.

Abnormality of the thymus (or anterior mediastinum) is suspected when the thymic silhouette has an abnormal shape or an abnormal size in relationship to the patient's age. Displacement or compression of the airway or other structures is suspicious for abnormality. CT, ultrasound, MRI, and fluoroscopy can be used to help to differentiate the normal thymus from an abnormal mass, but CT is probably used most commonly. When CT is performed to evaluate suspicious cases, the normal thymus should appear homogeneous in attenuation, typically is quadrilateral in shape in young children (Fig. 3-46) and triangular in teenagers (Fig. 3-47, *A* and *B*), and may have slightly convex margins. Heterogeneity, calcification, and displacement or compression of the airway or vascular structures

indicate an abnormality (Fig. 3-48, *A-D*; and see Fig. 3-42). True pathologic masses of the thymus are actually quite rare in children.

Thymic rebound is another source of confusion concerning normal thymic tissue. After a patient has ceased receiving chemotherapy for a malignancy, it is normal for the thymus to grow back, as seen in serial CT examinations. Thymic volume has been shown to vary cyclically by as much as 40% during rounds of chemotherapy (see Fig. 3-47). This intervallic increase in soft tissue attenuation in the anterior mediastinum should not be considered abnormal when encountered on cross-sectional imaging.

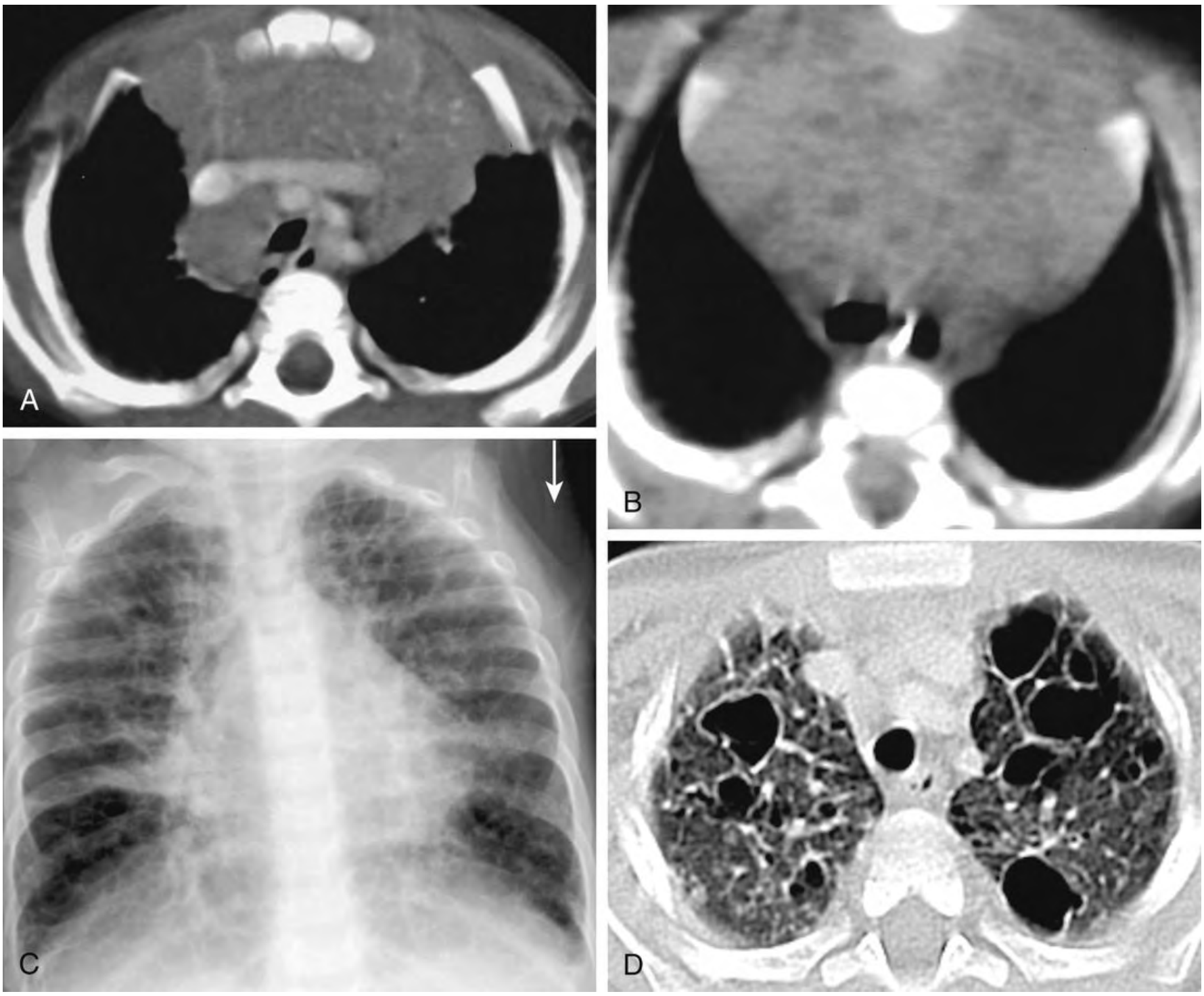
Lymphoma

Lymphoma is the third most common tumor in children, exceeded only by leukemia and brain tumors. It is by far the most common abnormal anterior mediastinal mass in children, particularly in older children and teenagers. Therefore lymphoma is the working diagnosis for newly diagnosed anterior mediastinal masses in children. Age is helpful in differentiating a normal thymus from lymphoma because a normal thymus is most common in small children and lymphoma is most common in teenagers. The most problematic case is the slightly prominent anterior mediastinum in an approximately 10-year-old child. One helpful clinical clue in identifying lymphoma is that mediastinal lymphoma is commonly associated with cervical lymphadenopathy.

TABLE 3-4

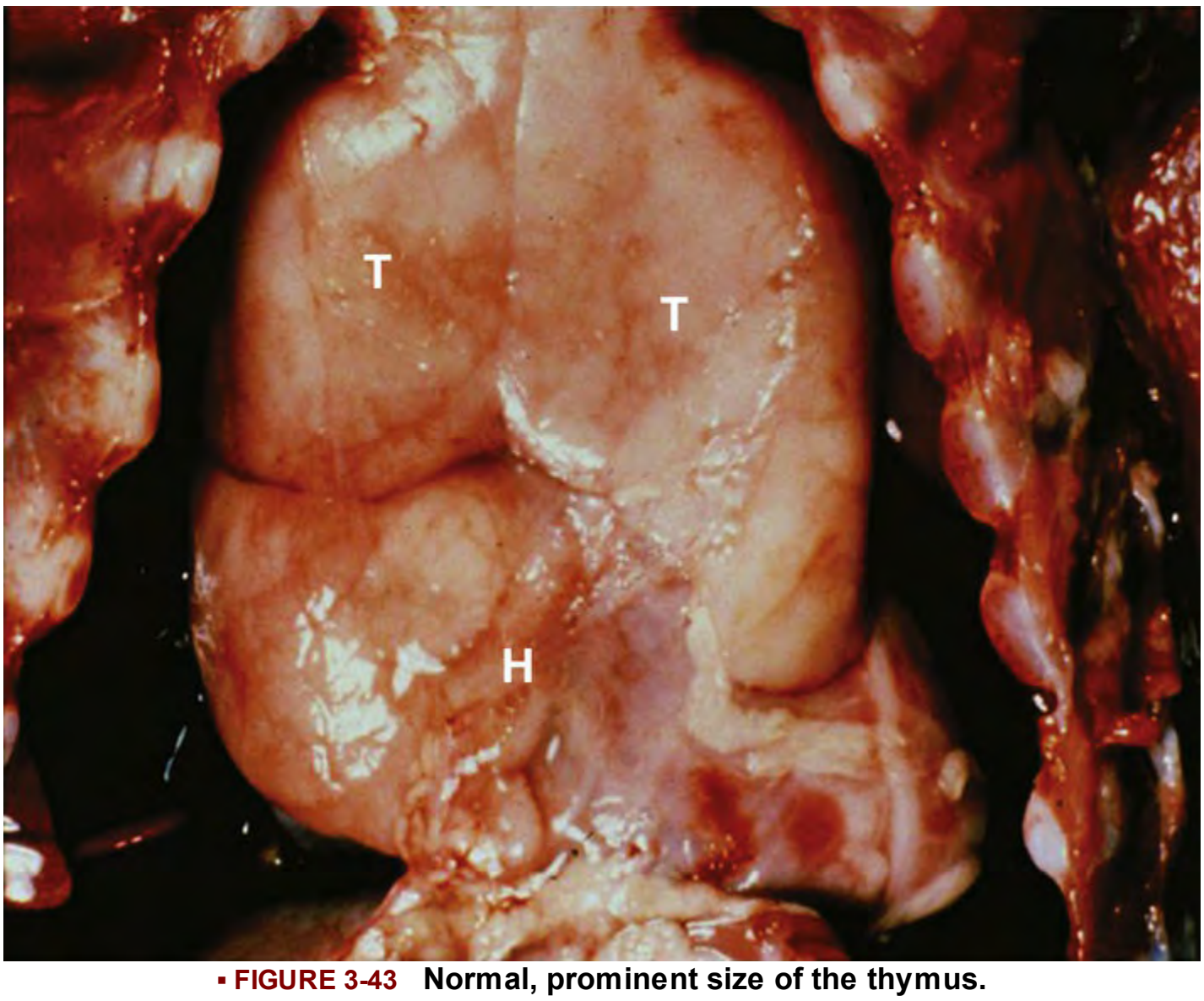
Common Mediastinal Masses by Location

Anterior	Middle	Posterior
Normal thymus	Lymphadenopathy	Neuroblastoma
Lymphoma	Duplication cyst	
Teratoma (germ cell tumor)		



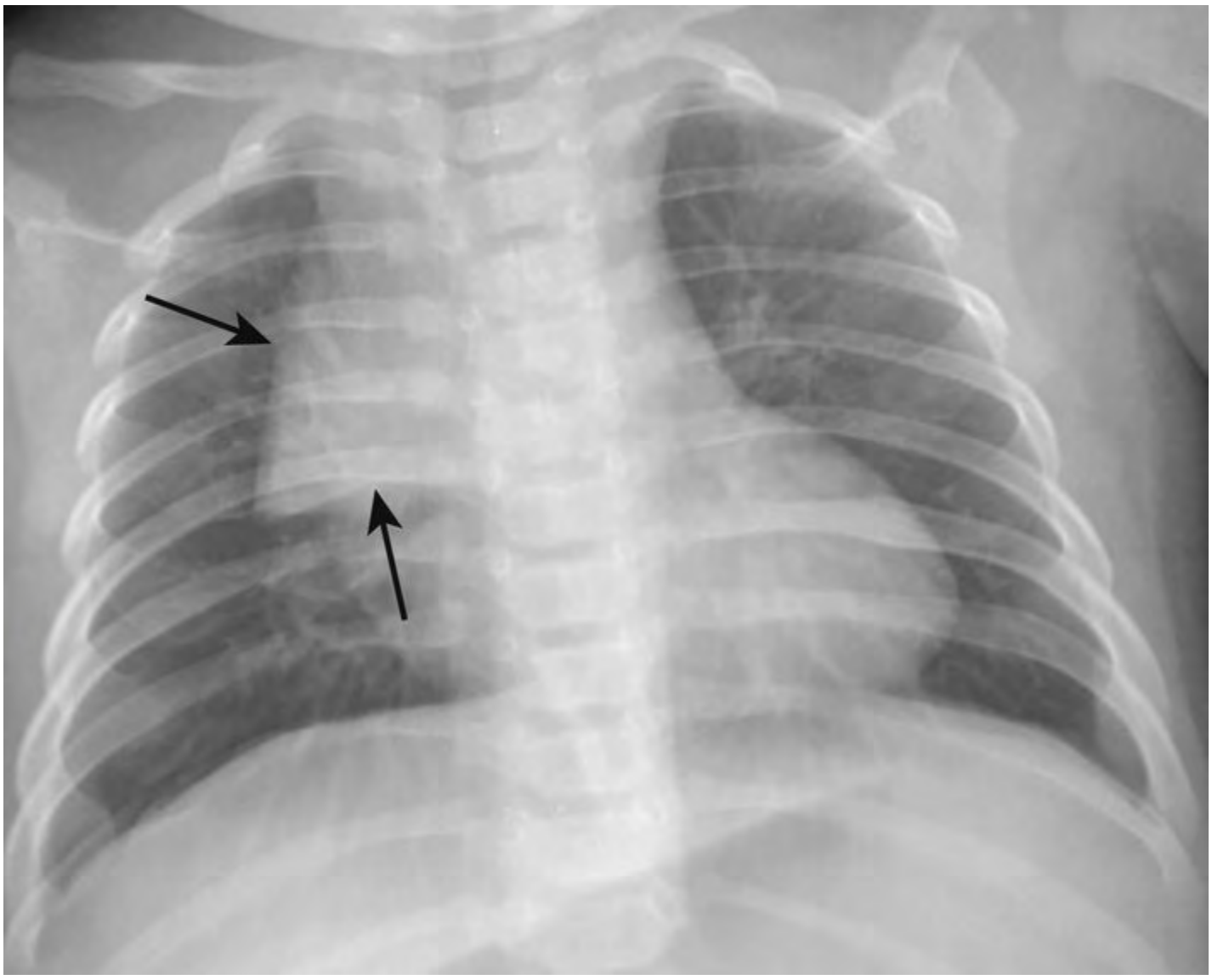
▪ **FIGURE 3-42** **Thymus in langerhans cell histiocytosis.**

A, In this child the thymus is enlarged and shows multiple punctate calcifications. **B,** Different child with Langerhans cell histiocytosis. CT shows a prominent thymus with numerous tiny cysts. Chest radiograph (**C**) and axial high-resolution CT image (**D**) of pulmonary Langerhans cell histiocytosis in another child show numerous cysts and coarsening of the pulmonary interstitium throughout both lungs.

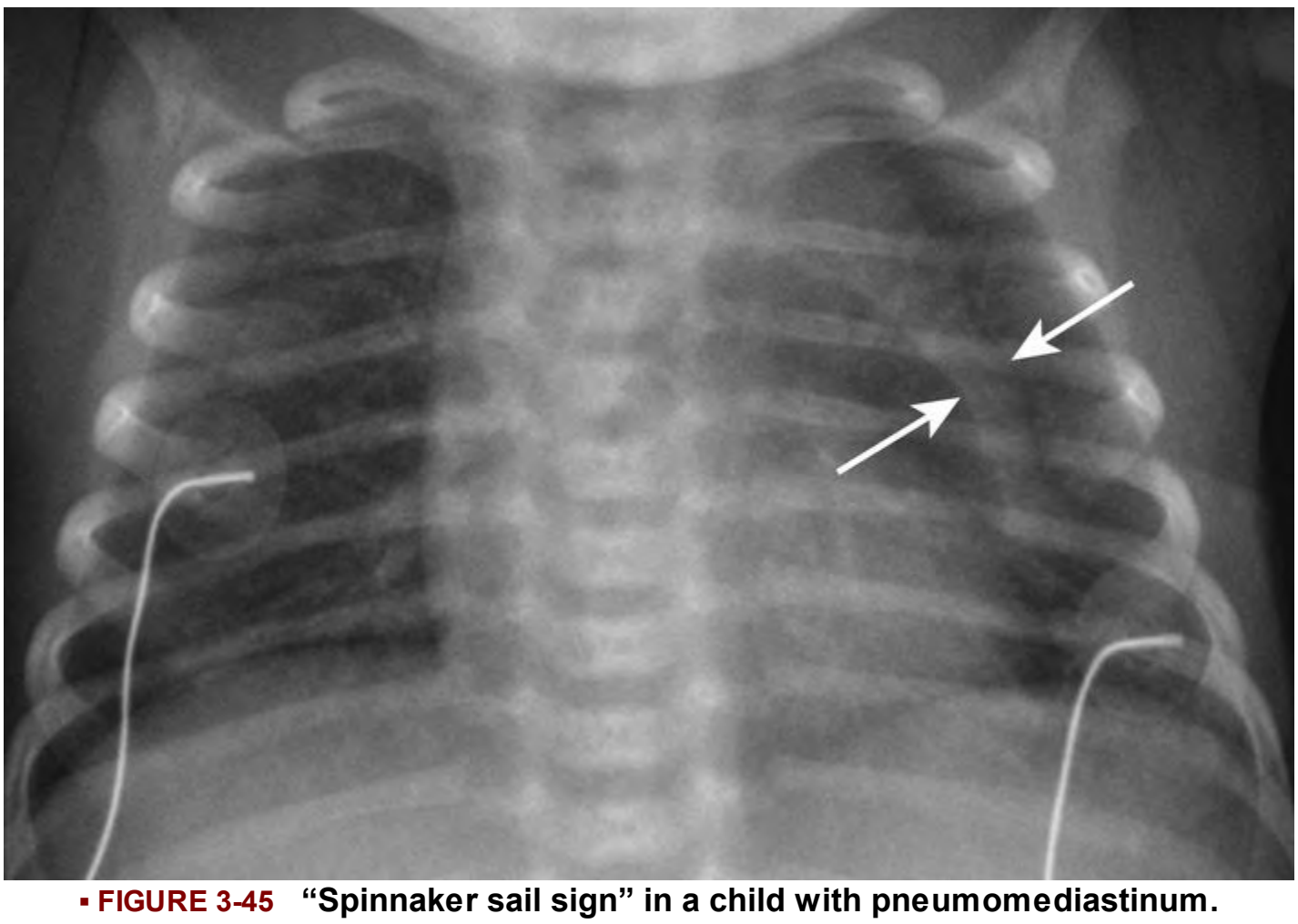


▪ **FIGURE 3-43** **Normal, prominent size of the thymus.**

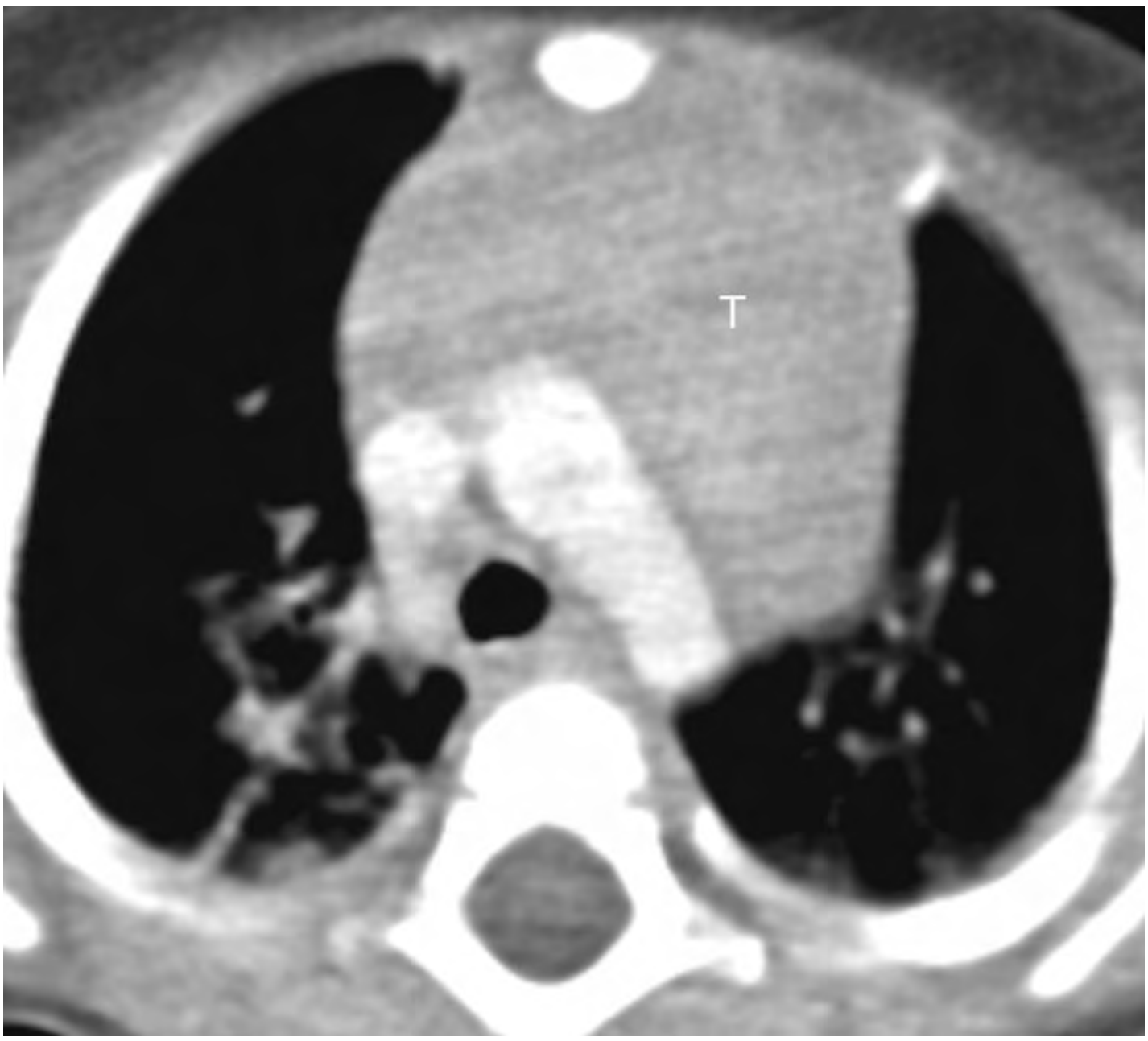
Photograph from autopsy of an infant who died of sudden infant death syndrome shows frontal view of thymus *(T)* after thoracotomy. Note the prominent size of the thymus in relation to the heart *(H)*. The thymus is bilobed. In this patient the left lobe is larger than the right. (Image courtesy Janet L. Strife, MD, Cincinnati, OH.)



▪ **FIGURE 3-44** **Normal, prominent thymus with “sail” sign.**
Radiograph shows prominent but normal thymus with rightward triangular extension *(arrows)*. This appearance should not be confused with right upper lobe pneumonia.

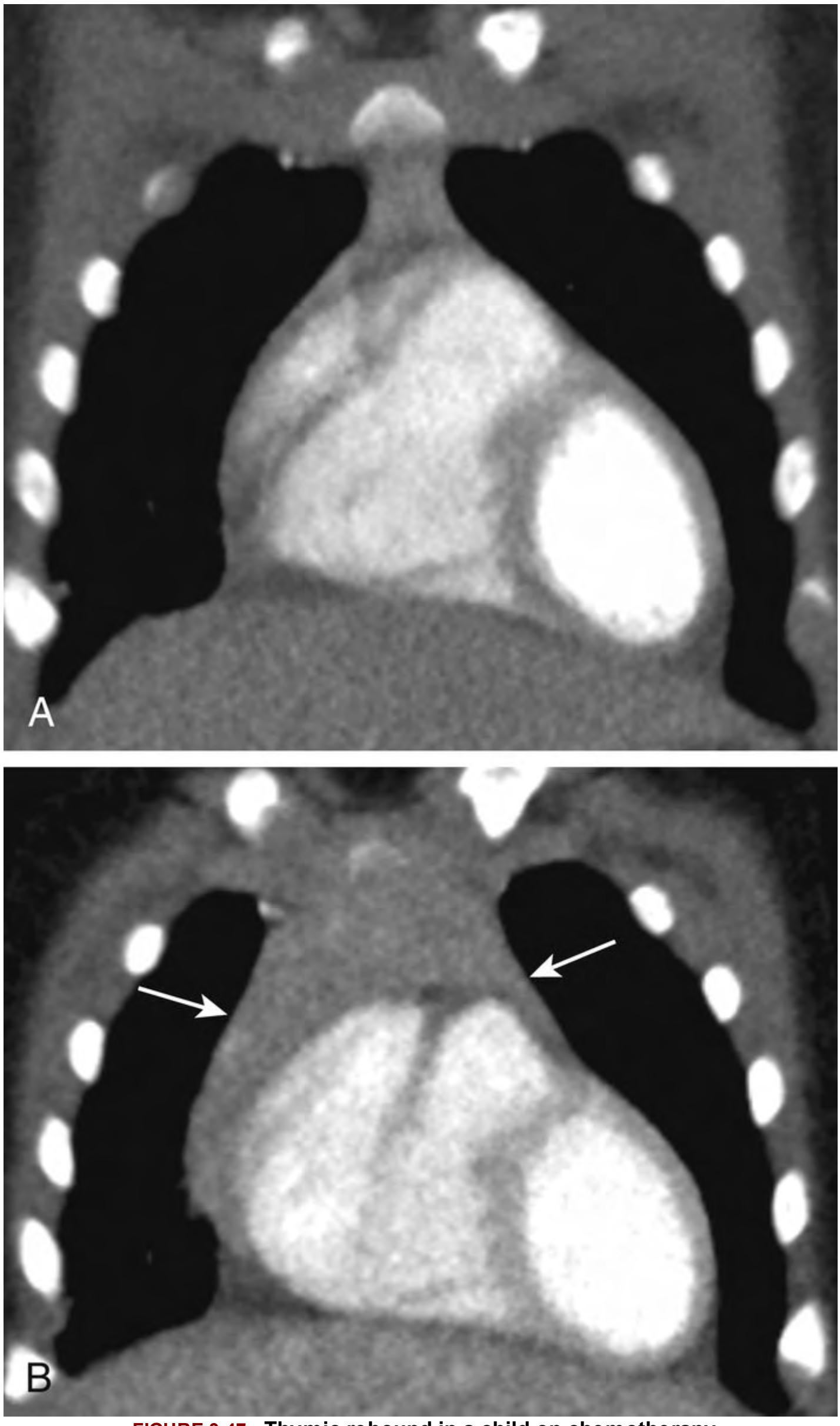


▪ **FIGURE 3-45** **“Spinnaker sail sign” in a child with pneumomediastinum.**
Radiograph shows thymus *(arrows)* lifted off of mediastinum by air in mediastinum. The uplifted thymus resembles a spinnaker sail.



▪ **FIGURE 3-46** **Normal thymus on cross-sectional imaging.**
CT in a young child shows thymus *(T)* to be quadrilateral in shape, have convex margins, and be of homogeneous attenuation. There is no compression of the trachea or superior vena cava.

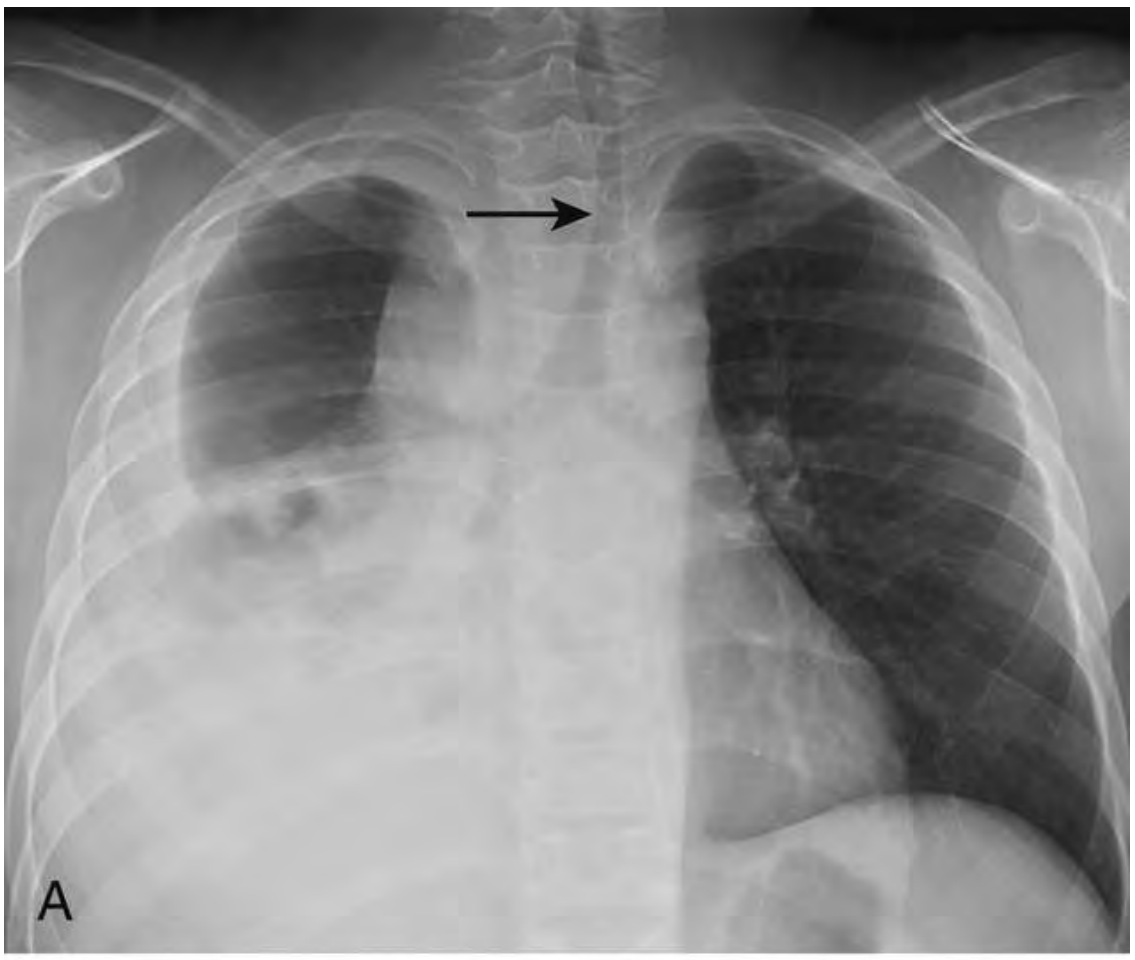
The most common types of lymphoma that involve the mediastinum include Hodgkin lymphoma and the lymphoblastic type of non-Hodgkin lymphoma. Both lesions can appear as discrete lymph nodes or as a conglomerate mass of lymph nodes, most commonly within the anterior mediastinum (see Fig. 3-48). Lung involvement, when present, is usually contiguous with mediastinal and hilar disease. Calcifications are rare in untreated lymphoma and when present should raise the possibility of other diagnoses, such as teratoma (Fig. 3-49), a form of germ cell tumor.

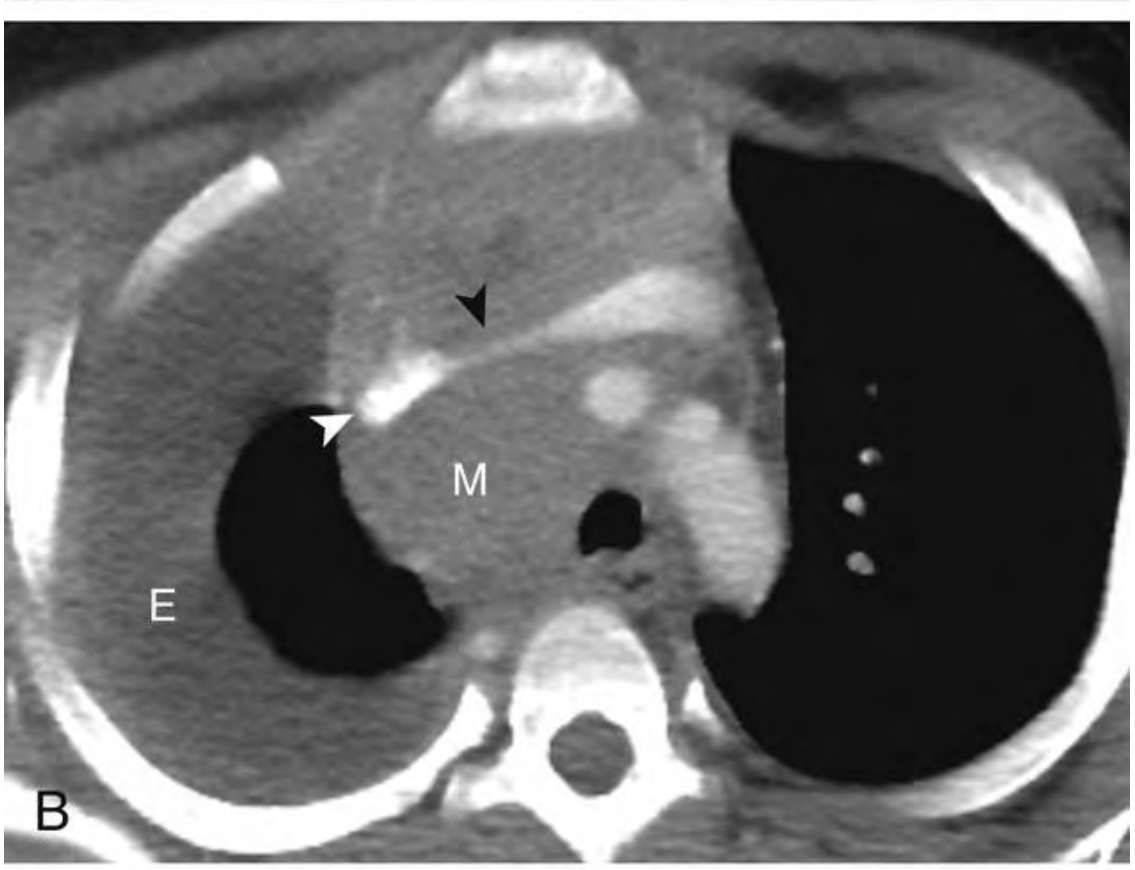


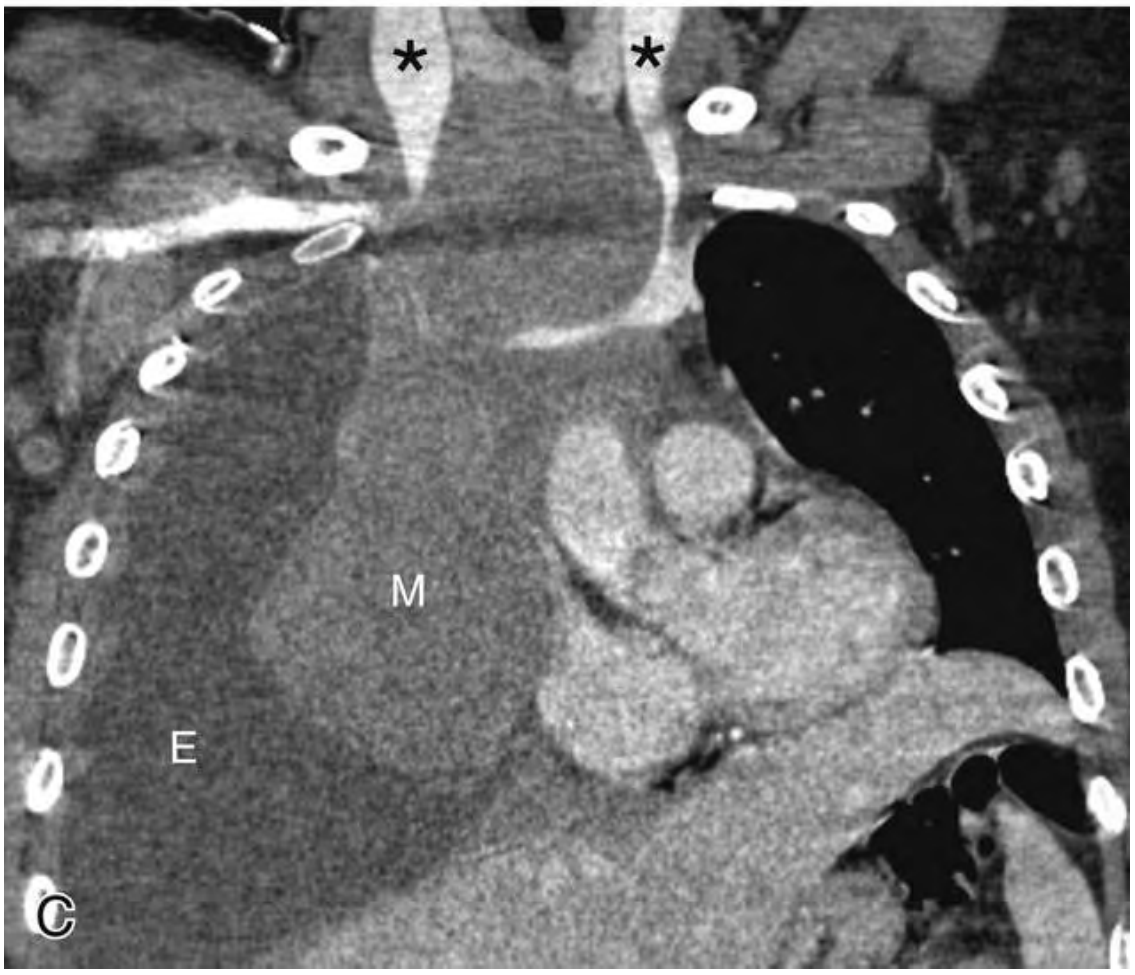
▪ **FIGURE 3-47** **Thymic rebound in a child on chemotherapy.**
A, Coronal reformatted CT image taken while the child was on chemotherapy shows little thymic tissue. **B,** CT taken 3 months later when child was off chemotherapy shows regrowth of thymus *(arrows)*.

Most mediastinal masses are initially identified on chest radiography and then further evaluated by CT, which confirms the presence of an anterior mediastinal mass, evaluates the extent of disease, and evaluates for potential complications. The potential complications related to mediastinal lymphoma

include airway compression, compressive obstruction of venous structures (superior vena cava, pulmonary veins), and pericardial effusion (Fig. 3-50; see Fig. 3-48). Airway compression is especially important because it may influence decisions concerning surgical biopsy with general anesthesia versus percutaneous biopsy with local anesthesia. If a patient cannot lie recumbent for CT imaging because of airway compression, the images can usually be obtained with the patient positioned prone because the anterior mediastinal mass falls away from the airway. Compression of the airway by more than 50% from the expected round shape has been shown to be associated with a high risk for complications related to anesthesia. Because of this, some such mediastinal masses are biopsied using ultrasound guidance and local anesthesia.


A


M
E
B


*
*
M
E
C

▪ **FIGURE 3-48** **Lymphoma.**
A, Frontal radiograph shows marked enlargement of superior mediastinum and associated large right pleural effusion. Note leftward displacement and compression of the trachea *(arrow)*, further supporting the presence of an abnormal mediastinal mass. Axial (**B**) and coronal (**C**) reformatted CT images show a large anterior mediastinal mass *(M)* with compression and posterior displacement of trachea *(arrow)* and compression of the superior vena cava *(white arrowhead)* and left brachiocephalic vein *(black arrowhead)*, which is markedly narrowed. The mass and large right pleural effusion *(E)* result in mass effect and leftward displacement of the heart. Note right atrial compression. Notice engorgement of the bilateral internal jugular veins *(asterisks)*.

Middle Mediastinal Masses

Middle mediastinal masses are less common than anterior or posterior mediastinal masses and are usually related to lymphadenopathy or duplication cysts. Lymphadenopathy can be inflammatory, most often secondary to granulomatous disease, such as tuberculosis or fungal infection; or to neoplastic growth secondary to metastatic disease or lymphoma. Duplication cysts can be bronchogenic enteric, or neurenteric. Duplication cysts are well-defined masses that appear cystic on cross-sectional imaging. Neurenteric cysts, by definition, have associated vertebral anomalies. Pathologic processes related to the esophagus can also cause middle mediastinal abnormalities. Chronic foreign bodies can erode through the esophagus and cause a middle mediastinal mass, typically in the cervical esophagus at the level of the thoracic inlet (Fig. 3-51, *A* and *B*). A dilated esophagus resulting from achalasia or a hiatal hernia may also appear as a middle mediastinal mass on chest radiography.

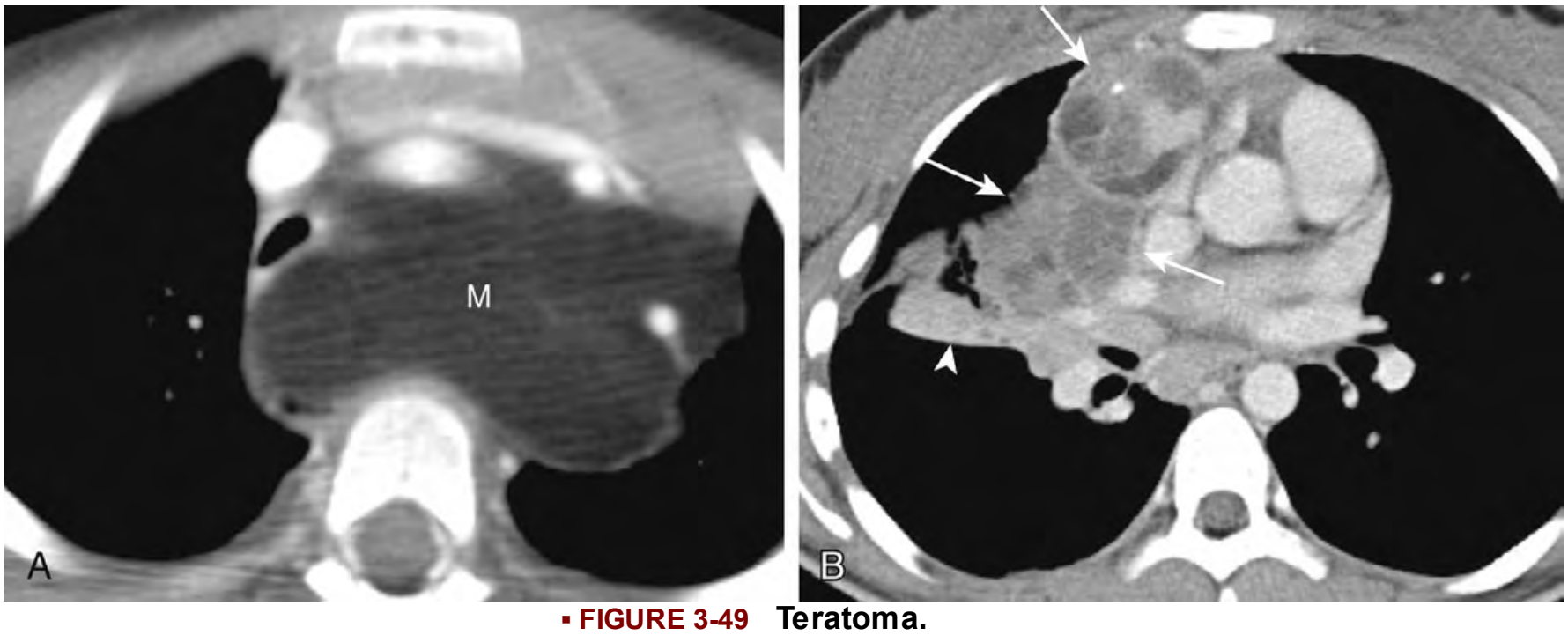
Posterior Mediastinal Masses

There are a number of causes of posterior mediastinal masses in children. They include neural crest tumor, neurofibroma, lateral menigocele, diskitis, hematoma, and extramedullary hematopoiesis. However, just as anterior mediastinal masses in older children are considered to be lymphoma, the working diagnosis for posterior mediastinal masses in young children is neuroblastoma until proven otherwise.

Neuroblastoma

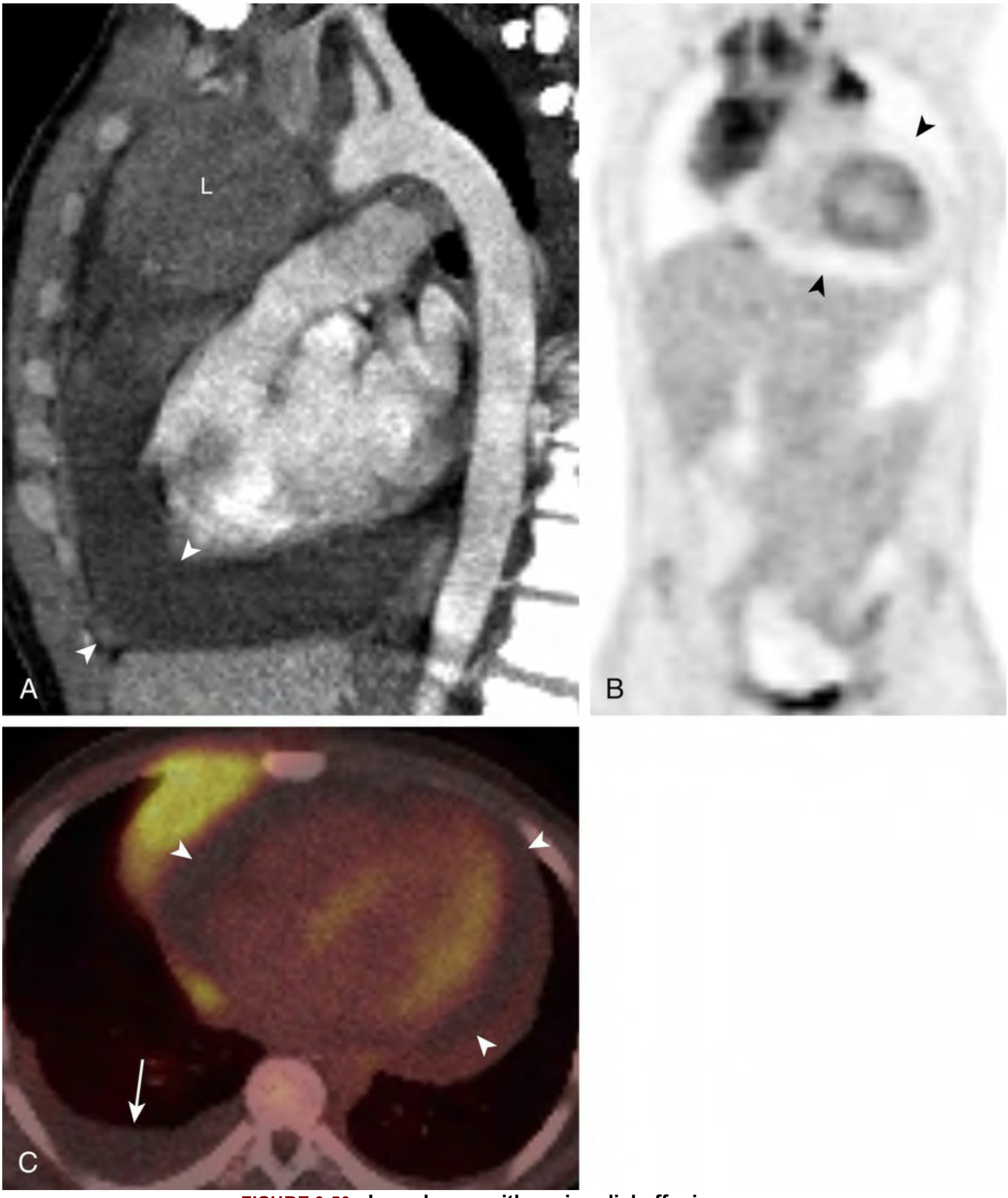
Neurogenic tumors (neuroblastoma, ganglioneuroblastoma, ganglioneuroma) are the most common posterior mediastinal masses in childhood. Neuroblastoma is discussed in detail in the genitourinary section. Approximately 15% of neuroblastomas occur in the posterior mediastinum, most occurring before a child is 2 years of age.

Most neuroblastomas are visible on frontal radiographs of the chest as a posterior opacity (Fig. 3-52, *A-D*). The soft tissue mass is often surprisingly poorly visualized on the lateral view. There is frequently erosion, destruction, or splaying of the adjacent posterior ribs. These findings may be subtle; so whenever a posterior chest opacity is identified, an effort should be made to look for rib erosion. The neuroforamina may appear enlarged on the lateral view, secondary to intraspinal extension of the tumor. Calcifications are reported to be visible on chest radiography in as many as 25% of cases, although in the author's experience it is less than that. Cross-sectional imaging with CT or MRI confirms the presence of the tumor and evaluates extent of disease, particularly whether there is intraspinal extension. Thoracic neuroblastomas have better prognosis than abdominal neuroblastomas.



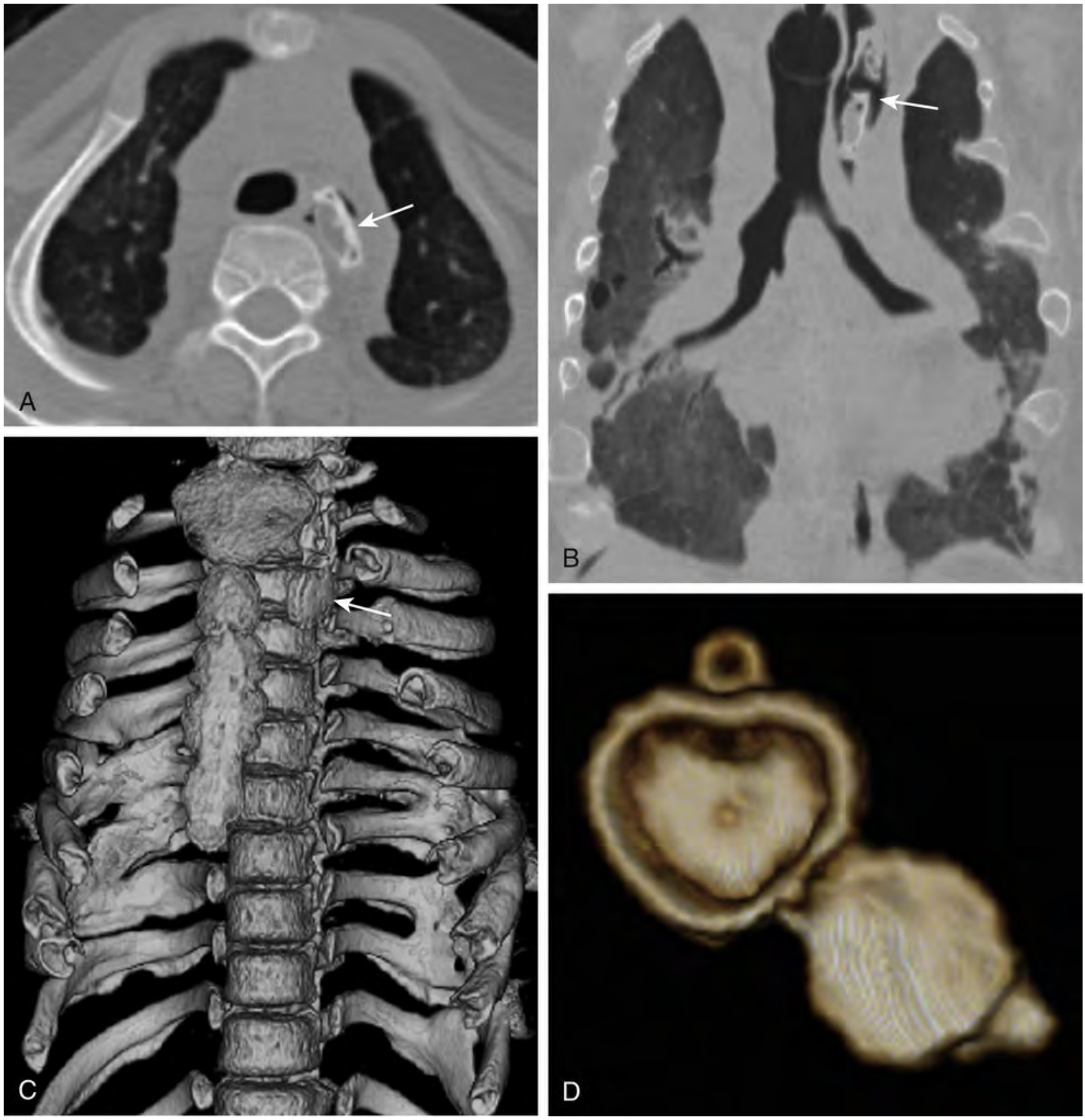
▪ **FIGURE 3-49** **Teratoma.**

A, CT shows anterior mediastinal mass *(M)* that is of fat attenuation. **B,** Axial CT image in another patient shows a large anterior mediastinal mass *(arrows)* with fatty, cystic, and calcific components. The lesion resulted in postobstructive pneumonia in the right middle lobe *(arrowhead)*.



▪ **FIGURE 3-50** **Lymphoma with pericardial effusion.**

A, Sagittal-reformatted CT image in an adolescent shows an anterior mediastinal mass *(L)*. Note adjacent, large pericardial effusion *(arrowheads)* encircling the heart. Coronal positron emission tomography (PET) (**B**) and axial fused PET (**C**) CT images show hypermetabolism corresponding to the pathologic mediastinal lymphadenopathy, a fairly sized pericardial effusion *(arrowheads)* and right pleural fluid *(arrow)*.



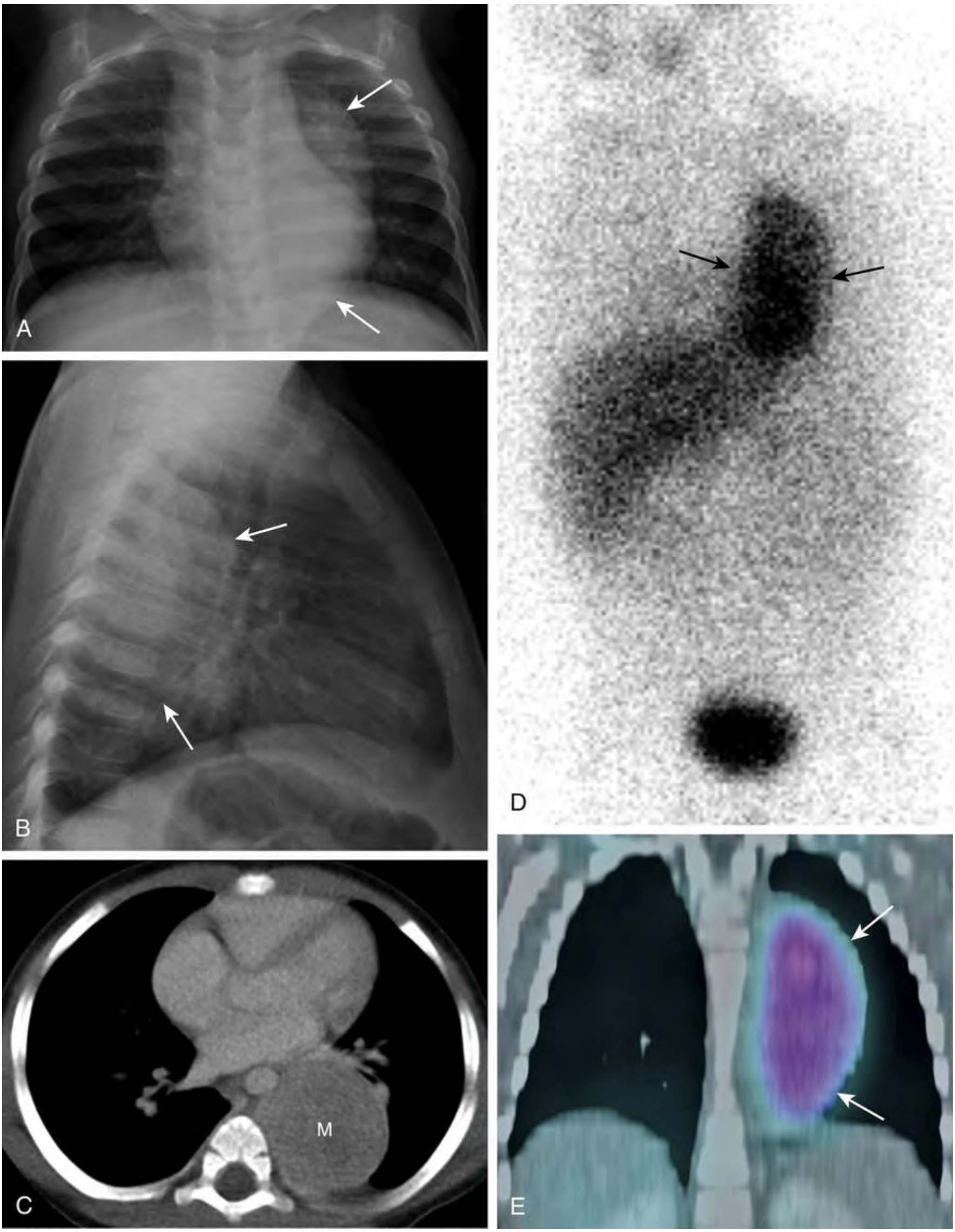
▪ **FIGURE 3-51** **Chronic esophageal foreign body presenting as worsening respiratory symptoms in a young child with Jeune syndrome.**

Axial (**A**) and coronal (**B**) reformatted CT images show a distended upper esophagus with an internal metallic density *(arrows)* suspicious for a chronic foreign body within the upper esophagus with adjacent inflammatory changes. **C,** Volume rendered three-dimensional reconstruction CT images show a heart-shaped locket *(arrow)* lodged in the upper esophagus. At surgical retrieval, the foreign body was found to be a locket heart. CT reconstruction of locket alone shown in **D**.

Pediatric Chest Wall Masses

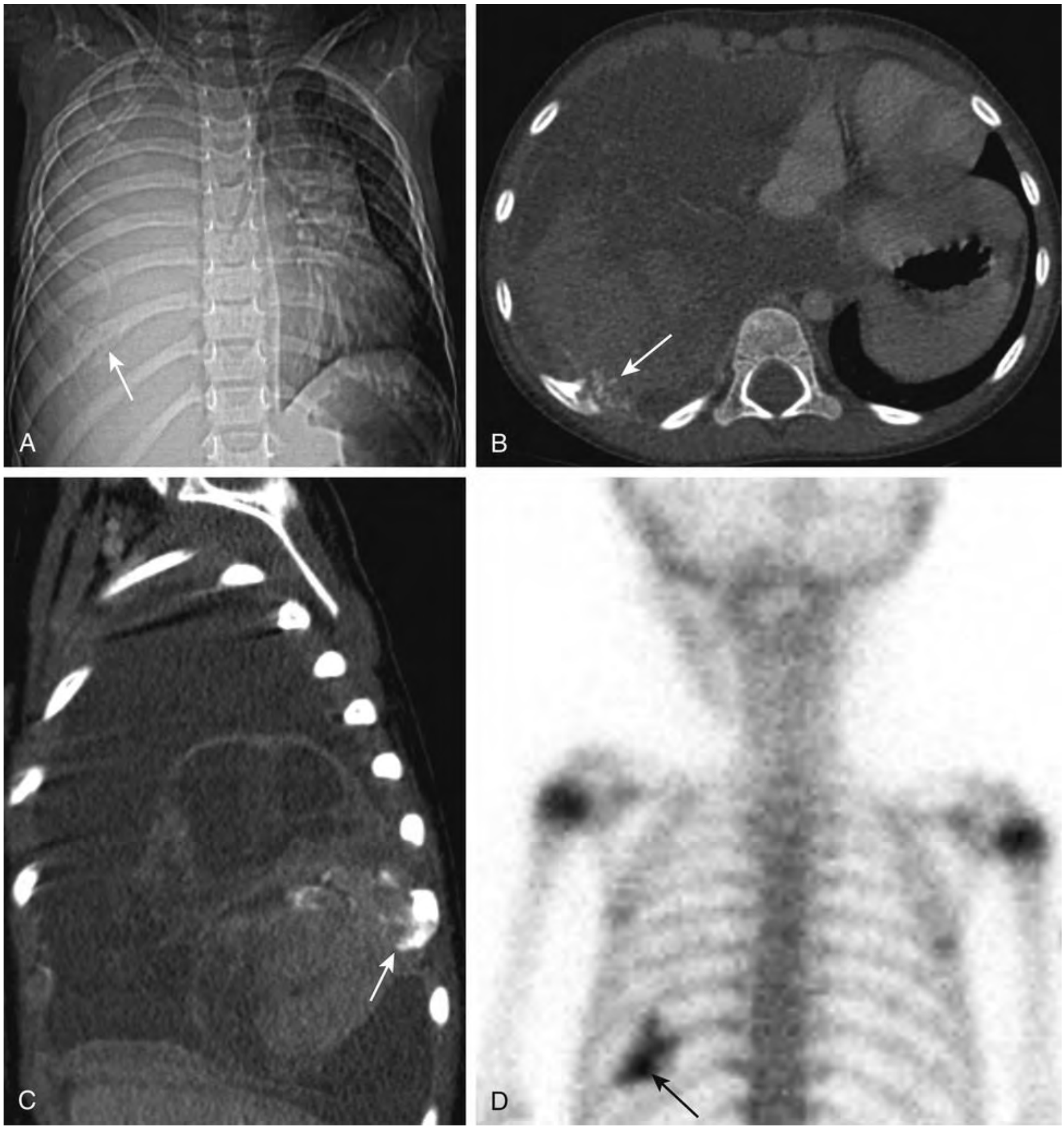
A number of primary malignant processes can arise in the chest walls of children. They include Ewing sarcoma (Fig. 3-53), Askin tumor (primitive neuroectodermal tumor of the chest wall), and other sarcomas. Most of these lesions present with painful enlargement of the chest wall. Metastatic involvement by neuroblastoma, lymphoma, or leukemia is actually more common than are primary tumors. On imaging, all of these malignancies typically appear as nonspecific aggressive lesions with poorly defined margins that include bony destruction and pleural involvement. However, one must consider that as much as one third of children have variations in the configuration of the anterior chest wall, including asymmetric findings, such as tilted sternum (Fig. 3-54), prominent convexity of anterior

rib or costal cartilage, prominent asymmetric costal cartilage, parachondral nodules, or mild degrees of pectus excavatum or carinatum. It is common for these asymmetric variants to be palpated by the pediatrician, parent, or patient, and because of the fear of malignancy, cross-sectional imaging is requested. In a previous study that reviewed cross-sectional examinations performed to evaluate children with suspected chest wall masses, all of the palpable lesions that were asymptomatic were related to normal anatomic variations. Knowledge that such variations are common should be communicated to referring physicians and parents when imaging is being contemplated in a child with an asymptomatic chest wall “lump.” Ultrasound is the initial imaging test of choice to demonstrate these anterior chest wall variations and exclude more concerning masses.



▪ **FIGURE 3-52** **Neuroblastoma.**

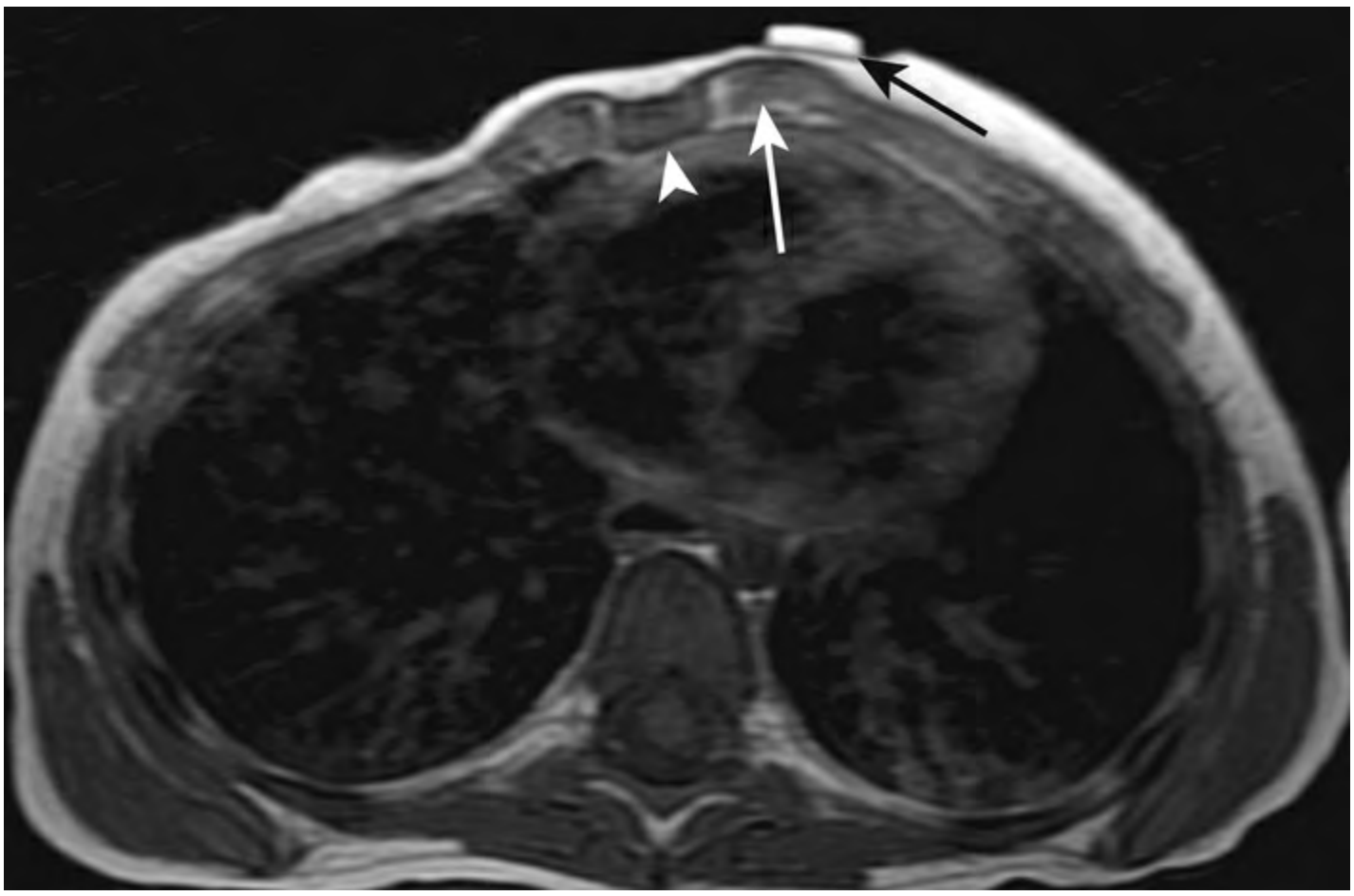
Frontal (**A**) and lateral (**B**) radiographs show a large mass in left hemithorax *(arrows)*. **C,** CT shows a large posterior mediastinal mass *(M).* Metaiodobenzylguanidine (MIBG) scan (**D**) and fused MIBG CT scan (**E**) images show avid uptake of radiotracer within the mass *(arrows)*, consistent with a neural crest tumor.



▪ **FIGURE 3-53** **Ewing sarcoma of the right tenth rib in a 3-year-old male.**

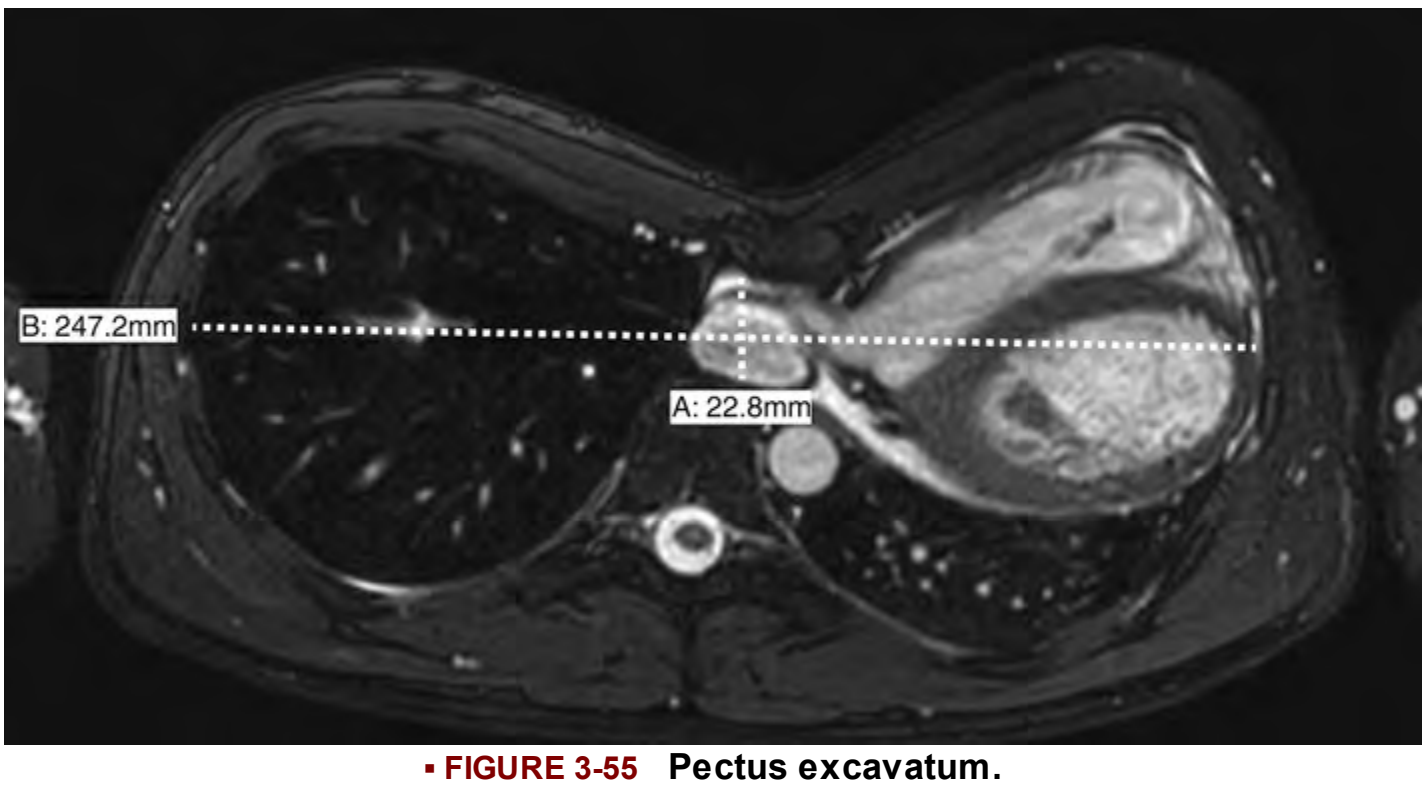
A, Initial chest radiograph shows extensive opacification of the right hemithorax with leftward mediastinal shift. Note the ill-defined, lytic lesion *(arrow)* involving the posterior inferior aspect of the right ninth rib. Axial (**B**) and sagittal (**C**) reformatted CT images show ill-defined lysis and expansion of the rib with a large, associated soft tissue mass and pleural effusion. **D,** Increased radionuclide activity is noted in the affected rib on bone scan.

One of the most common abnormalities in chest wall configuration is pectus excavatum. Although the majority of associated problems due to this deformity are cosmetic, pectus deformities can cause chest pain, fatigue, dyspnea on exertion, palpitations, and restrictive lung disease. When the deformities are severe, surgical repair can be performed. Pectus excavatum is commonly treated by the minimally invasive Nuss procedure. Before performing a Nuss procedure, surgeons commonly request CT or MR examination to document the Haller index, which quantifies the severity of the pectus deformity (Fig. 3-55). To calculate the Haller index, cross-sectional images are obtained through the level of the greatest degree of pectus deformity. The Haller index is equal to the transverse left-to-right diameter of the chest divided by the anterior-to-posterior diameter. The greater the Haller index, the more severe the pectus. A patient with a Haller index greater than 3.2 is considered a surgical candidate.



▪ **FIGURE 3-54 Tilted sternum with prominent costal cartilage presenting as a palpable mass on physical exam.**

MR image shows the sternum *(arrowhead)* to be tilted with respect to the horizontal right-to-left axis of the body. The left margin of the sternum is more anterior than the right. The associated anterior position of the left costal cartilage *(white arrow)*, a normal variant, caused the palpable finding on physical exam. Note the external skin marker overlying the region of palpable abnormality (*black arrow*).



▪ **FIGURE 3-55 Pectus excavatum.**

MR image shows severe concavity of anterior chest wall. Measurement lines are the anterior-to-posterior and left-to-right diameters of the chest. These are measured to calculate the Haller index, a quantitative measure of pectus severity. Note the degree of cardiac displacement and compression.

Suggested Readings

Agrons G.A, Courtney S.E, Stocker J.T, Markowitz R.I. From the archives of the AFIP: lung disease in premature neonates: radiologic-pathologic correlation. *Radiographics*. 2005;25(4):1047–1073.

Bramson R.T, Griscom N.T, Cleveland R.H. Interpretation of chest radiographs in infants with cough and fever. *Radiology*. 2005;236(1):22–29.

Donnelly L.F. Maximizing the usefulness of imaging in children with community-acquired

pneumonia. *AJR*. 1999;172:505–512.

Donnelly L.F. Imaging issues in CT of blunt trauma to the chest and abdomen. *Pediatr radiol*. 2009;39(Suppl 3):406–413.

Donnelly L.F, Frush D.P. Abnormalities of the chest wall in pediatric patients. *AJR*. 1999;173:1595–1601.

Donnelly L.F, Frush D.P. Localized lucent chest lesions in neonates: causes and differentiation. *AJR*. 1999;172:1651–1658.

Epelman M, Kreiger P.A, Servaes S, et al. Current imaging of prenatally diagnosed congenital lung lesions. *Semin Ultrasound CT MR*. 2010;31(2):141–157.

Erasmus J.J, McAdams H.P, Donnelly L.F, Spritzer C.E. MR imaging of mediastinal masses. *Magn Reson Imaging Clin N Am*. 2000;8(1):59–89.

Eslamy H.K, Newman B. Pneumonia in normal and immunocompromised children: an overview and update. *Radiol Clin North Am*. 2011;49(5):895–920.

Griscom N.T. Respiratory problems of early life now allowing survival into adulthood: concepts for radiologists. *AJR*. 1992;158:1–8.

Griscom N.T, Wohl M.B, Kirkpatrick J.A. Lower respiratory infections: how infants differ from adults. *Radiol Clin North Am*. 1978;16:367–387.

Lee E.Y. Interstitial lung disease in infants: new classification system, imaging technique, clinical presentation and imaging findings. *Pediatr Radiol*. 2013;43(1):3–13 quiz p128–129.

Marcovici P.A, LoSasso B.E, Kruk P, Dwek J.R. MRI for the evaluation of pectus excavatum. *Pediatr Radiol*. 2011;41(6):757–758.

Mong A, Epelman M, Darge K. Ultrasound of the pediatric chest. *Pediatr Radiol*. 2012;42(11):1287–1297.

Ranganath S.H, Lee E.Y, Restrepo R, Eisenberg R.L. Mediastinal masses in children. *AJR*. 2012;198(3):W197–W216.

Swischuk K.E, John S.D. Immature lung problems: can our nomenclature be more specific? *AJR*. 1996;166:917–918.

Thacker P.G, Mahani M.G, Heider A, Lee E.Y. Imaging evaluation of mediastinal masses in children and adults: practical diagnostic approach based on a new classification system. *J Thorac Imaging*. 2015;30(4):247–267.

CHAPTER 4

Cardiac

Daniel J. Podberesky

▪ Imaging Modalities in Congenital Heart Disease

Multiple imaging modalities are used to define the morphology, vascular connections, and function of the heart in children with congenital heart disease. Such modalities include radiography, echocardiography, nuclear scintigraphy, computed tomography (CT), magnetic resonance imaging (MRI), and catheter angiography.

Multiple insults can occur in utero that can lead to congenital heart disease. In many cases a specific insult results in a single type of anatomic lesion, such as ventricular septal defect (VSD) or coarctation of the aorta. However, insults can result in a variety of anatomic abnormalities or "complex" congenital heart disease. Historically, chest radiography and clinical symptoms played a large role in narrowing the differential diagnosis of the types of congenital heart disease that may be present in a particular patient. With technologic advances and increased use of other imaging modalities, the dependency on chest radiography findings to diagnose the specific type of congenital heart disease has decreased, though it remains important in the identification of the possible presence of congenital heart disease.

Diagnosing a specific type of congenital heart disease by radiography is difficult. The role of radiography in making the diagnosis of congenital heart disease has probably been overemphasized in education. This is particularly true nowadays because most of the classically described radiographic findings of specific congenital heart disease do not manifest until after the neonatal period, and most patients in developed nations are diagnosed with congenital heart disease and are treated surgically during the neonatal period. However, in some cases the radiologist may be the first person to recognize that the radiographic findings in a newborn suggest that congenital heart disease rather than a pulmonary disorder is the cause of respiratory distress. Therefore it is important to understand the radiographic findings and role of radiography in relation to the other imaging modalities in the management of congenital heart disease.

Echocardiography

Echocardiography is the mainstay of congenital heart disease identification and diagnosis. This is particularly true during the fetal and neonatal periods. Most of the highly detailed anatomic and functional information needed for the medical and surgical management of patients with congenital heart disease can be obtained by ultrasound. Color Doppler can be used to identify areas of stenosis or regurgitation. However, there are populations of patients in whom echocardiography is less easily obtained and more prone to inaccuracy. These populations include older children, adults, and postsurgical patients. In these patients the acoustic window is decreased and echocardiography is more difficult. It is in these circumstances that echocardiography may not provide the necessary information needed for care, so CT and MRI play a role. It is important to keep in perspective the current relatively small (albeit growing) role of CT and MRI in cardiac imaging as compared with that of ultrasound.

Computed Tomography Angiography

The role of CT in the evaluation of congenital heart disease has rapidly increased as a result of the advent of multidetector CT technology, improved temporal resolution, and decreased ionizing radiation doses. The rapid speed of acquisition, ability to acquire volumetric data, and ability to obtain thin collimation have made CT very useful in patients with congenital heart disease. CT is beneficial in depicting those anatomic structures that are not easily seen on echocardiography, such as the

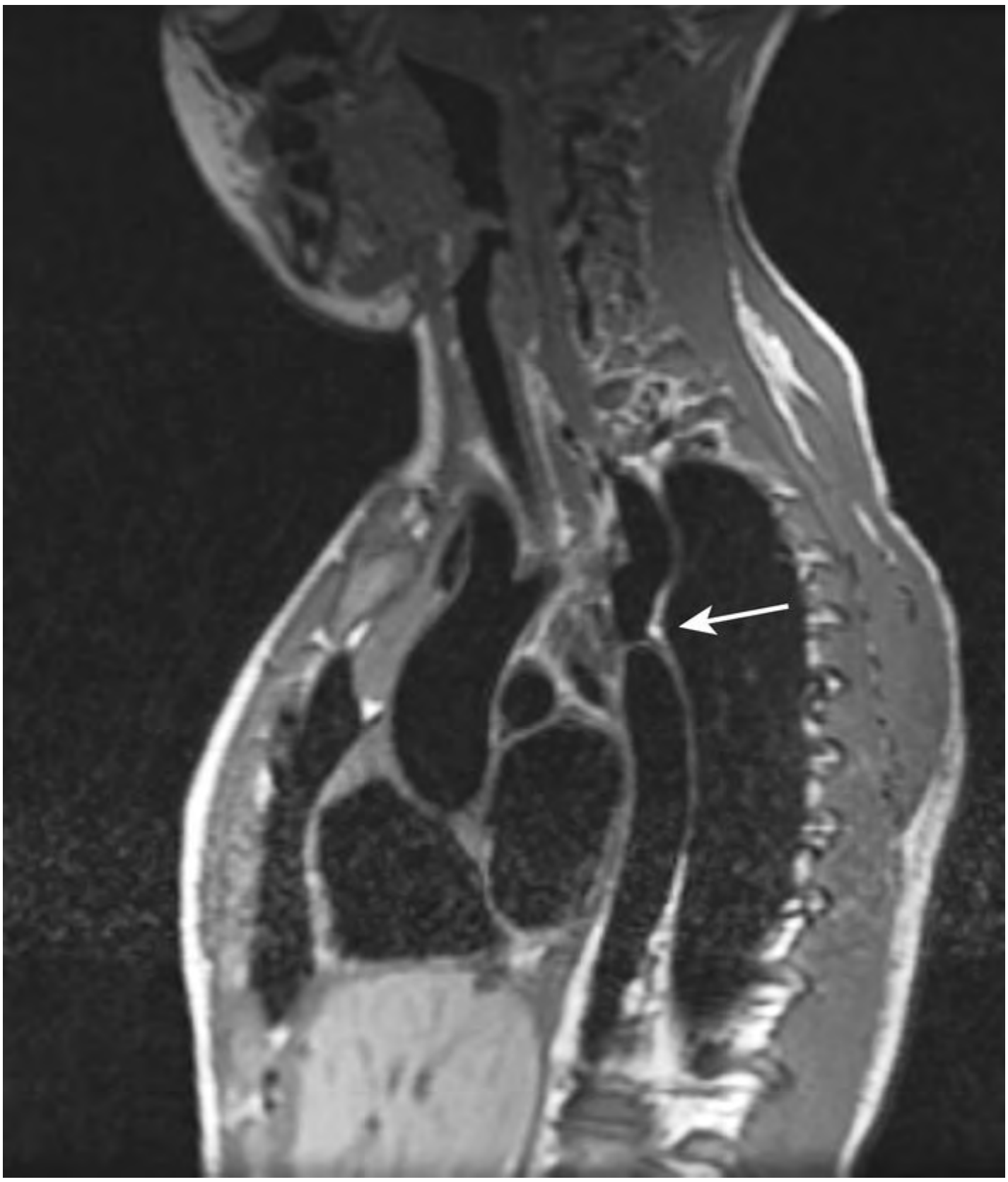
pulmonary arteries, aorta, pulmonary veins, right-sided chambers, and vascular conduits. CT also enables a more global assessment of the airway and pulmonary parenchyma, which may also be abnormal in patients with congenital heart disease. CT is often used to depict complex congenital heart disease preoperatively and to evaluate the postoperative patient (Fig. 4-1) for potential complications, such as stenoses, occlusions, and pseudoaneurysms. It is useful in evaluating the pulmonary veins, such as in suspected anomalous pulmonary venous return. CT is also useful in patients in whom pacemakers may preclude the use of MRI. Evaluation of metal stents is often less hampered by artifact in CT than in MRI, especially with new metal reduction algorithms on modern CT scanners. Although ionizing radiation exposure remains of paramount concern in medical imaging of children, the advent of newer technologies, such as iterative reconstruction, volume acquisition, and dual source scanners, has resulted in dramatic decreases in radiation exposure, improvement in temporal resolution associated with cardiac CT, and a resultant renewal of interest in its role in congenital heart disease evaluation.



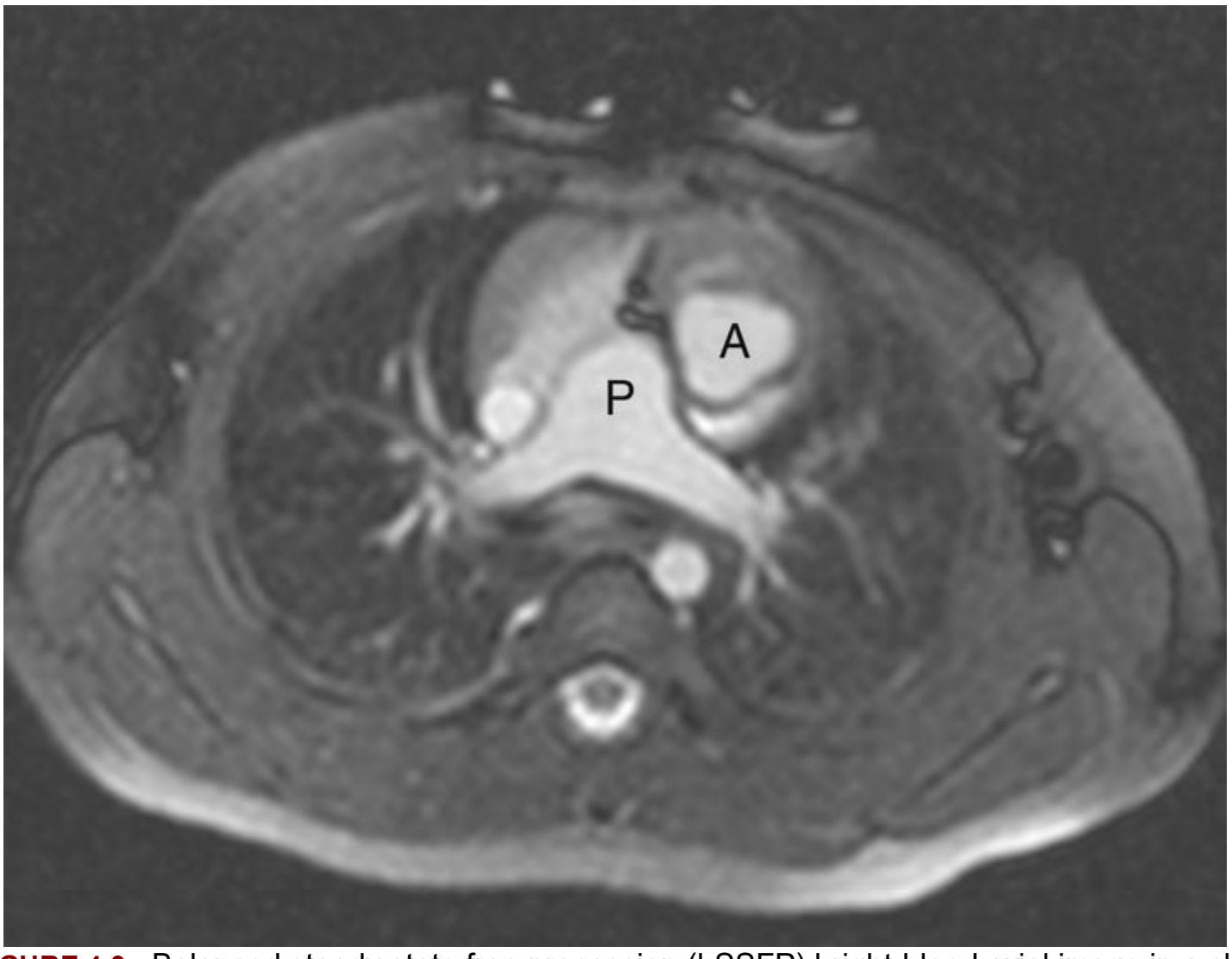
▪ **FIGURE 4-1** Three-dimensional reconstruction from a CT angiogram performed to evaluate patency of a Glenn shunt. The image shows a widely patent Glenn shunt (direct connection between the superior vena cava *(S)* and the pulmonary arteries *[arrow]*). The ascending aorta *(A)* courses anterior to the pulmonary arteries.

Magnetic Resonance Imaging

MRI has become a mainstay in the evaluation of certain types of congenital heart disease. MRI studies offer both anatomic and functional information. Cardiac gated spin echo imaging and double inversion recovery imaging, also known as "black-blood" imaging (Fig. 4-2), are the main sequences used to demonstrate anatomic detail and spatial relationships between adjacent structures. These sequences allow for precise measurement of anatomic structures.



▪ **FIGURE 4-2** Double inversion recovery, T1-weighted, black-blood, oblique sagittal ("candy cane") image shows a focal narrowing of the aortic isthmus *(arrow)* consistent with coarctation.



▪ **FIGURE 4-3** Balanced steady state free precession (bSSFP) bright-blood axial image in a child with L-transposition of the great arteries (L-TGA) shows the aorta *(A)* to the left and anterior to the main pulmonary artery *(P)*. Such images through the heart can be obtained in cine mode and are used to evaluate cardiac motion and functional parameters, such as ventricular ejection fraction.

Cardiac gated cine MRI, or "bright-blood" imaging, can be obtained with a number of sequences. Predominantly a balanced steady-state free precession (bSSFP) sequence is used (e.g., FIESTA, TRUFISP, bFFE; Fig. 4-3), but a T2* GRE sequence (e.g., FLASH, SPGR) can also be used for "bright-blood" imaging. Data from these sequences can be processed to provide functional information, such as ventricular ejection fractions, and can also be used to demonstrate dynamic findings, such as turbulent blood flow related to stenosis or regurgitation. Phase-contrast imaging can be used to evaluate flow dynamics within vasculature structures. MR angiography using gadolinium and maximum intensity projection or shaded surface three-dimensional reconstructions is also useful in demonstrating complex anatomic relationships.

Computed Tomography versus Magnetic Resonance Imaging

With both CT and MRI becoming increasingly useful in the evaluation of patients with congenital heart disease, there is frequent debate regarding which examination is better for specific clinical indications. Although there are no clear-cut answers, there are advantages and disadvantages of both examinations. The benefits of CT include rapid acquisition time, avoiding the need for sedation in many cases, greater access for critically ill infants, less artifact resulting from metal stents and other structures, lack of pacemaker safety issues, and visualizing the airway and lungs. The major disadvantage of CT is radiation exposure. Techniques used in adults, including cardiac gating, thin collimation, overlapping imaging acquisition, and acquiring multiple sets of images, result in very high radiation doses relative to other CT examinations. Because of the radiosensitivity of children, many of these techniques are not appropriate when imaging children. Other disadvantages of CT include dependence on intravenous contrast bolus and relative lack of functional information. The primary advantages of MRI include lack of ionizing radiation, ability to show more detailed anatomy in some circumstances, and greater depiction of functional information. A disadvantage of MRI is the requirement for sedation or anesthesia in younger children who may otherwise be able to undergo a CT without the need for sedation or anesthesia.

Catheter Angiography

The use of diagnostic angiography in cases in which percutaneous intervention is not performed is dramatically decreasing because of improvements in noninvasive imaging tools, such as echocardiography, MRI, and CT. At the same time that the role of diagnostic angiography in the evaluation of congenital heart disease is decreasing, percutaneous interventional procedures, such as ductus arteriosus, atrial septal defect (ASD), and VSD closure device deployment, are increasing in number. Diagnostic angiography is commonly performed as part of these interventional procedures to define the anatomy of these abnormalities and provide procedure guidance.

Approach to the Chest Radiograph in Congenital Heart Disease

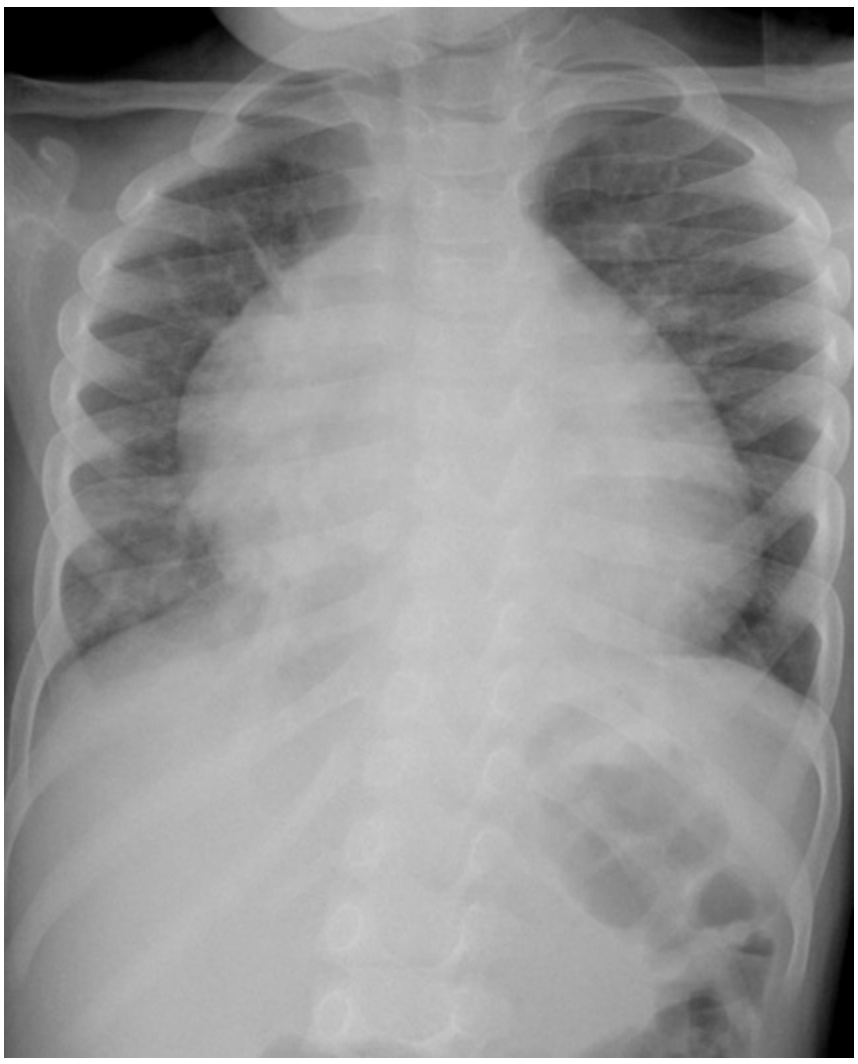
It is important to have a basic understanding of the radiographic findings of congenital heart disease because the radiologist may be the first to recognize that respiratory symptoms are secondary to cardiac rather than respiratory disease. In addition, understanding the radiographic findings provides a framework for understanding the pathophysiology behind congenital heart disease. When evaluating a chest radiograph in a patient with potential congenital heart disease, it is important to evaluate pulmonary vascularity, cardiac size, situs, and the position of the aortic arch.

Pulmonary Vascularity

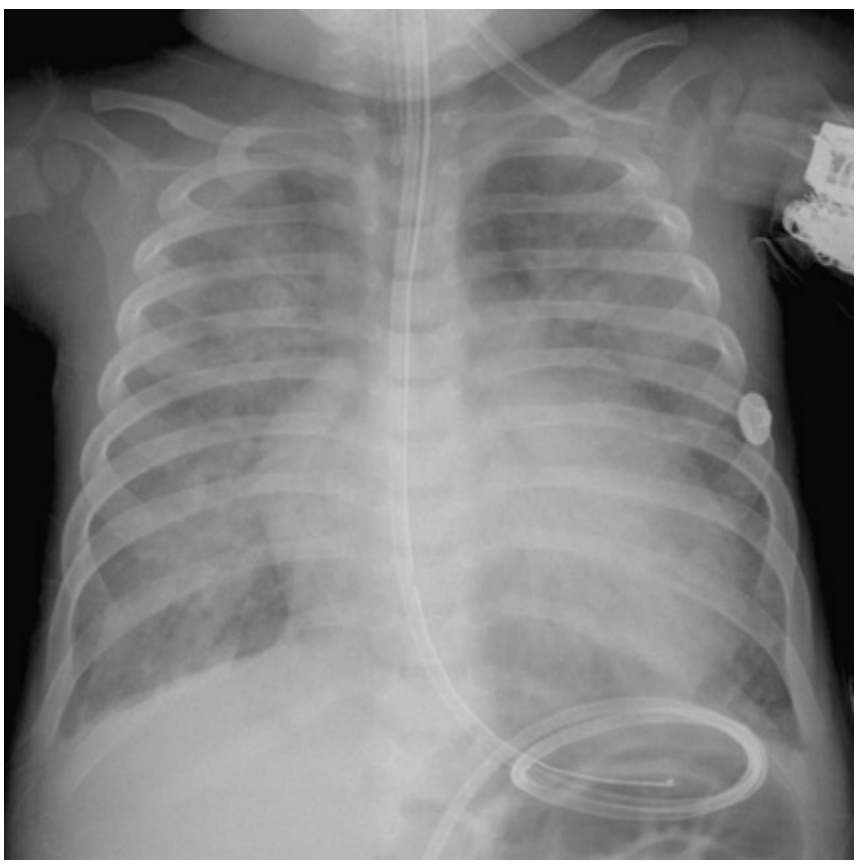
An important radiographic feature for determining the appropriate differential diagnosis in congenital heart disease is the pulmonary vascularity. Unfortunately, it is probably also the most difficult radiographic finding to evaluate and one that can be altered iatrogenically by the administration of fluids or diuretics to a patient. In addition, the appearance of pulmonary vascular prominence can be increased by low lung volumes and portable radiographic technique. The pulmonary vascularity can be normal or can reflect increased pulmonary arterial flow, increased pulmonary venous flow, or decreased pulmonary flow.

In cases of increased pulmonary arterial flow, the pulmonary arteries appear too prominent both in size and in the number of visualized pulmonary arterial structures (Fig. 4-4). A helpful rule is that if the right interlobar pulmonary artery is larger in diameter than the trachea, one should consider increased pulmonary arterial flow to be present. The prominent vascular structures seen in increased pulmonary arterial flow are very distinct and have well-defined borders. It can at times be difficult to differentiate increased pulmonary arterial flow from the increased peribronchial markings seen with reactive airway disease or viral pneumonia.

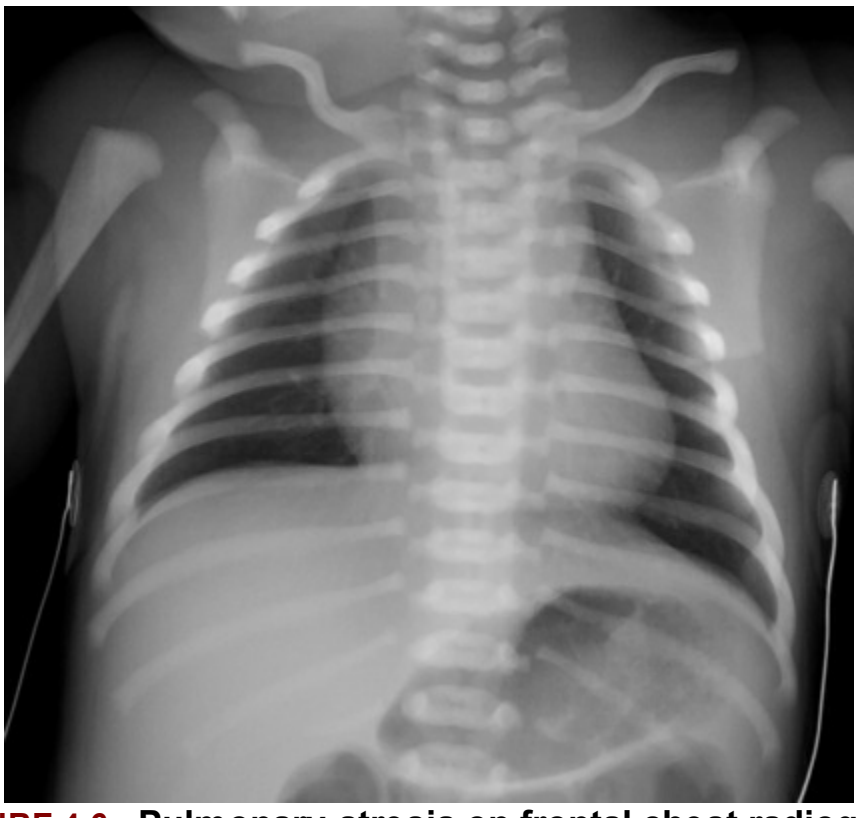
In cases with increased pulmonary venous flow, although the pulmonary vascular structures appear prominent in size and distribution, they are very indistinct and poorly defined (Fig. 4-5). Increased pulmonary venous flow is akin to pulmonary venous congestion or mild pulmonary edema. In many cases, such as in left-to-right shunts, there is both increased pulmonary arterial flow resulting from left-to-right shunting and increased pulmonary venous flow due to congestive heart failure. If any of the pulmonary arteries in a particular case appear very well defined, it is important to consider at least a component of increased pulmonary arterial flow to be present.



▪ **FIGURE 4-4** Frontal chest radiograph in a child with Down syndrome with atrioventricular canal defect shows shunt vascularity with increased number and size of visible pulmonary arteries. Cardiomegaly is present as well.



▪ **FIGURE 4-5** **Increased pulmonary venous flow in neonate with cardiomyopathy.** Note the prominent but indistinct pulmonary vascularity.



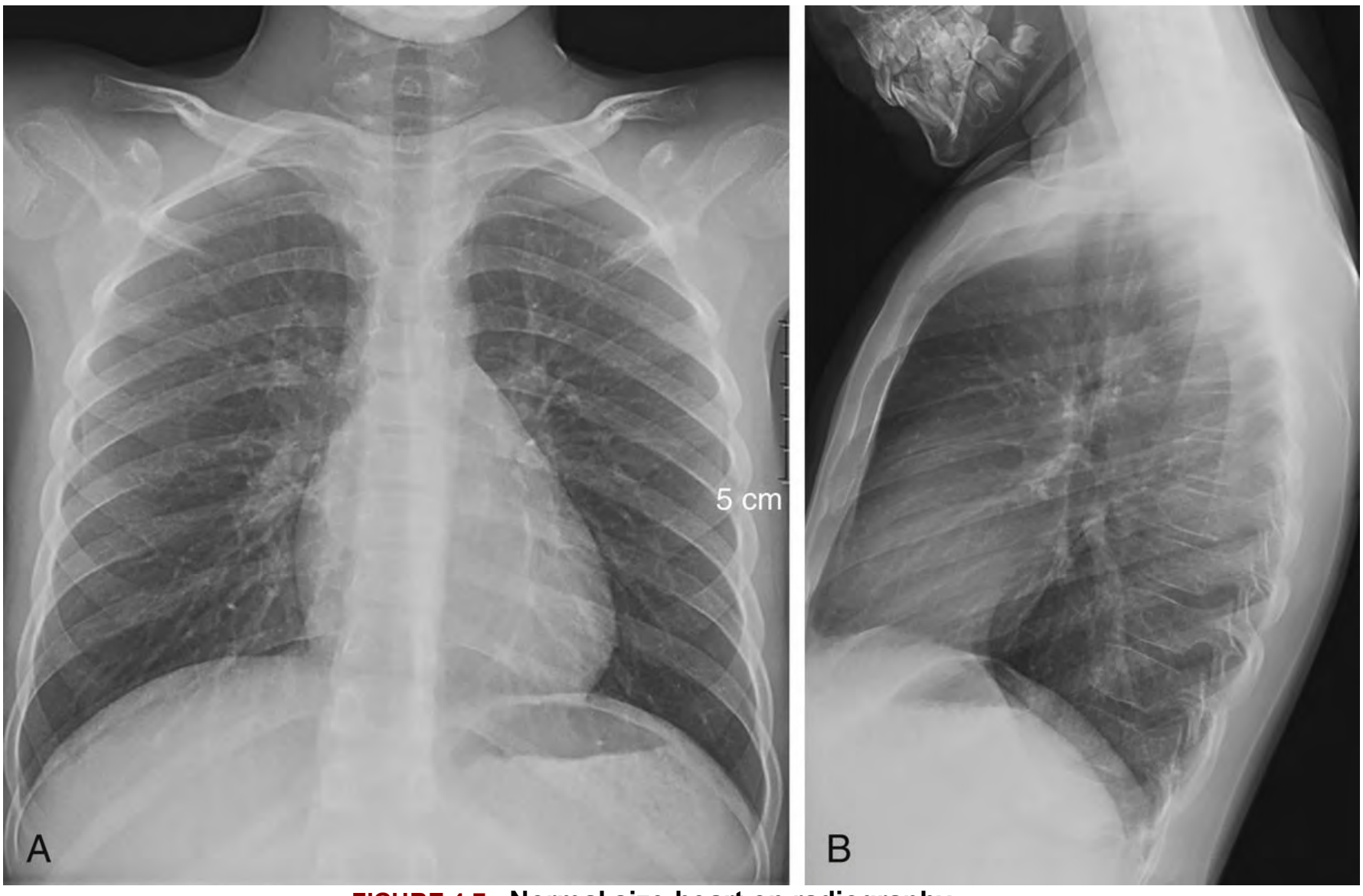
▪ **FIGURE 4-6** **Pulmonary atresia on frontal chest radiograph.**
Note the decrease in identifiable pulmonary markings consistent with decreased pulmonary flow.

In decreased pulmonary arterial flow, there is a paucity of visualized arterial structures throughout the lung (Fig. 4-6).

Cardiac Size

Cardiac size may be normal or enlarged. In older children and adults there may be findings that suggest specific chamber enlargement. However, specific chamber enlargement may be difficult to ascertain in infants because they usually undergo an anteroposterior radiographic technique and have large thymus glands. It is for this same reason that measuring the transverse diameter of the cardiac silhouette and comparing it with the transverse diameter of half the thoracic base may overestimate cardiac size. In these infants the lateral view commonly offers greater insight into whether cardiomegaly is truly present than does the frontal view (Figs. 4-7, *A* and *B*, and 4-8, *A* and *B*). On the lateral view, if the posterior aspect of the cardiac silhouette extends over the vertebral bodies, cardiomegaly should be considered present.

Cardiac axis is the term given to the configuration of the apex of the heart; it indicates whether the apex points superiorly or inferiorly. If the cardiac apex is oriented superiorly, right-sided cardiac enlargement is suggested, and if the cardiac axis or apex is oriented inferiorly, left-sided cardiac enlargement is suggested.



▪ **FIGURE 4-7** **Normal size heart on radiography.**

A, Frontal chest radiograph shows that the transverse diameter of the cardiac silhouette is less than 50% of the diameter of the chest. **B,** Lateral radiograph demonstrates the posterior border of the heart to be normally positioned and not to extend posteriorly beyond the spine. No cardiomegaly is present.

Situs

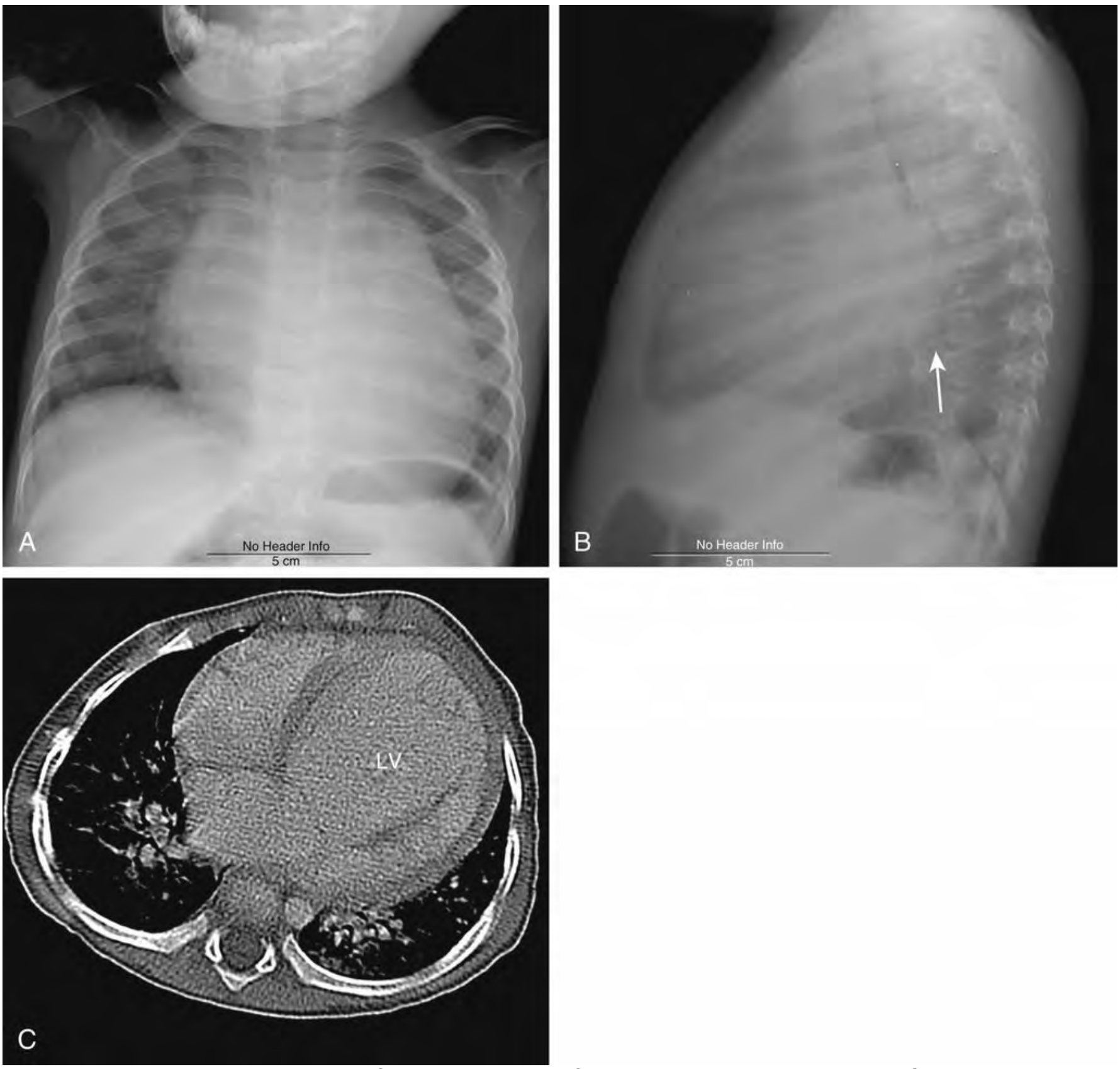
Situs is defined as the relationship of asymmetric organs to the midline. Identifying disturbances in normal situs (the presence of heterotaxy syndromes) is important because they are associated with the presence of congenital heart disease. Situs should not be confused with the actual location of the heart within the thoracic cavity. Levoposition describes a heart mainly located in the left chest, whereas dextroposition describes a heart located primarily within the right chest. The term *mesoposition* is used to describe a heart located in the midline. The term *dextrocardia* strictly refers to a heart located in the right hemithorax with the base-apex relationship tilted rightward.

The important structures when evaluating situs on chest radiography are the cardiac apex, stomach bubble, and position of the liver. When the cardiac apex and gastric bubble appear on the same side, left or right, there is a much lower incidence of congenital heart disease than in cases in which the cardiac apex is on the opposite side of gastric bubble. When there is discordance between the side of the cardiac apex and gastric bubble, there is a near 100% incidence of congenital heart disease. Situs solitus is the name given to the normal configuration; it is associated with a 0.6% incidence of congenital heart disease. Situs inversus is the mirror image of normal and is associated with a 3% to 5% incidence of congenital heart disease. With situs ambiguous, there is no clear, straightforward left- or right-sidedness. The major types of situs ambiguous include asplenia (bilateral right-sidedness) and polysplenia (bilateral left-sidedness). Definitive determination of situs requires identifying the relationship between the atrial chambers and adjacent organs, which is not possible radiographically.

Asplenia (Fig. 4-9, *A* and *B*) is associated with complex, cyanotic congenital heart disease. Patients are susceptible to infections by encapsulated bacteria because of the lack of a spleen. Other abnormalities that may be present include malrotation, microgastria, and midline gallbladder. Radiographic findings include a midline liver, bilateral right-sided-appearing bronchi, decreased pulmonary arterial flow, azygous continuation of the inferior vena cava (IVC), and other findings reflecting the specific type of cyanotic heart disease

Polysplenia (Fig. 4-10, *A* and *B*) is typically associated with less complex acyanotic heart disease, usually left-to-right shunts. Other associations include azygous continuation of the IVC, bilateral

superior vena cava (SVC), malrotation, and absent gallbladder. Radiographic findings include absence of the IVC shadow, prominent azygous vein, midline liver, and increased pulmonary arterial flow.

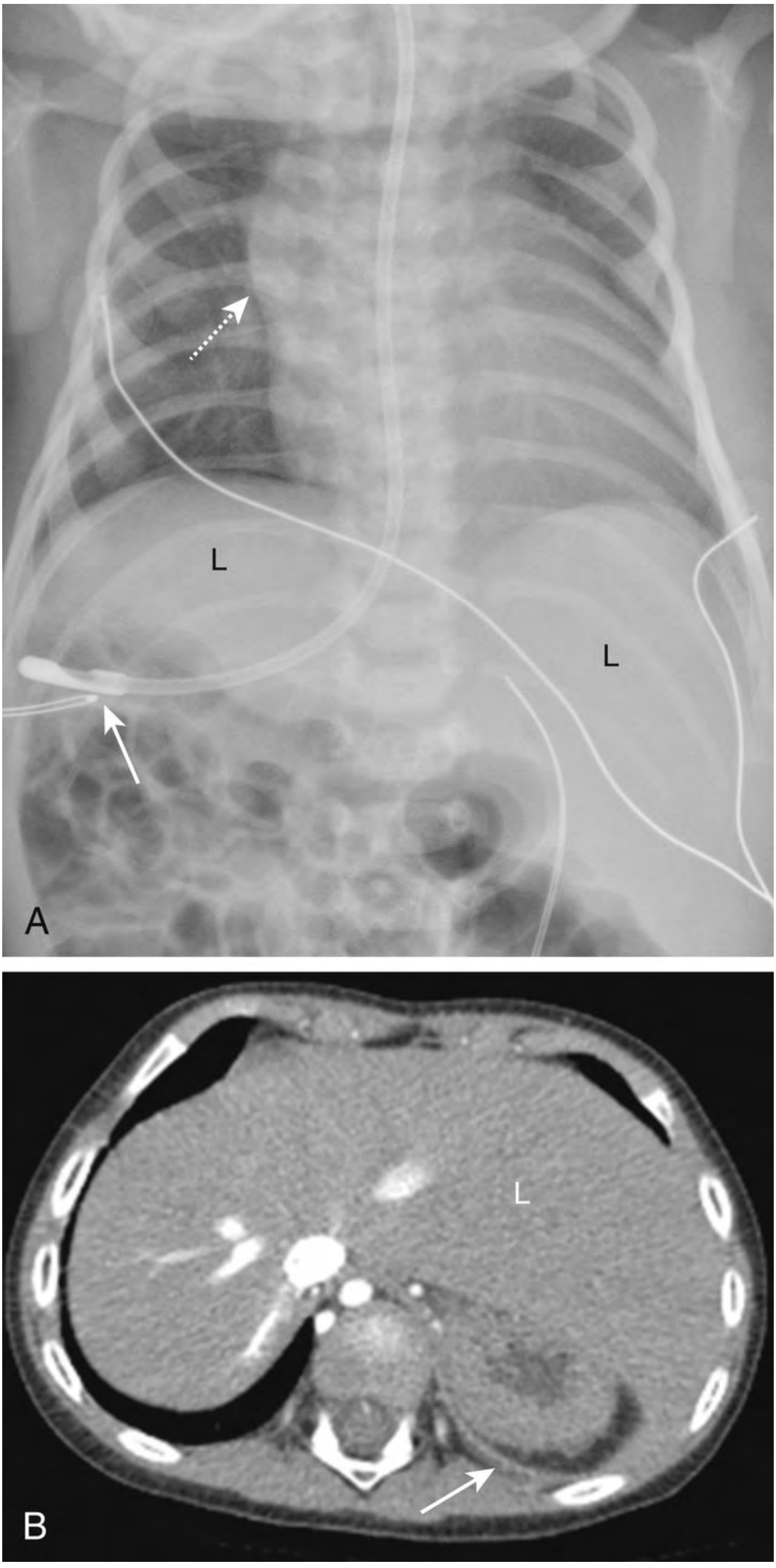


▪ **FIGURE 4-8** **Anomalous left coronary artery from the pulmonary artery (ALCAPA).** **A,** Frontal chest radiograph demonstrates prominent cardiac silhouette. **B,** Lateral radiograph better shows cardiomegaly. Note that the posterior aspect of the cardiac silhouette *(arrow)* extends beyond the anterior border of the spine. **C,** Axial contrast-enhanced CT image shows the markedly enlarged left ventricle *(LV)* secondary to myocardial ischemia and infarction from the anomalous coronary artery flow.

Position of Aortic Arch

The identification of a right-sided aortic arch should increase suspicion for the presence of congenital heart disease. The most common congenital heart lesions that have an associated right-sided aortic arch are tetralogy of Fallot, truncus arteriosus, tricuspid atresia, and transposition of the great arteries. When the aortic knob can be identified, as in most cases in adults and older children, it is obvious which side the aortic arch is on. However, in infants the aortic knob is often not easily identified. In such cases, secondary findings for the presence of the aortic arch must be used. Such findings include the position of the descending aorta (though this does not universally correspond with the side of the arch), tracheal displacement, and tracheal indentation. In a normal left-sided aortic arch, the trachea is displaced slightly toward the right as it moves inferiorly. Also in such cases there is an indentation on the left aortic border of the trachea as visualized on the frontal view of the chest. If the trachea deviates

slightly leftward as it moves inferiorly or if there is a soft tissue indentation on the right aortic border of the trachea, a right-sided aortic arch should be suspected. A double aortic arch may manifest on a chest radiograph simply as a midline trachea with no indentation.


L
L
A
L
B

▪ **FIGURE 4-9** **Asplenia.**
A, Frontal chest radiograph shows cardiomegaly with left-sided cardiac apex and levoposition of the heart and a right-sided aortic knob *(dashed arrow)*. Note that the stomach with the nasogastric tube *(solid arrow)* is on the right and the liver shadow *(L)* is predominantly on the left but crosses midline. No splenic shadow is seen. **B,** Axial contrast-enhanced CT image in a different patient shows a midline liver *(L)*, a left-sided stomach *(arrow)*, and absence of the spleen. Both patients had complex congenital heart disease.

▪ Categorization of Congenital Heart Disease

In the traditional classification of congenital heart disease, two of the major features that place the disease into a particular diagnostic category include (1) whether the patient is cyanotic (blue) and (2) whether the pulmonary arterial flow is decreased, normal, or increased (Table 4-1). Once these two major features have been identified, other radiographic findings will help to limit the differential diagnosis.

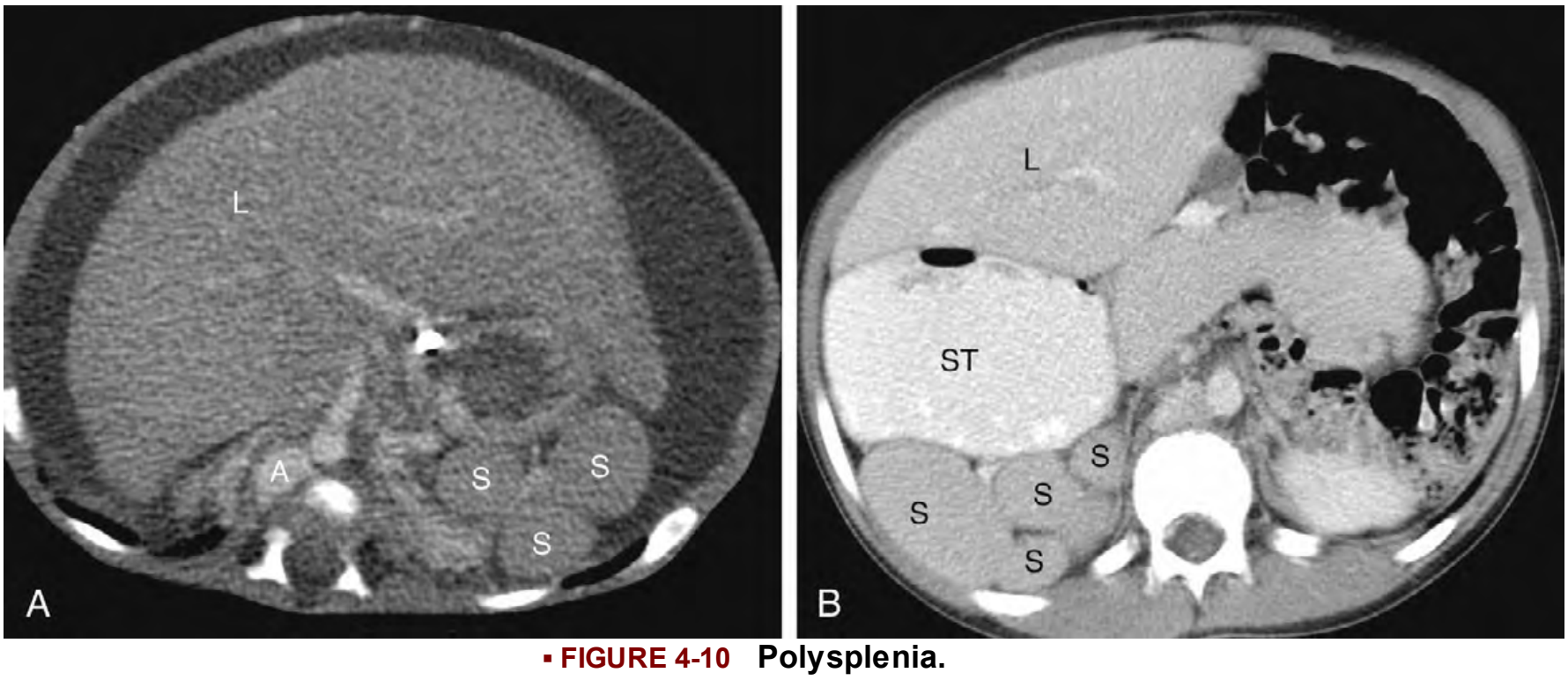
Another important factor to consider is the frequency of occurrence of the various types of congenital heart disease (Table 4-2). Approximately 50% of cases of congenital heart disease are left-to-right shunts. Many of the types of congenital heart disease discussed here are highlighted because of striking anatomic findings but are actually quite rare. It is also important to remember that there are other systems for classifying congenital heart disease that are used by cardiac imagers, most commonly the segmental approach described by Van Praagh (see Suggested Readings). The following discussion serves as a basic introduction to the classification of congenital heart teaching from a traditional radiography approach.

Blue, Decreased Pulmonary Arterial Flow, Mild Cardiomegaly

The differential diagnosis of patients who are cyanotic and demonstrate decreased pulmonary arterial flow on chest radiograph can be narrowed according to whether the patient has mild or massive cardiomegaly. In the cases in which the heart size is normal or there is only mild cardiomegaly, the differential diagnosis includes tetralogy of Fallot and pulmonary atresia with an associated VSD. These two entities are essentially different spectrums of the same disease.

Tetralogy of Fallot

Tetralogy of Fallot is the most common type of cyanotic congenital heart disease in children. It is usually diagnosed by 3 months of age. There are four classic anatomic components of tetralogy of Fallot: (1) right ventricular outflow tract obstruction, (2) VSD, (3) overriding aorta, and (4) right ventricular hypertrophy. Radiographic features include a normal-sized to slightly enlarged cardiac silhouette with uplifting of the ventricular apex (a superiorly oriented cardiac axis) secondary to right ventricular hypertrophy The main pulmonary artery segment is concave because of the small associated pulmonary arteries. The combination of the deficient main pulmonary artery and the upturned cardiac apex makes the configuration of the cardiac silhouette appear to be boot shaped. The pulmonary vascularity is generally decreased. In tetralogy of Fallot the central pulmonary arteries may be confluent or nonconfluent. This is often difficult to evaluate with echocardiography, so MRI can be used to evaluate the status of the pulmonary arteries in patients with tetralogy of Fallot (Fig. 4-11, *A* and *B*). A right aortic arch is present in approximately 25% of tetralogy of Fallot patients (see Fig. 4-11, *B* and *C*). Pulmonary atresia with a VSD is considered to be the most severe form of tetralogy of Fallot. It is synonymous with pseudotruncus or truncus arteriosus type 4 because of the larger bronchial arteries, or collaterals, arising from the aorta and supplying the lungs.



▪ **FIGURE 4-10** **Polysplenia.**

A, Axial contrast-enhanced CT image shows multiple spleens *(S)* in the left upper quadrant, a midline liver *(L)*, and azygous continuation of the IVC *(A)*. **B,** Axial contrast-enhanced CT image shows multiple spleens *(S)* in the right upper quadrant, a right-sided liver *(L)*, and a right-sided stomach *(ST)*.

TABLE 4-1

Categorization of Congenital Heart Disease

Blue

Decreased flow
- Normal heart size
  - Tetralogy of Fallot
- Giant heart size
  - Ebstein anomaly
  - Pulmonary atresia with intact ventricular septum

Increased flow
- Truncus arteriosus
- Total anomalous pulmonary venous return

Variable flow
- D-TGA
- Tricuspid atresia

Pink

Increased pulmonary arterial flow and left-to-right shunt (VSD, ASD, AVC, PDA)

Increased pulmonary venous flow
- Congestive heart failure in the newborn

Normal pulmonary flow
- Obstructive lesions
  - Coarctation of the aorta
  - Aortic stenosis
  - Pulmonary artery stenosis
- Postsurgery

ASD, Atrial septal defect; *AVC,* atrioventricular canal; *D-TGA,* D-transposition of the great arteries; *PDA,* patent ductus arteriosus; *VSD,* ventricular septal defect.

TABLE 4-2

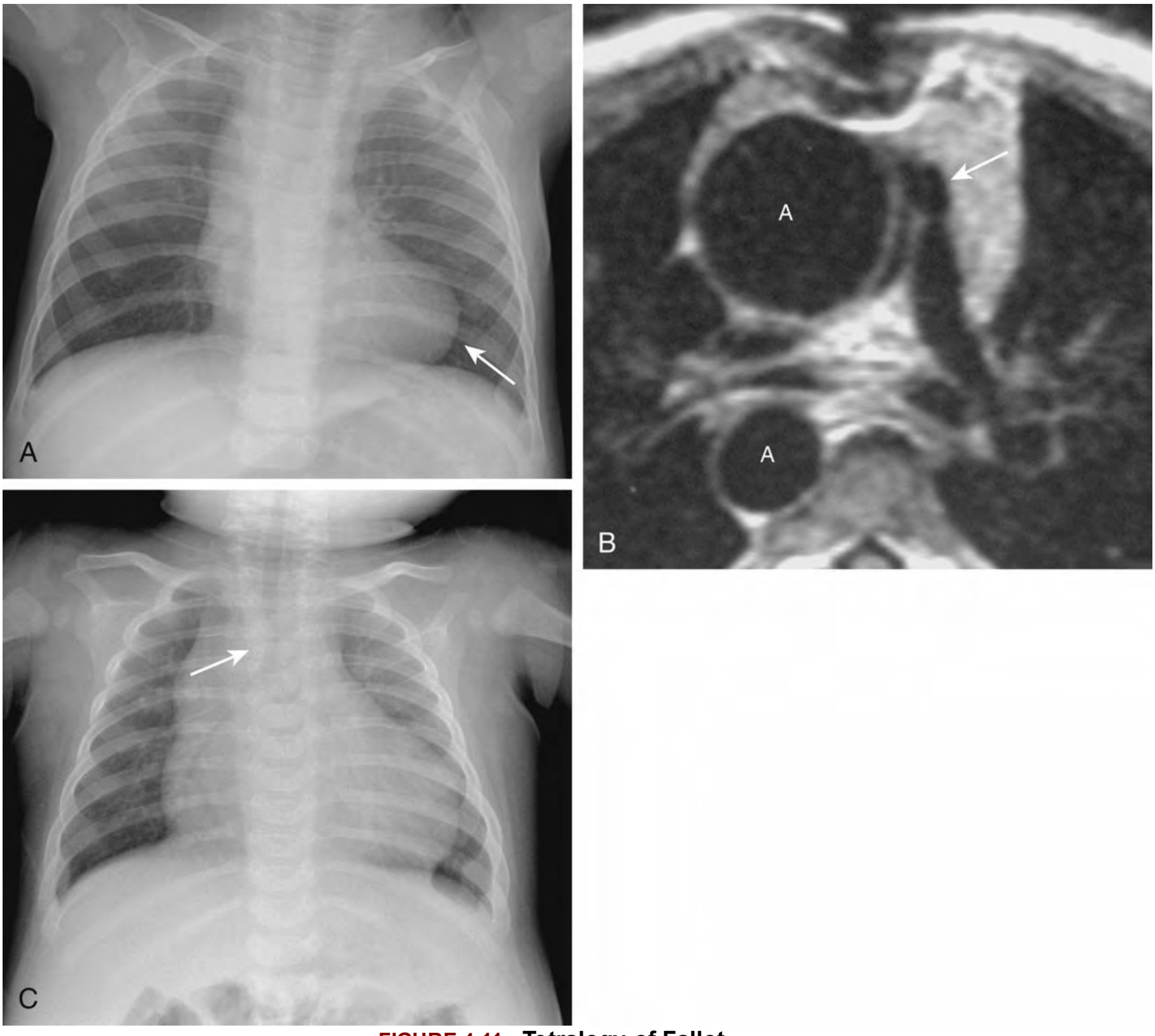
Incidence of More Common Types of Congenital Heart Disease

Diagnosis	% Congenital Heart Disease
Left-to-right shunts (VSD, ASD, atrioventricular canal, persistent PDA)	50 (VSD, 28)
Pulmonic stenosis	9.3
Aortic stenosis-bicuspid aortic valve	7.7
Tetralogy of Fallot	7.5
Coarctation of the aorta	3.8
Single ventricle	2.7
Hypoplastic left heart syndrome	1.8
D-TGA	1.8
Tricuspid atresia	1.6
Total anomalous pulmonary venous return	1.4
Truncus arteriosus, L-transposition of great arteries, pulmonary atresia, Ebstein anomaly	Each ≤1

ASD, Atrial septal defect; *D-TGA*, D-transposition of the great arteries; *PDA*, patent ductus arteriosus; *VSD*, ventricular septal defect.

Blue, Decreased Pulmonary Arterial Flow, Massive Cardiomegaly

In patients who are cyanotic and demonstrate decreased pulmonary flow but have massive cardiomegaly, the first two entities that should be considered are Ebstein anomaly and pulmonary atresia with an intact ventricular septum. With these two entities the degree of cardiomegaly may be the most massive encountered on radiography. The right atrium can dilate to massive size, rather like a balloon; therefore, when massive cardiomegaly is encountered, abnormalities that lead to marked enlargement of the right atrium should be considered.



▪ **FIGURE 4-11** **Tetralogy of Fallot.**

A, Frontal chest radiograph shows upturned cardiac apex *(arrow)* and decreased pulmonary arterial flow. **B,** Axial T1-weighted, black-blood MR image shows a right-sided aorta *(A)* and atretic pulmonary arteries *(arrow)*. **C,** Frontal chest radiograph shows a right-sided aortic arch *(arrow)*. Note the indentation on the right aspect of the trachea.

Ebstein Anomaly

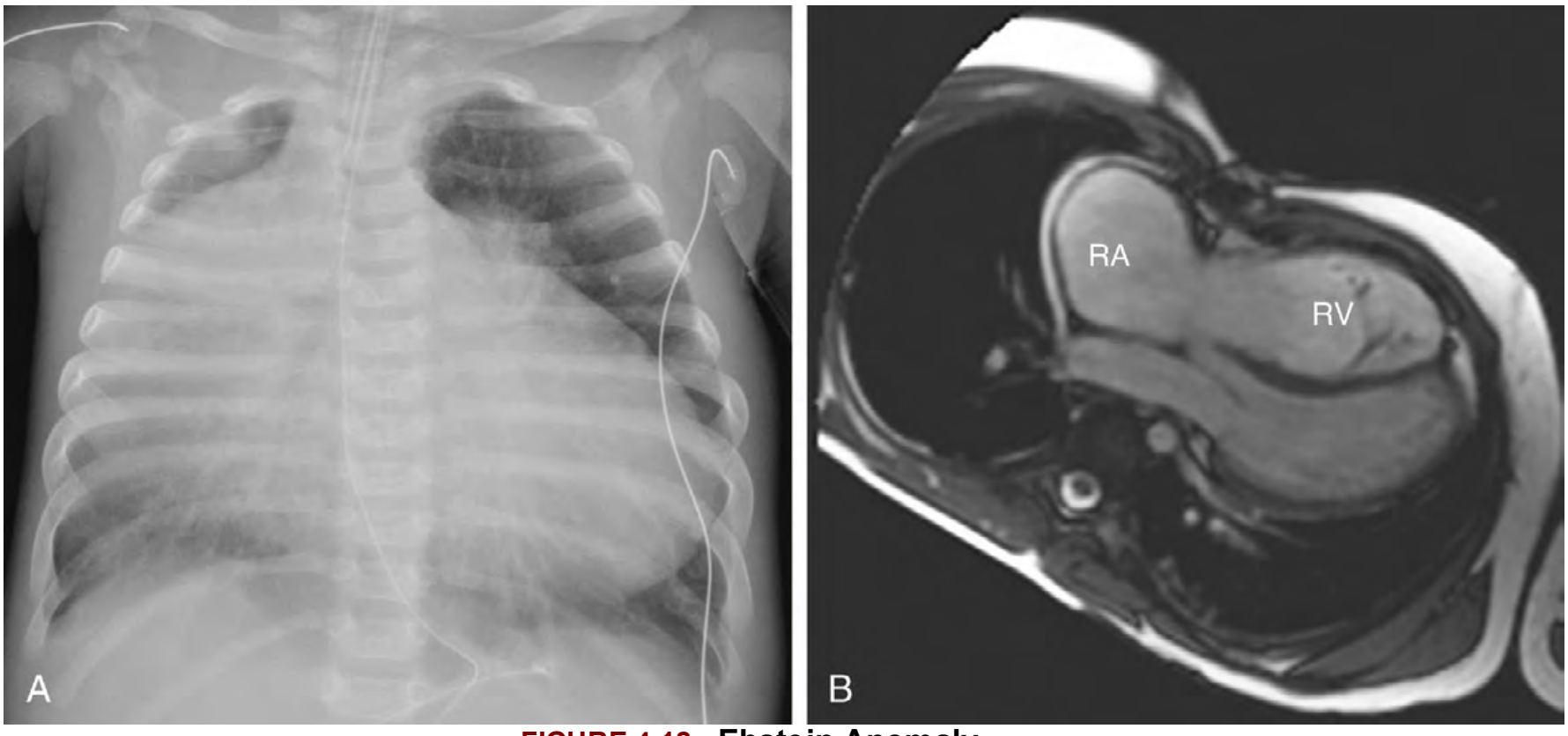
In Ebstein anomaly there is redundancy of the tricuspid valve, which is displaced into the right ventricle, causing atrialization of part of the right ventricle. There is functional obstruction at the level of the tricuspid valve that results in massive dilatation of the right atrium and the atrialized portion of the right ventricle. The age of presentation is variable. When the anomaly is severe, infants present with severe cyanosis. On radiography, massive cardiomegaly and decreased pulmonary arterial flow are seen (Figs. 4-12, *A* and *B*, and 4-13). Ebstein anomaly is a rare entity.

Pulmonary Atresia with Intact Ventricular Septum

Unlike cases of pulmonary atresia with VSD (tetralogy of Fallot), patients with pulmonary atresia and an intact septum have no forward flow from the right heart. This leads to massive dilatation of the right atrium and, to a lesser degree, the right ventricle. Such patients present with marked cyanosis in infancy. The radiographic appearance (Fig. 4-14) may be indistinguishable from that of Ebstein anomaly.

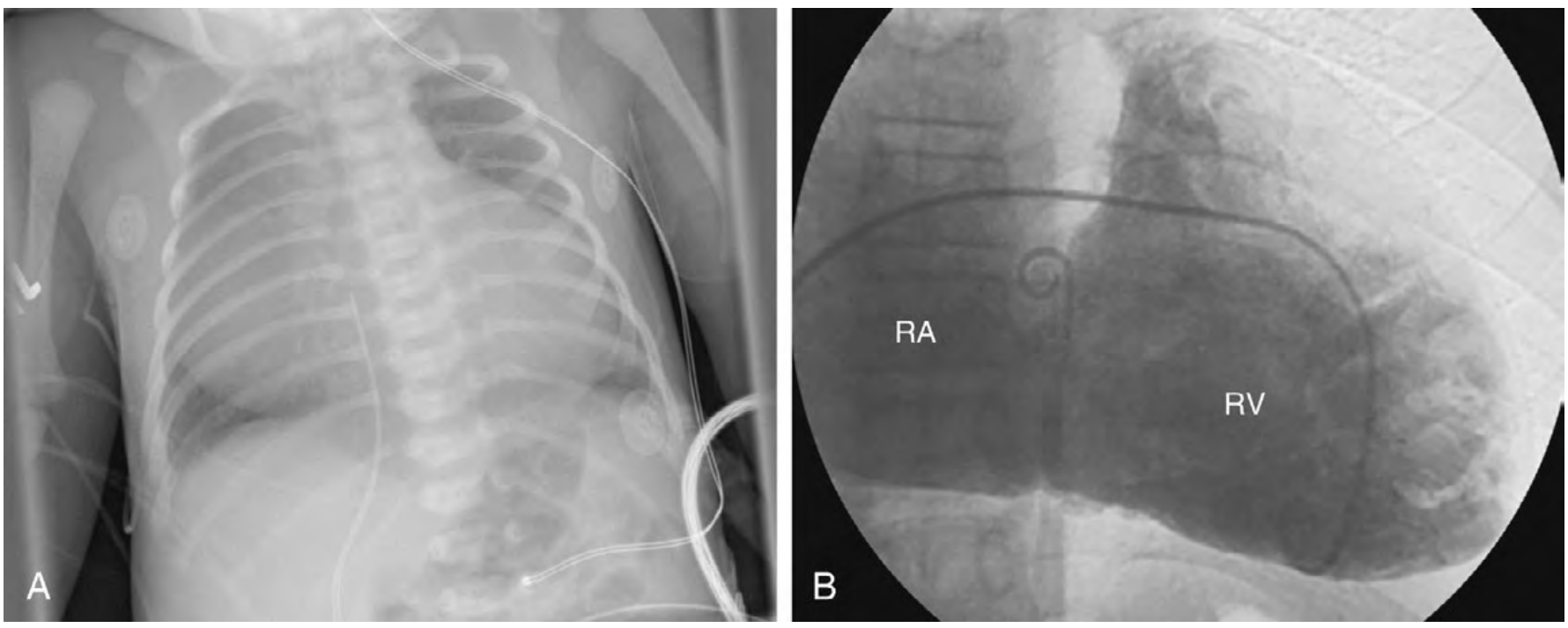
Note that there are many other abnormalities that may cause the appearance of a massive cardiopericardial silhouette on the chest radiograph of a newborn. They include cardiac tumors, such as rhabdomyoma (Fig. 4-15, *A* and *B*), noncardiac mediastinal masses, congenital diaphragmatic hernia before aeration of the herniated bowel, and peripheral arterial venous fistulas with associated high output failure. However, when massive cardiomegaly is encountered in the presence of decreased

pulmonary flow, Ebstein anomaly and pulmonary atresia with intact septum should be the primary considerations.



▪ **FIGURE 4-12** **Ebstein Anomaly.**

A, Frontal chest radiograph in a newborn shows massive cardiomegaly. **B,** Axial bSSFP MR image in a different patient with Ebstein anomaly shows marked enlargement of the right atrium *(RA)*. *RV,* Right ventricle.



▪ **FIGURE 4-13** **Ebstein anomaly with marked cardiomegaly.**

A, Frontal radiograph shows marked cardiac enlargement. **B,** Angiogram with catheter in the right heart demonstrates marked enlargement of the right atrium *(RA)* and atrialization of a portion of the right ventricle *(RV)*, a hallmark of Ebstein anomaly.

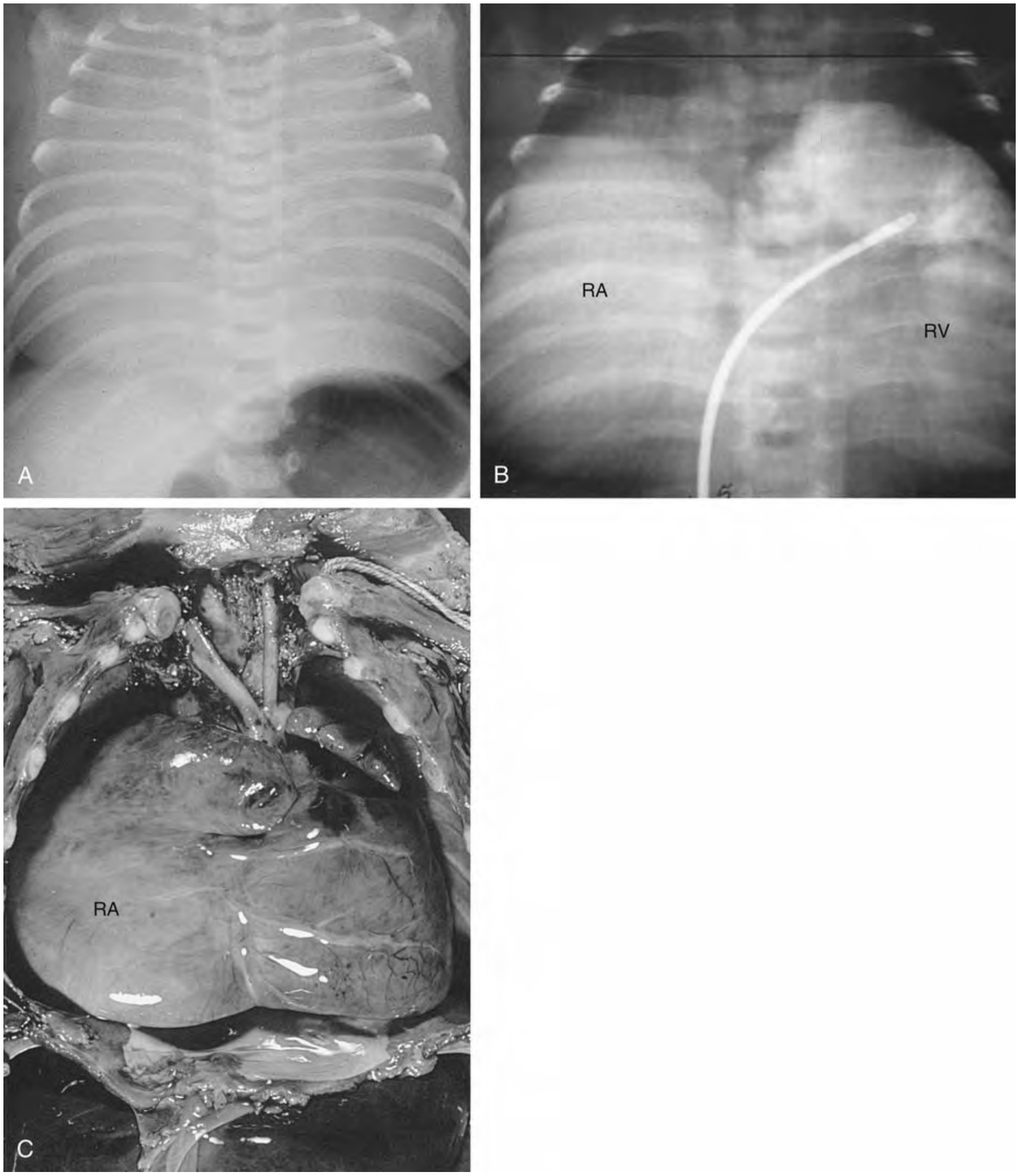
Blue, Increased Flow

Patients who are cyanotic and have increased pulmonary arterial flow have admixture lesions, in which the systemic and pulmonary circulations are mixed. In infancy the two entities that should be considered most likely are truncus arteriosus and total anomalous pulmonary venous return (TAPVR).

Truncus Arteriosus

In truncus arteriosus there is failure of the normal division of the primitive truncus arteriosus into an aorta and a pulmonary artery. Therefore one single vessel arises from the heart and gives rise to the

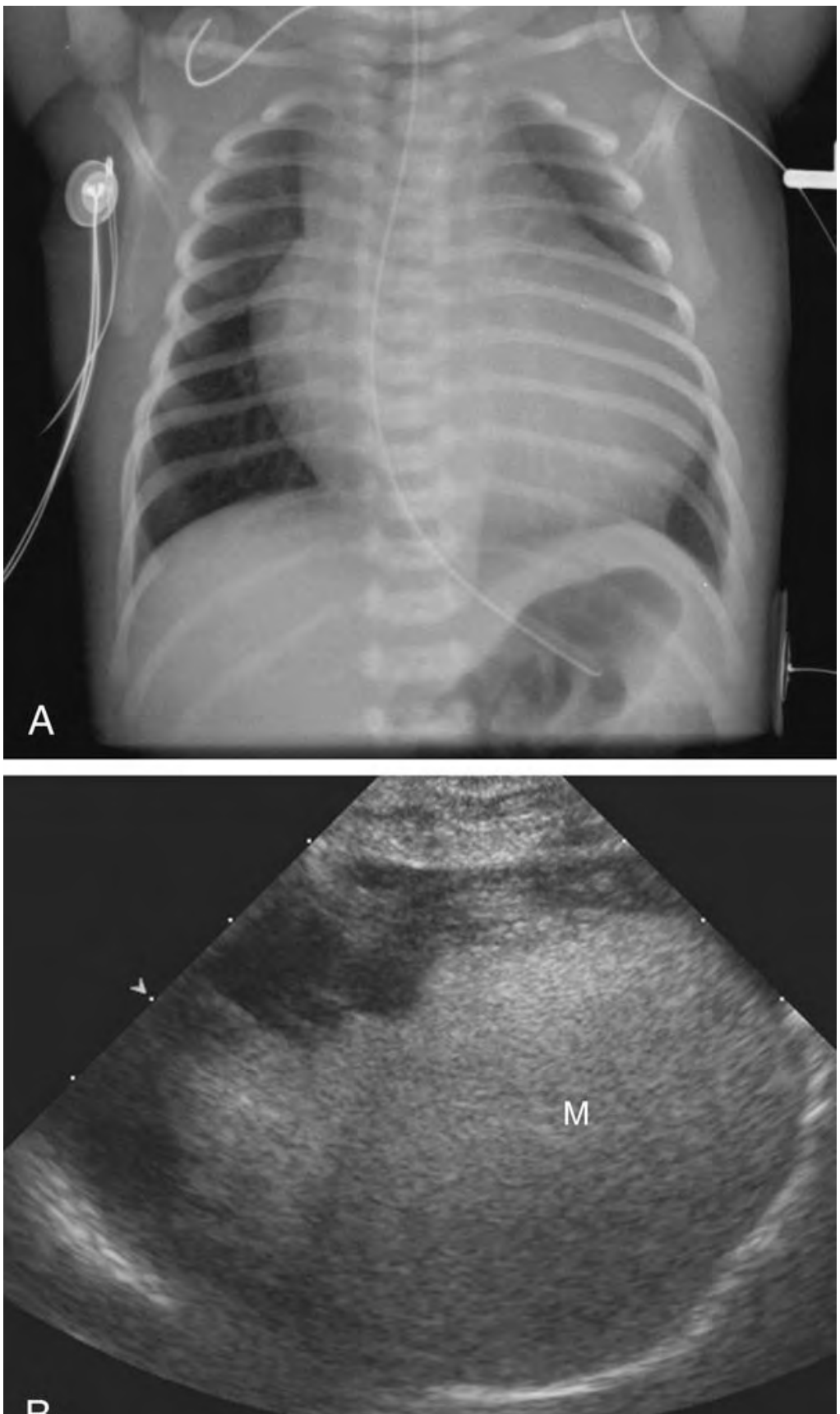
coronary, systemic, and pulmonary circulations. There is always an associated VSD. The types of truncus arteriosus are classified according to how the pulmonary arteries arise from the primitive truncus. It is an uncommon lesion and usually presents with cyanosis early in infancy.



▪ **FIGURE 4-14** **Pulmonary atresia with intact ventricular septum in a newborn.** **A,** Radiograph shows massive cardiomegaly filling the entire chest. **B,** Contrast injection of the right ventricle shows massive dilatation of the right atrium *(RA)* and right ventricle *(RV)*. **C,** Postmortem photograph after thoracotomy shows massively dilated right atrium. *(Donnelly LF, Gelfand KJ, Schwartz DC, et al.: The wall-to-wall heart: differential diagnosis for massively large cardiothymic silhouette in newborns,* Applied Radiol *26:23-28, 1997. Used with permission.)*

On chest radiography there is increased pulmonary arterial flow. A right aortic arch is present in approximately one third of patients. The identification of a right aortic arch in the presence of increased pulmonary arterial flow in a cyanotic child is highly suggestive of the diagnosis (Fig. 4-16). There is

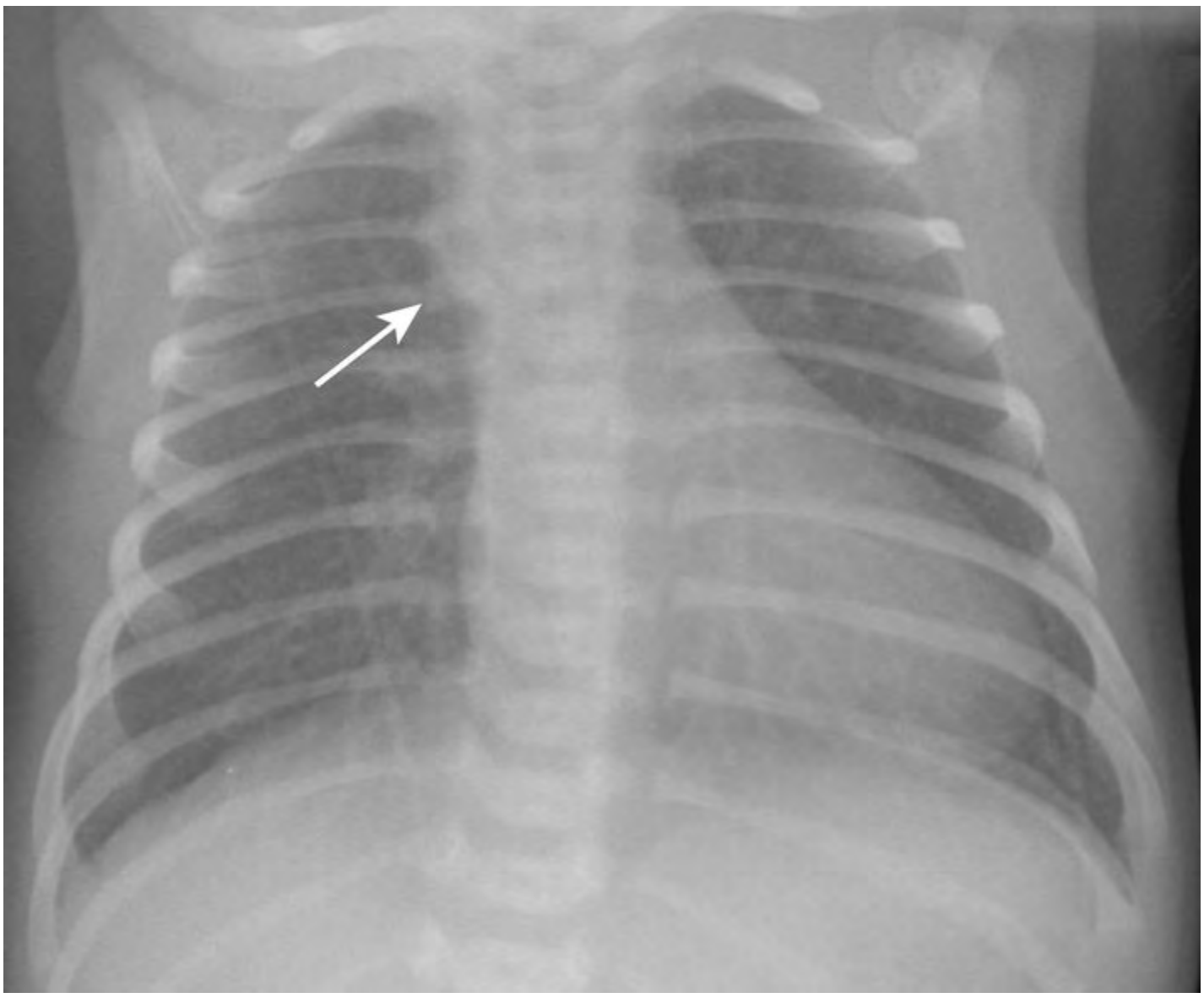
usually moderate cardiomegaly, as well as superimposed pulmonary venous congestion.


A

M
B


M
C

▪ **FIGURE 4-15** **Cardiac rhabdomyoma with cardiomegaly.**
A, Frontal chest radiograph demonstrates cardiomegaly. There even appears to be decreased pulmonary arterial flow. **B,** Substernal longitudinal ultrasound image demonstrates large infiltrative mass *(M)* arising from the heart. **C,** Coronal T1-weighted MR image shows an isointense mass *(M)* in the heart.



▪ **FIGURE 4-16** **Truncus arteriosus.**
Frontal chest radiograph shows increased pulmonary arterial flow, cardiomegaly, and right-sided aortic arch *(arrow)*.

Total Anomalous Pulmonary Venous Return

In TAPVR the pulmonary venous return does not connect to the left atrium but instead connects to the SVC, IVC, right atrium, or portal vein. TAPVR can be divided into supracardiac, cardiac, or infracardiac subtypes. Supracardiac is the most common form; in this form the pulmonary veins converge and form a left vertical vein that runs superiorly and connects into the innominate vein. With infracardiac TAPVR the returning veins penetrate the diaphragm and connect to the IVC or portal veins below the level of diaphragm. These veins may become obstructed, and the patient may present with a pulmonary edema pattern on chest radiography (Fig. 4-17). If the veins are not obstructed, the lesion may appear with cardiomegaly and increased pulmonary arterial flow, similar to other left-to-right shunts (Fig. 4-18, *A* and *B*). Supracardiac TAPVR classically demonstrates a "snowman" appearance, in which the dilated left vertical vein and dilated SVC form the superior portion of the snowman and the cardiac silhouette forms the inferior portion (Fig. 4-19, *A* and *B*). This classic appearance does not develop until later in life and is not often seen now because these lesions are repaired during infancy.

Blue, Variable Pulmonary Arterial Flow

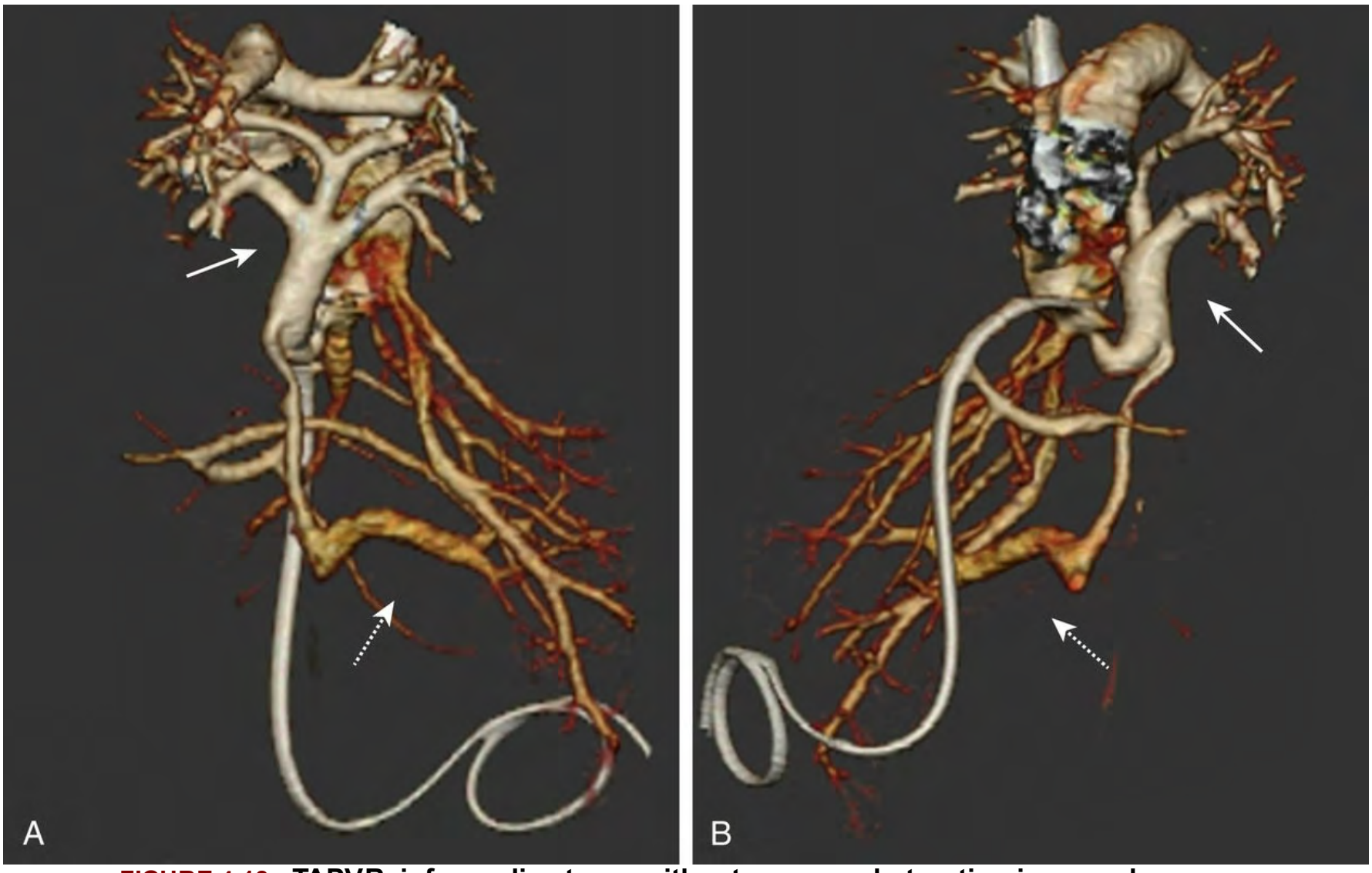
Both D-transposition of the great arteries (D-TGA) and tricuspid atresia can present with variable flow, depending on the anatomy associated with the lesion, as well as the age of the patient.



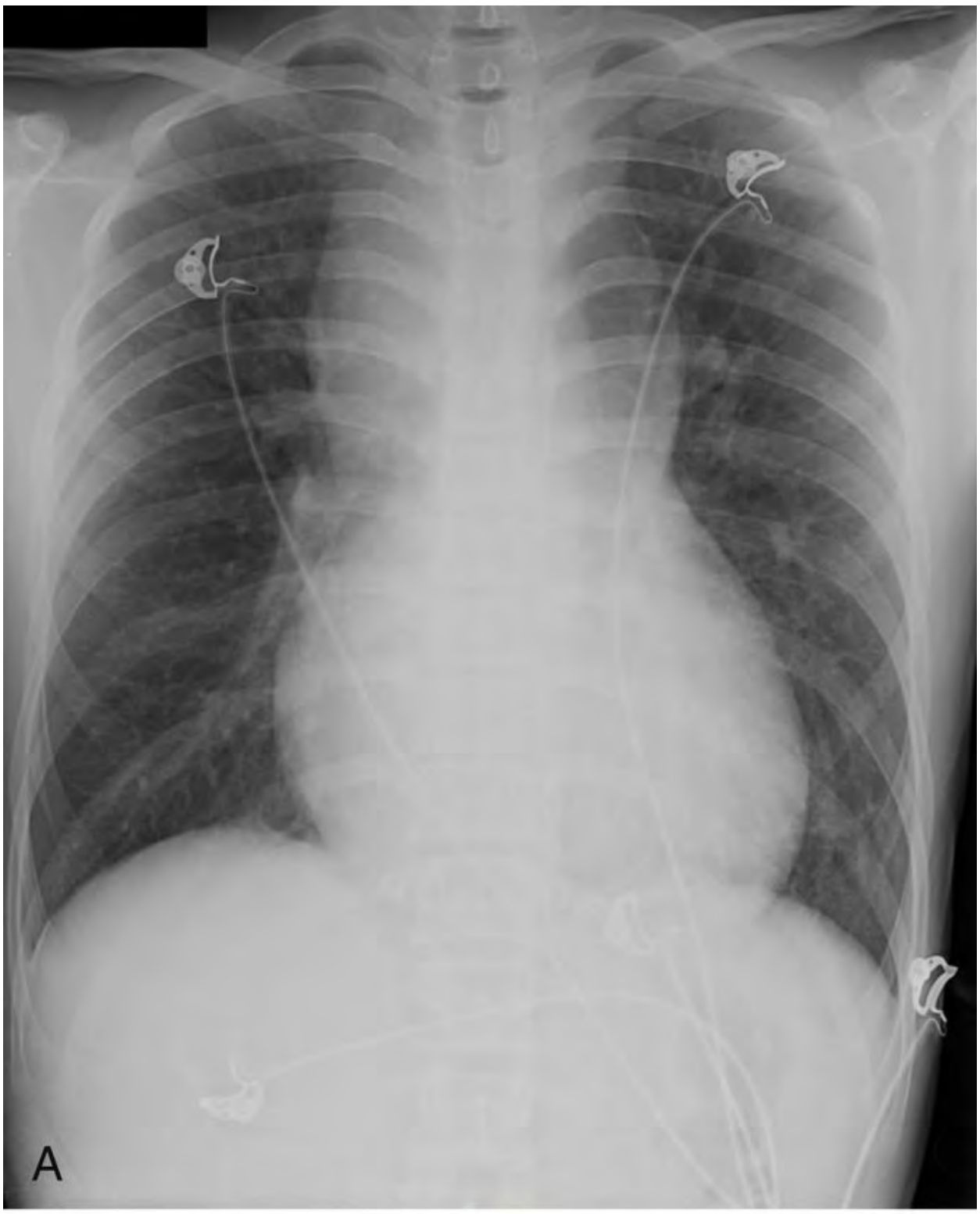
▪ FIGURE 4-17 **TAPVR, infracardiac type, with venous obstruction in a newborn.**
Frontal chest radiograph demonstrates diffuse pulmonary opacity with indistinctness of the pulmonary vascularity.

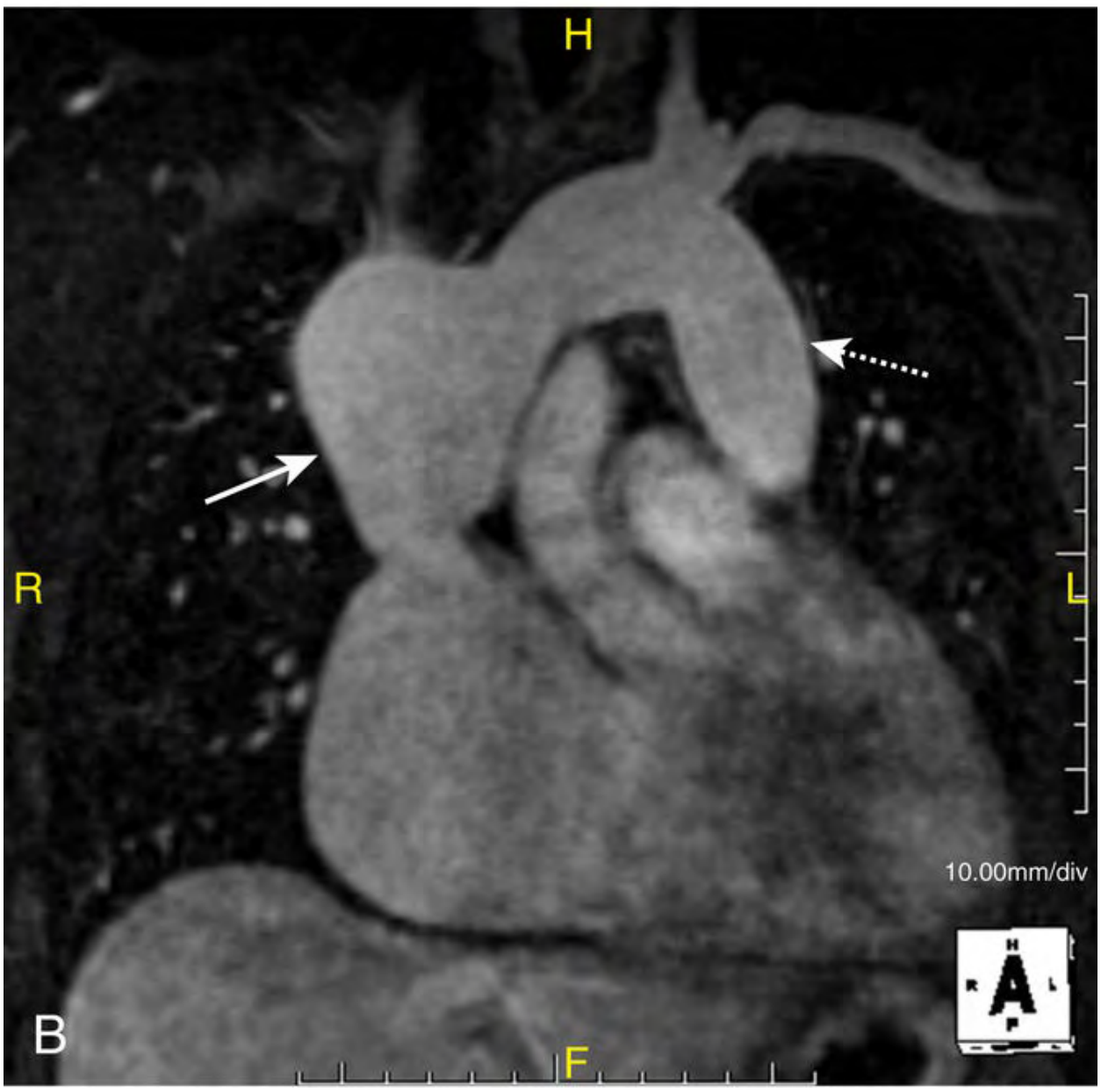
D-Transposition of the Great Arteries

D-TGA is the most common congenital heart disease presenting with cyanosis during the first 24 hours of life. With this abnormality the aorta and pulmonary arteries are transposed. The ascending aorta arises from the right ventricle, and the pulmonary artery arises from the left ventricle. Therefore blood flow runs in two parallel circuits, systemic and pulmonary. Survival depends on communication between these two circuits via a patent foramen ovale, ASD, VSD, or patent ductus arteriosus (PDA). Historically, D-TGA was categorized as a cardiac lesion associated with increased pulmonary arterial flow. However, in areas with developed health care systems, pulmonary arterial switch procedures are performed during the first week of life; therefore increased pulmonary flow, which is seen in older children with transposition, is now rarely seen. The most common chest radiographic appearance of a newborn child with D-TGA is normal. Classically described radiographic findings include narrowing of the superior mediastinum due to decreased thymic tissue and abnormal relationships of the great vessels and to increased pulmonary arterial flow, as previously mentioned. The appearance of the mediastinum has been likened to that of an egg on a string (Fig. 4-20).



▪ **FIGURE 4-18** **TAPVR, infracardiac type, without venous obstruction in a newborn.**
A and **B,** Three-dimensional reformations from a CT angiogram demonstrate all four pulmonary veins draining anomalously to a common vein *(solid arrows)*, which then drains toward the IVC and portal venous system *(dashed arrows)*.

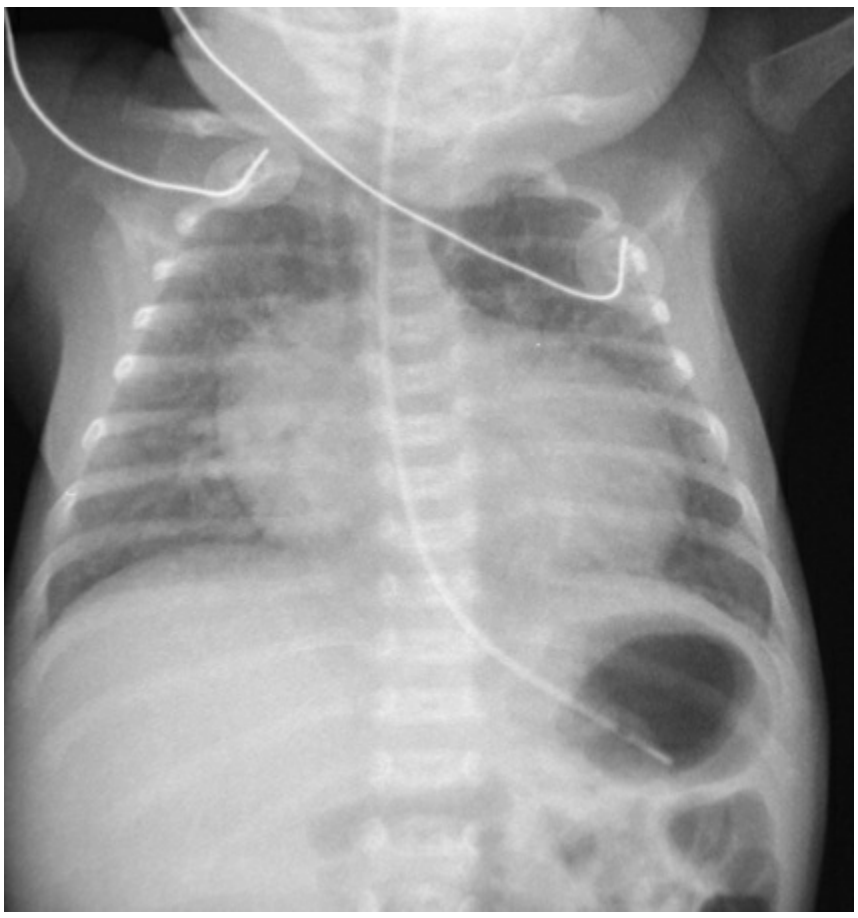

A


H
R
L
10.00mm/div
B
F

▪ **FIGURE 4-19** **TAPVR, supracardiac type, in an older child.**
A, Frontal chest radiograph shows the classic "snowman" appearance of the cardiomediastinum. There is enlargement of the superior mediastinum secondary to dilated left vertical vein and SVC. **B,** MRI coronal maximum intensity projection (MIP) MR angiogram image shows the vertical vein *(dashed arrow)* draining into SVC *(solid arrow)*.

Tricuspid Atresia

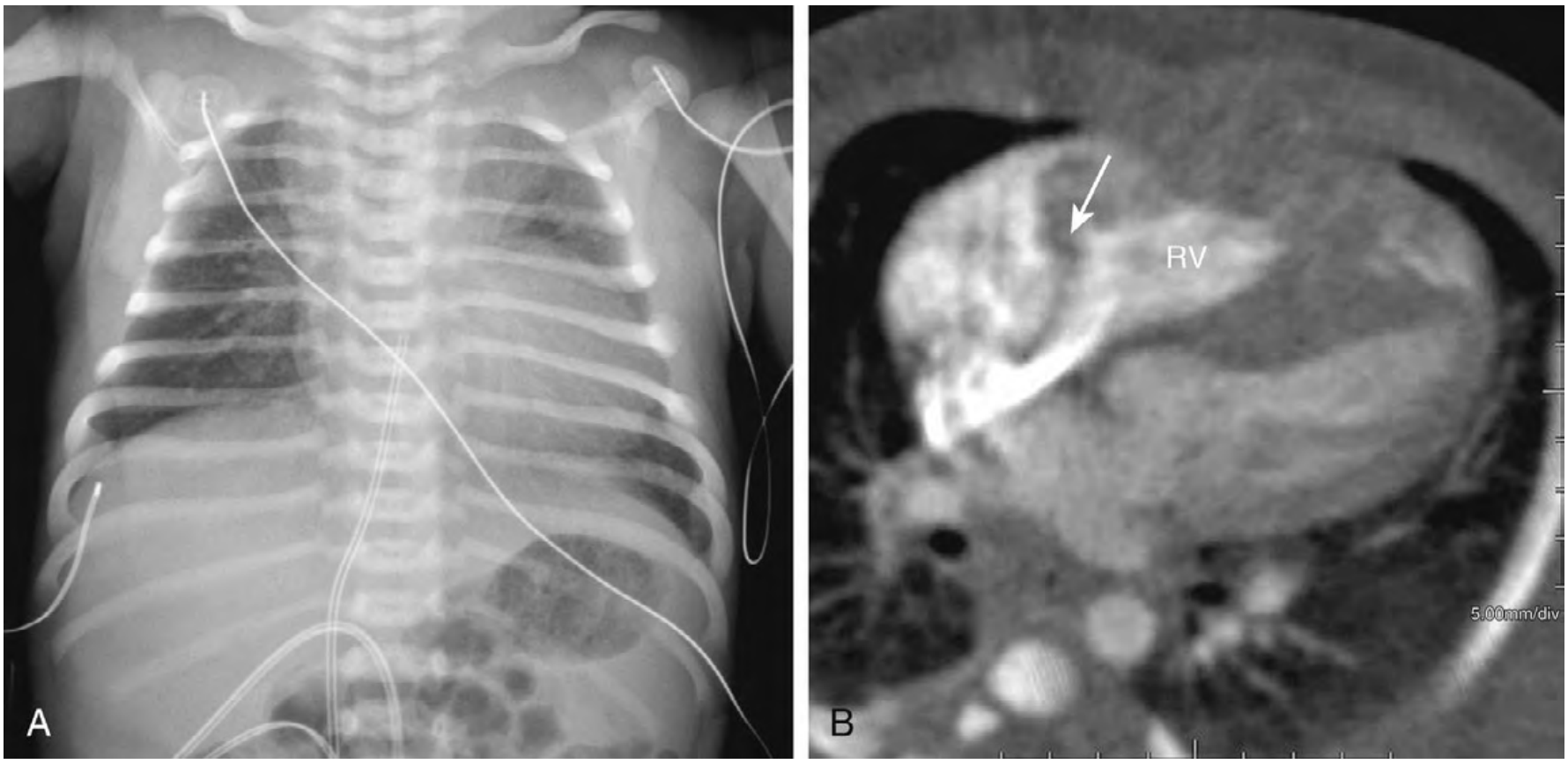
In tricuspid atresia the classic description is that the right atrium is markedly enlarged, causing marked cardiomegaly associated with decreased pulmonary flow. However, this classic appearance is seen only in a minority of patients. The radiograph can vary greatly in cases of tricuspid atresia, making radiographic diagnosis a humbling experience (Fig. 4-21, *A* and *B*).



▪ **FIGURE 4-20** **D-TGA in a newborn male.**
Frontal chest radiograph shows classic "egg-on-a-string" appearance of the heart and mediastinum. This is a relatively rarely encountered appearance for TGA. More commonly the chest radiograph is normal in these patients.

Pink, Increased Pulmonary Arterial Flow

Children who are acyanotic and demonstrate increased pulmonary arterial flow on chest radiography have left-to-right shunts. Potential shunts include ASD, VSD, PDA (Fig. 4-22, *A* and *B*), atrioventricular canal, partial anomalous pulmonary venous return, and aortopulmonary window. The particular cardiac chamber enlargement is a clue to which type of shunt is present. In ASD the right atrium and right ventricle are enlarged. In VSD the right ventricle, left atrium, and left ventricle are enlarged. In PDA the left atrium, left ventricle, and aorta are enlarged. However, as previously mentioned, determining chamber enlargement on chest radiographs is next to impossible in infants. Perhaps a more practical way of predicting which type of shunt is present is by determining the age at presentation. Patients with very large shunts, such as VSDs or atrioventricular canals, present in infancy. ASDs typically present later in childhood or in early adulthood. PDAs occur most commonly in premature infants. Atrioventricular canals occur with increased prevalence in patients with Down syndrome (see Fig. 4-4).



▪ FIGURE 4-21 **Tricuspid atresia in a 3-day-old girl.**
A, Frontal chest radiograph shows a prominent heart with increased pulmonary vascularity. **B,** Axial contrast-enhanced CT image shows a small, hypertrophied right ventricle *(RV)* with an atretic tricuspid valve *(arrow)*.

On chest radiography, neonates with left-to-right shunts demonstrate increased pulmonary arterial flow, a variable amount of associated increased pulmonary venous flow (pulmonary edema), and cardiomegaly (see Figs. 4-4 and 4-22). It is common for infants with large left-to-right shunts also to have marked hyperinflation on chest radiography. This hyperinflation is thought to be secondary to air trapping due to the peribronchial edema. Therefore the presence of marked hyperinflation should not dissuade one from the diagnosis of a left-to-right shunt in favor of viral small airway disease.

Pink (or Dusky) With Increased Pulmonary Venous Flow

An acyanotic patient with increased pulmonary venous flow is essentially a patient with congestive heart failure. In the neonate the differential diagnosis of congestive heart failure is quite extensive and somewhat different from that seen in older children and adults. Radiology trainees often have difficulty providing a reasonable differential diagnosis of congestive heart failure in a newborn. An easy way to approach the differential diagnosis is to consider two large categories of disease. The first category is anatomic left-sided obstruction (Table 4-3). Anything that obstructs the left side of the heart can cause congestive heart failure. If one works his or her way proximally, starting at the level of the aorta, one will not forget to mention any of the likely candidates. In the aorta, both coarctation of the aorta (Fig. 4-23) and critical aortic stenosis can cause left-sided obstruction. Anything that causes the left ventricle to be dysfunctional also can cause left-sided heart obstruction. The list of possibilities is long and includes cardiomyopathy (see Fig. 4-5), glycogen storage disease, anomalous origin of the left coronary artery with associated cardiac ischemia, birth asphyxia (shock myocardium), infants of diabetic mothers, myocarditis, and hypoplastic left heart syndrome (Fig. 4-24). Within the region of the left atrium, both mitral valve stenosis and cor triatriatum can cause left-sided heart failure. Cor triatriatum is defined as the presence of a membrane dividing the left atrium into two separate chambers. The membrane has a pinlike hole centrally that is the only route for forward blood flow and causes relative obstruction. Pulmonary venous atresia can also cause left-sided heart failure. The most commonly encountered of these abnormalities include hypoplastic left heart syndrome and coarctation of the aorta.

The second large category of entities that can cause left-sided heart failure includes systemic causes of failure, such as anemia and polycythemia, sepsis, or high output failure resulting from a peripheral arteriovenous malformation.

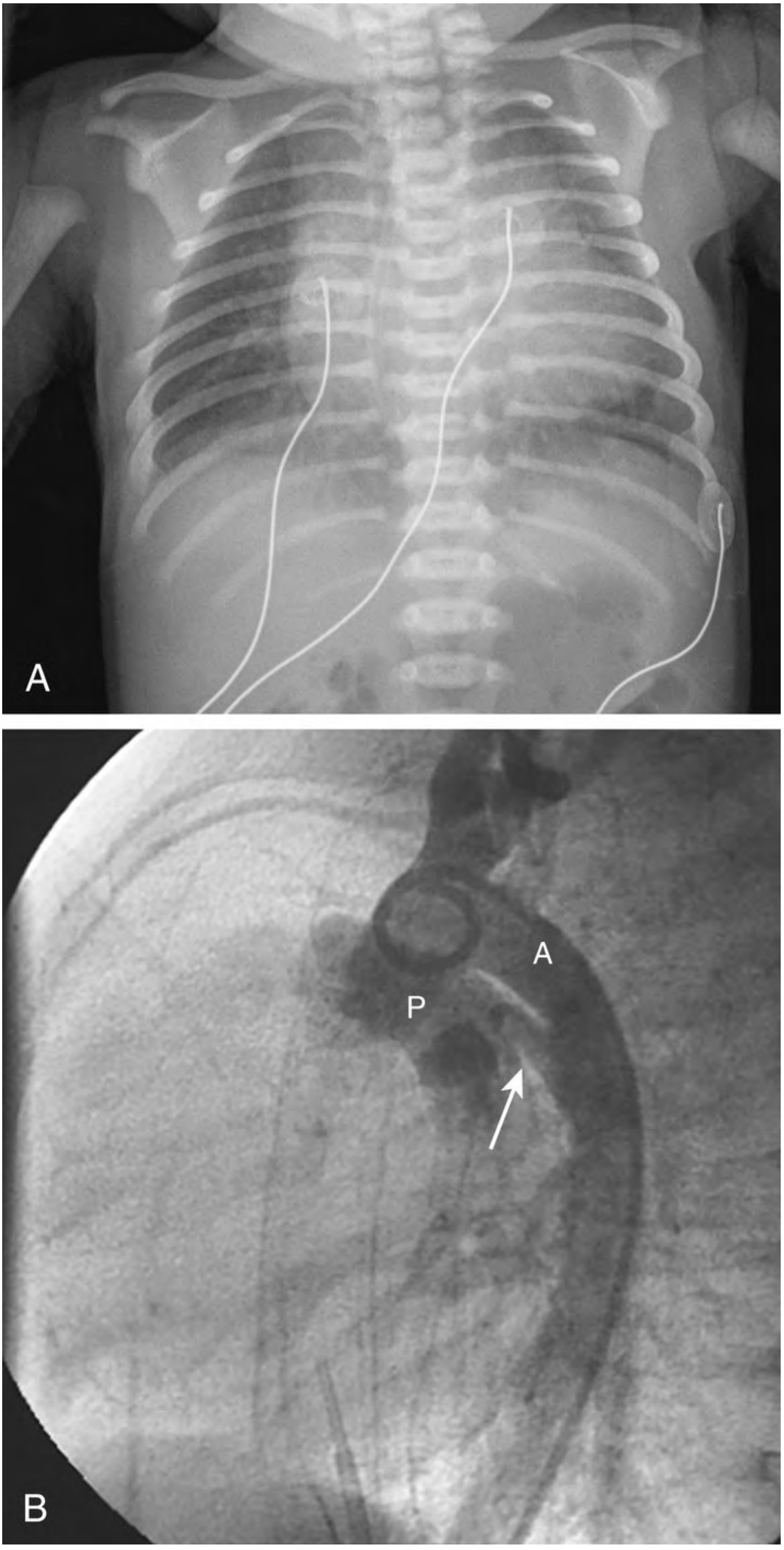
Hypoplastic Left Heart Syndrome

Hypoplastic left heart syndrome refers to a combination of hypoplasia or aplasia of the ascending aorta, aortic valve, left ventricle, and mitral valve. Children present with congestive heart failure at birth. The

lesion is dependent on a PDA. Systemic flow goes from the main pulmonary artery to the descending aorta via the PDA. Flow to the coronary and cranial areas is retrograde via the hypoplastic ascending aorta. On radiography there is cardiomegaly and increased pulmonary venous flow (pulmonary edema; see Fig. 4-24). Treatment is typically the Norwood procedure (Table 4-4).

Pink, Normal Pulmonary Arterial Flow

The three main categories of congenital heart disease that are associated with acyanosis and normal pulmonary arterial flow include obstructive lesions, extrinsic airway compression, and congenital heart disease with increased or decreased pulmonary arterial flow that has been surgically corrected. (Extrinsic airway compression was discussed in Chapter 2.)


A
A
P
B

▪ **FIGURE 4-22 PDA.**

A, Frontal chest radiograph shows an enlarged heart with increased pulmonary vascularity (shunt vascularity). **B,** Lateral angiogram image with catheter tip in the aortic arch *(A)* shows contrast traversing a PDA *(arrow)* and entering into the pulmonary artery *(P)*.

TABLE 4-3

Differential Diagnosis for Congestive Heart Failure in the Newborn

Anatomic

Coarctation
Aortic stenosis
Left ventricular dysfunction and
- Anomalous origin of the left coronary artery
- Myocarditis
- Shock myocardium (birth asphyxia)
- Glycogen storage disease
- Infant of diabetic mother

Hypoplastic left heart
Mitral stenosis
Cor triatriatum
Pulmonary venous atresia or stenosis

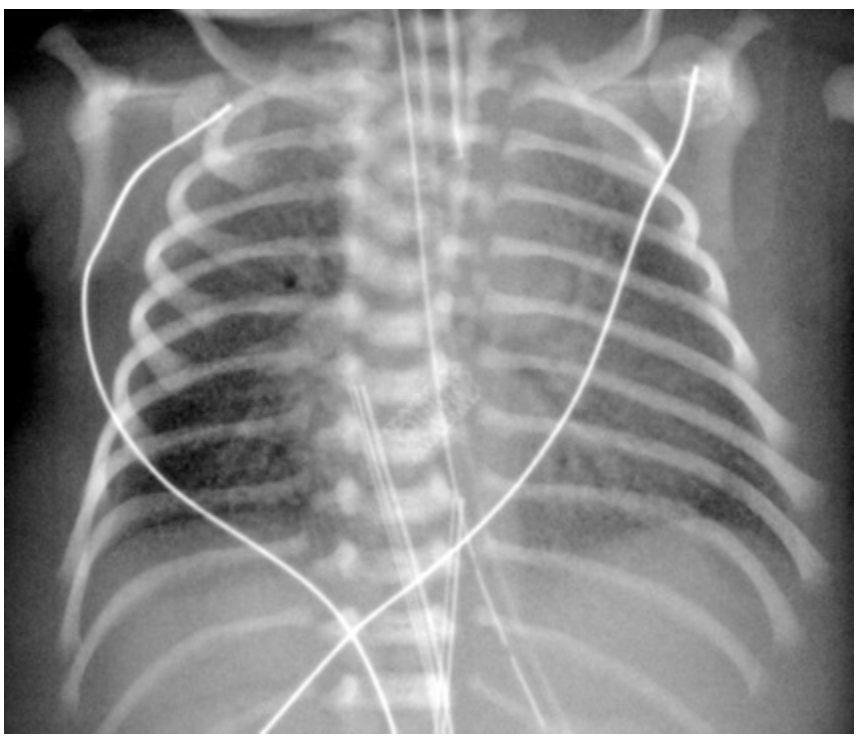
Systemic

Anemia-polycythemia
Hypoglycemia and hyperglycemia
Hypothyroidism and hyperthyroidism
Sepsis
Peripheral arteriovenous malformation
- Vein of Galen malformation
- Hepatic hemangioendothelioma





▪ **FIGURE 4-23** **Coartation of the aorta.**
Three-dimensional reformation of a CT angiogram demonstrates a coarctation at the aortic isthmus *(arrow)*.



▪ **FIGURE 4-24** **Hypoplastic left heart with associated congestive heart failure in a newborn.**
Frontal chest radiograph shows cardiomegaly and indistinct pulmonary vasculature. Note that patients with hypoplastic left heart do not necessarily have hearts that appear to be small.

Obstructive Lesions

Obstructive lesions of the great arteries include aortic stenosis, pulmonic stenosis, and coarctation of the aorta. These lesions can have subtle findings on chest radiography, so when there is a scenario that suggests congenital heart disease but one's initial impression is that the chest radiograph is normal, a second glance for subtle mediastinal contour abnormalities may prove fruitful.

Aortic Stenosis

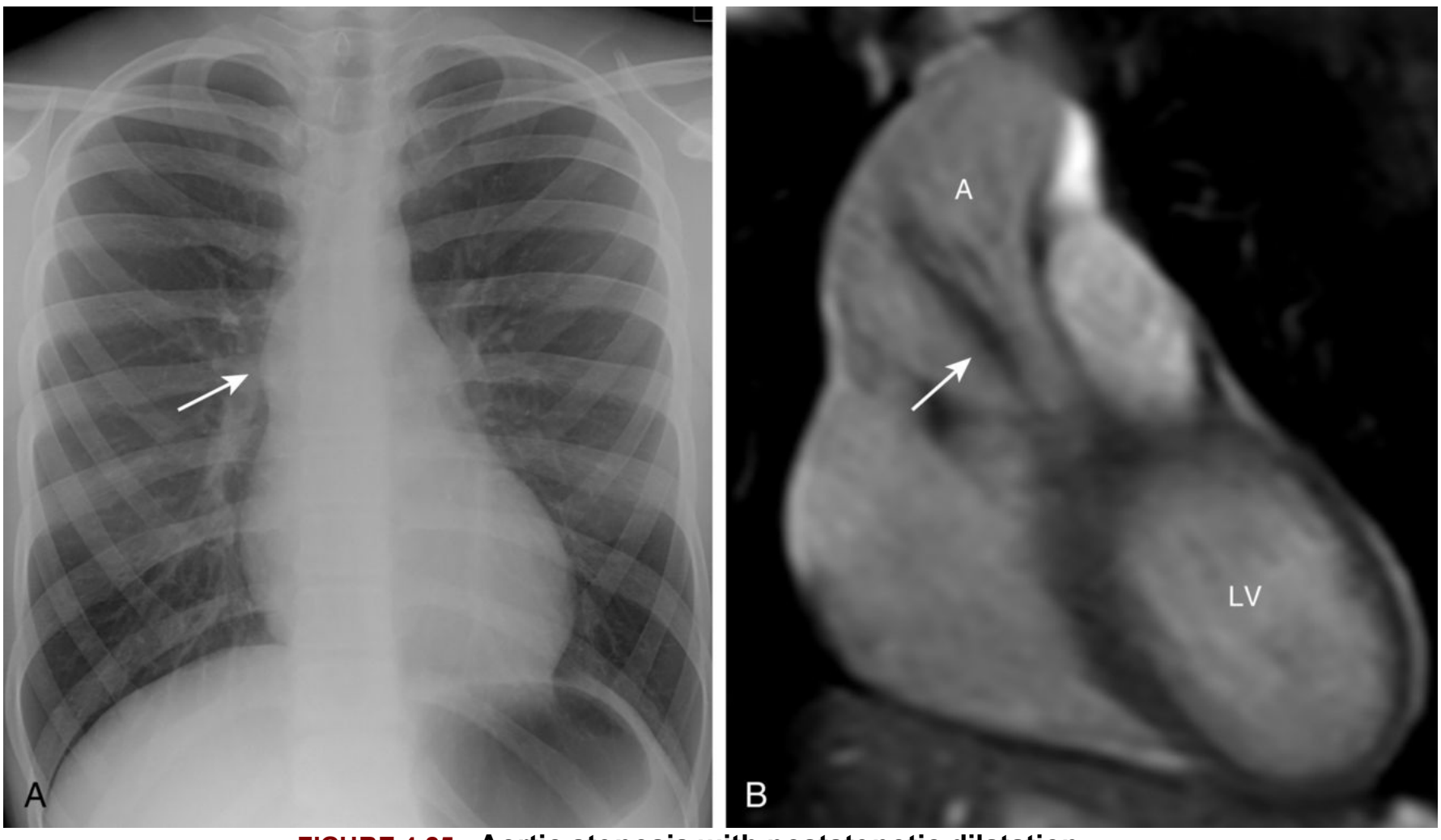
Aortic stenosis may occur secondary to a bicuspid aortic valve or previous rheumatic disease. With aortic valvular stenosis, there may be dilatation of the ascending aorta secondary to the "jet" effect through the stenotic valve (Fig. 4-25, *A* and *B*). The ascending aorta should never be identified in a normal child on frontal radiography. If the rightward border of the ascending aorta is visualized, a dilated aorta should be suspected (see Fig. 4-25). In addition to aortic stenosis, another cause of a dilated ascending aorta is an aneurysm secondary to a disorder such as Marfan syndrome. Another supporting sign for aortic stenosis is left ventricular enlargement secondary to hypertrophy. Aortic stenosis can also be supravalvular in location. Williams syndrome is associated with supravalvular stenosis, peripheral pulmonary artery stenosis, and other symptoms, including mental retardation.

TABLE 4-4

Common Surgical Procedures for Congenital Heart Disease

Procedure	Indication	Connection
Fontan	Tricuspid atresia	RA-to-PA conduit or anastomosis
	Single ventricle	
	Hypoplastic right ventricle	
	Complex congenital heart disease	
Glenn	Tricuspid atresia	SVC-to-right PA anastomosis (bidirectional provides flow to both pulmonary arteries)
	Hypoplastic RV	
	Pulmonary atresia	
Rastelli	Pulmonary atresia	RV-to-PA conduit
Mustard-Senning (intraatrial baffle)	D-TGA	Atrial rerouting of venous blood flow. Mustard uses pericardium to create baffle and Senning uses atrial wall
Arterial switch procedure (Jatene)	D-TGA	Switch of aorta and PA with reanastomosis of coronary arteries
Norwood	Hypoplastic left heart syndrome	First stage: use of main PA as ascending aorta, enlargement of aortic arch, systemic or right ventricle shunt to PA
		Second stage: Glenn
		Third stage: Fontan
Blalock-Taussig shunt	Palliative shunt for obstruction of pulmonary blood flow (TOF, pulmonary atresia, tricuspid atresia)	Subclavian artery-to-PA graft
Sano shunt	Palliative shunt for obstruction of pulmonary blood flow (TOF, pulmonary atresia, tricuspid atresia)	Right ventricle-to-PA graft
Closure device deployment	Left-to-right shunts (ASD, PDA)	Percutaneous catheter placement of "plugging" closure device across left-to-right shunt
Waterston-Cooley	Palliative shunt for obstruction of pulmonary blood flow	Ascending aorta-to-right PA anastomosis
Potts	Palliative shunt for obstruction of pulmonary blood flow	Descending aorta-to-right PA anastomosis
PA banding	Left-to-right shunting	Band around main PA

ASD, Atrial septal defect; *D-TGA,* transposition of the great arteries; *PA,* pulmonary artery; *PDA,* patent ductus arteriosus; *RA,* right atrium; *RV,* right ventricle; *RV,* right ventricle; *SVC,* superior vena cava; *TOF,* tetralogy of Fallot.



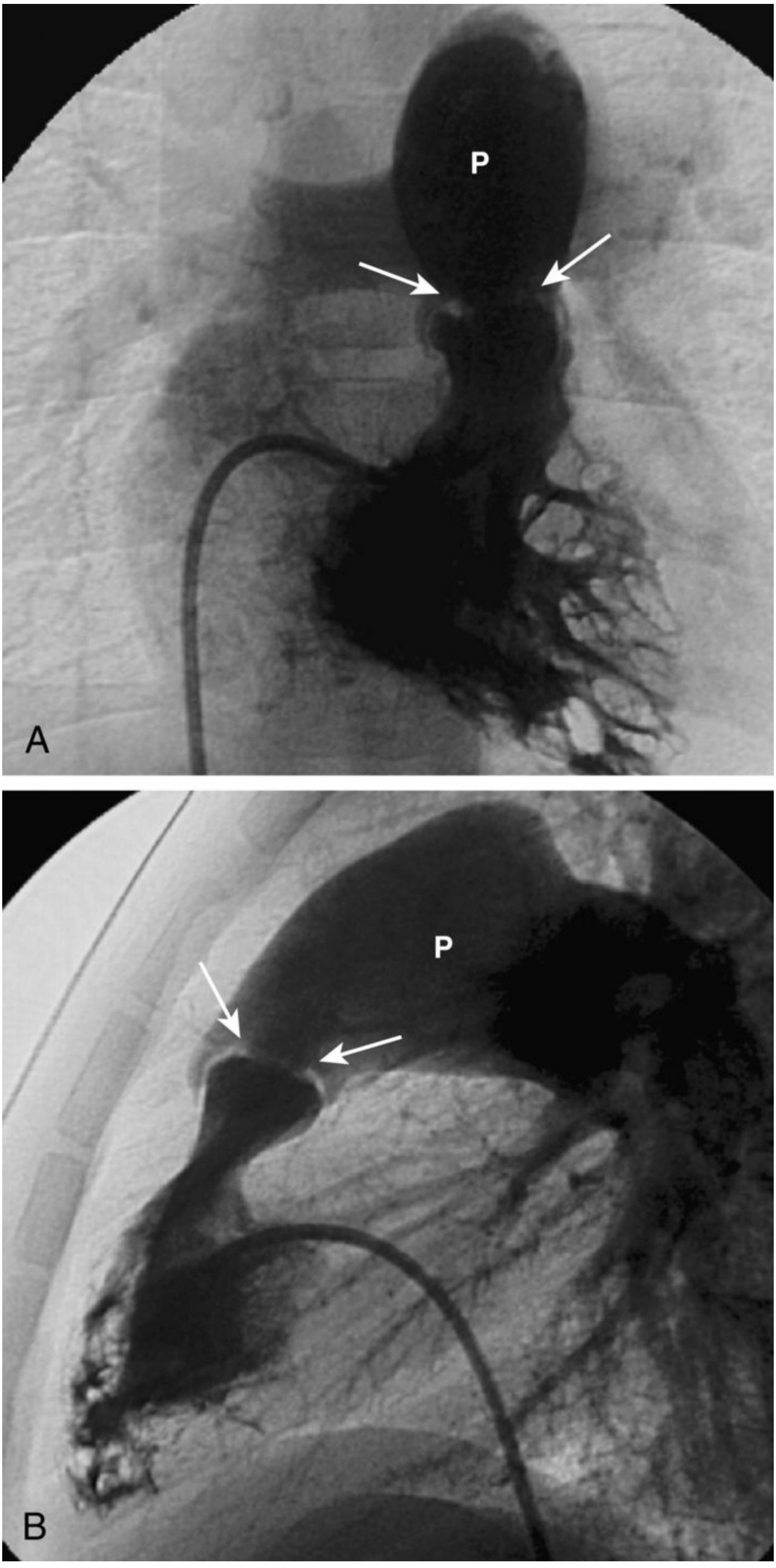
▪ **FIGURE 4-25 Aortic stenosis with poststenotic dilatation.**
A, Frontal chest radiograph shows visualization and prominence of the shadow of the ascending aorta *(arrow)*. Normally, the shadow of the ascending aorta is not seen in children. **B,** bSSFP MR image in the same patient shows a dilated ascending aorta *(A)* resulting from a flow jet *(arrow)* through the stenotic aortic valve from the left ventricle *(LV)*.

Pulmonic Stenosis

In pulmonary valvular stenosis there may be dilation of the main pulmonary artery secondary to the jet effect (Fig. 4-26, *A* and *B*). On frontal chest radiography this appears as a prominent main pulmonary arterial segment (Fig. 4-27).

Coarctation of the Aorta

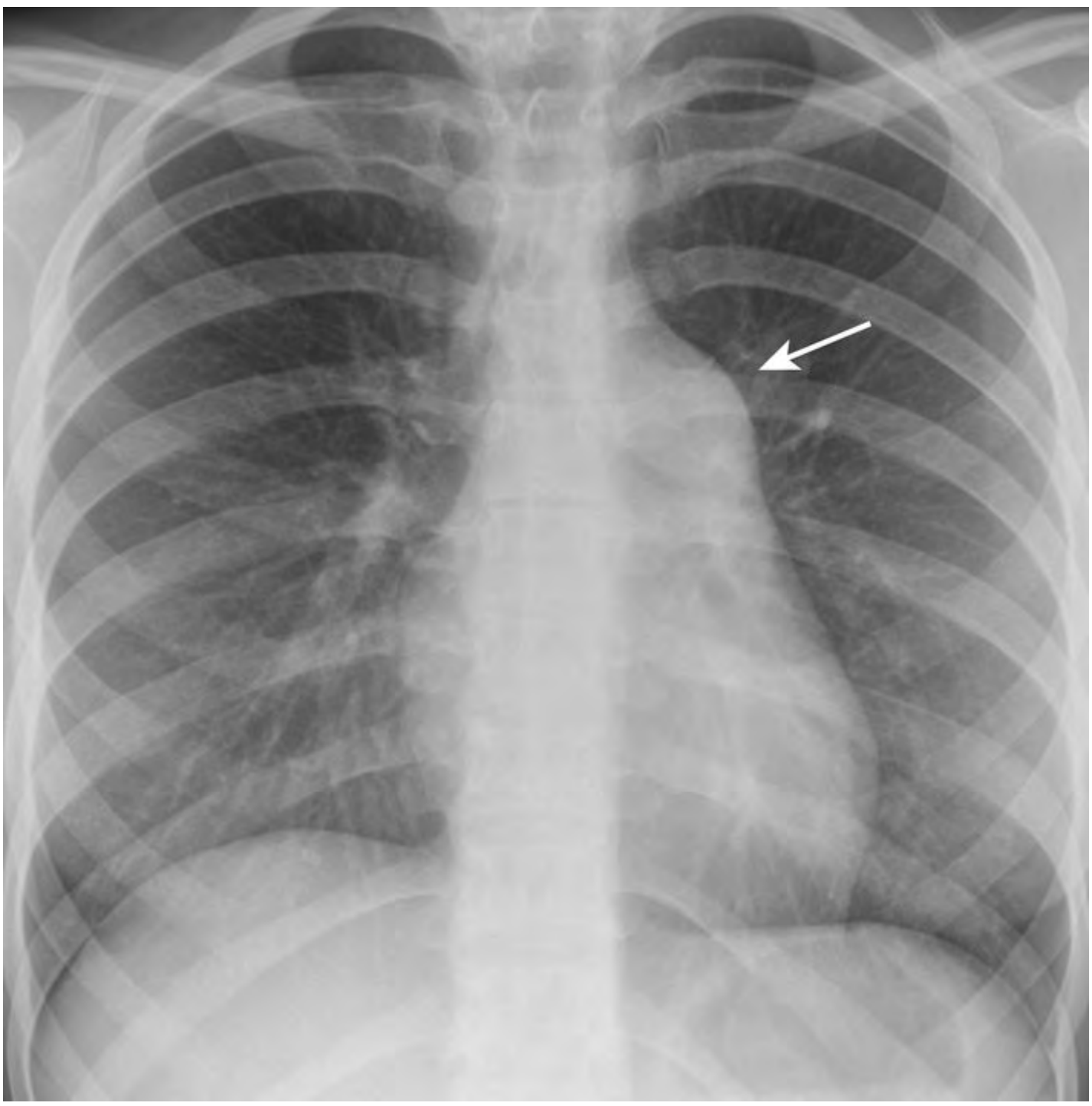
Coarctation is defined as a congenital narrowing of the aorta. This narrowing can be either diffuse or localized. The localized type, which is more common, is typically located just beyond the left subclavian artery origin in the vicinity of the level of ductus arteriosus. The clinical presentation is determined by the severity of the narrowing. Severe narrowing presents in infancy with congestive heart failure. Coarctation can be an isolated lesion or can appear as part of more complex anatomic anomalies (Fig. 4-28). Less severe narrowing may present later in childhood with upper extremity hypertension. On chest radiography the appearance of the leftward border of the superior mediastinum has been likened to the numeral 3 in coarctation (Fig. 4-29, *A*-*C*), particularly in older children. The superior portion of the 3 is caused by the prestenotic dilation of the aorta above the coarctation. The middle or narrow part of the 3 is caused by the coarctation itself, and the inferior part of the 3 is caused by the poststenotic, dilated portion of the descending aorta. Inferior rib notching may be present secondary to pressure from dilatated intercostal arteries (see Fig. 4-29); it most commonly occurs at the level of the fourth through eighth ribs. In patients with coarctation of the aorta there is increased association with bicuspid aortic valve, which can present later in life with resultant aortic stenosis. Treatment involves balloon dilation and stent placement (see Fig. 4-29) or surgical resection. In cases of coarctation, CT and MRI can be used for diagnosis and presurgical planning (site, length, severity, relationship to left subclavian artery, and extent of collateralization), as well as for postsurgical follow-up in the evaluation of restenosis, aneurysm, or left ventricular hypertrophy.


P
A
P
B

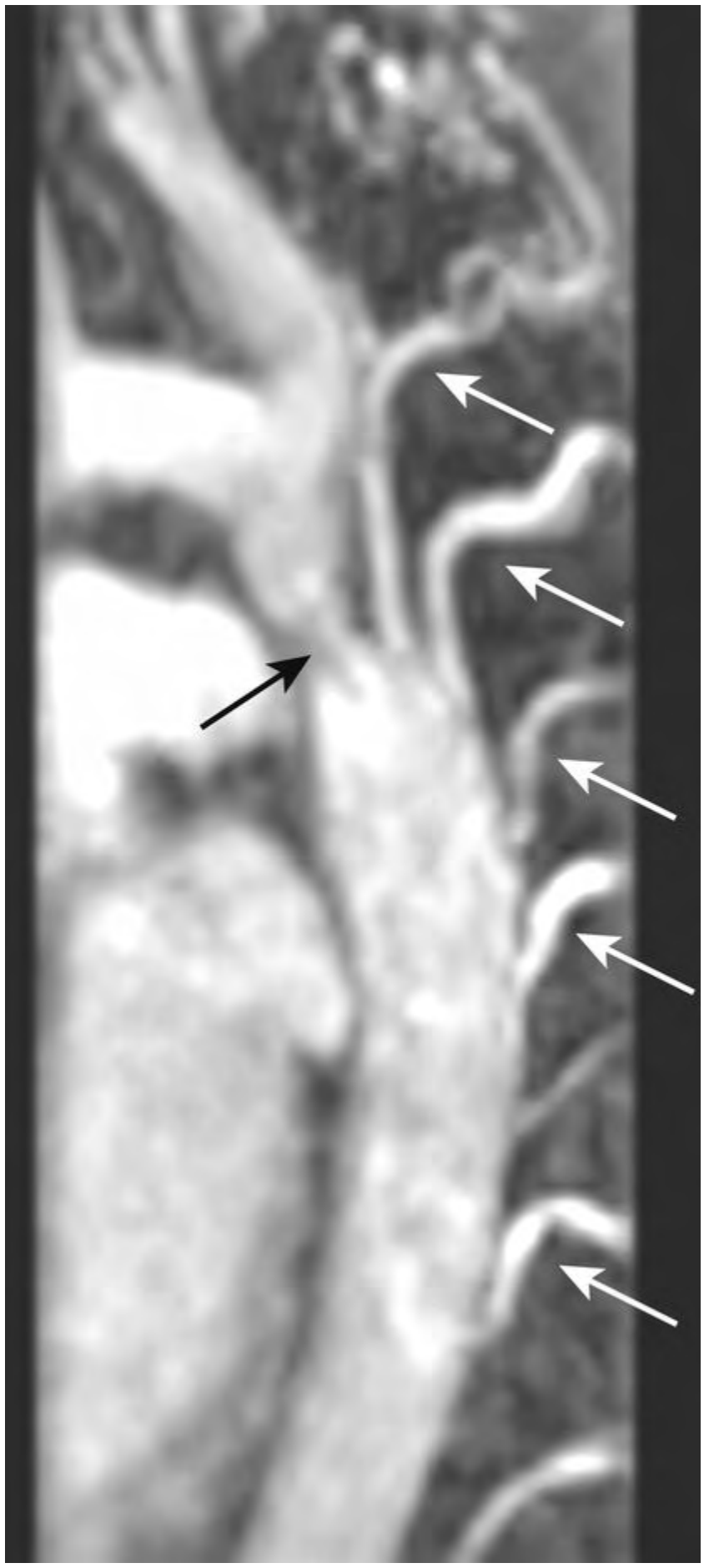
▪ **FIGURE 4-26** **Pulmonic stenosis in a 3-year-old boy.**
Arteriogram performed by injection of contrast via the right ventricle. **A,** Frontal projection. **B,** Lateral projection. Both images show a stenotic valve and jet *(arrows)* and poststenotic dilation of the main pulmonary artery *(P)*.

▪ Abnormalities of Conotruncal Rotation

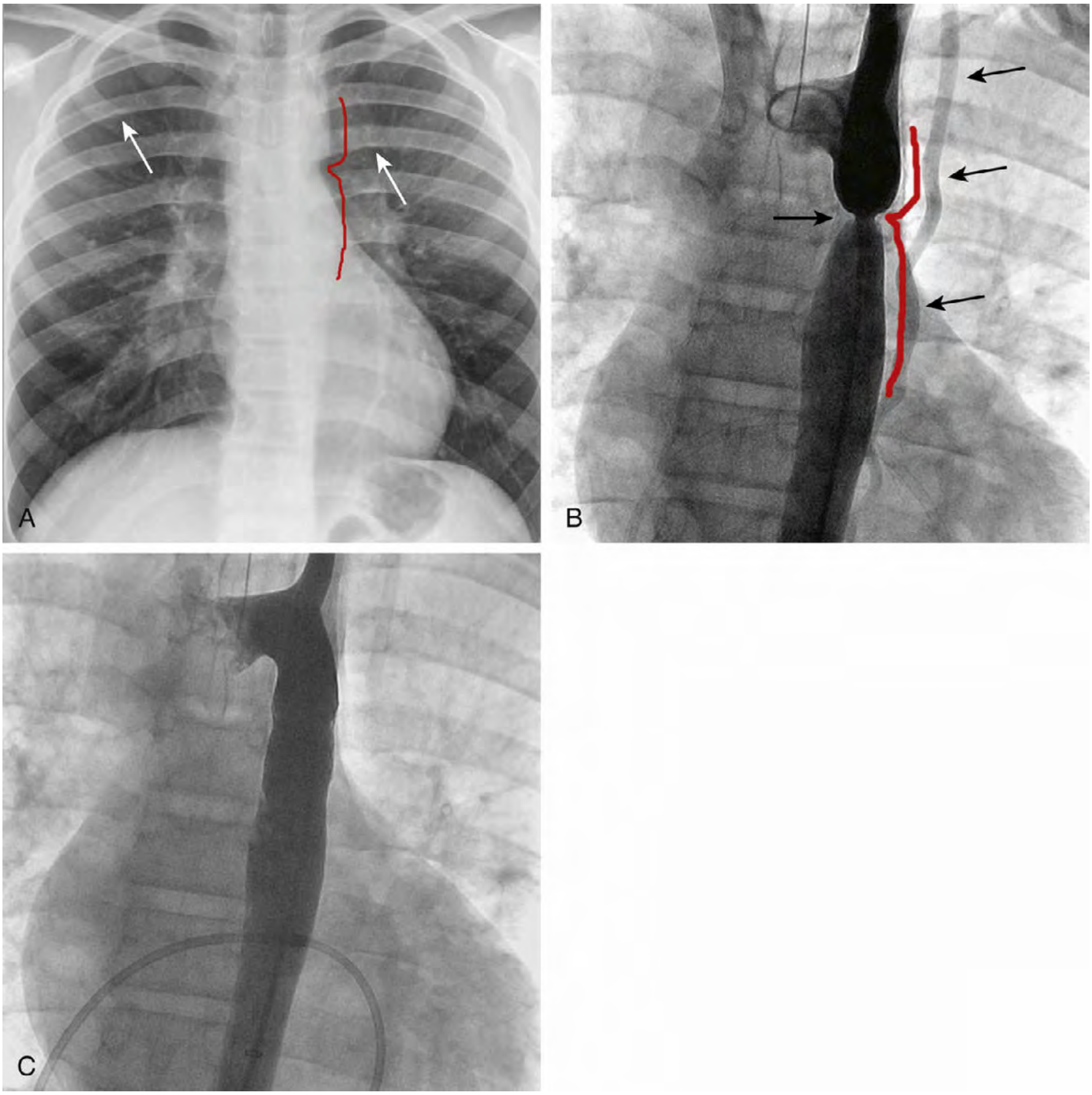
Several types of congenital heart disease can result from abnormalities of conotruncal rotation. There is often confusion concerning this group of diseases. The primitive truncus is an anterior midline structure during fetal development. Normally, the primitive truncus divides into the aorta and pulmonary artery, which rotate clockwise 150 degrees (Figs. 4-30 and 4-31). As a result, the pulmonary artery ends up anterior and to the left of the aorta. Abnormal division or rotation of this primitive truncus may result in a number of diseases, including L-transposition of the great arteries (L-TGA; Fig. 4-32); D-TGA (Figs. 4-33, *A* and *B*, and 4-34); truncus arteriosus; double-outlet right ventricle; and situs inversus. The anatomic relationship between the aorta and pulmonary artery as viewed in cross-section at the level of the semilunar valves is characteristic of these abnormalities. With truncus arteriosus there is a failure of division of the primitive truncus into a separate aorta and pulmonary artery. Therefore a single large vessel gives rise to the coronary, systemic, and pulmonary arterial circulation. Truncus arteriosus was discussed previously.



▪ **FIGURE 4-27** **Pulmonic stenosis in a 7-year-old girl.**
Frontal chest radiograph shows prominence of the main pulmonary artery *(arrow)*.

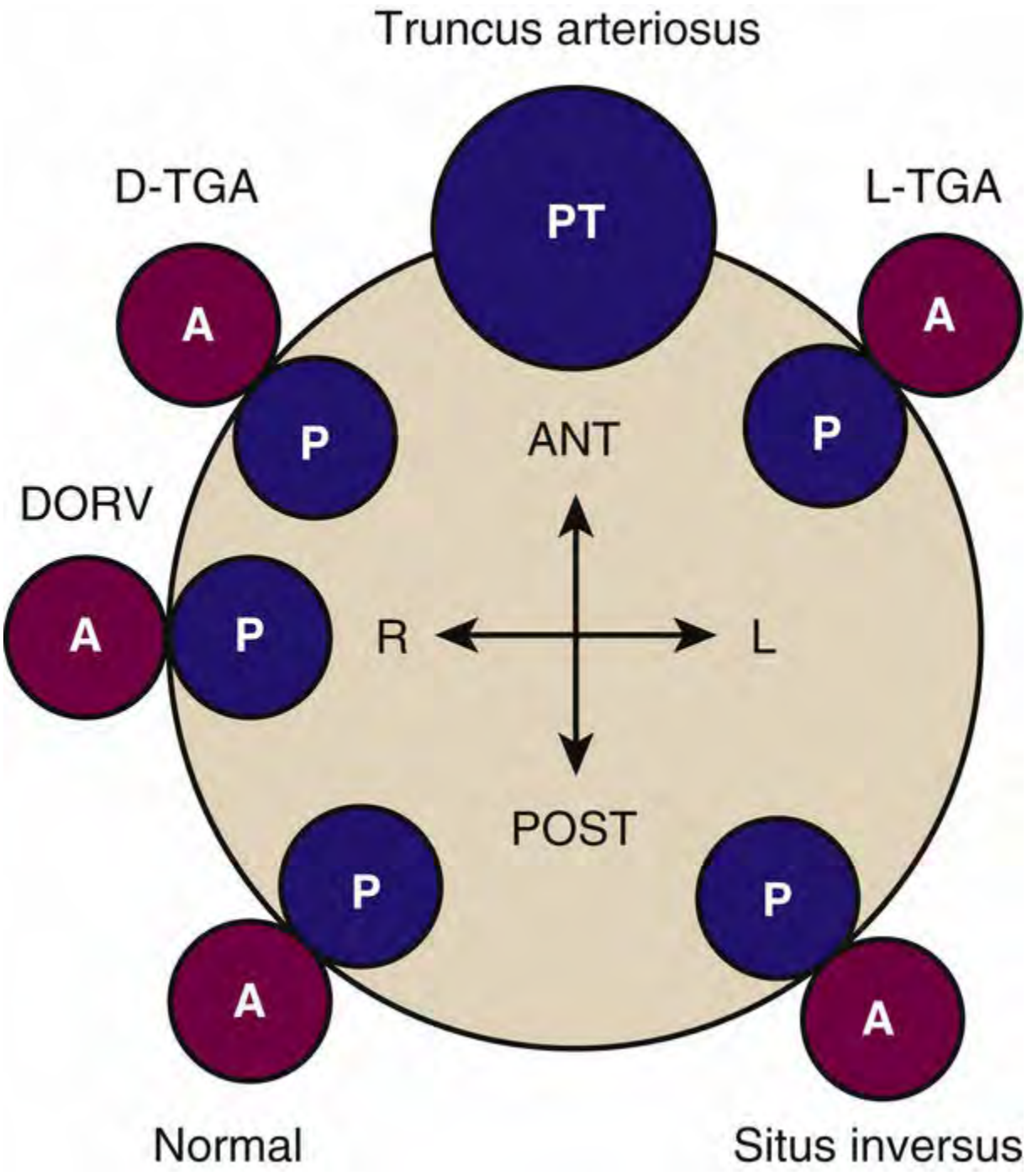


▪ **FIGURE 4-28** **Coarctation of the aorta.**
MIP postcontrast MR image demonstrates coarctation at the aortic isthmus *(black arrow)* and multiple collateral vessels *(white arrows)*.



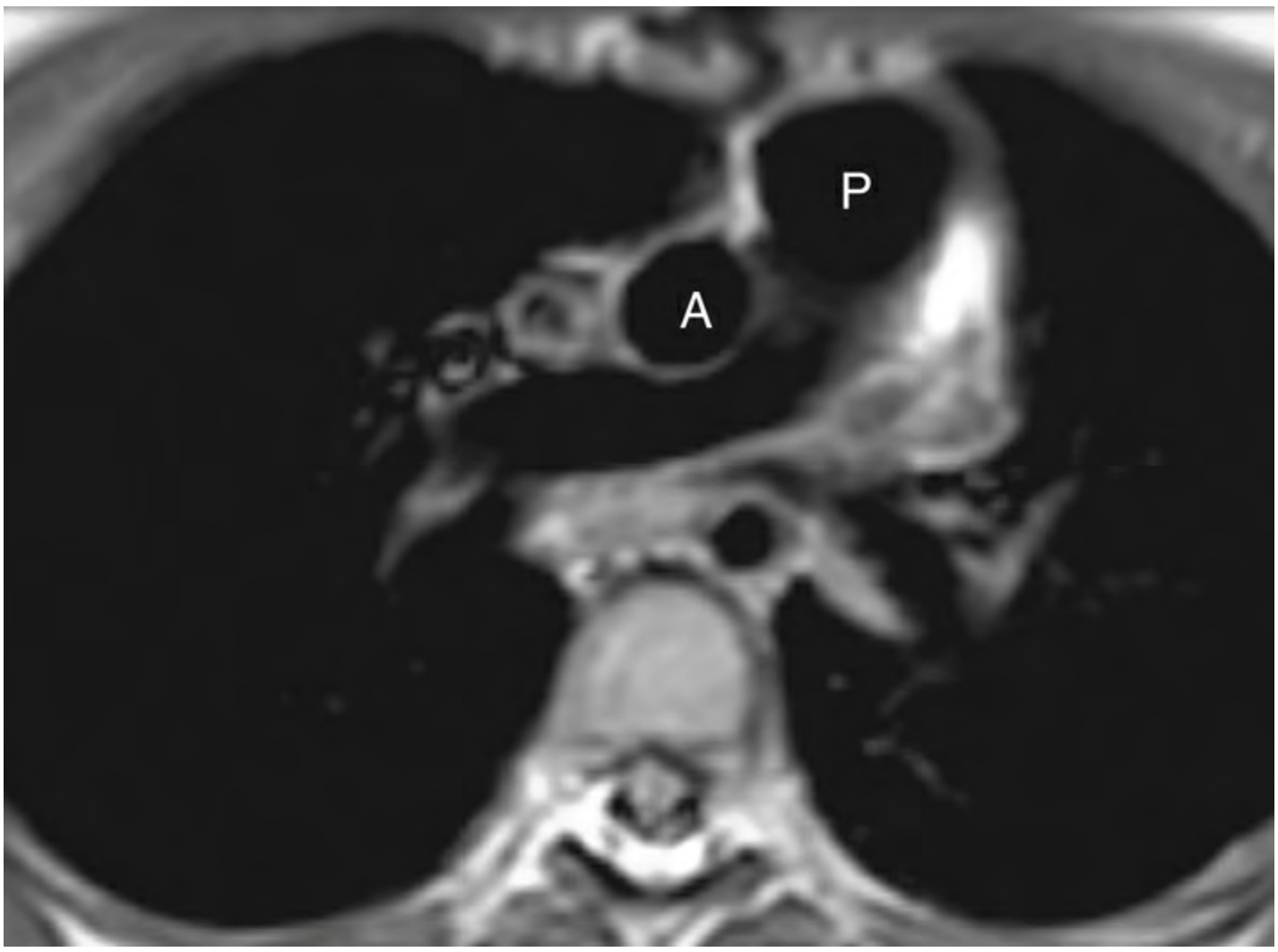
▪ **FIGURE 4-29 Coarctation of the aorta treated with balloon dilation and stent placement.** **A,** Frontal chest radiograph shows a 3-shaped appearance of the left superior mediastinal border (indicated by red line) made up of dilated aorta above the coarctation, coarctation, and poststenotic dilation of the descending aorta inferior to the coarctation. Also note rib notching *(arrows)*. **B,** Arteriogram performed before dilation shows coarctation *(long arrow)*. Note the 3-shaped appearance (indicated by red line). Note collateral flow via dilated internal mammary artery *(short arrows)*. **C,** Post-dilation and stent placement, the coarctation has been resolved. Note resolution of flow (nonvisualization on contrast study) within the dilated collateral mammary artery.

In L-TGA or congenitally corrected transposition of the great arteries, the ventricles and atrioventricular valves are inverted such that there is both atrioventricular and ventriculoarterial discordance. Therefore the morphologic right ventricle is in the position of and serves as the anatomic left ventricle. L-TGA is often associated with complex congenital heart disease but may occur as an isolated lesion. With L-TGA there is 30-degree clockwise rotation of the primitive truncus, which causes the aorta to be anterior and leftward as compared with the pulmonary artery (see Figs. 4-30 and 4-32).



▪ **FIGURE 4-30 Conotruncal rotation.**

Diagram shows relationship of the great arteries at the level of the semilunar valves as depicted by axial cross-sectional CT or MRI. During embryologic development, the primitive truncus is an anterior midline structure. With normal development, the primitive truncus divides into the aorta and the pulmonary artery, which then rotate 150 degrees clockwise. The pulmonary artery then lies anterior to and left of the aorta. Variations in this rotation are characteristic of various conotruncal abnormalities. *A,* Aorta; *DORV,* double outlet right ventricle; *P,* pulmonary artery; *PT,* primitive truncus; *TGA,* transposition of the great arteries.



▪ **FIGURE 4-31** Normal conotruncal position on axial T1-weighted black-blood MR. The pulmonary artery *(P)* is anterior and leftward in relationship to the aorta *(A)*.

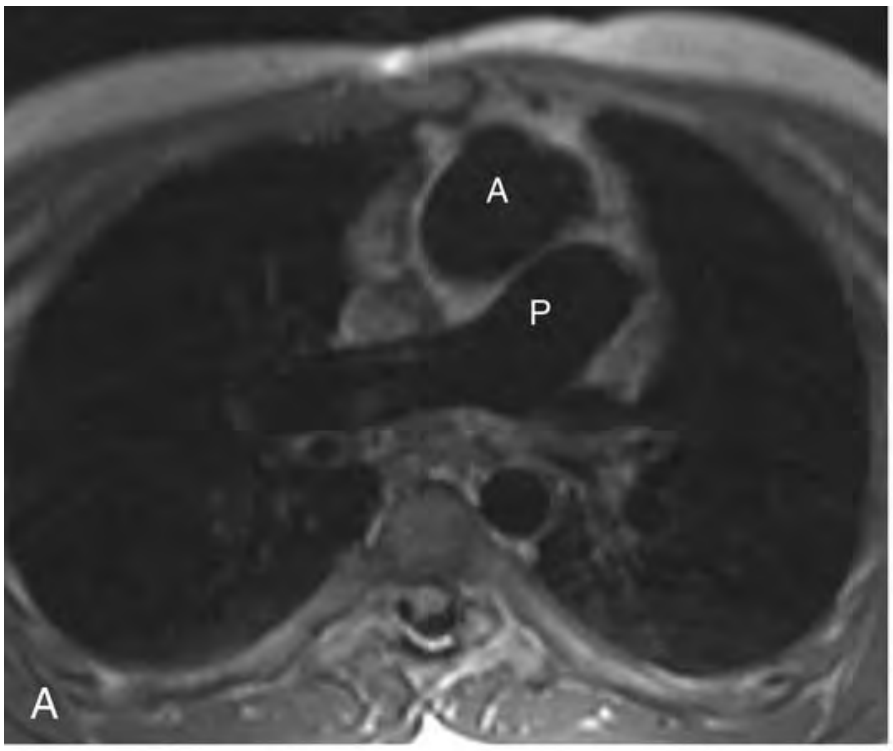
In contrast, with D-TGA or complete transposition of the great arteries, there is ventricular-great vessel discordance, in which the aorta arises from the right ventricle and the pulmonary artery arises from the left ventricle. With D-TGA there is a 30-degree counterclockwise rotation of the primitive truncus, which means that the aorta is rightward and anterior to the pulmonary artery (see Figs. 4-30, 4-33, and 4-34).

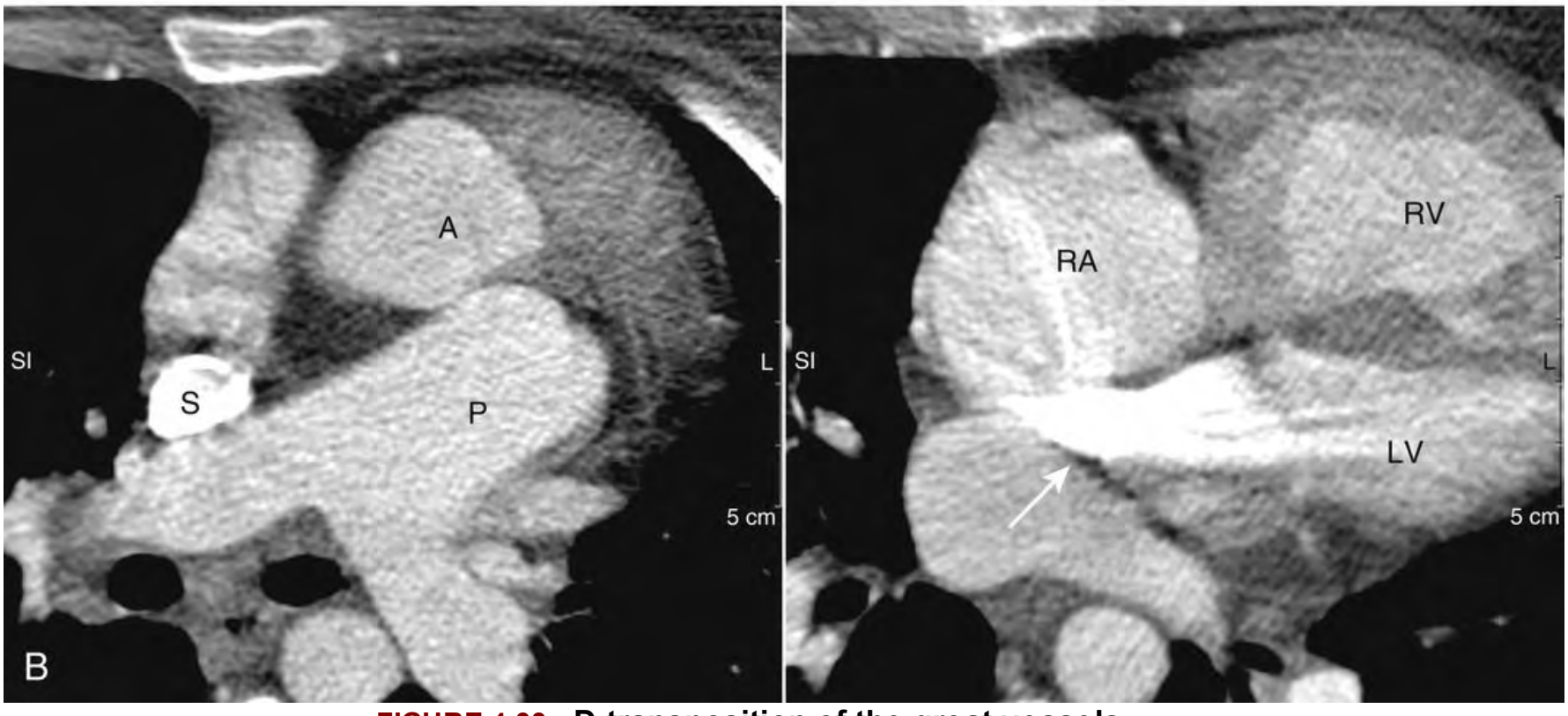
In the case of a double-outlet right ventricle, more than half of the origins of the great arteries arise from the morphologic right ventricle. The only outlet for the left ventricle is a VSD. This lesion is commonly associated with other complex congenital heart disease. During development, there is 45-degree counterclockwise rotation of the primitive truncus, which causes the aorta and pulmonary artery to be side by side with the aorta on the right (see Fig. 4-30).



▪ **FIGURE 4-32** L-transposition of the great vessels shown on axial T1-weighted, black-blood MR. The aorta *(A)* is to the left of and slightly anterior to the pulmonary artery *(P)*.

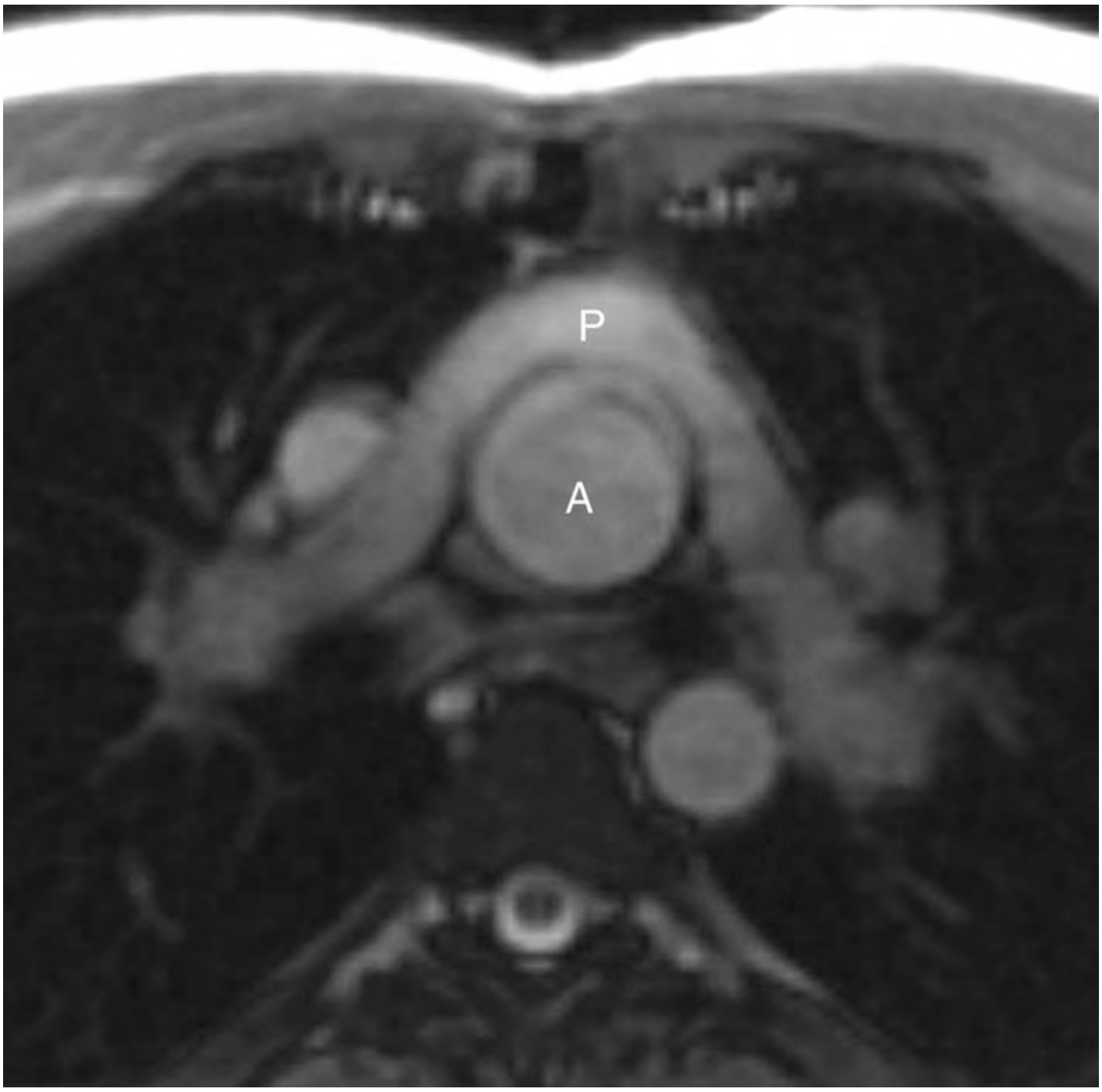
In situs inversus the rotation of the aorta and pulmonary artery is completely opposite of that which would be considered normal (see Fig. 4-30).





▪ **FIGURE 4-33** **D-transposition of the great vessels.**

A, Axial T1-weighted, black-blood image shows the aorta *(A)* is anterior and rightward in relationship to the pulmonary artery *(P)*. **B,** Contrast-enhanced axial CT images after Mustard intraatrial baffle demonstrate the aorta (*A*) anterior and to the right of the pulmonary artery *(P)*. Contrast within the SVC *(S)* has been baffled toward the left atrium and left ventricle (*LV*) instead of the right atrium *(RA)* and right ventricle *(RV)*. Thus deoxygenated blood is directed toward the left side of the heart, which pumps to the pulmonary artery to the lungs.



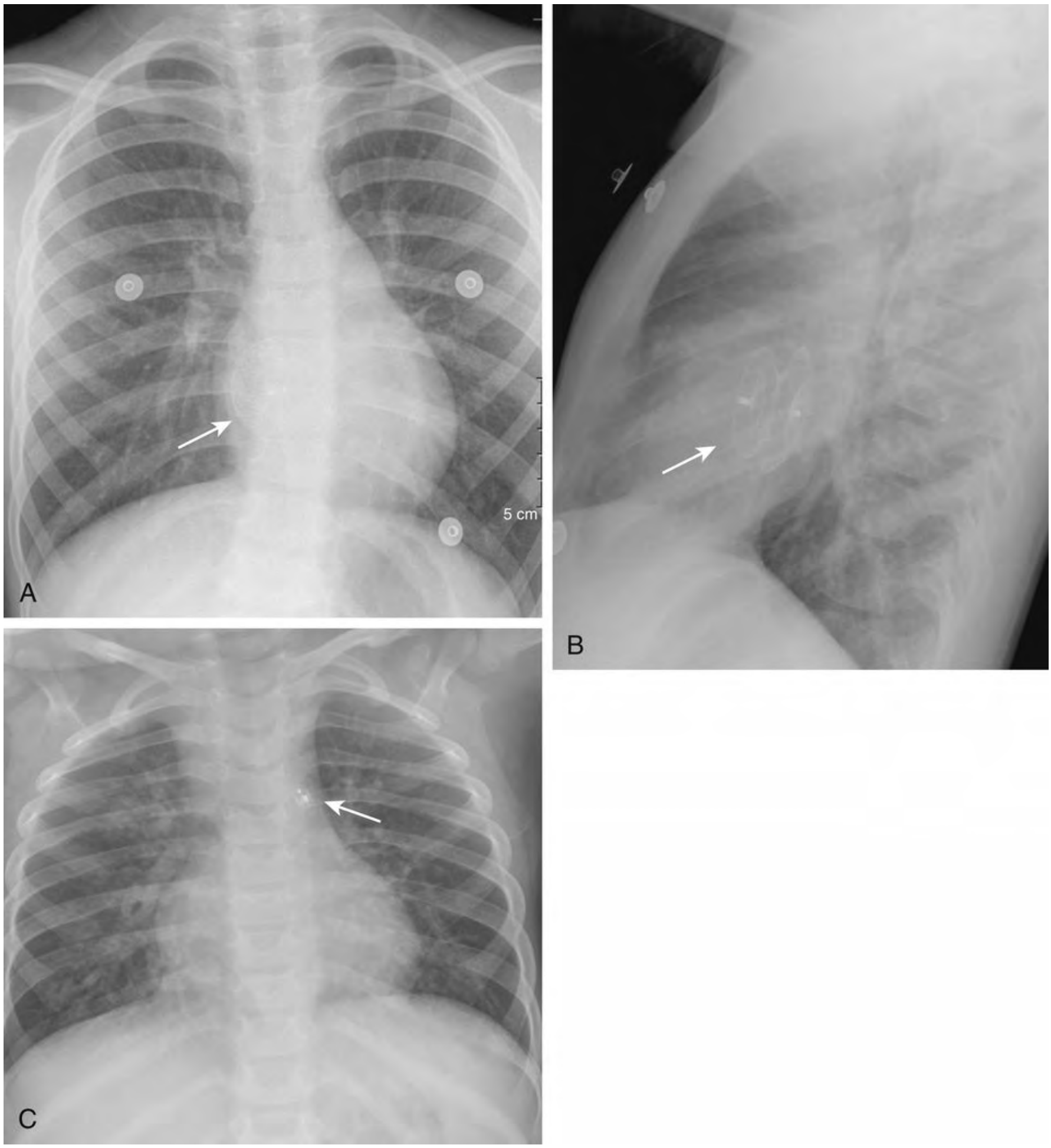
▪ **FIGURE 4-34** Axial bSSFP MR image shows D-transposition of the great vessels following an arterial switch (Jatene) procedure with Lecompte maneuver, with typical postswitch anatomy. The pulmonary artery *(P)* is now anterior to and draped over the more posteriorly positioned ascending aorta *(A)*.

▪ Surgeries for Congenital Heart Disease

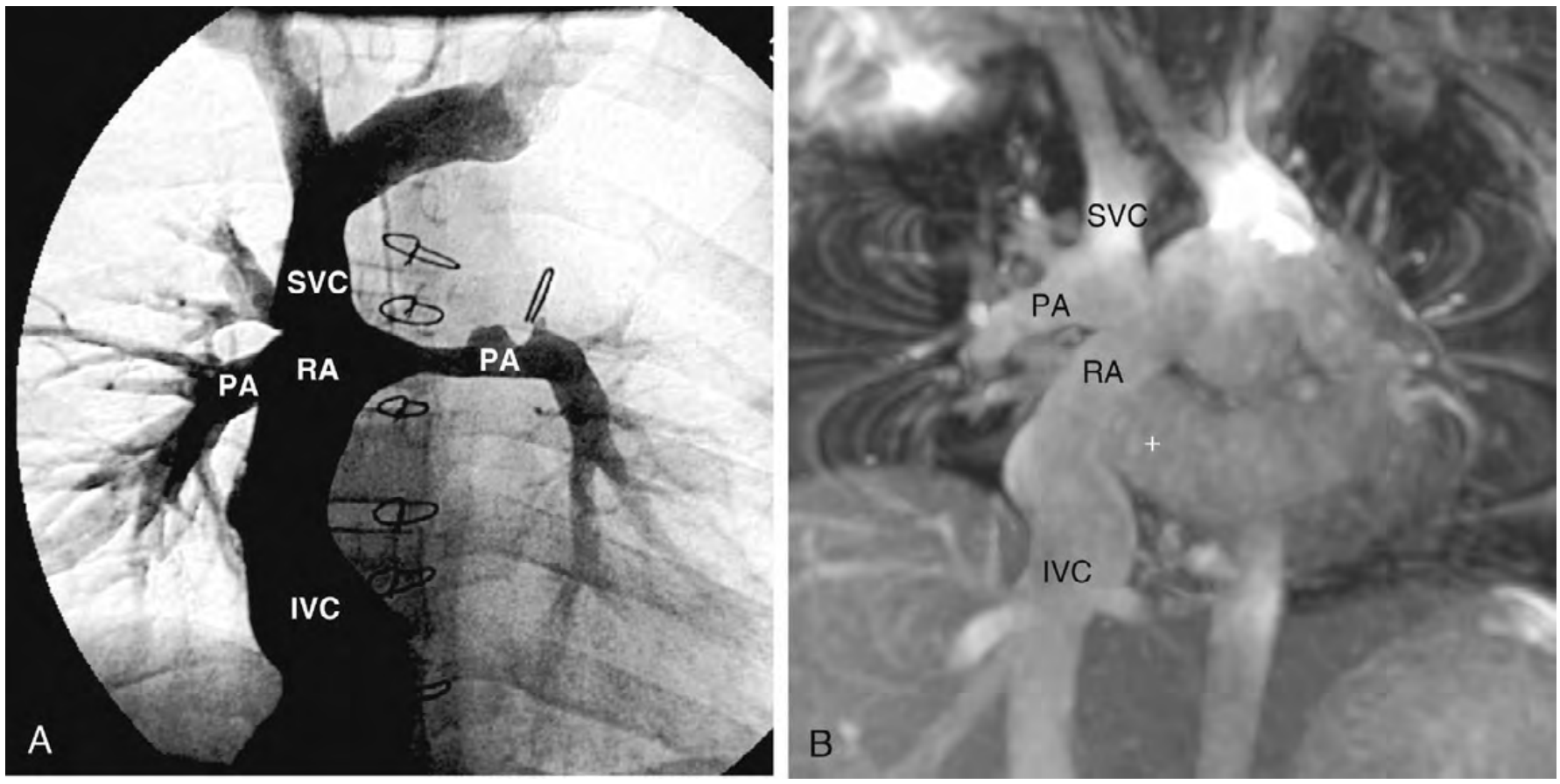
To understand the imaging appearances on chest radiography and cross-sectional studies of patients who have undergone surgery or interventional procedures for congenital heart disease, basic knowledge of the types of procedures performed is required. Table 4-4 lists the names, indications, and flow alterations of commonly performed cardiac procedures. The imaging findings related to a number of procedures are also illustrated: balloon angioplasty of coarctation of the aorta (see Fig. 4-29), intraatrial baffle (see Fig. 4-33), arterial switch procedure (see Fig. 4-34), Amplatzer occlusion devices (Fig. 4-35, *A*-*C*), Glenn shunt (see Fig. 4-1), and Fontan procedure (Fig. 4-36, *A* and *B*).

Acquired Heart Disease

In addition to congenital heart disease, there are multiple types of acquired heart disease that can occur during childhood. Many of these, such as cardiomyopathy and rheumatic heart disease, have features in common with those found in adult disease. One of the unusual types of acquired heart disease that can occur in children is Kawasaki disease.



▪ **FIGURE 4-35** **Amplatzer occlusion devices.**
Frontal (**A**) and lateral (**B**) chest radiographs show Amplatzer septal occluder device *(arrows)* in the location of an ASD. Note the two disk-shaped portions, each one resting on one or the other side of the defect, holding the device in place and blocking flow. **C**, Frontal chest radiograph shows an Amplatzer duct occluder device *(arrow)* closing a PDA.



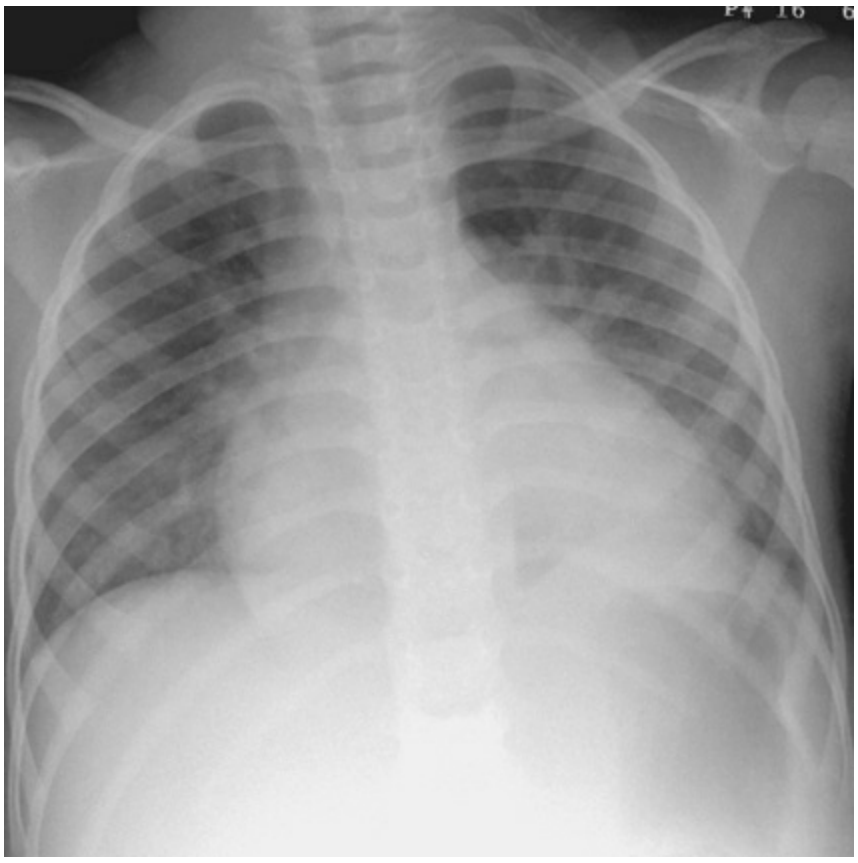
▪ **FIGURE 4-36 Fontan procedure.**
Venogram (**A**) and coronal (**B**) MIP bSSFP MRI show anatomy of the Fontan procedure. The SVC and IVC are connected directly to the pulmonary arteries *(PA)* via the right atrium *(RA)*.

Kawasaki Disease

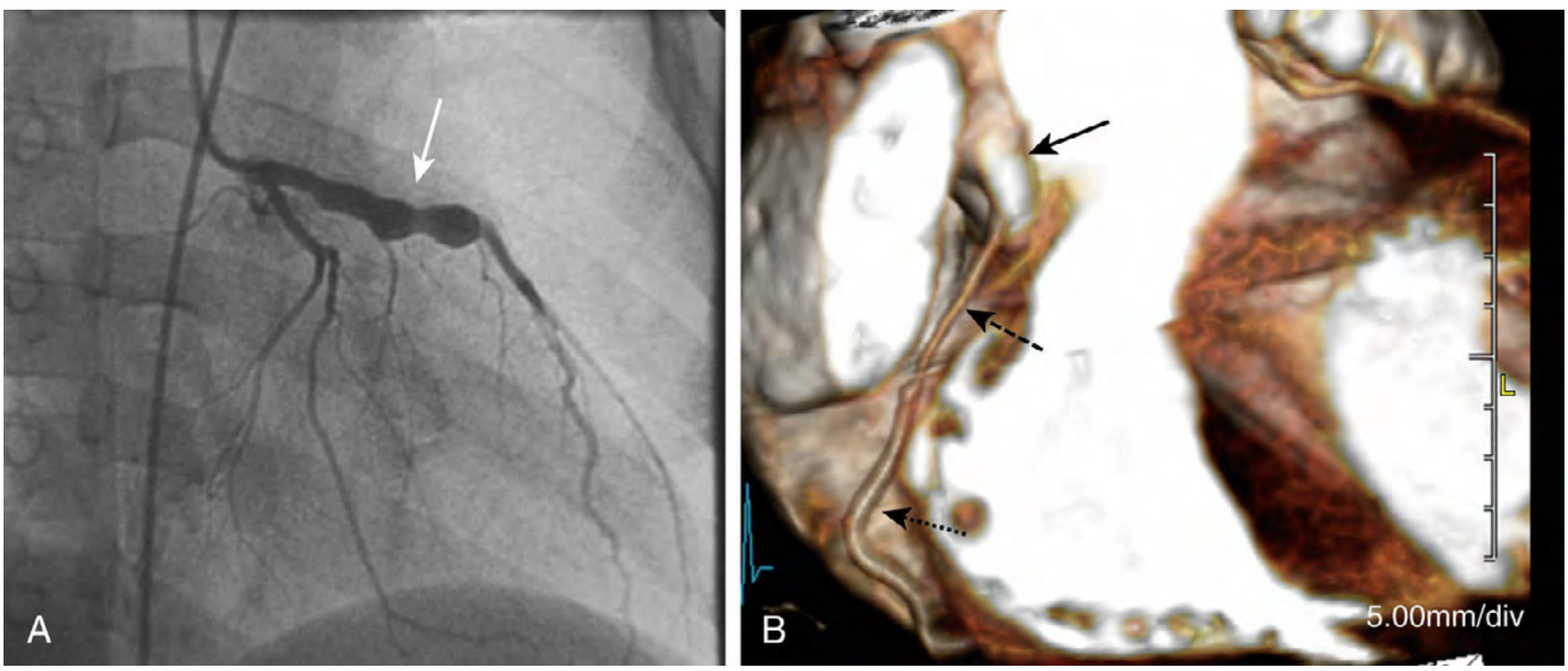
Kawasaki disease (mucocutaneous lymph node syndrome) is an inflammatory disease of unknown cause. Characteristic findings include fever, rash, conjunctivitis, erythema of the lips and oral cavity, and cervical lymphadenopathy. There is an associated generalized vasculitis. Cardiac involvement includes an acute myocarditis, which can lead to congestive heart failure (Fig. 4-37). Delayed cardiac complications include the development of coronary artery aneurysms (Fig. 4-38, *A* and *B*), as well as coronary artery stenoses. Chest radiographs can show findings of congestive heart failure when the myocarditis is severe. Rarely the coronary artery aneurysms can calcify. Gallbladder hydrops, as seen on ultrasound, has also been described as a finding. However, this is not included as one of the criteria in making the diagnosis, and ultrasound of the upper abdomen is rarely useful in diagnosing the disease. Treatment with gamma globulin can decrease the severity of the illness and can decrease the likelihood of delayed complications such as coronary aneurysms.

Cardiac Masses

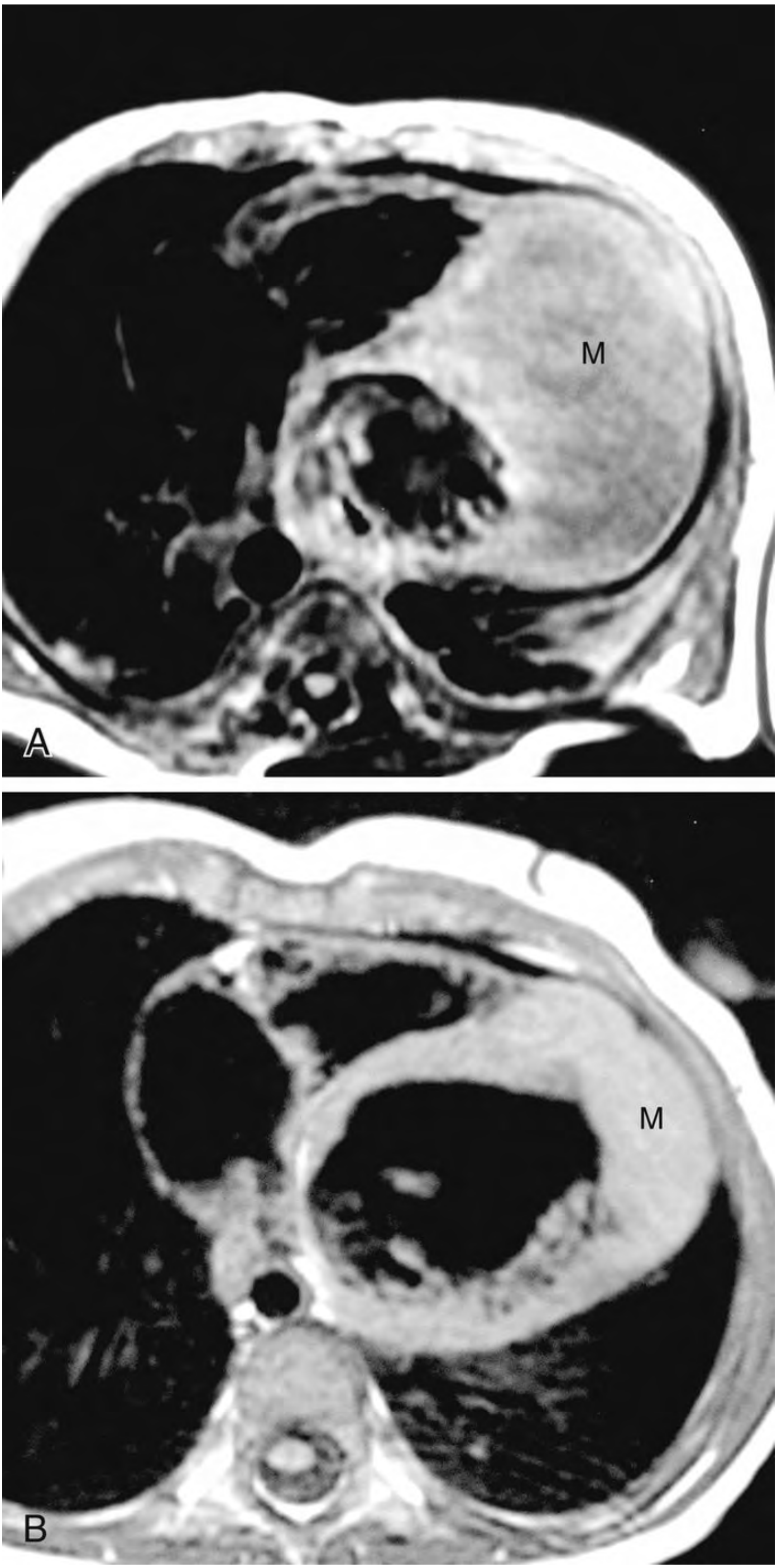
There are a number of causes of cardiac masses in children. The majority of pediatric cardiac masses are present during the newborn period. By far the most common type of congenital heart mass is rhabdomyoma (Fig. 4-39, *A* and *B*). This lesion is most commonly seen in patients with tuberous sclerosis. Rhabdomyomas typically involute over time and are usually treated conservatively (see Fig. 4-39). Other potential cardiac masses include angiosarcoma, fibroma (Fig. 4-40), teratoma, and hemangioma. The most common cause of cardiac tumor associated with pericardial effusion is a hemangioma. These cases are often initially diagnosed on in utero or postnatal sonography and then further characterized by MRI.



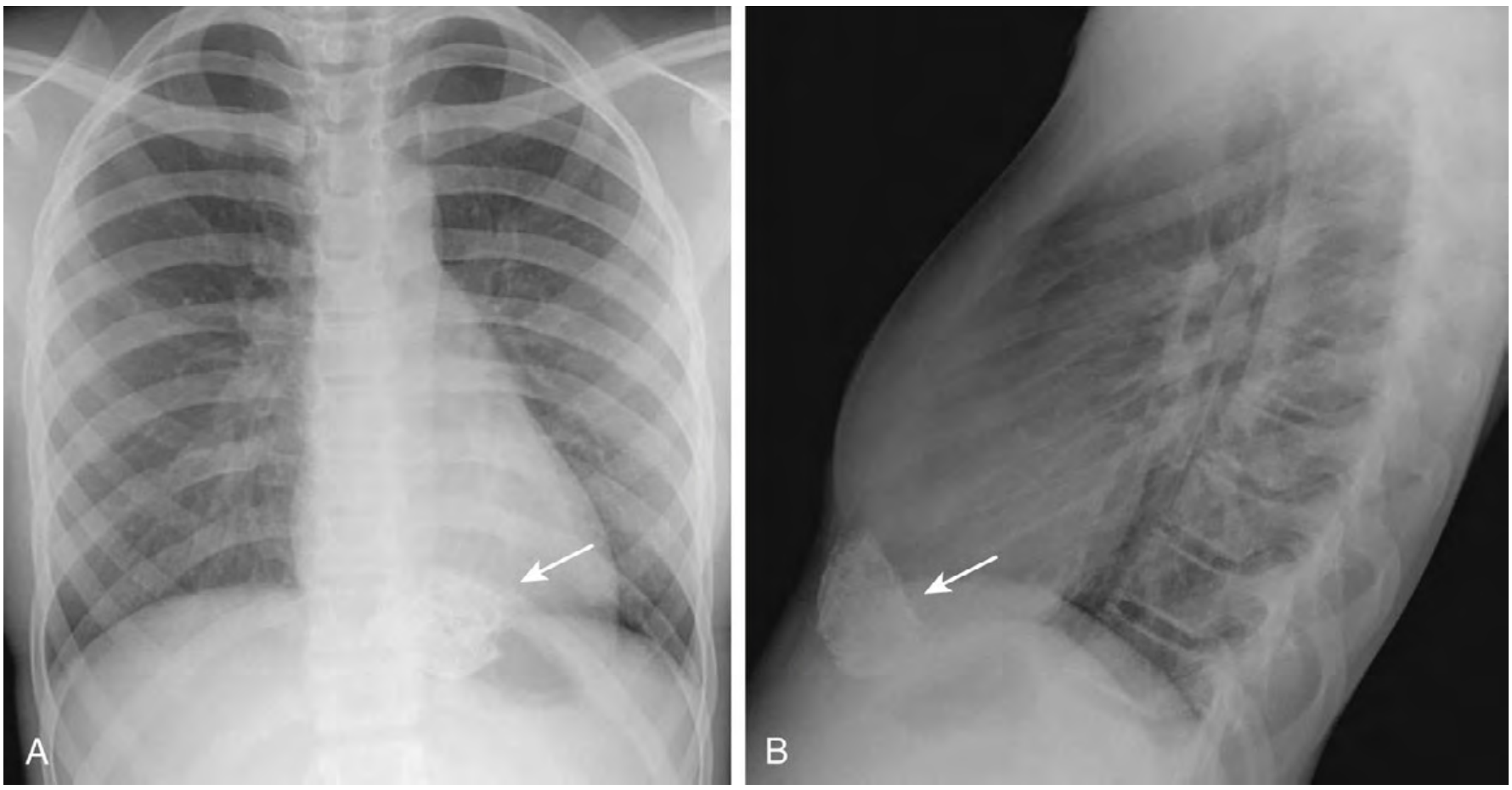
▪ FIGURE 4-37 **Kawasaki disease in a 4-year-old child resulting in acute myocarditis.**
Chest radiograph shows cardiomegaly and indistinct, prominent pulmonary vasculature consistent with venous congestion.



▪ FIGURE 4-38 **Kawasaki disease with coronary artery aneurysms.**
A, Left coronary arteriogram shows aneurysms proximally *(arrow)*. **B,** Three-dimensional reformation from a CT angiogram in a different patients shows an aneurysm of the proximal right coronary artery *(solid arrow)*, followed by a segment of stenotic artery *(dashed arrow)*, followed by normal-caliber artery *(dotted arrow)*.


M
A
M
B

▪ **FIGURE 4-39** **Rhabdomyoma in a girl with tuberous sclerosis.**
A, Axial T1-weighted image obtained at 2 days of life shows large mass *(M)* arising from the myocardium of the left and right ventricles, splaying the interventricular septum. **B,** Axial T1-weighted image obtained at 2 years of life shows interval decrease in size of mass *(M)*.



▪ **FIGURE 4-40** Frontal (**A**) and lateral (**B**) chest radiographs demonstrate a calcified fibroma within the anterior aspect of the heart *(arrows)*.

Suggested Readings

Applegate K.E, Goske M.J, Pierce G, Murphy D. Situs revisited: imaging of the heterotaxy syndrome. *Radiographics*. 1999;19:837–852.

Coussement A.M, Gooding C.A. Objective radiographic assessment of pulmonary vascularity in children. *Radiology*. 1973;109:649–654.

Donnelly L.F, Gelfand K.J, Schwartz D.C, et al. The wall to wall heart: differential diagnosis for massively large cardiothymic silhouette in newborns. *Appl Radiol*. 1997;26:23–28.

Donnelly L.F, Higgins C.B. MR imaging of conotruncal abnormalities. *AJR*. 1996;166:925–928.

Gaca A.M, Jaggers J.J, Dudley L.T, Bisset G.S. Repair of congenital heart disease: a primer Part 1. *Radiology*. 2008;247:617–631.

Gaca A.M, Jaggers J.J, Dudley L.T, Bisset G.S. Repair of congenital heart disease: a primer Part 2. *Radiology*. 2008;248:44–60.

Goo H.W. State-of-the-art CT imaging techniques for congenital heart disease. *Korean J Radiol*. 2010;11:4–18.

Kellenberger C.F, Yoo S.J, Valsangiacomo Büchel E.R. Cardiovascular MR imaging in neonates and infants with congenital heart disease. *Radiographics*. 2007;27:5–18.

Leschka S, Oechslin E, Husman L, et al. Pre- and postoperative evaluation of congenital heart disease in children and adults with 64-section CT. *Radiographics*. 2007;27:829–846.

Ntisnjana H.N, Hughes M.L, Taylor A.M. The role of cardiovascular magnetic resonance in pediatric congenital heart disease. *J Cardiovasc Magn Reson*. 2011;13:51.

Schallert E.K, Danton G.H, Kardon R, Young D.A. Describing congenital heart disease by using three-part segmental notation. *Radiographics*. 2013;33:E33–E46.

Siripornpitak S, Pornkul R, Khowsathit P, et al. Cardiac CT angiography in children with congenital heart disease. *Eur J Radiol*. 2013;82:1067–1082.

Strife J.S, Sze R.W. Radiographic evaluation of the neonate with congenital heart disease. *Radiol Clin North Am*. 1999;37:1093–1107.

Swischuk L.E, Stansberry S.D. Pulmonary vascularity in pediatric heart disease. *J Thorac Imaging*. 1989;4:1–6.

van der Hulst A.E, Roest A.A, Westenberg J.J, et al. Cardiac MRI in postoperative congenital heart disease patients. *J Magn Reson Imaging*. 2012;36:511–528.

Winer-Muram H.T, Tonkin I.L. The spectrum of heterotaxic syndromes. *Radiol Clin North Am*. 1989;27(6):1147–1170.

CHAPTER 5

Gastrointestinal

Lane F. Donnelly

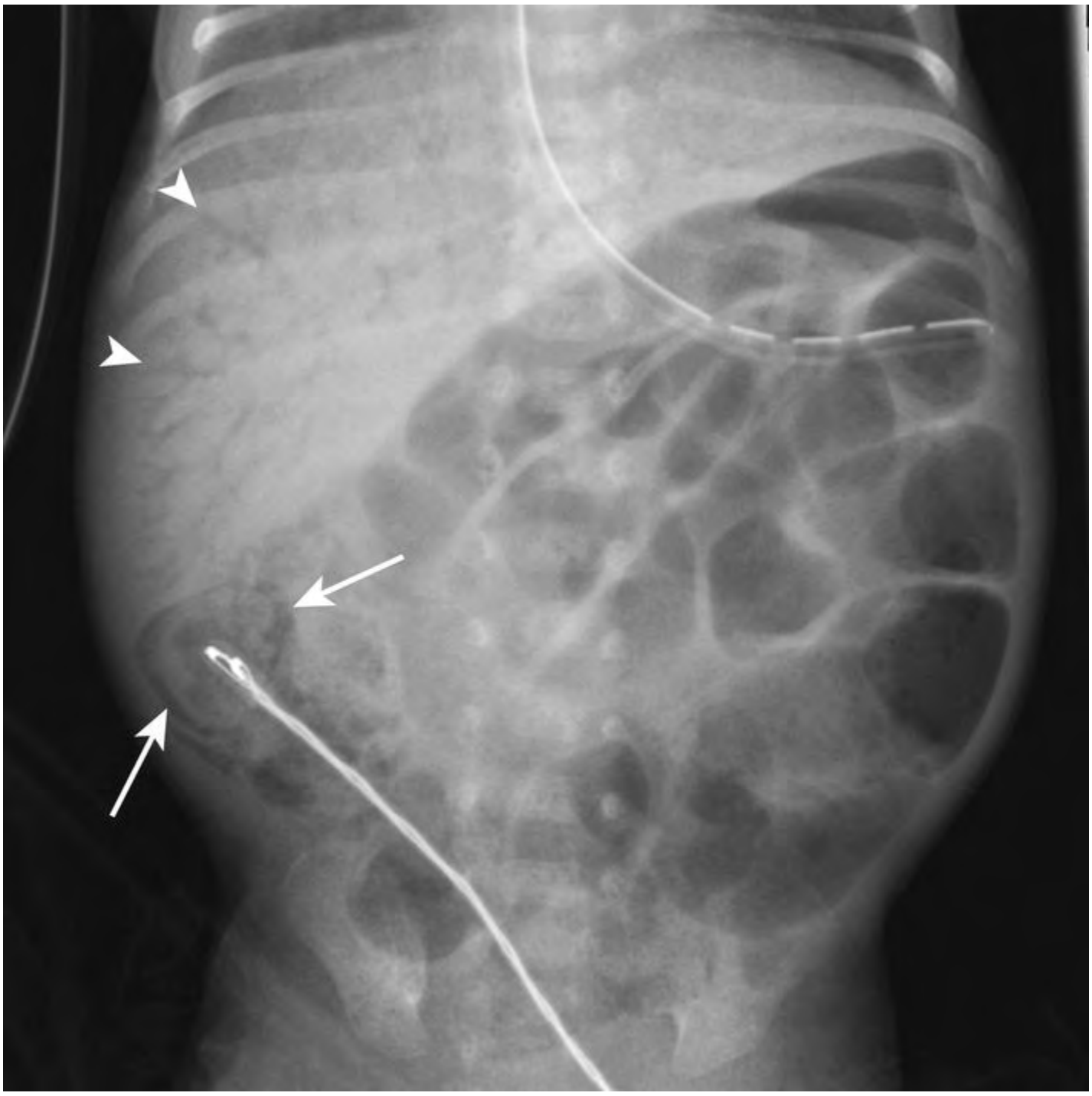
▪ Neonatal

Necrotizing Enterocolitis

Necrotizing enterocolitis (NEC) is a disease primarily of premature infants in the intensive care unit. It most often occurs 1 to 3 weeks after birth in infants weighing less than 1000 g but can also less commonly occur in older, nonpremature infants under extreme stress, such as after cardiac surgery. The overall mortality rate is 20% to 30%. NEC is an idiopathic enterocolitis that is most likely related to some combination of infection and ischemia. Symptoms include abdominal distention, feeding intolerance, increased aspirates from nasogastric tube, and sepsis. It is interesting to note that the only parameter associated with decreased incidence of NEC is the use of maternal breast milk. When NEC is suspected, infants are placed in the status of nil per os (NPO), treated with antibiotics, and monitored by serial abdominal radiographs (anteroposterior supine and a free air view [cross-table lateral or left lateral decubitus]).

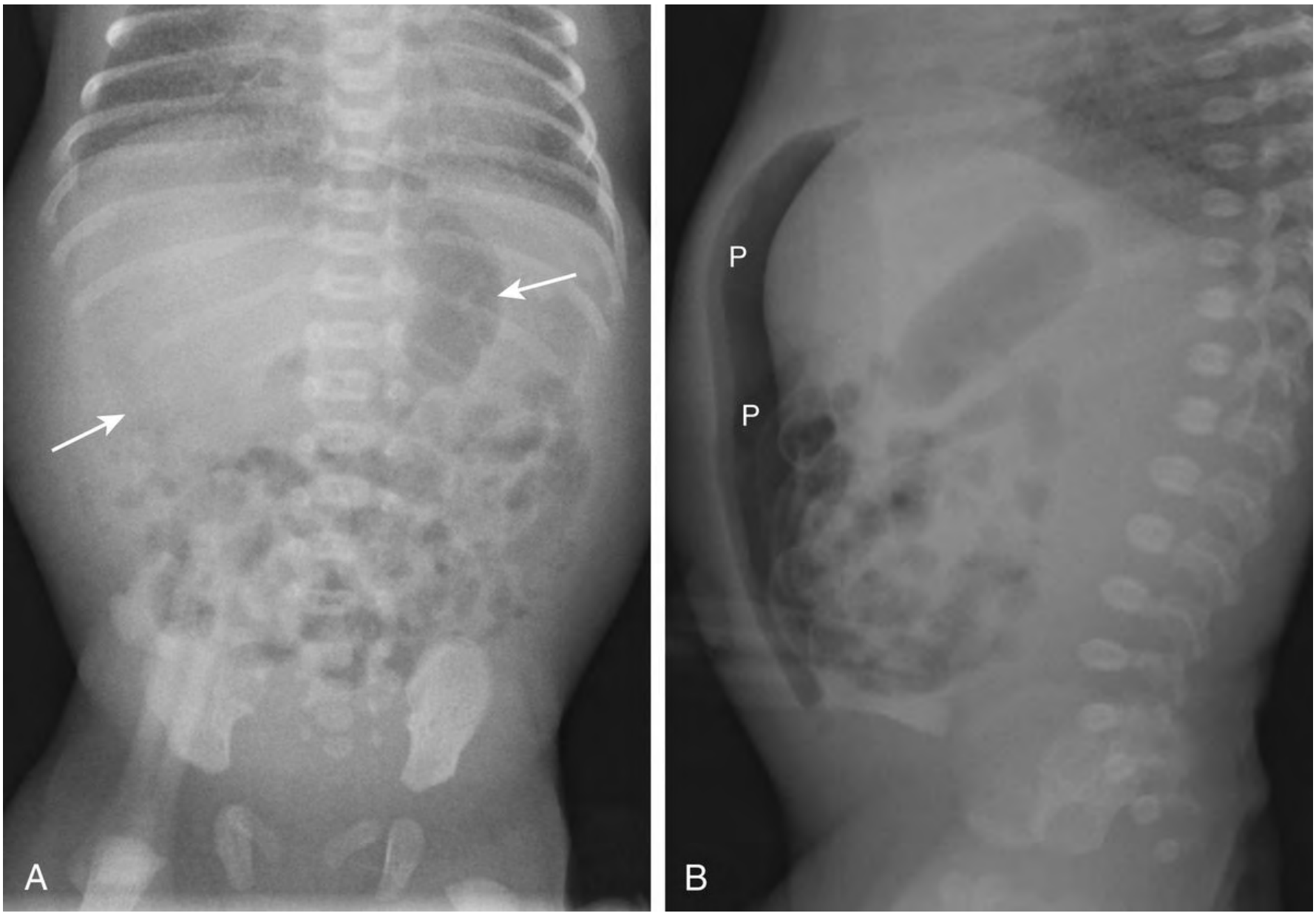
NEC most commonly affects the ileum and right colon. Radiographic findings range from normal to suggestive to diagnostic. Suggestive findings include focal dilatation of bowel (especially within the right lower quadrant) or featureless, unfolded-appearing small bowel loops with separation of the loops, suggesting bowel wall thickening. An unchanging bowel gas pattern over serial films is worrisome. The most definitive finding of NEC is the presence of pneumatosis (gas in the bowel wall) (Fig. 5-1). Pneumatosis appears as multiple bubblelike or curvilinear lucencies overlying the bowel. Its appearance can be similar to that of stool. However, stool is uncommon in sick premature neonates in the intensive care unit. Portal venous gas can also occur (see Fig. 5-1). This appears as branching linear lucencies overlying the liver. Free intraperitoneal air is the only radiographic finding seen in NEC that is considered an absolute indication for surgery. Free air may be seen as triangles of anterior lucency on cross-table laterally positioned radiographs (Fig. 5-2); as overall increased lucency on supine-positioned radiographs (see Fig. 5-2); in visualization of both sides of the bowel wall (Rigler sign); or as outlining the intraperitoneal structures, such as the falciform ligament (football sign). In the absence of free air, the decision to perform surgery is made by using a combination of clinical and radiographic findings.

Ultrasound has also been advocated as a means of monitoring infant for NEC (Figs. 5-3 through 5-6) and is used primarily instead of radiography to monitor NEC in some places. In cases of NEC in which the abdomen is distended but relatively gasless, ultrasound is particularly helpful. The identification of thickened bowel loops with increased or absent abnormal degrees of color Doppler flow is suggestive of inflamed (increased flow) or infarcted (decreased flow) bowel. A large amount of free fluid is also a poor prognostic finding. Ultrasound depicts pneumatosis as areas of hyperechoic foci in the bowel wall (see Figs. 5-3 and 5-4). In contrast to intraluminal gas, gas related to pneumatosis does not change position with changes in position of the patient. Portal venous gas is also easily depicted by ultrasound as hyperechogenic foci moving within the portal vein (see Fig. 5-5). Free air can also be depicted by ultrasound as areas of hyperechogenicity.



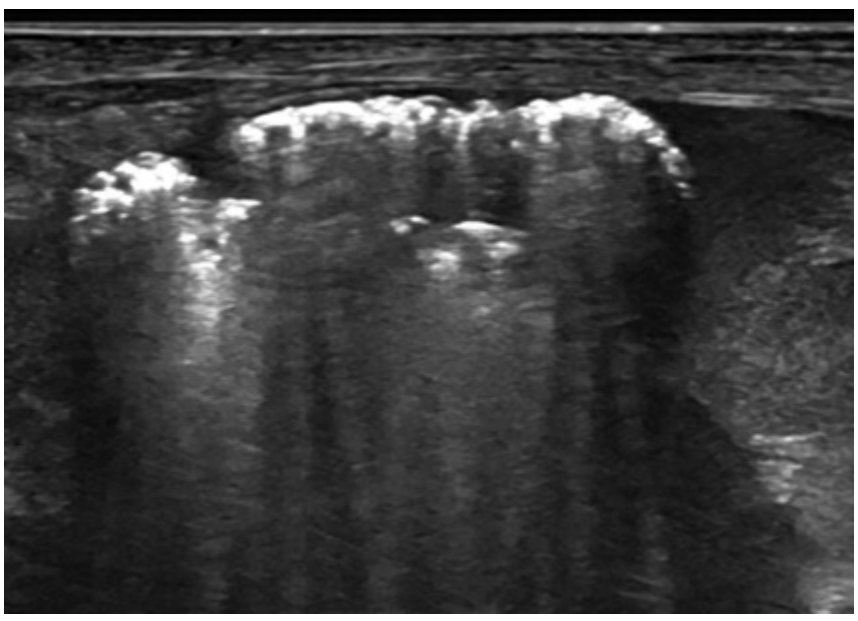
▪ **FIGURE 5-1** **NEC in a premature infant.**
Radiography shows multiple dilatated bowel loops with multiple areas of linear lucency *(arrows)* along the bowel wall, consistent with pneumatosis. In addition, note portal venous gas *(arrowheads)* as branching, tubular lucencies overlying the liver.

A delayed complication seen in survivors of NEC is bowel stricture (Fig. 5-7). These strictures most commonly involve the left colon.



▪ **FIGURE 5-2** **NEC in a newborn premature infant.**

A, Frontal supine radiograph shows increased lucency over right upper quadrant *(arrows)*, indicative of free air. **B,** Cross-table lateral radiograph shows pneumoperitoneum *(P)* adjacent to liver. Note how much more definitive the free air appears on the cross-table lateral as compared with the frontal supine view.



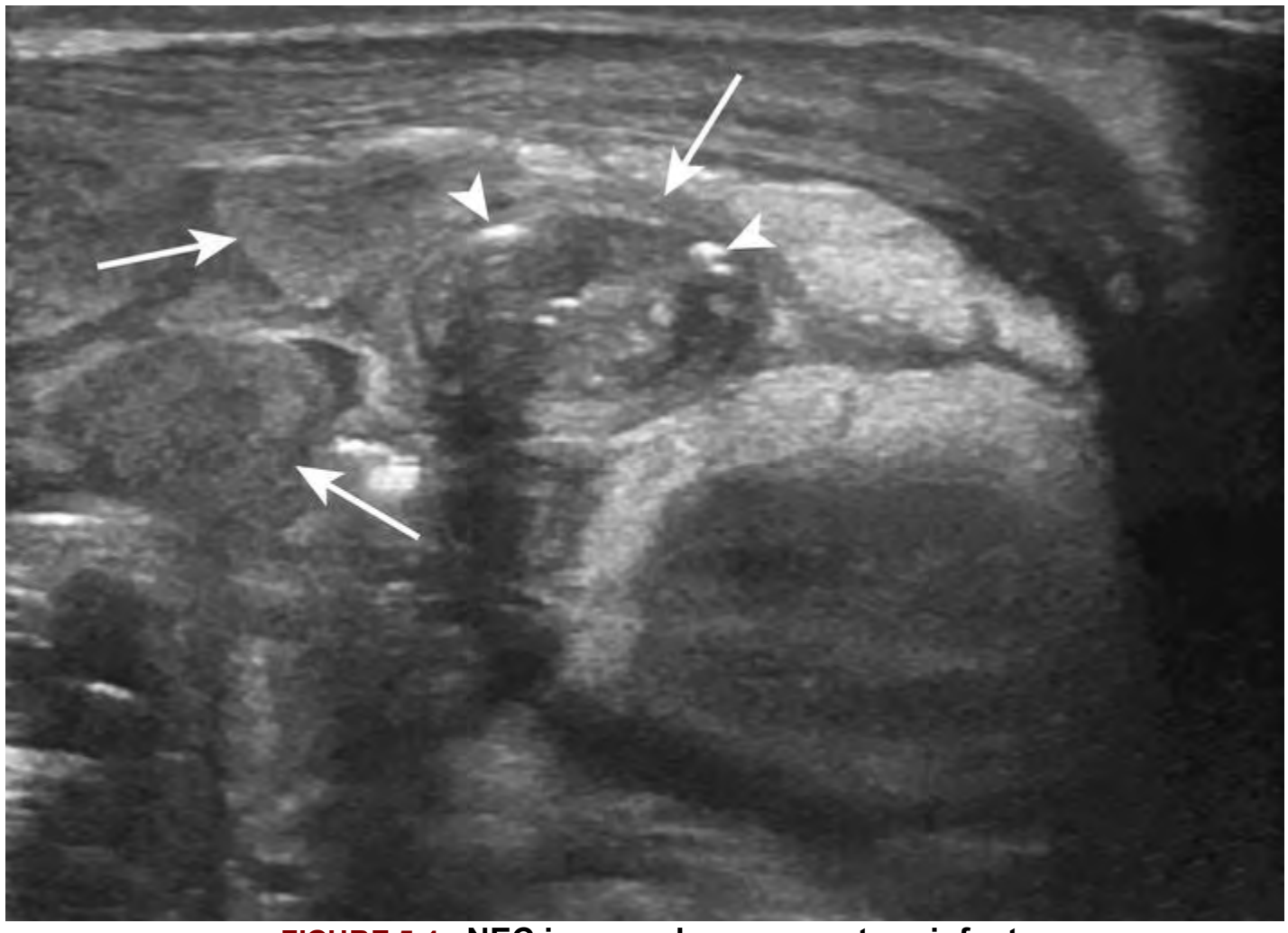
▪ **FIGURE 5-3** **NEC in a newborn premature infant.**

Ultrasound shows multiple shadowing echogenic foci representing pneumatosis (bubbles of gas in bowel wall).

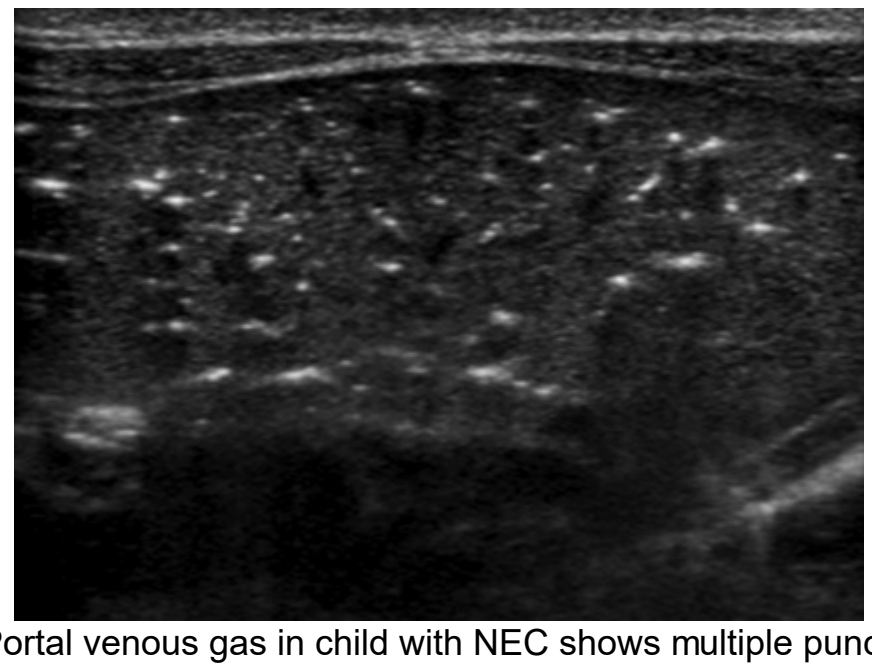
High Intestinal Obstruction in Neonates

Neonates with suspected intestinal obstruction can be divided into those with upper gastrointestinal obstruction and those with lower intestinal obstruction on the basis of clinical symptoms and radiographic findings. Infants with high intestinal obstruction present predominantly with vomiting. Radiographs may show distension involving the stomach, duodenum, jejunum, or all three, depending on the level of the obstruction. The number of distended small bowel loops is much fewer than that

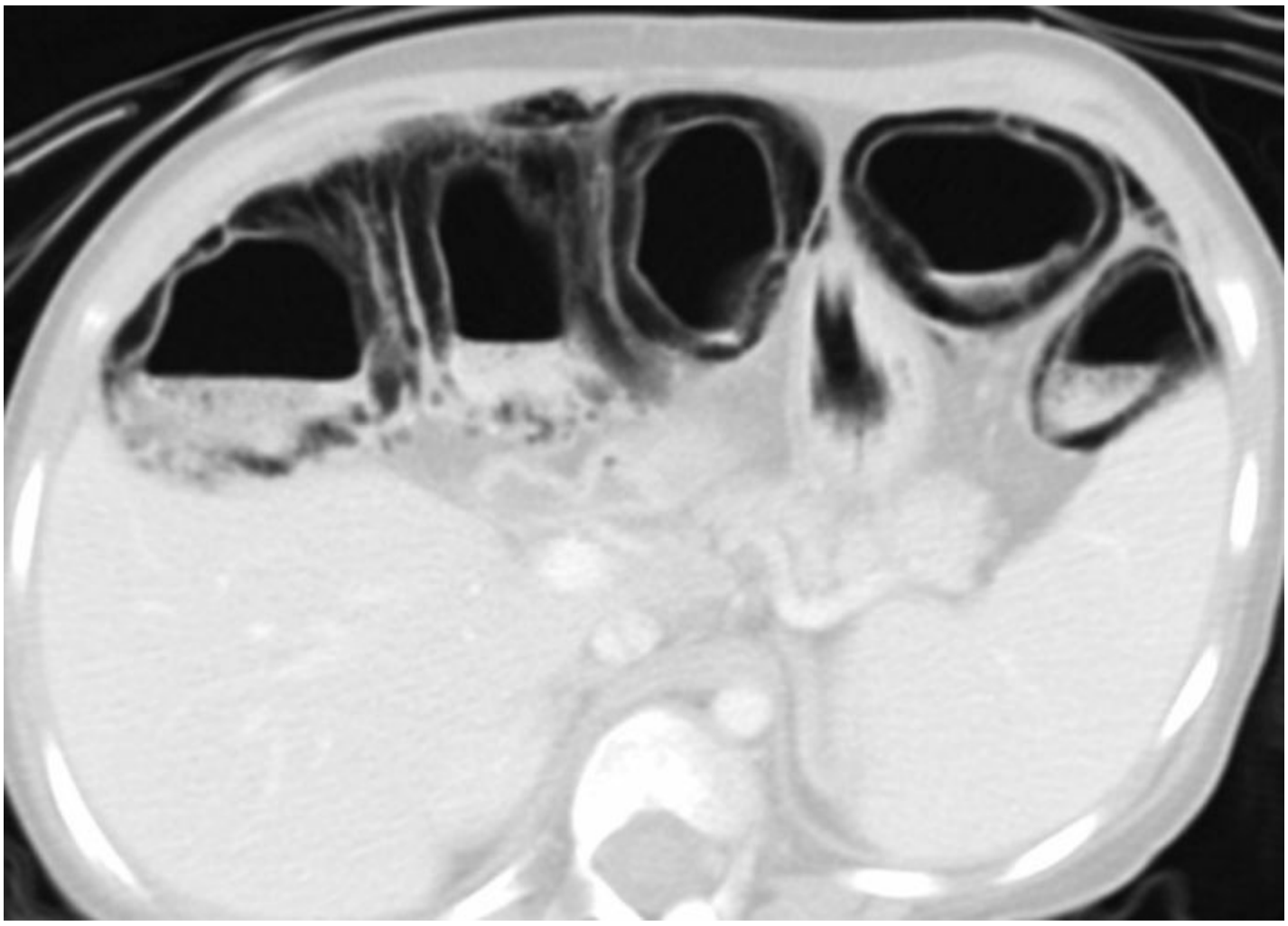
seen with distal bowel obstruction. The most common causes of upper gastrointestinal tract obstruction in neonates include duodenal atresia or stenosis, duodenal web, annular pancreas, midgut volvulus or obstruction by Ladd bands, and jejunal atresia (Table 5-1).



▪ **FIGURE 5-4** **NEC in a newborn premature infant.**
Ultrasound shows multiple loops of bowel with bowel wall thickening *(arrows)*. Note shadowing echogenic foci representing pneumatosis *(arrowheads)* in one area of bowel wall thickening.



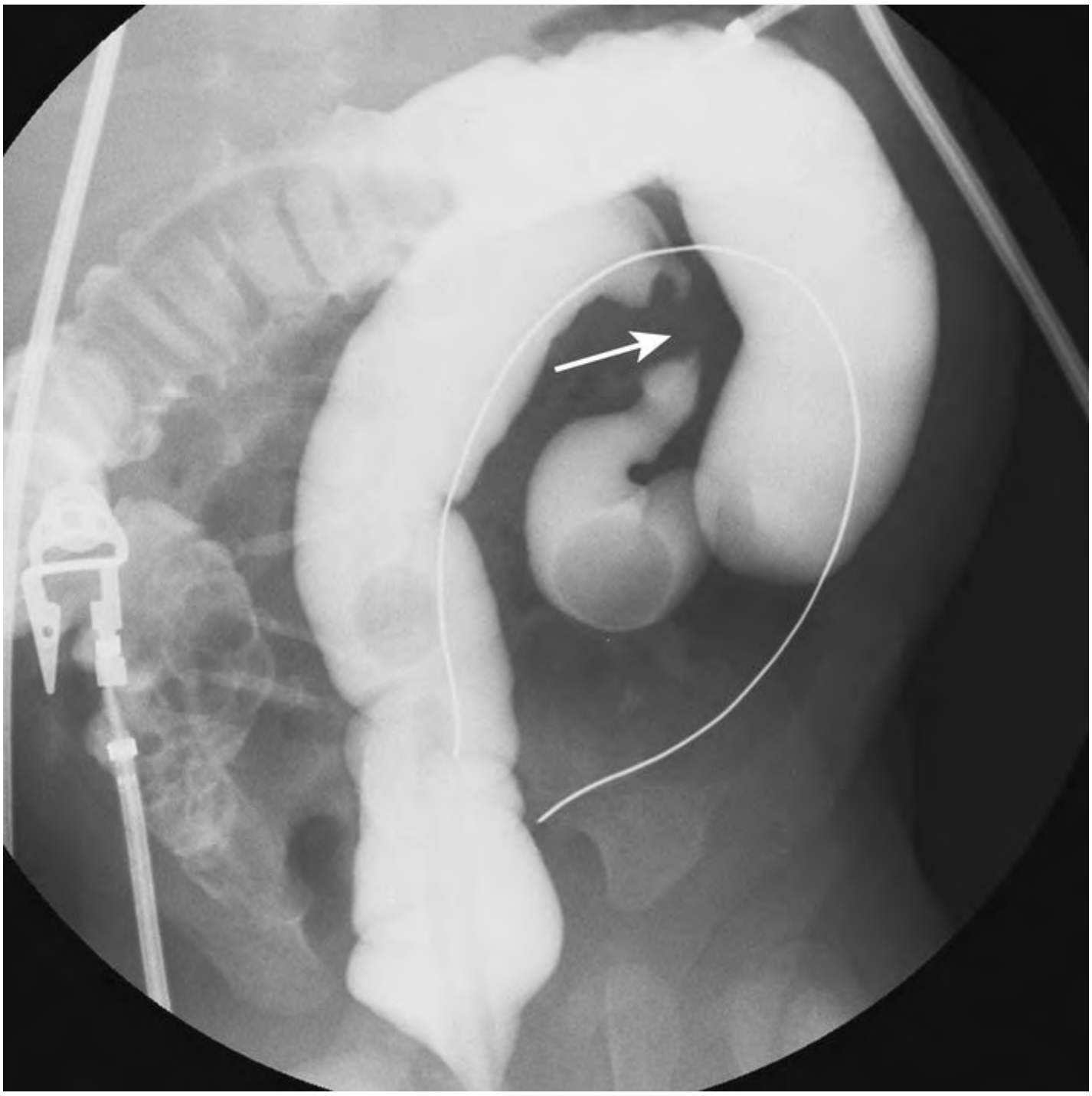
▪ **FIGURE 5-5** Portal venous gas in child with NEC shows multiple punctate shadowing echogenicities within the portal venous structures of the liver. Note that these findings are often shown to be dynamic and transient at real time ultrasound.



▪ **FIGURE 5-6** Pneumatosis shown on CT in older child, for illustration purposes. Axial image shows curvilinear areas of gas in the bowel wall completely encircling the fluid-gas filled bowel lumen of the transverse colon.

Duodenal Atresia, Stenosis, Web, and Annular Pancreas

Duodenal atresia, stenosis, web, and annular pancreas are all part of a spectrum of similar abnormalities. All cause either complete or partial duodenal obstruction and usually present at birth or within the first few days of life. Often, components of more than one diagnosis are present. For example, many cases of duodenal atresia have a component of annular pancreas, and annular pancreas almost never occurs without a component of intrinsic duodenal stenosis.



▪ **FIGURE 5-7** **Colonic stricture resulting from previous NEC.**
Contrast enema shows persistent narrowing of the sigmoid colon *(arrow)* due to stricture.

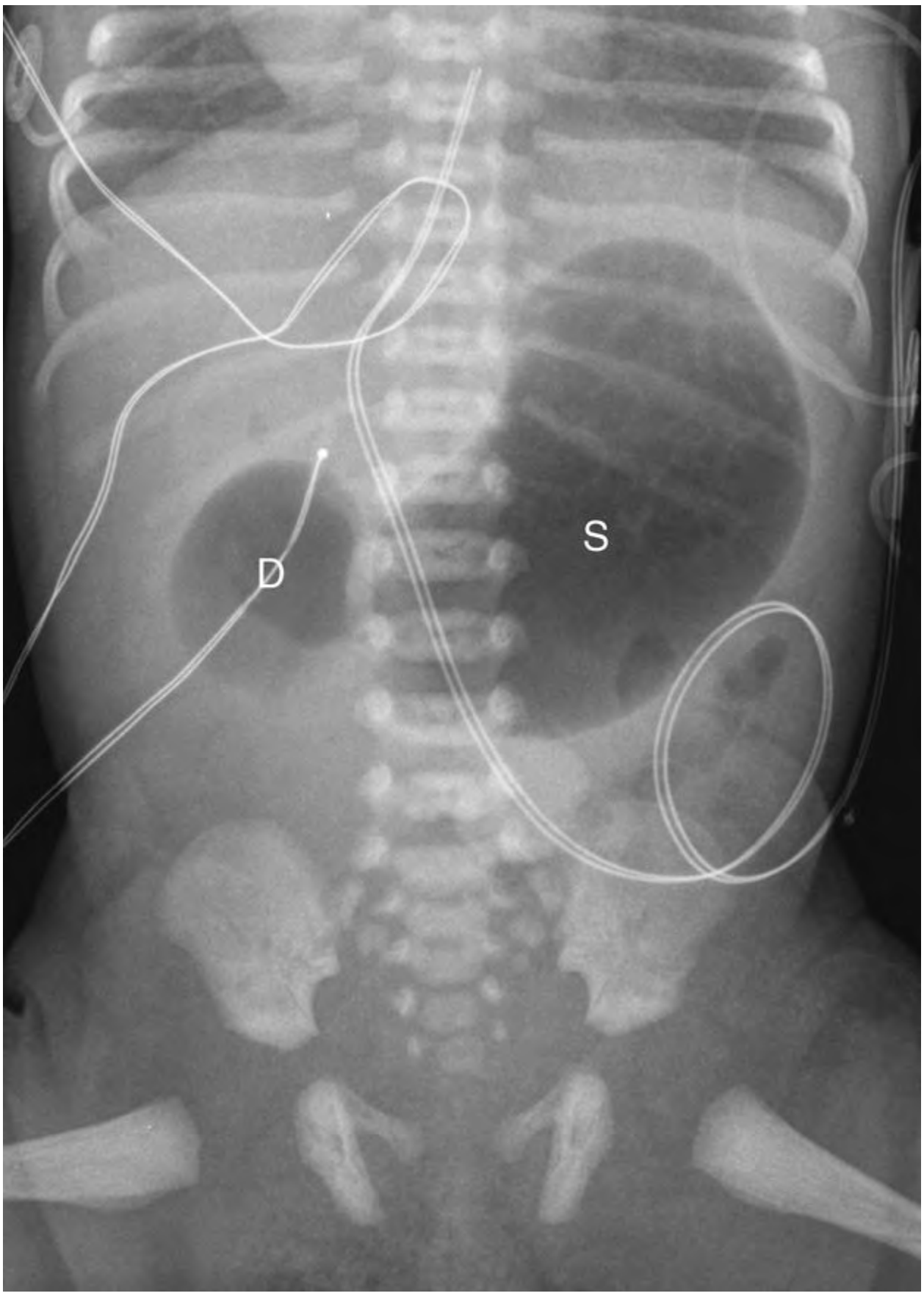
TABLE 5-1
Common Causes of Intestinal Obstruction in Neonates

High
- Midgut volvulus and malrotation
- Duodenal atresia and stenosis
- Duodenal web
- Annular pancreas
- Jejunal atresia

Low
- Hirschsprung disease
- Meconium plug syndrome (small left colon syndrome)
- Ileal atresia
- Meconium ileus
- Anal atresia and anorectal malformations

The duodenum is the most common site of intestinal atresia. Duodenal atresia and stenosis almost always occur in the region of the ampulla of Vater. Approximately 30% of cases of duodenal atresia are associated with Down syndrome. Other associations with duodenal atresia include other intestinal atresias, biliary abnormalities, congenital heart disease, and associations with the complex known as

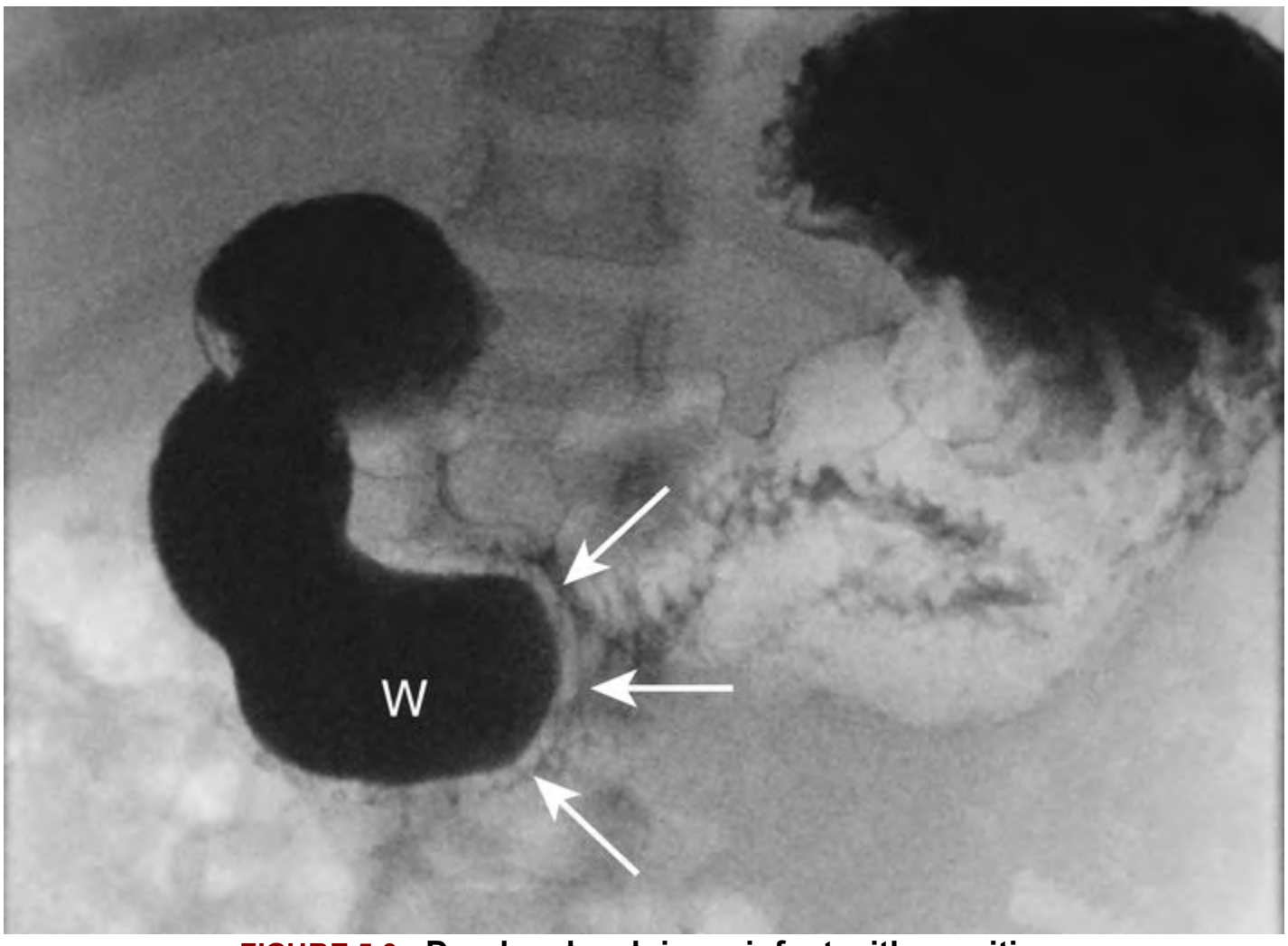
VATER (vertebral defects, imperforate anus, tracheoesophageal fistula, and radial and renal dysplasia). Radiographs of neonates with duodenal atresia typically demonstrate a dilatated stomach and dilatated proximal duodenum with no gas distal to the proximal duodenum. The two dilatated structures are referred to as a "double bubble" sign (Fig. 5-8). In the appropriate clinical setting, a double bubble is diagnostic of duodenal atresia, and additional imaging by an upper gastrointestinal series (UGI) is unnecessary. The question that often arises is how does one know that this is not an acute obstruction caused by a midgut volvulus, which is a surgical emergency? The answer is that dilatation of the duodenal bulb is seen only with chronic causes of obstruction. There is not enough time for the bulb to become dilated in acute obstruction, such as with an acute midgut volvulus. If it is not clear, a UGI can be performed to document the cause of obstruction. With duodenal stenosis, the double bubble is seen in association with the presence of distal bowel gas.



▪ **FIGURE 5-8** **Duodenal atresia in a newborn infant.**
Radiograph shows air-filled, dilated stomach *(S)* and dilated duodenal bulb *(D)*, giving the appearance of a double bubble. There is no distal bowel gas.

Duodenal web is another cause of congenital duodenal obstruction. Typically a web consists of an obstructing membrane; a pin-sized hole in its center is the only lumen. The web may stretch downstream, forming a windsock configuration seen on a UGI (Fig. 5-9). Because the obstruction is not complete, these patients may present later in life than those with atresia. The presence or absence of a

component of annular pancreas is not something that can be determined on a UGI in the setting of congenital duodenal obstruction.



▪ **FIGURE 5-9** **Duodenal web in an infant with vomiting.**
Frontal view from a UGI shows obstruction of the duodenum with a rounded, windsocklike appearance *(W)*. Note the membrane *(arrows)* obstructing the windsock. The obstruction is not complete, as some contrast passes into more distal collapsed bowel.

Malrotation and Midgut Volvulus

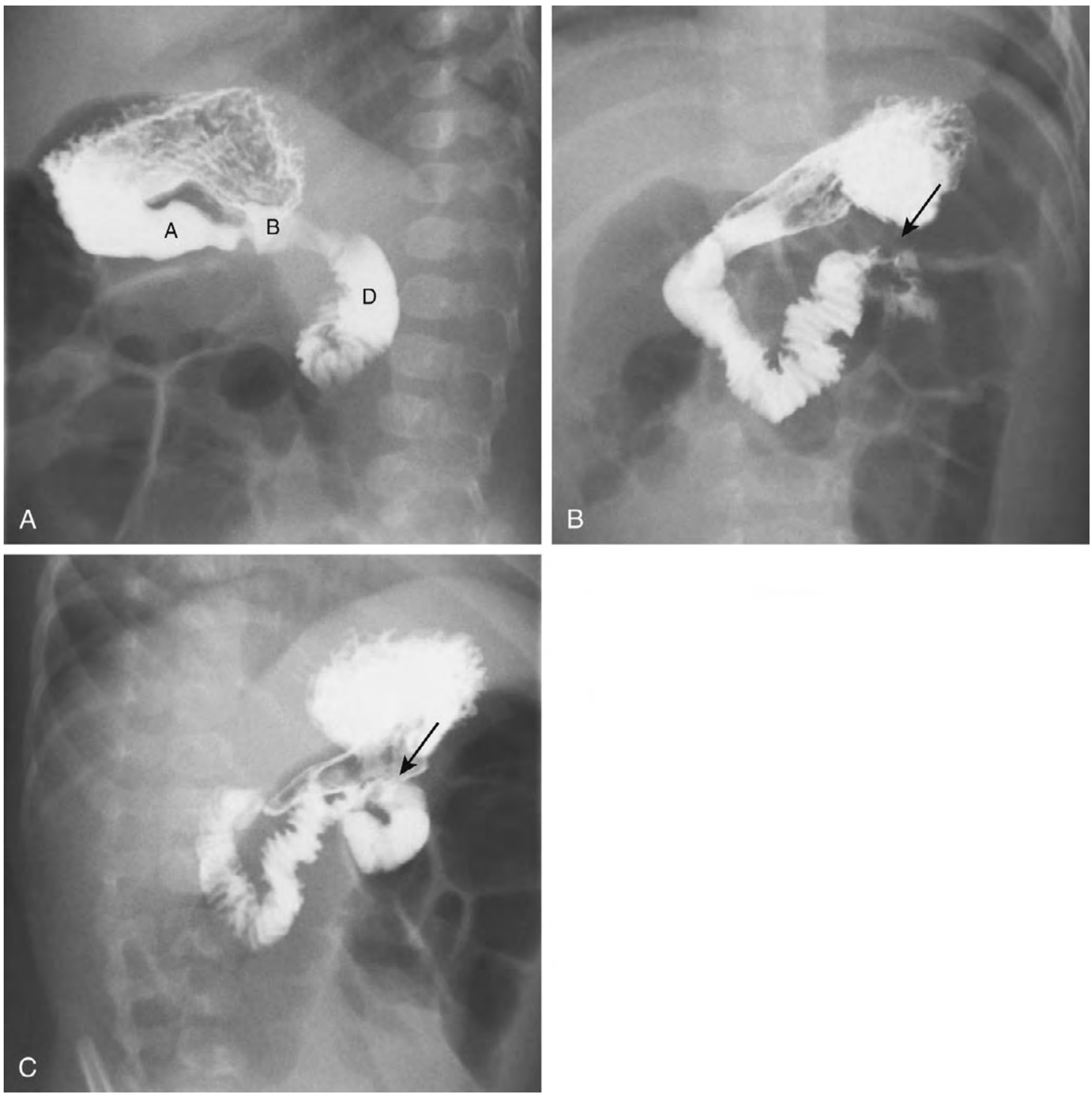
Midgut volvulus is one of the few true emergencies in pediatric gastrointestinal imaging. A delay in the diagnosis of midgut volvulus can result in ischemic necrosis of large portions of the bowel and possibly death. An understanding of midgut embryogenesis is often emphasized, but an understanding of the end result is more important. With normal embryonic rotation, both the duodenojejunal and ileocolic portions of the bowel rotate 270 degrees about the axis of the superior mesenteric artery (SMA). The result is that the duodenojejunal junction (DJJ) is positioned in the left upper quadrant and the cecum is positioned in the right lower quadrant. This results in a long, fixed base that keeps the small bowel mesentery from twisting. If the duodenojejunal and ileocecal junctions are not in their normal positions, the base of the small bowel mesentery may be short and predispose the small bowel to twisting, resulting in a midgut volvulus.

For clarification, note the following definitions:

- *Malrotation:* Embryologic abnormality of rotation that results in abnormal fixation of the small bowel mesentery that results in a short mesenteric base.
- *Midgut volvulus:* Abnormal twisting of the small bowel around the axis of the SMA. Volvulus can result in bowel obstruction, ischemia, or infarction but is not defined by the presence or absence of obstruction or ischemia.
- *Ligament of Treitz:* Also referred to as the DJJ. This is the anatomic location where the duodenum passes through the transverse mesocolon and becomes jejunum. It is also where the bowel changes from retroperitoneal (duodenal) to intraperitoneal (jejunum). This anatomic location is not visualized but is inferred on imaging.
- *Ladd bands:* Abnormal fibrous peritoneal bands that can occur in patients with malrotation; they are potential causes of duodenal obstruction, in addition to volvulus.

The diagnosis of malrotation has traditionally been made on a UGI by determining that the DJJ is abnormally positioned. The DJJ, the point at which the proximal bowel turns inferiorly on a frontal view, is considered normal when it meets the following two criteria—(1) *right to left*: it is to the left of

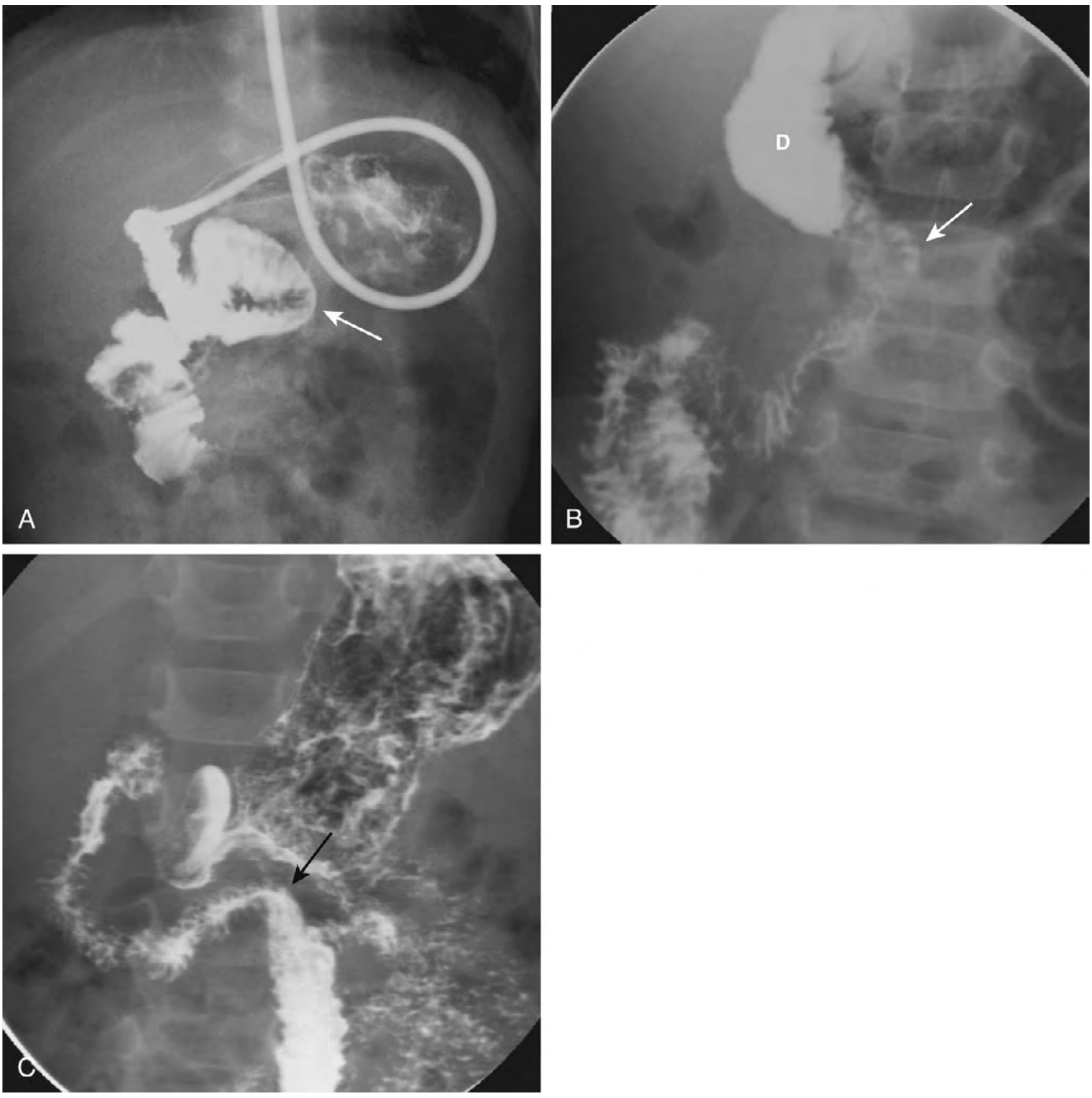
the spine and (2) *superior to inferior*: it is at the same level as or superior to the duodenal bulb. In addition, on the lateral view, the duodenum normally moves posteriorly and then inferiorly before moving back anteriorly. The "inferior" moving position on the lateral view is the retroperitoneal portion. If on the lateral view the duodenum moves posteriorly and then back anteriorly without the portion moving from superior to inferior (the retroperitoneal part), it is suspicious for malrotation. It is important to evaluate the position of the DJJ during the first pass of contrast through the duodenum and jejunum (see subsequent material; Figs. 5-10 and 5-11).



▪ **FIGURE 5-10** **Normal position of the DJJ (ligament of Treitz) on standard views from a UGI.** **A,** Lateral view shows antrum *(A)*, duodenal bulb *(B)*, and duodenal sweep *(D)*. Note that the duodenum normally extends posteriorly and inferiorly during the retroperitoneal course. **B,** Frontal view obtained during first pass shows the DJJ *(arrow)* identified by the point in the bowel that angles inferiorly. The DJJ is normally to the left of the spine and at the same level (superiorly to inferiorly) as the level of the duodenal bulb. **C,** Oblique view of patient with left side down again shows the level of the DDJ *(arrow)* at the level of duodenal bulb and proximal jejunum in left upper quadrant.

In many cases of malrotation the findings are grossly obvious; the duodenum courses rightward, rather than leftward and never crosses the spine (Fig. 5-12 and see Fig. 5-11). However, when performing UGIs in children, there are many cases that do not quite meet the criteria for normal but are very close. It is probably inappropriate to send all of these cases to the operating room. As one becomes more experienced in imaging, some things become more and more clear. Others become less clear, and one realizes that many of the rules one was taught should really be thought of more as guidelines. Although germane to the fabric of pediatric radiology, the diagnosis and exclusion of malrotation are not straightforward or easy. In cases with borderline-positioned DJJs (not quite as high as the bulb, not quite to the left of the spine), most pediatric radiologists follow the contrast through the small bowel (see Fig. 5-11). If the jejunum is in the left upper quadrant and the ileum and cecum are in the right lower quadrant, the patient is probably not at risk for midgut volvulus. Furthermore,

the DJJ is a mobile structure in children and can “factitiously” be moved into an abnormal position by a space-occupying lesion, such as a mass or distended bowel loops. In addition, the presence of a nasojejunal tube may alter the apparent position of the DJJ.



▪ **FIGURE 5-11** **Abnormal position of the DJJ.**
A, Marked abnormal position of the DJJ. UGI performed via nasogastric tube shows the DJJ *(arrow)* to be lower than the duodenal bulb and not to the left of the spine. Proximal jejunum is on right of spine. Findings are consistent with malrotation. **B,** Abnormal position of the DJJ associated with dilatation of the proximal duodenum. UGI shows that the DJJ *(arrow)* is not to the left of the spine and is lower than the duodenal bulb. The proximal jejunum is on right of spine. Findings are consistent with malrotation. Dilatation of the proximal duodenum *(D)* is suspicious for obstruction due to volvulus or Ladd bands. **C,** DJJ that does not quite meet normal criteria. The DJJ *(arrow)* is not quite to the left of the spine and not quite at same level as the bulb. In such cases, most radiologists will follow the contrast through the small bowel. If the cecum is in the right lower quadrant, the small bowel mesentery is most likely long enough not to be at risk for volvulus.



▪ **FIGURE 5-12 Malrotation.**
The duodenum courses rightward and never crosses the spine. The opacified proximal small bowel is in the right upper quadrant. The unopacified colon is in the left abdomen.

In patients who are malrotated, midgut volvulus may happen at any age; however, more than 90% are present during first 3 months of life. Midgut volvulus can be seen on a UGI as a corkscrew appearance of the duodenum and proximal jejunum or as duodenal obstruction (Fig. 5-13). The presence of bilious vomiting and findings of malrotation on a UGI, with or without findings of midgut volvulus, is considered a surgical emergency.

Malrotation and midgut volvulus may also be encountered on cross-sectional imaging studies, such as computed tomography (CT) or ultrasound, when these studies are ordered to evaluate abdominal pain or vomiting. This is particularly true in older children in whom malrotation is often not initially suspected as the cause of acute abdominal symptoms. On cross-sectional imaging the bowel may be seen to form a swirling pattern around the superior mesenteric vessels (Fig. 5-14).

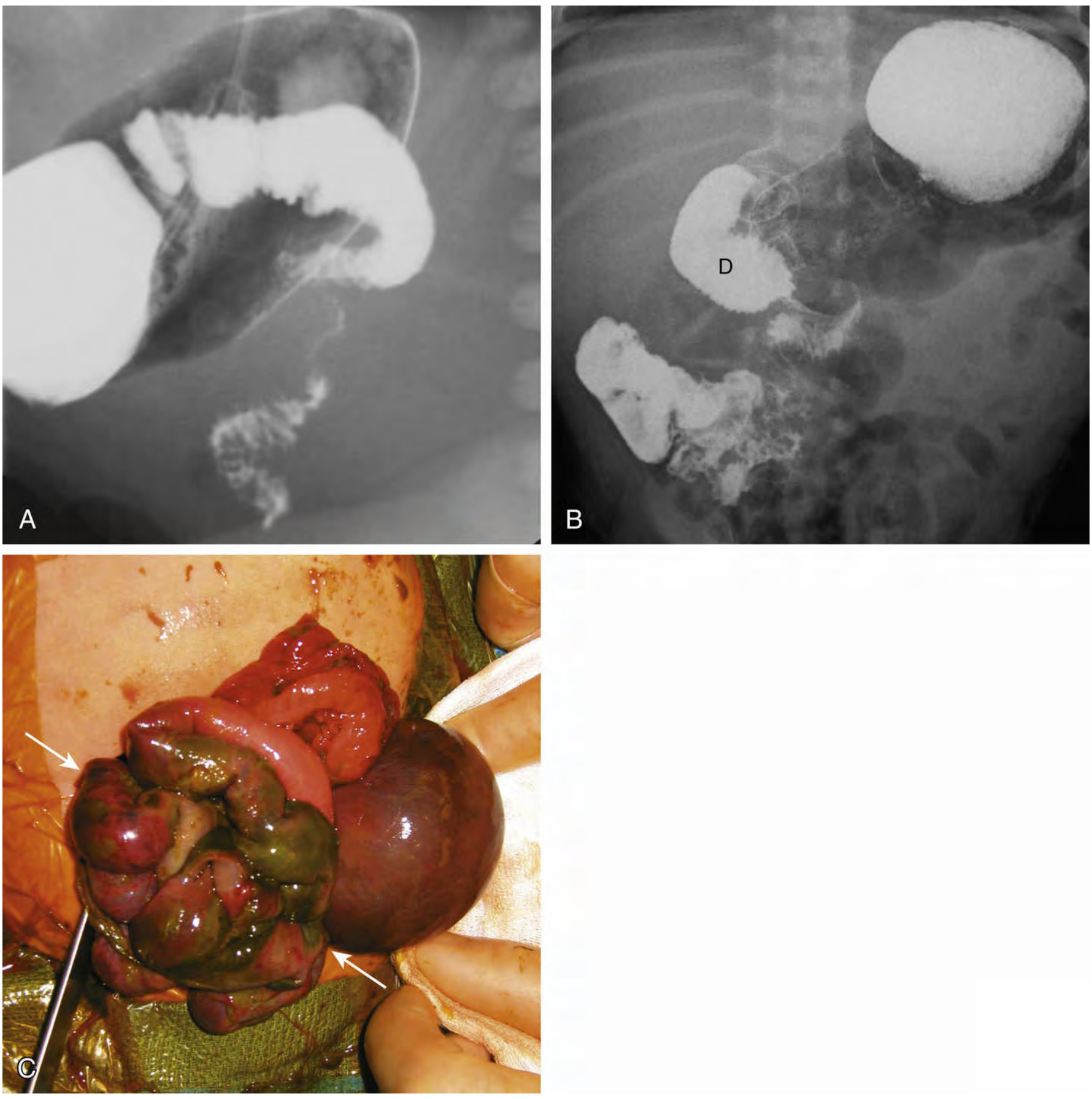
Today, there are an increasing number of people advocating ultrasound as the primary modality for infants with bilious vomiting, mainly because of the previously mentioned difficulties in using a UGI to make the diagnosis of malrotation. If an ultrasound shows a swirling pattern of bowel and vessels about the SMA, this is diagnostic of midgut volvulus. Such a child can go straight to the operating room without documenting the finding by a UGI.

Whether ultrasound can also accurately make or exclude the diagnosis of malrotation without volvulus has been more controversial. Initially, a reversal of the normal relationship between the SMA and superior mesenteric vein (SMV) was advocated as a finding of malrotation (see Fig. 5-11). Normally the SMV is to the right of the SMA (the SMA is smaller and rounder and surrounded by echogenic fat). However, this has been shown to be neither sensitive nor specific. One study showed that the SMA-SMV relationship was normal in 29% of malrotated patients and only 79% of normal controls. However, more recently, it has also been advocated that if ultrasound shows the third part of the duodenum traversing left to right between the aorta and the SMA, documenting that the duodenum travels retroperitoneal, this excludes malrotation. Conversely, if the duodenum does not traverse between the aorta and the SMA (Fig. 5-15), the child is malrotated. A study has shown that a normal retroperitoneal location of the third portion of the duodenum was seen in 100% of controls and only 2.5% (1 out of 38) of children with malrotation. This suggests this finding is fairly accurate at confirming and excluding malrotation in neonates.

Performing an Upper Gastrointestinal Series in an Infant

There are various ways to accomplish a UGI in an infant, and many pediatric radiologists disagree about the details. The following is the way I was taught to perform them. I prefer to have the infant secured to an octagon board (an immobilization device). This allows the radiologist to concentrate on

the examination (rather than on keeping the child from wiggling or getting hurt), get images in appropriate positions rapidly, and minimize the radiation dose. Some think that use of the octagon board is inhumane. The babies do dislike being immobilized and often cry; however, in my experience, if time is taken to explain the procedure and its benefits to the accompanying parent, things usually go well. Some radiologists prefer to administer barium orally and some by placing a nasogastric tube. When the child is willing and able to drink, I administer the contrast orally, usually by bottle. In contrast to adults, in whom many images of the stomach and duodenum are obtained to exclude ulcers and cancer, in children, few images are needed. The most important task is to document the position of the DJJ.

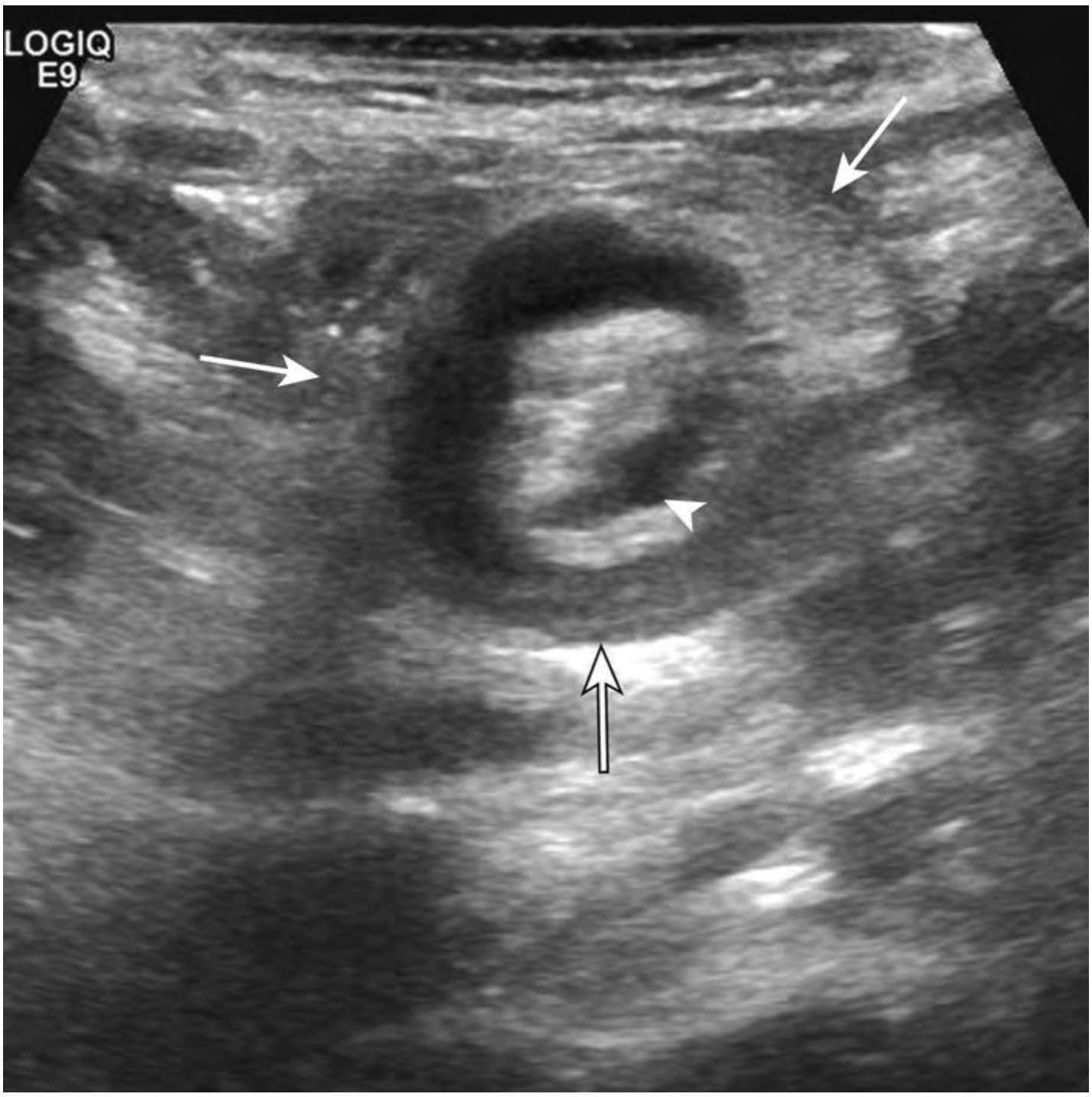


▪ **FIGURE 5-13** **Midgut volvulus.**
A, Lateral view from UGI shows corkscrew appearance of the duodenum and distention of the proximal duodenum. Findings are consistent with volvulus. **B,** Frontal view from UGI in another patient shows distention of proximal duodenum *(D)* and beaklike area of narrowing. Note that the DJJ is not in the normal position and the proximal small bowel is in the right lower quadrant. Findings are consistent with malrotation and volvulus. **C,** Surgical image from a different patient shows multiple loops of necrotic small bowel secondary to infarction from the volvulus.

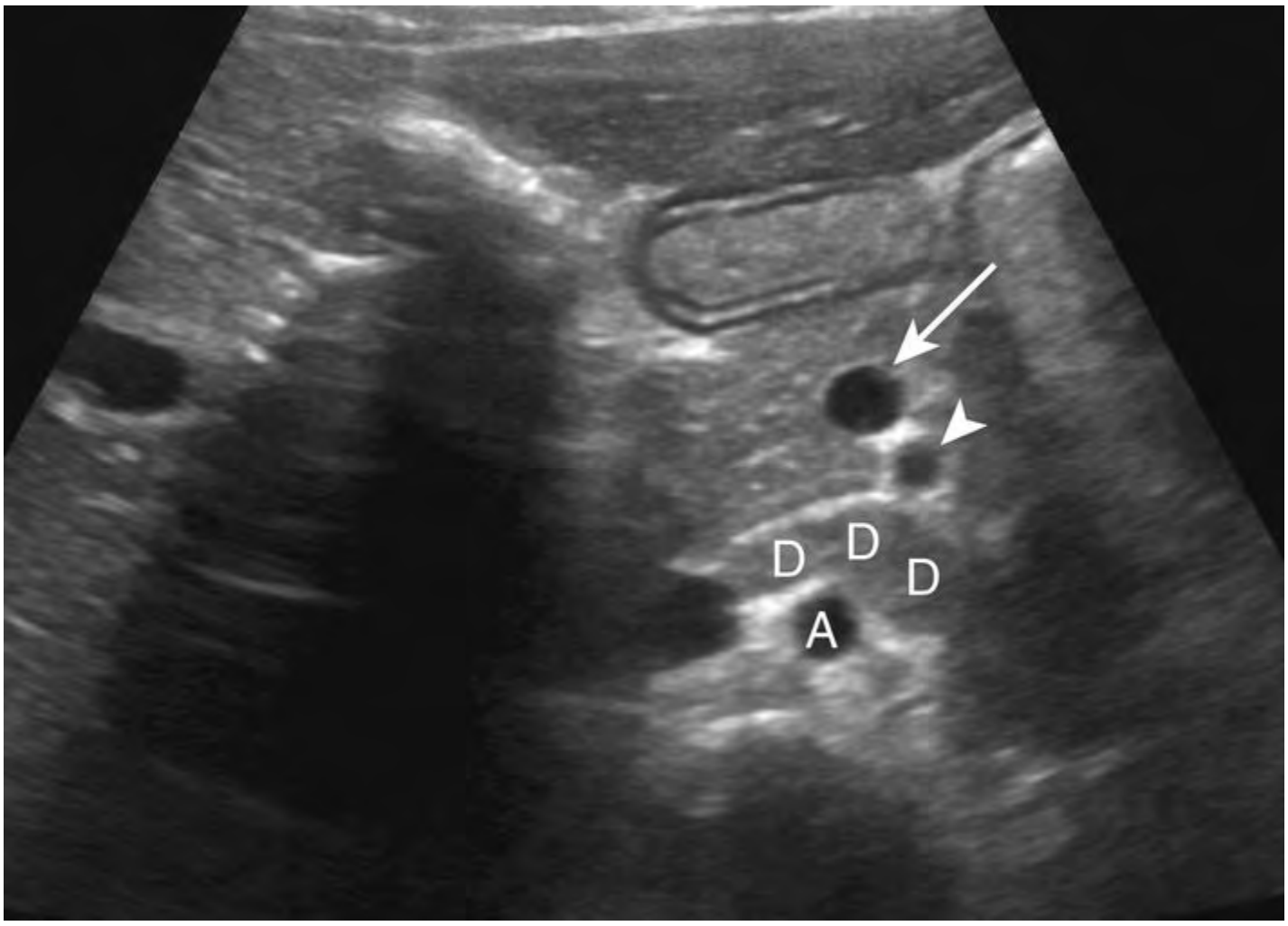
I start off with the child feeding in the supine position because they typically are more likely to suck in this position. Once they begin drinking, I obtain an anteroposterior image of the esophagus and then turn them to the lateral position, right side down. I obtain a lateral view of the esophagus and then wait for contrast to pool in the antrum. When the contrast passes through the pylorus and begins to fill the first and second portions of the duodenum, I obtain a lateral view documenting that the pylorus appears normal and that the duodenum courses posteriorly. This is the crucial point in the examination. The infant is then quickly turned supine, and an image is obtained as the contrast courses into the duodenum and proximal jejunum (see Fig. 5-10). If the infant is turned supine too early and not enough contrast is in the duodenum, the contrast will not pass leftward over the spine. You can always put the child back into the right-side-down position and get more contrast in the duodenum. If the child is turned supine too late (the worst-case scenario), the contrast will have passed into more distal loops of the jejunum and will obscure visualizing the position of the DJJ. Appropriate timing

comes with experience.

The next image that I obtain is an oblique with the left side down, producing an image of the air-filled antrum and bulb. Finally, I obtain an anterior-posterior (AP) image once more contrast has passed into the jejunum to document nondilatation of the jejunum and show that there is no gastroesophageal reflux. Therefore a normal UGI in an infant should consist of only six images. To reduce radiation dose, all of these images can be last-image hold fluoroscopic images rather than true radiographic spot views.



▪ **FIGURE 5-14** **Malrotation with volvulus in an infant.**
Ultrasound shows circle *(arrows)* of twirling bowel and vessels about the SMA *(arrowhead)* consistent with volvulus.

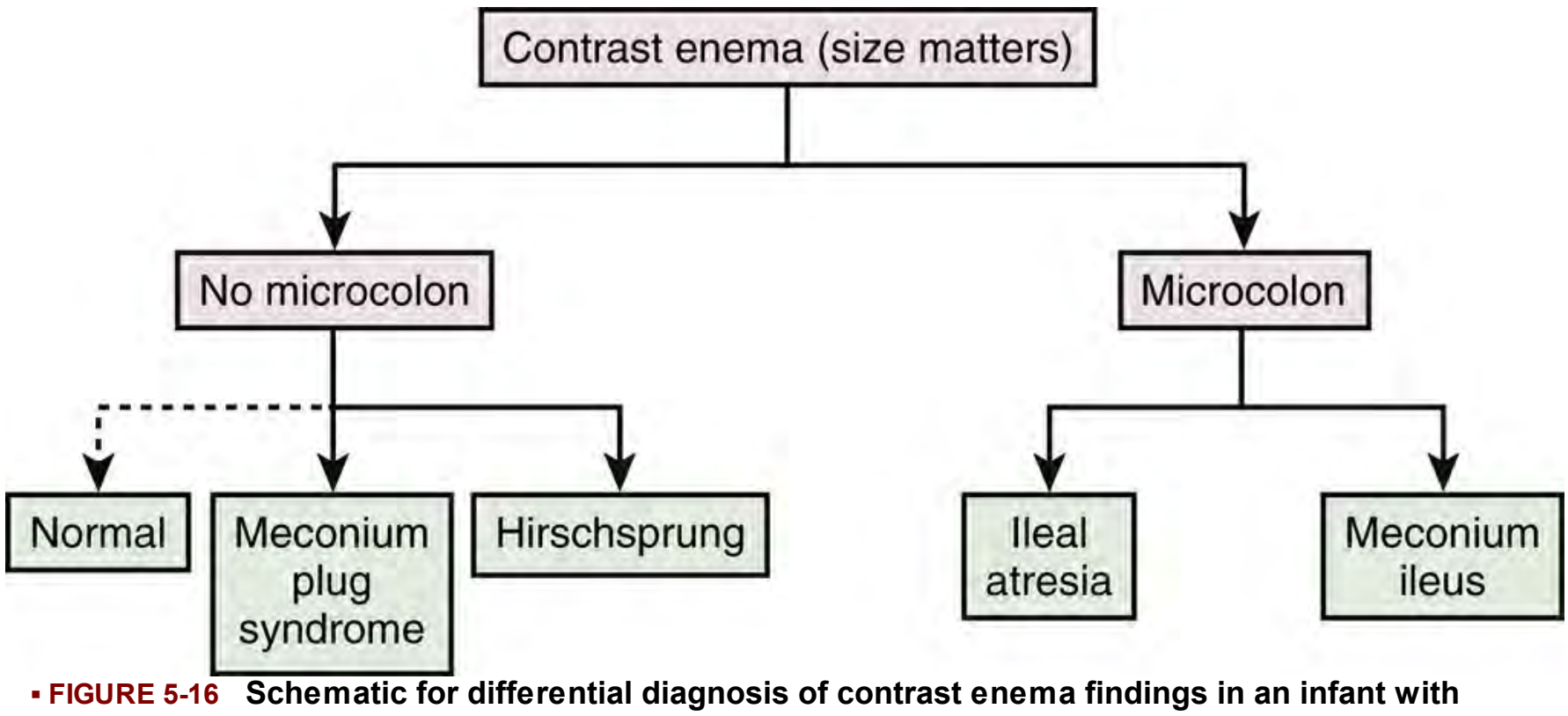


▪ **FIGURE 5-15** Ultrasound in a vomiting infant shows normal retroperitoneal location of the third portion of the duodenum. D3 *(D)* passes between SMA *(arrowhead)* and aorta *(A)*. Note SMV *(arrow)* to right of SMA.

Low Intestinal Obstruction in Neonates

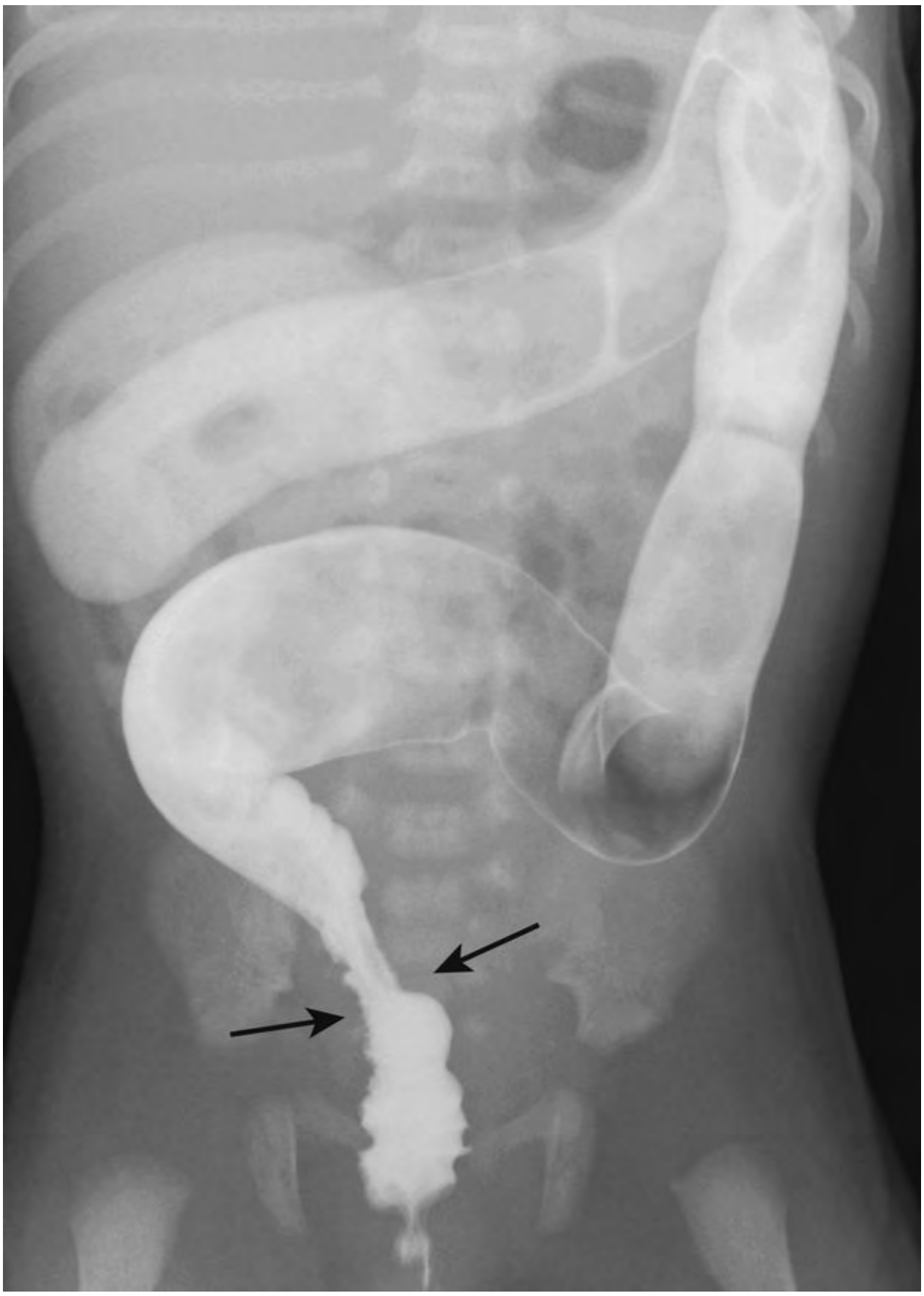
It is not uncommon for neonates to fail to pass meconium because of a distal obstructive process. On radiographs of the abdomen, dilatation of multiple loops of bowel is consistent with a distal obstructive process. The only proximal bowel process that may be associated with multiple dilatated loops of bowel is midgut volvulus, when the bowel dilates secondary to ischemia or infarction. However, these infants are very ill. The neonate who has multiple dilatated loops of bowel on radiographs along with abdominal distention and failure to pass adequate amounts of meconium but is otherwise well on physical exam does not have midgut volvulus as a cause of bowel dilatation and should be evaluated by a contrast enema rather than a UGI. In such a patient without anal atresia on physical examination, the diagnosis is likely to be one of four entities (see Table 5-1; Figs. 5-16 through 5-22). Of these, Hirschsprung disease and meconium plug syndrome involve the colon, and ileal atresia and meconium ileus involves the ileum.

Neonatal contrast enemas are typically performed using dilute ionic, water-soluble agents and a nonballoon-tip catheter of appropriate size. Barium is not typically used because it can make the evacuation of meconium plugs or meconium ileus more difficult, whereas water-soluble enemas can be therapeutic.



▪ **FIGURE 5-16** **Schematic for differential diagnosis of contrast enema findings in an infant with failure to pass meconium and distended abdomen.**

In this scenario there is a high incidence of pathology, and a normal study is uncommon. If the child has a microcolon, it indicates ileal pathology. If the child does not have a microcolon, the cause is probably colonic.



▪ **FIGURE 5-17 Hirschsprung disease in a newborn with abdominal distention and failure to pass meconium.**

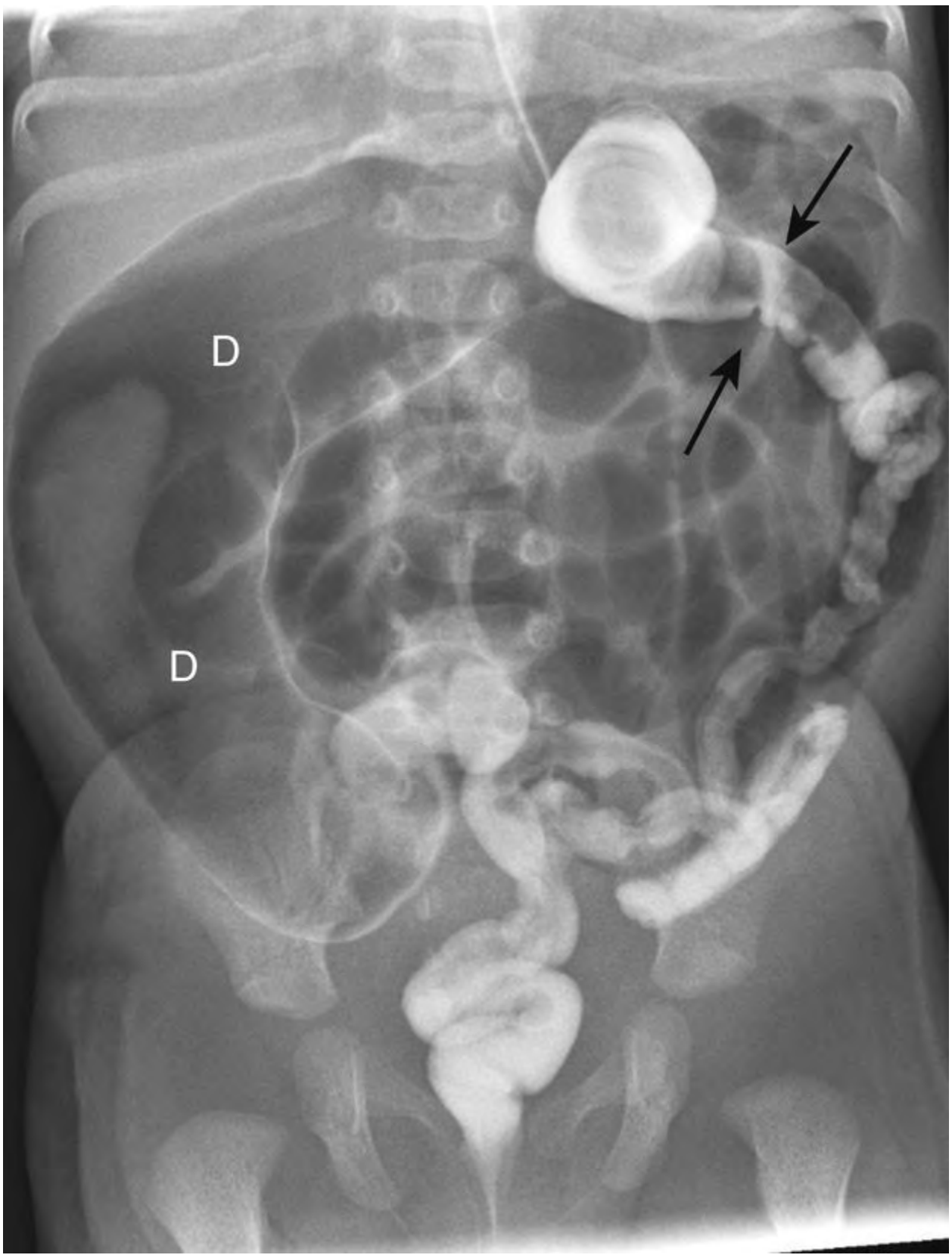
Frontal view from contrast enema shows rectum and distal sigmoid to be narrow in caliber *(arrows)*. Note serrated appearance of the mucosa in the narrowed area. The more proximal sigmoid colon is wider than is the distal sigmoid and rectum.

A microcolon is a narrow-caliber colon secondary to disuse; if it is identified on the enema, the cause is likely to be ileal pathology (see Fig. 5-16). If contrast is refluxed into a collapsed terminal ileum and the more proximal noncontrast-filled bowel loops are disproportionately dilatated, the diagnosis is likely to be ileal atresia (see Fig. 5-20). If the terminal ileum is distended and has multiple filling defects, the diagnosis is meconium ileus (see Fig. 5-21).

Meconium Ileus

Meconium ileus occurs secondary to obstruction of the distal ileum due to accumulation of abnormally tenacious meconium. It occurs exclusively in patients with cystic fibrosis and is the presenting finding of cystic fibrosis in approximately 10% of cases. It may be complicated by perforation, volvulus of the bowel, or meconium peritonitis (Fig. 5-23). Radiographs show findings of distal obstruction, which may be associated with bubblelike lucencies secondary to the accumulated meconium or with calcification when perforation is present (see Figs. 5-21 and 5-22). Serial water-soluble enemas are commonly used in an attempt to remove the obstruction nonsurgically. There is debate about the optimal contrast agent to use for such serial therapeutic enemas (see Fig. 5-21). Table 5-2 shows a summary of the meconium-

related gastrointestinal diseases.



▪ **FIGURE 5-18** **Meconium plug syndrome (small left colon syndrome) in a newborn infant with distended abdomen and failure to pass meconium.**
Contrast enema demonstrates a small left colon to the level of the splenic flexure *(arrows)*. The more proximal colon *(D)* is distended. Note several filling defects with opacified portion of colon consistent with meconium plugs. Rectal biopsy, performed to exclude Hirsch sprung disease, demonstrated normal ganglion cells.

Hirschsprung Disease

In contrast enemas performed to examine neonatal distal obstruction, if the proximal colon is distended, the cause of distal obstruction is likely to be colonic secondary to Hirschsprung disease or meconium plug syndrome.

Hirschsprung disease is related to the absence of the ganglion cells that innervate the colon. The denervated colon spasms and causes a functional obstruction. Therefore the affected portions of colon are small in caliber, and the more proximal, normally innervated colon is dilatated secondary to the obstruction. The rectum and a variable amount of more proximal colon are affected in a contiguous fashion; there are no skip lesions. Most patients with Hirschsprung disease (90%) present in the neonatal period with failure to pass meconium (see Fig. 5-17). However, patients can present later in life with problems related to constipation. Hirschsprung disease is much more common in boys (4:1) and is associated with Down syndrome in 5% of cases.



▪ **FIGURE 5-19** **Meconium plug syndrome (small left colon syndrome) in a newborn infant with distended abdomen and failure to pass meconium.**

A, Radiograph shows multiple dilated loops of bowel consistent with a distal bowel obstruction. **B,** Contrast enema demonstrates a small left colon to the level of the splenic flexure *(arrow)*. The more proximal colon is distended. Note several filling defects with opacified portion of colon consistent with meconium plugs.

When an enema is being performed to evaluate for possible Hirschsprung disease, it is essential to obtain early filling views, collimated to include the rectum and sigmoid colon, in both the lateral and then the frontal position. Findings of Hirschsprung disease include a transition zone from an abnormally small rectum and distal colon to a dilatated proximal colon (see Figs. 5-14 and 5-19). In a normal patient the rectum has the largest luminal diameter of the left-sided colon. When the rectum alone is involved by Hirschsprung disease, the sigmoid colon is larger than the rectum (see Fig. 5-17). This is referred to as an abnormal rectosigmoid ratio. Another, but less common, finding is fasciculations or saw-toothed irregularity of the denervated segment (see Fig. 5-17). If the entire colon is involved by Hirschsprung disease (very rare), the entire colon may appear small in caliber and may mimic a microcolon.

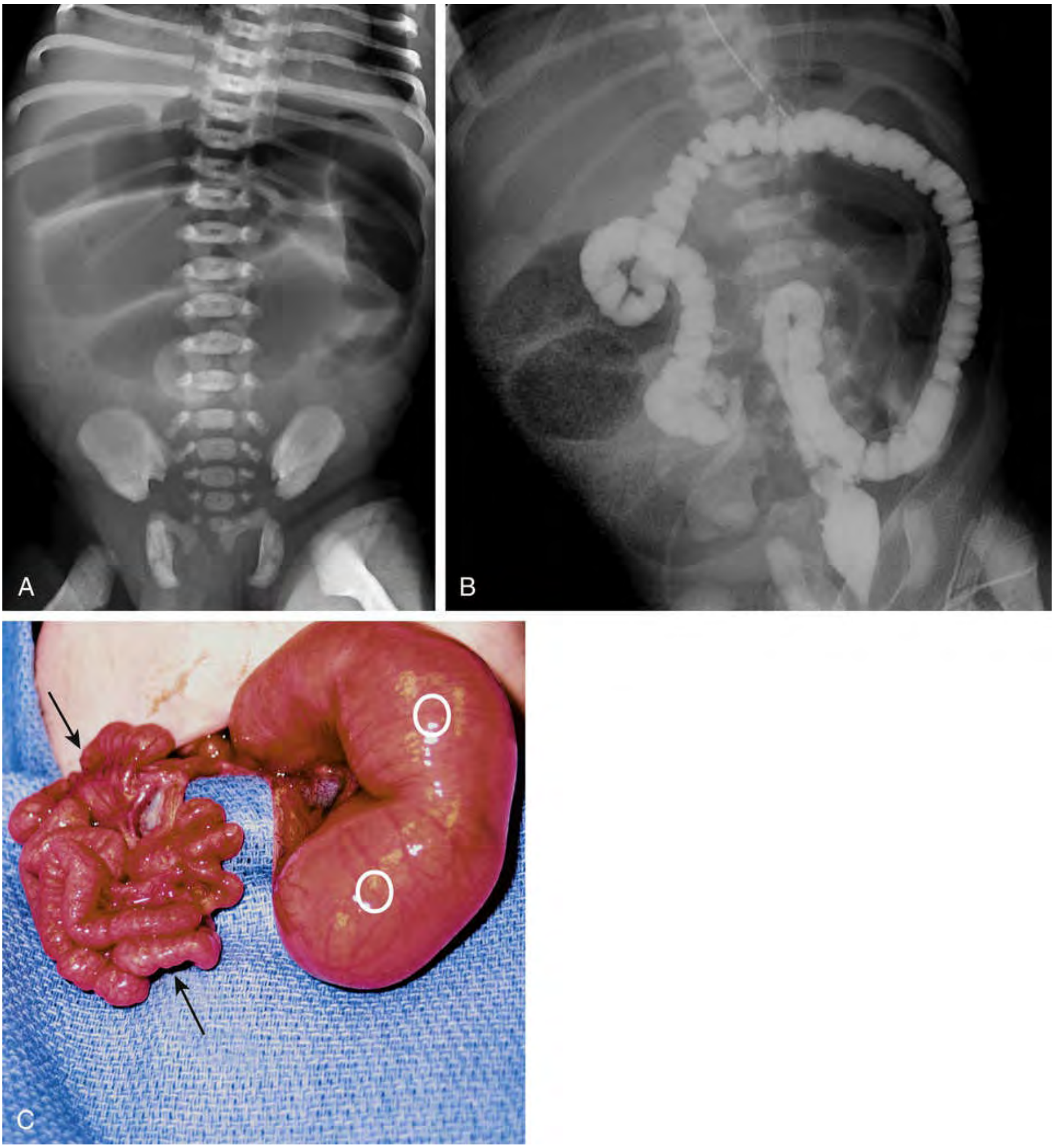
Patients with Hirschsprung disease may present with associated colitis. Therefore, in patients who are suspected to have Hirschsprung disease and are ill, contrast enemas should be avoided.

Definitive diagnosis is obtained by rectal biopsy, and patients are treated by surgical resection of the denervated segment. The transition zone depicted on enema does not always accurately predict where the transition from absent to present ganglion cells occurs histologically.

Meconium Plug Syndrome

Meconium plug syndrome, also referred to as functional immaturity of the colon or small left colon syndrome, is a common cause of distal neonatal obstruction. It is the most commonly encountered diagnosis in neonates who fail to pass meconium. It is thought to be related to functional immaturity of the ganglion cells. As in Hirschsprung disease, the distal colon does not have normal motility, which causes functional obstruction. Unlike Hirschsprung disease, it is a temporary phenomenon and resolves. Although most neonates with meconium plug syndrome are otherwise normal and have no abnormal associations, increased incidence occurs in patients who are infants of diabetic mothers or of mothers who have received magnesium sulfate for eclampsia. In neonates with meconium plug syndrome, there is always concern about underlying Hirschsprung disease, so at many centers, all neonates who have findings of meconium plug syndrome undergo rectal biopsy. In contrast to

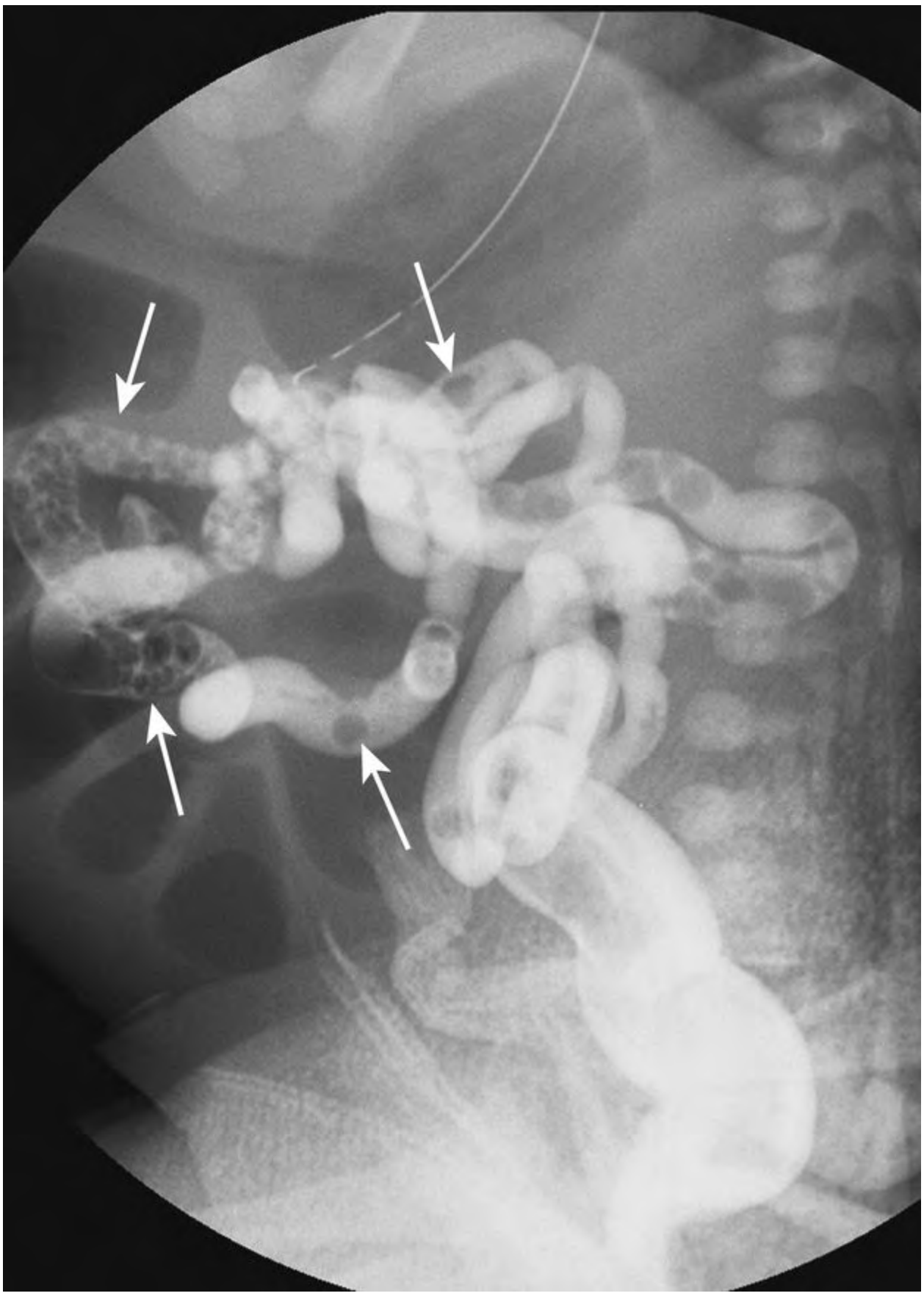
meconium ileus, there is no significant relationship between meconium plug syndrome and cystic fibrosis.



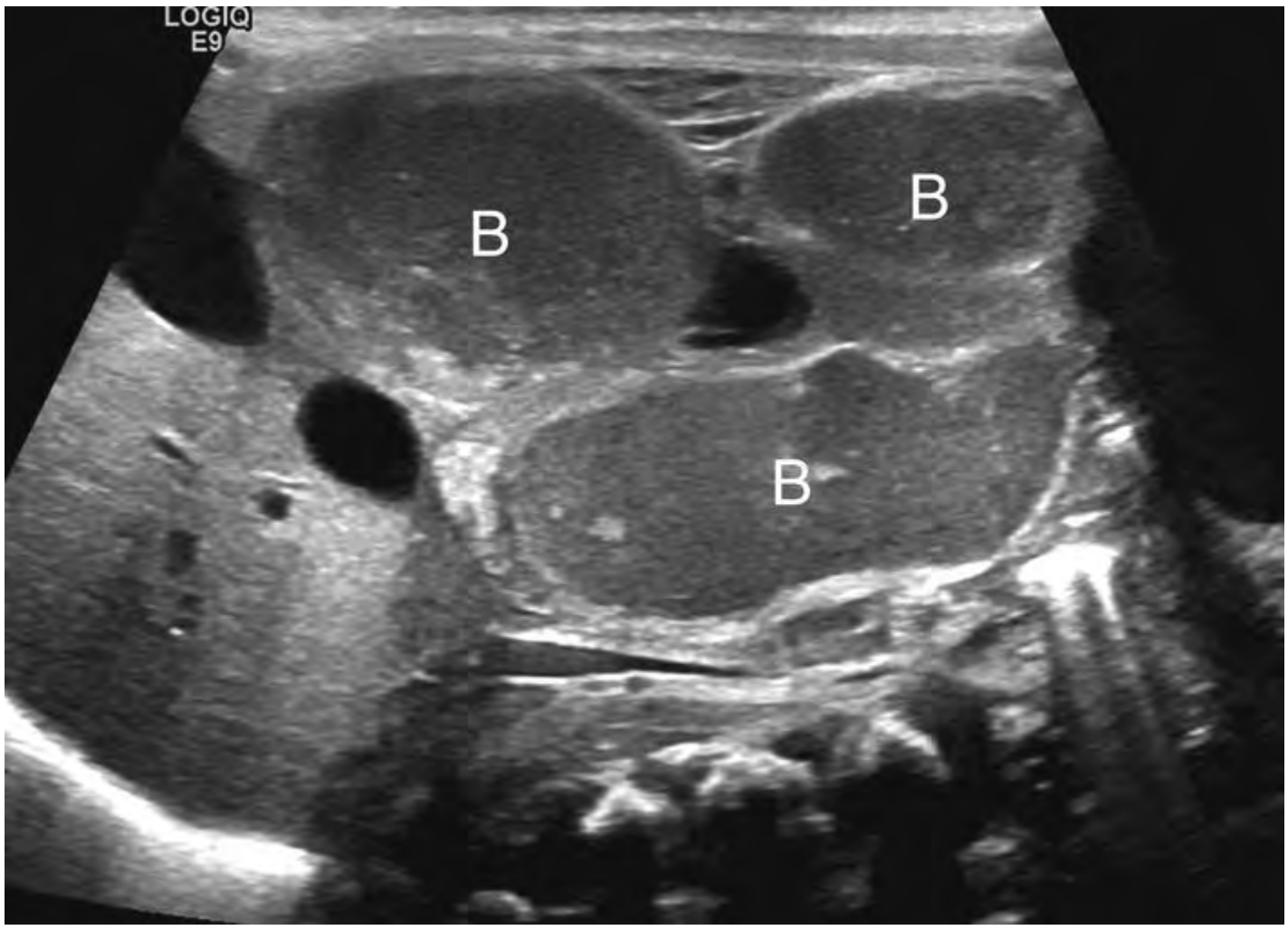
▪ **FIGURE 5-20 Bowel atresia.**
A, Radiograph shows multiple dilated loops of bowel consistent with a distal bowel obstruction. **B,** Contrast enema shows a relative microcolon. There are multiple, very dilated loops of nonopacified small bowel. Contrast is not able to be passed into the more proximal dilated loops. Findings are consistent with ileal atresia. **C,** Surgical photograph shows dilated loops of bowel *(O)* above the level of obstructive atresia. Distal to the atresia, there are multiple collapsed loops of ileum *(arrows)*.

On contrast enema, multiple filling defects (meconium plugs) are seen within the colon (see Figs. 5-18 and 5-19). The right and transverse colons may be more dilated than the left colon (small left colon syndrome; see Figs. 5-18 and 5-19), although these findings are variable. Microcolon does not occur. The rectum tends to be normal in luminal diameter, as compared with the rectums in infants with Hirschsprung disease. The enema is often therapeutic; plugs of meconium are commonly passed during or shortly after the enema, and symptoms of obstruction often resolve within hours after the

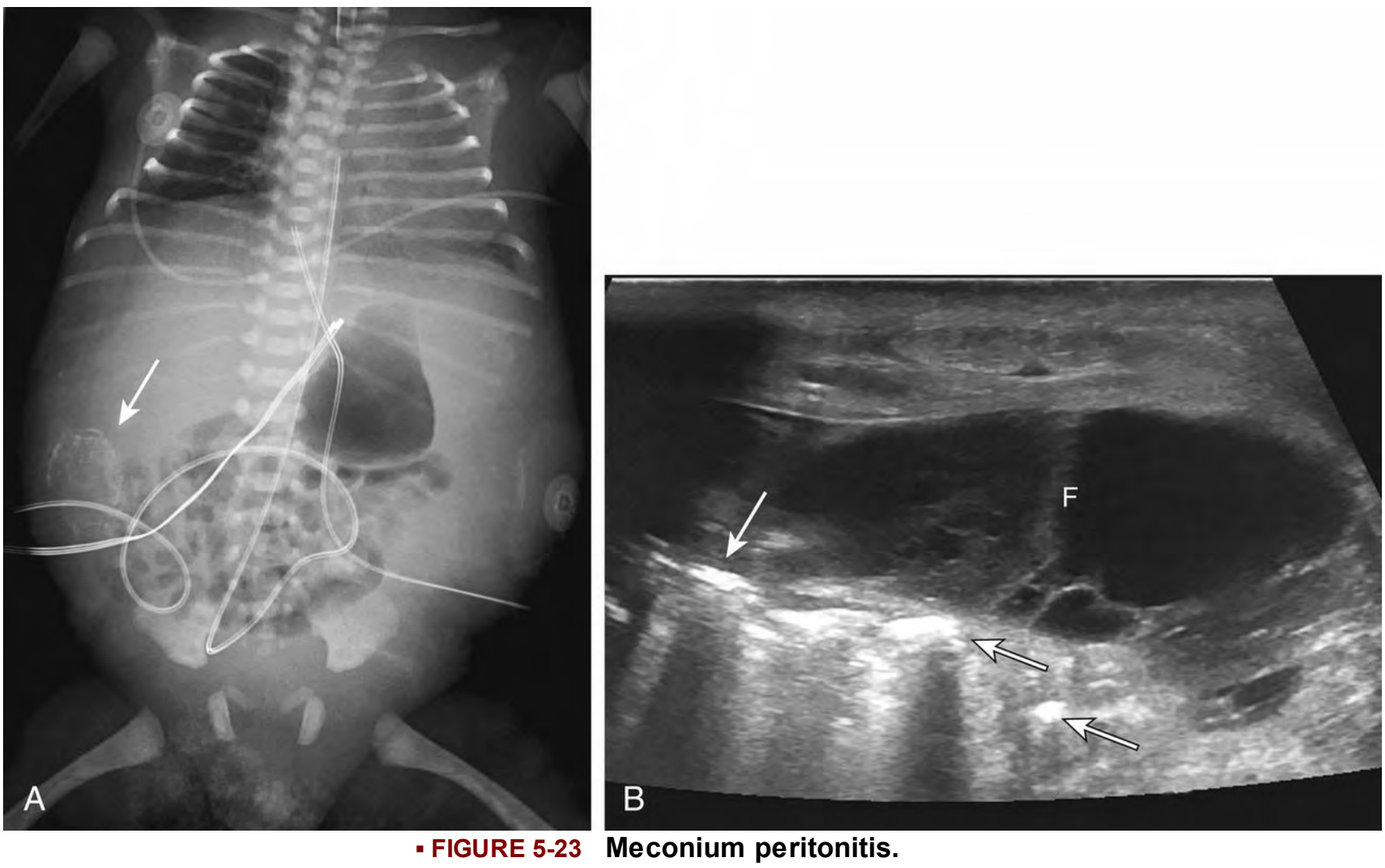
enema.



▪ **FIGURE 5-21** **Meconium ileus in a newborn infant with abdominal distention and failure to pass meconium.**
The infant was confirmed to have cystic fibrosis. Contrast enema in lateral view demonstrates a small-caliber microcolon and opacification of the distal ileum, which contains multiple filling defects *(arrows)*, consistent with meconium.



▪ **FIGURE 5-22** **Meconium ileus in a newborn infant with cystic fibrosis.**
Ultrasound shows multiple dilated bowel loops *(B)* with echogenic contents within the bowel.



▪ **FIGURE 5-23** **Meconium peritonitis.**
A, Radiograph of a neonate demonstrates multiple curvilinear calcifications *(arrow)* in the right side of the abdomen. **B,** Ultrasound shows large, complex fluid collection *(F)* and multiple adjacent shadowing echogenicities *(arrows)*, consistent with calcifications.

TABLE 5-2
Summary of Meconium-Related Gastrointestinal Diseases

Meconium Ileus

- Occurs only in patients with cystic fibrosis
- Tenacious meconium causes obstruction of distal ileum
- Contrast enema: Microcolon, dilatated distal small bowel with filling defects (meconium pellets)

Meconium Plug Syndrome (Small Left Colon Syndrome)

- Not associated with cystic fibrosis
- Immaturity of colon; functional obstruction
- Self-limited, often relieved by contrast enema
- Contrast enema: Filling defects (meconium plugs) in colon, small-caliber left colon

Meconium Peritonitis

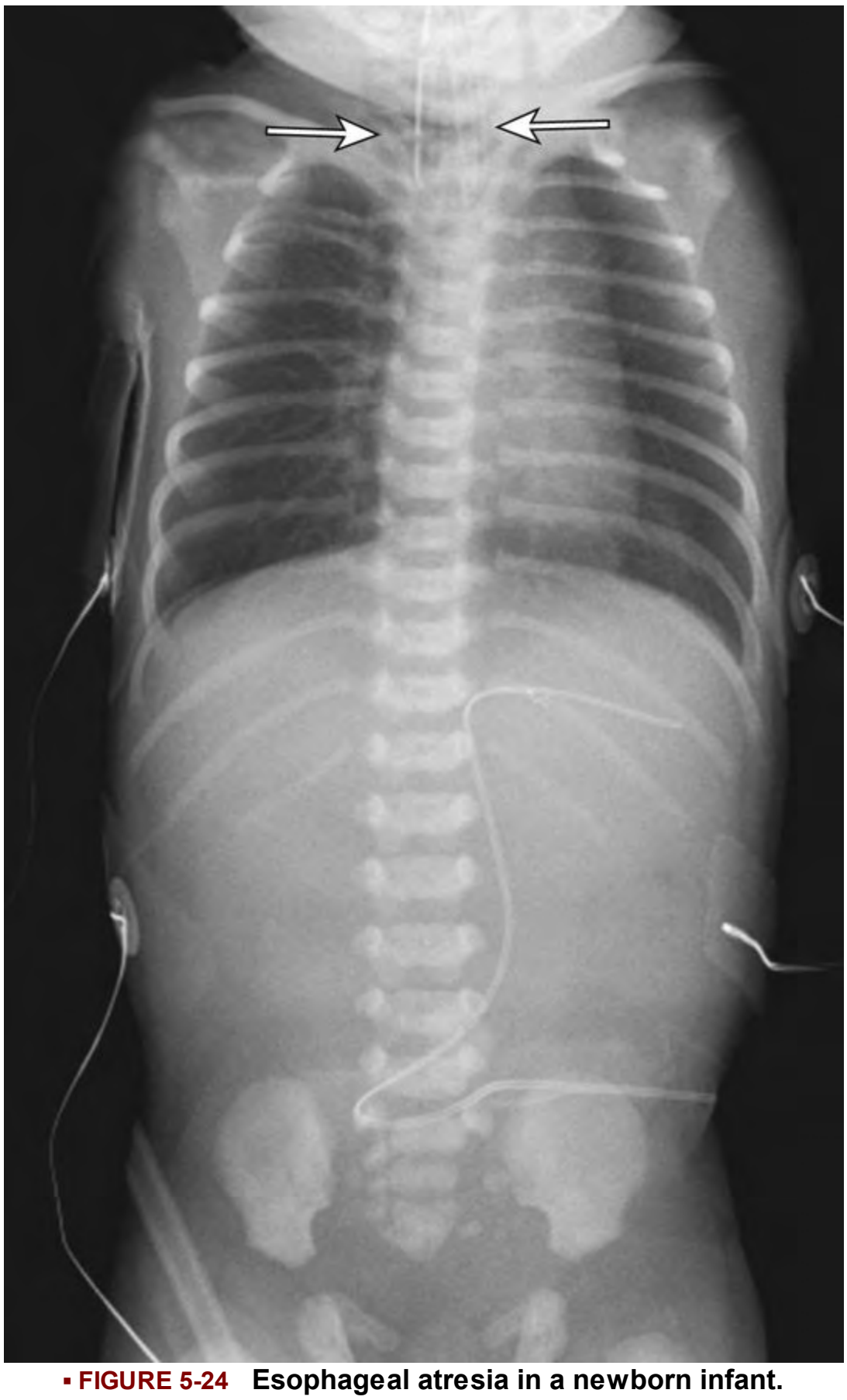
- Result of in utero perforation of bowel secondary to bowel atresia, in utero volvulus, or meconium ileus
- Imaging: bowel obstruction, peritoneal calcifications, meconium cysts in peritoneal cavity

Esophageal Atresia and Tracheoesophageal Fistula

In esophageal atresia the esophagus is atretic for a variable length, usually at the junction of the proximal and middle thirds of the esophagus. Esophageal atresia can occur in the presence or absence of a tracheoesophageal fistula. The most common type of esophageal atresia is that with a fistulous communication between the distal esophageal segment and trachea. Much less commonly, the fistula can connect the proximal or both the proximal and distal esophageal segments to the trachea. Rarely, tracheoesophageal fistulas can occur in the absence of esophageal atresia; this is called an H-type fistula.

Esophageal atresia presents at birth and is usually encountered by the radiologist after there is failure to pass an orogastric tube. Radiographic findings include a distended, air-filled pharyngeal pouch (Fig. 5-24), with or without an indwelling tube. If there is no abdominal bowel gas, a tracheoesophageal fistula is not present; if there is distal bowel gas, there is a distal fistula. Further imaging, such as with a UGI, is rarely needed. Because the surgery for esophageal atresia is performed through a thoracotomy contralateral to the aortic arch, it is important to determine on which side the arch is located. Often, echocardiography is used.

Esophageal atresia is usually associated with other congenital anomalies. The acronym VACTERL is used: vertebral anomalies, anal atresia, **c**ardiac anomalies, tracheoesophageal fistula, renal anomalies, and limb (radial array) anomalies. Chest radiographs in such patients should be scrutinized for vertebral and cardiac anomalies.



▪ **FIGURE 5-24** **Esophageal atresia in a newborn infant.**
Radiograph shows gasless abdomen and lucent circular area *(arrows)* over upper mediastinum with suction tube in place. This represents the pharyngeal pouch above the atresia.

Children with an H-type fistula present with coughing or choking during feeds or with recurrent pneumonia. Often a UGI is requested to exclude an H-type fistula. Some authors advocate that such an examination should be performed with the patient in the prone position, with a tube positioned in the esophagus, to fully distend the esophagus and maximize potential visualization of the fistula. Others state that this offers no advantage over routine oral administration of contrast via a bottle.

Complications following repair of esophageal atresia include recurrent fistula and esophageal leak during the immediate postoperative period. A large extrapleural fluid collection seen on chest radiography is highly suggestive of a leak. Long-term sequelae include esophageal stricture, esophageal dysmotility, and gastroesophageal reflux.

Abnormalities of Anterior Abdominal Wall

The closure of the anterior abdominal wall occurs during fetal life; failure of proper closure may result in a number of abnormalities, of which the most common are omphalocele, gastroschisis, and cloacal exstrophy. Many of these abnormalities are now diagnosed and evaluated prenatally by ultrasound or fetal magnetic resonance imaging (MRI). Omphalocele results from failure of fusion of the lateral folds. It is a midline defect in which the herniated abdominal contents (bowel or liver) are covered by a sac of peritoneum (Fig. 5-25). As much as two thirds of patients with omphalocele have associated congenital

anomalies, most commonly cardiac anomalies. On fetal MRI and ultrasound, with omphalocele, the cord is shown to insert directly into the herniated sac.

In contrast, in gastroschisis the defect is lateral to midline, there are typically no associated abnormalities, and the herniated content (usually only bowel) is not covered by a membrane (Fig. 5-26). On fetal MRI the umbilical cord inserts adjacent to the defect rather than directly to the hernia sac as in omphalocele. Because of the lack of a covering membrane, the bowel is exposed to the amniotic fluid, which is toxic to the bowel. These patients often have severe dysmotility problems and present with multiple episodes of pseudoobstruction. Often, small-bowel follow-throughs are requested in an effort to differentiate between pseudoobstruction and obstruction related to adhesions. This is a daunting task because these studies can last for days. In this scenario some have advocated giving the oral contrast and obtaining a film every 24 hours to help to minimize radiation exposure.



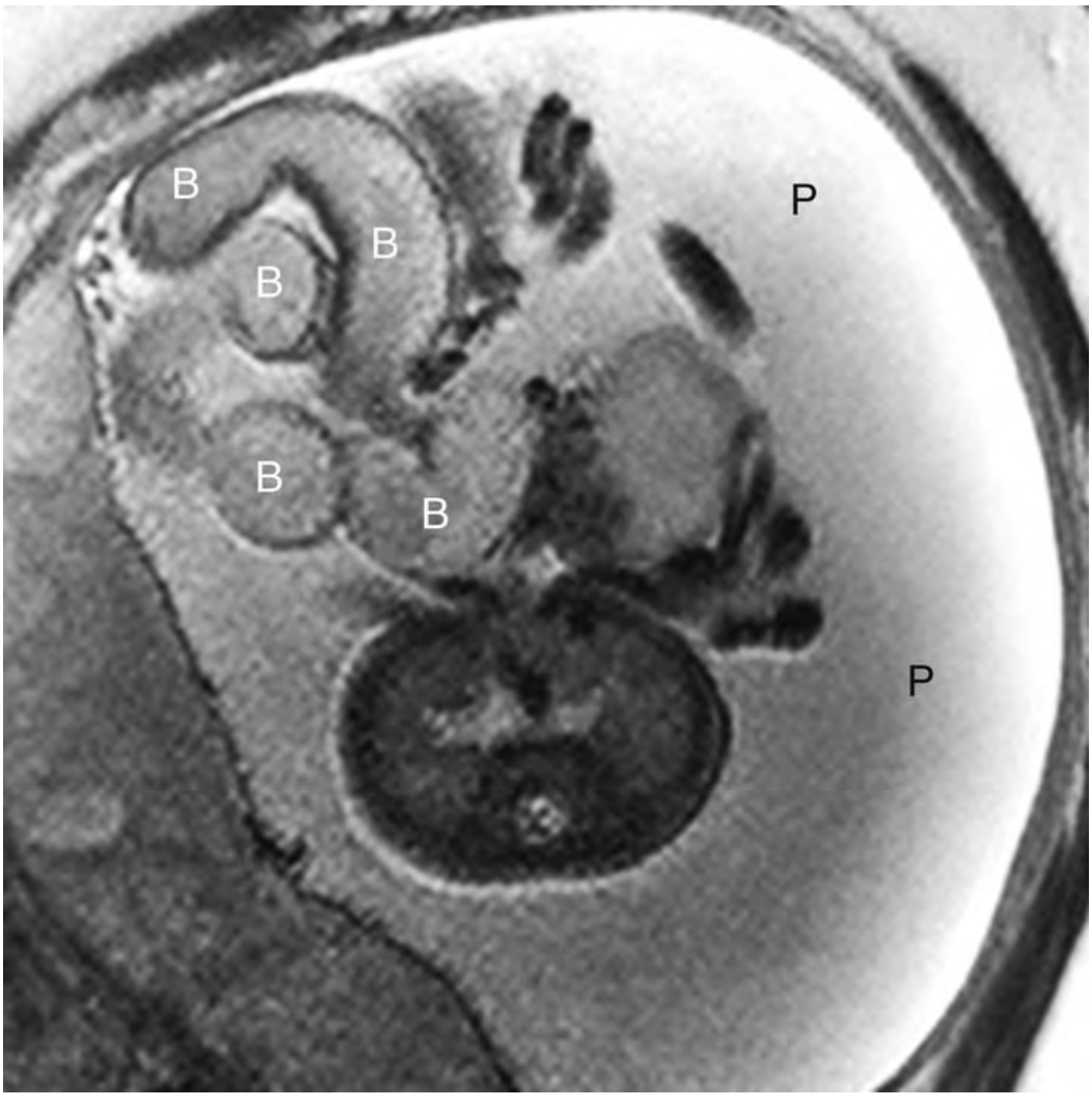
▪ **FIGURE 5-25** **Omphalocele demonstrated on fetal MRI.**
Sagittal image of fetus shows omphalocele *(arrows)* as an anterior pouch containing the liver *(L)*. Note the smooth appearance of the membrane covering the sac.

Cloacal exstrophy is a severe malformation in which there is bladder exstrophy and omphalocele. There is associated diastasis of the pubic bones and spinal dysraphism. Hydrometrocolpos can be associated with cloacal exstrophy and cause renal failure if not identified because it causes compression and extrinsic obstruction of the distal ureters.

The Vomiting Infant

The referral of an infant for a UGI to rule out reflux is a common event. Typically such infants are referred to radiology because of excessive "spitting up," or vomiting. There are a number of significant causes of excessive vomiting in infants. They include hypertrophic pyloric stenosis, gastroesophageal reflux, congenital stenosis, lactobezoar, and possibly midgut volvulus. The problem for pediatricians is

that spitting up (regurgitation) after feedings is a common and normal event. The degree of such spitting up is also variable. How do pediatricians differentiate prominent but normal regurgitation from vomiting secondary to obstruction or pathologic amounts gastroesophageal reflux? Associated problems such as failure to gain weight, failure to thrive, or respiratory symptoms suggest pathology. However, this difficult question often results in performing a UGI. Although such UGIs are often ordered to rule out reflux, they are actually performed to exclude an anatomic reason for excessive reflux, rather than to exclude reflux itself. Although it is appropriate to document the presence and anatomic extent of gastroesophageal reflux when it occurs, it is not necessary to perform maneuvers to provoke reflux.



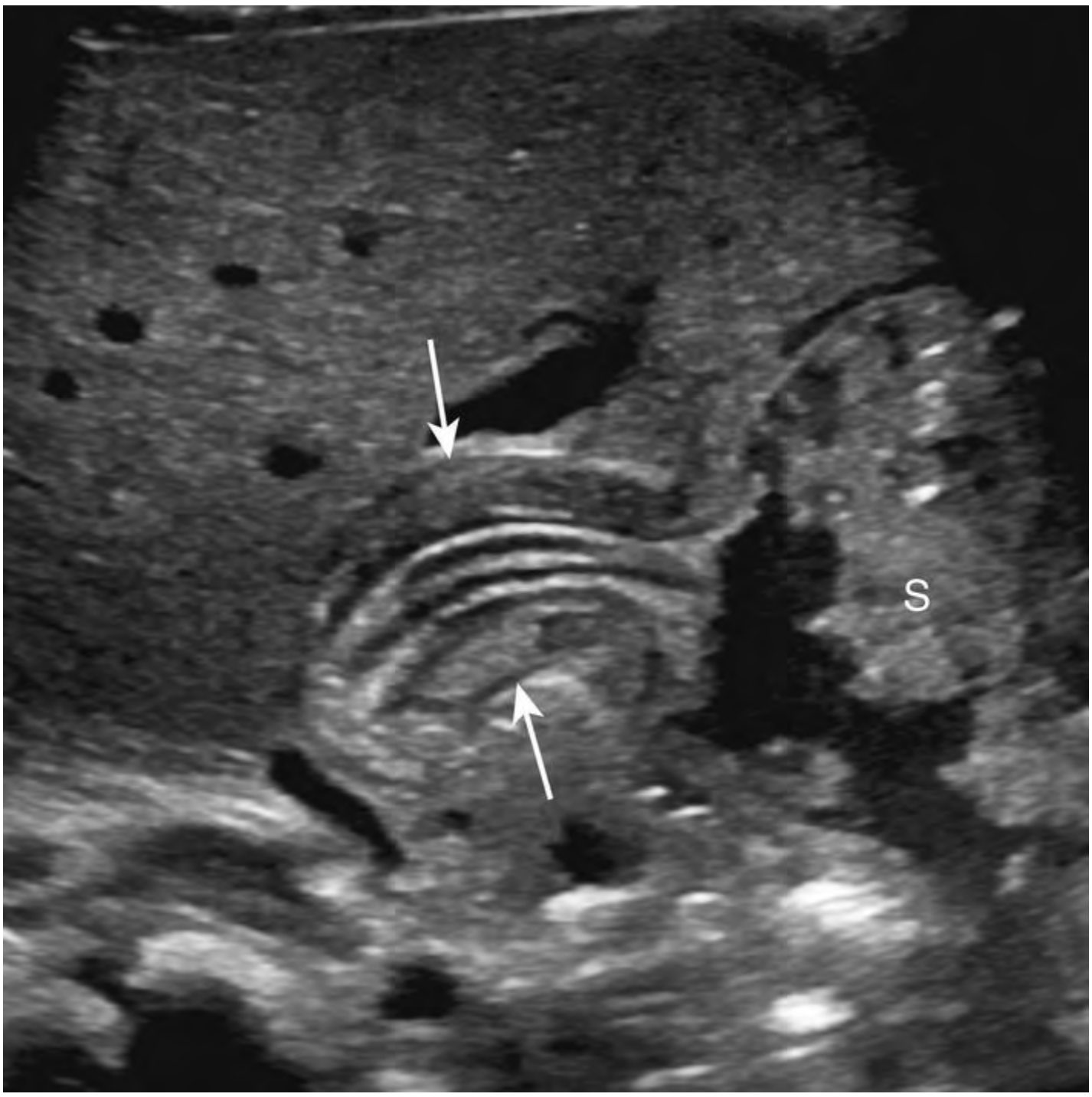
▪ **FIGURE 5-26 Gastroschisis shown on sagittal fetal MRI.**
There is eviscerated bowel *(B)* external to the fetus. Note the irregular configuration of bowel, consistent with the lack of an enveloping membrane. Note polyhydramnios *(P)*.

Hypertrophic Pyloric Stenosis

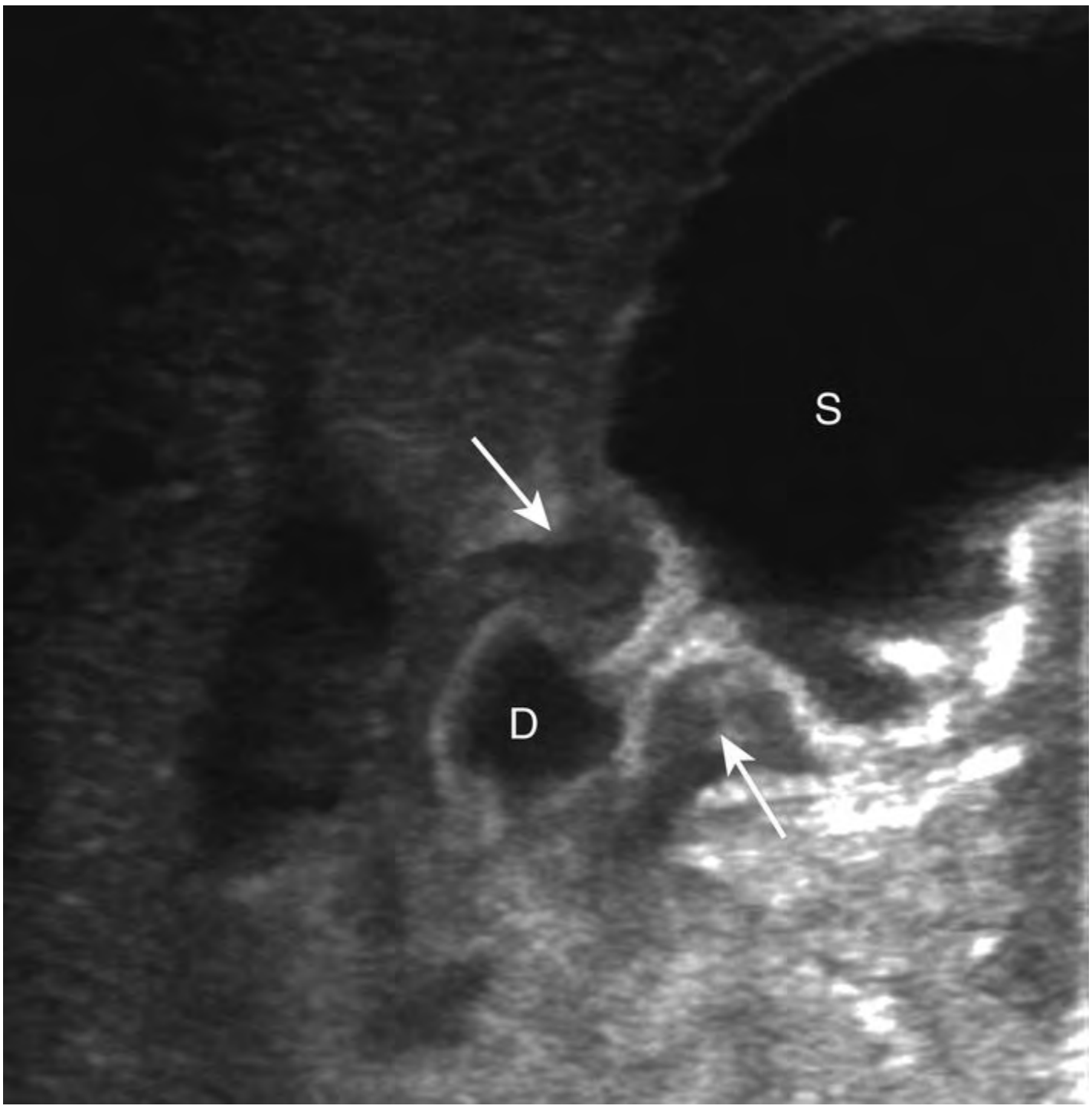
Hypertrophic pyloric stenosis is a common idiopathic thickening of the muscle of the pylorus that results in a progressive gastric outlet obstruction. It usually occurs in otherwise healthy infants (between 1 week and 3 months of age) who typically present with projectile, bile-free emesis. It is much more common in males (5:1 ratio). On physical examination the hypertrophied pylorus can be palpated as an olive-sized mass in the right upper quadrant. It is suggested that palpation of an "olive" in the presence of the appropriate clinical symptoms is diagnostic and that such infants do not need confirmatory imaging studies. However, in practicality, hypertrophic pyloric stenosis is a diagnosis made at imaging, and almost all children have imaging before surgery. It should be noted that imaging to confirm or exclude hypertrophic pyloric stenosis is not a medical emergency.

Ultrasound is the modality of choice to make a diagnosis of hypertrophic pyloric stenosis. Ultrasound

allows direct visualization of the pyloric muscle and does not use radiation. On ultrasound, the diagnosis of hypertrophic pyloric stenosis is often obvious and made on the gestalt of the appearance. The pylorus is anatomically located near the gallbladder, so an easy technique is to find the gallbladder and turn obliquely sagittal to the body in an attempt to visualize the pylorus longitudinally. The hypertrophied muscle is hypoechoic, and the central mucosa is hyperechoic (Fig. 5-27). With hypertrophic pyloric stenosis the pylorus does not open during real-time evaluation. There are measurement criteria that vary slightly from source to source. The pyloric muscle thickness (diameter of a single muscular wall on a transverse image) should normally be less than 3 mm. The length (longitudinal diameter) should not exceed 15 mm. Another good rule of thumb is that if one sends an inexperienced sonographer or resident in to scan the child and they find the pylorus easily, it is probably abnormal. A normal pylorus (Fig. 5-28) is much harder to image than is an abnormal pylorus.



▪ **FIGURE 5-27** Hypertrophic pyloric stenosis on ultrasound. Longitudinal ultrasound image demonstrating findings of hypertrophic pyloric stenosis. The hypertrophied pyloric muscle *(arrows)* is hypoechoic and the mucosa is echogenic. Stomach *(S)*, containing contents.



▪ **FIGURE 5-28 Longitudinal ultrasound appearance of the normal pylorus.**
The pylorus *(arrows)* is seen between the stomach *(S)* and duodenal bulb *(D)*. Note that the pylorus is not excessively long or thickened and has a patent lumen.

Findings of hypertrophic pyloric stenosis can also be seen on a UGI. On a UGI there is delayed gastric emptying with hypertrophic pyloric stenosis. When some contrast does pass into the duodenum, the pylorus appears elongated with a narrow pyloric channel (string sign). The lumen may be puckered and have more than one apparent lumen (the double-track sign). The pylorus may indent the contrast-filled antrum (the shoulder sign) or the base of the duodenal bulb (the mushroom sign), and the entrance to the pylorus may be beak-shaped (the beak sign). After the diagnosis is made, excess barium should be removed from the stomach by nasogastric tube to avoid the risk for aspiration.

On radiographs, children with hypertrophic pyloric stenosis may show gastric distension, peristaltic waves (caterpillar sign), and mottled retained gastric contents.

▪ Intestinal Obstruction in Children

As in adults the key finding of bowel obstruction on radiography is the presence of disproportionately dilatated proximal small bowel as compared with less dilatated more distal small bowel or colon. In contrast with adults, in infants and small children, it may be difficult to differentiate small bowel from colon secondary to a lack of well-defined haustra and valvulae conniventes. The addition of a prone view to the standard two-view abdomen (supine and either upright, cross-table lateral, or left decubitus) can be helpful when differentiation between small and large bowel is difficult. On the prone view, gas moves into the more posterior structures of the colon—the ascending and descending colon and the rectum. On supine views, the colonic gas lies in the more anterior structures, the transverse and sigmoid colon. The position of gas on the combination of these two views is often helpful in identifying that gas is in the colon rather than in the dilatated small bowel. Demonstration of the presence or absence of gas in the ascending colon can be of particular help when evaluating for potential ileocolic intussusception.

The most common causes of bowel obstruction in children older than infants are listed in Table 5-3. The pneumonic *take AAIIMM* against small bowel obstruction, championed by Donald R. Kirks, MD, is helpful for recalling this list when under pressure. Each letter in AAIIMM represents two diagnoses. Appendicitis, intussusception, and Meckel diverticulum are discussed in more detail subsequently.

Appendicitis

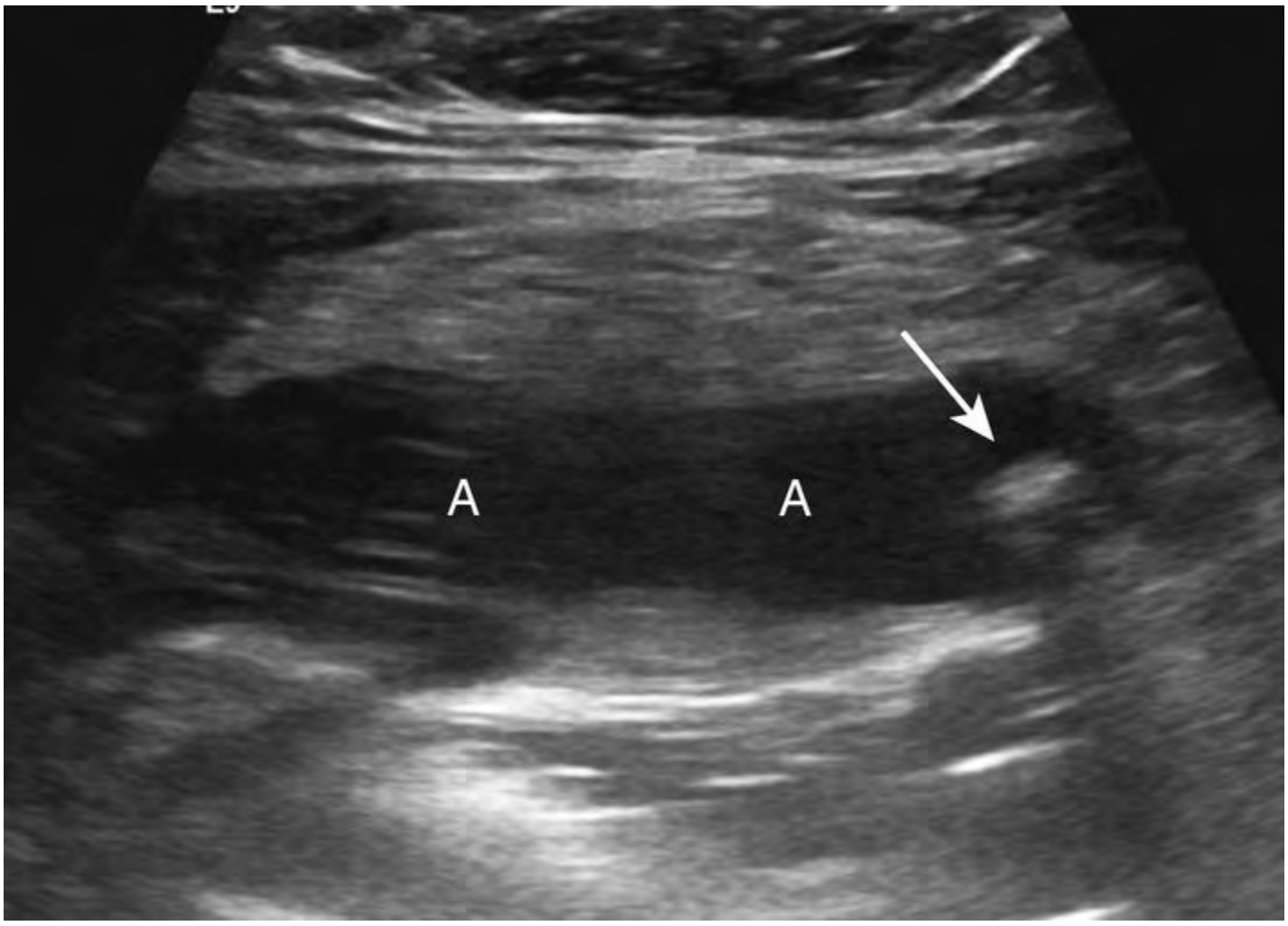
Appendicitis is the most common reason for abdominal surgery in children. Obstruction of the appendiceal lumen results in distention of the appendix, superimposed infection, ischemia, and eventually perforation. In older children with nonperforated appendicitis, the classic symptoms include pain that begins in the periumbilical region and migrates to the right lower quadrant, tenderness over the McBurney point, and a combination of anorexia, nausea, vomiting, diarrhea, and fever. The clinical presentation is nonspecific in up to one third of patients. This is particularly true in young patients, whose diagnoses often end up being delayed and who therefore have higher rates of perforation. Although historically the diagnosis and decision to operate have been made on physical examination and laboratory results alone, nowadays most patients undergo imaging studies before going to surgery. The goals of imaging include decreasing the negative laparotomy rate, increasing the rapidity of diagnosis to reduce the rate of perforation, and identifying other alternative diagnoses.

There is much debate about appropriate imaging algorithms for suspected appendicitis. Many advocate ultrasound as the primary diagnostic test. However, skilled performance of pediatric ultrasound for appendicitis is not available at all or around the clock in many health centers, and this leads to performing CT. Some have advocated primary use of ultrasound, with CT being performed in questionable cases. There is also debate about the technical factors related to CT: intravenous contrast, oral contrast, rectal contrast, or noncontrast studies. Noncontrast enhanced MRI with rapid sequences is becoming an increasingly used tool in the diagnosis of appendicitis. Imaging algorithms for appendicitis will continue to vary among institutions. However, several factors may be helpful in making such decisions. Ultrasound is certainly more useful in girls and in patients of thin body habitus than in boys and patients who are fat. In girls, in whom ovarian causes of right lower quadrant pain (such as hemorrhagic cyst or torsion) are not uncommon, ultrasound is the first test of choice. CT is favored in cases in which perforated appendicitis is highly suspected, in evaluation for abscess, in postoperative evaluation, and in obese patients.

TABLE 5-3
Common Causes of Intestinal Obstruction in Older Children: Take AAIIMM

Adhesions
Appendicitis
Intussusception
Incarcerated inguinal hernia
Malrotation with volvulus
Meckel diverticulum

The technique of ultrasound evaluation of appendicitis is graded compression of the right lower quadrant using a high-frequency transducer. Findings include a shadowing, echogenic appendicolith (Figs. 5-29 and 5-30), a noncompressible, blind-ending tubular structure that measures greater than 6 mm in diameter (see Fig. 5-29), increased color Doppler flow to the appendix wall, or right lower quadrant fluid, phlegmon, or abscess (Fig. 5-31). A negative ultrasound examination in which a normal appendix is identified has a higher negative predictive value than does an otherwise negative examination in which the normal appendix is not identified.



▪ **FIGURE 5-29** **Nonperforated appendicitis demonstrated by ultrasound.**
Longitudinal view of the appendix shows a tubular structure *(A)* that was noncompressible. The appendix contains a shadowing appendicolith *(arrow)*.

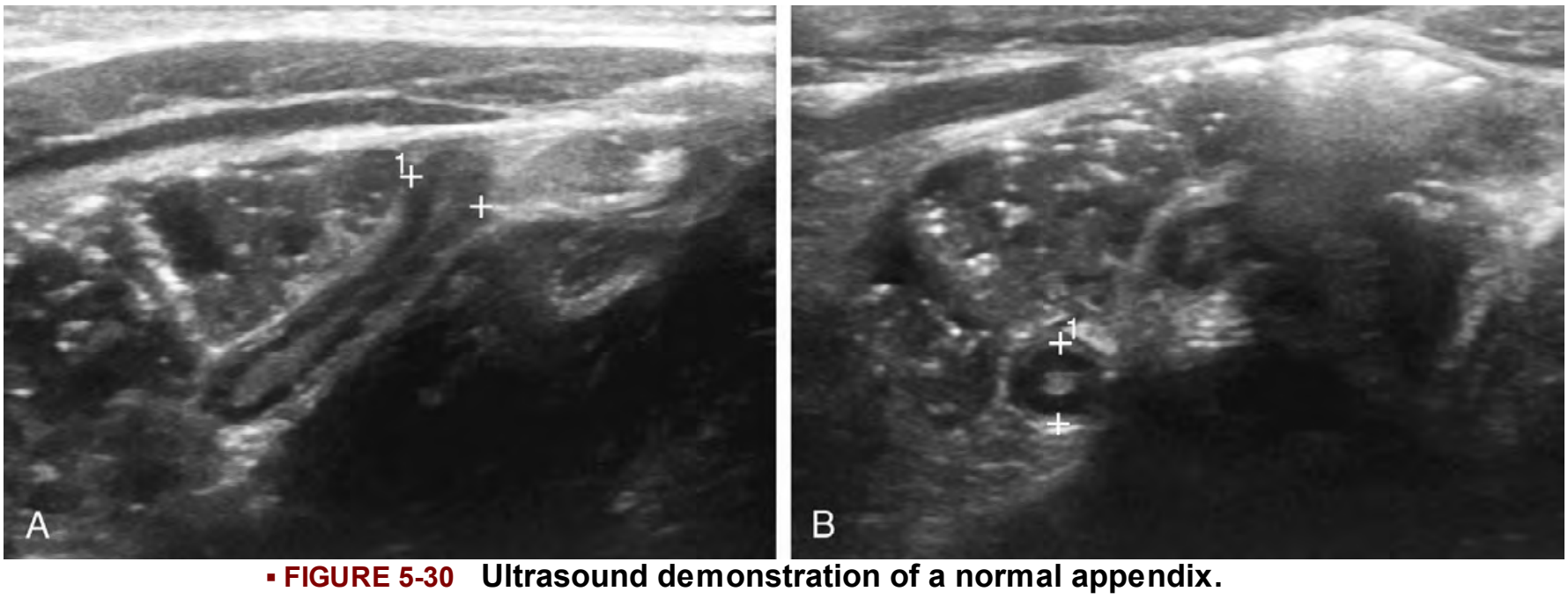
CT findings include identification of an appendicolith, a distended appendix, periappendiceal soft tissue stranding, and wall thickening of the cecum or terminal ileum. In cases of perforated appendicitis, findings of small bowel obstruction may be present, and inflammatory fluid collections may be seen in the right lower quadrant (see Fig. 5-31) or in the pelvic cul-de-sac.

Radiographs no longer play a primary role in the evaluation of a patient with suspected appendicitis. Radiographs demonstrate an appendicolith in 5% to 10% of patients (Fig. 5-32) with appendicitis. Other findings may include air-fluid levels within the right lower quadrant, splinting, and loss of the psoas margin. With perforated appendicitis there may be findings of small bowel obstruction, right lower quadrant extraluminal gas, and displacement of bowel loops from the right lower quadrant. Free intraperitoneal gas is extremely uncommon secondary to appendicitis.

Intussusception

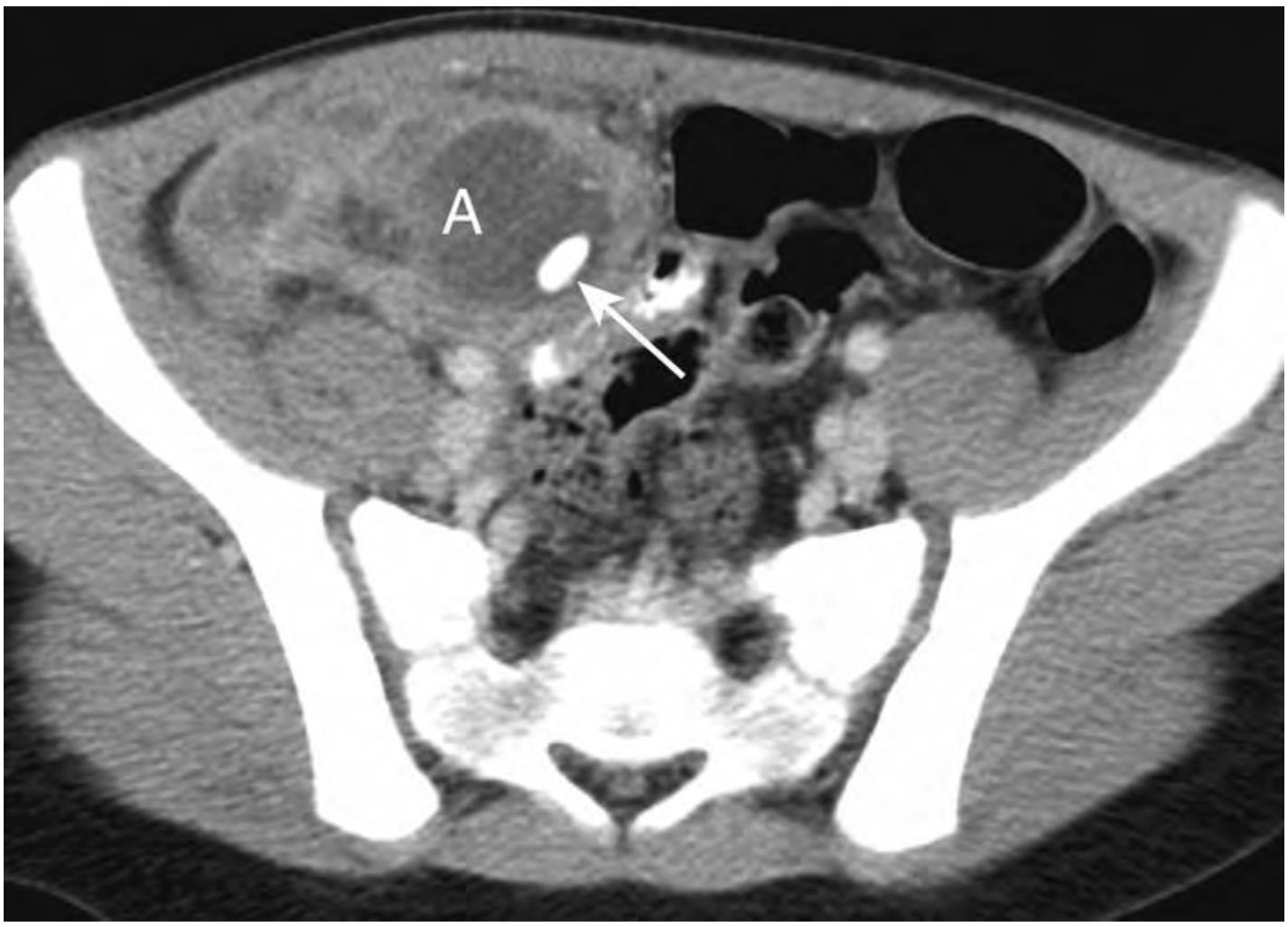
Intussusception occurs when forward peristalsis results in invagination of the more proximal bowel (the intussusceptum) into the lumen of the more distal bowel (the intussuscipiens) in a telescopelike manner. There are three primary types of intussusception: idiopathic ileocolic intussusception, intussuception secondary to pathologic lead points, and incidentally noted small bowel–small bowel intussusception.

In children, most cases of intussusception (90%) are idiopathic ileocolic. Therefore, when intussuception is referred to in children, this is the type that is generally meant. The idiopathic ileocolic intussusception is thought to be related to lymphoid hypertrophy in the terminal ileum secondary to viral disease. It is more common during the viral months of winter and spring and occurs more commonly in girls than in boys. The typical age for patients to present is between 3 months and 1 year (mean age 8 months), with almost all cases occurring before 3 years of age. If the child is less than 3 months of age or older than 3 years of age, a pathologic lead point should be increasingly suspected. Presenting symptoms include crampy abdominal pain, bloody (currant jelly) stools, vomiting, and palpable right-sided abdominal mass.



▪ **FIGURE 5-30** **Ultrasound demonstration of a normal appendix.**
A, Longitudinal view of the appendix shows a tubular structure which measured 5 mm in diameter *(cursers)*. **B,** Transverse view of appendix shows tubular structure again measuring 5 mm *(cursers)*.

Ultrasound has become the primary imaging study to evaluate children with suspected intussusception. On ultrasound the intussusception appears as a mass with alternating rings of hyperechogenicity and hypoechogenicity (Fig. 5-33). In the transverse plane the mass has been likened to a donut and in the longitudinal plane to a pseudokidney. When using ultrasound to evaluate for intussusception, it is important to image all four quadrants of the abdomen (Fig. 5-34). The intussusception can travel the entire route of the colon and therefore may be in any quadrant. If only the right lower quadrant is evaluated, the intussusception may be missed.



▪ **FIGURE 5-31** **Perforated appendicitis on CT.**
CT shows fluid collection *(A)* consistent with an abscess in the right lower quadrant. Within the abscess, there is a rounded calcification *(arrow)*, consistent with an appendicolith.



▪ **FIGURE 5-32 Appendicitis shown on radiography.**
Radiograph shows calcified appendicolith *(arrows)* in right lower quadrant, overlying the right sacrum.

The use of radiographs in the evaluation of intussusception has become less clear now that ultrasound is typically regarded as the primary imaging study. Radiographs are rarely completely normal in cases of intussusception. Findings include a paucity of gas within the right abdomen, the absence of an air-filled cecum or ascending colon, the meniscus of a soft tissue mass typically within the ascending or transverse colon (see Fig. 5-33), and small bowel obstruction. Because the key to identifying or excluding the diagnosis is related to seeing or not seeing gas in the right colon, left-side-down decubitus- and prone-positioned radiographs are helpful. If air-fluid levels are identified within the distal colon, intussusception is unlikely and viral gastroenteritis is a more likely cause of the patient's symptoms.

CT plays no role in the work-up of suspected intussusception. However, intussusception may be seen on CT when it is obtained for nonspecific abdominal pain, particularly in older children. When encountered on CT, ileocolic intussusception appears as a mass in the cecum or ascending colon with alternating rings of low and high attenuation (see Fig. 5-34).

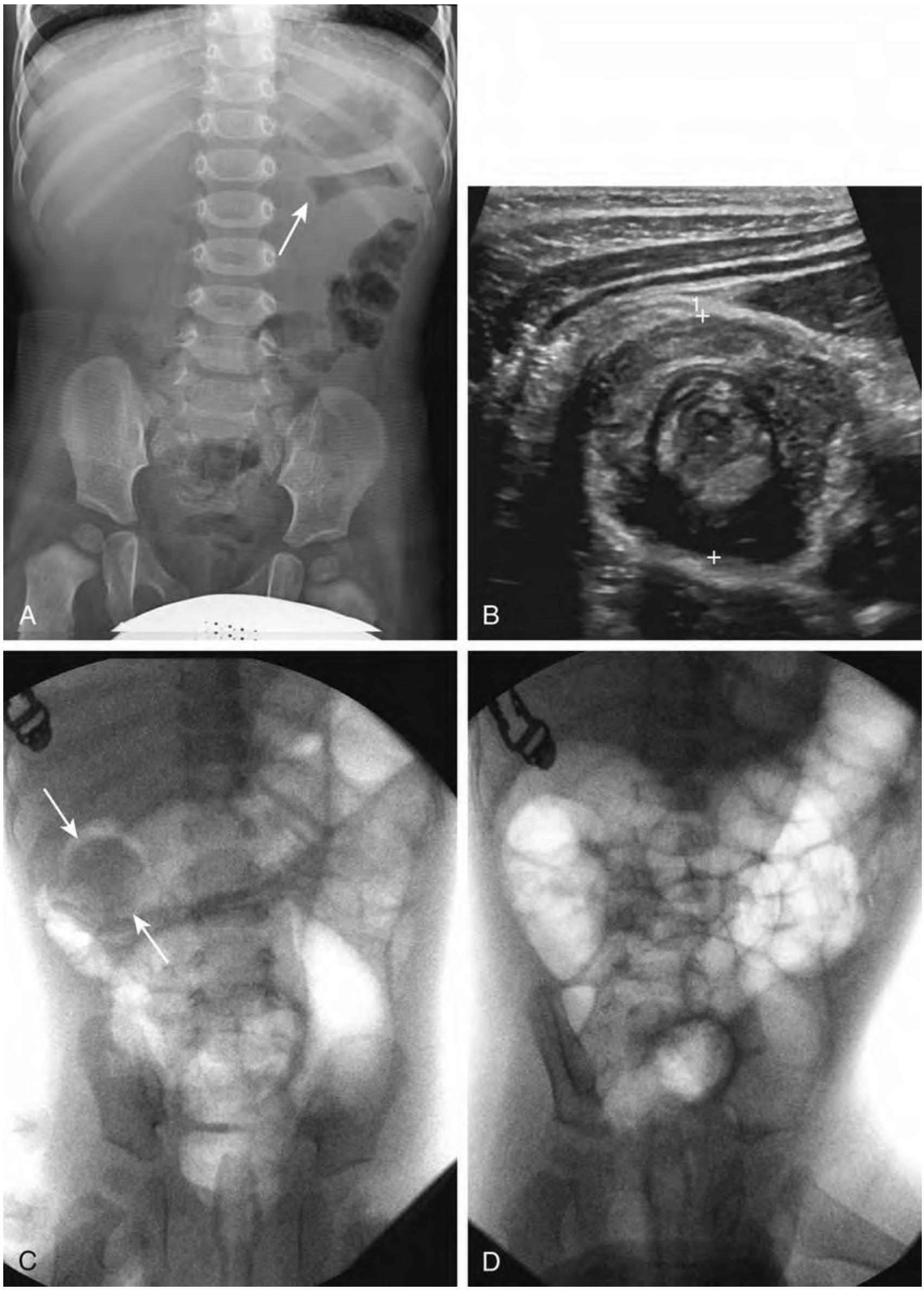
It is being increasingly recognized that small bowel–small bowel intussusceptions are often seen incidentally on ultrasound or CT examinations and that they are a normal, transient phenomenon (Fig. 5-35). However, there are pathologic causes of small bowel–small bowel intussusceptions as well, including lymphoma, Meckel diverticulum, duplication cyst, and Henoch-Schönlein purpura (see Fig. 5-35). Findings that help to favor incidental instead of pathologic intussusception include transient presence, lack of associated small bowel obstruction, and length less than 3.5 cm.

Imaging-Guided Reduction of Intussusception

There are several methods of increasing the pressure within the colon in an attempt to invert the intussusception into the normal position using imaging guidance. They include air insufflation with

fluoroscopic guidance, contrast enema with fluoroscopic guidance, and hydrostatic reduction with ultrasound guidance. Such methods are the primary therapy for intussusception; surgery is reserved for cases in which imaging-guided reduction fails. The choice of reduction method varies with the institution. At our institution, we use air reduction, which is described.

We use the following guidelines in preparing a patient for attempted reduction: adequate hydration with intravenous fluids if needed, a working intravenous port, abdominal examination by an experienced physician, and consultation with the pediatric surgery service. The members of the surgery service must at least know that the reduction is going to be attempted, and it is preferable that they have examined the patient. Some institutions give preprocedure antibiotics because of the risk of perforation, although the logic for this is not completely clear. Contraindications for attempting pressure reduction of an intussusception include peritonitis on physical examination or pneumoperitoneum on radiography (thus the argument for the use of radiographs in the work-up of intussusception). Findings that are not contraindications but are associated with decreased success include small bowel obstruction, long duration of symptoms (>24 hours), and lethargy. In a child with suspected intussusception, lethargy is a sign that the patient is potentially very ill. If a 1-year-old child does not fight you during placement of an enema tip, something is potentially wrong. Members of the surgical or emergency team should be present when performing an enema in a lethargic patient.



▪ **FIGURE 5-33** **Intussusception.**

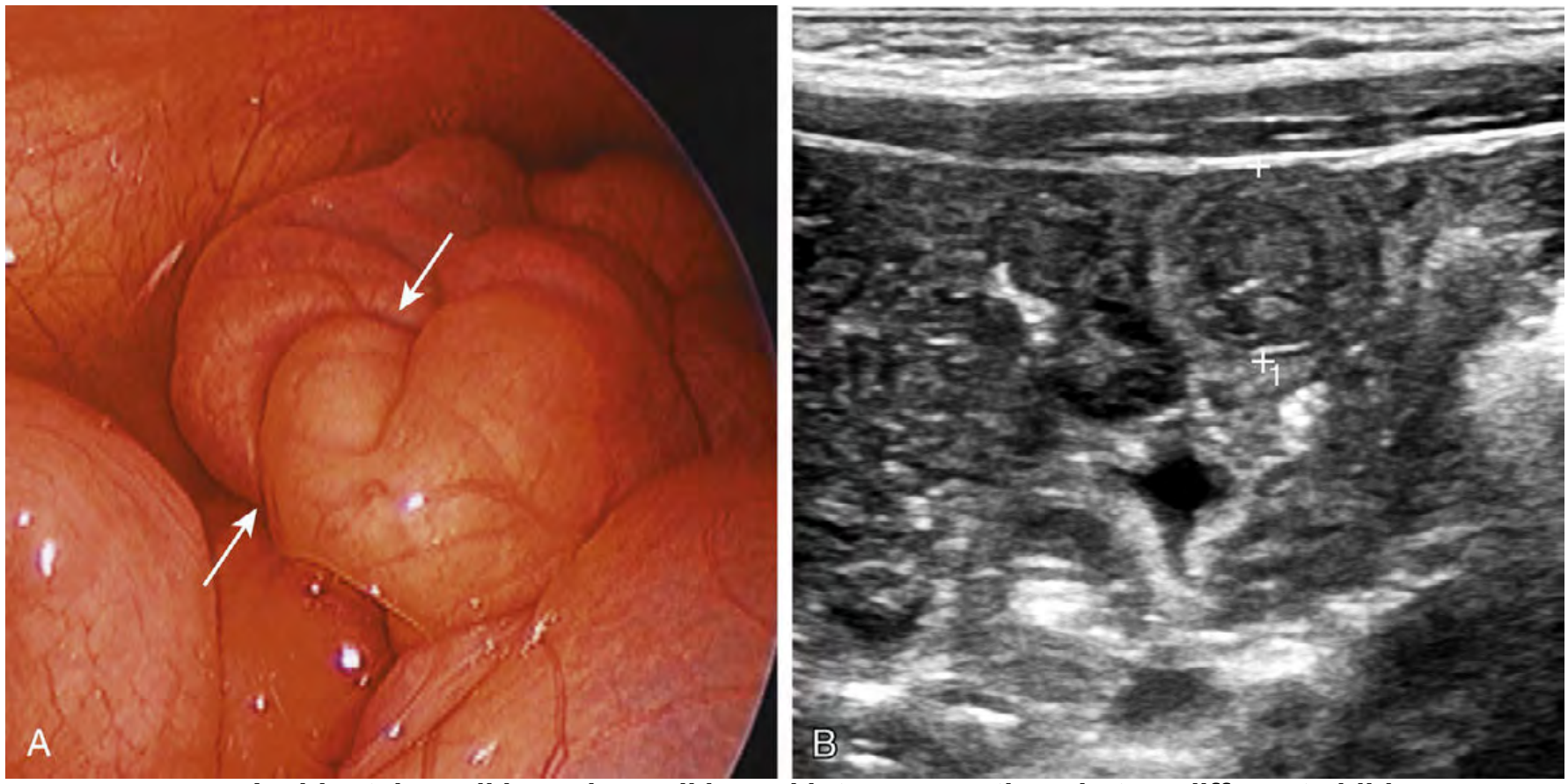
A, Radiograph demonstrates nonvisualization of gas in the ascending colon or cecum and a soft tissue meniscus *(arrows)* overlying the transverse colon, consistent with intussusception. **B,** Ultrasound shows concentric alternating hyperechogenic and hypoechogenic rings consistent with intussusception *(cursors)*. **C,** Image from reduction air-enema shows intussusception encountered in hepatic flexure as soft tissue mass *(arrows)*. **D,** Later image from enema shows resolution of soft tissue mass, as well as reflux of air into distal small bowel—meeting criteria for a successful reduction.



▪ **FIGURE 5-34** Intussusception shown on CT, which indicates a mass *(black arrows)* of alternating rings of density. Note that intussusception has progressed into the descending colon in the left lower quadrant of the abdomen. This illustrates why it is important to perform ultrasound in all four abdominal quadrants when evaluating for intussusception. Note the lymph node *(arrowhead)* in the intussusception, probably acting as lead point. Note no colon in right lower quadrant *(white arrow)*.

For air reduction the patient is immobilized and a Shiels intussusception air-reduction system (Custom Medical Products, Maineville, OH) is used. A key to success is generating an adequate rectal seal, so that sufficient colonic pressures can be obtained without leakage of air from the rectum. Some also use a Foley balloon catheter to help to create a rectal seal. Pressure generated within the colon should not exceed 120 mm Hg when the child is at rest. With air insufflation, the intussusception is encountered as a mass. The reducing intussusception moves retrograde to the level of the ileocecal valve. Criteria for successful reduction include resolution of the soft tissue mass and free reflux of gas into the small bowel (see Fig. 5-33).

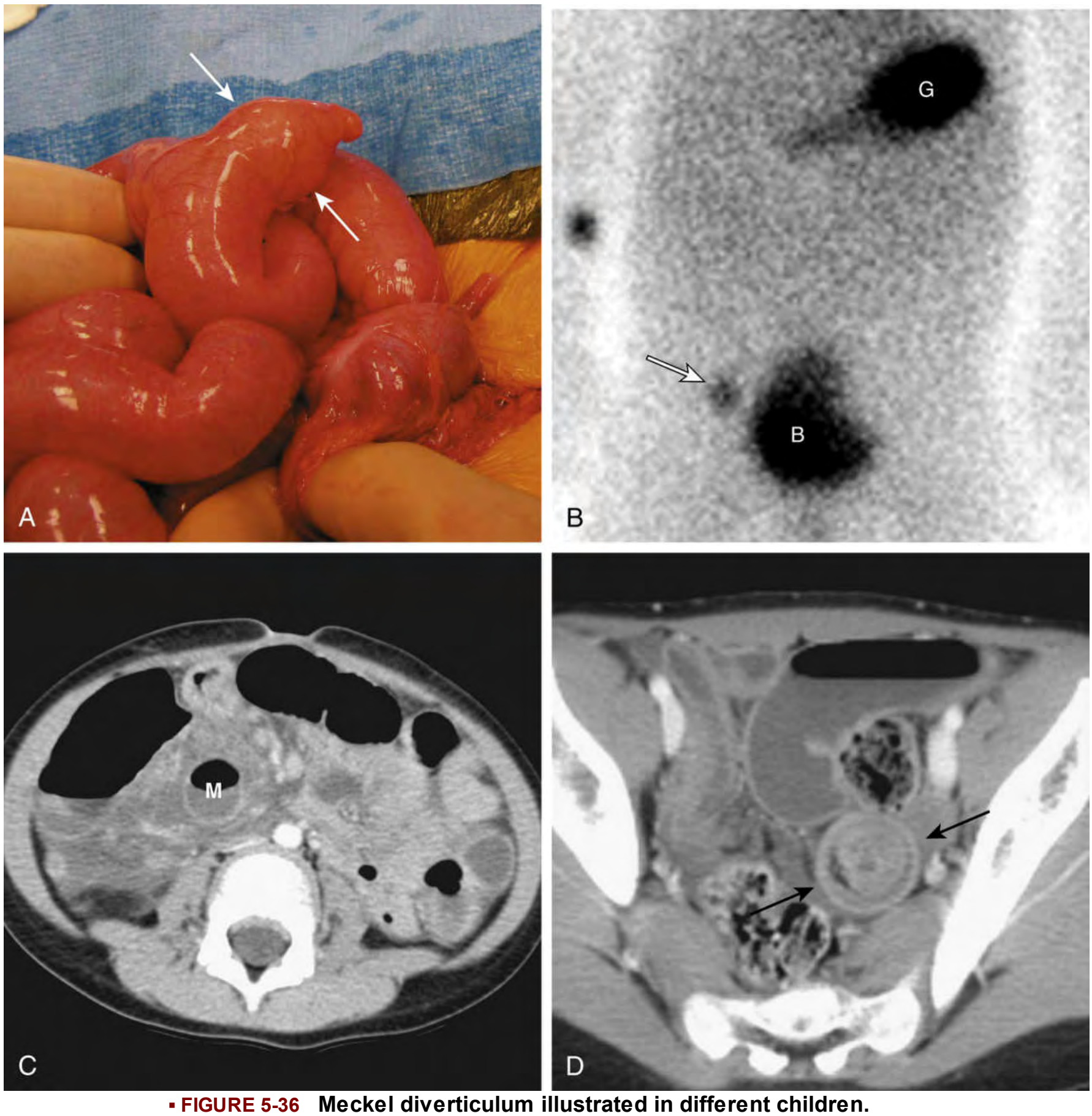
The "mass" often gets stuck at the ileocecal valve. In this case some radiologists give the child some time to rest and let the edema decrease and then repeat the reduction enema. This is often successful. Overall success rates for reduction enemas are approximately 70% to 90%. The risk for perforation is less than 0.5%. The risk for recurrent intussusception after a successful reduction is 5% to 10%, with most occurring within the first 72 hours after the reduction. Recurrence can be treated with repeated reduction enemas up to a recommended three times.



▪ **FIGURE 5-35 Incidental small bowel–small bowel intussusceptions in two different children.** **A,** Laparoscopic view of small bowel–small bowel intussusception *(arrows)*. **B,** Ultrasound shows small bowel–small bowel intussusception *(cursers)* in a child without abdominal pain. The lesion was shown to be intermittent.

Meckel Diverticulum

The omphalomesenteric duct is a fetal structure that connects the umbilical cord to the portion of the gut that becomes the ileum. Any or all of the structure can abnormally persist into postnatal life, resulting in cysts, sinuses, or fistulae from umbilicus to ileum. Most commonly, the portion adjacent to the ileal end persists and results in a Meckel diverticulum. Meckel diverticula can cause symptoms secondary to bleeding, focal inflammation, perforation, or intussusception (Fig. 5-36). Bleeding is a common complication and occurs secondary to the presence of ectopic gastric mucosa. Although most Meckel diverticula do not contain gastric mucosa, almost all of those associated with bleeding do. Therefore the imaging modality of choice to detect bleeding Meckel diverticula is nuclear scintigraphy with technetium (Tc) 99m pertechnetate, which accumulates in gastric mucosa. Such studies demonstrate foci of increased activity within the right lower quadrant of the abdomen (see Fig. 5-36).



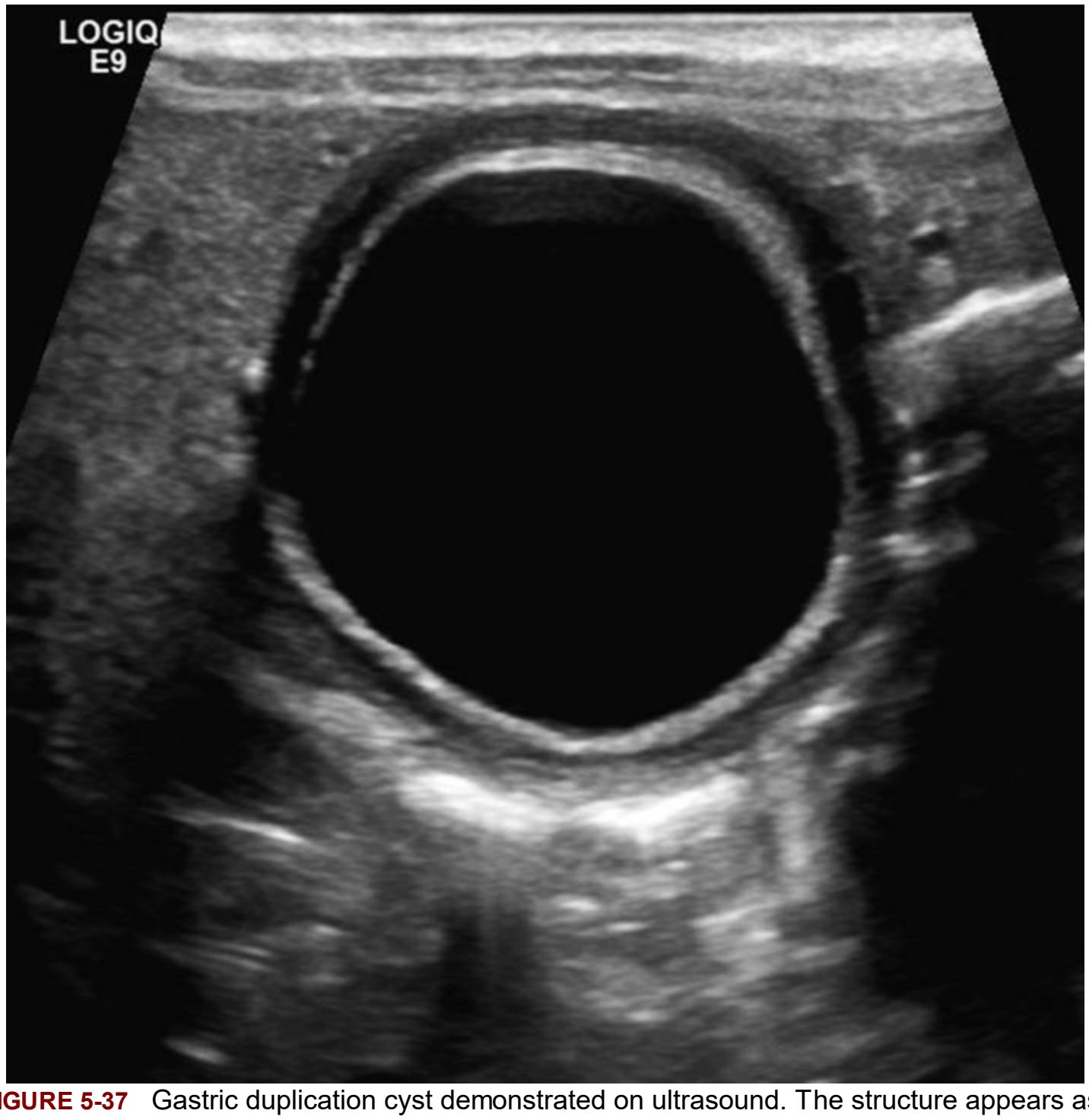
▪ **FIGURE 5-36** **Meckel diverticulum illustrated in different children.**
A, Surgical photograph showing Meckel diverticulum *(arrows)* arising from the ileum. **B,** Tc 99m pertechnetate image demonstrates abnormal increased activity *(arrow)* within the anterior right lower quadrant. Normal activity is seen within the stomach *(G)* and bladder *(B)*. **C,** Meckel diverticulitis. CT shows round structure *(M)* in right abdomen with surrounding inflammatory change. **D,** Intussusception secondary to Meckel lead point. CT shows bowel *(arrows)* with alternating high and low attenuation consistent with small bowel–small bowel intussusception.

In the authors' experience, Meckel diverticulum are encountered on the CT evaluation of pediatric abdominal pain more commonly then those who present with bleeding. On CT there are three patterns associated with the diagnosis of Meckel diverticulum: a lower abdominal cystic mass with surrounding inflammatory changes, small bowel obstruction without other findings, or small bowel–small bowel intussusception often associated with small bowel obstruction (see Fig. 5-36).

Gastrointestinal Duplication Cysts

Gastrointestinal duplication cysts are congenital lesions that are typically round, attached to the gastrointestinal tract, and do not communicate with the gastrointestinal lumen. The most common locations are the terminal ileum and distal esophagus. These cysts may present because of a palpable mass, compression of adjacent anatomic structures, bowel obstruction, or ulceration and perforation. They are most likely to be present during the first year of life. Duplication cysts have a typical

ultrasound appearance. They appear as a cystic mass with a "bowel wall signature" on ultrasound. The cyst wall demonstrates alternating hypoechoic and hyperechoic layers that correlate with the mucosa (hyperechoic) and muscular layers (hypoechoic) (Fig. 5-37). Much less commonly, duplications can appear tubular rather than round and can communicate with the gastrointestinal lumen.

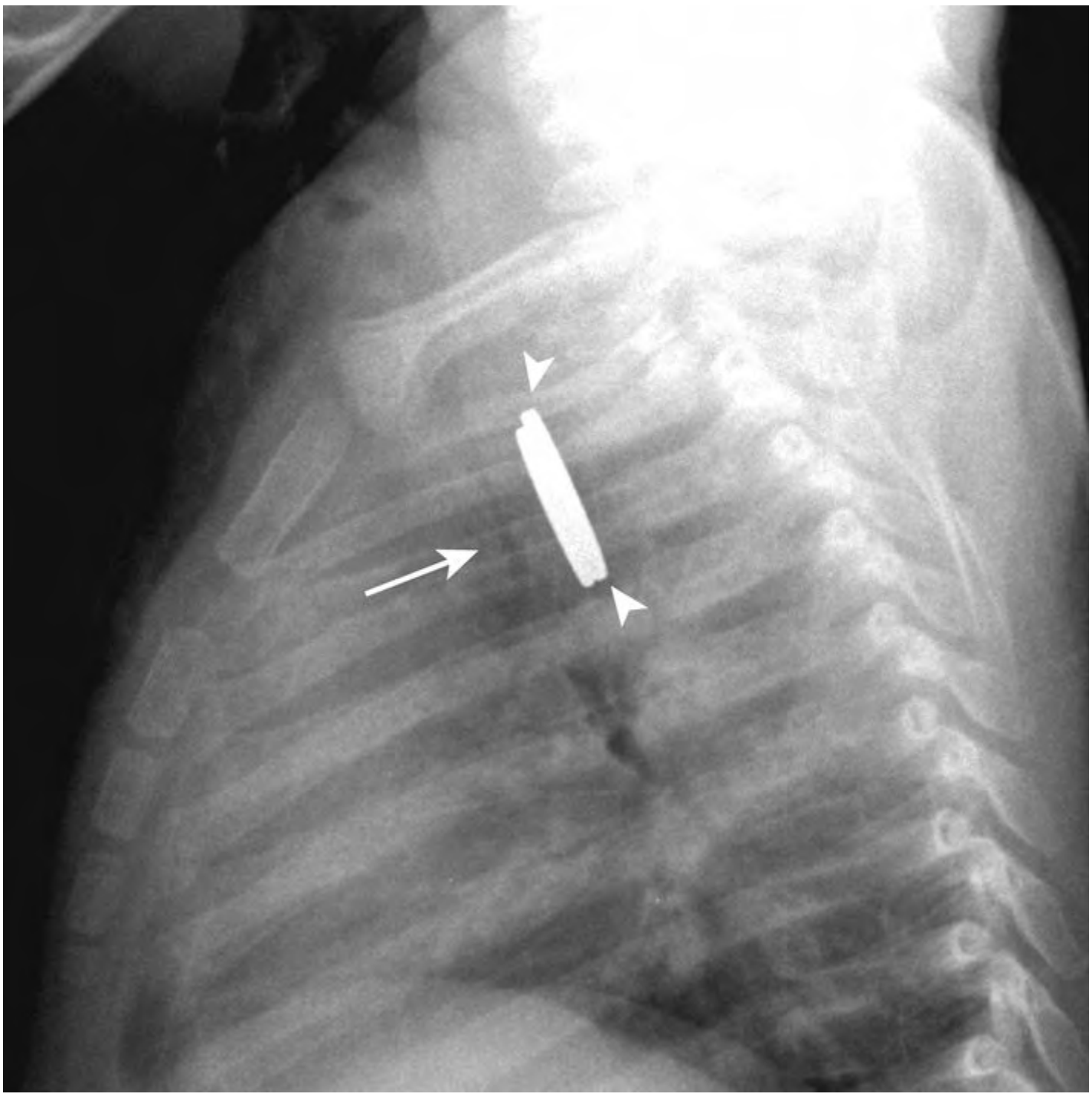


▪ **FIGURE 5-37** Gastric duplication cyst demonstrated on ultrasound. The structure appears as a cystic lesion with bowel wall signature of alternating hyperechoic and hypoechoic rings, adjacent to liver.

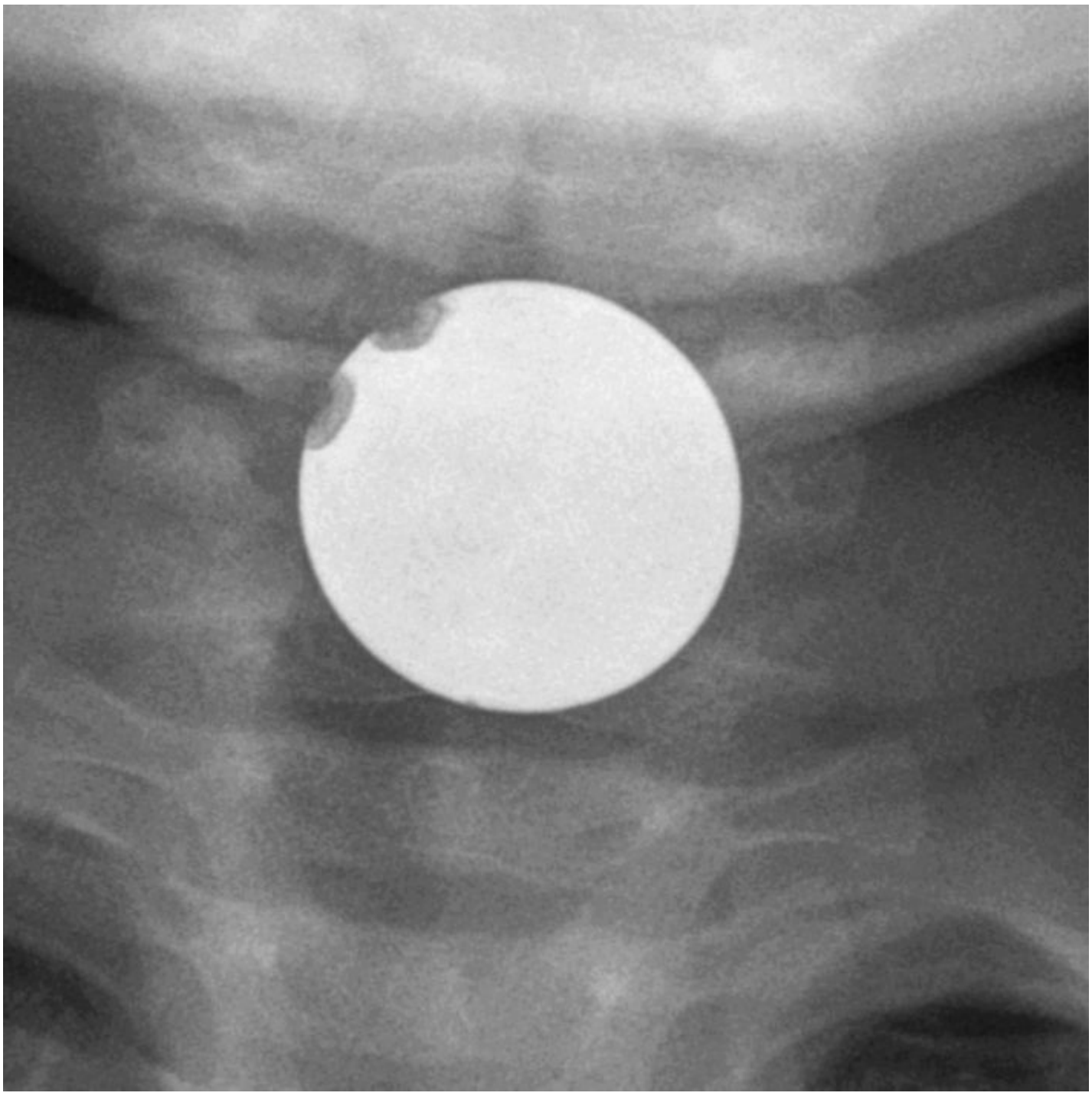
▪ Swallowed Foreign Bodies

The majority of foreign bodies swallowed by children pass through the gastrointestinal tract without complication. If the initial series of radiographs demonstrates that the foreign body lies within the stomach or more distally in the gastrointestinal tract, follow-up films are not indicated unless the child develops obstructive symptoms or peritonitis. However, foreign bodies may lodge within the esophagus. The most common site of esophageal foreign bodies, and also the least likely area from which foreign bodies will spontaneously pass, is the proximal esophagus at the thoracic inlet. Because, amazingly, many infants with esophageal lodgment of foreign bodies are initially asymptomatic, radiographs should be obtained when ingestions are witnessed, regardless of whether symptoms are present, to confirm that the foreign body has passed into the stomach.

The most common foreign body to lodge in the esophagus is a coin (Figs. 5-38 and 5-39). Chronic esophageal foreign bodies may result in complications, such as a tracheoesophageal fistula. They may also cause an inflammatory mass that leads to compression of the trachea. Such foreign bodies may present with respiratory rather than gastrointestinal symptoms. With chronic foreign bodies, inflammation can be seen on lateral radiographs as increased distance caused by soft tissue between the coin and the airway, anteriorly.



▪ **FIGURE 5-38** **Coins lodged within the esophagus at the thoracic inlet.**
Lateral view shows two coins *(arrowheads)* in esophagus posterior to airway. Note that the two coins can be seen as adjacent metallic objects with a step off between coins. Note that there is soft tissue thickening between the coin and airway, as well as compression of the adjacent trachea *(arrow)*, which suggest chronic inflammation.

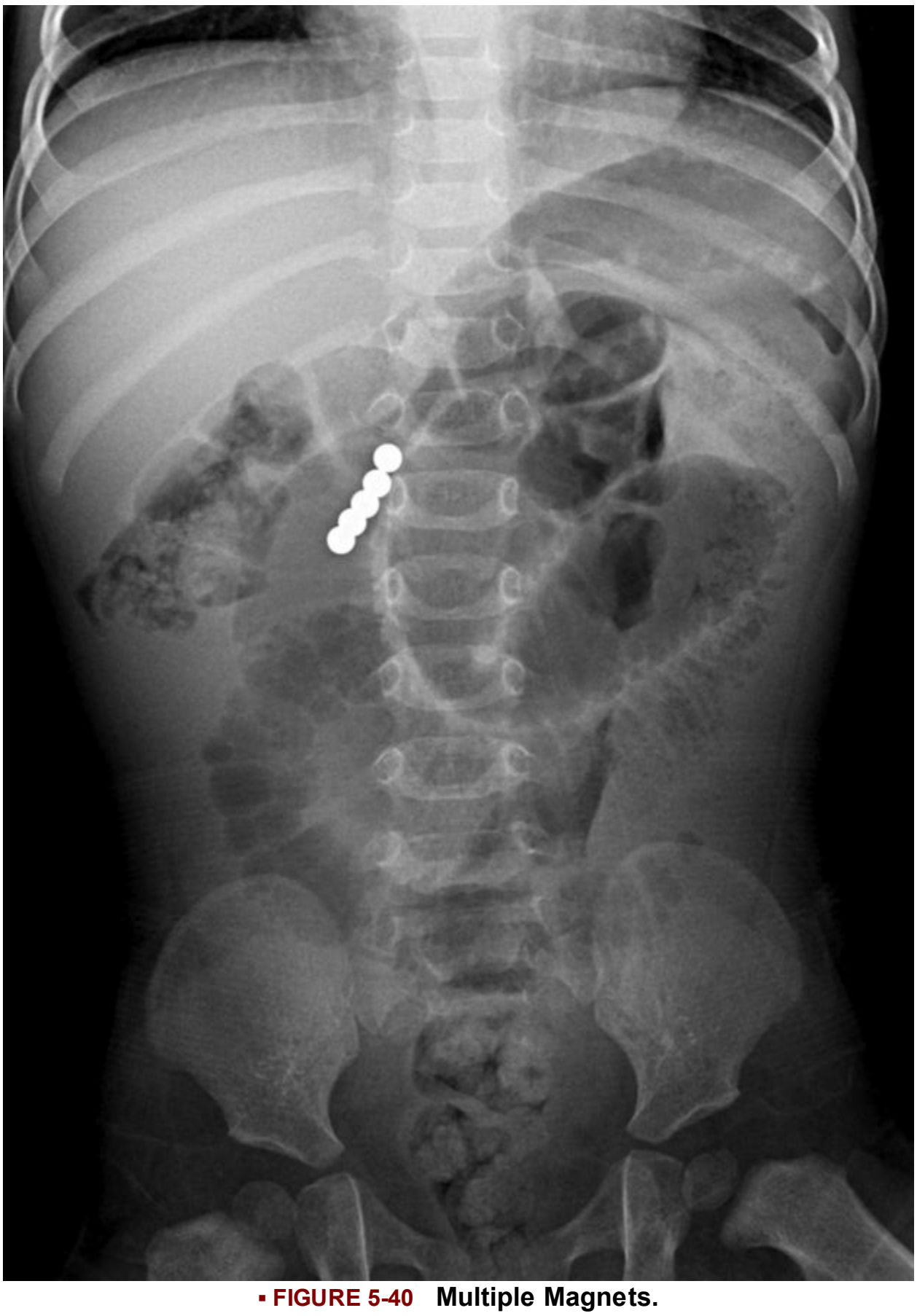


▪ **FIGURE 5-39** **Coin lodged at thoracic inlet.**
Note that there are erosions on the external portions of the metallic disc. This can be seen with lodged post-1982 American pennies, most likely in this case related to acid reflux.

Lodged esophageal foreign bodies may also be a sign of underlying pathology, such as a stricture or vascular ring that did not allow the foreign body to pass. Esophageal strictures can occur secondary to a number of causes in children, including corrosive ingestion, previous esophageal atresia repair, epidermolysis bullosa, and gastroesophageal reflux. Such strictures are often dilated using balloon catheters and fluoroscopic guidance.

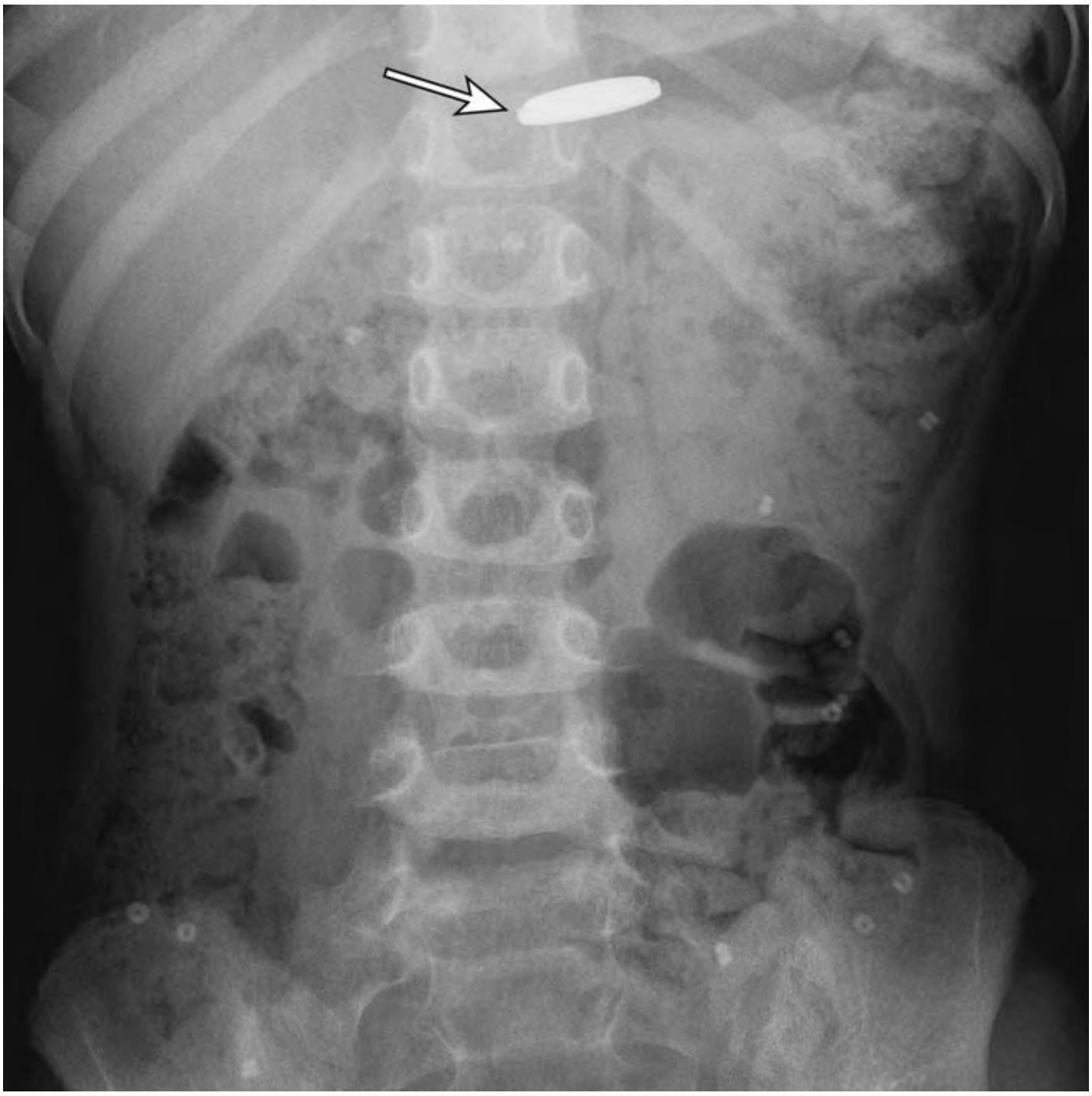
There are several circumstances and types of foreign bodies that deserve special mention: zinc pennies, multiple magnets, and button batteries.

- *Zinc pennies:* Post-1982 U.S. pennies are constructed with a zinc-based core and copper coding (rather than the pre-1982 solid copper pennies), and if retained in the stomach, the zinc-based coins can corrode, allowing the zinc to escape and react with the hydrochloric acid in the stomach to create a reaction that can lead to gastric ulceration. Radiography of such coins retained in the stomach can show irregular margins and developing radiolucent holes in the coins (see Fig. 5-39). If a penny is retained in the stomach and the patient is symptomatic, the coin should be removed endoscopically.



▪ **FIGURE 5-40** **Multiple Magnets.**
Radiograph shows multiple radiodense structures adjacent to each other, consistent with multiple swallowed magnets. There is an associated small bowel obstruction.

- *Multiple magnets:* Reports have shown that small colorful pieces of certain toys that contain magnets can be swallowed by children. When multiple magnets are swallowed, they can become attracted to each other across the walls of the small bowel, and this may lead to ischemia, necrosis, obstruction, and perforation (Fig. 5-40). It should be considered a surgical emergency when identified. When multiple metallic densities are seen lining up in tandem, multiple magnets should be suspected.
- *Button batteries:* Button batteries are disk-shaped batteries, such as those used in cameras, watches, and hearing aids. When swallowed by children, these batteries can cause caustic injury to the mucosa, particularly when lodged in the esophagus. The shape of these batteries is slightly different from that of a coin (Fig. 5-41). On a lateral view, the front edge of the battery is beveled with a central protrusion. In other words, the central portion is thicker than the peripheral portion. On a frontal view of a coin, the periphery may appear to have two circular edges. These batteries may develop corrosive holes if they are present internally for some time. The potential presence of a button battery should be communicated to the caregivers immediately to allow for expedited removal.

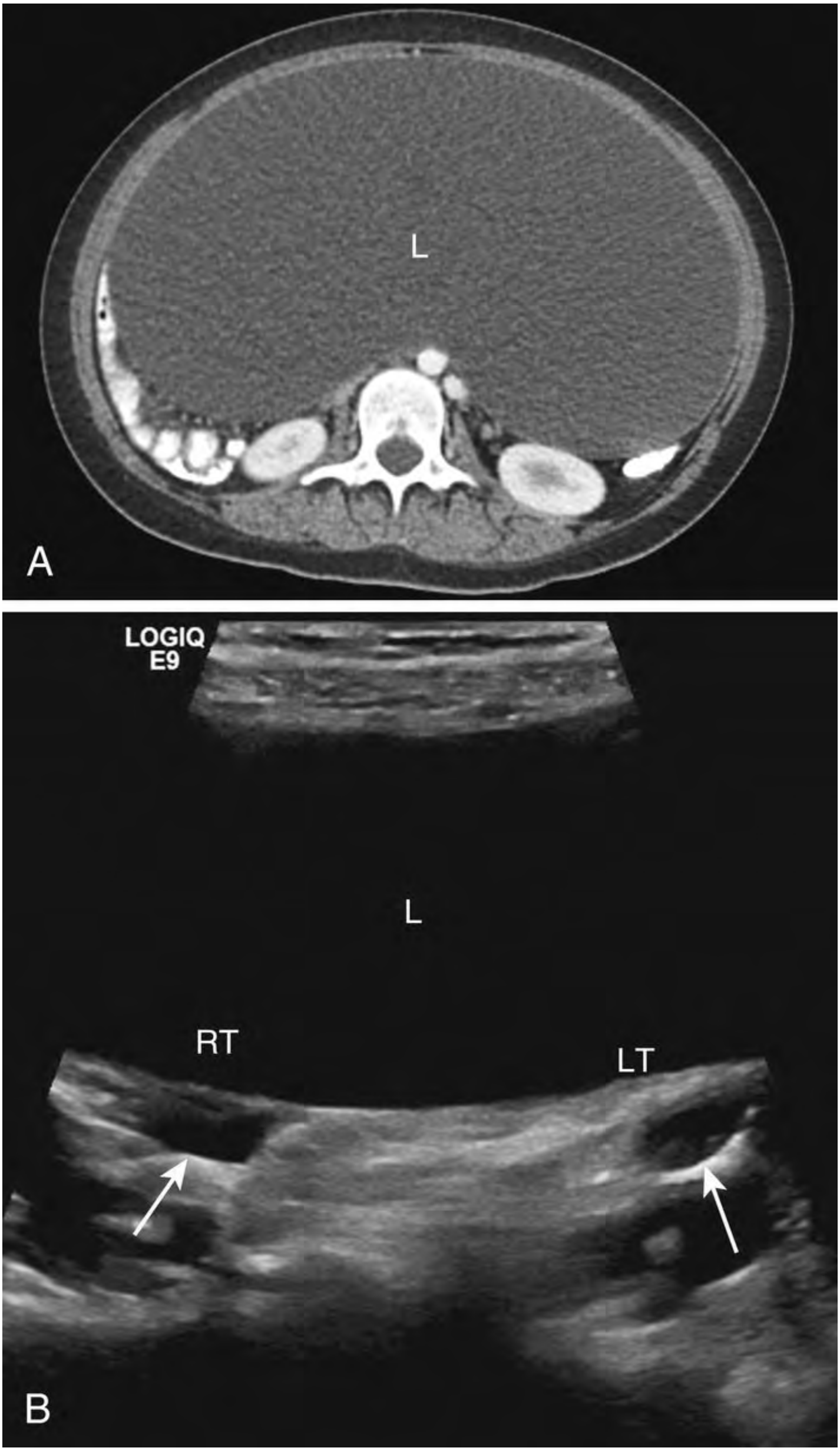


▪ **FIGURE 5-41** **Button battery.**
Frontal radiograph shows radiopaque round structure in stomach. On close inspection, the edge of the circle is beveled *(arrow)*, suspicious for a button battery. Note multiple other smaller metallic ingested foreign bodies in more distal bowel.

▪ Abnormalities of the Pediatric Mesentery

The mesentery does not have easily recognizable boundaries on imaging. Therefore localization of an abnormality to the mesentery can be difficult. The relative paucity of mesenteric fat seen in the pediatric population can make detection and localization of processes in the mesentery even more difficult than in adults, in whom fat is typically more abundant. The following criteria are helpful in localizing a process to the mesentery in children: (1) partial or complete envelopment of the SMA or SMV, (2) peripheral displacement of jejunal or ileal bowel loops, or (3) extension of the process from superocentral to inferoperipheral in a conelike manner. Mesenteric disorders are divided into the specific patterns of involvement that can readily be identified by imaging: developmental abnormalities of mesenteric rotation, diffuse mesenteric processes, focal mesenteric masses, and multifocal mesenteric masses. Abnormalities of mesenteric rotation have been discussed.

Processes that can involve the mesentery diffusely include edema, hemorrhage, and inflammation. Diffuse mesenteric processes characteristically demonstrate replacement of mesenteric fat by soft tissue attenuation with resultant loss of vascular definition. Focal masses within the mesentery in the pediatric population can be secondary to lymphoma, mesenteric cysts, desmoids, teratomas, and lipomas. Mesenteric cysts, also known as lymphatic malformations, are developmental anomalies in which focal lymphatic channels fail to establish connections with the central lymphatic system. Lymphatic malformations are often multiseptated and quite large (Fig. 5-42).



▪ **FIGURE 5-42** **Mesenteric lymphatic malformation (mesenteric cyst).**
A, CT shows large unilocular cyst *(L)* in central abdomen displacing the left and right colon peripherally. **B,** Ultrasound shows anechoic cyst *(L)* to be separate from both the left *(LT)* and right *(RT)* ovaries *(arrows)*. This excluded the other main differential consideration in this case—a large ovarian cyst.

Multifocal mesenteric masses most commonly represent lymphadenopathy. On imaging studies such

as CT, mesenteric lymph nodes are considered abnormal if they are greater than 5 mm in diameter. Mesenteric lymphadenopathy can be a manifestation of either a malignant neoplastic or an inflammatory process. Malignant entities include lymphoma, lymphoproliferative disorder, and metastatic disease. Lymphomatous involvement of the mesentery most often occurs in association with non-Hodgkin disease and usually involves both the mesentery and retroperitoneum. Most cases of non-Hodgkin lymphoma that involve the abdomen demonstrate lymphadenopathy rather than parenchymal masses. Mesenteric lymphadenopathy can also be caused by infectious disorders, such as tuberculosis, cat-scratch disease, or fungal infection. Central low attenuation with peripheral enhancement favors an inflammatory over a neoplastic cause. Central low attenuation of lymph nodes has been described as characteristic of tuberculosis and is present in as many as 60% of cases. With tuberculosis, it has been suggested that the mesenteric adenopathy is often more pronounced relative to the degree of retroperitoneal adenopathy.

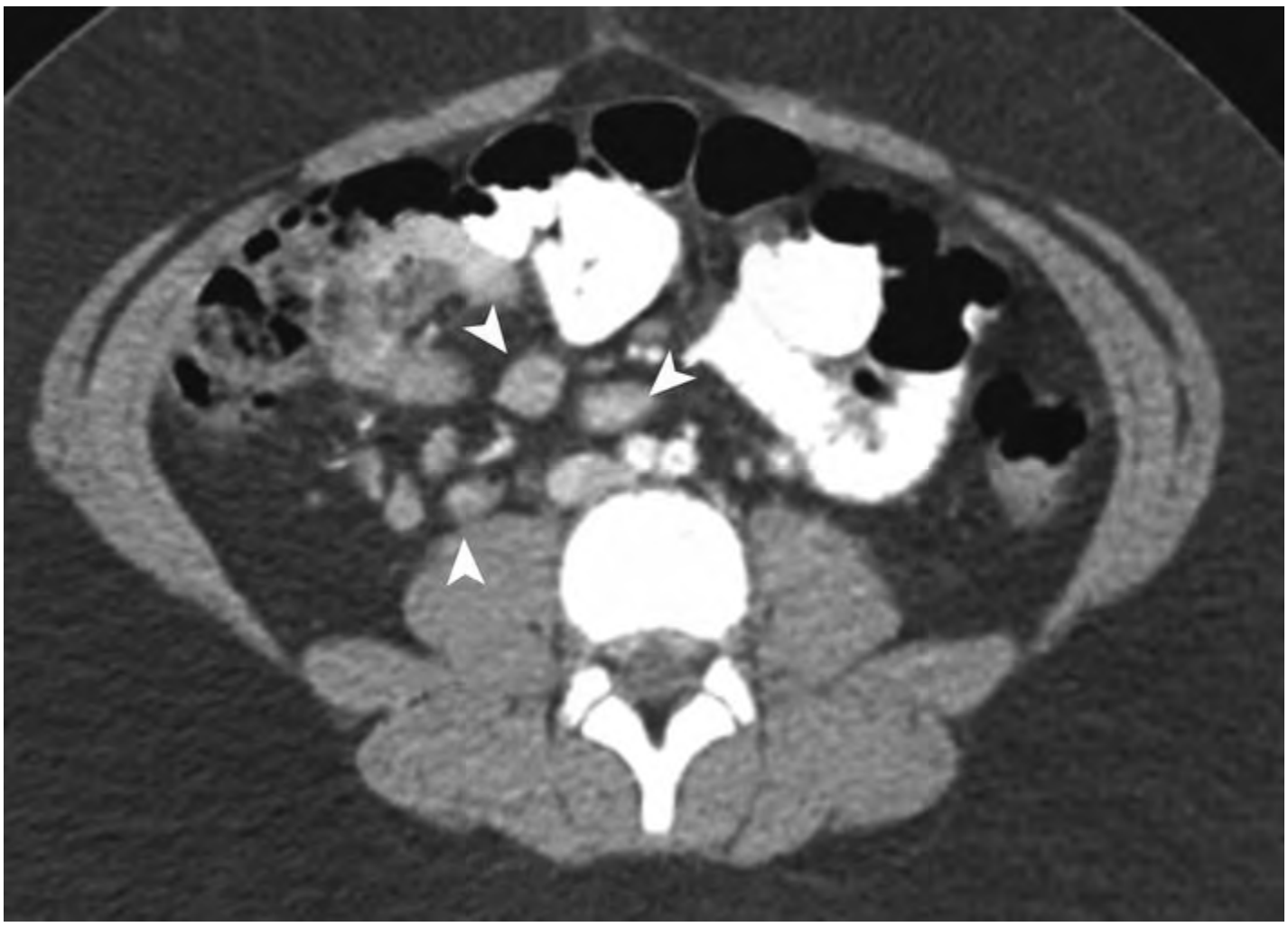
Note that visualization of prominent but smaller than 5-mm lymph nodes in the inferior mesentery and right lower quadrant is common in children and has no clinical significance.

Mesenteric Adenitis

Mesenteric adenitis is a clinical entity that is related to benign inflammation of the mesenteric lymph nodes, sometimes associated with enteritis. Patients present with nausea, vomiting, diarrhea, right lower quadrant abdominal pain and tenderness, fever, and leukocytosis. Because of the marked overlap in clinical symptomatology, differentiation between appendicitis and mesenteric adenitis can be extremely difficult, if not impossible, on a clinical basis. The diagnosis is often made at laparotomy and nontherapeutic appendectomy. Ultrasound or CT findings include enlarged and clustered lymphadenopathy in the bowel mesentery just anterior to the right psoas muscle (78%) or in the small bowel mesentery (56%) or ileal wall thickening (33%) and inflammatory changes in the mesentery (Fig. 5-43). The presence of diffuse mesenteric lymph nodes and the absence of findings of appendicitis suggest mesenteric adenitis as the cause of right lower quadrant pain. When the diagnosis is made at imaging, unnecessary surgical exploration may be avoided.

▪ Neonatal Jaundice

Some degree of "physiologic jaundice," or hyperbilirubinemia, is common in neonates and is related to physiologic destruction of red blood cells in the polycythemic newborn. Jaundice that persists beyond 4 weeks of age is due to biliary atresia or neonatal hepatitis in 90% of cases.



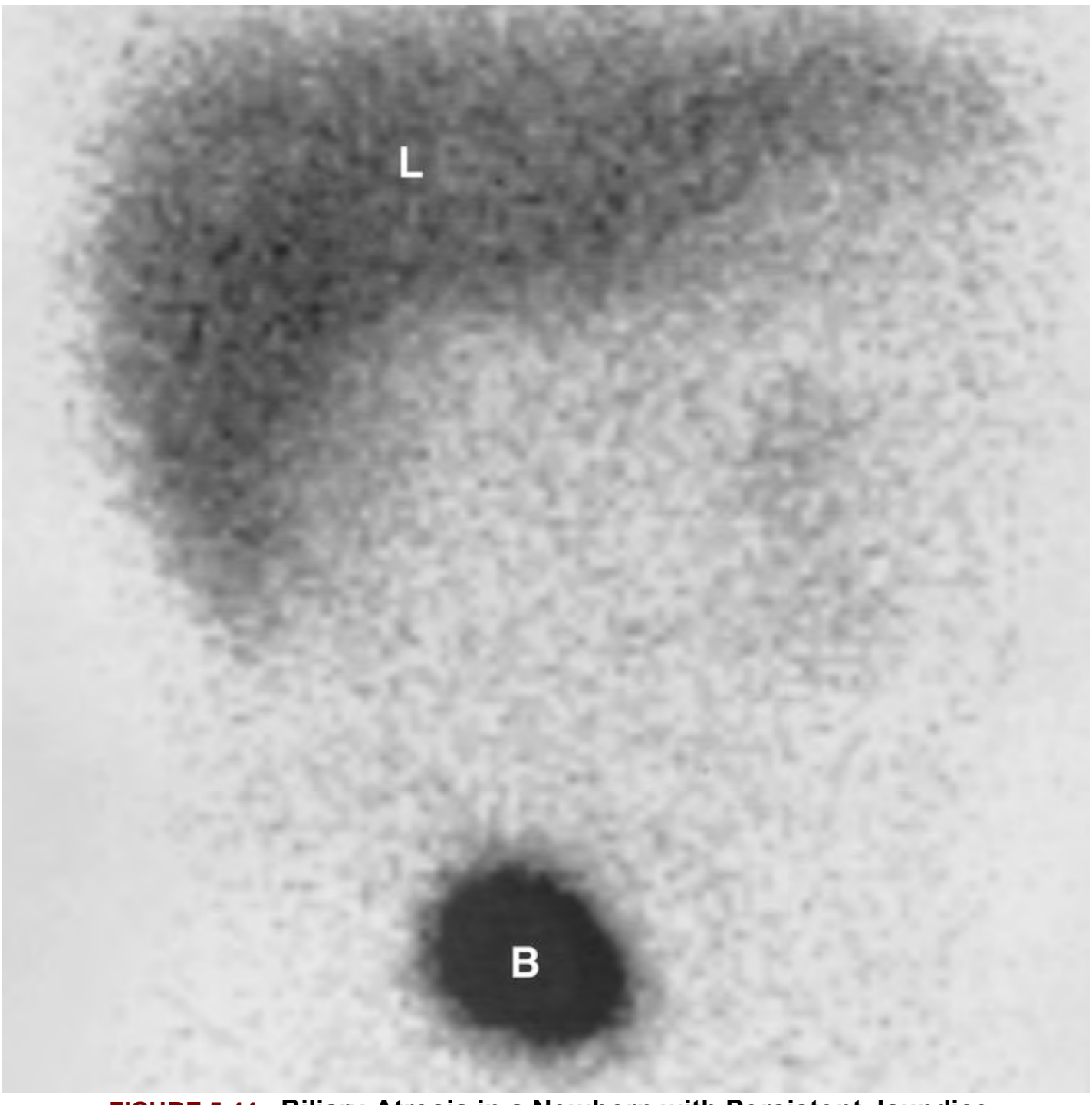
▪ **FIGURE 5-43** **Mesenteric adenitis in an obese teenage girl with right lower quadrant pain.** CT shows a cluster of lymph nodes in the mesentery *(arrowheads)*, centrally located in relationship to adjacent bowel.

Biliary Atresia versus Neonatal Hepatitis

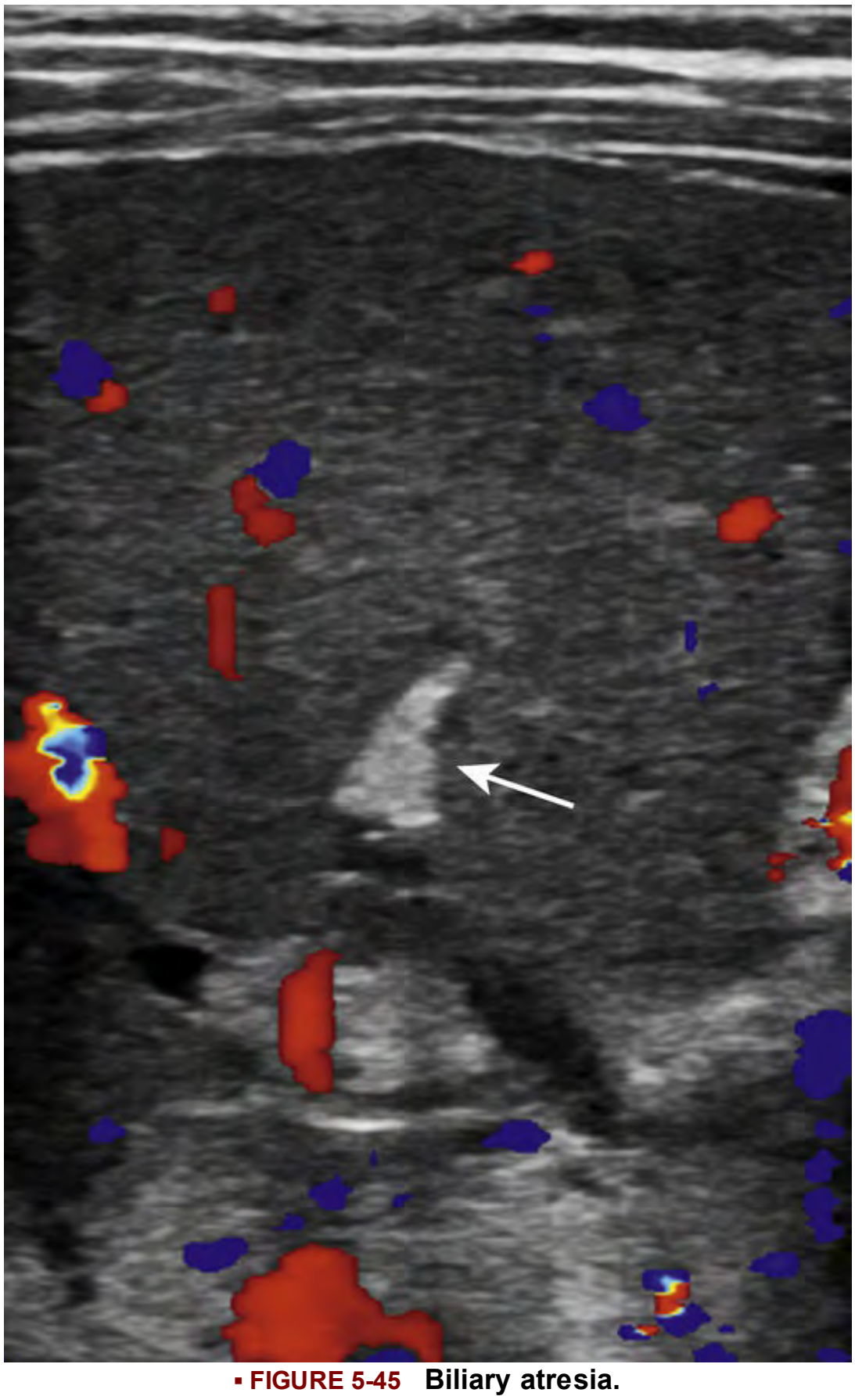
It is important to identify children with biliary atresia (Figs. 5-44 and 5-45) because they can benefit from early surgical intervention (before 3 months of age). In contradistinction, it is essential to avoid unnecessary laparotomies in patients with neonatal hepatitis. Because the two entities have similar clinical, laboratory, and pathologic findings, diagnostic imaging plays an important role in differentiating them. In biliary atresia there is congenital obstruction of the biliary system with bile duct proliferation intrahepatically and focal or total absence of the extrahepatic bile ducts. Cirrhosis ultimately develops unless there is corrective surgery. There is an association with the abdominal heterotaxy syndromes, such as polysplenia, and with trisomy 18.

Ultrasound is the initial imaging procedure in neonates with jaundice. It can exclude the presence of choledochal cysts and dilatation of the bile duct system due to other causes of obstruction. Absence of a visualized gallbladder is suggestive of biliary atresia, although 20% of normal patients have small or barely visible gall bladders. The finding of a normal or enlarged gall bladder helps to exclude the diagnosis of biliary atresia and therefore is supportive of the diagnosis of neonatal hepatitis. Visualization of a triangular echogenic structure adjacent to the main portal vein is called the *triangular cord sign* (see Fig. 5-45) and is thought to be the remnant of the common bile duct in biliary atresia. The hepatic parenchyma and intrahepatic bile ducts usually appear normal in patients with neonatal hepatitis and biliary atresia.

Hepatobiliary scintigraphy with Tc 99m-iminodiacetic acid derivatives can be one of the most reliable ways to differentiate between neonatal hepatitis and biliary atresia. The radiopharmaceutical is usually administered after pretreatment with oral phenobarbital. Normally, radiopharmaceutical uptake and clearance by hepatocytes exceeds cardiac blood pool tracer activity. Radiotracer can normally be visualized within the biliary tree and intestines 15 minutes after administration. Classically described scintigraphic appearance of neonatal hepatitis includes delayed uptake of radiotracer by hepatocytes, slow clearance of blood pool radiotracer, but eventual radiotracer excretion in the intestines. In biliary atresia, radiotracer uptake and clearance by hepatocytes are adequate, with prominent hepatic activity identified, but the tracer never reaches the gastrointestinal tract, even on 24-hour delayed imaging (see Fig. 5-44).



▪ **FIGURE 5-44** **Biliary Atresia in a Newborn with Persistent Jaundice.**
Radionuclide hepatobiliary image obtained at 4 hours shows prompt uptake in liver *(L)* and faint activity in kidneys. No activity is present in the gastrointestinal tract. Radioactivity is seen in the urinary bladder *(B)*.



▪ **FIGURE 5-45** **Biliary atresia.**
Doppler ultrasound shows a triangular echogenic structure *(arrow)* adjacent to the porta hepatis, consistent with a *triangular cord sign* of biliary atresia.

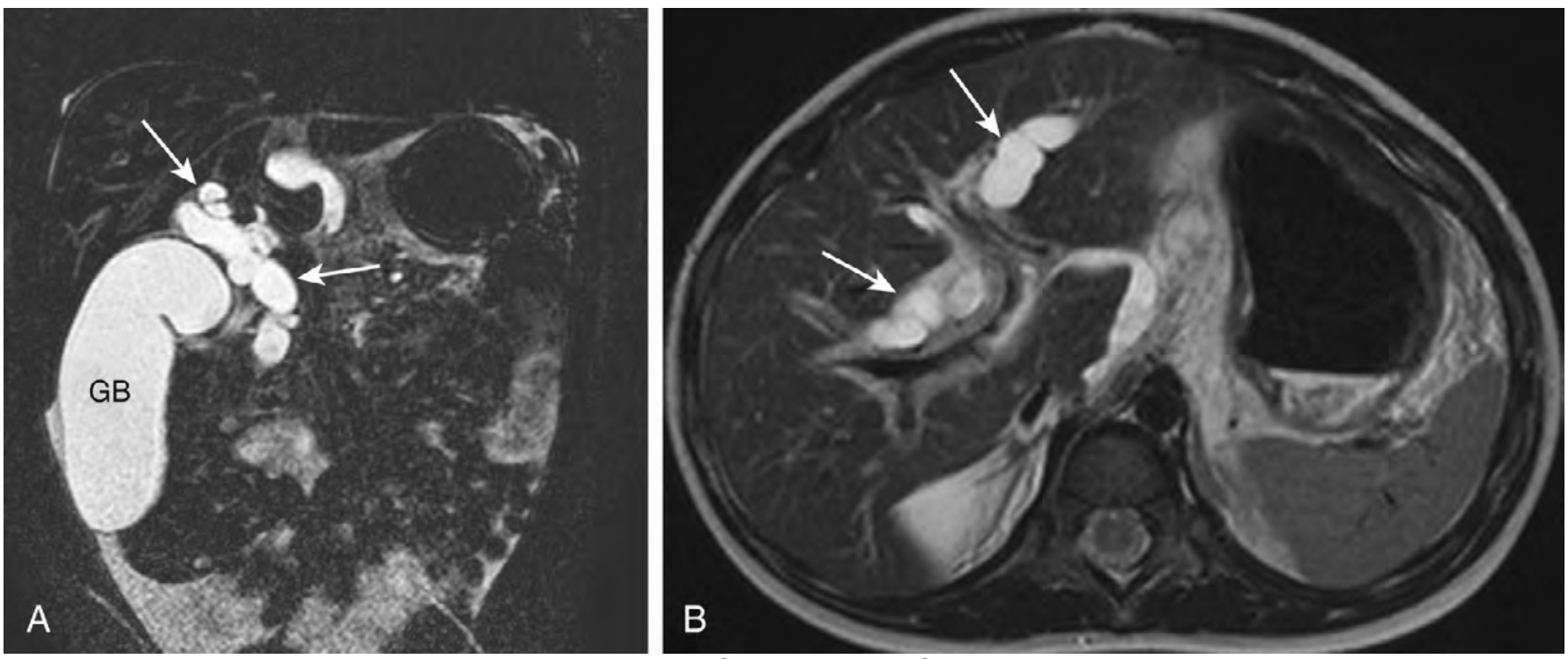
Choledochal Cyst

Choledochal cyst is defined as a local dilatation of the biliary ductal system and is categorized into types based on the anatomic distribution of dilatation. These types include localized dilatation of the common bile duct below the cystic duct, dilatation of the common bile and hepatic ducts, localized cystic diverticulum of the common bile duct, dilatation of the distal intramedullary portion of the common bile duct (choledochocele), and multiple cystic dilatations involving both the intrahepatic and extrahepatic bile duct radicals (Caroli disease). Choledochal cysts are uncommon, and the cause is unknown. They most commonly present early in life with jaundice (80%), abdominal mass (50%), or abdominal pain (50%). Ultrasound demonstrates a cystic mass in the region of the porta hepatis that is separate from an identifiable gallbladder (Fig. 5-46). The presence of a dilatated common bile duct or cystic duct or visualization of the hepatic duct directly emptying into the cystic mass confirms the diagnosis. In cases in which there is a nonspecific cyst in the region of the porta hepatis, hepatobiliary scintigraphy can be used to demonstrate radiotracer accumulation within the cyst, confirming the diagnosis.

▪ Liver Masses

Hepatic masses constitute only 5% to 6% of all intraabdominal masses in children, and primary hepatic neoplasms constitute only 0.5% to 2% of all pediatric malignancies. Primary hepatic neoplasms are the third most common abdominal malignancy in childhood, after Wilms tumor and neuroblastoma, and are by far the most common primary malignancy of the gastrointestinal tract.

Most children with benign or malignant liver masses present with a palpable mass on physical examination. Other presenting symptoms include pain, anorexia, jaundice, paraneoplastic syndromes, hemorrhage, and congestive heart failure. Although it is commonly obvious that these children have an upper abdominal mass, the organ of origin may not be clear without imaging. Whether CT or MRI is the modality of choice for definitive imaging of liver masses is a controversial issue. There are no pathognomonic imaging features for hepatic malignancies. The major role of imaging is to define accurately the extent of the lesion in relation to hepatic lobar anatomy and vascular and biliary structures for preoperative planning and to monitor tumor response to chemotherapy or radiation. For most hepatic malignancies, complete tumor resection or liver transplantation is essential for cure. The types of liver resection performed include left lobectomy, left lateral segmentectomy, right lobectomy, or trisegmentectomy (right lobe and medial segment of the left lobe). Therefore a mass must be confined to the left or right lobe or the right lobe plus the medial segment of the left lobe to be considered resectable. If a lesion does not meet anatomic requirements for resectability at initial imaging, the child is often initially treated with chemotherapy, with or without radiation, and then reimaged.



▪ **FIGURE 5-46 Choledochal Cyst.**
Coronal (**A**) and axial (**B**) T2-weighted MR images from magnetic resonance cholangiopancreatography (MRCP) show marked dilation of intrahepatic and extrahepatic bile ducts *(arrows)*, as well as distention of the gallbladder *(GB)*.

The differential diagnosis for liver masses in children includes benign and malignant neoplasms, such as hepatoblastoma, hepatic hemangioma, mesenchymal hamartoma, hepatocellular carcinoma, hemangiomas, lymphoproliferative disorder, lymphoma, hepatic adenomas, metastatic disease, and uncommon sarcomas, such as undifferentiated embryonal sarcoma and angiosarcoma. Nonneoplastic causes of liver masses include abscesses (fungal, bacterial, or granulomatous) and hematomas. Several factors help to focus the differential diagnosis, including the age of the child, the presentation, the alpha fetoprotein level, and whether the lesion is solitary or multiple (Table 5-4). The differential diagnosis of liver tumors is different in younger and older children. The most common hepatic tumors in children younger than 5 years of age include hepatoblastoma, hepatic hemangioma, mesenchymal hamartoma, and metastatic disease resulting from neuroblastoma or Wilms tumor. In children older than 5 years of age, the previously mentioned lesions are uncommon. The most common tumors include hepatocellular carcinoma, undifferentiated sarcoma, hepatic adenoma, hemangioma, and metastatic disease. Liver tumors that are associated with elevated serum alpha fetoprotein levels include hepatoblastoma and hepatocellular carcinoma. Hepatic hemangioma can show elevated serum alpha fetoprotein levels in a minority (less than 3%) of lesions. Other liver masses are not associated

with an elevated serum alpha fetoprotein. The presence of multiple liver lesions favors metastatic disease (Fig. 5-47), abscesses, cat-scratch disease, lymphoproliferative disorder, or hepatic adenomas associated with a predisposing syndrome (Fanconi anemia, Gaucher disease).

Hepatoblastoma

Hepatoblastoma is the most common primary liver tumor of childhood, composing 43% of total liver masses. Hepatoblastoma is usually seen in infants and young children and occurs primarily in those less than 3 years of age. Predisposing conditions include Beckwith-Wiedemann syndrome, hemihypertrophy, familial polyposis coli, Gardner syndrome, Wilms tumor, and biliary atresia. However, most hepatoblastomas are seen in patients without associated conditions. The most common presentation is a painless mass. There is usually not a history of underlying liver disease. Serum alpha fetoprotein levels are elevated in more than 90% of patients. Therefore a liver mass presenting in a child younger than 3 years of age with an elevated alpha fetoprotein level is almost always hepatoblastoma. On imaging, the lesions are most commonly well defined and have a tendency to displace rather than invade adjacent structures, such as the falciform ligament (Fig. 5-48). The lesions may be heterogeneous secondary to necrosis or hemorrhage.

TABLE 5-4

Causes of Pediatric Hepatic Masses

Age Less Than 5 Years

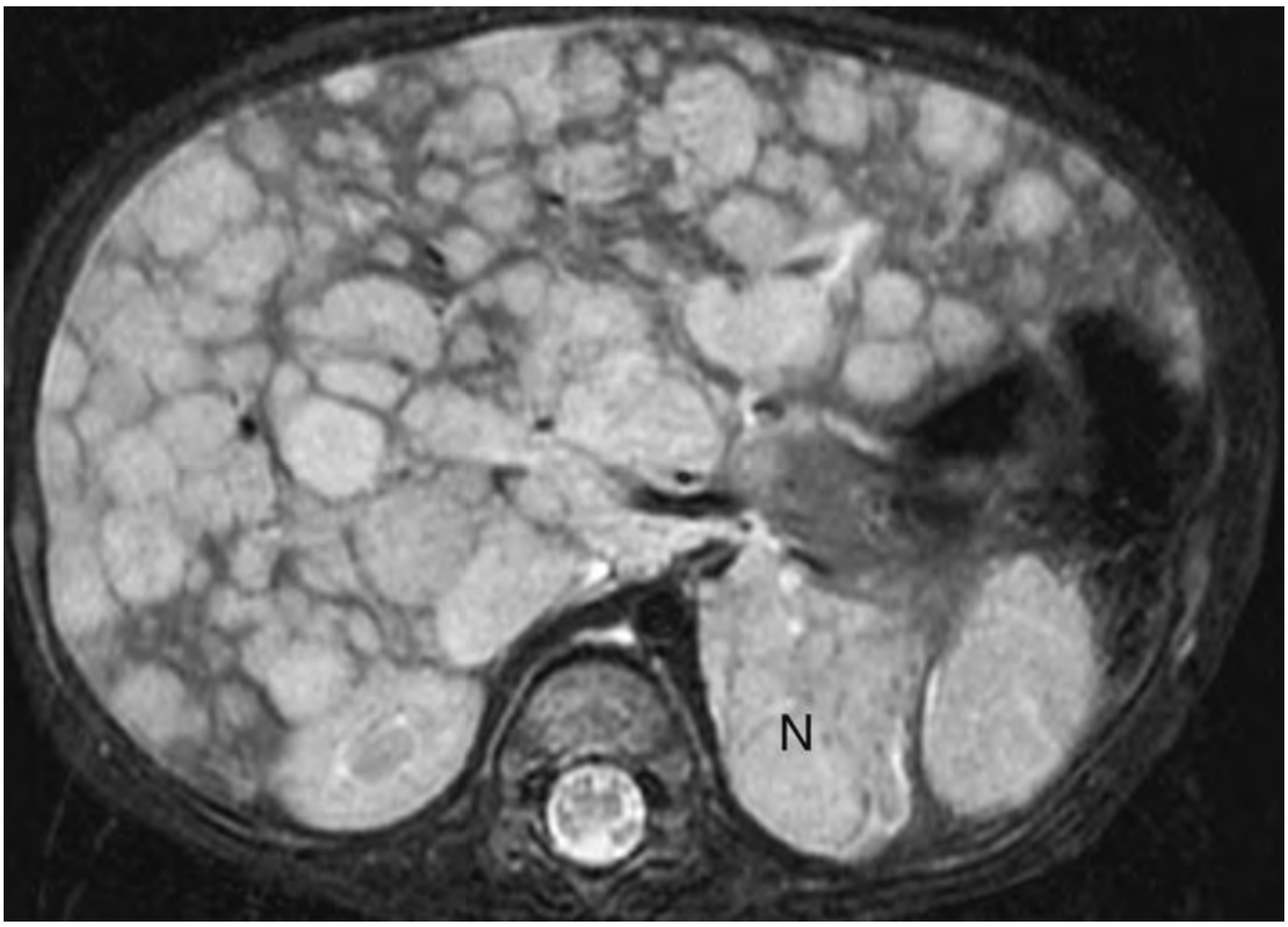
- Hepatoblastoma (+AFP)
- Congenital or infantile hepatic hemangioma
- Mesenchymal hamartoma
- Metastatic disease (Wilms, neuroblastoma)

Age Greater Than 5 Years

- Hepatocellular carcinoma (+ alpha fetoprotein level)
- Undifferentiated embryonal sarcoma
- Hepatic adenoma
- Hemangioma
- Metastatic disease

Immunocompromised State

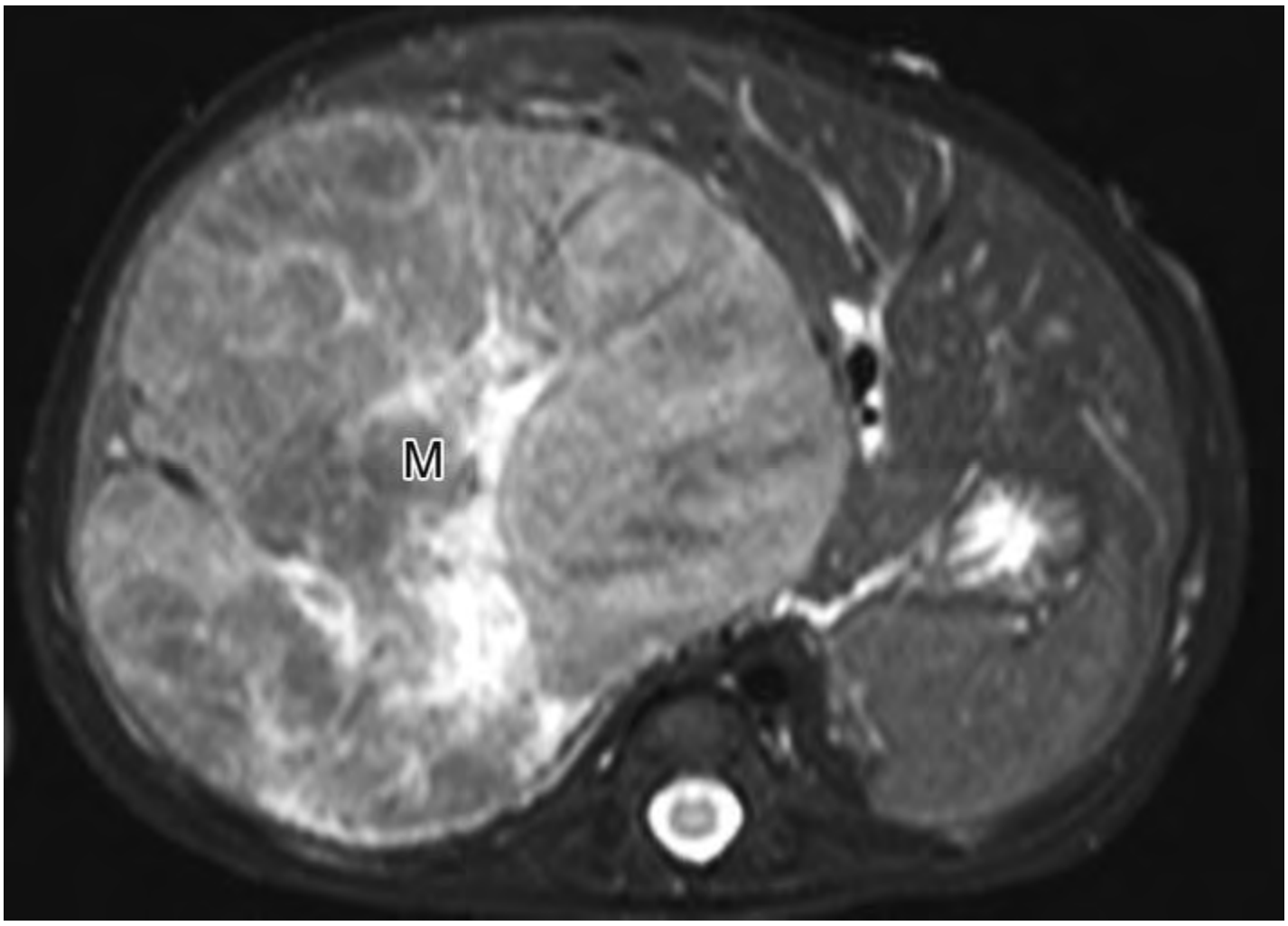
- Lymphoproliferative disorder
- Fungal infection



▪ **FIGURE 5-47** **Liver metastasis from neuroblastoma.**
T2-weighted MRI shows multiple high-signal masses replacing the majority of the liver parenchyma. Note the left adrenal neuroblastoma *(N)*.

Childhood Liver Hemangiomas

Childhood liver hemangiomas are the most common symptomatic vascular lesion of infancy. The lesions most commonly present in young infants as abdominal masses associated with either high-output congestive heart failure, consumptive coagulopathy (thrombocytopenia), or hemorrhage. They are categorized as either congenital or infantile. Congenital hemangiomas are present at birth and tend to be solitary lesions. Infantile hemangiomas are often diffuse or multiple lesions in appearance but are more apt to be asymptomatic. Approximately 85% of the lesions present by 6 months of age. The imaging appearance is variable; however, the lesions are most often heterogeneous and typically enhance with contrast (Fig. 5-49). There may be prominent vessels within the lesions. On all imaging modalities, the descending aorta superior to the level of the hepatic branches of the celiac artery may appear abnormally enlarged as compared with the infrahepatic aorta because of differential flow.

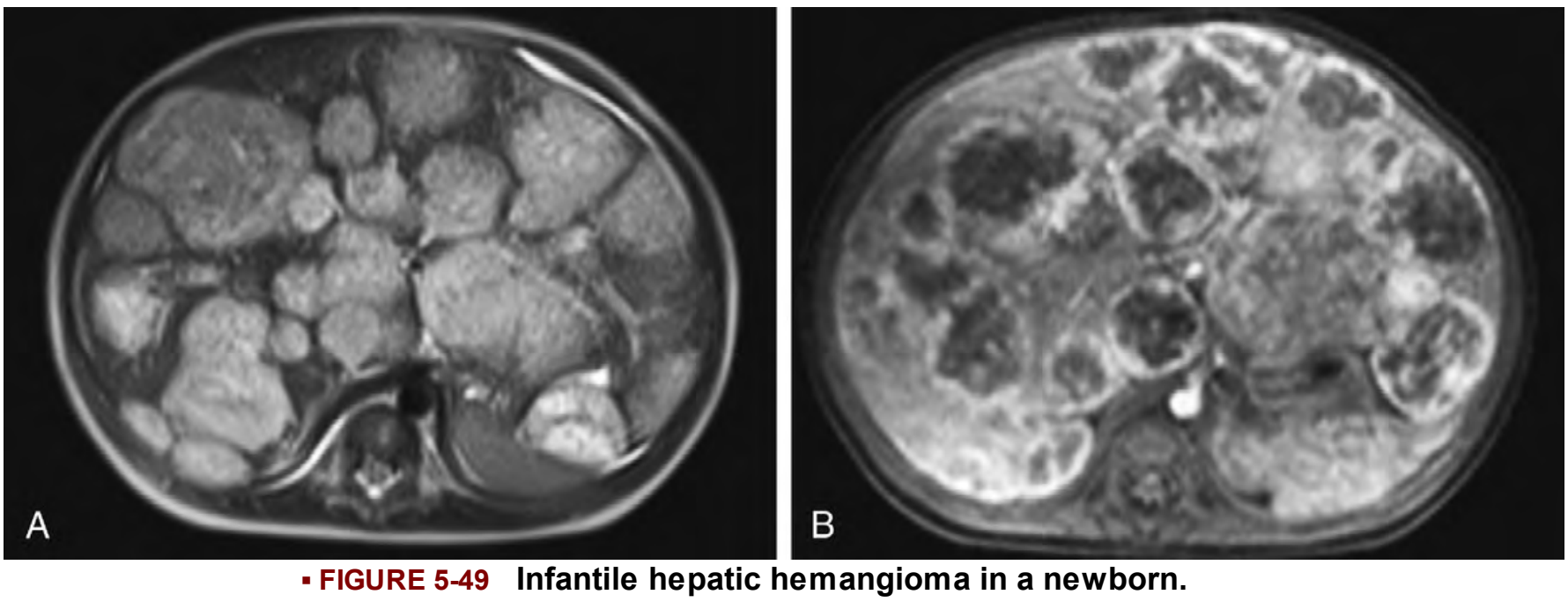


▪ **FIGURE 5-48** **Hepatoblastoma.**
Axial T2-weighted image shows well-defined mass *(M)* arising from the liver to be heterogeneously high in the T2-weighted signal. Note the central, high signal "scar-" appearing area.

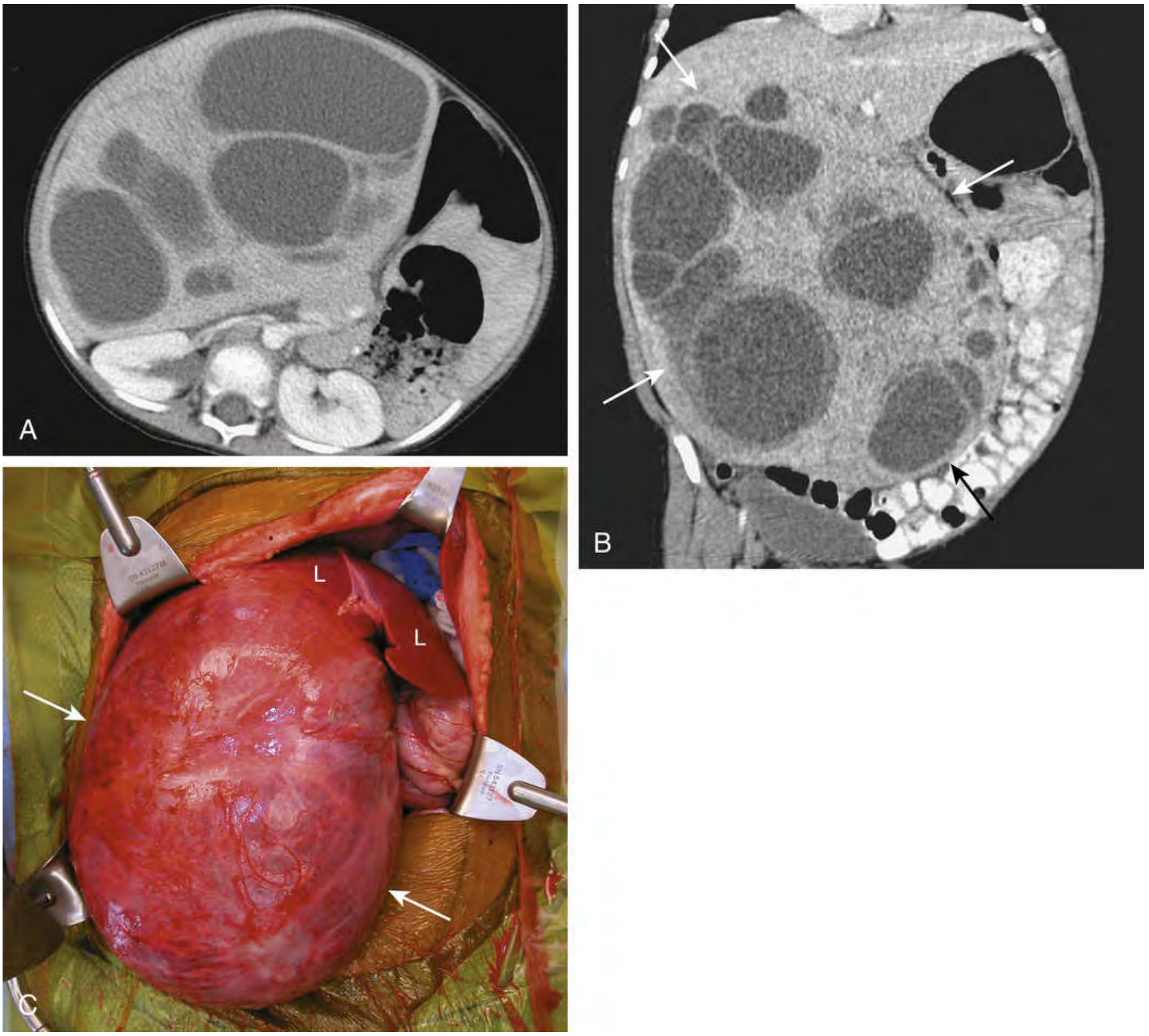
Infantile hepatic hemangiomas tend to spontaneously involute without therapy over a course of months to years. Sequential ultrasounds are often used to follow lesions and most often demonstrate a progressive decrease in size and an increase in degree of calcification.

Mesenchymal Hamartoma of the Liver

Mesenchymal hamartoma of the liver is a very rare, benign, predominately cystic liver mass that most commonly presents in infancy, almost always before 2 years of age. The lesion is considered a developmental anomaly rather than a true neoplasm. Patients usually present with a large painless abdominal mass and a normal serum alpha fetoprotein level. At imaging, lesions appear as large, multilocular, cystic masses with thin internal septations (Fig. 5-50). Occasionally the solid component of the lesion can be more predominant, with multiple smaller cysts giving the lesion the appearance of Swiss cheese.



▪ **FIGURE 5-49** **Infantile hepatic hemangioma in a newborn.**
A, T2-weighted MRI shows multiple high signal masses throughout the liver. **B,** Postcontrast MRI shows early peripheral enhancement of the multiple lesions.



▪ **FIGURE 5-50** **Mesenchymal hamartoma of the liver in a 3-week-old girl with an asymptomatic abdominal mass.**

A, Axial CT shows multicystic mass within liver. **B,** Coronal CT shows the multicystic mass *(arrows)* to be pedunculated off the inferior aspect of the liver. **C,** Operative photograph shows large pedunculated mass *(arrows)* extending off of the inferior aspect of the liver *(L)*.

▪ Blunt Abdominal Trauma

Blunt abdominal trauma is a common indication for CT of the abdomen and pelvis in children. In children the most common cause of blunt abdominal trauma is motor vehicle accidents. Other causes include a direct blow resulting from abuse or from a handlebar when falling off a bike. Many aspects of the imaging of pediatric trauma, such as the appearance of parenchymal lacerations, are similar in children and adults and are not discussed in detail here. However, there are several significant differences that are emphasized.

Focused abdominal ultrasound for trauma has been advocated as a way of triaging patients with potential blunt abdominal trauma. It consists of a rapid ultrasound search for free fluid in all four quadrants. However, it has been shown that many significant parenchymal injuries can occur without associated free fluid.

Parenchymal Organ Injuries

The order of frequency of parenchymal organ injuries in children is liver (36%), spleen (34%), kidney (22%), adrenal gland (11%), and pancreas (6%). Injury to multiple organs occurs in up to 21% of trauma cases. Most solid organ injuries are treated conservatively; operation is reserved for cases that are

hemodynamically unstable. The size and appearance of a parenchymal organ injury have been shown to be inaccurate predictors of which patients with solid organ injury will need surgery. However, the visualization of active extravasation of contrast from a lacerated organ (density as high as the enhancing aorta seen within the peritoneum) strongly predicts the need for operation (Fig. 5-51).

Artifactual areas of low attenuation can be seen within the spleen; this is known as transient splenic heterogeneity, which is a normal flow phenomenon commonly seen during the arterial phase of contrast enhancement. These artifacts should not be mistaken for splenic injury. Patterns of splenic heterogeneity include archiform (alternating bands of low and high attenuation [Fig. 5-52]), focal, and diffuse heterogeneity.

Bowel Injury

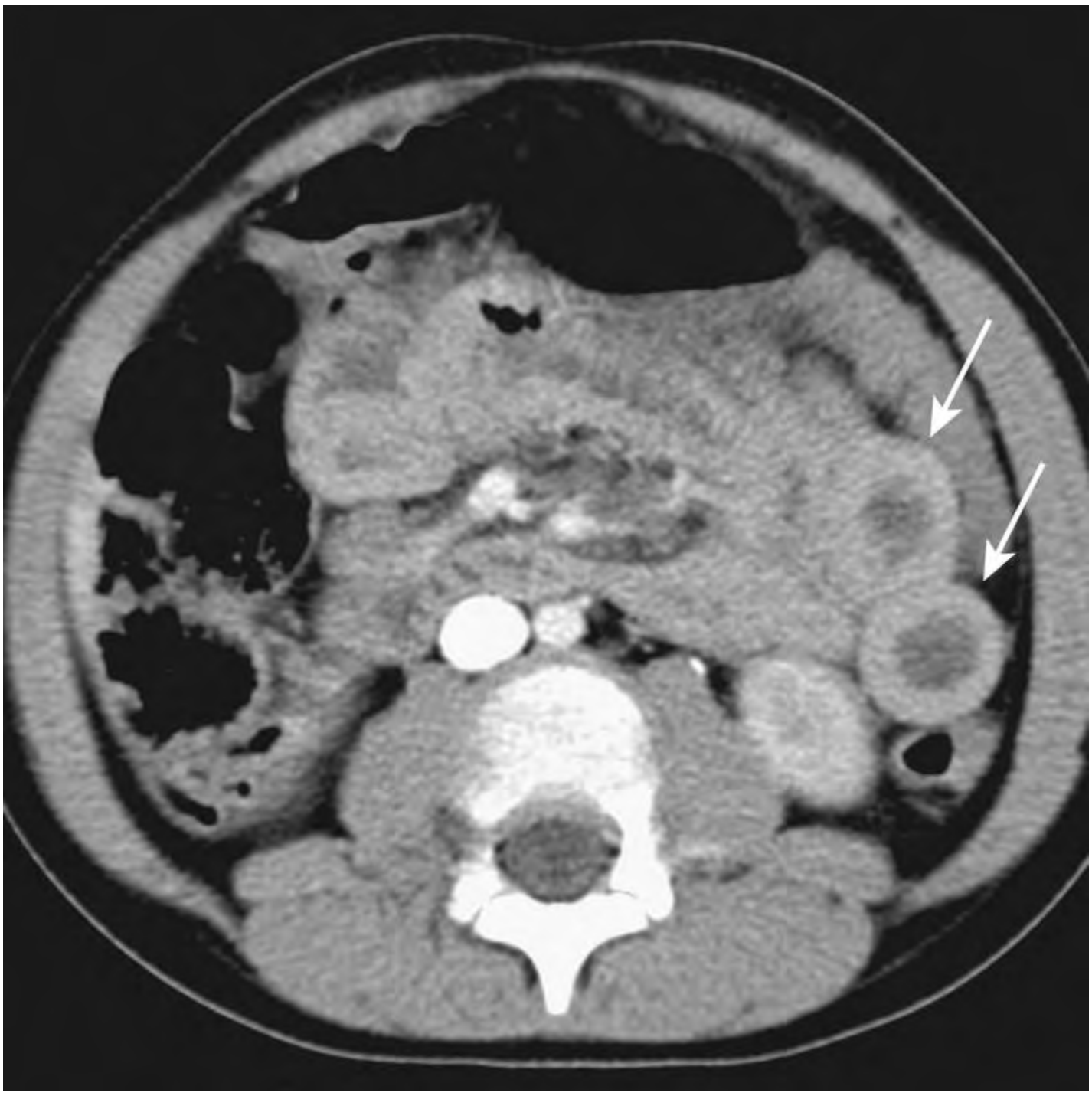
Injury to the bowel represents approximately 8% of abdominal injuries after trauma. Bowel injury is more common in children who have had lap belt-type injuries. The most commonly encountered CT findings include focal bowel wall thickening (Fig. 5-53), associated prominent bowel wall enhancement, mesenteric soft tissue stranding, and unexplained free peritoneal fluid (fluid in the absence of solid organ injury). When subtle, these findings may be suggestive but not diagnostic of a bowel injury. It is inappropriate to send all of such patients to the operating room. More often the findings are communicated to the surgical team and kept in mind in case the patient develops increasingly severe abdominal symptoms. More specific findings of bowel injury are less common and include free intraperitoneal air, extraluminal bubbles of gas in the vicinity of the injury, and, much less commonly, active extravasation of enteric contrast.



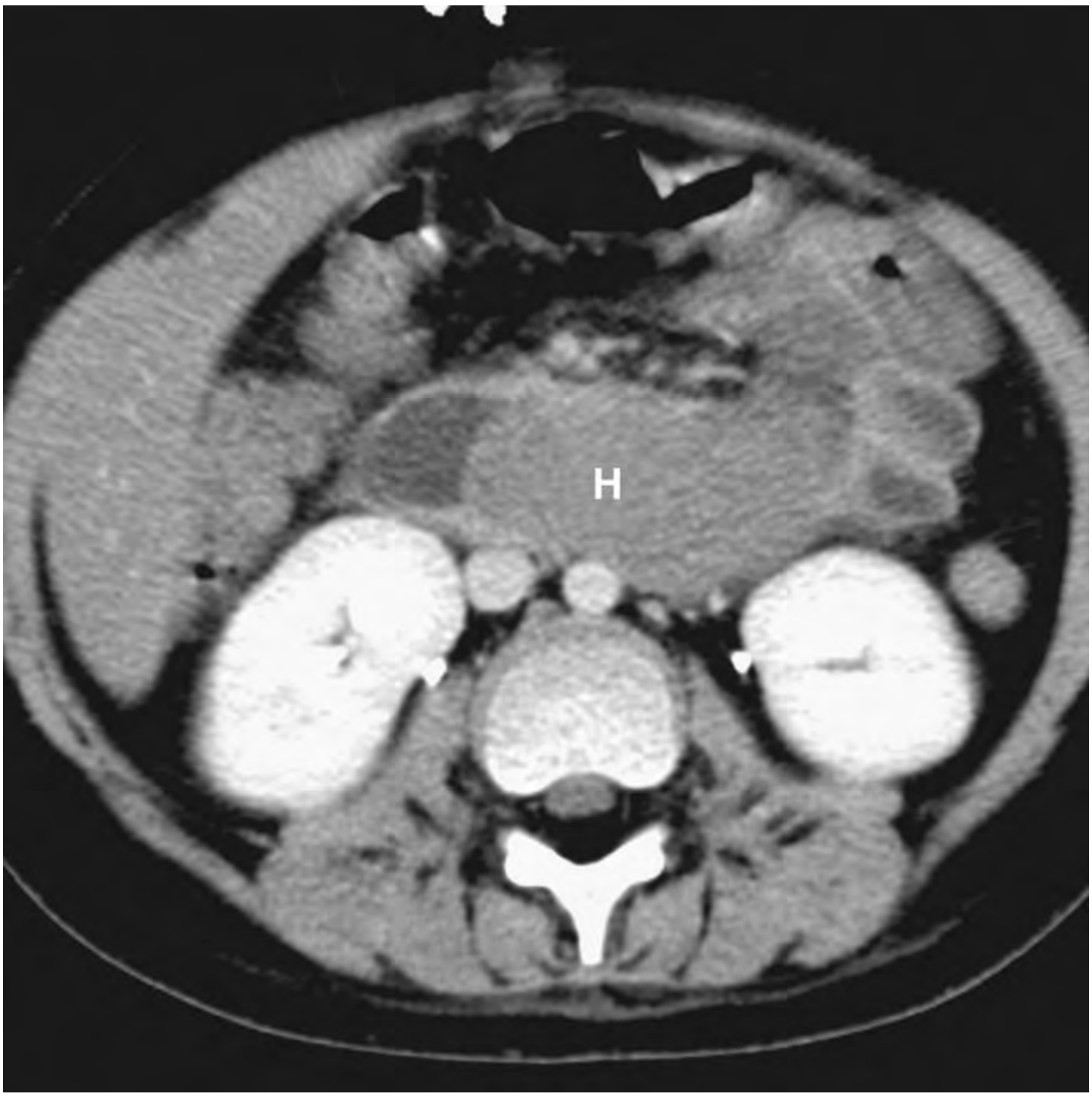
▪ **FIGURE 5-51** Active arterial extravasation resulting from traumatic splenic rupture. CT shows rupture of the spleen *(S)* with arterial extravasation *(arrows)* shown as high-attenuation material exuding from the spleen. Note the active extravasation directly from the torn splenic artery *(arrowhead)*. There is also a large amount of hemoperitoneum *(A)*.



▪ **FIGURE 5-52** Heterogeneous splenic enhancement related to imaging during the arterial phase of enhancement. Note “zebra” stripe pattern within the spleen. This artifact should not be mistaken for splenic injury.

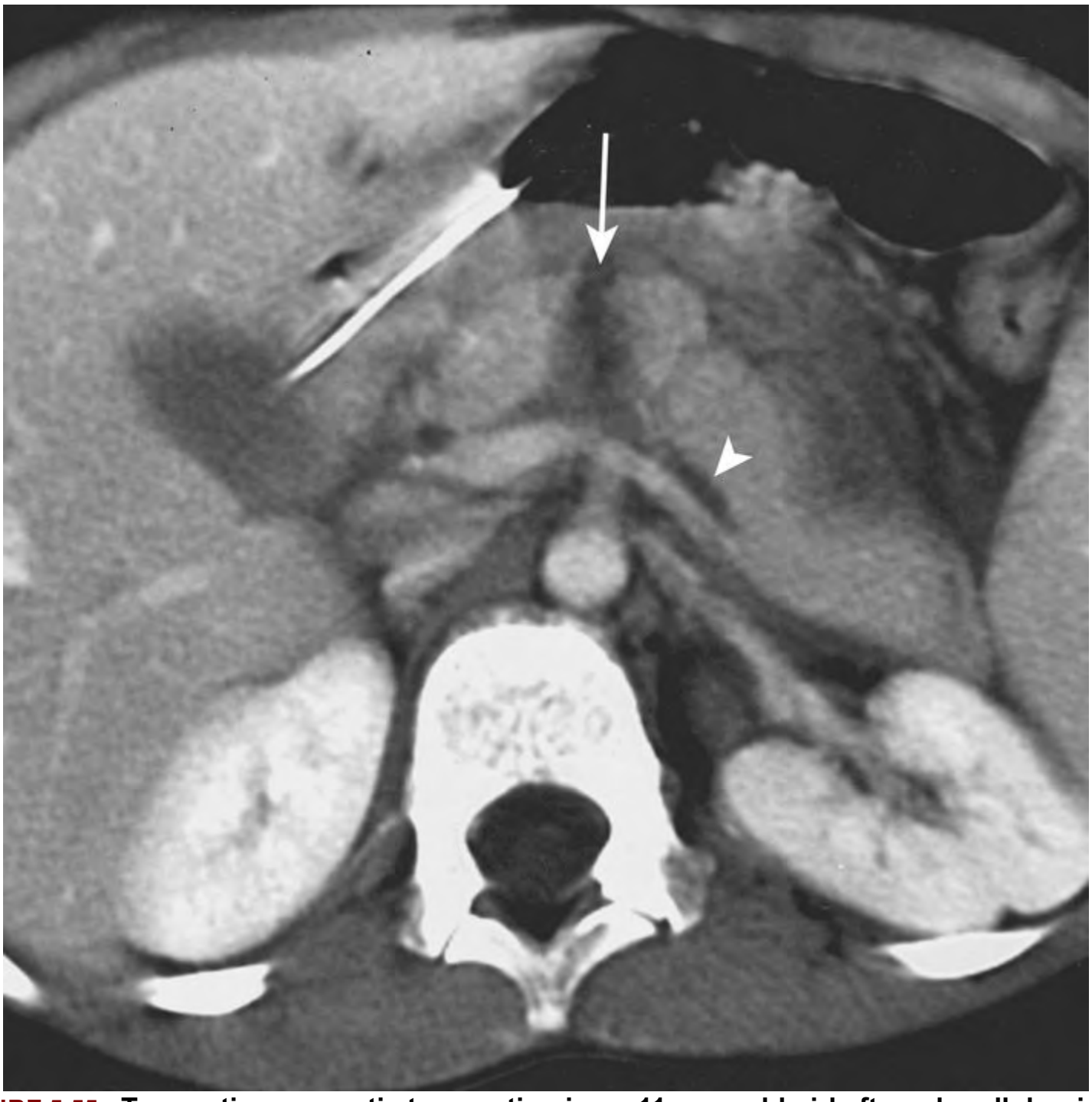


▪ **FIGURE 5-53** **Bowel injury.**
CT shows focal bowel wall thickening *(arrows)* involving several jejunal loops. There is also edema in the base of the mesentery.



▪ **FIGURE 5-54** **Duodenal hematoma.**
CT scan shows increased attenuation mass *(H)* within the portion of the duodenum that crosses the spine. This is the portion of the duodenum most commonly injured by blunt trauma.

A patient who receives a focal, direct blow to the upper abdomen, most commonly caused by either a bicycle handle when falling or by abuse, is at increased risk for having a duodenal hematoma or laceration or pancreatitis (Figs. 5-54 and 5-55). On CT, duodenal hematomas appear as high- or low-attenuation masses or as wall thickening in the third portion of the duodenum.

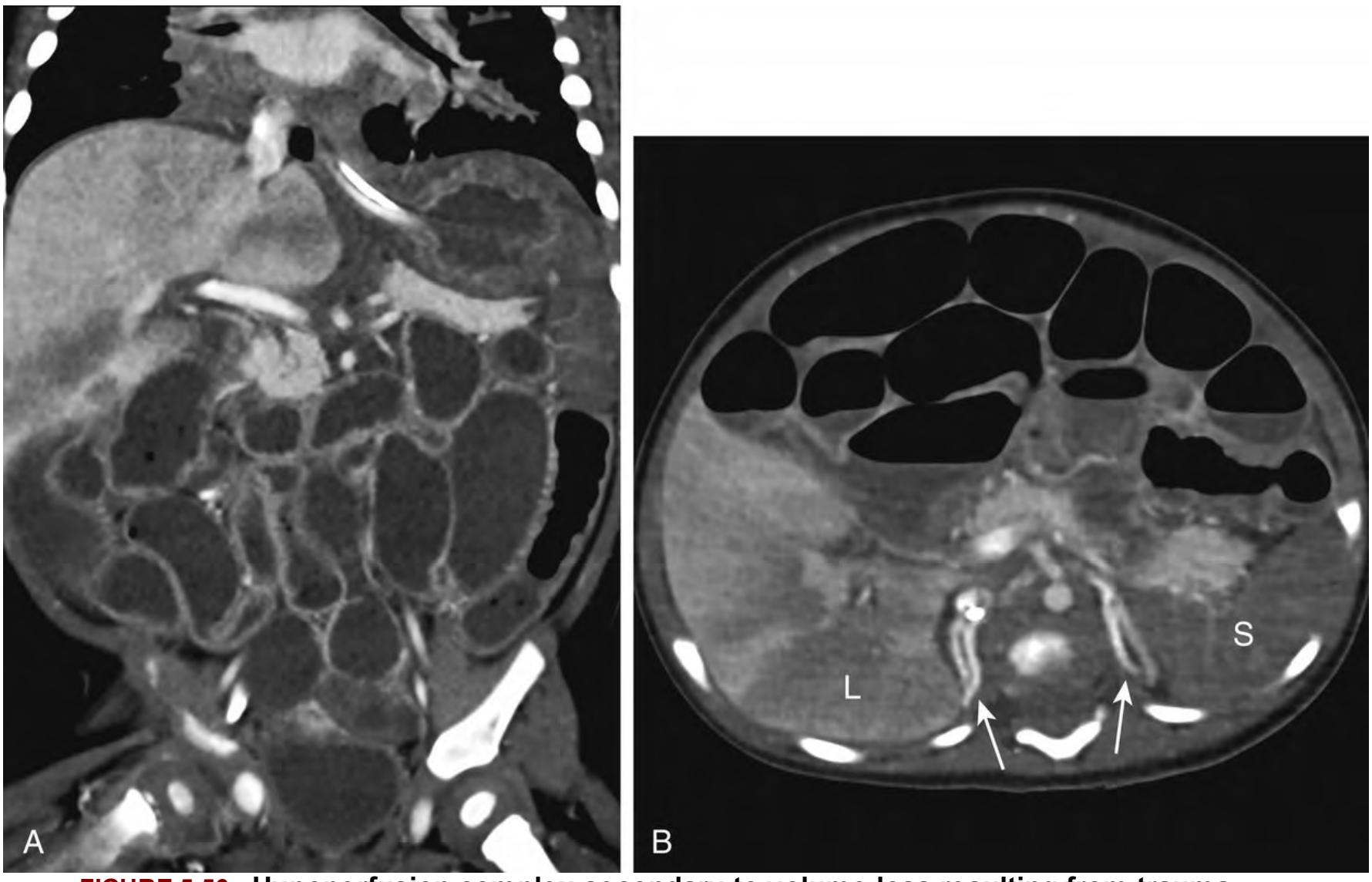


▪ **FIGURE 5-55** **Traumatic pancreatic transection in an 11-year-old girl after a handlebar injury.** CT shows low-attenuation cleft *(arrow)* traversing the pancreas and soft tissue stranding in the peripancreatic portion of the anterior pararenal space. There is also fluid *(arrowhead)* between the pancreas and splenic vein, a sensitive finding of pancreatic injury.

Fluid seen between the splenic vein and the pancreas is said to be the most sensitive finding of pancreatic trauma. Lacerations of the pancreas are seen as hypoattenuating linear structures through the pancreas.

Hypoperfusion Complex

The clinical findings of hypovolemic shock can be masked for a longer time in children than in adults because of more pronounced peripheral vasospasm and tachycardia. The CT appearance of such children has been referred to as the hypoperfusion complex or as "shock bowel." CT findings include abnormal intense enhancement of the bowel wall, mesentery, adrenal glands, liver, kidneys, and pancreas; intense enhancement and decreased caliber of the inferior vena cava and aorta; and diffusely dilatated, fluid-filled bowel loops (Fig. 5-56). This appearance on CT may be identified before clinical findings of shock being recognized and is associated with the potential development of hemodynamic instability. The bowel findings (bowel wall enhancement and dilatation over a diffuse distribution) should not be confused with the focal dilatation and bowel wall thickening or enhancement more typical of bowel injury. In cases in which the cause of the bowel findings is unclear, identifying other findings of the hypoperfusion complex is helpful.



▪ **FIGURE 5-56** **Hypoperfusion complex secondary to volume loss resulting from trauma.** **A,** Coronal CT shows diffuse abnormal bowel enhancement and free intraperitoneal fluid. **B,** Axial CT shows intense enhancement of the adrenal glands *(arrows)*. Note the low attenuation of the spleen *(S)* and multiple areas of the liver *(L)* related to areas of trauma.

▪ The Immunocompromised Child

The population of immunocompromised children has greatly increased. Children can be immunocompromised because of therapy for malignancy, bone marrow transplantation, solid organ transplantation, primary immunodeficiency, and acquired immunodeficiency syndrome. These patients can have many different types of problems, including those related to immunodeficiency (infection, lack of neoplasm surveillance); thrombocytopenia (bleeding); other therapy-related complications, including mucositis, radiation injury, and the development of secondary neoplasm; recurrence of the primary neoplasm; and normal childhood illnesses that are unrelated to the patients' oncologic problems. The gastrointestinal tract is commonly involved with such processes. These patients commonly present with nonspecific symptoms, and imaging, usually with CT, is requested.

Immunocompromised children are often referred for abdominal CT imaging to rule out abscess. However, drainable focal intraabdominal fluid collections are uncommon in immunocompromised children. More often, the abdominal source of sepsis is related to bowel wall compromise secondary to a variety of types of enterocolitis. Common bowel diseases in immunocompromised children are listed in Table 5-5. Most of these enterocolitides are managed medically unless there is evidence of perforation (extraluminal gas, fluid collection). When intraabdominal abscesses are present, they are often related to systemic fungal infection with such organisms as *Candida albicans* or *Aspergillus* species. These abscesses appear as multiple small, low-attenuation lesions within the liver, spleen, or kidneys.

Pseudomembranous Colitis

Because immunocompromised patients commonly receive antibiotics, they are at risk for developing pseudomembranous colitis, which is related to the overgrowth of and toxin production by *Clostridium difficile*, usually after the use of antibiotics. On gross inspection of the colon, there are discrete yellow plaques (pseudomembranes) involving the mucosal surface. The plaques are usually separated by normal-appearing mucosa. The CT findings, although nonspecific, are often highly suggestive of

pseudomembranous colitis (Fig. 5-57). In the majority of cases, there is diffuse colonic involvement (pancolitis). There is marked colonic wall thickening (average 15 mm), greater in degree than that seen in most other types of colitis. It is common for contrast material to insinuate between the pseudomembranes and swollen haustra creating an accordion sign, which is highly suggestive of the diagnosis. Because pseudomembranous colitis involves predominantly the mucosa and submucosa, the degree of inflammatory change in the pericolonic fat is often disproportionately subtle compared with the degree of colonic wall thickening (see Fig. 5-57).

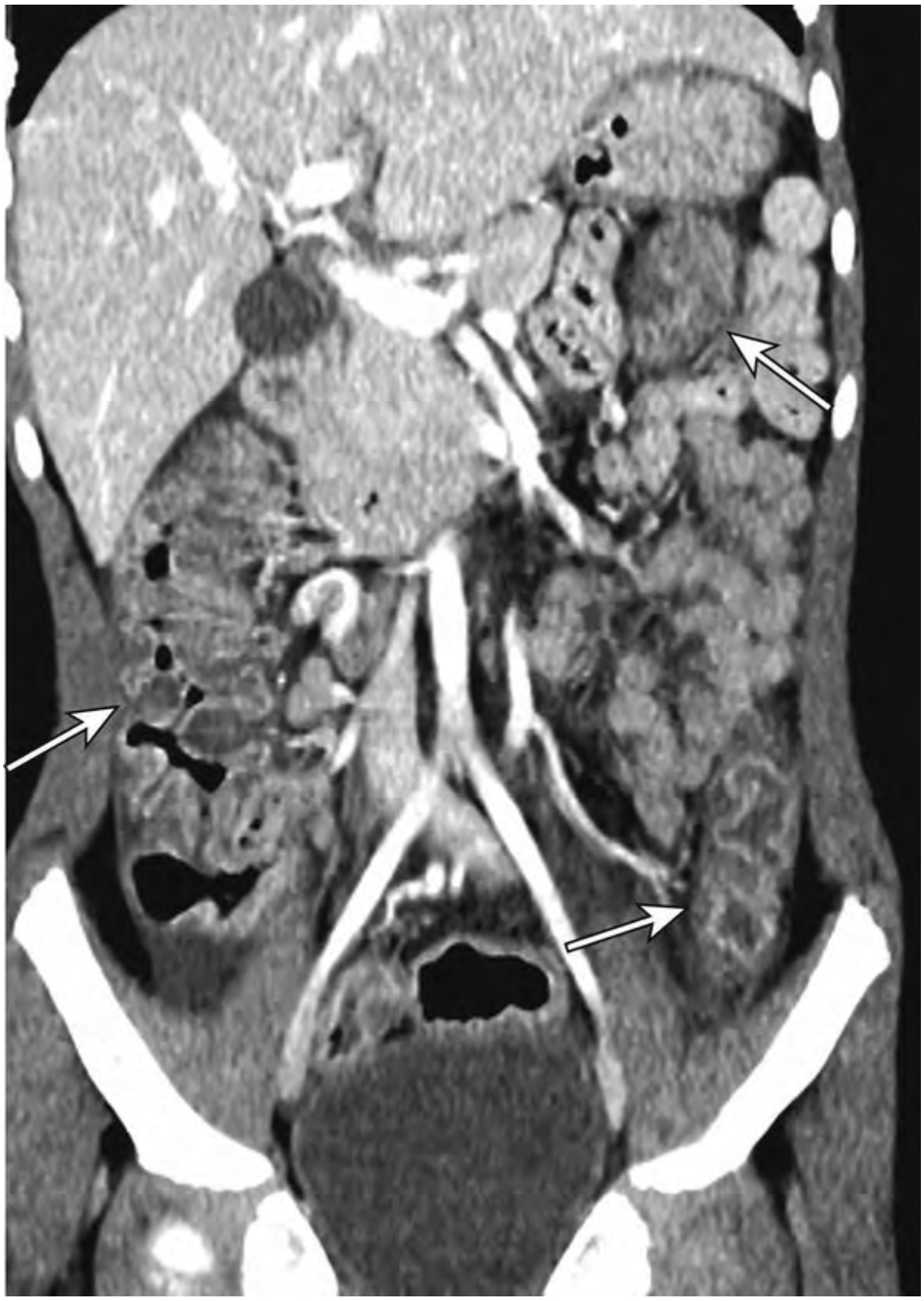
TABLE 5-5

Computed Tomography Findings Helpful in Differentiating Bowel Diseases in Immunocompromised Children

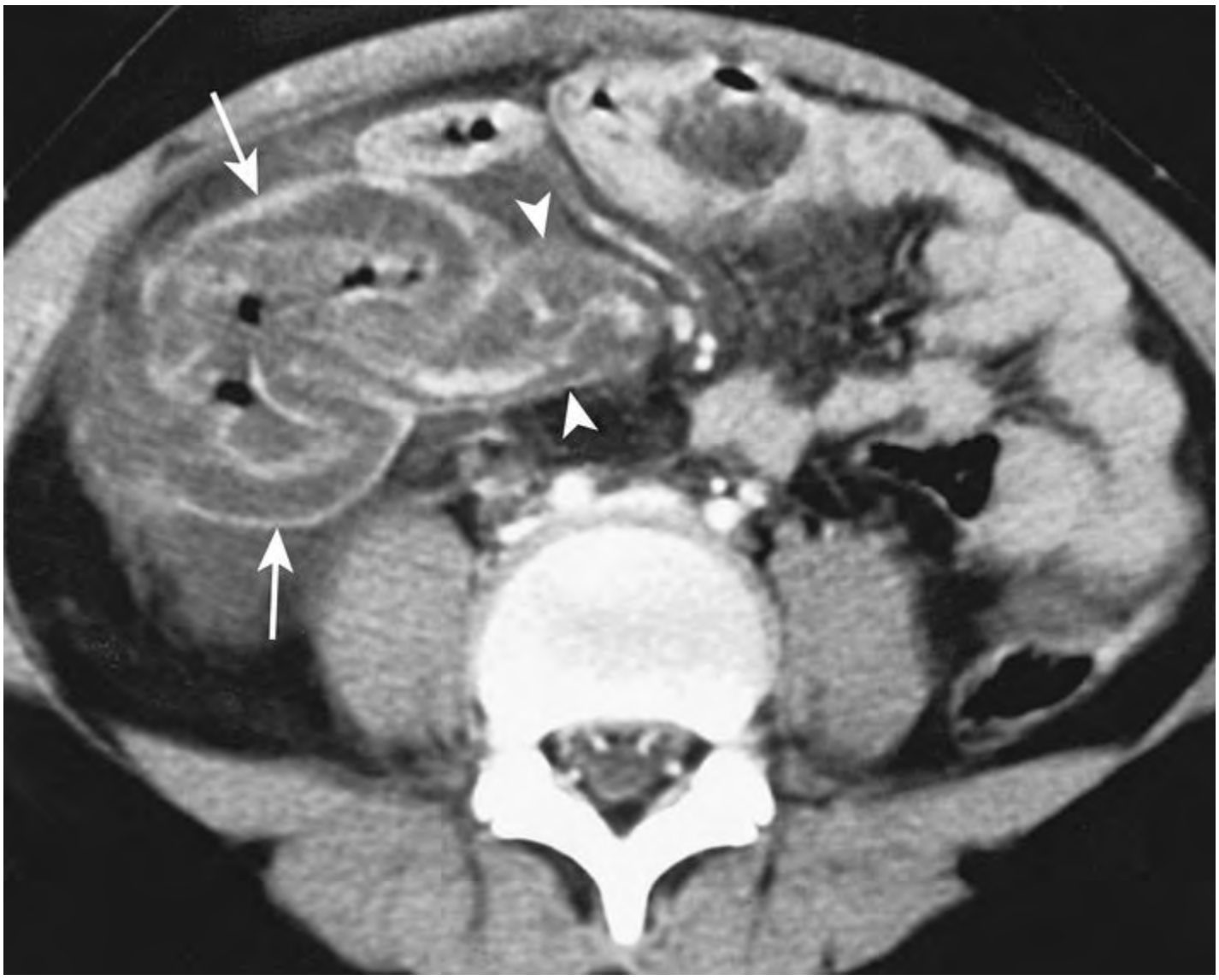
Entity	Typical Distribution	Imaging Features
Pseudomembranous colitis	Pancolitis	Marked bowel wall thickening
		Nonprominent pericolonic inflammatory changes
Neutropenic colitis	Cecum, right colon, terminal ileum	Bowel wall thickening
		Pericolonic inflammatory changes
Cytomegalovirus colitis	Cecum, right colon, terminal ileum	Bowel wall thickening
		Pericolonic inflammatory changes
Mucositis	Small and large bowel	Fluid-filled, dilatated small and large bowel
		Thin but enhancing bowel wall
		Absent bowel wall thickening or adjacent inflammatory changes
Graft-versus-host disease	Diffuse small and large bowel	Mucosal enhancement
		Fluid-filled dilatated bowel
		Mild wall thickening, isolated to small bowel
		Prominent mesenteric inflammatory changes
Lymphoproliferative disorder	Focal involvement, typically small bowel	Marked focal bowel wall thickening
		Aneurysmal dilatation of bowel lumen
		Parenchymal (liver) masses
		Lymphadenopathy-mesenteric masses
Gastrointestinal bleeding	Anywhere	High-attenuation fluid or heterogeneous mass (solid thrombus) within lumen
		Associated underlying enterocolitis

Neutropenic Colitis

Neutropenic colitis (typhlitis, necrosing enteropathy) is a life-threatening, right-sided colitis associated with severe neutropenia. Pathologically there is necrosing inflammation of the cecum and ascending colon with associated ischemia and secondary bacterial invasion. CT shows bowel wall thickening, pericolonic fluid, and inflammation of the pericolonic fat, usually isolated to the cecum and ascending colon (Fig. 5-58). The adjacent terminal ileum may also appear abnormal, but involvement of other portions of the small bowel or left colon is unusual.



▪ **FIGURE 5-57** **Pseudomembranous colitis.**
CT shows marked thickening of the colon *(arrows)* in the ascending colon, splenic flexure, and descending colon. There is mucosal enhancement, low-attenuation bowel wall thickening, and disproportionately little pericolonic inflammatory change as compared with the degree of bowel wall thickening.



▪ **FIGURE 5-58** **Neutropenic colitis.**
CT shows marked bowel wall thickening, adventitial enhancement, low-attenuation of the central bowel wall, and pericolonic inflammatory change involving both the cecum *(arrows)* and terminal ileum *(arrowheads)*. The descending colon and the remainder of the small bowel appear to be normal.

Graft-versus-Host Disease

Acute graft-versus-host disease is a process specific to bone marrow transplant recipients, in which donor T lymphocytes cause selected epithelial damage of recipient target organs. Histopathologically there is extensive crypt cell necrosis and, in severe cases, diffuse destruction of the mucosa throughout both the large and small bowel and replacement with a thin layer of highly vascular granulation tissue. CT findings include diffuse enterocolitis from the duodenum to the rectum. Compared with the previously discussed causes of enterocolitis, bowel wall thickening may be mild, isolated to the small bowel, or absent. More characteristically there is abnormal bowel wall enhancement in a central, mucosal location corresponding pathologically with the thin layer of vascular granulation tissue replacing the destroyed mucosa (Fig. 5-59). Both the small and large bowel are usually filled with fluid and dilatated. There is often prominent infiltration of the mesenteric fat and soft tissue attenuation.

Mucositis

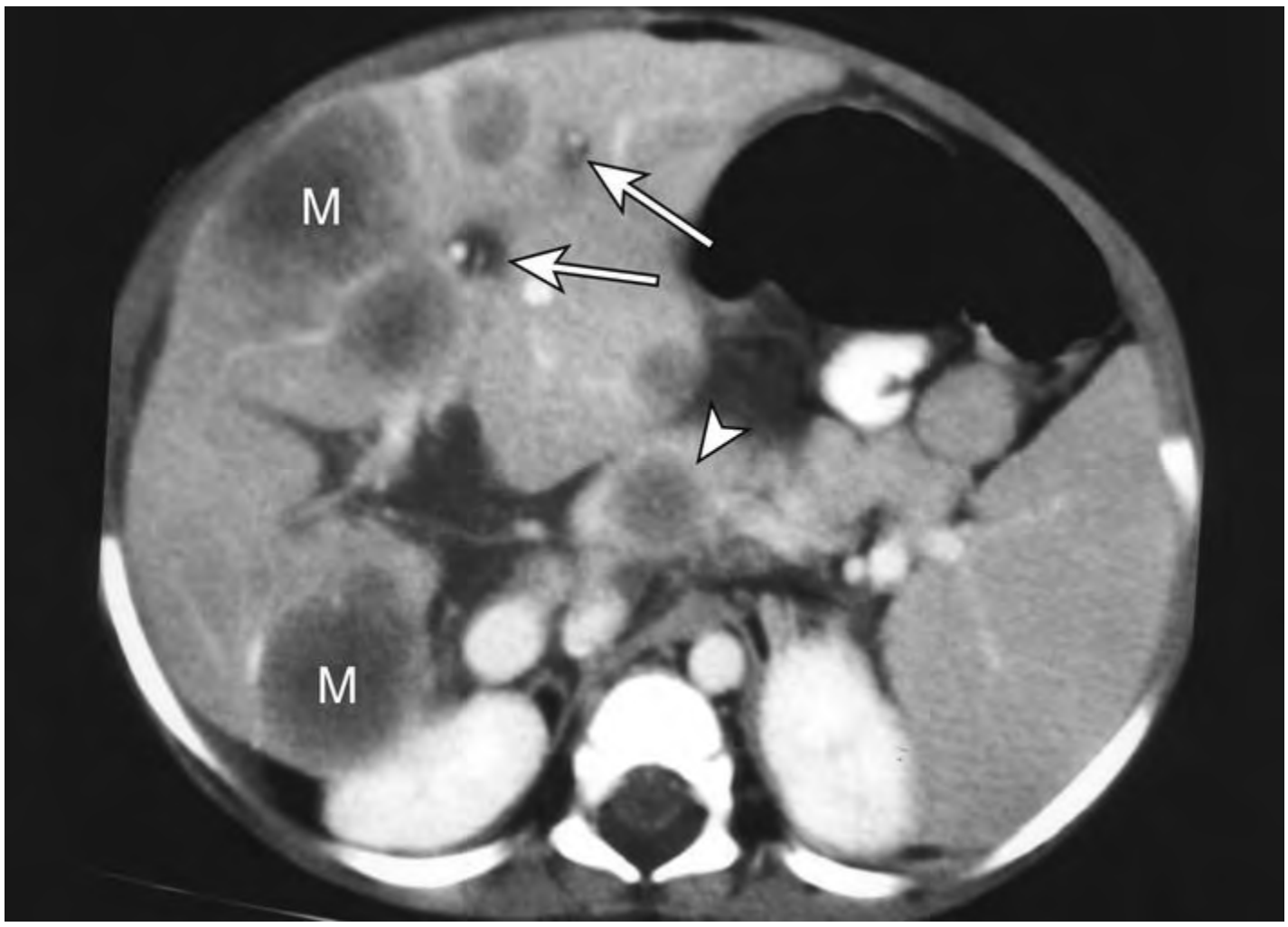
Gut toxicity has been described in association with multiple chemotherapeutic agents. The damage to the mucosa, impaired ability of the bowel to regenerate its protective cell lining (mucosa), and resultant inflammation are often referred to as mucositis. Patients present with nonspecific abdominal complaints, including nausea, vomiting, and abdominal pain, and they demonstrate an ileus pattern on abdominal radiographs. The symptoms may be severe and difficult to separate clinically from the previously discussed processes. On CT, the predominant finding of mucositis is dilatated, fluid-filled loops of small and large bowel. There may be mild associated small bowel wall enhancement. Marked bowel wall thickening, predominance of colonic involvement, and marked abdominal inflammatory changes suggest other diagnoses. Treatment for mucositis is supportive.



▪ **FIGURE 5-59** **Acute graft-versus-host disease.**
CT shows abnormal mucosal enhancement and mild diffuse wall thickening in all visualized bowel loops. There is also mesenteric edema.

Lymphoproliferative Disorder

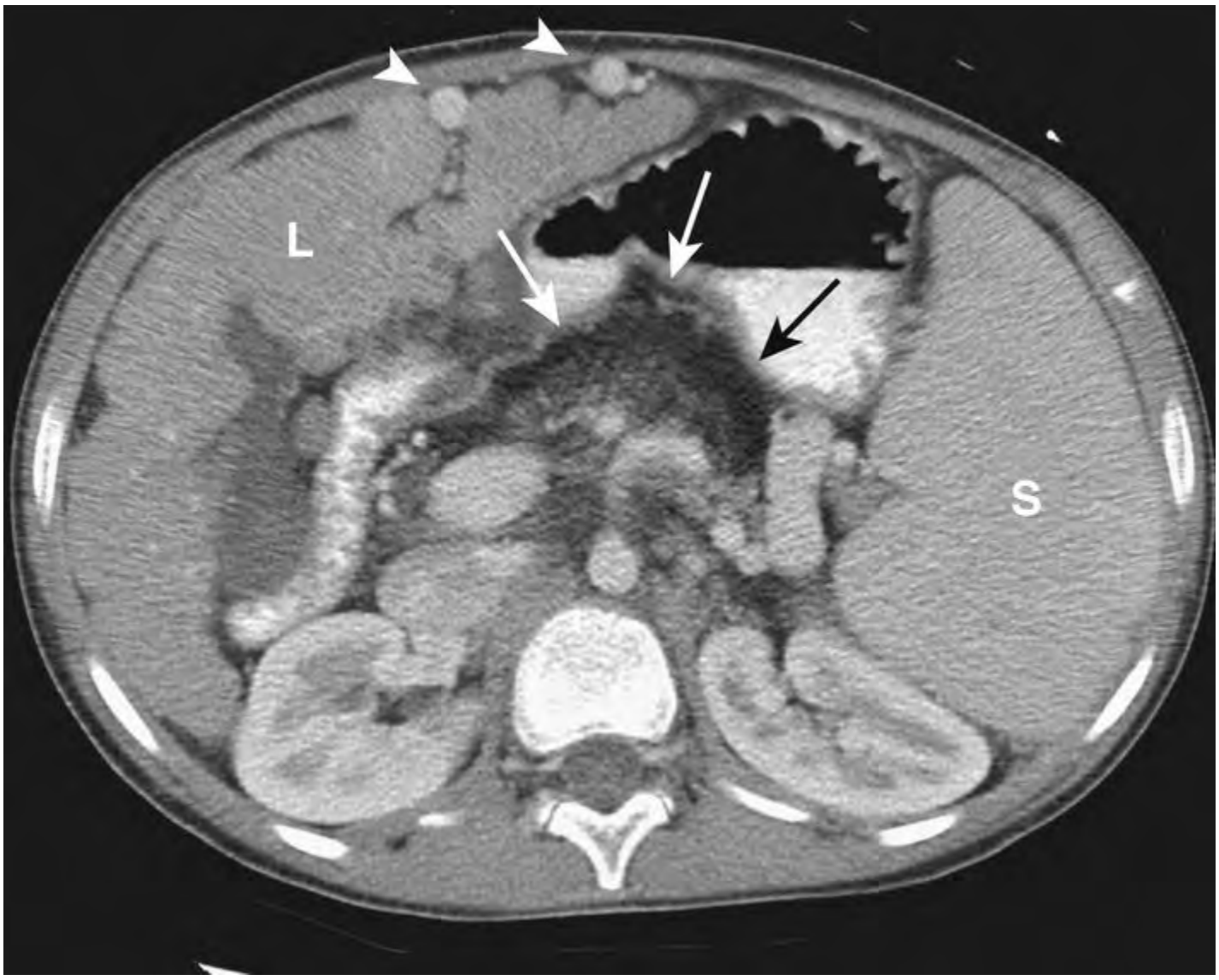
Lymphoproliferative disorders are lymphoma-like diseases related to an uncontrolled proliferation of cells infected by the Ebstein-Barr virus in an immunocompromised host. Although they can occur in any immunocompromised individual, they are most commonly encountered in patients after solid organ transplantation. Similar to the variable appearances of lymphoma, there are a spectrum of imaging findings of abdominal involvement in lymphoproliferative disorders, including focal parenchymal mass (Fig. 5-60), diffuse lymphadenopathy, mesenteric mass, bowel wall thickening, and associated aneurysmal dilatation of the small bowel lumen. In contrast to typical non-Hodgkin lymphoma, which manifests more commonly as abdominal lymphadenopathy, lymphoproliferative disorder is more often associated with parenchymal organ involvement, most commonly the liver. In solid organ transplant recipients, the distribution of disease tends to occur in the vicinity of the transplant organ. Therefore, liver transplant recipients are more likely to have abdominal disease than are heart transplant recipients. Therapeutic options include reduction of immunosuppressive therapy, when possible, and chemotherapy.



▪ **FIGURE 5-60** **Lymphoproliferative disorder in a liver transplant recipient.**
CT shows multiple masses *(M)* in liver. There are also periportal, low-attenuation masses surrounding the portal vein branches *(arrows)*. Note also mass in pancreatic head *(arrowhead)*.

▪ Complications Related to Cystic Fibrosis

Newborn infants with cystic fibrosis presenting with meconium ileus have already been discussed. Older children and adults can present with a similar syndrome, distal intestinal obstruction syndrome, also known as meconium ileus equivalent. These children develop obstruction secondary to inspissated, tenacious intestinal contents lodging within the bowel lumen. On radiographs there is abundant stool within the right colon and distal small bowel and findings of obstruction. When other therapies fail to resolve the obstruction, contrast enemas with Gastrografin (diatrizoate meglumine) may be effective. However, it should be noted that patients with cystic fibrosis who develop pseudomembranous colitis can develop abdominal pain and bloating, much like those with distal intestinal obstruction syndrome, and often do not have the diarrhea typically seen with pseudomembranous colitis. If colonic wall thickening is identified on imaging studies, such as CT or contrast enemas, the possibility of pseudomembranous colitis should be raised. In these cases, enemas are definitely not indicated.



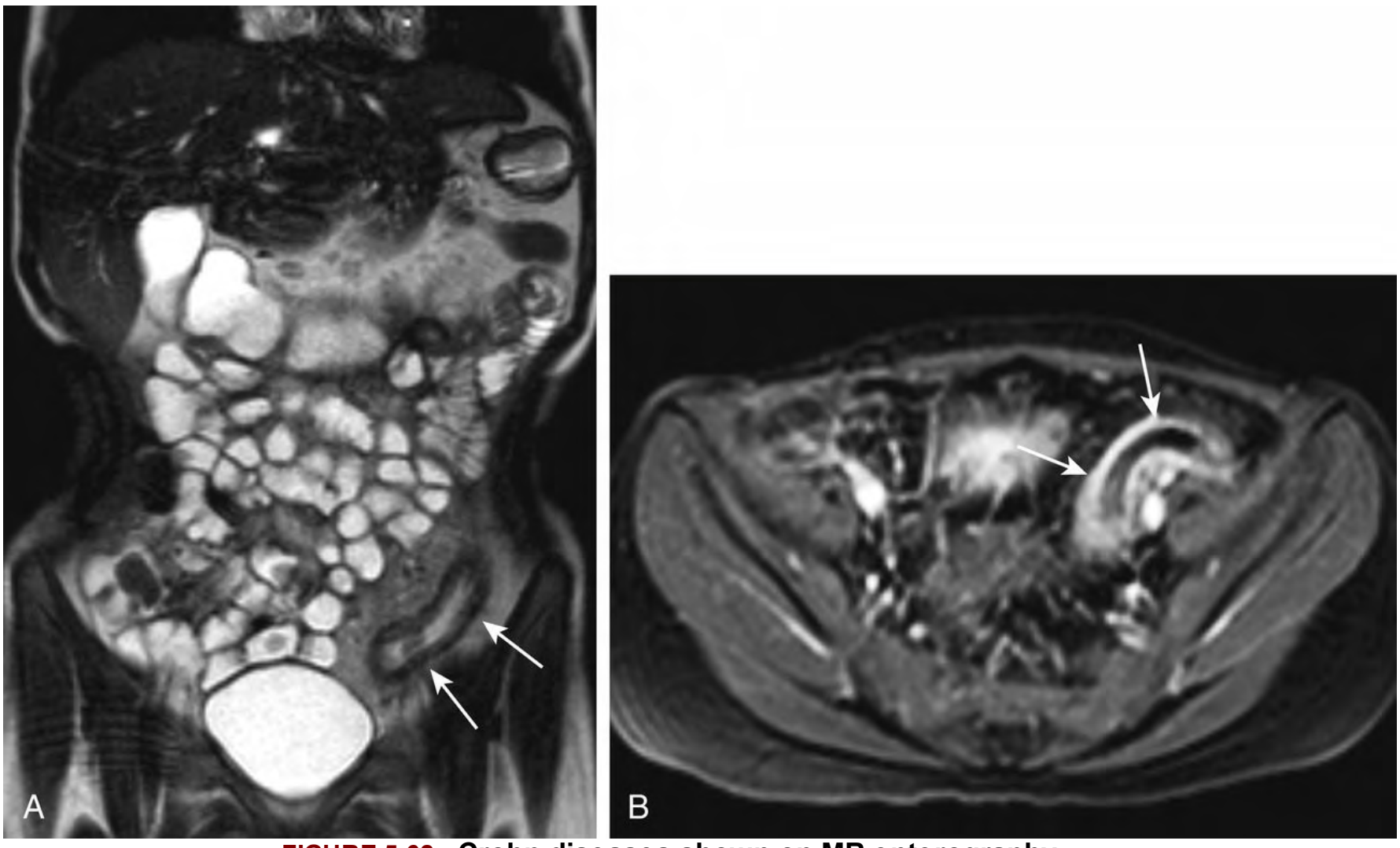
▪ **FIGURE 5-61 Abdominal Complications of Cystic Fibrosis.**
CT shows irregular liver *(L)* consistent with cirrhosis. There are findings consistent with portal hypertension, including splenomegaly *(S)* and multiple varices *(arrowheads)*. Note atrophy and fatty replacement of pancreas *(arrows)*.

Another cause of bowel pathology in cystic fibrosis is the development of colonic thickening or stricture resulting from iatrogenic damage caused by pancreatic enzyme replacement therapy.

Other gastrointestinal problems associated with cystic fibrosis include cirrhosis, portal hypertension and varices, gallstones, and pancreatic atrophy (Fig. 5-61). Patients with cystic fibrosis may have striking atrophy and fatty replacement of the pancreas on imaging studies, such as CT, sonography, and MRI.

▪ Inflammatory Bowel Disease in Children

Although typically considered a disease of adults, inflammatory bowel disease (IBD) often occurs in children, with as many as 25% of cases presenting during childhood. Crohn disease accounts for 65% of childhood IBD, and ulcerative colitis and nondefined cases make up the remaining 35%. Childhood Crohn disease more often involves the distal small bowel and colon than does adult disease. CT and MR enterography have become the imaging tests of choice in the evaluation of IBD. Both CT and MR enterography are both excellent studies and both have advantages and disadvantages. MR enterography has become favored in many clinical scenarios because of the lack of radiation. Imaging findings include bowel wall thickening, mucosal hyperenhancement, mural stratification (ability to see three layers), skip lesions (Crohn disease), strictures, fistula, engorgement of the vasa recta, pericolonic inflammation, enlarged lymph nodes, abscess, and free fluid (Fig. 5-62).



▪ **FIGURE 5-62** **Crohn diseases shown on MR enterography.**
A, Coronal T2-weighted image shows abnormal loop of large bowel in left lower quadrant *(arrows)* with bowel wall thickening and surrounding fatty infiltration. **B,** Axial postcontrast image shows abnormal enhancement *(arrows)* of thickened bowel wall.

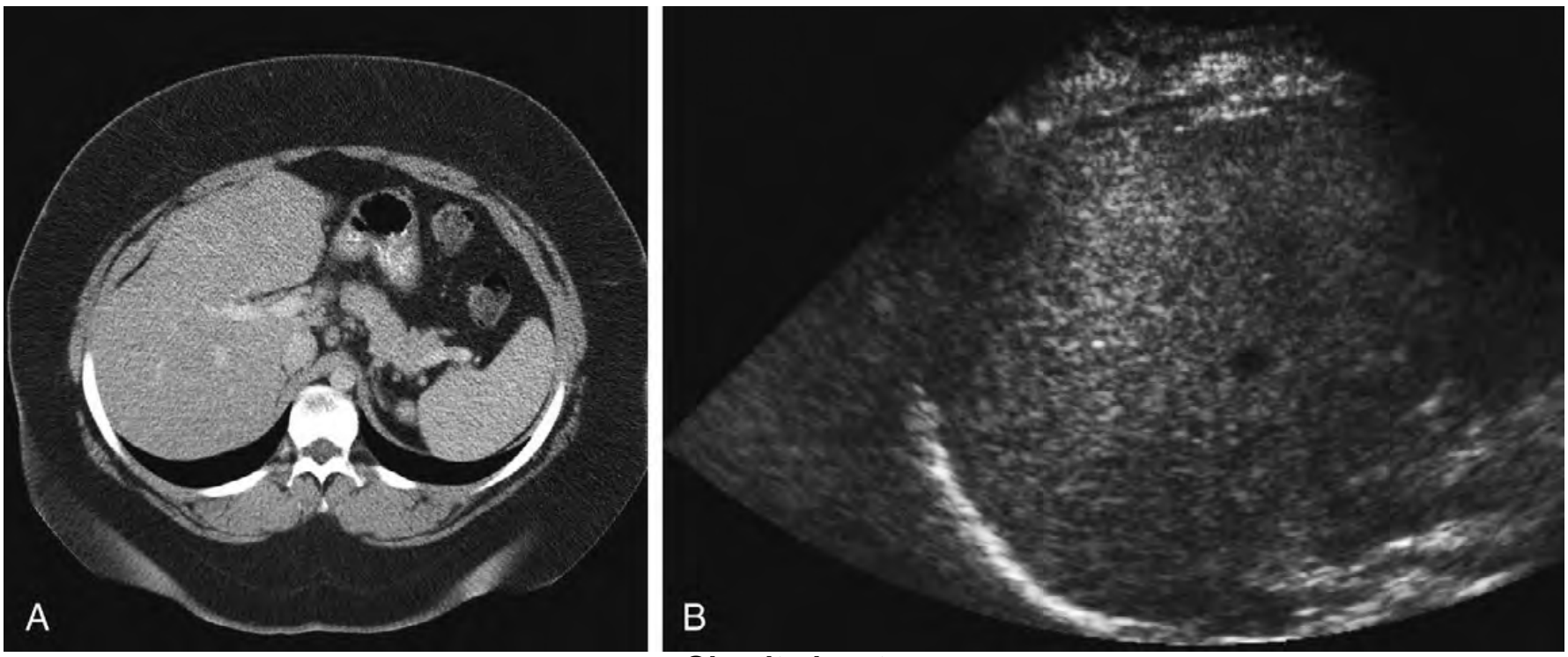
▪ Pediatric Obesity

Pediatric obesity has reached epidemic proportions. It is estimated that somewhere between one fifth and one third of children in the United States are obese. Pediatric obesity is also becoming a worldwide trend. If you consider which pediatric diseases are common and which cause significant morbidity and mortality in adulthood, pediatric obesity may well be the number one pediatric health concern. Obesity is a multiorgan system problem but is included here in the musculoskeletal chapter.

Pediatric obesity has a well-documented association with several diseases of childhood, such as slipped capital femoral epiphysis, but is also associated with a host of other potential problems, including psychosocial problems (poor self-esteem, depression), glucose intolerance and type 2 diabetes mellitus (the frequency of pediatric type 2 diabetes mellitus has increased 100 times in the past 20 years), hyperlipidemia, steatohepatitis (Fig. 5-63), cholelithiasis, obstructive sleep apnea, hypertension, and pulmonary embolism. Many of these traditionally adult disorders are now being encountered in obese children. Perhaps most concerning, approximately 80% of obese children will go on to be obese adults and have all of the associated morbidity.

Obesity poses multiple challenges for imaging in a pediatric setting. Most children's hospitals are geared toward dealing with the small end of the human spectrum, but they have not traditionally been well equipped to deal with the large end. Issues of image quality, imaging equipment weight limits, and diameter size limits can all be problematic.

Some have suggested that pediatric radiologists can take an advocacy role in raising awareness of pediatric obesity by including mention of obesity, when obviously present, within the impression of radiology reports. Written documentation of obesity in an official report can increase caregivers' and parents' awareness of a child's obesity.



▪ **FIGURE 5-63** **Obesity in a teenager.**

A, CT shows large amounts of subcutaneous fat. Note low attenuation in liver consistent with fatty infiltration. The image is of low quality related to the patient's large mass. **B,** Transverse ultrasound of the liver shows heterogeneous increased echogenicity related to fatty infiltration. Note low quality of exam related to patient's large size and difficulty with ultrasound penetration.

Suggested Readings

Buonomo C. Neonatal gastrointestinal emergencies. *Radiol Clin North Am*. 1997;35:845–864.

Choudhary A.K, Donnelly L.F, Racadio J.M, Strife J.L. Diseases associated with childhood obesity. *AJR*. 2007;188:1118–1130.

Donnelly L.F. CT imaging of immunocompromised children with acute abdominal symptoms. *Am J Roentgenol*. 1996;167:909–913.

Donnelly L.F, Bisset G.S. Pediatric liver imaging. *Radiol Clin North Am*. 1998;36:413–427.

Kirks D.R. Air intussusception reduction: "the winds of change.". *Pediatr Radiol*. 1995;25:89–91.

Muchantef K, Epelman M, Darge K, et al. Sonographic and radiographic imaging features of the neonate with necrotizing enterocolitis: correlation findings with outcomes. *Pediatr Radiol*. 2013;43:1444–1452.

Olson D.E, Kim Y.W, Donnelly L.F. CT findings in children with Meckel diverticulum. *Pediatr Radiol*. 2009;39:659–663.

Orth R.C, Guillerman R.P, Zhang W, et al. Prospective comparison of MR imaging and US for the diagnosis of pediatric appendicitis. *Radiology*. 2014;272:233–240.

Sivit C.J, Taylor J.A, Bulas D.I, et al. Posttraumatic shock in children: CT findings associated with hemodynamic instability. *Radiology*. 1992;182:723–726.

Taylor G.A. CT appearance of the duodenum and mesenteric vessels in children with normal and abnormal bowel rotation. *Pediatr Radiol*. 2011;41:1378–1383.

Teele R.L, Smith E.H. Ultrasound in the diagnosis of idiopathic hypertrophic pyloric stenosis. *N Engl J Med*. 1977;296:1149–1150.

Towbin A.J, Sullivan J, Denson L.A, et al. CT and MR enterography in children and adolescents with inflammatory bowel disease. *RadioGraphics*. 2013;33:1843–1860.

Yousefzadeh D.K. The position of the duodenojejunal junction: the wrong horse to bet on in diagnosing or excluding malrotation. *Pediatr Radiol*. 2009;39:s172–s177.

Zarewych Z.M, Donnelly L.F, Frush D.P, Bisset J.S. Imaging of pediatric mesenteric abnormalities. *Pediatr Radiol*. 1999;29:711–719.

CHAPTER 6

Genitourinary

Monica Epelman

Urinary Tract Infections

Urinary tract infection (UTI) is the most common problem of the genitourinary system encountered in children. The urinary tract is the second most common site of infection in children overall, with the upper respiratory tract being the first. The incidence of UTI is higher in girls than in boys, probably because of the short length of the female urethra. There is some current controversy concerning when children with UTIs should be imaged. According to the revised 2011 American Academy of Pediatrics (AAP) guidelines on UTI in febrile infants and young children, voiding cystourethrograms (VCUGs) are no longer routinely performed after the first febrile UTI. The immediate goals of imaging children with UTIs include identifying underlying congenital anomalies that predispose the child to UTI, identifying vesicoureteral reflux (VUR), identifying and documenting any renal cortical damage, providing a baseline renal size for subsequent evaluation of renal growth, and establishing prognostic factors. The long-term goal is to eliminate the chance of renal damage leading to chronic renal disease and hypertension.

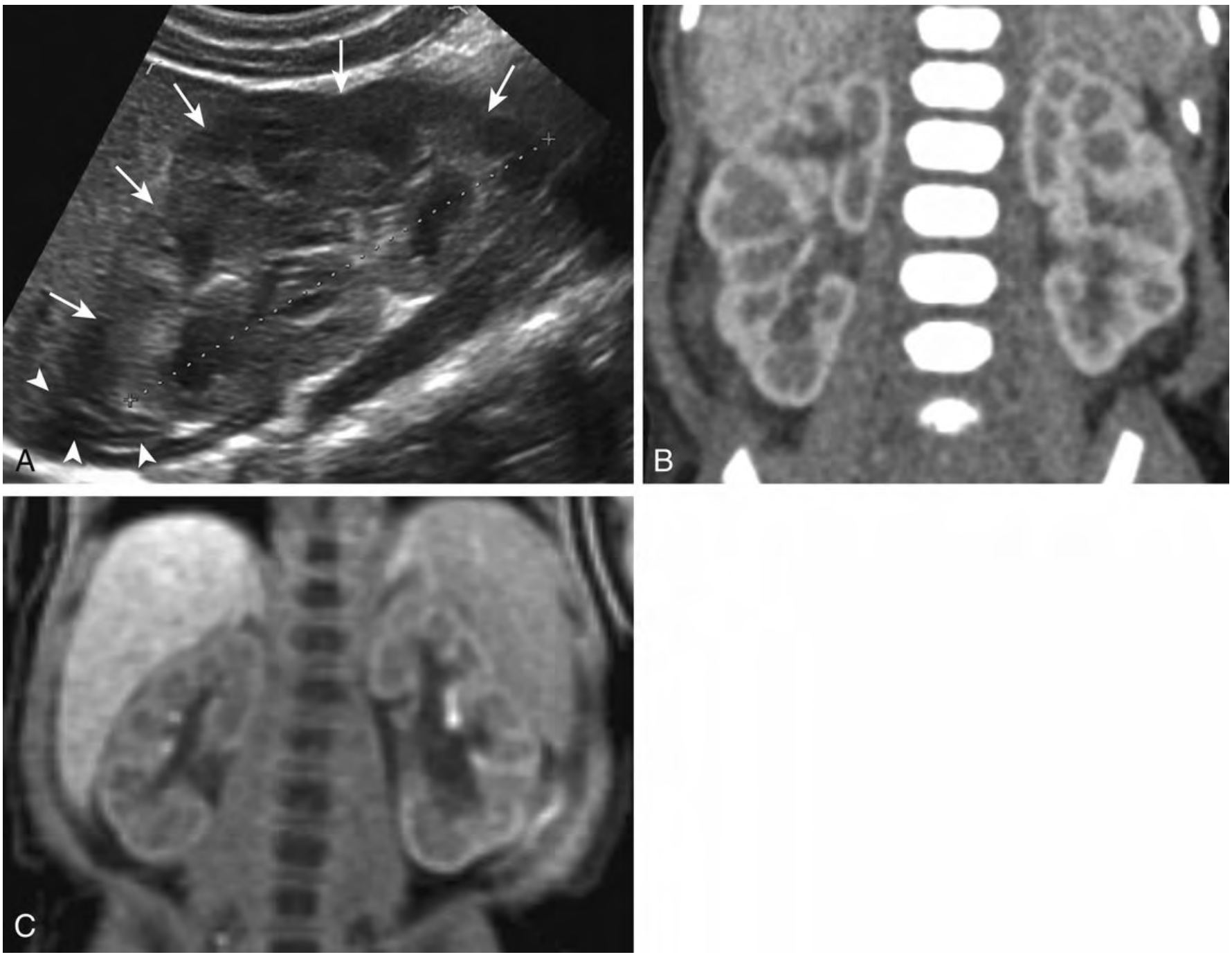
The work-up of a child with a first febrile UTI typically involves a renal and bladder ultrasound. However, routine VCUGs after a first febrile UTI are currently no longer recommended. Ultrasound is a poor screening test for the diagnosis of VUR; therefore the current imaging recommendations in young infants and children are widely debated. Under the current guidelines, VCUG should be obtained only if (1) the renal and bladder ultrasound shows hydronephrosis, scarring, obstructive uropathy, or masses; (2) any complex medical condition is associated with the UTI; (3) other findings that suggest high-grade VUR or obstructive uropathy are appreciated; or (4) there is a recurrence of febrile UTI. VCUGs can be performed using fluoroscopy or nuclear medicine. There is some debate about the indications for one or the other of the two studies. The advantage of the fluoroscopic cystourethrogram is that it demonstrates better anatomic detail. The advantage of the nuclear cystogram is that the patient is exposed to less radiation. However, in modern fluoroscopic units with pulse fluoroscopy, the difference in radiation dose between the two techniques is minimal. Because of the need for sharp anatomic detail in all boys and in girls with anatomic abnormalities demonstrated on ultrasound, most would advocate fluoroscopic cystograms for those patients. Nuclear cystograms are adequate for girls with normal ultrasound examinations. In other portions of the globe, the VCUG has been nearly entirely substituted by voiding urosonography, an ultrasound examination using intravesical contrast agent (microbubbles).

Renal Ultrasound

In many pediatric institutions, renal ultrasounds are performed with the patient in both the supine and prone positions. Transverse and longitudinal images are obtained of the kidney and bladder. Renal lengths are measured in both the prone and supine positions but are often more accurate with the patient in the prone position. In every case it is important to compare the patient's renal length with tables that plot normal renal length against age. In addition, the left and right kidneys should normally be within 1 cm of each other in length. If there is a discrepancy of more than 1 cm, an underlying abnormality should be suspected. A size discrepancy may result from a disorder that causes one of the kidneys to be too small, such as global scarring, or from a process that causes one of the kidneys to be too large, such as acute pyelonephritis or renal duplication.

The kidneys of infants have several characteristics that are different from those of older children and adults. They commonly have a prominent undulating contour. This is a normal appearance secondary

to fetal lobulation (Fig. 6-1). In addition, infants' kidneys can demonstrate prominent hypoechoic renal pyramids (see Fig. 6-1) in contrast to the more echogenic renal cortex. These findings should not be mistaken for hydronephrosis.



▪ **FIGURE 6-1** **Normal imaging appearance of neonatal kidney.**
A, Longitudinal ultrasound of a normal neonatal kidney *(between calipers)* shows prominent hypoechoic renal pyramids, which are regularly arranged. This normal finding should not be confused with hydronephrosis. No discrete central sinus echogenicity is noted. Also note fetal lobulation as focal indentations *(arrows)* located between medullary pyramids. The renal cortex appears thinner, when compared with older children or adults. Note the relatively prominent, normal neonatal adrenal gland *(arrowheads)*. **B,** Early postcontrast coronal reformatted CT image and **C,** MR T1-weighted fat suppressed images of normal neonatal kidneys in different patients show similar findings.

Magnetic Resonance Urography

With the advent of improved magnetic resonance imaging (MRI) technology, MR urography (MRU) has been increasingly used because of its superb delineation of the anatomy as a result of its intrinsic, high soft tissue contrast resolution and multiplanar three-dimensional reconstruction capabilities. MRU is considered a "one-stop shop" examination because it can provide both anatomical and functional information in one examination without the use of ionizing radiation. MRU plays an important role in the evaluation of ureteral ectopia and genital anomalies. However, the widespread use of MRU is limited by its cost, availability, and the need for sedation.

Fluoroscopic Voiding Cystourethrogram

The most common indication for a fluoroscopic VCUG is the evaluation of UTI. Other indications include voiding dysfunction, enuresis, and the work-up for hydronephrosis. The VCUG demonstrates

the presence or absence of VUR and also documents anatomic abnormalities of the bladder and urethra. Because catheterization is used for the procedure, there can be a great deal of anxiety for both the patient and the parents. Education of the parents and patient before the examination is crucial to optimizing the patient's experience. VCUGs are performed under fluoroscopy with the patient awake. The patient is catheterized under sterile conditions on the fluoroscopy table, typically using an 8F catheter. A precontrast scout view of the abdomen can be obtained to evaluate for calcifications, document the bowel pattern so that it is not later mistaken for VUR, and document the catheter position within the bladder. Contrast is then instilled into the bladder. An early filling view of the bladder should be obtained to exclude a ureterocele. A ureterocele appears as a round, well-defined filling defect on early filling views. On later full views of the bladder a ureterocele can be compressed and obscured. Once the patient's bladder is full, bilateral oblique views are obtained to visualize the regions of the ureteral vesicular junctions. These views are typically obtained with the collimators open from top to bottom, with the bladder positioned at the inferior aspect of the screen and the expected path of the ureter included on the film. During voiding, the male urethra is optimally imaged with the patient in the oblique projection. The female urethra is best seen on the anteroposterior view. It is critical to obtain an image of the urethra during voiding, particularly in males. In order to ensure that a view of the urethra is obtained, an image should be obtained during urination with the catheter in place and then a second view can be obtained after the catheter has been removed. After the patient has completed voiding, images are obtained of the pelvis and over the kidneys, documenting the presence or absence of VUR and evaluating the extent of postvoid residual contrast within the bladder and renal collecting systems. The use of fluoroscopy should be brief and intermittent during bladder filling. Fluoroscopic last-image hold images can often substitute for true exposures to further decrease radiation dose.

Sometimes, particularly in older children, it may be difficult to get the child to void on the table. Almost all children will eventually void, and a great deal of patience is required during such prolonged examinations. There are several maneuvers that may help the child to void. They include placing warm water on the patient's perineum or toes; placing a warm washcloth on the patient's lower abdomen; tilting the table so that the head is up; letting the patient hear the sound of running water in the sink; and dimming the lights.

The expected bladder capacity of small children can be calculated by adding 2 to the patient's age in years and multiplying that number by 30. This yields the bladder capacity in milliliters. Obviously this formula works only up to a certain age.

Acute Pyelonephritis

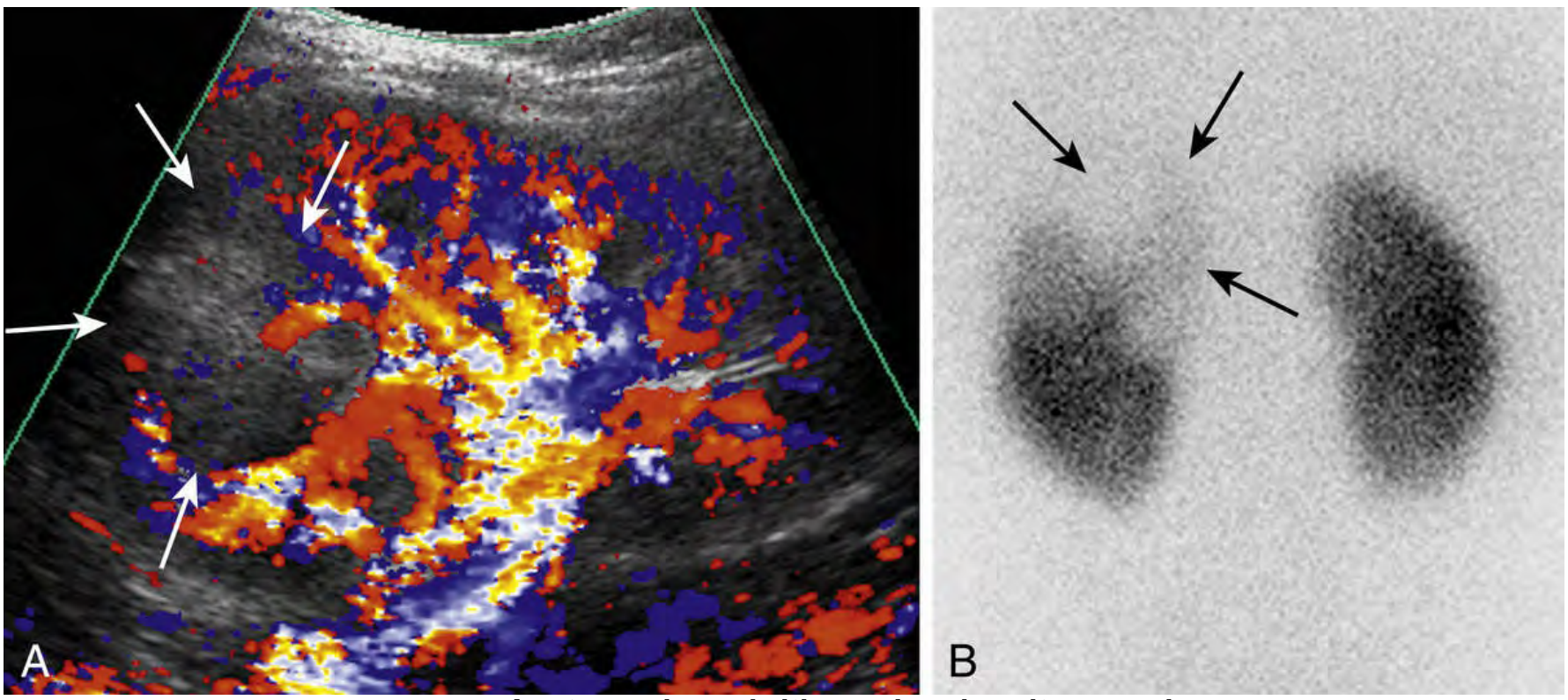
There is some confusion concerning the terminology used for infections of the urinary tract in children. The definition of UTI is the presence of bacteria in the urine, but the term typically refers to infections of the lower urinary tract. Acute pyelonephritis is defined as UTI that involves the kidney. Young children may present with nonspecific symptoms, such as fever, irritability, and vague abdominal pain. In older children the findings may be more specific, such as fever associated with flank pain. In patients in whom the diagnosis is straightforward, no imaging is needed during the acute infection. Cortical scintigraphy using dimercaptosuccinic acid (DMSA) has been advocated as being the most sensitive test for the diagnosis of pyelonephritis, demonstrating single or multiple areas of lack of renal uptake of the radiotracer. These areas tend to be triangular and peripheral (Fig. 6-2). Other imaging studies that have also been advocated to detect acute pyelonephritis include color Doppler ultrasound and contrast-enhanced computed tomography (CT). These studies typically demonstrate lack of color flow or contrast enhancement of triangular, peripheral portions of the kidney (Fig. 6-3). CT may show a striated nephrogram (Fig. 6-4). In addition, pyelonephritis can be very focal and can mimic a mass on all of these studies (Fig. 6-5, *A* and *B*). Ultrasound and CT may also demonstrate disproportionate enlargement and swelling of the affected kidney as compared with the contralateral side. Sometimes the findings of pyelonephritis will be encountered on these imaging studies when the studies were obtained for other suspected causes of abdominal pain, such as appendicitis.



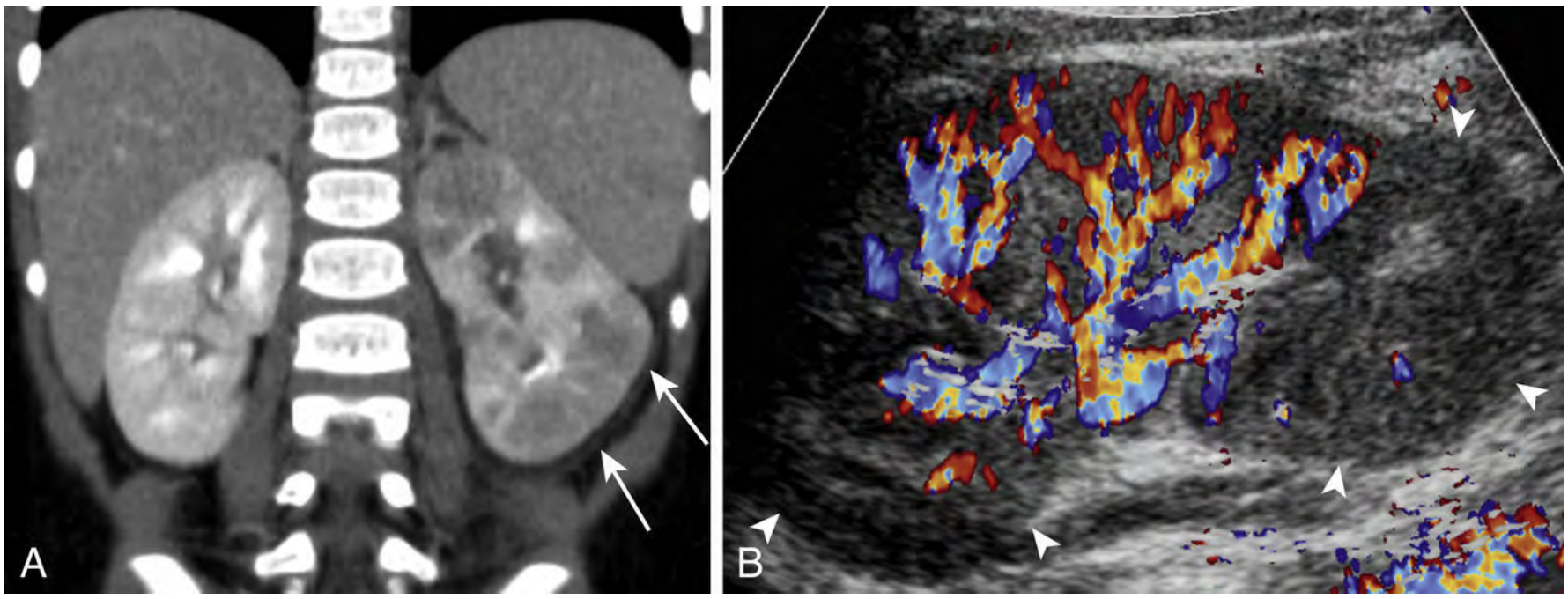
▪ **FIGURE 6-2** **Acute pyelonephritis.**
Nuclear scintigraphy with DMSA shows a focal, wedge-shaped area of decreased uptake *(arrow)* in the upper pole of the left kidney, consistent with pyelonephritis in a child with known reflux and flank pain.

Chronic Pyelonephritis

Chronic pyelonephritis is defined as the loss of renal parenchyma resulting from previous bacterial infection. It is synonymous with renal scarring. Normally the renal cortical thickness should be symmetric and equal within the upper, mid, and lower poles of the kidneys. The loss of renal cortical substance as seen by ultrasound, most commonly at one of the renal poles, is suggestive of the diagnosis (Fig. 6-6). This should not be confused with fetal lobulation (also known as an interrenicular septum; Fig. 6-7), a normal variant. In pyelonephrotic scarring the indentations of the renal contour tend to overlie the renal calyces, whereas in fetal lobulation the indentations are between renal calyces (see Fig. 6-7).



▪ **FIGURE 6-3** **Acute pyelonephritis on doppler ultrasound.**
A, Longitudinal color Doppler ultrasound shows lesion *(arrows)* as peripheral area of absent color flow. **B,** Corresponding nuclear scintigraphy with DMSA show a wedge-shaped defect of decreased uptake *(arrows)* in the upper pole of the left kidney.



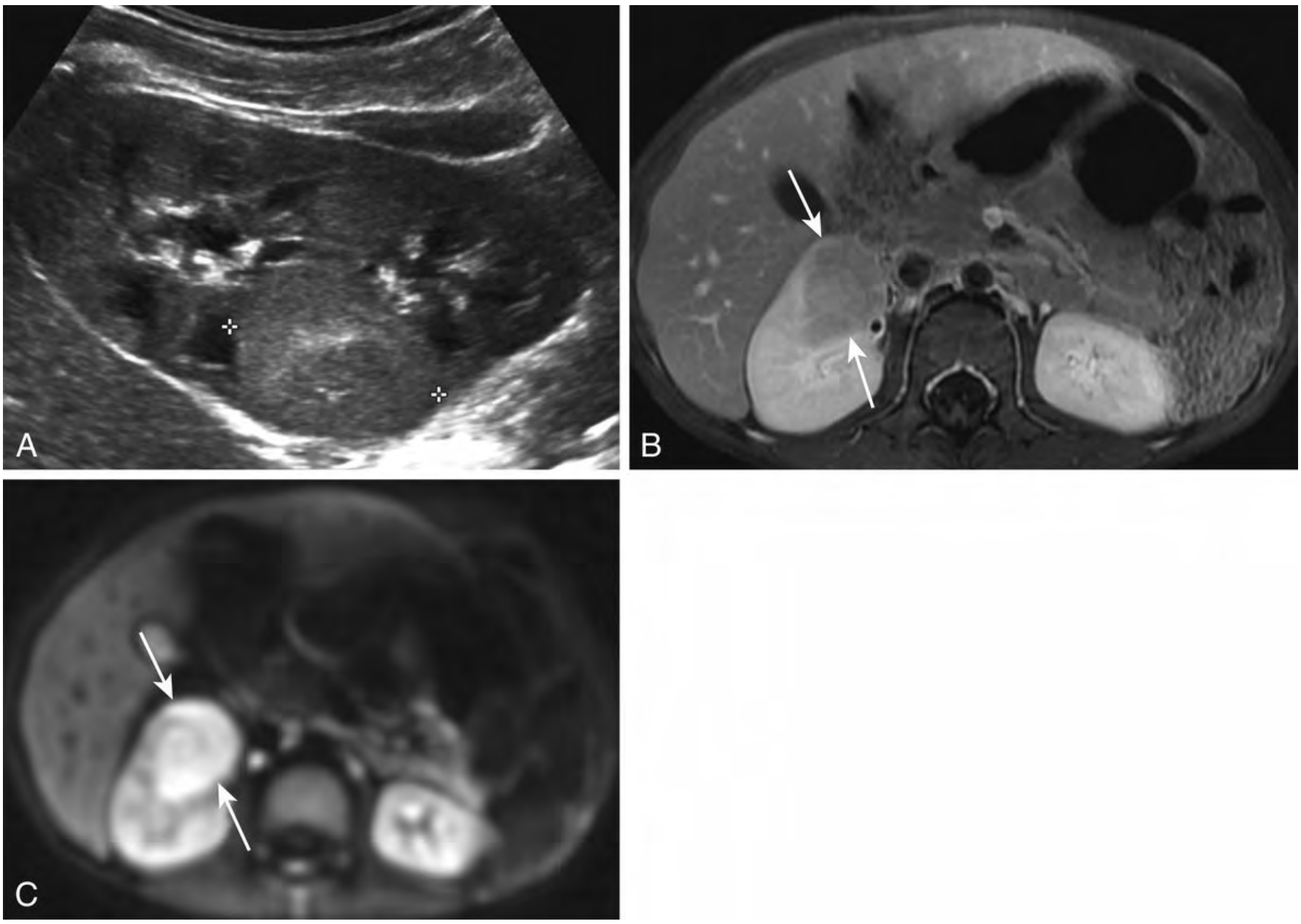
▪ **FIGURE 6-4** **Acute pyelonephritis on CT obtained for abdominal pain.**
A, Pyelonephritis appears as asymmetric increased volume of left kidney, with focal, wedge-like regions of hypoenhancement in the left upper and lower kidney poles. Note perinephric stranding with thickening of Gerota fascia *(arrows)*. **B,** Corresponding color Doppler ultrasound image shows focal areas of hyperechogenicity with loss of the corticomedullary differentiation and decreased flow in both left kidney poles *(arrowheads)*.

▪ Evaluation of Prenatally Diagnosed Hydronephrosis

As a result of the increasing use of prenatal ultrasound, pediatric radiologists are more frequently having to perform postnatal work-ups of prenatally diagnosed hydronephrosis. The evaluation of such patients typically includes both. The controversy revolves around the timing of the ultrasound evaluation. In neonates there is a relative state of dehydration that occurs after the first 24 hours of life. Reports have shown that this relative state of dehydration can lead to underestimation or nondetection of hydronephrosis by ultrasound. Therefore it is recommended that the postnatal evaluation of prenatally diagnosed hydronephrosis be performed during the first 24 hours of life or after 1 week of age. The disadvantage of doing the ultrasound during the first 24 hours of life is the interruption of mother-child bonding, whereas the disadvantage of performing the examination at 7 days of life is the potential of parental noncompliance and losing the patient for follow-up.

Congenital Anomalies

Congenital anomalies of the genitourinary tract are commonly encountered during work-ups for UTIs or other abnormalities.



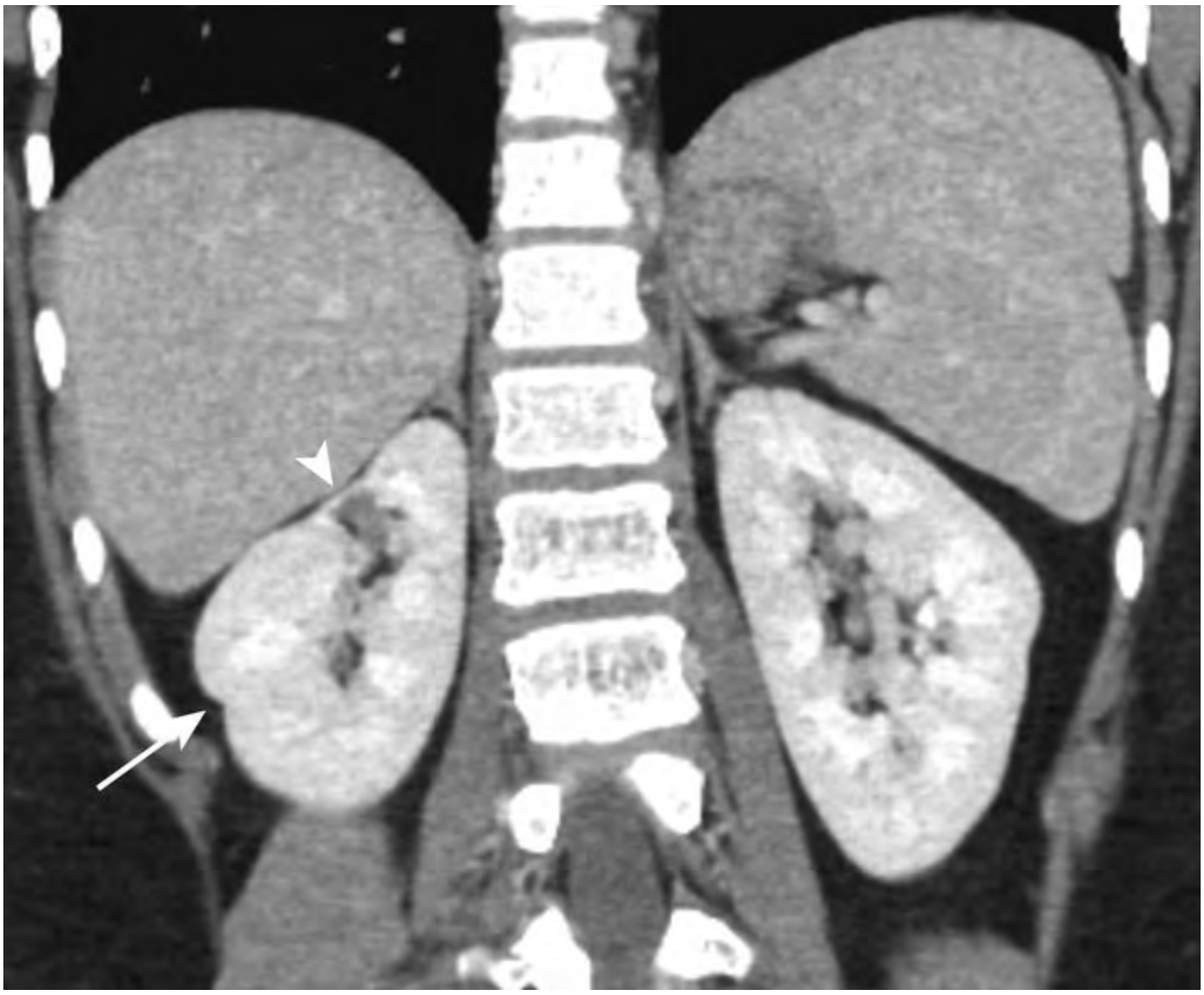
▪ **FIGURE 6-5** **Acute, focal pyelonephritis presenting as a mass.**
A, Longitudinal ultrasound shows a heterogeneous mass *(between calipers)* with areas of increased echogenicity. **B,** Corresponding axial postcontrast T1-weighted fat suppressed MR image shows a heterogeneous mass *(arrows)* with reduced enhancement (**C**), and restricted diffusion of diffusion-weighted imaging.



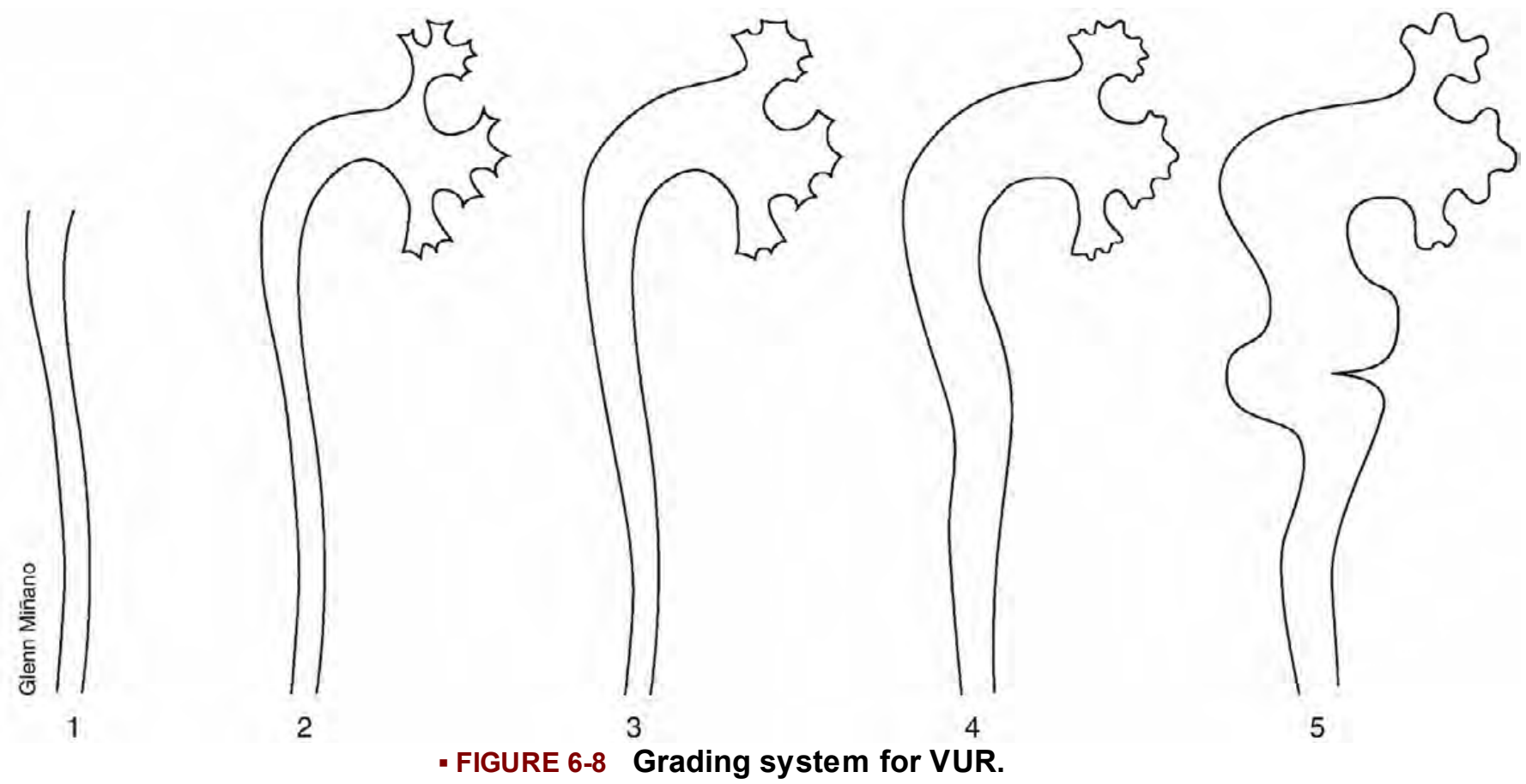
▪ **FIGURE 6-6** Global renal scarring shown on longitudinal ultrasound of the left kidney. There is diffuse thinning of the renal parenchyma, most striking in the upper pole *(arrow)*, where the renal surface is in close approximation to the collecting system.

Vesicoureteral Reflux

VUR is defined as retrograde flow of urine from the bladder into the ureter. It is thought to be a primary abnormality related to immaturity or maldevelopment of the ureterovesicular junction. Normally the ureter enters the ureterovesicular junction in an oblique manner such that the intramural ureter traverses the bladder wall for an adequate length to create a passive antireflux valve. In VUR the angle of entrance of the ureter is abnormal and the intramural tunnel is short, resulting in VUR. VUR occurs in less than 0.5% of asymptomatic children but is present in as much as 50% of children with UTIs. There is an increased incidence of VUR in siblings of children with VUR and in children of parents who had VUR. VUR incidence is lower in individuals of West African descent. The importance of VUR is its association with renal parenchymal scarring. VUR is present in almost all children with severe renal scarring. In addition, a direct correlation between the grade of VUR and prevalence of scarring has been demonstrated. Other complications associated with VUR include acute pyelonephritis, interference with the normal growth of the kidney, and development of hypertension. The degree of VUR is graded on the basis of several characteristics (Fig. 6-8): the level to which the reflux occurs (ureteral versus ureteral and collecting system); the degree of dilatation; the calyceal blunting; and papillary impressions. Grade 1 reflux is confined to the ureter. Grade 2 reflux fills the ureter and collecting system, but there is no dilatation of the collecting system. Grade 3 reflux is associated with blunting of the calyces. In deciding whether a calyx is dilated or not, it has been taught that if it looks like you could pick your teeth with a calyx, it is not dilated (Fig. 6-9). Grade 4 reflux is identified by progressive, tortuous dilatation of the renal collecting system. Grade 5 reflux is defined by the presence of a very tortuous dilated ureter. Both grade 4 and 5 reflux can be associated with intrarenal reflux. It is surprising, but significant VUR can be present in spite of a normal renal ultrasound. Lack of dilatation on ultrasound in no way excludes the presence of VUR. Dilatation of the ureter or collecting systems can sometimes be seen intermittently when VUR is present.



▪ **FIGURE 6-7** Differentiation between fetal lobulation and focal scarring; both are demonstrated in the same patient. Coronal CT shows indentation and thinning of the right upper pole renal cortex directly over the medullary pyramids *(arrowhead)*. This area represents focal scarring. There is also an indentation in the renal cortex between the medullary pyramids *(arrow)*. This is consistent with fetal lobulation.



▪ **FIGURE 6-8** **Grading system for VUR.**
Grade 1: Reflux is confined to the ureter. Grade 2: Reflux fills the ureter and collecting system without dilatation of the collecting system. Grade 3: Reflux is associated with blunting of the calyces. Grade 4: Reflux results in progressive, tortuous dilatation of the renal collecting system. Grade 5: Reflux is defined by the presence of a very tortuous, dilated ureter.

Most low-grade VUR resolves spontaneously by the age of 5 to 6 years unless there is an underlying anatomic abnormality. In children without anatomic reasons that prohibit spontaneous resolution of

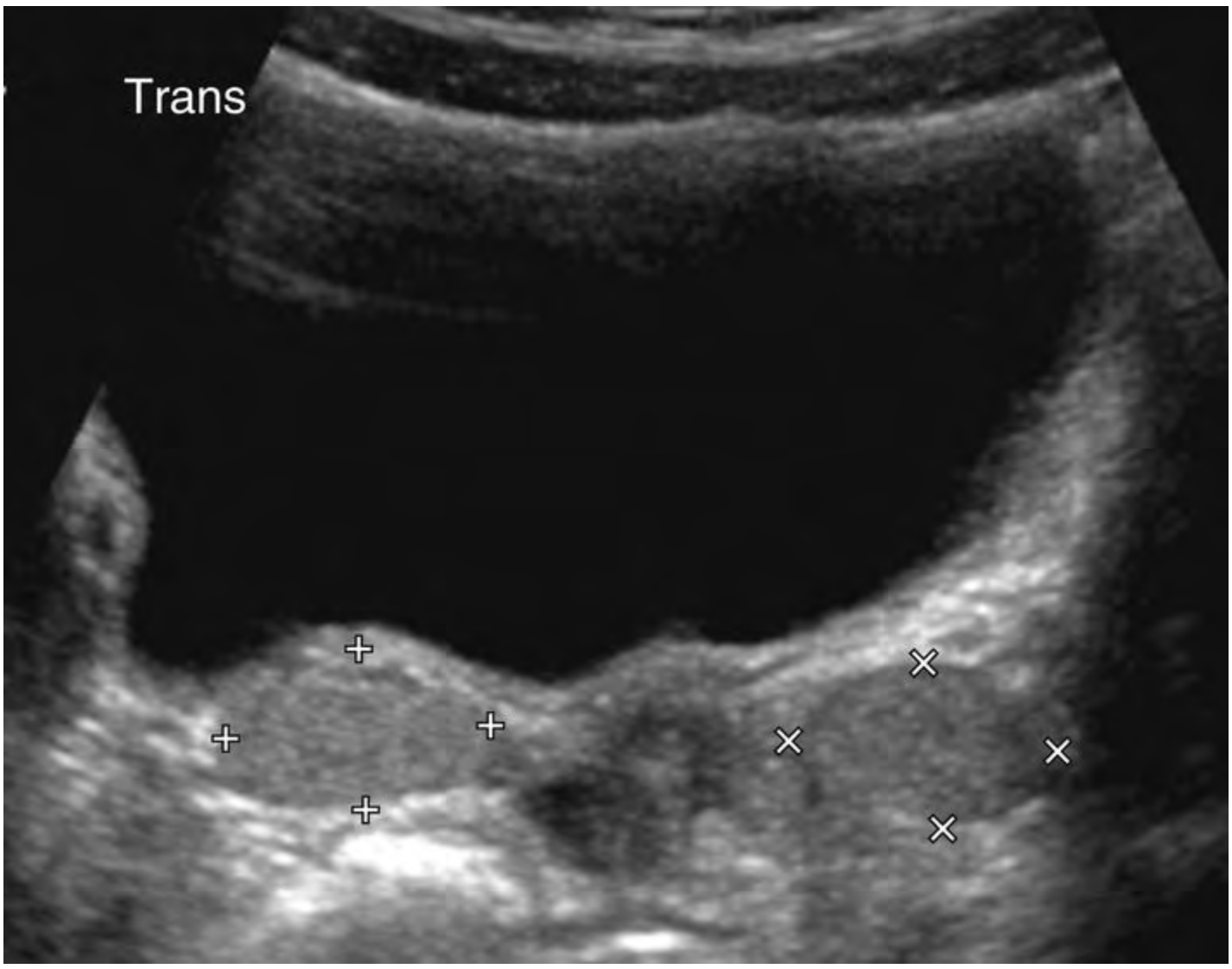
reflux, most are treated with prophylactic antibiotics alone, although this is controversial. Antibiotic therapy is discontinued when the reflux has resolved. Surgical reimplantation of the ureter or injection of a bulking agent below the ureteric orifice (minimally invasive endoscopic treatment) is considered when the degree of VUR is severe, if there is evidence of renal scarring, if the VUR has not resolved over a reasonable time, or if breakthrough infections occur frequently. After periureteral injection, ultrasound will show an echogenic mound in the bladder wall in the region of the treated ureteral orifice (Fig. 6-10).

Ureteropelvic Junction Obstruction

Ureteropelvic junction (UPJ) obstruction is defined as an obstruction of the flow of urine from the renal pelvis into the proximal ureter. It is the most common congenital obstruction of the urinary tract. There is an increased incidence of other congenital anomalies of the urinary tract in patients with UPJ obstruction. They include VUR and renal duplication, among others. Males are more often affected than females, and there is a predilection for the left side. In addition, UPJ obstruction may be present bilaterally, but the severity may be asymmetric. The cause of most UPJ obstructions is intrinsic narrowing at the UPJ. However, extrinsic compression secondary to anomalous vessels is also occasionally identified. On ultrasound there is dilatation of the renal collecting system without dilatation of the ureter (Fig. 6-11). The degree of dilatation may be severe. Renal scintigraphy using technetium 99m mercaptoacetyltriglycine (MAG 3) with diuretic (furosemide) challenge is often used to evaluate the severity of the UPJ obstruction. Most neonates with UPJ obstruction are characteristically asymptomatic, and the condition is usually detected following postnatal ultrasound evaluation of antenatal hydronephrosis. Children with UPJ obstruction and other congenital anomalies are predisposed to renal injury even by minor abdominal trauma (Fig. 6-12). Mild to moderate UPJ obstructions are sometimes treated conservatively, but most urologists treat severe UPJ obstruction surgically, with the gold standard, open pyeloplasty, being increasingly replaced by robotic or laparoscopic pyeloplasty, with similar rates of success.



▪ **FIGURE 6-9** **VUR shown on VCUG: right, grade 2, and left, grade 4.**
Image shows reflux of contrast filling a nondilated right renal collecting system. Note that the calyces are sharp in appearance and are not blunted. On the left, there is reflux of contrast filling a dilated ureter and collecting system. The calyces are markedly blunted.

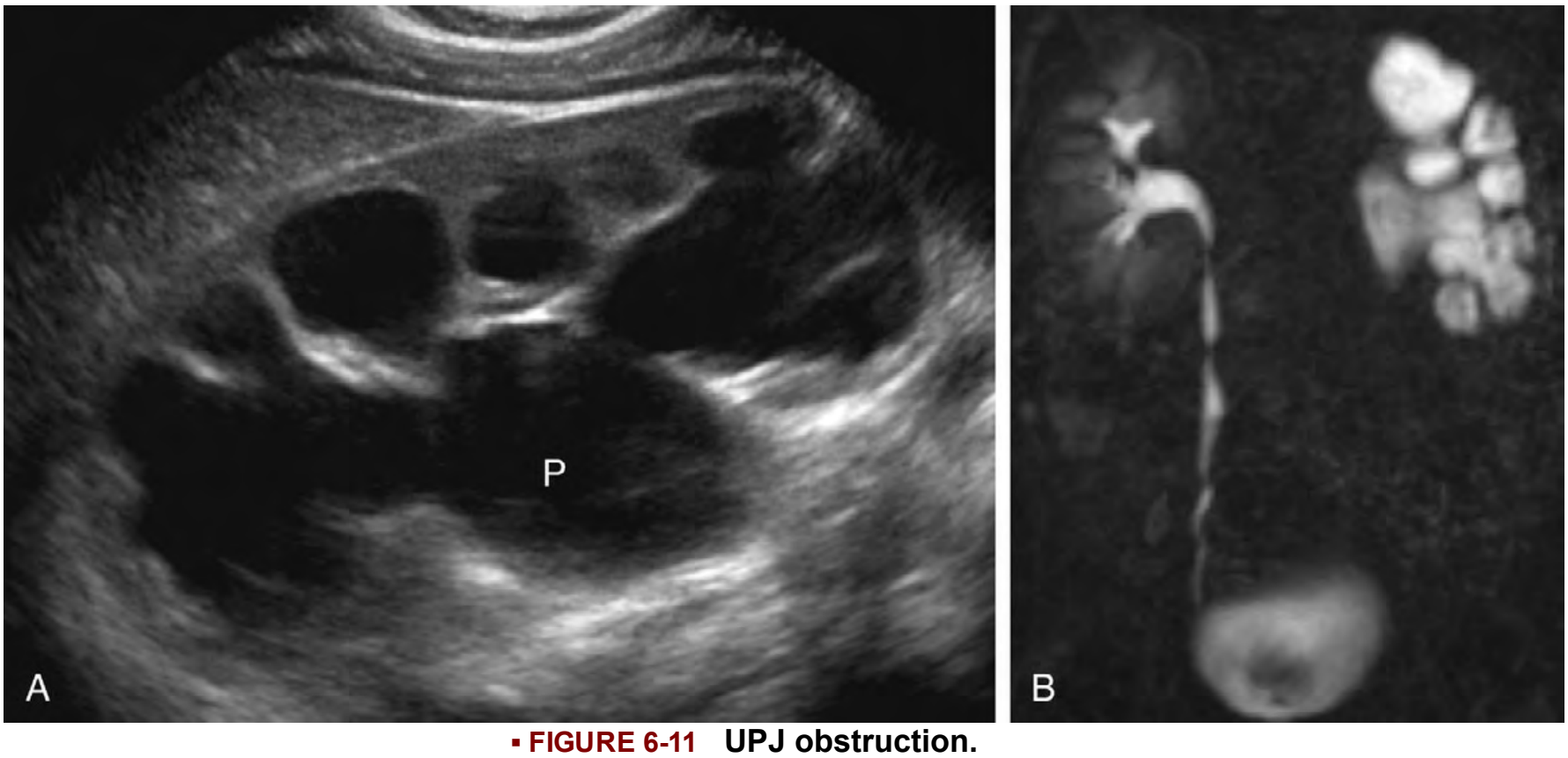


▪ **FIGURE 6-10** Ultrasound appearance following minimally invasive endoscopic treatment of VUR using periureteral injection of Deflux. Transverse (trans) ultrasound image shows bilateral echogenic mounds *(between calipers)* at base of bladder in region of the ureterovesicular junctions.

Multicystic Dysplastic Kidney

Multicystic dysplastic kidney (MCDK) is thought to be related to severe obstruction of the renal collecting system during fetal development. The site of the obstruction determines the imaging appearance. The most common appearance of MCDK is that of a grapelike collection of variably sized cysts that do not appear to communicate (Fig. 6-13). Historically the diagnosis of MCDK has been made on the basis of DMSA scans demonstrating trace or no renal uptake on 4-hour images. Currently, high-quality ultrasound scans may suffice for the diagnosis in most instances. In patients with MCDK it is important to exclude other associated congenital anomalies of the contralateral kidney. UPJ obstruction is commonly identified. Rarely, MCDK can be isolated to an upper or lower pole.

Most MCDKs slowly decrease in size over time. Often the remaining residual dysplastic renal tissue will no longer be visualized by imaging techniques. Although in the past, nephrectomy was the usual treatment for MCDK, most patients are currently treated nonoperatively. However, they are followed by ultrasound because there is some controversy as to whether there may be an increased risk for developing malignancy in an MCDK. MCDK can also predispose patients to hypertension, and if hypertension develops, nephrectomy is usually performed.



▪ **FIGURE 6-11** **UPJ obstruction.**
A, Longitudinal ultrasound shows dilatation of renal collecting system, which connects to central, dilated renal pelvis *(P)*. The ureter was not dilated. **B,** Coronal maximum intensity projection (MIP) image from an MR urogram obtained from an acquisition performed approximately 10 min after intravenous gadolinium administration shows normal contrast excretion on the right and delayed excretion on the left with marked pelvicaliectasis and no delineation of the left ureter.



▪ **FIGURE 6-12** **Renal injury to child with UPJ obstruction following minor trauma.**
CT shows findings of left UPJ obstruction with dilatation of the renal collecting system and central, dilated renal pelvis *(P)*. There is a large amount of perinephric fluid secondary to injury to the dilated collecting system.

Ureteropelvic Duplications

The term *ureteropelvic duplication* refers to a broad range of anatomic variations ranging in severity from incomplete to complete. The incomplete form of duplication is more common than the complete form and is the most common anomaly affecting the upper renal collecting system. It occurs most often in

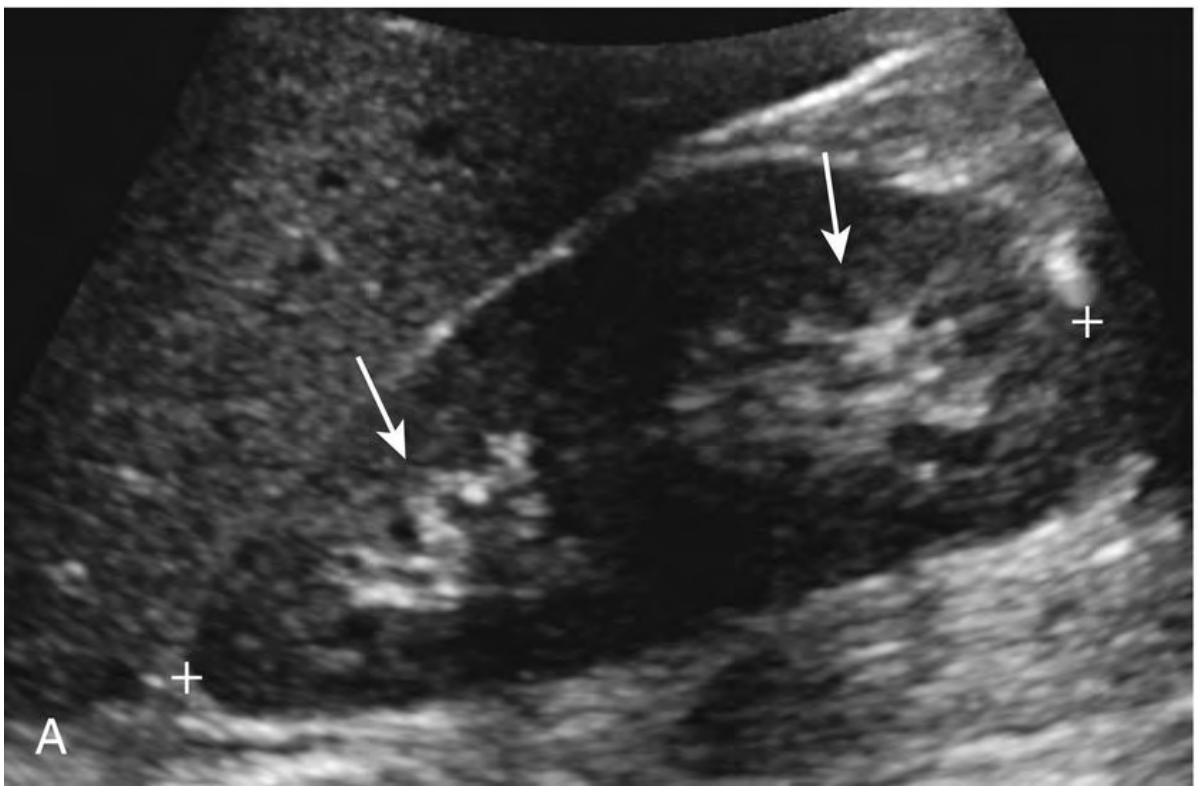
females. With incomplete duplication, there can be a bifid renal pelvis, two ureters superiorly that join in midureter, or duplicated ureters that join just before insertion into the bladder wall. With complete duplication there are two completely separate ureters that have separate orifices into the bladder. Ureteropelvic duplication is thought to occur secondary to premature division or duplication of the ureteral bud. Such duplications are five times more common unilaterally than bilaterally. On ultrasound, incomplete renal duplication may appear as an area of echogenicity similar to the renal cortex separating the echogenic central renal fat into superior and inferior components (Fig. 6-14). Noncomplicated, incomplete renal duplications have little significance and should be thought of as a normal variation. Children with incomplete duplication are not at increased risk for urinary tract disease as compared with children without duplications.

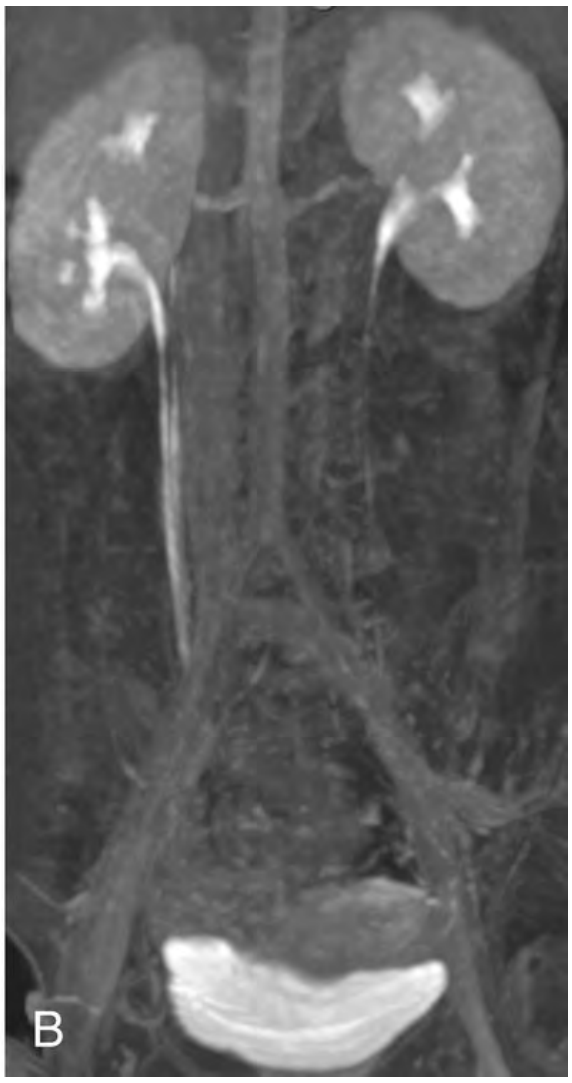
In patients with complete ureteropelvic duplication, there is a higher incidence of UTI, obstruction, VUR, and parenchymal scarring. In these patients the ureteral orifice of the upper pole moiety inserts more medially and more inferiorly than the orifice of the lower pole ureter. This is known as the Weigert-Meyer rule. The lower pole system is more prone to VUR. The upper pole system is more prone to obstruction secondary to an ectopic ureterocele (Figs. 6-15 and 6-16).



▪ **FIGURE 6-13** **Right MCDK.**

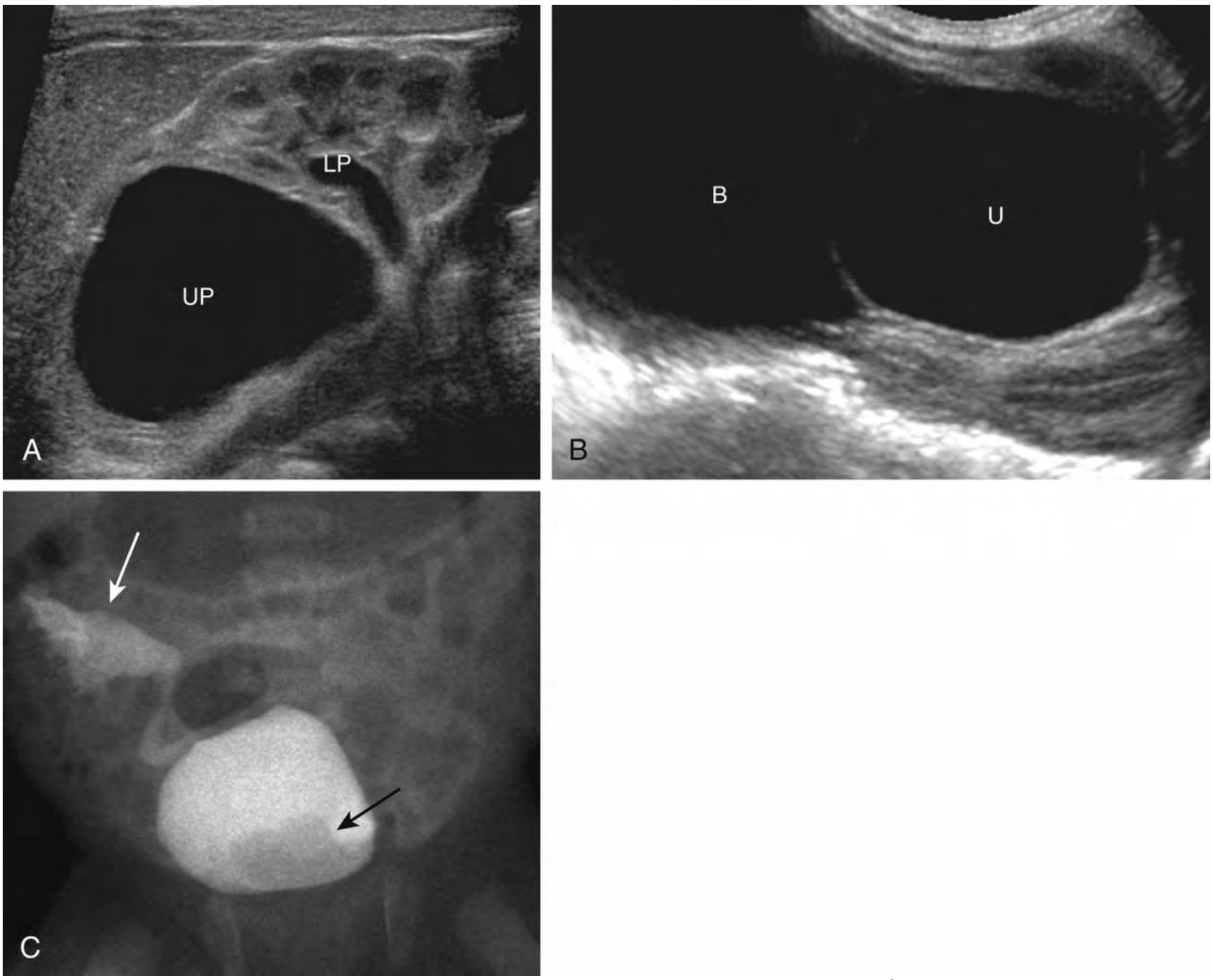
A, Coronal fetal T2-weighted MR image shows an enlarged right kidney *(arrows)* composed by multiple noncommunicating cysts of varying sizes. The right renal pelvis is not identified. The *arrowheads* denote the normal-appearing left kidney. **B,** MCDK shown on longitudinal ultrasound as cluster of anechoic cysts without dominant central cyst. **C,** Scintigraphy shows normal perfusion and function of the left kidney with no renal activity on the right. **D,** Axial T2-weighted spinal MR image redemonstrates the multicystic nature of the lesion.





▪ **FIGURE 6-14** **Duplex configuration.**

A, Intrarenal duplication shown on longitudinal ultrasound as an area of echogenicity similar to that of the renal cortex separating the central pelvicalyceal fat into separate superior and inferior components *(arrows)*. **B,** Coronal MIP image from an MR urogram confirms a duplex configuration of the right kidney with incomplete ureteral duplication, both ureters join in their middistal portion.

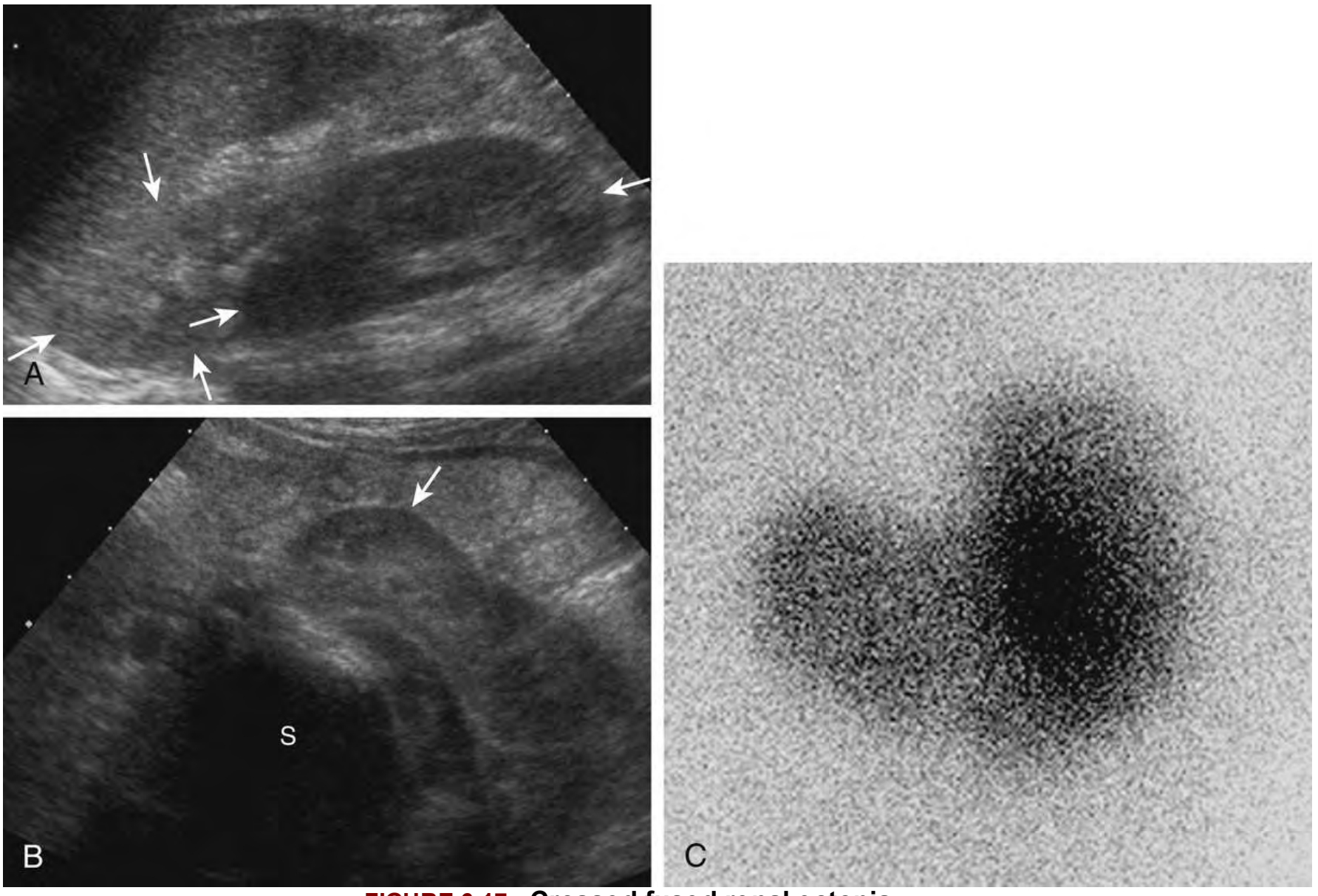


▪ **FIGURE 6-15** **Duplicated right renal collecting system with lower pole reflux and ureterocele causing obstruction of the upper pole.**

A, Longitudinal ultrasound of right kidney shows a markedly dilated upper pole collecting system *(UP)*, secondary to an obstructing ureterocele, and a mild dilatation of lower pole collecting system *(LP)*, secondary to VUR. **B,** Longitudinal ultrasound, right paramidline, of pelvis shows a ureterocele *(U)* as a thin-walled cystic structure within the bladder *(B)*. **C,** Image from VCUG shows a ureterocele *(black arrow)* as a round filling defect within the bladder. Note reflux into the lower pole collecting system *(white arrow)*. Also note that the opacified lower pole collecting system is displaced inferiorly by the dilatated, nonopacified, obstructed upper pole collecting system. This is called the *drooping lily sign.*



▪ **FIGURE 6-16** **Left renal collecting system duplication shown on an MRI urogram.** **A,** MRI urogram shows marked dilatation of the upper pole collecting system and ureter *(arrowheads)*, secondary to obstruction by ectopic ureter insertion *(arrow)*. **B,** Axial T2-weighted MR image shows ectopic *(arrow)* low-inserting left upper pole ureter which drained into the vagina. The *arrowhead* denotes the Foley catheter coursing within the urethra.



▪ FIGURE 6-17 **Crossed fused renal ectopia.**

A, Longitudinal ultrasound image shows fusion of the "left" and right kidneys to the left of the midline on ultrasound. The *arrows* point to the upper and lower poles of the two kidney units. **B,** Transverse ultrasound scan demonstrates the crossed fused right renal moiety *(arrow)* to overlie the spine *(S)*. **C,** DMSA scan shows the right kidney lying inferior to the left kidney in the midline and connecting to the left lower pole.

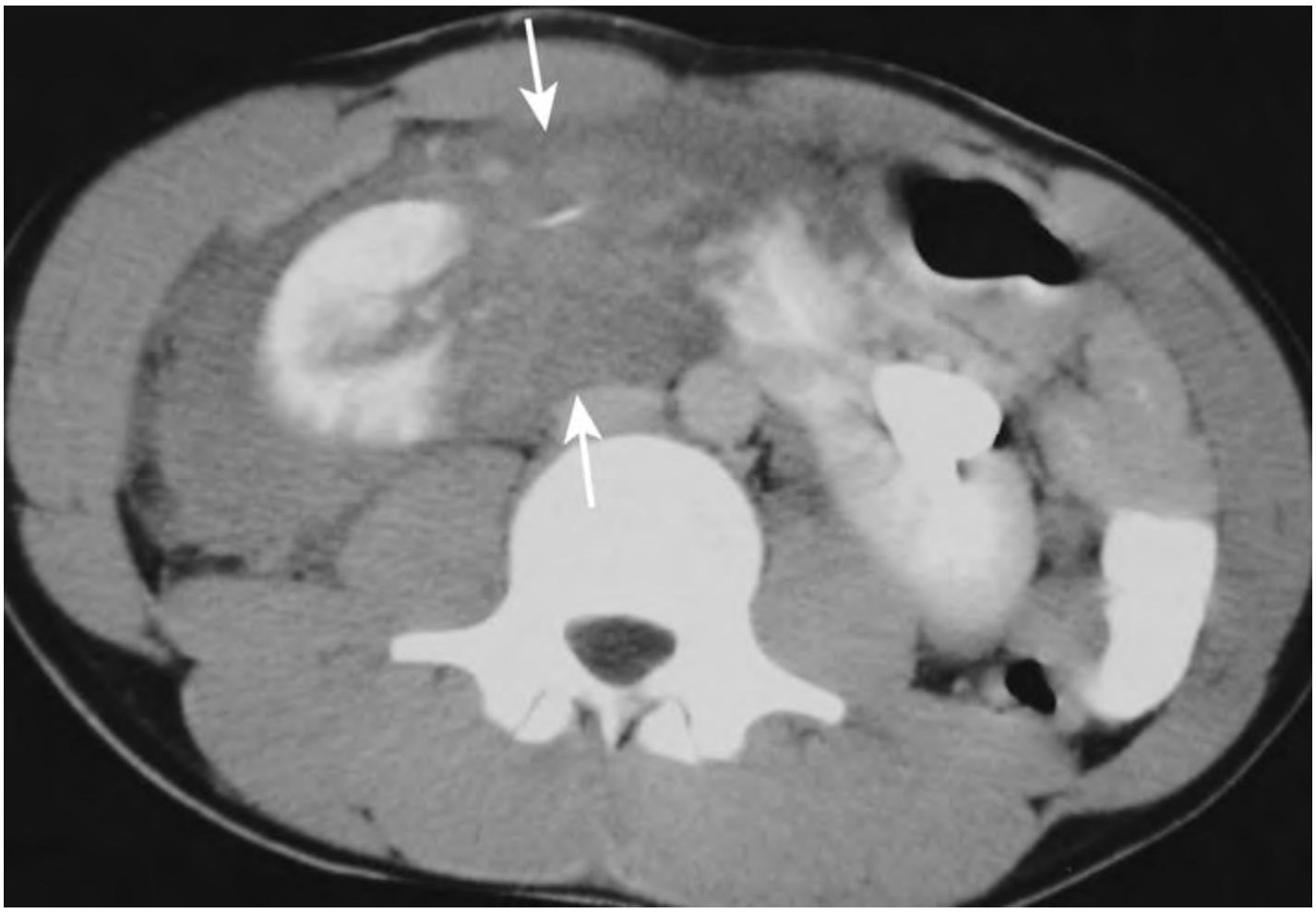
Ureterocele

A ureterocele is defined as dilatation of the distal ureter. The dilated portion of the ureter lies between the mucosal and muscular layers of the bladder. The ureteral orifice is usually stenotic or obstructed. Ureteroceles are defined as simple when they are positioned at the expected orifice of the ureter at the lateral aspect of the trigone. Ureteroceles are defined as ectopic when they are associated with an ectopic insertion of the ureter. Ectopic ureteroceles can be quite large and are almost always associated with a duplicated collecting system (see Fig. 6-15). The ureter from the upper pole moiety is the one associated with the ureterocele. There can be marked associated dilatation of that ureter and the upper pole moiety collecting system. On VCUGs, ureteroceles appear as round, well-defined filling defects, best visualized on early filling views (see Fig. 6-15). Ureteroceles may be compressed and not visualized when the bladder is distended by contrast. Sometimes the ureteroceles can invert and appear as diverticula. On ultrasound, typically a dilatated ureter is seen to terminate in a round, anechoic intravesicular cystic structure (see Fig. 6-15). Usually there is associated dilatation of the upper pole moiety.

Renal Ectopia and Fusion

Renal ectopia is defined as abnormal position of the kidney. It results from abnormal migration of the kidney from its fetal position within the pelvis to its expected position in the renal fossa. Renal fusion is defined as a connection between the two kidneys. It results from failure of separation of the primitive nephrogenic cell masses into two separate left and right blastemas. With ectopia the ectopic kidney most commonly lies within the pelvis. Most ectopic kidneys are also malrotated. With crossed fused renal ectopia, both kidneys lie on the same side of the abdomen and are fused (Fig. 6-17). In this anomaly, both ureters drain normally in their expected positions. Single kidneys and crossed fused ectopia are commonly observed in association with VACTERL (vertebral defects, anal atresia, cardiac

defects, tracheo-esophageal fistula, renal and limb abnormalities). The most common type of renal fusion is horseshoe kidney, which occurs in approximately 1 in 400 live births. With horseshoe kidney there is fusion of the lower pole of the two kidneys across the midline. The connecting isthmus may consist of functional renal tissue or fibrous tissue and cross the midline anterior to the aorta and inferior vena cava. Most horseshoe kidneys are located more inferiorly than normal. Horseshoe kidneys may be seen in association with Turner syndrome (XO) and trisomy 18. The number of ureters arising from a horseshoe kidney is variable, and they exit the kidney ventrally rather than ventromedially. Horseshoe kidneys and other types of renal fusions are at increased risk for infection, injury from mild traumatic events (Fig. 6-18), renal vascular hypertension, stone formation, and hydronephrosis (Fig. 6-19). There is also a slight increase in incidence of Wilms tumor. On ultrasound, horseshoe kidney may be more difficult to diagnose on the standard longitudinal and axial planes than one might expect. It may also be difficult to obtain accurate measurements of the kidneys in the longitudinal plane because of the poorly defined inferior pole. If the ultrasound probe is moved posterolaterally and the patient is scanned in the coronal plane, the two kidneys and connecting isthmus can be visualized on a single image (Fig. 6-20, *A-C*). Such images are most easily obtained in infants. Horseshoe kidneys are readily visualized on CT scanning (see Fig. 6-20).



▪ **FIGURE 6-18** CT of horseshoe kidney with laceration due to bike handle trauma. There is an area of low attenuation *(arrows)* within the horseshoe kidney, consistent with a grade V injury.

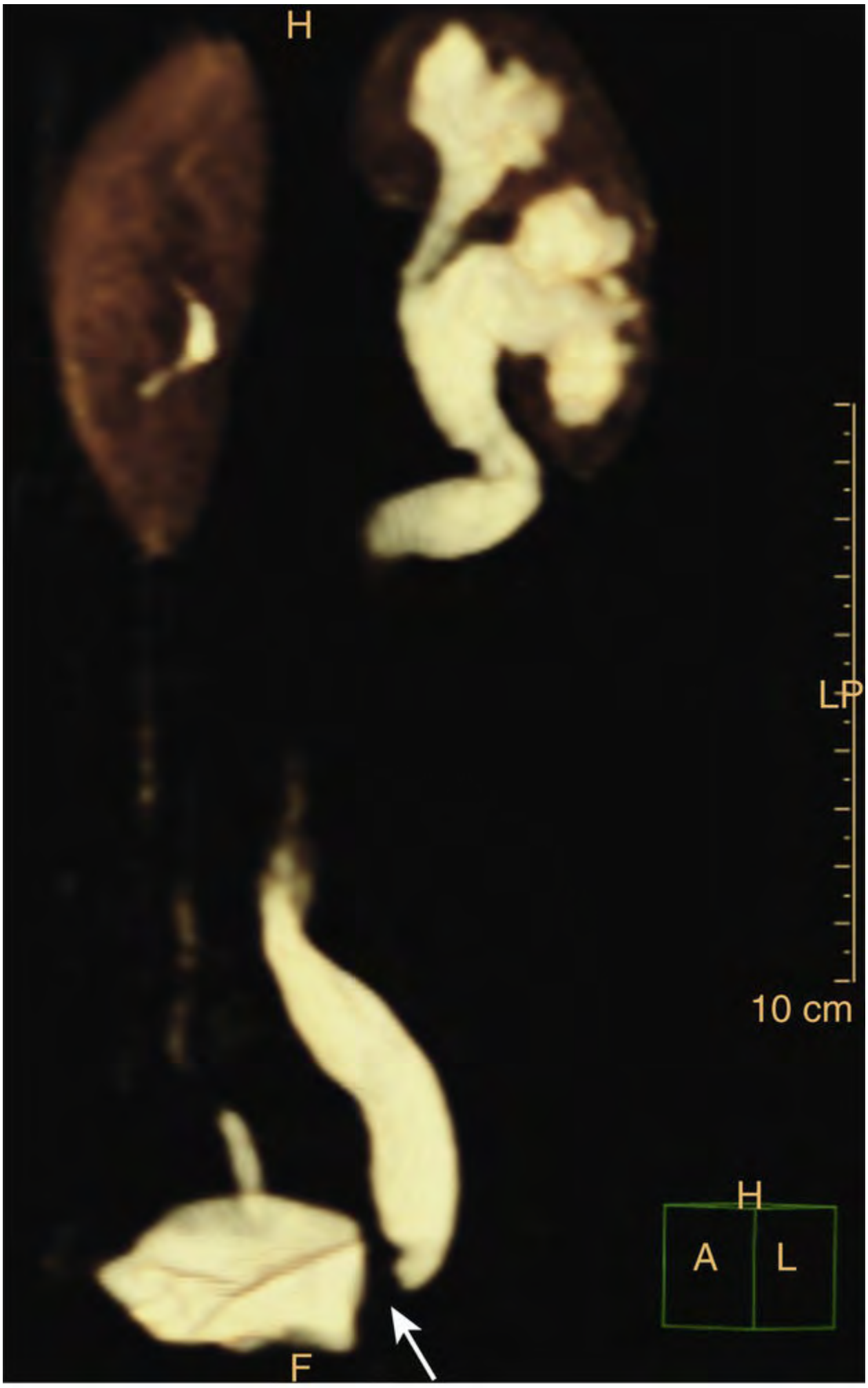


▪ **FIGURE 6-19** **Horseshoe kidney with associated right hydronephrosis.**
Axial T2-weighted MRI (**A**) and coronal (**B**) MIP image show a horseshoe kidney with a parenchymal connection of the kidneys across the midline *(arrows)*. Note hydronephrosis of the right renal moiety.



▪ **FIGURE 6-20** **Horseshoe kidney in two children.**

A, Horseshoe kidney shown on axial ultrasound of an infant. The right and left kidneys *(arrows)* are connected by a parenchymal isthmus. *A,* Aorta; *S,* spine. **B,** Axial T2-weighted MR image of a different child shows right and left kidneys joined by a parenchymal bridge *(arrows)*.



▪ **FIGURE 6-21** **Primary MU.**
An MIP MRU image shows marked hydroureteronephrosis due to a narrowed distal ureter *(arrow)* with dilatation of the more proximal ureter secondary to relative obstruction.

Primary Megaureter

A primary megaureter (MU) consists of a dilated ureter with or without associated pelvicalyceal dilation. Four main types have been described. These types include (1) obstructive MU, which can be thought of as the ureteral equivalent of Hirschsprung disease. With primary obstructive MU, there is an aperistaltic segment of the distal ureter that results in a relative obstruction (Fig. 6-21). The normal more proximal ureter dilates as a consequence of the relative obstruction. It is more common on the left and in boys. Children affected with primary MU may present with infection or be diagnosed prenatally. Ultrasound demonstrates hydronephrosis and enlargement of the ureter above the aperistaltic segment. Other types include (2) refluxing MU, which is the result of a derangement at the ureterovesical junction (UVJ); (3) refluxing MU with obstruction; and (4) nonrefluxing, nonobstructed

MU, which is the most common cause of a neonatal MU. In the aforementioned type, no VUR or focal stenosis at the UVJ can be demonstrated. Imaging algorithms are aimed to define the roles of VUR or obstruction in the presence of a MU, which may be quite challenging as the MU acts as a reservoir.

Posterior Urethral Valves

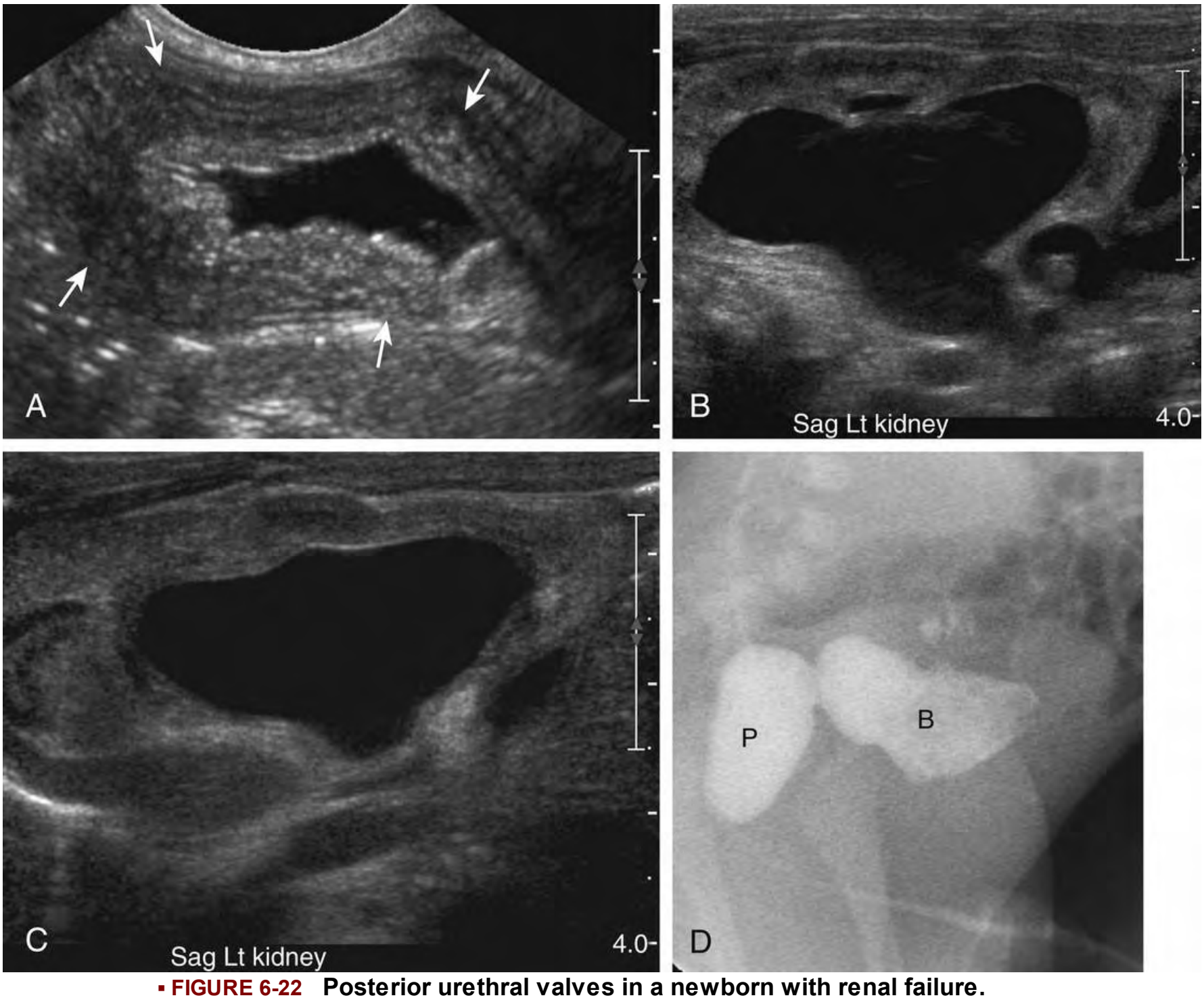
Posterior urethral valves are the most common cause of urethral obstruction in male infants. They are identified most commonly in infancy but can be diagnosed in older children. The high back pressure and associated reflux can damage the kidneys and result in renal failure. Affected children can be diagnosed prenatally and present with renal failure or with UTI.

Typical ultrasound features include a thick-walled bladder with associated bilateral dilatation of the renal collecting systems and ureters (Figs. 6-22, *A-D*, and 6-23, *A-C*). Occasionally a dilatated posterior urethra can be identified inferior to the bladder. On VCUG the posterior urethra appears very dilated (see Figs. 6-22 and 6-23). The actual valve itself may be difficult to visualize but can appear as a membranelike obstruction (see Fig. 6-22). The bladder is trabeculated. VUR is present in approximately 50% of patients with posterior urethral valves.

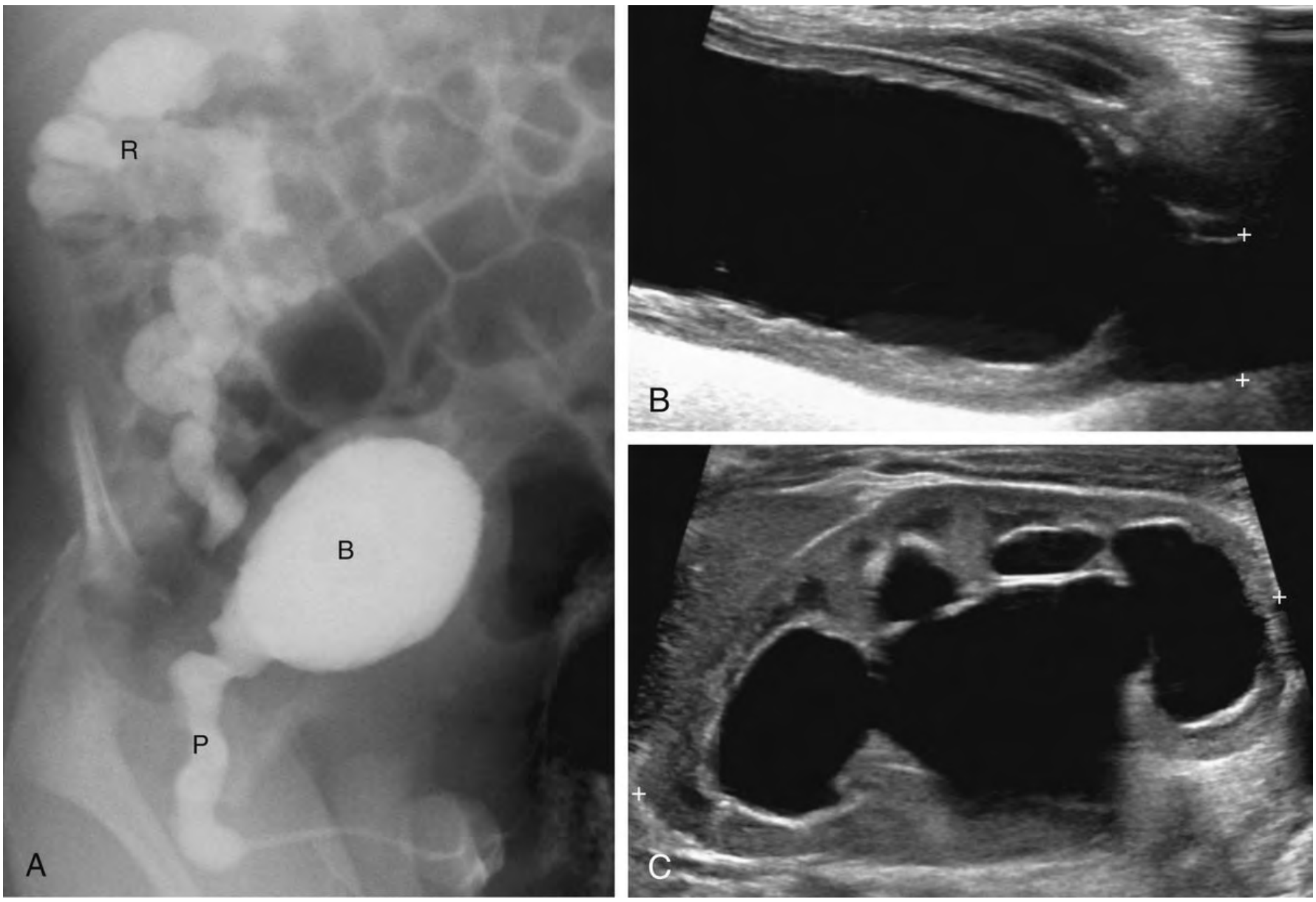
Anything that relieves the increased pressure within the urinary system of patients with posterior urethral valves protects the patients from developing renal failure and is associated with a better prognosis by lowering the urinary back pressure on the renal parenchyma and decreasing the potential for renal damage. Such entities include unilateral VUR (with protection of the kidney contralateral to the reflux; see Fig. 6-23), large bladder diverticula, or development of intrauterine urinary ascites. The spectrum of clinical severity is wide, and the prognosis is typically poor in cases of moderate to severe upper tract dilatation before 20 weeks of gestation. On the contrary, the outcome is generally favorable if the diagnosis of posterior urethral valves was made after the twenty-fourth week of gestation. It is the potential of posterior urethral valves that makes obtaining an image of the urethra during voiding a vital part of every VCUG performed on boys.

Urachal Abnormalities

The urachus is an embryologic structure that communicates between the apex of the bladder and the umbilicus. Normally it closes by birth. If any portion of this embryologic structure remains patent, an urachal abnormality results. The type of the urachal anomaly present is determined by which portion of the urachus remains patent (Figs. 6-24 and 6-25, *A-C*). If the urachus remains patent in its entirety from the umbilicus to the bladder, it is a patent urachus (see Fig. 6-25). A neonate with a patent urachus will have urine draining from the umbilicus. Patent urachus can be demonstrated by VCUG, fistula tract injection, or ultrasound.

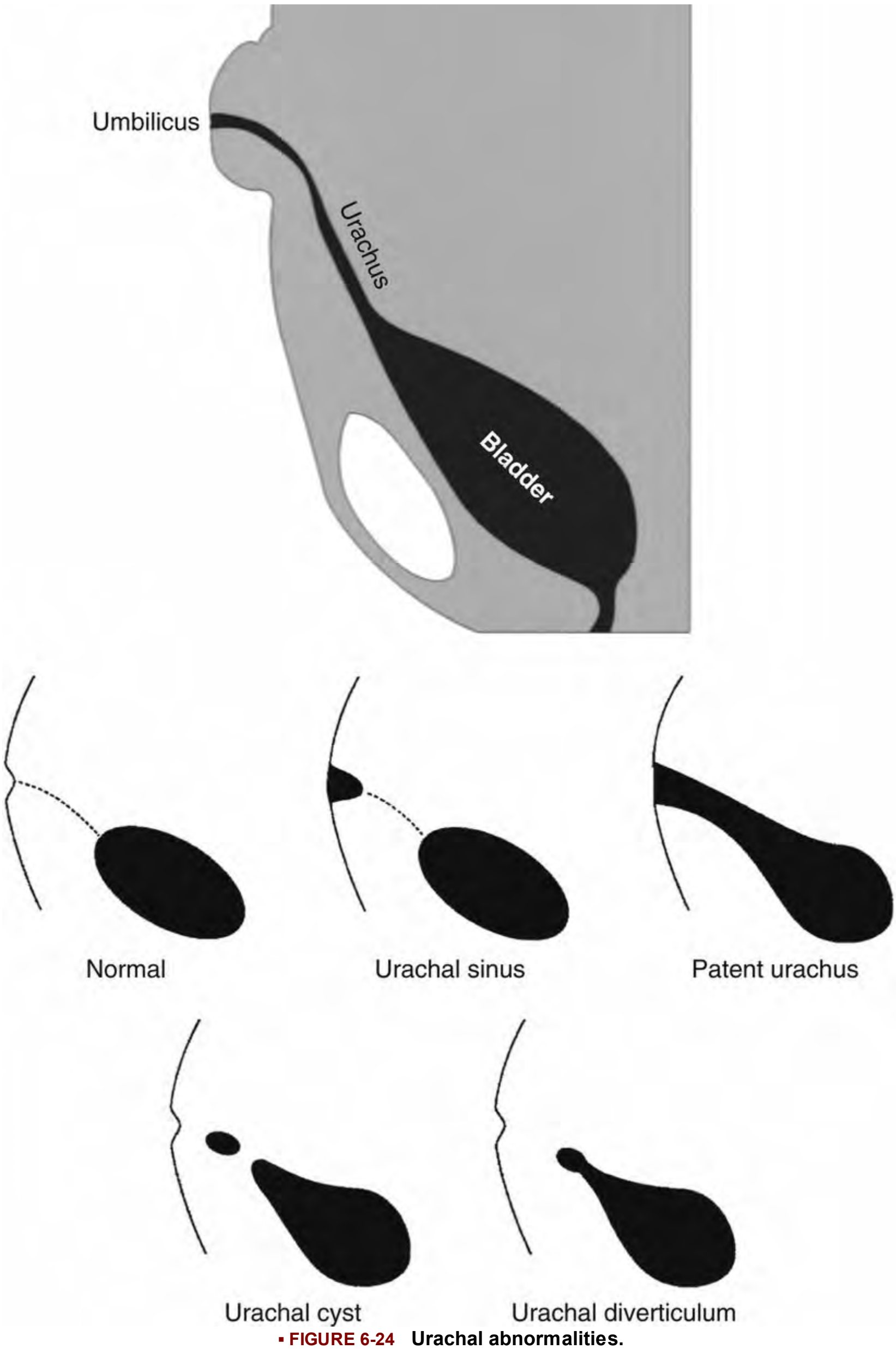


▪ **FIGURE 6-22** **Posterior urethral valves in a newborn with renal failure.**
A, Longitudinal ultrasound shows a markedly thick-walled bladder *(arrows)*. **B,** Longitudinal ultrasound of the left kidney shows hydronephrosis and echogenic renal parenchyma. **C,** Longitudinal ultrasound of the right kidney shows hydronephrosis and echogenic renal parenchyma. **D,** VCUG shows trabeculated, thick-walled bladder *(B)* and dilated posterior urethra *(P).*



▪ **FIGURE 6-23** **Posterior urethral valves and unilateral VUR serving as a protective mechanism for the contralateral kidney.**

A, VCUG shows trabeculated, thick-walled bladder *(B)*, dilated posterior urethra *(P)*, and narrowing of the anterior urethra without the valves being directly visualized. There is unilateral right, grade 5 VUR *(R)*. **B,** Longitudinal ultrasound scan of the pelvis shows bladder wall thickening and a dilated posterior urethra *(between calipers)*. **C,** Longitudinal ultrasound of right kidney shows marked dilatation of the renal collecting system and cortical thinning. The left protected kidney was normal (image not shown).

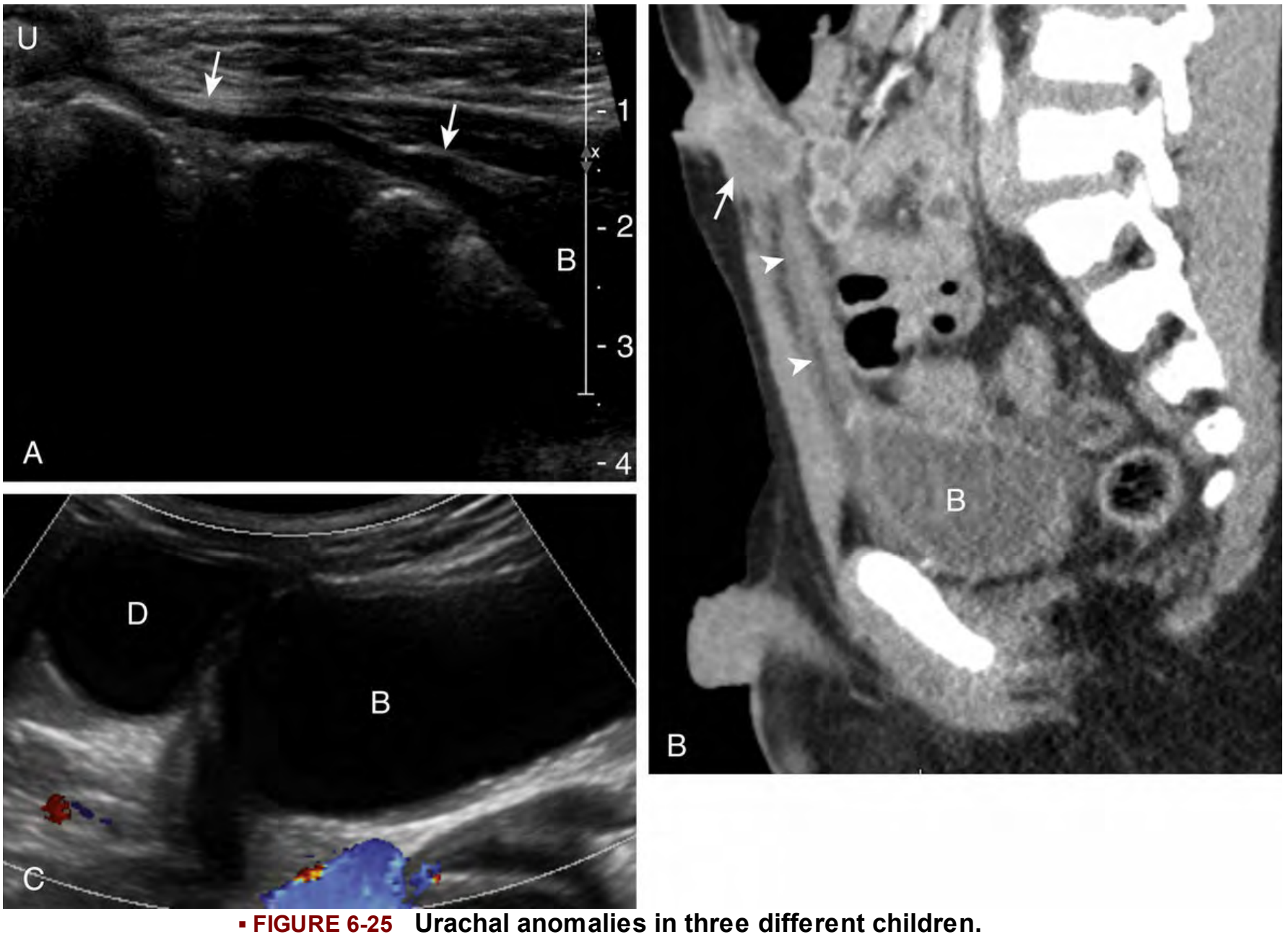


▪ **FIGURE 6-24** **Urachal abnormalities.**
The superior image demonstrates the urachus as a patent connection between the umbilicus and bladder during fetal life. The inferior row of images demonstrates the potential urachal anomalies that occur when a portion or all of the urachus remains patent after birth. The type of urachal abnormality present depends upon which portion of the urachus remains patent.

If the urachus remains patent only at the bladder end of the urachus, an urachal diverticulum is present. On ultrasound or VCUG, a diverticulum of variable size is demonstrated arising from the

anterosuperior aspect of the dome on the bladder (see Fig. 6-25). Ultrasound may also demonstrate a fibrous tract extending from the diverticulum to the umbilicus.

If the urachus remains patent only at the umbilical end, a urachal sinus is present. If the urachus remains patent only at its midportion and is closed at both its umbilical and its bladder ends, a urachal cyst is present. Urachal cysts may present as palpable masses but more commonly present with inflammatory changes after becoming infected. Ultrasound or CT will show a cystic mass anterior and superior to the bladder dome in the midline (see Fig. 6-25). Urachal carcinoma is rare in adults and extraordinarily rare in children.



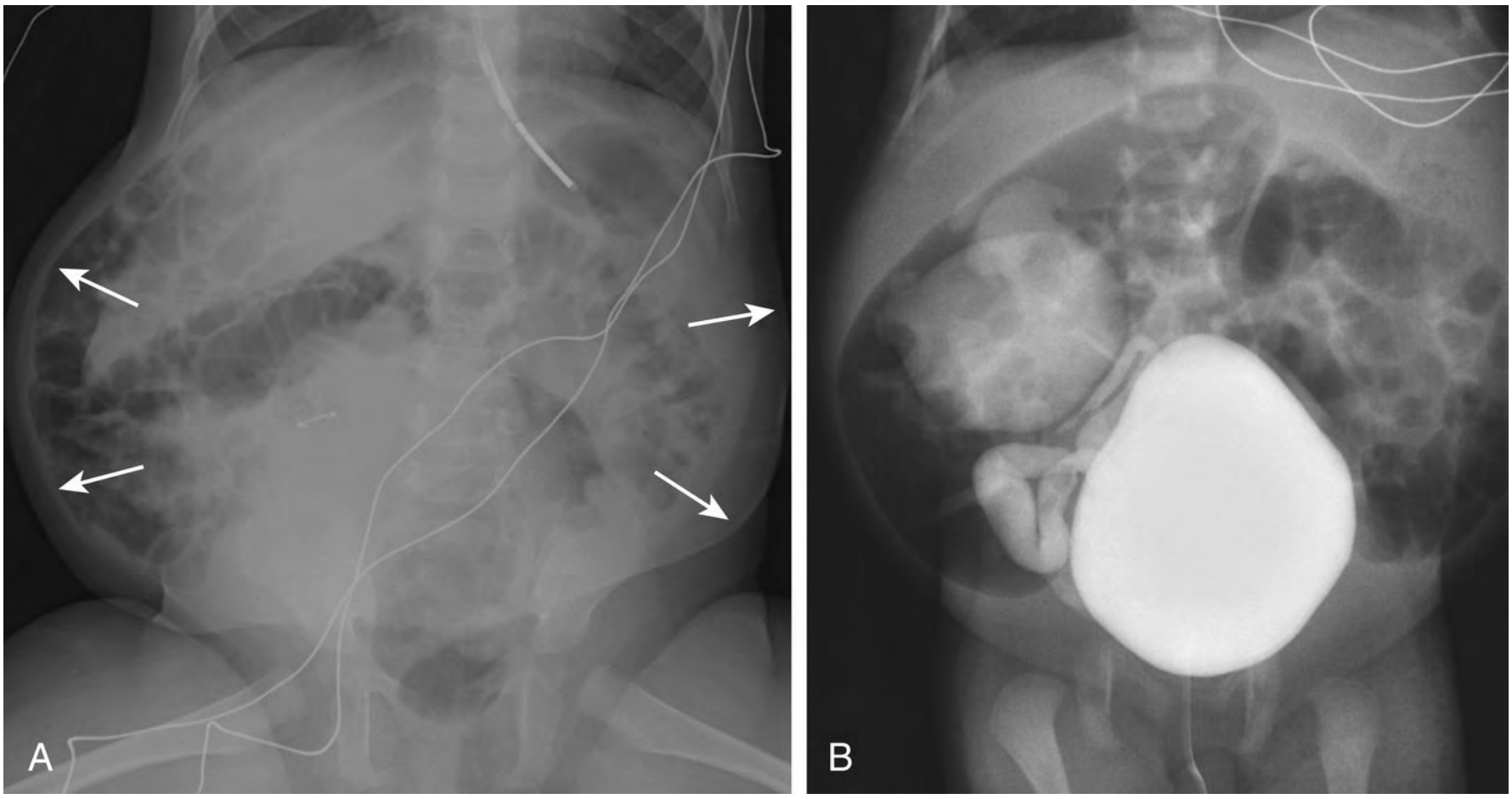
▪ **FIGURE 6-25** **Urachal anomalies in three different children.**
A, Patent urachus. Longitudinal ultrasound shows midline from umbilicus to bladder. There is a patent connection between bladder *(B)* and umbilicus *(U)* evidenced by a hypoechoic tract *(arrows)*. **B,** Infected urachal cyst. Enhanced sagittal reformatted CT image shows heterogeneous lesion *(arrow)* with surrounding inflammatory changes with associated tract *(arrowheads)* to the bladder *(B)*. **C,** Urachal diverticulum. Ultrasound demonstrates diverticulum *(D)* extending from the superior aspect of the bladder *(B)*.

Prune-Belly Syndrome

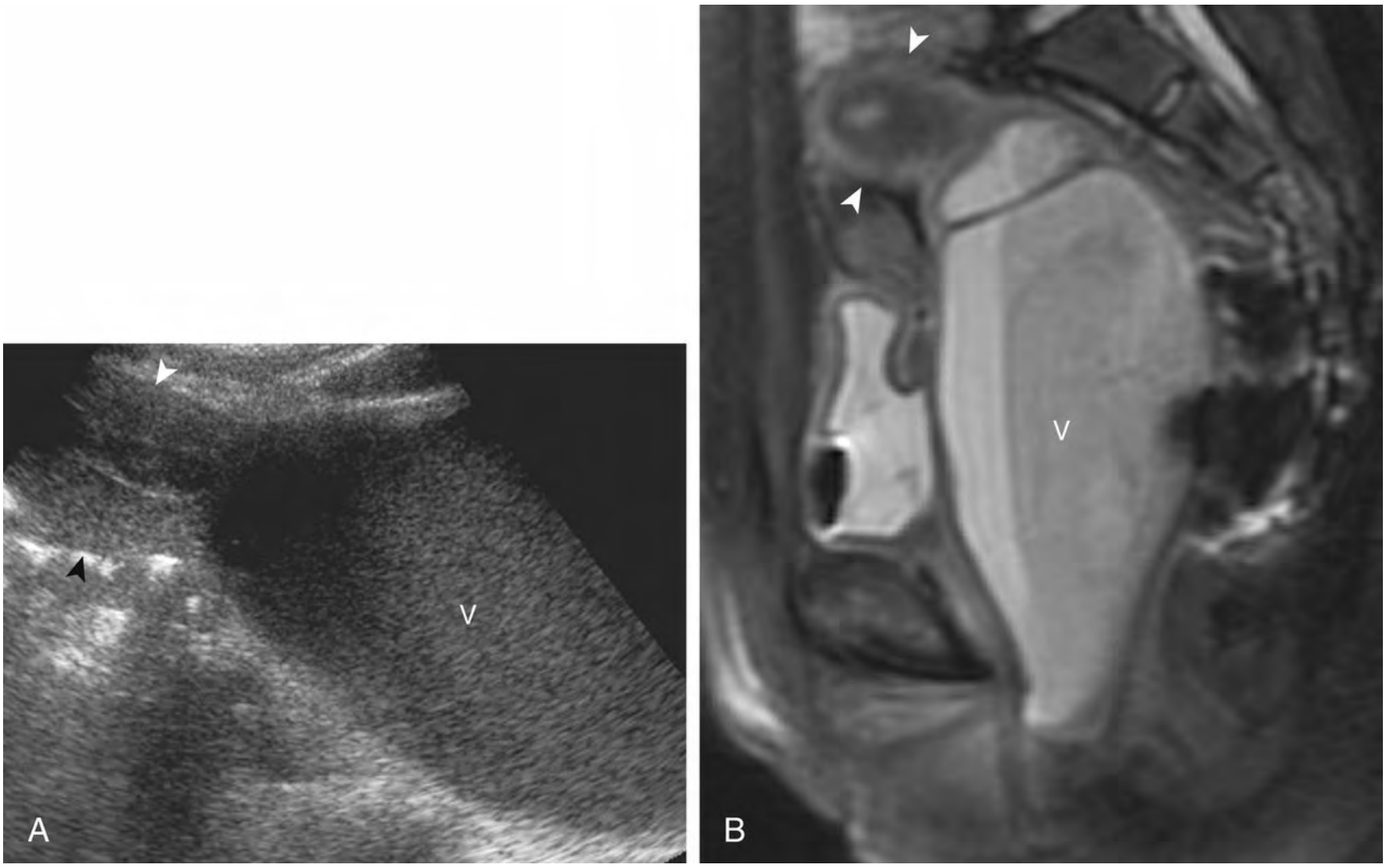
Prune-belly syndrome, or Eagle-Barrett syndrome, is the name given to the rare condition in which there is a triad of hypoplasia of the abdominal muscles, cryptorchidism, and abnormalities of the urinary tract system. The etiology of prune-belly syndrome is not fully understood. Potential urinary tract abnormalities include severe bilateral hydronephrosis, a large capacity, trabeculated and hypertrophied bladder, urachal diverticulum, and hydroureter. Radiographic manifestations include the characteristic bulging flanks secondary to abdominal wall hypoplasia and the previously described renal manifestations (Fig. 6-26, *A* and *B*). There are multiple associated congenital anomalies. The condition affects almost exclusively boys. Even more rarely, the syndrome can be incomplete (pseudo prune-belly syndrome) in girls, who obviously cannot have cryptorchidism, and it can occur unilaterally.

Hydrometrocolpos

Genital outflow tract obstructions may lead to hydrometrocolpos or hematometrocolpos. *Hydrometrocolpos* is the term given to a rare condition in which the vagina and uterus dilate when fluid accumulates in the reproductive tract. This occurs in response to hormonal stimulation, so it occurs during infancy, secondary to maternal hormones, or during puberty. Hematometrocolpos is the accumulation of blood in a dilated vagina and uterus that occurs after menarche in patients with a genital outflow tract obstruction. In both hydrometrocolpos and hematometrocolpos, a fixed midline mass may be palpable; the mass can become large enough to cause ureteral obstruction and result in hydronephrosis. Radiography or ultrasound can demonstrate the midline abdominal mass. On ultrasound the mass appears tubular or elliptical and at the midline. In hematometrocolpos there is heterogeneous echogenicity secondary to the underlying hemorrhage (Fig. 6-27, *A*). Because the vagina is more elastic, it becomes markedly dilated and composes the bulk of the mass. The uterus may also be dilated but cannot expand to the degree that the vagina can. Often the uterus can be identified as a small C-shaped cavity arising from the anterosuperior aspect of the distended vagina on ultrasound (see Fig. 6-27, *A*). Ultrasound also can reveal the degree of obstructive hydronephrosis. In problematic cases, MRI can be helpful in confirming the cause and the anatomy of the lesion (see Fig. 6-27).



▪ **FIGURE 6-26** **Prune-belly syndrome.**
A, Radiograph shows bulging flanks *(arrows)*. **B,** VCUG shows right grade 5 VUR and a large, hypotonic bladder. The right ureter is dilated and markedly tortuous.



▪ **FIGURE 6-27 Hematometrocolpos shown in two different girls.**
A, Longitudinal midline ultrasound shows elliptical echogenic mass *(V)*, which represents the vaginal cavity markedly distended with blood products. The uterus *(arrowheads)* extends from the superior aspect of the mass. The uterine cavity is slightly dilated but not nearly as much as the vaginal cavity. **B,** Sagittal T2-weighted MRI of a different girl shows massively dilated vaginal cavity *(V)*. The uterus *(arrowheads)* extends from the superior aspect of the mass.

Renal Cystic Disease

In children, renal cysts can occur secondary to polycystic kidney disease, can be associated with a variety of syndromes, can occur secondary to cystic neoplasms, or can be related to other cystic processes, such as MCDK (Table 6-1). The categorization of and nomenclature for renal cystic disease in children can sometimes be confusing. Many cystic diseases involving the kidney have a known genetic basis, and their nomenclature is clearly defined. However, these entities may be difficult to differentiate on imaging. In addition, it is important to note that although much less common than in adults, solitary simple renal cysts are not uncommonly identified in children. When such unilocular, solitary cysts are encountered during the work-up for a UTI or hematuria, they are usually of no clinical significance and do not necessarily suggest an underlying developing polycystic kidney disease. As in adults, the ultrasound criteria for diagnosing a simple renal cyst include an anechoic, well-defined, round lesion; an imperceptible wall; and increased through-transmission. No central echoes or vascular flow is present within the lesion or within its walls.

Autosomal Recessive Polycystic Kidney Disease

Autosomal recessive polycystic kidney disease (ARPKD), also known as infantile polycystic kidney disease, encompasses a range of recessive diseases that are associated with varying amounts of cystic disease in the kidneys as well as with hepatic fibrosis. It is a very rare condition. When the renal findings (severe renal tubular ectasia) predominate, the disease most commonly presents on in utero imaging or during infancy and is termed *infantile polycystic kidney disease*. When the liver disease (severe fibrosis) predominates and there is minimal renal disease, the disease usually presents later in childhood and is referred to as juvenile polycystic kidney disease. In the infantile form the kidneys are markedly enlarged and replaced by numerous small, 1- to 2-mm cysts throughout the cortex and medulla. On ultrasound the kidneys are grossly enlarged and demonstrate diffuse increased echogenicity (Fig. 6-28, *A* and *B*). Discrete cystic structures are sometimes not identified because of the small size of the cysts. In the juvenile form, patients usually present with hepatosplenomegaly and

portal hypertension. The kidneys may demonstrate enlargement and cysts of varying sizes. The liver usually shows increased echogenicity related to the diffuse hepatic fibrosis. Hepatosplenomegaly, portal hypertension, and portosystemic collaterals are not typically observed in the neonatal period and develop later in life.

TABLE 6-1
Renal Cysts in Children

Solitary simple cyst
Autosomal recessive polycystic renal disease
Autosomal dominant polycystic renal disease
Multicystic dysplastic kidney
Syndromes
Tuberous sclerosis
von Hippel-Lindau
Meckel-Gruber
Cystic neoplasms
Wilms tumor
Multilocular cystic nephroma
Calyceal diverticulum

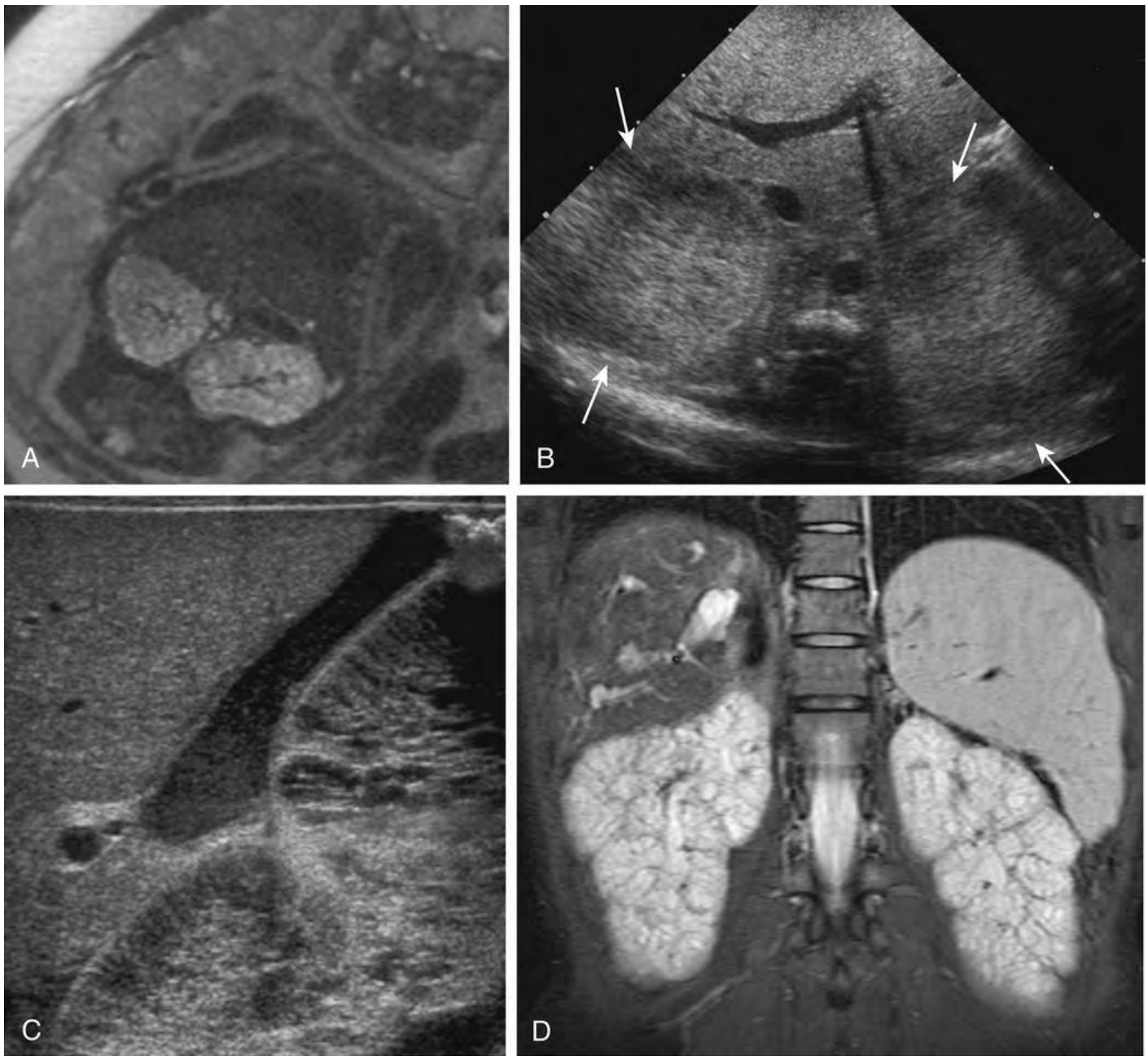
Autosomal Dominant Polycystic Kidney Disease

Autosomal dominant polycystic kidney disease (ADPKD) is a dominantly inherited disease with variable penetrance. It is relatively common. ADPKD is a ciliopathy that occurs as a result of a mutation in one of two genes, PKD1 and PKD2. Usually the diagnosis is first encountered in early adulthood, when the patient presents with hypertension, hematuria, or renal failure. However, the cysts can be encountered during childhood. Some patients even present during the neonatal period. During childhood, several cysts of varying sizes may be identified in both the cortex and medulla. The intervening renal parenchyma appears normal. The cysts are usually macroscopic and gradually progress in size and number with time, and the normal renal parenchyma can be compressed and destroyed. Cysts may also be found in other organs, most commonly in the liver or pancreas. When encountered, pancreatic cysts are useful in distinguishing between ADPKD and ARPKD. There is an association between the disease and the presence of intracranial berry aneurysms (10% of cases).

▪ Renal Tumors

Wilms Tumor

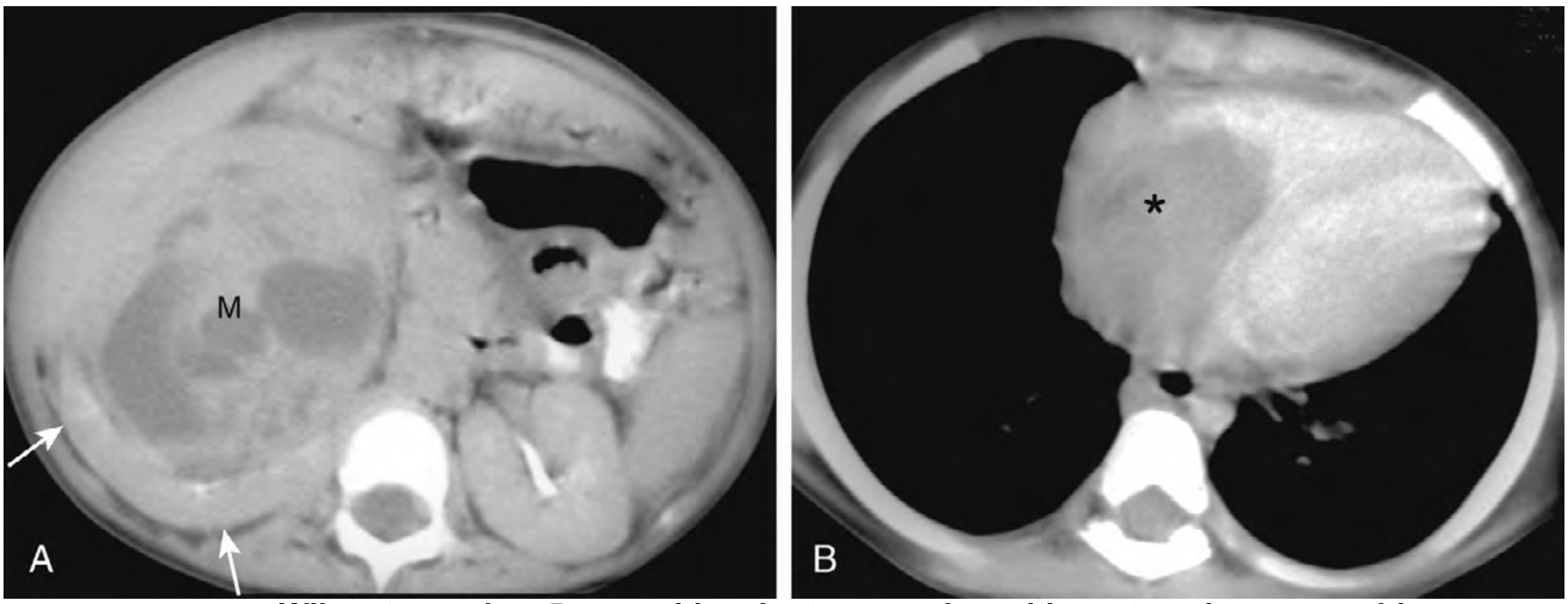
Wilms tumor is the most common renal malignancy in children. It accounts for approximately 8% of all childhood malignant tumors. Also referred to as nephroblastoma, Wilms tumor is a malignant embryonal neoplasm. Its peak incidence occurs at approximately 3 years of age, with approximately 80% of cases detected between 1 and 5 years of age. Wilms tumor presents most commonly as an asymptomatic abdominal mass but may present with abdominal pain, particularly when there is intratumoral hemorrhage (Fig. 6-29, *A-C*). Although most cases of Wilms tumor occur in otherwise normal children, there is an association between the development of Wilms tumor and overgrowth disorders (congenital hemihypertrophy, Beckwith-Wiedemann syndrome), sporadic aniridia, and other malformations. Wilms tumor can be bilateral in approximately 5% of cases. Invasion of the renal vein and extension into the renal vein and into the inferior vena cava occurs commonly in Wilms tumor. Lung metastatic disease occurs in as many as 20% of cases.



▪ **FIGURE 6-28** **ARPKD.**

A, Fetal MRI shows enlarged kidneys with multiple tiny cysts. There is severe oligohydramnios with a bell-shaped thoracic cage configuration related to pulmonary hypoplasia. **B,** Longitudinal ultrasound image shows massive enlargement of bilateral kidneys *(arrows)*, which fill the majority of the abdominal cavity. The kidneys are of diffusely increased echogenicity, and no discrete cysts are identified. **C,** Longitudinal ultrasound scan obtained with a linear-array transducer shows to better advantage the multiple, radiating-appearing, distended ducts in the pyramids and cortex. **D,** Coronal T2-weighted MR image in an older child shows enlarged kidneys with innumerable, uniform cysts, in keeping with ARPK
D. Notice the inhomogeneous liver parenchyma with dilated ducts with findings consistent with congenital hepatic fibrosis.

On ultrasound, Wilms tumors typically appear as large, well-defined masses arising from the kidney (see Fig. 6-29). The masses are typically of increased echogenicity and may show heterogeneity related to areas of intratumoral hemorrhage, necrosis, or calcification. Doppler ultrasound is excellent in detecting extension of the tumor into the renal vein or inferior vena cava. It is especially important to document extension of the tumor thrombus into the right atrium because in such cases cardiothoracic surgery usually also becomes involved.



▪ **FIGURE 6-29 Wilms tumor in a 5-year-old patient presenting with acute pain presumably secondary to intratumoral hemorrhage.**

A, CT shows heterogeneous mass *(M)* arising from right kidney *(arrows)*. The parenchyma of the right kidney forms a claw sign, indicating that the mass is truly arising from the right kidney and is not a suprarenal mass. **B,** CT shows tumor thrombosis *(asterisk)* as a filling defect within the right atrium.

Confirmation of the lesion and evaluation of the anatomic extent of disease is usually performed using CT or MRI (Fig. 6-30 and see Fig. 6-29). When evaluating a suspected Wilms tumor with either modality, it is important to document the following features: lymph node involvement, liver and lung metastases, involvement of the contralateral kidney by a synchronous Wilms tumor, the anatomic distribution of the intrarenal tumor, involvement of the renal vein or inferior vena cava, and the path of the ureters in relation to the mass. Identification of the ureter as anterior or posterior to the mass is important so that the ureters are not inadvertently injured when the mass is removed.

One of the most important issues when evaluating a mass in the region of the suprarenal fossa is determining whether the mass arises from the kidney and is therefore most likely a Wilms tumor or whether it arises from the suprarenal region and is a neuroblastoma. Differential features between these two lesions are described in Table 6-2. In the case of a Wilms tumor, the mass usually appears as a well-defined, large, round mass on CT and MRI. The mass tends to grow in a ball, displacing blood vessels rather than engulfing them, as does neuroblastoma. As Wilms tumor arises in the kidney, the renal parenchyma often surrounds a portion of the mass, resulting in the "claw sign." When the mass crosses the midline, the lesion usually passes anterior to the aorta, as compared with neuroblastoma, which can surround the aorta posteriorly and raise it anteriorly, away from the spine. Wilms tumors commonly appear to be solid, but larger lesions may have areas of heterogeneity or cystic components due to previous hemorrhage or necrosis.

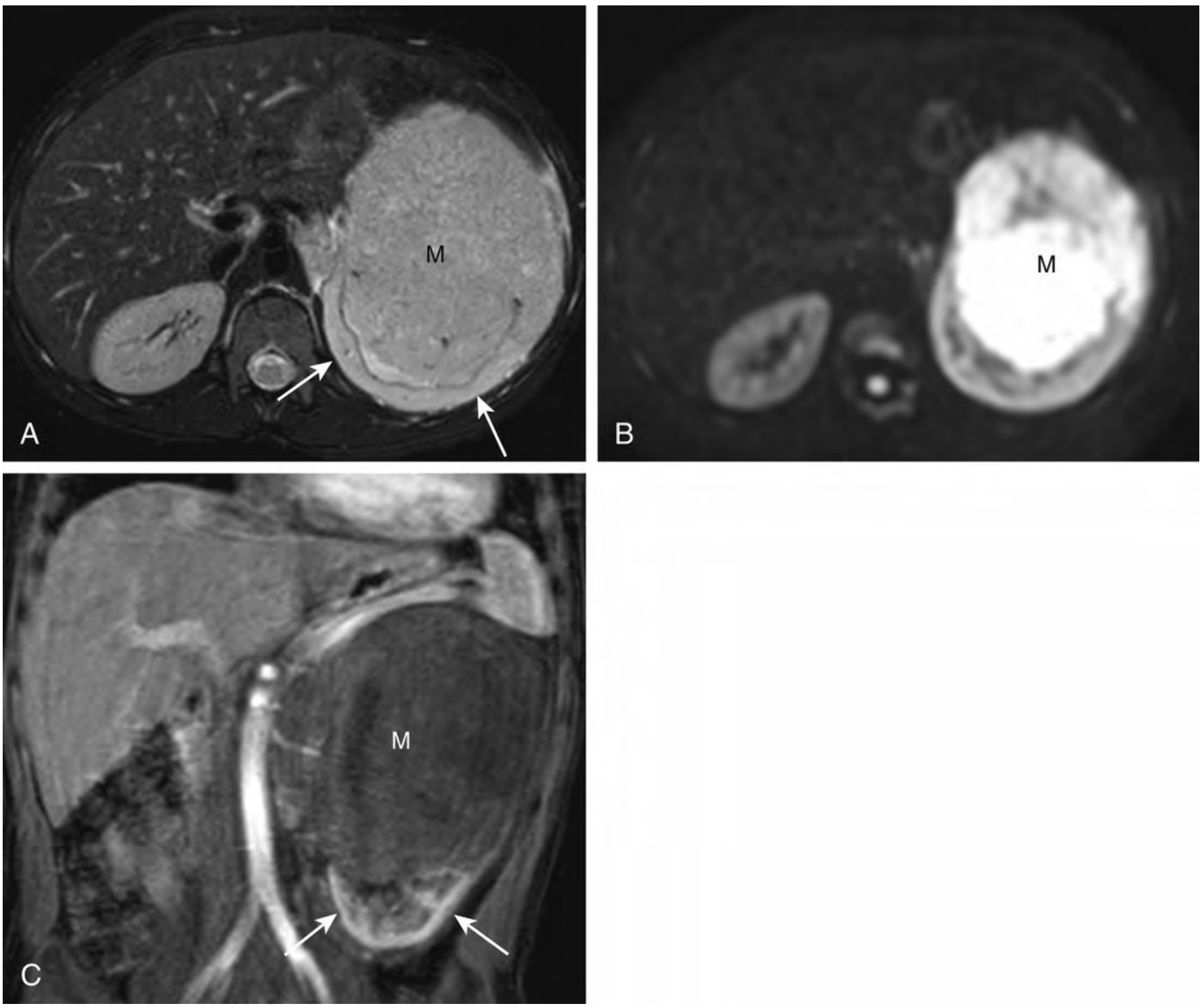
Nephroblastomatosis

Nephroblastomatosis is a rare entity that is related to the persistence of nephrogenic rests within the renal parenchyma after 36 weeks of gestation. These nephrogenic rests are precursors of Wilms tumors. Most patients with nephroblastomatosis are monitored by ultrasound, MRI, or CT for the development of Wilms tumors. On imaging, nephrogenic rests appear as plaquelike peripheral renal lesions and may be confluent (Fig. 6-31). The development of a Wilms tumor is suggested when a lesion appearing spherical demonstrates an increase in size compared with previous studies or demonstrates progressively increasing inhomogeneous enhancement as compared with the more nonenhancing nephrogenic rests. Typically, cases of Wilms tumor associated with syndromes are the ones that develop from nephroblastomatosis.

Multilocular Cystic Nephroma

Multilocular cystic nephroma is a rare type of cystic mass that contains multiple septa. The lesions have an unusual bimodal distribution in that they affect primarily young boys (3 months to 2 years) and adult women (during the fifth to sixth decades). Typically the lesions present as a painless abdominal mass. These lesions may be associated with the pleuropulmonary blastoma family cancer syndrome,

occurring in patients with mutations in the *DICER1* gene. By definition, the lesions do not contain malignant cells but can be difficult to distinguish from a well-differentiated Wilms tumor on imaging. On ultrasound, CT, and MRI the lesions appear as well-circumscribed, multiseptated masses (Fig. 6-32, *A* and *B*). Because the lesions cannot be differentiated from malignancy at imaging, surgical resection is performed.



▪ **FIGURE 6-30** **Wilms tumor on MRI.**
A, Axial T2-weighted image shows a mass *(M)* arising from left kidney *(arrows)*. The lesion is heterogeneous in signal and rounded in shape. **B,** The lesion shows high signal, restricted diffusion on diffusion-weighted imaging. **C,** Coronal postcontrast image shows a low signal mass *(M)* and enhancement of the surrounding renal parenchyma *(arrows)*.

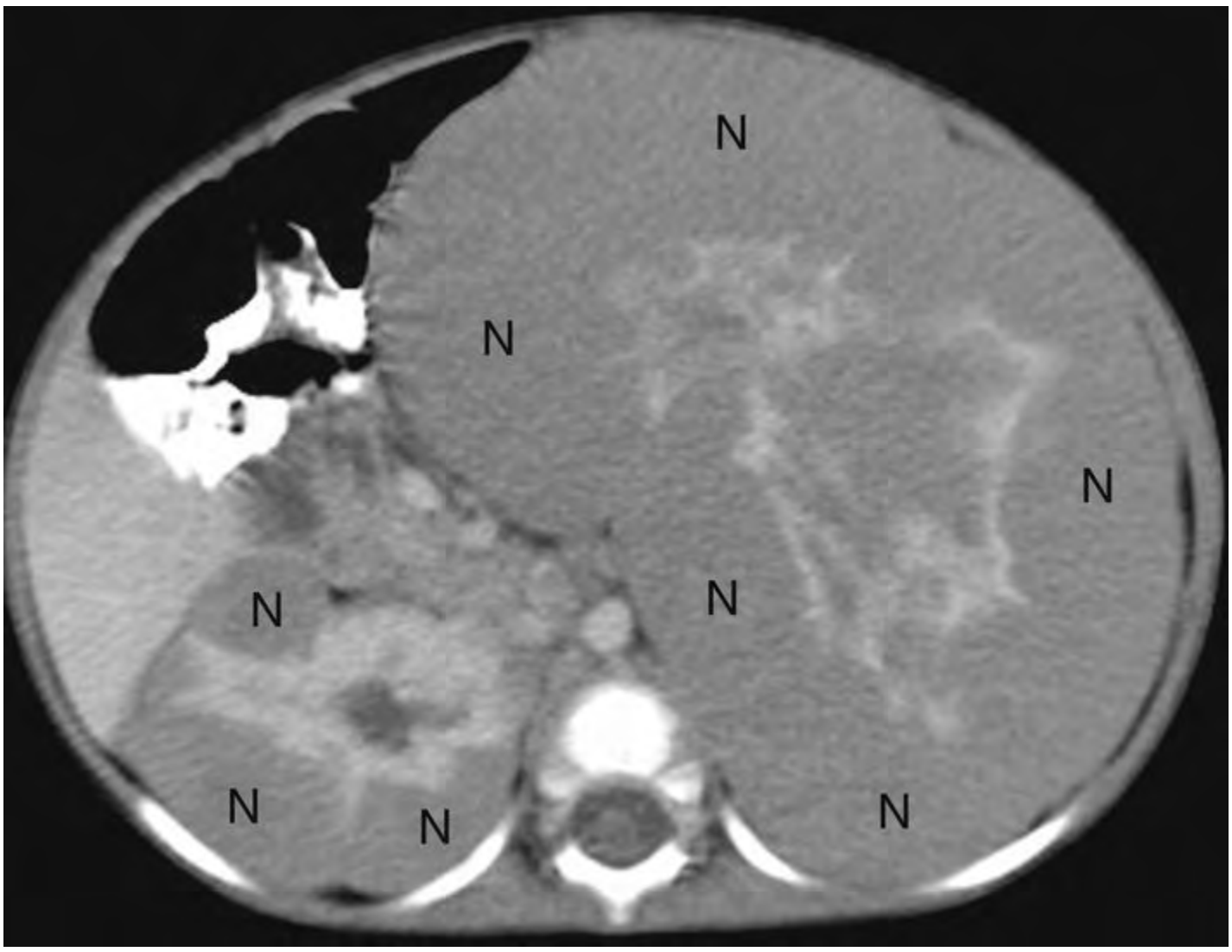
TABLE 6-2
Differentiating Features Between Neuroblastoma and Wilms Tumor

Feature	Neuroblastoma	Wilms Tumor
Age	Most common before age 2 yr	Peak incidence at 3 yr
Calcification	Calcifications common (85% on CT) and stippled	Calcifications uncommon (15% on CT) and often curvilinear or amorphous
Growth pattern	Surrounds and engulfs vessels	Grows like ball, displacing vessels
Relation to kidney	Inferiorly displaces and rotates kidney	Arises from kidney, claw sign
Lung metastasis	Uncommon	More common (20%)
Vascular invasion	Does not occur	Invasion of renal vein and/or inferior vena cava

CT, Computed tomography.

Mesoblastic Nephroma

Mesoblastic nephroma, or fetal renal hamartoma, is the most common solid renal mass in neonates. Typically it is encountered prenatally or during the first few months of life; the mean age of diagnosis is approximately 3 months. Neonates most commonly present with a nontender, palpable abdominal mass. The lesion consists of benign spindle-type cells. Ultrasound demonstrates a mixed echogenic mass that is intrarenal in location and indistinguishable from a Wilms tumor. CT demonstrates a solid intrarenal mass with variable enhancement (Fig. 6-33, *A* and *B*).



▪ **FIGURE 6-31** **Nephroblastomatosis.**
CT shows peripheral plaquelike lesions *(N)* of low attenuation. The lesions circumferentially involve both kidneys and distort the central renal parenchyma.

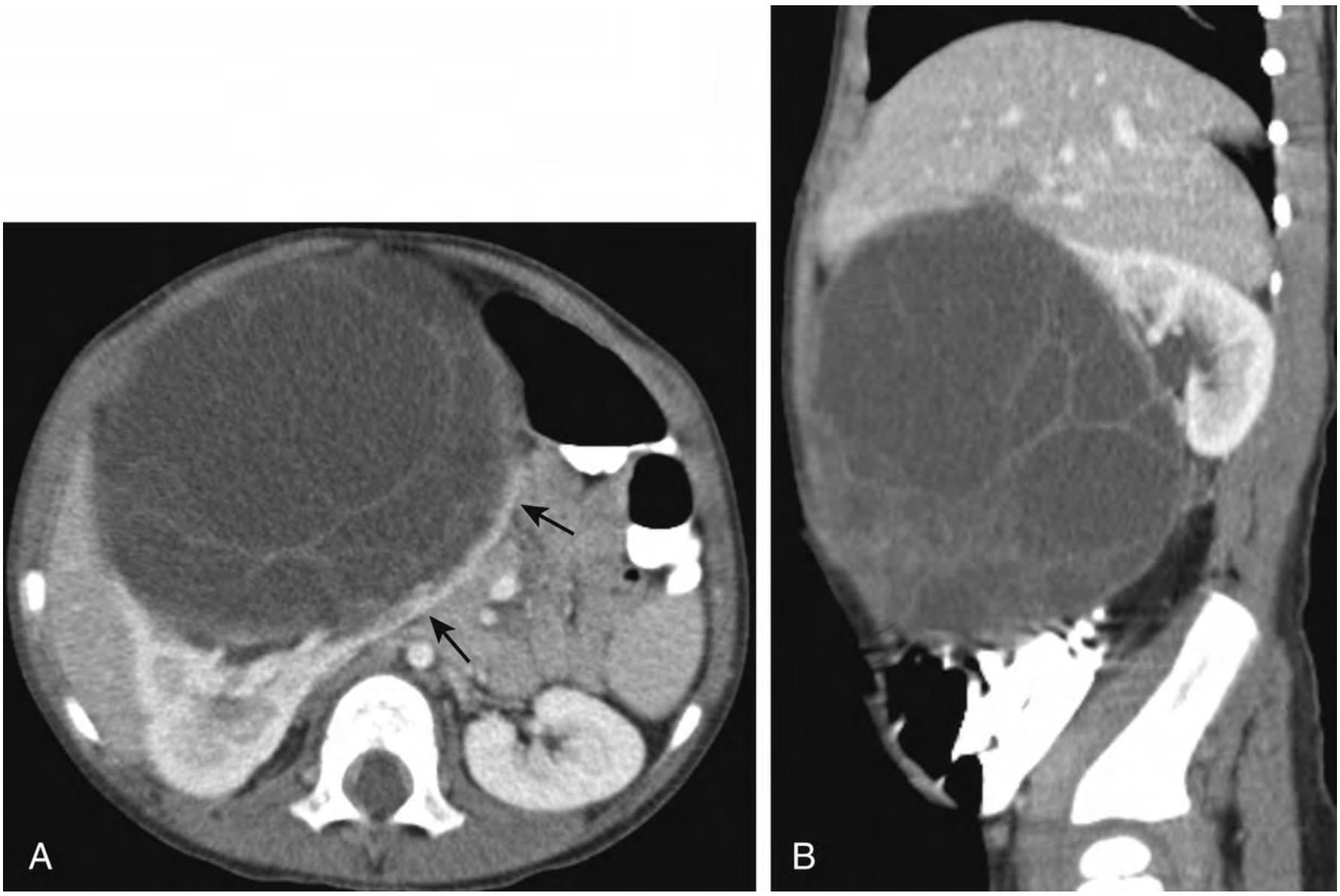
Other Renal Tumors

Other, less common causes of malignant renal lesions include renal cell carcinoma (RCC), renal lymphoma, clear cell carcinoma, and rhabdoid tumor. RCC is the most common cause of renal malignancy in older children, although it is still much less common than in adults. There is an increased risk of developing multiple RCCs at an early age in patients with von Hippel-Lindau syndrome (VHL); therefore all pediatric patients who develop RCC are usually screened for VHL. Ultrasound and CT typically show a nonspecific solid renal mass. Calcification is more common with RCC (25%) than with Wilms tumor.

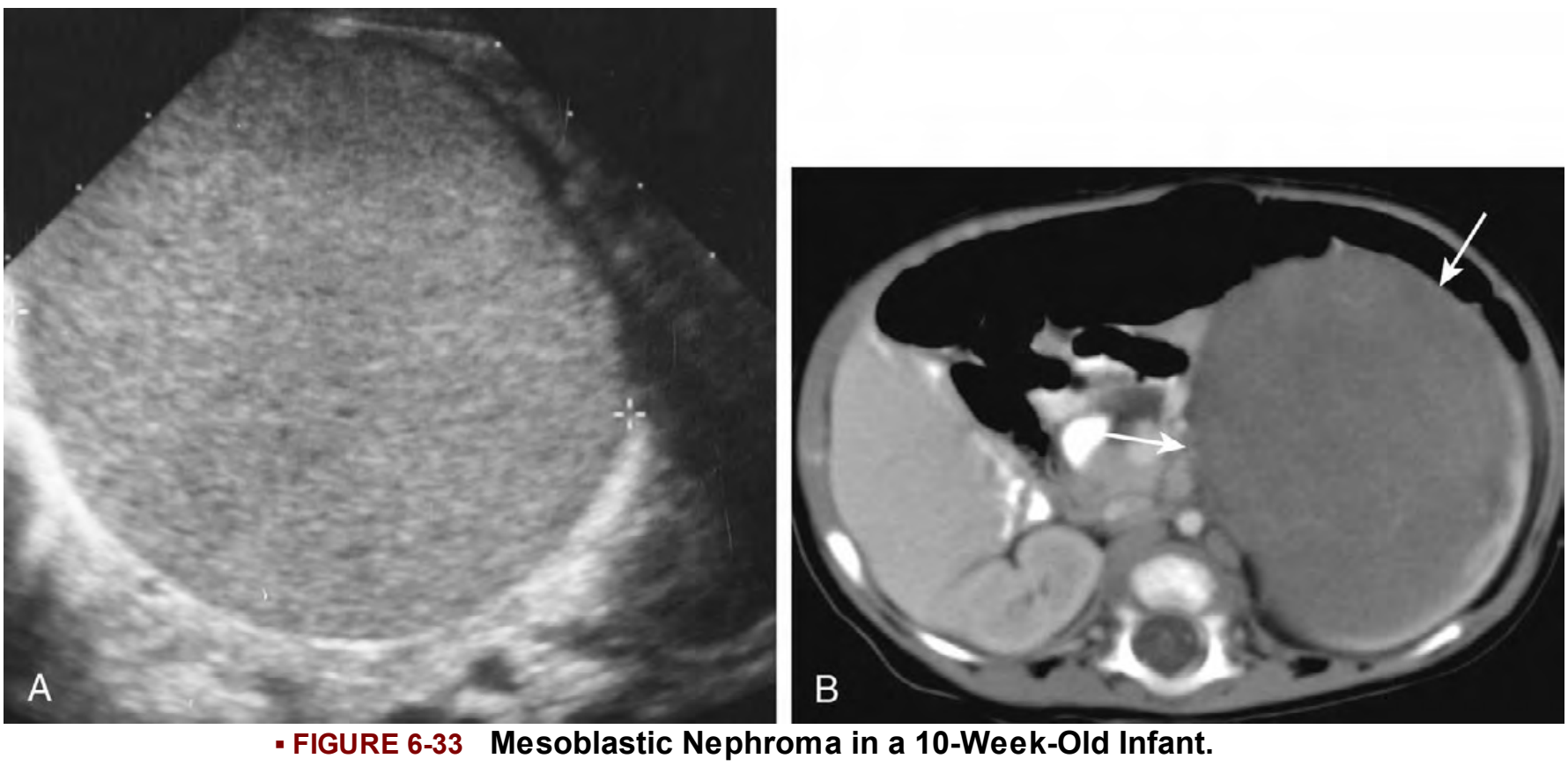
Angiomyolipoma

Patients with tuberous sclerosis are predisposed to developing angiomyolipomas. These lesions commonly demonstrate fatty components on imaging (Fig. 6-34, *A* and *B*) and may spontaneously hemorrhage. Hemorrhage from angiomyolipomas is the leading cause of death in tuberous sclerosis patients. Angiomyolipomas larger than 4 cm in diameter are particularly predisposed to contain dysplastic arteries and aneurysms that may hemorrhage; they are commonly treated by prophylactic embolization. The angiomyolipomas start as small echogenic foci within the kidneys during early childhood (Fig. 6-35) and grow into large infiltrative masses that enlarge the kidneys (see Fig. 6-34). Angiomyolipomas can usually be diagnosed conclusively on MRI, due to the presence of internal fatty tissue. However, on occasions, fat-poor angiomyolipomas pose a diagnostic dilemma and are difficult to differentiate from malignancy. Tuberous sclerosis is also associated with ADPKD and renal cysts. The gene for tuberous sclerosis (TSC2 on chromosome 16) is contiguous with the polycystic kidney disease

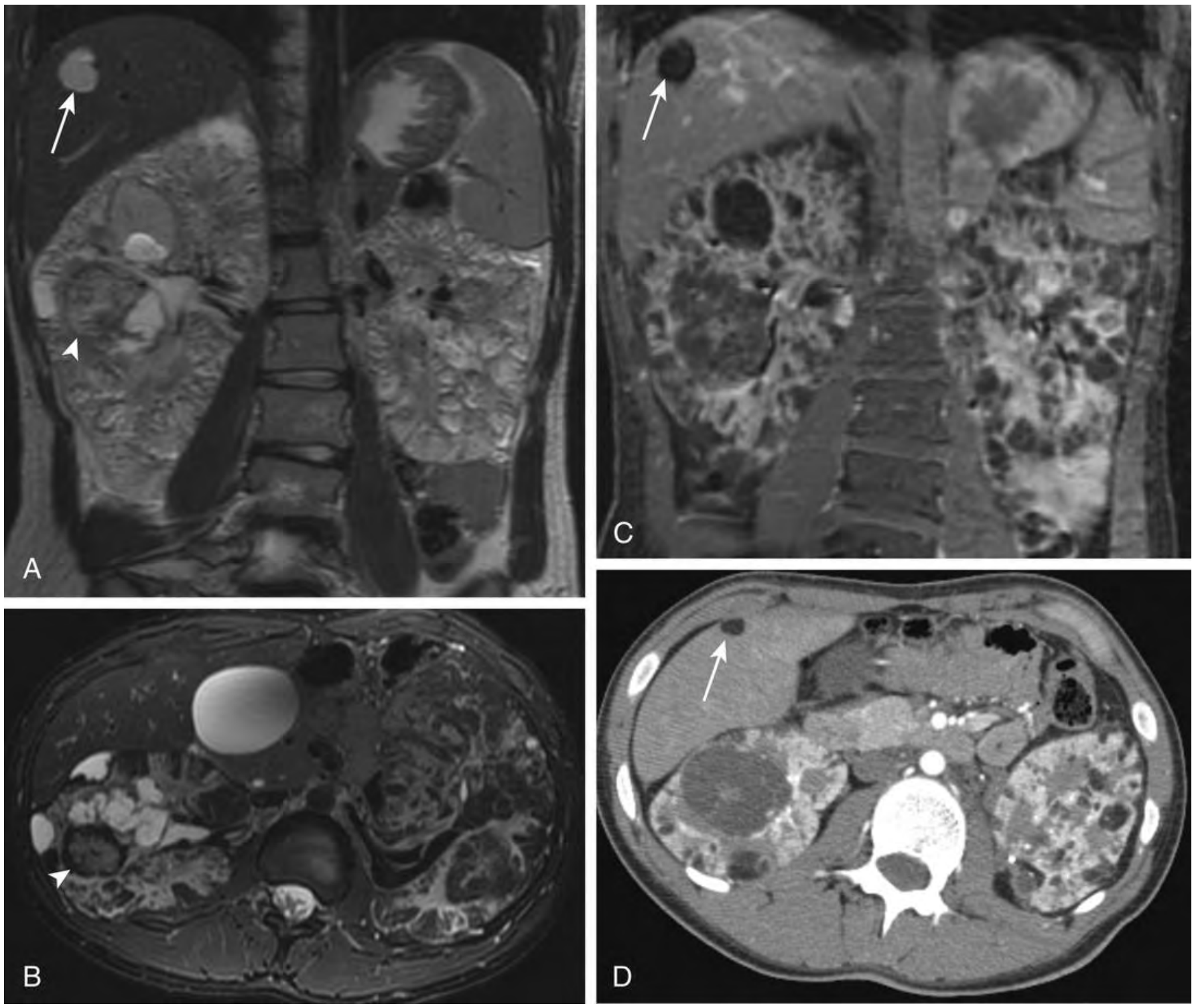
gene (PKD 1), and on occasions individuals with tuberous sclerosis have manifestations of polycystic kidney disease.



▪ **FIGURE 6-32** **Multilocular cystic nephroma.**
Axial (**A**) and sagittal postcontrast (**B**) CT images show a multiseptated cystic mass. Note claw sign indicating origin of mass in right kidney (*arrows* in **A**). Note renal parenchyma surrounding the medial aspect of the mass. There is only septal enhancement of cyst walls without solid components.



▪ **FIGURE 6-33** **Mesoblastic Nephroma in a 10-Week-Old Infant.**
A, Ultrasound shows a homogeneous mass in the right kidney. **B,** CT shows a homogeneously enhancing right renal mass *(arrows)*.



▪ **FIGURE 6-34** **Tuberous sclerosis.**
Coronal T2-weighted (**A**), axial T2-weighted fat suppressed (**B**), and coronal T1-weighted fat suppressed (**C**) postcontrast MR images show enlarged kidneys with diffuse fatty infiltration, from multiple angiomyolipomas, innumerable kidney cysts, and several hepatic angiomyolipomas *(arrows)*. Mild hemorrhagic changes (*arrowheads* in **A** and **B**) were noted within some of the cysts. **D,** Axial CT shows diffuse fatty infiltration and enlargement of the bilateral kidneys. The arrow denotes a hepatic angiomyolipoma.

Adrenal Glands

A number of pathologic processes can involve the adrenal glands in children. The most commonly encountered adrenal disorders are neuroblastoma and neonatal adrenal hemorrhage.



▪ **FIGURE 6-35** **Angiomyolipomas in a 5-year-old patient with tuberous sclerosis.** Ultrasound shows multiple echogenic foci in the kidney. The most prominent echogenic foci are denoted by *arrows*.

Neuroblastoma

Neuroblastoma is a malignant tumor of primitive neural crest cells that most commonly arises in the adrenal gland but can occur anywhere along the sympathetic chain. It is differentiated from its more benign counterparts, ganglioneuroma and ganglioneuroblastoma, by the degree of cellular maturation. Neuroblastoma is an aggressive tumor with a tendency to invade adjacent tissues. The tumor metastasizes most commonly to liver and bone. It is the most common extracranial solid malignancy in children and the third most common malignancy of childhood, with only leukemia and primary brain tumors being more common. Approximately 90% to 95% of patients with neuroblastoma have elevated levels of catecholamines (vanillylmandelic acid) in their urine, a useful diagnostic tool.

Neuroblastoma is a very unusual tumor in that the prognosis and the patterns of distribution of disease depend strongly on age. In children who are less than 1 year of age, the disease tends to spread to liver and skin. These children usually have a good prognosis. In those older than 1 year of age, the disease tends to spread to bone. These children have a poorer prognosis. The previous staging (Evans)

system for neuroblastoma has been replaced by the International Neuroblastoma Risk Group (INRG) Staging System (Table 6-3), which heavily relies on imaging-defined risk factors (IDRFs) (Table 6-4). IDRFs are 20 well-defined surgical risk factors, identified on imaging, that make complete tumor resection risky or complicated at the time of diagnosis. Stage MS is similar to prior stage 4S, except for primary tumor size and patient age, and is given to children less than 18 months of age with metastatic disease that is confined to skin, liver, and bone marrow (Fig. 6-36, *A-D*). Cortical bone involvement demonstrated by radiography or nuclear bone scintigraphy is not considered stage MS. It is intriguing that patients with stage M disease have very poor prognoses and commonly require therapy, such as bone marrow transplantation, whereas patients with stage MS disease have excellent prognoses and at many institutions are watched with imaging and receive no therapy. Other factors associated with better prognoses are listed in Table 6-5.

TABLE 6-3

International Neuroblastoma Risk Group Staging System

Stage	Definition
L1	Localized tumor that does not involve vital structures, as defined by the IDRFs. Tumors are primarily confined to the organ of origin and to one body compartment.
L2	Local regional tumor with the presence of one or more IDRFs
M	Distant, noncontiguous metastatic disease (except stage MS)
MS	Metastatic disease in children younger than 18 mo with metastases confined to skin, liver, and/or bone marrow

IDRF, Image-defined risk factor.

Reprinted with permission. © 2009 American Society of Clinical Oncology. All rights reserved. Monclair T, Brodeur GM, Ambros PF, et al. The International Neuroblastoma Risk Group (INRG) staging system: an INRG Task Force report. *J Clin Oncol* 2009; 27:298-303.

TABLE 6-4

Image-Defined Risk Factors in Neuroblastic Tumors

Ipsilateral Tumor Extension Within Two Body Compartments
- Neck-chest, chest-abdomen, abdomen-pelvis

Neck
- Tumor encasing carotid and/or vertebral artery and/or internal jugular vein
- Tumor extending to base of skull
- Tumor compressing the trachea

Cervicothoracic Junction
- Tumor encasing brachial plexus roots
- Tumor encasing subclavian vessels and/or vertebral and/or carotid artery
- Tumor compressing the trachea

Thorax
- Tumor encasing the aorta and/or major branches
- Tumor compressing the trachea and/or principal bronchi
- Lower mediastinal tumor, infiltrating the costovertebral junction between T9 and T12

Thoracoabdominal
- Tumor encasing the aorta and/or vena cava

Abdomen/Pelvis
- Tumor infiltrating the porta hepatis and/or the hepatoduodenal ligament
- Tumor encasing branches of the superior mesenteric artery at the mesenteric root
- Tumor encasing the origin of the coeliac axis, and/or of the superior mesenteric artery
- Tumor invading one or both renal pedicles
- Tumor encasing the aorta and/or vena cava
- Tumor encasing the iliac vessels
- Pelvic tumor crossing the sciatic notch
- Intraspinal tumor extension whatever the location, provided that more than one third of the spinal canal in the axial plane is invaded and/or the perimedullary leptomeningeal

spaces are not visible and/or the spinal cord signal is abnormal.
- Infiltration of adjacent organs and structures: pericardium, diaphragm, kidney, liver, duodenopancreatic block, and mesentery

Conditions to Be Recorded but *not* Considered IDRFs

- Multifocal primary tumors
- Pleural effusion, with or without malignant cells
- Ascites, with or without malignant cells

Reprinted with permission. © 2009 American Society of Clinical Oncology. All rights reserved. Monclair T, Brodeur GM, Ambros PF, et al. The International Neuroblastoma Risk Group (INRG) staging system: an INRG Task Force report. *J Clin Oncol* 2009; 27:298-303.

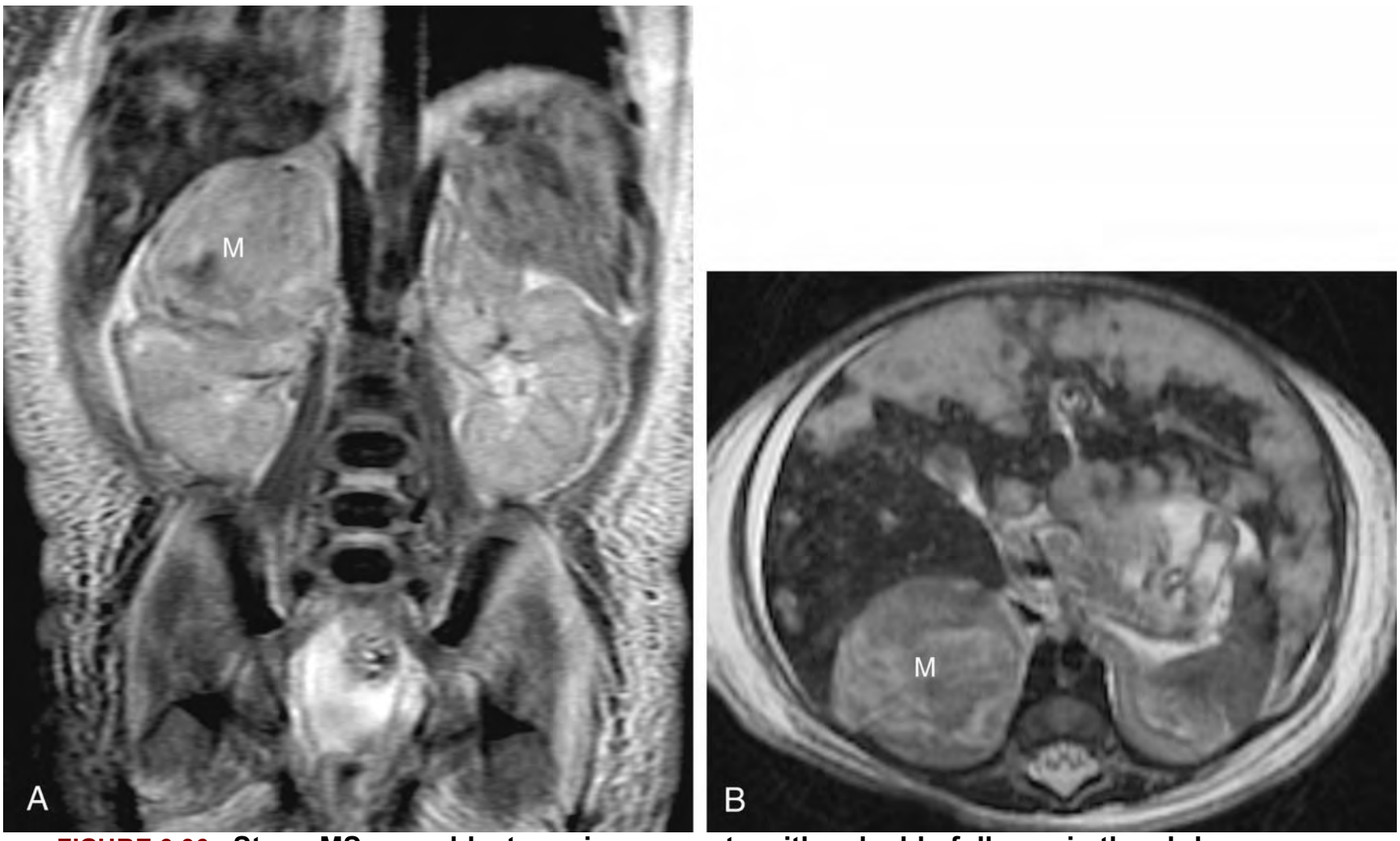
Although neuroblastoma may be encountered initially as a mass on abdominal radiographs or ultrasound, confirmation of the diagnosis and definition of the exact extent of disease is obtained with either CT or MRI. Some investigators have advocated MRI over CT because of its superior ability to identify tumor extension into the neuroforamina. Neuroforaminal involvement is important to identify because at many institutions it will lead neurosurgery services to become involved in the surgical resection. In the authors' experience, both CT and MRI are excellent in identifying neuroforaminal and spinal canal involvement.

On CT, neuroblastoma is detected with a sensitivity of nearly 100%. The tumors tend to appear lobulated and grow in an invasive pattern, surrounding and engulfing, rather than displacing, vessels such as the celiac axis, superior mesenteric artery, and aorta (Fig. 6-37). The masses are often inhomogeneous secondary to hemorrhage, necrosis, and calcifications. Calcifications are seen by CT in as much as 85% of cases (see Fig. 6-37, *A*). On MRI, neuroblastoma, like most other malignancies, appears bright on T2-weighted images and can be heterogeneous in signal. Calcifications are less commonly seen on MRI. During the staging of neuroblastoma, most patients also undergo evaluation by metaiodobenzylguanidine (MIBG) and bone scintigraphy. The role of positron emission tomography (PET) and PET-CT or PET-MR is still being defined.

Other adrenal tumors that occur in childhood, but much less commonly than neuroblastoma, include pheochromocytoma and adrenal carcinoma.

Neonatal Adrenal Hemorrhage

Adrenal hemorrhage can occur in neonates secondary to birth trauma or stress. Like neuroblastoma, adrenal hemorrhage may present as an asymptomatic flank mass and may be seen on imaging as an adrenal mass. Surgical intervention is unnecessary in adrenal hemorrhage, so differentiation from neuroblastoma is important. Ultrasound is usually able to differentiate the two. Neuroblastoma typically appears as an echogenic mass with diffuse vascularity (color Doppler), whereas adrenal hemorrhage typically appears as an avascular mass (Fig. 6-38). The internal hemorrhagic components may reveal a variable appearance, depending on the age of the blood products and their echogenicity, or MR signal may vary accordingly comparable to hemorrhages elsewhere in the body. Performing serial ultrasounds over time (see Fig. 6-38) is an acceptable way of differentiating problematic cases because the prognosis for neonates with stage L1 neuroblastoma is excellent. With time, adrenal hemorrhages decrease in size. MRI can also be useful in differentiating adrenal hemorrhage (low T2-weighted signal, blood product signal) from neuroblastoma (high T2-weighted signal) in very problematic cases.



▪ **FIGURE 6-36** **Stage MS neuroblastoma in a neonate with palpable fullness in the abdomen.**
Coronal (**A**) and axial T2-weighted (**B**) MR images show multiple heterogeneous masses throughout the liver parenchyma and a right suprarenal mass *(M)*.

TABLE 6-5

Features Associated With Better Prognosis in Patients With Neuroblastoma

- Age of diagnosis less than 18 mo
- Histologic grade
- No extra copies of the MYCN gene
- Stage MS
- Thoracic primary

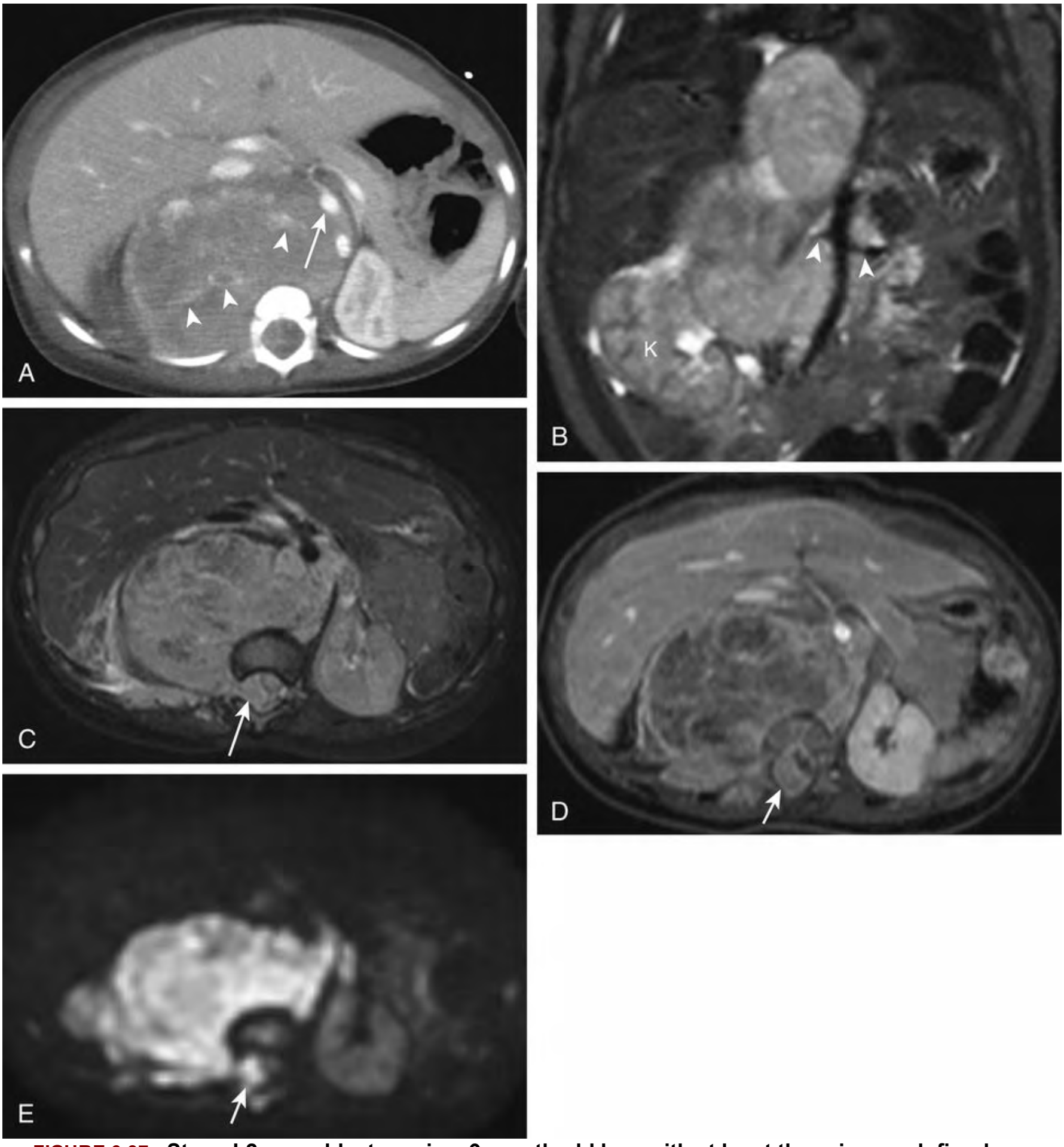
▪ Pelvic Rhabdomyosarcoma

Rhabdomyosarcoma is a highly malignant tumor that can occur in numerous locations throughout the body. It is the most common malignant sarcoma of childhood and typically presents during the first 3 years of life. Its most common locations include the pelvis and genitourinary tract (15%) and head and neck (40%). The most common locations within the genitourinary tract include the bladder (Fig. 6-39, *A* and *B*), prostate, spermatic cord, paratesticular tissues, uterus, vagina, and perineum. It affects girls and boys equally. When the lesion involves the bladder, it typically appears as a multilobulated mass, likened to a bunch of grapes. Pelvic rhabdomyosarcoma may result in hydronephrosis. Patients with cervicovaginal rhabdomyosarcoma, specifically botryoid-type embryonal, often have a cancer predisposition syndrome related to *DICER1* mutation.

▪ Sacrococcygeal Teratoma

Sacrococcygeal teratomas typically present as large cystic or solid masses either on prenatal imaging or at birth. Less commonly they present as buttock asymmetry or a presacral mass later in childhood. The majority are benign, but there is an increased risk for malignancy with delayed diagnosis. The mass can be primarily external, protruding from the sacral region, which is the most common type, accounting for nearly half of the cases; internal within the pelvis; or dumbbell-shaped, with both internal and

external components. On imaging, the lesions appear heterogeneous, with variable cystic, solid, and fatty components (Fig. 6-40, *A-E*).

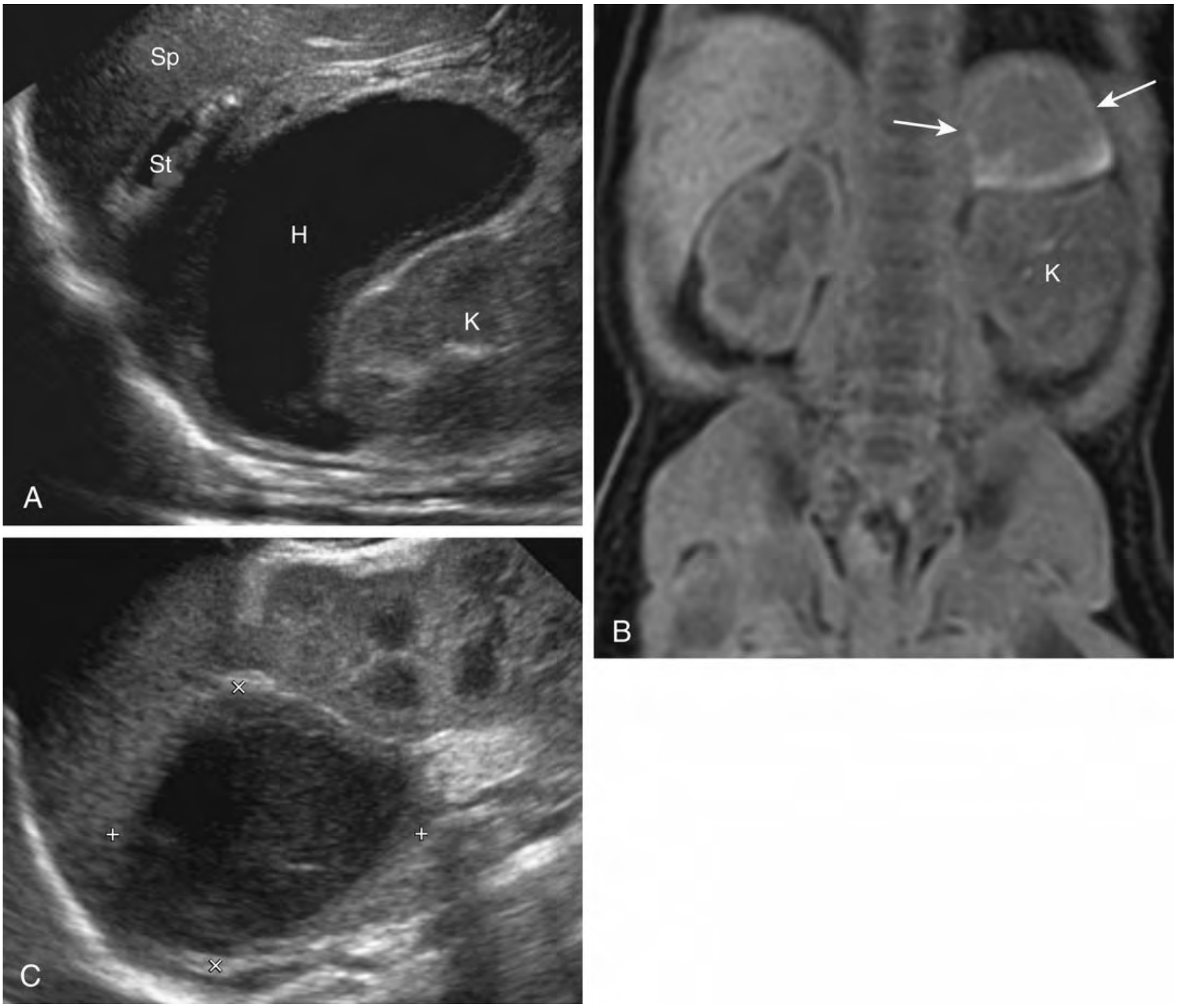


▪ **FIGURE 6-37** **Stage L2 neuroblastoma in a 9-month-old boy with at least three image-defined risk factors.**

A, CT shows heterogeneously enhancing retroperitoneal mass that surrounds and anteriorly displaces the abdominal aorta *(arrow)* and engulfs the origin of the celiac artery. Note the heterogeneous calcifications *(arrowheads)*. **B,** Coronal T2-weighted MR image shows the lesion crossing the midline as well as extending into the mediastinum. The lesion encircles the abdominal aorta and bilateral renal arteries' origins *(arrowheads)*. Note inferolateral displacement of the right kidney *(K)*. Axial T2-weighted (**C**), and axial T1-weighted (**D**) fat suppressed MR images show tumoral extension into the spinal canal *(arrows)*, as well as encasement of the aorta and celiac axis origin. **E,** Diffusion-weighted MR image shows corresponding marked restricted diffusion and demonstrates to better advantage extension of the lesion into the spinal canal *(arrow)*.

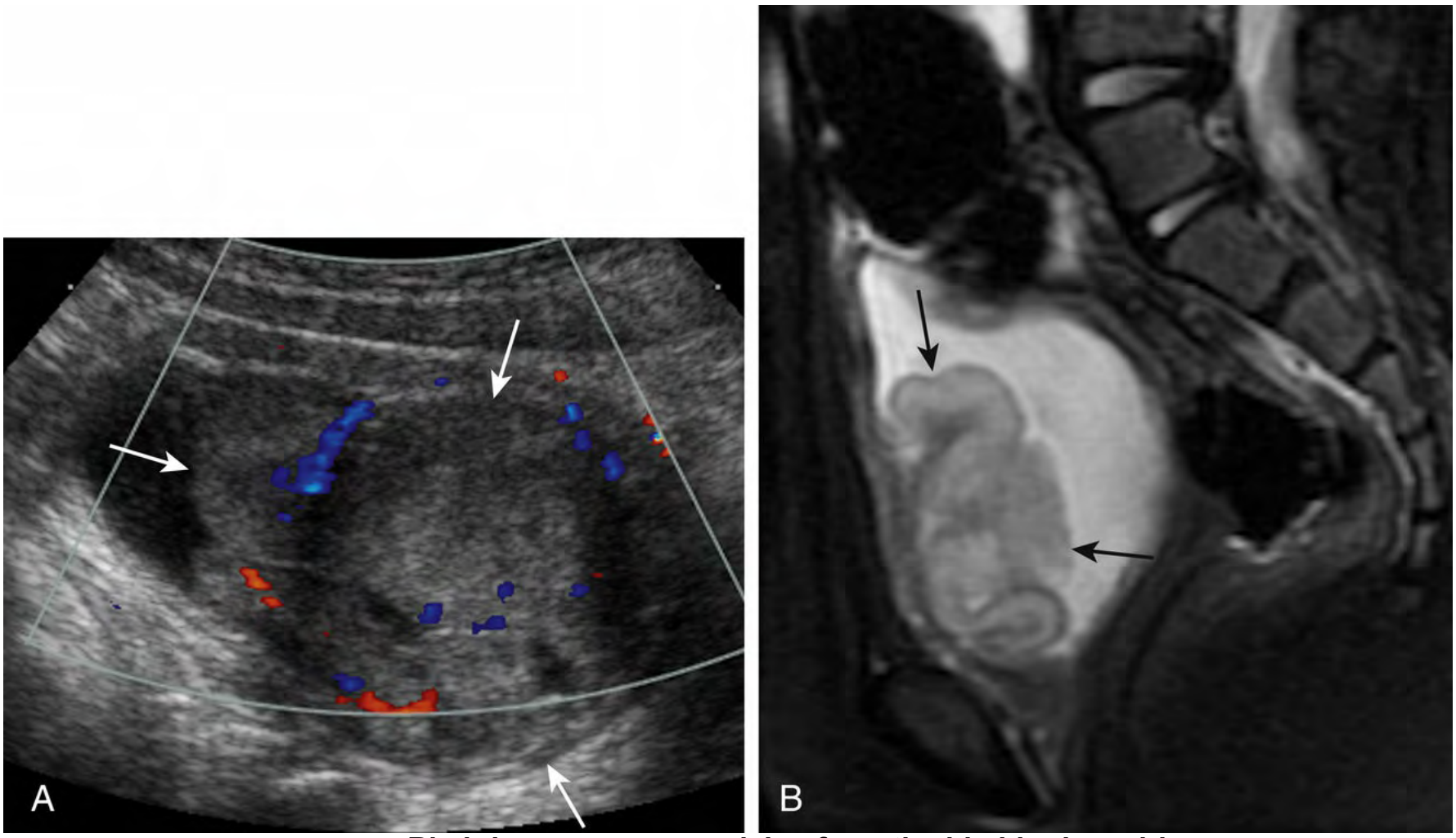
▪ Scrotum

The commonly encountered imaging issues in the pediatric scrotum include testicular neoplasm, testicular microlithiasis, and the acutely painful scrotum. Most intratesticular neoplasms (>90%) are germ cell tumors with a stratification according to age. In the first decade yolk sac tumors and teratomas are the most common types, whereas in the second decade, choriocarcinoma is the most common. Less than 10% of testicular tumors are metastatic from leukemia or lymphoma. Most primary testicular tumors present with a nontender, firm scrotal mass. Ultrasound confirms an intratesticular mass (Fig. 6-41). However, there are no ultrasound findings that suggest a specific histologic diagnosis. If a scrotal mass is extratesticular in location, the most likely diagnosis is embryonal rhabdomyosarcoma arising from the spermatic cord or epididymis.

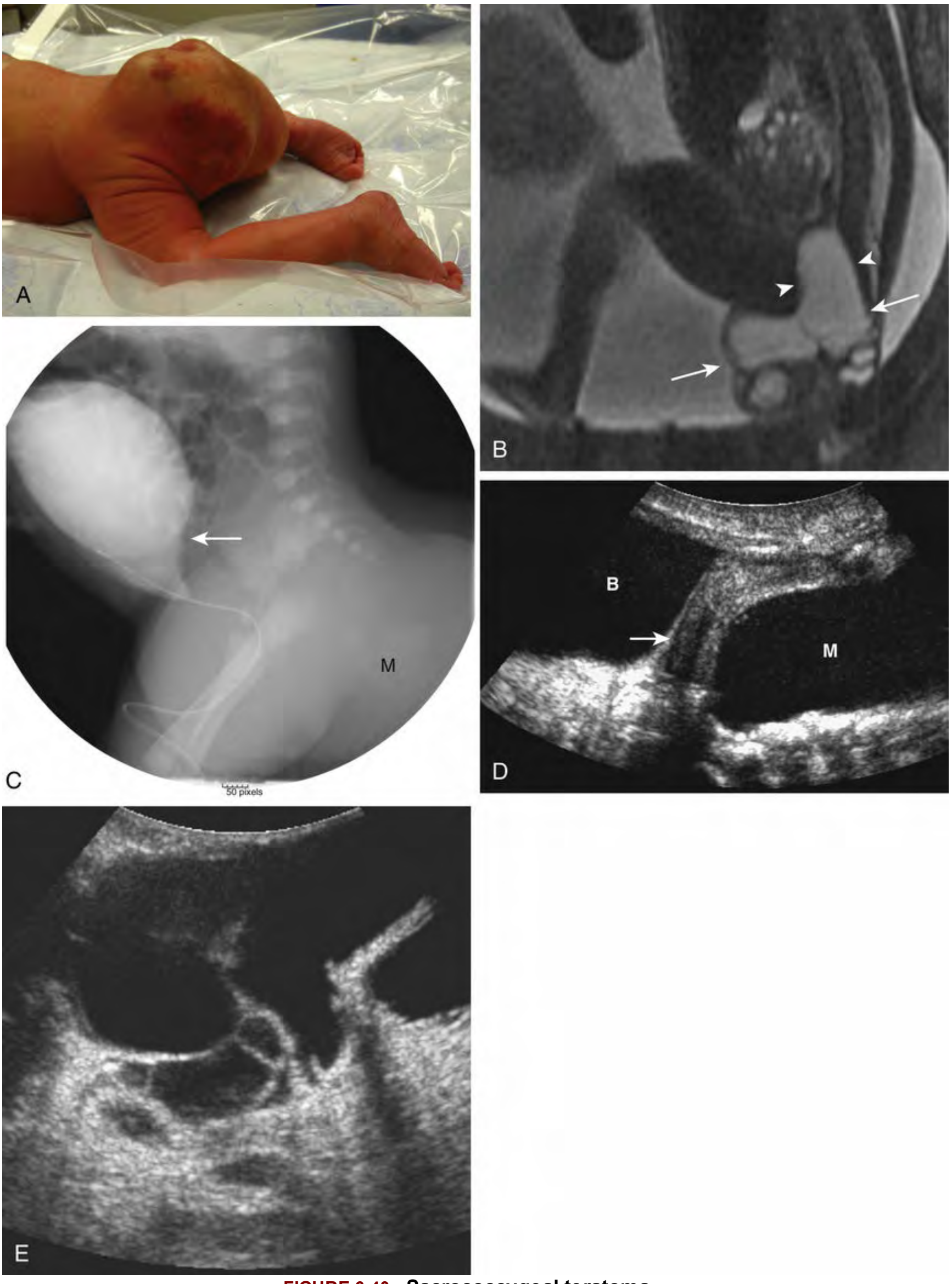


▪ **FIGURE 6-38** **Adrenal hemorrhage in a 2-day-old neonate.**

A, Initial sonogram shows a complex, predominantly cystic-appearing, hypoechoic mass *(H)* in a suprarenal location. The kidney *(K)* is displaced inferiorly. *Sp,* Spleen; *St,* stomach. **B,** Coronal T1-weighted fat suppressed MR image obtained at day 5 of life shows a complex suprarenal lesion *(arrows)* with high signal, blood degradation products consistent with an adrenal hemorrhage. The left kidney (K) is displaced inferiorly. **C,** Follow-up ultrasound from approximately 1 month later shows marked interval decrease in the size of the adrenal gland *(between calipers)*, a more adrenoform shape, consistent with resolving hematoma.

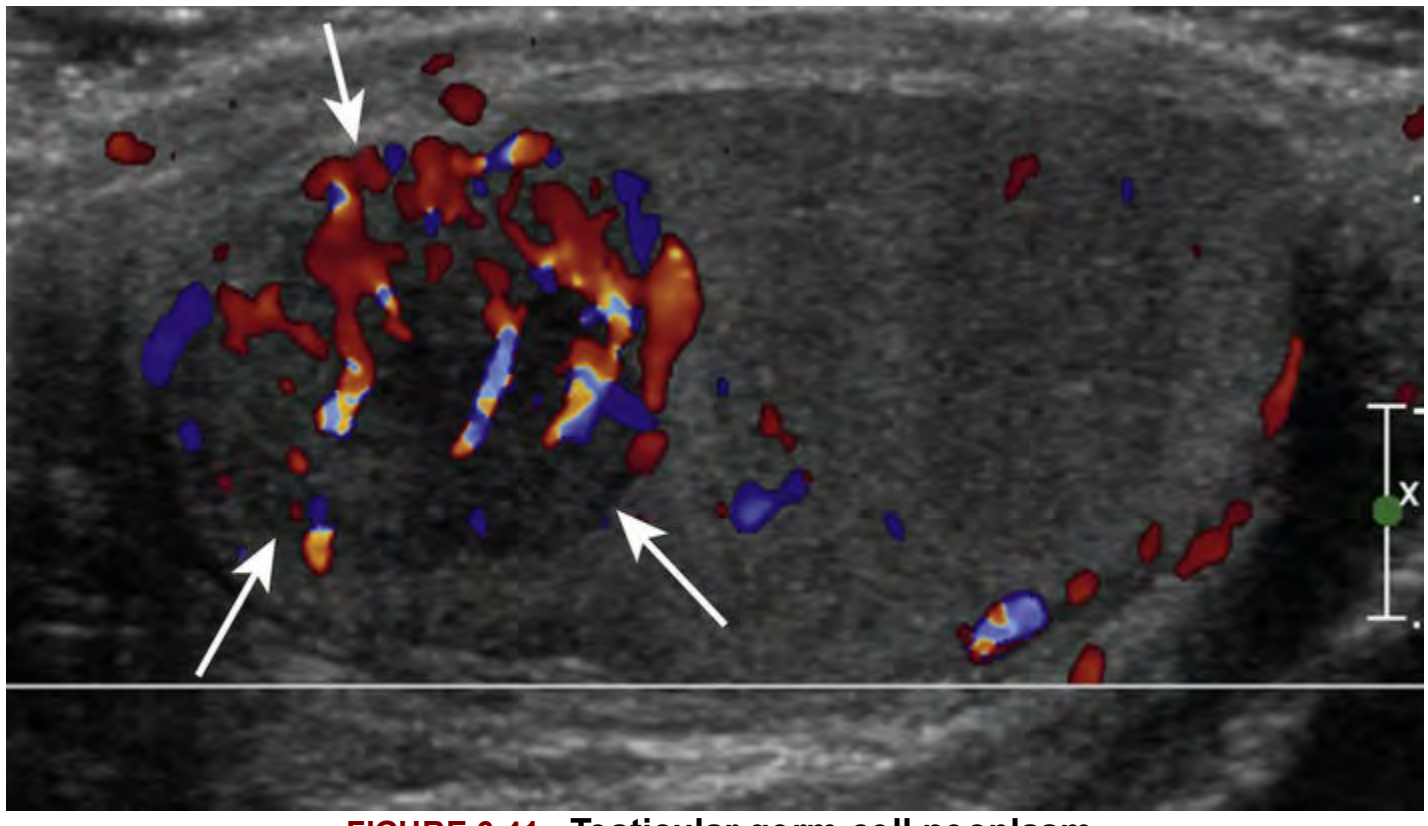


▪ **FIGURE 6-39** **Rhabdomyosarcoma arising from the bladder in a girl.**
A, Longitudinal ultrasound shows a large, intravesical heterogeneous mass *(arrows)* showing internal vascularity. **B,** Sagittal T2-weighted MR image redemonstrates the large heterogeneous intravesical mass *(arrows)*.



▪ **FIGURE 6-40** **Sacrococcygeal teratoma.**

A, Photograph of a newborn demonstrates skin-covered mass extending from buttocks region. **B,** Sagittal, T2-weighted prenatal MR image shows a multicystic mass *(arrows)* predominantly external, with component *(arrowheads)* extending within the internal pelvis. **C,** VCUG from postnatal work-up shows sacrococcygeal teratoma as a mass *(M)*. Note that the bladder is displaced anteriorly *(arrow)*. **D,** Longitudinal ultrasound shows that the cystic component of the mass *(M)* extends superiorly to the level of the inferior bladder *(B)*. The uterus *(arrow)* is displaced posteriorly and superiorly. **E,** Ultrasound over the external portion of the mass shows its multicystic nature.



▪ **FIGURE 6-41** **Testicular germ cell neoplasm.**
Transverse ultrasound shows focal, heterogeneous, hypoechogenic mass *(arrows)* in left testicle. Increased blood flow is shown on color Doppler.

Testicular Microlithiasis

Testicular microlithiasis appears on ultrasound as multiple small echogenicities within the testes (Fig. 6-42), reflecting calcium deposits within seminiferous tubules. There is often no posterior acoustic shadowing because of the small size of the calcifications. The finding is typically seen incidentally when the scrotum is being imaged for other reasons. It was initially reported that the risk for development of testicular neoplasm was between 18% and 75% in patients with ultrasound-demonstrated testicular microlithiasis. This led to recommendations for serial screening ultrasounds in patients with testicular microlithiasis to exclude development of neoplasm. However, more recent reports have shown that testicular microlithiasis is much more common than initially suspected, occurring in approximately 6% of the male population between 17 and 35 years of age. These reports have also shown that the overwhelming majority of these patients will not develop malignancies. Most now advocate following such patients with physical examination rather than ultrasound. Ultrasound could be obtained in symptomatic patients or in patients with a history of malignancy.



▪ **FIGURE 6-42** **Testicular microlithiasis.**
Transverse ultrasound of both testicles shows multiple punctate areas of increased echogenicity without posterior shadowing.

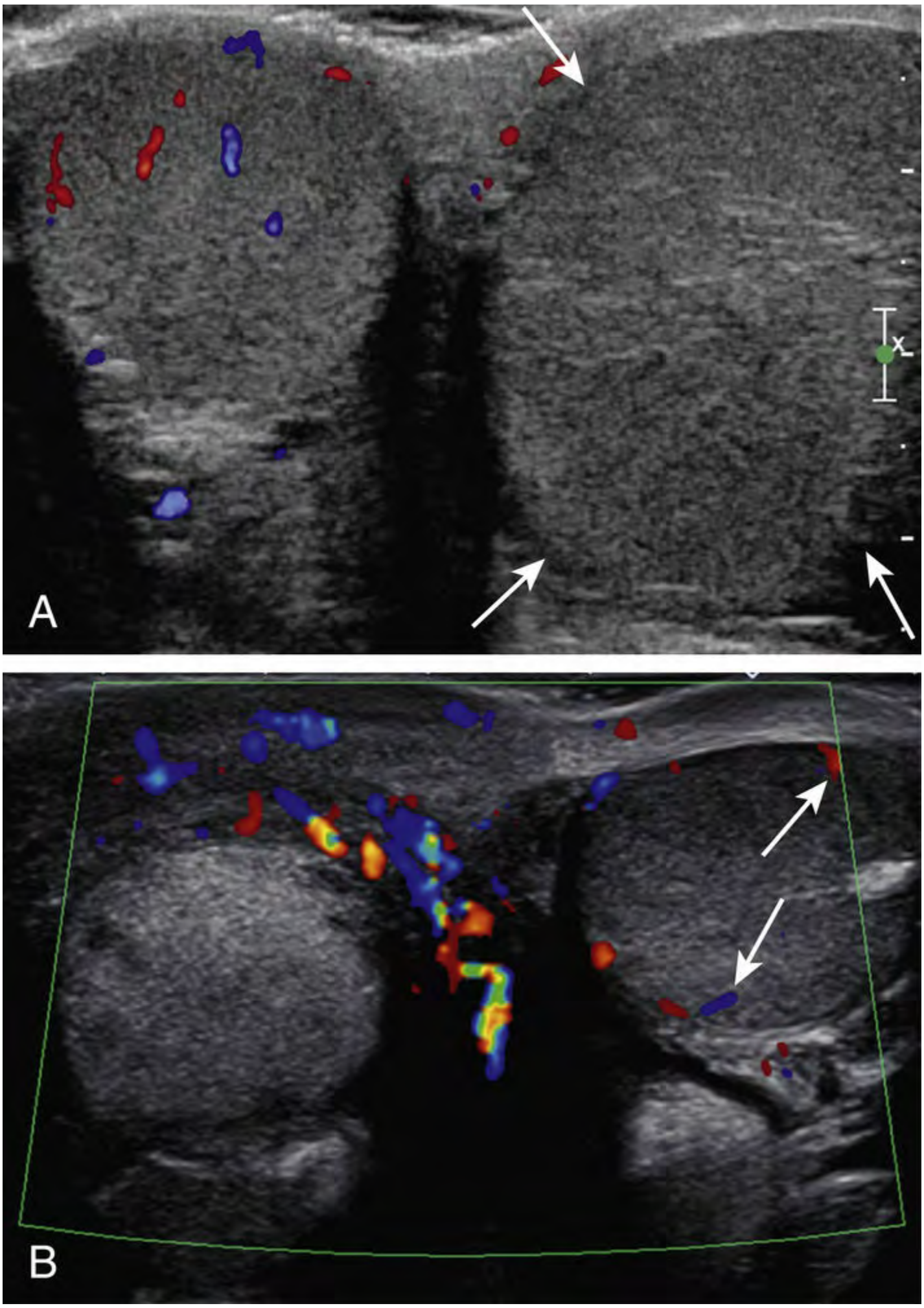
The Acute Scrotum

Because of the possibility of testicular torsion, imaging of the acutely painful scrotum is an emergency.

The major differential considerations in a child with acute scrotal pain include testicular torsion, epididymo-orchitis, and torsion of the testicular or epididymal appendage. Testicular hematoma is another less commonly encountered entity. The most common entities encountered in the setting of acute scrotal pain are actually epididymo-orchitis and torsion of an appendage. Although ultrasound examinations are performed to rule out testicular torsion, it is actually much less common than the other entities.

Testicular torsion occurs when the testis and cord twist within the serosal space and cause testicular ischemia. Prompt diagnosis and therapy are important because preservation of the testis is possible only in patients whose torsion is relieved within 6 to 10 hours. Color Doppler ultrasound is the modality of choice in evaluating an acute scrotum and demonstrates absence of flow or asymmetrically decreased flow within the affected testis. Demonstration of flow within a normal testis is more difficult in children less than 2 years of age. Grayscale ultrasound may demonstrate asymmetric enlargement and slightly decreased echogenicity of the affected testis. With progressive ischemia or infarction, hemorrhage and necrosis may cause increasing asymmetric heterogeneity (Fig. 6-43). This is a late finding.

Epididymo-orchitis usually occurs without an identifiable cause. In contrast to testicular torsion, in epididymo-orchitis the affected testis and epididymis demonstrate asymmetric and sometimes strikingly increased flow on Doppler ultrasound (Fig. 6-44, *A* and *B*). Gray-scale ultrasound demonstrates enlargement and decreased echogenicity of the testis and epididymis. Reactive hydroceles are common.

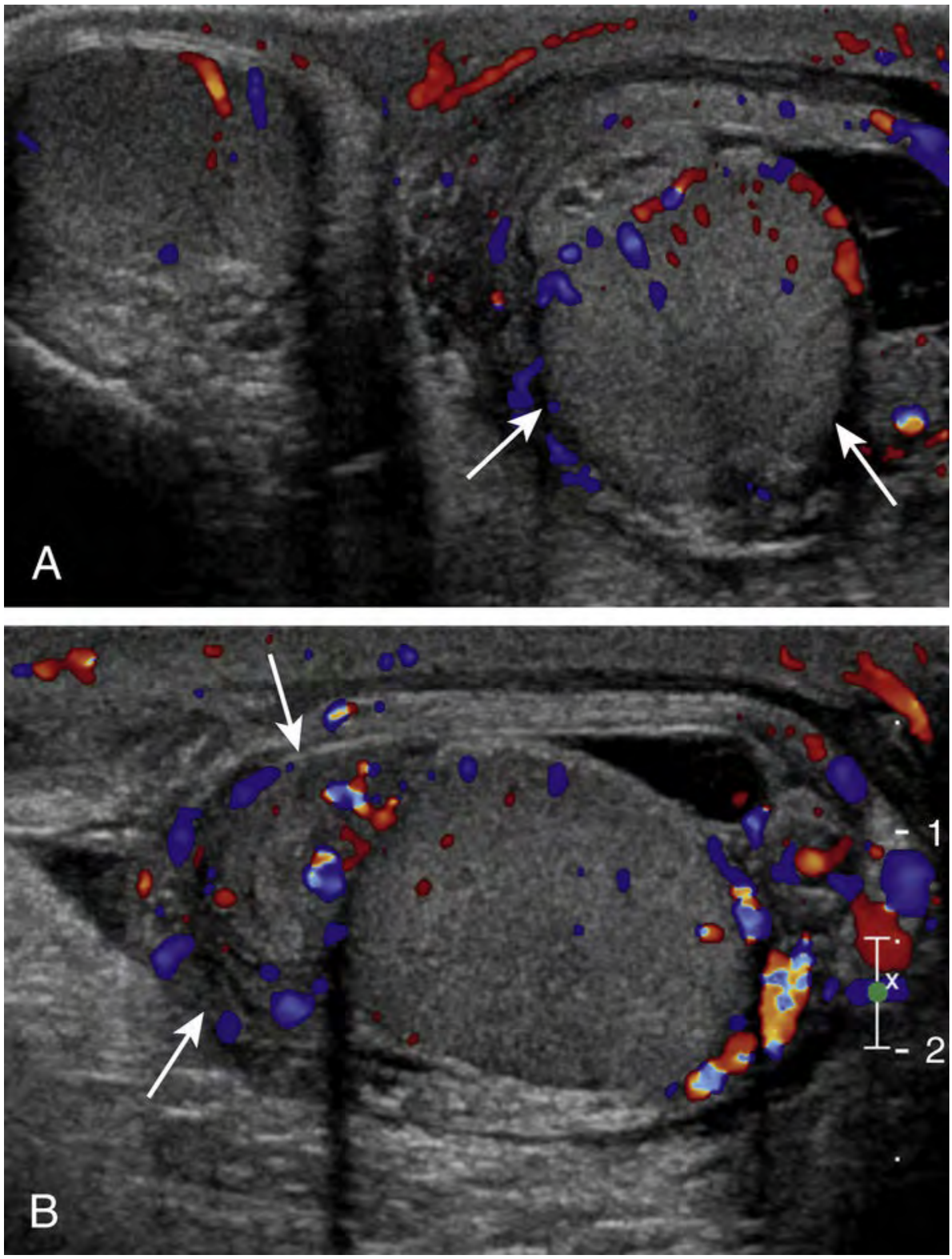


▪ **FIGURE 6-43 Testicular torsion, two examples.**
A, Transverse Doppler ultrasound showing both testes in a boy with left scrotal pain demonstrates absent flow and heterogeneous echotexture of left testicle *(arrows)*. Note normal echotexture and present flow on right. **B,** Later findings of torsion in a different patient. Transverse Doppler ultrasound showing both testes in a boy with right scrotal pain demonstrates absent flow and heterogeneous echotexture of right testicle. Note the flow detected *(arrows)* in the normal left testicle. There is a large amount of flow surrounding the right testicle, related to inflammatory reaction secondary to the necrosis.

Another cause of acute scrotum is torsion of a testicular or epididymal appendage, which are normal embryonic remnants. A mass of increased echogenicity may be seen between the superior pole of the testis and the epididymis. Enlargement of an appendage to greater than 5 mm has been touted as the best indicator of torsion. Periappendiceal hyperemia and normal testicular flow are supportive findings (Fig. 6-45, *A* and *B*). Torsion of the testicular appendage is a self-limited entity and does not require surgical management. The importance of making the diagnosis is to avoid unnecessary surgical exploration.

Trauma may result in a testicular hematoma. On ultrasound, hematomas appear as avascular masses

of abnormal echogenicity. Associated hematoceles are common.

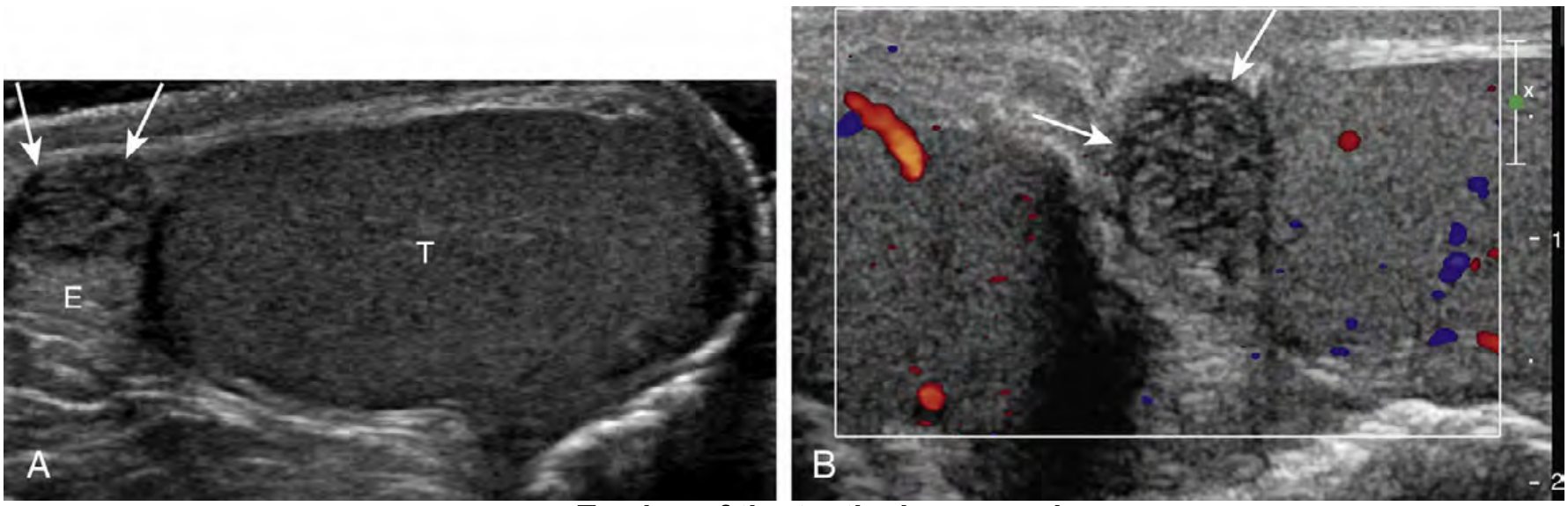


▪ **FIGURE 6-44** **Epidydimoorchitis in a boy with acute onset of left scrotal pain.**
A, Transverse color Doppler ultrasound shows asymmetric increased flow to the symptomatic left testis *(arrows)*. There is an associated hydrocele with a few thin septations. Note left scrotal thickening, more conspicuous when compared to the left side. **B,** Longitudinal color Doppler ultrasound shows enlarged epidydimis *(arrows)*. There is increased flow to both the epidydimis and testicle.

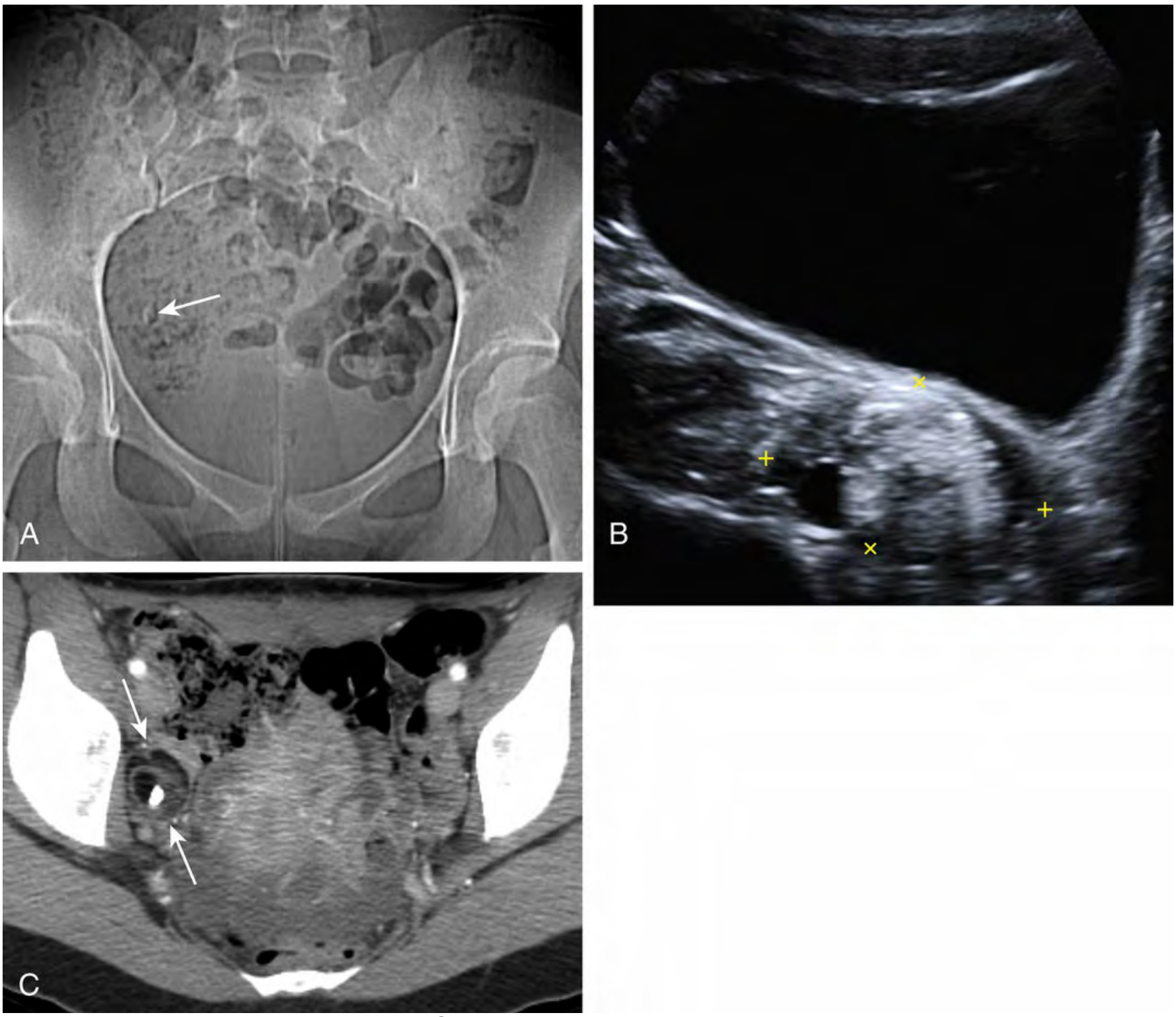
▪ Acute Pelvic Pain in Older Girls and Adolescents

Acute pelvic pain in older girls and adolescents is a commonly encountered problem that has many possible causes. Pain can be related to menstruation, multiple ovarian pathologies, or appendicitis. Ovarian causes of pain include ovarian cysts, hemorrhagic cysts, ectopic pregnancy, ovarian torsion, endometriosis, pelvic inflammatory disease, or other masses, such as teratoma (Fig. 6-46, *A* and *B*) or other neoplasms (Fig. 6-47, *A* and *B*). Ovarian dermoids (mature teratoma) can show fluid-fluid levels, fat, and calcifications on imaging (see Fig. 6-46). Other ovarian neoplasms are usually large at the time

of presentation (see Fig. 6-47), can have a cystic or solid appearance, and typically do not have differentiating features at imaging. In girls with right lower quadrant pain, appendicitis is also a possibility. The high incidence and variety of pathologic processes that may involve the ovaries make ultrasound the initial imaging modality for right lower quadrant pain in girls.



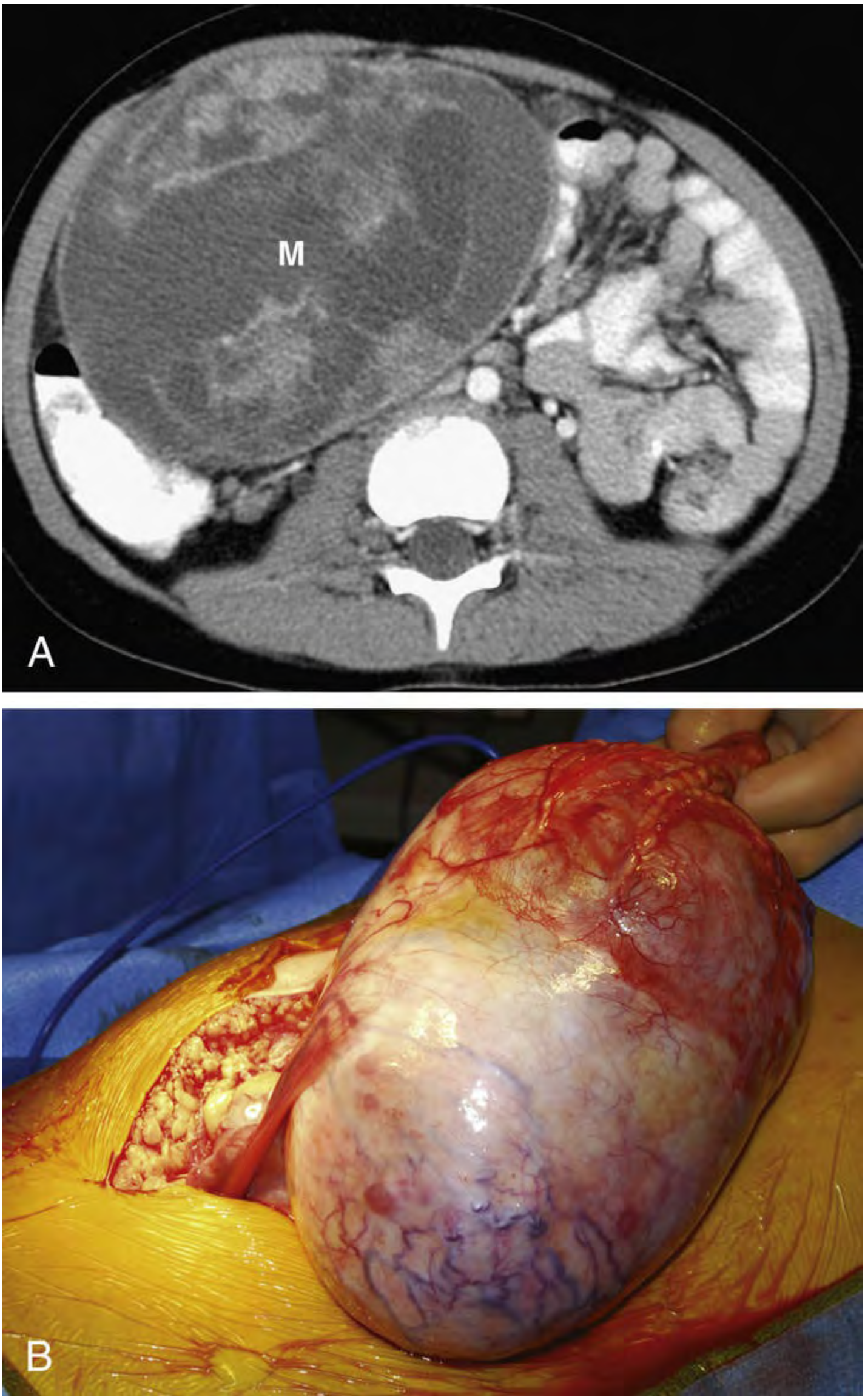
▪ **FIGURE 6-45 Torsion of the testicular appendage.**
A, Longitudinal view of the symptomatic side shows testicular appendage *(arrows)* to be enlarged (>5 mm). The appendage sits between the testicle *(T)* and the epididymis *(E)*. **B,** Color Doppler ultrasound image shows absence of flow to the testicular appendage *(arrows)*.



▪ **FIGURE 6-46** **Ovarian dermoid (mature teratoma).**
A, Pelvic radiograph shows a toothlike calcific density concerning for a teratoma in the right hemipelvis *(arrow)*. **B,** Pelvic ultrasound reveals an echogenic adnexal mass (between calipers) with posterior acoustic shadowing. The various interfaces in the near field, as a result of the mixture of fat and hair, obscure the remainder of the lesion, and the term *tip of the iceberg sign* is commonly used for this appearance. **C,** Corresponding CT image shows fatty tissue within the lesion *(arrows)*, a typical imaging feature of mature ovarian teratomas.

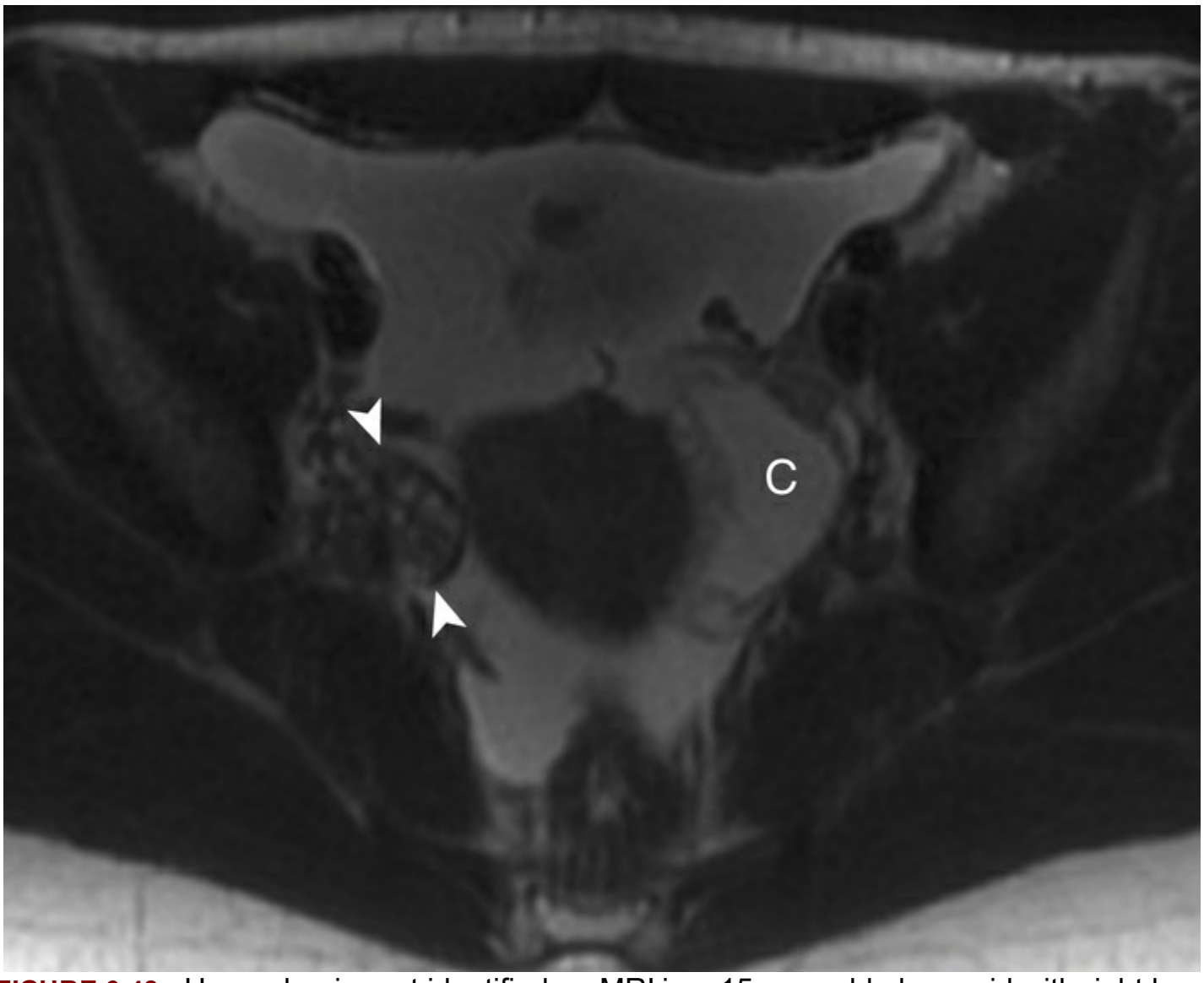
Hemorrhagic cysts are a common cause of pelvic pain in adolescent girls. On ultrasound the lesions appear as heterogeneous masses that often have enhanced through-transmission. Sometimes the masses can be quite large. Ovarian cysts can be discovered when CT or MRI is performed to evaluate for appendicitis (Fig. 6-48).

Ovarian torsion, which is less common than hemorrhagic cysts, can appear as an enlarged and echogenic ovary secondary to edema. There can be prominent peripheral follicular cysts, which are highly suggestive of the diagnosis (Figs. 6-49, *A* and *B*, and 6-50). However, the most commonly encountered positive finding is asymmetric ovarian volumes, with the larger ovary located on the side of pain. Doppler ultrasound demonstration of decreased or absent blood flow has not been shown to be accurate in diagnosing or excluding ovarian torsion. Note that a hemorrhagic cyst compressing the ovarian parenchyma peripherally can have a similar appearance and at times cannot be differentiated from ovarian torsion.

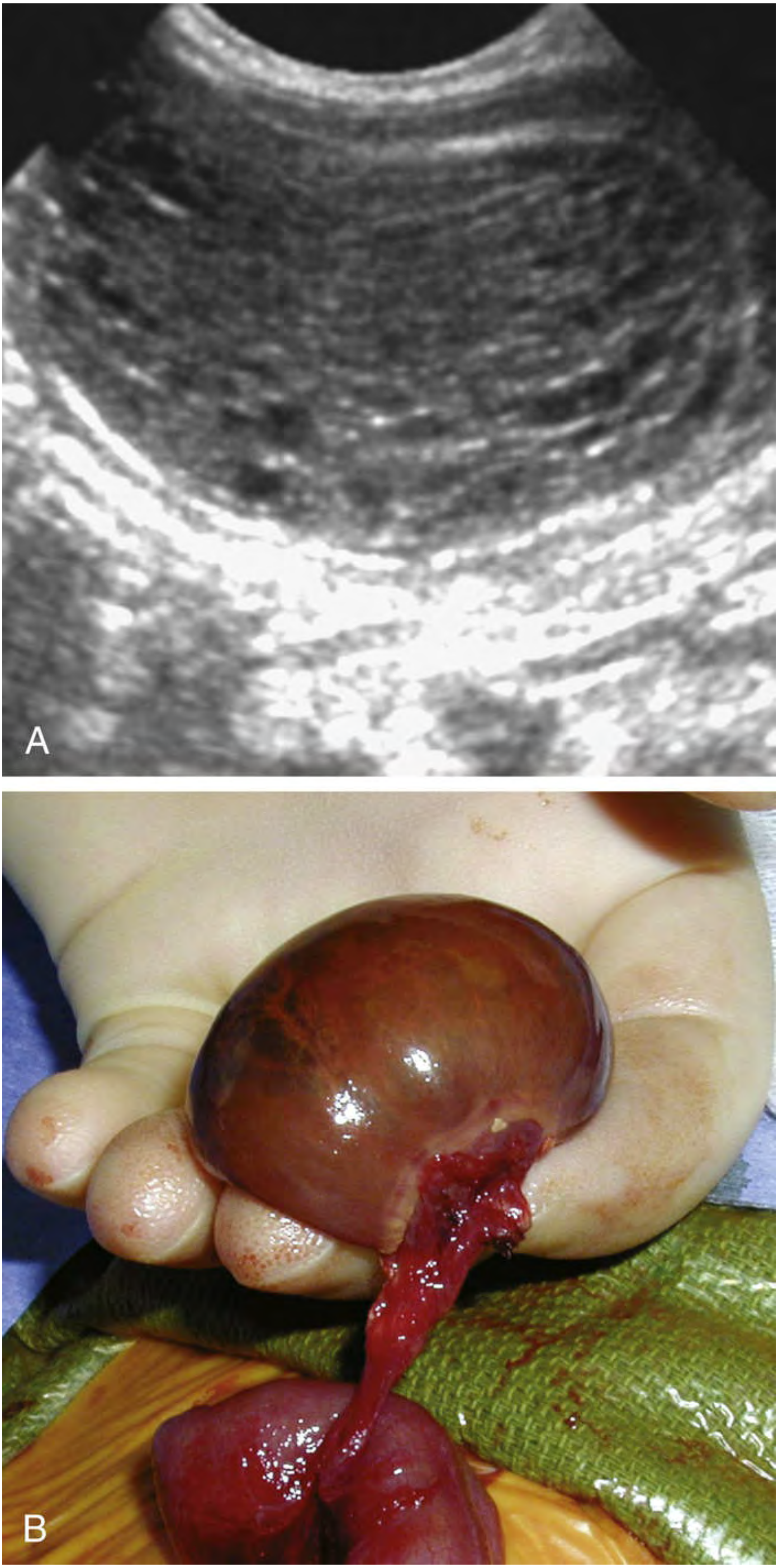


▪ **FIGURE 6-47** **Sertoli cell neoplasm of the ovary.**

A, CT shows heterogeneous mass arising from right superior pelvis *(M)*. **B,** Surgical photograph shows large mass arising from right ovary.

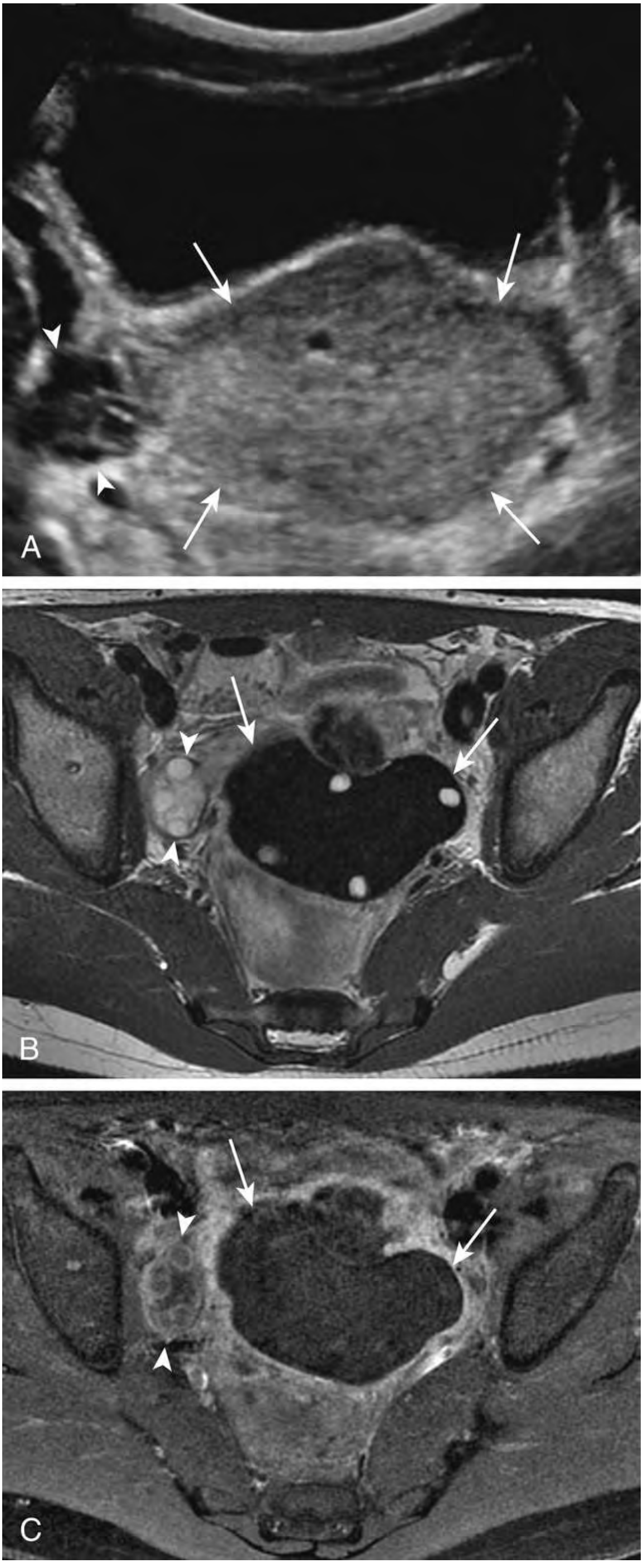


▪ **FIGURE 6-48** Hemorrhagic cyst identified on MRI in a 15-year-old obese girl with right lower quadrant pain and suspected appendicitis. Axial T2-weighted MR image shows an approximately 5 × 4 cm cyst *(C)* in region of left adenexa. It shows T2-shading and a crenated appearance suggestive of rupture. A mild to moderate amount of free fluid is noted. A normal ovary is seen on the right *(arrowheads)*.


A
B

▪ **FIGURE 6-49** **Ovarian torsion.**

A, Ultrasound shows asymmetrically enlarged ovary with increased echogenicity and some peripheral cysts. Doppler evaluation (not shown) showed no vascular flow. **B,** Surgical photograph showing infarcted ovary.


A
B
C

▪ **FIGURE 6-50** **Ovarian torsion in an 8-year-old girl with pelvic pain.**
A, Transverse ultrasound image shows asymmetrically enlarged left ovary *(arrows)* with heterogeneous echogenicity. The right ovary *(arrowheads)* is normal in appearance. Doppler evaluation showed no vascular flow to the left ovary. **B,** Axial T2-weighted MR image demonstrates an enlarged left ovary *(arrows)*, which is abnormally hypointense presumably due to stromal hemorrhage and necrosis. The right ovary *(arrowheads)* is normal in appearance. **C,** Axial postcontrast T1-weighted fat suppressed MR image shows no enhancement of the torsed right ovary *(arrows)*. Normal enhancement is seen in the left ovary *(arrowheads)*.

Suggested Readings

Avni F.E, Hall M. Renal cystic diseases in children: new concepts. *Pediatr Radiol*. 2010;40:939–946.

Brisse H.J, McCarville M.B, Granata C, et al. Guidelines for imaging and staging of neuroblastic tumors: consensus report from the International Neuroblastoma Risk Group Project. *Radiology*. 2011;261:243–257.

Daneman A, Navarro O.M, Somers G.R, et al. Renal pyramids: focused sonography of normal and pathologic processes. *RadioGraphics*. 2010;30:1287–1307.

Epelman M, Daneman A, Donnelly L.F, et al. Neonatal imaging evaluation of common prenatally diagnosed genitourinary abnormalities. *Semin Ultrasound CT MR*. 2014;35:528–554.

Gee M.S, Bittman M, Epelman M, et al. Magnetic resonance imaging of the pediatric kidney: benign and malignant masses. *Magn Reson Imaging Clin N Am*. 2013;21:697–715.

Gould S.W, Epelman M. Magnetic resonance imaging of developmental anomalies of the uterus and the vagina in pediatric patients. *Semin Ultrasound CT MR*. 2015;36:332–347.

Han B.K, Babcock D.S. Sonographic measurements and appearance of normal kidneys in children. *AJR*. 1985;145:611–618.

Heo S.H, Kim J.W, Shin S.S, et al. Review of ovarian tumors in children and adolescents: radiologic-pathologic correlation. *RadioGraphics*. 2014;34:2039–2055.

Khrichenko D, Darge K. Functional analysis in MR urography—made simple. *Pediatr Radiol*. 2010;40:182–199.

Lebowitz R.L, Olbing H, Parkkulainen K.V, et al. International system of radiographic grading of vesicoureteral reflux: international reflux study in children. *Pediatr Radiol*. 1985;15:105–109.

Monclair T, Brodeur G.M, Ambros P.F, et al. The International Neuroblastoma Risk Group (INRG) staging system: an INRG Task Force report. *J Clin Oncol*. 2009;27:298–303.

Roberts K.B. Urinary tract infection: clinical practice guideline for the diagnosis and management of the initial UTI in febrile infants and children 2 to 24 months. *Pediatrics*. 2011;128:595–610.

Roberts K.B. Revised AAP guideline on UTI in febrile infants and young children. *Am Fam Physician*. 2012;86:940–946.

Sung E.K, Setty B.N, Castro-Aragon I. Sonography of the pediatric scrotum: emphasis on the Ts—torsion, trauma, and tumors. *AJR*. 2012;198:996–1003.

CHAPTER 7

Musculoskeletal

Alexander J. Towbin

▪ Normal Variants and Common Benign Entities

Probably more than in any other organ system, the normal imaging appearance of the skeletal system is strikingly different in children from its appearance in adults (Fig. 7-1). This is related to the changing appearance of growing and maturing bone. The most striking changes occur near the physes and apophyses. Many of the more common mistakes made in pediatric skeletal radiology are related to the misinterpretation of normal structures as being abnormal. Textbooks such as Keats's *Atlas of Normal Roentgen Variants That May Simulate Disease* are dedicated to the normal radiographic appearances and variations of bones in children. The details of all of the normal changes in the radiographic appearance throughout the maturing skeleton cannot be covered here. The following section describes several commonly misinterpreted normal variants and benign entities.

Apophyseal and Epiphyseal Irregularity

The terms *apophysis* and *epiphysis* sound similar and have similar meanings. Their differences can be confusing. The term *epiphysis* refers to the part of bone that articulate with the adjacent bone. The primary growth plate, or physis, of the epiphysis is typically perpendicular to the longitudinal axis of the bone. *Apophyses* do not have an articular surface. The physis of an apophysis often courses parallel to the long axis of the bone. Apophyses act as a site of attachment for tendons.

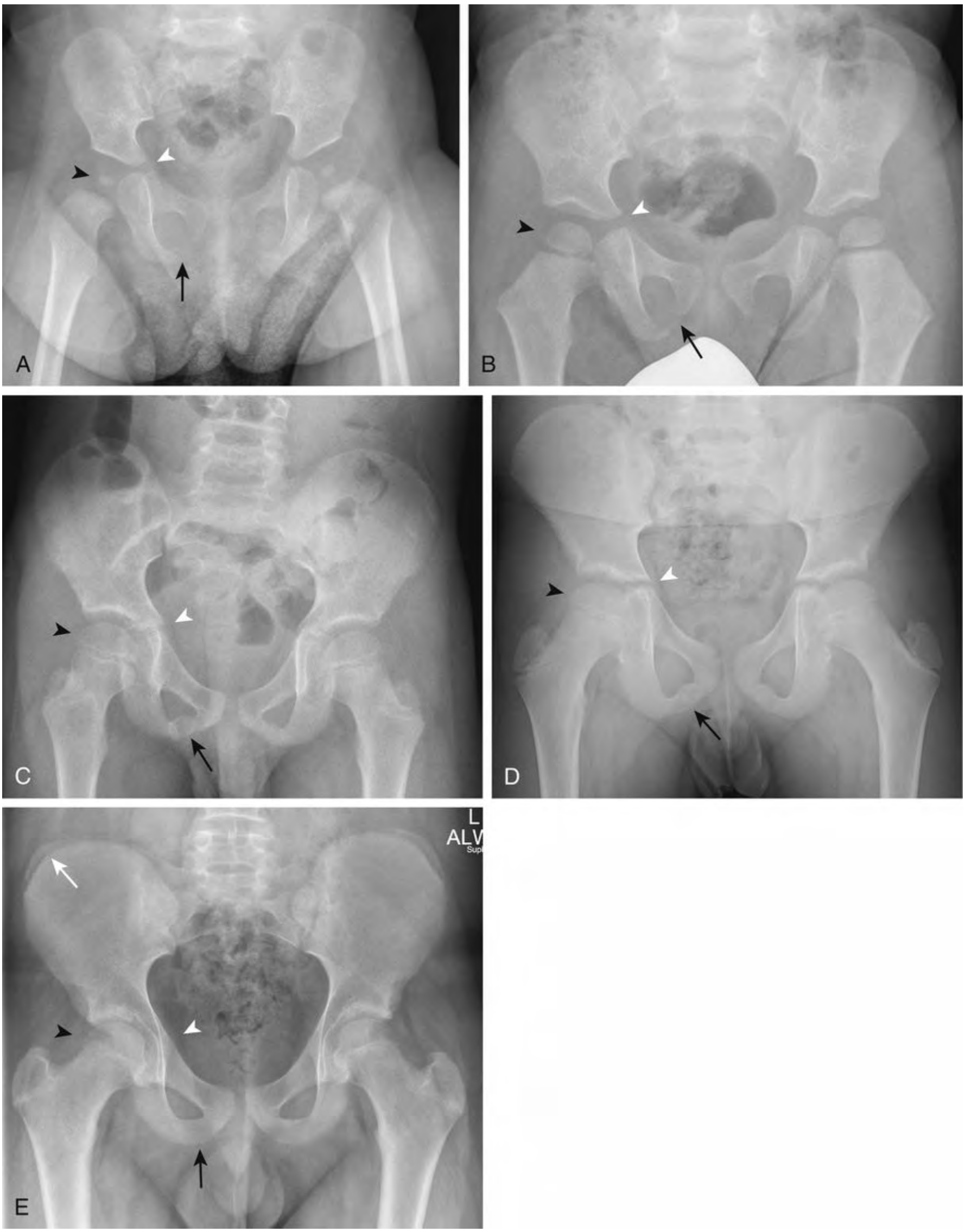
In the growing child, apophyses and epiphyses in various parts of the body can have variable and often somewhat irregular appearances. Separate ossicles of an apophysis can mimic fragments, irregularity can mimic periosteal reaction, and mixed sclerosis and lucency can be confused with findings of an inflammatory or neoplastic process. Common apophyses that may have this appearance include tibial tuberosity, ischeal tuberosity, ischeal pubic synchondrosis, posterior calcaneal apophysis (Fig. 7-2), and medial malleolus of the ankle (Fig. 7-3). Irregularity and fragmentation are commonly seen in the normal tibial tuberosity. The calcaneal apophysis can often demonstrate a strikingly sclerotic appearance (see Fig. 7-2, *C*). The ischeal pubic synchondrosis can appear very prominent (see Fig. 7-1, *D*) and asymmetric.

Epiphyses can also appear irregular and even fragmented. The most common epiphyses with this irregular appearance are the distal femoral epiphysis (Fig. 7-4) and the capitellum (Fig. 7-5). It is important to recognize these irregularities as a normal stage of development and not confuse them with osteochondral lesions (in the distal femoral epiphysis or the capitellum) or with fracture (medial malleolus).

Distal Femoral Metaphyseal Irregularity

Distal femoral metaphyseal irregularity, also referred to as cortical desmoid or cortical irregularity syndrome, refers to the presence of irregular cortical margination and associated lucency involving the posteromedial aspect of the distal femoral metaphysis. It occurs in as many as 11% of boys aged 10 to 15 years. Although debated, its presence is thought to be related to chronic avulsion at the insertion of the adductor magnus muscle. Although this lesion can be associated with pain, it is often discovered incidentally, and its significance lies in its alarming radiographic appearance. On radiography there is cortical irregularity present along the posteromedial cortex of the distal femoral metaphysis, best seen on the lateral view (Fig. 7-6). On frontal radiographs there may be an associated lucency (see Fig. 7-6, *B*). Familiarity with the typical location, appearance, and patient age is important so that these lesions are

not confused with aggressive malignancies. Because the lesions are often bilateral, confirmation of their benign nature can be made by demonstrating a similar lesion on radiographs of the opposite knee. In problematic cases, computed tomography (CT) or magnetic resonance imaging (MRI) can be used to demonstrate the characteristic findings: a characteristic scooplike defect with an irregular but intact cortex; no associated soft tissue mass; and a subtle contralateral lesion.



▪ **FIGURE 7-1 Changes in Radiographic Appearance of Bony Structures with Age.** Radiographs of the pelvis are shown in different patients. **A,** At 6 months of age; **B,** at 2 years of age; **C,** at 6 years of age; **D,** at 10 years of age; and **E,** at 15 years of age. Note the dramatic changes in the appearance of the pelvis as structures ossify over time. At 6 months of age (in **A**),

the femoral heads are just starting to ossify. The triradiate cartilage is open, and large portions of the ischium are not yet ossified. As children age, the femoral heads (*black arrowhead* on right femoral head) become more ossified, the ischium and pubis *(white arrow)* fuse, and the triradiate cartilage *(white arrowhead)* closes. As the ischiopubic synchondrosis (*black arrows* in **C** and **D**) closes, it can mimic a healing fracture to the untrained eye. The final portion of the pelvis to ossify is the iliac crest apophysis (in **E**, *white arrow*). This starts fusing only after the triradiate cartilage is closed.

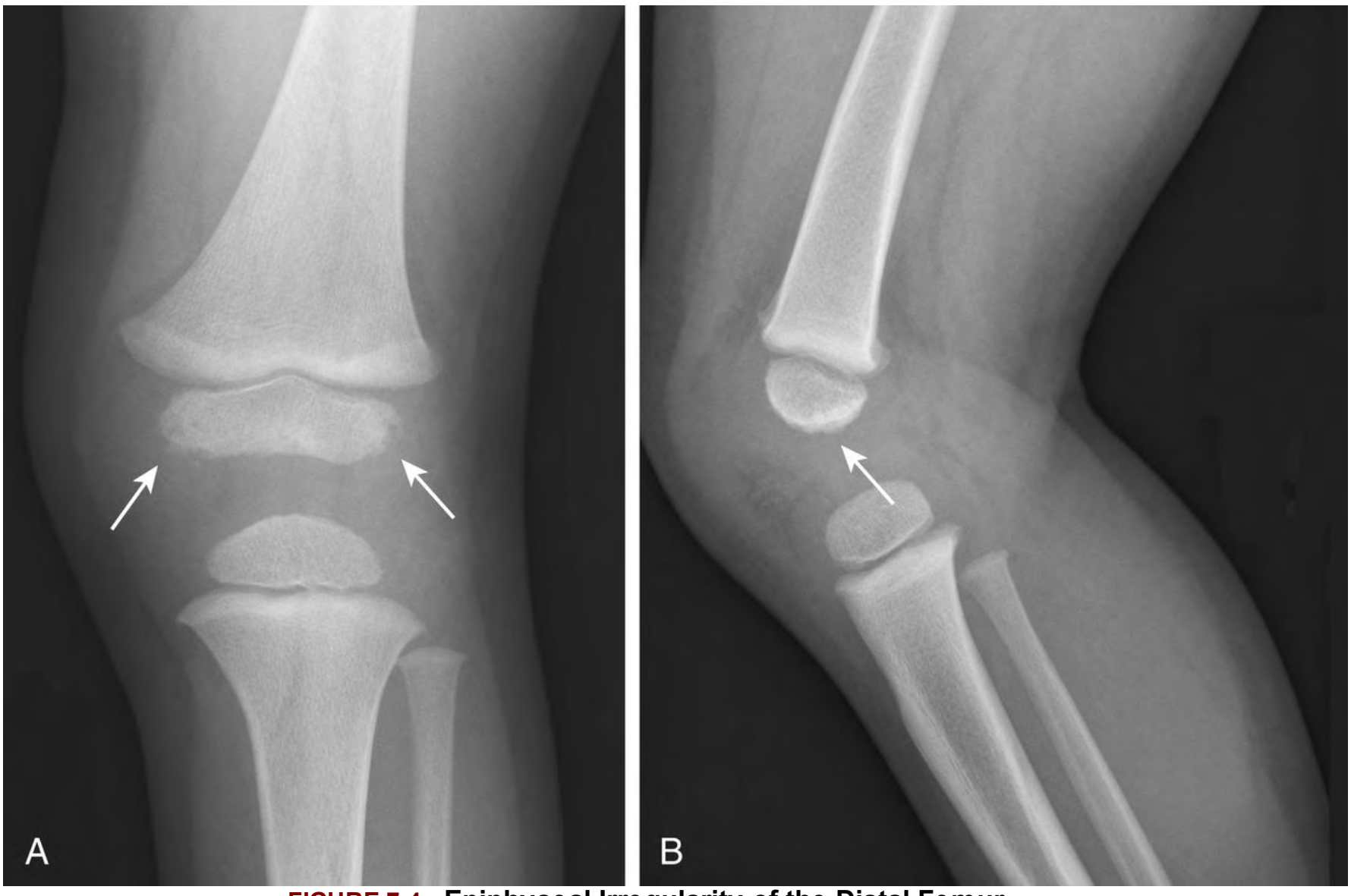


▪ **FIGURE 7-2 Examples of Apophyseal Irregularity in the Calcaneus in Four Separate Children Showing the Wide Variation in Normal.**

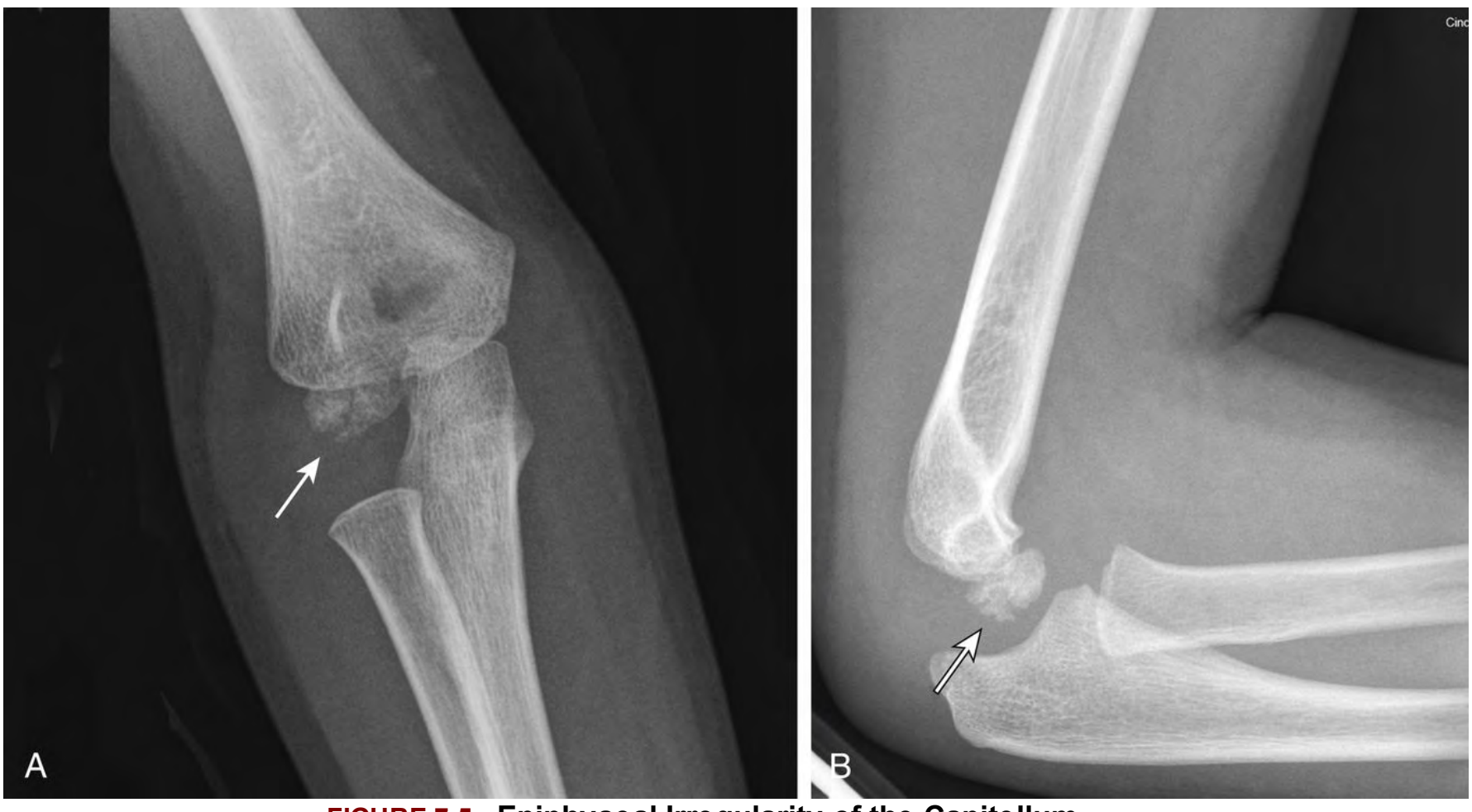
A, The calcaneal apophysis *(arrow)* is just beginning to ossify in this 6-year-old male. **B,** Both the metaphyseal and apophyseal edges of the calcaneus are irregular in this 9-year-old female. **C,** The calcaneal apophysis is mostly ossified in this 10-year-old male. In some children, as in this one, the normal calcaneal apophysis is sclerotic and mildly fragmented.



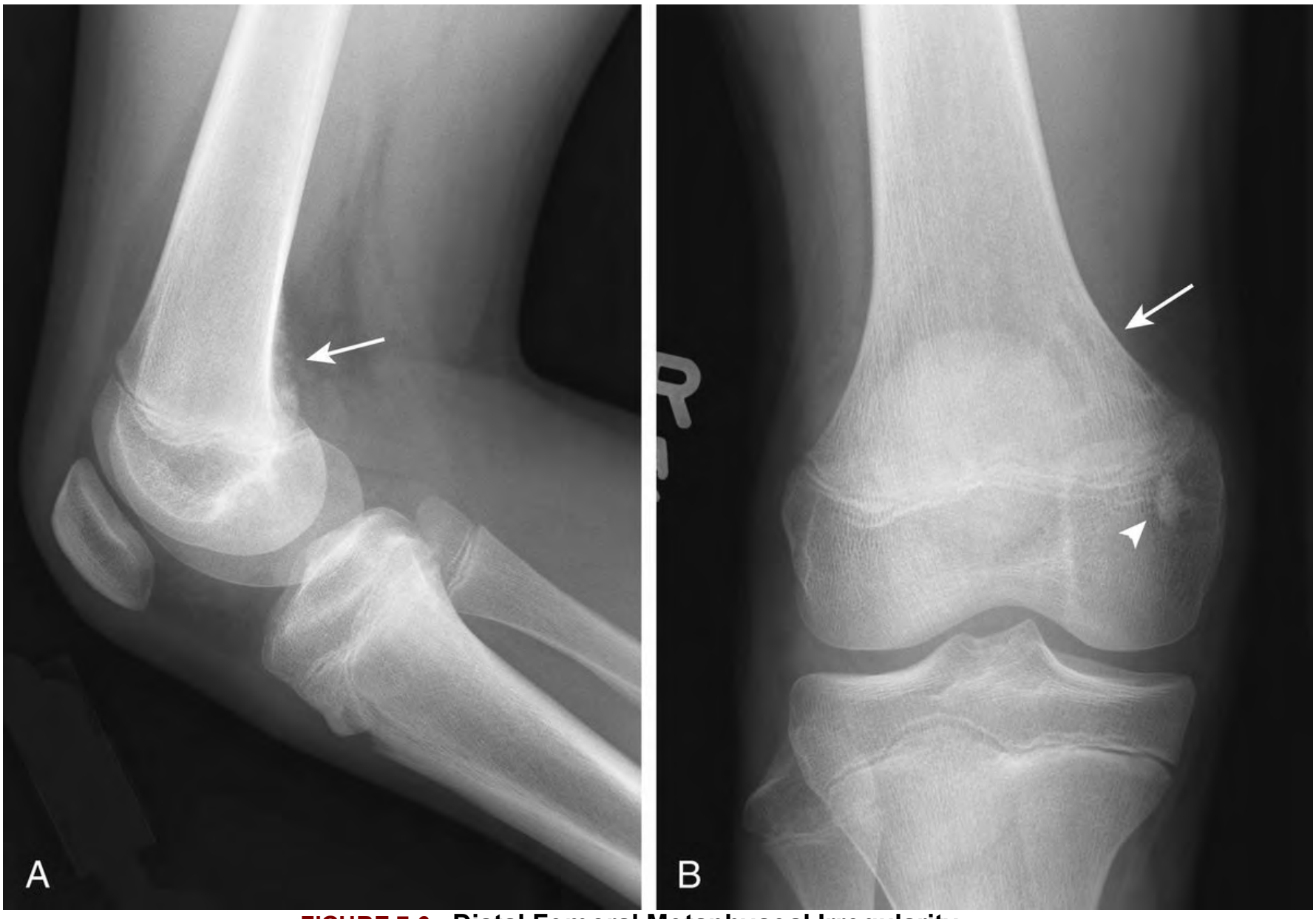
▪ **FIGURE 7-3** **Apophyseal Irregularity in the Medial Malleolus of the Distal Tibia.** Mortise view of the ankle in a 10-year-old male shows an irregular ossification center of the medial malleolus *(arrow)*. Fragmentation of the medial malleolus is almost always a part of normal development. The absence of soft tissue swelling helps to confirm that this is not related to trauma. Although there can be fragmentation of the medial malleolus, there should not be fragmentation of the distal fibula. When present, as in this case, it is related to trauma.



▪ **FIGURE 7-4** **Epiphyseal Irregularity of the Distal Femur.**
AP (**A**) and lateral (**B**) views of the knee in a 2-year-old female show developmental irregularity of the distal femoral epiphysis *(arrows)*. As children age, the irregularity may become more focal and can mimic an osteochondral lesion.



▪ **FIGURE 7-5** **Epiphyseal Irregularity of the Capitellum.**
AP (**A**) and lateral (**B**) views of the elbow in a 3-year-old male show developmental irregularity of the capitellum *(arrow)*. The lack of soft tissue swelling and a joint effusion help to confirm that no fracture is present. Follow-up radiographs (not shown) confirmed that the findings were developmental and not related to trauma.



▪ **FIGURE 7-6** **Distal Femoral Metaphyseal Irregularity.**
A, Lateral radiograph of the knee in a 14-year-old male shows irregularity *(arrow)* of the posterior aspect of the distal femoral metaphysis. Irregularity in this location is thought to represent chronic avulsion of the insertion of the adductor magnus muscle. **B,** On the AP view, the lesion appears as a well-marginated lucent lesion *(arrow)* along the medial aspect of the distal femoral metaphysis. In this patient a bone island is also present in the distal femoral epiphysis *(arrowhead)*.

Benign Fibrous Cortical Defects

Benign fibrous cortical defects, or nonossifying fibromas, are commonly encountered lesions of no clinical significance. They are seen in as many as 40% of children at some time during development and are most common between 5 and 6 years of age. The term *nonossifying fibroma* is typically reserved for lesions larger than 3 cm. They occur most commonly within the bones around the knee and in the distal tibia. They appear as eccentrically based, well-defined, bubbly, lucent lesions. These benign tumors have a narrow zone of transition with thin cortical rims (Figs. 7-7 through 7-9) and are typically round or oval in shape. When the characteristic pattern is identified, no further imaging or follow-up is necessary. Occasionally a pathologic fracture can occur through the lesion (see Fig. 7-9). Over time, benign fibrous cortical defects become more sclerotic and eventually resolve (see Fig. 7-7). When imaged during this healing process, they are sometimes referred to as ossifying nonossifying fibromas.



▪ **FIGURE 7-7** **Benign Fibrous Cortical Defect.**
AP radiograph of the ankle in a 14-year-old male shows an eccentrically based lucent lesion *(arrow)* with a narrow zone of transition and a sclerotic border. The eccentric location in bone and appearance are typical of a fibrous cortical defect. This lesion is slightly more sclerotic than the typical benign fibrous cortical defect representing early healing.


A
B



▪ **FIGURE 7-8** **Nonossifying Fibroma.**
AP (**A**) and lateral (**B**) radiograph in a 14-year-old male shows a large, expansile lucent lesion *(arrow)* of the distal tibia. This lesion is eccentrically based with a narrow zone of transition and a sclerotic border. The lesion *(arrow)* is hypointense on both the sagittal T1-weighted (**C**) and T2-weighted (**D**) images of the ankle. The abnormal signal (*arrowheads* in **C** and **D**) in the anterior aspect of the talus is due to a stress fracture.



▪ **FIGURE 7-9** **Pathologic Fracture Through a Nonossifying Fibroma.**
AP (**A**) and lateral (**B**) views of the ankle show a spiral fracture *(arrows)* centered in an eccentrically based lucent lesion of the distal tibia. This fracture extends to the physis, making it a Salter-Harris type II fracture.

▪ Trauma

Fractures in children differ from those in adults for multiple reasons. Children's bones have higher water content and are thus more pliable with a greater propensity to deform before breaking. This is akin to a new branch on a tree. Green sticks, with their higher water content, bend and deform before breaking.

The term *incomplete fracture* refers to a fracture that does not extend through the entire diameter of the cortex. Because children's bones are more elastic, incomplete fractures occur more commonly in children than adults. There are a number of types of incomplete fractures. *Plastic bowing deformity* (Figs. 7-10 and 7-11) is diagnosed when there is a greater than expected curvature of the bone after trauma

without a discrete fracture line. This type of fracture occurs almost exclusively in the radius, ulna, or fibula. At times this injury can be difficult to diagnose, and it is not until the follow-up image, when periosteal new bone is present, that the fracture can confidently be diagnosed. A *buckle fracture* is a concave buckling of the cortical surface of a long bone. Buckle fractures may be subtle and may appear only as an increase in acute angulation of a normally gentler curve (Figs. 7-12 and 7-13). Buckle fractures are most common in the distal radius and ulna, the metacarpals and metatarsals, the phalanges, and the tibia. Finally, a *greenstick fracture* is an incomplete fracture along the cortex of the convex margin of the bowing (Figs. 7-11 and 7-14). Greenstick fractures are most common in the forearm. Which name you give an incomplete fracture is not important. What is important is recognizing that a fracture is present when it has one of these incomplete appearances.



▪ **FIGURE 7-10** **Plastic Bowing Deformity.**
AP radiograph of the ankle in an 11-year-old male shows a transverse fracture *(arrow)* of the distal tibial diaphysis and a plastic bowing deformity *(arrowhead)* of the distal fibula.



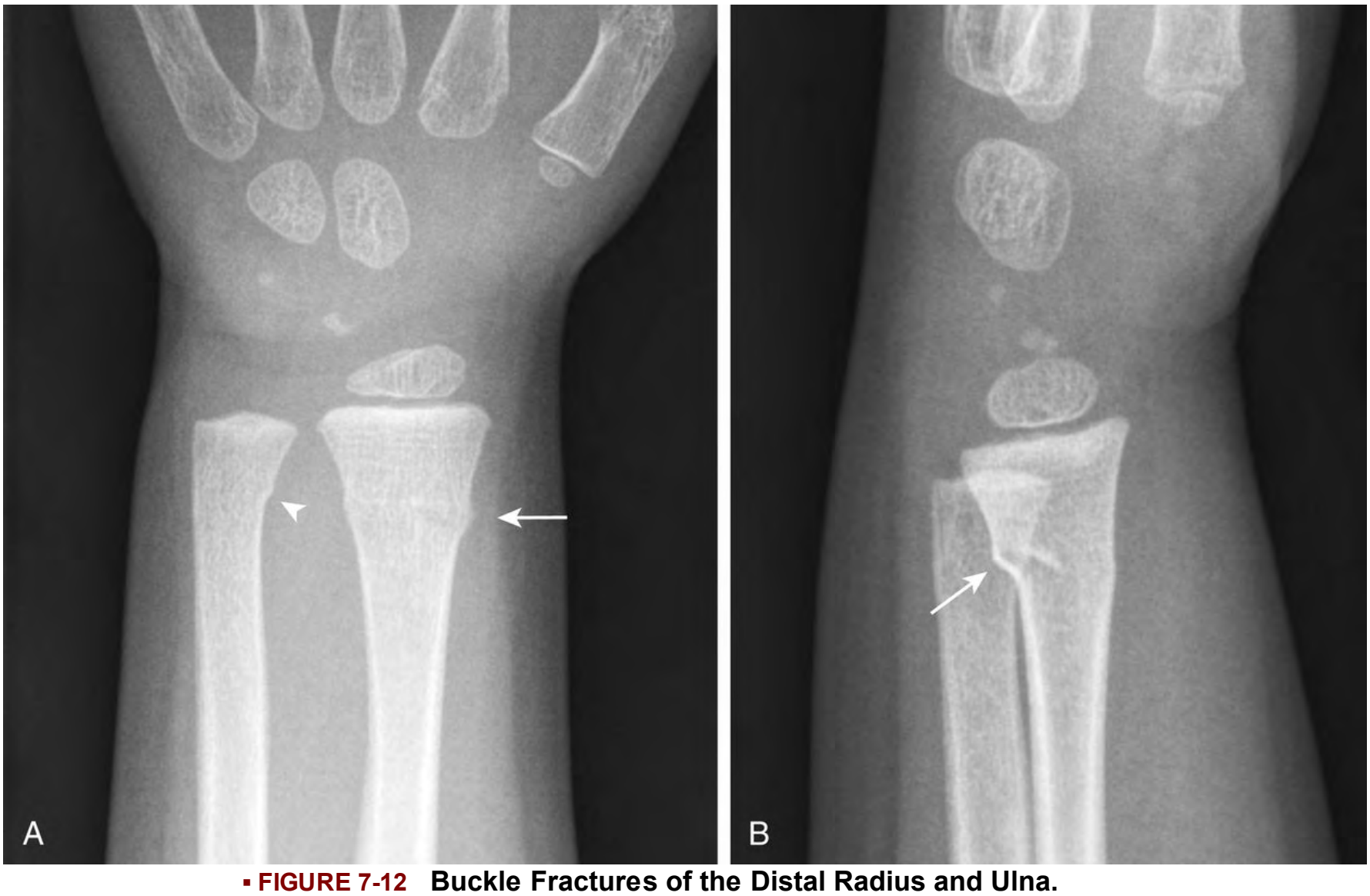
▪ **FIGURE 7-11** **Incomplete Fractures of the Radius and Ulna.**
AP (**A**) and lateral (**B**) radiographs of the forearm in a 4-year-old female show a greenstick fracture of the radius *(arrow)* and plastic bowing deformity of the ulna *(arrowhead)*. The lateral view better shows the bowing and greenstick fractures. In greenstick fractures the fracture line is along the convex margin of the cortex.

The potential for healing and the healing rate of fractures also differ in children and adults. Younger children heal very quickly. Periosteal reaction can be expected to be radiographically present 10 to 14 days after injuries in children. Children also tend to heal completely. Nonunited fractures are very uncommon in children. Fracture remodeling is also rapid and impressively complete in fractures of pediatric long bones. Normal alignment is typically restored.

Involvement of the Physis

One of the potential problematic issues with fractures in children is involvement of the physis. The physis is involved in as many as 18% of pediatric long bone fractures. Physeal involvement may result in growth arrest of that limb and in a higher rate of necessary internal fixation. The standard classification for physeal fractures is that by Salter and Harris. It divides fractures into five types according to whether there is involvement of the physis, epiphysis, or metaphysis, as determined by radiography (Fig. 7-15). Fractures with higher numbers by the *Salter-Harris classification* system have a

greater incidence of complications. Type 1 fractures involve only the physis (Fig. 7-16). They tend to occur in children younger than 5 years of age. On radiography the epiphysis may appear to be displaced in comparison with the metaphysis. However, type 1 fractures often reduce before the radiographs being obtained, making diagnosis extremely difficult. The potential findings of a type 1 fracture include soft tissue swelling adjacent to the physis, asymmetric widening of the physis, and/or displacement of the epiphysis. Salter-Harris type 1 injuries are uncommon and may only occur at the distal fibula and the proximal femur (as in a slipped capital femoral epiphysis [SCFE]). Type 2 fractures involve the metaphysis and physis but do not involve the epiphysis (Figs. 7-9 and 7-17). They are the most common type of physeal injury, accounting for up to 75% of Salter-Harris fractures. On radiography there is typically a triangular fragment of the metaphysis attached to the physis and epiphysis. Type 3 fractures involve the physis and epiphysis but not the metaphysis(Figs. 7-18 and 7-19). Type 3 injuries have a greater predisposition for growth arrest. Type 4 injuries involve the epiphysis, physis, and metaphysis and, like type 3 injuries, are associated with a high rate of growth arrest (Figs. 7-20 and 7-21). Type 5 fractures consist of a crush injury to part of or all of the physis. Like type 1 injuries, type 5 injuries are extremely difficult to diagnose. Often a diagnosis can be made only with a suspicious clinical history and comparison to the contralateral physis. With all Salter-Harris type fractures, it is important to assess the physis on follow-up images. Posttraumatic growth arrest is detected radiographically by demonstration of a bony bridge across the physis (Fig. 7-22).



▪ **FIGURE 7-12 Buckle Fractures of the Distal Radius and Ulna.**
AP (**A**) and lateral (**B**) radiographs of the wrist show buckle fractures of the distal radius *(arrow)* and ulna *(arrowhead)*. Buckle fractures can be very subtle on the AP view.



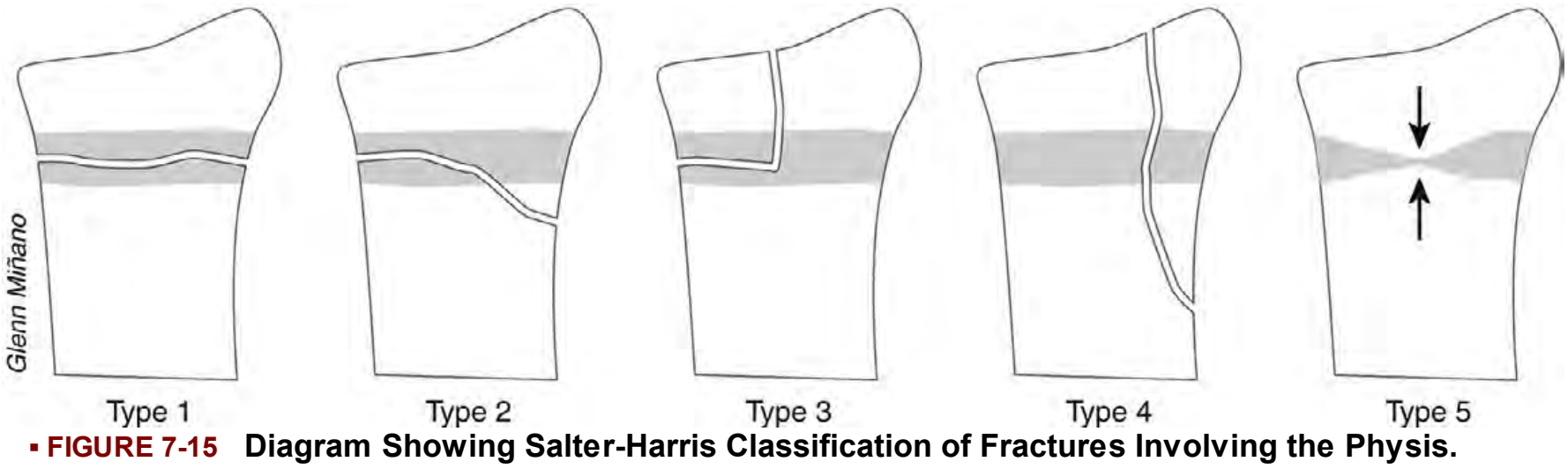
▪ **FIGURE 7-13** **Buckle Fractures of the Proximal Phalanx of the Ring and Small Fingers.** AP (**A**) and lateral (**B**) radiographs of the ring finger in a 4-year-old male show a subtle contour irregularity of the proximal aspect of the proximal phalanx of the ring finger *(arrow)*. On the AP view a small portion of the small finger is included and shows a similar buckle fracture *(arrowhead)*.



▪ **FIGURE 7-14** **Greenstick Fractures.**
AP (**A**) and lateral (**B**) radiographs of the forearm in an 11-year-old male show incomplete fractures of the proximal third of the radius *(arrow)* and ulna *(arrowhead)*.

Commonly Encountered Fractures by Anatomic Location

Pediatric fractures have unique features in almost all locations. The following material reviews several of the more commonly encountered areas.



▪ **FIGURE 7-15** **Diagram Showing Salter-Harris Classification of Fractures Involving the Physis.**



▪ **FIGURE 7-16** **Salter-Harris Type I Fracture.**

AP (**A**) and oblique (**B**) radiographs of the ankle in a 13-year-old female show widening of the distal fibular physis *(arrow)* compared with the distal tibial physis. There was associated lateral soft tissue swelling. AP (**C**) and oblique (**D**) images in the same patient 2 weeks later show mild healing with faint periosteal new bone formation *(arrow)* adjacent to the distal fibular metaphysis.



▪ **FIGURE 7-17 Salter-Harris Type II Fracture.**
AP radiograph of the small finger in a 9-year-old male shows a fracture of the proximal metaphysis of the proximal phalanx of the small finger. The fracture extends to the physis along its radial side *(arrow)*.



▪ **FIGURE 7-18** **Salter-Harris Type III Fracture.**
AP radiograph of the ankle in a 9-year-old male shows a fracture of the epiphysis of the distal tibia *(arrow)*. The ankle joint is disrupted by this fracture.



▪ **FIGURE 7-19** **Salter-Harris Type III Fracture.**
AP radiograph of the wrist in a 17-year-old male shows a fracture *(arrow)* of the distal epiphysis of the radius.



▪ **FIGURE 7-20** **Salter-Harris Type IV Fracture.**
AP radiograph of the ankle in a 14-year-old male shows a fracture *(arrow)* of the distal tibial metaphysis and epiphysis.



▪ **FIGURE 7-21** **Salter-Harris Type IV Fracture.**
Oblique radiograph of the hand in a 13-year-old female shows a fracture of the proximal epiphysis of the proximal phalanx of the middle finger. There are small fragments of bone *(arrow)* arising from the proximal metaphysis making this a Salter-Harris type IV fracture.

Wrist

The wrist is the most common fracture site in children. Most fractures of the distal forearm are buckle or transverse fractures of the distal metaphysis of the radius, with or without fracture of the distal ulnar metaphysis or styloid (Figs. 7-13 and 7-23). It is important to assess all fractures of the distal radius for extension of the fracture line to the physis because the distal radius is also the most common area of physeal fracture (28% of physeal injuries occur in the distal radius). Displacement or obliteration of the pronator fat pad indicates a fracture or deep soft tissue injury. The normal pronator fat pad is visualized on a lateral view of the forearm as a thin line of fat with a mildly convex border. In most distal forearm fractures the convexity of the pronator fat pad is increased or the fat pad becomes obliterated by soft tissue attenuation.

Elbow

There are several unusual features that make elbow injuries in children different from those in adults. In contrast to adults, in whom fracture of the radial head is the most common injury, children most commonly experience supracondylar fractures (Figs. 7-24 and 7-25). They occur secondary to hyperextension that occurs when falling on an outstretched arm. As many as 25% of such fractures are

incomplete and may be subtle on radiography. On radiographs there can be posterior displacement of the distal fragment such that a line drawn down the anterior cortex of the humerus (anterior humeral line) no longer bisects the middle third of the capitellum (see Fig. 7-24). The fracture line is usually best seen through the anterior cortex of the distal humerus on the lateral view. A joint effusion is typically evident. Elbow effusions are identified when there is displacement of the posterior fat pad, resulting in its visualization on a lateral view (Figs. 7-24 through 7-26). Normally the posterior fat pad rests within the olecranon fossa and is not visible on a true lateral view of the elbow. The anterior fat pad, which is often visible normally, may become prominent and have a prominent apex anterior convexity.

There is much debate about the significance of a traumatic elbow effusion in the absence of a visualized fracture (see Fig. 7-26). It is often taught that such a joint effusion is synonymous with an occult fracture. However, studies have shown that fractures are probably present in 50% or fewer cases. The point is moot because traumatic injury to the elbow is treated by splinting, whether a subtle fracture is identified or not. If pain persists, a repeat radiograph if often obtained at the follow-up orthopedic appointment and can be used to assess for signs of healing.

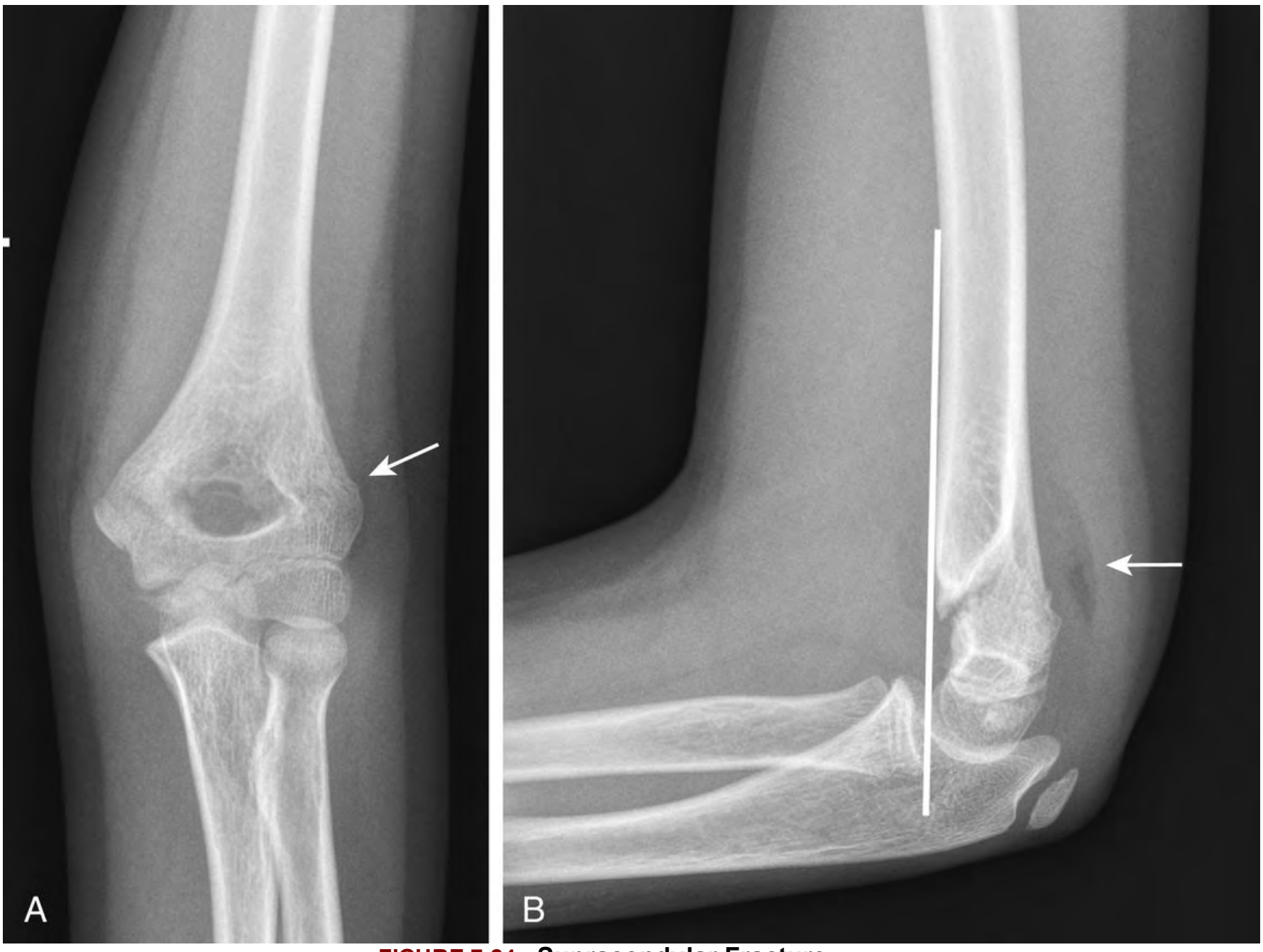


▪ **FIGURE 7-22** **Premature Physeal Fusion Secondary to a Salter-Harris Type II Fracture.** **A,** AP radiograph of the left ankle at time of injury in an 11-year-old female shows widening *(arrow)* of the medial aspect of the distal tibial physis. There are small ossific fragments adjacent to the distal metaphysis, making this a Salter-Harris type II fracture. **B,** AP radiographs of both ankles 1 year later show premature fusion of the left distal tibial physis *(arrow)*. **C,** The premature fusion *(arrow)* is confirmed on CT. The oblique lucency along the lateral aspect of the

distal tibial metaphysis is related to hardware used to fix the fracture internally.



▪ **FIGURE 7-23** **Salter-Harris Type II Fracture of the Distal Radius and Ulnar Styloid Fracture.** AP (**A**) and lateral (**B**) radiographs of the wrist in an 8-year-old female show fractures of the distal radius and ulna. The fracture of the ulna is mildly complex. There is a faint vertical component of the fracture *(arrowhead)* extending to the physis (seen on **A**), making this a Salter-Harris type II fracture. In addition to the fracture of the radius, an ulnar styloid fracture *(arrow)* is also present.



▪ **FIGURE 7-24** **Supracondylar Fracture.**

AP (**A**) and lateral (**B**) radiographs of the elbow in a 9-year-old male show a supracondylar fracture. The fracture line is often difficult to see on the AP view. In this case there is contour deformity on the lateral aspect of the humeral metaphysis *(arrow)*. The fracture line extends through the metaphysis at this plane. On the lateral view the line drawn along the anterior cortex of the humerus does not intersect the capitellum. The fracture line is more visible on this view. Note the large joint effusion *(arrow)*.



▪ **FIGURE 7-25** **Supracondylar Fracture.**
Lateral radiographs of the elbow in a 3-year-old female show a supracondylar fracture and large joint effusion. The fracture line *(arrow)* is seen along the anterior surface of the distal humerus.



▪ **FIGURE 7-26** **Elbow Effusion.**
Lateral radiograph of the elbow in a 4-year-old male shows a moderate joint effusion, as demonstrated by the elevation of the posterior fat pad *(arrow)*. The anterior fat pad is also displaced. No fracture was present on this image or on subsequent follow-up (not shown).

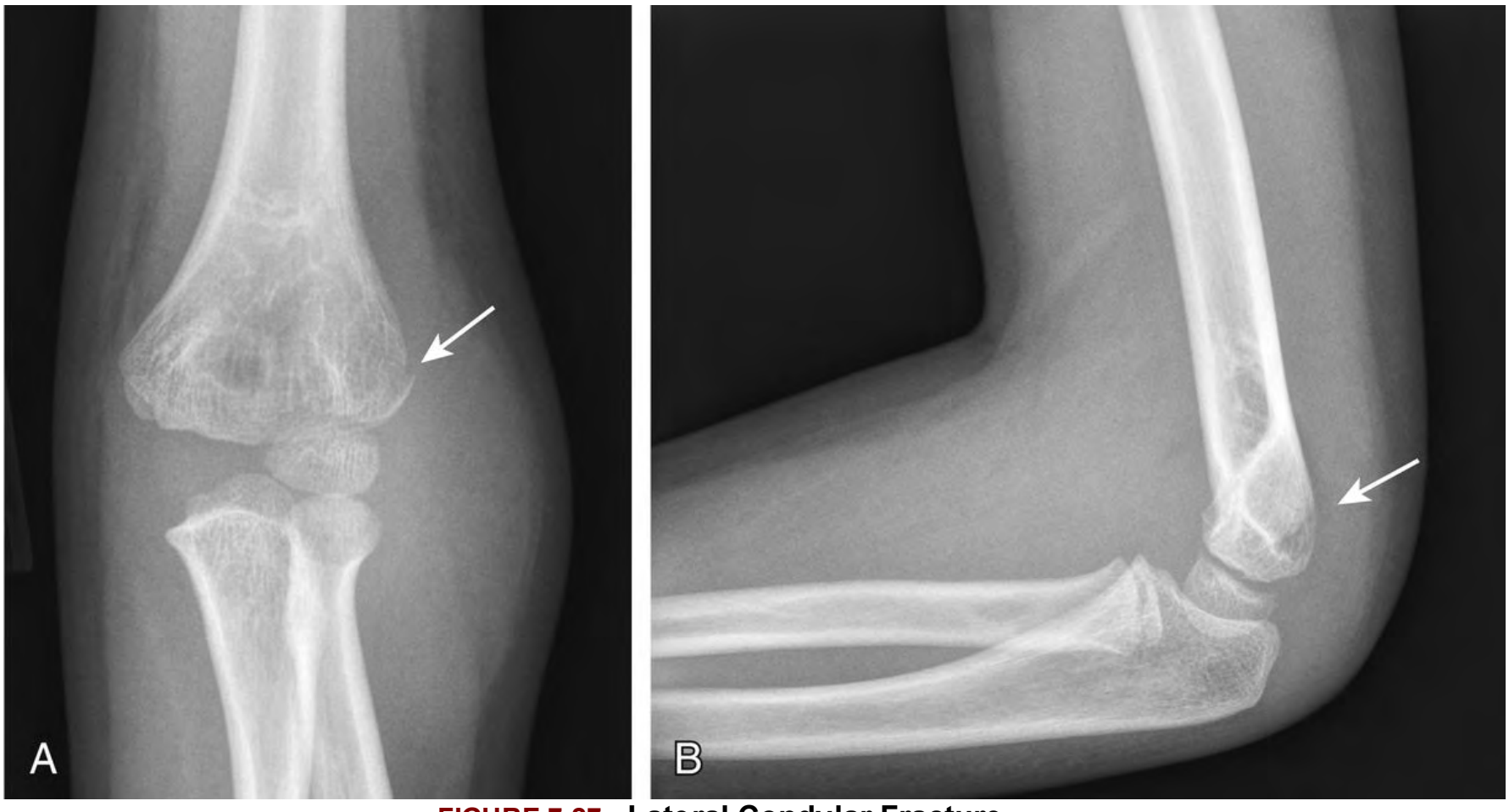
Other elbow injuries include fractures of the radial neck and lateral condyle (Fig. 7-27) and avulsion of the medial epicondyle (Little League elbow; Figs. 7-28 and 7-29). With avulsion of the medial epicondyle (10% of elbow injuries), the medial epicondyle may become displaced and even entrapped within the elbow joint (see Fig. 7-29). It is important to know the predictable order of maturity of the elbow ossification centers so that a displaced medial epicondyle is not missed. The order can be remembered by the mnemonic CRITOE (capitellum, radial head, internal [medial] epicondyle, trochlea, olecranon, external [lateral] epicondyle).

Whenever there is a fracture of the forearm, it is important to evaluate the radial-capitellar joint for potential dislocation of the radial head. The radial head should align with the capitellum on both the anteroposterior (AP) and lateral views. If it does not, radial head dislocation should be suspected (Fig. 7-30). When a radiocapitellar dislocation is present, it is important to image the entire forearm to look for a fracture-dislocation injury. A Monteggia fracture is a dislocation of the head of the radius with an associated fracture of the ulnar diaphysis (see Fig. 7-30).

Ankle

The ankle in a commonly injured joint due to combination of inversion and eversion injuries with weight bearing. There are two common fractures that are unique in adolescents, triplane fractures and juvenile Tillaux fractures. Like the name implies, a triplane fracture is a fracture in three planes: the coronal plane through the tibial metaphysis, transverse plane through the physis, and sagittal plane through the epiphysis (Fig. 7-31). Because the fracture extends through the metaphysis and epiphysis, this is a Salter-Harris type IV fracture. Triplane fractures occur in adolescents in whom the growth plate is beginning to close. It is important to evaluate the fracture carefully because internal fixation is

performed if there is more than 2-mm displacement of the fracture fragment. Often a CT is performed to evaluate the fracture and the degree of displacement more accurately. Fibular fractures are present approximately half of the time.



▪ **FIGURE 7-27** **Lateral Condylar Fracture.**

AP (**A**) and lateral (**B**) radiographs of the elbow in a 6-year-old male show a lateral condylar fracture. The fracture is better seen on the AP view, where there is a thin sliver of bone adjacent to the fracture line *(arrow)* in the distal lateral humeral metaphysis. There is also considerable lateral soft tissue swelling. The fracture is harder to see on the lateral view. However, a small posterior elbow effusion is present.



▪ **FIGURE 7-28** **Medial Epicondyle Avulsion.**
AP radiograph of the elbow in a 14-year-old female shows avulsion of the medial epicondyle *(arrow)*. The remainder of the physes of the elbow are fused. There is marked medial soft tissue swelling.



▪ **FIGURE 7-29** **Elbow Dislocation with Avulsion and Entrapment of the Medial Epicondyle.** AP (**A**) and lateral (**B**) radiographs of the elbow in a 10-year-old female show a lateral dislocation of the elbow. There is a circular ossific density *(arrow)* overlying the distal humerus on the AP view that represents the avulsed medial epicondyle. On the lateral view the avulsed fragment *(arrow)* is shown to be entrapped in the elbow joint. Note that the capitellum, radial head, trochlea, and olecranon are already ossified.



▪ **FIGURE 7-30** **Monteggia Fracture.**

AP (**A**) and lateral (**B**) radiographs of the forearm show a fracture of the midulna diaphysis *(arrow)* and dislocation of the proximal radius. On both views the line drawn through the center of the radius (parallel to its long axis) does not intersect the capitellum.



▪ **FIGURE 7-31** **Triplane Fracture.**

Oblique (**A**) and lateral (**B**) radiographs of the ankle in a 14-year-old female show fractures of the tibia *(arrow)* and fibula *(arrowhead)*. The tibia fracture extends from the tibial metaphysis, through the physis, and into the epiphysis. The lateral epiphysis is displaced laterally. The metaphyseal component of the fracture is better seen on the lateral view. Coronal (**C**) and sagittal (**D**) images from a CT of the ankle in the same patient show the fractures more obviously. The tibia fracture *(arrow)* is a Salter-Harris type IV fracture extending in three different planes.



▪ **FIGURE 7-32 Juvenile Tillaux Fracture.**
AP (**A**) and oblique (**B**) radiographs of the ankle in a 12-year-old female show a fracture *(arrow)* of the lateral aspect of the distal epiphysis of the tibia. The fracture fragment is displaced laterally by 2 mm. **C,** Coronal CT of the ankle shows the Salter-Harris type III fracture *(arrow)* of the distal tibia.

Juvenile Tillaux fractures are Salter-Harris type III fractures of the distal tibia. Like triplane fractures, they occur in adolescents in whom the growth plate is beginning to close. The fracture occurs because the medial tibial physis closes before the lateral physis. The differences in structural stability lead to this fracture pattern when there is abduction and external rotation of the ankle. On x-ray there is a fracture line through the distal tibial epiphysis and widening of the medial aspect of the ankle mortise (Fig. 7-32). CT is performed to evaluate the amount of fracture displacement. Orthopedic surgeons will perform internal fixation if the fracture is displaced by more than 2 mm.

Toddler Fracture

There are a number of fractures referred to as toddler fractures. The most common of these is a nondisplaced oblique or spiral fracture of the midshaft of the tibia (Fig. 7-33). Such an injury is relatively common and occurs when a child first begins to walk. Most children present with failure to continue to walk or refusal to bear weight on that extremity. Oblique views often demonstrate the fracture better than do frontal or lateral views. When diagnosing this fracture, it is important to look at the patient's age because a spiral fracture in a child who is not yet walking can be a fracture of abuse. Other types of toddler fractures include stress-type fractures involving the calcaneus or cuboid (Figs. 7-34 and 7-35).


A
B
C

▪ FIGURE 7-33 **Spiral Fracture of the Tibia.**
AP (**A**), oblique (**B**), and lateral (**C**) radiographs of the ankle in a 1.5-year-old male show a spiral fracture of the distal tibia *(arrows)*. The fracture plane is continuous throughout its course, even though it appears as two fracture lines on the AP and lateral views.

Avulsion Fractures in Adolescents

An avulsion injury is a structural failure of bone at a tendon or aponeurotic insertion and is related to a tensile force being applied by a musculoskeletal unit. Adolescents are prone to avulsive injuries because of a combination of their propensity to have great strength, their ability to sustain extreme levels of activity, and their immature, growing apophyses. The growing apophysis is often more prone to injury than the adjacent tendons. The sites of insertion of muscles capable of generating great forces are most predisposed to avulsion injuries.



▪ FIGURE 7-34 **Stress Fractures of the Calcaneus and Cuboid.**
A, Lateral radiograph of the foot at time of injury shows an oblique fracture of the distal tibia. **B,** Repeat radiograph of the foot performed 1 month later shows new linear areas of sclerosis in the posterior calcaneus *(arrowhead)* and posterior cuboid *(arrow)*. The tibial fracture is not well seen, related to healing.



▪ **FIGURE 7-35** **Stress Fractures of the Calcaneus.**
Oblique (**A**) and lateral (**B**) radiographs of the foot in a 2.5-year-old male show a linear area of sclerosis in the cuboid *(arrow)* consistent with a stress fracture.

Radiologists may encounter findings of chronic avulsion when patients are imaged for pain or incidentally when imaging is performed for other reasons. The irregularity and periostitis that can be associated with chronic avulsions should not be misinterpreted as suspicious for malignancy. In addition, if unwarranted biopsies of these areas are performed, the histologic changes associated with the healing callus of the avulsion injury may be misinterpreted as malignancy. The most common sites of avulsion occur within the pelvis, where muscles capable of great force attach. Common sites of pelvic apophyseal avulsions and their associated muscular attachments include the iliac crest (transversalis, internal oblique abdominalis, external oblique abdominalis; Fig. 7-36); anterior superior iliac spine (Sartorius; Fig. 7-37); anterior inferior iliac spine (rectus femoris; Fig. 7-38); ischial apophysis (hamstring muscles: biceps femoris, gracilis, semimembranosus, semitendinosus; Fig. 7-39); and lesser trochanter (iliopsoas). The radiographic findings of avulsion injuries include displacement of the ossified apophysis from normal position and variable, often exuberant amounts of associated periosteal new bone formation.

When involving a joint, avulsive injuries can occur at the cortical insertion site of a ligament or tendon. The knee is the joint most commonly associated with avulsive injuries. Many of these injuries occur exclusively in children and adolescents. Common sites of knee avulsion fractures and their associated tendinous or ligamentous attachments include the anterior medial tibial spine (anterior cruciate ligament; Fig. 7-40); lateral tibial rim, also known as a Segond fracture (lateral collateral ligament; Fig. 7-41); fibular head (conjoined tendon with biceps femoris; Fig. 7-42); tip of the fibular head (arcuate ligament); inferior pole of the patella, also known as the patellar sleeve (proximal patellar tendon; Figs. 7-43 and 7-44); and tibial tubercle (distal patellar tendon Fig. 7-45). Many of these injuries present with sudden pain and a joint effusion. MRI is often indicated because these injuries are associated with other internal derangement.

Chronic avulsion injuries are also common in the adolescent knee. Avulsion of the patellar tendon at its attachment to the patella is called Sinding-Larsen-Johansson syndrome. It occurs most commonly in

children between the ages of 10 and 14 years. Symptoms include localized pain and swelling over the inferior aspect of the patella associated with restricted knee motion. Radiography demonstrates irregular bony fragments at the inferior margin of the patella, associated with adjacent soft tissue swelling and thickening and indistinctness of the patellar tendon (Fig. 7-46). Chronic avulsive injury of the patellar tendon at its inferior attachment is referred to as Osgood-Schlatter disease (tibial tuberosity avulsion). It is a common disorder that most often affects active adolescent boys. Symptoms include pain and swelling over the tibial tuberosity. Radiography demonstrates bony fragmentation of the tibial tuberosity, associated adjacent soft tissue swelling, and thickening and indistinctness of the patellar tendon (Fig. 7-47).

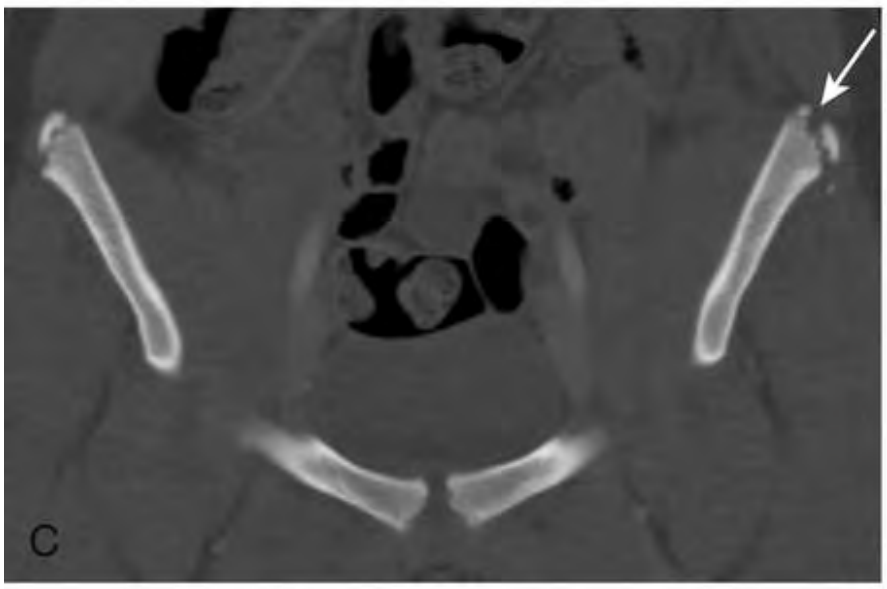
Child Abuse

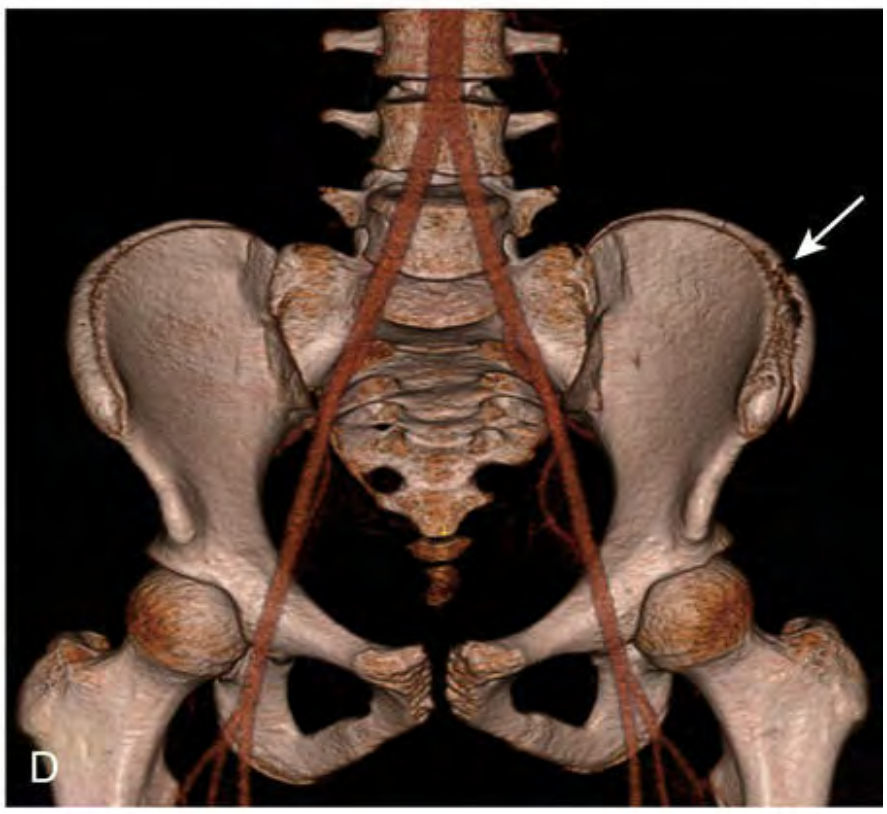
Child abuse, also referred to as the more politically correct and less graphic *nonaccidental trauma*, is unfortunately common. According to data from the U.S. Department of Health and Human Services, it is estimated that approximately 750,000 children are abused and 1600 killed each year in the United States (http://www.acf.hhs.gov/programs/cb/resource/cwo-08-11). Most abused children are less than 1 year of age and almost all are less than 6 years of age. When clinical or imaging findings are suspicious for potential abuse, a radiographic skeletal survey is typically obtained. The purpose of the skeletal survey is to document the presence of findings of abuse. In young children a head CT is often performed to identify intracranial signs of abuse. Other tests sometimes used include a repeat skeletal survey after approximately 2 weeks to look for healing injuries not seen on the initial skeletal survey, skeletal scintigraphy, abdominal CT, and MRI of the brain. The identification and reporting of findings of child abuse by the radiologist is an important task. False-positive cases can cause a nonabused child to be removed from his or her family, whereas false-negative cases can result in a child's returning to a potentially life-threatening environment.

The radiographic findings of abuse vary in their specificity. One of the highly specific findings is the presence of posterior rib fractures occurring near the costovertebral joints (Fig. 7-48). These are thought to occur when an adult squeezes an infant's thorax. Such rib fractures may be subtle before development of callus formation. The evaluation for rib fractures should be a routine part of the evaluation of the chest radiograph of any infant. Another finding that is highly specific for abuse is the metaphyseal corner fracture (Fig. 7-49). This fracture extends through the primary spongiosa of the metaphysis, the weakest portion, and usually occurs secondary to forceful pulling of an extremity. The broken metaphyseal rim appears as a corner fracture (a triangular piece of bone) when seen tangentially or as a crescentic rim of bone (referred to as a bucket-handle fracture) when seen obliquely. Other fractures associated with abuse include those of the scapula, spinous process, and sternum. Spiral long bone fractures in nonambulatory children are also highly suspicious. Multiple fractures in children of various ages (some with callus and some acute), as well as multiple fractures of various body parts, are highly suspicious for abuse (see Fig. 7-48). In fact, any fracture in an infant should be viewed with suspicion because as many as 30% of fractures in infants are secondary to abuse. Extraskeletal findings seen in abuse include acute or chronic subdural hematoma, cerebral edema (asphyxia), intraparenchymal brain hematoma (Fig. 7-50), lung contusion, duodenal hematoma, solid abdominal organ laceration, and pancreatitis.





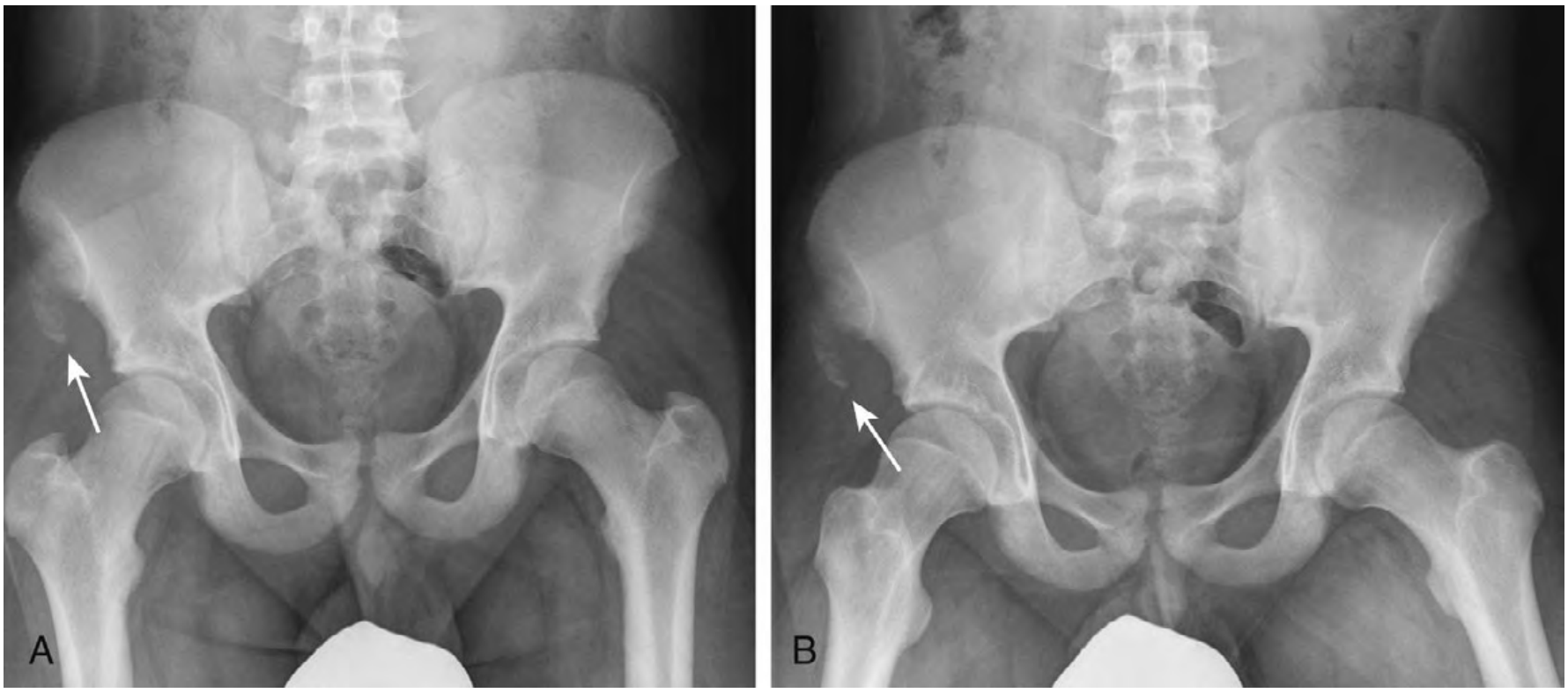




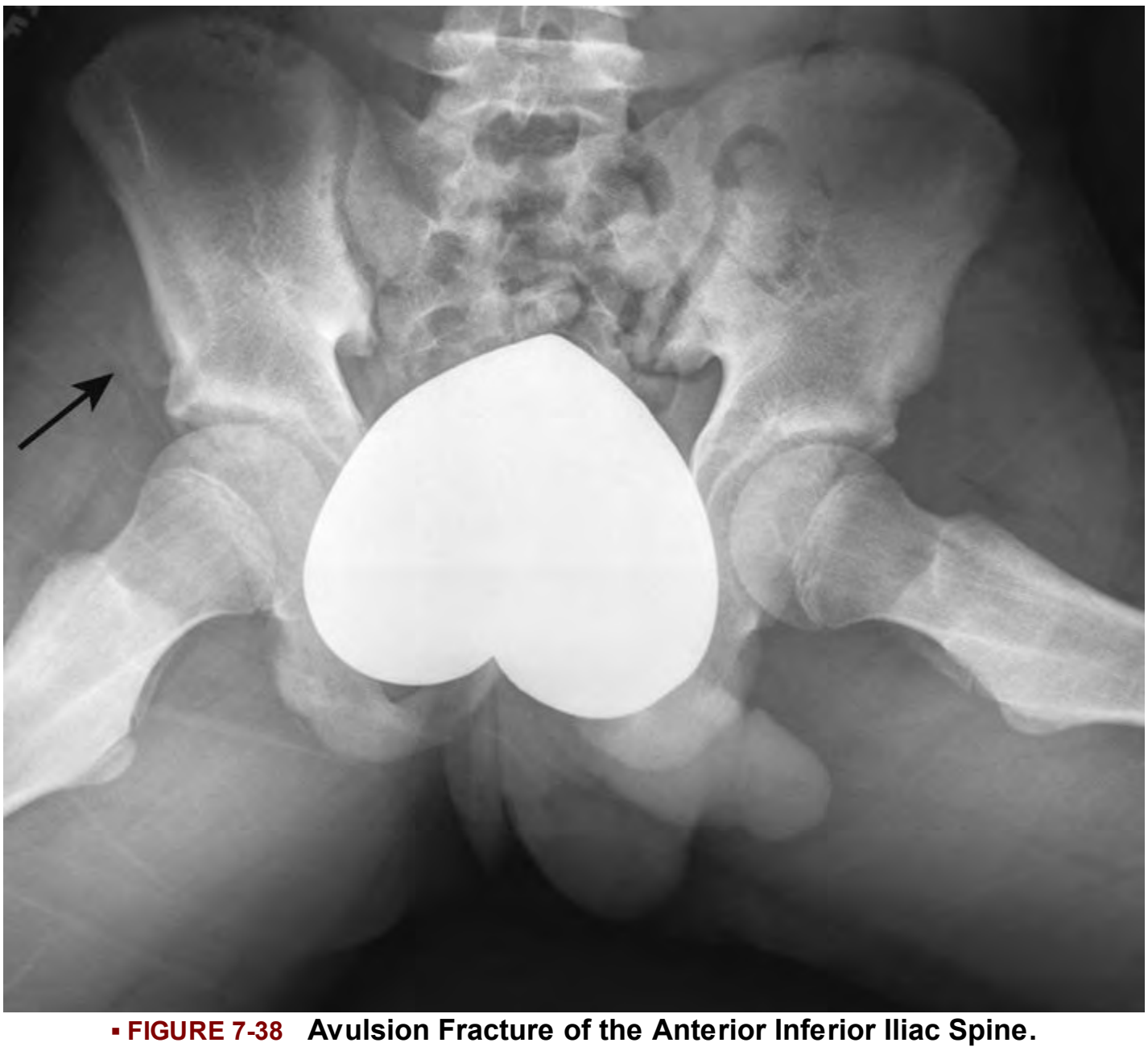


▪ **FIGURE 7-36** **Avulsion Fracture of the Iliac Crest.**

AP (**A**) and frog-leg lateral (**B**) radiographs of the pelvis in a 13-year-old female show asymmetric widening of the left lateral iliac crest *(arrow)*. Coronal (**C**) and three-dimensional reconstructed (**D**) images from a CT confirm the findings *(arrow)*. **E,** AP radiograph of the pelvis obtained 3 weeks later shows healing with new bone formation *(arrow)* inferior to the avulsed fragment.



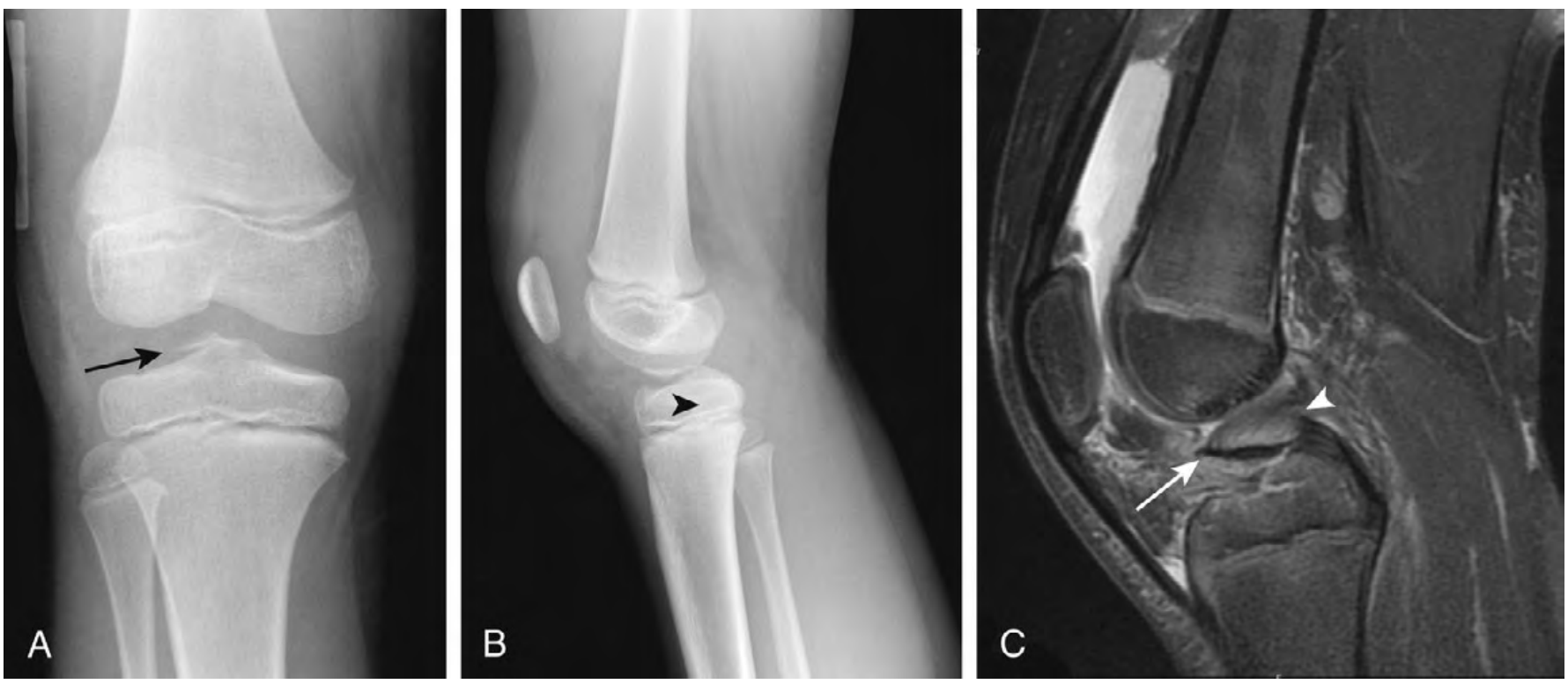
▪ **FIGURE 7-37** **Avulsion Fracture of the Anterior Superior Iliac Spine.**
AP (**A**) and frog-leg lateral (**B**) radiographs of the pelvis in a 16-year-old male show a large avulsion fracture of the right anterior superior iliac spine *(arrow)*. The fracture fragment is displaced inferiorly.



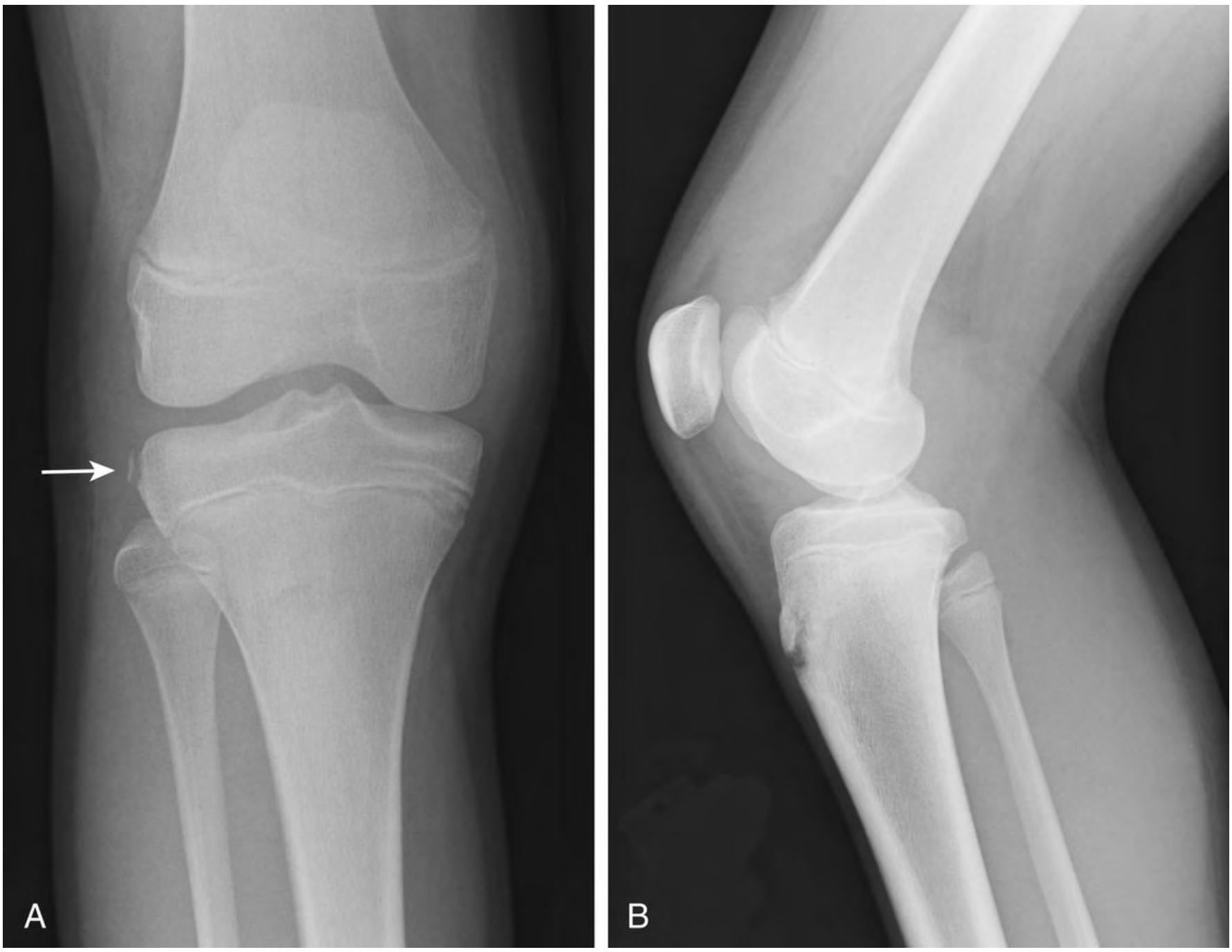
▪ **FIGURE 7-38** **Avulsion Fracture of the Anterior Inferior Iliac Spine.**
Frog-leg lateral radiograph of the pelvis in a 15-year-old male shows an avulsion fracture of the right anterior inferior iliac spine *(arrow)*. Pelvic avulsion fractures are often subtle as in this case.



▪ **FIGURE 7-39** **Avulsion Fracture of the Ischium.**
AP radiograph of the pelvis in a 13-year-old female shows a large avulsion fracture of the left ischial apophysis *(arrow)*.

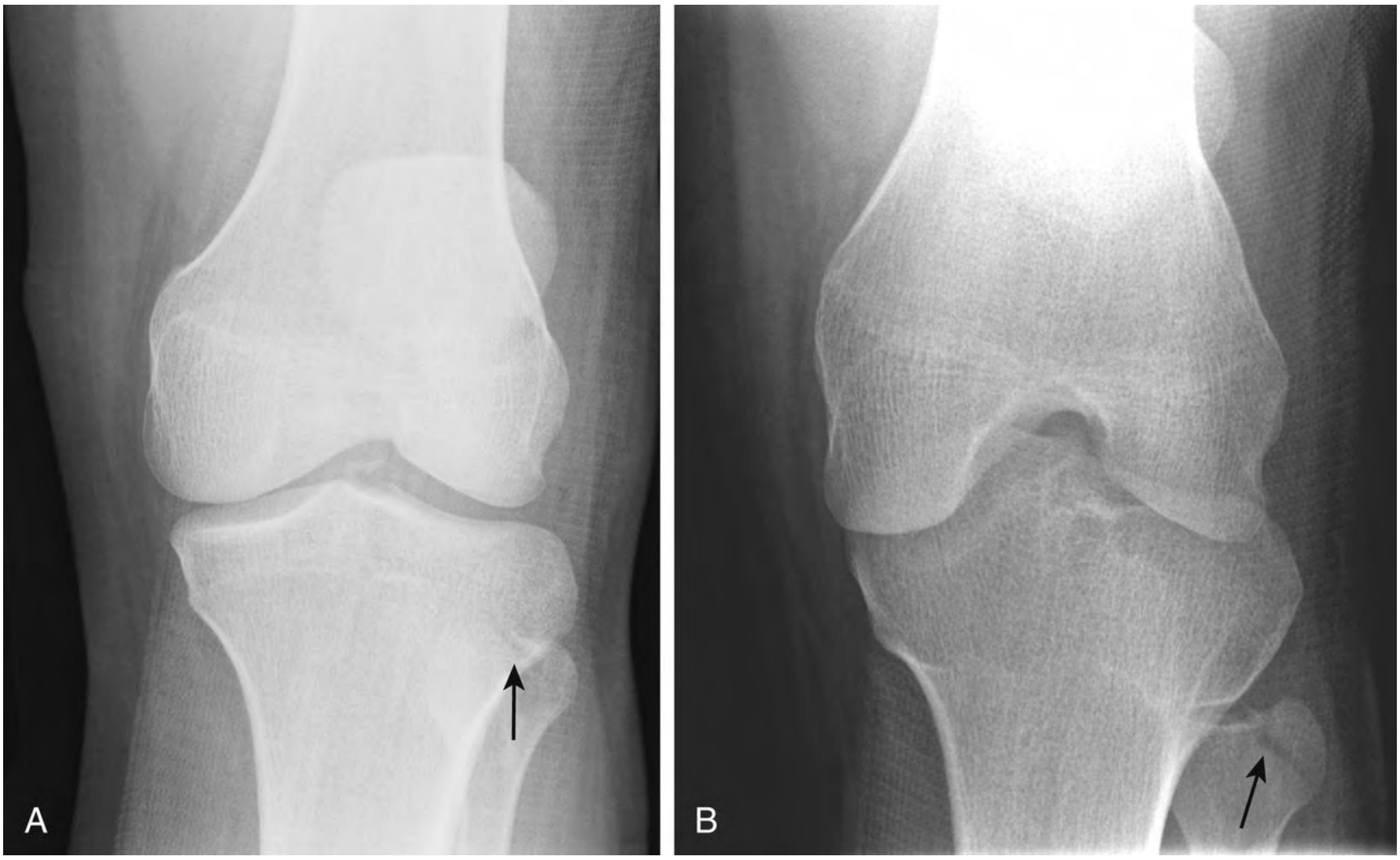


▪ **FIGURE 7-40** **Tibial Spine Avulsion Fracture.**
AP (**A**) and lateral (**B**) radiographs of the knee in a 7-year-old male show an avulsion fracture of the tibial spine. The avulsed fragment *(arrow)* is easier to see on the AP view, where it resides just lateral to the tibial spine. On the lateral view the donor site *(arrowhead)* is visible and there is a large joint effusion. **C,** Sagittal T2-weighted MRI with fat saturation shows the avulsed fragment *(arrow)* as a linear area of low signal in the knee joint. The anterior cruciate ligament *(arrowhead)* is attached to the fragment and is no longer taut. There is also a large hemarthrosis.

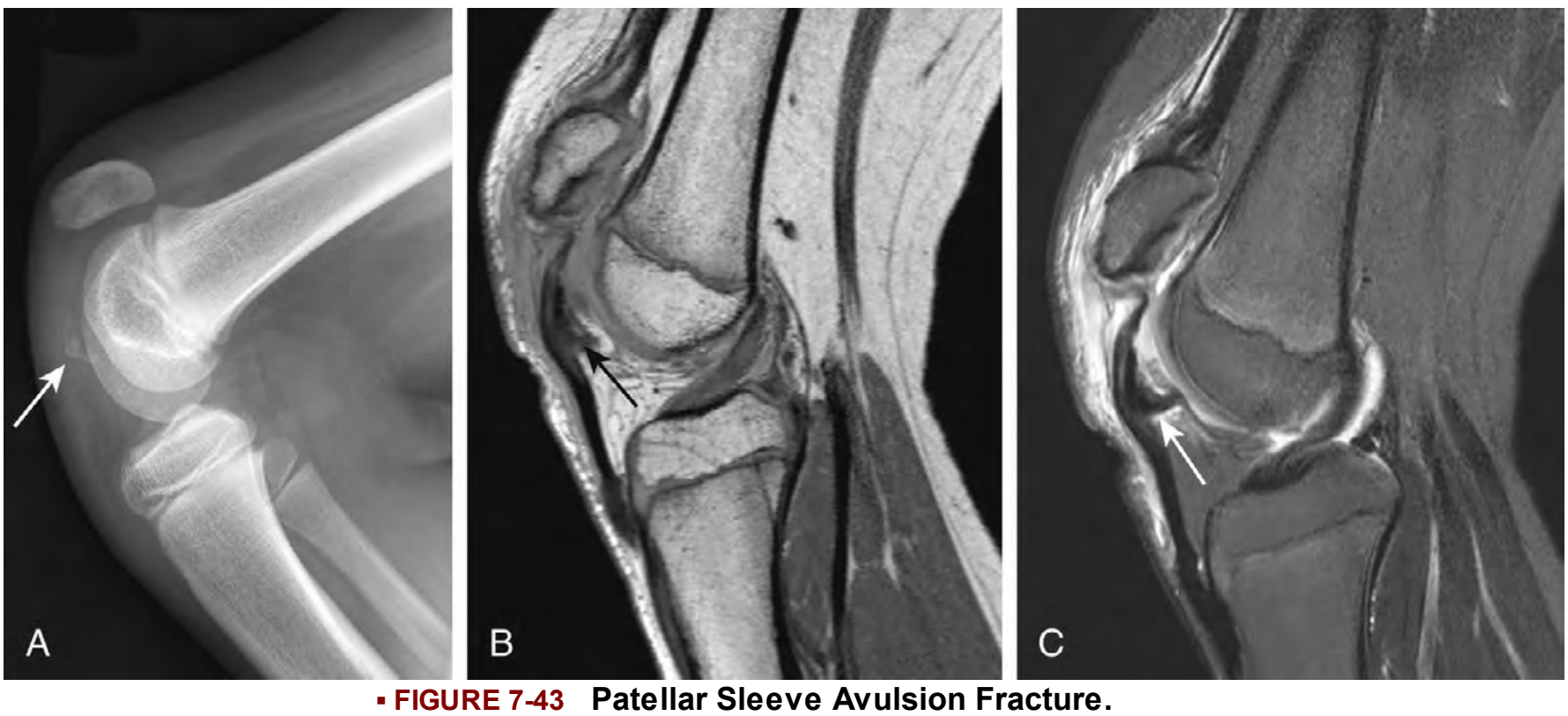


▪ **FIGURE 7-41** **Segond Fracture.**

AP (**A**) and lateral (**B**) radiographs of the knee in a 12-year-old female show an avulsion fracture of the lateral aspect of the proximal tibial epiphysis *(arrow)*. There is moderate lateral soft tissue swelling and a large joint effusion.



▪ **FIGURE 7-42** **Fibular Head Avulsion Fracture.**
AP (**A**) and PA (**B**) radiographs of the knee in a 14-year-old female show an avulsion fracture of the lateral aspect of the proximal fibula *(arrow)*. A tibial spine avulsion is also present and better seen on the AP view.



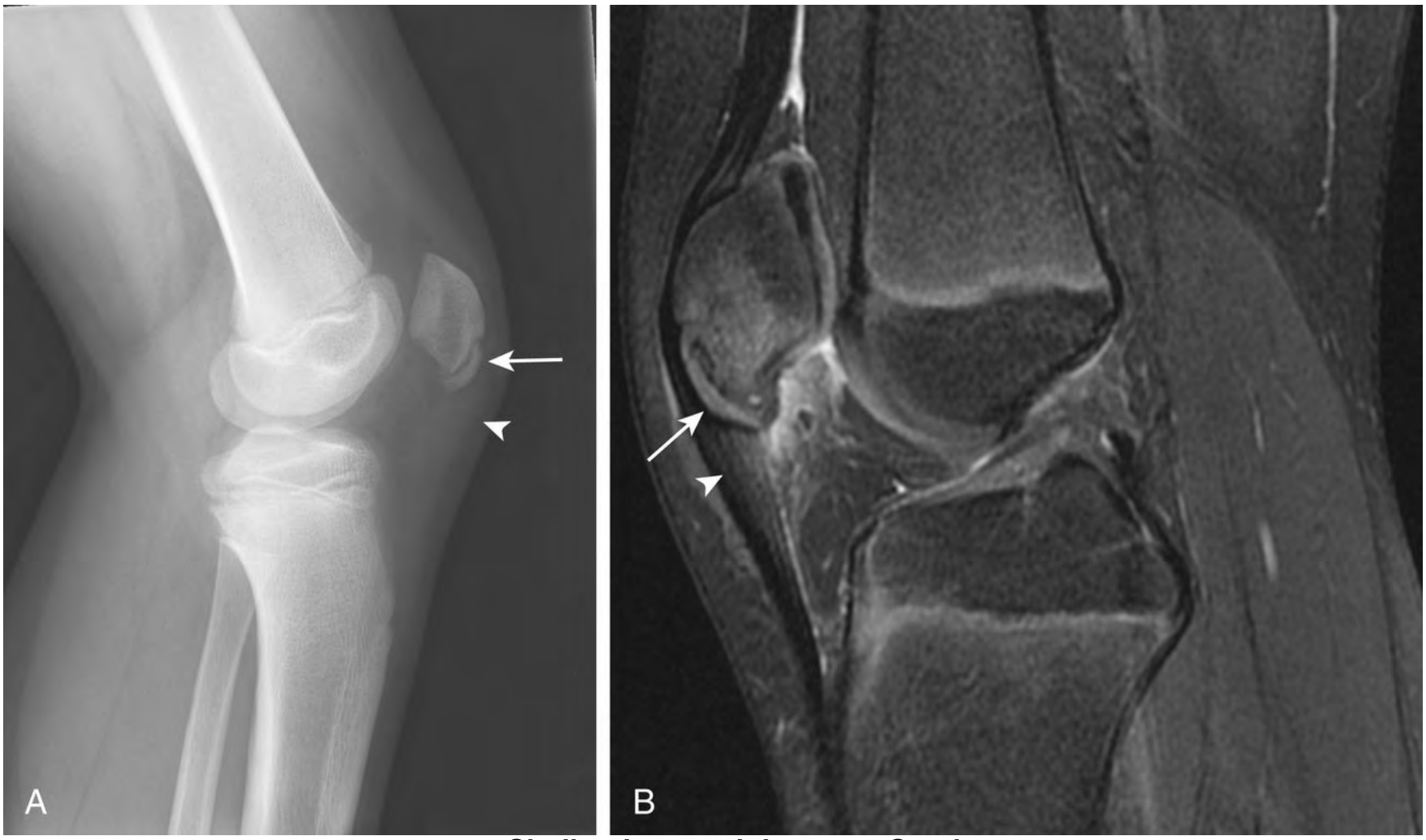
▪ **FIGURE 7-43** **Patellar Sleeve Avulsion Fracture.**
A, Lateral radiograph of the knee in a 10-year-old female shows an avulsion fracture *(arrow)* of the inferior pole of the patella. Sagittal proton density (**B**) and sagittal T2-weighted (**C**) images show the avulsed fragment *(arrow)* is attached to the patellar tendon. The donor site along the anterior inferior aspect of the patella is irregular.



▪ **FIGURE 7-44** **Patellar Sleeve Avulsion Fracture.**
Lateral radiograph of the knee in a 12-year-old male shows an avulsion fracture of the inferior pole of the patella *(arrow)*. The patella is slightly higher than expected, in an alta position. There is thickening and irregularity of the proximal patellar tendon.

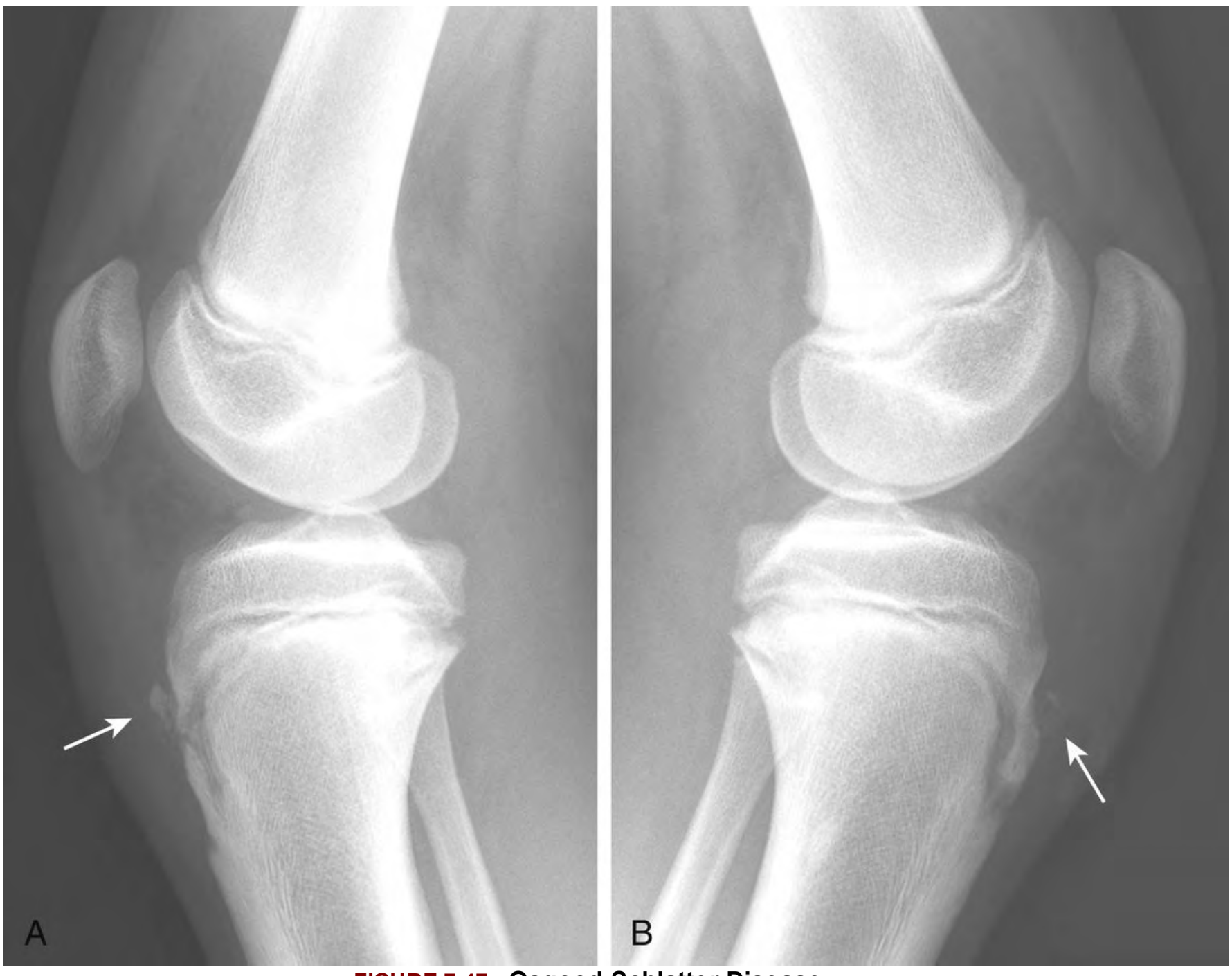


▪ **FIGURE 7-45** **Tibial Tubercle Avulsion Fracture.**
Lateral radiograph of the knee in a 16-year-old male shows an avulsion fracture of the tibial tuberosity *(arrow)*. A second avulsion fragment is present adjacent to the patella tendon insertion *(arrowhead)*.



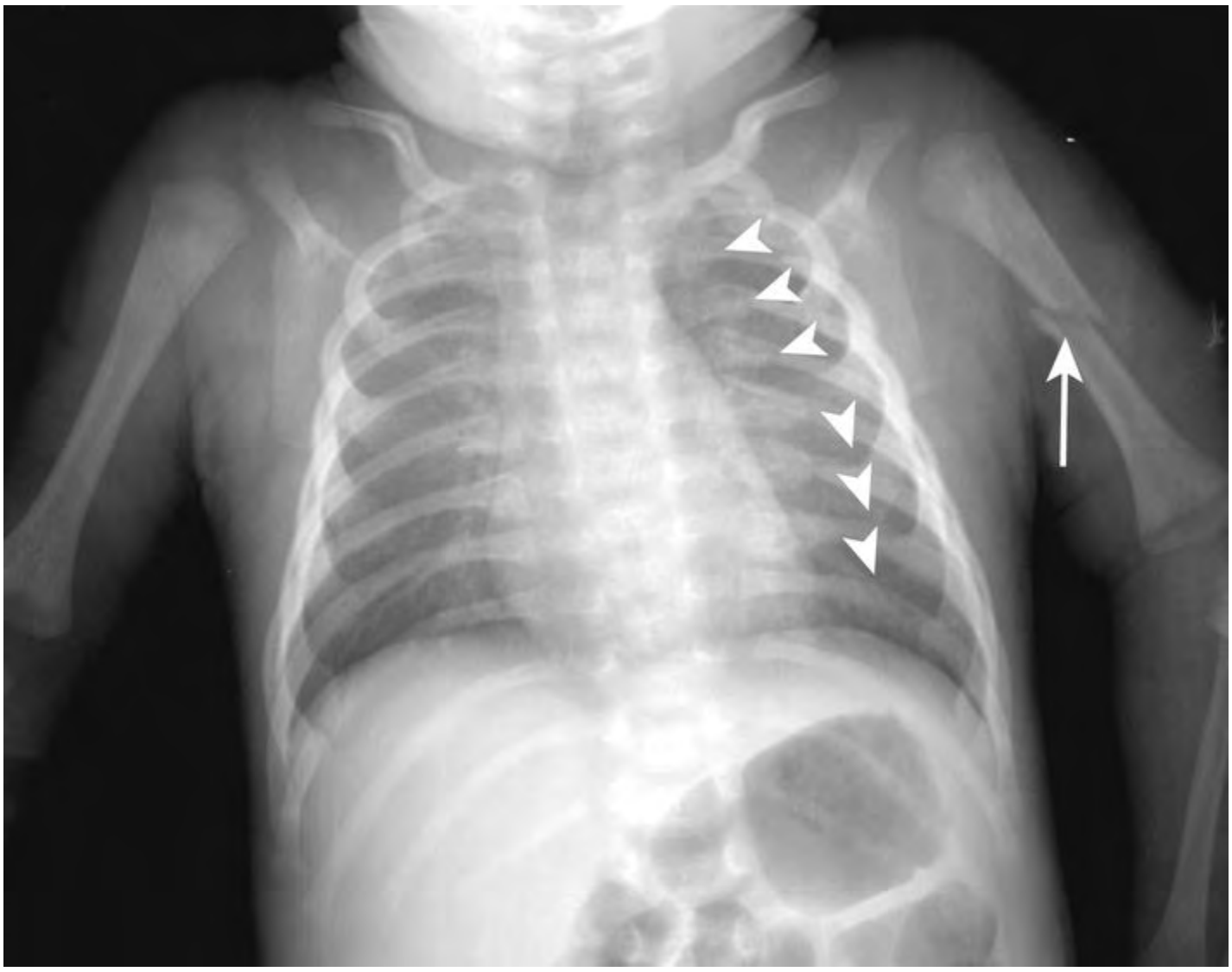
▪ **FIGURE 7-46** **Sinding-Larsen-Johansson Syndrome.**

A, Lateral radiograph of the knee in a 10-year-old male with chronic knee pain shows fragmentation of the inferior pole of the patella *(arrow)* and thickening of the origin of the patellar tendon *(arrowhead)*. **B,** Sagittal T2-weighted image of the knee shows the ossific fragment *(arrow)* of the lower pole of the patella along with bone marrow edema pattern in the fragment and the inferior patella. The proximal patella tendon is thickened *(arrowhead)* with edema in the tendon and within Hoffa fat pad.

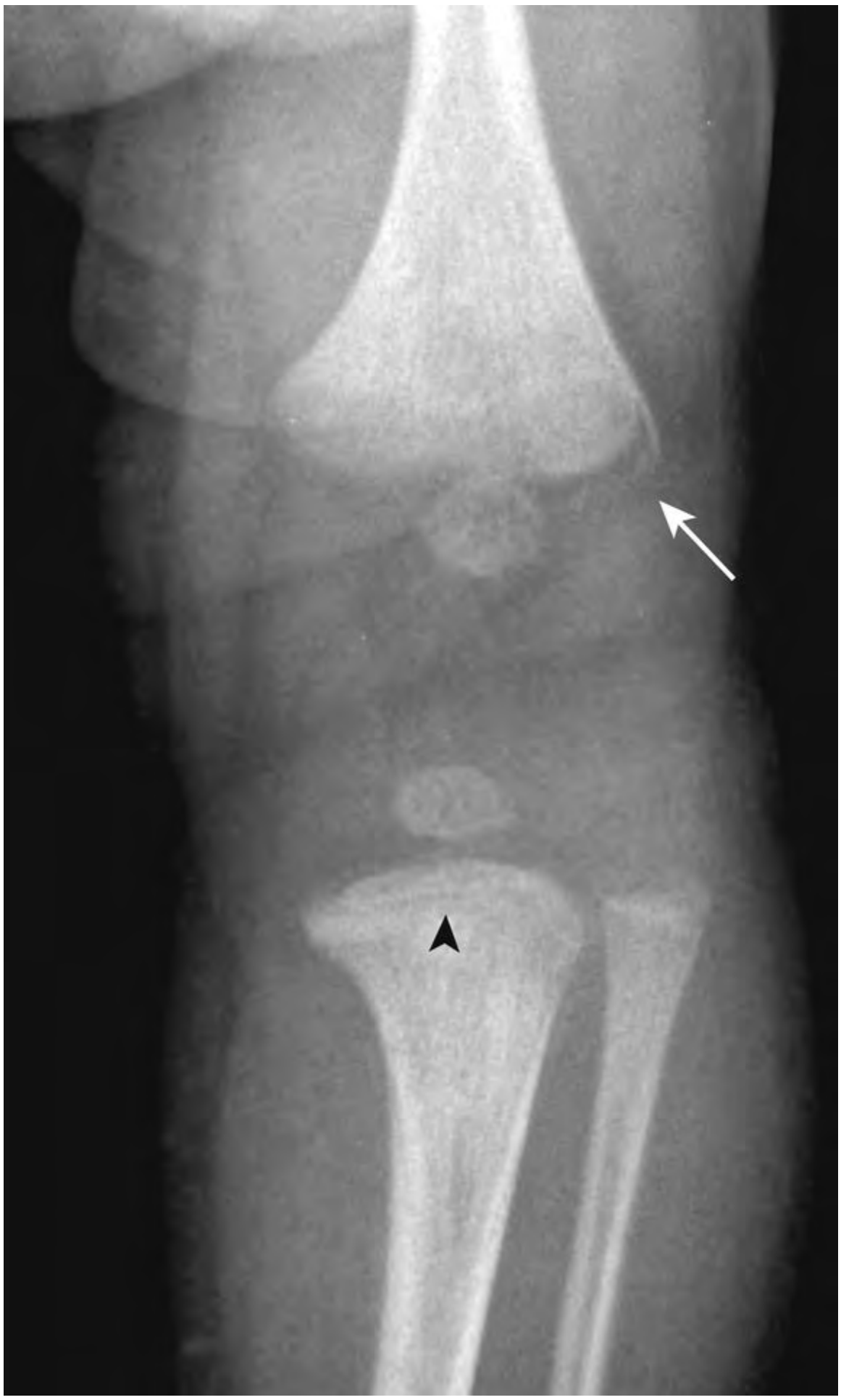


▪ **FIGURE 7-47 Osgood-Schlatter Disease.**
Lateral radiographs of the right (**A**) and left (**B**) knee in a 13-year-old male show fragmentation and irregularity of the tibial tuberosity *(arrow)* at the site of the patellar tendon insertion. The patellar tendon is thickened bilaterally, and there is overlying soft tissue swelling.

The clinical and imaging findings of abuse do not usually require differential diagnosis. However, other entities that may cause multiple fractures or that may cause radiographic findings that could be confused with injury, such as periosteal reaction, should always be considered. The other disorders that may present with multiple fractures in an infant are osteogenesis imperfecta (OI) and Menkes syndrome. Both of these entities are also associated with excessive wormian bones and osteopenia. There has been some debate about whether some patients diagnosed with child abuse do not suffer from vitamin D deficiency. Rickets, caused by vitamin D deficiency, is not a cause of the fractures specific for abuse, and most pediatric radiologists believe that the imaging appearance of child abuse and that of rickets do not overlap.



▪ **FIGURE 7-48** **Child Abuse.**
Frontal view of the chest in a 1-month-old male shows multiple fractures of different ages. There are healing fractures of the left third through eighth posterior ribs *(arrowheads)*. In addition, there is an acute fracture of the mid left humerus *(arrow)*.



▪ **FIGURE 7-49** **Child Abuse.**
AP view of the knee in a 1-month-old male shows a metaphyseal corner fracture of the distal, lateral femoral metaphysis *(arrow)*. A fracture in a bucket handle configuration *(arrowhead)* is present in the proximal tibia.

▪ Periosteal Reaction in the Newborn

When periosteal reaction is encountered in a newborn, there are a number of entities that must be considered (Table 7-1). They include physiologic new bone formation, TORCH infections (osteomyelitis), prostaglandin therapy, Caffey disease, metastatic neuroblastoma, and abuse. Physiologic periosteal new bone formation is commonly seen in infants during the first few months of life. It typically involves rapidly growing long bones, such as the femur, tibia, and humerus. Differential features that support physiologic growth as the cause of periosteal reaction include symmetric distribution, benign appearance of the periosteal reaction, and appropriate age of the child. When periosteal reaction involves the femur, tibia, or humerus, the other two bones are usually involved too. Radiographs may show one or several dense lines of periosteal reaction paralleling the cortex of the diaphysis of the long bones. Neonates with congenital heart disease are commonly treated with

prostaglandins to maintain patency of the ductus venosus. These children commonly demonstrate prominent periosteal reaction (Fig. 7-51).

TORCH Infections

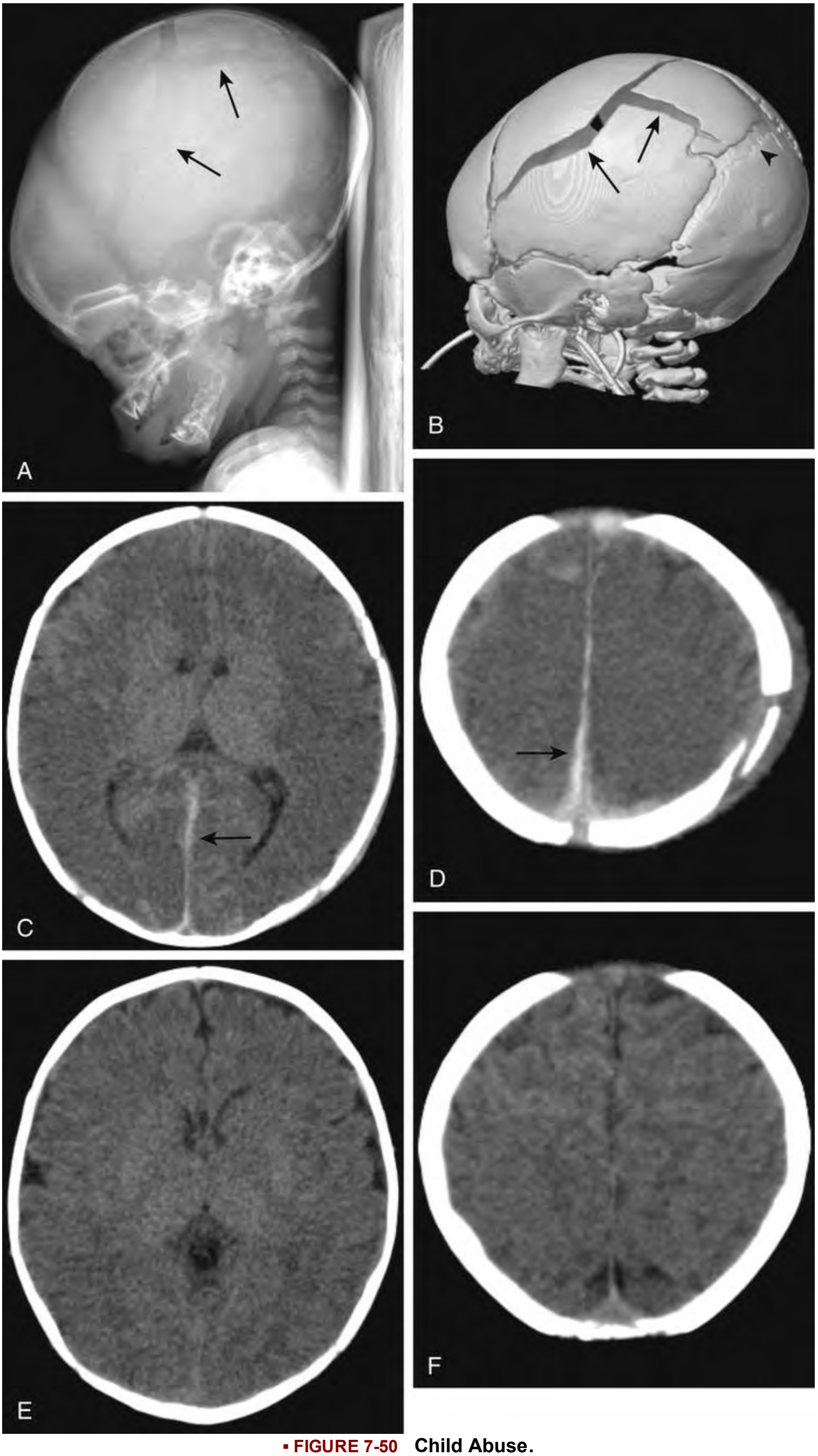
The differential diagnosis for transplacentally acquired infections can be remembered by the mnemonic TORCH: toxoplasmosis, other (syphilis), rubella, cytomegalovirus, and herpes.

Congenital Rubella Syndrome

Rubella was once the most common transplacental viral infection. Since the introduction of the rubella vaccine, the incidence of congenital rubella has plummeted. Its features include eye abnormalities, deafness, hepatosplenomegaly, aortic and pulmonic stenosis, and intrauterine growth restriction. Bony changes are present in as many as 50% of cases. They include irregular fraying of the metaphyses of long bones and generalized lucency of the metaphyses. The findings have been likened to a celery-stalk appearance. These radiographic findings are most apparent during the first few weeks of life. The bony manifestations of rubella are currently extremely rare.

Syphilis

Congenital syphilis occurs secondary to transplacental infection, usually occurring during the second or third trimester. Clinical findings include hepatosplenomegaly, rash, rhinorrhea, anemia, and ascites. Bony changes are present in as many as 95% of patients but often do not appear until 6 to 8 weeks after the time of infection. The radiographic findings may be present before the blood serology turns positive. Findings include nonspecific metaphyseal lucent bands, serrated metaphyses, multiple fractures, lytic skull lesions, and periosteal reaction involving multiple long bones. The *Wimberger corner sign* is the most specific finding of syphilis and consists of destruction of the medial portion of the proximal metaphysis of the tibia, resulting in an area of irregular lucency. Bony manifestations of syphilis are much more commonly encountered than those of rubella or other TORCH infections.



▪ **FIGURE 7-50** **Child Abuse.**

A, Lateral view of the skull shows a diastatic fracture of the left parietal bone *(arrows)*. **B,** The fracture *(arrows)* is more visible on the three-dimensional, reformatted image from a subsequent

CT. Note the difference between the fracture with its smooth borders and the sutures *(arrowhead)* with their jagged borders. Axial CT images through the lateral ventricles (**C**) and at the vertex (**D**) show edema with loss of gray matter–white matter differentiation, loss of the normal gyral pattern, and effacement of the sulci. In addition, there is a small hyperdense collection adjacent to the posterior falx cerebri *(arrow)*. The findings were new in comparison with a **E** and **F** CT performed 2 days earlier for a different event.

Caffey Disease (Infantile Cortical Hyperostosis)

Caffey disease is an idiopathic syndrome that consists of periosteal reaction shown on radiographs, irritability, fever, and soft tissue swelling over the areas of periosteal reaction. It occurs during the first few months of life. The bones most commonly involved include the mandible, clavicle, ribs, humerus, ulna, femur, scapula, and radius. Imaging shows periosteal new bone formation, sclerosis, and adjacent soft tissue swelling. The disease is self-limited and currently occurs much less commonly now than in the past, for reasons that are not well understood.

TABLE 7-1
Differential Diagnosis for Periosteal Reaction in a Newborn

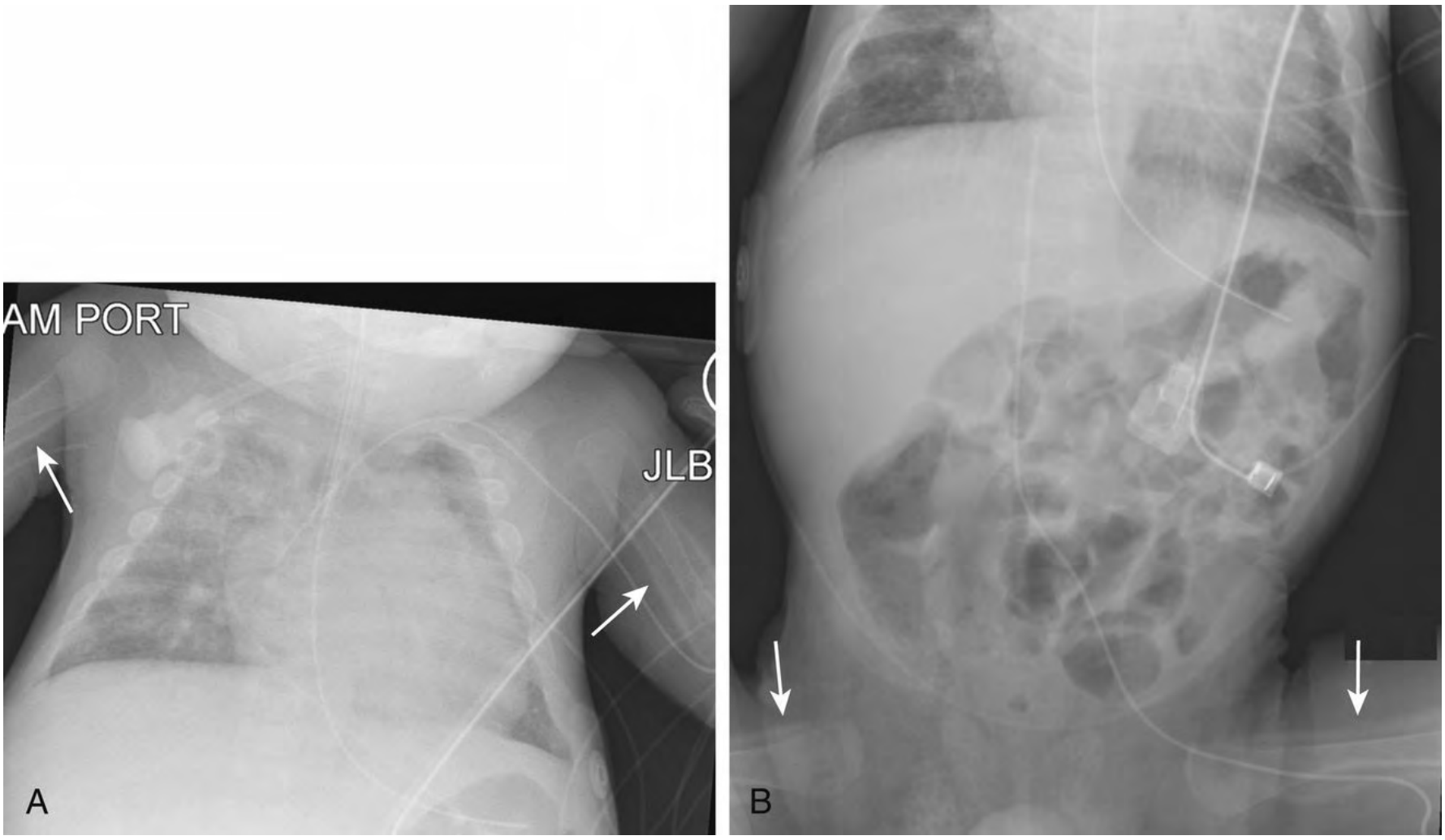
- Physiologic growth
- TORCH infections
- Prostaglandin therapy
- Caffey disease (infantile cortical hyperostosis)
- Neuroblastoma metastasis
- Healing fractures, abuse

▪ Lucent Permeative Lesions in Children

A bone lesion is considered permeative when it has poorly defined borders, a wide zone of transition, and multiple small, irregular holes centrally. As in an adult a permeative bone lesion in a child is consistent with an aggressive inflammatory or neoplastic lesion. The more common causes of a permeative lesion in a child include osteomyelitis, Langerhans cell histiocytosis (LCH), neuroblastoma metastasis, Ewing sarcoma, and lymphoma or leukemia. The differential diagnosis can be further limited by considering the patient's age (Table 7-2). If the patient is younger than 5 years of age, the most likely diagnoses include osteomyelitis, LCH, and metastatic neuroblastoma. Ewing sarcoma and lymphoma are exceedingly rare in children younger than 5 years of age. In older children, Ewing sarcoma and lymphoma or leukemia become candidates, and metastatic neuroblastoma becomes much less likely.

Osteomyelitis

Acute osteomyelitis is a relatively common cause of clinically significant bone pathology in children. It is primarily a disease of infants and young children; one third of cases occur in children younger than 2 years of age, and one half of cases occur before 5 years of age. Because of the young age of most of the children, the presentation is often nonspecific, and diagnosis is delayed. Erythrocyte sedimentation rate is elevated in a vast majority of cases. Most cases of osteomyelitis are hematogenous in origin; many patients have a recent history of respiratory tract infection or otitis media. *Staphylococcus aureus* is the most common cause, accounting for more than 80% of cases.



▪ **FIGURE 7-51** **Diffuse Periosteal New Bone Formation.**
AP radiographs of the chest (**A**) and abdomen (**B**) in a 3-month-old male treated with prostaglandin therapy show diffuse, symmetric periosteal new bone formation of the humeri and femurs *(arrows)*.

Osteomyelitis tends to occur in the metaphyses or metaphyseal equivalents of children. This is thought to be related to the rich and slow-moving blood supply to these regions. Approximately 75% of cases involve the metaphyses of long bones; the most common sites are the femur, tibia, and humerus. The other 25% of cases occur within metaphyseal equivalents of flat bones, most typically involving the bony pelvis.

TABLE 7-2
Differential Diagnosis of a Permeative Bone Lesion in a Child on the Basis of Age

Younger than 5 yr	Older than 5 yr
Osteomyelitis	Ewing sarcoma
Langerhans cell histiocytosis	Lymphoma or leukemia
Neuroblastoma metastasis	Osteomyelitis
	Langerhans cell histiocytosis

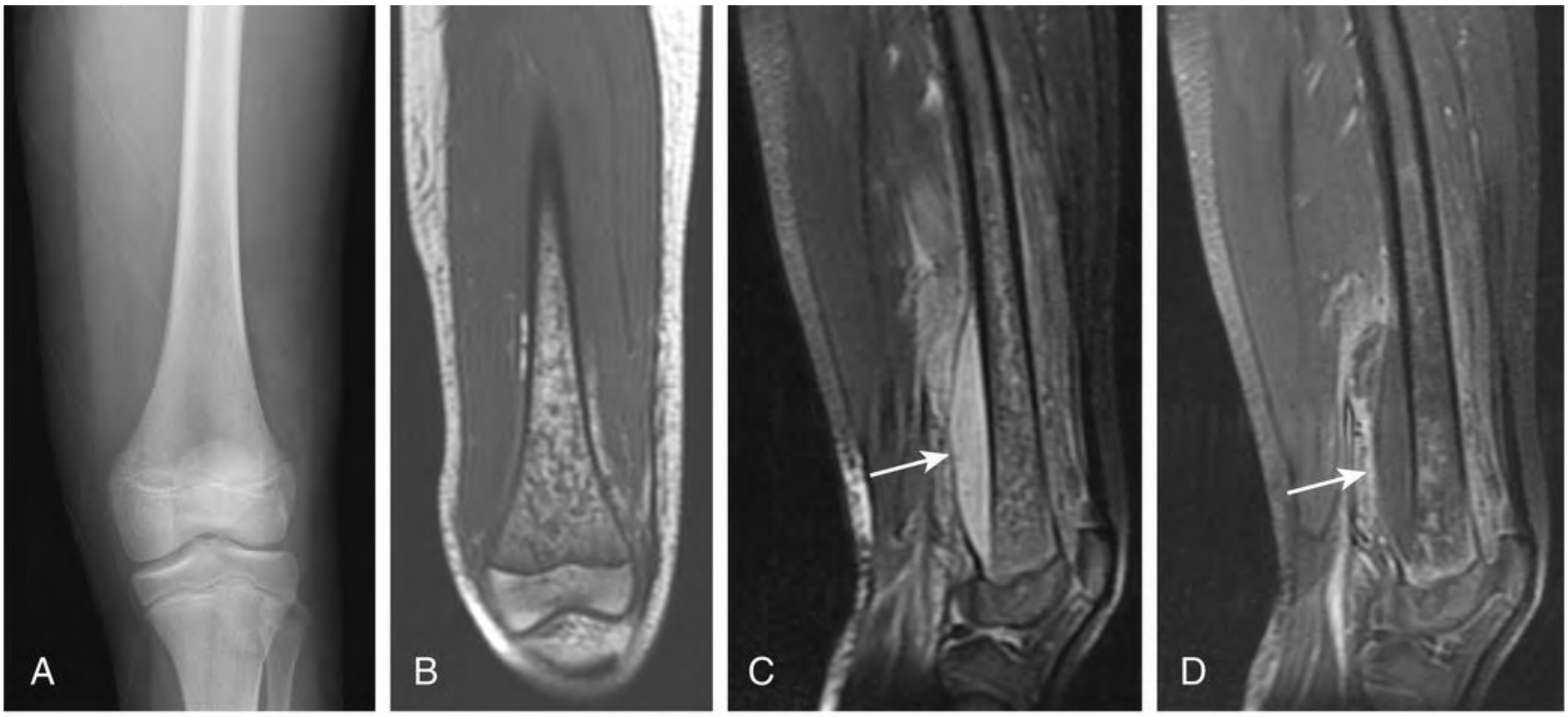
The earliest radiographic finding of osteomyelitis is deep soft tissue swelling evidenced by displacement or obliteration of the fat planes adjacent to a metaphysis. Bony changes may not be present until 10 days after the onset of symptoms. Initial bony changes consist of poorly defined lucency involving a metaphyseal area (Fig. 7-52). Commonly, progressive bony destruction is present. Periosteal new bone formation begins at approximately 10 days. Osteomyelitis can appear as sclerotic, rather than lucent, when it is a chronic process (Fig. 7-53).

MRI has become the dominant imaging study in the work-up of osteomylitis. Many institutions use a wide field of view T2-weighted MRI sequence to screen the lower extremities for osteomyelitis in symptomatic young children and then perform a more focused exam in areas of identified abnormalities. MRI demonstrates abnormal findings early after the onset of osteomyelitis. Osteomyelitis appears as an area of increased T2-weighted signal within a metaphysis. There are usually large areas of surrounding edema that are seen as an increased T2-weighted signal within the adjacent bone marrow and soft tissues. Gadolinium administration may show areas of nonenhancement suspicious for necrosis or abscess formation. Identification of drainable fluid for surgical planning is one of the advantages of MRI.



▪ **FIGURE 7-52 Osteomyelitis of the Great Toe.**

AP (**A**) and lateral (**B**) radiographs of the great toe in a 10-year-old female show a poorly defined lytic lesion *(arrowhead)* of the metaphysis of the distal phalanx of the great toe. The medial physis of the distal phalanx is widened, and there is a small Salter-Harris type II fracture. The initial injury occurred 1 week before these films were obtained.



▪ **FIGURE 7-53** **Methicillin-Resistant *Staphylococcus aureus*.**

A, AP radiograph of the femur in an 11-year-old female is essentially normal. There is minimal irregularity of the cortex of the lateral metaphysis. The radiographs are strikingly normal as compared with the MRI performed the same day. **B,** Coronal T1-weighted image of the distal femur shows the classic mottled heterogeneous signal of the marrow cavity. **C,** Sagittal T2-weighted image shows a similar mottled appearance of the marrow with a large subperiosteal abscess *(arrow)* along the posterior surface of the femur. **D,** Postcontrast T1-weighted MRI shows peripheral enhancement of the subperiosteal abscess *(arrow)* and lack of enhancement of the affected bone. AP (**E**) and lateral (**F**) radiographs of the distal femur after therapy show extensive changes from infection with sclerosis, cortical irregularity, and periosteal new bone.

Skeletal scintigraphy has become a much less common test to evaluate for osteomyelitis. On skeletal scintigraphy, osteomyelitis appears as a focal area of increased activity on the angiographic, soft tissue, and skeletal phase images. Skeletal scintigraphy becomes positive early after the onset of osteomyelitis and is often positive before development of changes seen on radiography. Another advantage of scintigraphy is the ability to evaluate for multiple sites of involvement.

A Brodie abscess is a unique form of osteomyelitis. It represents a subacute pyogenic osteomyelitis. On x-ray or CT, a Brodie abscess appears as a focal lucent lesion surrounded by a rim of sclerosis (Fig. 7-54). Periosteal new bone formation may be present. While not always present, a tract extending from the focal lucency to the physis is considered pathognomonic. On MRI the lesion can have variable signal appearance. The classic penumbra sign of increased T1 signal lining the rim of the abscess can help to confirm the diagnosis.

Methicillin-resistant *S. aureus* (MRSA) deserves special mention as it accounts for over half of call cases of pediatric osteomyelitis. Patients with MRSA osteomyelitis often have a more severe infection and require more therapy than those children with methicillin-sensitive *S. aureus*. MRSA osteomyelitis

has a unique pattern on MRI, with a mottled heterogeneous appearance of the marrow (see Fig. 7-53) and extensive subperiosteal rim-enhancing collections. At times, the marrow signal abnormalities are only identified on contrast-enhanced images, where they appear as areas of absent enhancement.



▪ **FIGURE 7-54 Brodie Abscess of the Patella.**
AP (**A**) and lateral (**B**) radiographs of the patella in a 6-year-old female show a poorly defined lytic lesion of the patella *(arrow)*. On the AP view there is a linear track extending superiorly and medially. **C,** Sagittal T1-weighted MRI shows a heterogeneous lesion in the patella with a thin rim of increased T1 signal along the superior aspect *(arrow)* of the abscess. **D,** Axial T2-weighted MRI shows the heterogeneous abscess in the center of the patella *(arrow)* with surrounding edema signal.

Langerhans Cell Histiocytosis

LCH, previously known as eosinophilic granuloma and histiocytosis X, is an idiopathic disorder that can manifest as focal, localized, or systemic disease. It remains unclear whether the disease process is inflammatory or neoplastic. It is characterized by abnormal proliferation of Langerhans cells. The disease is twice as common in boys as in girls and occurs most commonly in whites. Historically the disorder was characterized into one of three forms: eosinophilic granuloma (localized disease), Hand-Schüller-Christian (a chronic disseminated form), and Letterer-Siwe (acute disseminated form).

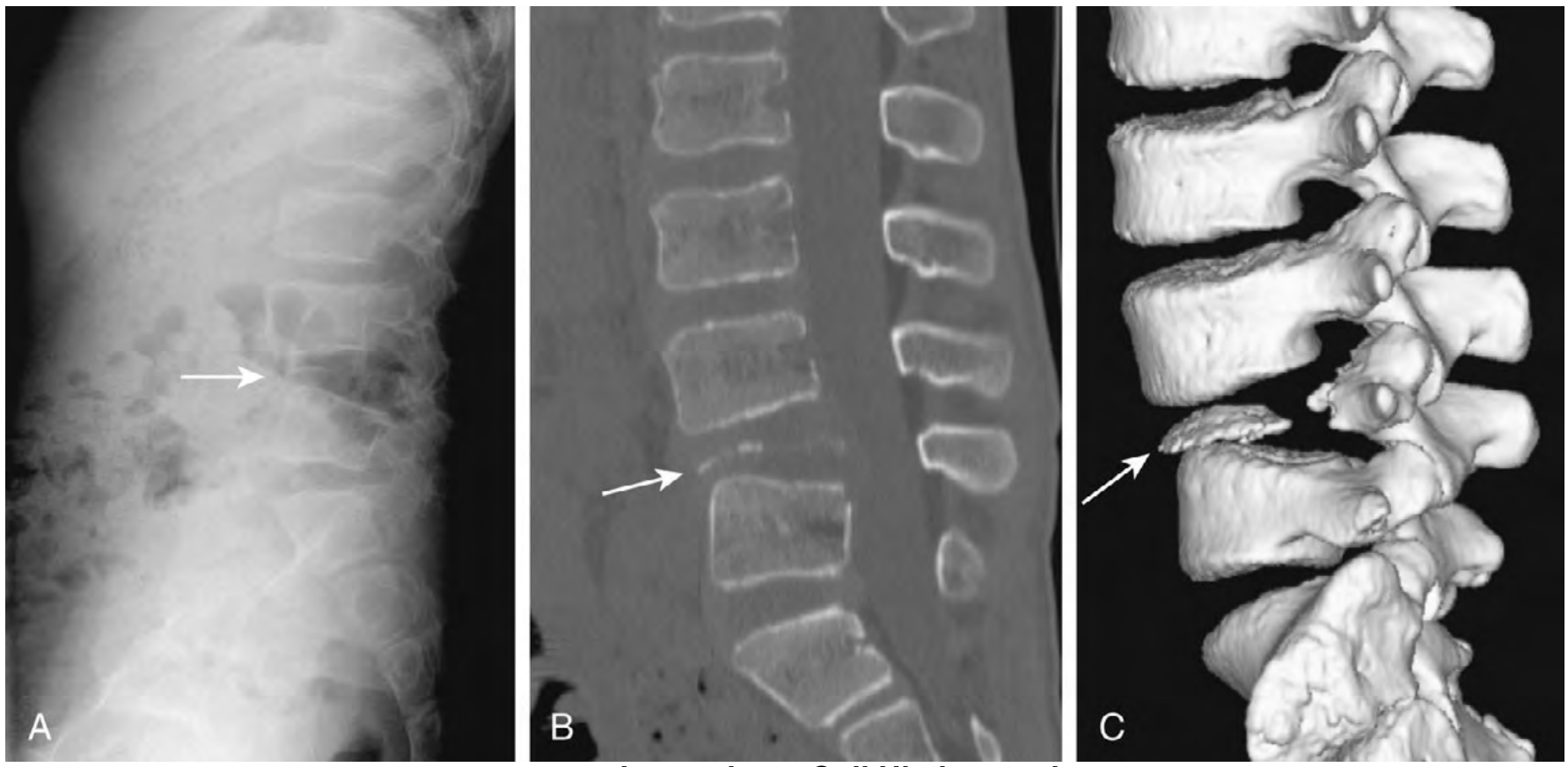
Currently, LCH is stratified into single-system or multisystem disease with or without risk organ involvement. Risk organs include the liver, spleen, lungs, and bone marrow.

Common sites of disease include bones, the skin, and pituitary. Bone is the most common site of disease, occurring in up to 80% of patients. Up to half of all lesions occur in the skull, with the remaining sites of involvement scattered throughout the appendicular skeleton, including the proximal limbs (20%), pelvis and scapula (12%), vertebral bodies (10%), and the distal limbs (5%). On radiograph, lesions typically appear as a well-demarcated, lytic lesion with no peripheral sclerosis (Fig. 7-55). Skull lesions may have a beveled edge when viewed en face or a target appearance when viewed straight on due to uneven destruction of the inner and outer tables of the skull. When the spine is involved, a classic finding is vertebral plana (vertebral destruction with severe collapse; Fig. 7-56).



▪ **FIGURE 7-55** **Langerhans Cell Histiocytosis.**

A, Lateral view of the skull in a 13-month-old male shows multiple lytic lesions in the skull *(arrows)*. **B,** Axial CT image through the largest skull lesion shows that the lesion is affecting the skull asymmetrically, with inner table being less affected than outer table. **C,** AP radiograph of the right hip shows a poorly defined lesion of the right acetabulum *(arrow)*. **D,** CT of the hip shows the poorly defined lesion.



▪ FIGURE 7-56 **Langerhans Cell Histiocytosis.**
Lateral radiograph (**A**), sagittal CT (**B**), and three-dimensional (**C**) reformat from CT of the lumbar spine show flattening of the L4 vertebral body *(arrow)*. Although the vertebral body is barely perceptible, the posterior elements are intact. The L5 vertebral body is rotated posteriorly.

A child who presents with a lesion suspicious for LCH should be evaluated by a skeletal survey to identify other bony lesions; a chest radiograph to exclude pulmonary involvement; and often an MRI or CT to characterize and evaluate the anatomic extent of disease or intraabdominal organ involvement. When positron emission tomography (PET)-CT or bone scan is performed, affected areas show increased uptake.

Ewing Sarcoma

After osteosarcoma, Ewing sarcoma is the second most common primary malignancy of bone in children. It is an aggressive, small, round, blue cell tumor similar to primitive neuroectodermal tumor. Ewing sarcoma most commonly occurs in the second decade of life, and its occurrence in children younger than 5 years of age is exceedingly rare. The most common sites of involvement, in decreasing order of frequency, are the femur, pelvis, tibia, humerus, and ribs. Two thirds of cases involve the pelvis or lower extremity. Overall, Ewing sarcoma has a greater propensity for flat bones as compared with other primary bone malignancies.

The radiographic appearance of Ewing sarcoma is variable. Most lesions involve the metaphysis, but diaphyseal involvement is more common than it is in other bone malignancies. Most lesions have an aggressive appearance: a lucent lesion with poorly defined borders and a permeative appearance in the cortex (Fig. 7-57). Aggressive-appearing periosteal new bone formation (spiculated, onion skin, Codman triangle) is commonly present. However, Ewing sarcoma can appear predominantly sclerotic in as many as 15% of cases. MRI demonstrates a destructive bony mass, often with an associated soft tissue component. The 5-year survival rate for those with Ewing sarcoma is 70% in those with localized disease and 30% in those in whom metastatic disease is present. Metastases primarily occur in other sites of bone and the lungs.

Metastatic Disease

In children, most cases of metastatic disease result from small, round, blue cell tumors. The most common primary neoplasms to metastasize to bone are neuroblastoma and leukemia or lymphoma. In any child younger than 3 years of age with a neoplastic bony lesion, metastatic neuroblastoma (Figs. 7-58 and 7-59) should be considered and is much more likely than a primary bone neoplasm. Leukemia and lymphoma may deposit in the regions of the metaphyses and cause bony destruction. The appearance is often that of lucent metaphyseal bands (Fig. 7-60). These nonspecific bands are often referred to as leukemic lines. Primary bone lymphoma is rare in children.

▪ Focal Sclerotic Lesions in Children

There are multiple causes of focal sclerotic bone lesions in children. The more common causes are listed in Table 7-3.

Osteoid Osteoma

Osteoid osteoma is a relatively common bone lesion. Most cases occur within the second decade of life and usually present with pain. Classically, the pain is worse at night and is relieved by nonsteroidal antiinflammatory medication. The lesions are more common in boys. The cause is unknown, and it is currently unclear whether the lesion is a benign neoplasm or an inflammatory lesion. Most commonly, osteoid osteomas occur within the cortex of the metadiaphyses or diaphyses of the long bones of the lower extremities.

On radiography an osteoid osteoma appears as a lucent cortical nidus surrounded by an area of reactive sclerosis (Fig. 7-61). By definition, the nidus is less than 2 cm in diameter. Lesions larger than 2 cm are referred to as osteoblastoma. Classically, a punctate radiodensity is identified within the central lucency (a dense dot within a lucent area, surrounded by sclerotic density). CT is commonly used to further characterize the lesion because the punctate central radiodensity and lucency are often better demonstrated on CT than on radiography (see Fig. 7-61), and it defines the anatomic position of the nidus. CT can be used as guidance for percutaneous ablation or drill removal of the osteoid osteoma. MRI can also be used to diagnose and characterize the lesions. Skeletal scintigraphy demonstrates a "double-density" sign of intense increased uptake by the nidus, surrounded by less intense but abnormally increased uptake by the surrounding sclerotic bone. Single-photon emission computed tomography (SPECT)-CT helps to increase the sensitivity of detecting subtle lesions.

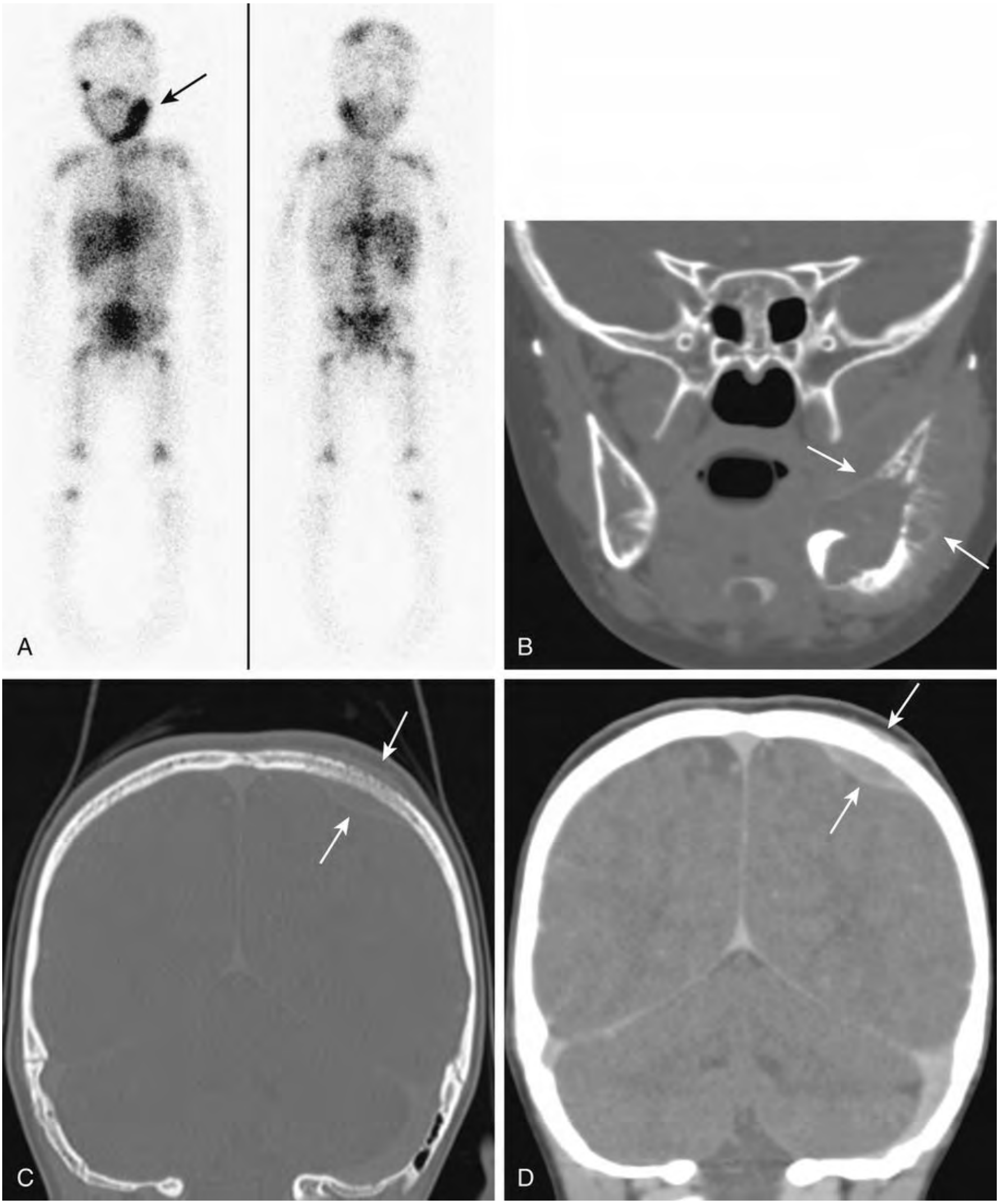
Stress Fracture

A stress fracture is defined as an injury resulting from repetitive trauma. It usually occurs when a new or intense activity has recently been initiated. The most common sites of stress fractures in children, in decreasing order of frequency, are the tibia, fibula, metatarsals, and calcaneus. A stress fracture appears on radiographs as a transverse or oblique band of sclerosis or as a lucent line surrounded by sclerosis or periosteal new bone formation. Periosteal new bone formation may be the only finding. In the tibia the most common location is the proximal posterior cortex, although the anterior cortex can also be involved. In the calcaneus there is typically a vertical sclerotic band paralleling the posterior cortex. Calcaneal stress fractures most commonly occur when a child has had a cast removed after a preceding lower extremity injury and returns to activity after a period of prolonged disuse (see Figs. 7-34 and 7-35). Skeletal scintigraphy demonstrates a stress fracture as an area of focal increased uptake days to weeks before the development of radiographic findings. CT may be helpful in demonstrating the linear nature of the lesion when trying to evaluate whether a sclerotic lesion is a stress fracture, osteoid osteoma, or osteomyelitis. Stress fractures may be identified on MRI when it is performed to evaluate for pain. They appear as low-signal linear structures with surrounding high T2-weighted signal edema.



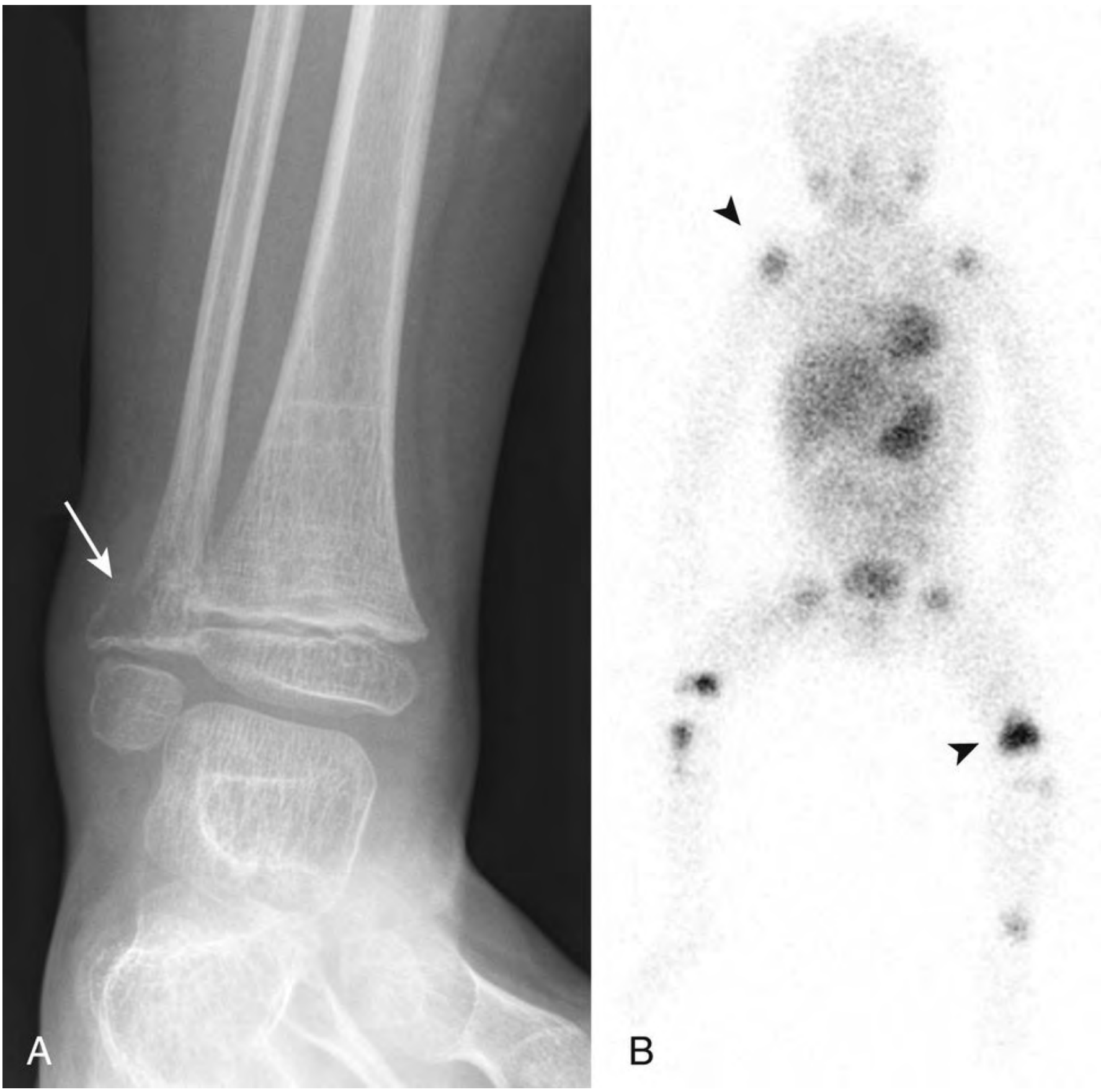
▪ **FIGURE 7-57** **Ewing Sarcoma.**

AP (**A**) and lateral (**B**) radiographs of the femur in a 17-year-old male show a poorly defined, expansile lytic lesion *(arrow)* of the mid femoral diaphysis. The medial cortical margin of the femur is irregular, and there is an associated soft tissue mass. On the lateral view (**B**), there is aggressive periosteal new bone formation with a Codman triangle *(arrowhead)* along the superior/medial aspect of the mass. **C,** Coronal FSEIR MRI of the lower extremities from the hips to the knees shows the solitary right femoral mass. There is a large hyperintense soft tissue mass *(arrow)* along the medial aspect of the tumor. Axial T2-weighted (**D**) and axial T1-weighted (**E**) MRIs show the tumor occupying the medullary cavity of the femur, infiltrating the bone, and extending as a soft tissue mass on the posterior and medial aspect of the leg. **F,** Coronal image of the lower extremities shows FDG uptake in the right femoral mass *(arrow)*. There are no other areas of abnormal FDG uptake. **G,** Anterior projection from a technetium (Tc) 99m MDP bone scan shows uptake *(arrow)* in the right femur. There are no other areas of tumoral uptake. *FDG,* 18f Fluorodeoxyglucose; *FSEIR,* fast spin echo inversion recovery; *MDP,* methylene diphosphonate; *MRI,* magnetic resonance imaging.



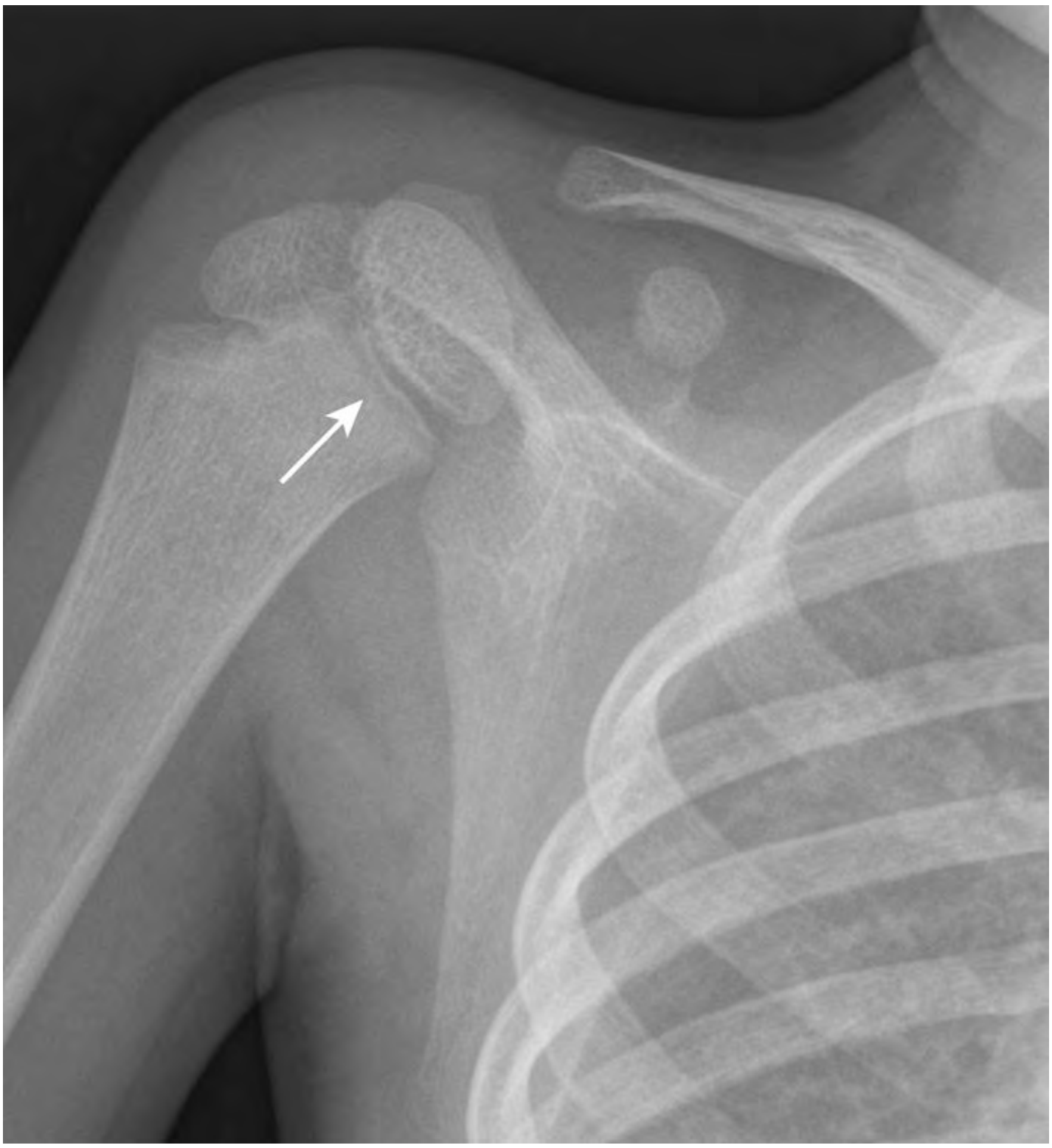
▪ **FIGURE 7-58** **Metastatic Neuroblastoma.**

A, I 123 MIBG scan in the anterior and posterior projection in a 1-month-old male with neuroblastoma shows extensive metastatic disease throughout the skeleton and liver. Any bone uptake is indicative of metastatic disease. The most intense area of uptake is in the mandible (*arrow* in anterior projection). **B,** Coronal CT of the mandible shows a large destructive mass of the left mandible *(arrows)*. The mandible is expanded with speculated cortical bone. Coronal head CT with contrast displayed in the bone algorithm (**C**) and soft tissue algorithm (**D**) shows a metastatic lesion of the left parietal bone. The bone has a permeative appearance. There is a soft tissue component of the metastasis along both the inner and outer table of the skull *(arrows)*.



▪ **FIGURE 7-59** **Metastatic Neuroblastoma.**

A, Radiograph of the ankle in a 3-year-old male with neuroblastoma shows a destructive lesion of the left fibula *(arrow)*. The lesion is lucent and expansile. The nearby trabeculae are coarsened. **B,** I 123 metaiodobenzylguanidine (MIBG) scan in the anterior projection show focal areas of uptake in the shoulders *(arrowhead)*, proximal and distal femurs *(chevron arrowhead)*, proximal tibias, and distal left fibula.



▪ **FIGURE 7-60** **Leukemic Lines.**
Radiograph of the shoulder in a 3-year-old male with acute lymphoblastic leukemia shows a thin metaphyseal lucency *(arrow)* of the proximal humerus.

TABLE 7-3

Common Causes of Focal Sclerotic Lesions in Children

- Osteoid osteoma
- Chronic osteomyelitis
- Stress fracture
- Osteosarcoma



▪ **FIGURE 7-61** **Osteoid Osteoma.**

AP (**A**) and lateral (**B**) radiographs of the tibia show a small lucent lesion in the anterior cortex of the mid tibia *(arrow)*. There is associated diffuse cortical thickening of the tibia. **C,** Sagittal image from a CT scan shows a geographic lucent lesion in the anterior cortex of the tibia *(arrow)*. There is a faint lucent tract extending anteriorly from the main lesion. The anterior cortex is thickened. **D,** Spot images of the lower leg from a bone scan using Tc 99m MDP bone scan shows a focus of uptake in the mid right tibia *(arrow)* surrounded by less intense, but abnormal uptake. Compare the right leg with the normal left leg.

Osteosarcoma

Osteosarcoma, or osteogenic sarcoma, is the most common primary bone malignancy of childhood. It occurs most commonly in patients between 10 and 15 years of age and is more common in boys than in girls. Although most cases of osteosarcoma arise in otherwise healthy children, there are certain predisposing conditions, such as hereditary retinoblastoma, Li-Fraumeni syndrome, and previous radiation therapy. Osteosarcoma is a very malignant lesion that uniquely gives rise to neoplastic osteoid and bone. The majority of osteosarcomas arise from the medullary cavity, although the lesion may arise from the surface of bone. The latter scenario gives rise to the periosteal and parosteal forms. The most common sites for development of osteosarcoma are the metaphyses of long bones. More than 60% of

cases of osteosarcoma arise in the region of the knee (distal femur or proximal tibia).

The radiographic appearance of osteosarcoma is dependent on the amount of bony destruction and new bone formation. The lesions are typically large at the time of presentation. The destructive component of the tumor is demonstrated by lucent destruction of a metaphysis with aggressive features (aggressive periosteal reaction, poorly defined borders). Tumor bone is seen in more than 90% of cases of osteosarcoma and helps to differentiate this tumor from other types of bone malignancies (Fig. 7-62). It appears as a cloudlike density. One feature that helps to differentiate tumor bone from sclerotic reactive bone is that tumor bone often extends beyond the expected confines of the bony shaft. In most cases of osteosarcoma there is a large soft tissue mass present at the time of diagnosis. In poorly differentiated, very aggressive lesions, tumor bone may not be present and the lesion may appear as a nonspecific, aggressive lucent lesion.

MRI is used to evaluate the extent of bone and soft tissue involvement for presurgical planning. The extent of marrow abnormality, soft tissue mass, and cortical destruction is well demonstrated as abnormal increased T2-weighted signal on MRI. However, MRI is not accurate in differentiating peritumoral marrow edema from tumor-involved marrow. Therefore all abnormal signals in the marrow are generally considered to be involved by tumor for the sake of surgical planning. MRI is accurate in depicting the relationship between the soft tissue mass and adjacent nerves and vascular structures. It is important to image the entire length of the long bone (from joint to joint) involved by the tumor because osteosarcoma can occasionally have discontinuous bone involvement (skip lesions), and identification of such skip lesions affects surgical planning. Surgery in conjunction with chemotherapy is standard therapy. Limb salvage procedures are currently being performed in as much as 80% of patients.



▪ **FIGURE 7-62** **Osteosarcoma.**

A, AP radiograph of the left shoulder in a 16-year-old female shows a large mass of the proximal humerus. The humeral head is sclerotic with a permeative pattern. There is extensive osteoid formation in the soft tissue adjacent to the humerus. The osteoid formation is amorphous. **B,** Coronal short tau inversion recovery (STIR) MRI of the humerus shows the extent of the heterogeneous mass *(arrows)* of the proximal humerus.

The 5-year survival of patients diagnosed with osteosarcoma has increased to 77% in recent years. However, patients with early metastases continue to have a poor prognosis. MRI has been shown to be useful in documenting chemotherapeutic response by demonstrating decrease in the size of the soft tissue mass and the amount of peritumoral edema. The best predictor of survival is the percentage of tumoral necrosis following chemotherapy. Patients with more than 90% necrosis have an 80% to 90% chance of achieving a long-term cure. The most common type of metastatic disease is pulmonary (lung nodules), which is evaluated by CT. Lung metastases can appear calcified or ossified. Skeletal metastatic disease is reported to be present in as many as 15% of patients and is evaluated by skeletal scintigraphy or PET-CT.

▪ Multifocal Bone Lesions in Children

The presence of multifocal involvement narrows the differential diagnosis for bone lesions in children (Table 7-4). Osteomyelitis, LCH, and metastatic disease have already been discussed. In addition, there are several hereditary syndromes that cause multifocal bone lesions in children.

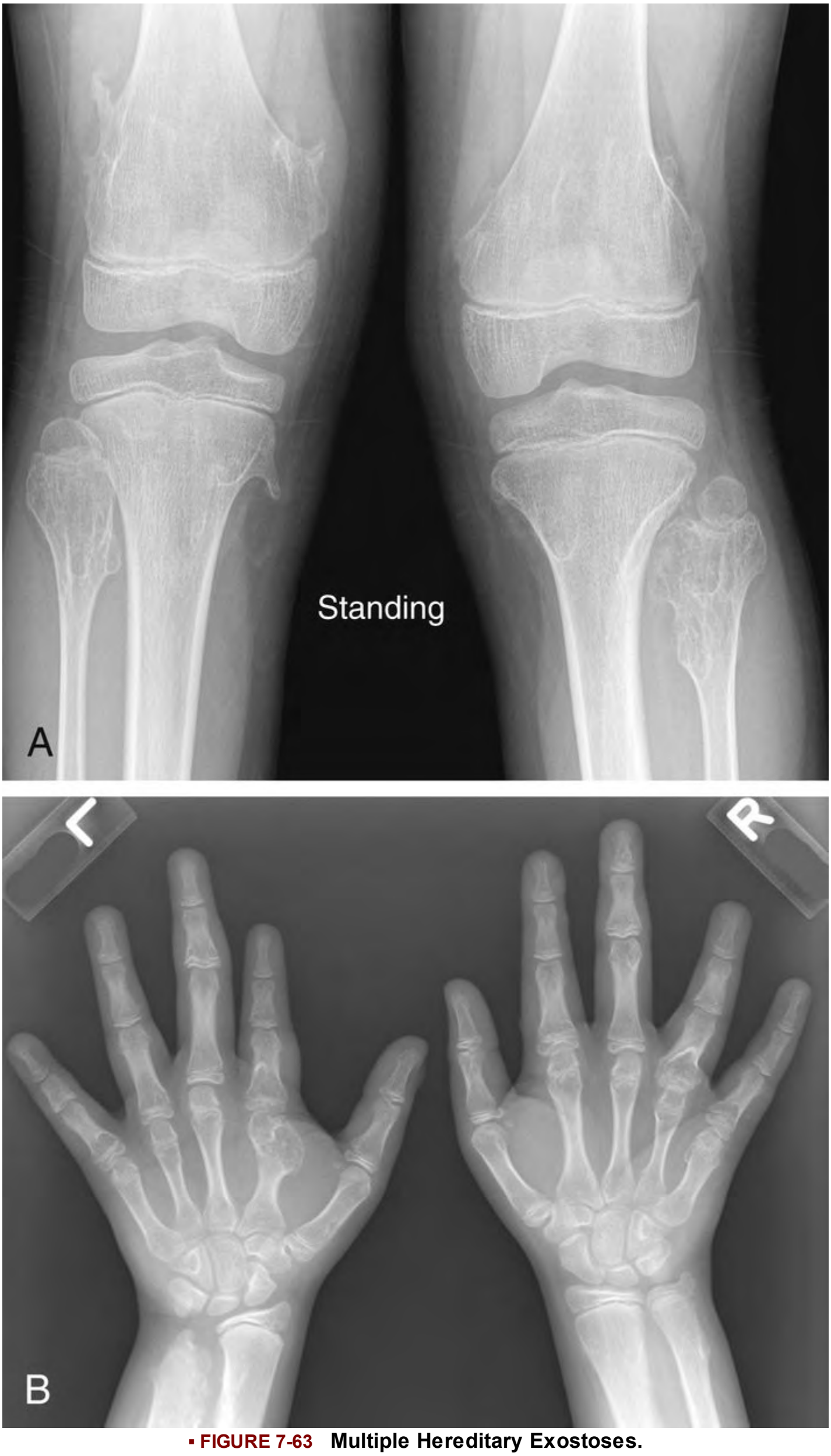
In multiple hereditary exostoses (osteochondromatosis), there is a propensity to develop multiple bilateral osteochondromas. Osteochondromas appear as bony growths that arise from the metaphysis and are continuous with the adjacent bony cortex (Fig. 7-63). They have a tendency to point away from joints. The most common location is the bones surrounding the knee. With osteochondromatosis the lesions can lead to a number of problems, including limb shortening, leg length discrepancy, bowing and deformity, compression of adjacent nerves and vessels, and malignant degeneration into chondrosarcoma (5%). Concerning features for the development of chondrosarcoma include new onset

of pain or lesion growth. In adults, MRI is used to evaluate at-risk lesions to help to identify malignant degeneration. Although evaluation of the thickness of the cartilaginous cap is important in adults, it is not a useful marker in children because the cartilage is normally thicker around growing bone.

TABLE 7-4

Multifocal Bone Lesions in Children

- Multifocal osteomyelitis
- Langerhans cell histiocytosis
- Metastatic disease
- Multiple hereditary exostoses (osteochondromatosis)
- Enchondromatosis (Ollier disease, Maffucci syndrome)
- Polyostotic fibrous dysplasia (McCune-Albright syndrome)
- Neurofibromatosis



▪ **FIGURE 7-63** **Multiple Hereditary Exostoses.**
AP radiograph of the knees (**A**) and hands (**B**) in a 10-year-old female shows multiple exostoses. The radiograph of the knees shows multiple lesions on each bone. The fibular lesions have a more sessile appearance, whereas the femoral and tibial lesions are more pedunculated. The lesions in the hand are more difficult to diagnose. The largest lesion is of the left second metacarpal. Most of the lesions are sessile. Several metaphyses are overhanging.

In Ollier disease (enchondromatosis) there are multiple enchondromas (Fig. 7-64). Although they most commonly occur bilaterally, it is possible for all the lesions to be located on one side of the body. Solitary enchondromas tend to occur in the hands and feet (Fig. 7-65), whereas lesions of enchondromatosis tend to be located within the metaphyses of long bones. With growth, the lesions may take on an oblong or flame-shaped, linear configuration perpendicular to the physis. Malignant degeneration to chondrosarcoma occurs in approximately 30% of lesions. When soft tissue venous malformations are seen in conjunction with multiple enchondromas, the syndrome is called Maffucci syndrome (Fig. 7-66). In those patients, phleboliths may be seen within the soft tissue masses on radiographs. Patients with Maffucci syndrome have an even higher risk of malignant degeneration than do those with Ollier syndrome and are also at increased risk for malignant neoplasms of the abdomen and central nervous system.



▪ **FIGURE 7-64** **Ollier Disease.**

A, AP radiograph of the right hand in a 16-year-old female shows multiple expansile lucent lesions of the middle phalanx of the index finder, proximal and middle phalanx of the middle finger, and third metacarpal. Coronal T1-weighted (**B**), coronal intermediate weighted (**C**), and coronal postcontrast, fat saturated T1-weighted (**D**) MRI of the hand shows expansile lesions of the index and middle fingers. The lesions are hypointense on T1-weighted images, hyperintense on the intermediate weighted image, and have peripheral and septal enhancement.

McCune-Albright syndrome is the presence of polyostotic fibrous dysplasia, café au lait spots, and endocrine abnormalities. The most common endocrine abnormality is precocious puberty in girls. Polyostotic fibrous dysplasia most commonly involves the facial bones, pelvis, spine, and proximal humeri. When the lesions affect the femur, patients can have an exaggerated coxa vara deformity referred to as a shepherd crook deformity. The fibrous dysplasia lesions tend to be unilateral in patients with McCune-Albright syndrome. Many patients present with pathologic fracture by 10 years of age (Fig. 7-67). There is no predisposition to malignancy. Fibrous dysplasia has a variable appearance

radiographically. It can be purely lytic or sclerotic and can be expansile or nonexpansile. The classic description is that of "ground-glass" matrix, which is a smudged and somewhat dense appearance of the central portion of the lesion. Periosteal reaction should be present only if there is a pathologic fracture.



▪ **FIGURE 7-65** **Solitary Enchondroma.**
AP radiograph of the hand in a 16-year-old female shows an expansile lucent lesion *(arrow)* of the third metacarpal.

▪ Constitutional Disorders of Bone

The term *constitutional disorder of bone* refers to any developmental abnormality of bone resulting in diffuse skeletal abnormality. The skeletal dysplasias, mucopolysaccharidoses, and OI fall into this category.

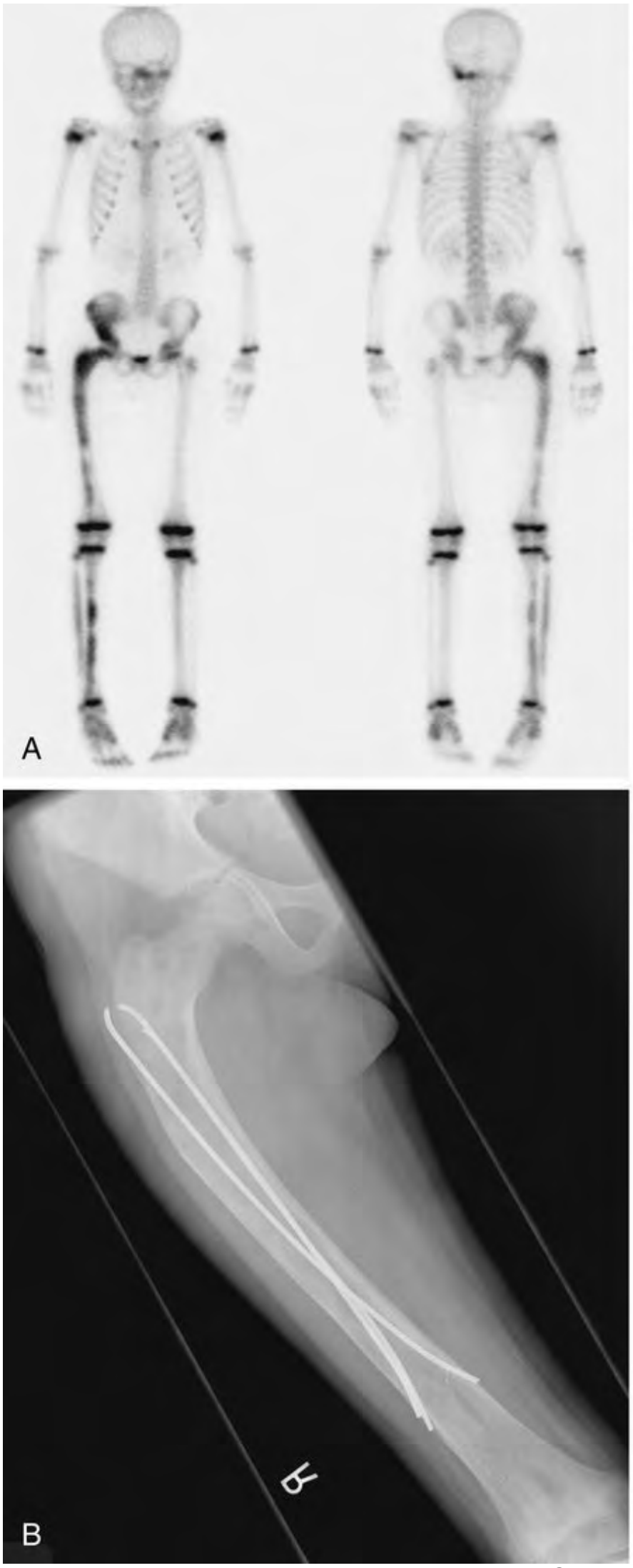
Skeletal Dysplasias

For some reason, many people think that those trained in pediatric radiology have a textbook knowledge of skeletal dysplasias. This unfortunate rumor could not be farther from the truth. Most pediatric radiologists deal with skeletal dysplasia fairly infrequently and typically know only enough to

be able to recognize that a dysplasia is present and that they need help. Most large children's hospitals have one person who is enthralled with and knowledgeable about skeletal dysplasias, and that person is consulted whenever a dysplasia arises. Anyone who is in a situation in which such a person is not available should consult the excellent textbooks available. The author recommends the text by Taybi and Lachman. It is practical to have an understanding of the approach to the dysplasias and to know something about the more common ones. The radiographic identification of a particular dysplasia can be helpful for prognostication and genetic counseling for the parents (e.g., is the identified dysplasia a dominant or recessive trait?).



▪ **FIGURE 7-66** **Maffucci Syndrome.**
AP radiograph of the hands in a 15-year-old female shows multiple enchondromas of the majority of bones of the hand. Each lesion is expansile with a heterogeneous internal matrix. Some of the lesions have a typical ground-glass matrix, whereas others have features more typical of a chondroid matrix. In addition to the bone lesions, the fingers are deformed with obvious soft tissue abnormality and calcifications.



▪ **FIGURE 7-67** **McCune-Albright Syndrome.**

A, Anterior and posterior projection from a Tc 99m MDP bone scan in an 11-year-old female shows abnormal uptake in the right iliac bone, right femur, and right tibia. There is a varus configuration of the right hip. **B,** AP radiograph of the right femur 4 years later shows a varus configuration of the femur, also known as the shepherd crook deformity, as well as expansion of the medullary cavity. **C,** Coronal CT of the pelvis shows an expansile lesion of the right iliac bone *(arrow)*. The lesion is lucent compared with the left side, with the more superior portion having a ground-glass matrix and the inferior portion being more lucent. **D,** Oblique radiograph of the right foot shows expansile lesions of the second, third, and fourth toes, as well as the second and fourth metacarpals. The affected toes are sclerotic and expansile. The metatarsal lesions *(arrows)* are expansile with a ground-glass matrix.

Radiographic evaluation of dysplasia requires images of the skull, spine, thorax, pelvis, and

extremities. An important feature for categorization is identifying whether the extremities are shortened and, if so, which portion is short. Extremity shortening can be classified as rhizomelic, mesomelic, or acromelic. *Rhizomelic* refers to proximal shortening (humerus, femur) and is seen in achondroplasia (Fig. 7-68) and thanatophoric dwarfism (Fig. 7-69). *Mesomelic* refers to middle narrowing (radius-ulna, tibia-fibula). Most of the mesomelic dysplasias are quite rare. *Acromelic* refers to distal shortening and is seen with asphyxiating thoracic dystrophy (Jeune syndrome; Fig. 7-70) and chondroectodermal dysplasia (Ellis-van Creveld syndrome). Other features helpful in categorizing dysplasias include determining whether there are skull enlargement, short ribs, a short spine, abnormal vertebral bodies, and an abnormal pelvic configuration. The pelvis may demonstrate abnormalities in the configuration of the iliac wings or in the appearance of the acetabulum. The iliac wings may be abnormally tall or short or may have a squared appearance. The acetabular roof may appear horizontal (a decreased acetabular angle). *Trident acetabulum* refers to a case in which the acetabulum is seen to have three inferior pointing spikes resembling an upside-down trident. This is a buzzword for Jeune syndrome but also can be seen in Ellis-van Creveld syndrome and thanatophoric dysplasia. Some of the more common dysplasias and their radiographic manifestations are described in Table 7-5.

Achondroplasia

Achondroplasia is discussed in greater detail because it is the most common short-limbed dwarfism. It is an autosomal dominant disease in which the heterozygous form demonstrates the clinical manifestations, and the homozygous form is lethal. Patients with achondroplasia have rhizomelic limb shortening (see Fig. 7-68). They also have craniofacial disproportion, an enlarged skull, a small skull base, and a small foramen magnum and jugular foramina. The last may result in brainstem compression. In the spine the vertebral bodies are short and decreased in anterior-to-posterior diameter. The disk spaces appear too tall. There is a decrease in the interpedicular distance (left to right), with this distance being narrower in the more inferior lumbar spine than in the more superior lumbar spine (the opposite of normal; see Fig. 7-68, *C*). The pedicles are also short in the anterior-to-posterior diameter. Because of these findings, achondroplasts are prone to spinal stenosis. The shortened long bones show metaphyseal flaring. In infancy there is commonly space between the middle fingers, resulting in a trident appearance of the hand. The iliac bones are short in height, and the acetabular roof is horizontal (a decreased acetabular angle), making the iliac bones resemble old-fashioned tombstones.

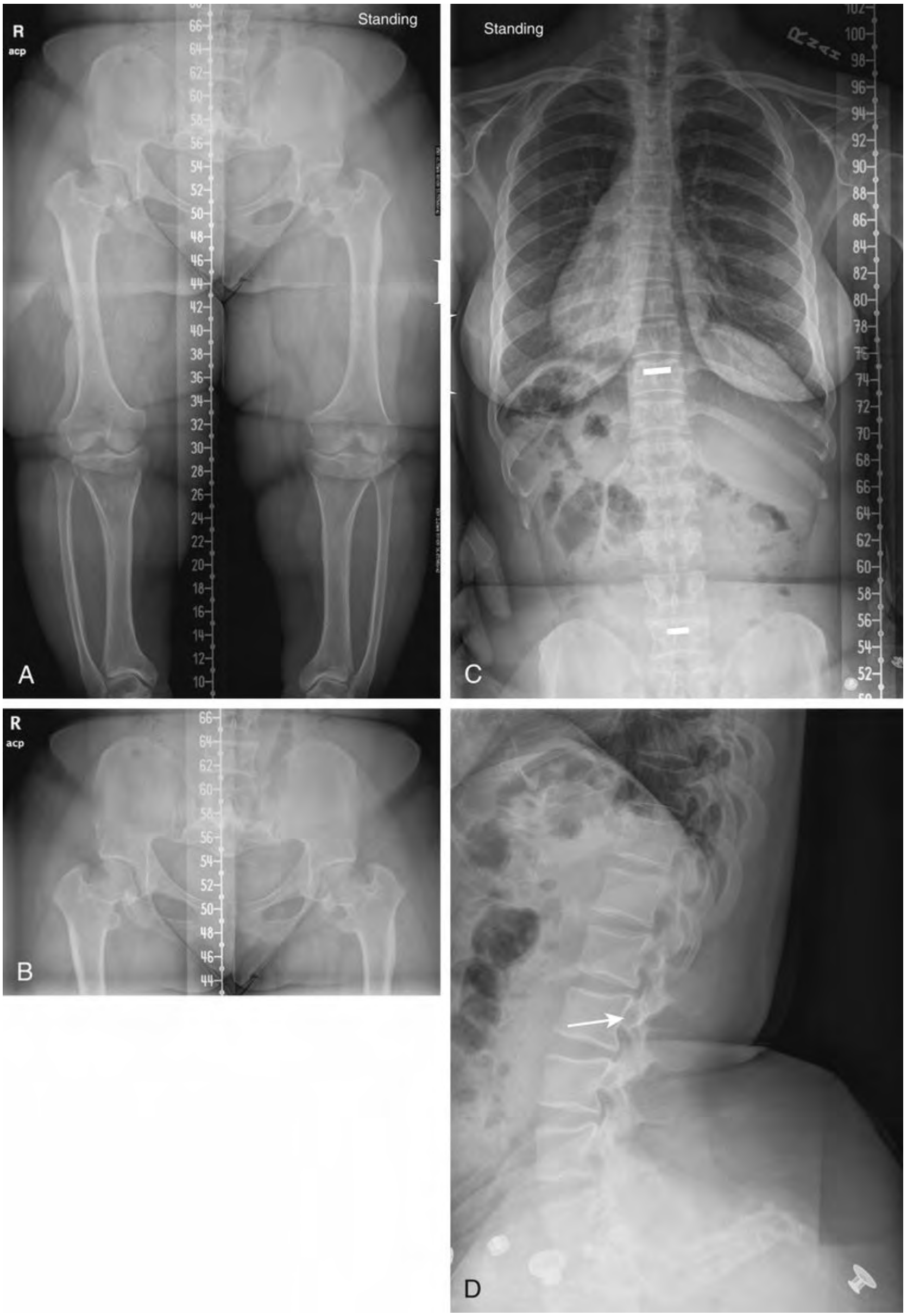
Mucopolysaccharidoses

Mucopolysaccharidoses are a group of hereditary disorders manifested by defects in lysosomal enzymes. They include such disorders as Hunter, Hurler, and Morquio syndromes. The skeletal findings in this group of diseases are similar and have been referred to as dysostosis multiplex (Fig. 7-71). The vertebral bodies are oval in shape and often have a beak extending from the anterior cortex (see Fig. 7-71, *C*). This is located in the midportion of the vertebral bodies in Morquio syndrome and in the inferior portion in Hunter or Hurler syndrome. Beaking is most prominent in the lumbar vertebral bodies. There can be focal kyphosis (gibbous deformity; see Fig. 7-71, *D*) at the thoracolumbar junction. The clavicles and ribs are commonly thickened. The ribs are narrower posteromedially, giving them a "canoe paddle" appearance. The appearance of the pelvis is essentially the opposite of that in achondroplasia. The iliac wings are tall and flared, and the acetabuli are shallow (increased acetabular angles; see Fig. 7-71, *E*). The femoral heads are dysplastic, and femoral necks are gracile and demonstrate coxa valga (loss of angle between the neck and the shaft of the femur). The hands have a characteristic appearance that includes proximal tapering of the metacarpal bones (see Fig. 7-71, *B*). The pituitary fossa can have a J-shaped appearance (see Fig. 7-71, *F*).

Osteogenesis Imperfecta

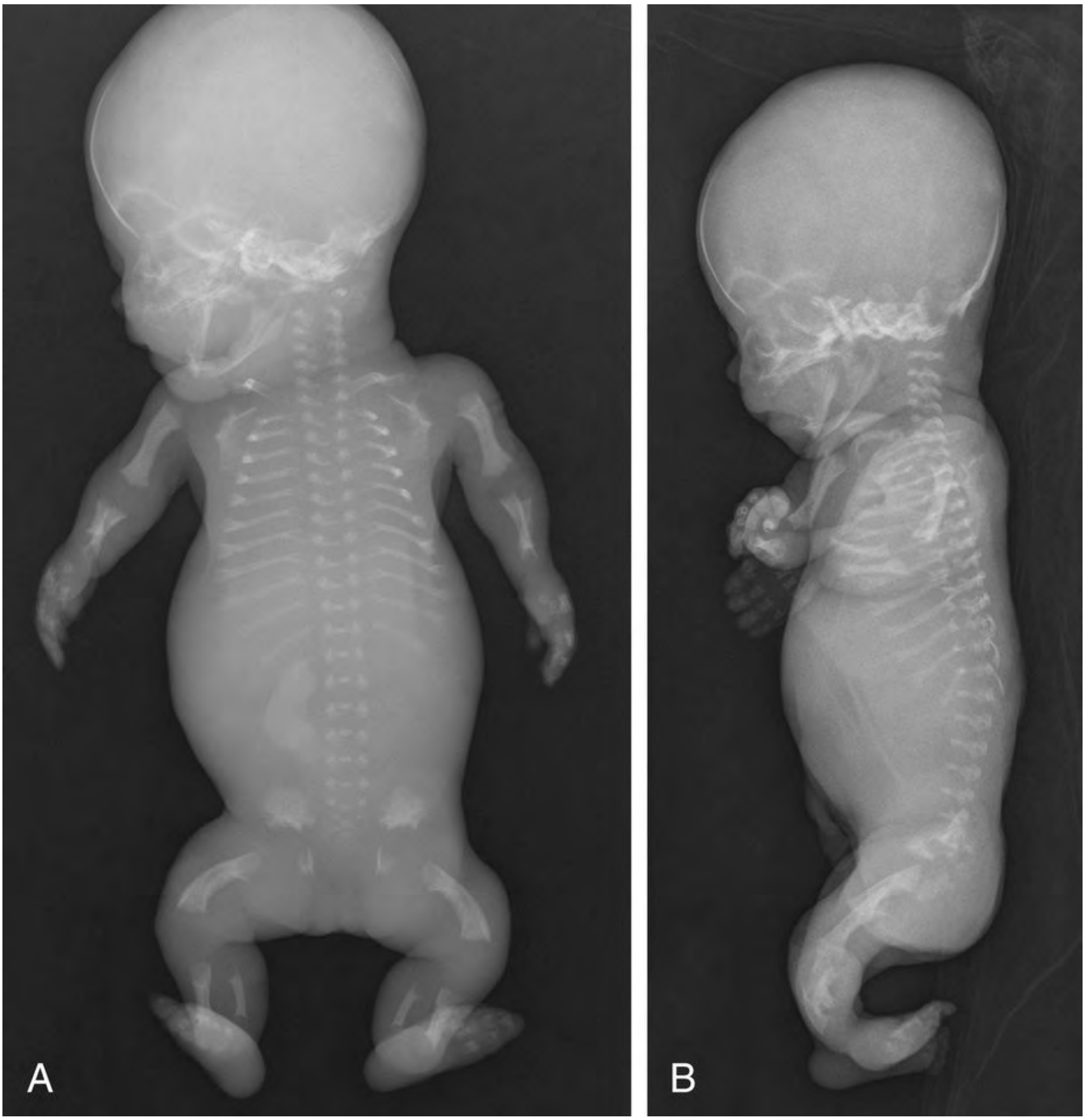
OI represents a group of eight different genetic disorders that result in the formation of abnormal type 1 collagen. In all types there is osteopenia and a propensity for fracture. The different types of OI range in severity from mild to severe. The more severe types are usually lethal in the prenatal period. Types I-V have an autosomal dominant mode of inheritance, whereas types VI-VIII are autosomal recessive. Patients with moderate to severe disease have evidence of multiple fractures of various ages. In such cases, other findings, such as osteopenia, should be clues to a diagnosis of OI rather than child abuse.

In moderate to severe cases there are thick tubular bones (Fig. 7-72) that result from the healing of multiple fractures, resulting in short-limb dwarfism. OI patients are commonly treated with bisphosphonate therapy to increase bone calcium deposition. Such therapy can result in a striking pattern of alternating sclerotic and lucent bands within the metaphyses of fast-growing bones. Multiple wormian bones (small ossicles along the cranial sutures) and thin skin are also commonly noted in association with OI (Fig. 7-73). Type I and III OI are associated with blue sclera.



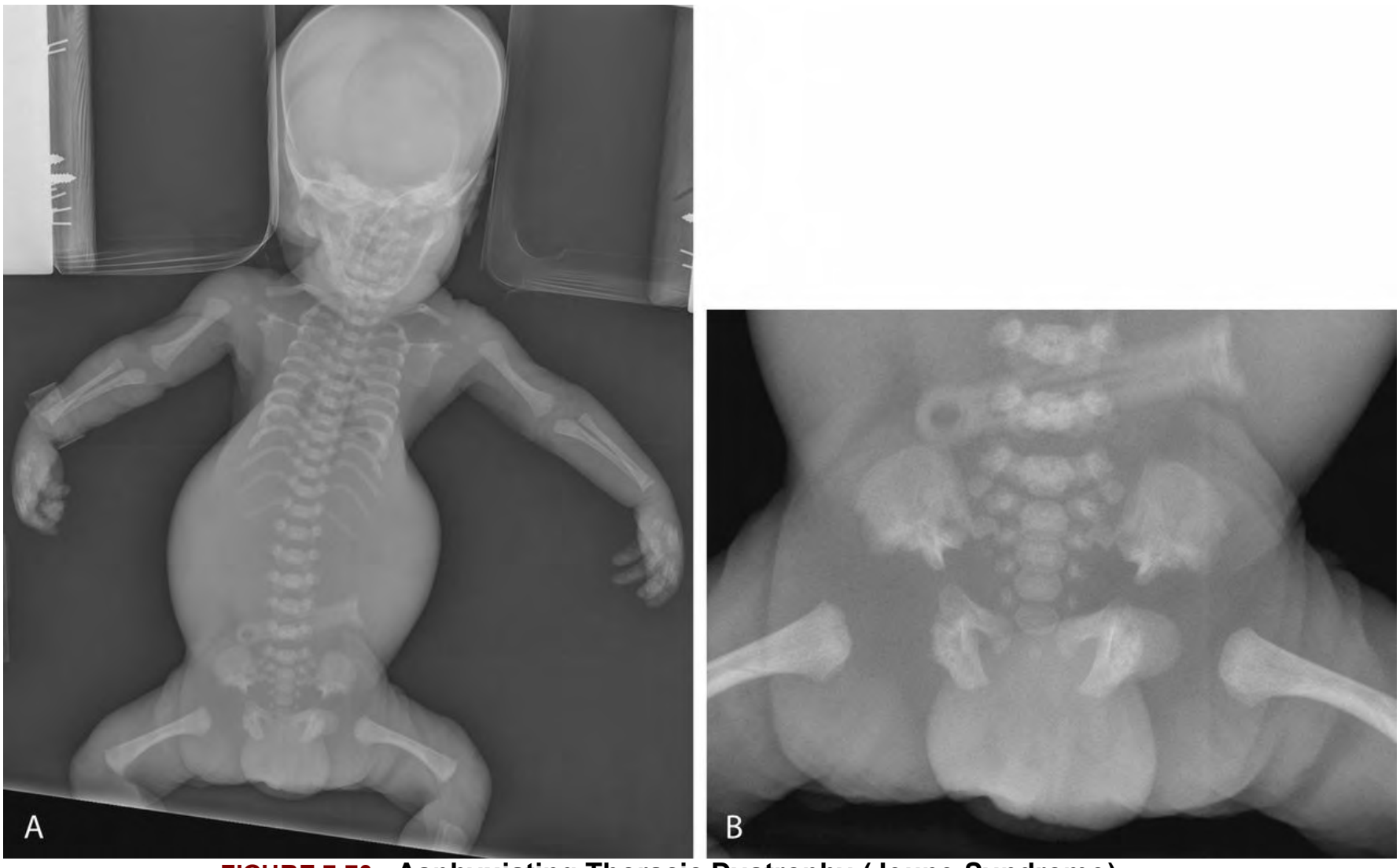
▪ **FIGURE 7-68** **Achondroplasia.**

A, AP radiograph of the lower extremities in a 25-year-old female shows shortened bones of the legs, affecting the femurs to a greater degree than the lower legs. In addition, there is metaphyseal flaring of all bones, shortened femoral necks, and relative overgrowth of the trochanters. **B,** AP view of the pelvis shows shortened iliac bones and horizontal acetabular roofs. **C,** AP view of the thoracic and lumbar spine shows narrowing of the interpedicular distance more inferiorly *(lines)*. **D,** Lateral view of the lumbar spine shows shortening of the pedicles *(arrow)*, making the spinal canal narrowed.



▪ FIGURE 7-69 Thanatophoric Dwarfism.

AP (**A**) and lateral (**B**) radiograph of a stillborn child show severe shortening of all long bones. The femurs are bowed and have a telephone receiver configuration. The lateral radiograph highlights the severe platyspondyly and shortened ribs.



▪ **FIGURE 7-70 Asphyxiating Thoracic Dystrophy (Jeune Syndrome).**
A, AP radiograph of a stillborn child shows severe shortening of the ribs. The abdomen seems to protrude due to the small size of the thorax. **B,** AP radiograph of the pelvis shows a trident configuration of the iliac bone around the acetabulum.

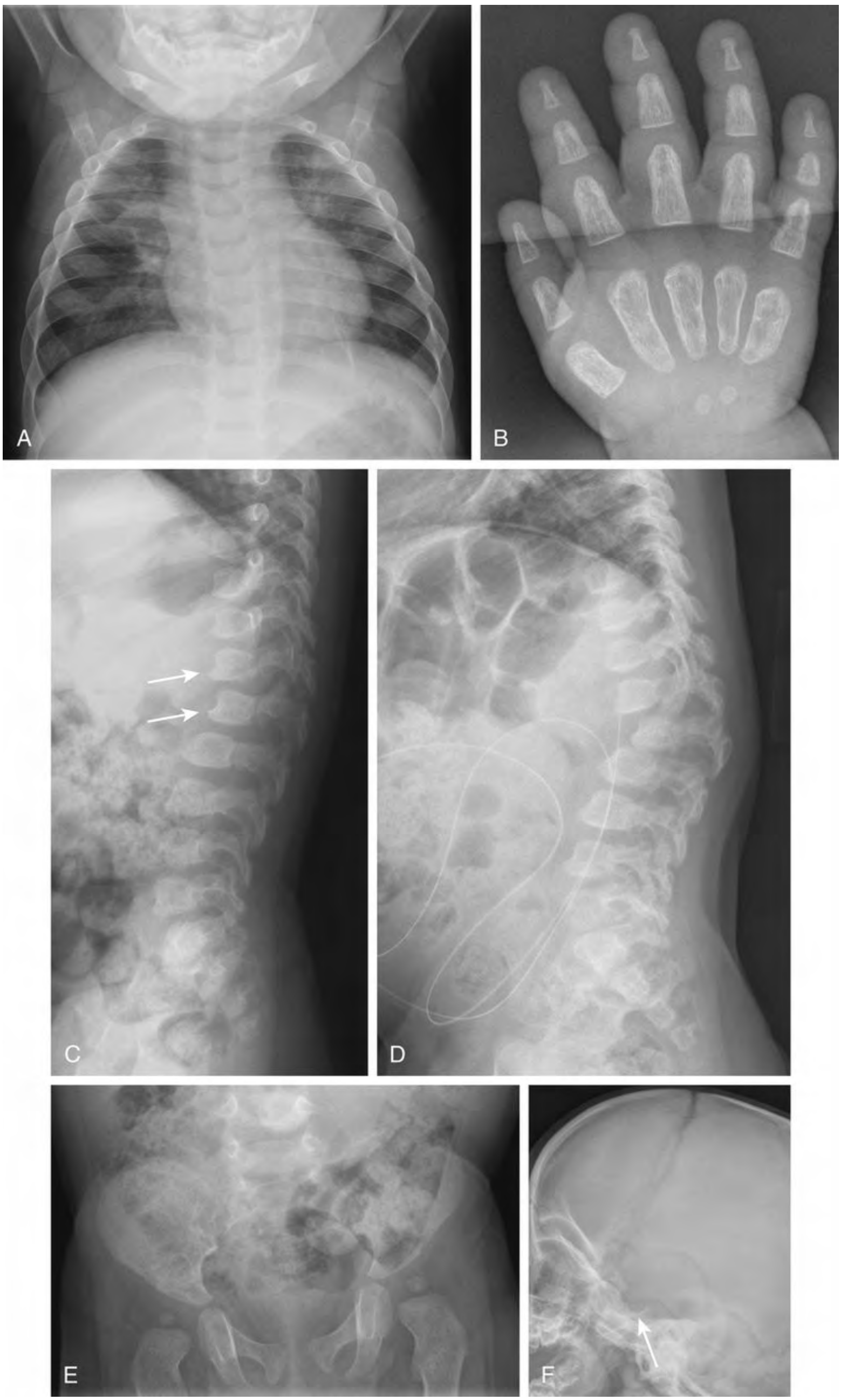
TABLE 7-5
Radiographic Manifestations of Several Skeletal Dysplasias

Dysplasia	Type of Extremity Shortening	Pelvis	Short Ribs	Spine	Enlarged Skull	Other
Achondroplasia	Proximal	Squared iliac wings Small sacroiliac notch Decreased acetabular angle (looks like tombstones)	Yes	Short vertebral bodies Narrow interpedicular distance	Yes	Metaphyseal flaring
Thanatophoric dysplasia	Proximal	Squared iliac wings Decreased acetabular angle Trident acetabulum	Yes	Platyspondyly	Yes	Early death Metaphyseal flaring "Telephone receiver" femurs
Chondrodysplasia punctata	Proximal	Normal	No	Stippled epiphysis	No	Stippled epiphyses
Asphyxiating thoracic dystrophy (Jeunc)	Distal	Decreased acetabular angle Trident acetabulum	Yes	Normal	No	Very short ribs Respiratory distress Metaphyseal irregularity and beaking
Chondroectodermal dysplasia (Ellis-van Creveld)	Distal	Decreased acetabular angle Trident acetabulum	Yes	Normal	No	Polydactyly, abnormal nails Congenital heart disease Amish community
Cleidocranial dysplasia	All	Squared iliac wings Decreased acetabular angle Widened pubic symphysis	No	Abnormal ossification	Yes	Absent or small clavicles Widened pubic symphysis Wormian bones
Camptomelic dysplasia	All	Tall, narrow iliac wings Increased acetabular angle	No	Ossification defects	Yes	Bowing of long bones (campto = bent limb) Airway obstruction

Osteopetrosis

Osteopetrosis is a rare bone disorder in which the osteoclasts are defective in resorbing and remodeling bone. As a result, bone is laid down and not resorbed. This results in dense bony sclerosis. There is often a bone-within-bone appearance on radiographs. The skull base is thickened and encroachment upon cranial nerves is a common complication. Although the total body calcium stores are increased, serum calcium levels are often paradoxically low, and radiographic findings of superimposed rickets are not uncommon. Lack of normal marrow space results in pancytopenia, which

often leads to complications and death.



▪ **FIGURE 7-71** **Hurler Syndrome.**

A, AP radiograph of the chest in a 1-year-old male with Hurler syndrome shows thickening of the ribs. The ribs are narrower in their posteromedial aspect. **B,** AP radiograph of the hand shows proximal tapering of the metatarsal bones. **C,** Lateral radiograph of the thoracolumbar spine shows anterior beaking along the inferior aspect of the T12 and L1 vertebral bodies *(arrows)*. **D,** Lateral radiograph of the spine obtained 1.5 years later shows a focal kyphosis at this location. **E**, AP radiograph of the pelvis shows tall and flared iliac wings with shallow acetabula. **F,** Lateral view of the base of the skull shows a J-shaped pituitary fossa *(arrow)*.



▪ **FIGURE 7-72** **Osteogenesis Imperfecta.**

AP radiograph of the chest (**A**) and lower extremities (**B**) in a newborn female shows multiple fractures of virtually every bone. Many of the fractures are healing, giving the bones a thickened appearance.



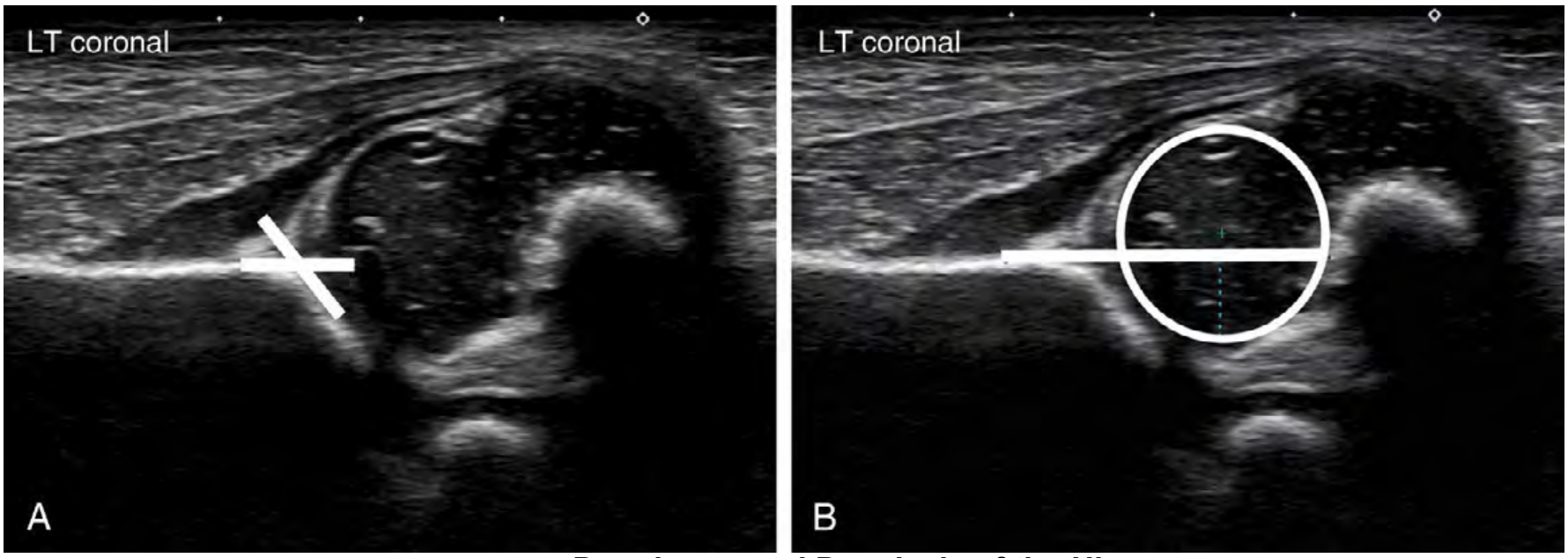
▪ **FIGURE 7-73** **Osteogenesis Imperfecta.**
AP (**A**) and lateral (**B**) radiographs of the skull show multiple wormian bones.

▪ Hip Disorders

There are a number of unique abnormalities that can involve the pediatric hip.

Developmental Dysplasia of the Hip

Development dysplasia of the hip (DDH), also previously referred to as congenital hip dislocation, refers to a condition related to abnormal development and configuration of the acetabulum and to increased ligamentous laxity around the hip. The cause is debated. DDH is much more common in females (in a ratio of as much as 9:1), in whites, and in children born in breech deliveries. One third of children with DDH are affected bilaterally. Clinical evaluation for DDH is part of routine neonatal screening. Neonates may demonstrate asymmetric gluteal folds, limited abduction, or a positive clunk felt on Ortolani (relocation) or Barlow (dislocation) maneuvers. If not detected and treated in infancy, DDH can lead to chronic abnormalities of the hip.

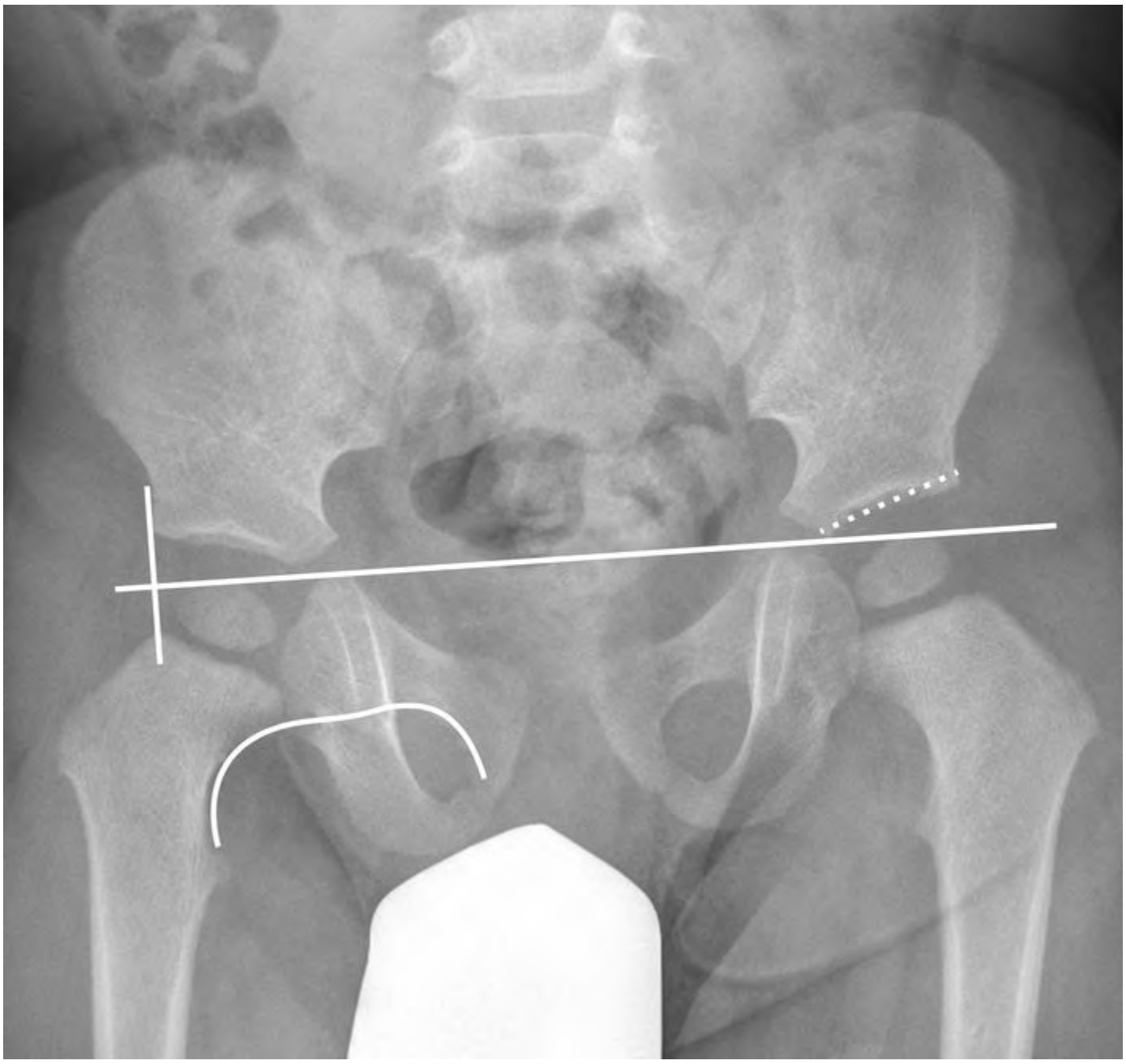


▪ **FIGURE 7-74** **Developmental Dysplasia of the Hip.**

A, Ultrasound of the left hip in a 2-week-old female shows a shallow acetabulum. The alpha angle, measured as the acute angle between the horizontal line of the iliac bone and the diagonal line of the acetabular roof is 55 degrees. **B,** Ultrasound of the left hip shows decreased coverage of the left hip. The line drawn along the iliac bone only covers 38% of the femoral head *(circle)*.

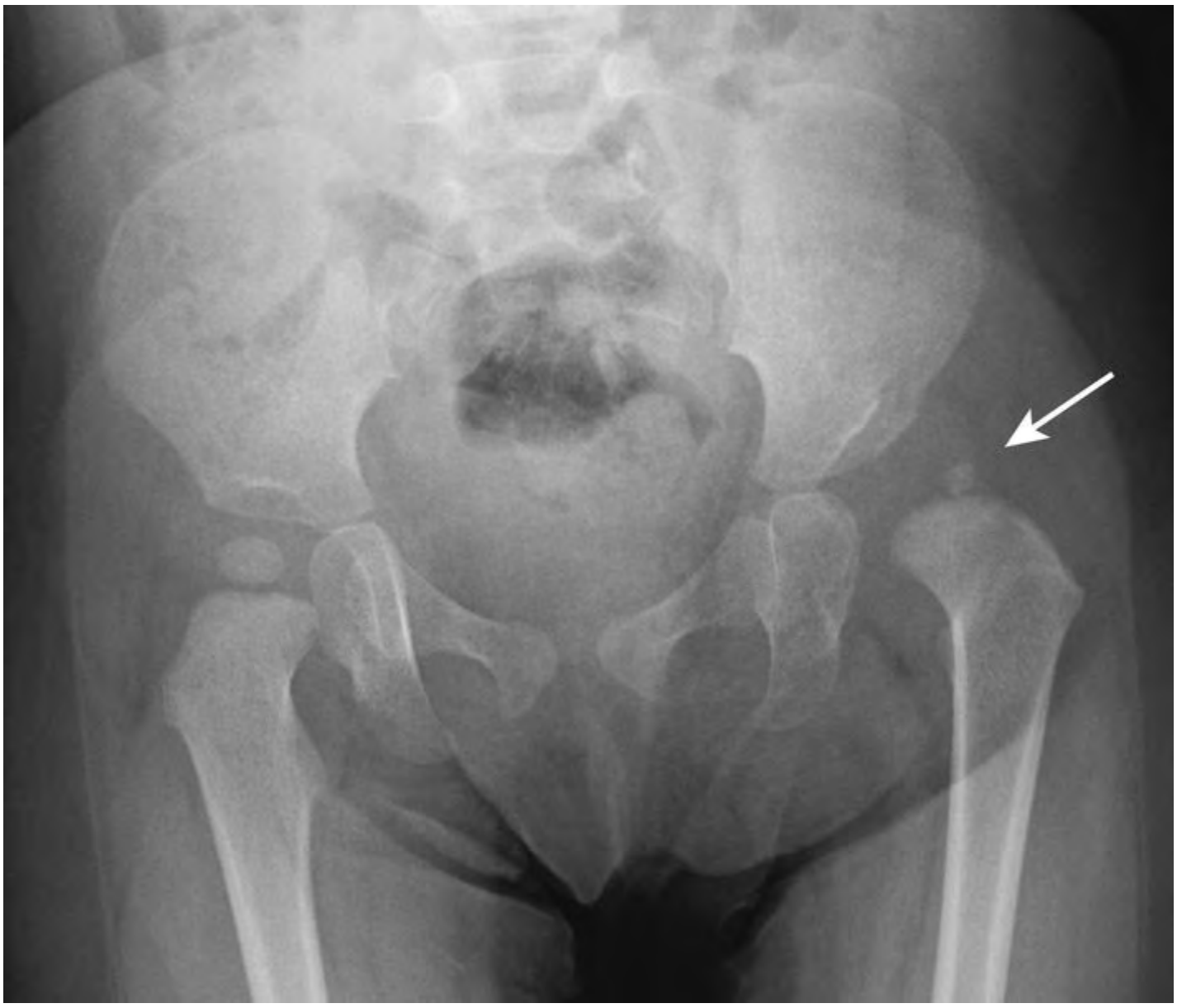
Ultrasound is used to evaluate the hips of infants who have clinical findings suggestive of DDH. Both the morphology of the acetabulum and any abnormal mobility of the hip are evaluated. Because there is physiologic ligamentous laxity during the first days of life, it is better to wait 2 weeks before performing hip ultrasound. The static morphologic evaluation is performed with the ultrasound probe coronal to the hip. Stress (Barlow) maneuvers are performed while evaluating the hip in the axial plane. On the static coronal view the anatomy simulates that seen on a frontal radiograph of the pelvis (Fig. 7-74). On such a view the iliac bone appears as a horizontal echogenic line on the right-hand side of the image. This line should bisect a nondislocated femoral head. A dislocated femoral head will be positioned posterior and lateral to the iliac line. The angle created between lines drawn along the straight part of the iliac bone and the acetabular roof form the alpha angle (see Fig. 7-74). Normally the alpha angle is greater than 60 degrees (55 degrees in newborns). In DDH the acetabulum is shallow, resulting in a decreased alpha angle on ultrasound, which correlates with an increased acetabular angle on radiographs (see subsequent material). A decreased alpha angle may be followed on repeat static ultrasound during therapy to evaluate for morphologic improvement.

DDH can also be evaluated by radiography. Radiographs are particularly useful after the femoral heads begin to ossify around 3 months of age, rendering ultrasound of limited value. In addition, it is important to know the radiographic findings of DDH so that such abnormalities may be identified when seen incidentally on other neonatal imaging studies that include the hips, such as abdominal radiographs. Because the femoral head and portions of the acetabulum are cartilaginous and not directly visualized on radiographs of the pelvis in the newborn period, landmarks are used to determine whether the hip is dislocated. With increasing age and ossification of the femoral head, direct visualization of a dislocated femoral head can be seen. Lines used to evaluate for DDH include the Hilgenreiner line, Perkin line, Shenton arc, and acetabular angle (Fig. 7-75). The **H**ilgenreiner line is a **h**orizontal line drawn through the bilateral triradiate cartilages, touching the inferior medial aspect of each acetabulum. A second line is then drawn connecting the inferior medial and superolateral aspects of the acetabulum, outlining the acetabular roof. The angle made between these two lines is the acetabular angle. Normally the acetabular angle is just less than 30 degrees at birth and decreases to 22 degrees at 1 year of age. With DDH, acetabular angles are abnormally increased. Another cause of increased acetabular angles is neuromuscular disorders. Abnormally decreased acetabular angles can be seen during the first year of life in Down syndrome and in multiple dysplasias, including achondroplasia (see Fig. 7-68, *B*). The vertical line of **Per**kin is drawn such that it is **per**pendicular to the Hilgenreiner line and traverses the superolateral corner of the acetabulum. When the femoral head is ossified and visible, it should lie medial to the Perkin line in the lower inner quadrant. When dislocated, the femoral head is usually in the upper, outer quadrant. When the head is not ossified, the Perkin line should bisect the middle third of the metaphysis. If the metaphysis is lateral to this position, the hip is subluxed or dislocated (Fig. 7-76). The Shenton arc is a continuous smooth arch connecting the medial cortex of the proximal metaphysis of the femur and the inferior edge of the superior pubic ramus. In DDH and dislocation, the arc is discontinuous (see Fig. 7-76).



▪ **FIGURE 7-75** **Normal Pelvis.**

AP radiograph of the pelvis in a 24-month-old male is used to highlight the normal lines of the pelvis. Hilgenreiner line is a horizontal line drawn connecting the triradiate cartilage. Perkin line is then drawn perpendicular to this line, starting from the lateral aspect of the acetabulum. The acetabular angle *(dashed line)* is calculated as the angle between Hilgenreiner line and the lateral margin of the acetabulum. Finally, Shenton arc is a continuous smooth arch connecting the medial cortex of the proximal metaphysis of the femur and the inferior edge of the superior pubic ramus.



▪ **FIGURE 7-76** **Developmental Dysplasia of the Hip.**
AP radiograph of the pelvis in a 14-month-old female shows left hip dysplasia. The left femoral head *(arrow)* is smaller and less mature than the right. In addition, the femoral head is subluxed superiorly and laterally, and the left acetabulum is shallow.

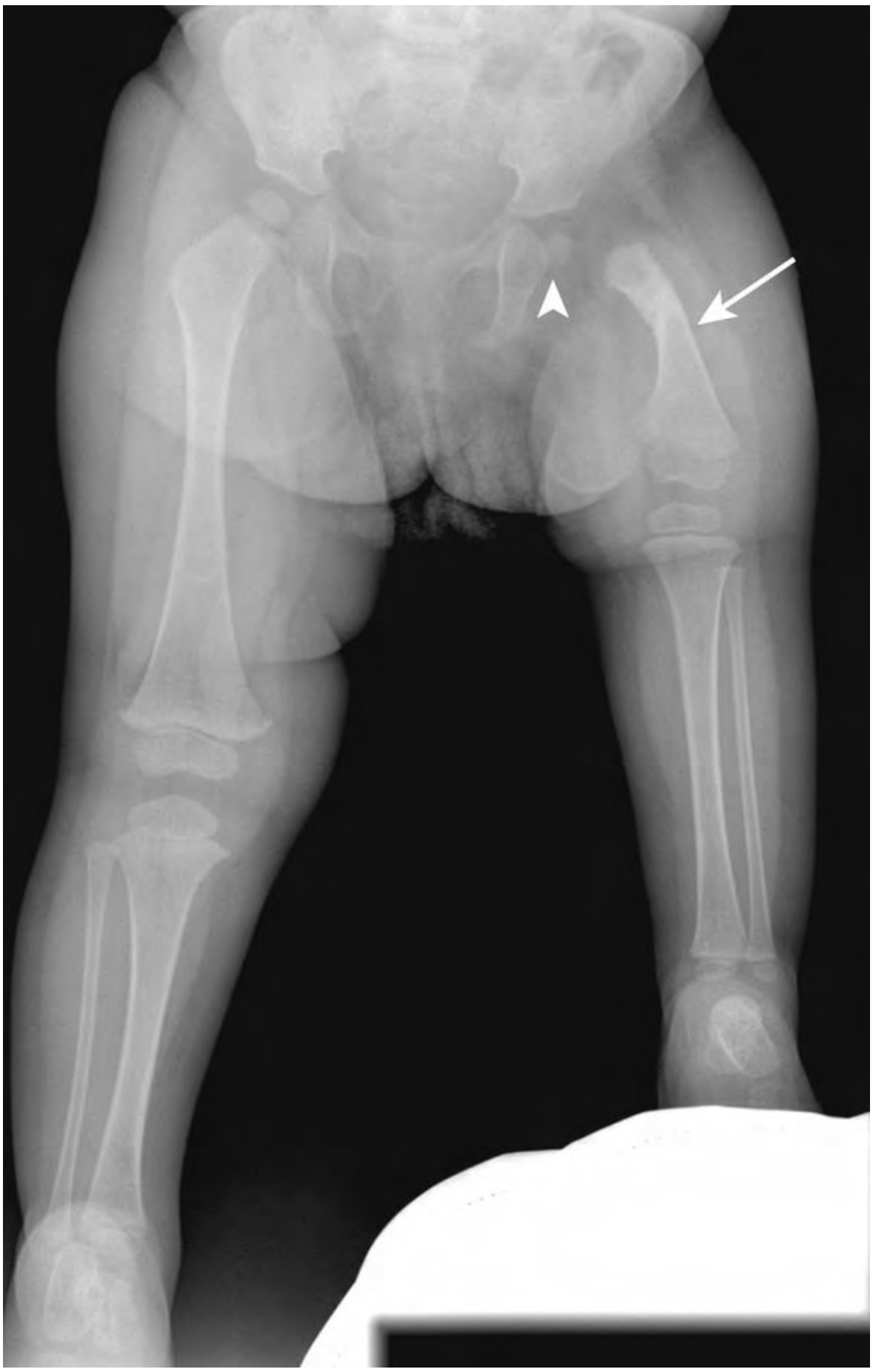


▪ **FIGURE 7-77** **Chronic Hip Dislocation.**
AP radiograph of the pelvis in a 20-year-old female shows chronic dislocation of both hips. The femoral heads are displaced superiorly and laterally and articulate with the iliac bones. The femoral heads are irregular and the femoral necks are shortened. The acetabula are flattened.

Chronic Hip Subluxation

In patients with neuromuscular disorders, such as cerebral palsy, development of progressive hip subluxation or dislocation may occur. Radiographs (Fig. 7-77) are used to evaluate how much the bony acetabulum covers the femoral head (percentage of coverage), degree of coxa valga (loss of angle

between the neck and shaft of the femur), and presence of complete dislocation.



▪ **FIGURE 7-78** **Proximal Focal Femoral Deficiency.**
AP radiograph of the lower extremities in a 14-month-old female show a shortened and irregular left femur *(arrow)*. The left femoral head *(arrowhead)* articulates with the acetabulum. There is a larger than expected nonossified section of the proximal femur, and the femoral diaphysis is bowed.

Proximal Focal Femoral Deficiency

Proximal focal femoral deficiency (PFFD) is a congenital disorder consisting of a range of hypoplasias to the absence of the proximal portions of the femur (Fig. 7-78). In its most severe form, the acetabulum, femoral head, and proximal femur may be absent. A varus deformity is commonly associated with the deficiency. It is important not to confuse the milder forms of PFFD with developmental dysplasia of the hip. In the latter the femur is of normal length. PFFD can be associated with ipsilateral fibular hemimelia and deformity of the foot.

Septic Arthritis

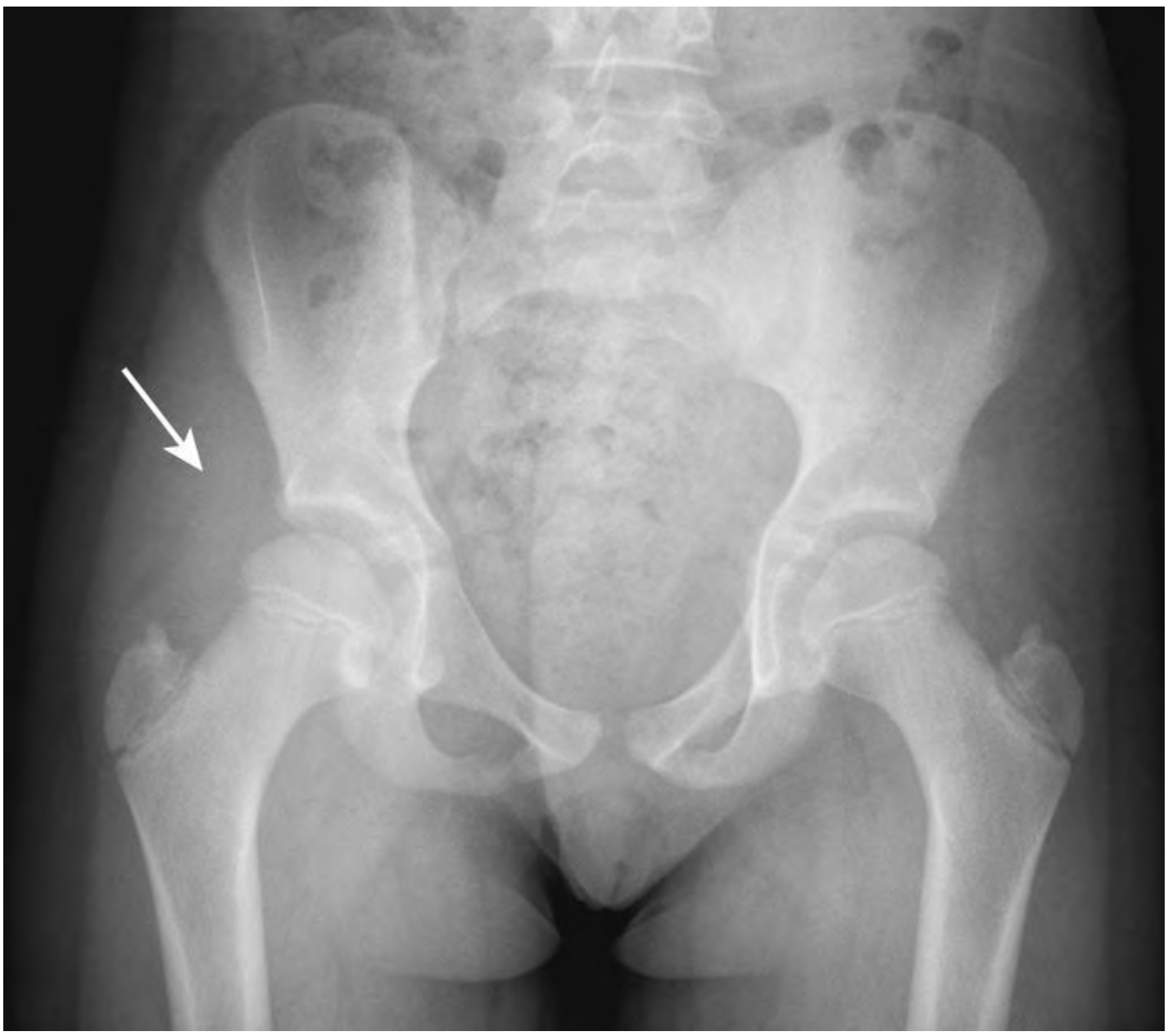
There are many potential causes of painful hips in children (Table 7-6). Many of these diagnoses present at specific ages, so the differential diagnosis can often be limited on the basis of age (see Table 7-6).

Septic arthritis is the most urgent diagnosis to exclude in a patient with a painful joint because delay in diagnosis can lead to destruction of the joint. In children, septic arthritis is thought to occur most commonly as a result of extension of infection from the adjacent metaphysis. In younger children it usually occurs secondary to bacterial sepsis, and the most common organisms are *S. aureus* (more than 50% of cases) and group A streptococci. Most cases of septic arthritis are monoarticular and involve large joints. The hip is the most common joint involved, followed by the knee.

TABLE 7-6

Potential Causes of Hip Pain in Children

Diagnosis	Typical Age at Presentation
Septic arthritis	Any age; most common in infants and teenagers
Toxic synovitis	<10 yr
Osteomyelitis	<5 yr
Langerhans cell histiocytosis	Any age, but pelvic bone involvement typically seen in those <5 yr
Slipped capital femoral epiphysis	12-15 yr
Legg-Calvé-PerthesLCP disease	5-8 yr
Juvenile rheumatoid arthritis	1-3 yr
Ewing sarcoma	Second decade
Osteoid osteoma	Second decade

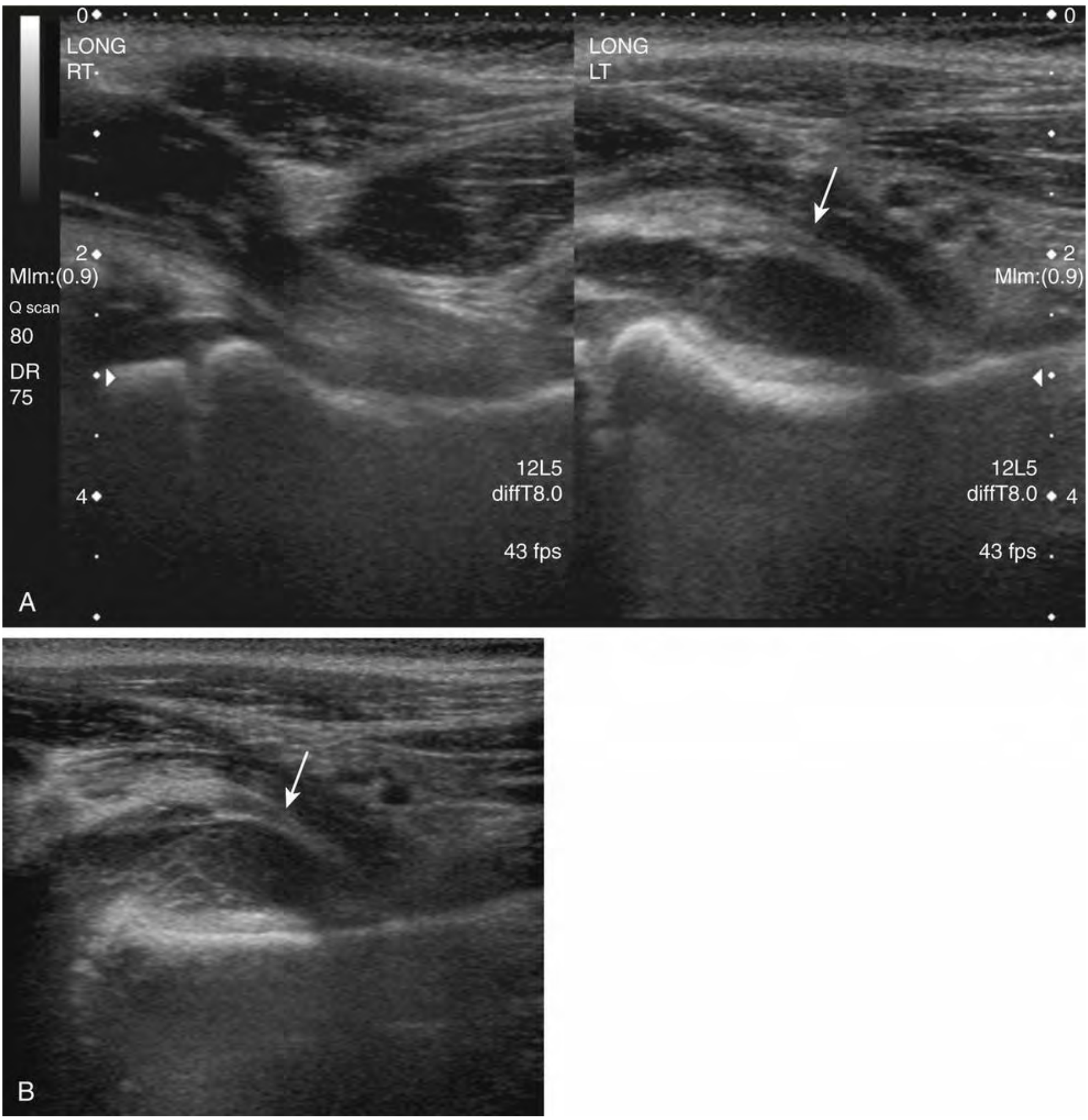


▪ **FIGURE 7-79** **Hip Effusion.**

AP radiograph of the pelvis in a 7-year-old female shows mild widening of the right hip joint space and obliteration of the fat plane *(arrow)* adjacent to the right femoral neck.

In septic arthritis of the hip, children usually present with pain, limp, or failure to bear weight. Radiographs of the pelvis and hips are usually obtained to exclude other diagnoses. The primary radiographic finding of septic arthritis is asymmetric widening of the hip joint space by more than 2

mm on a nonrotated film (Fig. 7-79). The joint spaces are evaluated by measuring the distance between the teardrop of the acetabulum and the medial cortex of the metaphysis of the femur. Unfortunately, this finding, although important when positive, is neither sensitive for a joint effusion nor specific for septic arthritis. Fluid tends to accumulate in the anterior recess of the hip joint before displacing the femur laterally. When septic arthritis is associated with osteomyelitis or another cause of soft tissue swelling, displacement or obliteration of the fat pads surrounding the hip may be noted. These include the obturator internus, gluteus muscle, and iliopsoas fat pads. Abnormalities of the fat pads are also neither sensitive nor specific. Therefore a normal pelvic radiograph in no way excludes a diagnosis of septic arthritis, and an abnormal radiograph does not cinch the diagnosis.

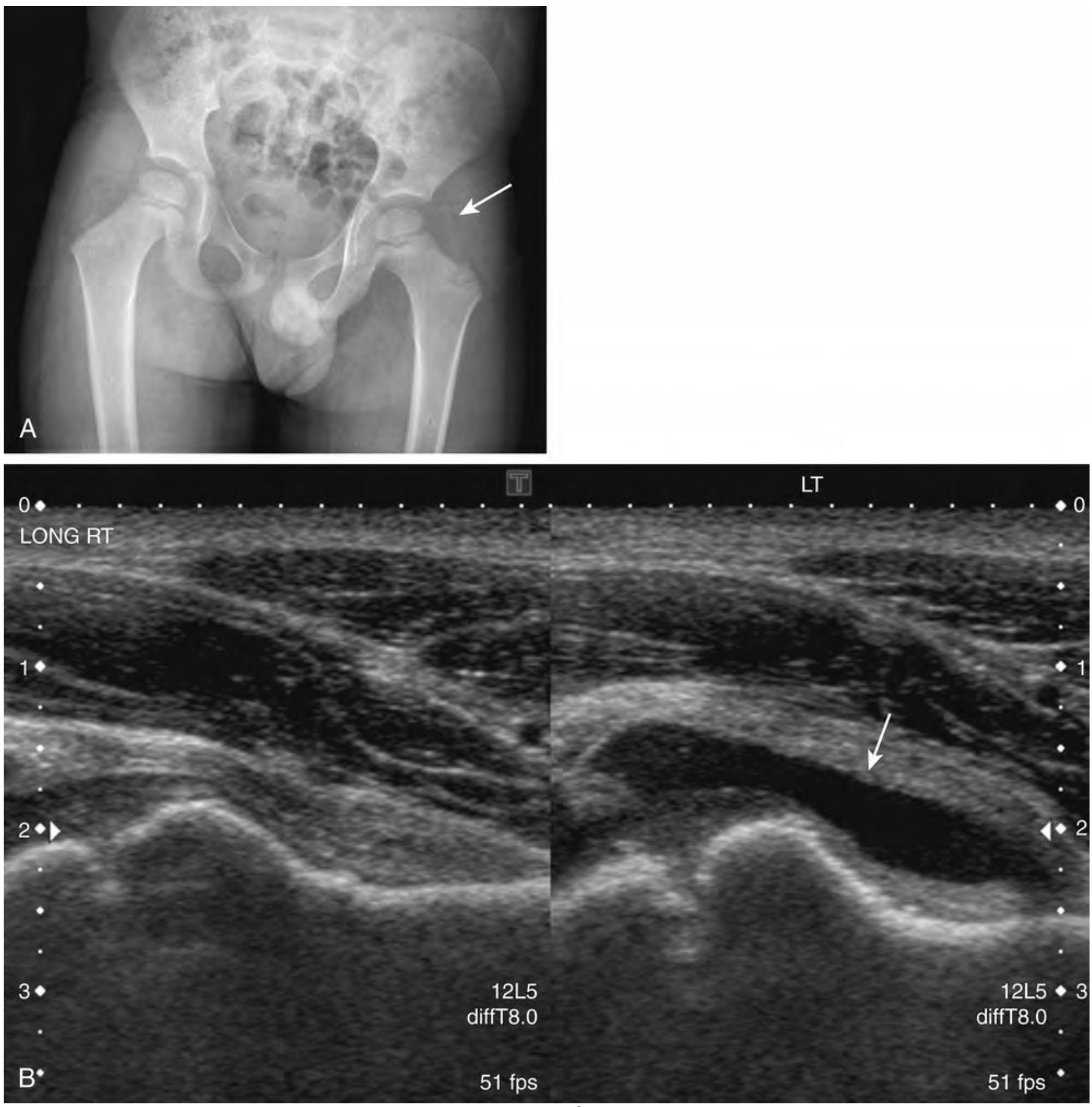


▪ FIGURE 7-80 **Septic Hip.**

A, Ultrasound of the right and left hip in a 3-year-old female show a left hip effusion *(arrow)* extending along the proximal femur. The synovium is thickened, and there is complexity of the effusion. **B,** Focused ultrasound of the left hip shows the complex left hip effusion. The fluid is echogenic, and there are multiple fine septations.

The presence of hip joint effusion can be evaluated by ultrasound. The probe is placed longitudinally, anterior to the hip joint. Asymmetric widening of a hypoechoic space between the shaft of the proximal femur and the joint capsule is diagnostic of a joint effusion (Fig. 7-80). The absence of fluid does

exclude a diagnosis of septic arthritis. When fluid is present, ultrasound guidance can be used to tap the effusion. There are causes of joint effusion other than septic arthritis. They include toxic synovitis, noninfectious arthritis, and Legg-Calvé-Perthes (LCP) disease.



▪ FIGURE 7-81 **Toxic Synovitis.**
A, AP radiograph of the pelvis in a 3-year-old male shows pelvic tilt with the left side down and bulging of the fat plane *(arrow)* adjacent to the left greater trochanter. **B,** Ultrasound of the right and left hip shows a moderate left hip effusion *(arrow)*.

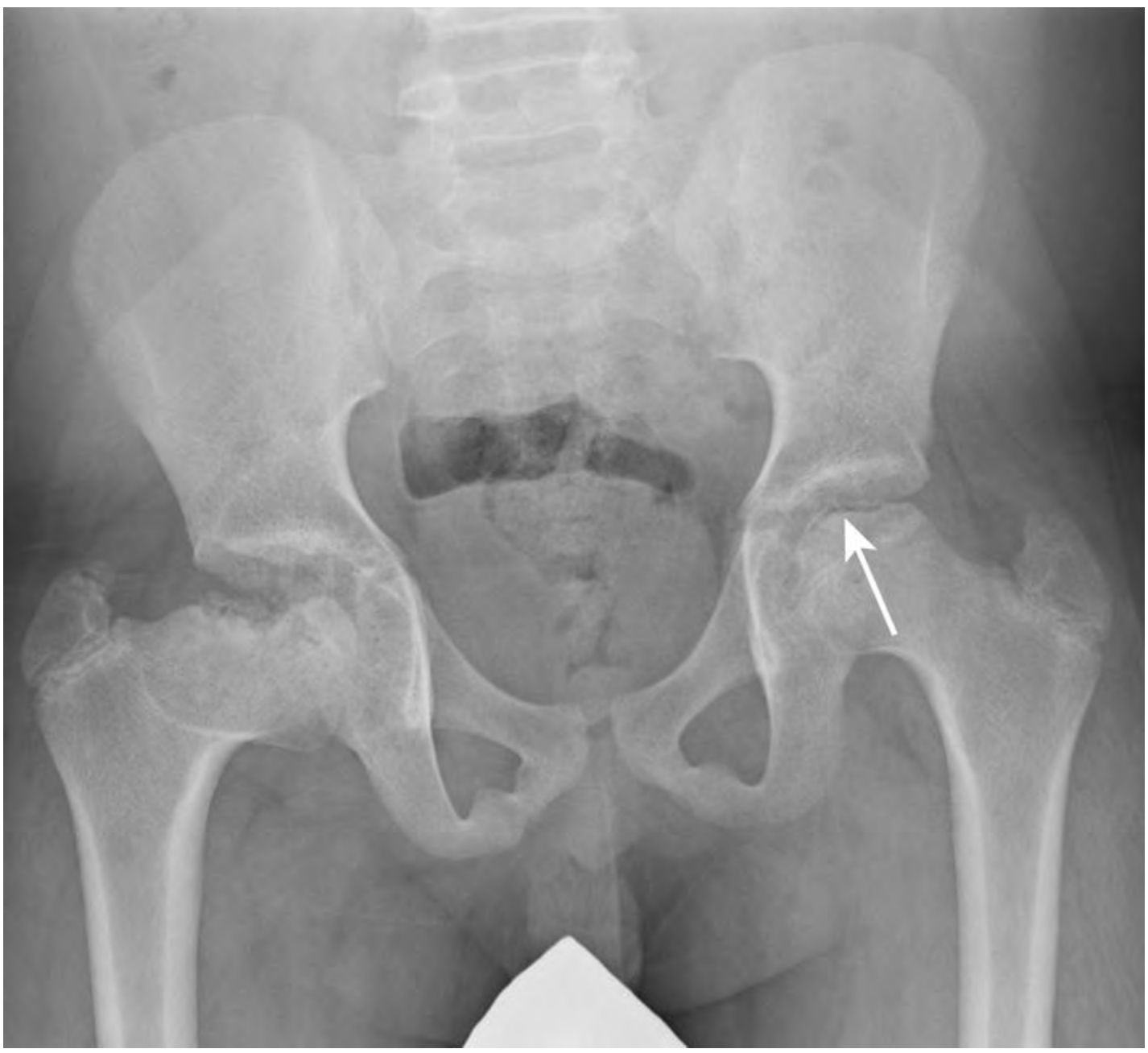
In the setting of suspected septic arthritis or osteomyelitis, many institutions have instituted a screening MRI examination with a wide field of view to identify the area of abnormality. A more focused examination is then performed in the abnormal area.

Toxic Synovitis

Toxic synovitis is the most common cause of acute hip pain in children younger than 10 years of age. It occurs most commonly in children between 4 and 7 years of age and typically follows an upper respiratory infection. Affected children present with pain or limping, have a joint effusion, have no findings of organisms in joint aspiration, and have symptoms that subside with rest (Fig. 7-81). It is a diagnosis of exclusion and is always in the differential diagnosis of septic arthritis.

Legg-Calvé-Perthes Disease

LCP disease is idiopathic avascular necrosis of the proximal femoral epiphysis. It occurs more commonly in boys than in girls (4:1), most commonly in whites, and typically between 5 and 8 years of age. Affected children present with pain in the groin, hip, or ipsilateral knee. The disease can be bilateral in as many as 13% of cases. It is often associated with skeletal immaturity (decreased bone age). Radiographs are usually positive, even early in the disease. Early findings include an asymmetric, small, ossified femoral epiphysis, widening of the joint space as a result of either joint effusion or synovial hypertrophy, and a subchondral linear lucency. The subchondral linear lucency (crescent sign) is best seen on frog-leg views and represents a fracture through the necrotic bone (Fig. 7-82). When the diagnosis is suspected and radiographs are nondiagnostic, the diagnosis of LCP can be made on MRI (high T2-weighted signal marrow edema, loss of fatty marrow signal on T1-weighted images, asymmetric decreased enhancement with gadolinium) or bone scintigraphy (asymmetric lack of uptake). Later changes in LCP include changes in the femoral epiphysis, such as fragmentation, areas of increased sclerosis and lucency, and loss of height (collapse; see Fig. 7-82). Lucencies may be seen in the adjacent metaphysis in as many as one third of patients. Chronic LCP may result in a broad, overgrown femoral head (coxa magna); a short, broadened femoral neck; and physeal arrest. Problems arise when the overgrown femoral head is not covered by the acetabulum, and this scenario may require surgical reconstruction of the acetabulum.

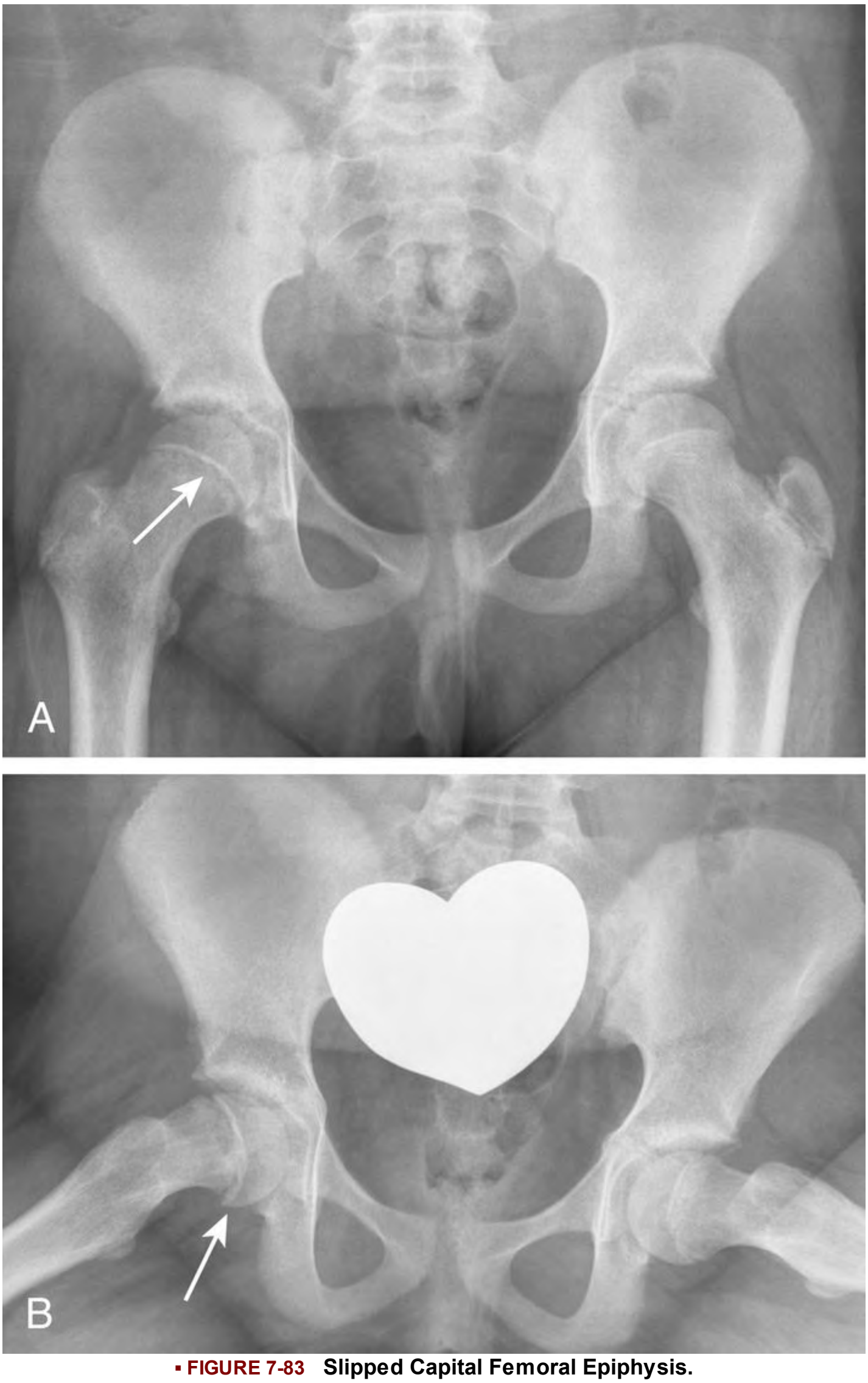


▪ **FIGURE 7-82 Legg-Calvé-Perthes Disease.**
AP view of the pelvis in a 10-year-old male shows advanced changes of bilateral LCP disease. There is a thin subchondral lucency *(arrow)* in the left femoral head. The underlying bone has already collapsed. There are severe destructive changes and collapse of the right femoral head.

Slipped Capital Femoral Epiphysis

SCFE is an idiopathic, Salter-Harris type 1 fracture through the proximal physis of the femur that results in displacement (slippage of the femoral epiphysis). It is more common in boys than in girls

(2.5:1), in African Americans, and in obese children. Certain groups, such as those with renal osteodystrophy, are predisposed. The hips can be involved bilaterally in up to one third of patients. However, both hips do not usually present at the same time. The typical age of diagnosis is 12 to 15 years.



▪ **FIGURE 7-83** **Slipped Capital Femoral Epiphysis.**
A, AP and view of the pelvis in a 13-year-old female shows asymmetric widening of the proximal femoral physis *(arrow)*. **B,** Frog-leg view shows medial displacement of the right femoral head *(arrow)* in relation to the femoral neck.

The slippage of the femoral head in SCFE is posterior and to a lesser extent medial. Because of this,

findings are more prominent on the frog-leg lateral view than on the frontal AP radiograph. On the frog-leg lateral view, the epiphysis is seen to be displaced in comparison to the metaphysis. The image has been likened to an ice cream cone with the dip of ice cream falling off the cone. A line drawn tangential to the lateral cortex of the metaphysis on the frog-leg lateral view should bisect a portion of the ossified epiphysis. If the physis is medial to this line, it has slipped. Findings of SCFE can be very subtle on the frontal view. They include asymmetric widening of the physis and indistinctness of the metaphyseal border of the physis (Fig. 7-83). SCFE is typically treated with pin fixation to prevent further slippage, but the epiphysis is not moved back to its normal position. Potential complications of SCFE include avascular necrosis of the femoral head and chondrolysis.



▪ **FIGURE 7-84** **Rickets.**

A, AP view of the right wrist in a 2.5-year-old female shows widening of the physes of the distal radius and ulna, as well as cupping and fraying of the distal metaphyses. **B,** The same changes are found about the knee.

▪ Metabolic Disorders

Rickets

Rickets is the bony manifestations of a heterogeneous group of problems resulting from a relative or absolute insufficiency of vitamin D or its derivatives. It may result from dietary deficiency, malabsorption, renal disease, or lack of end-organ response. The lack of vitamin D results in insufficient conversion of growing cartilage into mineralized osteoid and buildup of nonossified osteoid. The radiographic manifestations are most prominent in rapidly growing bones, and skeletal surveys to evaluate for rickets can be confined to frontal views of the knees and wrists. Radiographic findings include metaphyseal fraying, cupping, and irregularity along the physeal margin (Fig. 7-84). There is osteomalacia with unsharp, smudged-appearing trabecular markings. One of the more sensitive findings is loss of dense zone of provisional calcification. Patients may be predisposed to insufficiency fractures (Looser zones) and slipped capital femoral epiphyses.

Lead Poisoning

Lead poisoning most commonly occurs in children younger than 2 years of age secondary to consumption of lead-containing substances, such as old paint chips. The incidence of lead poisoning has decreased significantly since 1978, when lead paints were removed from the market. Findings of lead poisoning include broad sclerotic metaphyseal bands (lead lines) in areas of rapid growth, such as the knee (Fig. 7-85). Unfortunately, dense metaphyseal bands can be seen as a normal variant. One discriminating factor is that lead lines tend to affect all of the metaphyses surrounding the knee, whereas the normal variant type of dense bands tends to spare the proximal fibula. Other common entities that cause dense metaphyseal lines include chronic anemia, chemotherapy, growth arrest lines, treated leukemia, and bisphosphonate therapy.

▪ Miscellaneous Disorders

Scoliosis

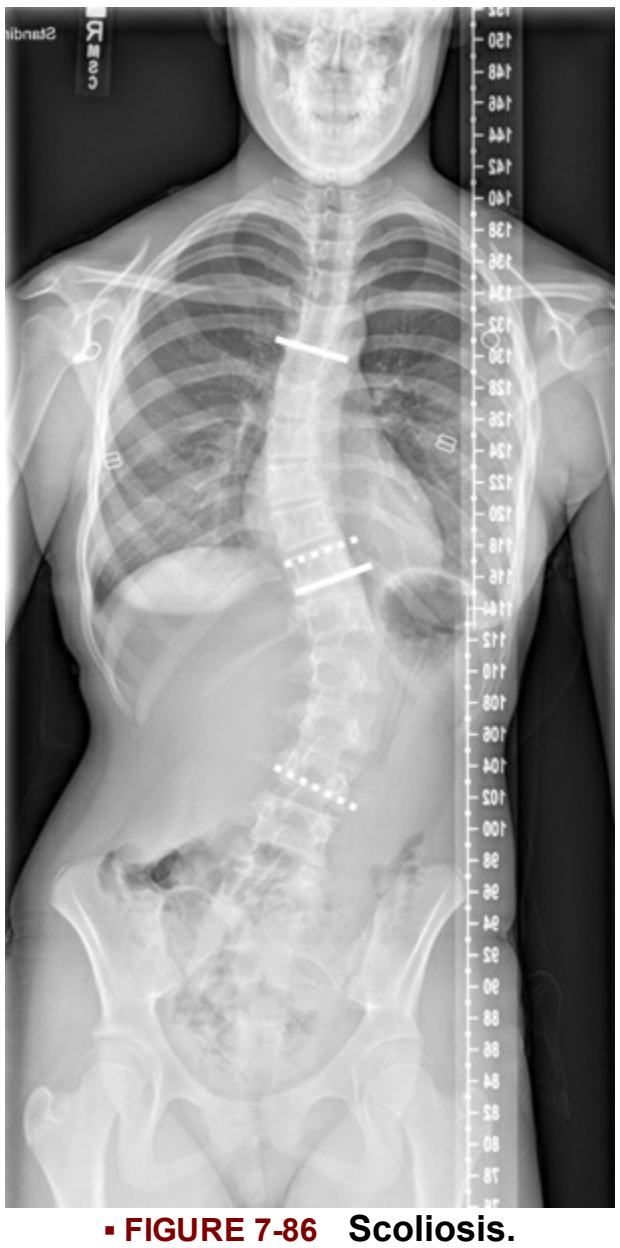
Scoliosis is defined as lateral curvature of the spine. Radiographic evaluation for spinal curvature after suspicion is raised on routine physical examination is a common occurrence in children. Most often, scoliosis is idiopathic in origin; the following discussion pertains to idiopathic scoliosis unless otherwise indicated. Idiopathic scoliosis is typically S-shaped, with the upper (thoracic) curvature convex to the right—a dextrocurvature. Congenital scoliosis occurs secondary to vertebral segmentation anomalies and is often associated with more abrupt short-segment curves than those found in idiopathic cases. Neuromuscular scoliosis results from neurologic impairment or muscular dystrophy and is typically C-shaped. Idiopathic scoliosis is usually identified in late childhood or adolescence and is 7 times more common in girls. In 80% of cases diagnosis is made between the ages of 10 years and maturity. The degree of curvature may change quickly during times of rapid growth, such as puberty. Severe scoliosis can be associated with respiratory compromise, neurologic symptoms, and pain.



▪ **FIGURE 7-85** **Lead Poisoning.**
AP radiograph of the right knee in an 18-month-old female with elevated lead levels shows dense metaphyseal lines of the femur *(arrows)*, tibia, and fibula.

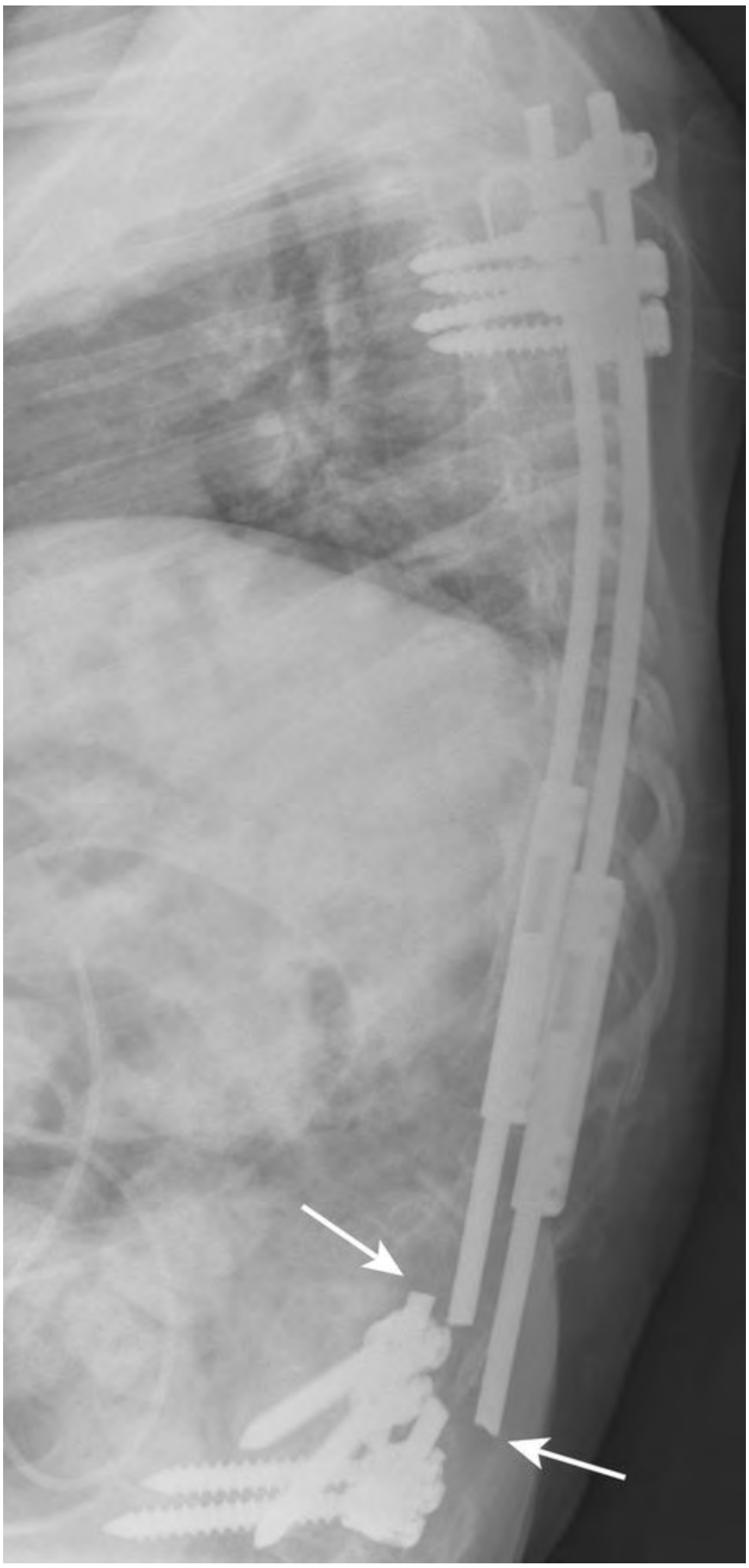
Radiographic evaluation is typically performed by means of a frontal view of the thoracolumbar spine. Studies are obtained with the patient standing (when possible) and in the posteroanterior projection to decrease the radiation dose to the breast. Depending on the situation, the frontal view may be complemented by a lateral view, bilateral bending views, or distraction views.

The curvature of the spine is measured by calculating the Cobb angle. Lines are drawn parallel to the end plates of two vertebral bodies, highlighting the greatest curvature (Fig. 7-86). The angle between those two lines represents the angle of curvature. Curves less than 10 degrees are considered normal. Curves less than 25 degrees are often treated by applying an external brace. Rapidly progressive curves or curves greater than 40 degrees are typically treated surgically with posterior spinal fusion.



▪ **FIGURE 7-86** **Scoliosis.**
AP radiograph of the spine in a 13-year-old female shows an S-shaped curvature of the spine. There is a 37-degree dextrocurvature from the superior end plate of T6 through the inferior end plate of T11 *(lines)* and a 42-degree levocurvature from the superior end plate of T11 through the inferior end plate of L3 *(dashed lines)*.

When reporting findings, it is important to note whether any vertebral anomalies are present, the degree of spinal curvature, any change in curvature compared with previous studies, and the Risser stage. Because the iliac crest apophysis matures in a predictable pattern from the lateral margin to the medial margin, the Risser stage can be used to define skeletal maturity. Risser stage 0 is the least mature and refers to an iliac crest apophysis that has not yet begun to ossify; Risser stages 1, 2, and 3 refer to an iliac crest in which the lateral 25%, 50%, and 75%, respectively, of the iliac crest apophysis have begun to ossify; Risser stage 4 occurs when the entire iliac crest apophysis ossifies; and finally, the most mature is Risser stage 5, when the iliac crest apophysis has fused to iliac wing. The Risser stage helps surgeons to plan the best time to operate because the more skeletally mature the patient, the less chance there is of further progression of the spinal curvature. In follow-up of postoperative cases it is important to evaluate the stability of the curve, as well as for fracture or change in position of hardware (Fig. 7-87).



▪ FIGURE 7-87 **Fractured Scoliosis Rods.**
Lateral view of the spine in an 11-year-old male with a history of scoliosis shows a fracture of the inferior aspect of the scoliosis rods bilaterally *(arrows)*.

Osteochondral Lesions

Osteochondral lesions, or osteochondritis dissecans, are lesions of adolescence and are typically seen in athletes. They most commonly occur in the lateral aspect of the medial femoral condyle (Fig. 7-88) but can also occur in the elbow (capitellum; Fig. 7-89) or ankle (Fig. 7-90). The defect can vary in size from a few millimeters to 1 to 2 cm depending on the location. Osteochondral lesions are often detected on radiographs obtained for joint pain. The lesions appear as a semicircular area of lucency and often have surrounding sclerosis or fragmentation. MRI can be important to help to determine stability of the lesion. Determinants of instability vary in children compared with adults but include fluid signal surrounding the lesion, multiple cysts, a large size, thick sclerotic margin, or a loose joint body. Treatment is often conservative because many lesions heal on their own. Surgical therapy is reserved

for unstable lesions, lesions that fail to heal with conservative therapy, and lesions in high performance athletes.

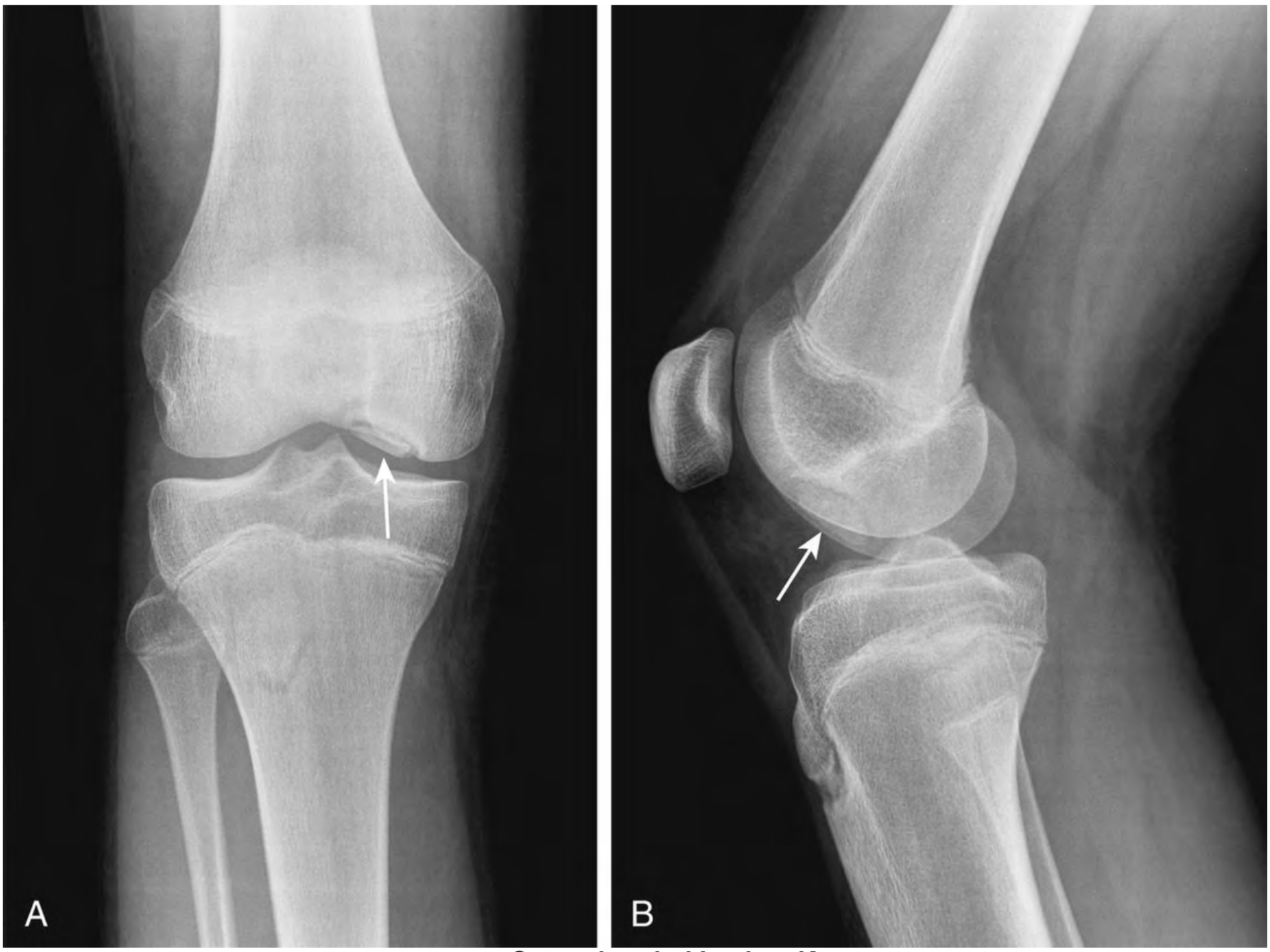
Panner Disease

Panner disease is an idiopathic avascular necrosis of the capitellum. It is distinguished from an osteochondral lesion by the patient's age and relation to activity. Panner disease typically occurs in children between 5 and 12 years of age; it is not associated with throwing sports. Osteochondral lesions are more common in patients 13 years of age and older and are usually a result of throwing sports. On radiographs Panner disease appears as irregularity and fragmentation of the capitellar ossification center (Fig. 7-91), similar to the appearance of the femoral head in LCP. An elbow effusion is not always present.

Abnormalities of Skeletal Maturity: Bone Age

Clinical indications for evaluating whether a child's skeletal maturity matches the child's true age include short stature, growth hormone deficiency, premature puberty, delayed puberty, and preoperative evaluation for orthopedic surgery (scoliosis, leg length discrepancy).

In such cases a single frontal view of the left hand is typically obtained and compared with a set of image standards (Greulich and Pyle). The degree of epiphyseal ossification is compared with the standards. The pattern of ossification of the more distal physes of the fingers is considered more accurate than the more proximal finger physes or carpal bones. When reporting such studies, the patient's chronologic age, gender, bone age based on the standards of Greulich and Pyle, calculated standard of deviation of bone age for chronologic age, and whether the bone age falls outside of two standard deviations (i.e., whether it is abnormal) should be included. Other methods of determining the bone age exist and may be useful for certain populations. For example, in the Sontag method, the number of ossification centers of the entire left upper and lower extremity are counted and compared to a standard. This method is useful in determining the bone age of infants and toddlers.



▪ **FIGURE 7-88** **Osteochondral Lesion, Knee.**

AP (**A**) and lateral (**B**) radiographs of the right knee show a large osteochondral lesion *(arrow)* of the lateral aspect of the medial femoral condyle. The lesion has an oval shape and is surrounded by a thin lucent rim and an outer sclerotic border.



▪ **FIGURE 7-89** **Osteochondral Lesion, Capitellum.**
AP radiograph of the elbow shows a semicircular lucency of the capitellum *(arrow)* with an irregular sclerotic border.



▪ **FIGURE 7-90** **Osteochondral Lesion, Talar Dome.**
AP radiograph of the ankle shows an oval ossific density *(arrow)* with a lucent border and a sclerotic rim in the medial aspect of the talar dome.



▪ **FIGURE 7-91** **Panner Disease.**

AP (**A**) and lateral (**B**) radiographs of the left elbow show irregularity and subchondral lucency of the capitellum *(arrow)*. A moderate elbow effusion is visible on the lateral view.

Juvenile Idiopathic Arthritis

Juvenile idiopathic arthritis (JIA) was formerly known as juvenile rheumatoid arthritis. JIA is an idiopathic systemic disease that affects primarily the musculoskeletal system. It differs from adult rheumatoid arthritis in many ways. In JIA most cases are seronegative, and the diagnosis is made clinically. In contrast to adult disease, in which small joint involvement predominates, large joint involvement is more common in children. The joints most commonly involved, in descending order, are the knee, ankle, wrist, hand, elbow, and hip. In most cases the disease is pauciarticular, with between two and four joints involved. Before development of radiologic findings, MRI with gadolinium enhancement may show abnormally enhancing thickened synovium, tenosynovitis, and a complex effusion (containing rice bodies or other debris) in involved joints. This may be used to aid in diagnosis and in monitoring therapy. Initial radiographs may be normal or may show only soft tissue swelling or joint effusion. With more advanced disease in the knee, there may be joint effusion, epiphyseal overgrowth, widening of the intracondylar notch, and accelerated bony maturation. There can be associated periosteal reaction. In the cervical spine there is often ankylosis of the apophyseal joints. When the hands and wrists are involved, the disease is typically most severe in the carpal bones (Figs. 7-92 and 7-93). Findings include small, square-appearing carpal bones and narrowing of the intercarpal joint spaces. Later changes include erosions, ankylosis, or subluxation. Children may also have splenomegaly or pleural effusions. Still disease is an acute form of JIA in which children present with fever, rash, hepatosplenomegaly, and lymphadenopathy. Skeletal involvement is rare in these children.

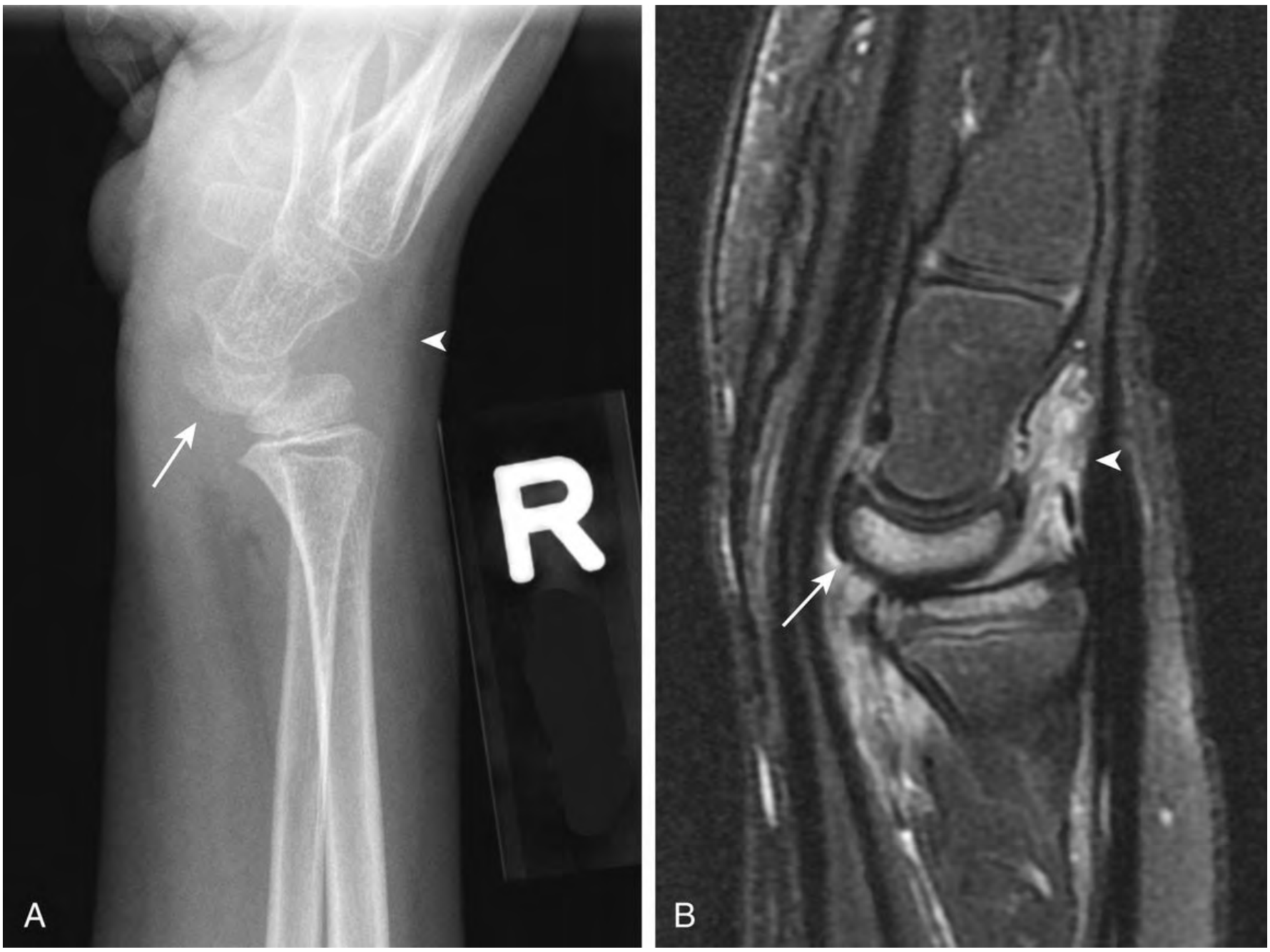
Hemophilia

With hemophilia, recurrent bleeding into a joint can result in a debilitating arthropathy. The joints

most commonly involved include (in decreasing order of frequency of occurrence) the knee, elbow, and ankle. The recurrent hemorrhage deposits hemosiderin within the synovium, and there is associated hypertrophy of the synovium and destruction of the underlying articular cartilage. On radiography, epiphyseal overgrowth may be seen particularly in the head of the radius (Fig. 7-94), and in the knee, there is often squaring of the margin of the patella and widening of the intracondylar notch. In more advanced disease, cartilage destruction, erosions, and subchondral cysts may be present. These findings can appear similar to those in JIA. On MRI there is destruction of articular cartilage and hypertrophy of the synovium. The hypertrophied synovium may be dark on T2-weighted images, secondary to the hemosiderin deposition (see Fig. 7-94), giving rise to an appearance similar to pigmented villonodular synovitis. Recurrent hematoma formation can also lead to the formation of pseudotumors, which usually occur in the soft tissues but can cause pressure necrosis and lucency of adjacent bone.



▪ **FIGURE 7-92** **Juvenile Idiopathic Arthritis.**
AP radiograph of the wrist in a 13-year-old female shows erosions of the distal radius, ulna, and carpal bones (*arrows* on some examples). The carpal bones have a jumbled appearance, making it difficult to identify all of the bones in proximal and distal carpal rows.



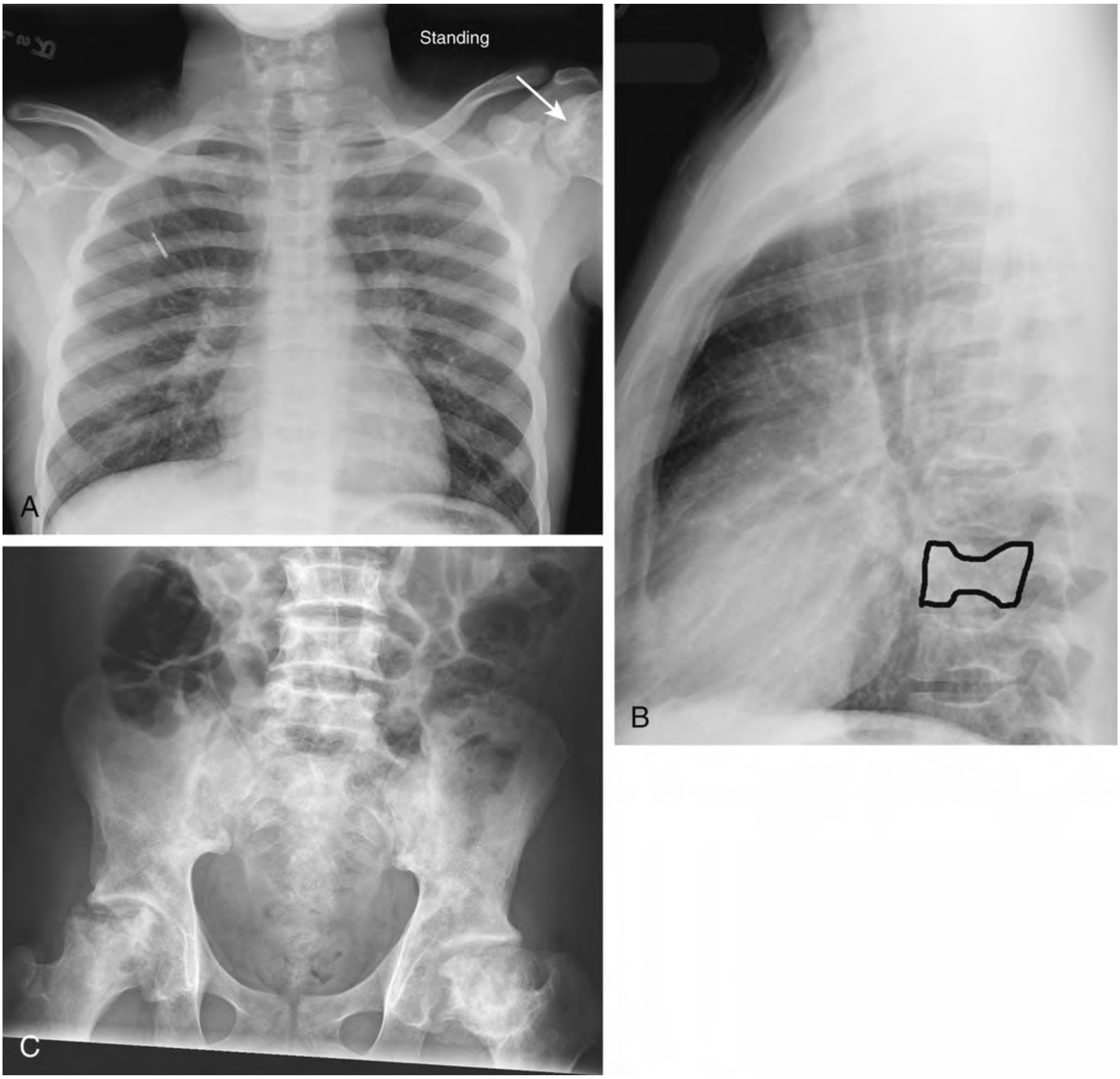
▪ **FIGURE 7-93** **Juvenile Idiopathic Arthritis.**

A, Lateral radiograph of the wrist in a 7-year-old female shows palmar subluxation of the wrist *(arrow)* and dorsal soft tissue swelling *(arrowhead)*. **B,** Sagittal T2-weighted MRI of the wrist also shows palmar subluxation of the wrist *(arrow)*. There is thickened synovium along the dorsum of the wrist *(arrowhead)*. The lunate and distal radius have abnormal signal.



▪ **FIGURE 7-94** **Hemophilia A.**

AP (**A**) and lateral (**B**) radiographs of the elbow in a 21-year-old male show overgrowth of bones about the elbow. This is most pronounced in the head of the radius *(arrow)*. In addition, the joint space is narrowed, the intercondylar notch is widened and deepened, and there are erosions and subchondral cysts of the capitellum. **C,** Sagittal proton density MRI with fat saturation shows overgrowth of the head of the radius *(arrows)*, darkened, hypertrophied synovium *(arrowheads)*, and marrow signal abnormality.



▪ **FIGURE 7-95** **Sickle Cell Anemia.**

A, AP radiograph of the chest in a 21-year-old male shows mild thickening of the ribs, sclerosis in the left humeral head *(arrow)* from avascular necrosis, and an H-shaped configuration of the vertebral bodies. **B,** The H-shaped vertebral bodies are better seen on the lateral view of the chest (example outlined). **C,** AP view of the pelvis shows chronic changes of avascular necrosis of both hips with flattening and sclerosis of both hips, and subchondral cysts. Overall, the bones are sclerotic with coarsened trabeculae.

Sickle Cell Anemia and Thalassemia

With severe causes of anemia, such as sickle cell anemia or thalassemia, skeletal changes related to marrow expansion may be seen on radiography. Findings include thinning of the cortex, coarsening of the trabeculae, and bony remodeling (Fig. 7-95). The ribs appear widened. In the skull the diploic space can become widened and have a hair-on-end appearance, particularly with thalassemia. In sickle cell anemia there are often areas of bone infarction that may appear as either sclerotic or lucent areas. The vertebral bodies in sickle cell anemia often demonstrate indented and flat portions of the superior and inferior end plates, giving the vertebral bodies a "Lincoln log" or H-shaped appearance (see Fig. 7-95).

With severe anemia, other imaging findings may include cardiomegaly, gallstones, and splenomegaly (or conversely, in sickle cell anemia there may be autoinfarction of the spleen and a small, calcified spleen). Extramedullary hematopoiesis and a predisposition to osteomyelitis may also be noted.



▪ **FIGURE 7-96** **Radial Dysplasia.**
Lateral radiograph of the right (**A**) and left (**B**) forearm in an 11-month-old male shows an absent right radius and a hypoplastic left radius *(arrow)*. Both ulnas are thickened and bowed with their apex directed dorsally. Note that the distal ulna is much wider than normal because it forms the primary articulation at the wrist.

Radial Dysplasia

Radial dysplasia, often referred to as radial ray syndrome, refers to a variable degree of hypoplasia or aplasia of the radius (Fig. 7-96). Often the first metatarsal or thumb may be hypoplastic or absent as well. Radial ray syndrome may be seen in conjunction with a number of syndromes, including association with VATER complex, Holt-Oram syndrome, Fanconi anemia, and thrombocytopenia-absent radius syndrome.

Blount Disease

Blount disease is excessive medial bowing of the tibias (tibia vara), most commonly occurring during infancy. It is an idiopathic disease but is thought to be related to excessive pressure on the medial metaphysis of the tibia, resulting in delayed endochondral ossification. It can be differentiated from physiologic bowing of the tibias by both the degree of angulation and the appearance of the medial metaphysis of the tibia. With Blount disease there is irregularity, fragmentation, and beaking of the medial tibial metaphysis (Fig. 7-97). Severe cases may require tibial osteotomy.

Neurofibromatosis

The nonmusculoskeletal aspects of neurofibromatosis type 1 are discussed in Chapter 8. Many changes

can occur in the bones of patients with this disorder, and most of them are thought to be related to mesodermal dysplasia. The bones may demonstrate overgrowth, bowing, areas of sclerosis, and numerous cortical defects. Characteristic findings include anterolateral tibial bowing (Fig. 7-98), pseudoarthrosis formation (commonly within the tibia and/or fibula), and twisted-appearing (ribbonlike) ribs. The vertebral bodies may demonstrate posterior scalloping due to either dural ectasia or multiple neurofibromas. There is often kyphoscoliosis.

Clubfoot (Talipes Equinovarus)

Talipes equinovarus, or clubfoot, refers to a common congenital abnormality of the foot. In order to understand both clubfoot and other congenital abnormalities of the foot, it is important to understand the descriptive terminology. The terms *valgus* and *varus* refer to the bowing of the shaft of a bone and bowing at a joint. The name given to the bowing is determined by whether the distal part is more lateral or medial than normal. *Valgus* refers to lateral (think the L in valgus stands for lateral) and *varus* refers to medial. In hindfoot varus the distal bone of the hindfoot (calcaneus) is angled too far medially in relationship to the more proximal bone of the hindfoot (talus), as seen on the AP view of the foot (Fig. 7-99). Normally this angle is approximately 30 degrees. With clubfoot this angle is decreased. In addition, on the lateral view of the foot, the lateral talocalcaneal angle is normally approximately 30 degrees. With clubfoot there is a decrease in the lateral talocalcaneal angle, with the talus and calcaneus being closer to parallel to each other. This same terminology is used to describe other parts of the body as well. Therefore genu varum is the bowing of the knee, with the distal part (tibia) being more medial than normal, and coxa valgus is bowing at the hip, with the distal part (femur) being more lateral than normal.



▪ **FIGURE 7-97** **Blount Disease.**
AP radiograph of the right (**A**) and left (**B**) lower extremity in a 16-year-old male shows excessive medial bowing of the tibias and beaking *(arrow)* of the medial tibial metaphyses.



▪ **FIGURE 7-98** **Neurofibromatosis Type 1.**
AP (**A**) and lateral (**B**) radiograph of the left tibia and fibula in a 5-year-old female shows anterolateral tibial bowing characteristic of neurofibromatosis type 1.

The terms *equinus* and *calcaneus* refer to the relationship between the ankle (tibia) and hindfoot (calcaneus) as viewed on a lateral radiograph. Equinus is fixed plantar flexion of the calcaneus (distal end pointing down, as a deer walks), and calcaneus is fixed dorsiflexion (distal end of the calcaneus pointing up). With clubfoot, or talipes equinovarus, there is hindfoot varus, hindfoot equinus, and forefoot varus. Normally a line drawn through the long axis of the talus on an AP view of the foot passes through the midsection to the medial section of the metatarsal bones. With forefoot varus the distal bones (the metatarsals) are located more medial to this drawn line.

Tarsal Coalition

Tarsal coalition is an abnormal fibrous or bony connection between two of the tarsal bones of the feet. Patients with tarsal coalition can present with chronic foot pain or a propensity for ankle injury. It is a common abnormality affecting approximately 1% of the population and usually presents during adolescence. Although there is debate concerning which of the tarsal coalitions is the most common, talocalcaneal and calcaneonavicular coalitions are by far more common than other types. More than half of cases are bilateral. Calcaneonavicular coalition is easily demonstrated on radiographs of the

foot. It is best visualized on the oblique view, in which the direct connection (bony coalition) or close proximity and irregularity of the joint margins (fibrous coalition) of the calcaneus and navicular bones (Fig. 7-100) is best depicted. On the lateral view the anterior superior calcaneus appears longer than normal as it extends toward the navicular bone. The appearance has been likened to an anteater's nose. Rarely, cross-sectional imaging may be needed to confirm the diagnosis. In contrast, findings of talocalcaneal coalition can be subtle on radiography, and CT is performed to make the diagnosis. Radiographic findings include secondary signs, such as talar beaking, poor visualization of the space within the talocalcaneal joint, and a prominent C-shaped band of overlapping bone overlying the calcaneus (Fig. 7-101). On the lateral view, if space can be seen within the talocalcaneal joint, talocalcaneal coalition is not present. However, this space may not be seen within a normal joint on an oblique film. On coronal (short-axis) CT images, talocalcaneal coalition is visualized as bony fusion or irregularity and close proximity (fibrous coalition) between the middle facet of the talus and the sustentaculum tali of the calcaneus. Treatment options include surgical excision of the coalition.



▪ **FIGURE 7-99** **Clubfoot.**

A, AP radiograph of the foot in a 16-month-old-male shows hindfoot varus. **B,** Lateral radiograph of the foot shows a near parallel configuration of the talus and calcaneus.



▪ **FIGURE 7-100 Calcaneonavicular Coalition.**

A, Oblique radiograph of the foot in a 16-year-old male shows close proximity and irregularity of the joint margins of the calcaneus and navicular bones *(arrow)*. **B,** Lateral radiograph shows elongation of the anterior process of the calcaneus *(arrow)*.



▪ **FIGURE 7-101** **Talocalcaneal Coalition.**
Lateral view of the hind foot in a 16-year-old male shows the C sign *(arrows)* with no visible talocalcaneal joint.

▪ Disorders Affecting Primarily Soft Tissues

Vascular anomalies

Vascular malformations and hemangiomas can cause significant morbidity and even mortality in both children and adults. For a number of reasons, there is often confusion regarding these lesions. The classification of and nomenclature used to describe endothelial malformations have been a source of confusion. Historically, lesions were named according to the sizes of channels within the lesions and the type of fluid the lesion contained. Blood-containing lesions were called hemangiomas, and lymph-containing lesions were referred to as lymphangiomas or cystic hygromas. This classification system was replaced by one described in 1982 by Mulliken and Glowacki, which separated endothelial malformations into two large groups, hemangiomas and vascular malformations, on the basis of their natural history, cellular turnover, and histology. More recently, the International Society for the Study of Vascular Anomalies published a revised classification system. This classification scheme recognizes two main classes of vascular anomalies: vascular tumors and vascular malformations (Table 7-7).

TABLE 7-7
Classification of Vascular Anomalies with Common Examples

Vascular Tumors
1. Benign and/or reactive
a. Infantile hemangioma
b. Rapidly involuting congenital hemangioma

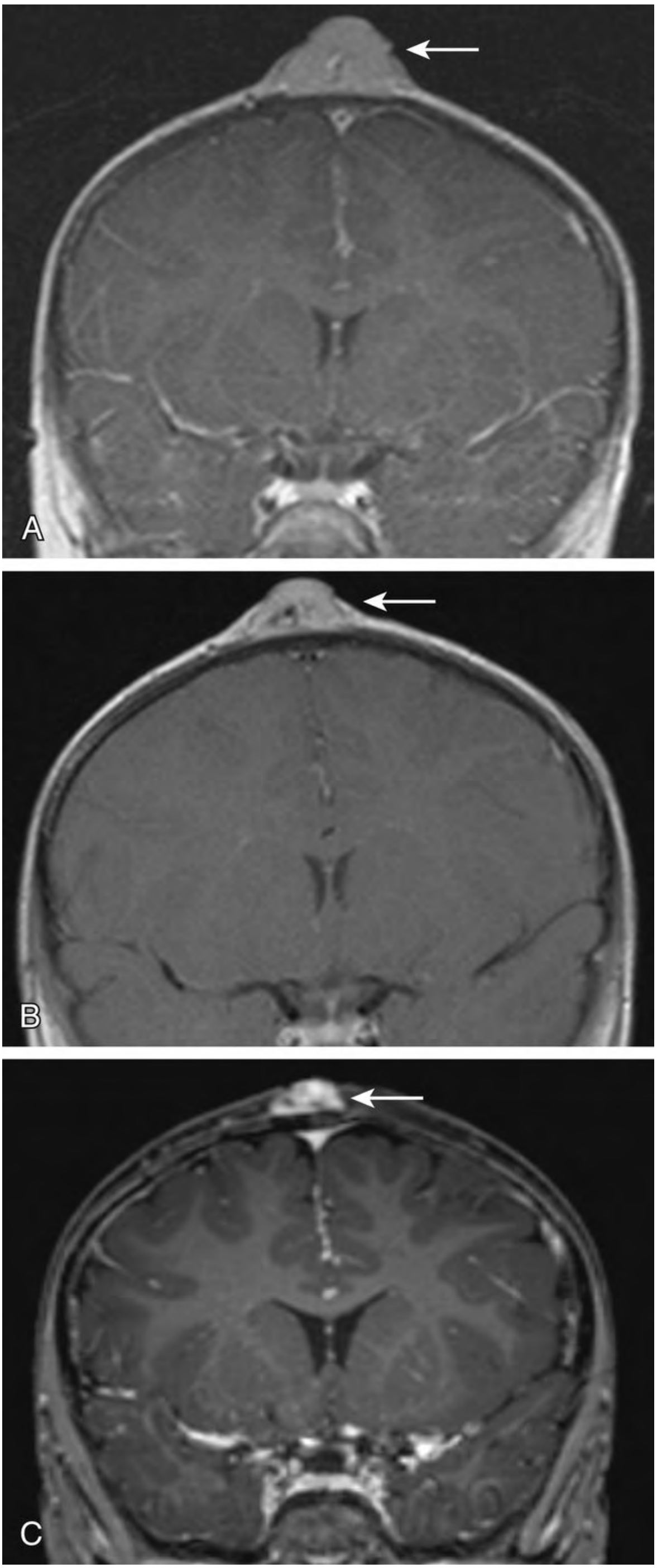
c. Noninvoluting congenital hemangioma
2. Locally aggressive
a. Kaposiform hemangioendothelioma
b. Retiform hemangioendothelioma
c. Kaposi sarcoma
3. Overtly malignant
a. Angiosarcoma
b. Epithelioid hemangioendothelioma

Vascular Malformations

1. Simple malformations
a. Capillary malformation
b. Lymphatic malformation
c. Venous malformation
d. Arteriovenous malformation
2. Combined malformations
3. Malformations of named vessels
4. Malformations associated with other anomalies
a. Klippel-Trénaunay syndrome
b. Parkes Weber syndrome
c. Sturge-Weber syndrome
d. CLOVES syndrome
e. Proteus syndrome

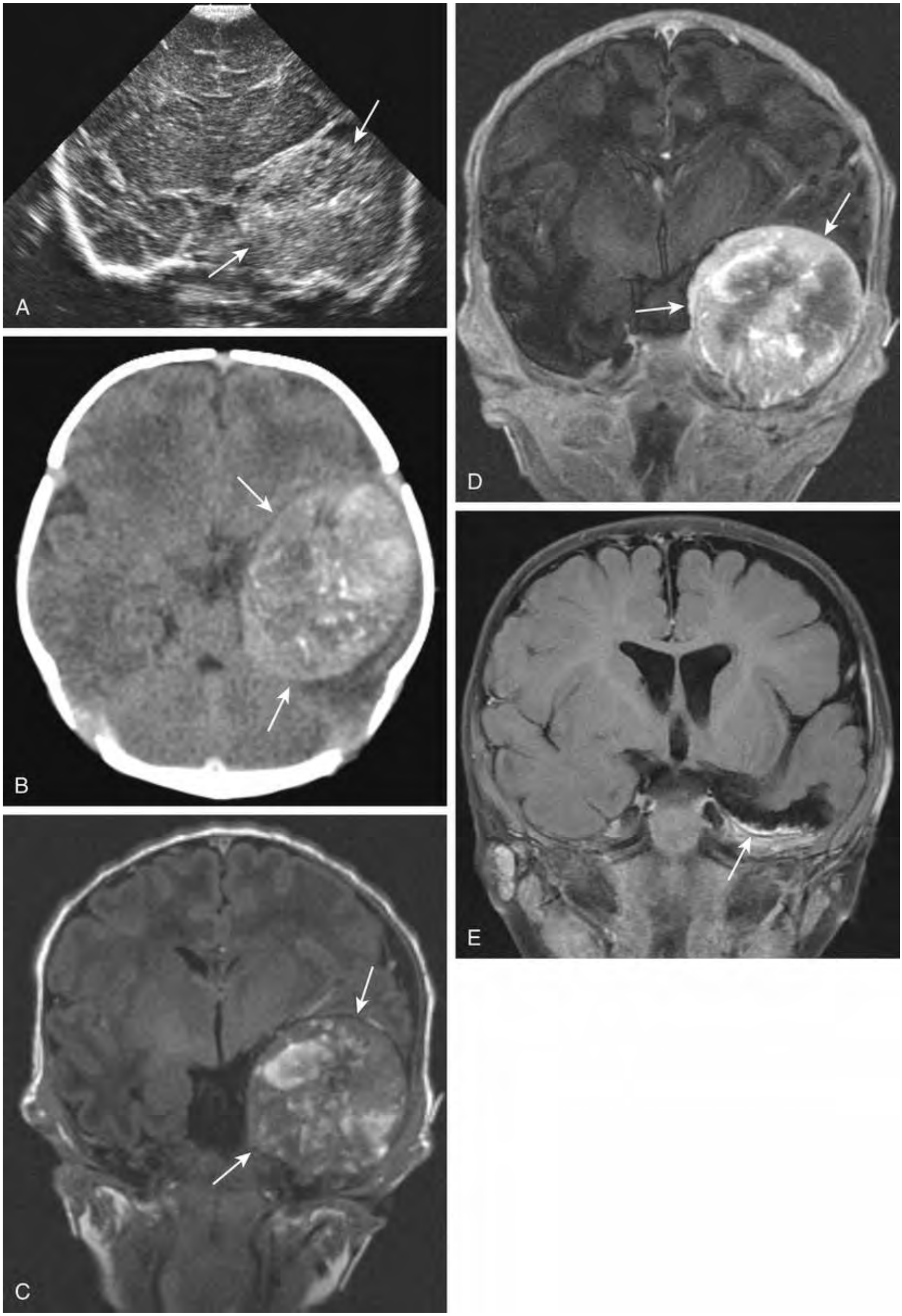
Vascular Tumors

Vascular tumors can be split into three categories: benign and reactive, locally aggressive, and overtly malignant. The locally aggressive and overtly malignant tumors are rare and will not be discussed further; however, examples of these lesions are provided in Table 7-7. Benign tumors are quite common. The two most common variants of benign tumors are infantile hemangiomas and congenital hemangiomas. Infantile hemangiomas are the most common tumor of infancy, affecting anywhere between 4% and 10% of all infants (Fig. 7-102). These tumors are more common in girls and in the craniofacial region. These tumors are not present at birth but appear within the first few weeks of life. After appearing, they progressively grow over the first few months of life before stabilizing and then regressing. Most infantile hemangiomas resolve by school age. Infantile hemangiomas are classified by their morphology, extent, distribution, and depth of involvement. Infantile hemangiomas can be associated with syndromes such as PHACES (posterior fossa anomaly, hemangioma, arterial anomaly, cardiovascular anomalies, eye anomalies, and sternal clefting).


A
B
C

▪ **FIGURE 7-102** **Infantile Hemangioma.**
A, Coronal T1-weighted MRI of the scalp after the administration of contrast in a 2-year-old female shows a hyperintense soft tissue mass at the top of the scalp *(arrow)*. Coronal T1-weighted postcontrast images 2 (**B**) and 3 (**C**) years after the initial imaging time point shows a continued reduction in size of the mass *(arrow)*.

Congenital hemangiomas are less common (Fig. 7-103). They differ from infantile hemangiomas in that they are present and fully grown at birth. They often regress rapidly, resolving before age 1. However, they can be subclassified based on the rapidity of involution. Rapidly involuting congenital hemangiomas (RICHs) resolve, whereas noninvoluting congenital hemangiomas (NICHs) do not. RICH lesions can be associated with transient thrombocytopenia or consumptive coagulopathy (Kasabach-Merritt syndrome).



▪ **FIGURE 7-103** **Rapidly Involuting Congenital Hemangioma.**

A, Coronal image from head ultrasound in a 3-day-old male shows a round echogenic mass *(arrows)* adjacent to the left temporal lobe. **B,** Axial noncontrast CT shows the mass *(arrows)* to be hyperdense with scattered areas of calcification. Coronal T1-weighted MRI before (**C**) and after (**D**) contrast administration shows the large mass *(arrows)* displacing the temporal lobe superiorly. The mass has some internal hyperintense T1-signal consistent with internal hemorrhage. **E,** Coronal T1-weighted MRI with contrast performed 18 months later shows that the mass has involuted. Only mild thickening remains at the site of the congenital hemangioma

(arrow).

Ultrasound, MRI, or CT can be used to evaluate lesions. Imaging of a hemangioma typically shows a discrete lobulated mass. On MRI the lesions are hyperintense on T2-weighted images and isointense to muscle on T1-weighted images. Typically, prominent draining veins are identified. Hemangiomas typically enhance diffusely with contrast and show increased flow on Doppler ultrasound. Involuting hemangiomas can demonstrate areas of fibrofatty tissue with an associated high signal on T1-weighted images and demonstrate less contrast enhancement than proliferating hemangiomas. Unfortunately, many of the soft tissue malignancies of infancy, such as fibrosarcoma and rhabdomyosarcoma, can show an imaging appearance similar to that of proliferating hemangiomas. Therefore cases that do not exhibit the typical appearance and growth patterns of hemangioma are often biopsied to exclude malignancy.

Vascular Malformations

Vascular malformations are divided into four groups based on their complexity and associated vessels: simple malformations, combined malformations, malformations of named vessels, and malformations associated with other anomalies. Simple malformations are typically composed of one type of vessels, although arteriovenous malformations (AVMs) and nontraumatic arteriovenous fistulas are included in this group. In general, the vascular malformations are present at birth and enlarge in proportion to the growth of the child. They remain present throughout the patient's life. MRI can be used to classify vascular malformations into either low-flow or high-flow lesions because their treatment options differ. Malformations with arterial components are considered high-flow lesions, and those without arterial components are considered low-flow lesions. Low-flow vascular malformations include primarily venous, lymphatic, and mixed malformations. A characteristic imaging finding in vascular malformations is that they tend to be infiltrative, without respecting fascial planes, and they often involve multiple tissue types, such as muscle and subcutaneous fat.

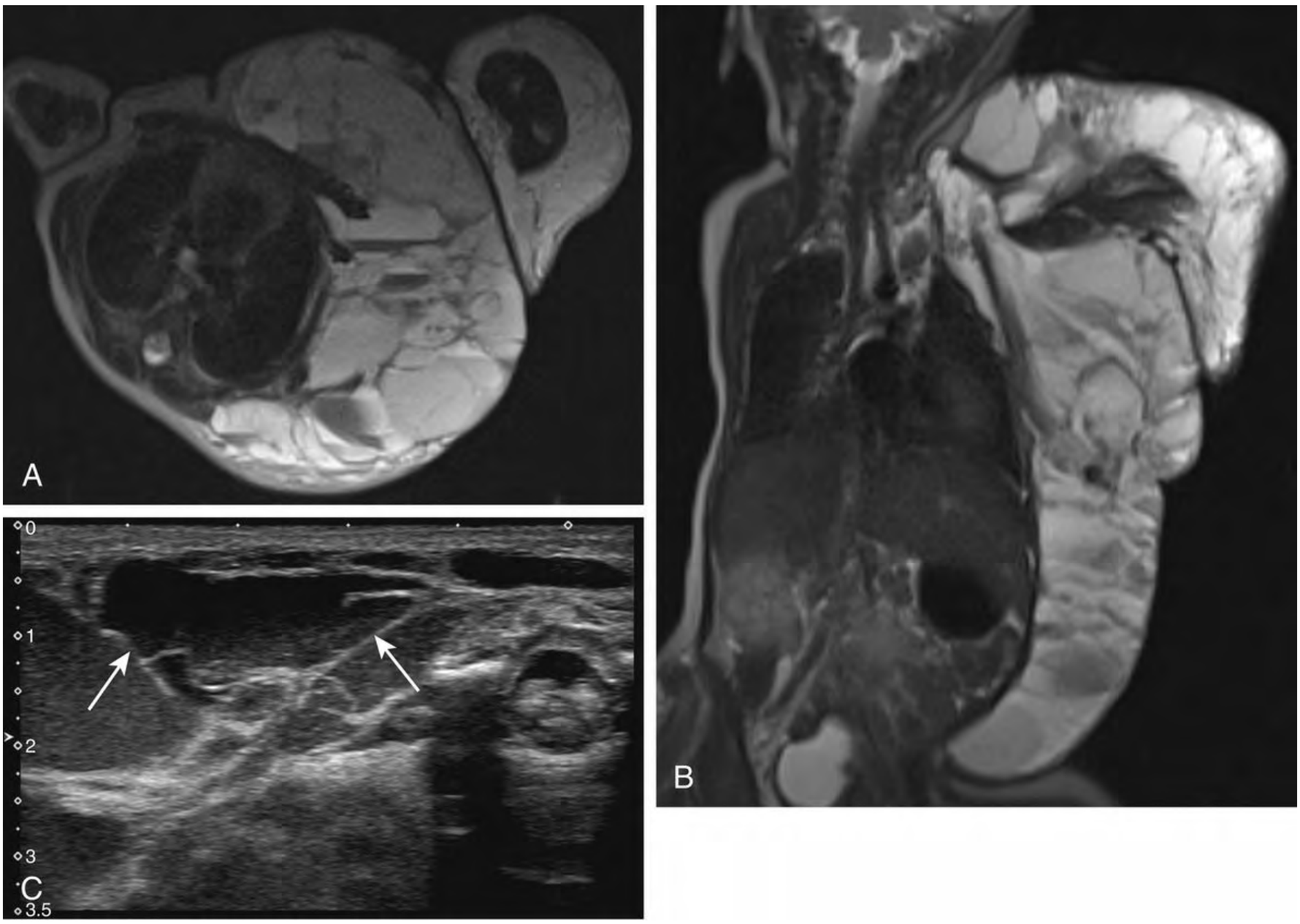
Capillary malformations affect the skin, appearing as pink to red macules (port-wine stain). Many times, the small, superficial lesions at midline near the forehead or on the back of the neck fade over time. The remainder of the lesions darken with time and persist. Lesions can be associated with soft tissue or bony overgrowth.

Lymphatic malformations are composed of variously sized lymphatic channels. They are classified according to the size of the channels as microcystic, macrocystic, or mixed. Macrocystic lesions have discrete cystic areas of various sizes. Macrocysts can be aspirated or sclerosed via interventional radiology. Lymphatic malformations are most common in the craniofacial and neck or axillary regions. The term *cystic hygroma* has been used to refer to lymphatic malformations in the neck. This term is no longer used. Lymphatic malformations can be distinguished on physical exam by their normal overlying skin color. On MRI, lymphatic malformations may contain cystic structures of various sizes, ranging from macrocystic to microcystic (Fig. 7-104). These cystic structures typically appear as high in signal intensity on T2-weighted MRI and do not exhibit central enhancement with gadolinium. Fluid-fluid levels are often present. Gorham-Stout disease is a special variant of a lymphatic malformation, also known as vanishing bone disease. It is characterized by lymphatic malformations affecting one or multiple bones with associated progressive osteolysis (Fig. 7-105). Therapy for lymphatic malformations includes percutaneous sclerotherapy or surgical excision.

Venous malformations appear as blue skin lesions that are soft and compressible on palpation. Many venous malformations cause pain; they may also cause decreased range of motion and deformity. Symptoms tend to increase in late childhood or early adulthood. Venous malformations are classified by their distribution as focal, multifocal, or diffuse. Treatment options for venous malformations include elastic compression garments, percutaneous sclerosis, and surgical excision. On MRI, venous malformations appear as a collection of serpentine structures separated by septations (Fig. 7-106). These serpentine structures represent slow-flowing blood within the venous channels and appear as high signals on T2-weighted images and intermediate signals on T1-weighted images. Phleboliths may be present; they appear as round, low-signal-intensity lesions on MRI. Gadolinium-enhanced T1-weighted images show enhancement of the slow-flowing venous channels.

AVMs are composed of a tangle of vessels with a central nidus and a direct arteriovenous communication. The lesions may present in childhood or adulthood and are often exacerbated during puberty or pregnancy. Presenting symptoms include congestive heart failure, embolism, pain, bleeding, and ulceration. High-flow vascular malformations are much less common than low-flow vascular malformations. On MRI the lesions appear as a tangle of multiple-flow voids (Fig. 7-107) that

demonstrate high flow on gradient echo images. Although the lesions can be associated with surrounding edema or fibrofatty stroma, there is usually no focal, discrete, soft tissue mass. Color Doppler ultrasound demonstrates arterial waveforms in the adjacent venous structures. The most effective treatment for AVMs is transarterial embolization.



▪ **FIGURE 7-104** **Lymphatic Malformation.**
Axial (**A**) and coronal (**B**) T2-weighted MRI of the chest and abdomen in a 5-day-old male shows a massive lymphatic malformation of the left lateral chest and abdominal wall. The mass is heterogeneous with fluid-fluid levels on the axial image. The malformation is made up of large and small cystic spaces. On the images provided, most of the cystic spaces are large. **C,** Ultrasound of the left back with the patient in prone position. There are large collections *(arrows)* on the left-hand side of the image. The cystic spaces have moderate internal debris. There is a fluid-debris level in the medial collection.

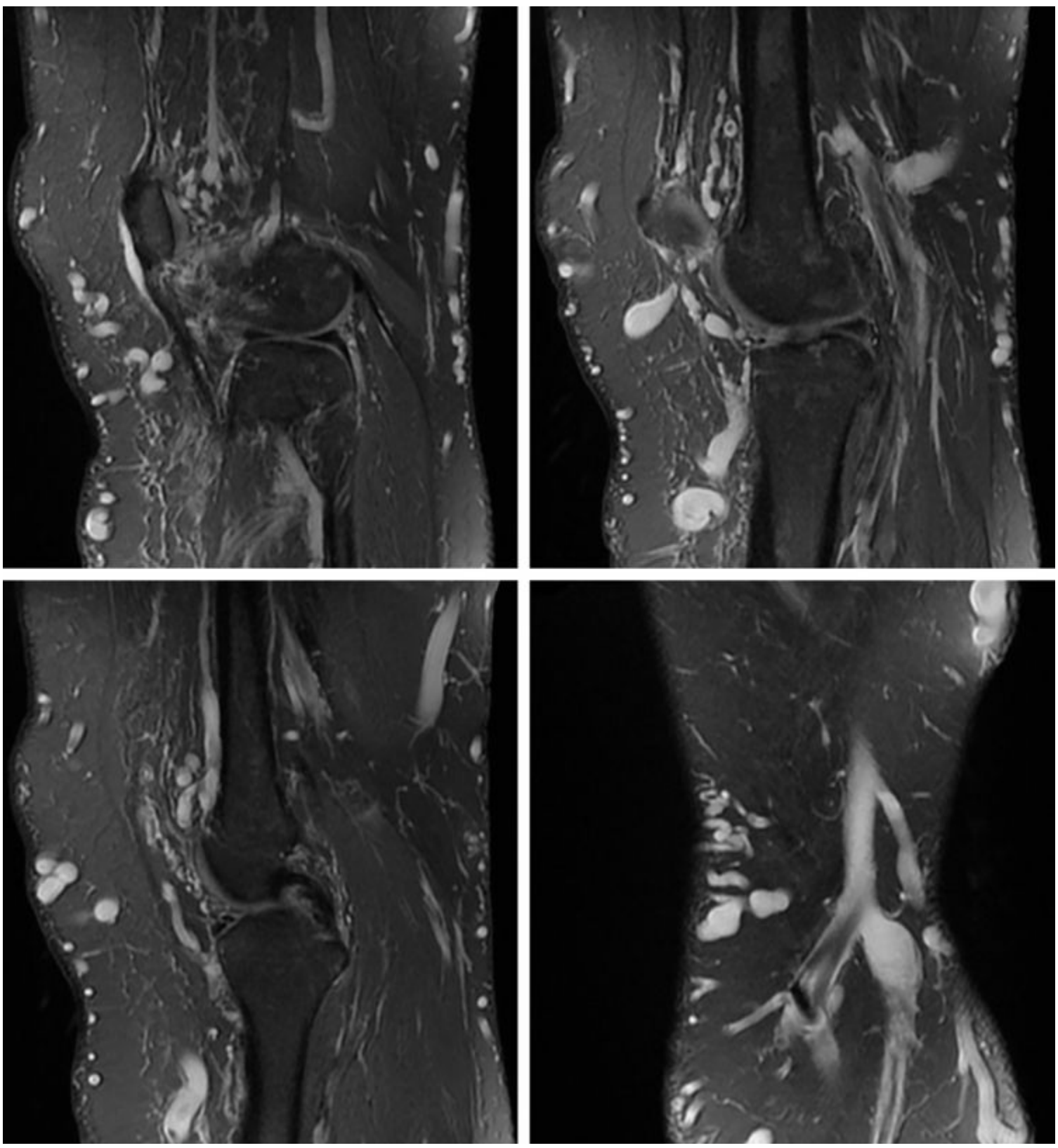


▪ **FIGURE 7-105** **Gorham-Stout Disease.**
AP radiograph (**A**) and coronal CT (**B**) of the cervical spine in a 23-year-old female show expansion of the medullary cavity of the lower cervical vertebral bodies, the posterior first and second ribs on the right, and the posterior first through third ribs on the left (between *arrowheads*).

Combined vascular malformations are said to be present if two or more simple components are present within a lesion. MRI is an important tool to help to define the combination of components, as well as the extent of the lesion. Malformations of major named vessels affect larger-caliber veins, arteries, or lymphatics. Again, imaging is important to define the extent of involvement, as well as the severity of disease. Finally, vascular malformations associated with other anomalies represent many named syndromes, such as Klippel-Trénaunay syndrome, Parkes Weber syndrome, Sturge-Weber syndrome, Maffucci syndrome, CLOVES (congenital, lipomatous, overgrowth, vascular malformations, epidermal nevi, and spinal or skeletal anomalies) syndrome, and Proteus syndrome.

Dermatomyositis

Dermatomyositis is an autoimmune disease that involves the skeletal muscle and skin. Children typically present with weakness and rash. MRI has been used to aid in making the diagnosis, directing biopsies to high-yield areas, and monitoring the response to therapy. On T2-weighted fat-saturated images, there is dramatically increased signal intensity in the involved muscles, myofascial planes, and subcutaneous tissues (Fig. 7-108). The most commonly involved muscles are those within the anterior compartment of the thigh and those surrounding the hip. There is typically rapid resolution of the abnormal high signal after therapy has been instituted. In patients with chronic dermatomyositis, calcifications may be seen in the soft tissues on radiography (Fig. 7-109).



▪ **FIGURE 7-106** **Venous Malformation.**
Four separate sagittal T2-weighted images from an MRI of the knee (from lateral to medial) show multiple hyperintense serpiginous structures surrounding the knee.

Soft Tissue Malignancies

Primary malignancies of the soft tissues are uncommon in children. MRI is the imaging modality of choice for evaluating soft tissue masses. The likely diagnosis is related to the patient's age. In infants, fibrosarcoma is the most common soft tissue malignancy, whereas rhabdomyosarcoma is the most common in children (Fig. 7-110).

Rhabdomyosarcoma is most common in children between 2 and 6 years of age. Although it can arise from any muscle, it is most common in the head and neck region and pelvis. When rhabdomyosarcomas arise in the extremities, they are more likely to represent the alveolar subtype and present later in adolescence. Metastases are most common in the lungs, lymph nodes, and bones.

Other potential malignancies include primitive neuroectodermal tumors and synovial sarcomas. Synovial sarcomas tend to occur around joints and are notoriously and deceptively benign-appearing on imaging studies, with smooth, well-defined borders.

Aggressive fibromatosis is a fibroproliferative disorder that is locally aggressive but does not metastasize. The lesions usually involve older children and occur in the deep soft tissues. On MRI the lesions tend to be high signal on T2-weighted images despite their fibrous nature. After resection, there is a tendency to recurrence along the proximal margin of the resection.

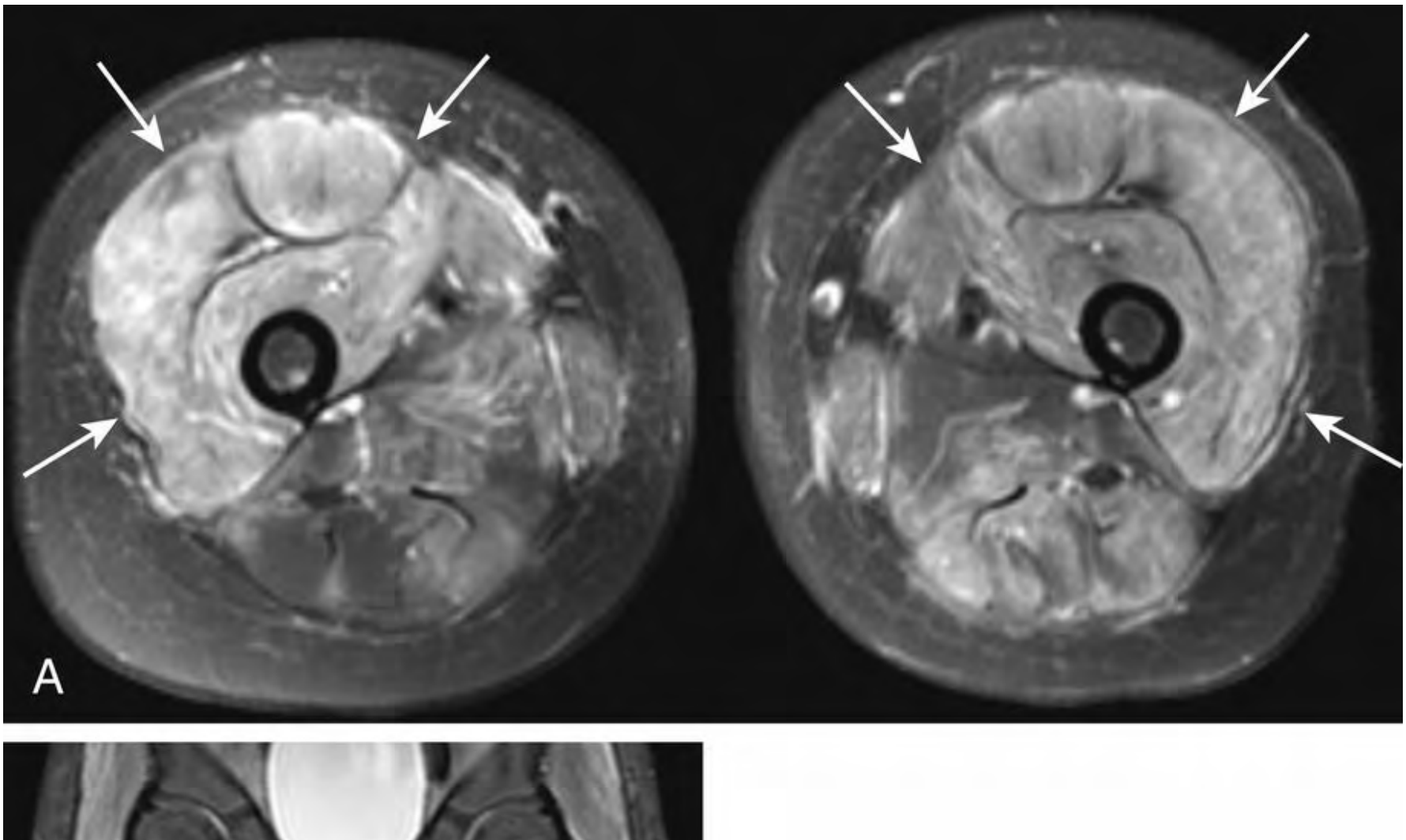
Mimickers of Soft Tissue Malignancies

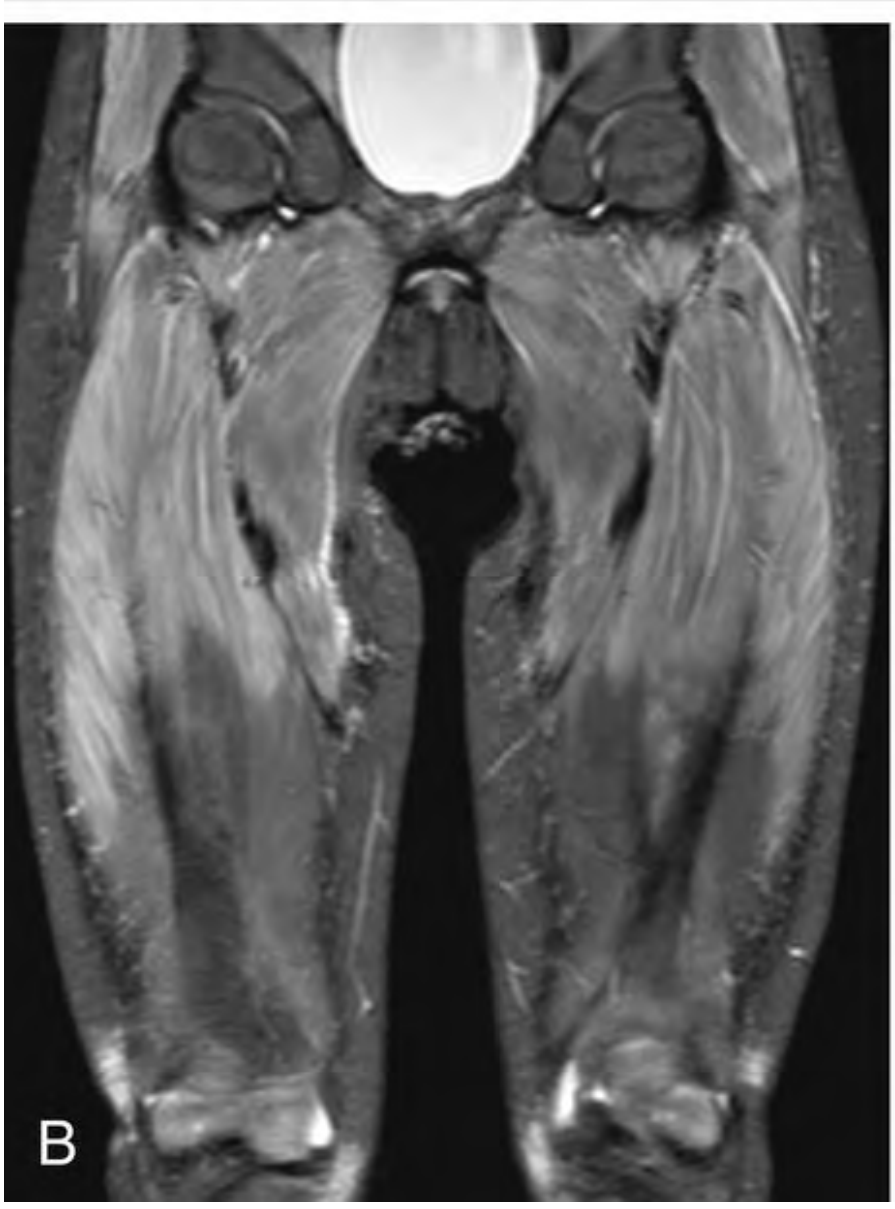
There are a number of benign entities that can present as palpable masses on physical examination and may lead to a request for imaging to rule out a malignant soft tissue mass. Knowledge of these entities will lead to accurate diagnosis and avoid potentially unnecessary or wrong procedures. Such entities include myositis ossificans, chronic foreign body, posttraumatic fat necrosis, and fibromatosis colli.



▪ **FIGURE 7-107** **Arteriovenous Malformation.**

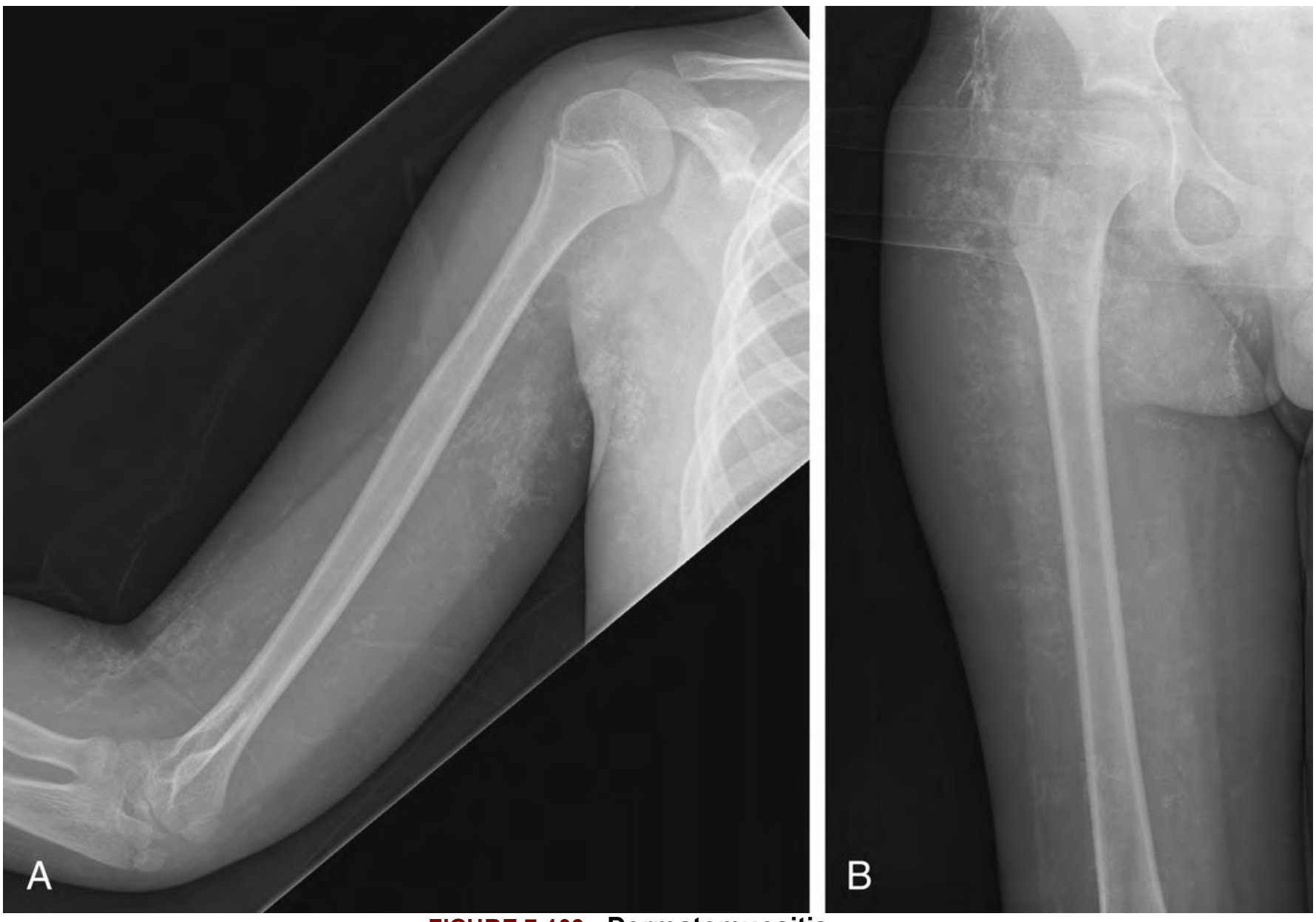
A, Maximum intensity projection from MR angiogram with intravenous contrast large vessels extending toward the foot. Once in the foot, there is a tangle of small vessels *(arrow)*. There is then brisk outflow into a large, bright vein *(arrowhead)*. **B,** Sequential images from catheter angiogram (left to right, top to bottom) show inflow of contrast from large arteries extending to the foot (*arrow* in 1). Once in the foot, there is a tangle of small vessels that gradually fills (*arrows* in 2 and 3). On the third image, there is early drainage into a large vein *(arrowhead)*. This progresses by the fourth image.





▪ **FIGURE 7-108** **Dermatomyositis.**

Axial (**A**) and coronal (**B**) T2-weighted images of the thighs in a 3-year-old female show diffuse abnormal hyperintense T2-signal within the muscles. Although all muscles are affected, the muscles of the anterior compartment *(arrows)* have more diffuse signal abnormality.



▪ **FIGURE 7-109** **Dermatomyositis.**
Radiographs of the right humerus (**A**) and femur (**B**) show diffuse amorphous soft tissue calcifications.



▪ **FIGURE 7-110** **Fibrosarcoma.**
AP (**A**) and lateral (**B**) radiograph of the tibia and fibula in a 5-month-old male shows an abnormal configuration of the fibula *(arrow)*. The fibula has a lucent lesion in its distal portion and is bowed laterally. There is a soft tissue mass posterior to the fibula (*arrowheads* in **B**), causing widening of the space between the tibia and fibula. **C,** Sagittal T2-weighted image of the lower leg shows a large hyperintense mass adjacent to the posterior tibia *(arrows)*.

Myositis Ossificans

Myositis ossificans typically presents as a tender soft tissue mass. It is thought to be related to an organizing hematoma, but a history of trauma may be difficult to elicit. Eventually (2 to 6 weeks after the event), calcifications within the soft tissues become evident and progress into a sharply circumscribed eggshell appearance. Initial radiographs may fail to show calcifications, and MRI performed at that time may show a nonspecific soft tissue mass. A low-signal ring may be seen on MRI on gradient echo sequences. CT may show calcifications before they are seen on radiography.

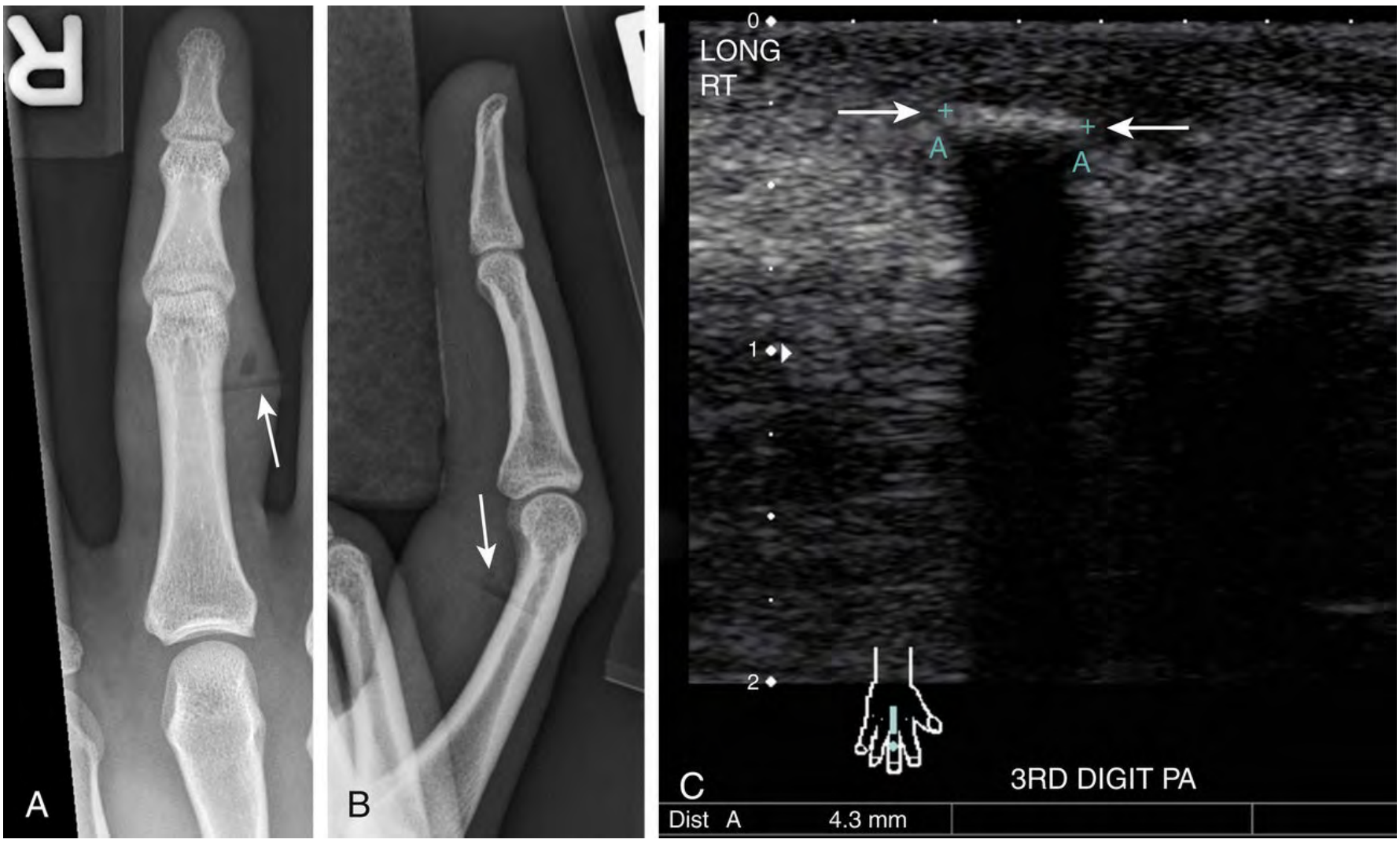
Chronic Foreign Body

A child may experience a penetrating trauma that introduces a small foreign body, but the trauma may not be remembered. Such a child may present months later with a palpable soft tissue mass related to formation of granulation tissue around the foreign body and be imaged for work-up of a soft tissue mass. Like acute foreign bodies (Fig. 7-111), typical locations for chronic foreign bodies are those predisposed to trauma, including the plantar aspect of the foot, anterior portion of the knee, and buttocks. Ultrasound is a useful modality to evaluate the soft tissue mass in both the acute and chronic phases. Often ultrasound will reveal the underlying foreign body as an echogenic structure with the center of soft tissue thickening, edema, and hyperemia. When MRI is performed to evaluate a soft tissue mass, the foreign body may appear as a low-signal structure surrounded by soft tissue mass.

Posttraumatic Fat Necrosis

As a result of minor trauma, children may develop fat necrosis in the area of the injured subcutaneous tissue. Months after the event, there may be scar formation in the area of fat necrosis, and it may present as a firm mass on physical examination. At the time of presentation, the traumatic event is

usually not remembered. The most common locations for posttraumatic fat necrosis are in the thin layer of subcutaneous tissue anterior to the tibia (take a look at any 8-year-old's shins; most have bruising) and the buttocks. On MRI, posttraumatic fat necrosis appears as a linear area of high T2-weighted signal and enhancement. It is confined to the subcutaneous tissues, associated with volume loss in the involved subcutaneous tissues, and not associated with a discrete soft tissue mass. There is a similar condition known as subcutaneous granuloma annulare that also involves the subcutaneous tissues anterior to the tibia and is thought to be related to trauma but does have soft tissue mass related to granulation tissue (Fig. 7-112).



▪ **FIGURE 7-111** **Foreign Body.**

AP (**A**) and lateral (**B**) radiograph of the middle finger in a 17-year-old male with a wooden splinter shows soft tissue swelling along the distal and lateral aspect of the proximal phalanx. There is a linear air collection *(arrow)* within the soft tissue swelling. **C,** Ultrasound of the finger shows a linear hyperechoic foreign body *(arrows)* with posterior acoustic shadowing.

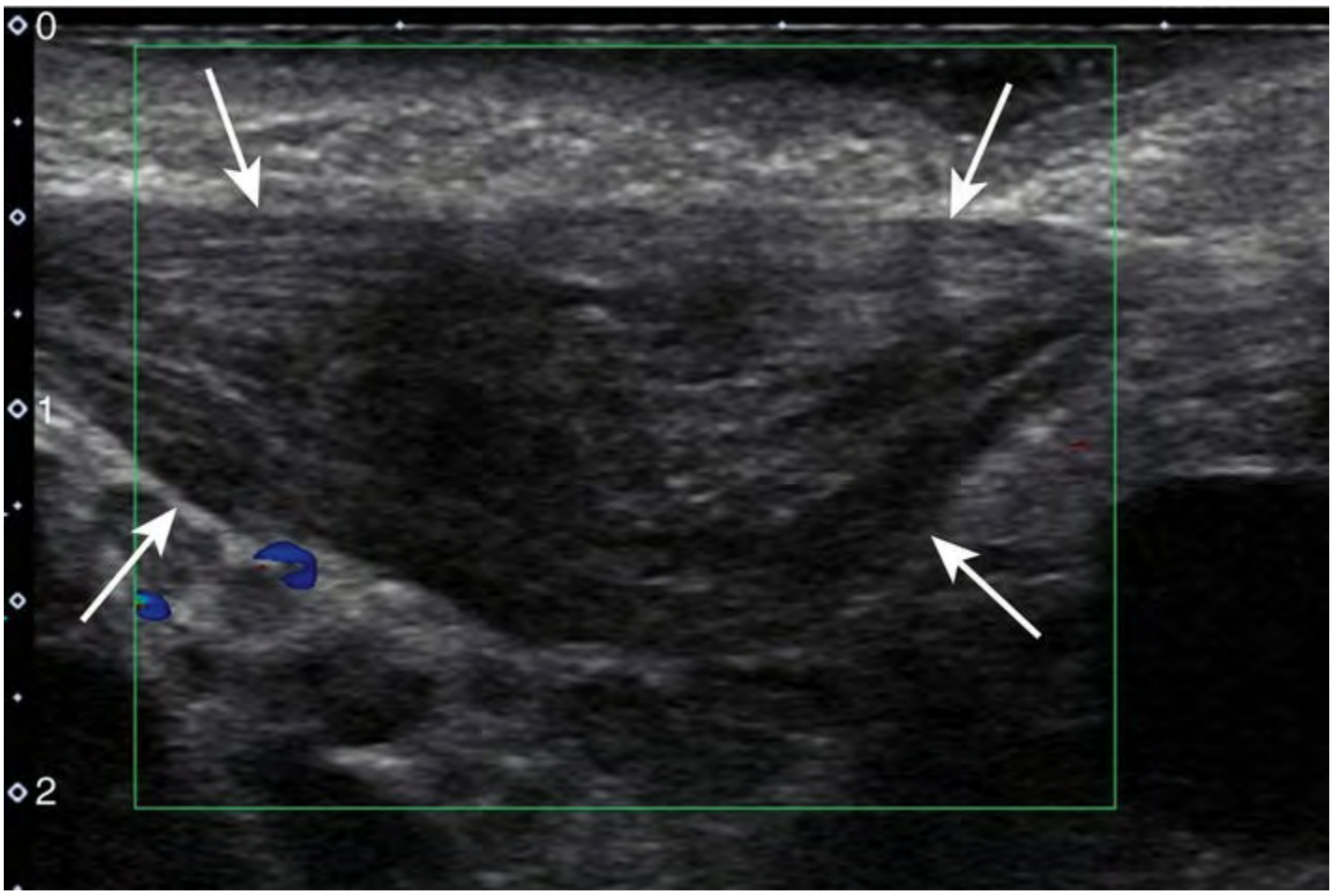


▪ FIGURE 7-112 **Subcutaneous Granuloma Annulare.**

A, Lateral radiograph of the tibia and fibula shows a soft tissue mass *(arrow)* along the anterior aspect of the mid tibia. **B,** On ultrasound the mass *(arrows)* is elongated, confined to the soft tissue, has no internal color Doppler flow, and has no effect on the underlying bone.

Fibromatosis Colli

Fibromatosis colli is a term that should not be confused with the more aggressive fibrotic processes of childhood. It is a benign mass in the sternocleidomastoid muscle in neonates who present with torticollis. The cause is poorly understood. Typically, ultrasound is performed to confirm the diagnosis. Ultrasound shows asymmetric fusiform thickening of the sternocleidomastoid muscle (Fig. 7-113), the echogenicity of which is typically heterogeneous and asymmetric but may be increased or decreased compared to the contralateral normal muscle. Most symptoms resolve over time with stretching exercises, and surgical intervention is rarely required.



▪ **FIGURE 7-113** **Fibromatosis Colli.**
Longitudinal ultrasound image of the neck in a 1-month-old female shows fusiform enlargement of the sternocleidomastoid muscle *(arrows)*.

Suggested Readings

Arndt C.A, Rose P.S, Folpe A.L, Laack N.N. Common musculoskeletal tumors of childhood and adolescence. *Mayo Clin Proc*. 2012;87:475–487.

Davis K.W, Gill K.G. Upper extremity injuries in young athletes. *Semin Musculoskelet Radiol*. 2012;16:269–279.

Grady M.F, Goodman A. Common lower extremity injuries in the skeletally immature athlete. *Curr Probl Pediatr Adolesc Health Care*. 2010;40:170–183.

Harcke H.T, Grissom L.E. Performing dynamic sonography of the infant hip. *AJR*. 1990;155:837–844.

Helms C.A. *Fundamentals of skeletal radiology*. 4th ed. Philadelphia, PA: Saunders; 2013.

Kahn S.L, Gaskin C.M, Sharp V.L, et al. *Radiographic atlas of skeletal maturation*. Stuttgart: Thieme; 2011.

Kaste S.C. Imaging pediatric bone sarcomas. *Radiol Clin North Am*. 2011;49:749–765.

Keats T.E, Anderson M.W. *Atlas of normal roentgen variants that may simulate disease*. 9th ed. Philadelphia, PA: Saunders; 2012.

Khanna G, Bennett D.L. Pediatric bone lesions: beyond the plain radiographic evaluation. *Semin Roentgenol*. 2012;47:90–99.

Kozlowski K. The radiographic clues in the diagnosis of bone dysplasias. *Pediatr Radiol*. 1985;15:1–3.

McKinney B.I, Nelson C, Carrion W. Apophyseal avulsion fractures of the hip and pelvis. *Orthopedics*. 2009;32:42.

Offiah A, van Rijn R.R, Perez-Rossello J.M, Kleinman P.K. Skeletal imaging of child abuse (non-accidental injury). *Pediatr Radiol*. 2009;39:461–470.

Panda A, Gamanagatti S, Jana M, Gupta A.K. Skeletal dysplasias: a radiographic approach and review of common non-lethal skeletal dysplasias. *World J Radiol*. 2014;6:808–825.

Rogers L.F, Poznanski A.K. Imaging of epiphyseal injuries. *Radiology*. 1994;191:297–308.

Strouse P.J. 'Keller & Barns' after 5 years—still inadmissible as evidence. *Pediatr Radiol*. 2013;43:1424.

Taybi H, Lachman R.S. *Radiology of syndromes, metabolic disorders, and skeletal dysplasias*. 5th ed. St. Louis, MO: Mosby; 2006.

Vanderhave K.L, Brighton B, Casey V, et al. Applications of musculoskeletal ultrasonography in pediatric patients. *J Am Acad Orthop Surg*. 2014;22:691–698.

Wassef M, Blei F, Adamas D, et al. Vascular anomalies classification: recommendations from the international society for the study of vascular anomalies. *Pediatrics*. 2015;136:e203–e214.

Wexler R, Wooton-Gorges S.L. *Pediatric orthopedic imaging*. New York, NY: Springer; 2014.

Zbojniewicz A.M, Sorger J.I. Posttreatment imaging of pediatric musculoskeletal tumors. *Radiographics*. 2014;34:724–740.

CHAPTER 8

Neuro

Carolina V. Guimaraes

Pediatric neuroimaging is a distinct subspecialty. Anatomic areas in neuroimaging include the skull, brain, orbits, face and sinuses, neck, and spine. At many children's hospitals, dedicated neuroradiologists perform and interpret all of the neuroimaging. The large amount of information included in pediatric neuroradiology is beyond the scope of this textbook. However, this chapter is a review of some of the more commonly encountered entities.

▪ Pediatric Neuroimaging Modalities: Magnetic Resonance, Computed Tomography, and Ultrasound

In pediatric neuroimaging, magnetic resonance imaging (MRI), computed tomography (CT), and ultrasound are all used, with some overlap. In general, MRI has become the definitive test in evaluating intracranial abnormalities. It is the test of choice for evaluating brain involvement in neoplasms, vascular lesions, inflammatory processes, demyelinating disorders, metabolic diseases, and developmental abnormalities, as well as for the evaluation of neurodegenerative disorders, focal seizures, unexplained hydrocephalus, and neuroendocrine disorders. CT is typically reserved for the evaluation of trauma and acute neurologic symptoms, such as those associated with ventriculoperitoneal shunt (VPS) malfunction. Sinus disease, orbital cellulitis, temporal bones, and head and neck abnormalities are also often evaluated by CT. The use of MRI for the evaluation of VPS function and temporal bone, head, and neck abnormalities is increasing and may complement initial CT evaluation. Neck ultrasound is used for thyroid evaluation and superficial masses. Head ultrasound is reserved for evaluating premature infants and newborns.

▪ Basic Review of Advanced Magnetic Resonance Imaging Techniques in Pediatric Neuroimaging

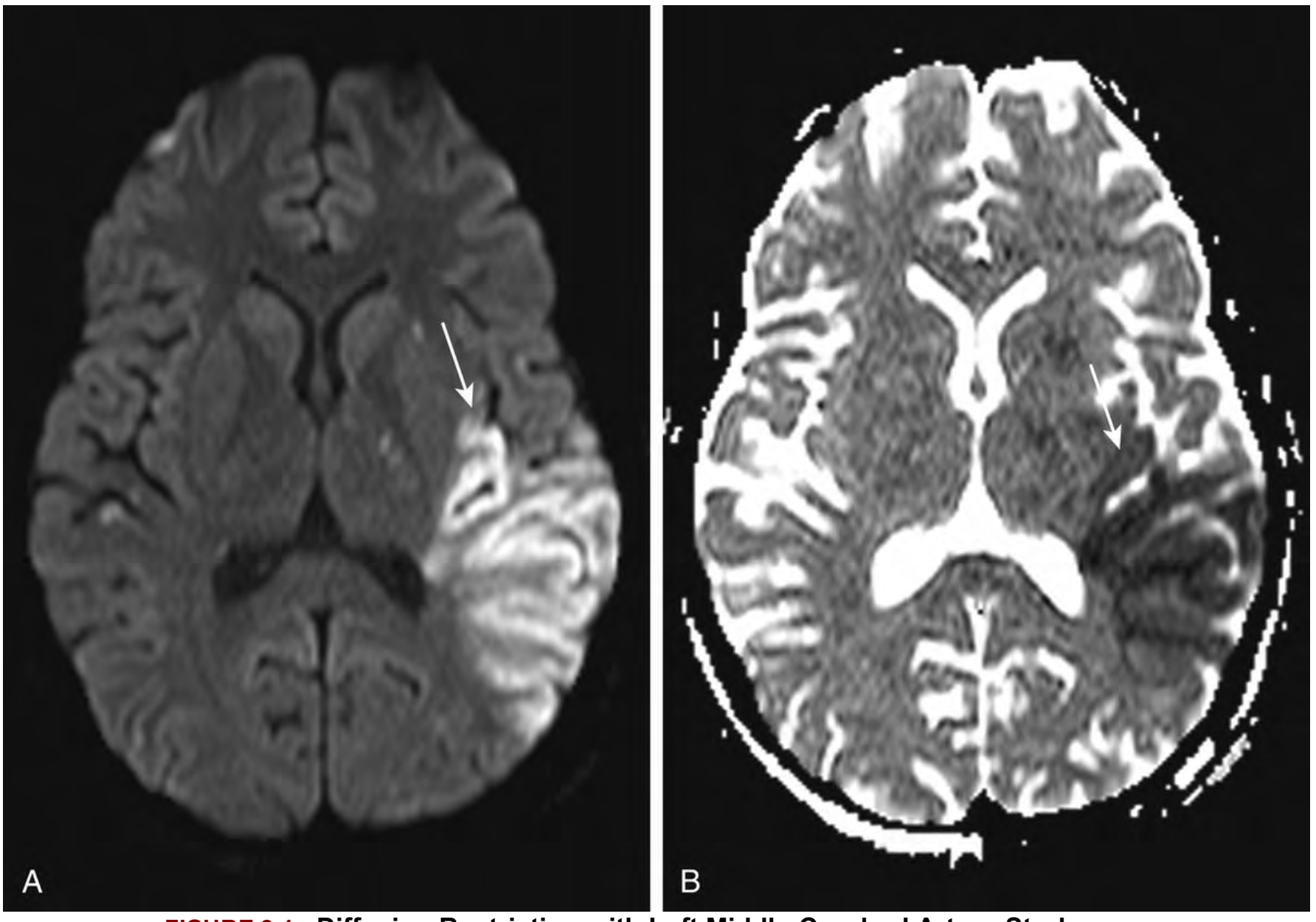
A number of advanced MRI techniques are playing an increasing role in the neuroimaging of children. Such techniques are summarized here. Basic vocabulary is reviewed (which is half the battle). Applications in pediatric patients are also discussed.

Diffusion-Weighted Imaging

Diffusion-weighted imaging (DWI) images are determined by the variability in the diffusivity of water molecules in tissues. The random movement of water molecules is known as Brownian motion. In tissues there is variable restriction of the movement of water molecules relative to tissue structure. Pathologic states may alter the diffusion characteristics of water molecules in the brain and therefore affect the appearance of the DWI images. Images on DWI are influenced not only by diffusion of water molecules but also by other tissue properties, such as T2. To eliminate the influences on imaging appearance of factors unrelated to diffusion of water molecules, the data are processed, most commonly by using a technique called *apparent diffusion coefficient (ADC) map*. For each DWI sequence, two sets of images are created: the DWI images and the ADC map. In a pathologic process in which there is true restricted diffusion, the involved area appears high in signal on the DWI images and low in signal on the ADC map (Fig. 8-1, *A* and *B*). Conversely, in pathologic processes in which there is facilitated diffusion, signal will be low on DWI images and high on the ADC map. Due to the

influences of T2 tissue properties on DWI imaging, an area of increased signal on T2-weighted sequences (including T2 fluid attenuated inversion recovery [FLAIR]) may show as increased DWI signal and not represent true diffusion restriction. In this case, signal will be normal or increased on ADC map, instead of decreased. This phenomenon is known as T2 shine-through (Fig. 8-2, *A-C*) and should not be confused with restricted diffusion.

Restricted diffusion is seen in pathologic processes that present with cytotoxic edema including brain infarct and/or ischemia, nonhemorrhagic traumatic injury, seizure-related edema, and encephalitis. Other causes of diffusion restriction include purulent fluid collections (Fig. 8-3, *A-C*), epidermoid cysts, subacute hematoma, and hypercellular tumors. Processes that show facilitated diffusion include vasogenic edema and cerebrospinal fluid (CSF) collections, such as an arachnoid cyst.



▪ **FIGURE 8-1 Diffusion Restriction with Left Middle Cerebral Artery Stroke.**
A, Increased signal on DWI sequence at the left middle cerebral artery inferior division territory *(arrow)*. **B,** ADC map demonstrates low signal corresponding to the area of increase DWI signal *(arrow)*, confirming diffusion restriction.

DWI has become an extremely important tool in neuroimaging. One of its major advantages is its high sensitivity for ischemia and infarction. It often reveals them before such findings are seen on conventional MR sequences. It is also helpful in differentiating among posterior fossa tumors. Hypercellular medulloblastomas have restricted diffusion, whereas low-grade astrocytomas typically do not. Restricted diffusion is also rare in ependymomas. Table 8-1 shows a glossary of terms related to DWI and diffusion tensor imaging (DTI).

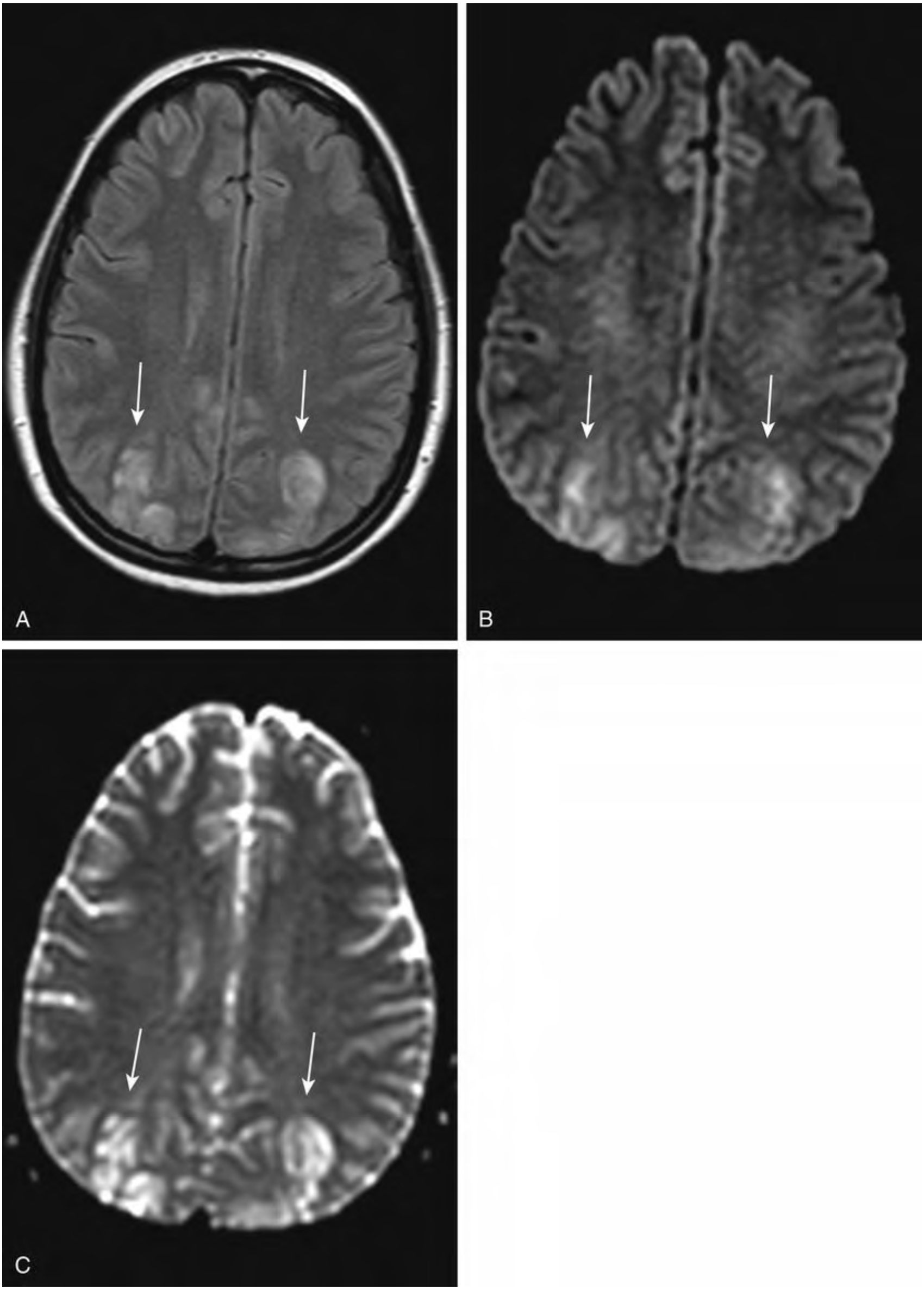
Diffusion Tensor Imaging and Tractography

Diffusion is anisotropic in white matter fibers, as axonal membranes and myelin sheaths act as barriers to the motion of water molecules in directions not parallel to their own orientation. By applying diffusion gradients in multiple directions during a diffusion MRI sequence, DTI technique enables the identification of the direction of maximum diffusivity in a voxel and therefore the identification of location, orientation, and directionality of the white matter tracts. DTI provides several capabilities not previously possible. (1) Large, individual white matter tracts can be depicted as discrete anatomic

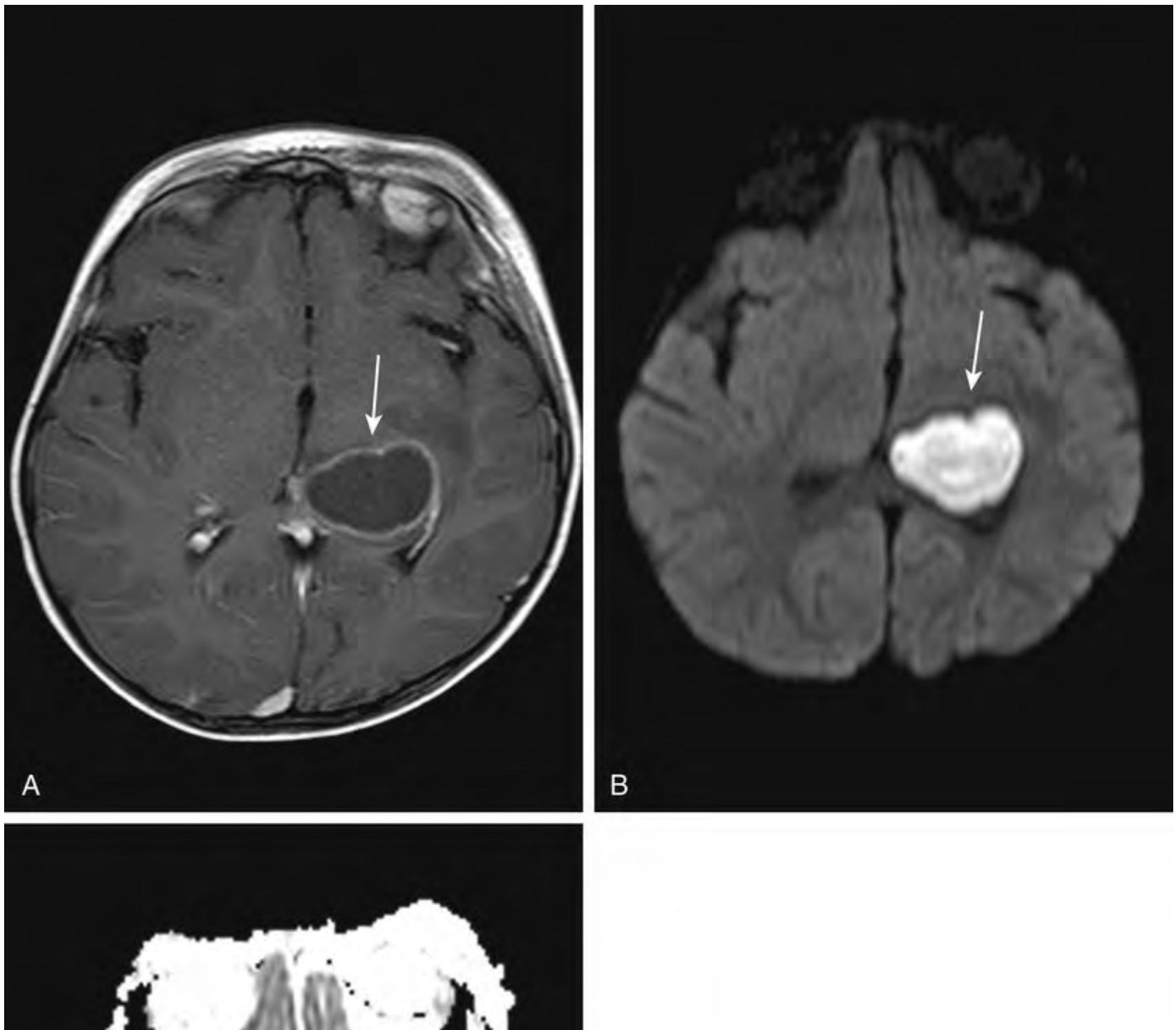
structures. The three-dimensional postprocessing technique used to create such images is tractography. (2) Metrics describing the microarchitecture of tissue can be calculated. They include fractional anisotropy, mean diffusivity, radial diffusivity, and axial diffusivity.

Tractography images are typically shown in color. By convention, white matter tracts oriented left to right are shown as red, cephalocaudad as blue, and anteroposterior as green (Fig. 8-4).

DTI and tractography can be used to evaluate myelination. Increased myelination increases anisotropy. Therefore, in normal infants, anisotropy increases with age. Most disease states that affect white matter decrease anisotropy. DTI has been used to evaluate stroke, hydrocephalus, trauma, and demyelinating disorders. DTI and tractography have also been used to study and depict the white matter tract abnormalities associated with congenital brain anomalies and in the presurgical evaluation of brain tumors (Fig. 8-5). One important limitation of DTI-based tractography is that it underestimates the white matter tracts in parenchymal locations where there are crossing fibers. This is because a single tensor can resolve only a single fiber direction within a voxel. Recent studies have described new diffusion-based nontensor tractography techniques that demonstrate fiber tracts more accurately, but these are not yet being used in the routine clinical practices.



▪ **FIGURE 8-2** **"T2 Shine-through" in a Case of Posterior Reversed Encephalopathy Syndrome.** **A,** Abnormal increased FLAIR signal within the bilateral occipital cortex and subcortical white matter *(arrows)* in a child presenting with an acute episode of hypertension and new neurologic signs. Corresponding increased signal on DWI *(arrows)* (**B**) and increased signal on ADC map *(arrows)* (**C**) compatible with T2 shine-through rather than diffusion restriction.



▪ **FIGURE 8-3** **Diffusion-weighted Imaging in a Brain Abscess.**
A, Axial T1-weighted sequence postcontrast shows a ring-enhancing fluid collection causing mass effect over the atrium of the left lateral ventricle *(arrow)*. **B,** DWI sequence demonstrate high signal within the abscess cavity *(arrow)*. **C,** ADC map demonstrates low signal *(arrow)*, consistent with restricted diffusion from purulent material.

TABLE 8-1

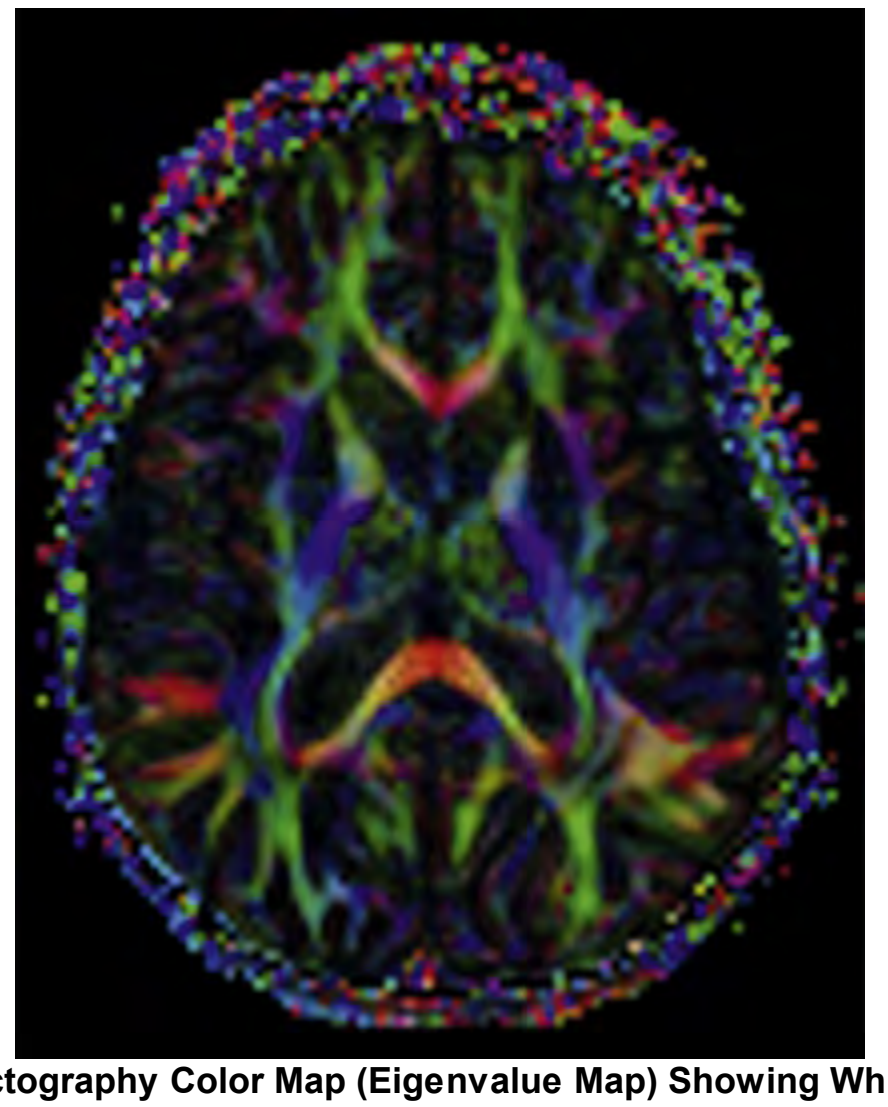
Glossary of Terms in Diffusion-Weighted and Diffusion Tensor Imaging

Term	Definition
Isotropy	Uniformity of physical properties of a molecule in all directions; in other words, the absence of any kind of polarity
Anisotropy	The opposite of isotropy; having polarity or directionality
Eigenvalue	The mathematical property of a tensor (vector) related to magnitude and direction
Fractional anisotropy	A metric measuring the degree of anisotropy (0 for isotropy and 1 for full anisotropy)
ADC	A measure of the freedom of water diffusion in a particular tissue; increased ADC = increased diffusivity
Tractography	A postprocessing method of creating images representing axonal fiber tracts from diffusion tensor data
Tensor	The magnitude and direction of diffusion; is used similarly to the term *vector*. A 3 × 3 matrix is used to calculate a tensor

ADC, Apparent diffusion coefficient.

Perfusion

Perfusion MRI evaluates cerebral microvascular parameters, including cerebral blood volume, mean transit time, and cerebral blood flow. It relies on the use of a tracer that may be exogenous (gadolinium) in dynamic susceptibility contrast-enhanced (DSC) and dynamic contrast-enhanced (DCE) techniques or endogenous in noncontrast arterial spin labeling (ASL) technique. The main applications of perfusion MRI are evaluation of vascular pathologies (ischemic strokes, vasculopathies, vasospasm) and tumors. In the evaluation of brain tumors, perfusion may help with preoperative tumor grading and biopsy guidance by identifying high perfusion areas suspicious to represent higher grade portions of the tumor. Perfusion also plays a role in the evaluation of, tumor treatment response, and in the attempt to answer the always difficult question of tumor recurrence versus radiation necrosis.



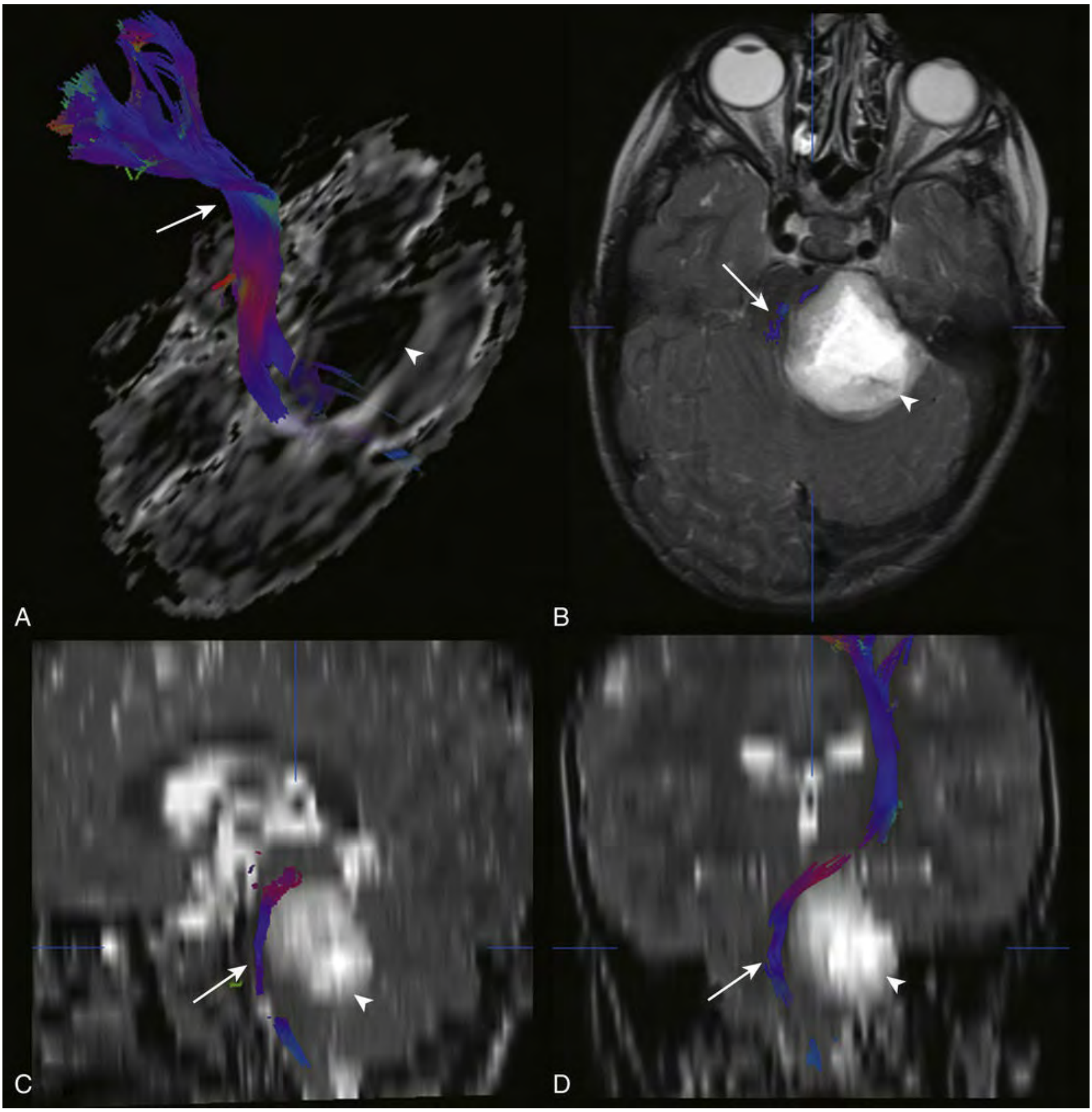
▪ **FIGURE 8-4 Tractography Color Map (Eigenvalue Map) Showing White Matter Tracts.** Note that *red* denotes tracts oriented left to right, *blue* denotes cephalocaudad, and *green* denotes anteroposterior.

Magnetic Resonance Spectroscopy

Proton (hydrogen) MR spectroscopy (MRS) is a tool that is used to help to characterize a number of pediatric neurologic conditions. Most often, single-voxel spectroscopy is created using a 1-cubic centimeter sample area. The results of spectroscopy are typically depicted as a spectrum, with each metabolic peak characterized by resonance frequency, height, width, and area (Fig. 8-6). Metabolic

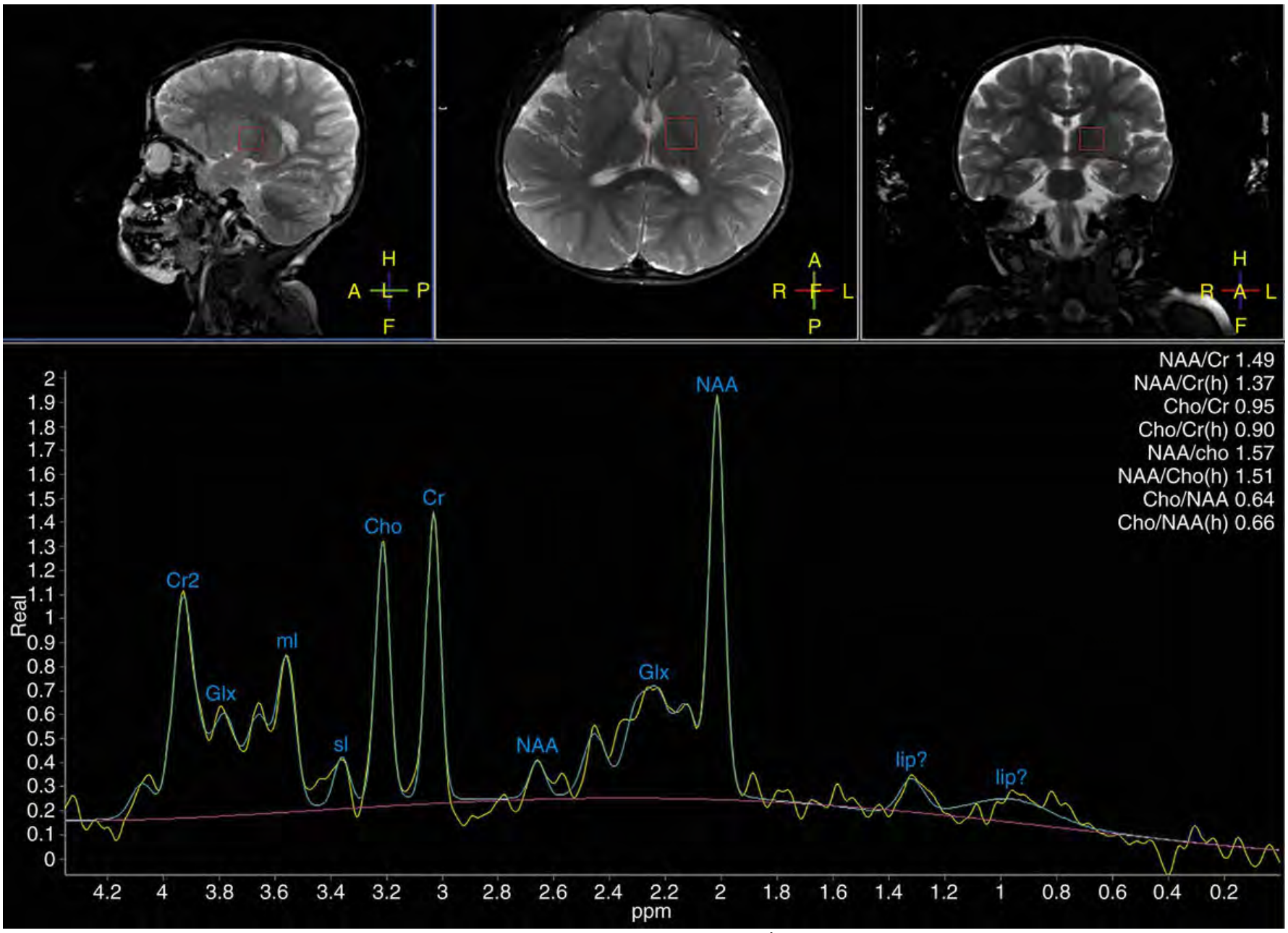
profiles depicted on MR spectroscopy have been much less specific than originally hoped. However, the information obtained can provide useful information that complements the information derived from conventional MRI in many pediatric disorders, including neoplasms, hypoxic ischemic insult, and metabolic diseases.

The most commonly evaluated brain metabolites include *N*-acetylaspartate (NAA), creatine (Cr), choline (Cho), myoinositol (mI), and lactate (Lac) (see Fig. 8-6). NAA is a neuronal marker and is decreased in most disorders that decrease neuronal viability and density, such as neoplasms (Fig. 8-7), infarcts, radiation injuries, and many white matter diseases. NAA is markedly elevated in Canavan disease and may also be elevated in Salla disease and Pelizaeus-Merzbacher disease. Cho compounds reflect the synthesis and degradation of cell membranes; therefore increased Cho is seen when there is high cellular turnover, as occurs with most tumors (see Fig. 8-7). Lactate is a product of anaerobic glycolysis, typically elevated in the setting of acute ischemia (Fig. 8-8), infarction, abscess, many high-grade tumors, and some metabolic diseases, such as mitochondrial disorders. Myoinositol is considered a glial marker, elevated in gliosis and astrocytosis in pediatrics. Creatine is relatively constant; therefore it is used as an internal reference for calculation of metabolite ratios. Creatine deficiency syndromes are rare causes of decreased creatine levels. Taurine (Tau) is not a commonly seen metabolite in clinical MR spectroscopy; however, it has been shown to be elevated in medulloblastoma and therefore is an important metabolite to recognize in pediatric posterior fossa tumors (at 3.3 ppm, above baseline on short TE 30-35 and below baseline on TE 144).



▪ **FIGURE 8-5** **Diffusion Tensor Imaging.**

Left brainstem glioblastoma multiforme in 5-year-old male extending into the brachium pontis. Tractography (**A**) and three-dimensional fiber representation of the left corticospinal tract (**B,** axial; **C,** sagittal; **D,** coronal) obtained for surgical planning. Left corticospinal tract *(arrow)* overlaid on anatomic images. Note the corticospinal tract *(arrow)* displaced medially by the large brainstem mass *(arrowhead)*. (Images courtesy of James L. Leach, MD.)

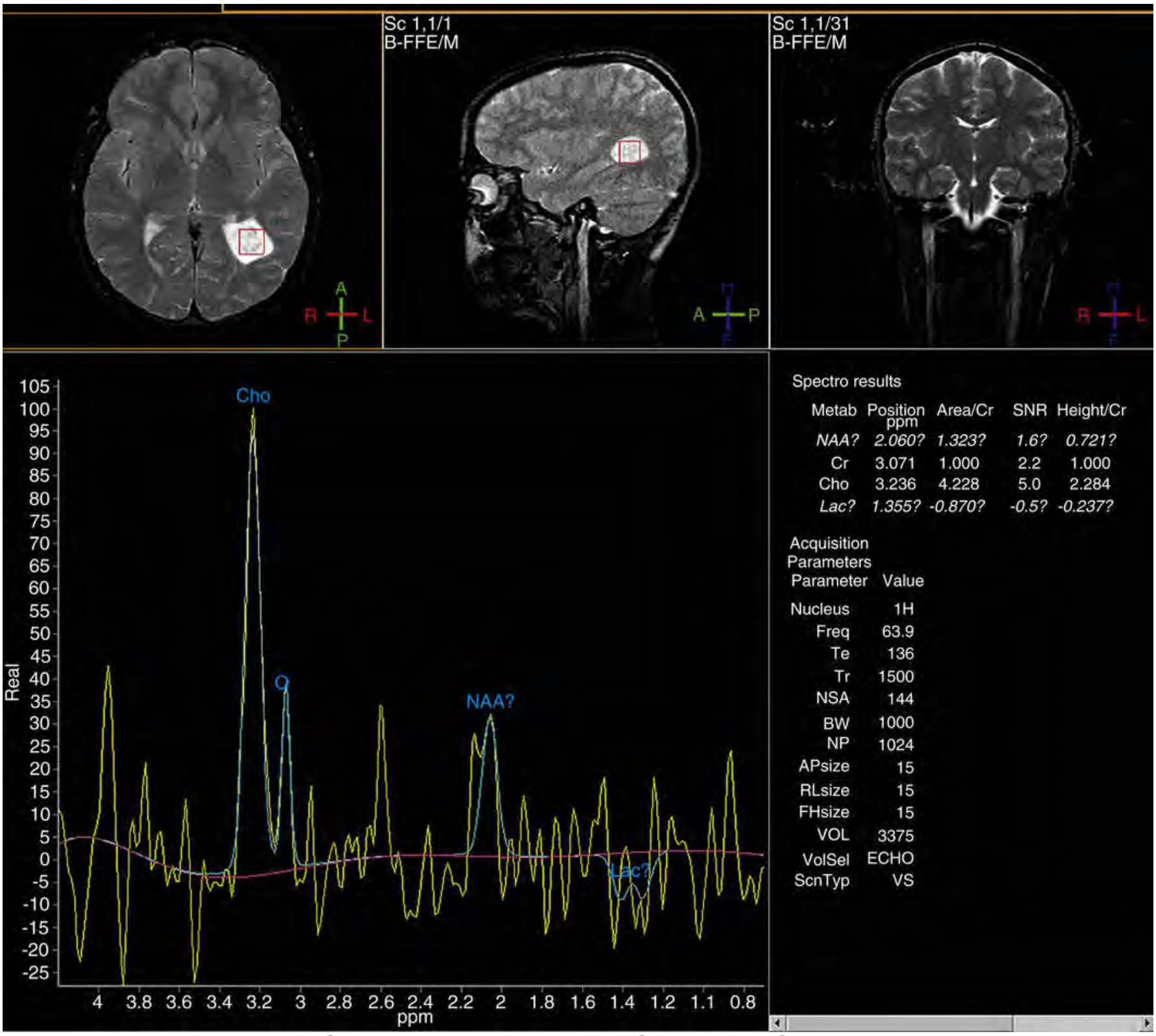


▪ **FIGURE 8-6 Normal Short Echo Single Voxel ^{1}H-MR Spectroscopy.**
Voxel placed at the left basal. Note the normal stair-step relationship of choline (Cho; 3.2 ppm), creatine (Cr; 3.0 ppm), and NAA (NAA; 2.0 ppm) peaks. A peak related to myoinositol is also noted (mI; 3.6 ppm). Location of pathologic lactate peak (not present in this normal example) is at 1.3 ppm.

There are differences in metabolite levels in the gray and white matter. The concentration of NAA in gray matter is higher than in white matter, and Cho concentration is typically higher in white matter. There are also differences in metabolite levels in the developing brain, especially during the first year of life. In the newborn period, NAA levels are low and mI and Cho levels are high (Fig. 8-9). Small lactate peak can also be found in healthy newborns.

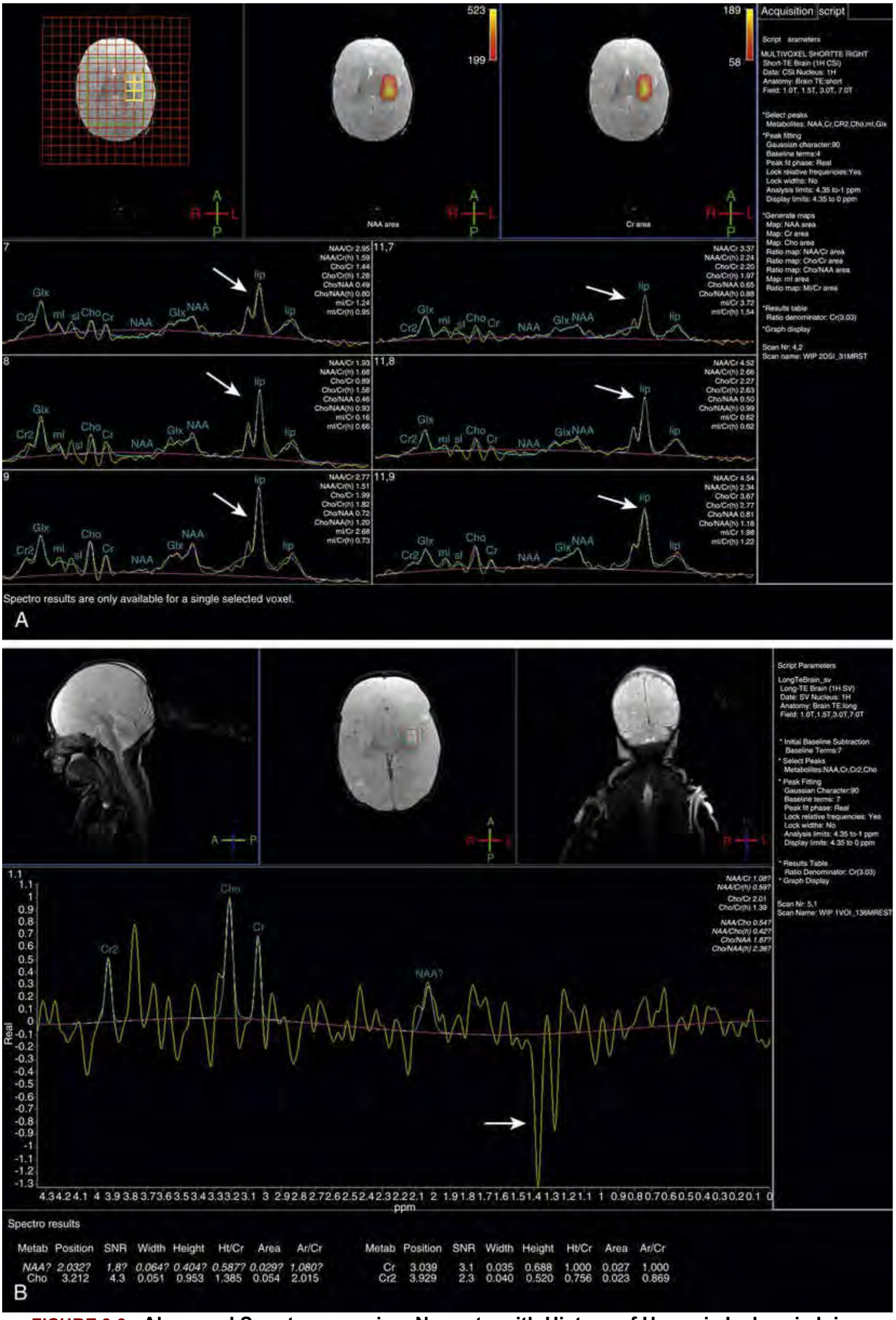
Functional Magnetic Resonance Imaging

Functional MRI (fMRI) is a noninvasive method of evaluating regional neuronal activity within the brain. Neuronal activity increases metabolic activity, which results in increased blood flow to that region and a relative increase in the ratio of oxygenated hemoglobin to deoxygenated hemoglobin. Deoxyhemoglobin is paramagnetic; therefore a change in the ratio affects the magnetic state of the tissue and, as a result, changes the local MRI signal. This phenomenon is called the *blood oxygenation level-dependent (BOLD) effect*. fMRI techniques show these changes superimposed on anatomic information. fMRI is used to document regional neuronal activity during a specific task. The most validated use is for localization of different body representations in the primary motor and somatosensory cortex, as well as language lateralization (Fig. 8-10, *A-F*). Clinically, fMRI has been used in the evaluation of patients with seizures and planning of surgical approaches to brain tumors. It also has been a very useful research tool in increasing our understanding of brain function. Current research is mostly focused on resting state techniques (R-fMRI), which measure BOLD fluctuations of spontaneous neuronal activity without the performance of a specific task.



▪ **FIGURE 8-7 Abnormal Spectroscopy (TE:135) in a Child With a Supratentorial Pilocytic Astrocytoma.**

Note a large Cho peak and diminished NAA, typical of neoplasms. There is also some elevation of lactate, depicted as an inverted doublet at 1.3 ppm. Although pilocytic astrocytoma is a low-grade tumor, spectra may mimic a more aggressive lesion.



Spectro results are only available for a single selected voxel.

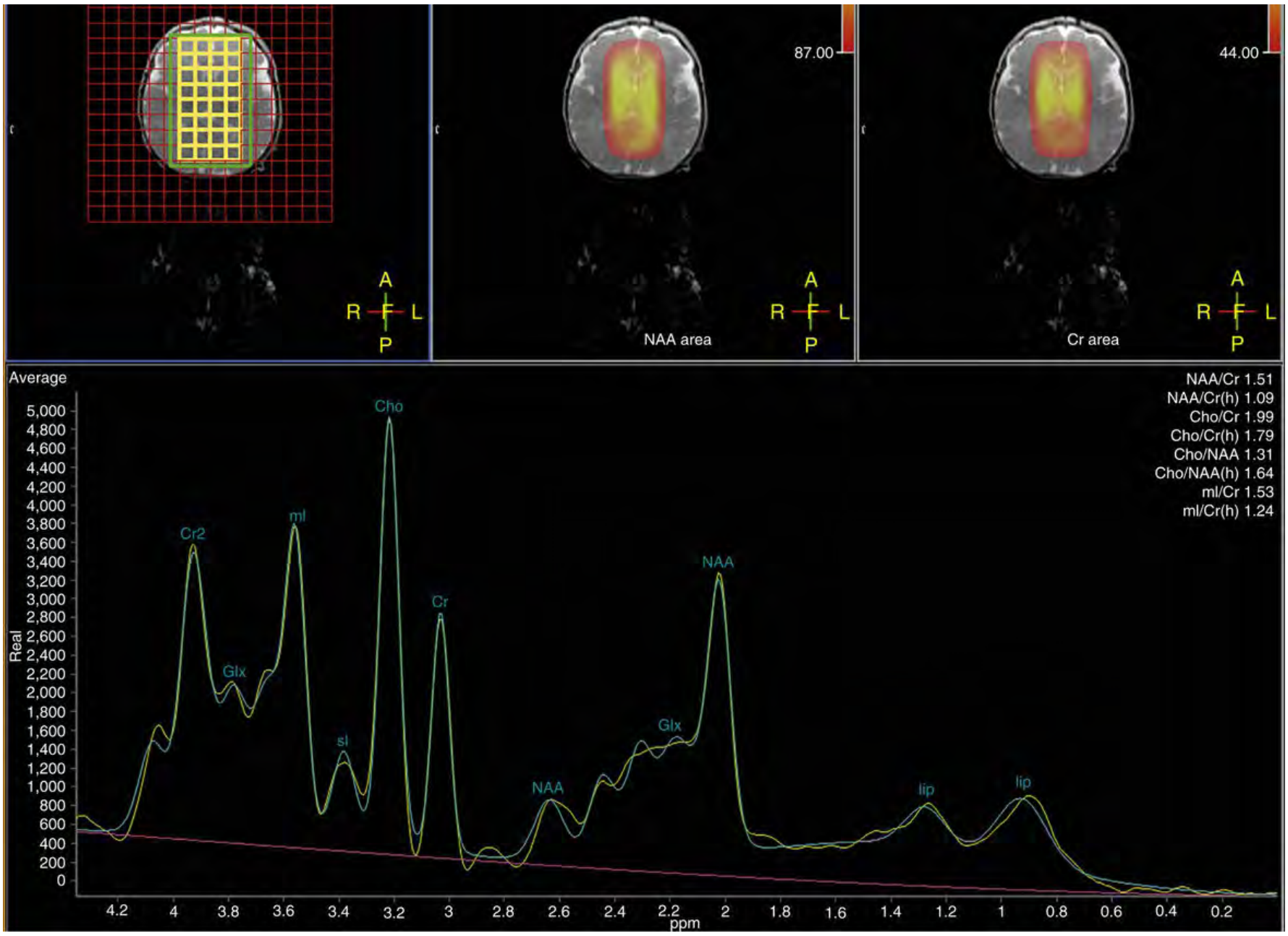
A

Spectro results

Metab	Position	SNR	Width	Height	Ht/Cr	Area	Ar/Cr	Metab	Position	SNR	Width	Height	Ht/Cr	Area	Ar/Cr
NAA?	*2.032?*	*1.8?*	*0.064?*	*0.404?*	*0.587?*	*0.029?*	*1.080?*	Cr	3.039	3.1	0.035	0.688	1.000	0.027	1.000
Cho	3.212	4.3	0.051	0.953	1.385	0.054	2.015	Cr2	3.929	2.3	0.040	0.520	0.756	0.023	0.869

B

▪ **FIGURE 8-8** **Abnormal Spectroscopy in a Neonate with History of Hypoxic Ischemic Injury.** **A,** Multivoxel short echo spectroscopy (TE:35) at the left basal ganglia. Note large doublet at 1.3 bpm *(arrows)*, likely a combination of lipids and lactate. **B,** Single voxel spectroscopy (TE:135) confirmed the presence of lactate, seen as an inverted doublet at 1.3 bpm *(arrow)*.



▪ **FIGURE 8-9** **Normal Neonate Spectroscopy.**

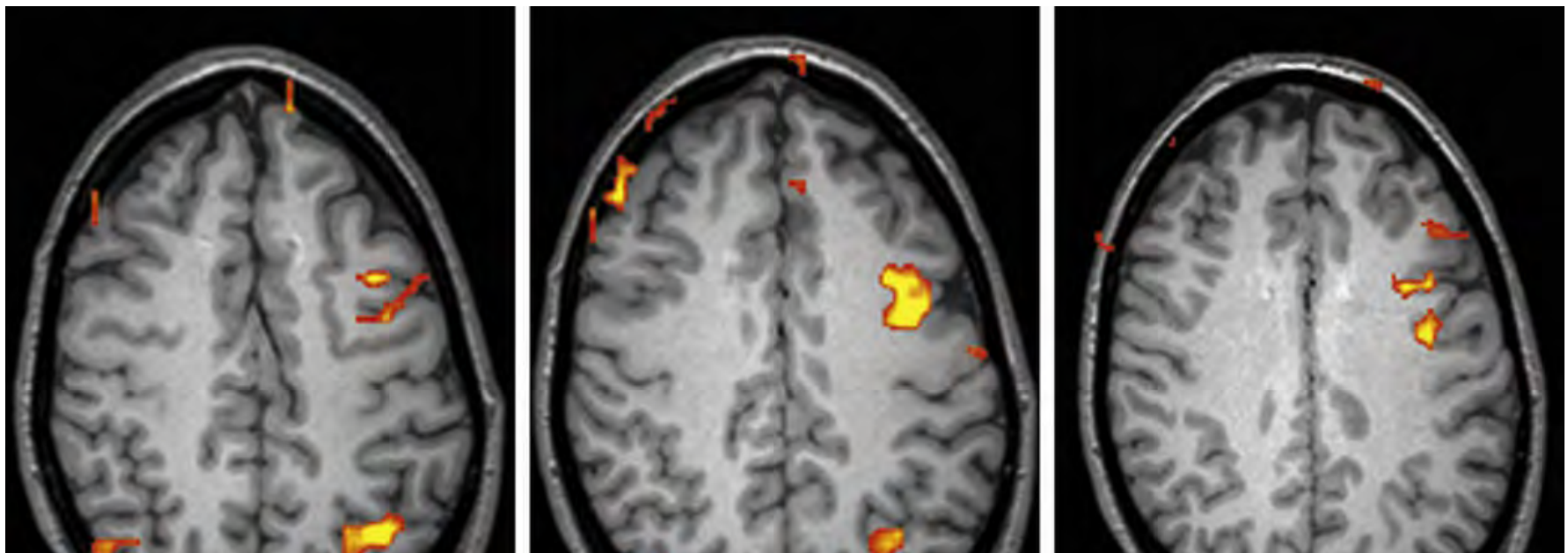
Multivoxel short echo spectroscopy of the deep gray matter structures in a normal neonate demonstrating low NAA peak relative to Cho and ml levels. This is typical in the neonatal period and should not be confused with an abnormal decrease in NAA.

▪ Neonatal Head Ultrasound

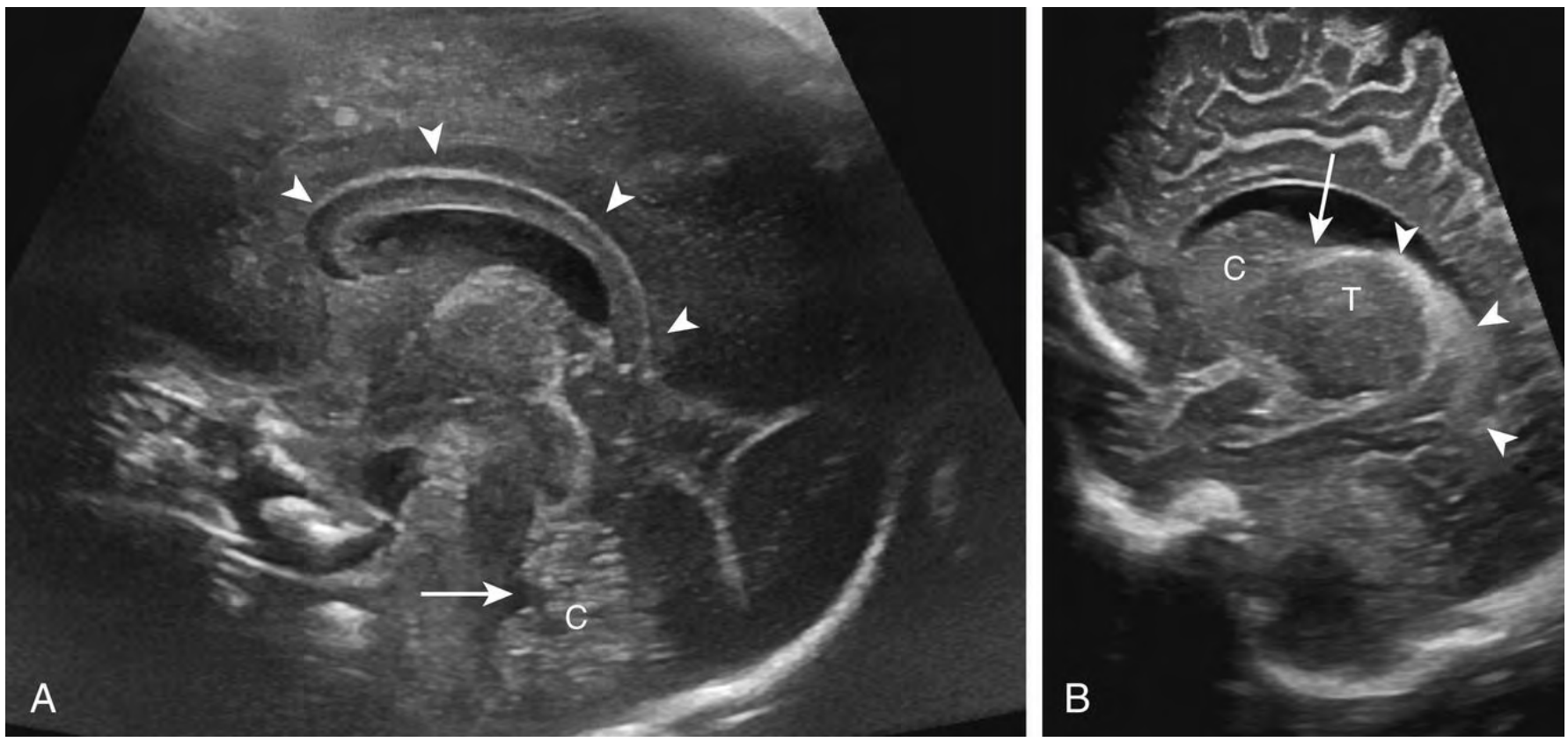
Neonatal head ultrasound is performed through the open fontanels of neonates and infants using high-frequency transducers. Images are commonly obtained in the sagittal and coronal planes via the anterior fontanel using a sector transducer (Fig. 8-11, *A* and *B*). Linear high-resolution transducers are used to assess the extraaxial spaces (Fig. 8-12, *A* and *B*) and superficial cortex. Additional images via the mastoid fontanel enable the detection of posterior fossa hemorrhages (Fig. 8-13, *A* and *B*) and congenital anomalies. Evaluation via the posterior fontanel can be use for differentiation of white matter injury versus anisotropy artifact in cases of abnormally increased posterior periventricular white matter echogenicity. In premature infants, head ultrasound is most commonly used to diagnose and follow up intracranial complications, such as germinal matrix hemorrhage and white matter injury of prematurity (periventricular leukomalacia). It can also be used to screen for congenital abnormalities and hydrocephalus. Another common indication is evaluation of an infant with a large head circumference.

Germinal Matrix Hemorrhage

The germinal matrix is a fetal structure that is a stem source for neuroblasts. It typically involutes by term but is still present in premature infants within the caudothalamic groove (the space between the caudate head and the thalamus). The germinal matrix is highly vascular and is subject to hemorrhaging with fluctuation in cerebral blood pressure. Germinal matrix hemorrhage most commonly occurs in premature infants during the first days after birth. Potential complications include destruction of the precursor cells within the germinal matrix, hydrocephalus, and hemorrhagic infarction of the surrounding periventricular tissues. Cerebellar hemorrhage can also be seen in very premature patients (see Fig. 8-13, *A* and *B*).

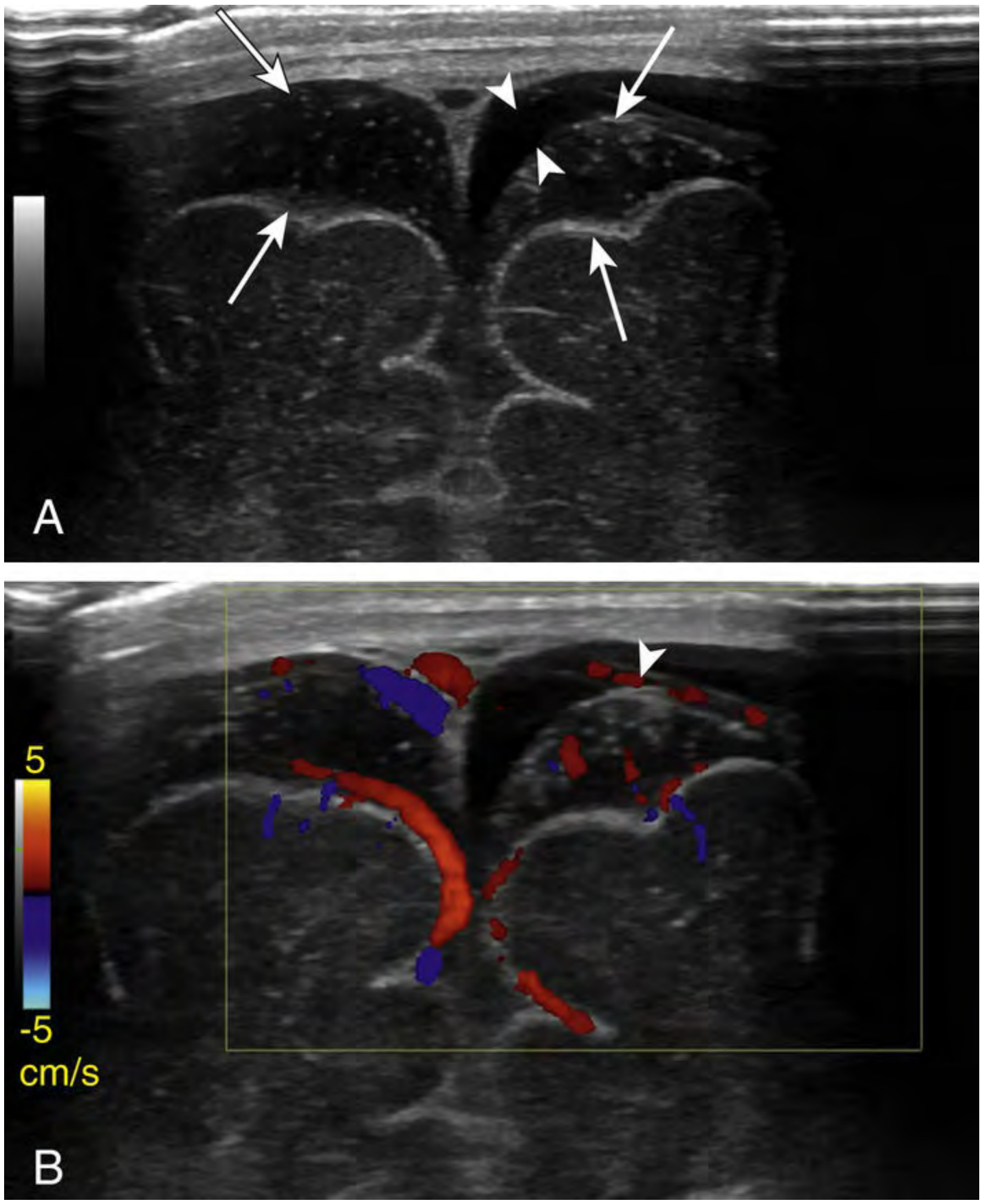


▪ **FIGURE 8-10** **Functional Magnetic Resonance Imaging.**
Right-handed child with chronic seizures and right frontal cortical dysplasia (not shown). Preoperative evaluation for hemispheric language dominance—verb generation task. **A-F,** Areas of significant BOLD-related signal change *(orange-yellow areas)* during silent verb production are noted to be predominately left sided, including left inferior frontal, consistent with left hemispheric language dominance.



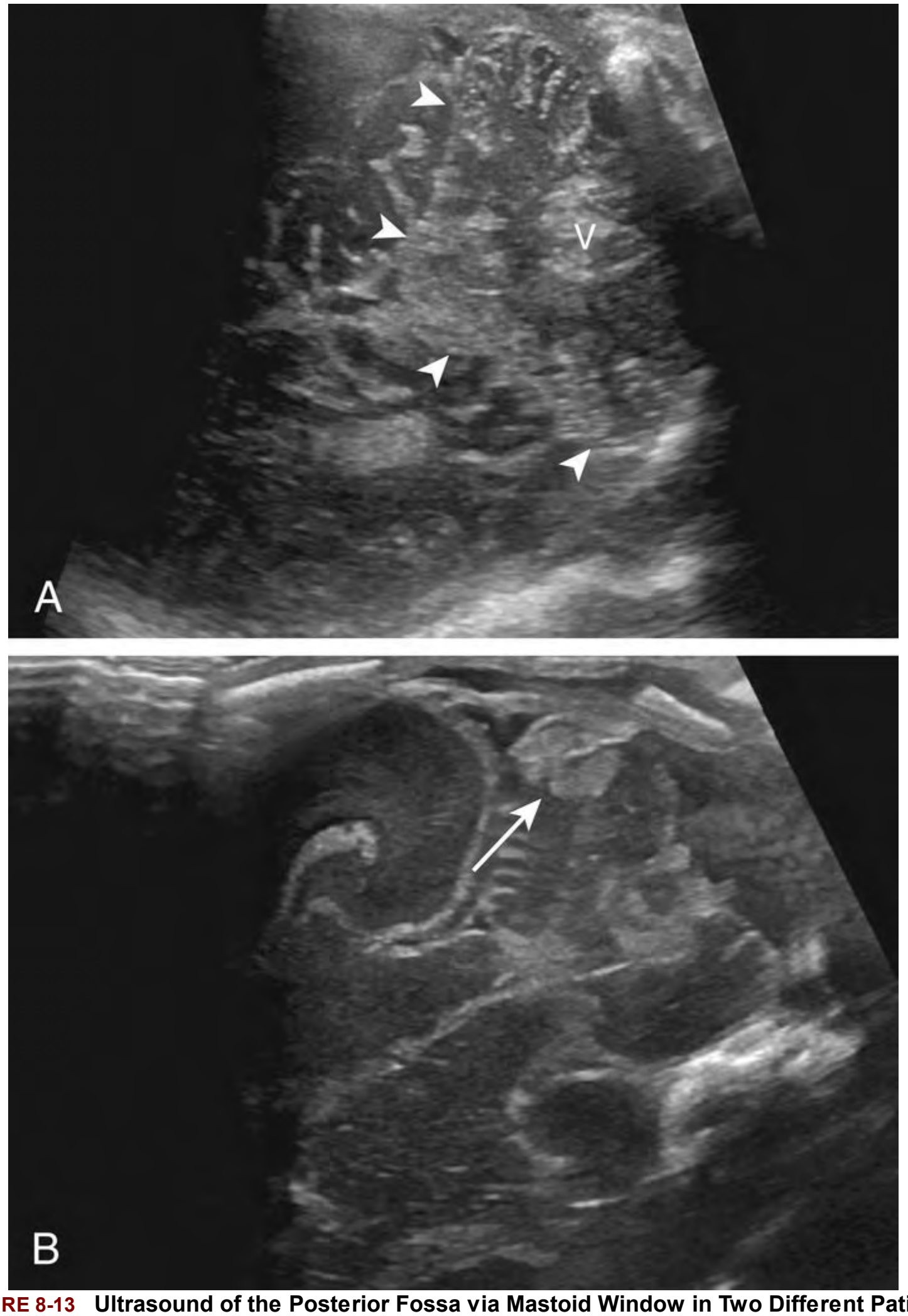
▪ **FIGURE 8-11** **Normal Findings in a Premature Neonate on Sagittal Ultrasound of the Head.**

A, Midline sagittal view demonstrates normal midline structures, including corpus callosum *(arrowheads)*, cerebellar vermis *(C)*, and fourth ventricle *(arrow)*. Note the normally increase echogenicity of cerebellar vermis. **B**, Off-midline sagittal view demonstrate normal caudothalamic groove *(arrow)*, between the caudate nucleus *(C)* and thalamus *(T)*. Note choroid plexus *(arrowheads)*.

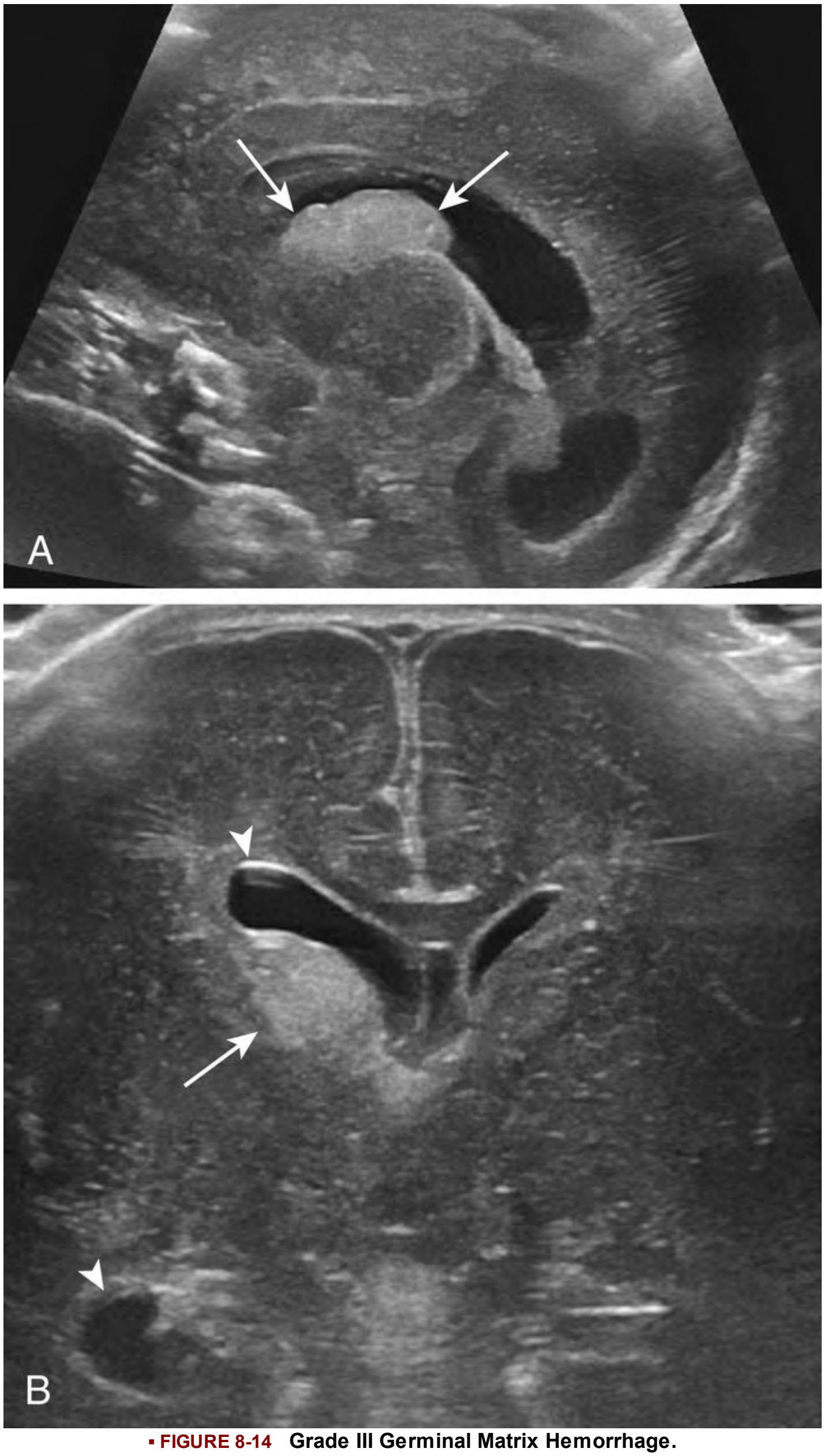


▪ **FIGURE 8-12 Ultrasound of the Extraaxial Spaces.**

A, Ultrasound via the anterior fontanel using high-resolution transducer demonstrates the subarachnoid spaces bilaterally (between *arrows*). Small subdural collection is seen on the left (between *arrowheads*). **B,** Doppler interrogation shows normal abundant vasculature within subarachnoid spaces. Note that a few bridging veins can be seen within a pathological subdural collection *(arrowhead)*.



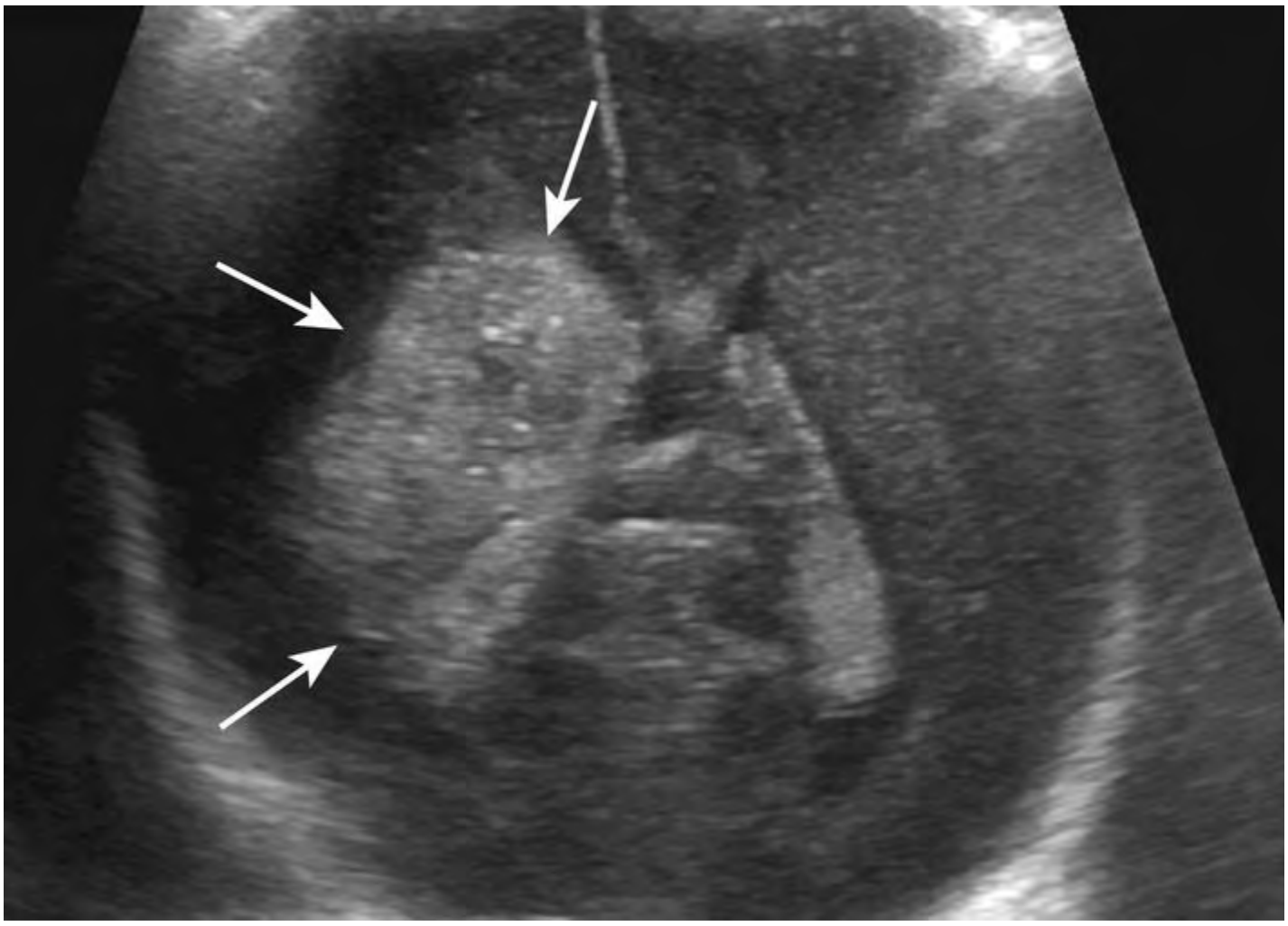
▪ **FIGURE 8-13 Ultrasound of the Posterior Fossa via Mastoid Window in Two Different Patients.** Note that images are oriented with patient anterior to left and posterior to right. **A,** Normal cerebellar hemispheres *(arrowheads)* and cerebellar vermis *(V)*. **B,** Different patient showing focal area of hemorrhage along the lateral inferior aspect of the right cerebellar hemisphere *(arrow)* compatible with cerebellar hemorrhage, depicted only with mastoid window views.



▪ **FIGURE 8-14** **Grade III Germinal Matrix Hemorrhage.**

A, Off-midline sagittal ultrasound demonstrates echogenic mass *(arrows)* in the caudothalamic groove, compatible with germinal matrix hemorrhage. **B,** Coronal view again demonstrates germinal matrix hemorrhage within the right caudothalamic grove *(arrow)* with associated enlargement of right lateral ventricle *(arrowheads)* compatible with grade III hemorrhage. Note the smooth-appearing brain with markedly diminished sulcation, consistent with prematurity.

On ultrasound, germinal matrix hemorrhage is seen as an ovoid echogenic mass within the caudothalamic groove (Figs. 8-14, *A* and *B*, and 8-15). For those not well acquainted with head ultrasound, there may be confusion in differentiating germinal matrix hemorrhage from the normally echogenic choroid plexus. In contrast to germinal matrix hemorrhage, normal choroid plexus should never extend as anterior as the caudothalamic groove on a parasagittal view (see Fig. 8-11, *B*). Hemorrhage may extend into the ventricular system and lead to hydrocephalus. Germinal matrix hemorrhage is categorized into one of four grades (Table 8-2). Intraparenchymal hemorrhage (grade IV) is secondary to venous infarction of the deep medullary veins rather than a direct extension of hemorrhage (Fig. 8-16 and see also Fig. 8-15). Grades I and II hemorrhages tend to have good prognosis. In contrast, grades III and IV hemorrhages tend to have poor prognosis, including high incidences of neurologic impairment, hydrocephalus, and death.



▪ **FIGURE 8-15** **Right Grade IV Germinal Matrix Hemorrhage.**
On coronal ultrasound there is a large echogenic area of hemorrhage *(arrows)* occupying the lateral ventricle and adjacent brain parenchyma.

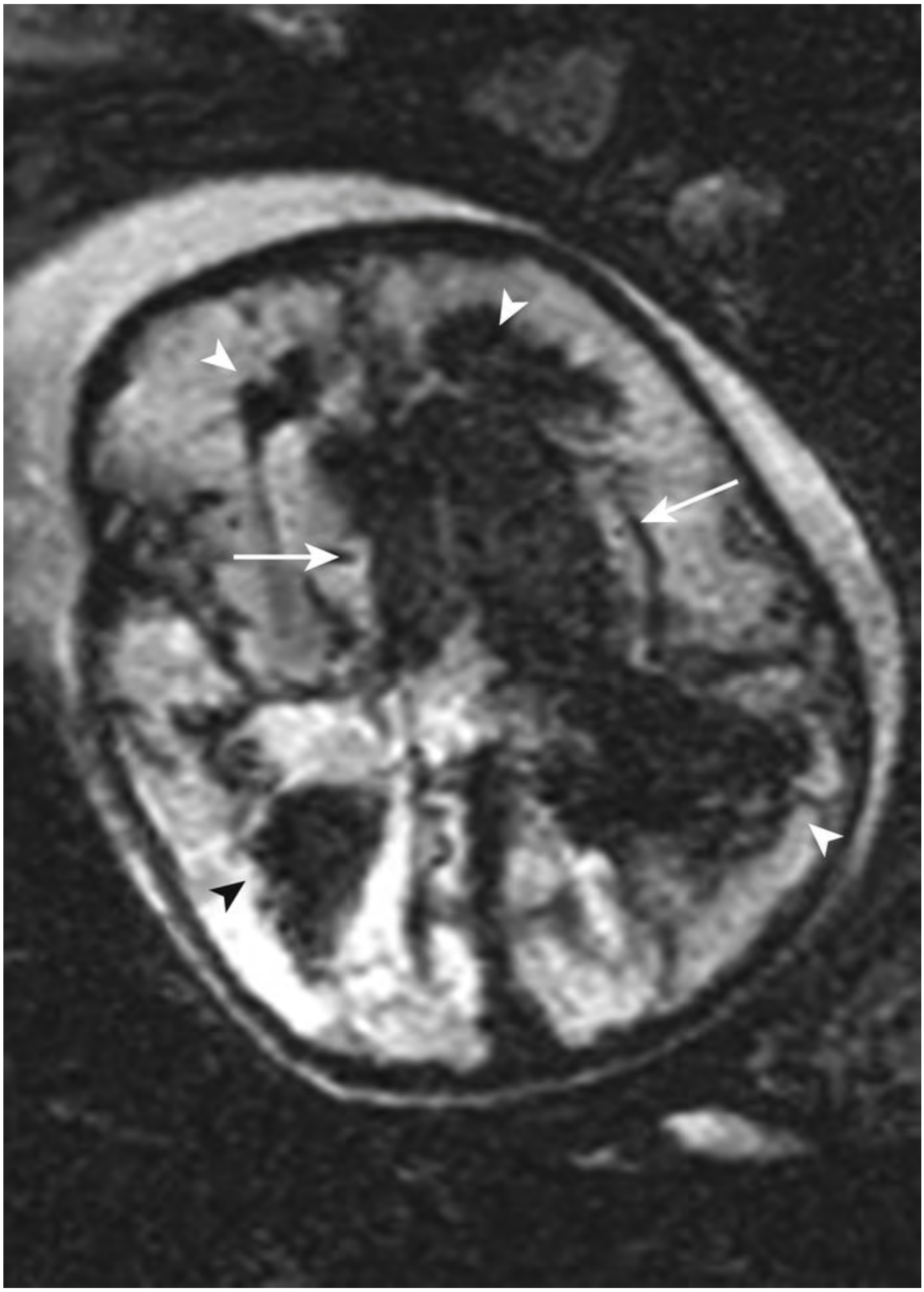
TABLE 8-2
Grades of Germinal Matrix Hemorrhage

Grade	Morphologic Findings
I	Hemorrhage confined to germinal matrix
II	Intraventricular hemorrhage without ventricular dilatation
III	Intraventricular hemorrhage with ventricular dilatation
IV	Intraparenchymal hemorrhage

Hypoxic Ischemic Insult and White Matter Injury of Prematurity

Perinatal partial asphyxia can result in damage to the periventricular white matter, the watershed zone of the premature infant, and result in white matter injury of prematurity (periventricular leukomalacia). It most commonly affects the white matter adjacent to the atria and the frontal horns of the lateral ventricles (Fig. 8-17). It is associated with neurologic sequelae, such as movement disorders, seizures, and spasticity. On ultrasound, increased heterogeneous echogenicity is seen within the periventricular white matter or basal ganglia. In severe cases there may be cystic necrosis and development of periventricular cysts (Fig. 8-18). With time, there is often volume loss of the involved white matter (Fig. 8-19, *A* and *B*). Head ultrasound can identify early signs of hypoxic ischemic insult,

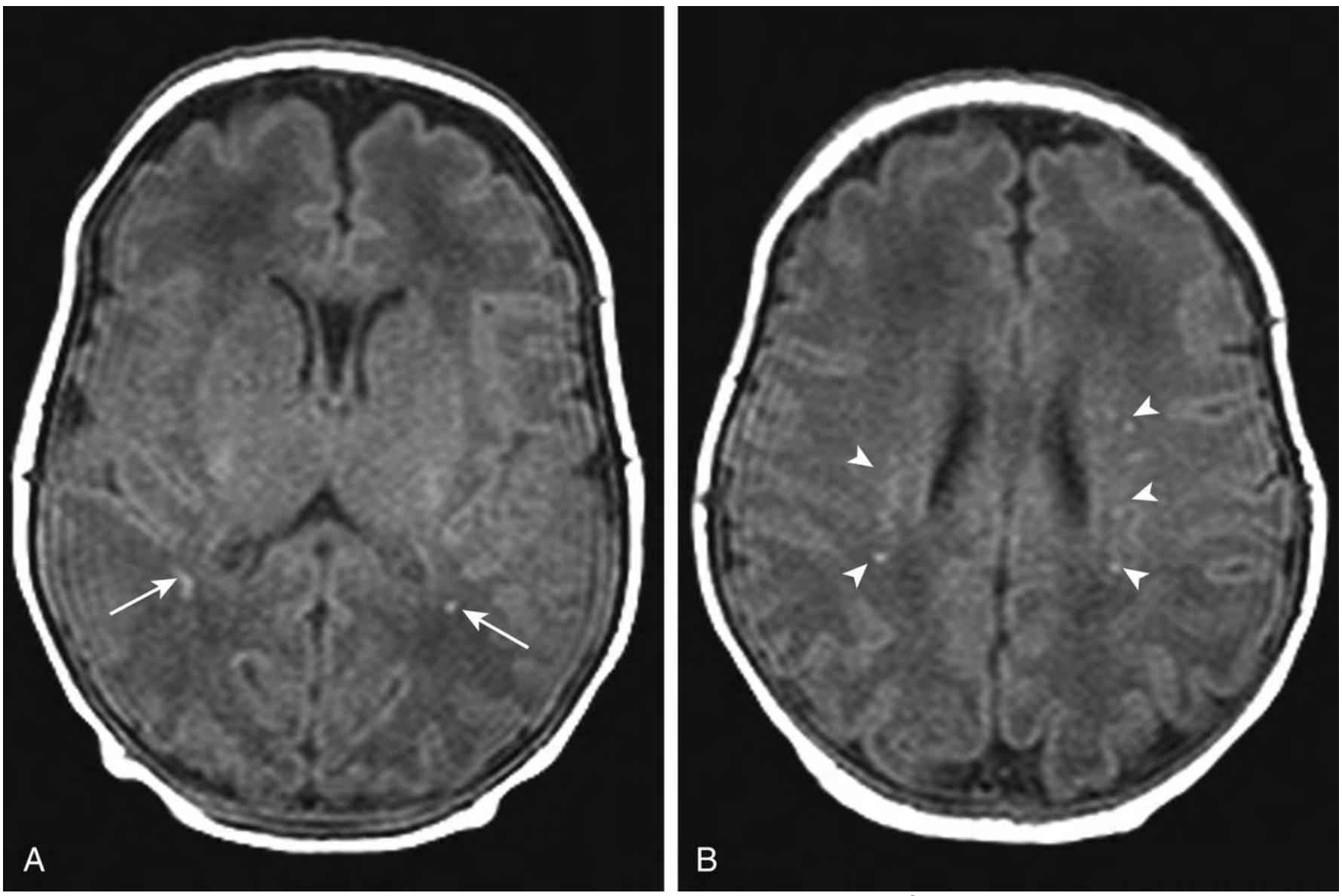
such as accentuated gray-white matter differentiation (Fig. 8-20, *A* and *B*), slitlike ventricles secondary to edema, and blurring of interhemispheric fissure. Doppler interrogation of the circle of Willis may add value in the evaluation of acute ischemia and increase intracranial pressure. Premature and full-term infants exhibit a generally accepted resistive index (RI) range of approximately 0.6 to 0.9, in the absence of cardiac disease or peripheral vascular disease. Lower values may indicate acute hypoxia or ischemia, as a result of increased diastolic flow through cerebral vasodilation. Higher values may suggest cerebral swelling where intracranial pressures rise higher than systemic pressures, leading to decreased diastolic flow.



▪ **FIGURE 8-16** **Prenatal Diagnosis of Bilateral Grade IV Hemorrhage on Fetal MRI.** Echo planar imaging (EPI) sequence demonstrates susceptibility artifact compatible with blood within the enlarged lateral ventricles *(arrows)* and at the periventricular white matter in the expected location of the deep medullary veins *(arrowheads)*.

Benign Enlargement of Extraaxial Spaces

Benign enlargement of extraaxial spaces (benign macrocrania) is a diagnosis of exclusion. The term refers to children with large heads (head circumference greater than 97% for age), prominent subarachnoid spaces, and normal development. Typically such children present between 6 months and 2 years of age. After 2 years of age, the head size usually normalizes, and the children have no long-term consequences. The parents of such children often have large heads or had large heads as infants. On imaging there is a prominent size of subarachnoid spaces and normal to borderline prominent ventricular system (Fig. 8-21, *A* and *B*). Imaging is otherwise normal. Clinical follow-up is necessary to exclude loss of milestones or continue increase in head circumference that may indicate communicating hydrocephalus.

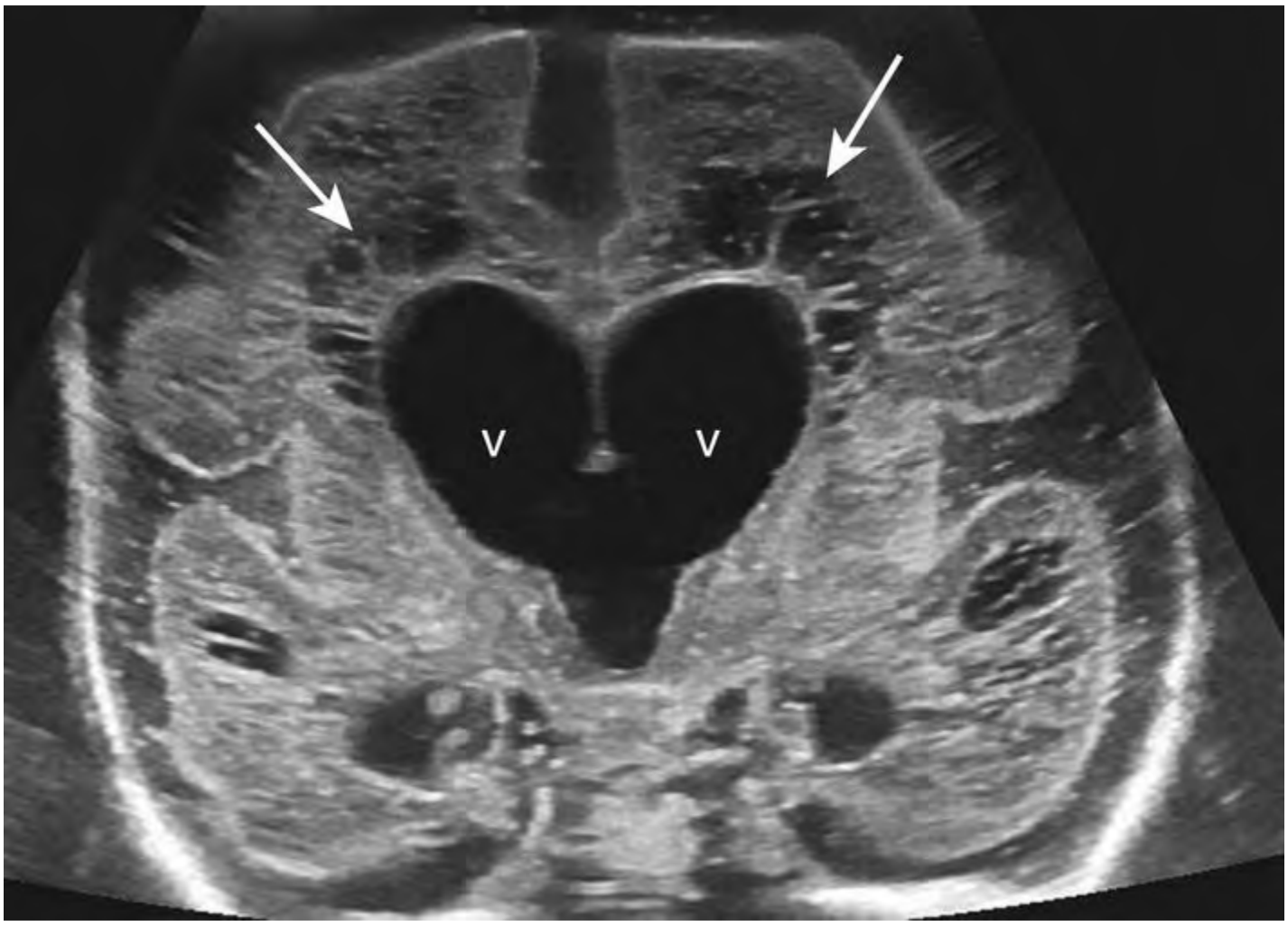


▪ **FIGURE 8-17** **Acute, Noncavitary White Matter Injury of Prematurity.**
Axial T1-weighted sequence demonstrates multiple punctate foci of increased T1 signal within the periventricular white matter bilaterally (**A,** *arrows*; **B,** *arrowheads*). This is compatible with early changes of white matter injury of prematurity and is often not depicted by ultrasound. DWI may demonstrate corresponding foci of restricted diffusion (not seen in this case).

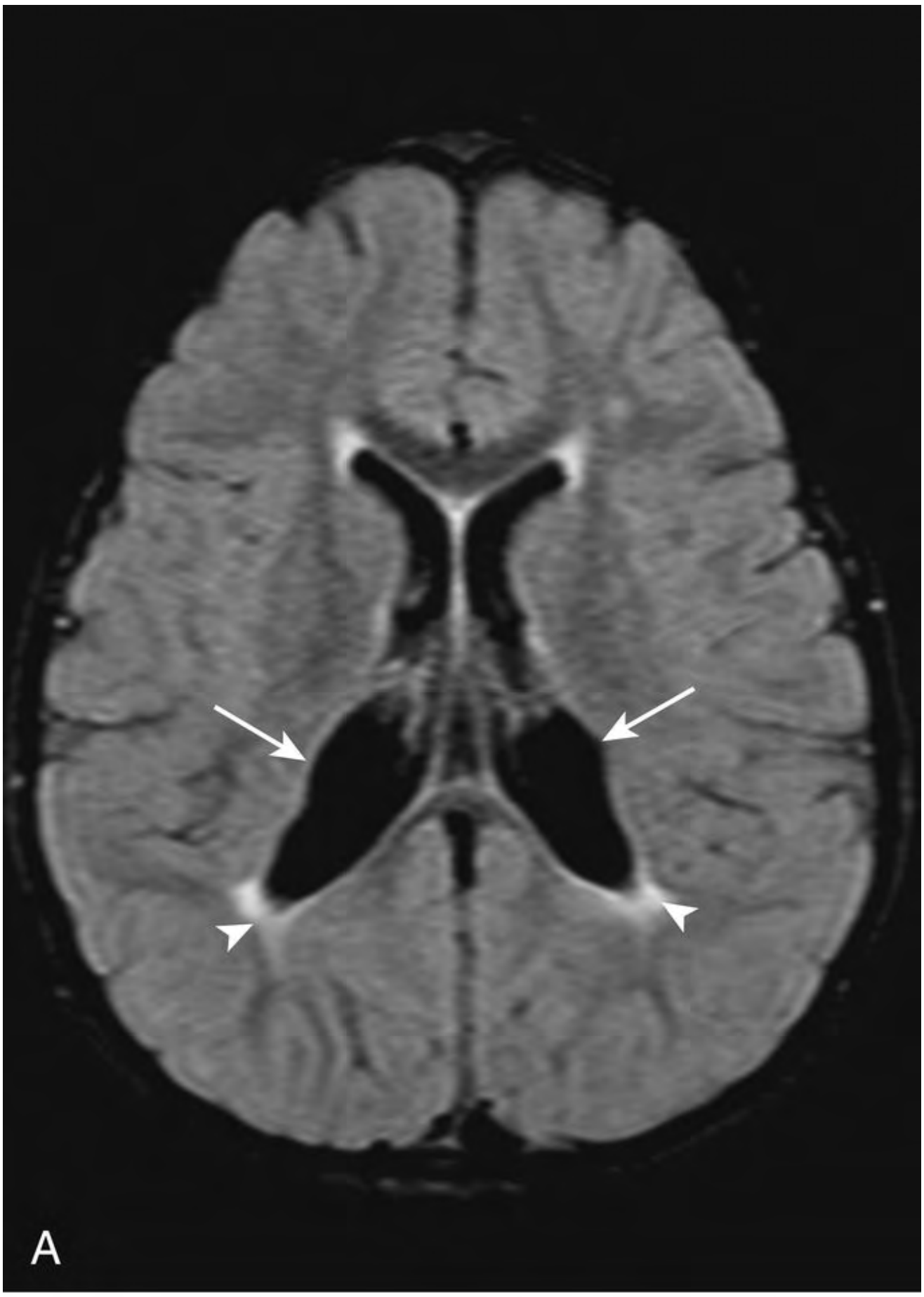
▪ Normal Myelination

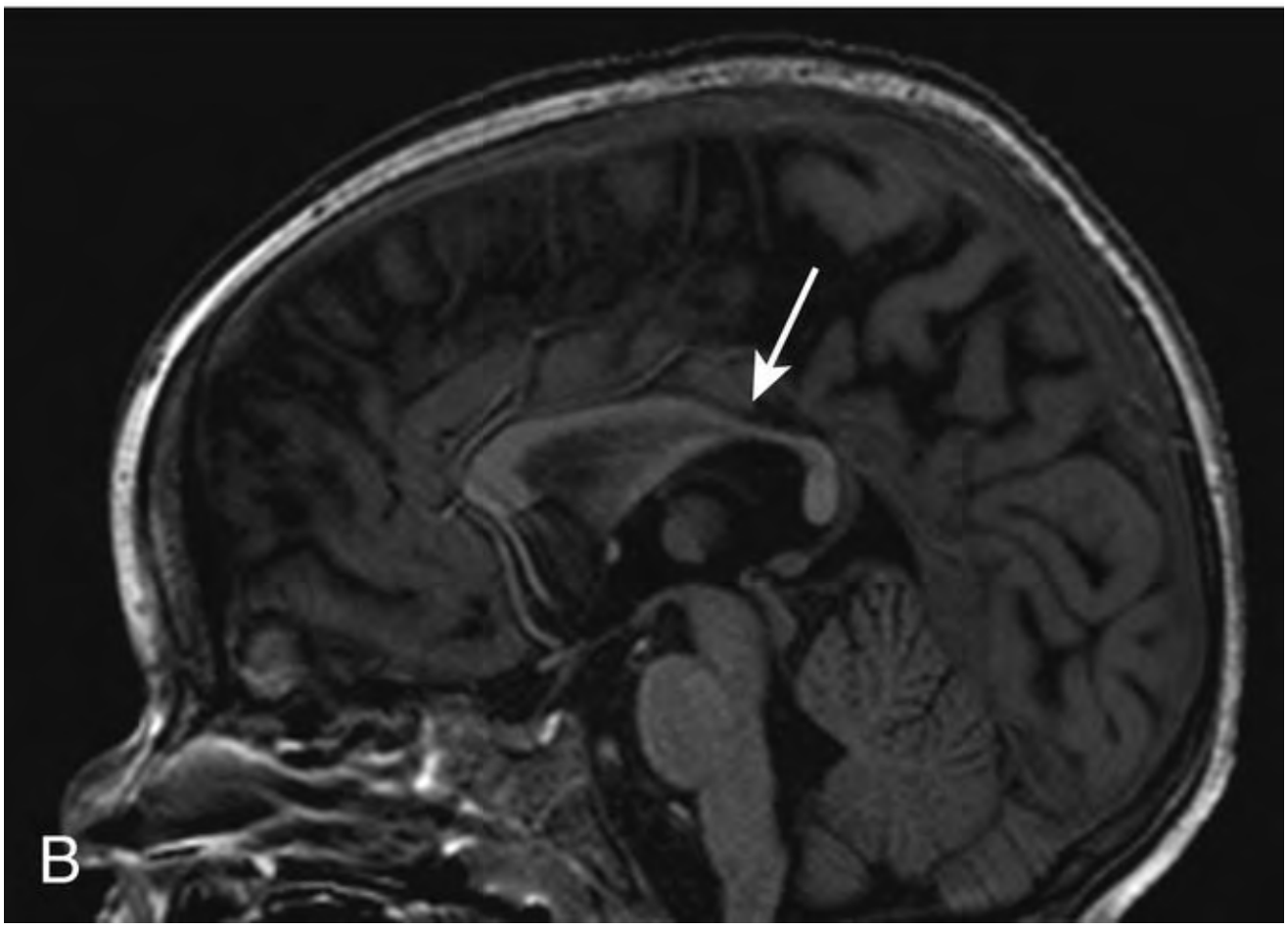
Great changes in brain myelination occur during the first 24 months of life. Before myelination, white matter is hydrophilic and, because it contains water, appears high in signal on T2-weighted images and low in signal on T1-weighted images (Fig. 8-22, *A-C*). With myelination, the white matter becomes hydrophobic and, because it contains less water, appears low in signal on T2-weighted images and high in signal on T1-weighted images (Fig. 8-23, *A* and *B*). Myelination starts in utero and progresses from caudal to cranial, central to peripheral, and dorsal to ventral, paralleling neurologic development. In myelinating white matter, T1 shortening precedes T2 shortening. Therefore T1-weighted sequence is the preferred sequence for the evaluation of normal myelination from birth until 6 month of age, whereas T2-weighted sequence is more frequently used after 6 months, especially after 1 year of age. Myelination in a term infant on T1-weighted sequence is seen along the dorsal brainstem, cerebellar peduncles, globus pallidi, lateral thalami, posterior limb of internal capsule, central corona radiata, rolandic and perirolandic regions, and optic tracts (Fig. 8-24). During the first 3 months of life, there is progressive myelination of the spinal cord and brainstem, followed by myelination of the cerebellar

white matter. The corpus callosum begins to myelinate in the splenium (posterior part) at 2 to 3 months of age, proceeds anteriorly, and is completely myelinated through the rostrum (anterior part) by 6 to 8 months of age. Table 8-3 summarizes the expected myelination milestones in T1 and T2 sequences, with key milestones highlighted in bold. Myelination becomes similar to adult patterns on T2-weighted sequence by 24 to 36 months of age, with the exception of few terminal zones. Terminal zones of myelination can be seen in the frontotemporal subcortical white matter until the age of 36 to 40 months, whereas the commonly identified posterior periventricular terminal zones of myelination can be seen as late as teenage years (Fig. 8-25).

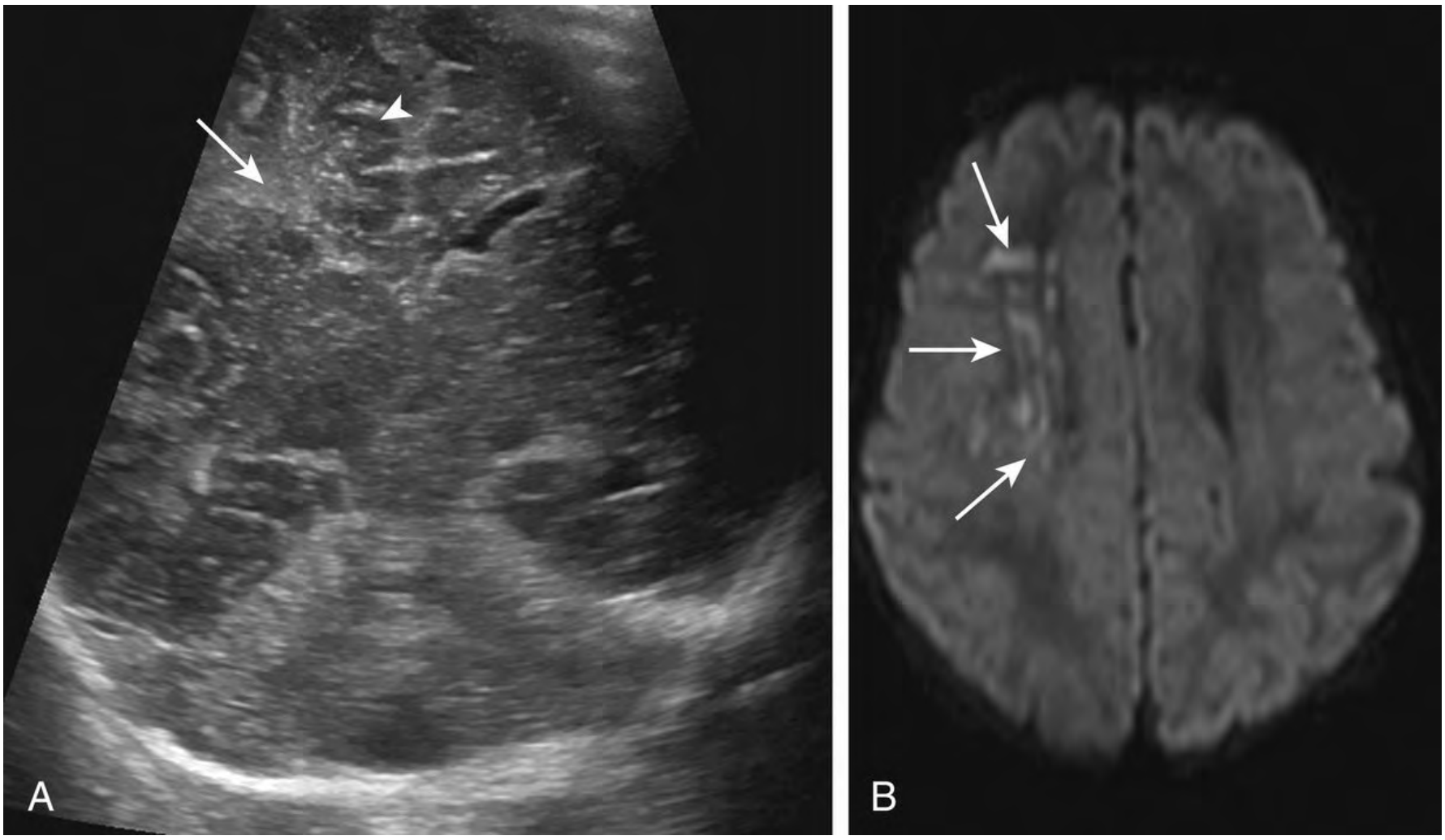


▪ **FIGURE 8-18** **Cystic White Matter Injury of Prematurity.**
Coronal ultrasound shows heterogeneous echogenicity in the frontal periventricular white matter with multiple cystic changes compatible with cavitary evolution of white matter injury of prematurity *(arrows)*. There are similar lesions in the temporal lobes. There is associated enlargement of ventricular system *(V)*. Note the markedly diminished sulcation consistent with prematurity.

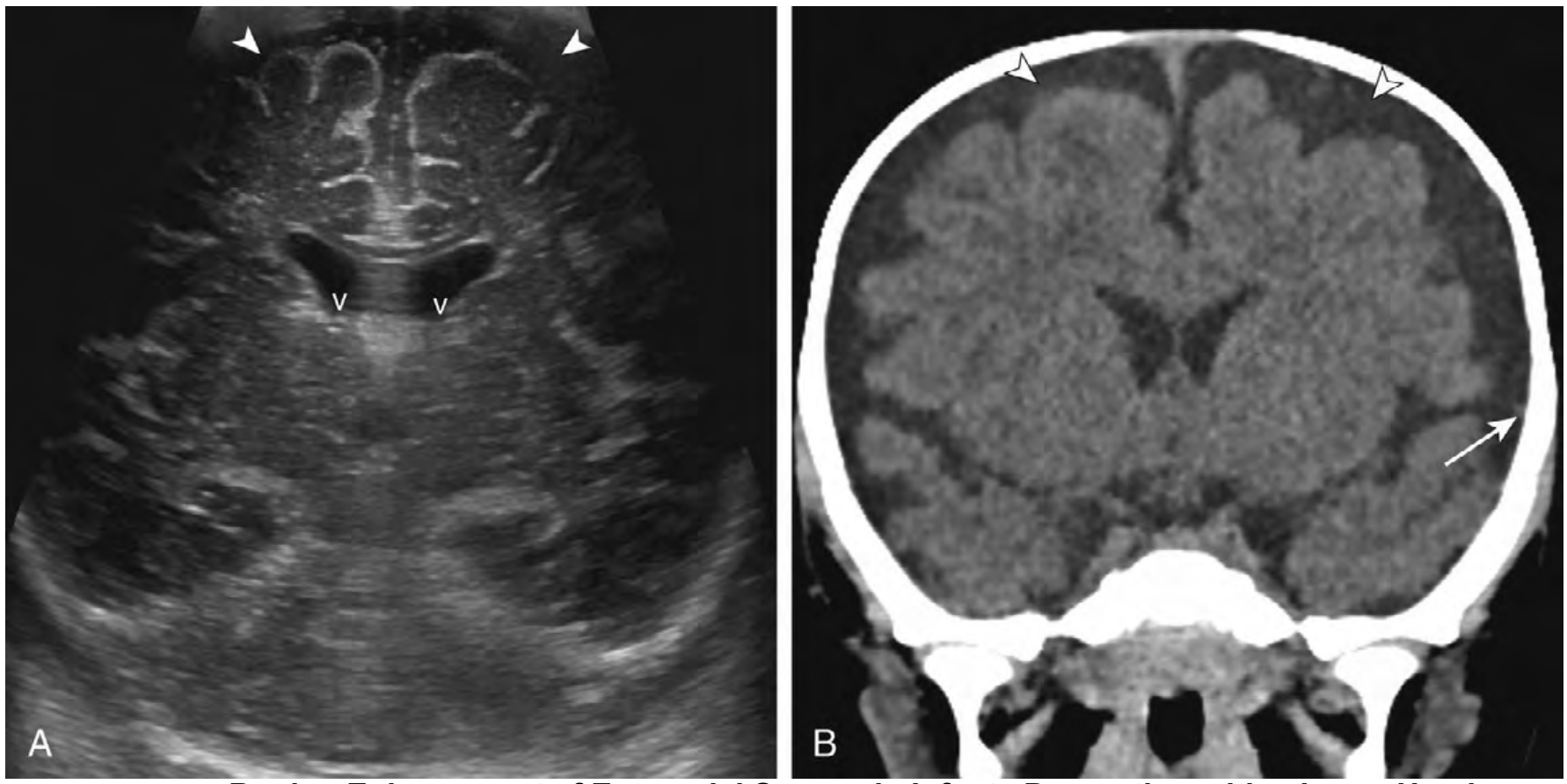

A


B

▪ **FIGURE 8-19** **Chronic Changes of White Matter Injury of Prematurity.**
A, Axial FLAIR image demonstrates periventricular white matter volume loss with mildly enlarged and dysmorphic lateral ventricles *(arrows).* There is also mildly increased periventricular white matter signal marginating the lateral ventricles, compatible with gliosis *(arrowheads)*. **B,** Sagittal T1-weighted sequence shows mild thinning of the corpus callosum, especially at its posterior body *(arrow)*, as a result of white matter volume loss.

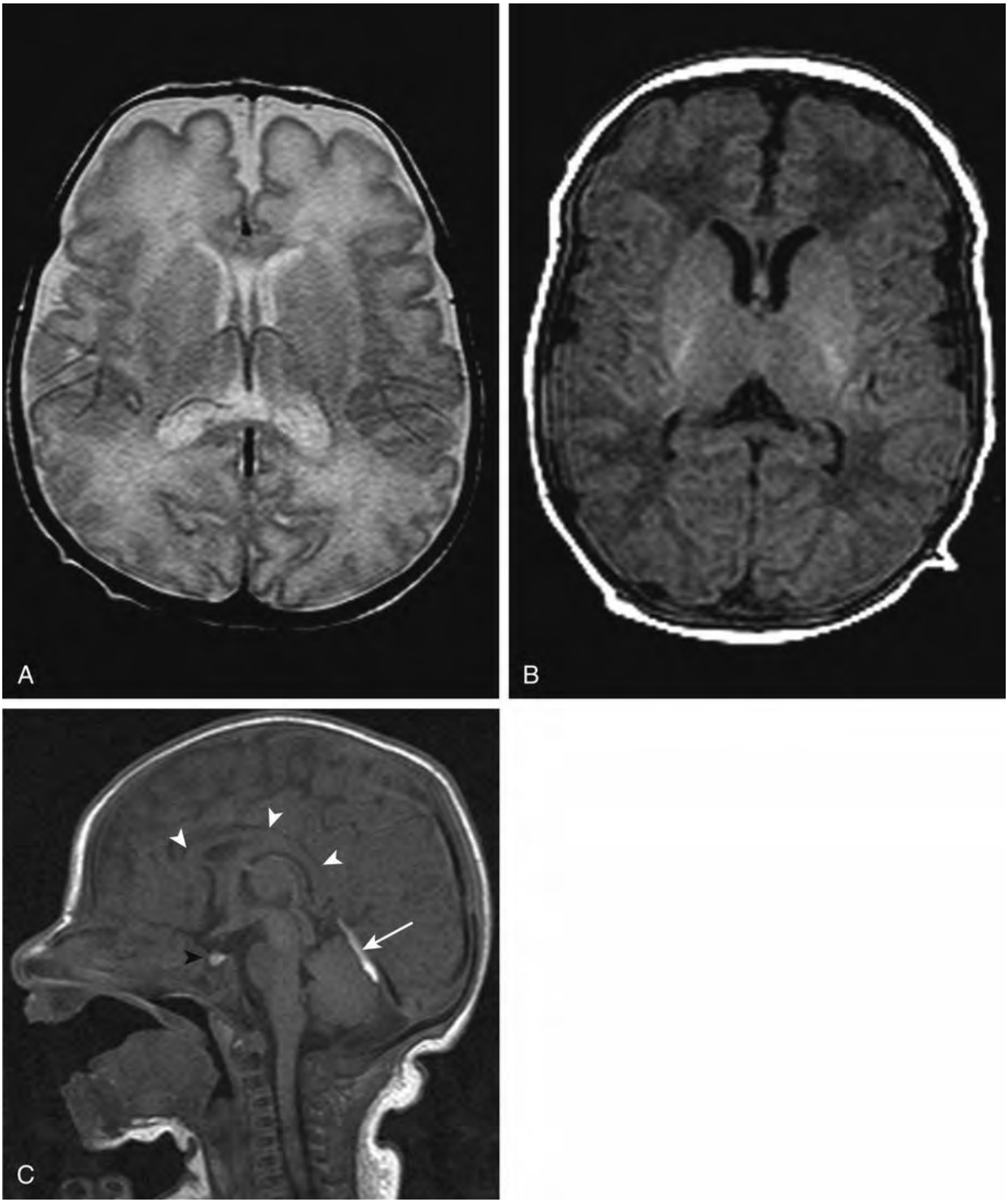


▪ **FIGURE 8-20** **Ischemic Insult by Ultrasound.**
A, Coronal ultrasound demonstrating increased right periventricular white matter echogenicity *(arrow)* and accentuated gray-white matter differentiation *(arrowhead)*. There is also decreased size of ipsilateral lateral ventricle due to edema. **B,** Diffusion-weighted sequence MRI confirmed area of diffusion restriction *(arrows)*.



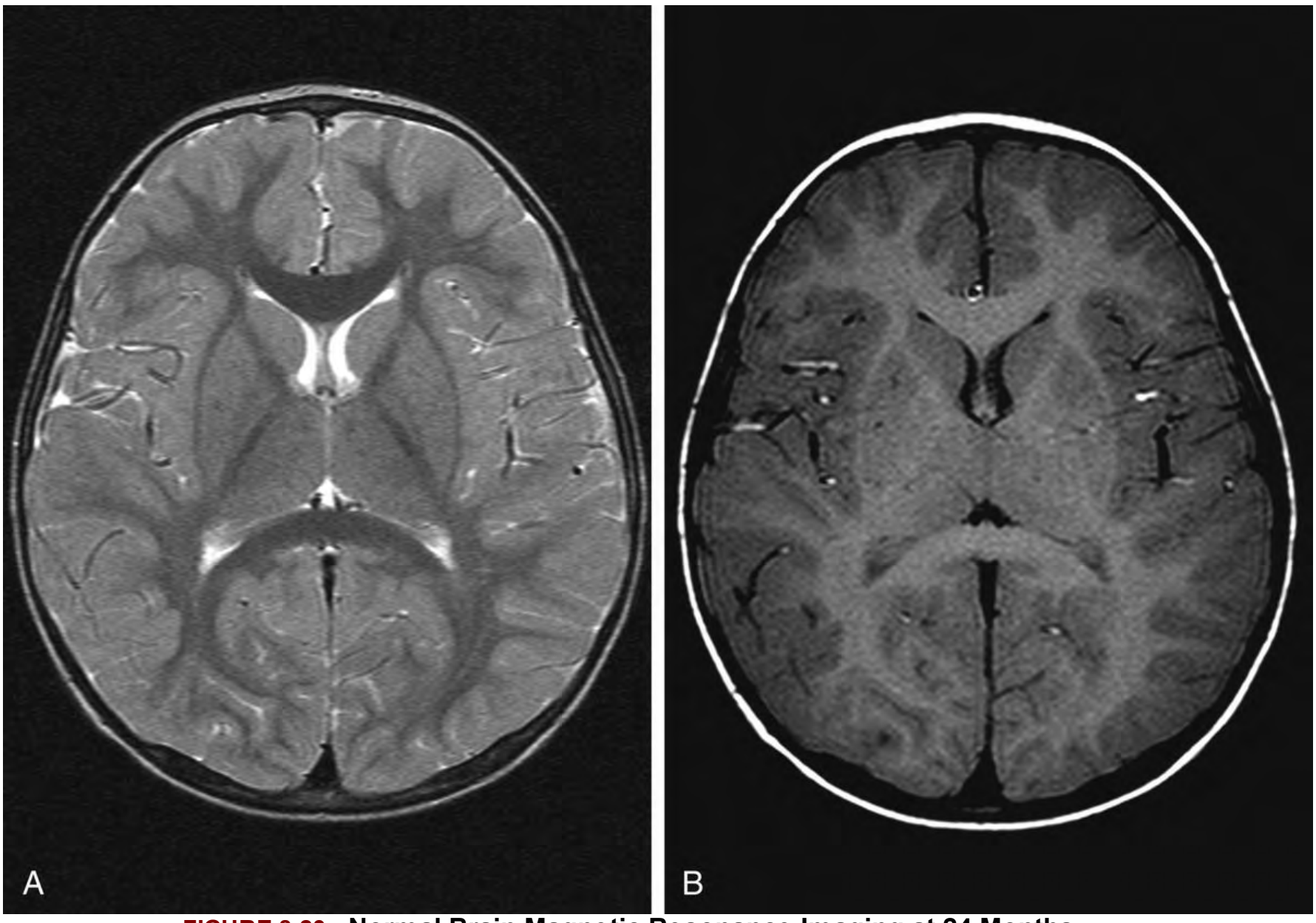
▪ **FIGURE 8-21 Benign Enlargement of Extraaxial Spaces in Infants Presenting with a Large Head Circumference.**

A, Image from coronal ultrasound shows prominent subarachnoid spaces *(arrowheads)* and borderline prominence of the lateral ventricles *(V)*. **B,** Coronal reformat from CT study also showing bilateral symmetric enlargement of subarachnoid spaces *(arrowheads)*. Note the peripherally located cortical vessel away from the brain parenchyma *(arrow)*, helping in the differentiation from chronic subdural collections, which are known to cause medial (towards the brain) displacement of these vessels.



▪ **FIGURE 8-22** **Normal Newborn Brain MRI.**

Axial T1- (**A**) and axial T2-weighted (**B**) sequences demonstrating normal low T1 signal and high T2 signal of unmyelinated white matter. **C,** Sagittal T1-weighted sequence shows low signal and mild thinning of the corpus callosum, normal in the neonatal period due to lack of myelination *(white arrowheads)*. The pituitary gland demonstrates increased T1 signal throughout *(black arrowhead)*, normal in neonates. Note small amount of hemorrhage along the tentorium near the straight sinus *(arrow)*. This is a common and clinically not significant finding related to recent delivery.



▪ **FIGURE 8-23** **Normal Brain Magnetic Resonance Imaging at 24 Months.**
Axial T2- (**A**) and axial T1-weighted (**B**) sequences demonstrating normal myelination characterized by increased T1 and decrease T2 white matter signal. Compare with neonatal MRI (see Fig. 8-22).

Assessing myelination has become a key component in the evaluation of children with developmental delay. Abnormal myelination is a nonspecific finding and can be secondary to a number of causes, including metabolic disease, infection, trauma, hypoxia-ischemia, and genetic or malformative syndromes.

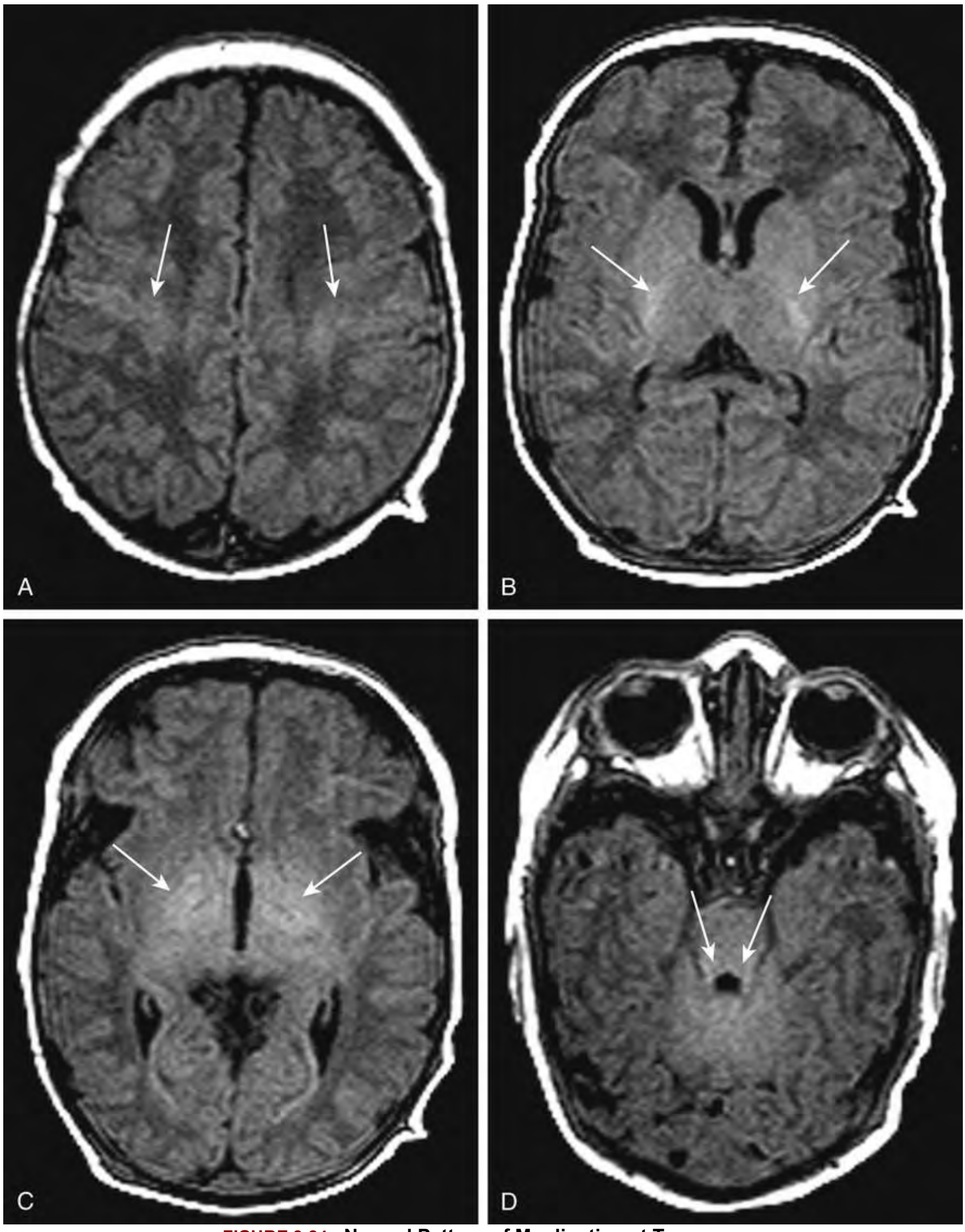
▪ Developmental Abnormalities

Developmental abnormalities can be classified on the basis of the embryologic event that fails, causing the abnormality (Table 8-4). Categories include abnormalities of dorsal induction, ventral induction, migration and cortical organization, neuronal proliferation and differentiation, and myelination. Abnormalities can also result from destruction of already formed structures. The type of developmental lesion often reflects the timing of the disturbance that occurred during development. Often, multiple distinct developmental abnormalities are present simultaneously.

Chiari

Chiari Type 1

Chiari type 1 is the presence of an abnormal inferior location of the cerebellar tonsils, at least 5 mm below the foramen magnum (Fig. 8-26). The cerebellar tonsils are typically elongated in morphology rather than round, and there are different degrees of CSF effacement at the craniocervical junction. The medulla and fourth ventricle are in normal positions. Complications of Chiari type 1 include hydrocephalus and hydromyelia (see Fig. 8-26). It may be suspected on CT when the foramen magnum appears "full" with soft tissue (Fig. 8-27). It is best visualized on sagittal MR images. Phase-contrast CSF flow MR sequence is often used to show CSF space effacement and pistoning movement of the cerebellar tonsils. Chiari 1 may be acquired with increase intracranial pressure and may also resolve with child growth.



▪ **FIGURE 8-24** **Normal Pattern of Myelination at Term.**

From superior to inferior, axial T1-weighted images of the brain parenchyma in a normal term neonate. Increased T1 signal compatible with myelinated white matter *(arrows)* is seen along the rolandic and perirolandic regions and central corona radiata (**A**), posterior limb of internal capsules (**B**), inferior globus pallidi and subthalamic nucleous (**C**), posterior brainstem, and superior cerebellar peduncle (**D**). See Table 8-3 for detailed list of myelinated structures at term and myelination milestones.

TABLE 8-3
Myelination Milestones

Age	T1 High Signal	T2 Low Signal
Term	Rolandic or perirolandic gyri (up to 2 mo)	Central CR
	Central CR	Posterior ⅓ of PLIC
	PLIC	Dorsal pons
	Globus pallidi	Vermis
	Lateral thalamus	
	Optic radiations	
	Dorsal brainstem	
	Cerebellar peduncles	
	Dentate nucleus	
	Vermis	
By 3-4 mo	Splenium of corpus callosum	½ PLIC
	Cerebellar white matter	Optic radiations
	ALIC	Middle cerebellar peduncle
	Anterior pons	Dentate nucleus
	Hippocampus	
	Central occipital white matter	
By 6 mo	Genu of corpus callosum	Splenium of corpus callosum
	Deep frontal white matter	PLIC
		Cerebellar white matter
		Anterior pons
By 8 mo	Near adult, except for most peripheral temporal and frontal subcortical branches	Genu of corpus callosum
		ALIC (at least partially)
		Increasing myelination of CR
By 12 mo	Temporal white matter	CR
		ALIC
		Deep occipital white matter
By 14-18 mo	Subcortical U fibers	Deep frontal white matter
		Branching occipital white matter
18-24 mo	Fully myelinated	Near adult, except for most peripheral temporal and frontal subcortical branches
24-36 mo		Fully myelinated

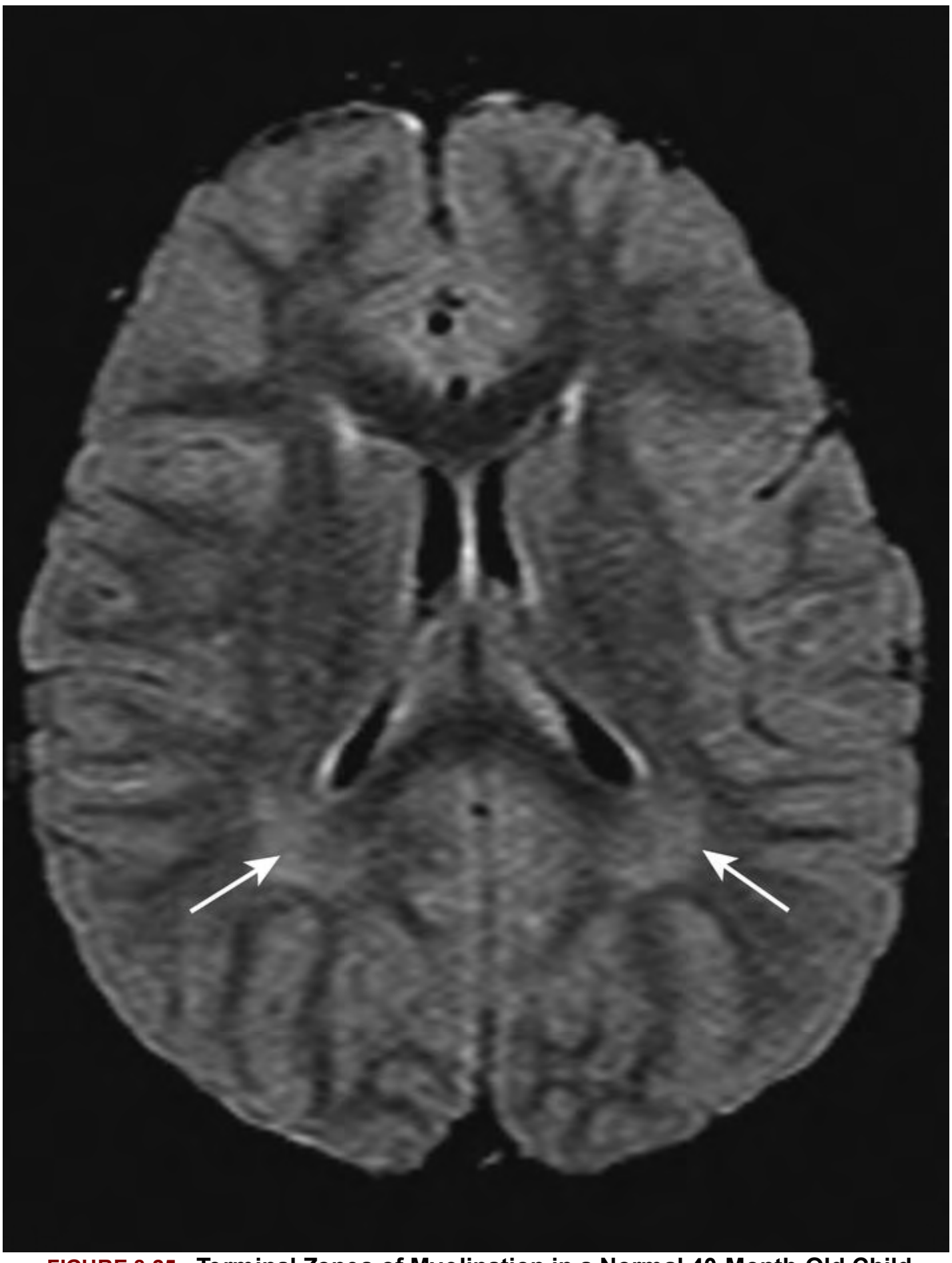
ALIC, Anterior limb of internal capsule; *CR,* corona radiata; *PLIC,* posterior limb of internal capsule.

Chiari Type 2

Chiari type 2 is a malformation of hindbrain and is almost always associated with myelomeningoceles. Conversely, almost all patients with myelomeningoceles have Chiari type 2 malformation. Patients with this abnormality have small posterior fossa and associated inferior displacement of the cerebellum, medulla, and fourth ventricle into the upper cervical canal (Fig. 8-28). Associated imaging findings include a kinked appearance of the medulla, colpocephaly (disproportionate enlargement of the posterior body of the lateral ventricles), fenestration of the falx associated with interdigitating gyri across the midline, enlargement of the massa intermedia, inferior pointing of the lateral ventricles, and tectal beaking (a pointed appearance of the quadrigeminal plate). Chiari type 2 malformations are usually associated with hydrocephalus diagnosed prenatally (Fig. 8-29, *A* and *B*).

Prenatal correction of myelomeningocele can be performed in a subset of fetuses, following specific inclusion criteria. The aim is to decrease hindbrain herniation and the postnatal use of VPSs, as well as to improve lower extremity function (Fig. 8-30, *A* and *B*).

Chiari type 3 and type 4 malformations are very rare.



▪ **FIGURE 8-25** **Terminal Zones of Myelination in a Normal 40-Month-Old Child.** Axial T2 FLAIR sequence shows focal increased FLAIR signal within the bilateral posterior periventricular white matter compatible with terminal zones of myelination *(arrows)*. Note the thin band of normal myelinated white matter between the terminal zones and the lateral ventricles. This helps in the differentiation from periventricular gliosis seen in white matter injury of prematurity.

TABLE 8-4

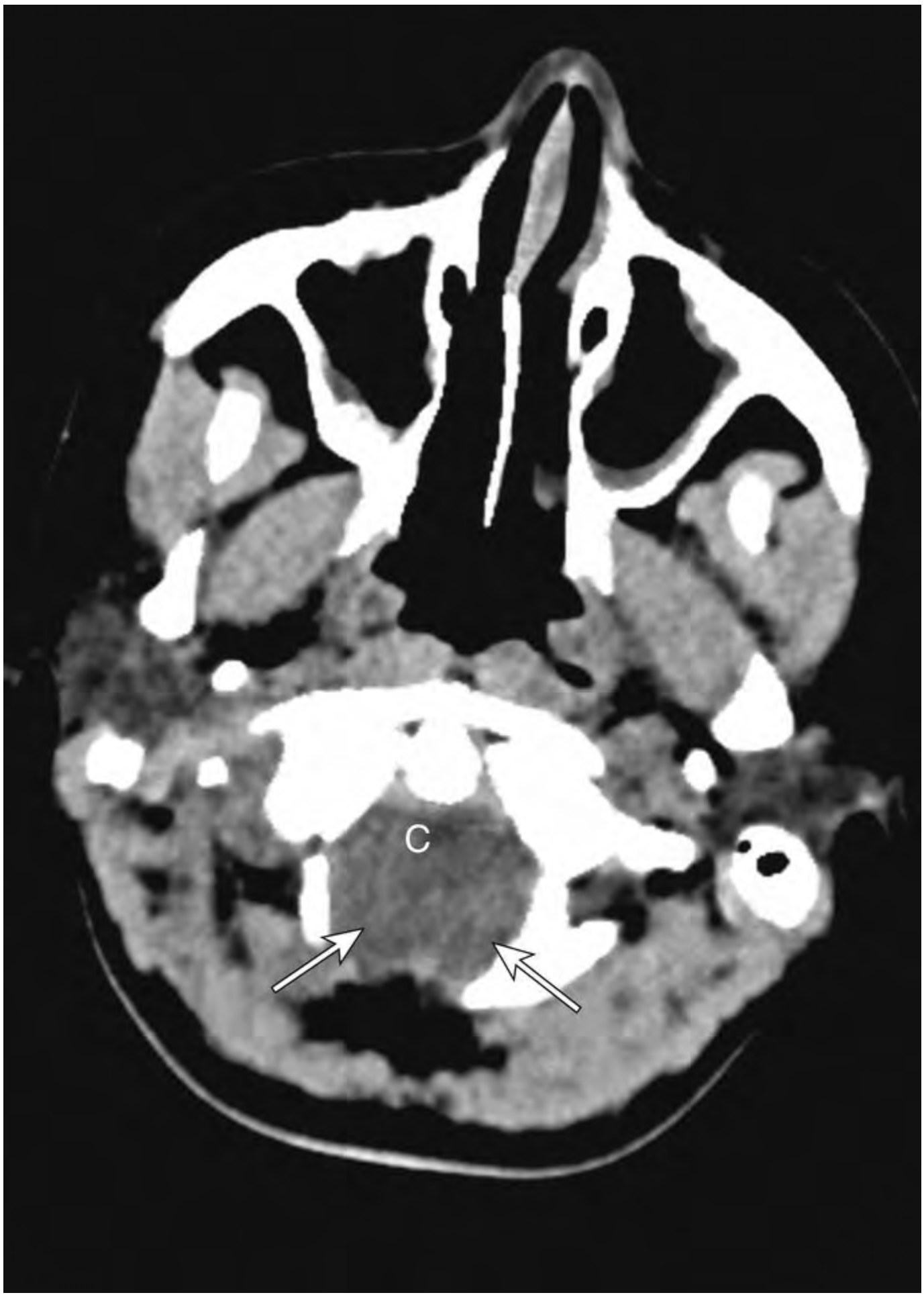
Common Development and Congenital Abnormalities of the Brain

Abnormality	Mechanism (Abnormality of)	Description	Associated Imaging Findings
Chiari type 2	Dorsal induction and complex hindbrain malformation	Small posterior fossa with inferior displacement of cerebellum, fourth ventricle, and brainstem into cervical canal; associated with myelomeningocele	Colpocephaly
			Fenestrated falx
			Large massa intermedia
			Tectal beaking
			Cervicomedullary kink
			Hydrocephalus
Holoprosencephaly	Ventral induction	Failure in cleavage of brain into two cerebral hemispheres	Alobar type:
			Single ventricle Fused thalami
			Absent corpus callosum and falx
Dandy-Walker malformation	Defect in rhombencephalon formation and/or abnormal fenestration of foramens of Magendie and Luschka	Complete or partial agenesis of the cerebellar vermis in conjunction with an enlarged retrocerebellar CSF spaces and/or cyst	Posterior fossa is enlarged (elevated torcula)
			May be an isolated posterior fossa anomaly or present with multiple associated supratentorial abnormalities
Gray matter heterotopia	Migration	Arrested migration of neurons, resulting in heterotopic areas of gray matter within the subependymal regions or white matter	Subependymal or subcortical
			Nodular or laminar appearance
			Isointense to gray matter
Schizencephaly	Late migration and cortical organization	Gray matter-lined cleft extending from lateral ventricle to cerebral surface	Absent septum pellucidum—common
			Other migration abnormalities, hippocampal and callosal anomalies may be seen
Lissencephaly (lissencephaly type I or classic lissencephaly)	Migration	Arrest neuronal migration causing failure of development of gyri and sulci	Smooth cortical surface ("figure eight" appearance of the brain)
			Cortical thickening
			Other migration abnormalities are common
			Part of many rare genetic disorders
Cobblestone complex (cobblestone lissencephaly or lissencephaly type II)	Migration	Overmigration with lack of normal laminar organization of the cortex.	Smooth cortical surface
			Pebbled appearance of the cortex
			Hypoplastic and kinked brainstem
			Often associated with aqueductal stenosis, eye abnormalities and congenital muscular dystrophies
Cortical dysplasia	Neuronal proliferation (FCD type II and glioneural tumors) Cortical organization (FCD type I and III)	Abnormality of neuronal proliferation and/or organization leading to dysplastic cortex	Imaging commonly normal
			Type II FCD may show focal cortical thickening, blurring of gray-white matter and triangular shaped white matter signal changes
			May have associated glioneuronal tumor (dual pathology)
Polymicrogyria	Late migration and cortical organization	Cortex showing multiple small gyri and sulci	Predilection to perisylvian region
			Small gyri may appear fused given appearance similar to pachygyria
			Part of many genetic syndromes
Hemimegalencephaly	Neuronal proliferation	Hamartomatous overgrow of one cerebral hemisphere	Enlarged and dysplastic cerebral hemisphere
			Enlarged ipsilateral ventricle
			Intractable epilepsy
Dysgenesis of the corpus callosum	Commissure formation	Complete or partial absence of the corpus callosum	Parallel lateral ventricles
			Bundles of Probst
			Colpocephaly
			High-riding third ventricle
Vein of Galen malformation	Disorder of vascular differentiation	Arteriovenous fistula to embryonic precursor of the vein of Galen resulting in large posterior midline venous varix	May cause brain ischemia or infarct from "steal phenomenon"
			May present with hydrocephalus
			Congestive heart failure may be the first identified symptom
Hydranencephaly	Injury of formed structures	Destruction of the cerebrum secondary to insult affecting the bilateral internal carotid arteries	Cerebrum replaced by CSF
			Falx is present
			Thalami separated
			Normal or enlarged head circumference
Porencephaly	Injury of formed structures	Cyst formation from injury to brain parenchyma during first or second trimester	Thin-walled CSF cyst
			May communicate with lateral ventricle (no cortical lining)
			No septations



▪ **FIGURE 8-26** **Chiari 1.**

Sagittal T2-weighted sequence showing low-lying, peg-shaped cerebellar tonsils *(white arrow)* causing crowding of CSF spaces at the craniocervical junction. There is also a posteriorly tilted C2 dens causing mild impression upon the anterior cervicomedullary junction *(black arrow).* Note associated hydromyelia *(arrowheads)* within the lower cervical and upper thoracic spinal cord.



▪ FIGURE 8-27 Chiari 1.

Axial noncontrast CT at the level of the posterior arch of C1, just below the foramen magnum. There is tissue crowding composed of normal upper spinal cord *(C)* and low-lying cerebellar tonsils *(arrows)*. Findings compatible with Chiari 1. This can be confirmed on sagittal reconstructions when equivocal on axial images.

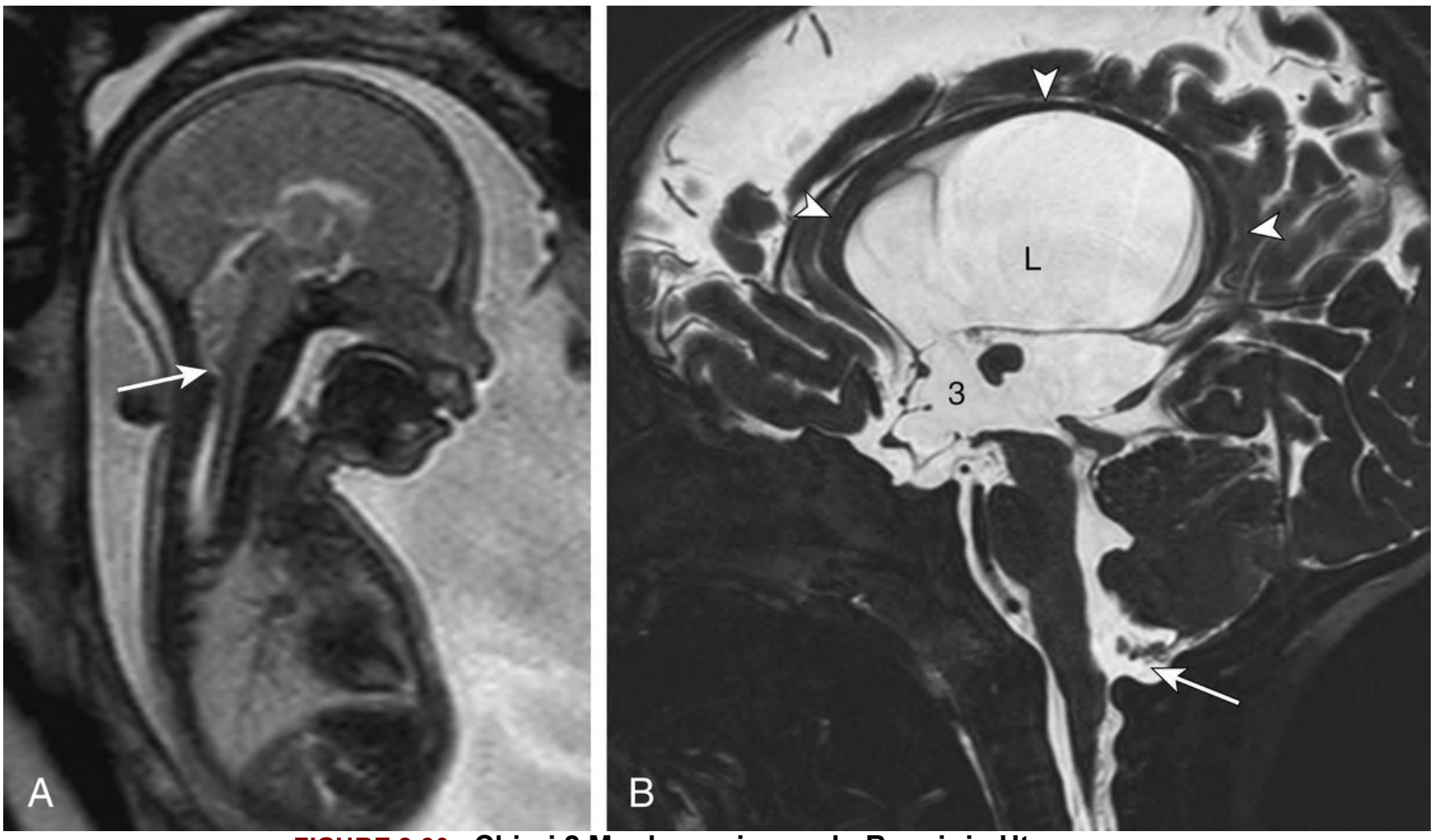


▪ **FIGURE 8-28** **Chiari 2 Malformation.**
Sagittal T1-weighted image shows downward displacement of cerebellar tonsils *(white arrow)*. The posterior fossa is small, and the fourth ventricle is compressed. There is a prominent massa intermedia *(black arrow)* and beaked tectum *(black arrowhead)*. Note marked enlargement of lateral ventricle *(L)* and consequent superiorly displaced and thinned corpus callosum *(arrowheads)*.



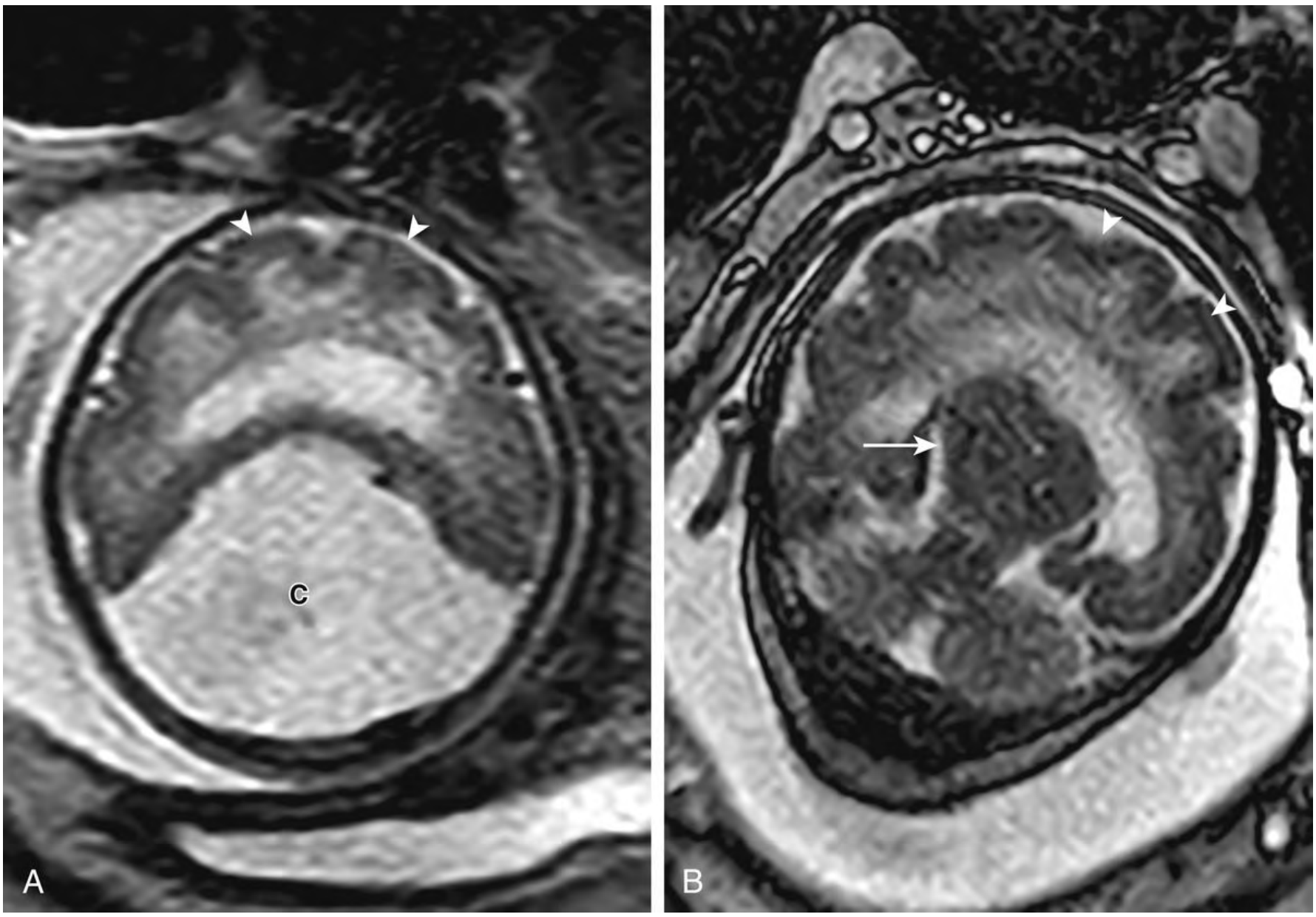
▪ **FIGURE 8-29 Chiari 2 Malformation on Fetal Magnetic Resonance Imaging.**

A, Axial, single-shot fast spin echo (SSFSE) sequence from fetal MRI of fetal head demonstrates bilateral enlargement of lateral ventricles *(V)* and bifrontal skull concavities compatible with classic lemon head sign *(arrows)*. **B**, Sagittal SSFSE sequence of the spine shows lumbosacral myelomeningocele sac *(black arrow)*. Note thin band of low T2 signal within myelomeningocele sac, representing neuroelements.



▪ **FIGURE 8-30** **Chiari 2 Myelomeningocele Repair in Utero.**

A, Fetal MRI: small posterior fossa and low-lying cerebellar tonsils *(arrow)* seen in this fetus with known myelomeningocele, compatible with Chiari 2 malformation. Fetus underwent successful in utero repair of myelomeningocele. **B,** Postnatal sagittal T2 balanced steady-state free precession (b-FFE) sequence of same patient shows resolution of hindbrain herniation *(arrow)*. However, there is persistent dilatation of third *(3)* and lateral ventricles *(L)*. Thinning of corpus callosum *(arrowheads)* is commonly seen in cases of neonatal hydrocephalus such as this one.



▪ **FIGURE 8-31** **Alobar Holoprosencephaly.**
A, Axial fetal MRI shows complete fusion of cerebral hemispheres *(arrowheads)*. A single ventricle is present, and a large CSF-containing structure is seen posterior to the fused parenchyma. This is known as a dorsal cyst *(C)*. Note the absence of falx. **B,** Coronal view again demonstrates fused cerebral parenchyma *(arrowheads)* and fused thalami *(arrow).*

Holoprosencephaly

Holoprosencephaly results from lack of complete cleavage of the brain into two hemispheres. Although there is a continuous spectrum of severity, holoprosencephaly is classically classified into one of three distinct groups: alobar, semilobar, or lobar. The severity of the brain abnormality is usually reflected in the severity of the midline facial abnormality.

Alobar holoprosencephaly (Fig. 8-31, *A* and *B*) is the most severe form and is characterized by a monoventricle. The thalami are fused and there is no attempt at cleavage of the cerebral hemispheres. There is no falx cerebri or corpus callosum. There is a single anterior cerebral artery (azygous artery). These infants are commonly stillborn or have a very short life span.

With the intermediate form, semilobar holoprosencephaly (Fig. 8-32, *A* and *B*), the cerebral hemispheres are partially cleaved from each other posteriorly. The temporal horns of the lateral ventricles may be formed, but there is a single ventricle anteriorly. There is at least partial separation of the thalami. Midline structures, such as the falx and corpus callosum, may be present posteriorly but not anteriorly.

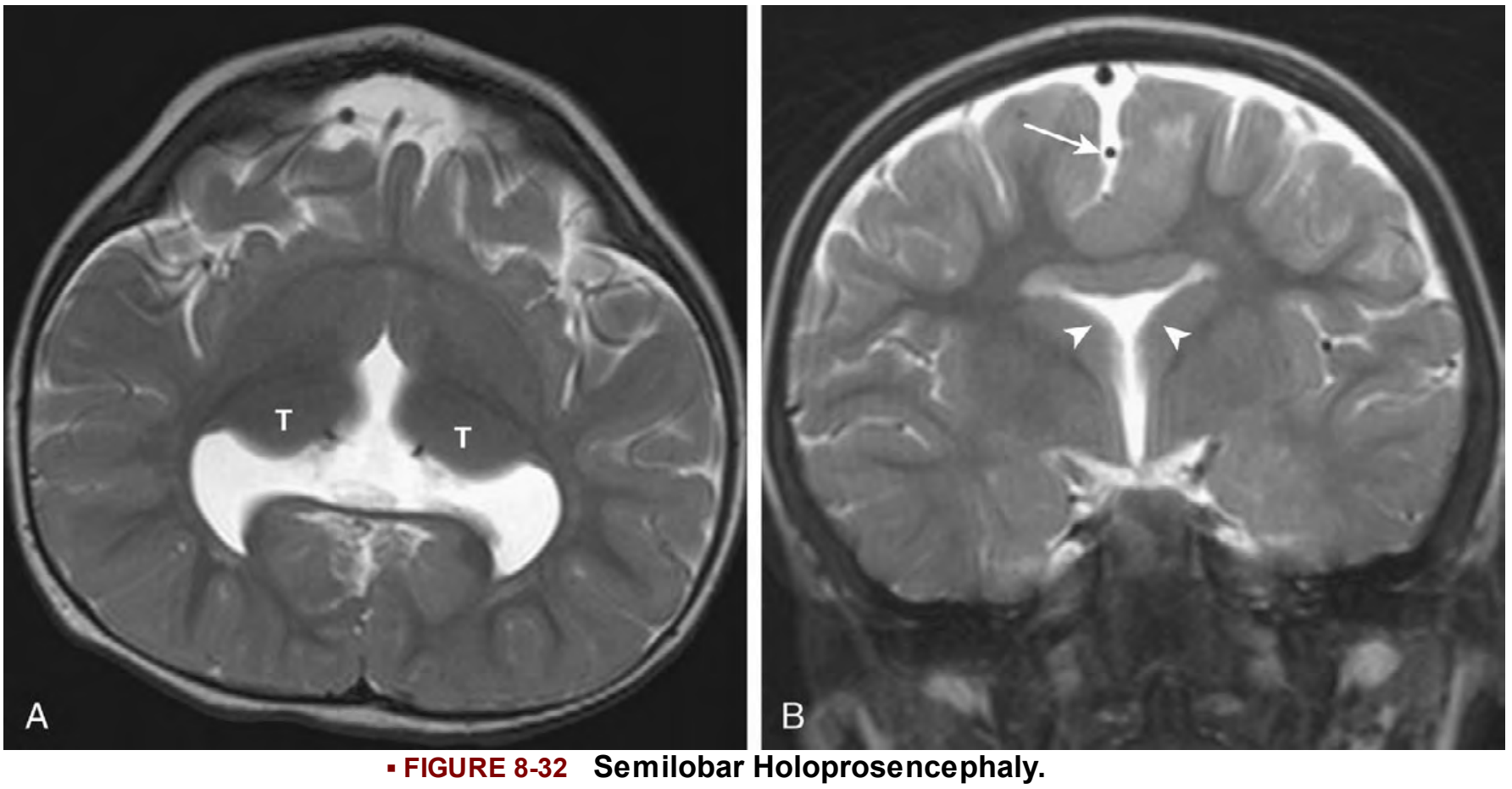
Lobar holoprosencephaly is a milder form in which the occipital and temporal horns are well formed but there is failure of cleavage of the frontal lobes. The septum pellucidum is absent, and the corpus callosum may be absent or dysplastic.

A less severe form of holoprosencephaly is syntelencephaly or middle interhemispheric variant, and may be seen as fusion only of the midline posterior frontal lobes and parietal lobes (Fig. 8-33). Different degrees of septum pellucidum and corpus callosum agenesis/dysgenesis can be present.

Septo-optic Dysplasia

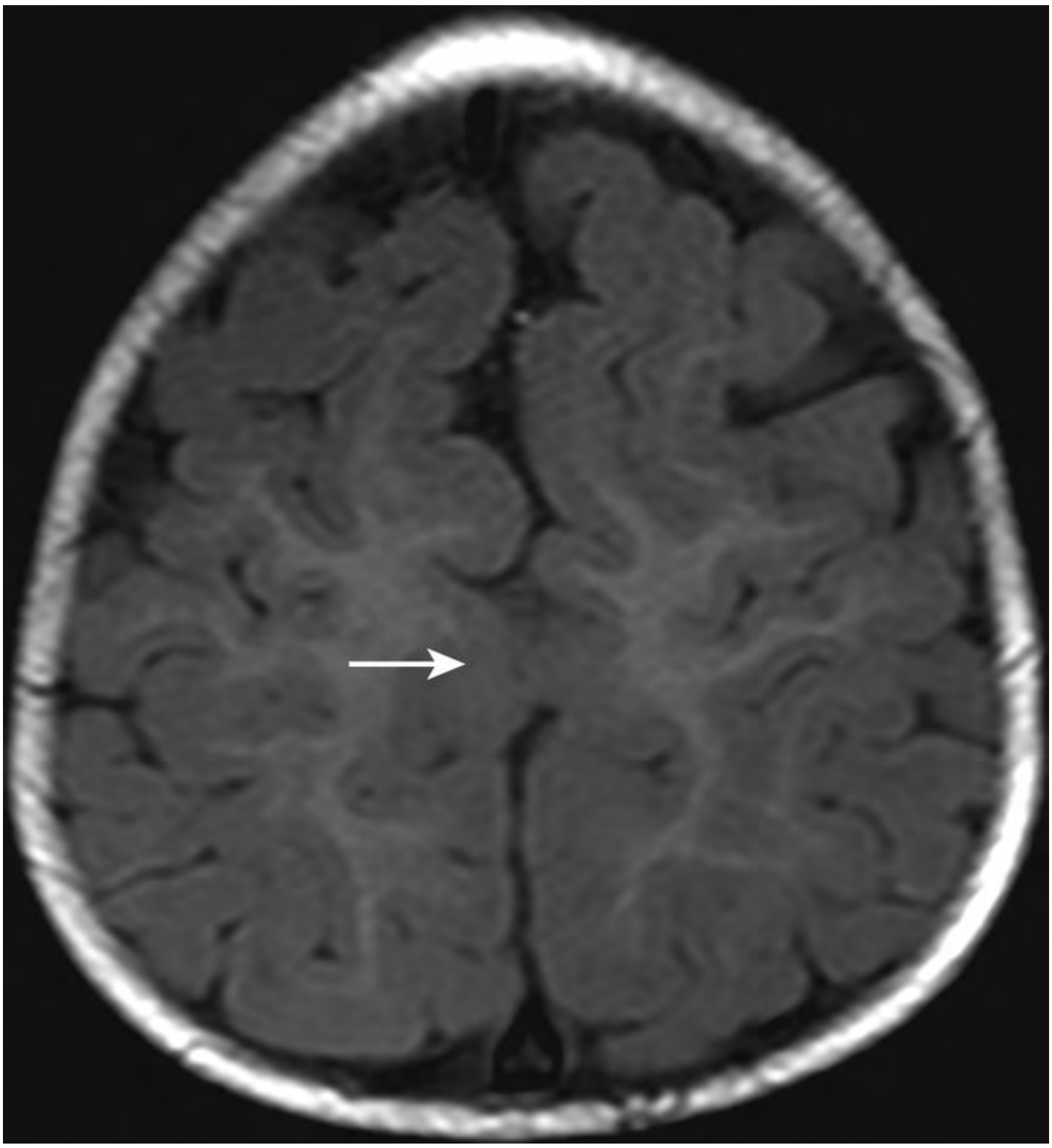
Septo-optic dysplasia is another type of ventral induction malformation, analogous to mild holoprosencephaly. It was originally described as absence of the septum pellucidum and hypoplasia of

the optic nerves (diagnosed most often by ophthalmological evaluation). It was later discovered that there is often associated pituitary abnormalities and dysfunction (approximately two thirds). Currently, several authors believe that a combination of any two of the three findings is part of the disease spectrum. Pituitary abnormalities may include absent visualization of T1 bright posterior pituitary gland, ectopic posterior pituitary gland (Fig. 8-34), interrupted or hypoplastic pituitary stalk, or hormonal abnormalities with no obvious imaging finding. Septo-optic dysplasia may also present with schizencephaly, heterotopia, and incomplete hippocampi inversion. In septo-optic dysplasia the frontal horns of the lateral ventricles have a squared appearance on coronal MR images.

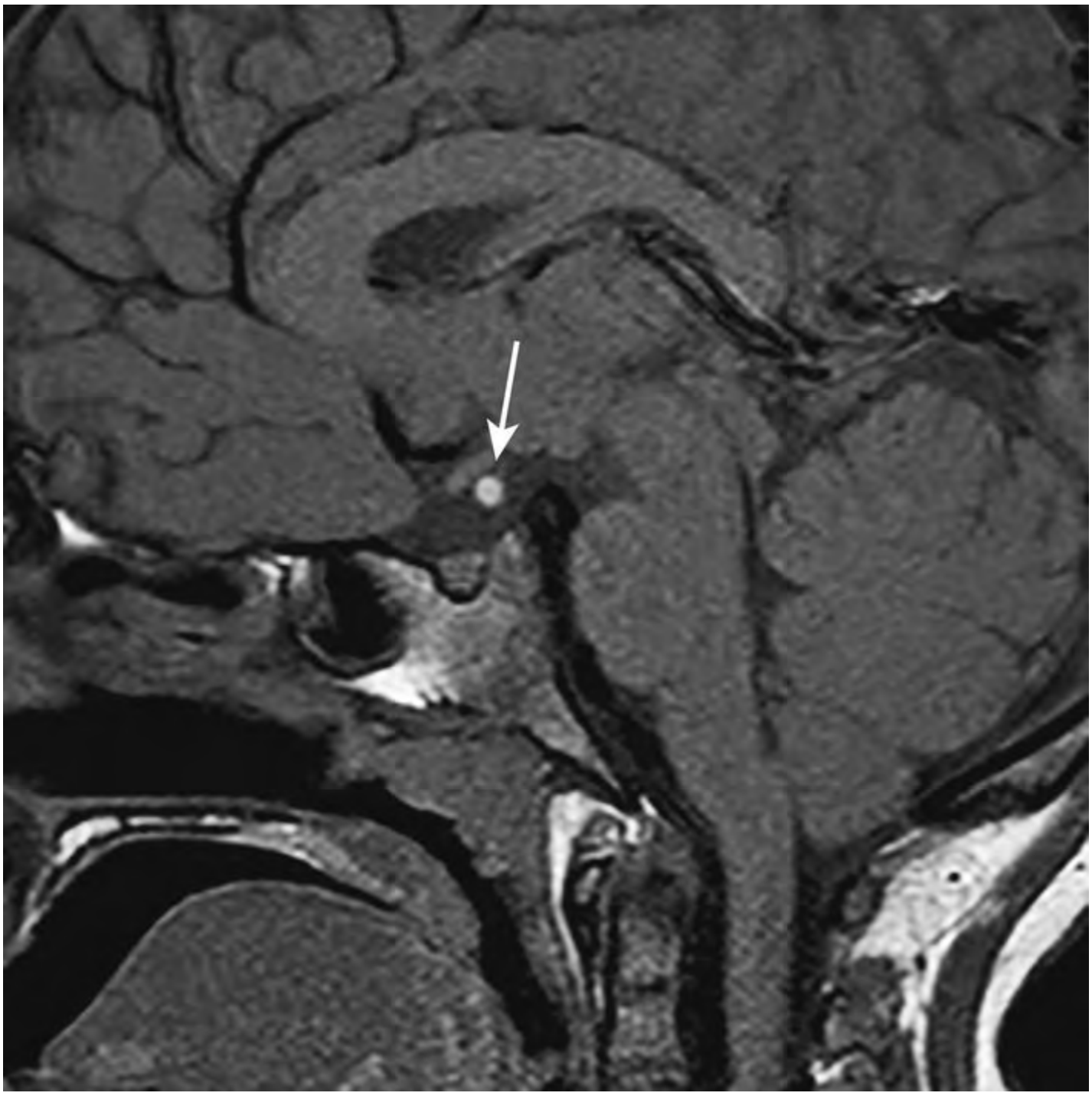


▪ **FIGURE 8-32** **Semilobar Holoprosencephaly.**

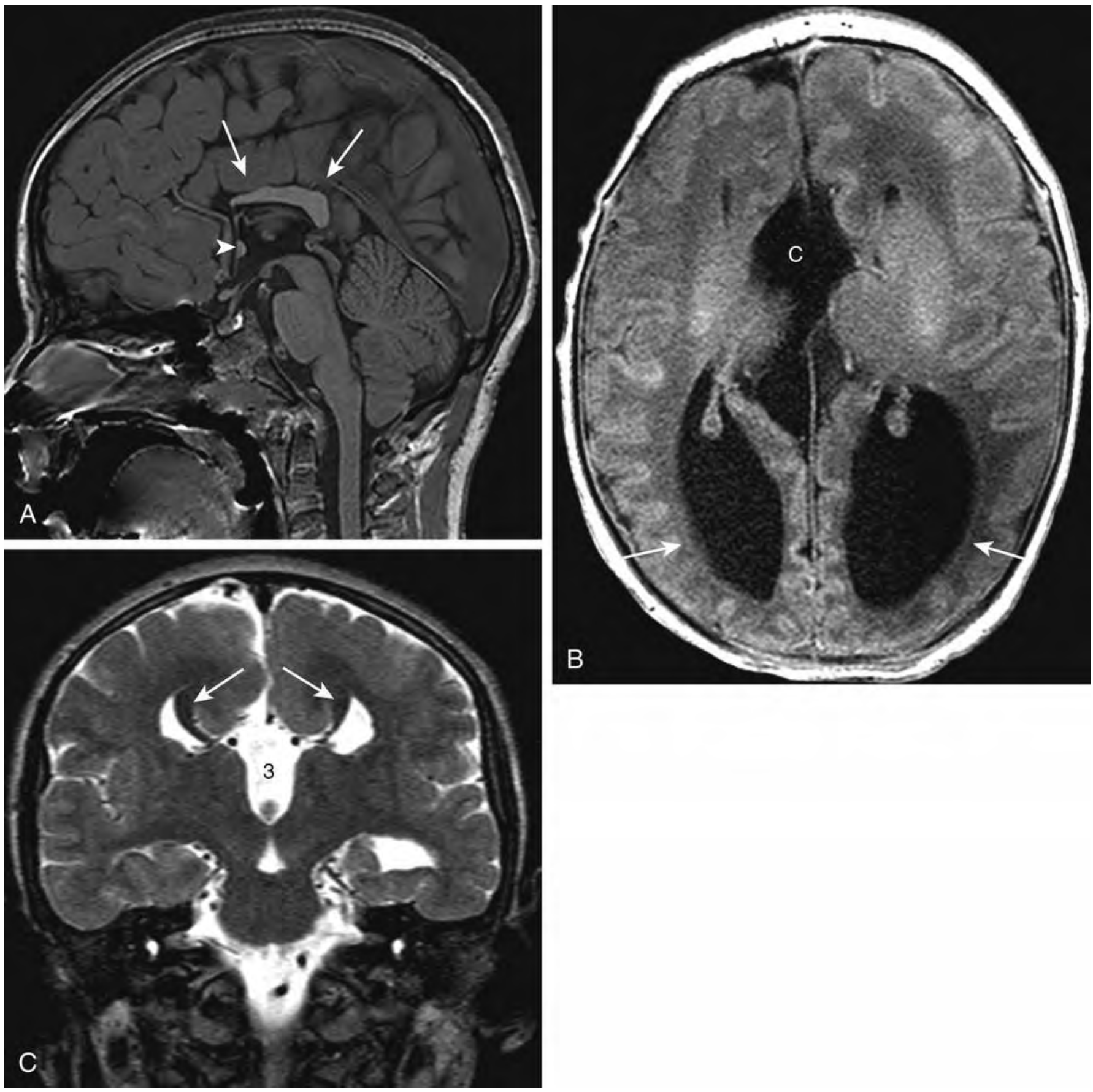
A, Axial T2-weighted image shows separation of the thalami *(T)* and separated occipital lobes but fusion of the frontal lobes. There is a single monoventricle and absence of the septum pellucidum. **B,** Coronal T2-weighted image shows monoventricle *(arrowheads)*. Note the single anterior cerebral artery (Azygous artery, *arrow*).



▪ **FIGURE 8-33** **Middle Interhemispheric Variant of Holoprosencephaly.**
Axial T1-weighted sequence shows abnormal midline fusion of brain parenchyma only at the high posterior frontal region *(arrow)*.



▪ **FIGURE 8-34** **Ectopic Posterior Pituitary.**
Patient with history of growth hormone deficiency. Sagittal T1-weighted sequence without contrast shows abnormal position of the posterior pituitary bright spot, located posterior to the optic chiasma *(arrow)* instead of within the posterior sella. Note also the absent visualization of the pituitary stalk (interrupted stalk).

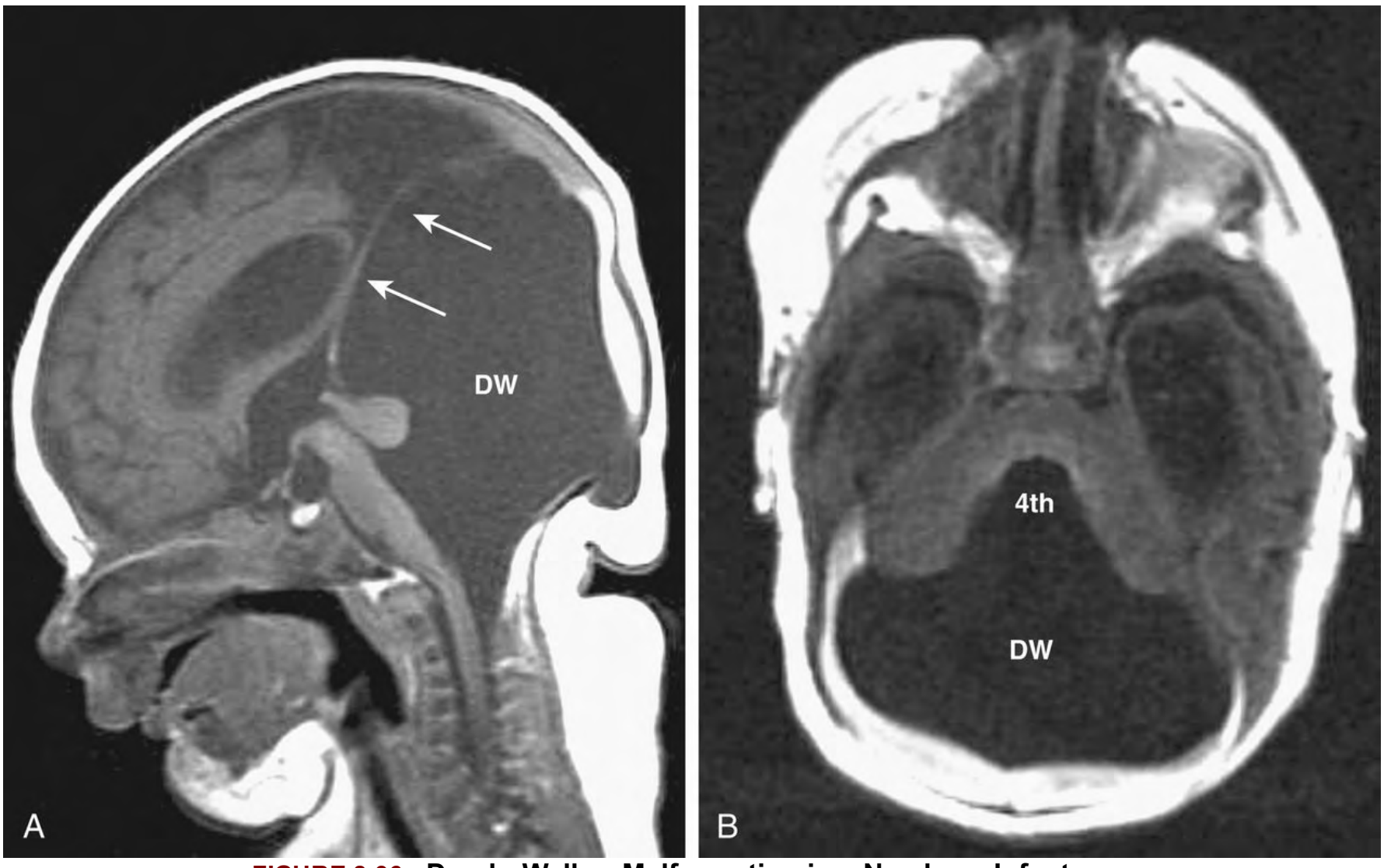


▪ **FIGURE 8-35 Agenesis and Dysgenesis of Corpus Callosum in Different Patients.**
A, Sagittal T1-weighted sequence shows an abnormally short corpus callosum *(arrows)* with lack visualization of its anterior portions. Note the presence of a preserved anterior commissure *(arrowhead)*. **B,** Axial view of a different patient shows the typical parallel configuration of the lateral ventricles with associated colpocephaly *(arrows)*. Note the presence of an interhemispheric cyst *(C)*, not uncommonly seen in cases of agenesis of corpus callosum. **C**, Probst bundles *(arrows)* visualized on coronal T2-weighed sequence. Also note "bull horn" configuration of lateral ventricles and high-riding third ventricle *(3)*.

Dysgenesis of Corpus Callosum

Dysgenesis of the corpus callosum includes both complete and partial absence. The corpus callosum normally develops from two independent portions, anterior and posterior, and the anterior corpus callosum enlarges and becomes visible earlier. More commonly the anterior portion is present with partial absence, although this is not always true (Fig. 8-35, *A-C*). Absence of the corpus callosum can occur in isolation or in conjunction with many of the other developmental abnormalities. On coronal MR images the lateral ventricles are separated, and the third ventricle extends more superiorly than normal, positioned between the lateral ventricles. The white matter tracts, which normally would cross the midline via the corpus callosum, run along the medial surface of the lateral ventricles and form the bundles of Probst (see Fig. 8-35, *C*). Lateral ventricles assume a parallel configuration on axial views, and colpocephaly (see Fig 8-35, *B*) is often present (dilatation of posterior horns of lateral ventricles).

Midline masses, such as lipoma and interhemipheric cyst (see Fig. 8-35, *B*), can also be associated.



▪ FIGURE 8-36 **Dandy-Walker Malformation in a Newborn Infant.**
A, Sagittal T1-weighted MR image shows large posterior fossa and posterior fossa CSF spaces *(DW)*. The cerebellar vermis is markedly hypoplastic. The torcula *(arrows)* is elevated. **B,** Axial T1-weighted MR image shows large posterior fossa CSF spaces *(DW)* and wide communication with the fourth ventricle *(4th)*.

Posterior Fossa Anomalies with Enlarged Cerebrospinal Fluid Spaces

Causes of enlarged posterior fossa fluid spaces include a spectrum of etiologies that vary from normal developmental variants (mega cisterna magna) to more significant malformations. They can be divided into five major groups: Dandy-Walker malformation, cerebellar vermian hypoplasia, Blake pouch cyst, mega cisterna magna, and arachnoid cyst.

Dandy-Walker malformation is characterized by complete or partial agenesis of the cerebellar vermis in conjunction with the presence of a large posterior fossa. The CSF spaces are enlarged, and the torcula is elevated (Fig. 8-36). The falx cerebelli is absent. Often there are also supratentorial abnormalities that may include holoprosencephaly, agenesis of the corpus callosum, polymicrogyria, and heterotopias. Hydrocephalus is also not uncommon. Outcome depends on severity of vermian hypoplasia and associated supratentorial abnormalities.

Cerebellar vermian hypoplasia (formerly known as Dandy-Walker variant or continuum) is characterized by mild, moderate, or severe hypoplasia of the cerebellar vermis. As a result there is enlargement of the normal communication between the fourth ventricle and posterior fossa extra axial spaces. The overall size of the posterior fossa is not enlarged, and there is a normally positioned torcula (Fig. 8-37).

Blake pouch cyst is more commonly seen in the prenatal scenario, when fetal MRI is performed to evaluate for Dandy-Walker malformation versus vermian hypoplasia. Blake pouch is a normal embryological CSF-filled structure, seen during the development of the posterior fossa as a CSF outpouching that extends posteriorly from the inferior aspect of the developing fourth ventricle. When there is absent, incomplete, or late fenestration of this pouch (future foramens of Luschka and Magendie), a persistent cystic structure causing enlarged communication of the fourth ventricle and retrocerebellar extraaxial spaces is seen and referred to as Blake pouch cyst. The cerebellar vermis is

usually uplifted but normally formed.



▪ **FIGURE 8-37 Cerebellar Vermian Hypoplasia.**
Sagittal T1-weighted MR image shows mild inferior vermian hypoplasia *(V)* and prominent retrocerebellar CSF spaces *(C)*. There is an enlarged communication *(arrowheads)* of the posterior fossa CSF spaces with the fourth ventricle *(arrow),* as a result of vermian hypoplasia. There is a normal position of the torcula, the posterior fossa is not enlarged.

When enlarged posterior fossa CSF spaces are present with a fully developed and normally positioned cerebellar vermis, there are two possibilities. If the CSF spaces exhibit no mass effect on the cerebellum and the falx cerebelli is present, a mega cisterna magna is considered to be present. A mega cisterna magna may be in the spectrum of a persistent Blake's pouch cyst, as proposed by recent articles, and is considered a developmental variant of no clinical significance. If the CSF spaces appear cystic and exhibit mass effect on the cerebellum, an arachnoid cyst is considered more likely (Fig. 8-38). The differentiation between a mega cisterna magna and an arachnoid cyst may be difficult. However, regardless of the name chosen, if there is minimal or no mass effect on the cerebellum, the finding is considered incidental and of no clinical significance.

Gray Matter Heterotopias

Heterotopias are abnormalities of neuronal migration characterized by arrest in radial migration of the neurons from the subependymal area to the cortex. Heterotopias may be isolated or associated with other migrational disorders. Common clinical presentation is focal seizures. On CT and MRI the lesions may appear as nodular (Fig. 8-39, *A* and *B*) or linear (Fig. 8-40) areas of gray matter signal within the white matter, most typically in the subependymal and subcortical regions. Bilateral periventricular subependymal nodular heterotopia may be familial with either X-linked or autosomal recessive patter

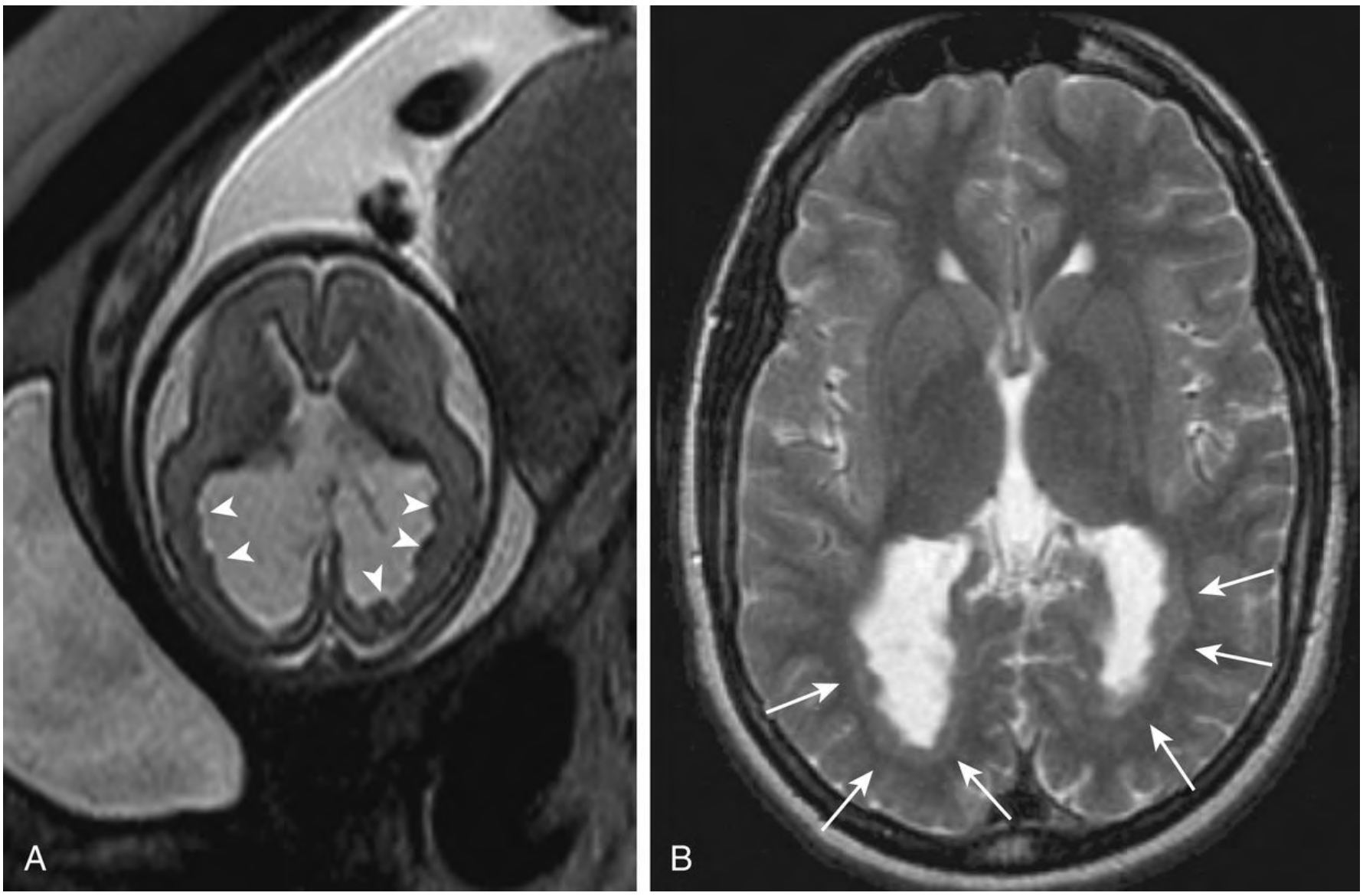
of inheritance.



▪ **FIGURE 8-38** **Posterior Fossa Arachnoid Cyst.**
Sagittal T2-weighted MR image shows posterior fossa cyst *(A)* that does not communicate with the fourth ventricle *(arrow)*. There is mass effect on the cerebellum *(C)*.

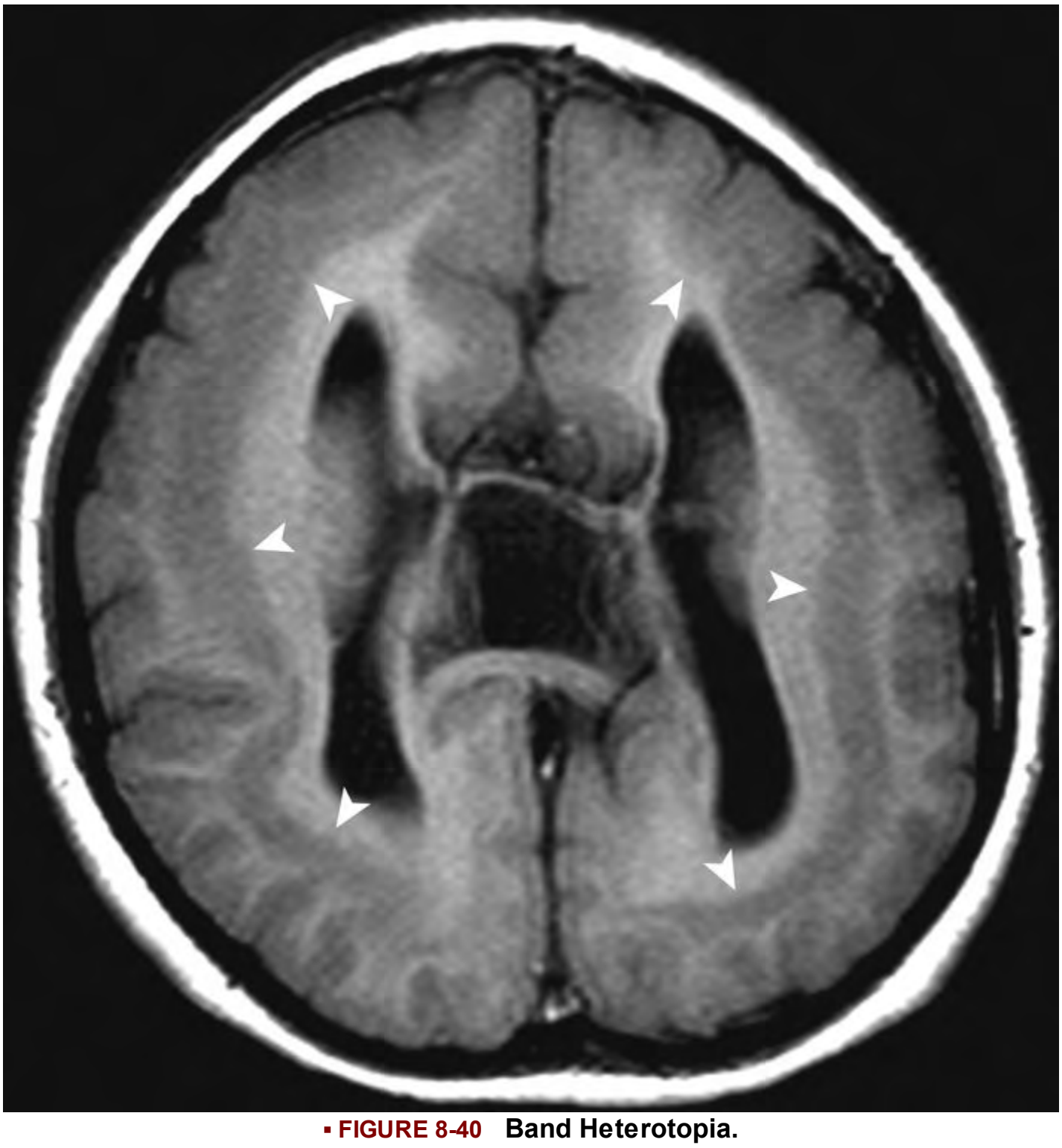
Lissencephaly (Agyria-Pachygyria)

Lissencephaly is a term applied to a smooth appearance of the brain secondary to absent or markedly decreased sulcation and gyration. Abnormal neuronal migration can result in total failure of development of sulci and gyri (agyria-complete lissencephaly) (Fig. 8-41) or development of abnormally broad and flat gyri with abnormally shallow sulci (pachygyria). Findings are best visualized with MRI, usually with patchy areas of both agyria and pachygyria. These abnormalities are commonly associated with other migrational abnormalities. They also occur as part of a number of rare syndromes. Two malformations often associated with agyria and pachyria are classic lissencephaly and cobblestone malformations. Classic lissencephaly that is due to arrest of neuronal migration is also known as lissencephaly type I. MRI demonstrates a smooth brain with thick cortex and a band of hyperintense T2 signal within the cortex (sparse cell zone). Brain may demonstrate the classic "figure eight" morphology (see Fig. 8.41). Cobblestone malformations are due to overmigration and are also known as cobblestone lissencephalies or lissencephalies type II. They are commonly associated with congenital muscular dystrophy. On imaging there is markedly decreased sulcation with a pebbled appearance of the cortex. Other findings may include vermian hypoplasia, cerebellar dysplasia (Fig. 8-42, *C*) brainstem hypoplasia, kinked pontomesencephalic junction, pontine cleft, ocular anomalies, and aqueduct stenosis leading to ventriculomegaly (Fig. 8-42, *A* and *B*).



▪ **FIGURE 8-39 Heterotopic Gray Matter in Two Different Patients.**

A, Fetal MRI showing multiple nodular areas of subependymal heterotopia *(arrowheads)* along the dilated posterior horns of the lateral ventricles. **B,** Axial T2-weighted MRI shows nodular foci *(arrows)* lining the posterior horns of the lateral ventricles. Nodules have the same signal as gray matter, consistent with heterotopic gray matter. There is associated enlargement of the occipital horns of the lateral ventricles.

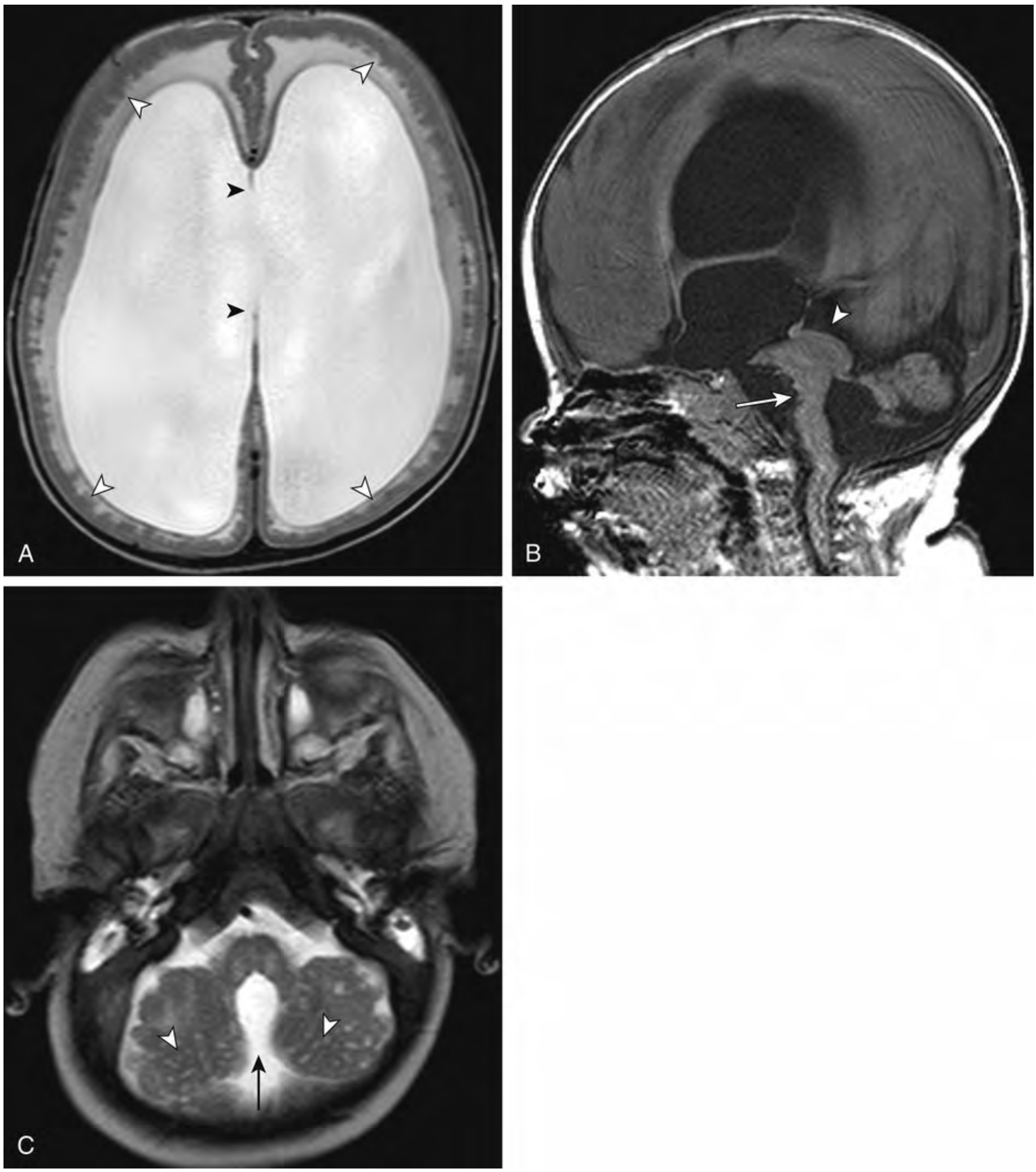


▪ **FIGURE 8-40** **Band Heterotopia.**
Axial T1-weighted sequence shows abnormal band of gray matter *(arrowheads)* located medially to the subcortical white matter. There is also an abnormal appearance of the cortex with areas of pachygyria. Note associated findings of callosum agenesis, including parallel lateral ventricles and high-riding third ventricle.



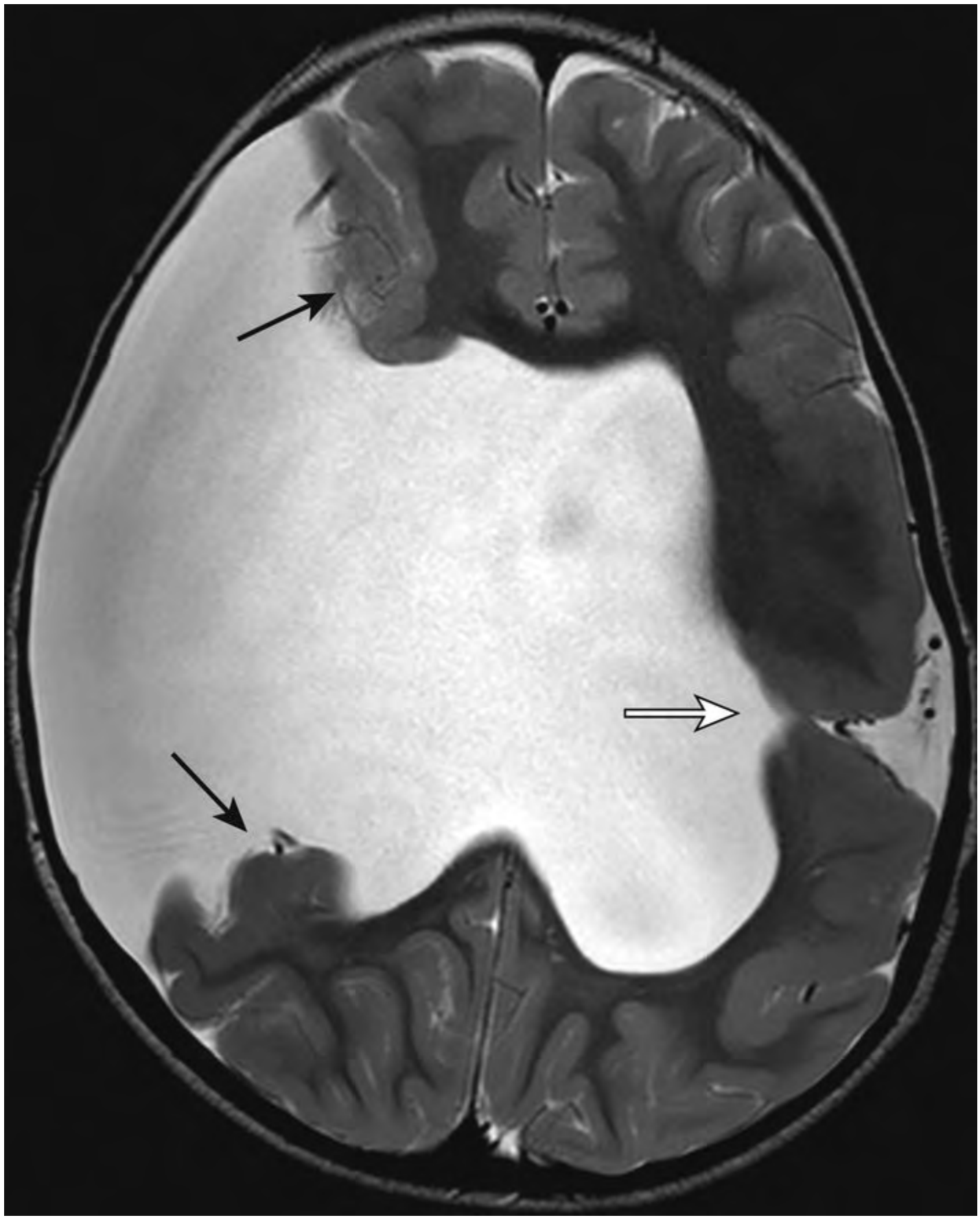
▪ **FIGURE 8-41** **Classic Lissencephaly.**

Axial T2-weighted image shows the smooth surface of the bilateral cerebral hemispheres with only a few frontal sulci present and shallow sylvian fissures (figure eight configuration). Note the thin band of increase T2 signal within the abnormal cortex (sparse cell zone) *(arrowheads)*. This is seen in cases of classic lissencephaly.



▪ **FIGURE 8-42 Cobblestone Lissencephaly.**

A, Axial T2-weighted sequence demonstrates smooth surface of the brain with "pebbled" appearance of the cerebral cortex *(white arrowheads)*. There is also marked lateral ventriculomegaly and partial absence of septum pellucidum *(black arrowheads)*. **B,** Sagittal T1-weighted sequence shows hypoplastic and kinked brainstem *(arrow)*. The cerebellar vermis is also hypoplastic, and the tectum is thickened *(arrowhead)*. Note the enlargement of the third and lateral ventricles secondary to tectal thickening resulting in aqueduct stenosis. Fourth ventricle is enlarged due to brainstem and cerebellar hypoplasia. **C,** Axial, T2 sequence of the posterior fossa confirmed hypoplasia of cerebellar vermis depicted here as an enlarged communication of fourth ventricle with extraaxial spaces *(black arrow)*. Cerebellar hemispheres are dysplastic with multiple small cystic changes, a few marked by *white arrowheads*.



▪ **FIGURE 8-43** **Schizencephaly.**
Axial T2-weighted image shows large fluid-filled space that is in communication with the right lateral ventricle. The communication is lined by gray matter *(black arrows)*, consistent with an open lip schizencephaly. On the left, a smaller closed lip schizencephalic cleft is seen *(white arrow)*. Note common association of absent septum pellucidum.

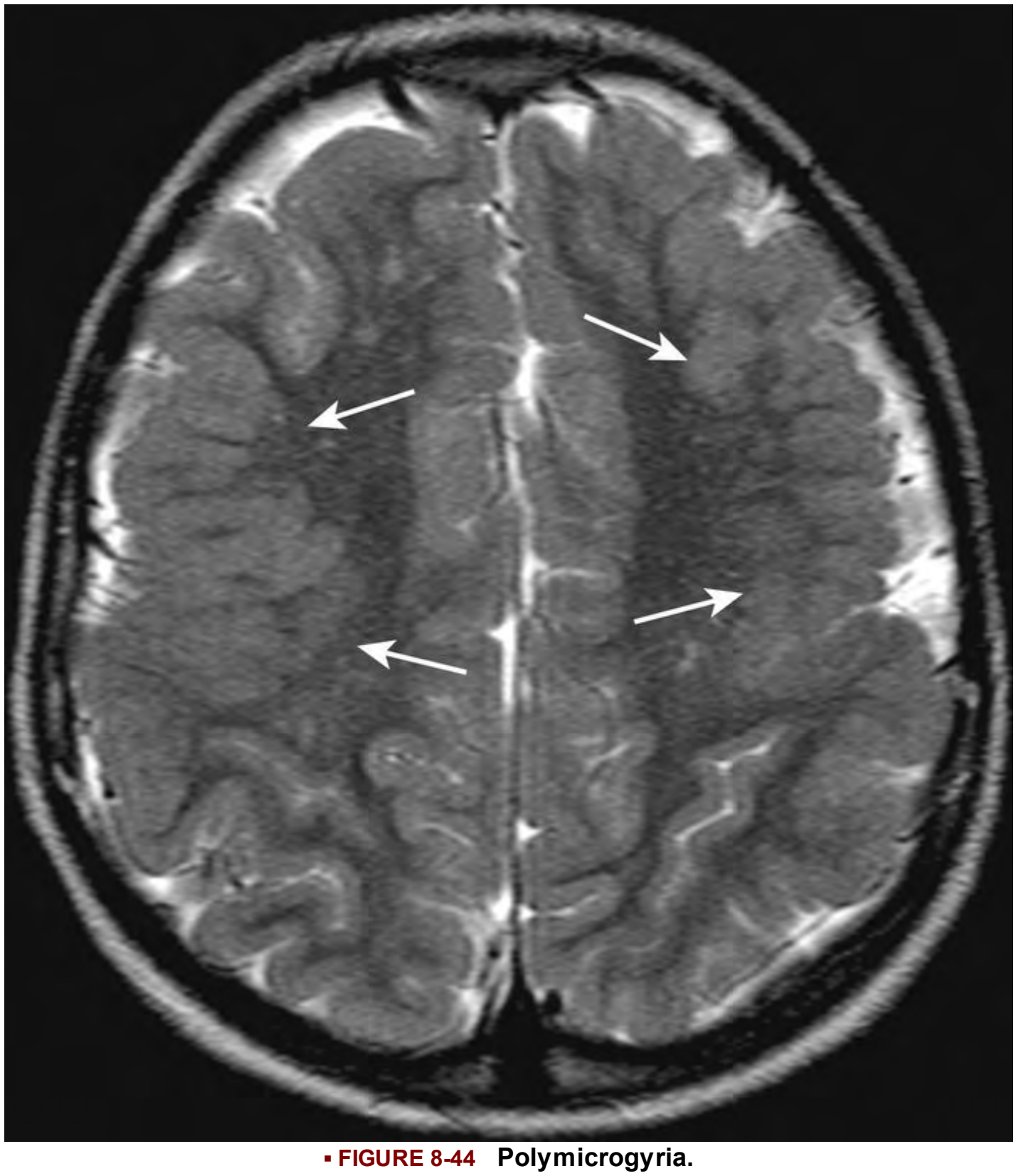
Schizencephaly

Schizencephaly is another migrational disorder. The term refers to a cleft in the cerebral hemisphere lined with dysplastic gray matter (Fig. 8-43). The cleft typically extends from the lateral ventricle to the surface of the brain. The presence of gray matter lining the entire cleft is the diagnostic feature that separates schizencephaly from other causes of clefts, such as porencephaly (see later material). Schizencephaly is often characterized as being open or close lipped (see Fig. 8-43). The lesion can be unilateral or bilateral and can occur anywhere in the cerebral hemispheres. In many cases there is associated absent septum pellucidum.

Polymicrogyria

Polymicrogyria is a disorder of late neuronal migration and cortical organization that results in multiple small, disorganized gyri (Fig. 8-44). It too is usually associated with other migrational abnormalities. It can be the result of prenatal infection (see Fig. 8-67), ischemia, or genetic

abnormalities.



▪ **FIGURE 8-44** **Polymicrogyria.**
Axial T2-weighted sequence demonstrates extensive bilateral frontoparietal polymicrogyria *(arrows)*.

Cortical Dysplasia

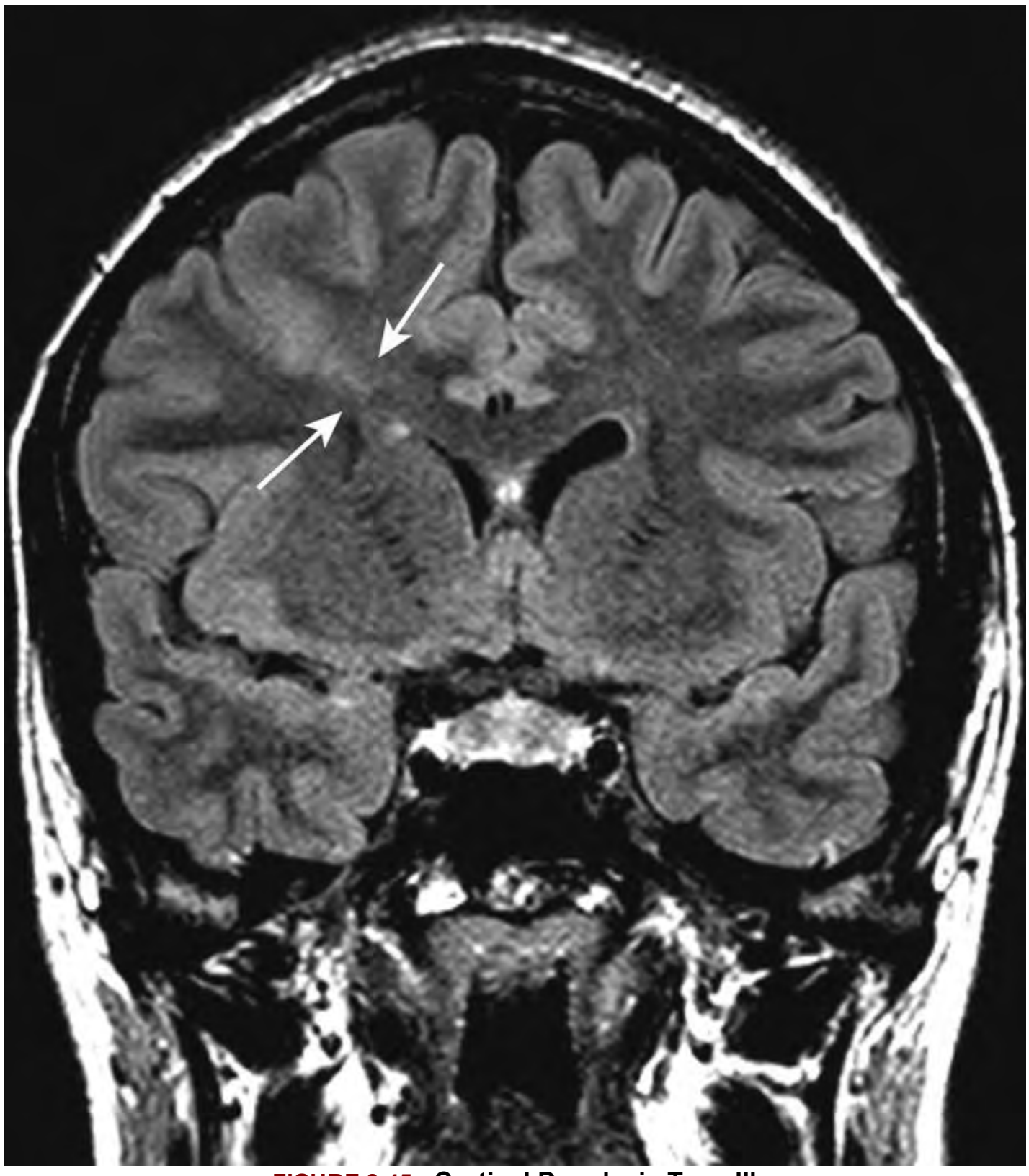
Focal cortical dysplasia (FCD) is the most common cause of intractable epilepsy in children. It is mostly sporadic but can be related to familial genetic causes. There are currently four different types of FCD described: mild malformations of cortical development (mMCD), FCD type I, FCD type II, and FCD type III.

FCD type II contains dysmorphic neurons and tends to present earlier in life and with higher incidence of medically refractory seizures. On imaging, FCD type II may demonstrate a focal area of altered cortical thickness, blurring of the gray-white matter differentiation, and increase T2 signal within the underlying white matter. The white matter signal changes are the result of glial proliferation and reduced myelination and frequently extend from the subcortical white matter to the surface of the adjacent lateral ventricle (Fig. 8-45).

Type I FCD and mMCD have more subtle cortical changes with no dysmorphic neurons. As a result the majority of cases have normal MRI imaging or present with subtle changes in cortical thickness and blurring of gray-white matter interface.

Type III FCD is a combination of type I cortical changes and an associated abnormality that can vary from hippocampal sclerosis (Fig. 8-46, *A* and *B*), glioneural tumors (Fig. 8-47), vascular malformations,

or porencephalic changes.



▪ **FIGURE 8-45** **Cortical Dysplasia Type IIb.**
Coronal FLAIR sequence shows a triangular-shaped area of increased signal extending from the right frontal cortex into the deep white matter near the surface of the right lateral ventricle *(arrows)*. Note also mild thickening of the involved cortex and focal blurring of the gray-white matter differentiation.

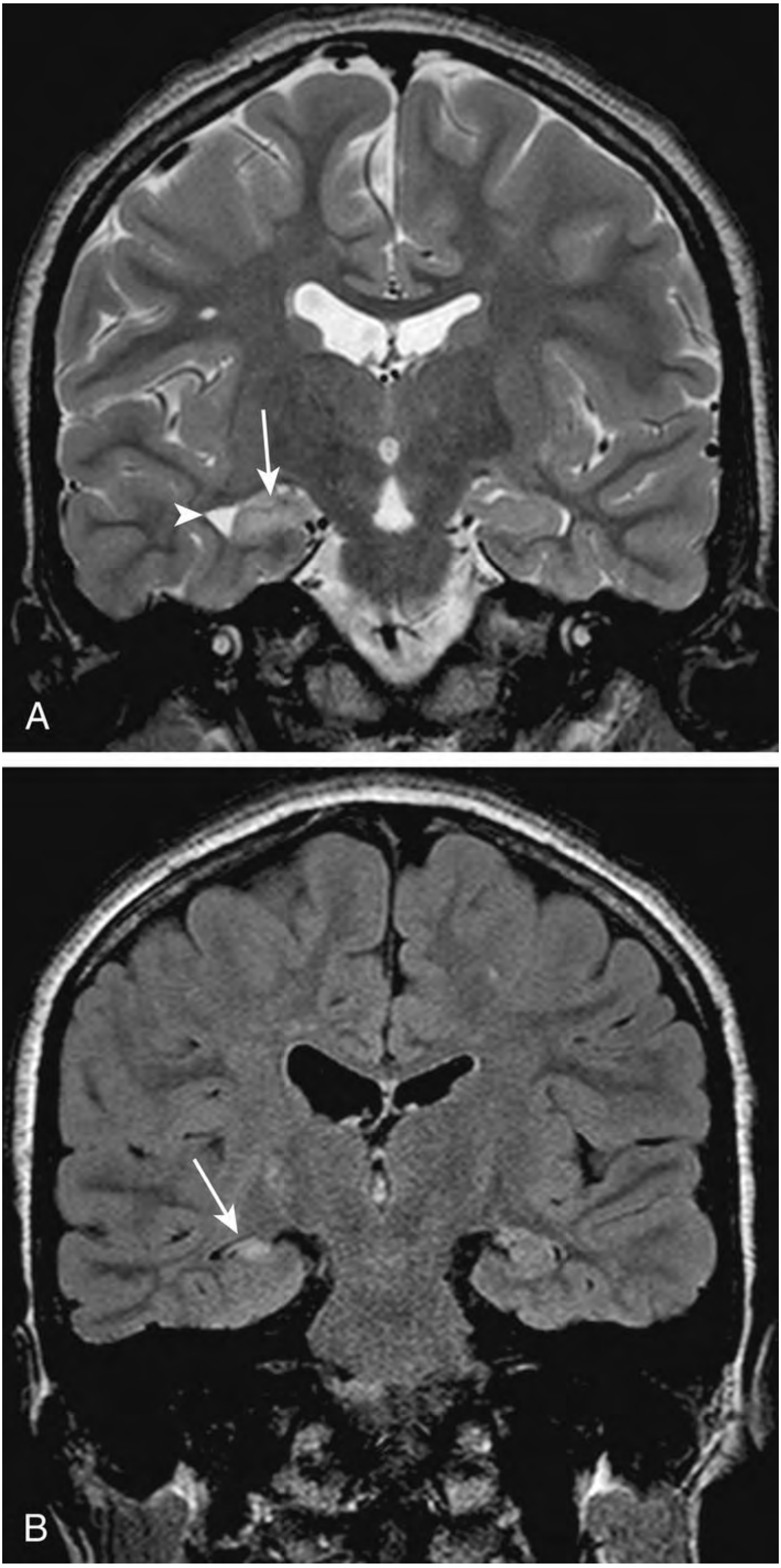
Hemimegalencephaly

Hemimegalencephaly is a hamartomatous overgrowth of one cerebral hemisphere or part of the cerebral hemisphere. It can be isolated or in association with many genetic disorders, including neurocutaneous and hemihypertrophy syndromes. Imaging findings include enlarged cerebral hemispheres and cortical malformations (Fig. 8-48). The most common clinical presentation is early onset intractable seizures. Other symptoms include hemiplegia and developmental delay.

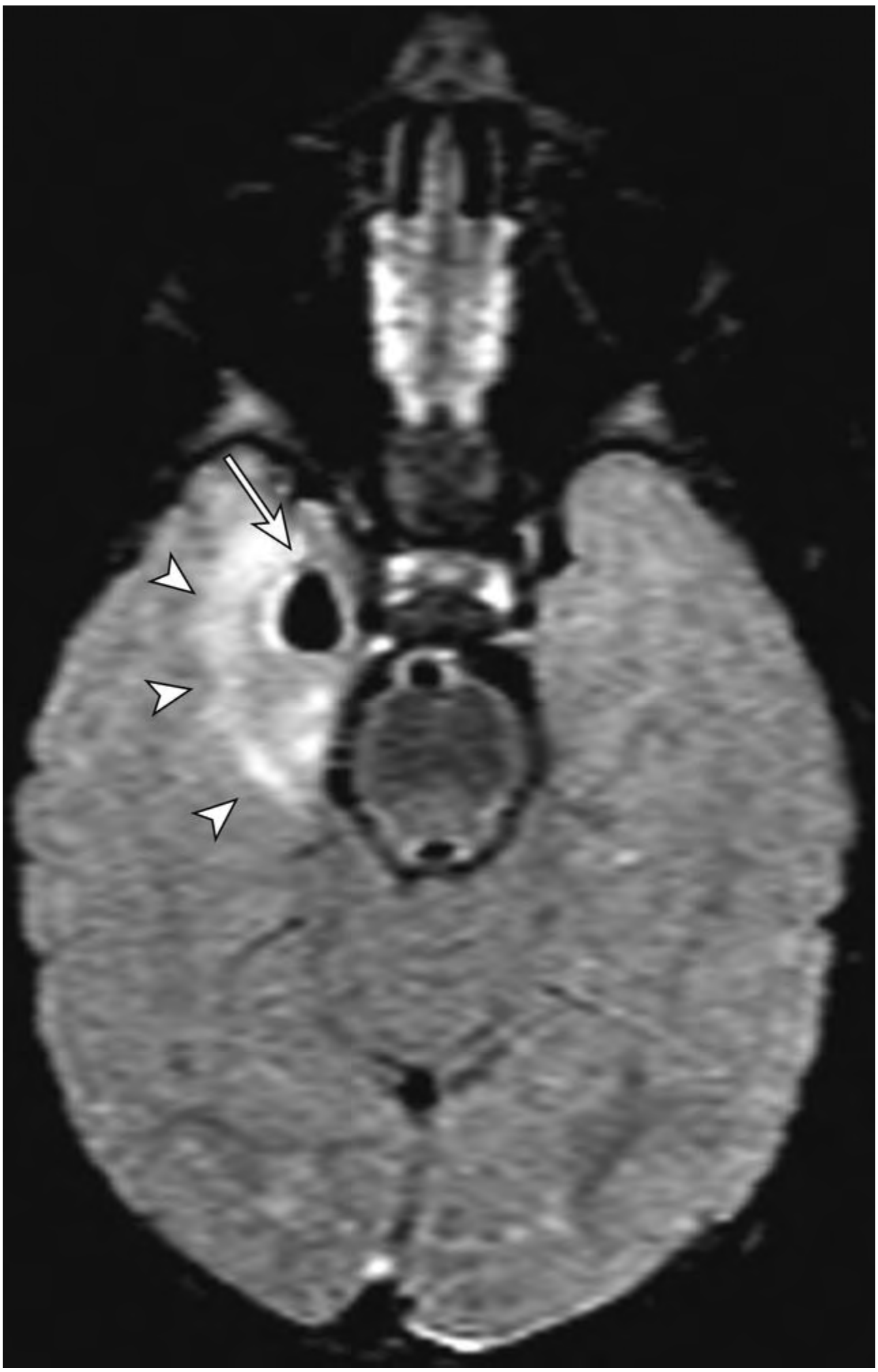
Vein of Galen Malformations

With vein of Galen malformation, or vein of Galen aneurysm, there are arteriovenous connections of cerebral arteries with a persistent embryonic vein (median prosencephalic vein of Markowski). On imaging there is an enlarged varix at the location of the vein of Galen and straight sinus, which corresponds to the enlarged persistent median prosencephalic vein (Fig. 8-49). The most common type of vein of Galen malformation is the "choroidal type," which presents with multiple abnormal vessel

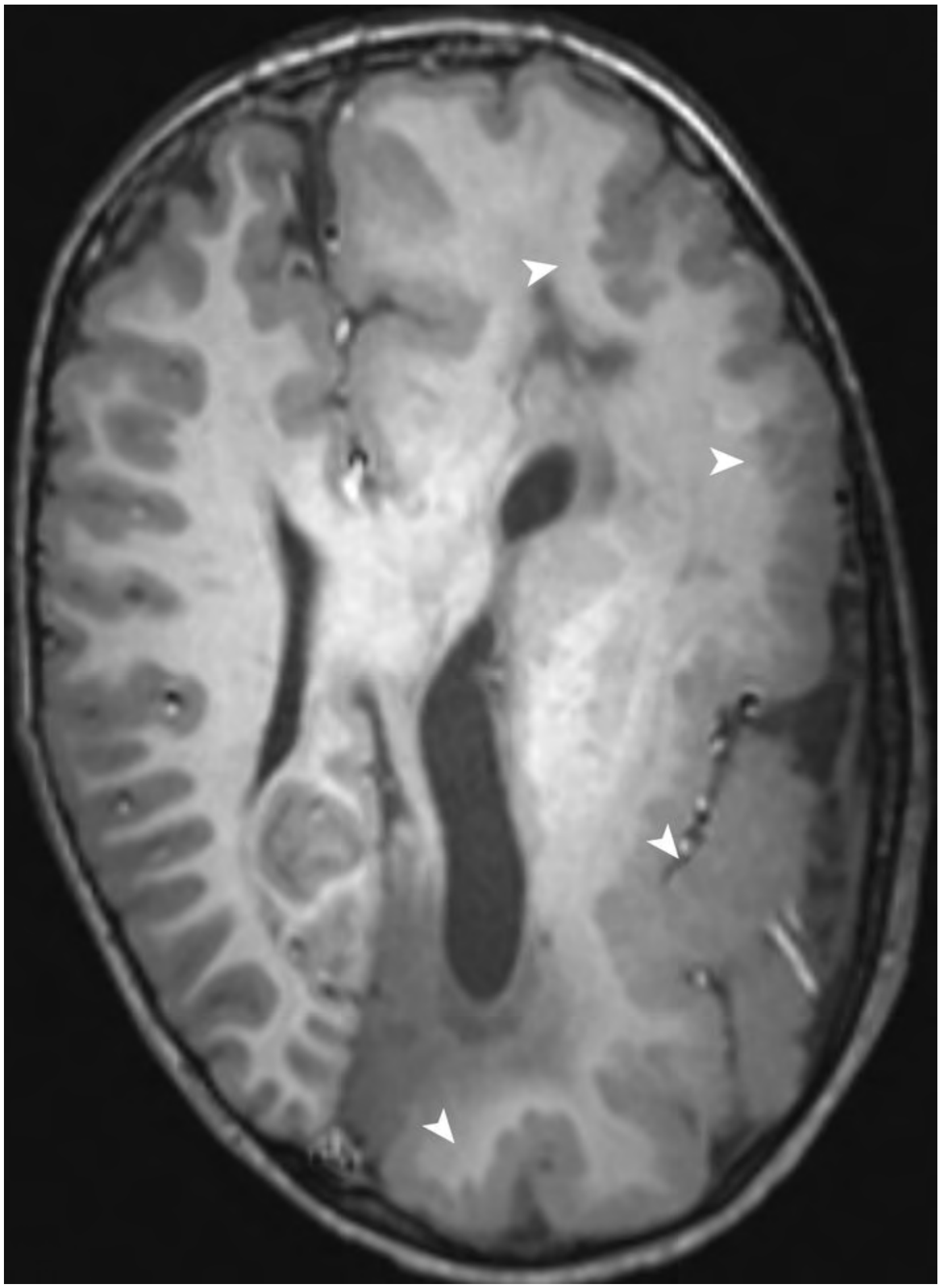
connections (usually thalamoperforators, choroidal and anterior cerebral arteries) to the anterior wall of the vein, causing significant arteriovenous shunting. These malformations may be depicted prenatally or present during the neonatal period. They often are associated with congestive heart failure due to associated left-to-right shunting of blood. On chest radiography there is cardiomegaly, signs of congestive heart failure, and widening of the superior mediastinum secondary to vascular enlargement caused by the increased blood flow to and from the head. There may be associated hydrocephalus and brain ischemic changes due to steal phenomenon (Fig. 8-50, *A* and *B*). A "mural type" vein of Galen malformation is seen when there are fewer larger caliber connections (usually posterior choroidal or collicular arteries). This type of malformation carries a better prognosis—with lower incidence of cardiac heart failure and brain ischemia, as well as better response to treatment. Most vein of Galen malformations are treated by arterial embolization. Outcome depends on the severity of the malformation and degree of shunting. Severe cases commonly die in the neonatal period. Mild cases can achieve cure.


A
B

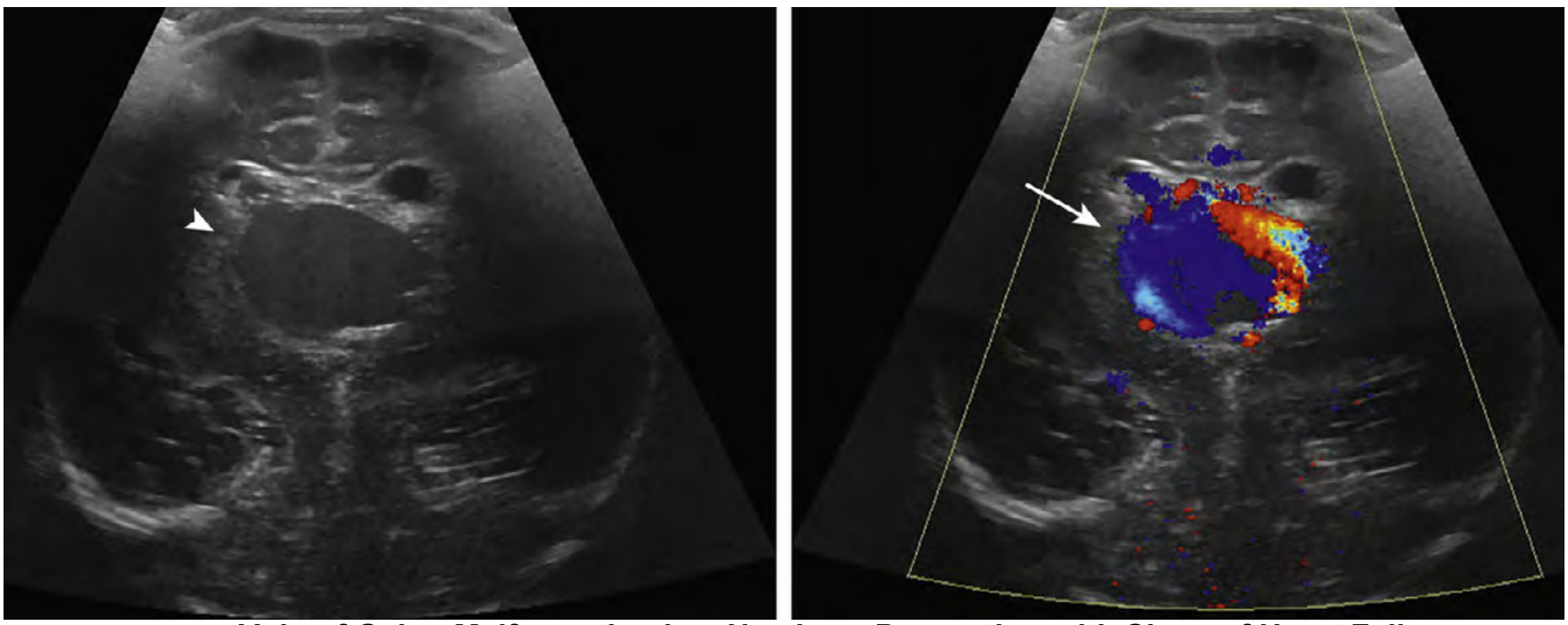
▪ **FIGURE 8-46** **Mesial Temporal Lobe Sclerosis.**
A, Coronal T2-weighted sequence shows decreased size of the right hippocampus *(arrow)* when compared with the normal contralateral side. Note also mild-prominence of the right temporal horn of the lateral ventricle *(arrowhead)*, which can be a secondary finding in cases of mesial temporal sclerosis. **B,** Coronal FLAIR sequence also shows increased signal within the small right hippocampus *(arrow)*.



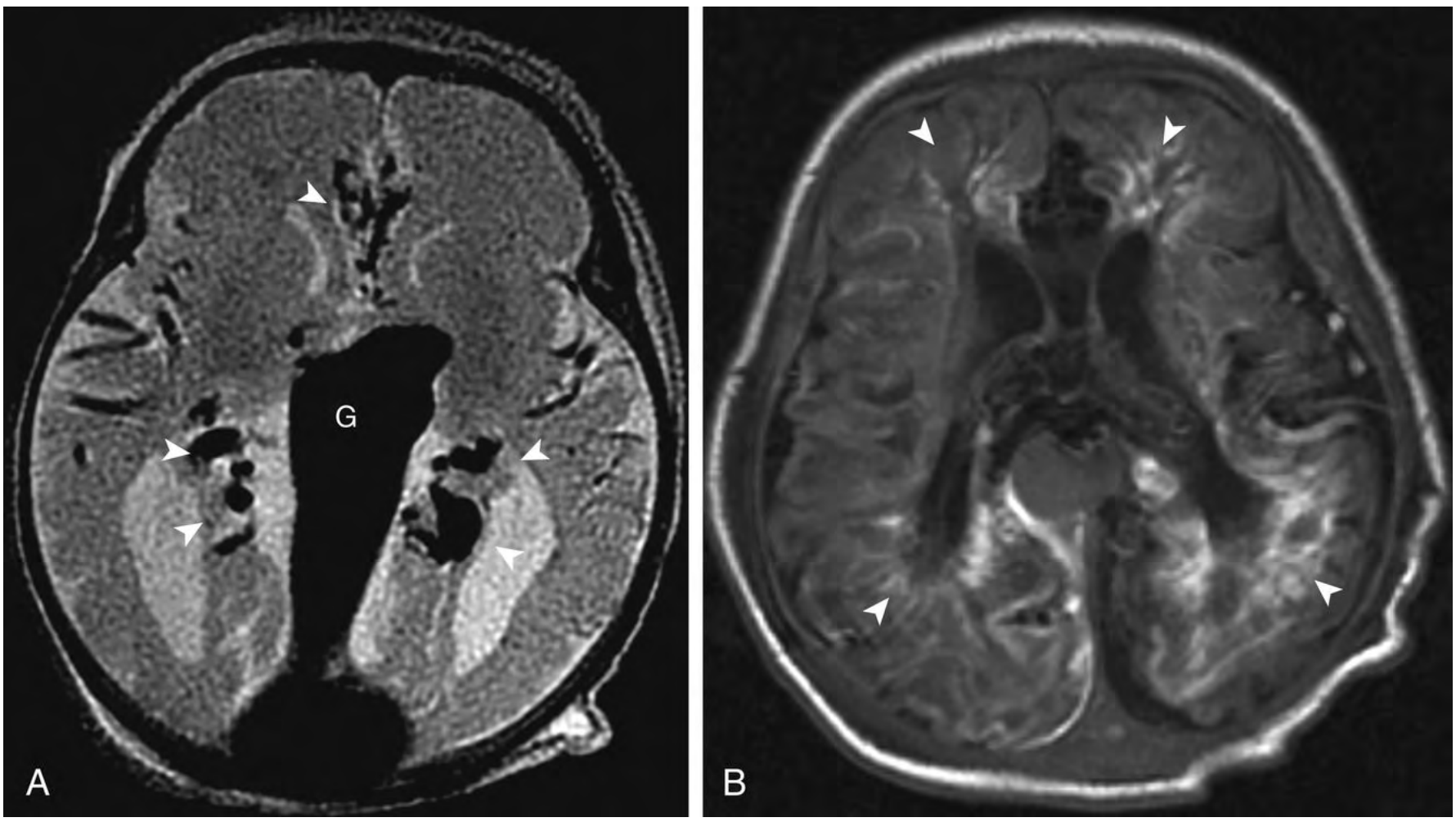
▪ **FIGURE 8-47** **Dysembryoplastic Neuroepithelial Tumor in a Patient Presenting with Seizures.**
Axial FLAIR sequence demonstrates right mesial temporal lobe abnormality, including a focal cyst *(arrow)* with surrounding increased FLAIR signal *(arrowheads)*. This was resected surgically and confirmed to represent a DNET and associated cortical dysplasia (dual pathology).



▪ **FIGURE 8-48** **Hemimegalencephaly.**
Axial T1-weighted sequence shows an enlarged and markedly dysplastic left cerebral hemisphere. Note diffuse cortical malformation compatible with polymicrogyria *(arrowheads)* and enlarged left lateral ventricle.



▪ **FIGURE 8-49 Vein of Galen Malformation in a Newborn Presenting with Signs of Heart Failure.**
Coronal, gray-scale ultrasound image shows a large midline fluid structure posterior to the third ventricle *(arrowhead)*. Color Doppler demonstrates vascular flow within it compatible with an enlarged median prosencephalic vein *(arrow)*.



▪ **FIGURE 8-50 Vein of Galen Malformation.**
A, Axial T2-weighted sequence demonstrates a markedly enlarged posterior midline flow-void at the expected location of the straight sinus and vein of Galen *(G)* compatible with an enlarged median prosencephalic vein. Note multiple enlarged and tortuous feeding arterial structures from the anterior and posterior circulation *(arrowheads)*. **B,** Follow-up, axial T1-weighted sequence demonstrates volume loss and periventricular signal abnormalities *(arrowheads)* compatible with chronic ischemic changes due to steal phenomenon from the malformation.

▪ Sequelae of in Utero Insults

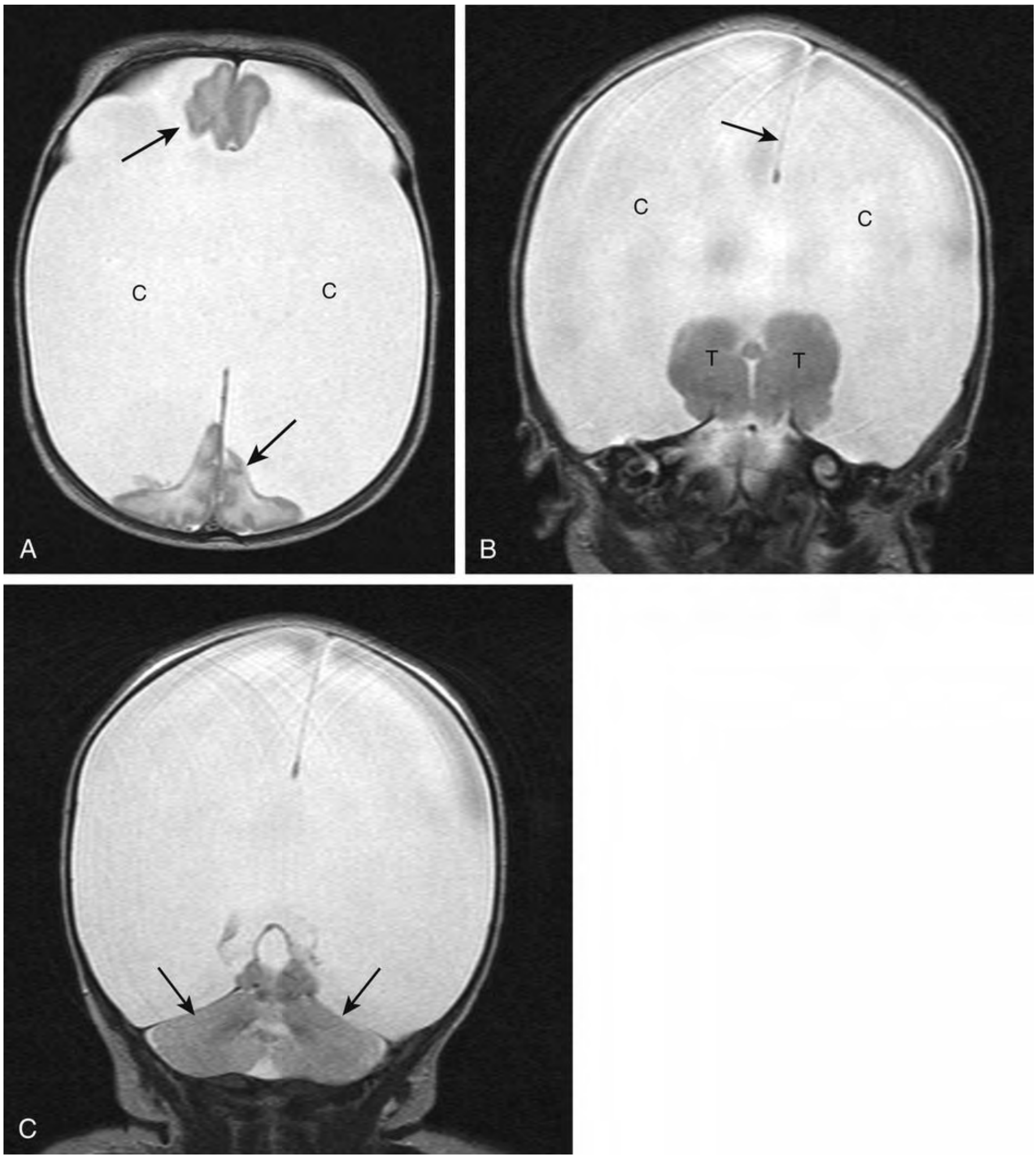
In contrast to developmental abnormalities that result from abnormal formation, other congenital abnormalities may arise from destruction of already developed structures. Most commonly they are related to vascular ischemia and infarction that can be the result of a number of underlying causes. The most commonly encountered lesions are porencephaly, encephalomalacia, and hydranencephaly.

Porencephaly and Encephalomalacia

Before the end of the second trimester, parenchymal injury does not result in glial scar formation. During this early time period, focal injury results in the development of a fluid-filled space called a *porencephalic cyst*. On imaging this appears as a thin-walled, CSF-containing cyst that may communicate with the ventricles (Fig. 8-51). There are no septations. During the third trimester and neonatal period, parenchymal injury incites some glial scar formation, resulting in encephalomalacia. Encephalomalacia appears as areas of high T2-weighted signal with septations in the region of injury.



▪ **FIGURE 8-51** Porencephalic cyst shown on coronal T1-weighted MRI as a large CSF cyst *(arrows)* that is contiguous with the right lateral ventricle. The communication is not lined by gray matter.



▪ **FIGURE 8-52** **Hydranencephaly.**

A, Axial T2-weighted sequence shows most of cerebrum replaced by CSF *(C)*. Note small portions of preserved cerebral parenchyma along the anterior and posterior parasagittal regions *(arrows)*. **B,** The thalami *(T)* are present bilaterally and are not fused. A falx cerebri *(arrow)* is present. **C,** Note normal cerebellar structures within the posterior fossa *(arrows)*.

Hydranencephaly

Hydranencephaly is the result of significant injury to the majority of the cerebral hemispheres secondary to an in utero destructive process. The cause is thought to be vascular in origin with involvement of both internal carotid arteries. Infectious vasculitis has been identified as a potential cause. The supratentorial compartment is almost entirely filled with CSF. A few areas of preserved parenchyma may be seen in the occipital lobes, inferior temporal lobes, and thalami (Fig. 8-52, *A-C*). The brainstem is usually hypoplastic, and the cerebellum is typically intact. These structures remain because they are supplied by the vertebrobasilar arterial system. The presence of the falx cerebri and the separation of the thalami seen in hydranencephaly help to differentiate this disorder from severe

(alobar) holoprosencephaly (see Fig. 8-52, *B*). It is sometimes very difficult to impossible to differentiate hydranencephaly from severe hydrocephalus.

TABLE 8-5

Diagnostic Criteria for Neurofibromatosis Type 1

Two or more of the following:
1. Six or more café au lait macules
2. Two or more neurofibromas or one plexiform neurofibroma
3. Axillary or inguinal freckles
4. Visual pathway gliomas
5. Two hamartomas of the iris (Lisch nodules)
6. Distinctive bony lesion (sphenoid wing dysplasia or thin long bones with pseudoarthrosis)
7. Parent, sibling, or child with NF-1

▪ Neurocutaneous Syndromes

The neurocutaneous syndromes (phakomatoses) are a group of related diseases that affect tissues of ectodermal origin, primarily the skin and nervous system. Some of the more common phakomatoses that present in childhood include neurofibromatosis, tuberous sclerosis (TS), and Sturge-Weber syndrome.

Neurofibromatosis

Neurofibromatosis is the most common of the phakomatoses and is divided into subcategories, of which neurofibromatosis type 1 (NF-1) and neurofibromatosis type 2 (NF-2) are the most common.

NF-1 is an autosomal dominant disorder. Diagnostic criteria for NF-1 are listed in Table 8-5. The neuroimaging manifestations of NF-1 are multiple. The most common lesions of the central nervous system (CNS) are the "NF-1 spots" that appear as high T2-weighted foci in the basal ganglia (especially globus pallidus), thalami, mesial temporal lobes, internal capsule, splenium, brainstem, and cerebellar white matter (Fig. 8-53, *A-C*). The lesions are areas of myelin vacuolization and typically become apparent at around 3 years of age, increase in number and size until approximately 12 years of age, and then regress. Other lesions of NF-1 include optic pathway gliomas (Fig. 8-54, *A-C*), cerebral astrocytomas, hydrocephalus, vascular dysplasia (including aneurysms and moyamoya vasculopathy), dural ectasia, and sphenoid wing dysplasia. Patients with NF-1 can develop cranial nerve schwannomas, peripheral neurofibromas, plexiform neurofibromas (Fig. 8-55, *A* and *B*), and malignant peripheral nerve sheath tumors. Plexiform neurofibromas are locally aggressive masses that are histologically more disorganized than typical neurofibromas. In the head and neck they often involve the scalp and orbit. They are often monitored by imaging to evaluate for findings suspicious for malignant degeneration. Spinal manifestations include posterior vertebral scalloping (resulting from dural ectasia or neurofibromas), scoliosis, and lateral meningoceles.

NF-2 is characterized by the presence of bilateral acoustic schwannomas (Fig. 8-56). Other associated lesions include meningiomas, gliomas, neurofibromas, and schwannomas of other cranial nerves. Patients most commonly present in adulthood.

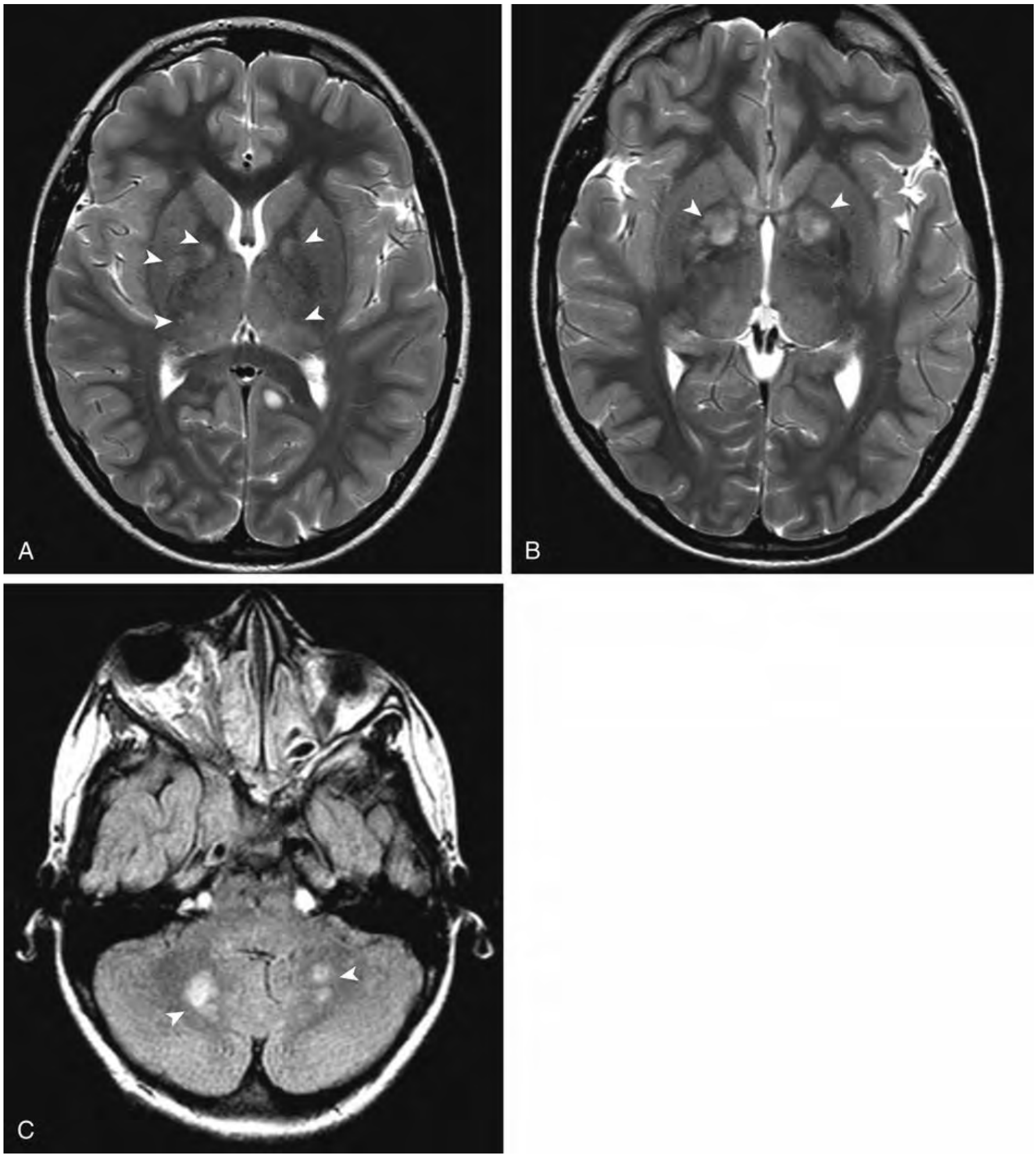
Tuberous Sclerosis

TS is an autosomal dominant syndrome associated with a classic triad of seizures, mental retardation, and adenoma sebaceous (facial angiofibroma of the skin). Although this triad is described as characteristic, the incidence of all three symptoms occurring in conjunction is actually low. The disease may affect the skin, CNS, orbits, skeletal system, lungs, and abdominal organs.

The most common neuroimaging finding is the presence of tubers. These are hamartomatous lesions that appear as subependymal nodules, typically along the walls of the lateral ventricles (Fig. 8-57), or parenchymal lesions within the subcortical white matter and cortex. The signal characteristics of subependymal nodules are variable and are related to age. In older patients lesions are often calcified.

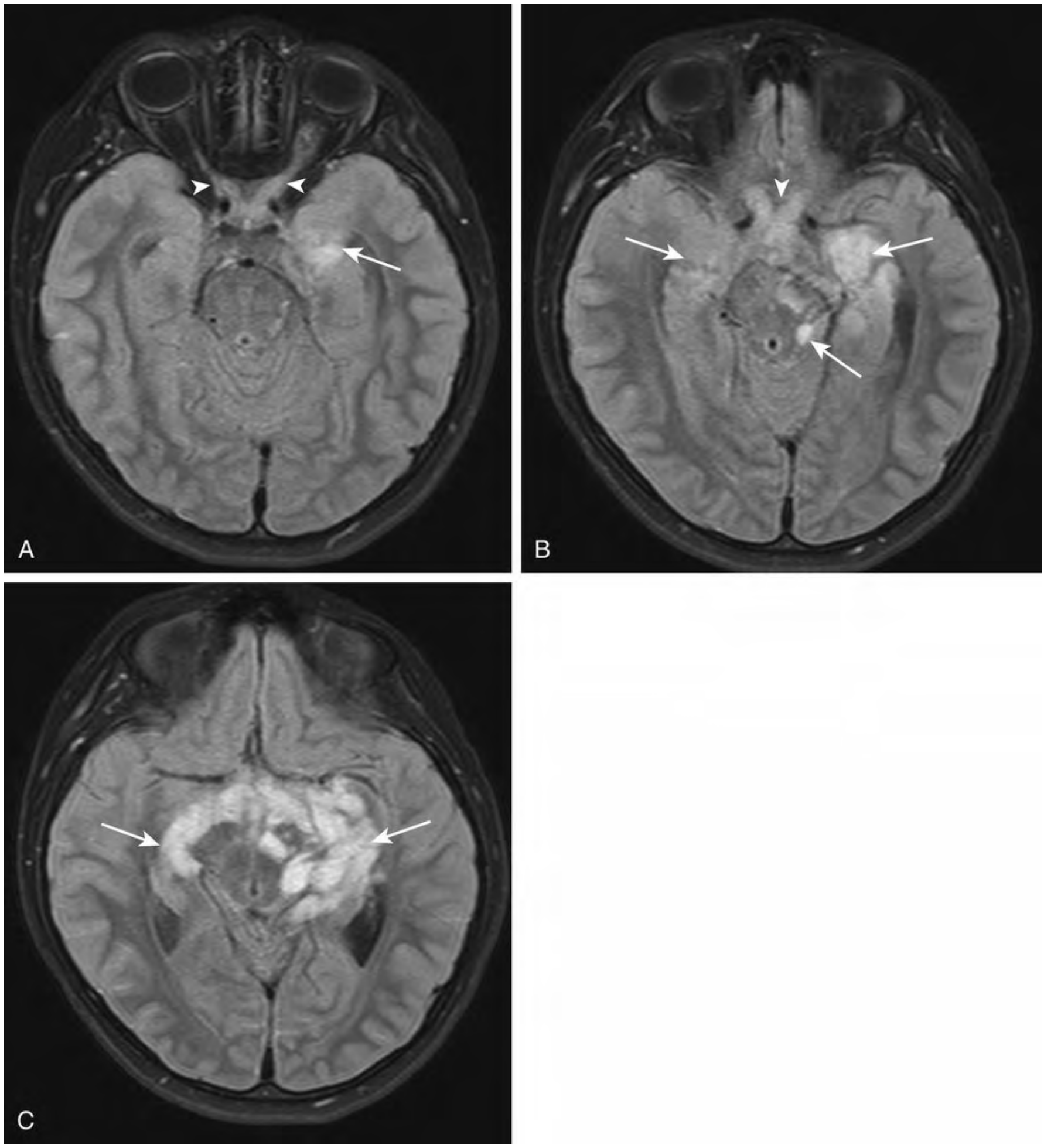
In younger children the lesions tend to be isointense to gray matter. Enhancement is variable. When a subependymal nodule near the foramen of Monro rapidly enlarges, malignant subependymal giant cell astrocytoma (SEGA) is suspected (Fig. 8-58). Such tumors frequently obstruct CSF flow and can lead to hydrocephalus. Parenchymal tubers are characterized as areas of increase T2 signal, predominantly within the subcortical white matter. Some of these lesions can involve the cortex and few may calcify. Parenchymal tubers are a cause of seizures, and determination of which lesion is the epileptogenic focus can be difficult. Other imaging findings include radial migration lines (Fig. 8-59) and gyri expansion associated with cystoid degeneration of parenchymal tubers (Fig. 8-60).

Visceral manifestations of TS are covered elsewhere and include renal cysts, renal angiomyolipomas, cardiac rhabdomyomas, pulmonary lymphangioleiomyomatosis, and hamartomas of other organs.

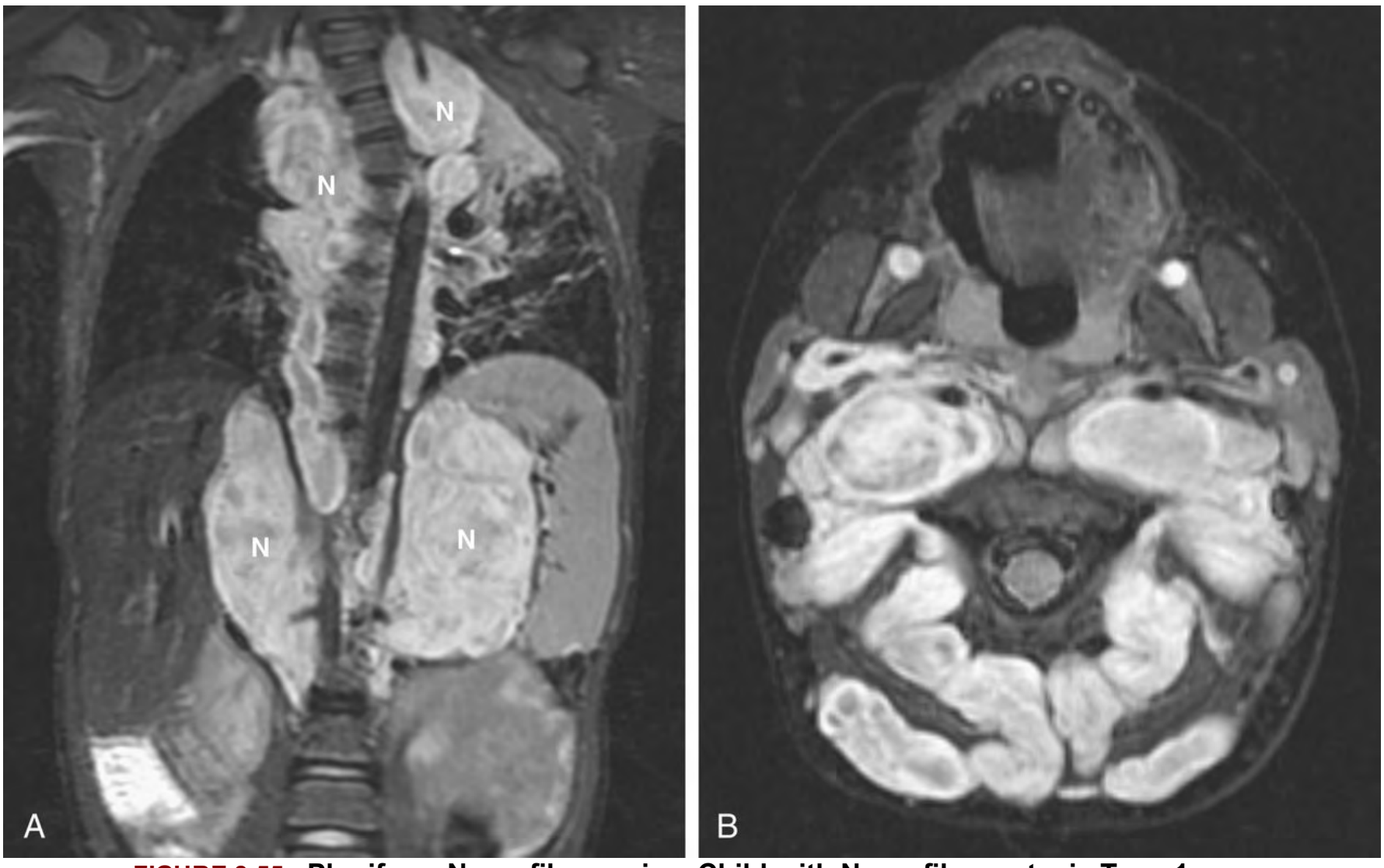


▪ **FIGURE 8-53** **Neurofibromatosis Type 1.**

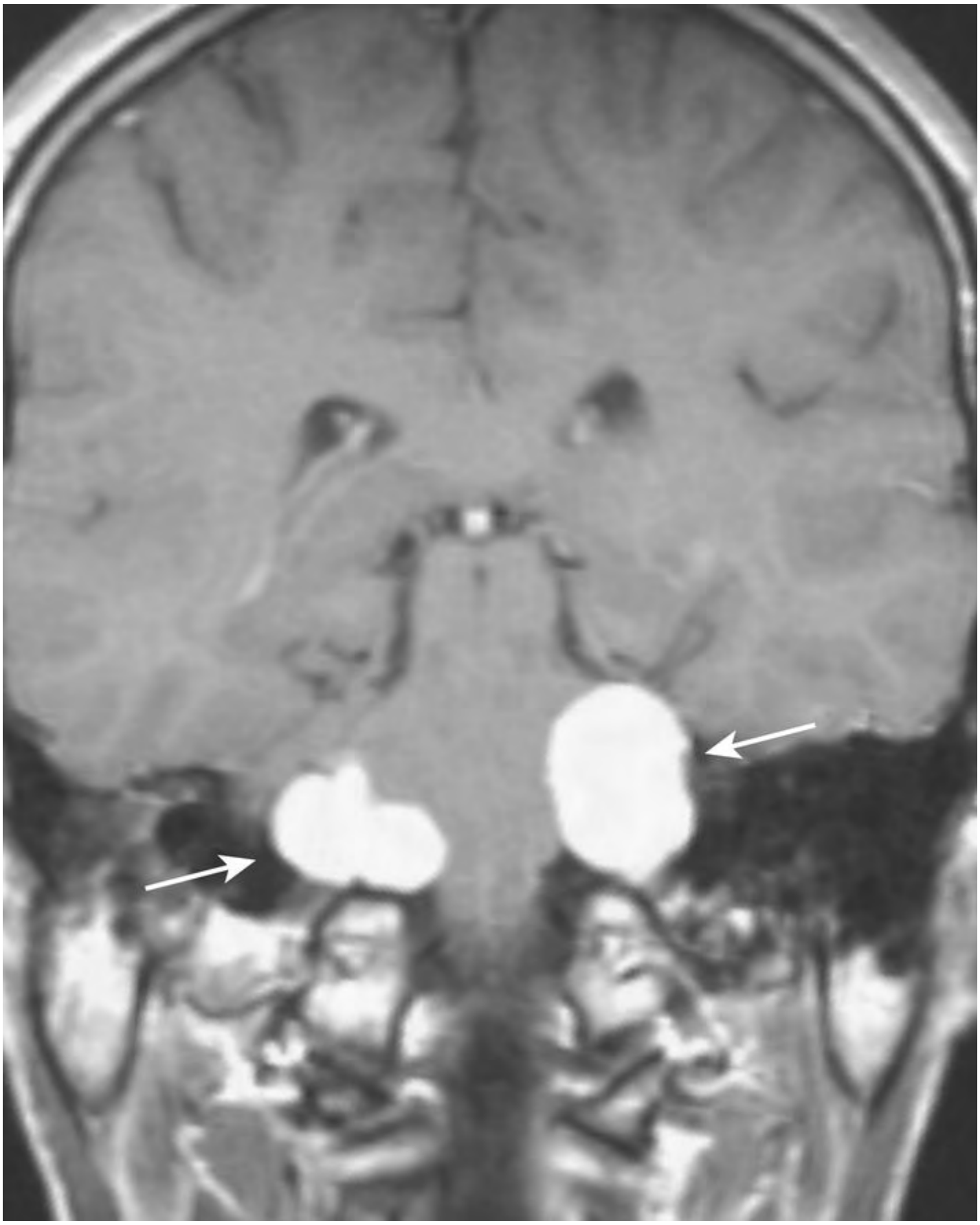
A and **B,** Axial T2-weighted MR image shows NF-1 spots as abnormal increased signal within the globus pallidi and thalami bilaterally *(arrowheads)*. **C,** Myelin vacuolization spots of NF-1 also noted within the bilateral cerebellar white matter *(arrowheads)*. Note also right eye proptosis secondary to intraorbital plexiform neurofibroma (not fully shown).



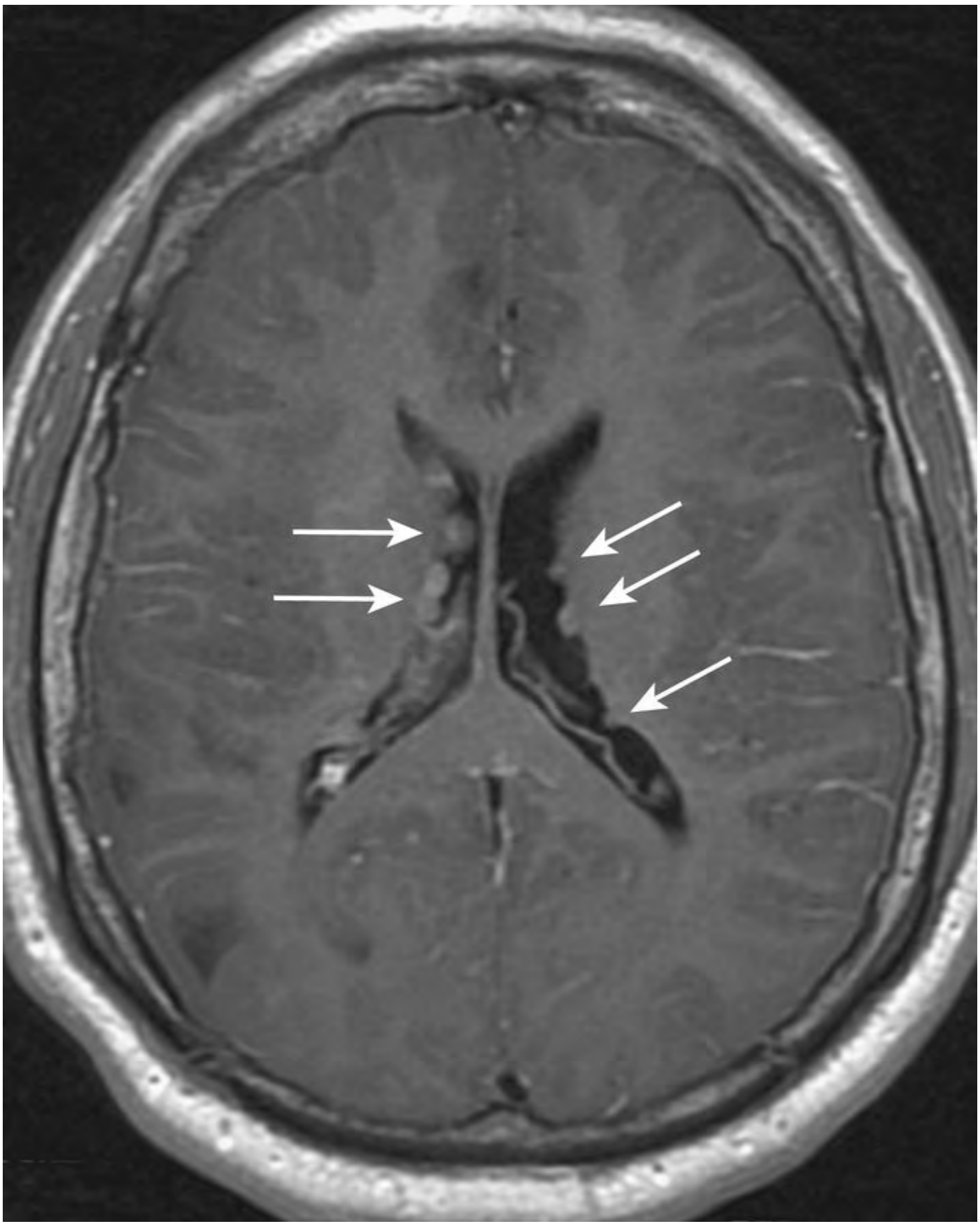
▪ **FIGURE 8-54 Optic Pathway Glioma in a Patient with Neurofibromatosis Type 1.** **A,** Axial FLAIR sequence shows enlarged bilateral prechiasmatic optic nerves *(arrowheads)* compatible with optic pathway glioma, as well as signal abnormality within the left mesial temporal lobe *(arrow)*. **B,** Optic pathway glioma extends into the chiasma *(arrowhead)*, optic radiations, and left aspect of midbrain *(arrows)*. **C,** Higher axial image demonstrates significant supratentorial extension bilaterally via optic radiations *(arrows)*. Note this is a case of extensive involvement of optic pathway glioma. In patients with NF-1 more subtle findings include focal enlargement and enhancement of optic nerves.



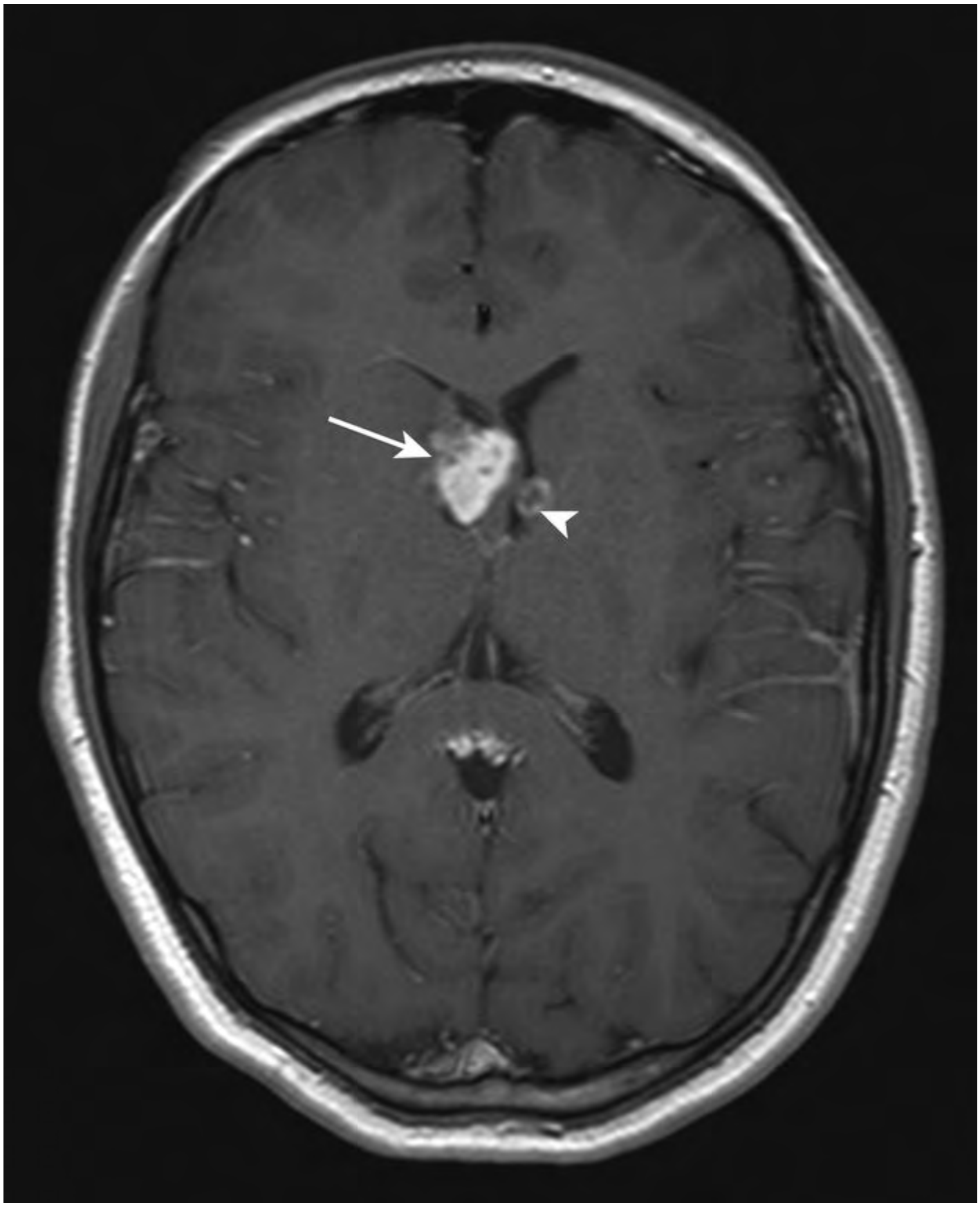
▪ **FIGURE 8-55** **Plexiform Neurofibroma in a Child with Neurofibromatosis Type 1.**
A, Coronal T2-weighted image shows multiple retroperitoneal masses *(N)* consistent with plexiform neurofibromas. **B,** Axial T2-weighted image of neck, in same patient, shows multiple high-signal lesions consistent with plexiform neurofibromas. In both **A** and **B,** note lower signal rounded areas within the masses. These are typical for plexiform neurofibromas.



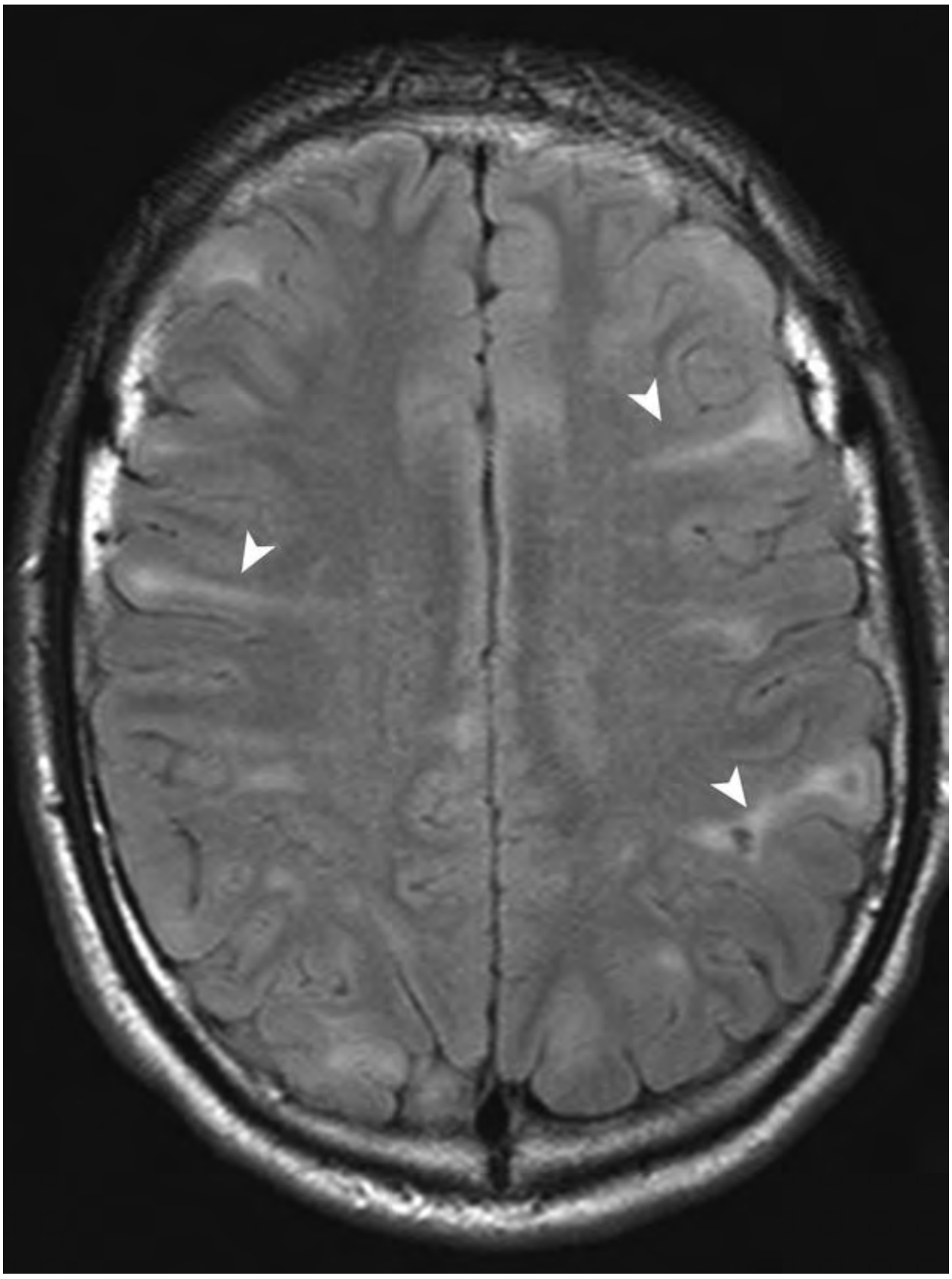
▪ **FIGURE 8-56** **Neurofibromatosis Type 2 with Bilateral Acoustic Schwannomas.** Coronal, postcontrast MR image shows bilateral enhancing masses *(arrows)* consistent with bilateral acoustic schwannomas.



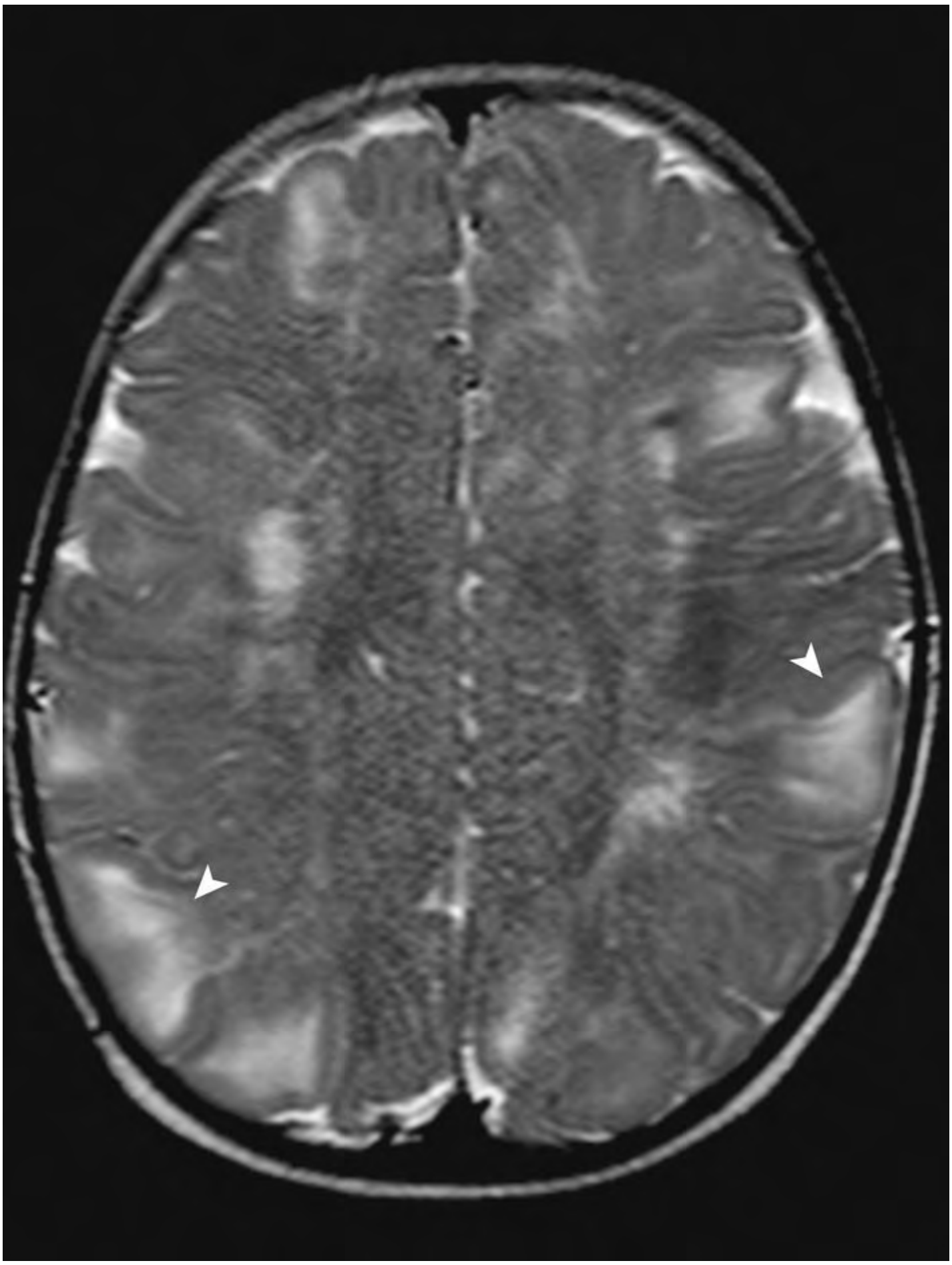
▪ **FIGURE 8-57** **Tuberous Sclerosis in a 9-Year-Old Boy with Seizures.**
Axial postcontrast T1-weighted MRI shows enhancing subependymal nodules *(arrows)* consistent with tubers.



▪ **FIGURE 8-58** **Tuberous Sclerosis.**
Axial T1-weighted image postcontrast demonstrates bilateral enhancing subependymal nodules near the foramen of Monro. The nodule on the right *(arrow)* is large and demonstrates an interval increase in size when compared with prior (not shown); suspicious for SEGA. Smaller left-side nodule *(arrowhead)* did not increase in size over time.



▪ **FIGURE 8-59** **Tuberous Sclerosis.**
Axial FLAIR sequence demonstrates radial migration lines seen in TS *(arrowheads)*.



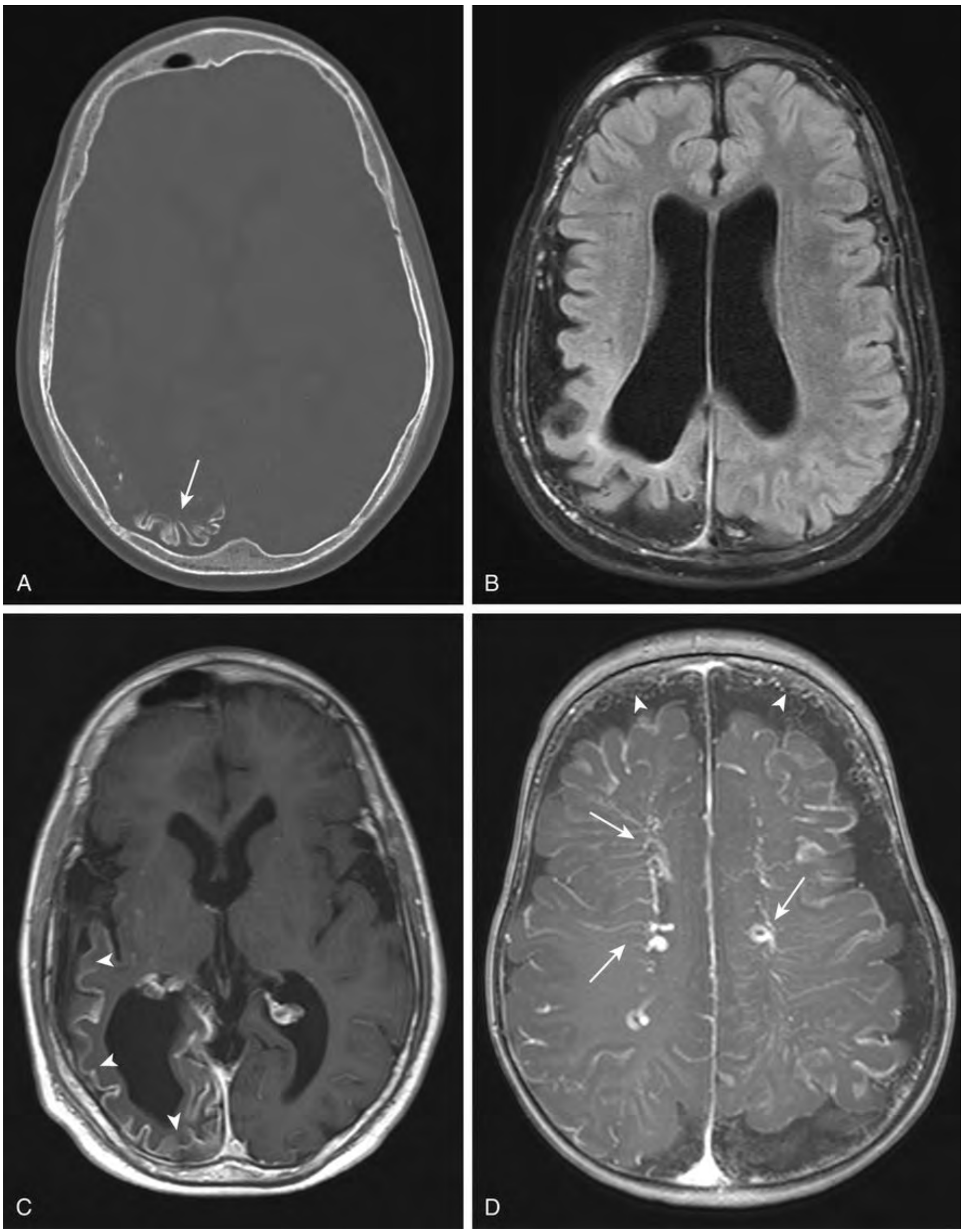
▪ **FIGURE 8-60** **Tuberous Sclerosis.**
Axial T2-weighted sequence showing multiple subcortical and cortical parenchyma tubers causing gyri expansion, a few of which are marked here *(arrowheads)*.

Sturge-Weber Syndrome

Sturge-Weber syndrome, or encephalotrigeminal angiomatosis, is characterized by low-flow vascular malformation both intracranially and extracranially. The syndrome manifests as abnormalities of the skin (facial port-wine nevus in the distribution of the trigeminal nerve), leptomeninges, and choroid of the eye. The altered leptomeningeal flow secondary to pial vascular malformation (angioma) results in venous stasis and chronic ischemic injury to the affected underlying brain. On neurologic imaging there is serpiginous calcifications, abnormal enhancement, and atrophy of the involved gyri (Fig. 8-61, *A-D*). Other findings may include prominence of choroid plexus on the involved side and choroidal angiomas of the orbits (Fig. 8-62). The cranium is commonly thickened adjacent to the brain abnormalities. Clinical manifestations include seizures, mental retardation, and hemiparesis.

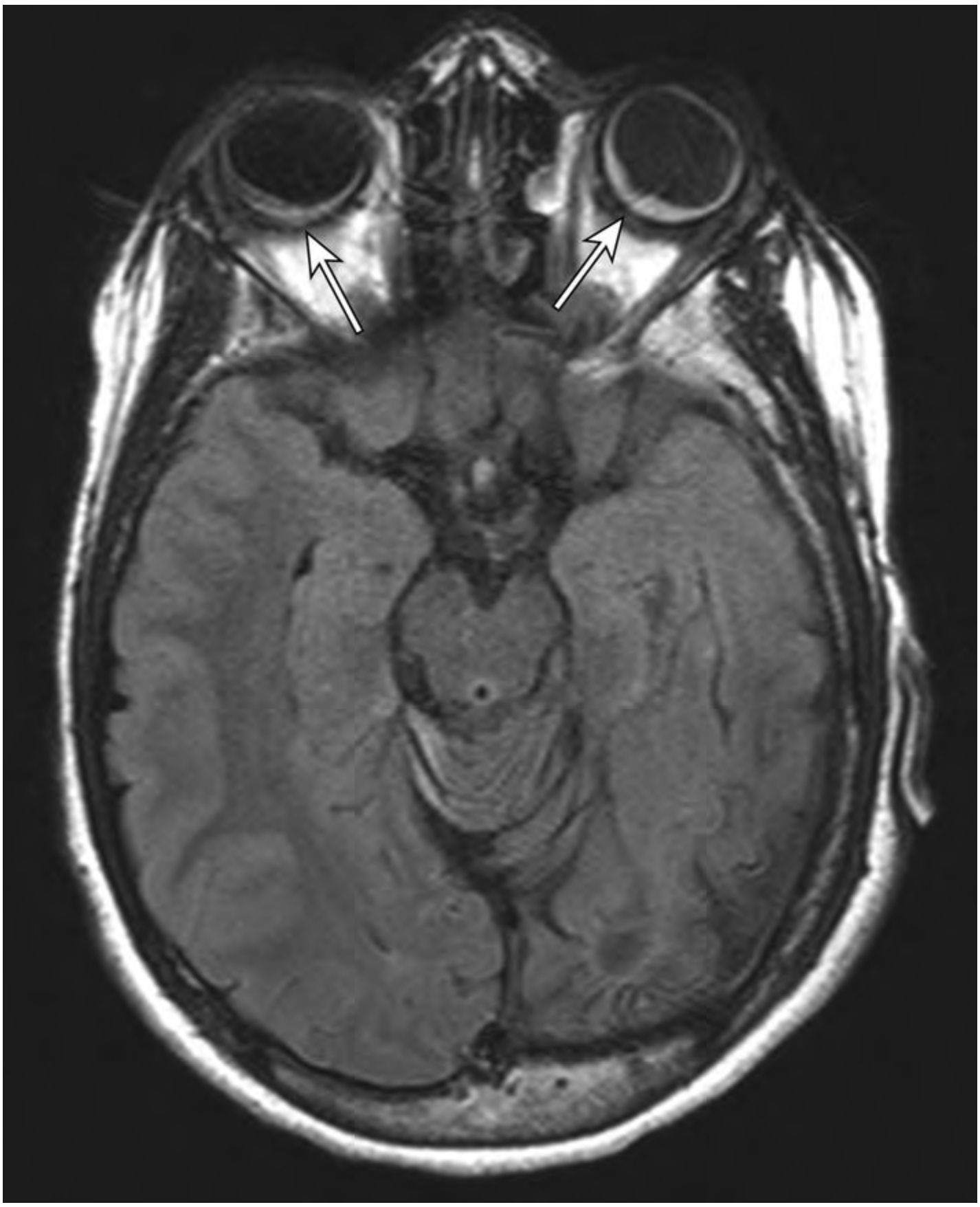
▪ Metabolic and Degenerative Disorders

A large number of metabolic and degenerative disorders can result in abnormal myelination patterns. Most of these diseases are rare and untreatable. Categories of disease include lysosomal storage disorders, mitochondrial disorders, peroxisomal disorders, and amino acid disorders. On MRI these disorders typically demonstrate abnormally increased T2-weighted signal involving portions of white matter, gray matter, or a combination of the two, most often in a bilateral symmetric pattern. There may be associated atrophy of the involved structures. The distribution of the abnormal signal can be helpful in narrowing the differential diagnosis (Figs. 8-63, *A-C* through 8-66, *A-C*). MR spectroscopy can also provide helpful information. Representative disorders and the associated distribution of abnormalities are listed in Table 8-6.



▪ **FIGURE 8-61** **Sturge-Weber Syndrome.**

A, Noncontrast CT in bone window shows abnormal gyriform calcifications *(arrow)* within the right parietooccipital region. **B,** Axial FLAIR sequence demonstrates regional parenchymal volume loss. **C,** Abnormal gyriform enhancement *(arrowheads)* is seen on postcontrast T1 sequence. **D,** Axial T1-weighted sequence postcontrast, in a different patient with bilateral involvement, demonstrates prominent and tortuous bilateral deep medullary veins *(arrows)* and peripheral cortical veins within the subarachnoid space *(arrowheads)*.



▪ **FIGURE 8-62** **Orbital Involvement of Sturge-Weber Syndrome.**
Axial FLAIR sequence demonstrates crescentic area of increased signal along the bilateral choroidal surface of the globes *(arrows)*, compatible with choroidal angiomas. This is not a very common finding on imaging, even when choroidal involvement is present. The diagnosis is typically made on ophthalmological evaluation.

▪ Infection

Many of the imaging findings in CNS infections (meningitis, cerebritis, empyema, encephalitis, and parenchymal abscess) are similar in children and adults and are not emphasized here. This section focuses on several of the issues unique to children.

Congenital Infections

There are a number of in utero infections (TORCH: toxoplasmosis, other [syphilis, HIV], rubella, cytomegalovirus [CMV], herpes; see Chapter 7) that can affect the CNS. They demonstrate unique findings as compared with CNS infections that occur later in life because in utero infections affect brain development. The severity of the abnormality commonly reflects the time period during which the infection occurred.

Infection by CMV is the most common TORCH infection to involve the CNS. Imaging findings include periventricular calcifications, migrational abnormalities (such as polymicrogyria and

lissencephaly), increased white matter T2 signal, cortical cysts (especially at the temporal lobes), cerebellar hypoplasia, and ventricular enlargement (Fig. 8-67, *A* and *B*). Clinical manifestations include microcephaly, hearing impairment, mental retardation, and developmental delay.

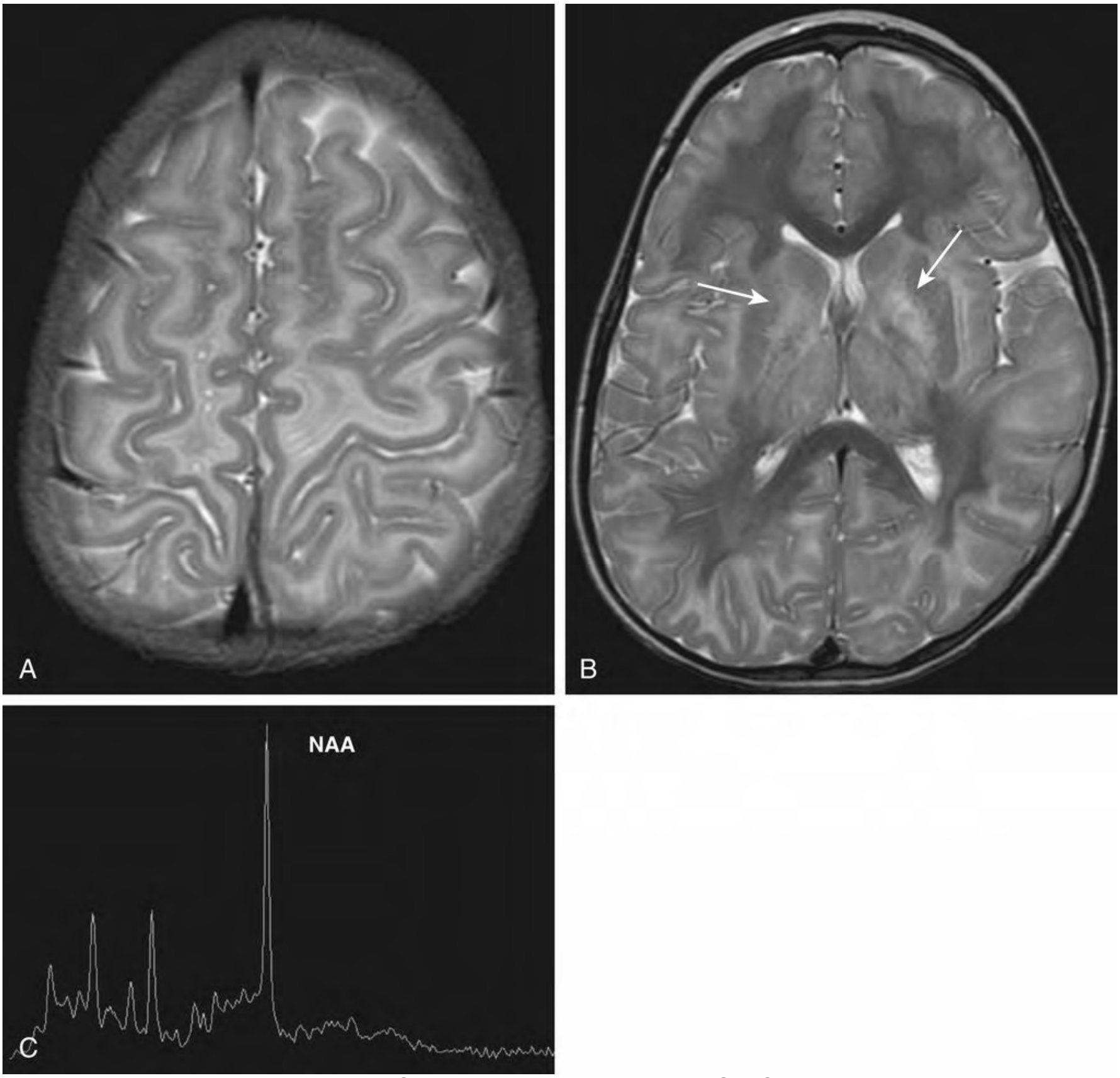
Toxoplasmosis is the second most common TORCH infection to involve the CNS. The parenchymal calcifications seen in toxoplasmosis are more variable in location than those seen with CMV, with predilection to basal ganglia and periventricular white matter. Other manifestations include hydrocephalus. No migrational abnormalities are seen. Differential diagnosis of periventricular calcifications in the neonatal period also includes more rare entities, such as lymphocytic choriomeningitis infection (LCMV) and pseudo-TORCH syndromes (Aicardi-Goutières syndrome and Baraitser-Reardon syndrome).

With congenital infection by human immunodeficiency virus (HIV), CNS abnormalities are mostly related to primary HIV involvement rather than secondary complications (opportunistic infections and tumors), as are seen in adults. The majority of children with congenital HIV infection have CNS manifestations, typically progressive encephalopathy. Imaging findings include diffuse atrophy, delayed myelination, and calcifications. The calcifications most commonly occur within the basal ganglia and subcortical white matter of the frontal lobes.

Congenital herpes is secondary to herpes simplex virus type 2 (HSV2), and imaging findings of meningoencephalitis include cortical and white matter signal abnormality, diffusion restriction, and meningeal enhancement. HSV2 infection has no predilection of location as opposed to HSV1, which typically affects the temporal lobes.

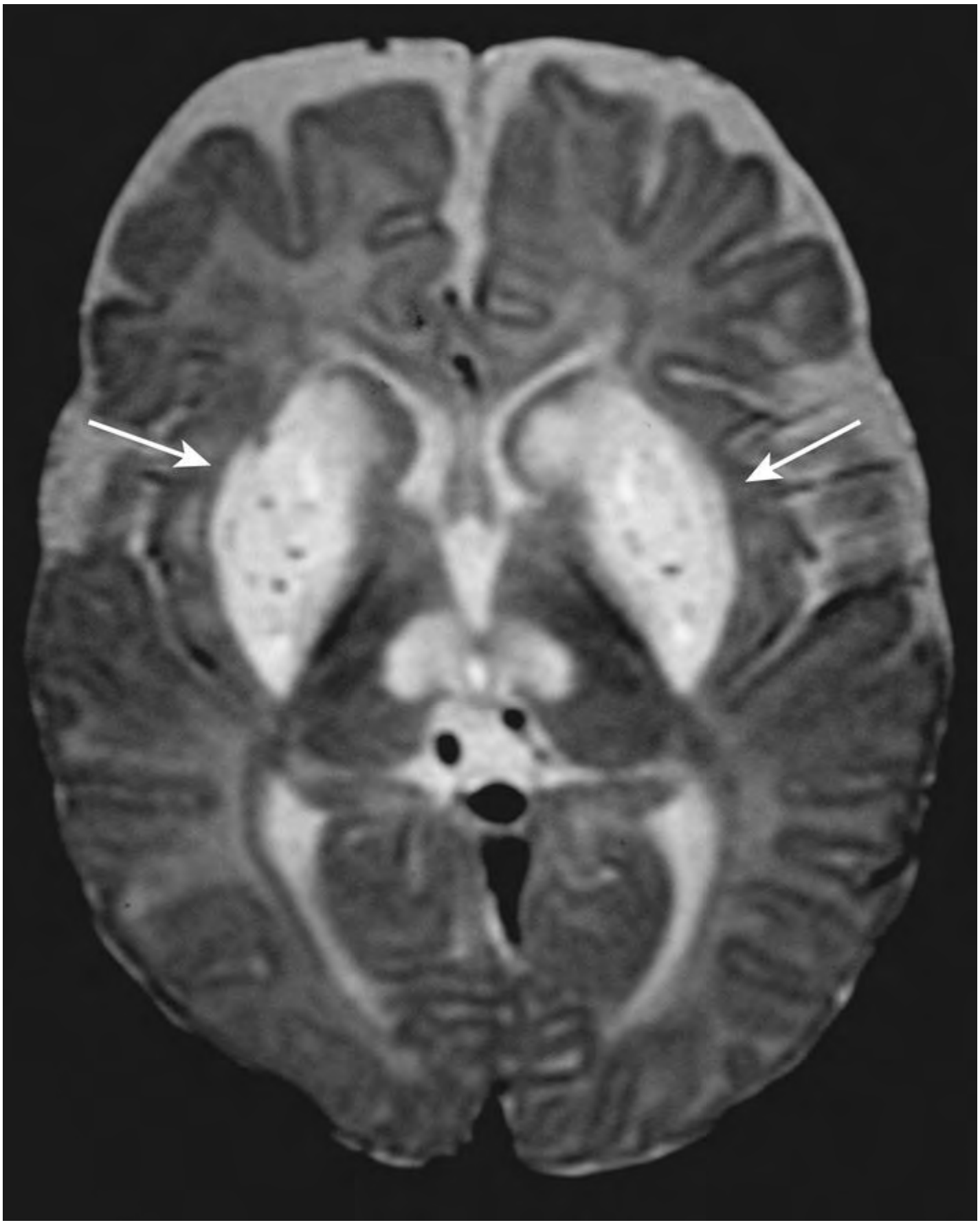
Encephalitis

Encephalitis is inflammation of the brain, sometimes seen in conjunction with meningeal inflammation. It can occur secondary to direct viral infection, can be associated with an autoimmune response to a virus or immunization, or can be the extension of a meningeal infection. Children typically present with seizures, lethargy, or focal neurologic deficits. Several types of encephalitis occur, predominantly during childhood.



▪ **FIGURE 8-63** **Canavan Disease in a 3-Year-Old Child.**
A, T2-weighted axial image shows increased signal diffusely throughout the subcortical white matter. **B,** T2-weighted axial image more inferiorly shows increased signal in globus pallidi bilaterally *(arrows)*. Again, there is increased signal in subcortical white matter. **C,** MR spectroscopy shows increased NAA peak.

1. *HSV1* can lead to necrotizing meningoencephalitis. When it occurs secondary to the reactivation and migration of a previous latent infection via the branches of the trigeminal nerve, it typically affects one or both temporal lobes (Fig. 8-68, *A-C*). On MRI, high signal is seen within the cortex of one or both temporal lobes, with or without diffusion restriction. There are often areas of hemorrhage within the affected areas.
2. *Subacute sclerosing panencephalitis* is thought to be an encephalitis that occurs secondary to reactivation of latent measles infection. It is a disease of childhood. Imaging demonstrates nonspecific atrophy and increased T2-weighted signal within the cerebral cortex and white matter (Fig. 8-69).
3. *Acute disseminated encephalomyelitis (ADEM)* is an immunologic disease that occurs in response to a recent viral infection or immunization. It typically occurs days to weeks after the preceding stimulus. On MRI, areas of increased T2-weighted signal are typically seen in the white matter (Fig. 8-70), brainstem, and cerebellum. Deep gray matter structures (basal ganglia) can also be affected. Treatment is typically with steroids, and most children completely recover.



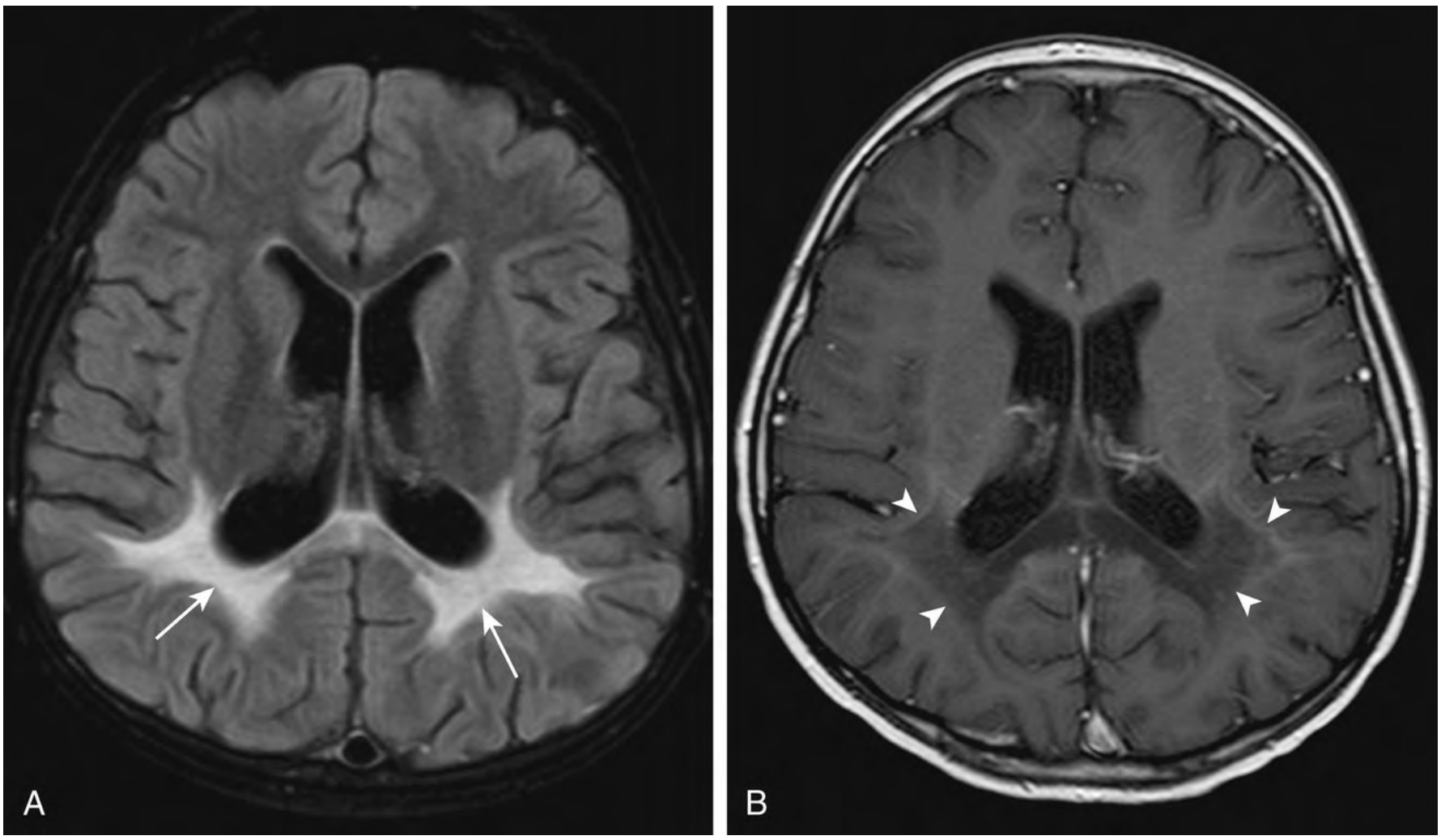
▪ **FIGURE 8-64** **Leigh Disease in a 5-Month-Old Boy.**
Axial T2-weighted MR image shows abnormal, increased signal within the basal ganglia *(arrows)* and medial thalami. There is bifrontal volume loss.

▪ Tumors

Tumors of the CNS are the most common solid malignancies of childhood. The imaging approach to differential diagnosis is based on the categorization of the tumors according to their anatomic location: posterior fossa, supratentorial, intraventricular, sellar-suprasellar, and pineal region.

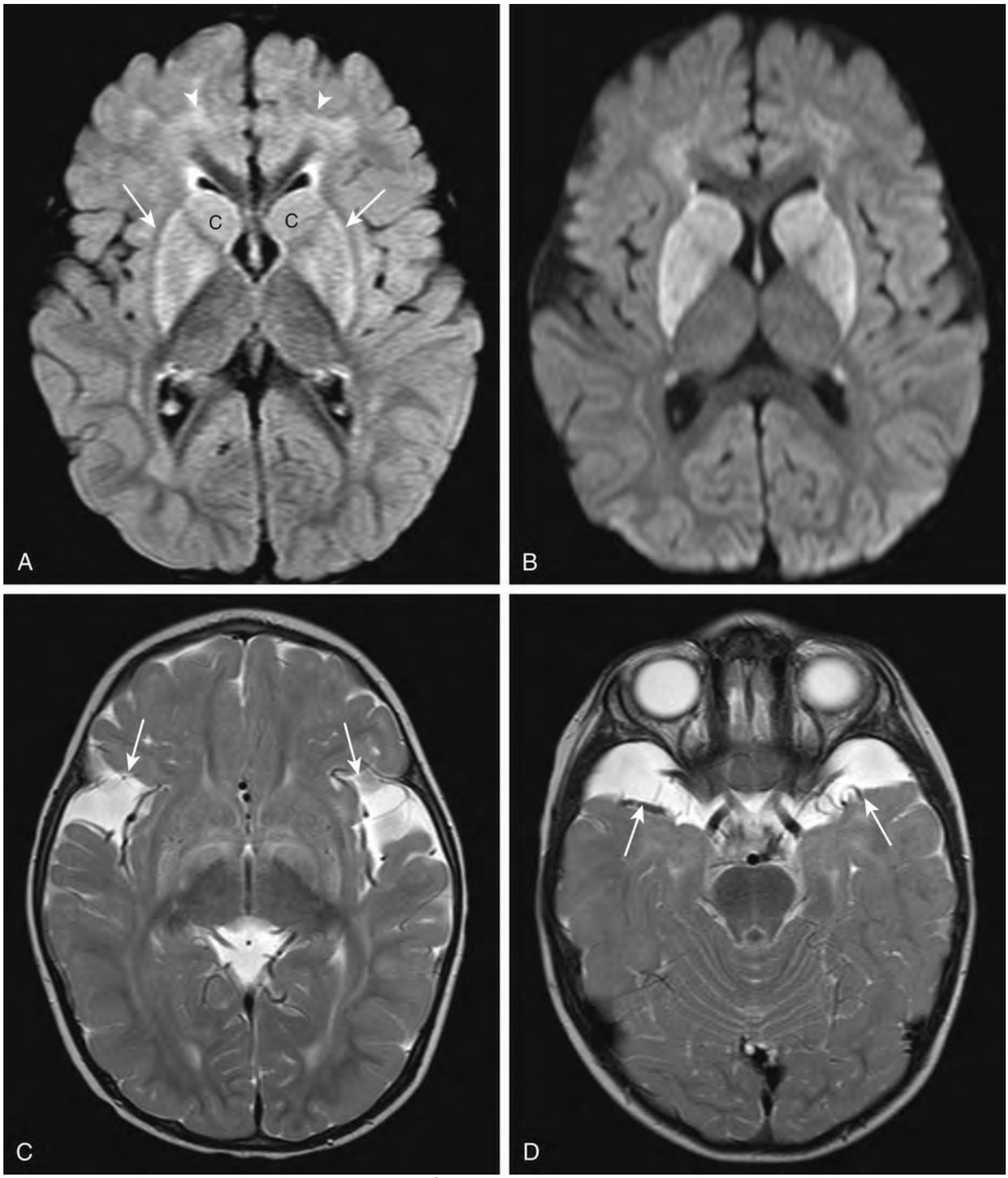
Posterior Fossa Tumors

Tumors of the posterior fossa are more common in childhood than in adulthood. The most common posterior fossa tumors in children include cerebellar astrocytoma, medullablastoma, brainstem glioma, and ependymoma (Table 8-7). Atypical teratoide rhabdoid tumor (ATRT) is a less common tumor that should be included in the differential diagnosis of a heterogeneous and hypercellular posterior fossa tumor in children under the age of 3. Posterior fossa tumors often present with obstructive hydrocephalus secondary to mass effect over the fourth ventricle and sylvian aqueduct.



▪ **FIGURE 8-65** **Adrenoleukodystrophy.**

A, Axial FLAIR sequence shows abnormal, increased signal in the posterior periventricular white matter *(arrows)*. **B,** Axial postcontrast image demonstrates abnormal enhancement along the outer margins of the signal abnormality *(arrowheads)*.



▪ **FIGURE 8-66** **Glutaric Aciduria Type 1.**

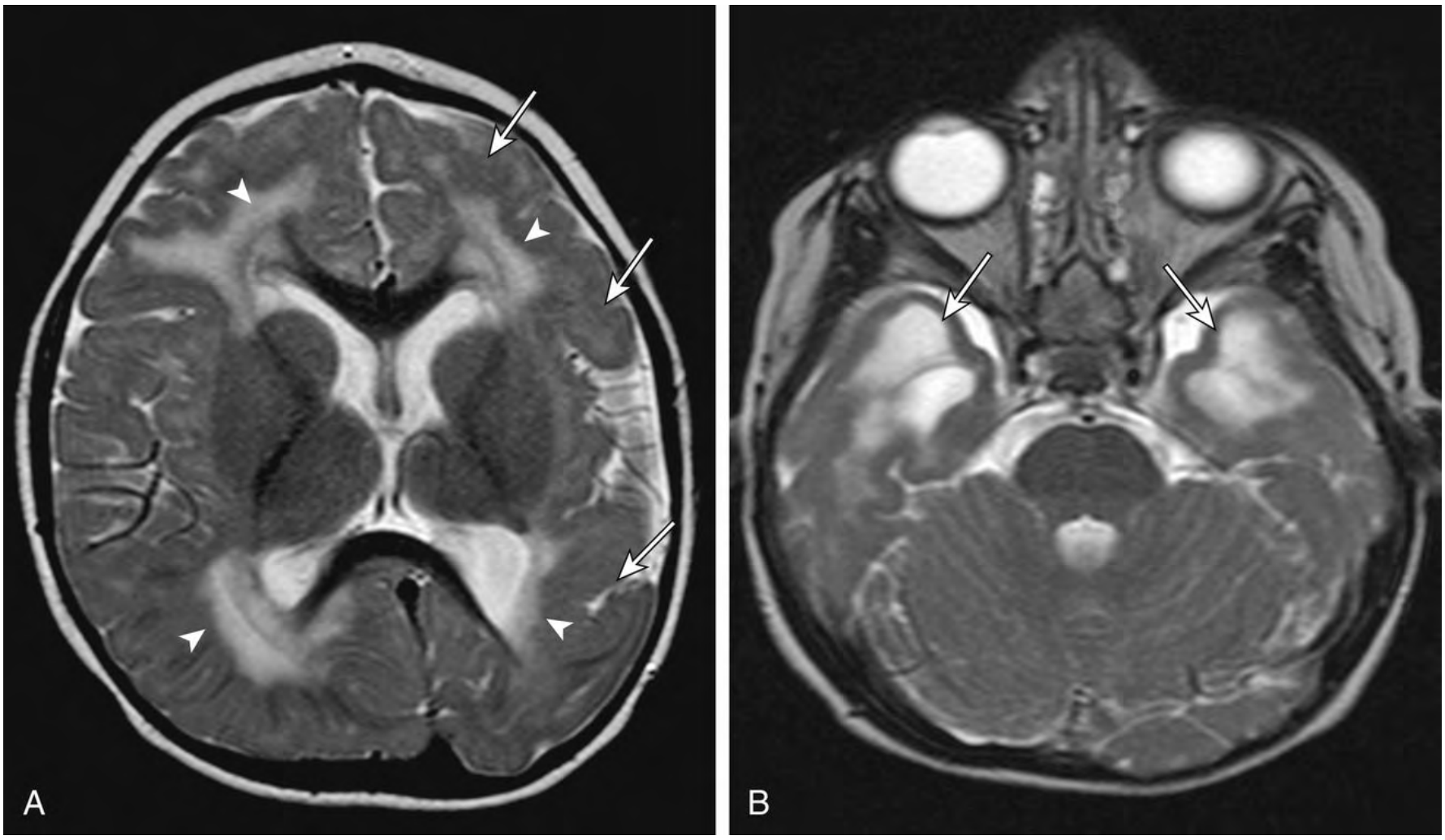
A, Axial FLAIR sequence demonstrates abnormal, bilateral, symmetric, increased signal within the head of caudate nucleus *(C)* and lentiform nucleus *(arrows)*, as well as bilateral anterior periventricular white matter *(arrowheads)*. **B,** Diffusion sequence shows restricted diffusion in corresponding areas. **C,** T2-weighted sequence demonstrates bilateral widening of sylvian fissures *(arrows)* due to underopercularization. **D,** Note also bilateral prominent CSF at the middle cranial fossa *(arrows)*. Glutaric aciduria type 1 can present with nontraumatic subdural collections and is part of the differential diagnosis for child abuse.

TABLE 8-6

Metabolic and Degenerative Disorders of the Central Nervous System

Disorder	Category of Disease	Primary Distribution of Abnormality and Key Features
Leigh disease	Mitochondrial disorder	**Deep gray matter** (especially striatum, periaqueductal gray matter, substancia nigra, subthalamic nuclei, dorsal pons, and cerebellar nuclei)
Kearns-Sayre disease	Mitochondria disorder	**Deep gray** (primarily globus pallidus) + **White matter** (subcortical U fibers and cerebellum)
		May have basal ganglia calcification
Pelizaeus-Merzbacher	Miscellaneous metabolic disorder	**White matter** (including subcortical fibers and early involvement of internal capsule)
Adrenoleukodystrophy	Peroxisomal disorder	**White matter** (initially central white matter, posterior periventricular more frequent)
		Leading edge enhancement is common
Phenylketonuria	Amino acid disorder	**White matter** (initially central white matter)
Maple syrup urine disease	Amino acid disorder	**Deep gray** (primarily globus pallidus and thalami) + **White matter** (edema or restricted diffusion in cerebellar white matter and brainstem)
Glutaric aciduria type 1	Mitochondrial disorder	**Deep gray matter** (striatum more than globus pallidus)
		Enlarged operculum
		Bilateral prominent middle cranial fossa CSF
Vanishing white matter	Miscellaneous metabolic disorder	**White matter** (begins in central white matter, extensive hypomyelination is seen on latter stages with signal of white matter becoming similar to CSF)
Mucopolysaccharidosis	Lysosomal storage disorders	**White matter** (associated enlarged perivascular spaces)
Metachromatic leukodystrophy	Lysosomal storage disorders	**White matter** (spare subcortical U fiber until late disease)
		Stripped appearance of affected white matter "tigroid" pattern
		May have enhancement of cranial nerves and cauda equina
Krabbe disease	Lysosomal storage disorders	**White matter** (initially central white matter, cerebellar white matter around dentate nucleus)
		May have hyperintense basal ganglia and thalami on CT
		Enhancement of lumbar nerve roots occasionally present
Canavan disease	Amino acid disorder	**Deep gray** (primarily globus pallidus, sparing caudate and putamen) + **White matter** (including peripheral white matter, sparing internal capsule, and corpus callosum)
		Macrocephaly
		Increase NAA on MRS
Alexander disease	Miscellaneous metabolic disorder	**White matter** (including peripheral white matter, bifrontal predominance)
		Macrocephaly
Megalencephaly leukoencephalopathy with subcortical cysts (MLC)	Miscellaneous metabolic disorder	**White matter**
		Macrocephaly
		Subcortical "cysts" (more common on temporal lobes)

CSF, Cerebrospinal fluid; *MRS*, magnetic resonance spectroscopy *NAA, N*-acetylaspartate.



▪ FIGURE 8-67 **Sequelae of Cytomegalovirus Infection.**

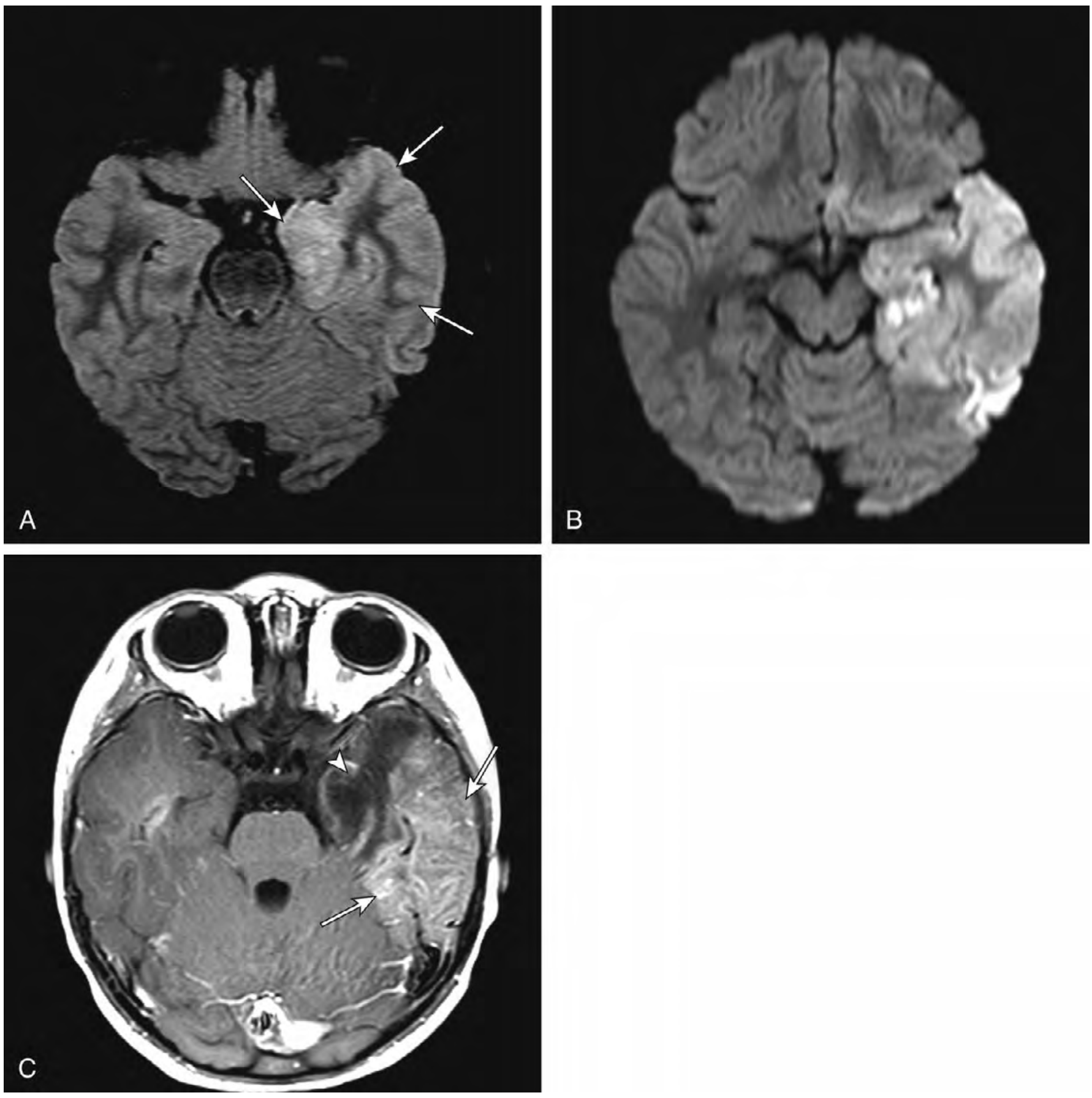
A, Axial T2-weighted sequence shows signal abnormality within the periventricular white matter *(arrowheads)* and extensive left hemisphere polymicrogyria *(arrows)*. **B,** Lower image shows increased subcortical T2 signal within the bilateral temporal lobes *(arrows)*. Signal abnormality is similar to CSF and referred to as temporal cysts. This finding is highly suggestive of CMV when congenital infection is suspected.

Cerebellar Astrocytoma

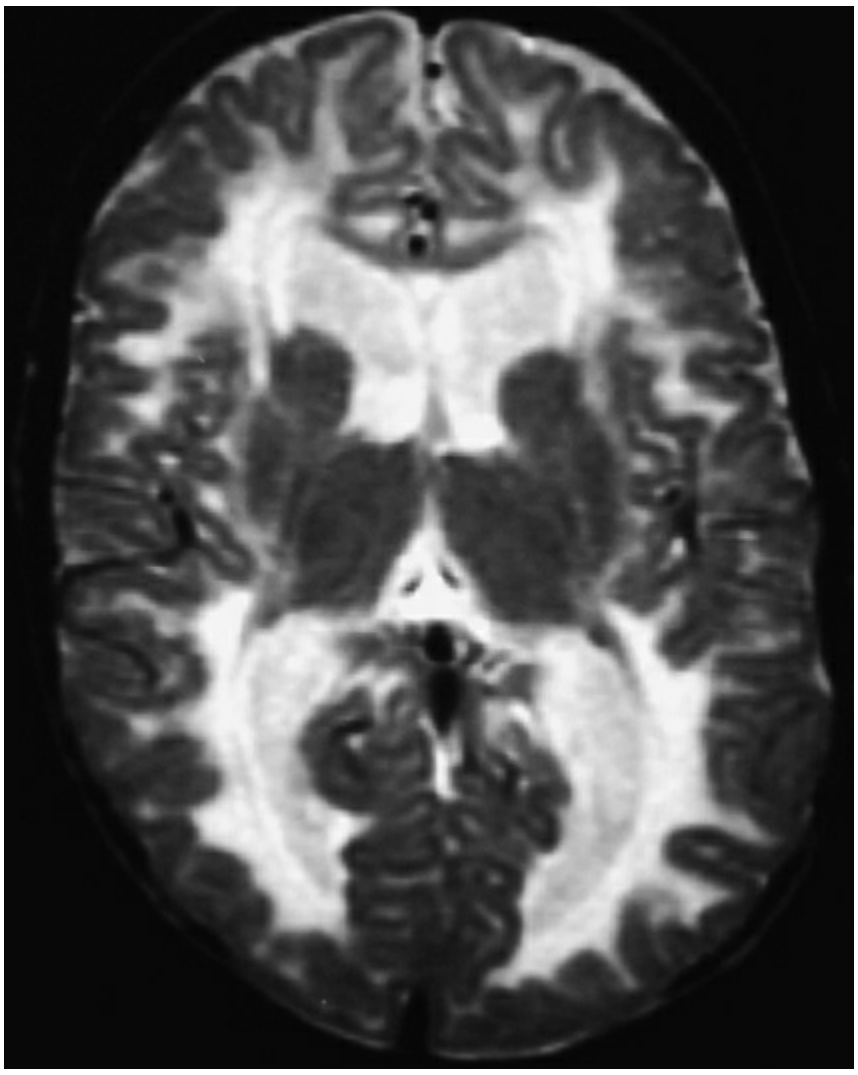
Cerebellar astrocytoma (pilocytic subtype) is the most common type of posterior fossa tumor. It is a low-grade malignancy and has the best prognosis of any CNS malignancy. Most require surgical treatment only, if full resection is achieved. The lesions occur most commonly in the cerebellar hemispheres. The classic appearance on imaging is a cystic cerebellar hemisphere mass with a peripheral enhancing nodule (Fig. 8-71). However, cerebellar astrocytomas can be predominantly cystic or completely solid in appearance (Fig. 8-72, *A* and *B*). The margins of the lesions are usually well defined. The fourth ventricle is displaced, and the margin between the lesion and the fourth ventricle is typically also well defined (see Fig. 8-72). Unlike medulloblastomas and ependymomas, cerebellar astrocytomas usually do not demonstrate areas of calcification or hemorrhage. The predominantly solid lesions enhance heterogeneously (see Fig. 8-72). Differential diagnosis of a well-circumscribed cystic cerebellar mass with mural nodule in children includes the less common ganglioglioma. Ganglioglioma is also a low-grade tumor; however, it is most commonly seen in the supratentorial compartment and may have calcifications.

Medulloblastoma

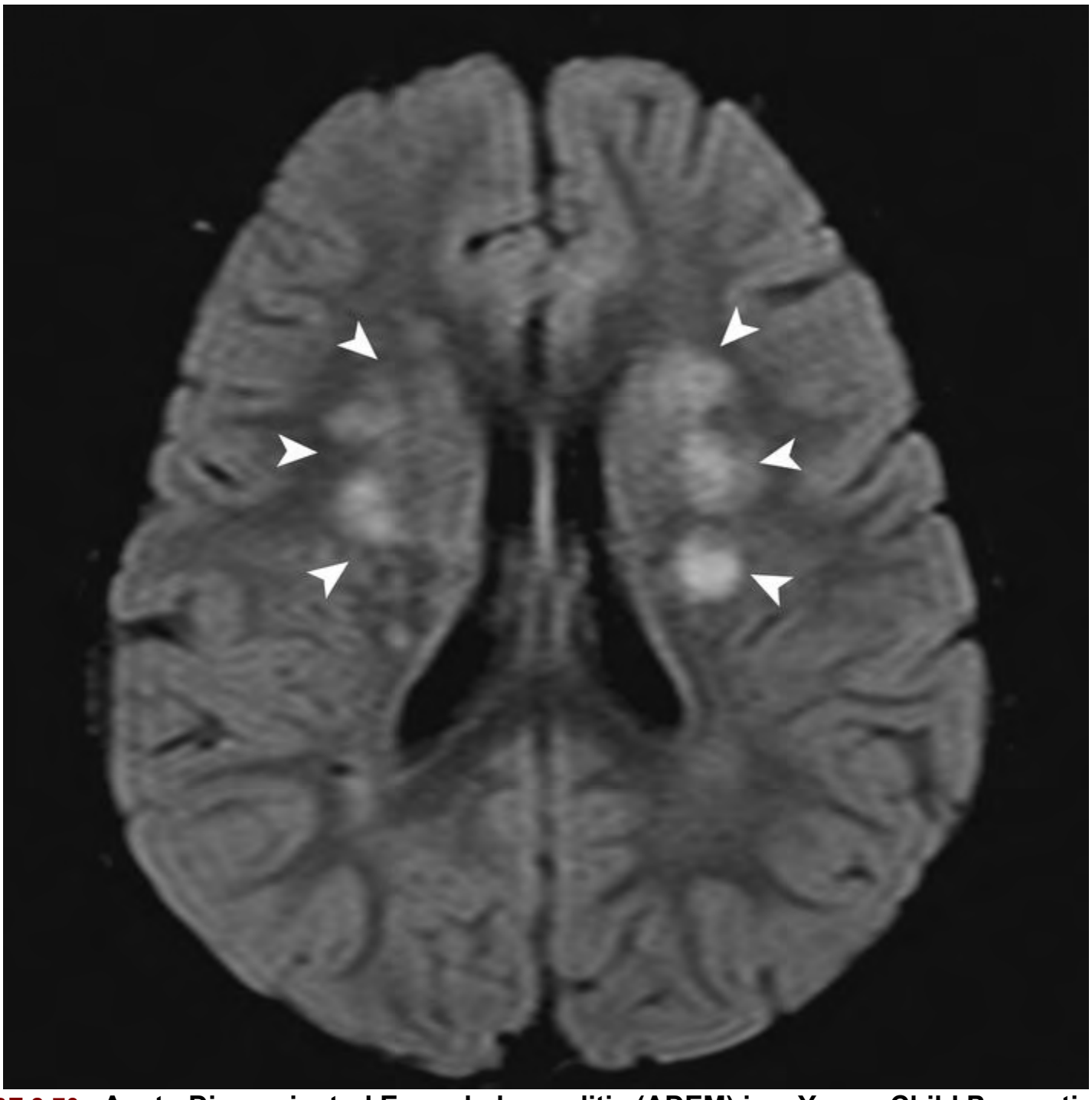
Medulloblastoma is the second most common posterior fossa tumor in children and is the most malignant. It is considered a primitive neuroectodermal tumor (PNET). On imaging the lesion appears as a mass filling the fourth ventricle (Fig. 8-73, *A-D*). Because it arises from the roof of the fourth ventricle, the border between the vermis and lesion, as seen on a sagittal MRI, is poorly defined. On CT the lesion may appear hyperdense (see Fig. 8-73, *A*). On MRI the lesions tend to be more homogeneous in signal than cerebellar astrocytomas or ependymomas and enhance diffusely (Fig. 8-73, *B*). Medulloblastomas tend to be hypointense (hypercellularity) to mildly hyperintense on T2-weighted images. Unlike most other posterior fossa tumors, medulloblastomas are hypercellular and as a result show restricted diffusion on DWI sequences (Fig. 8-73, *C* and *D*). Spectroscopy may show elevated Tau at 3.3 ppm. There is a propensity for seeding within the intracranial and intraspinal CSF spaces (Fig. 8-74). Evaluation of the entire spine with contrast is necessary to rule out drop metastases.



▪ **FIGURE 8-68** **Herpes Encephalitis.**
A, Axial FLAIR sequence shows focal abnormal, increased signal involving most of the left temporal lobe *(arrows)*. **B,** Restricted diffusion was noted on DWI sequence. **C,** Axial postcontrast T1-weighted sequence from a follow-up MRI demonstrates focal area of encephalomalacia *(arrowhead)* and abnormal peripheral enhancement of the reminder of the left temporal lobe *(arrows)*, sequelae of prior infarct and ischemia from herpes encephalitis.



▪ **FIGURE 8-69** **Subacute Sclerosing Panencephalitis.**
Axial T2-weighted MR image shows abnormal increased signal throughout periventricular white matter. There is associated volume loss and dilatation of the lateral ventricles.



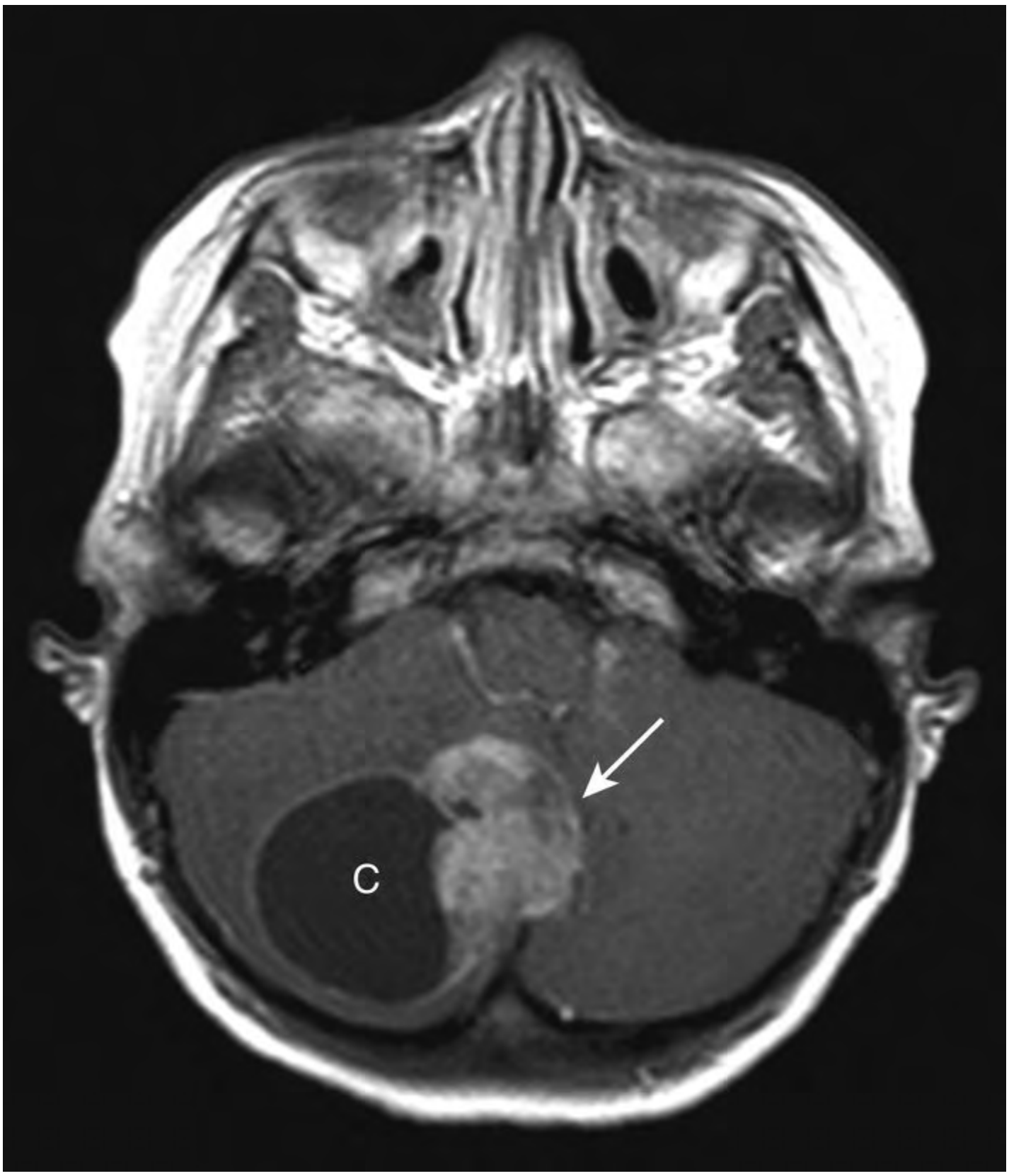
▪ **FIGURE 8-70** **Acute Disseminated Encephalomyelitis (ADEM) in a Young Child Presenting with Focal Neurological Symptoms and Recent Respiratory Illness.**

Axial FLAIR MR image shows multiple foci of abnormal, increased signal in the bilateral deep cerebral white matter *(arrowheads)*. Other demyelinating diseases, such as multiple sclerosis, can have similar findings, and differentiation may be impossible based soley on imaging. Demographics, clinical history, and course of disease are usually necessary to reach a final diagnosis.

TABLE 8-7

Posterior Fossa Tumors

Tumor	Imaging Characteristics
Cerebellar astrocytoma	Cystic or solid
	Most common presentation: cystic with mural nodule
	Mostly within cerebellar hemisphere, off midline
	Well defined
	Fourth ventricle displaced, with well-defined interface
	No calcification or hemorrhage
Medulloblastoma	Arises from roof of fourth ventricle; poorly defined interface
	Mostly a solid midline mass
	Increase attenuation on CT
	Restricted diffusion on DWI sequences
	CSF metastasis may be present
	Elevated Tau at 3.3 ppm on spectroscopy
Brainstem glioma	Circumferential enlargement or exophytic mass of brainstem (most commonly pons)
	Nonenhancing
	Fourth ventricle pushed posteriorly
	Hydrocephalus uncommon
Ependymoma	Arises from floor of fourth ventricle; poorly defined interface
	Mostly heterogeneous (hemorrhage, necrosis) midline mass
	"Plastic" tumor, tendency to extend through foramens magnum and Luschka
	Calcifications in 50% to 70%



▪ **FIGURE 8-71** **Cerebellar Pilocytic Astrocytoma.**
Contrast-enhanced T1-weighted MR image shows a predominantly cystic mass *(C)* in the right cerebellar hemisphere with an enhancing mural nodule *(arrow)*.

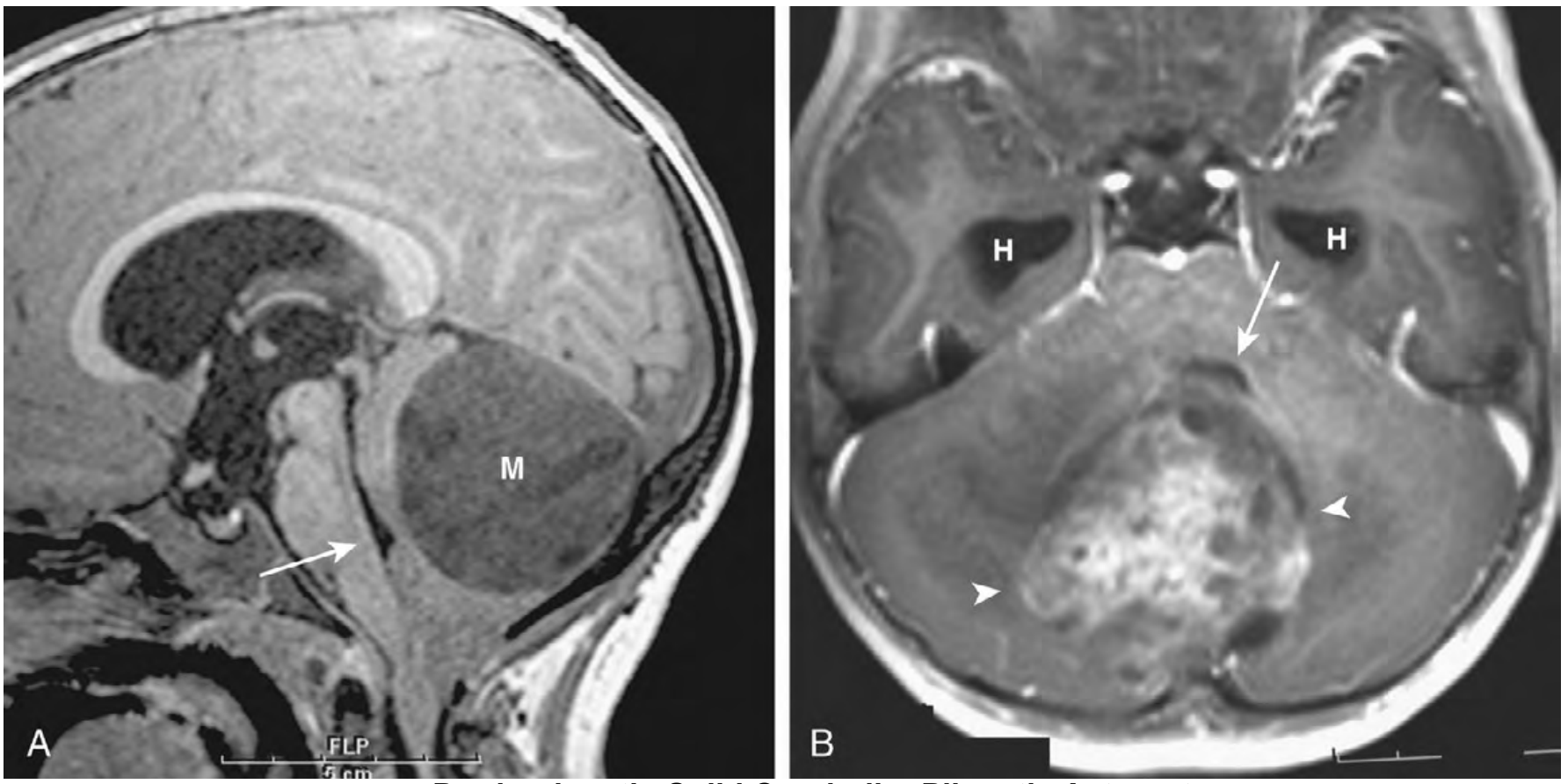
Brainstem Glioma

Brainstem gliomas are most commonly astrocytomas of moderate aggressiveness. They occur most often in the pons. Unlike other posterior fossa masses, the lesions tend to present with cranial nerve abnormalities, pyramidal tract signs, or cerebellar dysfunction rather than with signs of hydrocephalus. The lesions usually cause circumferential enlargement of the brainstem surrounding the basilar artery in diffuse intrinsic pontine glioma (Fig. 8-75, *A* and *B*) or, less commonly, grow in an exophytic fashion. On MRI the lesions tend to demonstrate a homogeneous high signal on T2-weighted images. Before treatment, enhancement is rare (see Fig. 8-75, *B*). Exophytic lesions more commonly enhance. Approximately 10% of lesions have a cystic component. If displaced, the fourth ventricle is pushed posteriorly (see Fig. 8-75, *A*). In the vast majority of these tumors, complete surgical resection is not possible. Radiation therapy remains the primary mode of therapy, although different types of chemotherapy agents and vaccines are currently being used in research trials throughout the country.

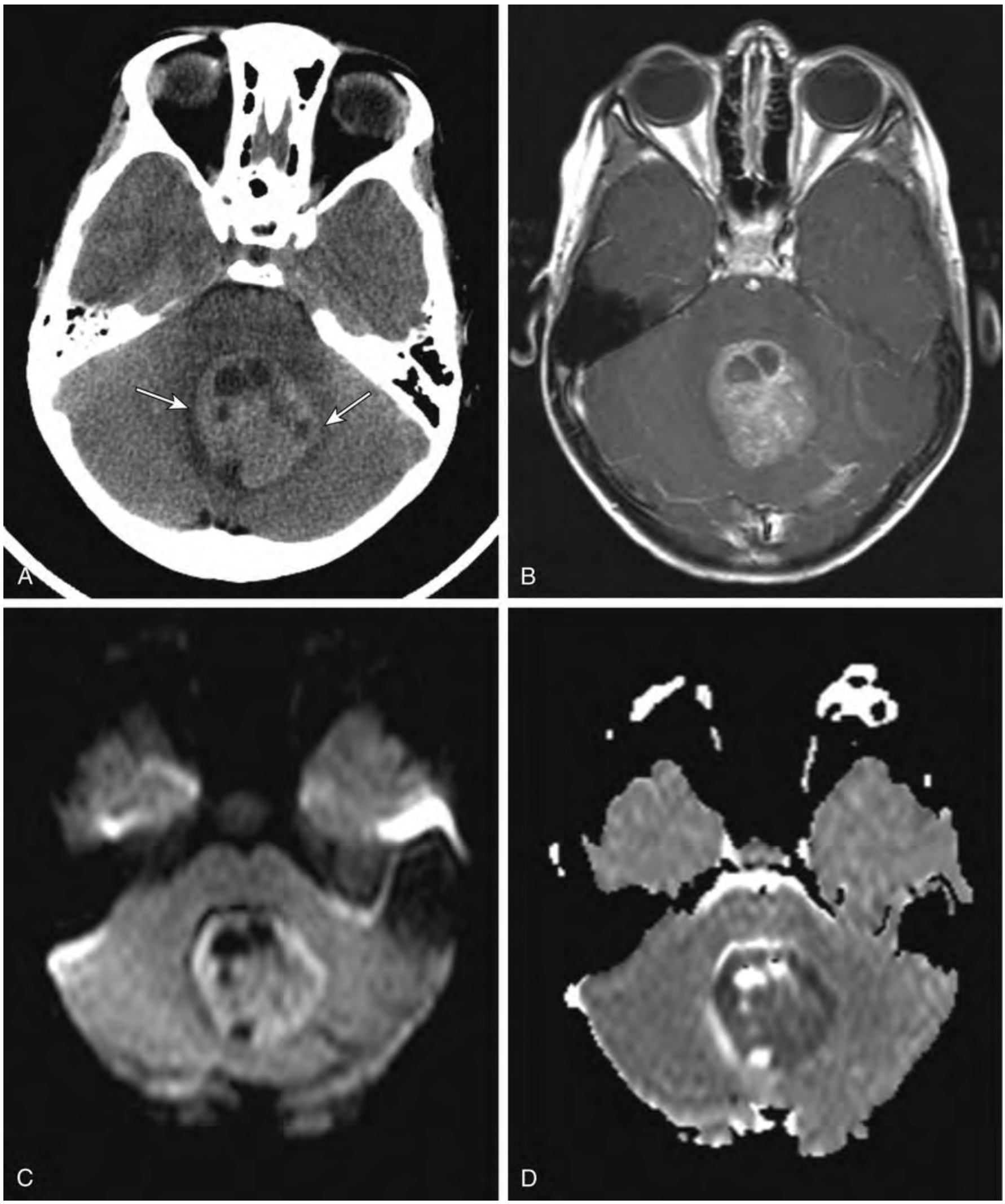
Ependymoma

Ependymomas are relatively slow-growing tumors that arise from the ciliated ependymal cells that line the ventricles. Two thirds occur in the fourth ventricle. When they occur in the fourth ventricle, ependymomas arise from and have a broad connection with the floor of the fourth ventricle, opposite from the roof involvement seen in medulloblastoma. Therefore the border between the lesion and floor

of the fourth ventricle is often poorly defined (Fig. 8-76, *A* and *B*). The lesions may fill and grow out of the fourth ventricle via the foramina into the cisterna magna and spinal canal ("soft" or "plastic" tumor) (Fig. 8-77, *A* and *B*). The lesions appear very heterogeneous and enhance heterogeneously on CT and MRI. Ependymomas have well-defined, lobulated margins. Calcifications are seen on CT in 50% to 70% of cases (see Fig. 8-76, *A*).



▪ **FIGURE 8-72** **Predominantly Solid Cerebellar Pilocytic Astrocytoma.**
A, Sagittal T1-weighted MRI shows large, heterogeneous, relatively low-signal mass *(M)* seen within the cerebellar vermis. Note anterior displacement of fourth ventricle *(arrow)*. The third ventricle is dilatated secondary to obstructive hydrocephalus. **B,** Axial postcontrast T1-weighted MRI shows heterogeneous enhancement of mass *(arrowheads)* and anterior displacement of fourth ventricle *(arrow)*. Note the dilatated temporal horns of lateral ventricles *(H)*, consistent with secondary obstructive hydrocephalus.



▪ **FIGURE 8-73** **Medulloblastoma.**

A, Noncontrasted axial CT shows a mostly solid mass within the posterior fossa *(arrows)*, at the expected location of the fourth ventricle. Note the increase attenuation suggestive of a high cellularity tumor. **B,** Postcontrast T1 MRI demonstrates diffuse enhancement of the solid portions of the tumor. **C** and **D,** Tumor diffusion restriction, suggesting a high cellularity and high-grade tumor, is seen as increased signal on DWI sequence (**C**) and decreased signal on ADC map (**D**).



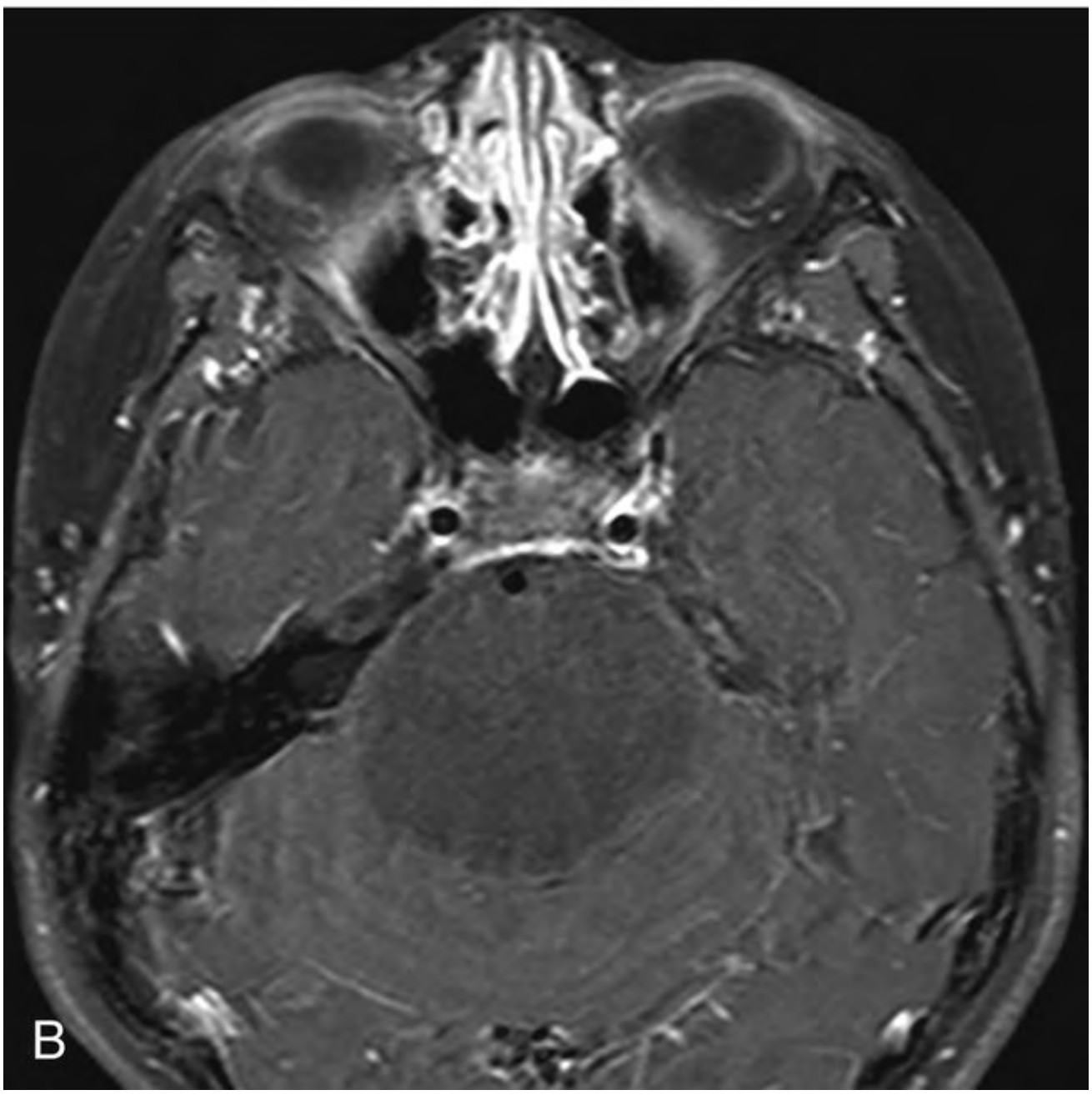
▪ FIGURE 8-74 **Metastatic Medulloblastoma.**
Follow-up MRI in a patient with previously resected posterior fossa medulloblastoma. Sagittal T1-weighted sequence postcontrast shows diffuse leptomeningeal metastasis seen as a focal enhancing nodule at the level of the obex *(arrow)*, as well as diffuse slightly nodular enhancement coating the surface of the brainstem anteriorly and spinal cord posteriorly *(arrowheads)*. Note high signal in vertebral bodies from prior radiation.

Supratentorial Tumors

In children, supratentorial tumors are much less common than those of the posterior fossa. Most cerebral tumors affecting children are glial in origin (astrocytoma, oliogodendroglioma, glioblastoma). Astrocytomas are the most common, varying from low to high grade and from well circumscribed to infiltrative. Imaging appearance does not always correlate with histologic grade. Low-grade, peripherally located tumors that involve the cerebral cortex and may act as an epileptogenic focus include ganglioglioma, dysembryoplastic neuroepythelial tumor (DNET) (Fig. 8-78, *A* and *B*), pleomorphic xanthoastrocytoma (PXA), and less commonly oligodendroglioma. Desmoplastic infantile ganglioglioma (DIG) are large, solid-cystic tumors usually in children less than 1 year of age. Less

common supratentorial tumors include embryonal tumors (PNETs) and ependymoma.

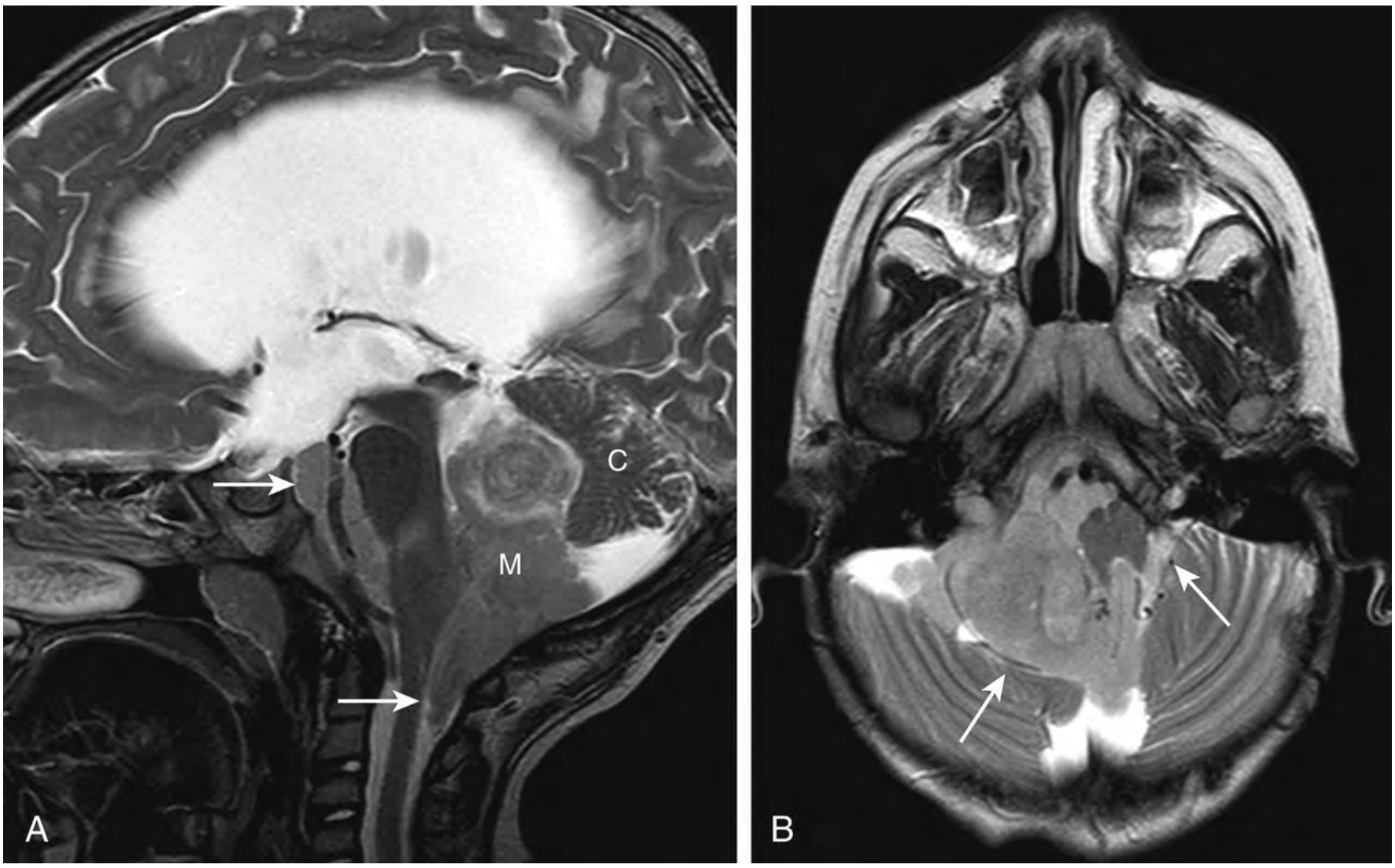

A


B

▪ **FIGURE 8-75** **Brainstem Glioma.**
A, Axial FLAIR sequence shows a large mass occupying and expanding the brainstem *(arrows)*. Note the lesion engulfing the basilar artery *(arrowhead)*. **B,** Axial postcontrast T1-weighted MR image shows no enhancement.

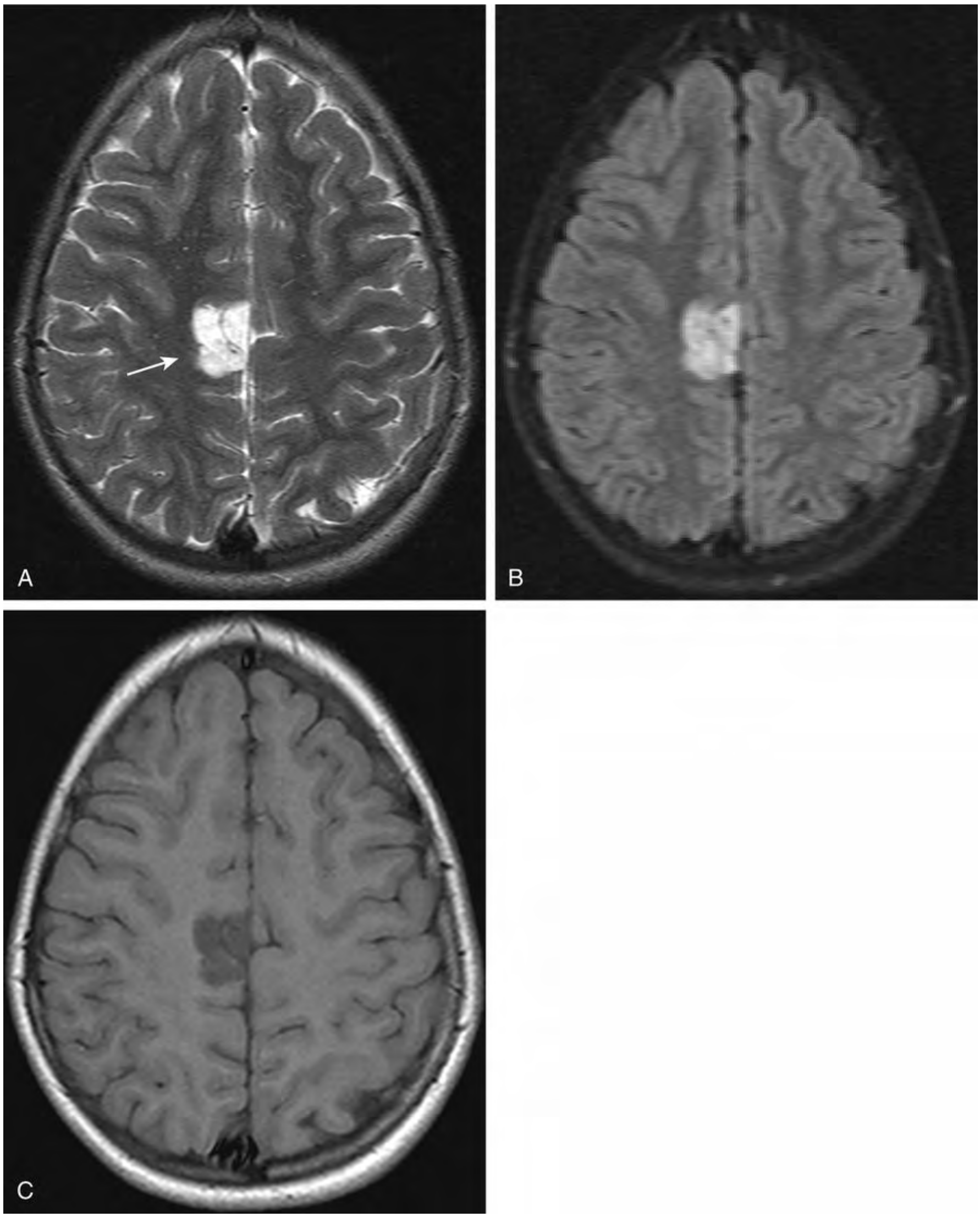


▪ **FIGURE 8-76** **Ependymoma in a 2-Year-Old Child with Headaches.**
A, Axial, noncontrast CT shows heterogeneous but well-defined mass *(arrows)* with calcifications filling the fourth ventricle. **B,** Sagittal contrast-enhanced T1-weighted MR image shows mass with heterogeneous enhancement. The border between the brainstem and mass *(arrow)* is poorly defined, whereas the outline of the roof of the fourth ventricle *(arrowhead)* is well defined.



▪ **FIGURE 8-77** **Ependymoma.**

A, Sagittal T2-weighted sequence shows a large midline posterior fossa mass *(M)* occupying the inferior fourth ventricle and displacing the cerebellum posteriorly *(C)*. Note the tumor "plasticity" characterized by inferior extension through the foramen magnum and anterior extension via foramen of Luschka *(arrows).* **B,** Axial T2-weighted sequence of the same patient demonstrating the bilateral tumor extension thought the foramen of Luschka *(arrows)*, right greater than left.



▪ **FIGURE 8-78** **Dysembryoplastic Neuroepithelial Tumor (DNET).**
A, Axial T2-weighted sequence shows a cortically based mass *(arrow)* within the right posterior frontal parasagittal region, demonstrating increased T2 signal. Note the "bubbly" appearance of the lesion. **B,** The mass demonstrates increased signal on FLAIR. **C,** There is decreased signal on T1-weighted images. Diagnosis of DNET was confirmed after surgical resection.

Intraventricular Tumors

Choroid plexus tumors are the most common intraventricular tumors in pediatrics and occur most commonly in the lateral ventricles. They are benign and slow growing in most cases (choroid plexus papilloma). However, there are malignant choroid plexus tumors (choroid plexus carcinoma) that have

similar imaging appearance to its benign counterpart, unless metastatic disease is present. These lesions are markedly vascular and demonstrate marked enhancement at imaging (Fig. 8-79). SEGAs are slow-growing tumors arising near the foramen of Monro in patients with TS and can cause hydrocephalus (see Fig. 8-59). Intraventricular meningiomas are rare in pediatrics; however, they may mimic choroid plexus papilloma. Central neurocytomas and subependymomas are uncommon in children.

Sellar and Suprasellar Tumors

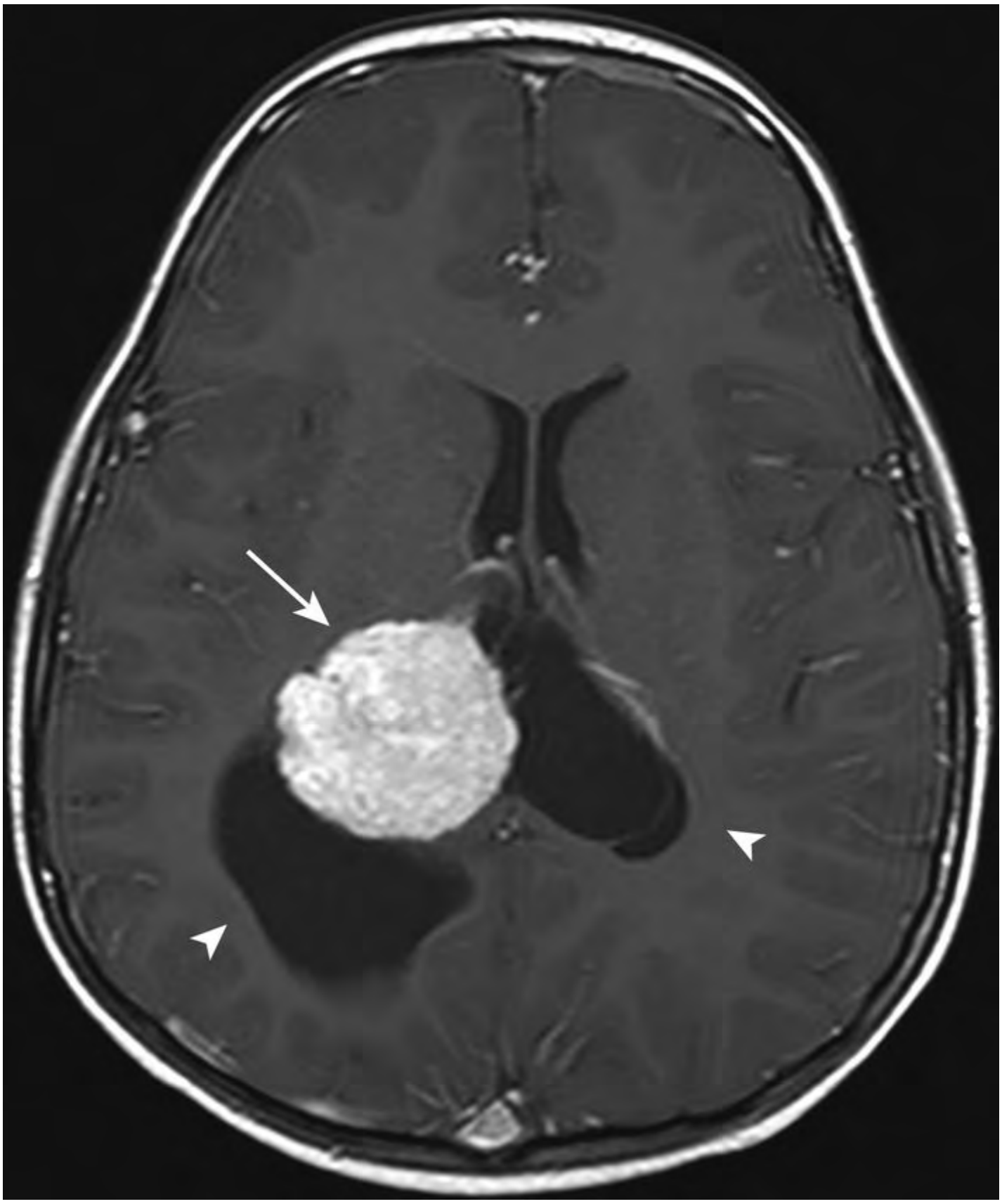
Although there is a long list of sellar and suprasellar tumors, the most common in children include optic and hypothalamic astrocytoma, craniopharyngioma, and germ cell tumor.

Optic and Hypothalamic Astrocytoma

Optic and hypothalamic astrocytoma is one of the most common suprasellar tumors in childhood. They are typically low-grade pilocytic tumors, with pilomyxoid variant being less common. It can involve any or all portions of the visual pathway and hypothalamus. There is an increased incidence of optic pathway tumors in patients with NF-1. Optic nerve involvement is demonstrated as bulbous enlargement of the optic nerves with increase enhancement on MRI (see Fig. 8-55, *A-C*). It is often difficult to differentiate optic gliomas of the chiasm from hypothalamic gliomas on MRI. Tumors arising in either location commonly extend into the other location. Both optic nerve and hypothalamic astrocytomas tend to be hyperintense on T2-weighted images and demonstrate heterogeneous enhancement of solid portions, sometimes difficult to differentiate from craniopharyngioma.

Germ Cell Tumor

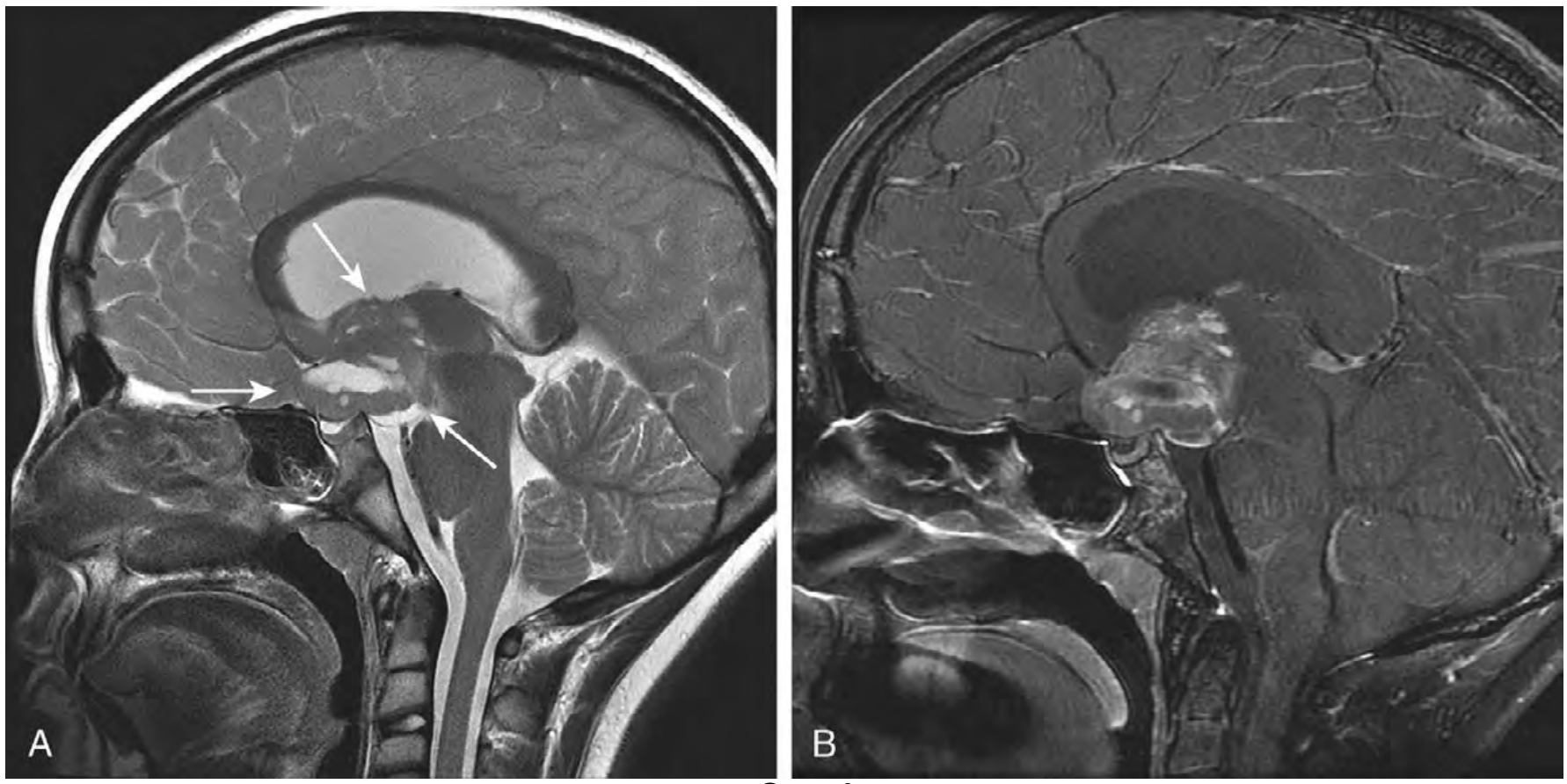
Germ cell tumors of the CNS most commonly occur in the region of the pineal gland and suprasellar region (Fig. 8-80, *A* and *B*). The most common histologic type is germinoma. Nongerminomatous types include teratoma, embryonal carcinoma, yolk sac tumor, and choriocarcinoma. Teratomas may demonstrate fatty tissue or calcifications. Germinomas are seen on MRI as an enhancing mass that may demonstrate diffusion restriction and CSF seeding. Sellar and suprasellar germinomas may present initially as absent posterior pituitary T1 bright spots with or without thickening of pituitary stalk. Diabetes insipidus is a common clinical presentation in this scenario, and differential diagnoses include Langerhans cell histiocytosis (LCH; Fig. 8-81). Other rare lesions presenting with homogeneous thickening or enhancing mass at the pituitary stalk include lymphocytic hypophysitis, lymphoma or leukemia, neurosarcoidosis, and pituicytoma.



▪ **FIGURE 8-79** **Choroid Plexus Papilloma.**
Axial postcontrast T1-weighted image shows homogeneously enhancing mass *(arrow)* within the posterior horn of the right lateral ventricle. There is associated enlargement of the bilateral posterior lateral ventricles *(arrowheads)*.

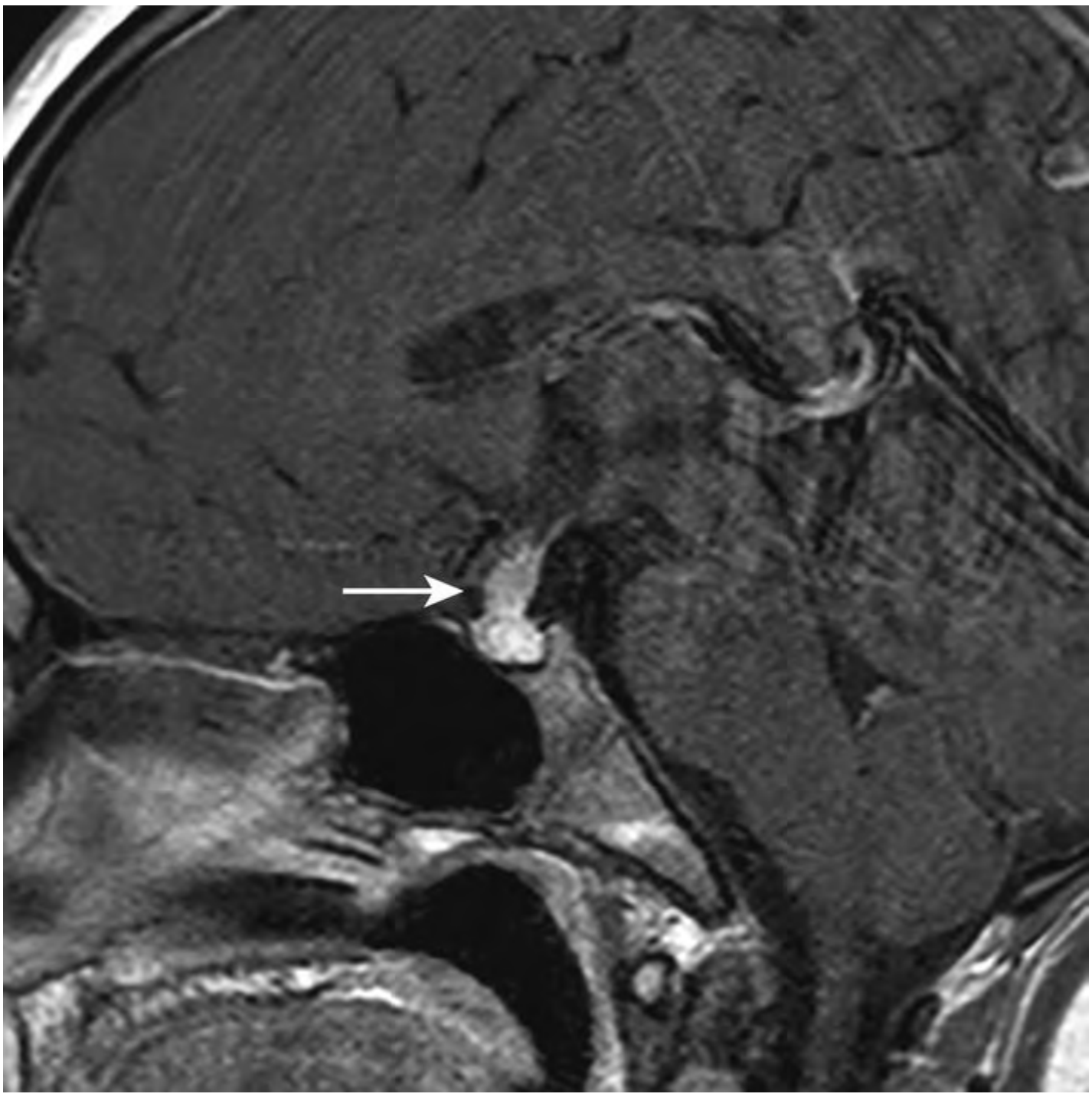
Craniopharyngioma

Craniopharyngiomas arise from the persistence and proliferation of squamous epithelial cells within the tract of an embryologic structure, the craniopharyngeal duct. They account for 7% of all intracranial tumors in children. They are benign and slow-growing lesions. Typically they are intrasellar and suprasellar in location. Calcifications are present in up to 80% of pediatric cases. Typically CT shows a large, partially calcified suprasellar mass with both cystic and solid enhancing portions. On MRI the cystic components tend to be high signal on all sequences because they contain proteinaceous and cholesterol-laden fluid (Fig. 8-82, *A-C*). The signal characteristics of the solid portions are variable on MRI.



▪ **FIGURE 8-80** **Germinoma.**

A, Sagittal T2-weighted image shows a large, solid-cystic mass within the supra-sellar region *(arrows)*. **B,** Heterogeneous enhancement seen on postcontrast images.



▪ **FIGURE 8-81** **Langerhans Cell Histiocytosis.**
Sagittal postcontrast T1-weighted sequence shows an enlarged pituitary stalk *(arrow)*. This patient was confirmed to have LCH. Aside from classic skull lesions and pituitary stalk abnormalities, intracranial findings of LCH also include choroid plexus masses and cerebellar white matter demyelination (not shown).

Hypothalamic Hamartoma

Hypothalamic hamartomas are actually considered a congenital gray matter heterotopia in the region of the tuber cinereum and mammillary bodies. It is described in this section because it presents as a suprasellar mass that should be differentiated from other neoplastic processes. This lesion may be sessile or pedunculated and presents clinically with seizures or precocious puberty. Gelastic seizures are classically associated with this lesion; however, this is not necessary the most common presentation. On imaging, this lesion is mostly isointense to gray matter and does not enhance (Fig. 8-83). If enhancement is seen, consider other pathologies.

Pineal Tumors

The majority of pineal region neoplasms arise from germ cells (60%) or from pineal parenchyma (15%). Pineal tumors arising from the pineal parenchyma range from benign pineocytomas to highly malignant pineoblastomas (histologically similar to PNETs). Clinical presentation is most often related to mass effect and hydrocephalus with symptoms of headache, nausea, vomiting, or Parinaud syndrome. Pineal germ cell tumors are classified as germinomas or nongerminomatous, and symptoms may also include precocious puberty. Germinomas and pineoblastomas are highly cellular tumors and often have similar imaging findings: isointense to hypointense T2 signal compared with gray matter, diffusion restriction on DWI, and CSF spread.



▪ **FIGURE 8-82** **Craniopharyngioma.**
A, Sagittal reconstruction from noncontrasted CT demonstrates a large suprasellar mass extending into the superior aspect of the sella. The mass is composed of a large cyst with proteinaceous components *(arrows)* and a smaller solid component inferiorly with internal calcifications *(arrowhead)*. **B,** Sagittal T2-weighted sequence MR image again shows the large cystic component *(C)* and smaller solid component *(arrow)*. **C,** Note the increased signal on noncontrasted T1-weighted sequence due to proteinaceous contents *(arrows)*.

▪ Trauma

Children with minor head trauma usually require no imaging. The evaluation of significant pediatric head trauma is usually performed by CT. Skull radiographs obtained to rule out skull fracture are grossly overused, result in increased cost and radiation, and offer little useful information. The presence of a skull fracture does not necessarily indicate intracranial injury, and the absence of a skull fracture certainly does not exclude it. Finally, the presence or absence of a skull fracture usually does not affect the management of a child with head trauma.

Most of the CT findings in intracranial trauma, including subdural hematoma, epidural hematoma, subarachnoid hemorrhage, and parenchymal contusion, are similar in appearance in adults and

children and are not discussed here.



▪ **FIGURE 8-83 Hypothalamic Hamartoma.**
Sagittal noncontrast T1-weighted sequence shows a midline hypothalamic mass *(arrow)* centered at the expected location of the tuber cinereum and mammillary bodies. The mass is isointense to the brain parenchyma and did not enhance after contrast administration (postcontrast not shown).

Abuse

For the most part the imaging appearance of intracranial trauma that occurs secondary to abusive head injury (child abuse) is similar to that seen with accidental trauma. Therefore imaging findings should be interpreted in the context of the clinical history. Intracranial injury is the number one cause of death in abused children. Types of injury that should increase the degree of suspicion for abuse include interhemispheric subdural hematoma (caused by shaking) (Fig. 8-84) and the combination of traumatic subdural or subarachnoid hematoma with anoxic-ischemic injury (Fig. 8-85, *A* and *B*). Subdural hemorrhages of varying ages, as shown on CT or MRI, are also highly suggestive (Fig. 8-86, *A-C*).

▪ Hydrocephalus and Ventriculoperitoneal Shunts

Hydrocephalus is a problem commonly encountered in pediatric neuroimaging. It may be secondary to overproduction (choroid plexus papilloma or choroid villous hyperplasia), disturbances of CSF flow or absorption (tumors or cysts, infection, hemorrhage or genetic causes), or the result of loss of ventricular wall compliance. A common cause of prenatally diagnosed hydrocephalus is aqueduct stenosis, which can be acquired or developmental (Fig. 8-87, *A-C*). Patients with hydrocephalus are often treated by the placement of ventricular shunts. The most commonly used shunt is the VPS, in

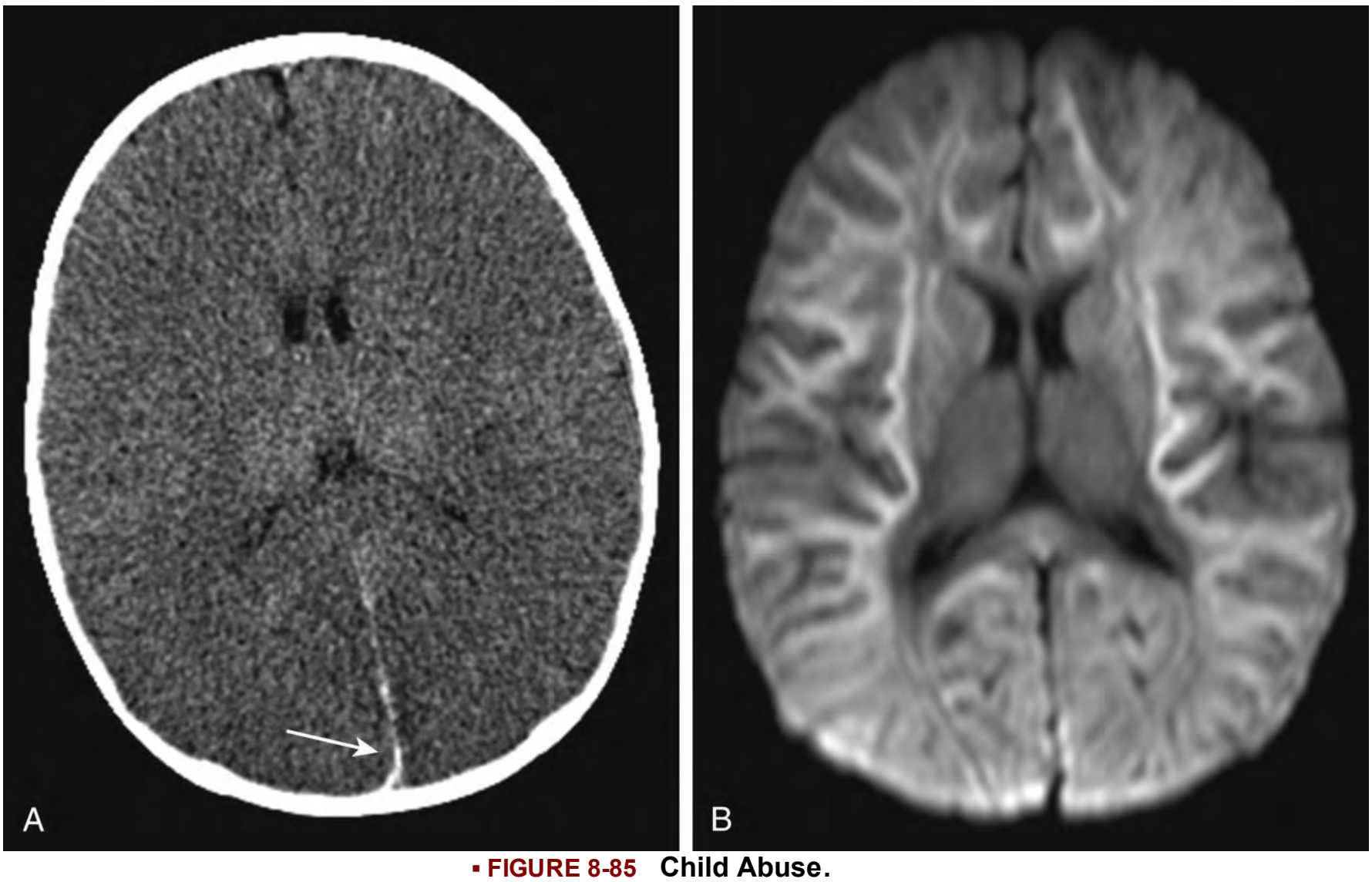
which the proximal portion of the shunt is positioned in one of the lateral ventricles, and the distal end is positioned in the peritoneal cavity. When a patient with a VPS presents with headaches, vomiting, or lethargy, increased intracranial pressure resulting from VPS malfunction should be investigated. Imaging includes radiographs of the shunt from cranium to abdomen (shunt series) to ensure that there is no evidence of shunt disconnection or kinking. The most common site for shunt dislocation is at the connection between the shunt tubing and shunt reservoir (Fig. 8-88, *A-D*), which usually overlies the cranium. Familiarity with the various types of commercially available shunts is important because some types have radiolucent portions that could be mistaken for areas of disconnection.



▪ **FIGURE 8-84** **Child Abuse.**
Axial noncontrasted CT image shows increased attenuation along the posterior falx *(arrow)*, asymmetric to the left, compatible with subdural blood. This is nonspecific, but subdural hemorrhage is frequently seen in child abuse.

A head CT is also obtained to evaluate for any interval change in the size of the cerebral ventricles (see Fig. 8-88). Fast MRI sequences can also be used in the evaluation of shunt malfunction, if available. Symptoms are most often related to insufficient shunting and interval increase in ventricular size but can occasionally be secondary to overshunting, which produces slit-like ventricles. It is important to evaluate the scout image from the CT for evidence of shunt dislocation or kinking. An abdominal pseudocyst surrounding and obstructing the intraabdominal tip of the VPS is also a possibility. This

may be suspected when interval radiographs demonstrate a static position of the distal shunt tubing. Further investigation for VPS pseudocysts is usually performed using ultrasound.



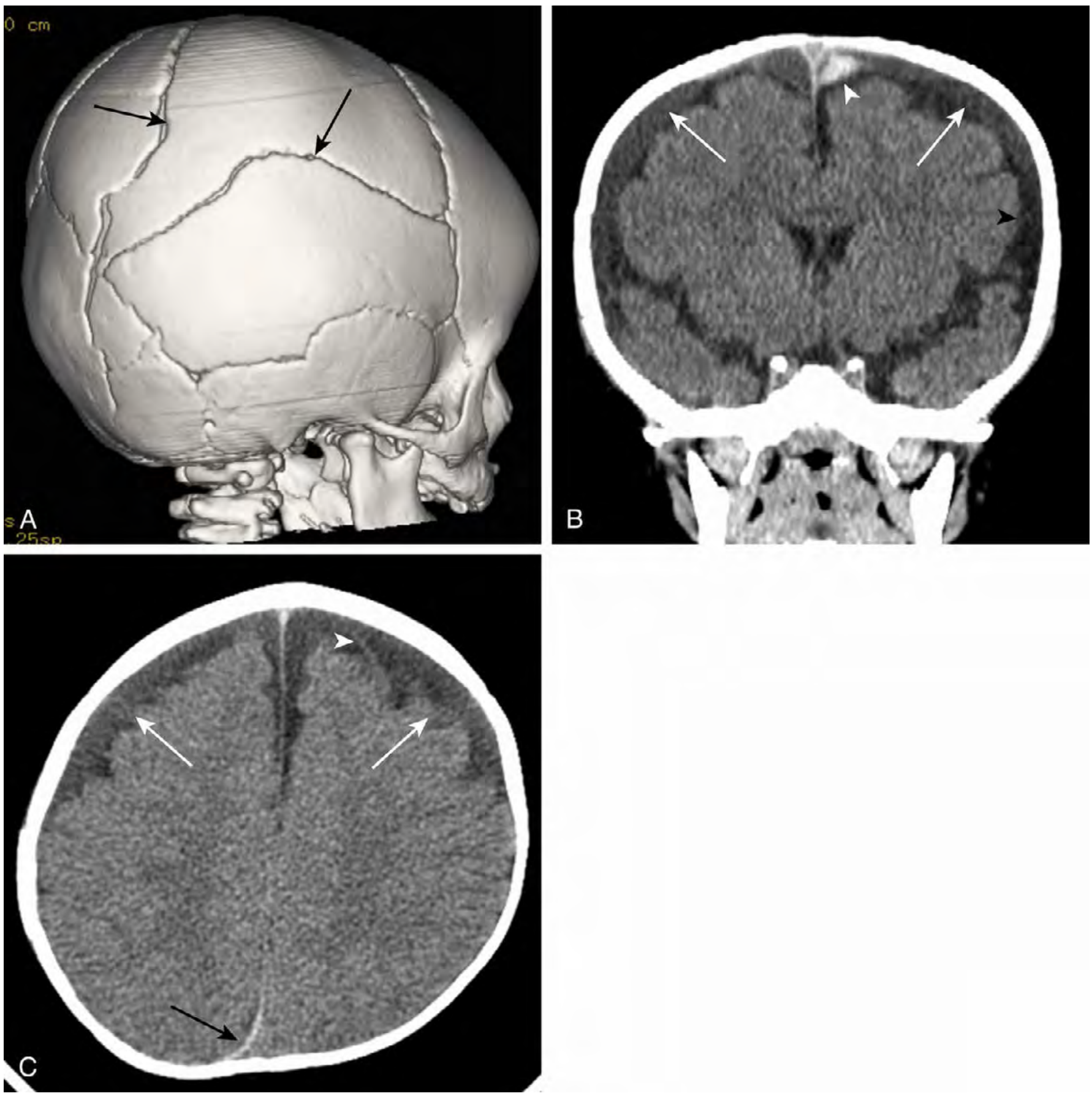
▪ **FIGURE 8-85** **Child Abuse.**

A, Nonenhanced CT shows diffuse low-attenuation throughout the majority of the brain parenchyma with loss of gray-white matter differentiation. Findings are consistent with edema and infarction, related to asphyxia. There is also high attenuation along the right aspect of the posterior falx *(arrow)*, consistent with subdural hemorrhage. **B,** Diffusion MR image shows diffuse parenchymal diffusion restriction.

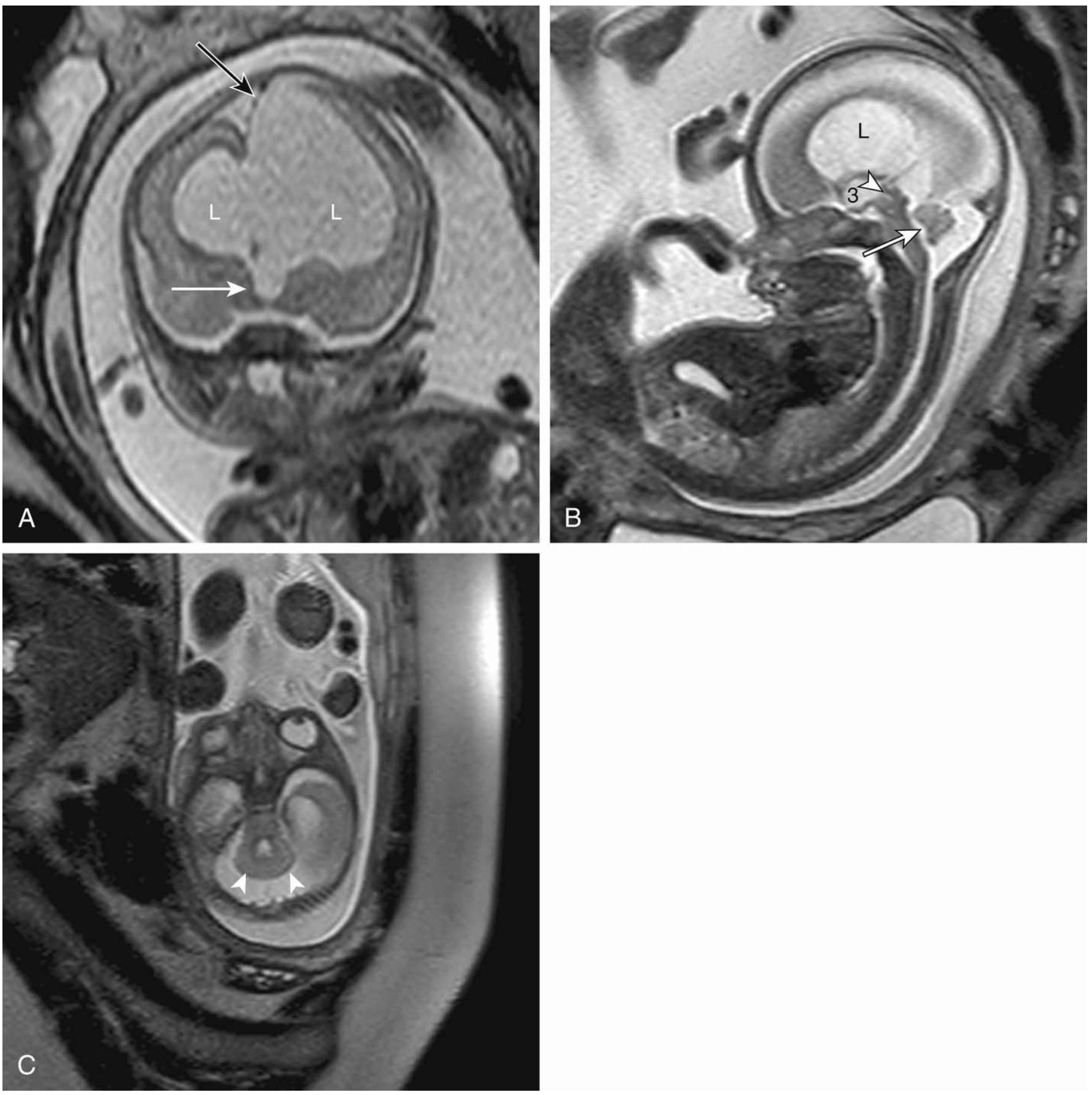
▪ Craniosynostosis

Craniosynostosis is premature closure of the sutures of the skull. It can occur as an idiopathic, primary condition, or it can be secondary to a number of genetic or metabolic disorders. Primary craniosynostosis is typically present at birth and occurs more commonly in boys than in girls. The sagittal suture is most commonly involved. Because the skull stops growing in the direction of the closed suture and continues to grow in the directions of the open sutures, craniosynostosis of a particular suture leads to a predictable abnormal head shape on physical exam and on imaging. With sagittal suture synostosis the head becomes long and narrow (dolichocephaly or scaphocephaly) (Fig. 8-89, *A* and *B*). With bilateral coronal or lambdoid suture synostosis, the head becomes short from anterior to posterior and is wide from left to right (brachycephaly). The orbits in coronal synostosis assume an oval, oblique lateral margin that is referred to as a harlequin-eye appearance (Fig. 8-90). With metopic suture craniosynostosis the forehead assumes a pointed or triangular appearance (trigonocephaly; Fig. 8-91, *A* and *B*), and the eyes are usually hypoteloric. Plagiocephaly refers to an asymmetric skull shape that can be seen with unilateral coronal and unilateral lambdoid suture synostosis (Fig. 8-92, *A*) or, more commonly, the result of positional molding with no synostosis (Fig. 8-92, *B*). Positional molding occurs due to preferential sleep positions in young infants. Synostosis of all of the sutures results in clover-leaf skull (kleeblattschädel). There is severe deformity of the skull, with bulging in the squamosal areas and in the bregma. It is associated with thanatophoric dwarfism.

The screening examination for craniosynostosis may be done by radiography, although many institutions are performing helical CT with three-dimensional surface-rendered reconstruction of the skull. In addition to the characteristic skull shapes, imaging may demonstrate complete or partial closure of the suture, bony ridging, and perisutural sclerosis.

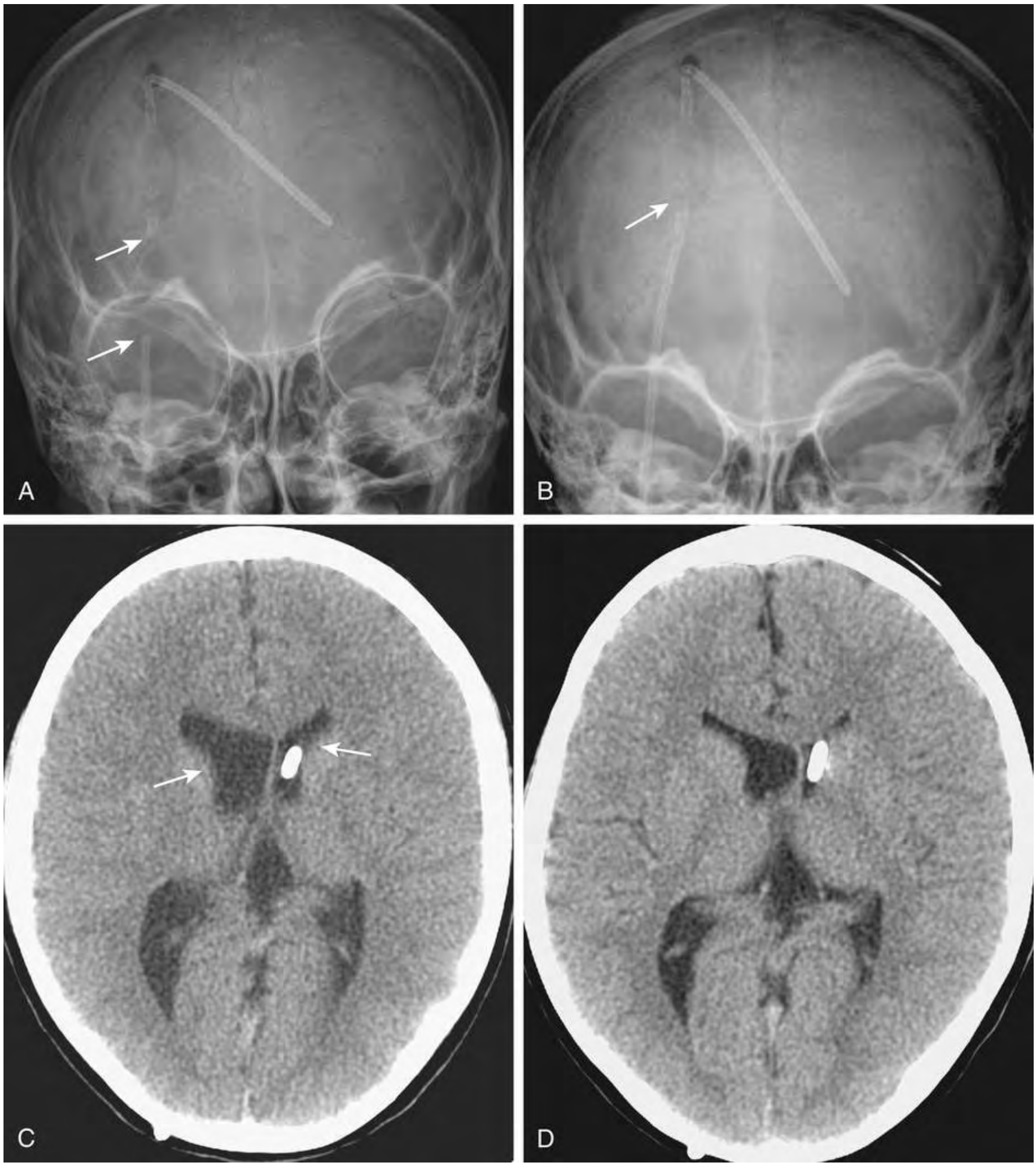


▪ **FIGURE 8-86 Child Abuse, Subdural Hematomas of Varying Ages.**
A, Volume rendered, three-dimensional reformat from noncontrasted CT shows a complex parietal skull fracture *(arrows).* **B,** Coronal reformat demonstrates bilateral subacute subdural hemorrhage along the convexities *(arrows)*. There is also a more acute hemorrhage along the left parasagittal subdural space *(white arrowhead)*. Note the medially displaced cortical vein *(black arrowhead)*, a finding that may help in the detection of a low-attenuation or chronic subdural collection. **C,** Axial CT image of the same patient again shows bilateral subacute subdural hemorrhages *(white arrows),* as well as a small amount of acute blood along the posterior falx *(black arrow)*. Note a bridging vein traversing the subdural collection on the right frontal region *(arrowhead)*. Bridging veins drain into the superior sagittal sinus and transverse the subdural space; therefore they can be seen within a subdural collection, usually along the superior and anterior midline regions. This should not be confused with the smaller and more numerous cortical vessels present in the subarachnoid spaces that do not transverse the subdural space and are usually displaced medially by a subdural collection (see **B**).

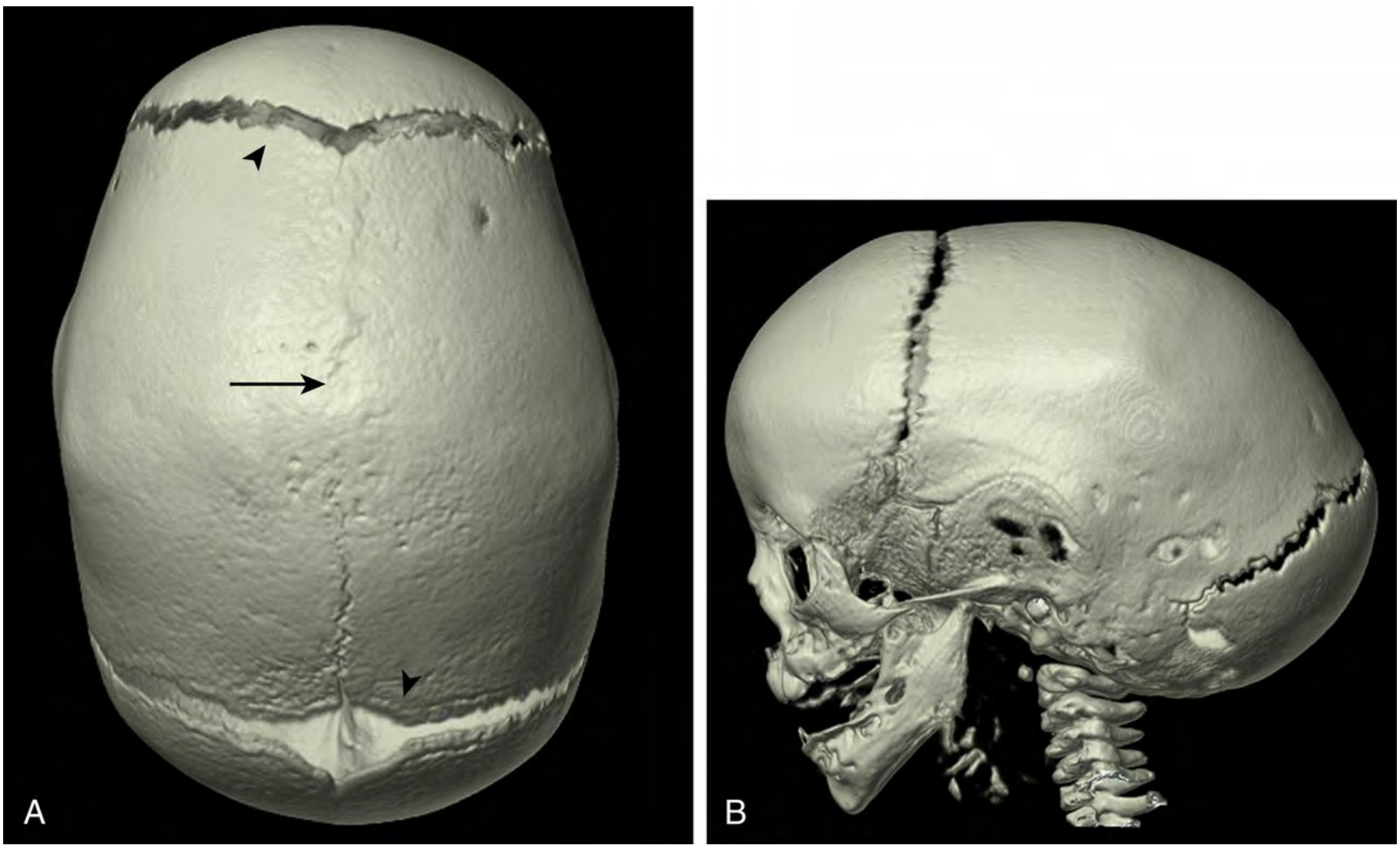


▪ **FIGURE 8-87** **Aqueductal Stenosis.**

A, Coronal SSFSE sequence from fetal MRI demonstrates marked enlargement of the lateral *(L)* and third *(white arrow)* ventricles. Note also the focal absence of left high parasagittal cerebral parenchyma covering the enlarged lateral ventricle *(black arrow)*. This is compatible with a ventricular diverticulum often seen in cases of marked prenatal hydrocephalus, most commonly due to aqueductal stenosis. **B,** Sagittal view of a different fetus shows also an enlarged lateral *(L)* and third *(3)* ventricles with normal size of the fourth ventricle *(arrow)*. Note also the "funnel" shape of the aqueduct *(arrowhead)* due to inferior aqueductal obstruction or stenosis. **C,** Axial image from same fetal MRI as shown in **B** also shows posterior fossa findings of rhombencephalosynapsis (RES). Note the small transverse cerebellar diameter, absence of cerebellar vermis, and cerebellar hemisphere fusion *(arrowheads)*. Although the etiology of aqueductal stenosis is multifactorial and may be secondary to infection and/or hemorrhage, careful evaluation of other fetal anatomical structures, especially the posterior fossa, is important to exclude associated malformations and genetic syndromes. RES is not uncommonly associated with aqueduct stenosis. Cobblestone malformations and X-linked hydrocephalus (in a male fetus) are also potential associated abnormalities.

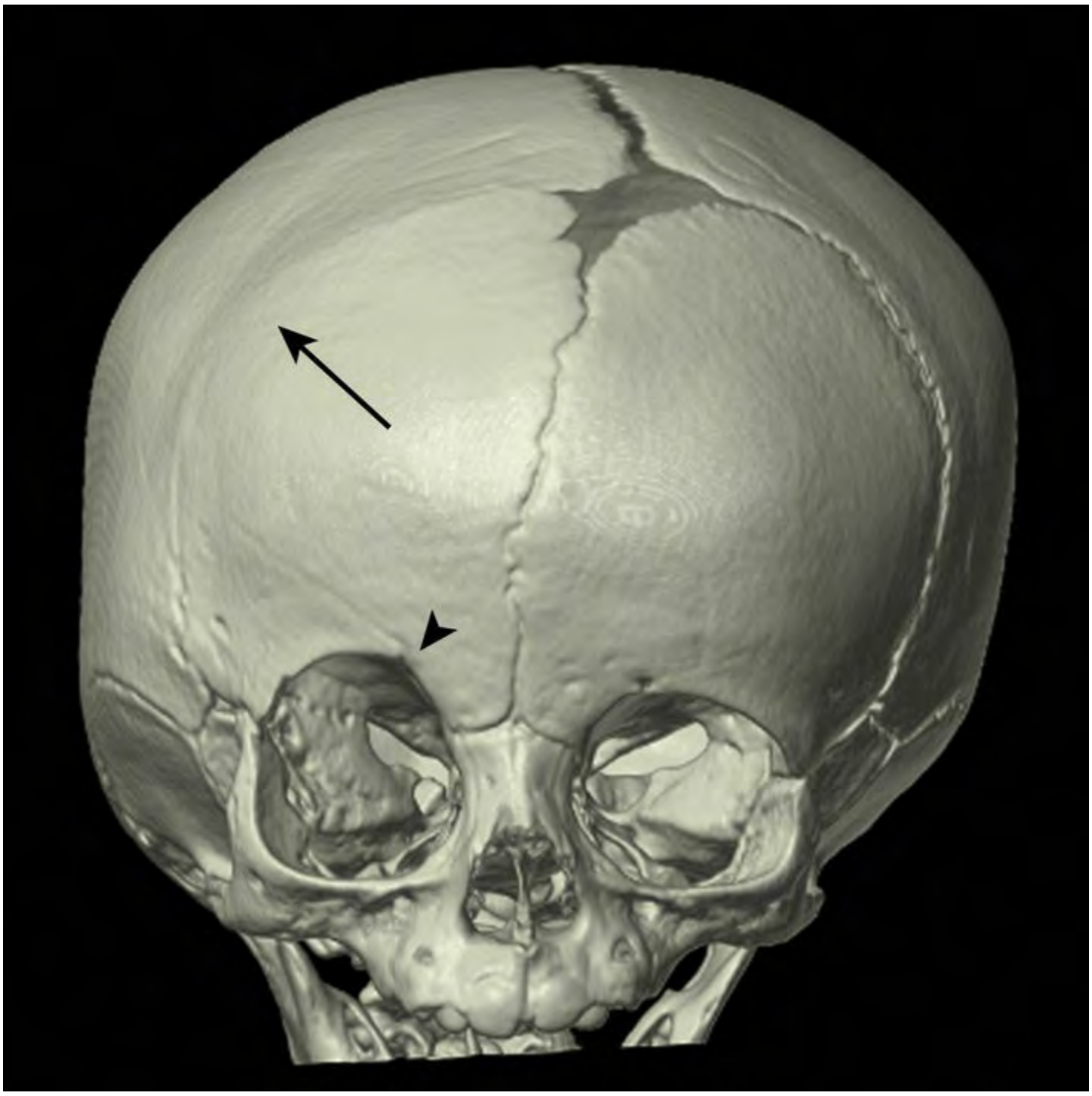


▪ **FIGURE 8-88** **Ventriculoperitoneal Shunt Malfunction in a Vomiting Child.**
A, Frontal view of skull from shunt series shows a gap *(arrows)* between the shunt reservoir and the more distal tubing. **B,** Previous comparison radiograph shows reservoir and tubing to have been contiguous previously *(arrow)*. **C,** CT at time of presentation shows interval increase in size of lateral ventricles, particularly in frontal horns *(arrows)*, consistent with increased hydrocephalus. Note the VPS tip in the left frontal horn. **D,** Previous baseline CT shows the smaller size of the ventricles.



▪ **FIGURE 8-89** **Sagittal Suture Synostosis.**

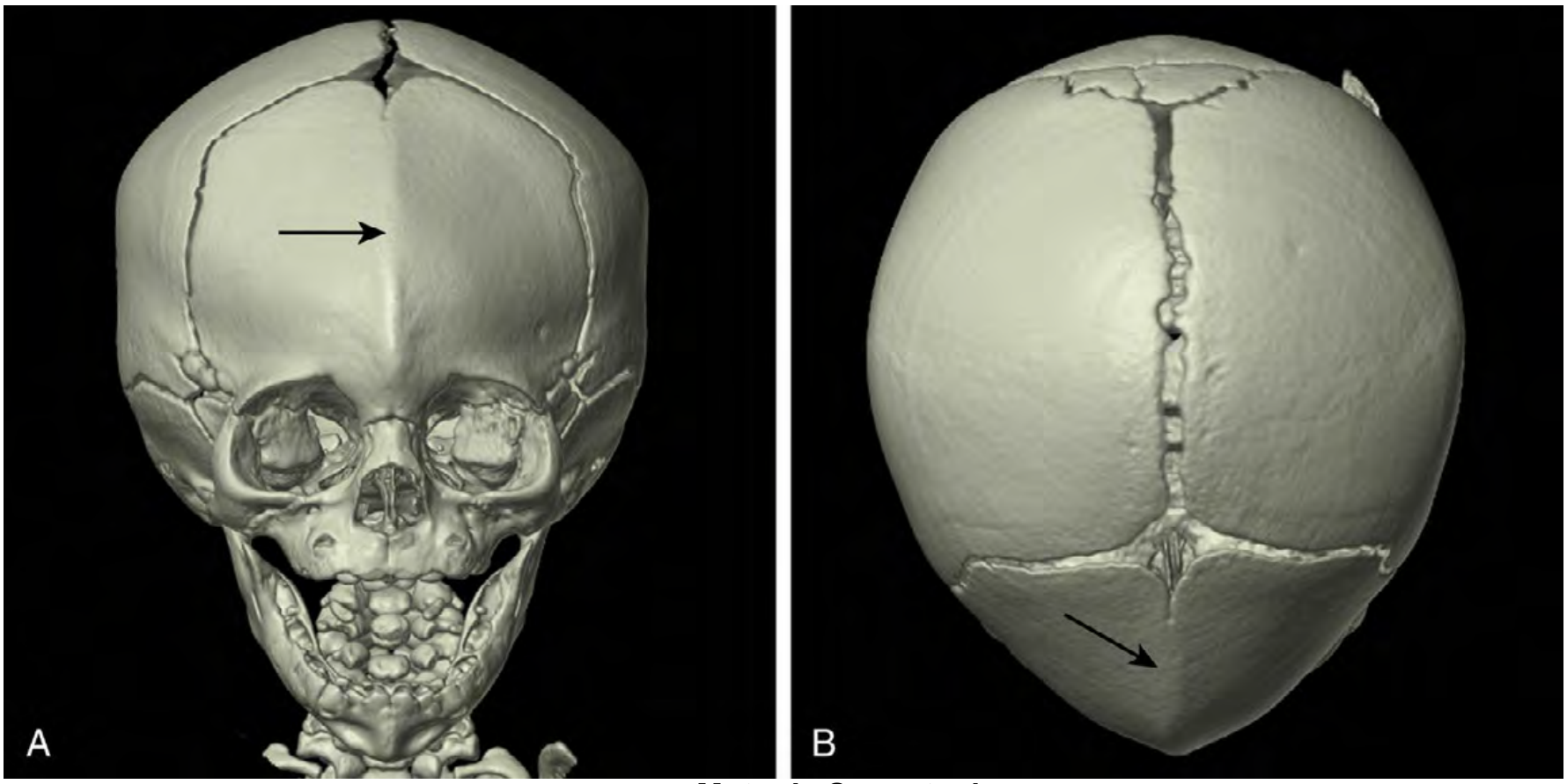
A, Volume rendered, three-dimensional CT image of the skull shows early fusion of sagittal suture *(arrow)*, as well as diastatic coronal and lambdoid sutures *(arrowheads)*. **B,** Note the increased anteroposterior dimension of the skull (scaphocephaly or dolicocephaly).



▪ **FIGURE 8-90** **Unilateral Coronal Synostosis.**
Volume- rendered, three-dimensional CT image shows early fusion of the right coronal suture *(arrow)*. Note also “harlequin eye” *(arrowhead)*.

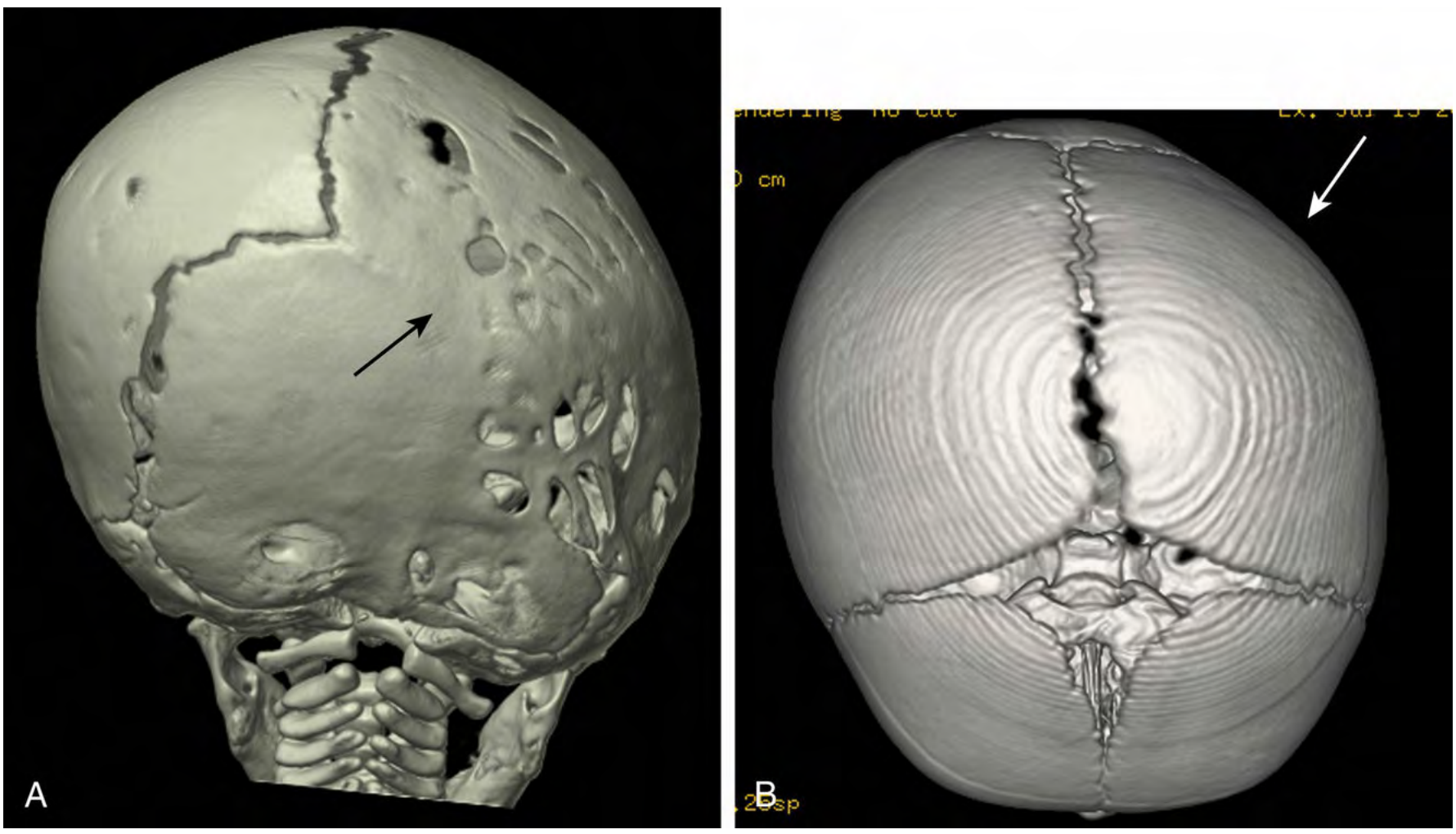
▪ Lacunar Skull

Lacunar skull, or lückenschädel, is a defect in the mesenchymal formation of the skull that is associated with myelomeningocele. The radiographic findings include multiple oval lucencies that occur secondary to the thinning of the inner table of the skull (Fig. 8-93) and are more prominent in the occipital and parietal regions. It is present in patients with myelomeningocele under 3 months of age. The imaging findings typically resolve by 6 months of age. It is always associated with myelomeningocele. Lacunar skull should not be confused with the skull changes related to increased intracranial pressure (Fig. 8-94). With increased intracranial pressure, there is marked accentuation of the normal convolutional markings. The appearance has been likened to hammer-beaten silver. Personally, the authors think that they appear rather similar, with lacunar skull appearing more severe. Other radiographic findings of increased intracranial pressure include sutural diastasis, sellar enlargement, and demineralization.



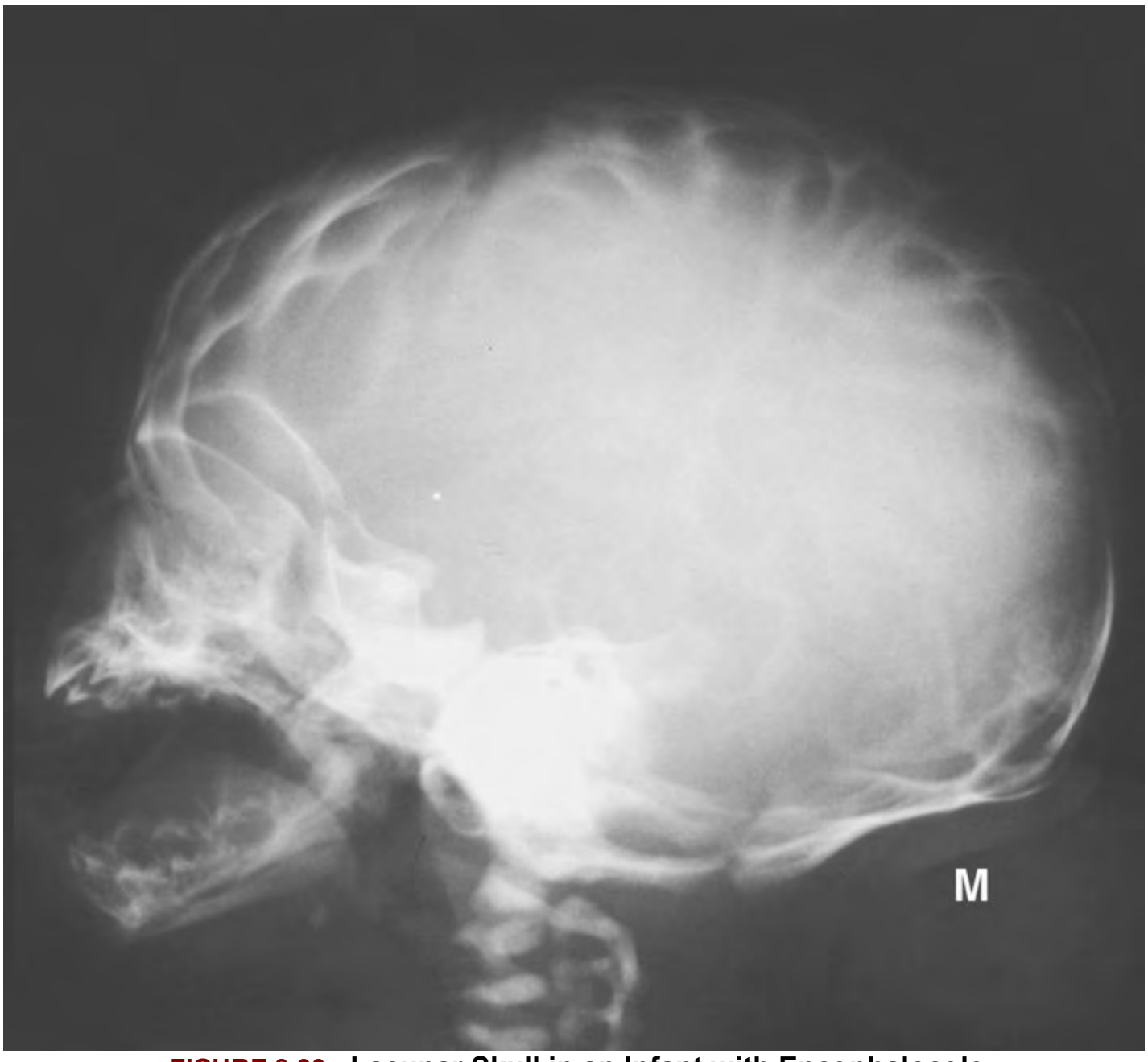
▪ FIGURE 8-91 **Metopic Synostosis.**

A, Volume rendered, three-dimensional CT shows fusion of the metopic suture with associated bony ridging *(arrow)*. **B,** Superior view again shows fusion of the metopic suture *(arrow)*, as well as triangular shape of the forehead (trigonocephaly).



▪ FIGURE 8-92 **Plagiocephaly.**

A, Volume rendered, three-dimensional CT image shows unilateral lambdoid suture synostosis *(arrow)* causing asymmetric posterior skull flattening of the involved side. **B,** Different patient showing positional plagiocephaly seen as an asymmetric flattening of the left occipital region *(arrow)* with no craniosynositosis (note patent skull sutures).

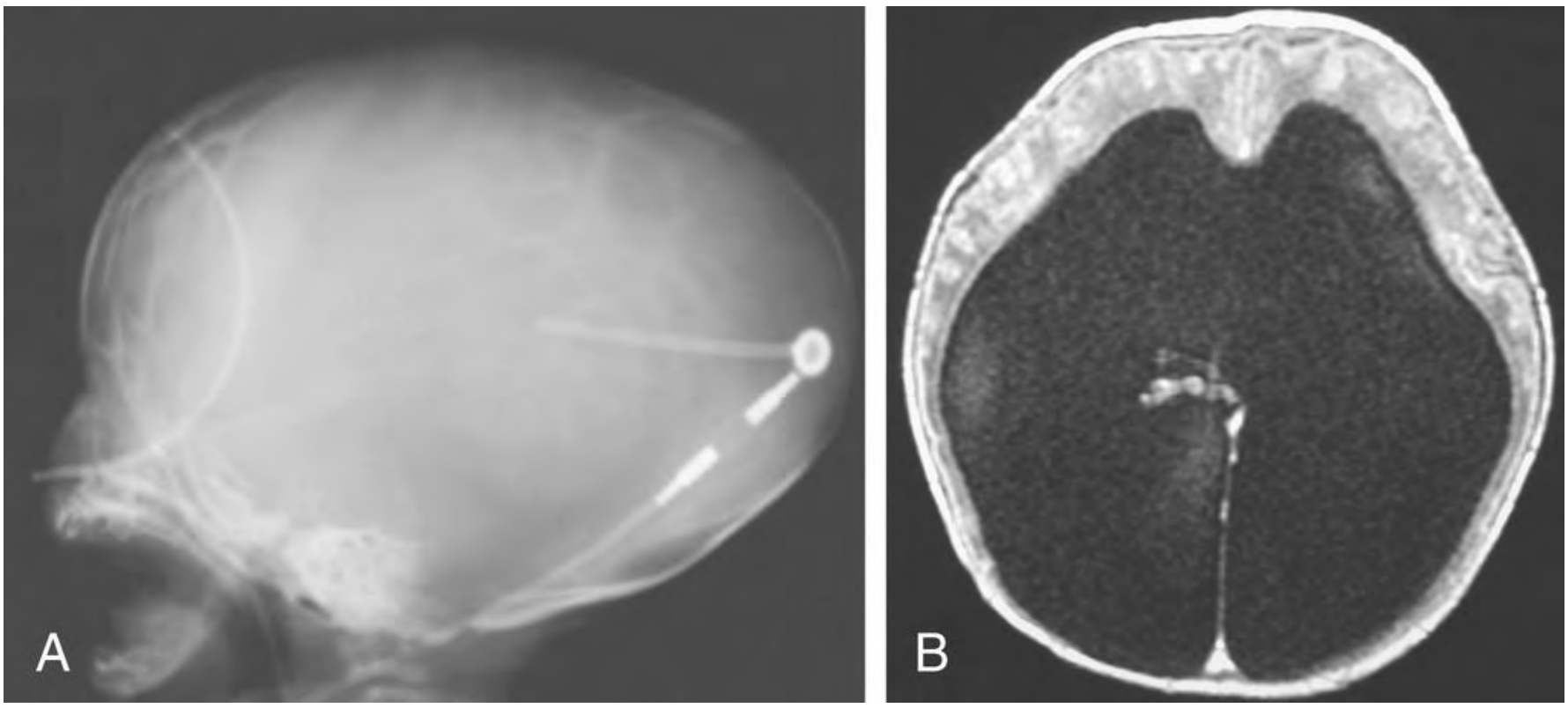


▪ **FIGURE 8-93** **Lacunar Skull in an Infant with Encephalocele.**
Radiograph shows multiple oval lucencies. The encephalocele can be seen as a subtle posterior soft tissue mass *(M)*.

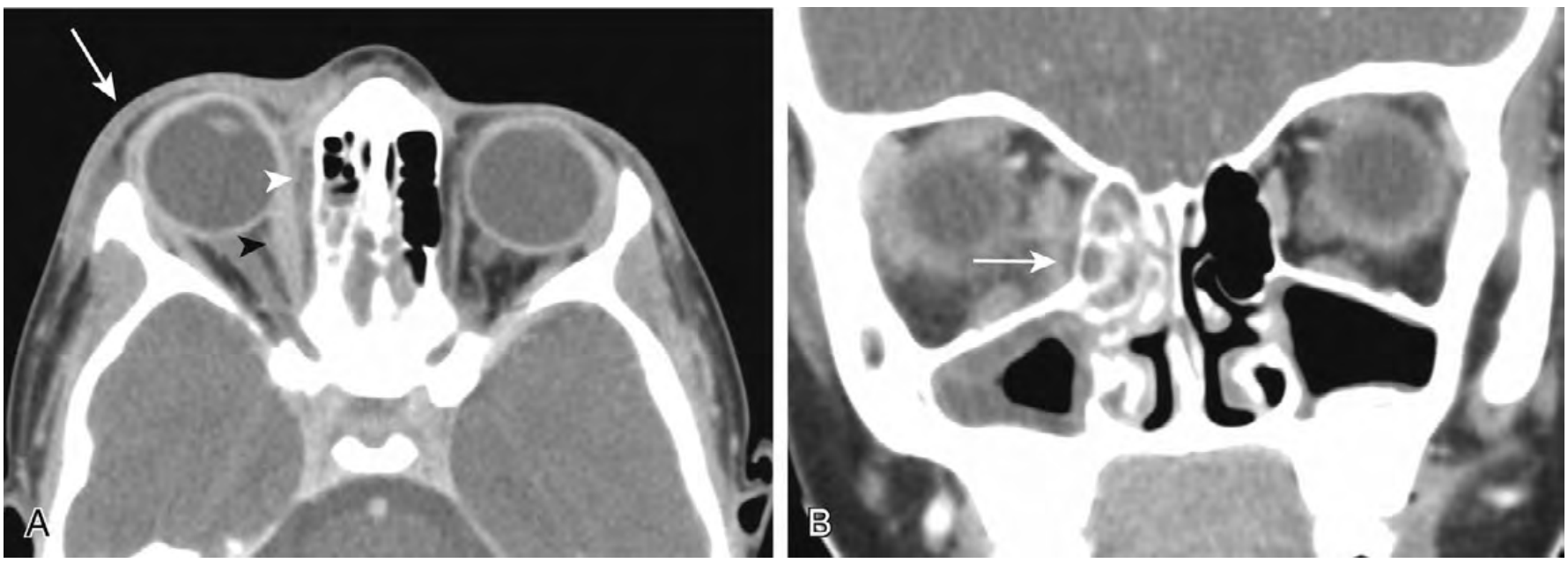
▪ Head and Neck Inflammatory and Infectious Processes

Orbital Cellulites

Orbital cellulitis is the most common abnormality of the pediatric orbit. It is most commonly due to a bacterial infection that arises from extension of sinus disease. Orbital cellulitis is categorized anatomically as being preseptal or postseptal on the basis of the relationship between the inflamed tissue and the orbital septum. Preseptal tissue is limited to the eyelid. When inflammation extends posterior to the septum, it is considered to be postseptal and typically involves the extraconal tissues, sometimes with the formation of a subperiosteal abscess (Fig. 8-95, *A* and *B*). Almost all cases of postseptal cellulitis are associated with ethmoid sinus disease (see Fig. 8-95) and may present clinically with ophthalmoplegia and visual loss. The presence of a drainable abscess is suggested on CT when rim enhancement is present surrounding an area of fluid attenuation with or without gas. Drainable abscesses are typically treated surgically. Cellulitis without abscess is treated with antibiotics alone. Less frequent complications of postseptal cellulitis include thrombosis of the ophthalmic vein and cavernous sinus (Fig. 8-96, *A* and *B*). When sinus disease involves the frontal sinus, complications may include frontal osteomyelitis with frontal soft tissue abscess formation (“Pott puffy tumor”) and intracranial empyema.



▪ **FIGURE 8-94** **Skull Changes in Increased Intracranial Pressure.**
A, Radiograph shows accentuation of convolutional markings. Note the VPS. **B,** Axial T1-weighted MRI shows massive dilatation of the lateral ventricles.



▪ **FIGURE 8-95** **Preseptal and Postseptal Cellulitis.**
A, Axial, contrast-enhanced CT of the orbits shows asymmetric thickening of the right preseptal soft tissues *(arrow)*. There is also involvement of the medial extraconal postseptal soft tissues *(white arrowhead)*. The medial rectus muscle is enlarged *(black arrowhead)* due to reactive myositis. Note partial ethmoid sinus opacification. **B,** Coronal contrast-enhanced CT of a different patient also showing right medial postseptal cellulitis with a small subperiosteal collection representing an early abscess *(arrow)*. Note again ethmoid sinusitis as the cause of orbital cellulitis.



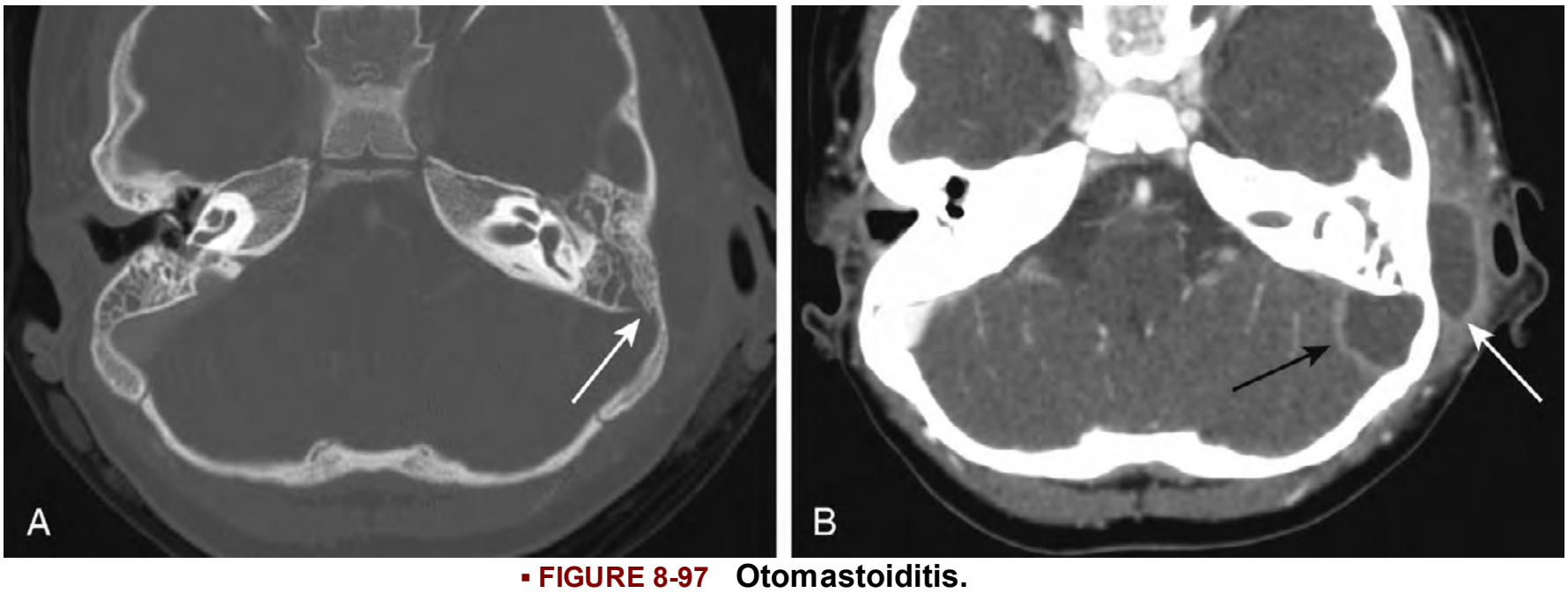
▪ **FIGURE 8-96** **Ophthalmic Vein and Cavernous Sinus Thrombosis.**
Axial contrast-enhanced CT in a patient with postseptal orbital cellulitis shows an enlarged and nonenhancing right superior ophthalmic vein compatible with thrombosis *(white arrow)*. Note normal enhancement of the contralateral vein *(white arrowhead)*. There is also lack of normal enhancement within the bilateral cavernous sinus (*black arrows*) due to thrombosis. Note also the small size of the cavernous portion of the right internal carotid artery due to spasm *(black arrowhead)*.

Acute Otomastoiditis

Acute otomastoiditis is a complication of otitis media. Clinical presentation may include fever, otalgia, otorrea, mastoid tenderness, and auricular proptosis. Imaging findings include middle ear and mastoid opacification with associated edema of the superficial retroauricular soft tissues (Fig. 8-97, *A-C*). Complications include retroauricular subperiosteal abscess, erosion of mastoid septations (coalescent otomastoiditis) or bony walls, intracranial empyema or abscess, and dural sinus thrombosis. Isolated opacification of middle ear and mastoid air cells without soft tissue edema or other complications is a common finding in pediatrics and should not be interpreted as acute otomastoiditis. More aggressive pathologies presenting with soft tissue attenuation and mastoid bony erosions include disorders such as LCH (Fig. 8-98, *A* and *B*), rhabdomyosarcoma, and cholesteatoma and are part of the differential diagnosis of acute coalescente otomastoiditis.

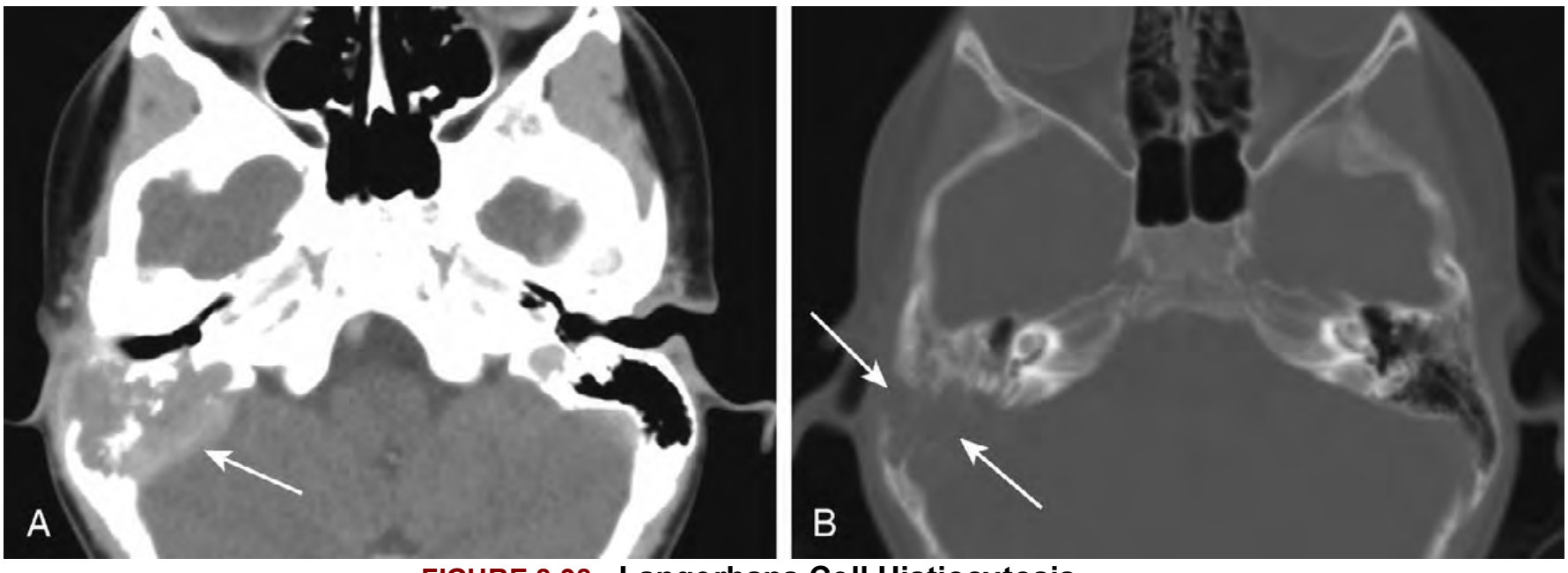
Suppurative Adenites

Neck suppurative adenitis is a complication of upper respiratory tract bacterial infection, resulting in lymph node enlargement and suppurative changes that can evolve to abscess formation (Fig. 8-99). Abscess as a result of suppurative adenitis occurs commonly in the lateral retropharyngeal spaces (see Chapter 2 for further details). Ultrasound is often the initial imaging study to determine whether a drainable fluid collection is present in superficial neck lymphadenopathy. CT can also be used and is the imaging test of choice for suspected retropharyngeal adenitis or abscess.



▪ **FIGURE 8-97** **Otomastoiditis.**

A, Axial CT image in bone window shows complete fluid opacification of the left mastoid air cells and middle ear cavity. There is a focal area of bony disruption along the posterior mastoid wall *(arrow)*. **B,** Soft tissue window demonstrates large retroauricular *(white arrow)* and intracranial *(black arrow)* ring-enhancing fluid collections compatible with abscesses.



▪ **FIGURE 8-98** **Langerhans Cell Histiocytosis.**

A, Axial contrast-enhanced CT of the temporal bones demonstrates an enhancing soft tissue lesion involving the right mastoid *(arrow)*. **B,** Bone window shows marked bony destruction *(arrows)*, not typical for otomastoiditis. Biopsy of the lesion confirmed LCH.



▪ FIGURE 8-99 Suppurative Adenitis.

Left neck ring-enhancing fluid collection, lateral to the carotid space, with surrounding inflammatory changes, compatible with suppurative adenitis and abscess formation *(arrow)*. Note compression of left internal jugular vein *(arrowhead)* due to mass effect from abscess.

▪ Retinoblastoma

Retinoblastoma is a malignant tumor that arises in the retina and may invade the optic nerve. It typically presents in children younger than 5 years of age. It is bilateral in as many as 25% of cases and can also rarely involve the pineal region (trilateral retinoblastoma) and suprasellar region. In bilateral cases there is often a genetic predisposition. Patients with retinoblastoma are also predisposed to secondary osteosarcoma after radiation therapy. On CT, retinoblastoma typically appears as a calcified, intraocular mass (Fig. 8-100, *A*-*C*). MRI demonstrates a heterogeneous intraocular mass of variable enhancement.

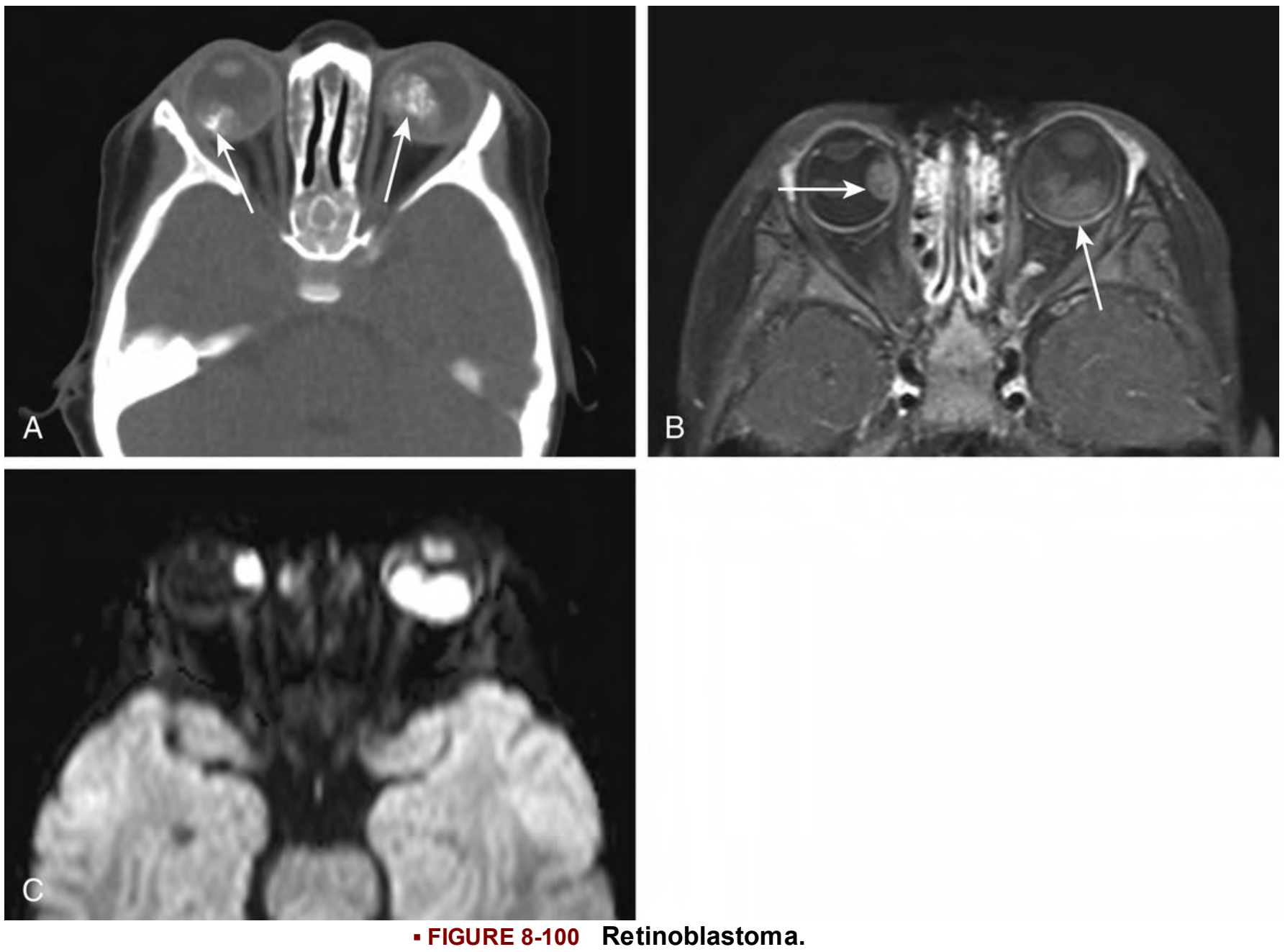
There are a variety of other causes of intraorbital masses, the most common of which are listed in Table 8-8. The differential diagnosis can be limited on the basis of the location of the mass: globe, intraconal, or extraconal. Aggressive lesions involving the orbital rim include metastatic neuroblastoma (Fig. 8-101, *A* and *B*), rhabdomyosarcoma, and LCH.

▪ Neck Masses

There are a large number of causes of pediatric neck masses (Table 8-9). The most common cause is suppurative lymphadenitis (see Fig. 8-99).

Of pediatric malignancies, 5% occur in the head and neck. Most malignant lesions present as painless masses. The head and neck area is one of the most common sites, along with the genitourinary tract, for rhabdomyosarcoma to occur. Rhabdomyosarcoma typically presents in the preschool age child. In older children, lymphoma is most common, presenting with malignant lymphadenopathy.

A number of congenital lesions can present with palpable neck masses, including branchial cleft cyst (Fig. 8-102), thyroglossal duct cyst (Fig. 8-103, *A* and *B*), lingual thyroid (Fig. 8-104), laryngocele, thymic cysts, lymphatic malformations, and dermoid or epidermoid. Branchial cleft cysts can persist from any of the developmental branchial arches, but those arising from the second branchial cleft are the most common. Typically, second branchial cleft cysts occur near the angle of the mandible—posterolateral to the submandibular gland, lateral to the carotid space, and anterior or anteromedial to the sternocleidomastoid muscle (see Fig. 8-102).



▪ **FIGURE 8-100 Retinoblastoma.**
A, CT shows calcified masses *(arrows)* within the posterior aspect of the bilateral globes. **B,** Axial contrast-enhanced T1-weighted sequence of a different patient shows bilateral enhancing intraocular masses *(arrows)*. **C,** Same patient as **B**; DWI sequence demonstrates diffusion restriction seen in highly cellular tumors.

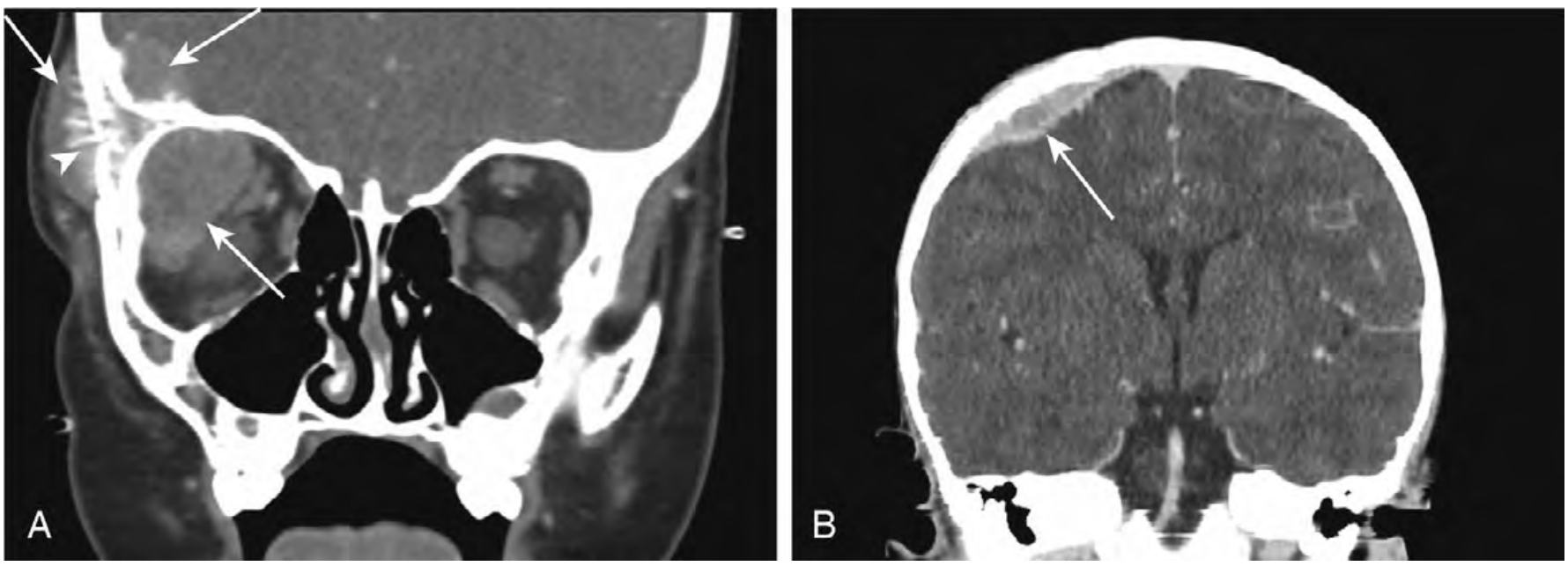
TABLE 8-8
Common Causes of Pediatric Orbital Masses (Extraocular)

- Orbital cellulitis or abscess
- Orbital pseudotumor
- Infantile hemangioma
- Lymphatic or venous malformation
- Optic nerve glioma
- Rhabdomyosarcoma

- Lymphoma or leukemia
- Retinoblastoma
- Langerhans cell histiocytosis
- Metastatic neuroblastoma
- Hematoma

▪ Congenital Vertebral Anomalies

A number of fairly common anomalies of the vertebral bodies occur as the result of abnormal development. There may be lack of fusion of the two cartilaginous centers of the vertebral bodies that results in a cleft in the sagittal plane. This is referred to as a butterfly vertebra. When one of the lateral cartilaginous centers fails to form, a hemivertebra results. It may be associated with scoliosis, rib anomalies, and other vertebral anomalies. Anterior and posterior hemivertebrae are also possible. If there is failure of separation of two or more adjacent vertebral bodies, a fusion anomaly with block vertebra is formed. The fusion of multiple cervical vertebral bodies can be seen in Klippel-Feil syndrome. A number of other associated anomalies may be seen in Klippel-Feil syndrome: a low posterior hairline, a short webbed neck, genitourinary anomalies, and congenital heart disease. A Sprengel deformity (high-riding scapula) in association with a bridging omovertebral bone is present in 25% of patients with Klippel-Feil syndrome.



▪ **FIGURE 8-101 Metastatic Neuroblastoma.**

A, Contrast-enhanced CT of the orbits in coronal plane demonstrates a large soft tissue mass *(arrows)* at the right superolateral orbital wall with associated "hair-on-end" periosteal reaction of involved bone *(arrowhead)*, characteristic of metastatic neuroblastoma. **B,** Contrast-enhanced CT of the head in coronal view of a different patient shows an enhancing subdural mass *(arrow)*.

TABLE 8-9

Common Causes of Pediatric Neck Masses

Congenital	Thyroglossal duct cyst
	Branchial cleft cyst
	Lingual thyroid
	Dermoid or epidermoid
Inflammatory	Suppurative lymphadenitis
	Abscess
	Inflamed salivary gland
	Ranula
Neoplastic	Rhabdomyosarcoma
	Lymphoma
	Metastatic disease
Vascular	Venous malformation
	Lymphatic malformation
	Infantile hemangioma

▪ Spinal Dysraphism

Spinal dysraphism is a group of disorders of the spine in which the posterior bony and neuronal tissues fail to fuse due to abnormal neurulation (Table 8-10). The abnormalities are categorized as open (neural tissue exposed through bone and skin defect) or closed (abnormality covered by skin).

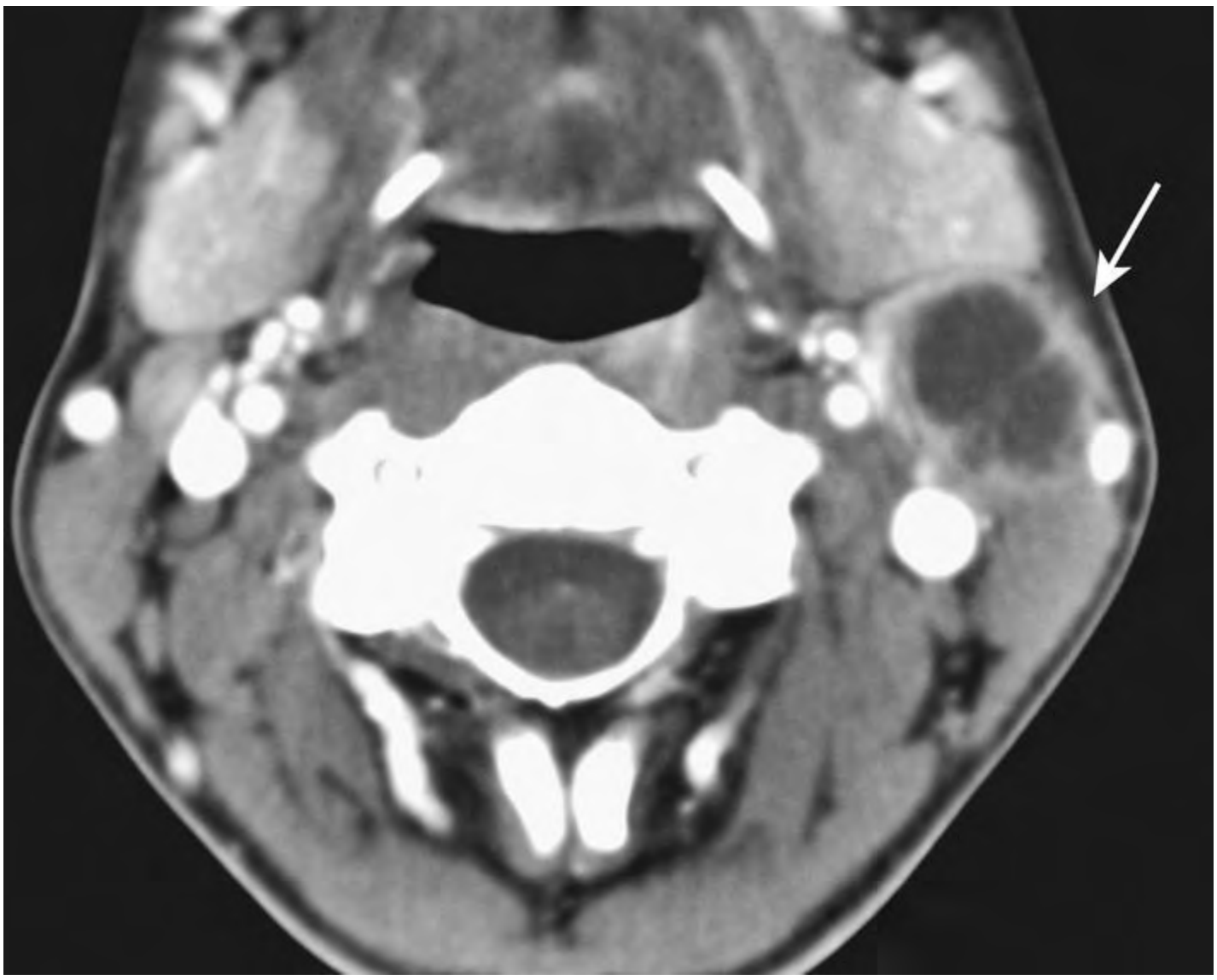
The most common of the open dysraphism are myelomeningoceles and myeloschisis. Myelomeningoceles contain the meninges, neuroplacode, and nerve roots protruding through the skin defect (see Fig. 8-29, *B*). Myeloschisis is a flat defect with neuroplacode and meninges contained within the dysraphic spinal canal. Although the lesions are most common in the lower lumbar spine, they can occur at any level. Encephaloceles occur through defects in the cranium. As previously discussed, essentially all patients with myelomeningoceles have associated Chiari II malformations, and the vast majority have hydrocephalus. Hydromyelia is also often present. On radiography the posterior elements of the spine are absent, and there is widening of the spinal canal and interpedicular distances (Fig. 8-105). Typically, multiple contiguous vertebral levels are involved. MRI is often used to look for delayed complications, such as syrinx, dermoid, or postoperative tethering.

With closed dysraphisms, children may be asymptomatic or may present with subcutaneous masses or dermal tracts, bladder dysfunction, lower-extremity neurologic abnormalities, or orthopedic deformities of the feet or legs.

Lipomyelomeningocele is a closed dysraphic defect characterized by a lipomatous mass and neural elements extending from the low-lying cord through a defect in the bone and contiguous with the subcutaneous fat (Fig. 8-106). A palpable mass may be present, but the overlying skin is intact. Other

less common closed defects include lypomyelocele, myelocystocele, and meningocele. A dermal sinus is an epithelium-lined tract that extends from the skin to the deep spinal soft tissues. If a true open tract is present, immediate surgical attention is necessary, given the risk of meningitis. It may connect to the spinal canal with no associate mass or end in a dermoid, epidermoid, or lipoma. When findings of occult dysraphism are found on ultrasound or are highly suspected clinically, definitive evaluation is performed using MRI.

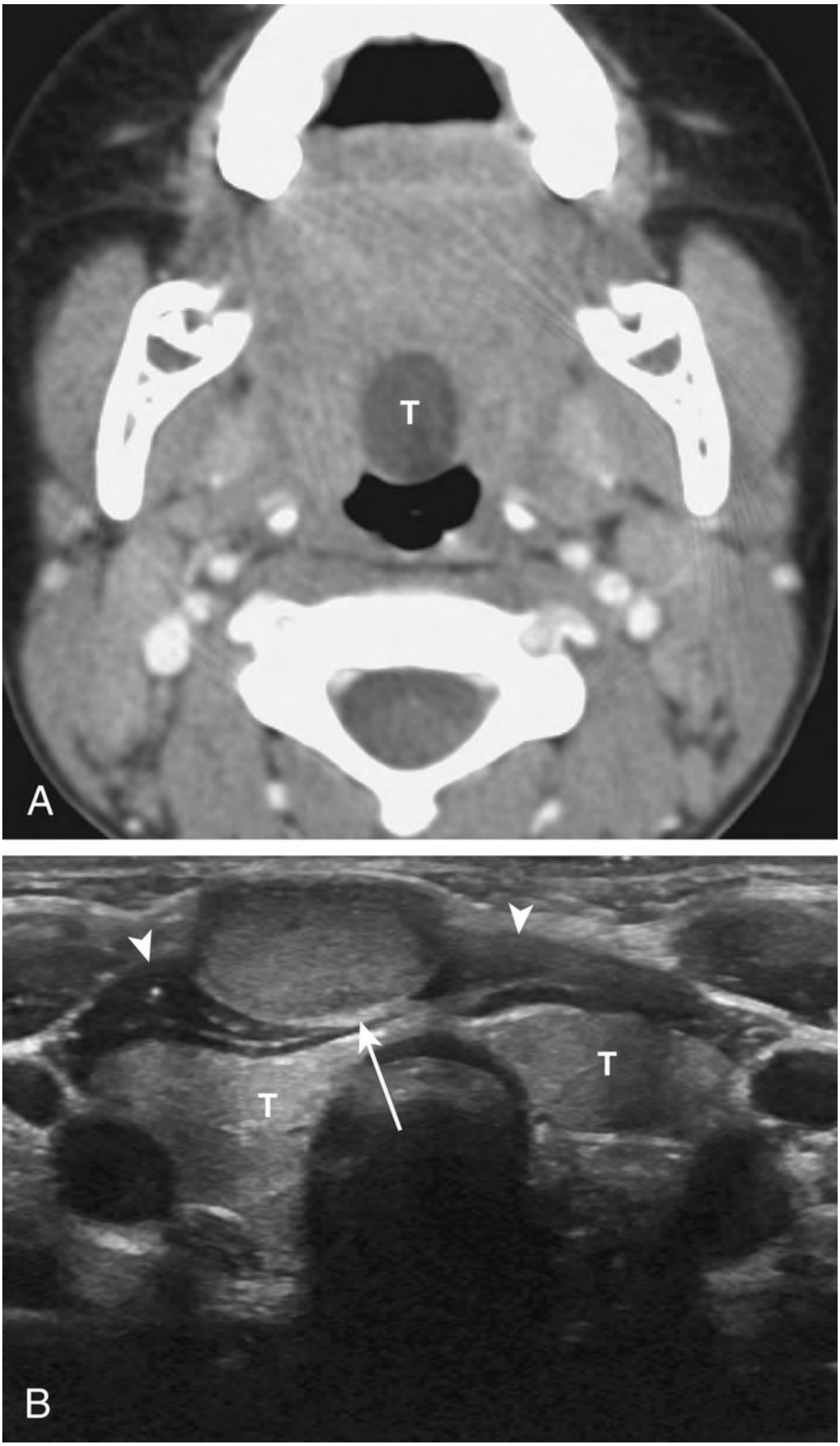
In infants who demonstrate a high skin dimple, patch of hair, or other findings suspicious for an occult dysraphism, the initial screening examination is often ultrasound. In a normal infant the conus medullaris is located superior to or at the level of L2-L3 (Fig. 8-107). The cord and nerve roots are seen to be freely moving during real-time ultrasound evaluation. In tethered cord the tip of the spinal cord is low-lying, below the level of L2-L3 (Fig. 8-108), and nerve roots do not float freely in the CSF space and are often posteriorly positioned.



▪ **FIGURE 8-102 A Second Branchial Cleft Cyst in an 18-Year-Old Girl with a Tender Mass.** CT shows a low-attenuation cystic lesion *(arrow)* just inferior to the left angle of the mandible. The lesion has an enhancing rim.

Tethered cord may occur as a primary problem or may be associated with a tethering lesion, such as a terminal lipoma (see Fig. 8-108) or multiple other dysraphic defects. With a tethered cord the filum terminale may be abnormally thick (>1 to 2 mm).

Caudal regression syndrome is a complex spinal dysraphism that results from abnormal formation of the caudal mesoderm. The most severe form of caudal regression syndrome results in sirenomelia with fusion of lower extremities. Potential etiologies include toxic, ischemic, infectious, or genetic causes. There is a high association with maternal diabetes, VACTERL, and OEIS (omphalocele, exstrophy of the cloaca, imperforate anus, and spinal defect) complex. There is lack of formation of the distal spinal cord and vertebrae. Associated abnormalities of the anal opening, genitalia, bladder, and kidneys are common. Findings on imaging include a blunted high conus medullaris, usually above L1, and sacral hypogenesis (Fig. 8-109).

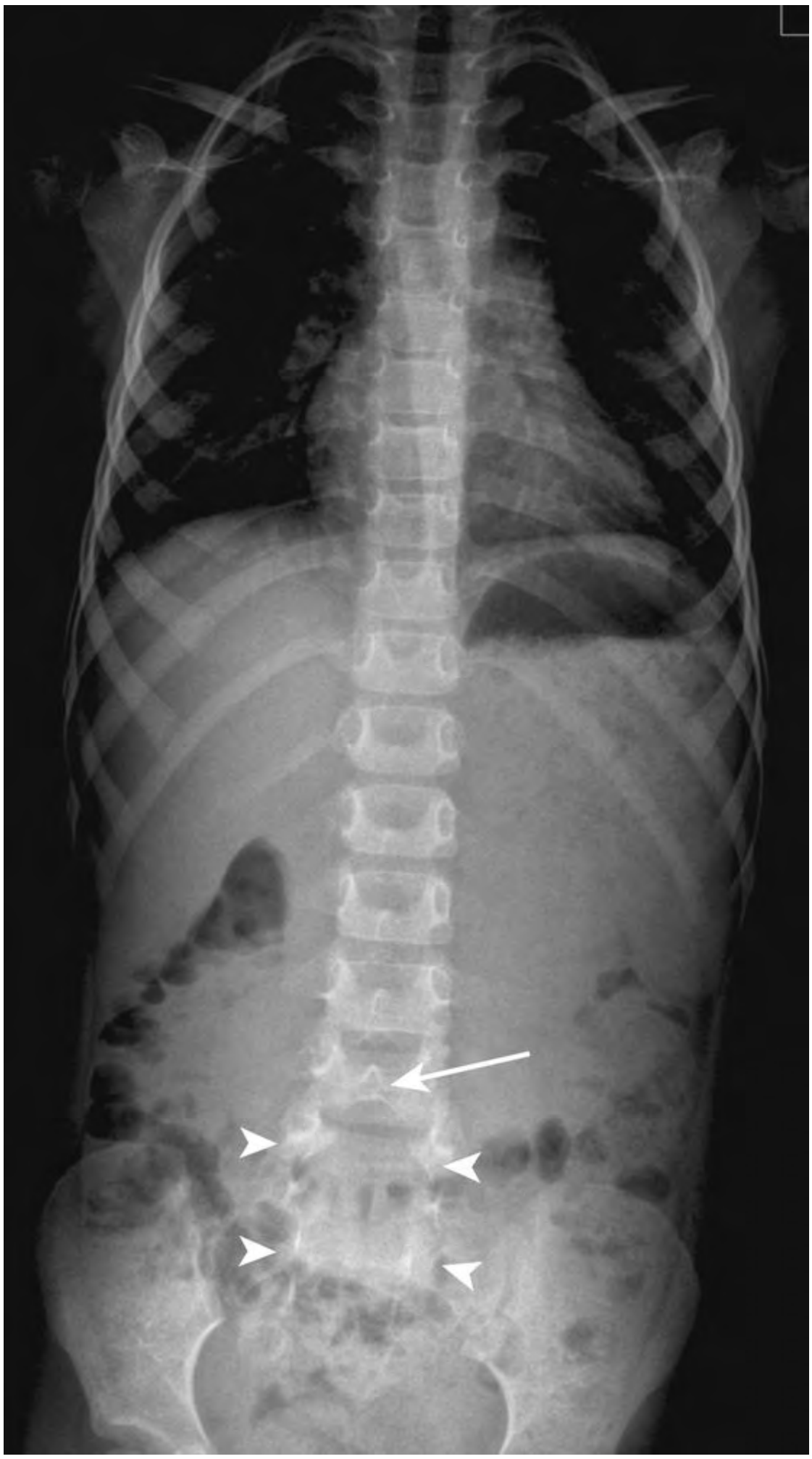


▪ **FIGURE 8-103 Thyroglossal Duct Cyst.**

A, Contrast-enhanced CT shows well-defined, nonenhancing mass *(T)* in the midline, just inferior to the base of the tongue. **B,** Ultrasound of the neck in a different patient shows an oval-shaped lesion *(arrow)* embedded in the strap muscles *(arrowheads)*, as demonstrated by presence of a "claw sign". The lesion is just to the right of midline and causing mild mass effect upon the right lobe of the thyroid gland *(T)*. Note homogeneous internal echos compatible with proteinaceous contents (pseudosolid lesion), as well as enhanced through transmission.



▪ **FIGURE 8-104** **Lingual Thyroid.**
Contrast-enhanced CT of the neck shows a hyperdense mass at the base of the tongue *(arrow)*, compatible with a lingual thyroid. High attenuation is not related to enhancement; it is secondary to thyroid tissue iodine content.



▪ **FIGURE 8-105** **Dysraphic Changes Within the Lumbosacral Spine.**
Radiograph shows absence of the posterior elements and widening of the interpeduncular distance *(arrowheads)*. The posterior elements superior to the level of the dysraphism appear normal *(arrow)*.

TABLE 8-10

Common Types of Spinal Dysraphism

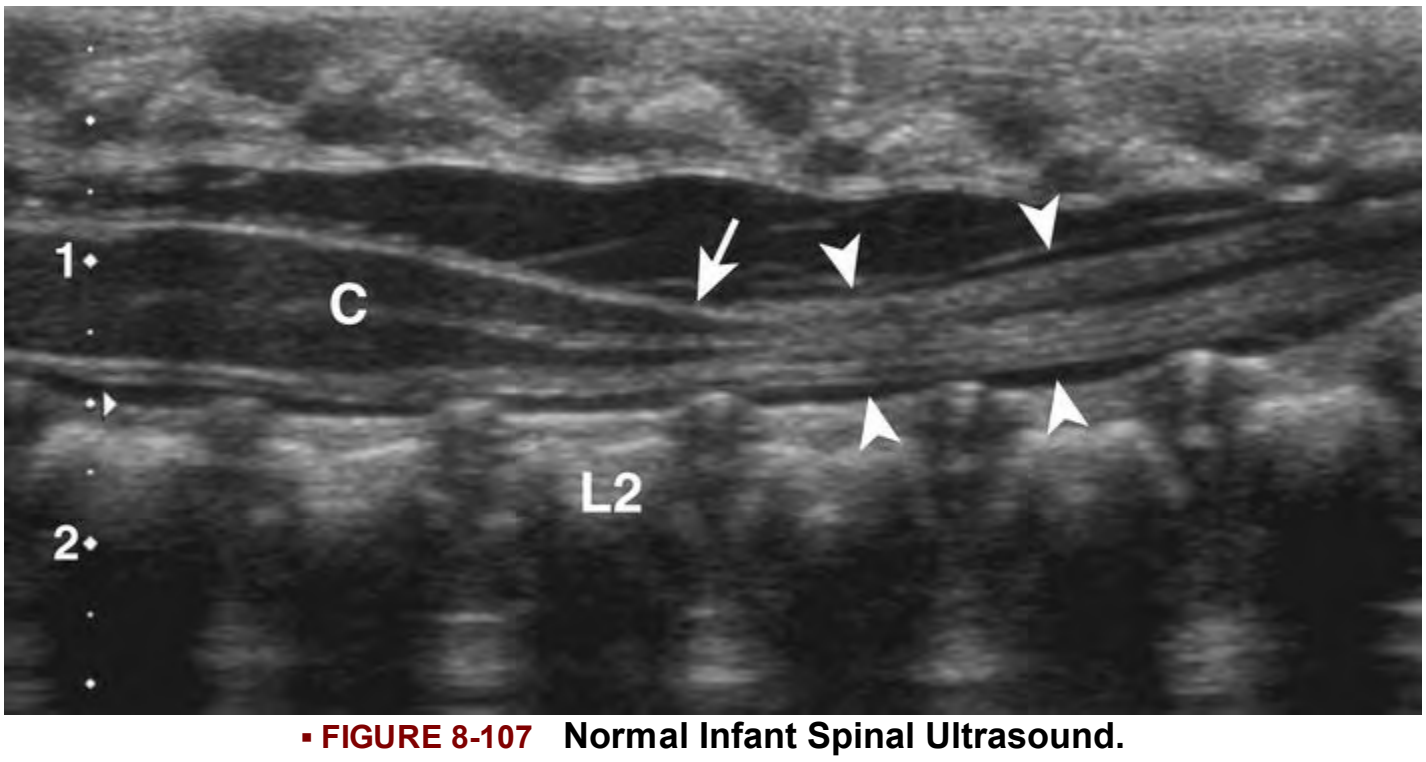
Open spinal dysraphism	Myelomeningocele
	Myeloschisis
Closed spinal dysraphism with a subcutaneous mass	Lipomyelomeningocele
	Lipomyelocele
	Myelocystocele
	Meningocele
Closed spinal dysraphism without a subcutaneous mass	Caudal regression syndrome
	Split notochord syndrome (dorsal enteric fistula and neurenteric cyst)
	Split cord malformation (diastematomyelia)
	Segmental spinal dysgenesis
	Dermal sinus tract
	Tethered cord syndrome
	Intraspinal lipoma

▪ Spinal Trauma

Injury to the spine is much less common in infants and young children than it is in adults. Most injuries that occur in older children and teenagers have the same appearances and locations as those seen in adults and are not discussed here. In infants and young children the majority of cervical spine injuries involve the superior cervical spine, as opposed to the lower cervical spine injuries seen in adults. This is thought to be related to the relatively large head size of young children and the immaturity of the spinal column. As with all cervical spine trauma, one must be diligent concerning the technical factors and the interpretation of radiographs.



▪ **FIGURE 8-106** **Lipomyelomeningocele.**
Sagittal T2-weighted sequence of the lumbar spine shows a low-lying conus medullaris *(white arrow)*. The neuroplacode terminates into a fatty mass *(black arrowheads)* that extends through a lumbosacral dysraphic defect *(white arrowheads)* and is in continuity with the subcutaneous fat tissues.



▪ **FIGURE 8-107** **Normal Infant Spinal Ultrasound.**
Midline sagittal image shows tip of conus medullaris *(arrow)* to be located at the level of *L2*, which is normal position. The cord *(C)* is shown as a hypoechoic structure, and nerve roots *(arrowheads)* are more echogenic. Note that the cord and nerve roots lay anteriorly, with gravity. On real-time ultrasound in a normal patient the cord and nerve roots float freely in the CSF and show motion.





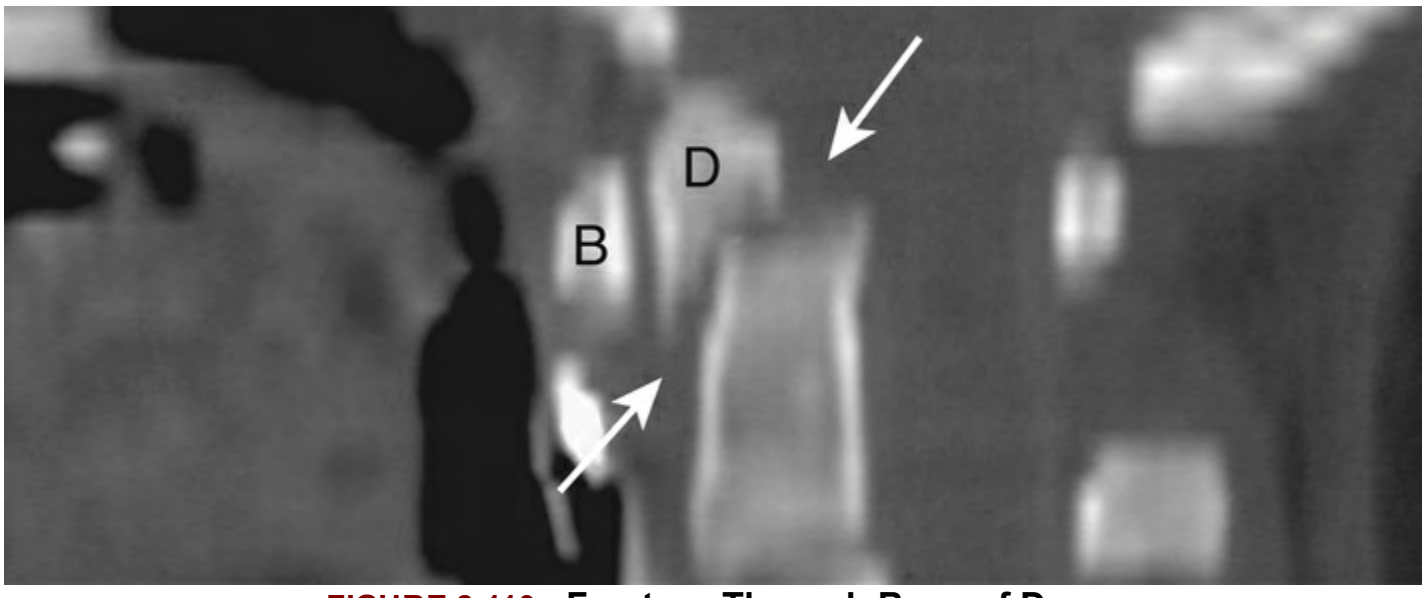
▪ FIGURE 8-108 Tethered Cord with Terminal Lipoma.
Sagittal T1-weighted image of the lumbar spine without contrast demonstrates a low-lying conus *(arrow)* tethered by a terminal lipoma *(arrowheads)*. Patient had a small associated syrinx. A sacral dimple was present clinically and is marked with a skin surface marker.

Fractures of the upper cervical spine in infants and young children often involve the atlas and axis. With flexion injuries, there can be a fracture through the base of the dens (at the synchondrosis between the dens and body of C2) (Fig. 8-110). With this injury there is typically anterior displacement of C1 in association with soft tissue swelling. Extension injuries in this region may result in fractures of the posterior arch of C1, the dens, or a "hangman fracture" (a fracture through the posterior arch of C2) (Fig. 8-111). Atlantooccipital dislocations can also occur (Fig. 8-112). Atlantooccipital dislocation is a severe injury that may result in death. On radiographs the distance between the occiput and C1 is increased, and there is marked soft tissue swelling. Atlantoaxial instability can also occur and is discussed subsequently.

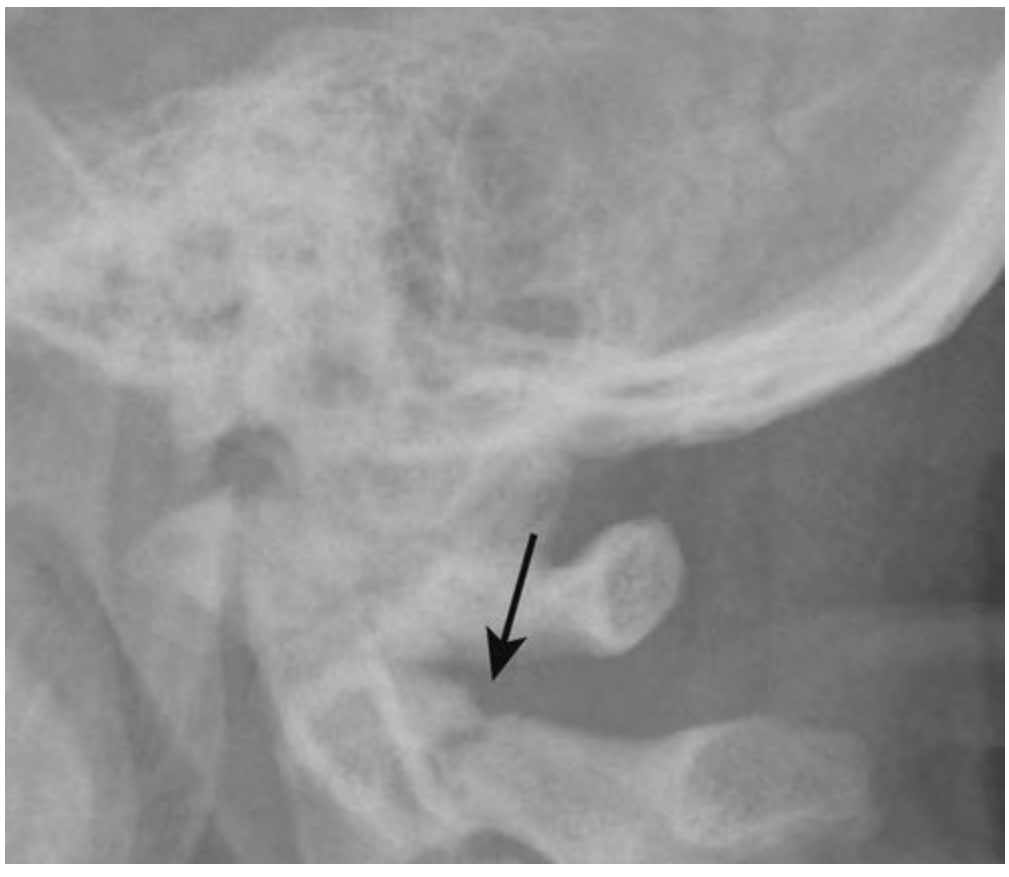
Lap belt injuries occur in children who are restrained by lap belts but not by shoulder belts. Anterior compression fractures of the lumbar vertebral bodies may occur in association with disruption of the posterior processes (Chance fractures; Fig. 8-113, *A* and *B*). These fractures are not commonly associated with neurologic injury but are frequently associated with intraabdominal injuries, particularly of the bowel.



▪ **FIGURE 8-109** **Caudal Regression Syndrome.**
Sagittal T2-weighted sequence of the lumbar spine shows a truncated conus medullaris *(arrow)*. There is also vertebral segmentation anomalies *(white arrowhead)* and a syrinx *(black arrowhead)*. Images of the sacrum also demonstrated sacral dysplasia (not shown).



▪ **FIGURE 8-110** **Fracture Through Base of Dens.**
Sagittal reconstructed CT shows fracture line *(arrows)* through base of dens with anterior displacement of dens *(D)* and anterior arch of C1 *(B)* in relationship to the base of C2.



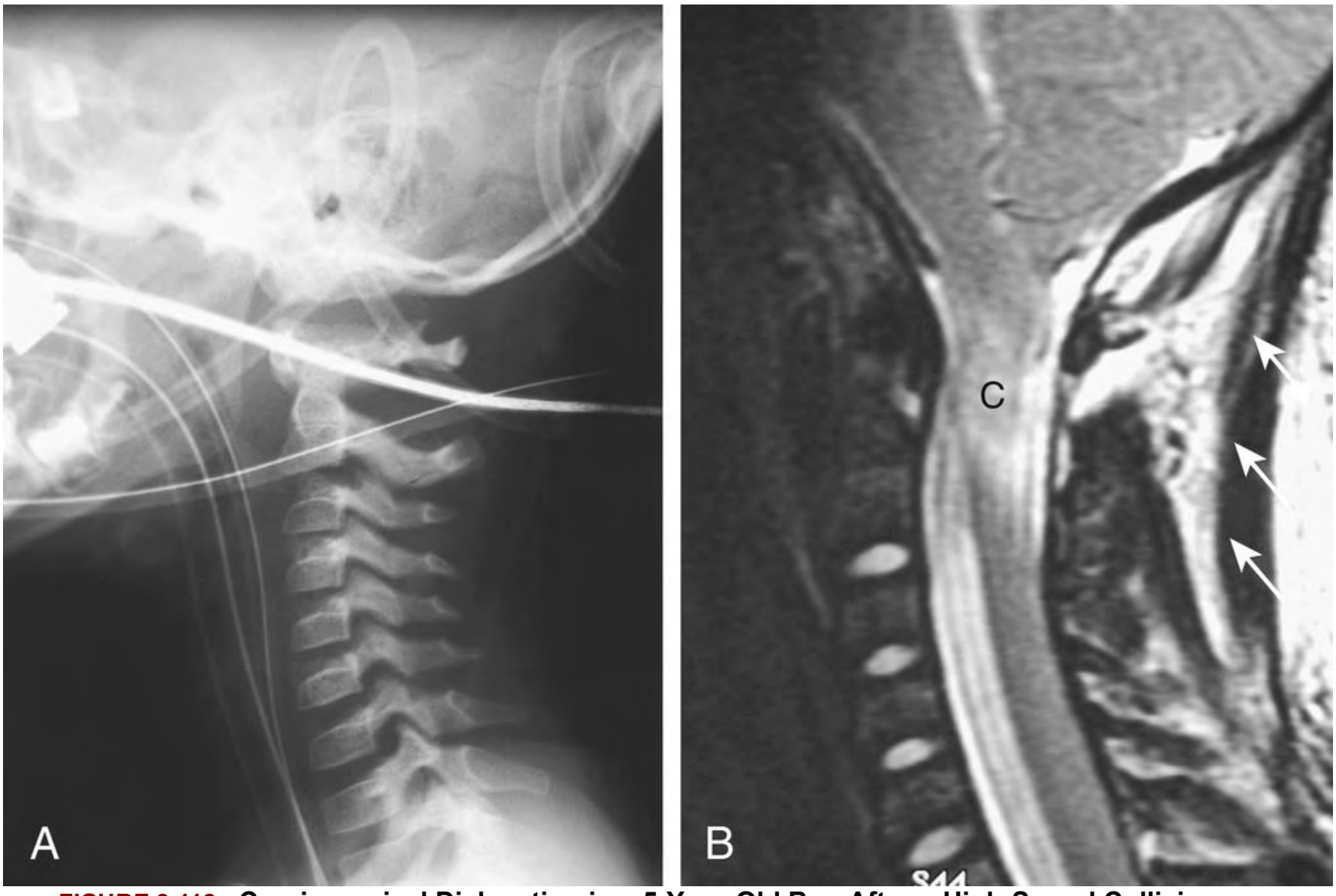


▪ **FIGURE 8-111 Hangman Fracture.**
Radiograph shows linear fracture *(arrow)* through the posterior elements of C2.

▪ Normal Variants and Congenital Anomalies of the Cervical Spine

Another difficulty in the interpretation of pediatric cervical spine radiographs is recognizing normal variants and not misinterpreting them as traumatic injury. One of the more common normal variants that may lead to confusion is cervical pseudosubluxation. In normal children there may be a slightly anterior position of C2 in relation to C3 (Fig. 8-114). However, in contrast to ligamentous injury, with pseudosubluxation the posterior cervical line (a line drawn along the anterior aspect of the posterior processes) remains straight. Pseudosubluxation may also be seen at the C3 to C4 level.

There are a number of age-related variations in C1 and C2. The ossification centers that make up the atlas fuse posteriorly by 1 year of age and laterally by 3 years of age. Before fusion, a lucent synchondrosis is seen radiographically. In addition, there may be a congenital defect in the posterior portion of C1 that should not be confused with a fracture (Fig. 8-115). C2 also has multiple ossification centers. These nonossified synchondroses should not be mistaken for fractures. The synchondrosis between the dens and body of C2 typically fuses between 3 and 6 years of age. Before fusion the lucent synchondrosis is seen through the base of the dens. The ossiculum terminale (tip of the dens) fuses to the body of the dens by 12 years of age. The dens may also be normally tilted slightly posteriorly in young children.

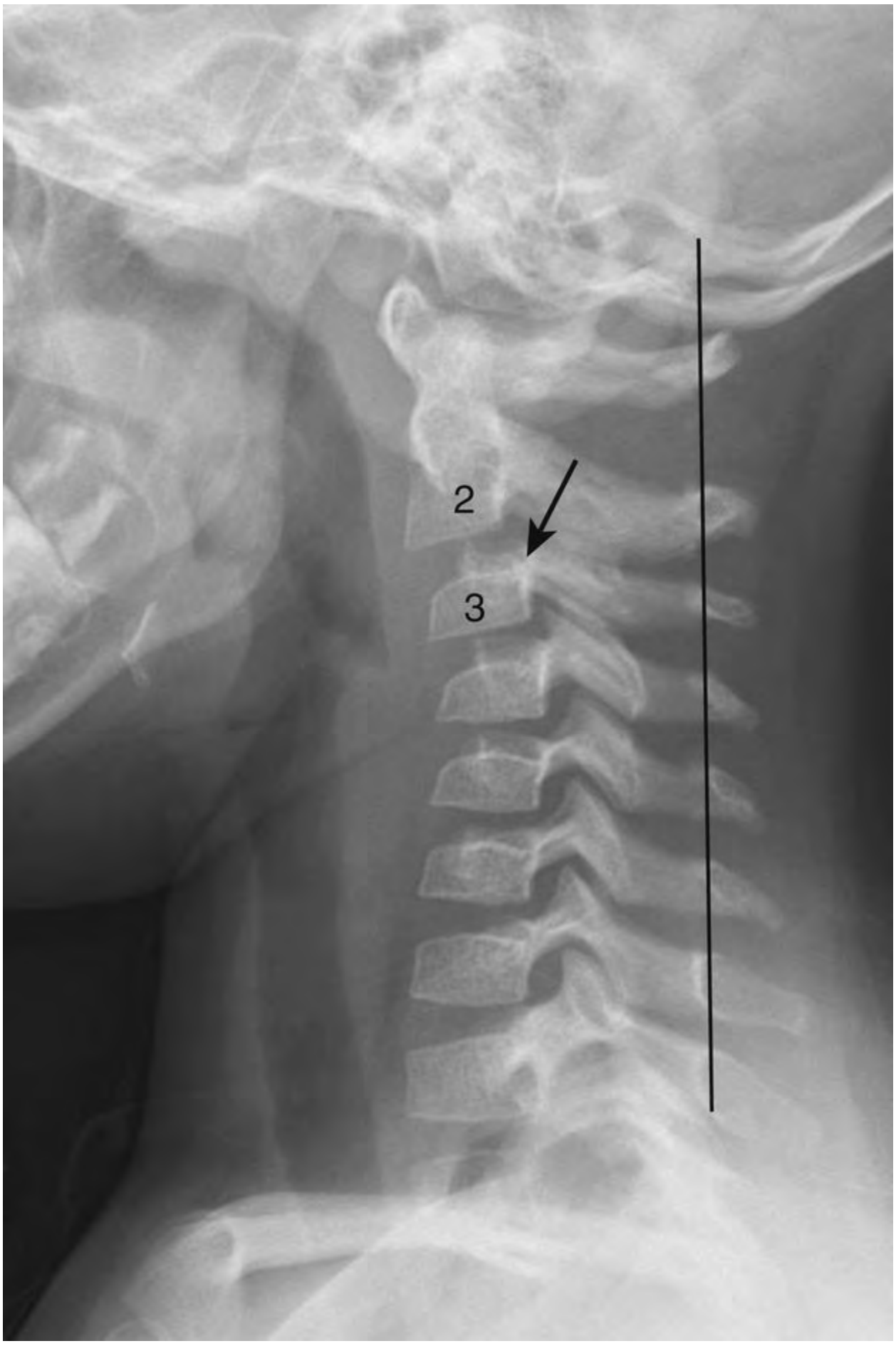


▪ **FIGURE 8-112 Craniocervical Dislocation in a 5-Year-Old Boy After a High-Speed Collision.** **A,** Radiograph shows increased distance between the skull base and C1 vertebral body. **B,** Sagittal T2-weighted MR image shows high signal within the cord *(C)*, representing a cord contusion. There is high-signal edema within the posterior soft tissues *(arrows)* secondary to ligamentous injury.



▪ **FIGURE 8-113** **Chance Fracture.**

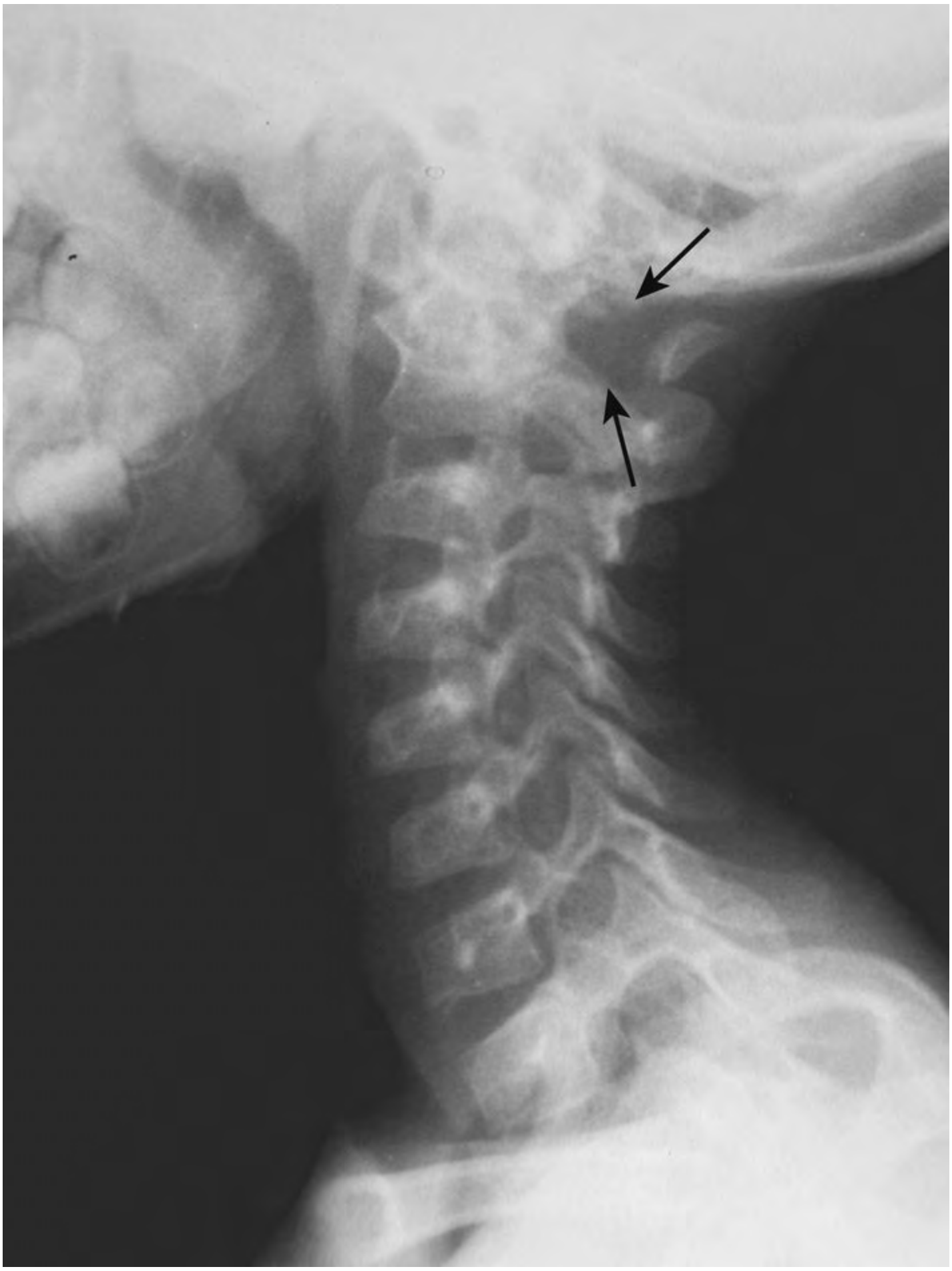
A, Radiograph shows fracture *(arrow)* through posterior elements of the spine and compression fracture of the vertebral body *(arrowhead)*. **B,** STIR MR sequence again shows the fracture through the posterior elements *(white arrow)* and vertebral body compression fracture *(black arrow)*. Note also subcutaneous edema *(arrowheads)*.



▪ **FIGURE 8-114** **Pseudosubluxation of C2 onto C3.**
Radiograph shows that the posterior aspect of C2 vertebral body is slightly more anteriorly positioned than is that of C3 *(arrow)*. However, the posterior cervical line shows that the posterior elements of C2 are not more anterior than the posterior elements of C3, consistent with pseudosubluxation rather than true injury.

▪ Atlantoaxial Instability

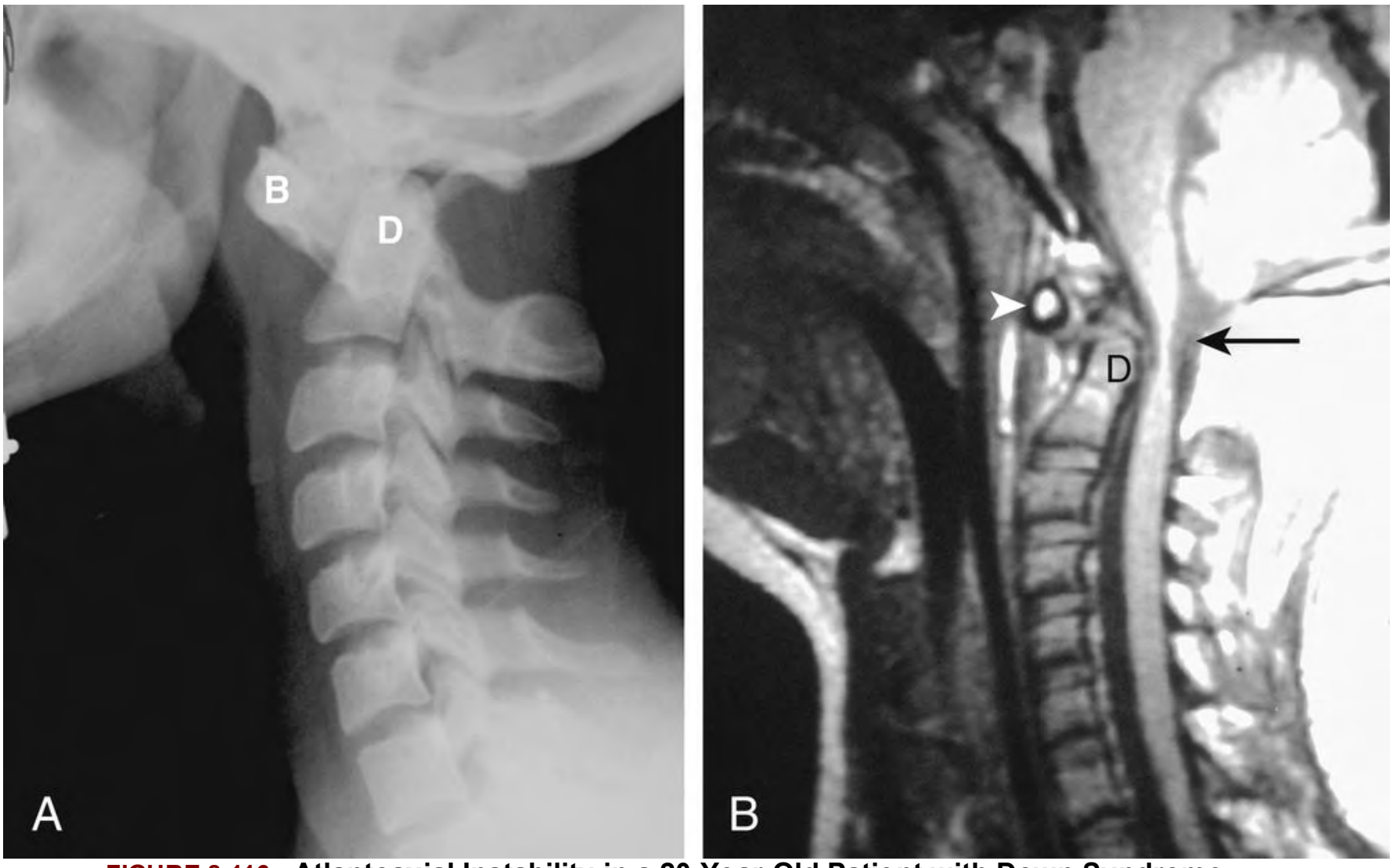
The atlantoaxial joint, or the articulation between the C1 and C2 vertebral bodies, is a unique joint that allows for lateral rotation of the cervical spine. The joint is stabilized by a number of ligaments. The transverse ligament is responsible for stabilizing the relationship between the dens of C2 and anterior arch of C1. In children the space between the dens and anterior arch of C1 should not exceed 5 mm. Atlantoaxial subluxation leads to an abnormal increase in this distance (Fig. 8-116) and decrease in the diameter of the spinal canal with potential cord compression (see Fig. 8-116). Causes of atlantoaxial instability include trauma, inflammation (juvenile idiopathic arthritis, retropharyngeal abscess), and congenital predisposition (Down syndrome, hypoplasia of the dens, os odontoideum [Fig. 8-117], absence of the anterior arch of C1). Patients with Down syndrome are typically screened for atlantoaxial instability with flexion and extension radiographs before participation in physical activities.



▪ **FIGURE 8-115** Congenital absence of the posterior portion of C1 is shown in the lucent area *(arrows)* on radiography.

▪ Spondylolysis and Spondylolisthesis

The most common abnormality identified on radiography in children who present with lower back pain is spondylolysis. Spondylolysis refers to a defect in the pars interarticularis of the posterior vertebral arch. It usually occurs bilaterally and at a single level. The overwhelming majority of cases (93%) occur at the L5 level; the second most common location is L4. It is a common lesion, affecting approximately 7.1% of adolescents. Symptoms usually present in late childhood, although many of these children are asymptomatic. There is debate concerning whether the cause is traumatic, congenital, or some combination of the two.



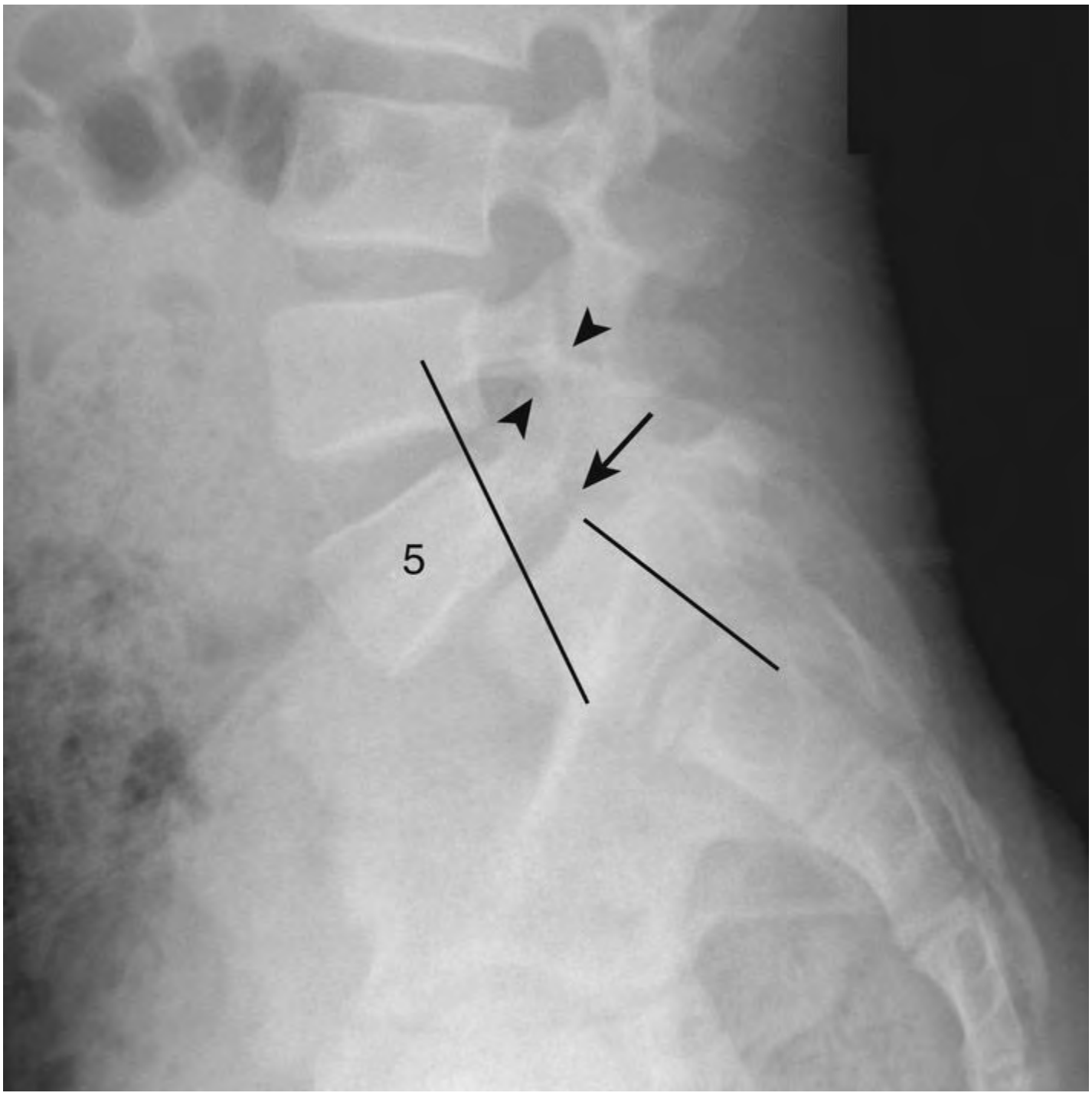
▪ **FIGURE 8-116 Atlantoaxial Instability in a 20-Year-Old Patient with Down Syndrome.** **A,** Radiograph shows increased distance between the anterior arch of C1 *(B)* and the dens of C2 *(D)*. **B,** Sagittal T1-weighted MR image again shows increased distance between the anterior arch of C1 *(arrowhead)* and the dens of C2 *(D)*. There is also narrowing of the spinal canal and severe spinal cord compression *(arrow)*.

Spondylolisthesis refers to anterior displacement of the more superior vertebral body as relate to the inferior vertebral body (Fig. 8-118). Spondylolisthesis is graded from 1 through 5 on the basis of increments of one quarter of the vertebral body. Grade 1 refers to anterior displacement of up to one quarter of the superior vertebral body beyond the anterior border of the inferior vertebral body. In grade 2 the displacement is up to one half; in grade 4 it is the entire vertebral body. Grade 5 is complete anterior displacement and inferior migration such that the superior vertebral body is anterior to the inferior vertebral body.

On lateral radiographs, spondylolysis appears as a lucent defect through the region of the pars interarticularis, with or without associated anterior slippage (spondylolisthesis). Oblique views demonstrate the lucency through the pars. The pars defect has been likened to a lucent broken neck of what appears to look like a Scottish terrier on the oblique views (see Fig. 8-118). Personally, the authors find the defect easier to see on the straight lateral films. In cases in which confirmation is necessary, CT or MRI can be used.



▪ **FIGURE 8-117** **Os Odontoideum.**
Sagittal STIR sequence shows an ossicle at the tip of the odontoid process of C2 *(arrow)*, which is separate from the remaining of the odontoid process. This is compatible with an orthotopic os odontoideum. There is no associated edema or ligamentous injury to suggest an acute fracture.



▪ **FIGURE 8-118** **L5-S1 Spondylolysis with Grade 2 Spondylolisthesis.**
Lateral radiograph shows anterior displacement of L5 vertebral body in relationship to the S1 vertebral segment. Lines are drawn parallel to the posterior aspect of L5 and S1, demonstrating the anterior displacement of L5. The normal, intact pars is seen at L4 *(arrowheads)* and resembles a “dog collar on a Scotty dog.” There is lucency through the pars *(arrow)* at the L5 level, consistent with the spondylolysis.

Suggested Readings

Barkovich A, Raybaud C. *Pediatric neuroimaging*. Philadelphia, PA: Lippincott Williams & Wilkins; 2012.

Brandao L.A, Mukherji S.K. MR spectroscopy of the brain. *Neuroimaging Clin N Am*. Aug 2013;23(3):359–562.

Cruz L.C.H, Mukherji S.K. Clinical applications of diffusion imaging of the brain. *Neuroimaging Clin N Am*. Feb 2011;21(1):1–196.

Dinan D, Daneman A, Guimaraes C.V, et al. Easily overlooked sonographic findings in the evaluation of neonatal encephalopathy: lessons learned from magnetic resonance imaging. *Semin Ultrasound CT MR*. Dec 2014;35(6):627–651.

Kline-Fath B, Bulas D, Bahado-Singh R. *Fundamental and advanced fetal imaging—ultrasound and MRI*. Philadelphia, PA: Wolters Kluwers; 2015.

Lowe L.H, Balley Z. State-of-the-art cranial sonography: part 1, modern techniques and imaging interpretation. *Am J Roentgenol*. May 2011;196(5):1028–1033.

Lowe L.H, Balley Z. State-of-the-art cranial sonography: part 2, pitfalls and variants. *Am J Roentgenol*. May 2011;196(5):1034–1039.

Pillai J.J, Mukherji S.K. Clinical applications of functional MRI. *Neuroimaging Clin N Am*. Nov 2014;24(4):557–728.

Welker K, Patton A. Assessment of normal myelination with magnetic resonance imaging. *Semin Neurol*. 2012;32:15–28.

Index

Page numbers followed by *f* indicate figure, by *t* table, and by *b* box.

A

Abdominal trauma, blunt, 122–123
  bowel injury due to, 122–123, 123f
  hypoperfusion complex due to, 123, 124f
  parenchymal organ injuries due to, 122, 122f
Abdominal wall, anterior, abnormalities of, 106, 106f
Abscess
  brain, 246f
  lung, 47–48, 47f
  retropharyngeal, 11–13, 12f–13f
Acetabulum, trident, 209
Achondroplasia, 209, 210f
Acoustic schwannomas, in neurofibromatosis type 2, 279, 282f
Acromelic extremity shortening, 209
Acute chest syndrome, in sickle cell anemia, 51, 52f
Acute diffuse pulmonary consolidation, 33–34, 34t
Acute disseminated encephalomyelitis (ADEM), 286–287, 292f
Acute laryngotracheobronchitis, 8, 9f
Acute pelvic pain, in older girls and adolescents, 160–163, 161f–163f
Acute scrotum, 159–160, 160f–161f
Acute stridor, 8
ADC (apparent diffusion coefficient) map, 243, 244f, 247t
Adenitis, mesenteric, 117, 117f
Adenoid tonsils, recurrent and enlarged, 20–21, 21f
Adenomatoid malformation, congenital cystic, 34–37
Adolescents
  acute pelvic pain in, 160–163, 161f–163f
  avulsion fractures in, 183–185
    of knee, 185, 188f–190f
    of pelvis, 185, 186f–187f
Adrenal disorders, 153

neonatal adrenal hemorrhage as, 154–155, 157f
neuroblastoma as, 153–154
CT of, 154, 155f–156f
prognosis for, 153–154, 155t
risk factors in, 154t
staging of, 153–154, 153t
Adrenal glands, 153
Adrenal hemorrhage, neonatal, 154–155, 157f
Adrenoleukodystrophy, 287f, 289t
Age-related changes, in imaging appearance, 5
Age-related differential diagnosis, 5
Aggressive fibromatosis, 238
Agyria-pachygyria, 271–273, 272f–273f
Air space consolidation, in pneumonia, 43
Airway, 8–25
Airway foreign body, 18, 20f
Airway obstruction
acute upper, 8–13
due to croup, 8, 9f
due to epiglottitis, 8–11, 10f
due to exudative tracheitis, 11, 11f
due to retropharyngeal cellulitis and abscess, 11–13, 12f–13f
congenital, 24–25, 24f–25f
lower, 13–24, 14f
due to abnormal soft palate, 23–24
due to enlarged lingual tonsils, 21–22, 22f
due to enlarged palatine tonsils, 21, 22f
due to glossoptosis, 22, 23f
due to hypopharyngeal (retroglossal) collapse, 22–23, 24f
due to recurrent and enlarged adenoid tonsils, 20–21, 21f
extrinsic, 14–17, 15f–16f
due to double aortic arch, 14, 16f
due to innominate artery compression syndrome, 16–17, 19f
due to pulmonary sling, 14–15, 17f
due to right aortic arch with aberrant left subclavian artery, 16, 18f
intrinsic, 17–18
due to airway foreign body, 18, 20f
due to tracheomalacia, 17
in obstructive sleep apnea, 18–20, 21f
Alexander disease, 289t
Anemia(s), sickle cell, 228–229, 228f

acute chest syndrome in, 51, 52f
Anesthesia, during procedure, 4
Aneurysm(s)
coronary artery, in Kawasaki disease, 89, 89f–90f
vein of Galen, 275–277, 276f
Angiography, catheter, of congenital heart disease, 68
Angiomyolipoma, 151–153, 152f–153f
Anisotropy, 247t
Ankle, fractures in, 178–182, 181f–182f
Annular pancreas, 94–95
Anterior abdominal wall, abnormalities of, 106, 106f
Anterior mediastinal mass(es), 55
lower airway obstruction due to, 14, 16f
lymphoma as, 57–60, 60f–61f
teratoma as, 59, 61f
Aorta, coarctation of, 80, 81f, 83, 84f–85f
Aortic arch
double, lower airway obstruction due to, 14, 16f
left-sided, 71
position of, 71
right-sided, 71
with aberrant left subclavian artery, 16, 18f
in truncus arteriosus, 76, 77f
Aortic injury, 54
Aortic knob, 71
Aortic stenosis, 82–83, 83f
Aortic valvular stenosis, 82–83, 83f
Apnea, obstructive sleep, *See* Obstructive sleep apnea (OSA).
Apophyseal irregularity, 164, 166f
Apparent diffusion coefficient (ADC) map, 243, 244f, 247t
Appendicitis, 108–109
with appendicolith, 109, 109f–110f
CT of, 109, 110f
nonperforated, 109f
perforated, 109, 110f
radiographs of, 109, 110f
ultrasound of, 109, 109f
Appendicolith, 109, 109f–110f
Arachnoid cyst, 271
posterior fossa, 271f
Arterial switch procedure, 82t

Aryepiglottic folds, in epiglottitis, 10, 10f
ASD (atrial septal defect), 79–80, 81f
Aspiration
  of airway foreign body, 18
  chronic, high-resolution computed tomography in, 53, 53f
  of hydrocarbons, 54–55, 57f
Asplenia, 70, 71f
Astrocytoma, cerebellar, 290, 292t, 293f
Atlantoaxial instability, 318, 319f
Atlantooccipital dislocations, 315, 317f
Atrial septal defect (ASD), 79–80, 81f
Autosomal dominant polycystic kidney disease (ADPKD), 147
Autosomal recessive polycystic kidney disease (ARPKD), 147, 148f
Avulsion fractures, in adolescents, 183–185
  of knee, 185, 188f–190f
  of pelvis, 185, 186f–187f

B

Bacterial pneumonia, 43, 44f

Bacterial tracheitis, *See* Exudative tracheitis.

Balloon dilation, for coarctation of the aorta, 83, 85f

Batteries, button, swallowed, 115, 116f

Benign fibrous cortical defects, 168, 168f

Benign macrocrania, 256–257

Biliary atresia, 117–118, 118f

"Black-blood" imaging, 67, 67f

Bladder capacity, 132

Blalock-Taussig shunt, 82t

Bleeding

See also Hemorrhage

gastrointestinal, in immunocompromised child, 125t

Block vertebra, 311

Blood oxygenation level-dependent (BOLD) effect, 249–252

Blount disease, 229, 230f

Blunt abdominal trauma, 122–123

bowel injury due to, 122–123, 123f

hypoperfusion complex due to, 123, 124f

parenchymal organ injuries due to, 122, 122f

Bochdalek hernia, 37–38

BOLD (blood oxygen level-dependent) effect, 249–252

Bone age, 223

Bowel atresia, 103f

Bowel injury, 122–123, 123f

Bowel stricture, in necrotizing enterocolitis, 93, 94f

Bowing deformity, plastic, 170–171, 170f

BPD (bronchopulmonary dysplasia), 34

Brachycephaly, 302

Brain abscess, 246f

Brainstem glioma, 292t, 293, 295f

Branchial cleft cysts, 311, 313f

"Bright-blood" imaging, 67–68, 67f

Brodie abscess, 196, 197f

Bronchiectasis, 48

Bronchogenic cyst, 39

lower airway obstruction due to, 14, 15f

Bronchopulmonary dysplasia, 34, 35f

Buckle fracture, 170–171, 172f

Butterfly vertebra, 311
Button batteries, swallowed, 115, 116f

C

Caffey disease, 194

Calcaneus, 231

apophyseal irregularity of, 164, 166f

stress fractures of, 182–183, 184f

Canavan disease, 289t

Capillary malformations, 235

Cardiac apex, 70

Cardiac axis, 69

Cardiac disease

acquired, 88–89

cardiac masses, 77f, 89, 90f–91f

Kawasaki disease as, 89

congenital

aortic stenosis as, 82–83, 83f

approach to chest radiograph in, 68–71

cardiac size as, 69, 70f–71f

position of aortic arch as, 71

pulmonary vascularity as, 68–69, 69f

situs as, 70, 72f–73f

atrial septal defect as, 79–80, 81f

cardiomyopathy as, 69f

categorization of, 72–83, 73t

blue

decreased pulmonary arterial flow, massive cardiomegaly in, 73–75, 75f–76f

decreased pulmonary arterial flow, mild cardiomegaly in, 72–73, 74f

increased flow in, 75–77, 77f–79f

variable pulmonary arterial flow in, 77–79

pink

increased pulmonary arterial flow in, 79–80, 81f

normal pulmonary arterial flow in, 81–83, 82f–85f

pink (or dusky), increased pulmonary venous flow in, 80–81, 81f, 81t

coarctation of the aorta as, 80, 81f, 83, 84f–85f

congestive heart failure due to, 80, 81t

double-outlet right ventricle as, 86

D-transposition of the great arteries as, 78–79, 79f, 86, 87f

due to abnormalities of conotruncal rotation, 84–86, 86f–87f

Ebstein anomaly as, 74, 75f

hypoplastic left heart syndrome as, 80–81, 82f

imaging modalities for, 66–71

catheter angiography as, 68
computed tomography angiography as, 66–67, 67f
echocardiography as, 66
magnetic resonance imaging as, 67–68, 67f
incidence of, 72, 73t
left-to-right shunts, 79–80, 81f
L-transposition of the great arteries as, 85, 86f
obstructive lesions of the great arteries as, 82
patent ductus arteriosus as, 79–80, 81f
pulmonary atresia with intact ventricular septum as, 74–75, 76f–77f
pulmonic stenosis as, 83, 84f
situs inversus as, 70, 86
surgeries for, 88–89, 88f–89f
surgical procedures for, 82t
tetralogy of Fallot as, 72–73, 74f
total anomalous pulmonary venous return as, 77, 78f–79f
tricuspid atresia as, 79, 80f
truncus arteriosus as, 75–76, 77f, 84–85
ventricular septal defect as, 79–80, 81f
Cardiac gated cine MRI, 67–68, 67f
Cardiac gated spin echo imaging, 67, 67f
Cardiac masses, 77f, 89, 90f–91f
Cardiac rhabdomyoma, 74–75, 77f, 89, 90f
Cardiac silhouette, 69, 70f–71f
Cardiac size, 69, 70f–71f
Cardiomegaly, 69, 70f–71f
decreased pulmonary arterial flow with
massive, 73–75, 75f–76f
mild, 72–73, 74f
Catheter(s)
extracorporeal membrane oxygenation, 31–32, 31f
peripherally inserted central, 31–32
umbilical arterial and venous, 30–31, 30f
Caudal regression syndrome, 316f
Cavitary necrosis, due to pneumonia, 48, 49f
CCAM (congenital cystic adenomatoid malformation), 34–37
CDH (congenital diaphragmatic hernia), 37–38, 39f–40f
Cellulitis
orbital, 308–309, 308f
retropharyngeal, 11–13, 12f–13f
Central catheters, peripherally inserted, 31–32

Central nervous system (CNS) infection(s), 285–287
congenital, 285
encephalitis as, 285–287, 291f
Central nervous system (CNS) tumor(s)
germ cell, 298, 299f
hypothalamic hamartoma as, 299, 301f
optic and hypothalamic astrocytoma, 298
pineal, 299–300
posterior fossa, 287–295, 292t
brainstem glioma as, 292t, 293, 295f
cerebellar astrocytoma as, 290, 292t, 293f
ependymoma as, 292t, 293–295, 296f
medulloblastoma as, 290–293, 292t, 294f–295f
sellar and suprasellar, 298–300
supratentorial, 295–298, 297f
Cerebellar astrocytoma, 290, 292t, 293f
Cerebellar vermian hypoplasia, 271f
Cerebral tumors, 295–298
Cerebrospinal fluid spaces, enlarged, posterior fossa anomalies with, 270–271
Cervical spine
congenital anomalies of, 316–318, 318f
normal variants of, 316–318, 318f
pseudosubluxation of, 316, 318f
Chance fractures, 316, 317f
Chemotherapy, thymic rebound and, 57
Chest, 26–65
chronic aspiration in, 53, 53f
cystic fibrosis in, 51–53, 52f
hydrocarbon ingestion in, 54–55, 57f
lymphoma in, 57–60, 60f–61f
mediastinal injury in, 54
mediastinal masses in, 55–60, 57t
anterior, 55
lymphoma as, 57–60, 60f–61f
teratoma as, 59, 61f
middle, 60
posterior, 60–62
neonatal, 26–39
acute diffuse pulmonary consolidation in, 33–34
bronchogenic cyst in, 39
bronchopulmonary dysplasia in, 34

congenital cystic adenomatoid malformation in, 34–37
congenital diaphragmatic hernia in, 37–38, 39f–40f
congenital lobar emphysema in, 36, 36f
diffuse pulmonary disease in, 26, 26t
exclusion of other pathologic processes in, 44
failure to resolve in, 44
focal pulmonary lesions in, 34–36, 35t
group B streptococcal pneumonia in, 29, 29f
meconium aspiration syndrome in, 26, 27f
neonatal intensive care unit support apparatus for, 29–30
extracorporeal membrane oxygenation as, 31–32, 31f
high-frequency oscillators as, 32
peripherally inserted central catheters as, 31–32
umbilical arterial and venous catheters as, 30–31, 30f
persistent pulmonary hypertension in, 29
pneumonia in, 27, 39–53
bacterial, 43, 44f
characterization and prediction of infectious agent in, 40–43, 42f–43f
complications of, 44–48
chronic lung, 48, 49f
lung parenchymal, 47–48
parapneumonic effusions as, 44–45, 46f
persistent or progressive symptoms as, 47
confirmation or exclusion of, 40, 42f
fungal, 50f
group B streptococcal, 29
in immunodeficient children, 51, 51f
neonatal, 27, 27f–28f
round, 43, 45f
viral, 43
pulmonary interstitial emphysema in, 32–33, 32f
sequestration in, 38–39, 38f, 41f
surfactant-deficient disease in, 27–28, 28f
surfactant replacement therapy for, 28–29, 28f
transient tachypnea in, 27, 27f
tuberculosis in, 50–51, 50f
neuroblastoma in, 60–62, 63f
pectus excavatum in, 64–65, 65f
pulmonary interstitial emphysema in, 32–33
rib fractures and lung contusion in, 54, 54f
teratoma in, 59, 61f

thymus in
abnormality of, 57
in Langerhans cell histiocytosis, 58f
normal, 55–57, 58f–59f
with sail sign, 55–57, 58f
with spinnaker sail sign, 55–57, 59f
Chest trauma, 54–55
Chest wall masses, pediatric, 62–65
Chiari malformation(s), 260–262
type 1, 260–262, 263t–264t, 265f
type 2, 262, 263t–264t, 265f–266f
Child abuse, 185–192, 191f–193f
head trauma secondary to, 301, 301f–302f
rib fractures in, 54, 56f
Child-friendly surroundings, 2, 2f–4f
Childhood interstitial lung disease, 53–54, 54f
Choledochal cyst, 118, 119f
Choline, in MR spectroscopy, 247–249, 249f
Choroid plexus tumors, 298, 298f
Chronic foreign body, in soft tissues, 240, 241f
Chronic hip subluxation, 216, 216f
Chronic lung disease of prematurity, 34
Church steeple, in croup, 8, 9f
Cisterna magna, mega, 271
"Claw sign," in Wilms tumor, 149
Cloacal exstrophy, 106
Clostridium difficile, 124–125
Closure device deployment, 82t
Clover-leaf skull, 302
Clubfoot (talipes equinovarus), 229–231, 231f
CMV (cytomegalovirus), CNS abnormalities due to, 285, 290f
Coarctation of the aorta, 80, 81f, 83, 84f–85f
Cobblestone complex, 263t–264t
Cobblestone lissencephaly, 273f
Coin, in esophagus, 114–115, 114f–115f
Colitis
cytomegalovirus, 125t
neutropenic, 125, 125t, 126f
pseudomembranous, 124–125, 125f, 125t
Colon, functional immaturity of, 102–103
Colonic stricture, in necrotizing enterocolitis, 94f

Communication, 2
Computed tomography (CT)
of appendicitis, 109, 110f
of bowel diseases, in immunocompromised children, 125t
in chronic aspiration, 53, 53f
contrast dosing for, 5
distraction for, 3f, 4
of intussusception, 110, 112f
for neuroimaging, 243
radiation safety of, 6
vs. magnetic resonance imaging, 68
Computed tomography angiography, of congenital heart disease, 66–67, 67f
Congenital airway obstruction, 24–25, 24f–25f
Congenital anomalies, 133
hydrometrocolpos as, 145–146, 146f
multicystic dysplastic kidney as, 136–137, 138f
posterior urethral valves as, 142, 143f
primary megaureter as, 142, 142f
prune-belly syndrome as, 145, 146f
renal cystic disease as, 147, 147t
autosomal dominant, 147
autosomal recessive, 147, 148f
renal ectopia and fusion as, 140–141, 140f–141f
urachal abnormalities as, 142–144, 144f–145f
ureterocele as, 139f, 140
ureteropelvic duplications as, 137–140, 138f–139f
ureteropelvic junction obstruction as, 135–136, 137f
vesicoureteral reflux as, 134–135, 135f–136f
Congenital cystic adenomatoid malformation (CCAM), 36–37
Congenital diaphragmatic hernia, 37–38, 39f–40f
Congenital heart disease
aortic stenosis as, 82–83, 83f
approach to chest radiograph in, 68–71
cardiac size as, 69, 70f–71f
position of aortic arch as, 71
pulmonary vascularity as, 68–69, 69f
situs as, 70, 72f–73f
atrial septal defect as, 79–80, 81f
cardiomyopathy as, 69f
categorization of, 72–83, 73t
blue

decreased pulmonary arterial flow, massive cardiomegaly in, 73–75, 75f–76f
decreased pulmonary arterial flow, mild cardiomegaly in, 72–73, 74f
increased flow in, 75–77, 77f–79f
variable pulmonary arterial flow in, 77–79
hypoplastic left heart syndrome as, 80–81, 82f
pink
increased pulmonary arterial flow in, 79–80, 81f
normal pulmonary arterial flow in, 81–83, 82f–85f
pink (or dusky), increased pulmonary venous flow in, 80–81, 81f, 81t
coarctation of the aorta as, 80, 81f, 83, 84f–85f
congestive heart failure due to, 80, 81t
double-outlet right ventricle as, 86
D-transposition of the great arteries as, 78–79, 79f, 86, 87f
due to abnormalities of conotruncal rotation, 84–86, 86f–87f
Ebstein anomaly as, 74, 75f
imaging modalities for, 66–71
catheter angiography as, 68
computed tomography angiography as, 66–67, 67f
echocardiography as, 66
magnetic resonance imaging as, 67–68, 67f
incidence of, 72, 73t
left-to-right shunts, 79–80, 81f
L-transposition of the great arteries as, 85, 86f
obstructive lesions of the great arteries as, 82
patent ductus arteriosus as, 79–80, 81f
pulmonary atresia with intact ventricular septum as, 74–75, 76f–77f
pulmonic stenosis as, 83, 84f
situs inversus as, 70, 86
surgeries for, 88–89, 88f–89f
surgical procedures for, 82t
tetralogy of Fallot as, 72–73, 74f
total anomalous pulmonary venous return as, 77, 78f–79f
tricuspid atresia as, 79, 80f
truncus arteriosus as, 75–76, 77f, 84–85
ventricular septal defect as, 79–80, 81f
Congenital hemangiomas, 233–235, 234f
Congenital high airway obstruction syndrome (CHAOS), 24–25, 24f–25f
Congenital infections, affecting central nervous system, 285, 290f
Congenital lobar emphysema, 36, 36f
Congenital pulmonary airway malformation, 36–37, 37f–38f
Congenital rubella syndrome, 192

Congenital vertebral anomalies, 311
Congestive heart failure, 80, 81t
Conotruncal rotation, abnormalities of, 84–86, 86f–87f
Conscious sedation, during procedure, 5
Constitutional disorders of bone, 207–214
  mucopolysaccharidoses as, 209, 213f
  osteogenesis imperfecta as, 209–212, 214f
  osteoporosis as, 212–214
  skeletal dysplasias as, 207–209, 212t
    achondroplasia as, 209, 210f
    distal shortening in, 209, 211f
    thanatophoric dwarfism as, 209, 211f
Contrast enemas, neonatal, 100
Conus medullaris, 312–313, 315f
Conventional ventilation, 32
Cooperation, 2–5
Coronary artery aneurysms, in Kawasaki disease, 89, 89f–90f
Corpus callosum, dysgenesis of, 263t–264t, 269–270, 269f
Cortical defects, fibrous, benign, 168, 168f
Cortical desmoid, 164–168, 168f
Cortical dysplasia, 263t–264t
Cortical hyperostosis, infantile, 194
Cortical irregularity syndrome, 164–168, 168f
Costal cartilage, prominent, 62–64, 65f
Craniocervical dislocation, 317f
Craniopharyngioma, 298–299, 300f
Craniosynostosis, 302, 306f–307f
Creatine, in MR spectroscopy, 249, 252f
Crohn disease, 127–128, 128f
Croup, 8, 9f
  membranous, *See* Exudative tracheitis.
CT, *See* Computed tomography (CT).
Cyanosis
  with Ebstein anomaly, 74, 75f
  with variable pulmonary arterial flow, 78–79
Cyst(s)
  arachnoid, 270
  branchial cleft, 311, 313f
  bronchogenic, 39
    lower airway obstruction due to, 14, 15f
  choledochal, 118, 119f

duplication
gastrointestinal, 114, 114f
in middle mediastinal masses, 60
mesenteric, 116, 116f
ovarian, 160
porencephalic, 277–278, 277f
renal, 147, 147t
autosomal dominant, 147
autosomal recessive, 147, 148f
thyroglossal duct, 310–311, 313f
urachal, 144, 145f
Cystic adenomatoid malformation, congenital, 34–37
Cystic fibrosis, 51–53, 52f
abdominal complications of, 127, 127f
Cystic hygroma, 235
Cystourethrogram, fluoroscopic voiding, 131–132
Cytomegalovirus (CMV), CNS abnormalities due to, 285, 290f
Cytomegalovirus colitis, 125t

D

Dandy-Walker malformation, 263t–264t, 270, 270f

Dandy-Walker variant, 270, 271f

DDH (developmental dysplasia of the hip), 214–216, 215f–216f

Degenerative disorders, affecting myelination, 283–285, 286f–288f, 289t

Dens, fracture through base of, 315, 316f

Dermal sinus, 312

Dermatomyositis, 237–238, 239f

Dermoids, ovarian, 160, 161f

Desmoid, cortical, 164–168, 168f

Developmental abnormality(ies), 260–277, 263t–264t

  Chiari malformations as, 260–262

    type 1, 260–262, 263t–264t, 265f

    type 2, 262, 263t–264t, 265f–266f

  cortical dysplasia as, 274, 275f–276f

  Dandy-Walker malformation as, 263t–264t, 270, 270f

  dysgenesis of corpus callosum as, 263t–264t, 269–270, 269f

  gray matter heterotopias as, 263t–264t, 271, 272f

  hemimegalencephaly as, 275, 276f

  holoprosencephaly as, 263t–264t, 267f–268f, 267

  lissencephaly (agyria-pachygyria) as, 263t–264t, 271–273, 272f–273f

  polymicrogyria as, 263t–264t, 274, 274f

  schizencephaly as, 263t–264t, 274, 274f

  septo-optic dysplasia, 263t–264t, 267–269, 268f

  vein of Galen malformations as, 263t–264t, 275–277, 276f–277f

Developmental dysplasia of the hip (DDH), 214–216, 215f–216f

Diaphragmatic hernia, congenital, 37–38, 39f–40f

Differential diagnosis, age-related, 5

Diffuse microatelectasis, 33–34, 34f

Diffuse pulmonary disease, in newborn, 26, 26t

Diffusion tensor imaging (DTI), 247t, 248f

Diffusion-weighted imaging (DWI), 243–244, 244f–246f

Distal femoral metaphyseal irregularity, 164–168, 168f

Diverticulum

  Meckel, 113–114, 113f

  urachal, 144, 145f

DJJ (duodenojejunal junction), 97f

  abnormal, 96, 97f

  in malrotation, 95

  normal, 96, 96f

Dolichocephaly, 302
Double aortic arch, 14, 16f
"Double bubble" sign, in duodenal atresia, 94–95, 95f
Double inversion recovery imaging, 67, 67f
Double-outlet right ventricle, 86
"Drooping lily" sign, 139f
DTI (diffusion tensor imaging), 244–247, 247t, 248f
D-transposition of the great arteries, 78–79, 79f, 86, 87f
Ductus arteriosus, patent, 79–80, 81f
  acute diffuse pulmonary consolidation and, 33–34, 33f
Duodenal atresia, 94–95
Duodenal hematoma, 123, 123f
Duodenal stenosis, 94–95
Duodenal web, 94–95, 95f
Duodenojejunal junction (DJJ)
  abnormal, 96, 97f
  in malrotation, 95
  normal, 96, 96f
Duplication cysts
  gastrointestinal, 114, 114f
  in middle mediastinal masses, 60
DWI (diffusion-weighted imaging), 243–244, 244f–246f
Dysgenesis of corpus callosum, 263t–264t, 269–270, 269f
Dysostosis multiplex, 209

E

Eagle-Barrett syndrome, 145, 146f

Ebstein anomaly, 74, 75f

Echocardiography, of congenital heart disease, 66

ECMO (extracorporeal membrane oxygenation), 31–32, 31f

Edema, vasogenic, 244, 246f

Eigenvalue, 247f, 247t

Elbow, fractures in, 175–178

  effusion, 175–178, 178f

  of lateral condyle, 178, 179f

  of medial epicondyle, 178, 179f–180f

  with radial head dislocation, 178, 180f

  supracondylar, 175, 177f–178f

Elbow effusions, 175

Ellis-van Creveld syndrome, 209

Emphysema

  congenital lobar, 36, 36f

  pulmonary interstitial, 32–33, 32f

Empyema, due to pneumonia, 44–45, 46f

Encephalitis, 285–287, 291f

  herpes, 291f

Encephaloceles, 312

Encephalomalacia, 277–278

Encephalomyelitis, acute disseminated, 286–287, 292f

Encephalotrigeminal angiomatosis, 283, 284f–285f

Enchondromatosis, 206–207, 206f–207f

Endotracheal tubes, 29–30

Enterocolitis, necrotizing, 92–93

  bowel stricture due to, 93

  free intraperitoneal air due to, 92

  pneumatosis due to, 92, 94f

  portal venous gas due to, 92, 94f

  ultrasound of, 92–93, 93f

Ependymoma, 292t, 293–295, 296f

Epididymo-orchitis, 159–160, 160f

Epiglottitis, 8–11, 10f

Epiphyseal irregularity, 164, 167f

Equinus, 231

Esophageal atresia, 105–106, 105f

Esophageal foreign bodies, 114

Esophageal intubation, 29–30, 30f
Esophageal strictures, 115
Evans staging system, for neuroblastoma, 153–154
Ewing sarcoma, 199, 200f
  in chest wall, 62–64, 64f
Extracorporeal membrane oxygenation, 31–32, 31f
Exudative tracheitis, 11, 11f

F

Family members, interacting with, 1–2

Fat necrosis, posttraumatic, 240–241, 241f

Fetal circulation, persistent, 29

Fetal renal hamartoma, 151, 152f

Fibroma, nonossifying, 168, 169f–170f

Fibromatosis

aggressive, 238

colli, 242, 242f

Fibrosarcoma, 238, 240f

Fibrous cortical defects, benign, 168, 168f

Fistula, tracheoesophageal, 105–106

Fluoroscopic voiding cystourethrogram, 131–132

fMRI (functional magnetic resonance imaging), 249–252, 253f

Focal pulmonary lesions, in newborn, 34–36, 35t

Focal sclerotic lesions, 199–205, 202t

due to osteoid osteoma, 199, 203f

due to osteosarcoma, 203–205, 204f

due to stress fracture, 199–203

Fontan procedure, 82t, 89f

Football sign, in necrotizing enterocolitis, 92

Foreign body(ies)

airway, 18, 20f

chronic, 60, 62f

swallowed, 114–115, 114f–115f

Fractional anisotropy, 247t

Fracture(s), 170–192

by anatomic location, 172–182

in ankle, 178–182, 181f–182f

avulsion, in adolescents, 183–185

of knee, 185, 188f–191f

of pelvis, 185, 186f–187f

buckle, 170–171, 171f

Chance, 316, 317f

due to child abuse, 185–192, 191f–193f

elbow, 175–178

effusion, 175–178, 178f

of lateral condyle, 178, 179f

of medial epicondyle, 178, 179f–180f

with radial head dislocation, 178, 180f

supracondylar, 175, 177f–178f
greenstick, 170–171, 172f
hangman, 315, 316f
incomplete, 170–171, 171f
physis in, involvement of, 171–172
plastic bowing, 170–171, 170f
rib, 54, 54f
in child abuse, 54, 56f
Salter-Harris classification of, 171–172, 173f–176f
skull, 300
stress, 182–183, 184f, 199–203
toddler, 182–183, 183f–184f
wrist, 172f, 175, 177f
Free intraperitoneal air, in necrotizing enterocolitis, 92
Functional immaturity of colon, 102–103
Functional MRI (fMRI), 249–252, 253f
Fungal pneumonia, 50f

G

Gastric bubble, 70

Gastrointestinal disorders, 92–129

abnormalities of anterior abdominal wall as, 106, 106f

in children

due to swallowed foreign bodies, 114–115, 114f–115f

inflammatory bowel disease as, 127–128, 128f

intestinal obstruction as, 108–114, 108t

due to appendicitis, 108–109

due to gastrointestinal duplication cysts, 114, 114f

due to intussusception, 109–110

due to Meckel diverticulum, 113–114, 113f

due to blunt abdominal trauma, 122–123

bowel injury as, 122–123, 123f

hypoperfusion complex as, 123, 124f

parenchymal organ injuries as, 122, 122f

due to cystic fibrosis, 127, 127f

due to mesenteric abnormalities, 116–117, 116f

esophageal atresia as, 105–106, 105f

hypertrophic pyloric stenosis as, 107–108, 107f

in immunocompromised child, 124–127

bleeding as, 125t

cytomegalovirus colitis as, 125t

due to graft-*versus*-host disease, 125t, 126, 126f

due to lymphoproliferative disorder, 125t, 126–127, 127f

mucositis as, 125t, 126

neutropenic colitis as, 125, 125t, 126f

pseudomembranous colitis as, 124–125, 125f, 125t

liver masses as, 118–122

causes of, 120t

due to hepatoblastoma, 119–120, 120f

due to infantile hepatic hemangioma, 120, 121f

due to mesenchymal hamartoma, 120–122, 121f

due to metastatic disease, 119, 120f

necrotizing enterocolitis as, 92–93

bowel stricture due to, 93

free intraperitoneal air due to, 92

pneumatosis due to, 92, 94f

portal venous gas due to, 92, 94f

neonatal, 92–108

high intestinal obstruction as, 93–98
due to annular pancreas, 94–95
due to duodenal atresia, 94–95
due to duodenal stenosis, 94–95
due to duodenal web, 94–95, 95f
due to malrotation, 95–98, 100f
due to midgut volvulus, 95–98, 99f
jaundice as, 117–118, 118f
low intestinal obstruction as, 100–105, 100f
due to Hirschsprung disease, 101–102, 101f
due to ileal atresia, 101, 103f
due to meconium ileus, 101, 104f, 105t
due to meconium peritonitis, 101, 104f, 105t
due to meconium plug syndrome, 101f–102f, 102–105, 105t
with microcolon, 101
upper gastrointestinal series for, 98–100
pediatric obesity as, 128, 129f
tracheoesophageal fistula as, 105–106
in vomiting infant, 106–107
Gastrointestinal duplication cysts, 114, 114f
Gastroschisis, 106, 106f
General anesthesia, during procedure, 4
Genitourinary disorders, 130–163
acute pelvic pain, in older girls and adolescents as, 160–163, 161f–163f
adrenal, 153
neonatal adrenal hemorrhage as, 154–155, 157f
neuroblastoma as, 153–154
CT of, 154, 155f–156f
prognosis for, 153–154, 155t
risk factors in, 154t
staging of, 153–154, 153t
vs. Wilms tumor, 150t
congenital, 133
hydrometrocolpos as, 145–146, 146f
multicystic dysplastic kidney as, 136–137, 138f
posterior urethral valves as, 142, 143f
primary megaureter as, 142, 142f
prune-belly syndrome as, 145, 146f
renal cystic disease as, 147, 147t
autosomal dominant, 147
autosomal recessive, 147, 148f

renal ectopia and fusion as, 140–141, 140f–141f
urachal abnormalities as, 142–144, 144f–145f
ureterocele as, 139f, 140
ureteropelvic duplications as, 137–140, 138f–139f
ureteropelvic junction obstruction as, 135–136, 137f
vesicoureteral reflux as, 134–135, 135f–136f
pelvic rhabdomyosarcoma as, 155, 157f
prenatally diagnosed hydronephrosis as, 133–147
renal tumors as, 147–155
angiomyolipoma as, 151–153, 152f–153f
mesoblastic nephroma as, 151, 152f
multilocular cystic nephroma as, 149–150, 151f
nephroblastomatosis as, 149, 151f
Wilms tumor as, 147–149, 149f–150f, 150t
sacrococcygeal teratoma as, 155–156, 158f
of scrotum, 156–160, 159f
acute, 159–160, 160f–161f
testicular germ cell neoplasm as, 159f
testicular microlithiasis as, 159, 159f
urinary tract infections as, 130–133
definition of, 132
fluoroscopic voiding cystourethrogram for, 131–132
magnetic resonance urography for, 131
pyelonephritis as
acute, 132, 132f–134f
chronic, 132–133, 134f
renal ultrasound for, 130, 131f
Germ cell tumors
of central nervous system, 298, 299f
testicular, 159f
Germinal matrix, 252–255
hemorrhage, 252–255, 256f
grades of, 255t
ultrasound of, 255, 255f
Glenn procedure, 82t
Glioma(s)
brainstem, 292t, 293, 295f
optic nerve, 298
Glossoptosis, 22, 23f
Glutaric aciduria type 1, 289t
Gorham-Stout disease, 235, 236f

Graft-*versus*-host disease, 125t, 126, 126f
Gray matter heterotopias, 263t–264t, 271, 272f
Great arteries
  D-transposition of, 78–79, 79f, 86, 87f
  L-transposition of, 85, 86f
  obstructive lesions of, 82
Greenstick fracture, 170–171, 172f
Group B streptococcal pneumonia, 29, 29f

H

Haemophilus influenzae, epiglottitis and, 8–10

Haller index, 64–65

Hamartoma

  fetal renal, 151, 152f

  mesenchymal, of liver, 120–122, 121f

Hand-Schüller-Christian disease, 197

Hangman fracture, 315, 316f

Head trauma, 300

Head ultrasound, neonatal, 252–257, 254f

Heart disease

  acquired, 88–89

    cardiac masses, 77f, 89, 90f–91f

    Kawasaki disease as, 89

  congenital, *See* Congenital heart disease.

Heart failure, congestive, 80, 81t

Heart size, 69, 70f–71f

Hemangiomas, 120

  infantile, 233, 233f

  lower airway obstruction due to, 18

Hematoma

  duodenal, 123, 123f

  subdural, 300, 303f

  testicular, 159–160

Hematometrocolpos, 145–146, 146f

Hemimegalencephaly, 263t–264t, 275, 276f

Hemivertebra, 311

Hemophilia, 225–228, 227f

Hemorrhage

  See also Bleeding

  germinal matrix, 252–255, 256f

    grades of, 255t

    ultrasound of, 255, 255f

  neonatal adrenal, 154–155, 157f

Hepatitis, neonatal, 117–118

Hepatobiliary scintigraphy, 117–118, 118f

Hepatoblastoma, 119–120, 120f

Hernia, congenital diaphragmatic, 37–38, 39f–40f

Herpes encephalitis, 291f

Heterotaxy syndromes, 70

Heterotopias, gray matter, 263t–264t, 271, 272f
High-frequency oscillators, 32
Hilgenreiner line, in DDH, 215–216, 216f
Hip disorders, 214–220
  chronic hip subluxation as, 216, 216f
  developmental dysplasia as, 214–216, 215f–216f
  Legg-Calvé-Perthes disease as, 219–220, 220f
  proximal focal femoral deficiency as, 217, 217f
  septic arthritis as, 217–219, 217f–218f, 217t
  slipped capital femoral epiphysis as, 220, 220f
  toxic synovitis as, 219, 219f
Hirschsprung disease, 101–102, 101f
Holoprosencephaly, 263t–264t, 267f–268f, 267
Horseshoe kidney, 140–141, 141f
Human immunodeficiency virus (HIV), CNS infection by, 285
Hunter syndrome, 209
Hurler syndrome, 209, 213f
Hyaline membrane disease, 27–28
Hydranencephaly, 263t–264t, 278–279, 278f
Hydrocarbon ingestion, 54–55, 57f
Hydrocephalus, 301–302, 304f–305f
  with Chiari malformation, type 1, 262
Hydrogen MR spectroscopy, 247, 249f
Hydrometrocolpos, 145–146, 146f
Hydronephrosis
  due to horseshoe kidney, 140–141, 141f
  prenatally diagnosed, 133–147
Hyperbilirubinemia, neonatal, 117
Hypertension, persistent pulmonary, of newborn, 29
Hypertrophic pyloric stenosis, 107–108, 107f
Hypoperfusion complex, due to blunt abdominal trauma, 123, 124f
Hypopharyngeal (retroglossal) collapse, 22–23, 24f
Hypoplastic left heart syndrome, 80–81, 82f
Hypothalamic hamartoma, 299, 301f
Hypovolemic shock, due to blunt abdominal trauma, 123, 124f
Hypoxic ischemic insult, 255–256, 256f–258f

I

IBD, *See* Inflammatory bowel disease (IBD).

Idiopathic ileocolic intussusception, 109–110

Ileal atresia, 101, 103f

Ileus, meconium, 101, 104f, 105t

Imaging appearance, age-related changes in, 5

Immobilization, during procedure, 4

Immunocompromised child, gastrointestinal disorders in, 124–127

  bleeding as, 125t

  cytomegalovirus colitis as, 125t

  due to graft-*versus*-host disease, 125t, 126, 126f

  due to lymphoproliferative disorder, 125t, 126–127, 127f

  mucositis as, 125t, 126

  neutropenic colitis as, 125, 125t, 126f

  pseudomembranous colitis as, 124–125, 125f, 125t

In utero insults, sequelae of, 277–279

  hydranencephaly as, 263t–264t, 278–279, 278f

  porencephaly and encephalomalacia as, 277–278

Incomplete fracture, 170–171, 171f

Increased intracranial pressure, 306–308, 308f

Infantile cortical hyperostosis, 194

Infantile hemangiomas, 233, 233f

Infantile hepatic hemangioma, 120, 121f

Infantile polycystic kidney disease, 147, 148f

Infection(s)

  central nervous system, 285–287

    congenital, 285

    encephalitis as, 285–287, 291f

  urinary tract, 130–133

    definition of, 132

    fluoroscopic voiding cystourethrogram for, 131–132

    magnetic resonance urography for, 131

    pyelonephritis as

      acute, 132, 132f–134f

      chronic, 132–133, 134f

    renal ultrasound for, 130, 131f

Inflammatory bowel disease (IBD), 127–128, 128f

Innominate artery compression syndrome, 16–17, 19f

International Neuroblastoma Risk Group (INRG) Staging System, 153–154, 153t

Interstitial lung disease, childhood, 53–54

Intestinal disorders, *See* Gastrointestinal disorders.
Intestinal obstruction
in children, 108–114, 108t
due to appendicitis, 108–109
with appendicolith, 109, 109f–110f
CT of, 109, 110f
nonperforated, 109f
perforated, 109, 110f
radiographs of, 109, 110f
ultrasound of, 109, 109f
due to gastrointestinal duplication cysts, 114, 114f
due to intussusception, 109–110
CT of, 110, 112f
idiopathic ileocolic, 109–110
imaging-guided reduction of, 110–113, 111f
radiographs of, 110, 111f
small bowel-small bowel, 110, 112f
ultrasound of, 110, 111f
due to Meckel diverticulum, 113–114, 113f
neonatal
high, 93–98, 94t
due to annular pancreas, 94–95
due to duodenal atresia, 94–95
due to duodenal stenosis, 94–95
due to duodenal web, 94–95
due to malrotation, 95–98, 98f, 100f
due to midgut volvulus, 95–98, 99f
duodenojejunal junction in, 95
low, 94t, 100–105, 100f
due to Hirschsprung disease, 101–102, 101f
due to ileal atresia, 101, 103f
due to meconium ileus, 101, 104f, 105t
due to meconium peritonitis, 101, 104f, 105t
due to meconium plug syndrome, 101f–102f, 102–105, 105t
with microcolon, 101
Intraatrial baffle, 82t
Intracranial pressure, increased, 306–308, 308f
Intracranial trauma, 300
Intraperitoneal air, free, in necrotizing enterocolitis, 92
Intravenous line, placement of, 4
Intrinsic lower airway obstruction, 17–18

Intussusception, 109–110
CT of, 110, 112f
idiopathic ileocolic, 109–110
imaging-guided reduction of, 110–113, 111f
radiographs of, 110, 111f
small bowel-small bowel, 110, 112f
ultrasound of, 110, 111f
Isotropy, 247t

J

Jaundice, neonatal, 117–118, 118f
Jeune syndrome, 209, 211f
Juvenile idiopathic arthritis (JIA), 225, 226f
Juvenile Tillaux fracture, 182, 182f

K

Kawasaki disease, 89, 89f–90f

Kearns-Sayre disease, 289t

Kidney

horseshoe, 140–141, 141f

multicystic dysplastic, 136–137, 138f

Kidney disorders, *See* Genitourinary disorders.

Kleeblattschädel, 302

Klippel-Feil syndrome, 311

Knee, avulsion fractures of, in adolescents, 185, 188f–191f

Kommerell diverticulum, 16

Krabbe disease, 289t

L

Lactate, in MR spectroscopy, 249, 251f

Lacunar skull, 306–308, 308f

Ladd bands, 96

Langerhans cell histiocytosis (LCH), 197–199, 198f

  thymus in, 58f

Lap belt injuries, 315–316, 317f

Laryngotracheobronchitis

  acute, 8, 9f

  membranous, *See* Exudative tracheitis.

Lateral condyle, fracture of, 178, 179f

Lead poisoning, 221, 222f

Left-to-right shunts, 79–80, 81f

Legg-Calvé-Perthes disease (LCP), 219–220, 220f

Leigh disease, 289t

Letterer-Siwe disease, 197

Leukomalacia, periventricular, 255–256, 256f

Ligament of Treitz

  in malrotation, 95–96

  normal position of, 96f

Lingual thyroid, 314f

Lingual tonsils, enlarged, 21–22, 22f

Lipomyelomeningocele, 312, 315f

Lissencephaly, 263t–264t, 271–273, 272f–273f

Liver masses, 118–122

  causes of, 120t

  due to hepatoblastoma, 119–120, 120f

  due to infantile hepatic hemangioma, 120, 121f

  due to mesenchymal hamartoma, 120–122, 121f

  due to metastatic disease, 119, 120f

Lower airway obstruction, 13–24, 14f

  due to abnormal soft palate, 23–24

  due to enlarged lingual tonsils, 21–22, 22f

  due to enlarged palatine tonsils, 21, 22f

  due to glossoptosis, 22, 23f

  due to hypopharyngeal (retroglossal) collapse, 22–23, 24f

  due to recurrent and enlarged adenoid tonsils, 20–21, 21f

  extrinsic, 14–17, 15f–16f

    due to double aortic arch, 14, 16f

    due to innominate artery compression syndrome, 16–17, 19f

due to pulmonary sling, 14–15, 17f
due to right aortic arch with aberrant left subclavian artery, 16, 18f
intrinsic, 17–18
due to airway foreign body, 18, 20f
due to tracheomalacia, 17
in obstructive sleep apnea, 18–20, 21f
L-transposition of the great arteries, 85, 86f
Lucent permeative lesions, in children, 194–199
differential diagnosis of, 194, 195t
due to Ewing sarcoma, 199, 200f
due to Langerhans cell histiocytosis, 197–199, 198f
due to metastatic disease, 199, 201f–202f
due to osteomyelitis, 194–197, 195f–197f
Lückenschädel, 306–308, 308f
Lumbar vertebral bodies, anterior compression fractures of, 315–316
Lung abscess, 47–48, 47f
Lung contusion, 54, 55f
Lung laceration, 54, 55f
Lung parenchymal complications, of pneumonia, 47–48
Lymphadenitis, suppurative, 310, 310f
Lymphadenopathy
mesenteric, 116–117
in middle mediastinal masses, 60
Lymphatic malformations, 235, 236f
mesenteric, 116, 116f
Lymphoma, 57–60, 60f–61f
mesenteric lymphadenopathy due to, 116–117
neck mass due to, 310
tracheal compression due to, 16f
Lymphoproliferative disorder, in immunocompromised child, 125t, 126–127, 127f

M

Macrocrania, benign, 256–257
Maffucci syndrome, 206–207, 207f
Magnetic resonance imaging (MRI)
  age-related changes in appearance on, 5
  of congenital heart disease, 67–68, 67f
  distraction for, 2–4, 4f
  for neuroimaging, 243
    basic review of advance, 243–252
    diffusion tensor, 247t, 248f
    diffusion-weighted, 243–244, 244f–246f
    functional, 249–252, 253f
    MR spectroscopy, 247–249, 249f–251f
    perfusion of, 247
  radiation safety of, 6
  sedation for, 4
  vs. computed tomography, 68
Magnetic resonance (MR) spectroscopy, 247–249, 249f–251f
Magnetic resonance urography, for urinary tract infections, 131
Malrotation, 95–98, 98f, 100f
Maple syrup urine disease, 289t
Mature teratoma, ovarian, 160, 161f
McCune-Albright syndrome, 207, 208f
MCDK (multicystic dysplastic kidney), 136–137, 138f
Measles, subacute sclerosing panencephalitis due to, 286
Meckel diverticulum, 113–114, 113f
Meconium aspiration syndrome, 26, 27f
Meconium ileus, 101, 104f, 105t
Meconium peritonitis, 101, 104f, 105t
Meconium plug syndrome, 101f–102f, 102–105, 105t
Medial epicondyle, fracture of, in elbow, 178, 179f–180f
Mediastinal injury, 54
Mediastinal mass(es), 55–60, 57t
  anterior, 55
    lower airway obstruction due to, 14, 16f
    lymphoma as, 57–60, 60f–61f
    teratoma as, 59, 61f
  middle, 60
  posterior, 60–62
Medulloblastoma, 290–293, 292t, 294f–295f

Mega cisterna magna, 271
Megalencephaly leukoencephalopathy with subcortical cysts (MLC), 289t
Megaureter, primary, 142, 142f
Meningoencephalitis, necrotizing, due to herpes simplex-1 virus, 286, 291f
Mesenchymal hamartoma, of liver, 120–122, 121f
Mesenteric adenitis, 117, 117f
Mesenteric cysts, 116, 116f
Mesenteric lymphadenopathy, 116–117
Mesentery, abnormalities of, 116–117, 116f
Mesoblastic nephroma, 151, 152f
Mesomelic extremity shortening, 209
Metabolic disorders
  affecting myelination, 289t
  in musculoskeletal system, 221
    lead poisoning as, 221, 222f
    rickets as, 221, 221f
Metachromatic leukodystrophy, 289t
Metastasis, to liver, 119, 120f
Metastatic disease, in children, 199, 201f–202f
Methicillin-resistant *S. aureus* (MRSA), 196–197, 196f
Metopic suture craniosynostosis, 302, 306f
Microatelectasis, diffuse, 33–34, 34f
Microcolon, 101
Middle mediastinal masses, 60
Midgut volvulus, 95–98, 99f
Monteggia fracture, 180f
Morquio syndrome, 209
MR (magnetic resonance) spectroscopy, 247–249, 249f–251f
MRI, *See* Magnetic resonance imaging (MRI).
Mucocutaneous lymph node syndrome, 89, 89f–90f
Mucopolysaccharidoses, 209, 213f, 289t
Mucositis, in immunocompromised child, 125t, 126
Multicystic dysplastic kidney (MCDK), 136–137, 138f
Multifocal bone lesions, 205–207, 205t
  due to McCune-Albright syndrome, 207, 208f
  due to multiple hereditary exostoses (osteochondromatosis), 205–206, 205f
  due to Ollier disease (enchondromatosis), 206–207, 206f–207f
Multilocular cystic nephroma, 149–150, 151f
Multiple hereditary exostoses (osteochondromatosis), 205–206, 205f
Multiple magnets, swallowed, 115, 115f
Musculoskeletal system, 164–242

common benign entities in, normal variants and, 164–168, 165f
apophyseal and epiphyseal irregularity as, 164, 166f–167f
benign fibrous cortical defects as, 168, 168f–170f
distal femoral metaphyseal irregularity as, 164–168, 168f
Mustard-Senning (intraatrial baffle) procedure, 82t
Mycoplasma pneumoniae, pneumonia due to, 41–42
Myelination
metabolic and degenerative disorders affecting, 289t
normal, 257–260, 259f–261f, 262t, 263f
Myelomeningoceles, 262, 312
with Chiari malformation type 2, 262
Myositis ossificans, 240

N

Neck masses, 310–311, 312t, 313f–314f

Necrotizing enterocolitis (NEC), 92–93

bowel stricture due to, 93

free intraperitoneal air due to, 92

pneumatosis due to, 92, 94f

portal venous gas due to, 92, 94f

ultrasound of, 92–93, 93f

Necrotizing meningoencephalitis, due to herpes simplex-1 virus, 286, 291f

Neonatal adrenal hemorrhage, 154–155, 157f

Neonatal chest, 26–39

acute diffuse pulmonary consolidation in, 33–34, 34t

bronchogenic cyst in, 39

bronchopulmonary dysplasia in, 34, 35f

congenital cystic adenomatoid malformation in, 34–37

congenital diaphragmatic hernia in, 37–38, 39f–40f

congenital lobar emphysema in, 36, 36f

diffuse pulmonary disease in, 26, 26t

focal pulmonary lesions in, 34–36, 35t

group B streptococcal pneumonia in, 29

meconium aspiration syndrome in, 26, 27f

neonatal intensive care unit support apparatus for, 29–30

extracorporeal membrane oxygenation as, 31–32, 31f

high-frequency oscillators as, 32

peripherally inserted central catheters as, 31–32

umbilical arterial and venous catheters as, 30–31, 30f

neonatal pneumonia in, 27

persistent pulmonary hypertension in, 29

pneumonia in, 27, 39–53

bacterial, 43, 44f

characterization and prediction of infectious agent in, 40–43, 42f–43f

complications of, 44–48

chronic lung, 48, 49f

lung parenchymal, 47–48

parapneumonic effusions as, 44–45, 46f

persistent or progressive symptoms as, 47

confirmation or exclusion of, 40, 42f

fungal, 50f

group B streptococcal, 29, 29f

in immunodeficient children, 51, 51f

neonatal, 27, 27f–28f
round, 43, 45f
viral, 43
pulmonary interstitial emphysema in, 32–33, 32f
sequestration in, 38–39, 38f, 41f
surfactant-deficient disease in, 27–28, 28f
surfactant replacement therapy for, 28–29, 28f
transient tachypnea in, 27, 27f
Neonatal gastrointestinal disorder(s), 92–108
abnormalities of anterior abdominal wall as, 106, 106f
esophageal atresia as, 105–106, 105f
high intestinal obstruction as, 93–98
due to annular pancreas, 94–95
due to duodenal atresia, 94–95
due to duodenal stenosis, 94–95
due to duodenal web, 94–95, 95f
due to malrotation, 95–98, 98f, 100f
due to midgut volvulus, 95–98, 99f
jaundice as, 117–118
low intestinal obstruction as, 100–105, 100f
due to Hirschsprung disease, 101–102, 101f
due to ileal atresia, 101, 103f
due to meconium ileus, 101, 104f, 105t
due to meconium peritonitis, 101, 104f, 105t
due to meconium plug syndrome, 101f–102f, 102–105, 105t
with microcolon, 101
necrotizing enterocolitis as, 92–93
bowel stricture due to, 93, 94f
free intraperitoneal air due to, 92
pneumatosis due to, 92, 92f, 94f
portal venous gas due to, 92, 92f, 94f
ultrasound of, 92–93, 93f
tracheoesophageal fistula as, 105–106
upper gastrointestinal series for, 98–100
Neonatal head ultrasound, 252–257, 254f
Neonatal intensive care unit support apparatus, 29–30
extracorporeal membrane oxygenation as, 31–32, 31f
high-frequency oscillators as, 32
peripherally inserted central catheters as, 31–32
umbilical arterial and venous catheters as, 30–31, 30f
Neonatal pneumonia, 27, 27f–28f

Nephroblastoma, 147–149, 149f–150f, 150t
Nephroblastomatosis, 149, 151f
Nephrogenic rests, 149, 151f
Nephroma
  mesoblastic, 151, 152f
  multilocular cystic, 149–150, 151f
Neuroblastoma, 153–154
  CT of, 154, 155f–156f
  metastatic, 199, 201f–202f
  in posterior mediastinal masses, 60–62, 63f
  prognosis for, 153–154, 155t
  risk factors in, 154t
  staging of, 153–154, 153t
  vs. Wilms tumor, 150t
Neurocutaneous syndrome, 279–283
  neurofibromatosis as, 279
    type 1, 279, 279t, 280f–282f
    type 2, 262, 263t–264t, 265f–266f, 279, 282f
  Sturge-Weber syndrome as, 283, 284f–285f
  tuberous sclerosis as, 279, 282f–283f
Neuroendocrine cell hyperplasia, of infancy (NEHI), 53f, 54
Neurofibroma(s), plexiform, in neurofibromatosis type 1, 279
Neurofibromatosis (NF), 229, 230f, 279
Neurofibromatosis type 1 (NF-1), 279, 279t, 280f
  plexiform neurofibromas in, 279
Neurofibromatosis type 2 (NF-2), 279, 282f
Neuroimaging
  CT for, 243
  MRI for, 243
    diffusion tensor, 247t, 248f
    diffusion-weighted, 243–244, 244f–246f
    functional, 249–252, 253f
    MR spectroscopy, 247–249, 249f–251f
    perfusion, 247
    vein of Galen malformations as, 263t–264t, 275–277, 276f–277f
  pediatric, 243
Neurologic disorder(s)
  acute otomastoiditis as, 309, 310f
  atlantoaxial instability as, 318, 319f
  benign enlargement of extraaxial spaces, 256–257
  benign macrocrania as, 256–257

congenital anomalies of cervical spine as, 316–318, 318f
congenital vertebral anomalies as, 311
craniosynostosis as, 302, 306f–307f
developmental, 260–277, 263t–264t
Chiari malformations as, 260–262
type 1, 260–262, 263t–264t, 265f
type 2, 262, 263t–264t, 265f–266f
cortical dysplasia as, 274, 275f–276f
Dandy-Walker malformation as, 263t–264t, 270, 270f
dysgenesis of corpus callosum as, 263t–264t, 269–270, 269f
gray matter heterotopias as, 263t–264t, 271, 272f
hemimegalencephaly as, 275, 276f
holoprosencephaly as, 263t–264t, 267f–268f, 267
lissencephaly (agyria-pachygyria) as, 263t–264t, 271–273, 272f–273f
polymicrogyria as, 263t–264t, 274, 274f
schizencephaly as, 263t–264t, 274, 274f
septo-optic dysplasia as, 263t–264t, 267–269, 268f
due to infection, 285–287
congenital, 285
encephalitis as, 285–287, 291f
due to trauma, 300–301
due to tumors, 287–300
germ cell, 298, 299f
pineal, 299–300
of posterior fossa, 287–295, 292t
brainstem glioma as, 292t, 293, 295f
cerebellar astrocytoma as, 290, 292t, 293f
ependymoma, 292t, 293–295, 296f
medulloblastoma as, 290–293, 292t, 294f–295f
sellar and suprasellar, 298–300
germinal matrix hemorrhage as, 252–255, 256f
grades of, 255t
ultrasound of, 255, 255f
hydrocephalus as, 301–302, 304f–305f
imaging modality(ies) for, 243
CT as, 243
functional, 249–252, 253f
head ultrasound as, 252–257, 254f
MRI as, 243
diffusion tensor, 247t, 248f
diffusion-weighted, 243–244, 244f–246f

MR spectroscopy, 247–249, 249f–251f
perfusion, 247
lacunar skull as, 306–308, 308f
metabolic and degenerative, 289t
neurocutaneous syndrome as, 279–283
neurofibromatosis as, 279
type 1, 279, 279t, 280f–282f
type 2, 279, 282f
Sturge-Weber syndrome as, 283, 284f–285f
tuberous sclerosis as, 279, 282f–283f
orbital cellulitis as, 308–309, 308f–309f
periventricular leukomalacia as, 255–256, 256f
retinoblastoma as, 310, 311f–312f, 311t
sequelae of in utero insults as, 277–279
encephalomalacia as, 277–278
hydranencephaly as, 263t–264t, 278–279, 278f
porencephaly as, 263t–264t, 277–278
spinal dysraphism(s) as, 312–314, 314f–315f, 314t
closed, 312
dermal sinus as, 312
encephaloceles as, 312
lipomyelomeningocele as, 312
myelomeningoceles as, 312
open, 312
spondylolysis and spondylolisthesis as, 318–320, 320f
suppurative adenitis as, 309–310
Neutropenic colitis, 125, 125t, 126f
NF, *See* Neurofibromatosis (NF).
Non-Hodgkin lymphoma, mesenteric lymphadenopathy due to, 116–117
Nonossifying fibroma, 169f–170f
Norwood procedure, 82t

O

Obesity, pediatric, 128, 129f

Obstruction

airway, *See* Airway obstruction.

intestinal, *See* Intestinal obstruction.

ureteropelvic junction, 135–136, 137f

Obstructive lesions, of the great arteries, 82

Obstructive sleep apnea (OSA), 18–20, 21f

due to abnormal soft palate, 23–24

due to enlarged tonsils

adenoid, 20–21, 21f

lingual, 21–22, 22f

palatine, 19, 21f

Ollier disease (enchondromatosis), 206–207, 206f–207f

Omphalocele, 106, 106f

Omphalomesenteric duct, 113–114

Optic nerve gliomas, 298

Orbital cellulitis, 308–309, 308f

OSA, *See* Obstructive sleep apnea (OSA).

Oscillator, high-frequency, 32

Osgood-Schlatter disease, 185, 191f

Osteochondral lesions, 223, 224f

Osteochondromatosis, 205–206, 205f

Osteogenesis imperfecta, 209–212, 214f

Osteogenic sarcoma, 203–205, 204f

Osteoid osteoma, 199, 203f

Osteomyelitis, 194–197, 195f–197f

Osteoporosis, 212–214

Osteosarcoma, 203–205, 204f

Otomastoiditis, acute, 309, 309f–310f

Ovarian causes, of acute pelvic pain, 160, 161f–163f

Ovarian dermoids, 160, 161f

Ovarian neoplasms, 160, 162f

Ovarian torsion, 162–163, 162f–163f

P

PA banding, 82t
Pain, acute pelvic, in older girls and adolescents, 160–163, 161f–163f
Palatine tonsils, enlarged, 21, 22f
  in obstructive sleep apnea, 19, 21f
Pancreas, annular, 94–95
Pancreatic injury, 123f
Panencephalitis, subacute sclerosing, 286, 292f
Panner disease, 223, 225f
Parapneumonic effusions, due to pneumonia, 44–45, 46f
Parenchymal organ injuries, 122, 122f
Parents, imager and, 1–2
Patent ductus arteriosus (PDA), 79–80, 81f
  acute diffuse pulmonary consolidation and, 33–34, 33f
Patient safety, quality and, 5–6
Pectus excavatum, 64–65, 65f
Pediatric imaging, special considerations in, 1–7
Pediatric neuroimaging, 243
Pediatric radiology, as career, 1
Pelizaeus-Merzbacher disease, 289t
Pelvic pain, acute, in older girls and adolescents, 160–163, 161f–163f
Pelvic rhabdomyosarcoma, 155, 157f
Pelvis, avulsion fractures of, in adolescents, 185, 186f–187f
Pennies, zinc, swallowed, 115, 115f
Perinatal partial asphyxia, 255–256
Periosteal reaction, in newborn, 192–194, 194f, 194t
  due to Caffey disease, 194
  due to congenital rubella syndrome, 192
  due to syphilis, 192–194
  due to TORCH infection, 192–194
Peripherally inserted central catheters, 31–32
Peritonitis, meconium, 101, 104f, 105t
Periventricular leukomalacia, 255–256, 256f
Perkin line, in DDH, 215–216, 216f
Persistent fetal circulation, 29
Persistent pulmonary hypertension, of newborn, 29
Phenylketonuria, 289t
Physeal involvement, in fractures, 171–172, 173f–176f
PICCs (peripherally inserted central catheters), 31–32
PIE (pulmonary interstitial emphysema), 32–33, 32f

Pineal tumors, 299–300
Pineoblastomas, 299–300
Plagiocephaly, 307f
Plastic bowing deformity, 170–171, 170f
Pleural effusion, in neonatal pneumonia, 27
Plexiform neurofibromas, in neurofibromatosis type 1, 279
Pneumatocele, due to pneumonia, 47–48, 48f
Pneumatosis, in necrotizing enterocolitis, 92, 92f, 94f
Pneumomediastinum, spinnaker sail sign in, 55–57, 59f
Pneumonia
  bacterial, 43, 44f
  characterization and prediction of infectious agent in, 40–43, 42f–43f
  complications of, 44–48
    chronic lung, 48, 49f
    lung parenchymal, 47–48
    parapneumonic effusions as, 44–45, 46f
    persistent or progressive symptoms as, 47
  confirmation or exclusion of, 40, 42f
  fungal, 50f
  in immunodeficient children, 51, 51f
  neonatal, 27, 27f–28f
  round, 43, 45f
  viral, 43
Polycystic kidney disease
  autosomal dominant, 147
  autosomal recessive (infantile), 147, 148f
Polymicrogyria, 263t–264t, 274, 274f
Polysplenia, 70, 73f
Porencephalic cyst, 277–278, 277f
Porencephaly, 263t–264t, 277–278
Portal venous gas, in necrotizing enterocolitis, 92, 92f, 94f
Posterior fossa tumor(s), 287–295, 292t
  brainstem glioma as, 292t, 293, 295f
  cerebellar astrocytoma as, 290, 292t, 293f
  ependymoma as, 292t, 293–295, 296f
  medulloblastoma as, 290–293, 292t, 294f–295f
Posterior mediastinal masses, 60–62
Posterior urethral valves, 142, 143f
Posttraumatic fat necrosis, 240–241, 241f
Potts procedure, 82t
Prematurity

chronic lung disease of, 34
white matter injury of, 255–256, 256f–258f
Professionalism, 2
Proton MR spectroscopy, 247, 249f
Proximal focal femoral deficiency (PFFD), 217, 217f
Prune-belly syndrome, 145, 146f
Pseudomembranous colitis, 124–125, 125f, 125t
Pulmonary airway malformation, congenital, 35–37
Pulmonary arterial flow
decreased, 69, 69f
with cardiomegaly
massive, 73–75, 75f–76f
mild, 72–73, 74f
increased, 68, 69f
blue, 75–77
pink, 79–80, 81f
normal, 81–83, 82f–85f
with coarctation of the aorta, 81, 82f
with pulmonic stenosis, 82f, 83
variable, blue, 77–79
Pulmonary artery, anomalous origin of left, 14–15, 17f
Pulmonary atresia
with intact ventricular septum as, 74–75, 76f–77f
in tetralogy of Fallot, 72–73
Pulmonary consolidation, acute diffuse, 33–34, 34t
Pulmonary hypertension, persistent, 29
Pulmonary interstitial emphysema, 32–33, 32f
Pulmonary lesions, focal, in newborn, 34–36, 35t
Pulmonary sequestration, 38–39, 38f, 41f
Pulmonary sling, 14–15, 17f
Pulmonary valvular stenosis, 83
Pulmonary vascularity, 68–69, 69f
Pulmonary venous flow, increased, 68–69
due to cardiomyopathy, 69f
due to coarctation of the aorta, 81f
due to hypoplastic left heart syndrome, 80–81, 82f
Pulmonary venous return, total anomalous, 77, 78f–79f
Pulmonic stenosis, 83, 84f
Pyelonephritis
acute, 132, 132f–134f
chronic, 132–133, 134f

Pyloric stenosis, hypertrophic, 107–108, 107f

Q

Quality, patient safety and, 5–6

R

RAA-ALSCA, *See* Right aortic arch with aberrant left subclavian artery (RAA-ALSCA).

Radial dysplasia, 229, 229f

Radiation safety, 6

Radiographs

of appendicitis, 109, 110f

of intussusception, 110, 111f

Rastelli procedure, 82t

Renal cell carcinoma (RCC), 151

Renal collecting system, duplication of, 137, 138f

Renal cystic disease, 147, 147t

autosomal dominant, 147

autosomal recessive, 147, 148f

Renal ectopia, 140–141, 140f–141f

Renal fusion, 140–141, 140f–141f

Renal hamartoma, fetal, 151, 152f

Renal tumors, 147–155

angiomyolipoma as, 151–153, 152f–153f

mesoblastic nephroma as, 151, 152f

multilocular cystic nephroma as, 149–150, 151f

nephroblastomatosis as, 149, 151f

Wilms tumor as, 147–149, 149f–150f, 150t

Renal ultrasound, 130, 131f

Respiratory distress syndrome, 27–28

Retinoblastoma, 310, 311f–312f, 311t

Retroglossal collapse, 22–23, 24f

Retropharyngeal cellulitis and abscess, 11–13, 12f–13f

Retropharyngeal soft tissue thickening, pseudo-, 11–12, 13f

Rhabdomyoma, cardiac, 74–75, 77f, 89, 90f

Rhabdomyosarcoma, 238

neck mass due to, 310

pelvic, 155, 157f

Rhizomelic extremity shortening, 209

Rib fractures, 54, 54f

in child abuse, 54, 56f

Rib notching, due to coarctation of the aorta, 83, 85f

Rickets, 221, 221f

Right aortic arch with aberrant left subclavian artery (RAA-ALSCA), 16, 18f

Right ventricle, double-outlet, 86

Rigler sign, in necrotizing enterocolitis, 92

Risser stages, 222–223
Round pneumonia, 43, 45f
Rubella syndrome, congenital, 192

S

Sacrococcygeal teratoma, 155–156, 158f

Sagittal suture synostosis, 302, 306f

Sail sign, thymus with, 55–57, 58f

Salter-Harris classification, of fractures, 171–172, 173f–177f

Sano shunt, 82t

Sarcoma(s)

Ewing, 199, 200f

fibro-, 238, 240f

osteogenic, 203–205, 204f

rhabdomyo-

neck mass due to, 310

pelvic, 155, 157f

synovial, 238

SCFE (slipped capital femoral epiphysis), 220, 220f

Schizencephaly, 263t–264t, 274, 274f

Schwannomas, acoustic, in neurofibromatosis type 2, 279

Scoliosis, 221–223, 222f–223f

Scrotum

acute, 159–160, 160f–161f

disorders of, 156–160, 159f

testicular germ cell neoplasm as, 159f

testicular microlithiasis as, 159, 159f

SDD (surfactant-deficient disease), 27–28, 28f

Sedation program, during procedure, 5

Septic arthritis, 217–219, 217f–218f, 217t

Septo-optic dysplasia, 263t–264t, 267–269, 268f

Sequestration, pulmonary, 38–39, 38f, 41f

Sertoli cell neoplasm, of ovary, 162f

Shock, hypovolemic, due to blunt abdominal trauma, 123, 124f

"Shock bowel," due to blunt abdominal trauma, 123

Sickle cell anemia, 228–229, 228f

acute chest syndrome in, 51, 52f

Sinding-Larsen-Johansson syndrome, 185, 190f

Situs, 70, 72f–73f

ambiguous, 70

inversus, 70, 86

solitus, 70

Size variability, physiology and, 5

Skeletal dysplasias, 207–209, 212t

achondroplasia as, 209, 210f
distal shortening in, 209, 211f
thanatophoric dwarfism as, 209, 211f
Skeletal scintigraphy, 196
Skull
clover-leaf, 302
fracture, 300
lacunar, 306–308, 308f
Slice thickness, size variability and, 5
Slipped capital femoral epiphysis (SCFE), 220, 220f
Small bowel-small bowel intussusception, 110, 112f
Small left colon syndrome, 101f–102f, 102–103, 105t
Soft palate, abnormal, 23–24
Soft tissues, disorders affecting, 232–242
dermatomyositis as, 237–238, 239f
malignancies as, 238, 240f
chronic foreign body in, 240, 241f
fibromatosis colli in, 242, 242f
mimickers of, 238–242
myositis ossificans in, 240
posttraumatic fat necrosis in, 240–241, 241f
vascular anomalies as, 232–237, 233t
malformations, 235–237, 236f, 238f
tumors, 233–235, 233f–234f
Solitary enchondromas, 206–207, 207f
Spinal dysraphism(s), 312–314, 314f–315f, 314t
closed, 312
dermal sinus as, 312
encephaloceles as, 312
lipomyelomeningocele as, 312
myelomeningoceles as, 312
open, 312
Spinal trauma, 314–316
Spinnaker sail sign, thymus with, 55–57, 59f
Splenic heterogeneity, transient, 122, 122f
Splenic rupture, 122f
Spondylolisthesis, 318–320, 320f
Spondylolysis, 318–320, 320f
Sprengel deformity, 311
Standardization, 6
Staphylococcus aureus

exudative tracheitis and, 11
pneumonia due to, 41–42
Steeple sign, in croup, 8, 9f
Sternum, tilted, 62–64, 65f
Stomach bubble, 70
Streptococcal pneumonia, group B, 29, 29f
Stress fractures, 182–183, 184f, 199–203
Stridor, acute, 8
Sturge-Weber syndrome, 283, 284f–285f
Subacute sclerosing panencephalitis, 286, 292f
Subclavian artery, right aortic arch with aberrant left, 16, 18f
Subdural hematoma, 300, 303f
Subglottic airway, in croup, 8, 9f
Superior mesenteric artery (SMA), superior mesenteric vein (SMV) and, 98, 100f
Suppurative adenitis, 309–310
Suppurative lymphadenitis, 310, 310f
Supracondylar fracture, 175, 177f–178f
Suprasellar tumors, 298–300
Surfactant replacement therapy, 28–29, 28f
Surfactant-deficient disease, 27–28, 28f
Swallowed foreign bodies, 114–115, 114f–115f
Swyer-James syndrome, 48
Syndrome, 16–17
Synovial sarcomas, 238
Syphilis, congenital, 192–194

T

Talipes equinovarus, 229–231, 231f

TAPVR (total anomalous pulmonary venous return), 77, 78f–79f

Tarsal coalition, 231–232, 232f

Tensor, 247t

Teratoma, 59, 61f

  mature ovarian, 160, 161f

  of neck, congenital airway obstruction due to, 25f

  sacrococcygeal, 155–156, 158f

Testicular appendage, torsion of, 159–160, 161f

Testicular germ cell neoplasm, 159f

Testicular hematoma, 159–160

Testicular microlithiasis, 159, 159f

Testicular torsion, 159, 160f

Tetralogy of Fallot, 72–73, 74f

TGA (transposition of the great arteries)

  D-, 78–79, 79f, 86, 87f

  L-, 85, 86f

Thalassemia, 228–229

Thanatophoric dwarfism, 209, 211f

Thymic rebound, 57, 59f

Thymus

  abnormality of, 57

  in Langerhans cell histiocytosis, 58f

  normal, 55–57, 58f–59f

  with sail sign, 55–57, 58f

  with spinnaker sail sign, 55–57, 59f

Thyroglossal duct cysts, 310–311, 313f

Tilted sternum, 62–64, 65f

Toddler fracture, 182–183, 183f–184f

Tonsils

  adenoid, recurrent and enlarged, 20–21, 21f

  lingual, enlarged, 21–22, 22f

  palatine, enlarged, 21, 22f

TORCH infections, 192–194

Total anomalous pulmonary venous return (TAPVR), 77, 78f–79f

Toxic synovitis, 219, 219f

Toxoplasmosis, CNS abnormalities due to, 285

Toys, for distraction, 2–4

Trachea, normal configuration of, 14, 16f

Tracheal compression, 13, 14f
See also Lower airway obstruction
Tracheal rings, tracheal compression due to, 14–15
Tracheitis, exudative, 11, 11f
Tracheoesophageal fistula, 105–106
Tracheomalacia, lower airway obstruction due to, 17
Tractography, 247t
Transient respiratory distress, 27
Transient splenic heterogeneity, 122, 122f
Transient tachypnea, of newborn, 27, 27f
Transposition of the great arteries
D-, 78–79, 79f, 86, 87f
L-, 85, 86f
Trauma
See also Fracture(s)
blunt abdominal, 122–123
bowel injury due to, 122–123, 123f
hypoperfusion complex due to, 123, 124f
parenchymal organ injuries due to, 122, 122f
chest, 54–55
head, 300
spinal, 314–316
Tricuspid atresia, 79, 80f
Tricuspid valve, in Ebstein anomaly, 74
Trident acetabulum, 209
Trigonocephaly, 302, 307f
Triplane fracture, 178, 181f
Truncus arteriosus, 75–76, 77f, 84–85
TTN (transient tachypnea of the newborn), 27, 27f
Tuberculosis, 50–51, 50f
Tuberous sclerosis, 279, 282f–283f
angiomyolipoma and, 151–153, 152f–153f
Typhlitis, 125

U

UGI (upper gastrointestinal) series, in infant, 98–100
Ultrasonography
  of germinal matrix hemorrhage, 252–255, 254f–256f
  of necrotizing enterocolitis, 92–93, 93f
  of neonatal head, 252–257, 254f
  renal, 130, 131f
Umbilical arterial and venous catheters, 30–31, 30f
UPJ (ureteropelvic junction) obstruction, 135–136, 137f
Upper airway obstruction, acute, 8–13
  due to croup, 8, 9f
  due to epiglottitis, 8–11, 10f
  due to exudative tracheitis, 11, 11f
  due to retropharyngeal cellulitis and abscess, 11–13, 12f–13f
Upper gastrointestinal (UGI) series, in infant, 98–100
Urachal abnormalities, 142–144, 144f–145f
Urachal carcinoma, 144
Urachal cysts, 144, 145f
Urachal diverticulum, 144, 145f
Urachal sinus, 144
Ureterocele, 131–132, 139f, 140
Ureteropelvic duplications, 137–140, 138f–139f
Ureteropelvic junction (UPJ) obstruction, 135–136, 137f
Urethral valves, posterior, 142, 143f
Urinary tract infections (UTIs), 130–133
  definition of, 132
  fluoroscopic voiding cystourethrogram for, 131–132
  magnetic resonance urography for, 131
  pyelonephritis as
    acute, 132, 132f–134f
    chronic, 132–133, 134f
  renal ultrasound for, 130, 131f

V

VACTERL acronym, 105
Vanishing white matter, 289t
Vascular anomalies, in soft tissues, 232–237, 233t
  malformations, 235–237, 236f–238f
  tumors, 233–235, 233f–234f
Vascular rings, in tracheal compression, 13
Vasogenic edema, 244, 246f
VATER complex, 94–95
VCUG (voiding cystourethrogram), fluoroscopic, 131–132
Vein of Galen malformations, 263t–264t, 275–277, 276f–277f
Venous malformations, 235, 237f–238f
Ventricular septal defect (VSD), 79–80, 81f
  in tetralogy of Fallot, 72–73
  in truncus arteriosus, 75–76
Ventriculoperitoneal shunt (VPS), 301–302, 304f–305f
Vertebra
  block, 311
  butterfly, 311
  hemi-, 311
Vertebral anomalies, congenital, 311
Vesicoureteral reflux (VUR), 134–135, 135f–136f
  due to posterior urethral valves, 143f
Video goggles, for distraction, 2–4, 4f
Video players, for distraction, 2–4
Viral pneumonia, 43
Voiding cystourethrogram (VCUG), fluoroscopic, 131–132
Volvulus, midgut, 95–98
Vomiting, in infant, 106–107
VPS (ventriculoperitoneal shunt), 301–302, 304f–305f
VSD (ventricular septal defect), 79–80, 81f
  in tetralogy of Fallot, 72–73
  in truncus arteriosus, 75–76
VUR (vesicoureteral reflux), 134–135, 135f–136f
  due to posterior urethral valves, 143f

W

Waiting area, child-friendly, 3f

Waterston-Cooley procedure, 82t

Weigert-Meyer rule, 137

Wet lung disease, 27

Wheezing, 13

Williams syndrome, 82–83

Wilms tumor, 147–149, 149f–150f, 150t

Wilson-Mikity syndrome, 34

Wimberger corner sign, 192–194

Wormian bones, in osteogenesis imperfecta, 214f

Wrist, fractures in, 172f, 175, 177f

Z

Zinc pennies, swallowed, 115, 115f

Table of Contents

Title page 2
Table of Contents 3
Copyright 6
Contributors 8
Preface 9
Chapter 1. Special Considerations in Pediatric Imaging 11
- Pediatric Radiology As a Potential Career 11
- Introduction: Special Considerations in Pediatric Imaging 11

Chapter 2. Airway 21
- Acute Upper Airway Obstruction 21
- Lower Airway Obstruction 30
- Congenital Airway Obstruction 49

Chapter 3. Chest 53
- Neonatal Chest 53
- Roles of Imaging in Pediatric Pneumonia 78
- High-Resolution Computed Tomography in Children 101

Chapter 4. Cardiac 126
- Imaging Modalities in Congenital Heart Disease 126
- Categorization of Congenital Heart Disease 137
- Abnormalities of Conotruncal Rotation 159
- Surgeries for Congenital Heart Disease 166

Chapter 5. Gastrointestinal 173
- Neonatal 173
- Intestinal Obstruction in Children 203
- Swallowed Foreign Bodies 213
- Abnormalities of the Pediatric Mesentery 217
- Neonatal Jaundice 219
- Liver Masses 223
- Blunt Abdominal Trauma 227
- The Immunocompromised Child 233
- Complications Related to Cystic Fibrosis 238
- Inflammatory Bowel Disease in Children 239
- Pediatric Obesity 240

Chapter 6. Genitourinary 241
- Urinary Tract Infections 241
- Evaluation of Prenatally Diagnosed Hydronephrosis 245
- Renal Tumors 268
- Pelvic Rhabdomyosarcoma 278
- Sacrococcygeal Teratoma 278
- Scrotum 280
- Acute Pelvic Pain in Older Girls and Adolescents 286

Chapter 7. Musculoskeletal 295
- Normal Variants and Common Benign Entities 295
- Trauma 303
- Periosteal Reaction in the Newborn 343
- Lucent Permeative Lesions in Children 346
- Focal Sclerotic Lesions in Children 353

- Multifocal Bone Lesions in Children 360
- Constitutional Disorders of Bone 365
- Hip Disorders 375
- Metabolic Disorders 385
- Miscellaneous Disorders 386
- Disorders Affecting Primarily Soft Tissues 406

Chapter 8. Neuro 422

- Pediatric Neuroimaging Modalities: Magnetic Resonance, Computed Tomography, and Ultrasound 422
- Basic Review of Advanced Magnetic Resonance Imaging Techniques in Pediatric Neuroimaging 422
- Neonatal Head Ultrasound 433
- Normal Myelination 441
- Developmental Abnormalities 447
- Sequelae of in Utero Insults 476
- Neurocutaneous Syndromes 479
- Metabolic and Degenerative Disorders 488
- Infection 491
- Tumors 494
- Trauma 517
- Hydrocephalus and Ventriculoperitoneal Shunts 518
- Craniosynostosis 520
- Lacunar Skull 527
- Head and Neck Inflammatory and Infectious Processes 529
- Retinoblastoma 533
- Neck Masses 533
- Congenital Vertebral Anomalies 535
- Spinal Dysraphism 536
- Spinal Trauma 541
- Normal Variants and Congenital Anomalies of the Cervical Spine 547
- Atlantoaxial Instability 550
- Spondylolysis and Spondylolisthesis 551

Index 555